



International Journal of
Molecular Sciences

Novel Strategies in the Development of New Therapies, Drug Substances and Drug Carriers

Edited by

Andrzej Kutner, Geoffrey Brown and Enikő Kallay

Printed Edition of the Special Issue Published in *International Journal of
Molecular Sciences*

Novel Strategies in the Development of New Therapies, Drug Substances and Drug Carriers

Novel Strategies in the Development of New Therapies, Drug Substances and Drug Carriers

Editors

Andrzej Kutner

Geoffrey Brown

Enikő Kallay

MDPI • Basel • Beijing • Wuhan • Barcelona • Belgrade • Manchester • Tokyo • Cluj • Tianjin



Editors

Andrzej Kutner

Department of Bioanalysis
and Drug Analysis
The Medical University
of Warsaw
Warsaw
Poland

Geoffrey Brown

Institute of Clinical Sciences
College of Medical and
Dental Sciences
University of Birmingham
Birmingham
United Kingdom

Enikő Kallay

Department of
Pathophysiology and
Allergy Research
Center of Pathophysiology,
Infectiology & Immunology
Medical University of Vienna
Vienna
Austria

Editorial Office

MDPI

St. Alban-Anlage 66
4052 Basel, Switzerland

This is a reprint of articles from the Special Issue published online in the open access journal *International Journal of Molecular Sciences* (ISSN 1422-0067) (available at: www.mdpi.com/journal/ijms/special_issues/ACCORD2021).

For citation purposes, cite each article independently as indicated on the article page online and as indicated below:

LastName, A.A.; LastName, B.B.; LastName, C.C. Article Title. <i>Journal Name</i> Year , <i>Volume Number</i> , Page Range.
--

ISBN 978-3-0365-4646-9 (Hbk)

ISBN 978-3-0365-4645-2 (PDF)

© 2022 by the authors. Articles in this book are Open Access and distributed under the Creative Commons Attribution (CC BY) license, which allows users to download, copy and build upon published articles, as long as the author and publisher are properly credited, which ensures maximum dissemination and a wider impact of our publications.

The book as a whole is distributed by MDPI under the terms and conditions of the Creative Commons license CC BY-NC-ND.

Contents

About the Editors	ix
Preface to “Novel Strategies in the Development of New Therapies, Drug Substances and Drug Carriers”	xi
Andrzej Kutner, Geoffrey Brown and Enikő Kallay Novel Strategies in the Development of New Therapies, Drug Substances, and Drug Carriers Volume I Reprinted from: <i>Int. J. Mol. Sci.</i> 2022 , <i>23</i> , 6635, doi:10.3390/ijms23126635	1
Robert Nawrot, Alicja Warowicka, Piotr Józef Rudzki, Oskar Musidlak, Katarzyna Magdalena Dolata and Jacek Musijowski et al. Combined Protein and Alkaloid Research of <i>Chelidonium majus</i> Latex Reveals CmMLP1 Accompanied by Alkaloids with Cytotoxic Potential to Human Cervical Carcinoma Cells Reprinted from: <i>Int. J. Mol. Sci.</i> 2021 , <i>22</i> , 11838, doi:10.3390/ijms222111838	7
Joanna Gracz-Bernaciak, Oliwia Mazur and Robert Nawrot Functional Studies of Plant Latex as a Rich Source of Bioactive Compounds: Focus on Proteins and Alkaloids Reprinted from: <i>Int. J. Mol. Sci.</i> 2021 , <i>22</i> , 12427, doi:10.3390/ijms222212427	23
Elżbieta U. Stolarczyk, Weronika Strzempek, Marta Łaszcz, Andrzej Leś, Elżbieta Menaszek and Katarzyna Sidoryk et al. Anti-Cancer and Electrochemical Properties of Thiogenistein—New Biologically Active Compound Reprinted from: <i>Int. J. Mol. Sci.</i> 2021 , <i>22</i> , 8783, doi:10.3390/ijms22168783	49
Martyna Zagórska-Dziok, Patrycja Kleczkowska, Ewa Oledzka, Ramona Figat and Marcin Sobczak Poly(chitosan-ester-ether-urethane) Hydrogels as Highly Controlled Genistein Release Systems Reprinted from: <i>Int. J. Mol. Sci.</i> 2021 , <i>22</i> , 3339, doi:10.3390/ijms22073339	69
Anna Jaromin, Beata Gryzłó, Marek Jamrozik, Silvia Parapini, Nicoletta Basilico and Marek Cegła et al. Synthesis, Molecular Docking and Antiplasmodial Activities of New Tetrahydro- β -Carbolines Reprinted from: <i>Int. J. Mol. Sci.</i> 2021 , <i>22</i> , 13569, doi:10.3390/ijms222413569	89
Karina Piatek, Andrzej Kutner, Dan Cacsire Castillo-Tong, Teresa Manhardt, Nadja Kupper and Urszula Nowak et al. Vitamin D Analogs Regulate the Vitamin D System and Cell Viability in Ovarian Cancer Cells Reprinted from: <i>Int. J. Mol. Sci.</i> 2021 , <i>23</i> , 172, doi:10.3390/ijms23010172	105
Ewa Maj, Beata Maj, Klaudia Bobak, Michalina Gos, Michał Chodyński and Andrzej Kutner et al. Differential Response of Lung Cancer Cells, with Various Driver Mutations, to Plant Polyphenol Resveratrol and Vitamin D Active Metabolite PRI-2191 Reprinted from: <i>Int. J. Mol. Sci.</i> 2021 , <i>22</i> , 2354, doi:10.3390/ijms22052354	117
John Wesley Pike and Mark B. Meyer New Approaches to Assess Mechanisms of Action of Selective Vitamin D Analogues Reprinted from: <i>Int. J. Mol. Sci.</i> 2021 , <i>22</i> , 12352, doi:10.3390/ijms222212352	139

Kaori Yasuda, Miyu Nishikawa, Hiroki Mano, Masashi Takano, Atsushi Kittaka and Shinichi Ikushiro et al. Development of In Vitro and In Vivo Evaluation Systems for Vitamin D Derivatives and Their Application to Drug Discovery Reprinted from: <i>Int. J. Mol. Sci.</i> 2021 , 22, 11839, doi:10.3390/ijms222111839	157
Fumihiko Kawagoe, Sayuri Mototani and Atsushi Kittaka Design and Synthesis of Fluoro Analogues of Vitamin D Reprinted from: <i>Int. J. Mol. Sci.</i> 2021 , 22, 8191, doi:10.3390/ijms22158191	173
Alicja Chrzanowska, Aleksandra Drzewiecka-Antonik, Katarzyna Dobrzyńska, Joanna Stefańska, Piotr Pietrzyk and Marta Struga et al. The Cytotoxic Effect of Copper (II) Complexes with Halogenated 1,3-Disubstituted Arylthioureas on Cancer and Bacterial Cells Reprinted from: <i>Int. J. Mol. Sci.</i> 2021 , 22, 11415, doi:10.3390/ijms222111415	199
Marta Woźniak, Gabriela Pastuch-Gawołek, Sebastian Makuch, Jerzy Wiśniewski, Tibor Krenács and Peter Hamar et al. In Vitro and In Vivo Efficacy of a Novel Glucose–Methotrexate Conjugate in Targeted Cancer Treatment Reprinted from: <i>Int. J. Mol. Sci.</i> 2021 , 22, 1748, doi:10.3390/ijms22041748	225
Katarzyna Kaławaj, Adrianna Sławińska-Brych, Magdalena Mizerska-Kowalska, Aleksandra Żurek, Agnieszka Bojarska-Junak and Martyna Kandefers-Szerszeń et al. Alpha Ketoglutarate Exerts In Vitro Anti-Osteosarcoma Effects through Inhibition of Cell Proliferation, Induction of Apoptosis via the JNK and Caspase 9-Dependent Mechanism, and Suppression of TGF- β and VEGF Production and Metastatic Potential of Cells Reprinted from: <i>Int. J. Mol. Sci.</i> 2020 , 21, 9406, doi:10.3390/ijms21249406	239
Agata Gurba, Przemysław Taciak, Mariusz Sacharczuk, Izabela Młynarczuk-Biały, Magdalena Bujalska-Zadrożny and Jakub Fichna Gold (III) Derivatives in Colon Cancer Treatment Reprinted from: <i>Int. J. Mol. Sci.</i> 2022 , 23, 724, doi:10.3390/ijms23020724	261
Łukasz Szczukowski, Edward Krzyżak, Benita Wiatrak, Paulina Jawień, Aleksandra Marciniak and Aleksandra Kotynia et al. New <i>N</i> -Substituted-1,2,4-triazole Derivatives of Pyrrolo[3,4- <i>d</i>]pyridazinone with Significant Anti-Inflammatory Activity—Design, Synthesis and Complementary In Vitro, Computational and Spectroscopic Studies Reprinted from: <i>Int. J. Mol. Sci.</i> 2021 , 22, 11235, doi:10.3390/ijms222011235	281
Marek Król, Grzegorz Ślifirski, Jerzy Kleps, Szymon Ulenberg, Mariusz Belka and Tomasz Baczek et al. Synthesis of Novel Pyrido[1,2- <i>c</i>]pyrimidine Derivatives with 6-Fluoro-3-(4-piperidynyl)-1,2-benzisoxazole Moiety as Potential SSRI and 5-HT _{1A} Receptor Ligands Reprinted from: <i>Int. J. Mol. Sci.</i> 2021 , 22, 2329, doi:10.3390/ijms22052329	319
Grzegorz Ślifirski, Marek Król and Jadwiga Turło 5-HT Receptors and the Development of New Antidepressants Reprinted from: <i>Int. J. Mol. Sci.</i> 2021 , 22, 9015, doi:10.3390/ijms22169015	341
Hyun-Sun Park, Jongmin Kim, Seong Hoon Ahn and Hong-Yeoul Ryu Epigenetic Targeting of Histone Deacetylases in Diagnostics and Treatment of Depression Reprinted from: <i>Int. J. Mol. Sci.</i> 2021 , 22, 5398, doi:10.3390/ijms22105398	373

Mickael Couty, Marie Dusaud, Mickael Miro-Padovani, Liuhui Zhang, Patricia Zadigue and Loussiné Zargarian et al. Antitumor Activity and Mechanism of Action of Hormonotoxin, an LHRH Analog Conjugated to Dermaseptin-B2, a Multifunctional Antimicrobial Peptide Reprinted from: <i>Int. J. Mol. Sci.</i> 2021 , 22, 11303, doi:10.3390/ijms222111303	389
Martin Schepelmann, Nadja Kupper, Marta Sladczyk, Bethan Mansfield, Teresa Manhardt and Karina Piatek et al. Stereo-Specific Modulation of the Extracellular Calcium-Sensing Receptor in Colon Cancer Cells Reprinted from: <i>Int. J. Mol. Sci.</i> 2021 , 22, 10124, doi:10.3390/ijms221810124	407
Bini Chhetri Soren, Jagadish Babu Dasari, Alessio Ottaviani, Beatrice Messina, Giada Andreotti and Alice Romeo et al. In Vitro and In Silico Characterization of an Antimalarial Compound with Antitumor Activity Targeting Human DNA Topoisomerase IB Reprinted from: <i>Int. J. Mol. Sci.</i> 2021 , 22, 7455, doi:10.3390/ijms22147455	421

About the Editors

Andrzej Kutner

Andrzej Kutner received his PhD in chemistry in 1982 and his DSc (habilitation) in pharmaceutical sciences in 1994, and in 2011 he was awarded the title of professor of pharmaceutical sciences. He has been a trainee at US universities (University of Wisconsin-Madison, New York University, University of Minnesota, Duluth, University of California, Riverside). He works at the Faculty of Pharmacy of the Medical University of Warsaw and lectures on pharmaceutical syntheses at the Chemistry Department of the University of Warsaw. The main area of interest is medicinal chemistry, synthesis of active substances, and analysis of the correlation between biological activity and molecular structure.

Geoffrey Brown

Geoffrey Brown received a BSc from Queen Elizabeth College, London, and a PhD from University College (with Prof Sir Mel Greaves), London. Postdoctoral research was at the MRC Immunochemistry Unit (with Alan Williams and Prof Rodney Porter) and the Nuffield Department of Clinical Medicine (in Prof Sir David Weatherall's Department), Oxford, where he was also IBM Fellow, University of Oxford and Research Lecturer, Christ Church College. He is now Reader in Cellular Immunology (Honorary), College of Medical and Dental Sciences, University of Birmingham. His research concerns the development of blood cells and the nature of leukemia stem cells.

Enikő Kallay

Enikő Kallay received her PhD in biochemistry in 1999 at the University of Vienna and her habilitation in experimental pathophysiology in 2004 at the Medical University of Vienna. She has been a trainee at several US universities (Harvard Medical School, John Hopkins University, MD, Strang Cancer Prevention Center, Cornell University, NY) and was a Marie Curie European Research Fellow at University of Oxford, UK. She works at the Dept. Pathophysiology and Allergy Research, Center of Pathophysiology, Infectiology and Immunology, Medical University of Vienna and lectures on cancer biology at the Karl Landsteiner University of Health Sciences, Krems, Austria. Her main area of interest is to unveil the biochemical and molecular mechanisms of the anti-tumourigenic and anti-inflammatory effects of vitamin D and dietary calcium in inflammatory bowel diseases and in cancers of the colon and ovaries.

Preface to “Novel Strategies in the Development of New Therapies, Drug Substances and Drug Carriers”

At present, there is a strong need for new therapies that are effective and safe for widespread diseases. In developing new treatments, areas of current interest include drug-development-related strategies, new therapeutic molecules, and new drug delivery systems. This book is conceived to promote synergy between research and industrial activities in the design and development of new drugs and, therefore, was not limited to any specific aspect of development. It covers the entire process from the identification of a molecular target, studies of drug–protein interactions, the modeling and optimization of the functional activity, design and chemical synthesis, biological evaluation, and the development of new pharmaceutical carriers.

The original articles and reviews are focused on the design and development of new anticancer treatments, new anticancer low-molecular-weight agents as potential drug substances, and the elucidation of their mechanisms of action. The book also includes studies on novel modulators of the serotonergic system used to treat central nervous system disorders, novel agents against infectious diseases, and the development of anti-plasmodial and anti-inflammatory agents. The successful identification of new compounds for development as drug substances comes from a rich source of medicinal plants and medicinal chemistry approaches. The molecular mechanism of potential drug substances is important to their development as drugs.

Andrzej Kutner, Geoffrey Brown, and Enikő Kallay
Editors



Editorial

Novel Strategies in the Development of New Therapies, Drug Substances, and Drug Carriers Volume I

Andrzej Kutner ^{1,*}, Geoffrey Brown ² and Enikő Kallay ³

¹ Department of Bioanalysis and Drug Analysis, Faculty of Pharmacy, Medical University of Warsaw, 1 Banacha, 02-097 Warsaw, Poland

² School of Biomedical Sciences, Institute of Clinical Sciences, College of Medical and Dental Sciences, University of Birmingham, Birmingham B15 2TT, UK; g.brown@bham.ac.uk

³ Department of Pathophysiology and Allergy Research, Center of Pathophysiology, Infectiology & Immunology, Medical University of Vienna, Währinger Gürtel 18-20, A-1090 Vienna, Austria; enikoe.kallay@meduniwien.ac.at

* Correspondence: akutner@chem.uw.edu.pl

At present, there is a strong need for new therapies that are effective and safe for widespread diseases. In developing new treatments, areas of current interest include drug development-related strategies, new therapeutic molecules, and new drug delivery systems. The Special Issue was conceived to promote synergy between research and industrial activities in the design and development of new drugs and, therefore, was not limited to any specific aspect of development. It covers the entire process from the identification of a molecular target, studies of drug substance–protein interactions, the modeling and optimization of the functional activity, design and chemical synthesis, biological evaluation, and the development of new pharmaceutical carriers.

The original articles and reviews are focused on the design and development of new anticancer treatments, new anticancer low-molecular-weight agents as potential drug substances, and the elucidation of their mechanisms of action. The Issue also includes studies on novel modulators of the serotonergic system used to treat central nervous system disorders, novel agents against infectious diseases, and the development of antiplasmodial and anti-inflammatory agents. The successful identification of new compounds for development as a drug substance is coming from the rich source of medicinal plants and medicinal chemistry approaches. The molecular mechanism of potential drug substances is important to their development as a drug.

The emergence of drug-resistant parasites makes malaria one of the most dangerous infectious diseases. In their research to fight this disease, Nawrot et al. [1] have examined a combination of macromolecular and low-molecular-weight compounds obtained from the latex-bearing plants, including *Chelidonium majus* L. This is a medicinal latex-bearing plant that has been used in traditional folk medicine to treat human papillomavirus (HPV)-caused warts, papillae, and condylomas. The authors have identified the novel major latex protein CmMLP1 and presented a model of its structure. CmMLP1 and the accompanying three alkaloids decreased the in vitro viability of human cervical cancer cells (HPV-negative and HPV-positive).

Gracz-Bernaciak et al. [2] have reviewed the general role of latex, a key part of a plant's defense system, in plant physiology. The authors have described a broad spectrum of active components that are beneficial not only for plants but also for human health. Examples include morphine and codeine from poppy latex. The significance of alkaloids and proteins to the defense system of plants was analyzed for *Chelidonium majus* L, from the poppy family. Their investigations of medicinal latex compounds are outlined, including functional studies of proteins and other pharmacological compounds, via the use of techniques such as CRISPR/Cas9 gene editing.

Citation: Kutner, A.; Brown, G.; Kallay, E. Novel Strategies in the Development of New Therapies, Drug Substances, and Drug Carriers Volume I. *Int. J. Mol. Sci.* **2022**, *23*, 6635. <https://doi.org/10.3390/ijms23126635>

Received: 13 May 2022

Accepted: 7 June 2022

Published: 14 June 2022

Publisher's Note: MDPI stays neutral with regard to jurisdictional claims in published maps and institutional affiliations.



Copyright: © 2022 by the authors. Licensee MDPI, Basel, Switzerland. This article is an open access article distributed under the terms and conditions of the Creative Commons Attribution (CC BY) license (<https://creativecommons.org/licenses/by/4.0/>).

The pharmacological actions of isoflavones of natural origin, such as genistein (GE), relate to their antioxidant activity, and they protect cells from carcinogenesis. Using a self-assembled monolayer on the gold electrode in simulated voltammetry, Stolarczyk et al. [3] have revealed that a new thiolated genistein analog (TGE) has antioxidant activity. The electroactive centers of TGE and its oxidation mechanism have been elucidated using infrared spectrometry supported by quantum chemical and molecular mechanics calculations. In vitro studies indicated that TGE exhibits a high cytotoxic activity towards the human prostate cancer cell line DU145 and that its activity against normal prostate epithelial cells is lower than that of GE.

Zagórska-Dziok et al. [4] studied the kinetic release of genistein (GE) from biomaterials such as polymeric hydrogels and observed favorable physicochemical properties and biocompatibility of the active substance. Non-toxic poly(chitosan-ester-ether-urethane) hydrogels were synthesized by ring-opening polymerization (ROP) and polyaddition. The release rate of GE from hydrogels was near-zero-order kinetics without “burst release” and with non-Fickian transport. The non-toxicity of hydrogels, together with a relatively highly controlled release profile of GEN, suggests that polymeric hydrogels are an effective drug substance carrier.

Drug substances of a natural origin continue to provide drug candidates that are effective against a variety of diseases. However, medicinal chemistry represents a dominant approach to new drug candidates and is well represented by papers in the Special Issue.

By using an advanced medicinal chemistry approach, Jaromin et al. [5] have identified a very high anti-plasmodial activity and selectivity, and a lack of cytotoxicity, for a diastereomeric mixture of *N*-(3,3-dimethylbutyl)-1-octyl-2,3,4,9-tetrahydro-1H-pyrido [3,4-b]-indole-3-carboxamides. The racemic mixture decreased the in vitro viability of human cervical cancer cells, including both HPV-negative and HPV-positive. In silico simulations have revealed possible interactions of the mixture with the enzymes that are essential for parasite metabolism.

Ovarian cancer is one of the most lethal cancers in women, and the current therapies are not sufficiently effective. Piątek et al. [6] have studied a potential new treatment strategy regarding the effectiveness of vitamin D against ovarian cancer cell lines. Synthetic analogs of the active hormonal form of vitamin D have different potencies against high-grade serous ovarian cancer cell lines. The efficacy of the most active analogs in increasing *CYP24A1* expression was cell line- and chemical-structure-dependent. Therefore, optimizing the chemical structure of analogs together with screening for activity in ovarian cancer cells might offer the prospect of a new treatment for ovarian cancer.

Vitamins D and plant polyphenols are both therapeutic anticancer agents and chemopreventive. Their mechanism of synergistic action is not fully elucidated. Maj et al. [7] have evaluated the biological effects of an active vitamin D metabolite and the plant polyphenol resveratrol (RESV) on lung cancer cells. The effectiveness of both agents was dependent on the genetic nature of the cells. The effect of vitamin D metabolite on the induction of *CYP24A1* expression was enhanced by RESV. There was a pronounced effect of the compounds on cytokine production. The authors have postulated that the differences in the responsiveness of the cell lines to vitamin D metabolite and RESV relates to inherent epigenetic differences.

Recent studies of transcription have revealed the principles that govern the action of vitamin D action on a genome-wide scale. Even so, the identification of analogs that are potentially useful therapeutically has had limited success. Pike and Meyer [8] have postulated that a better understanding of the action of vitamin D at the transcriptional level, by the identification of sequential molecular events that occur during activation of most genes, both in vivo and in vitro studies, may provide insight into beneficial structure/activity relationships. Therefore, a novel approach to identifying potent anticancer vitamin D analogs would be to identify the extent to which they lead to selective gene expression within certain cells and tissues.

To facilitate the selection of vitamin D analogs as potential drug candidates, Yasuda et al. [9] have developed and reviewed *in vitro* systems, examining their affinity for VDR and CYP24A1-mediated metabolism. The authors have developed an *in vivo* system, including a *Cyp27b1* gene-deficient rat (a type I rickets model), a *Vdr* gene-deficient rat (a type II rickets model), and a rat with a mutant *Vdr* (R270L) (another type II rickets model), by using genome editing. These models can be used to determine the efficacy of vitamin D analogs, the readout being the amelioration of the symptoms of rickets.

Fluorine substitution of drug substances offers a number of advantages, including changing the pKa and dipole moment of the molecule, improving the chemical or metabolic stability, and enhancing the binding affinity to the target protein. These unique features of fluorinated compounds encouraged Kittaka et al. [10] to review the molecular structures of fluorinated analogs of vitamin D, their synthetic methodologies, and the resulting biological activities, including their anticancer action. Fluorination of the CYP24A1 metabolic positions at the side chain of vitamin D led to strong VDR agonists that have a prolonged half-life *in vivo*.

Chrzanowska et al. [11] have designed and synthesized copper (II) complexes with 3-(4-chloro-3-nitrophenyl)thiourea. They were cytotoxic against human cancer cell lines at the low micromolar range, and this concentration did not affect normal cells. The complexes also induced lactate dehydrogenase (LDH) release from the cancer cell lines. They provoked the immediate apoptosis of cancer cells. The complexes also reduced the level of interleukin-6. An effect of the complexes on the detoxifying and reactive oxygen species of cells that scavenge tumor cells was demonstrated.

The use of methotrexate (MTX) chemotherapy is hampered by a lack of selectivity against the target tumor. To improve this therapy, Woźniak et al. [12] have designed and evaluated a novel glucose-methotrexate conjugate (GLU-MTX), whereby a cleavable linkage allows the intracellular release of MTX after selective uptake through the glucose transporter-1 (GLUT1). GLU-MTX inhibited the growth of colorectal, breast, and lung adenocarcinomas, squamous cell carcinoma, and osteosarcoma cell lines. For these cells, GLU-MTX uptake was increased 17-fold as compared with unconjugated MTX. In a mouse model of breast cancer, the GLUT-MTX conjugate caused growth inhibition *in vivo*.

Currently, there are limited treatments for metastatic osteosarcoma (OS). However, alpha-ketoglutarate (AKG) may represent a novel adjuvant therapy, and Kaławaj et al. [13] have tested whether supplementation of osteosarcoma cell lines with exogenous AKG exerts an anti-cancer effect. AKG inhibited the proliferation of the OS cell lines in a concentration-dependent manner. AKG blocked cell cycle progression at the G₁ stage, which was accompanied by a decrease in the level of cyclin D1. AKG activated both initiator and executioner caspases and induced the expression of Bax while inhibiting Bcl2.

Colorectal cancer (CRC) is the third most frequently diagnosed cancer in men and the second in women. The effectiveness of standard cisplatin therapy for CRC is low due to its lack of specificity and the frequent development of drug resistance. There are also severe side effects. Gurba et al. [14] have documented that Au(III) complexes are promising drug candidates for CRC treatment due to their structural similarity to Pt(II). The authors have reviewed the efforts that have led to stable Au(III) complexes that have potentially selective cytotoxic activity for cancer cells. Unexpectedly, rather than binding to DNA, the inhibition of proteins, such as thioredoxin reductase, mediates the anticancer effects of the complexes.

In the search for safer and more effective anti-inflammatory agents, Szczukowski et al. [15] have designed and synthesized a broad series of novel *N*-substituted-1,2,4-triazole-based derivatives of pyrrolopyridazinone. The derivatives showed significant inhibition of the activity of cyclooxygenase-2 (COX-2) and promising COX-2/COX-1 selectivity. A molecular docking study has demonstrated that the new derivatives occupied, in the active site of COX-2, a position that usually binds meloxicam, a known NSAID. The new derivatives increased the viability of cells that were pre-incubated with the pro-inflammatory lipopolysaccharide and reduced the level of reactive oxygen and nitrogen species (RONS) during induced oxidative stress.

Disturbances in serotonergic neurotransmission are closely related to central nervous system disorders such as depression, anxiety, and schizophrenia, and Król et al. [16] have searched for novel modulators of the serotonergic system. The authors have designed and synthesized novel 4-aryl-pyridopyrimidines. The compounds demonstrated very high binding affinities for the 5-HT_{1A} receptor and high affinities for the D₂, 5-HT_{2A}, and 5-HT₇ receptors. The lead compound had the activity profile of a presynaptic agonist.

The complex nature of the serotonergic system and interactions with other neurochemical systems indicate that the development of depression may be mediated by various pathologic mechanisms, including disturbance to the transmission within the central 5-HT synapses. Ślifirski et al. [17] have reviewed the potential that the serotonergic system offers for the development of new antidepressant therapies. Of importance is a combination of serotonin inhibition together with different agents that are directed towards the 5-HT system. In this regard, the authors summarized recent searches for new antidepressants.

A substantial subpopulation of depression patients is unresponsive to current therapies, and so there is a need for therapies that are more effective and also more tolerable. Pharmacological regulation of histone acetylation levels is considered a potential clinical strategy. Histone acetylation status is also a potential diagnostic biomarker for depression. Inhibitors of histone deacetylases (HDACs) are widely studied as novel therapeutics. Park et al. [18] have reviewed the histone acetylation status in depression and the therapeutic potential of HDAC inhibitors.

Prostate cancer is the most common cancer in men. For patients with advanced and metastatic disease, the available treatment is limited to delaying the progression of the tumor. Couty et al. [19] have examined a natural multifunctional antimicrobial peptide, dermaseptin-B2, that has shown some antitumor activity. To improve its pharmacological properties and decrease its peripheral toxicity and lethality, the authors have developed a hormonotoxin molecule composed of dermaseptin-B2 combined with d-Lys⁶-LHRH protein to target the luteinizing hormone-releasing hormone (LHRH) receptor. The new hormonotoxin reduced tumor burden in mice and was better tolerated than dermaseptin-B2, as it induced cell death by apoptosis rather than necrosis.

Calcimimetics, the pharmacological allosteric agonists of the extracellular calcium-sensing receptor (CaSR), show substantial gastrointestinal side effects and induce the expression of inflammatory markers (e.g., IL-8) in colon cancer cells. Schepelman et al. [20] have used both CaSR-specific (*R*) and -unspecific (*S*) enantiomers of a calcimimetic (NPS 568) and a calcilytic (allosteric CaSR antagonist; NPS 2143) to prove that these effects are mediated via the CaSR. As expected, only the CaSR-selective *R*-enantiomer of the calcimimetic induced CaSR and IL-8 expression, an effect inhibited only by *R*-NPS-2143 but not *S*-NPS-2143. The investigators have, therefore, proved that the pro-inflammatory effects of calcimimetics in colon cancer cells are mediated through CaSR activation.

In searching for an efficient anticancer molecule that targets the human DNA topoisomerase IB, Soren et al. have [21] investigated the catalytic steps of human DNA topoisomerase IB in the presence of a drug substance coded MMV024937, which was obtained from the open-access drug bank Medicines for Malaria Venture. The substance strongly and irreversibly inhibited the cleavage activity of the enzyme and reduced the cell viability of cancer cell lines. Molecular docking and molecular dynamics simulations have suggested that MMV024937 binds to the human DNA topoisomerase IB-DNA complex and sits inside the catalytic site of the enzyme. The investigators have, therefore, provided a molecular-level explanation for the cleavage-inhibition effect of the substance and a possible rationale for using this drug as a lead for the development of anticancer agents.

In summary, the papers within the Special Issue have cover a wide aspect to the development of new drug substances. Medicinal chemistry, supported by molecular modeling and quantum mechanical calculations, is at present the leading approach to drug discovery. The exploration of plant biodiversity is still an important avenue in this field.

Author Contributions: A.K. wrote the original draft that was revised by G.B. and E.K. All authors have read and agreed to the published version of the manuscript.

Funding: This research received no external funding.

Conflicts of Interest: The authors declare no conflict of interest.

References

1. Nawrot, R.; Warowicka, A.; Rudzki, P.J.; Musidlak, O.; Dolata, K.M.; Musijowski, J.; Stolarczyk, E.U.; Goździcka-Józefiak, A. Combined Protein and Alkaloid Research of *Chelidonium majus* Latex Reveals CmMLP1 Accompanied by Alkaloids with Cytotoxic Potential to Human Cervical Carcinoma Cells. *Int. J. Mol. Sci.* **2021**, *22*, 11838. [CrossRef] [PubMed]
2. Gracz-Bernaciak, J.; Mazur, O.; Nawrot, R. Functional Studies of Plant Latex as a Rich Source of Bioactive Compounds: Focus on Proteins and Alkaloids. *Int. J. Mol. Sci.* **2021**, *22*, 12427. [CrossRef] [PubMed]
3. Stolarczyk, E.U.; Strzemppek, W.; Łaszcz, M.; Leś, A.; Menaszek, E.; Sidoryk, K.; Stolarczyk, K. Anti-Cancer and Electrochemical Properties of Thiogenistein—New Biologically Active Compound. *Int. J. Mol. Sci.* **2021**, *22*, 8783. [CrossRef] [PubMed]
4. Zagórska-Dziok, M.; Kleczkowska, P.; Olędzka, E.; Figat, R.; Sobczak, M. Poly(chitosan-ester-ether-urethane) Hydrogels as Highly Controlled Genistein Release Systems. *Int. J. Mol. Sci.* **2021**, *22*, 3339. [CrossRef] [PubMed]
5. Jaromin, A.; Gryzłó, B.; Jamrozik, M.; Parapini, S.; Basilico, N.; Cegła, M.; Taramelli, D.; Zagórska, A. Synthesis, Molecular Docking and Antiplasmodial Activities of New Tetrahydro- β -Carbolines. *Int. J. Mol. Sci.* **2021**, *22*, 13569. [CrossRef] [PubMed]
6. Piatek, K.; Kutner, A.; Castillo-Tong, D.C.; Manhardt, T.; Kupper, N.; Nowak, U.; Chodyński, M.; Marcinkowska, E.; Kallay, E.; Schepelmann, M. Vitamin D Analogs Regulate the Vitamin D System and Cell Viability in Ovarian Cancer Cells. *Int. J. Mol. Sci.* **2022**, *23*, 172. [CrossRef] [PubMed]
7. Maj, E.; Maj, B.; Bobak, K.; Gos, M.; Chodyński, M.; Kutner, A.; Wietrzyk, J. Differential Response of Lung Cancer Cells, with Various Driver Mutations, to Plant Polyphenol Resveratrol and Vitamin D Active Metabolite PRI-2191. *Int. J. Mol. Sci.* **2021**, *22*, 2354. [CrossRef]
8. Pike, J.W.; Meyer, M.B. New Approaches to Assess Mechanisms of Action of Selective Vitamin D Analogues. *Int. J. Mol. Sci.* **2021**, *22*, 12352. [CrossRef]
9. Yasuda, K.; Nishikawa, M.; Mano, H.; Takano, M.; Kittaka, A.; Ikushiro, S.; Sakaki, T. Development of In Vitro and In Vivo Evaluation Systems for Vitamin D Derivatives and Their Application to Drug Discovery. *Int. J. Mol. Sci.* **2021**, *22*, 11839. [CrossRef]
10. Kawagoe, F.; Mototani, S.; Kittaka, A. Design and Synthesis of Fluoro Analogues of Vitamin D. *Int. J. Mol. Sci.* **2021**, *22*, 8191. [CrossRef]
11. Chrzanowska, A.; Drzewiecka-Antonik, A.; Dobrzyńska, K.; Stefańska, J.; Pietrzyk, P.; Struga, M.; Bielenica, A. The Cytotoxic Effect of Copper (II) Complexes with Halogenated 1,3-Disubstituted Arylthioureas on Cancer and Bacterial Cells. *Int. J. Mol. Sci.* **2021**, *22*, 11415. [CrossRef] [PubMed]
12. Woźniak, M.; Pastuch-Gawolek, G.; Makuch, S.; Wiśniewski, J.; Krenács, T.; Hamar, P.; Gamian, A.; Szeja, W.; Szkudlarek, D.; Krawczyk, M.; et al. In Vitro and In Vivo Efficacy of a Novel Glucose–Methotrexate Conjugate in Targeted Cancer Treatment. *Int. J. Mol. Sci.* **2021**, *22*, 1748. [CrossRef] [PubMed]
13. Kaławaj, K.; Sławińska-Brych, A.; Mizerska-Kowalska, M.; Żurek, A.; Bojarska-Junak, A.; Kandefer-Szerszeń, M.; Zdzisińska, B. Alpha Ketoglutarate Exerts In Vitro Anti-Osteosarcoma Effects through Inhibition of Cell Proliferation, Induction of Apoptosis via the JNK and Caspase 9-Dependent Mechanism, and Suppression of TGF- β and VEGF Production and Metastatic Potential of Cells. *Int. J. Mol. Sci.* **2020**, *21*, 9406. [CrossRef]
14. Gurba, A.; Taciak, P.; Sacharczuk, M.; Młynarczuk-Biały, I.; Bujalska-Zadrożny, M.; Fichna, J. Gold (III) Derivatives in Colon Cancer Treatment. *Int. J. Mol. Sci.* **2022**, *23*, 724. [CrossRef] [PubMed]
15. Szczukowski, Ł.; Krzyżak, E.; Wiatrak, B.; Jawień, P.; Marciniak, A.; Kotynia, A.; Świątek, P. New N-Substituted-1,2,4-triazole Derivatives of Pyrrolo[3,4-*d*]pyridazinone with Significant Anti-Inflammatory Activity—Design, Synthesis and Complementary In Vitro, Computational and Spectroscopic Studies. *Int. J. Mol. Sci.* **2021**, *22*, 11235. [CrossRef] [PubMed]
16. Król, M.; Ślifirski, G.; Kleps, J.; Ulenberg, S.; Belka, M.; Bączek, T.; Siwek, A.; Stachowicz, K.; Szewczyk, B.; Nowak, G.; et al. Synthesis of Novel Pyrido[1,2-*c*]pyrimidine Derivatives with 6-Fluoro-3-(4-piperidynyl)-1,2-benzisoxazole Moiety as Potential SSRI and 5-HT_{1A} Receptor Ligands. *Int. J. Mol. Sci.* **2021**, *22*, 2329. [CrossRef]
17. Ślifirski, G.; Król, M.; Turło, J. 5-HT Receptors and the Development of New Antidepressants. *Int. J. Mol. Sci.* **2021**, *22*, 9015. [CrossRef]
18. Park, H.-S.; Kim, J.; Ahn, S.H.; Ryu, H.-Y. Epigenetic Targeting of Histone Deacetylases in Diagnostics and Treatment of Depression. *Int. J. Mol. Sci.* **2021**, *22*, 5398. [CrossRef]
19. Couty, M.; Dusaud, M.; Miro-Padovani, M.; Zhang, L.; Zadigue, P.; Zargarian, L.; Lequin, O.; de la Taille, A.; Delbe, J.; Hamma-Kourbali, Y.; et al. Antitumor Activity and Mechanism of Action of Hormonotoxin, an LHRH Analog Conjugated to Dermaseptin-B2, a Multifunctional Antimicrobial Peptide. *Int. J. Mol. Sci.* **2021**, *22*, 11303. [CrossRef]

20. Schepelmann, M.; Kupper, N.; Sladczyk, M.; Mansfield, B.; Manhardt, T.; Piatek, K.; Iamartino, L.; Riccardi, D.; Kariuki, B.M.; Bassetto, M.; et al. Stereo-Specific Modulation of the Extracellular Calcium-Sensing Receptor in Colon Cancer Cells. *Int. J. Mol. Sci.* **2021**, *22*, 10124. [CrossRef]
21. Soren, B.C.; Dasari, J.B.; Ottaviani, A.; Messina, B.; Andreotti, G.; Romeo, A.; Iacovelli, F.; Falconi, M.; Desideri, A.; Fiorani, P. In Vitro and In Silico Characterization of an Antimalarial Compound with Antitumor Activity Targeting Human DNA Topoisomerase IB. *Int. J. Mol. Sci.* **2021**, *22*, 7455. [CrossRef] [PubMed]



Article

Combined Protein and Alkaloid Research of *Chelidonium majus* Latex Reveals CmMLP1 Accompanied by Alkaloids with Cytotoxic Potential to Human Cervical Carcinoma Cells

Robert Nawrot ^{1,*}, Alicja Warowicka ^{2,3}, Piotr Józef Rudzki ⁴, Oskar Musidlak ¹,
Katarzyna Magdalena Dolata ^{1,†}, Jacek Musijowski ⁴, Elżbieta Urszula Stolarczyk ^{4,‡} and
Anna Goździcka-Józefiak ¹

- ¹ Molecular Virology Research Unit, Institute of Experimental Biology, Faculty of Biology, Adam Mickiewicz University, Poznań, Uniwersytetu Poznańskiego 6, 61-614 Poznań, Poland; oskar.musidlak@amu.edu.pl (O.M.); katarzyna.dolata@fli.de (K.M.D.); agjozef@amu.edu.pl (A.G.-J.)
- ² Department of Animal Physiology and Developmental Biology, Institute of Experimental Biology, Faculty of Biology, Adam Mickiewicz University, Poznań, Uniwersytetu Poznańskiego 6, 61-614 Poznań, Poland; alicja@amu.edu.pl
- ³ NanoBioMedical Centre, Adam Mickiewicz University, Poznań, Wszechnicy Piastowskiej 3, 61-614 Poznań, Poland
- ⁴ Łukasiewicz Research Network—Pharmaceutical Research Institute, Rydygiera Street 8, 01-793 Warsaw, Poland; pj.rudzki@wp.pl (P.J.R.); j.musijowski@gmail.com (J.M.); elzbieta.stolarczyk@ichp.pl (E.U.S.)
- * Correspondence: rnawrot@amu.edu.pl; Tel.: +48-61-829-5931
- † Present address: Institute of Molecular Virology and Cell Biology, Friedrich Loeffler Institut, Südufer 10, 17493 Greifswald-Insel Riems, Germany.
- ‡ Present address: Łukasiewicz Research Network—Institute of Industrial Chemistry, Rydygiera Street 8, 01-793 Warsaw, Poland.

Citation: Nawrot, R.; Warowicka, A.; Rudzki, P.J.; Musidlak, O.; Dolata, K.M.; Musijowski, J.; Stolarczyk, E.U.; Goździcka-Józefiak, A. Combined Protein and Alkaloid Research of *Chelidonium majus* Latex Reveals CmMLP1 Accompanied by Alkaloids with Cytotoxic Potential to Human Cervical Carcinoma Cells. *Int. J. Mol. Sci.* **2021**, *22*, 11838. <https://doi.org/10.3390/ijms222111838>

Academic Editors: Andrzej Kutner, Geoffrey Brown and Enikő Kallay

Received: 2 October 2021

Accepted: 28 October 2021

Published: 31 October 2021

Publisher's Note: MDPI stays neutral with regard to jurisdictional claims in published maps and institutional affiliations.

Abstract: *Chelidonium majus* L. is a latex-bearing plant used in traditional folk medicine to treat human papillomavirus (HPV)-caused warts, papillae, and condylomas. Its latex and extracts are rich in many low-molecular compounds and proteins, but there is little or no information on their potential interaction. We describe the isolation and identification of a novel major latex protein (CmMLP1) composed of 147 amino acids and present a model of its structure containing a conserved hydrophobic cavity with high affinity to berberine, 8-hydroxychelerythrine, and dihydroberberine. CmMLP1 and the accompanying three alkaloids were present in the eluted chromatographic fractions of latex. They decreased in vitro viability of human cervical cancer cells (HPV-negative and HPV-positive). We combined, for the first time, research on macromolecular and low-molecular-weight compounds of latex-bearing plants in contrast to other studies that investigated proteins and alkaloids separately. The observed interaction between latex protein and alkaloids may influence our knowledge on plant defense. The proposed toolbox may help in further understanding of plant disease resistance and in pharmacological research.

Keywords: major latex protein; *Chelidonium majus*; greater celandine; defense-related proteins; alkaloids; molecular docking; cancer cells



Copyright: © 2021 by the authors. Licensee MDPI, Basel, Switzerland. This article is an open access article distributed under the terms and conditions of the Creative Commons Attribution (CC BY) license (<https://creativecommons.org/licenses/by/4.0/>).

1. Introduction

Chelidonium majus L. is a perennial herbal plant belonging to the family Papaveraceae that grows across Europe, western Asia, and North America [1–3]. It is a rich source of different biologically active substances (alkaloids, flavonoids, phenolic acids) and has been used in folk medicine for centuries. Over 27 alkaloids (e.g., chelerythrine, sanguinarine, chelidone, protopine, allocryptopine, berberine, coptisine) were identified in its extracts and latex [4,5]. Plant laticifer cells are filled with latex (milky sap) that contains condensed defense substances [6,7]. The plant exudes latex immediately at the site of damage caused by an insect attack [7,8]. In folk herbal medicine, extracts and latex of *C. majus* are used to

treat warts and condylomas caused by human papillomavirus (HPV) [9]. The medicinal interest in *C. majus* is based mainly on small molecules such as alkaloids, flavonoids, and phenolic acids, which may also act synergistically [4,5,10]. These compounds exhibit antitumor, antiviral, and antibacterial activities [5,11]. The proteins of *C. majus* also show mitogenic, cytotoxic, antibacterial, and antiviral activities [7]. Nucleases present in milky sap were found to exert apoptotic effects on a human cervical cancer HeLa cell line [12,13]. The antiviral activity of milky sap was suggested to be associated with major latex proteins (MLPs) [7,14].

MLPs, pathogenesis-related 10 (PR-10) proteins, cytokinin-specific binding proteins (CSBPs), and norcochlorogenic acid synthases belong to the Bet v 1 superfamily of proteins. Their characteristic hydrophobic cavity binds to secondary metabolites and hormones [15,16]. MLPs were discovered in *Papaver somniferum* as abundant, laticifer-specific peptides with unknown function [17]. MLPs constitute up to 50% of the soluble *P. somniferum* latex subproteome, which correlates with the relative abundance suggested by SDS-PAGE [18]. MLPs are also present in non-latex-bearing plants such as *Arabidopsis thaliana* and *Prunus persica* (peach) [15]. They influence fruit ripening in kiwi [16] and fruit and flower development in peach [19]. They protect cotton against *Verticillium dahliae* [20] and melon against cucumber mosaic virus [21]. The presence of MLP-like protein in the latex of *Chelidonium majus* L. was first reported using proteomic analysis against *C. majus* sequence database prepared after transcriptome sequencing and annotation [22]. The study identified previously uncharacterized nucleic acid binding protein and showed that it is highly overrepresented in the latex [22,23]. Statistical analysis confirmed that MLP is present in different stages of plant development until the fruit ripening period [14].

Our interest in *C. majus* originated from the traditional use of the fresh plant extracts and latex against warts and condylomas caused by the oncogenic human papillomavirus (HPV) infection. HPV infections can lead to cervical cancer in women, which can result from persistent infection with a group of “high-risk” HPVs [24]. However, previous studies on *C. majus* have shown that the proteins from this plant are also biologically active [3,13]. The antiviral activity of the *C. majus* milky sap is possibly linked with the presence of MLP [7,25]. Synergistic action of plant secondary metabolites with other components of the plant extracts is also postulated [10].

Hence, the goal of the study was to isolate the MLP from *C. majus* latex, identify accompanying low-molecular compounds and to analyze their joint cytotoxic activities against cervical cancer cell lines.

2. Results

To the best of our knowledge, no joint research has been performed before in separate fields of plant compounds research of different structures and sizes for latex-bearing plants. Such an approach requires multidisciplinary research with the use of biological, biotechnological, chemical, as well as analytical and theoretical techniques (Figure 1). Therefore, we employed a research scheme, which started with the use of two kinds of source materials—*C. majus* whole plant extract and latex samples. The second step enabled fractionation of the material with the use of affinity chromatography on heparin. All fractions were monitored with the use of proteomic and zymography techniques, as well as with the use of LC-ESI-MS/MS techniques for the identification of proteins and non-protein substances. This step allowed to indicate specific protein and alkaloids co-existing in the fractions, which was confirmed with the use of bioinformatic tools of molecular modeling and docking. Finally, the fractions were monitored in terms of their cytotoxic activities on cervical cancer cells (Figure 1).

2.1. Isolation of MLP from *C. majus* Whole Plant Extracts and Latex

To isolate and purify the MLP from whole plant extracts and latex samples, heparin column was selected due to its high affinity to DNA-binding proteins, coagulation factors, lipoproteins, and protein synthesis factors. In-gel DN-ase zymography was used to assess

the presence of MLP in separated fractions. We observed a strong nucleolytic activity for the selected fractions eluted (Figure 2). We collected protein bands showing nucleolytic activity and analyzed them by LC-ESI-MS/MS. We then applied Mascot analysis to MS results using the annotated *C. majus* CDS database [22]. We observed that MLP was the main constituent of the nucleolytic bands (MLP-like protein 28, Table 1, band 1A; Table S1). We visualized the protein content of the fractions by using SDS-PAGE and silver staining (Figure 2). The most representative bands were then collected and analyzed by LC-ESI-MS/MS. MLP was again found to be the main constituent of the fractions—both for the whole plant extracts (Table 1, band 1B; Table S2) and latex samples (Figure S1; Table S3).

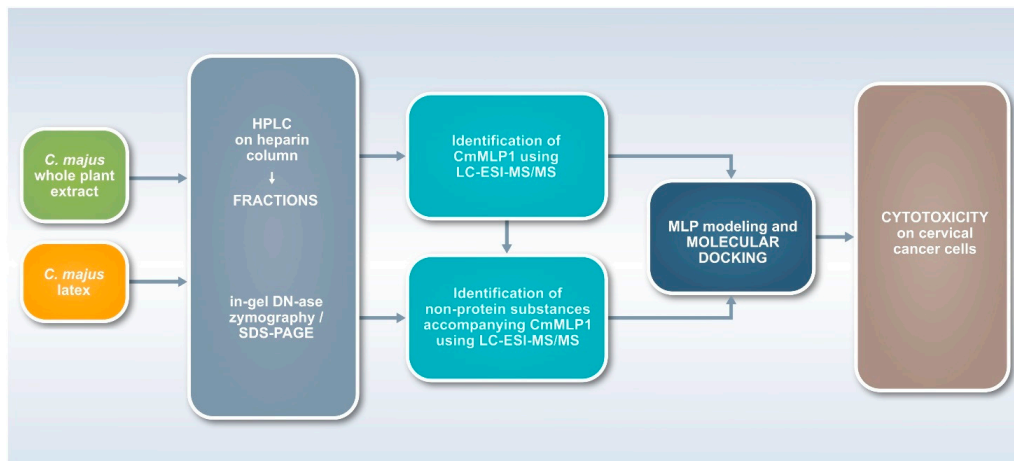


Figure 1. Workflow for the multidisciplinary study (toolbox) for two kinds of plants source materials—*C. majus* extracts and latex. The research scheme enabled fractionation with the use of affinity chromatography, monitoring of all fractions with the use of proteomic, zymography, as well as LC-ESI-MS/MS techniques for the identification of proteins and non-protein substances. Molecular interactions were confirmed with the use of bioinformatic tools of molecular modeling and docking, and their biological activities were finally analyzed using cell lines.

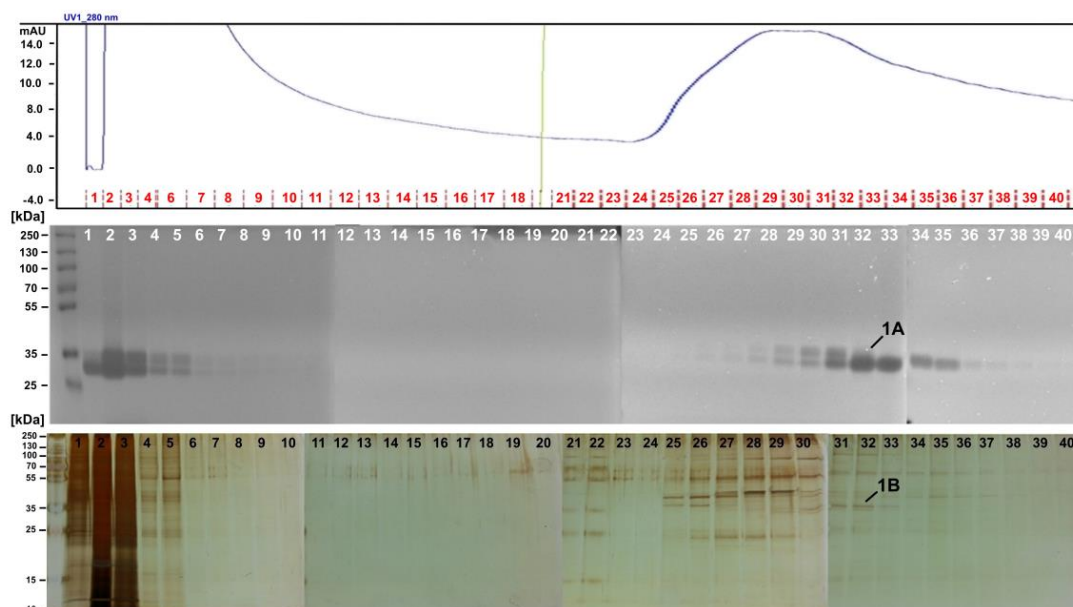


Figure 2. Fractionation of *C. majus* whole plant extract on a heparin column. Top: Absorbance at 280 nm—blue line—indicates protein content in fractions. Red lines and numbers represent fraction numbers. Middle: In-gel DNase assay zymography of protein fractions with high nucleolytic activity. Band 1A of ca. MW 33–35 kDa was cut, and MLP presence was confirmed by MS/MS. Bottom: Protein profiles of each fraction in SDS-PAGE stained with silver. Band 1B of ca. MW 36 kDa was cut from the gel, and MLP presence was confirmed by MS/MS.

Table 1. MS/MS results of protein bands cut from an in-gel DNase assay zymography gel (Figure 2, Band 1A) and a silver-stained SDS-PAGE gel (Figure 2, Band 1B) after electrophoretic separation of protein fractions isolated from whole plant extract. The main constituent of the fractions was MLP.

Accession Number	Protein Definition	Mascot Score	Mol. Mass (da)	Matched Peptides	Sequence Coverage (%)
Band 1A					
m.37898	m.37898 MLP-like protein 28	6205	39612	27	65.2
m.37901	m.37901 MLP-like protein 28	5490	41223	30	65.7
m.37897	m.37897 MLP-like protein 28	4549	22910	18	73.9
m.37895	m.37895 MLP-like protein 28	4202	22792	21	74.9
m.37902	m.37902 MLP-like protein 28	3868	22814	17	69.8
m.12632	m.12632 MLP-like protein 28	2459	26927	15	69.5
m.12634	m.12634 MLP-like protein 28	2334	21853	18	61.9
m.33033	m.33033 bifunctional epoxide hydrolase 2-like	1996	35790	17	59.9
m.37899	m.37899 MLP-like protein 28	1959	22825	18	56.6
uniq_06137	uniq_06137 14-3-3 protein	1309	29225	21	71.6
Band 1B					
m.60929	m.60929 ferredoxin–nadp leaf chloroplastic-like isoform 1	1978	40992	37	58.3
m.37898	m.37898 MLP-like protein 28	1951	39612	12	44.6
m.37901	m.37901 MLP-like protein 28	1656	41223	10	37.0
m.12632	m.12632 MLP-like protein 28	1190	26927	7	33.0
m.12634	m.12634 MLP-like protein 28	1137	21853	8	41.8
m.37897	m.37897 MLP-like protein 28	537	22910	7	42.7
m.37895	m.37895 MLP-like protein 28	267	22792	5	36.2
m.61102	m.61102 pectinesterase 3-like	218	63766	4	8.8
m.12630	m.12630 MLP-like protein 28	174	16874	2	17.7
m.60714	m.60714 glyceraldehyde-3-phosphate cytosolic-like	100	36972	1	4.1

2.2. LC-MS/MS Identification of Non-Protein Substances Accompanying MLP

We washed out the unbound small molecules and proteins with no affinity from the column (Figure 2, fractions 1–18). However, because we also aimed to identify non-protein substances that might possibly be present in the nucleolytic fractions, we extended our toolbox by adopting sample preparation from plasma/serum pharmacokinetics (Figures S2–S33) and combining it with LC-MS/MS screening of small molecules. In the fractions derived from the whole plant extract, we found the following alkaloids: berberine, chelidonine, coptisine, corysamine, dihydroberberine, dihydrosanguinarine, dihydrochelerythrine, dihydroxysanguinarine, norchelerythrine, norsanguinarine, and protopine (Figures S3–S21) [4,5]. For samples rich in low-molecular constituents, we semi-quantitatively compared 21 signals (Tables S4 and S5; Figures S34–S47). Finally, we identified 8 alkaloids co-localizing with proteins in the protein-rich fractions. The presence of these alkaloids suggest their molecular association with proteins. The highest relative signal intensities for coptisine, berberine, dihydroberberine, chelidonine, and protopine were found in fractions 22–23 (Figure 3, in green), while those for 8-hydroxychelerythrine, stylophine, and sanguinarine were found in fractions 25–26 (Figure 3, in green).

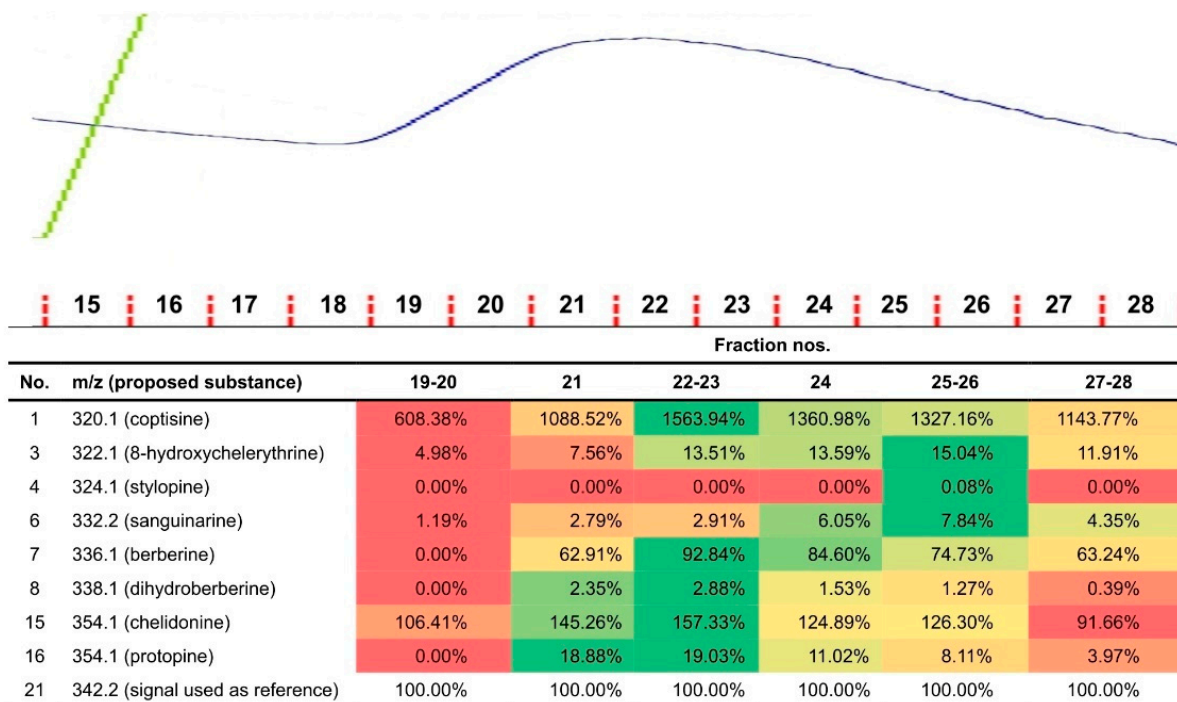


Figure 3. Correlation of the protein content (MLP) with the alkaloid content of the fraction. Top: Chromatogram of *C. majus* latex protein fractions adjusted to the numbers of fractions in the table. Blue line indicates protein content in fraction (monitored at 280 nm). The protein peak between fractions nos. 19–26 presents higher protein content in the fractions, which could be correlated with the higher quantity of identified alkaloids in the same fractions. Bottom: Relative signal intensities for latex fractions. Color coding ranges from red (lowest relative intensity of a particular compound in a group of samples) up to green (highest relative intensity).

We used the same approach for *C. majus* milky sap, which enabled to identify several alkaloids (Table S5). Although the proposed identifications were based only on mass spectrometry data, they were consistent with the compounds detected previously in *C. majus* [4,5].

2.3. CmMLP1 Domain Architecture

The identified MLP-like protein 28 (Figure 2b) belongs to the MLP-related protein family 28 as described for *A. thaliana* [26]. We conducted bioinformatics analysis by searching for MLP-like sequences in the *C. majus* CDS database derived from transcriptomic data (<http://webblast.ipk-gatersleben.de/chelidonium/>, accessed on 28 October 2021). The analysis revealed the presence of 19 transcript sequences of length 105–359 nucleotides (Figure 4), coding for MLP-like proteins of different sizes with a common “core” of approximately 100 amino acids (Figure 5 and Figure S48). We selected the sequence composed of 147 amino acids as the one coding for the MLP, with the calculated MW of 16.77 kDa and theoretical pI of 5.88 (MLP-like m.12630); this result was consistent with the size of MLPs derived from other plants [17]. The protein encoded by this sequence was named CmMLP1. By using bioinformatics tools, we predicted the conserved hydrophobic cavity for binding of small molecules in the structure of CmMLP1 and confirmed that the protein belongs to the “START/RHO_alpha_C/PITP/Bet_v1/CoxG/CalC (SRPBCC) ligand-binding domain superfamily” [12,19,27].

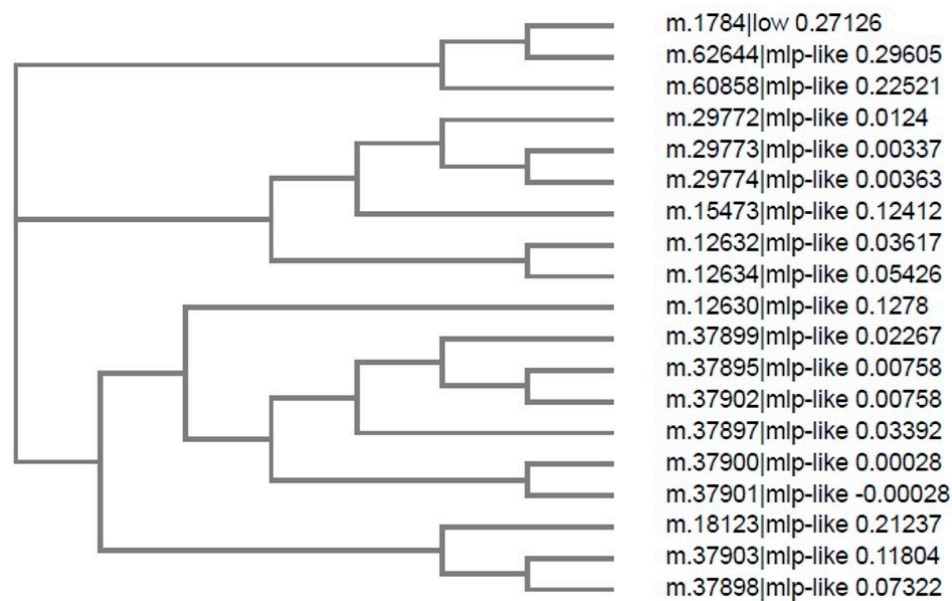


Figure 4. Phylogenetic tree showing relationships between 19 MLP-like sequences from *C. majus*. *C. majus* database accession numbers are shown (<http://webblast.ipk-gatersleben.de/chelidonium/>, accessed on 28 October 2021).

m.12630 mlp-like	-----	0
m.37900 mlp-like	AVYVKAYEDAPIPAKYIEFLVGF TKDLDAHLQKNHGHTHAVGDNNIEKIEVEVEVPYDAD	60
m.37901 mlp-like	AVYVKAYEDAPIPAKYIEFLVGF TKDLDAHLQKNHGHTHAVGDNNIEKIEVEVEVPYDAD	60
m.12630 mlp-like	-----TVKLWKYKLEGKSLYSKERMTVVDD	25
m.37900 mlp-like	KFYHMFKYDAKEIPKHLPHLIEHVEVLEGGDVHAGTVKLWKYKLEGKTLYLKERMTVVDD	120
m.37901 mlp-like	KFYHMFKYDAKEIPKHLPHLIEHVEVLEGGDVHAGTVKLWKYKLEGKTLYLKERMTVVDD *****.*.*****	120
m.12630 mlp-like	EKKIITHSVIEGDLLKDYKCFVVTLIITPKGGHGDGSVWKWIVEYEKATEDVHVPANYIE	85
m.37900 mlp-like	EKKIITYSILEGDLLKDYKCFGATFTATPKGGHGDGSVWKWILEYEKATKDAIPANYIE	180
m.37901 mlp-like	EKKIITYSILEGDLLKDYKCFGATFTATPKGGHGDGSVWKWILEYEKATKDAIPANYIE *****.*.:*****.*.:*****.*.:*****.*.:*****	180
m.12630 mlp-like	FAVWLTKDLDGSLPNHAHTAVGANNIEKIEGEVEVQCDADKFYSMFKHDVKEIPKNIPH	145
m.37900 mlp-like	FLVWVTKDLNAHLHNRSHSHSVGADNIEKIEVEVEVQSDADKFRILIKHDVKEIPKGVPH	240
m.37901 mlp-like	FLVWVTKDLNAHLHNRSHSHSVGADNIEKIEVEVEVQSDADKFRILIKHDVKEIPKGVPH * **.*.*.*.* * *.*:*.**:*.***** ***.***** *:*****.*:**	240
m.12630 mlp-like	LY-----	147
m.37900 mlp-like	LFEHVEVLEGGDINAGSVKLWKYLLLEGKHEYCKERMKVVDEKRMITHSFFEGDVMKDYT	300
m.37901 mlp-like	LFEHVEVLEGGDINAGSVKLWKYLLLEGKHEYCKERMKVVDEKRMITHSFFEGDVMKDYT *:	300
m.12630 mlp-like	-----	147
m.37900 mlp-like	YFDVIFTVTPKGGHGEESVVKW-----	322
m.37901 mlp-like	YFDVIFTVTPKGGHGEESVVKWDEVEVVRAREDVP IPTNLYLDHLIWTTKDLDAHQKDV*	358

Figure 5. Primary sequence alignment of three *C. majus* MLPs. The protein sequence is shown, with the number of amino acids for each sequence. Asterisks indicate conserved amino acids with the “core” common to all sequences. The shortest MLP-like m.12630 sequence contains 147 residues and has molecular weight of 16.77 kDa. *C. majus* database accession numbers are shown.

2.4. MLP Structure Prediction and Modeling

We used a homology modeling approach for constructing 3D protein structure. On the basis of the fold-recognition (FR) alignment proposed by GeneSilico MetaServer, we

selected template structures of 4IGV chain A—crystal structure of kirola (Act d 11, PubMed: 23969108). The structure of the protein covers the sequence in the region of 1–101 amino acids. The PROQ method to predict model quality evaluated the model as “fairly good” (predicted LGscore = 1.151, predicted MaxSub = 0.172, predicted GDT_TS: 36.39). Figure 6 and Figure S49 illustrate the predicted quality of the mature protein structure.

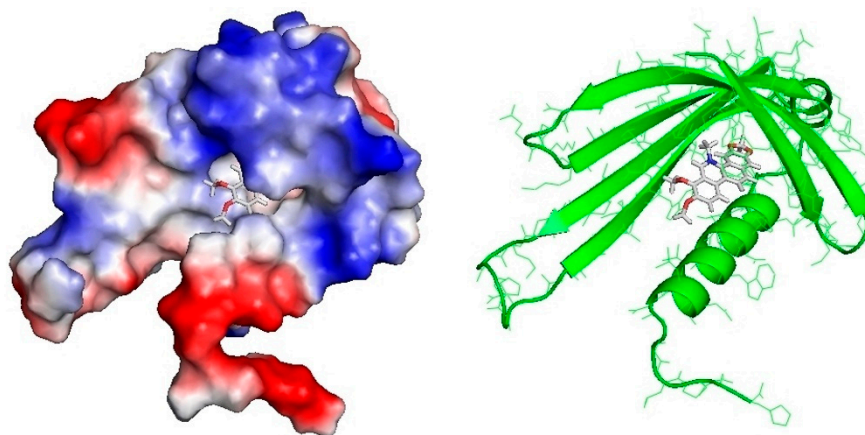


Figure 6. Left: 3D model of *C. majus* MLP with surface representation, colored according to the distribution of the electrostatic surface potential calculated with ABPS (PyMol). Positively charged regions in blue and negatively charged regions in red. Hydrophobic cavity filled by dihydroberberine (docking affinity 5.98). Right: MLP in a ribbon representation with docked 8-hydroxycheleritrine (docking affinity 5.94).

2.5. Molecular Docking of Alkaloids to CmMLP1

Eight alkaloid structures retrieved from ZINC database were docked in the hydrophobic pocket of the CmMLP1. Docking of ligand molecules to CmMLP1 was performed using the Autodock Vina program, which analyzes 20 possible conformations of the ligand molecule at the active site of the protein. Binding energy in the active site was calculated for each conformation. We observed high binding affinity for dihydroberberine and 8-hydroxycheleritrine as well as relatively high affinity for berberine (Table 2, nos. 1–3, Tables S6–S13; Figure S50).

Table 2. Molecular docking of alkaloids detected in *C. majus* milky sap fractions with nucleolytic activity to the 3D model of MLP. * Binding affinity below -5.00 kcal/mol is considered as high affinity. ** Binding affinity between -5.00 and -4.50 kcal/mol is considered as relatively high affinity.

No.	ZINC Database Number	Structure (Compound)	Binding Affinity (kcal/mol)	Docking Score
1	ZINC01575028	dihydroberberine	-5.98 *	-0.55
2	ZINC03872044	8-hydroxycheleritrine	-5.94 *	-0.50
3	ZINC03779067	berberine	-4.86 **	-0.37
4	ZINC20111233	protopine	-3.55	-1.09
5	ZINC01709414	coptisine	-3.45	-0.18
6	ZINC00000706	sanguinarine	-3.12	-0.80
7	ZINC20470298	stylopine	-2.84	-1.44
8	ZINC30727894	chelidonine	-2.14	-1.34

2.6. Cytotoxic Activity of CmMLP1 Accompanied with Alkaloids

To assess the biological activity of fractions containing CmMLP1 accompanied with alkaloids, we analyzed their cytotoxic effects on HeLa and C33A cell lines. We used two such cell lines—HeLa and C33A. Both of them originate from cervical samples of women,

however they differ with the HPV genetic material content. HeLa cells are considered as HPV positive (HPV+), and C33A as HPV negative (HPV-). The analysis was performed using the WST-1 colorimetric assay and normal fibroblasts (MSU-1.1) were used as a control.

We analyzed the whole spectra of the samples separated on heparin column both from whole plant extracts and from latex. The results indicated that the viability of HeLa and C33A cancer cells after 48 h of incubation with all fractions from latex as well whole plant extract was reduced on different levels. These cell lines showed similar viability after treatment with fractions derived from whole plant extract (Figures S51 and S52). However, an immediate decrease of at least 50% in viability was observed for HeLa and C33A cells when treated with latex fractions 24–26 as compared to that for MSU-1.1 (Figure 7). We previously confirmed the presence of CmMLP1 and alkaloids in the same fractions (Table 1). Moreover, the cell viability was the lowest for HeLa cells, with less than 10% living cells, what is comparable to negative control treatments (DMSO). The results suggest that the fractions containing CmMLP1 accompanied by alkaloids present the highest cytotoxic activity against cervical cancer HPV positive cells—less than 10% living cells left for each fraction (Figure 7a,c; Table 3). The viability of the cervical cancer cells was two-fold lower for HPV+ (HeLa) cells than for HPV- (C33A) cells ($p < 0.0001$) (Figure 7a).

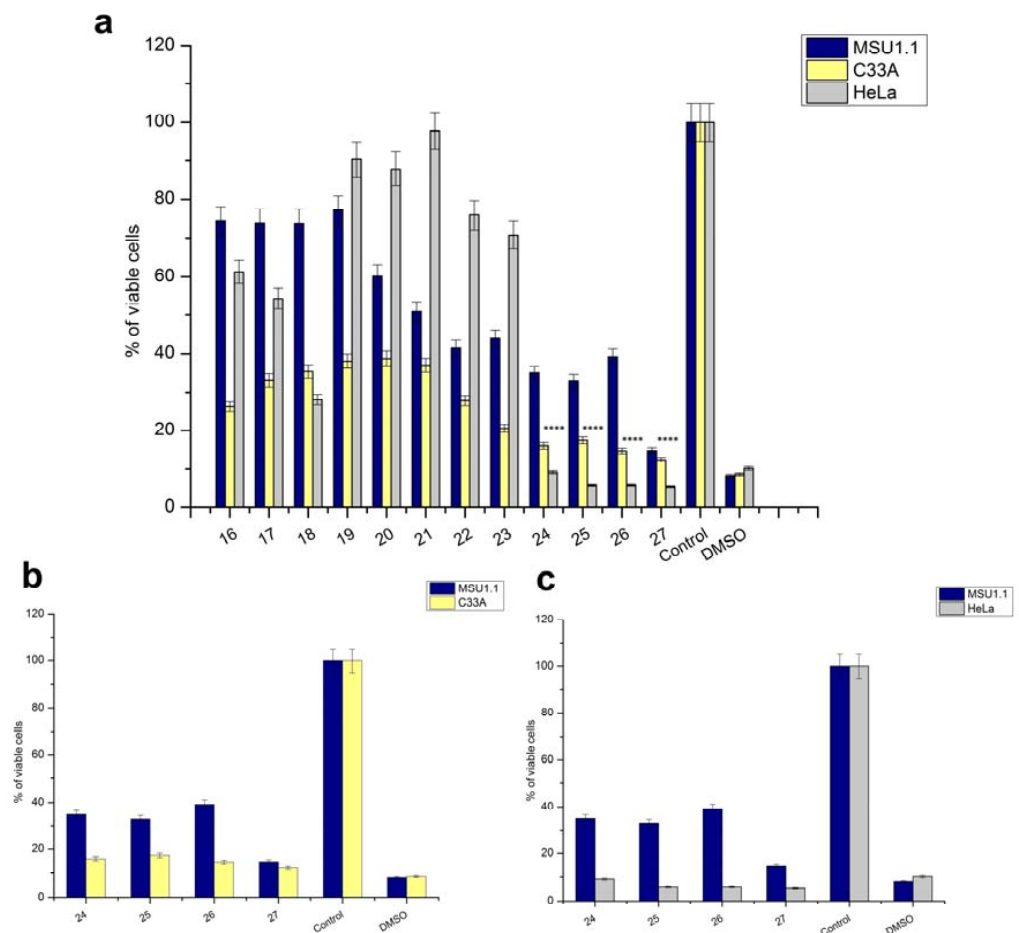


Figure 7. CmMLP1 and the accompanying three alkaloids decreased in vitro viability of human cervical cancer cells (HPV-negative and HPV-positive). (a–c) Viability (%) of C33A and HeLa cancer cells compared to that of normal MSU-1.1 fibroblasts after treatment with latex fractions for 48 h. Control (negative)—untreated cells; DMSO—positive control. (a) C33A, HeLa, and MSU-1.1 cell lines treated with fractions 16–27. (b) Both C33A HPV- cervical cancer cell line and MSU-1.1 treated with fractions 24–26 containing CmMLP1 accompanied with alkaloids and fraction 27. (c) Both HeLa HPV+ cervical cancer cell line and MSU-1.1 treated with fractions 24–26 containing CmMLP1 accompanied with alkaloids and fraction 27. ****, $p < 0.0001$.

Table 3. Viability of C33A and HeLa cancer cell lines vs. normal MSU1.1 treated with latex fractions containing CmMLP1 accompanied with alkaloids.

Cell Line (CmMLP1 Concentration)	Fraction 24 (2 ng/ μ L)	Fraction 25 (1.5 ng/ μ L)	Fraction 26 (1 ng/ μ L)
MSU1.1	22.8%	32.8%	39.2%
C33A	16.0%	17.4%	14.8%
HeLa	9.1%	5.8%	5.9%

3. Discussion

Our present study has enabled us to advance plant science because of multidisciplinary research on compounds of different structures: large and small molecules. MLP was accompanied with coptisine, stylopine, sanguinarine, chelidonine, protopine, berberine, 8-hydroxychelerythrine, and dihydroberberine (Figure 3). Molecular docking showed high affinity of the latter three molecules to the hydrophobic cavity of CmMLP1 (Figure 3d). To the best of our knowledge, these associations are reported for the first time. Previous studies focused solely on either macromolecules or alkaloids. Both these groups of compounds coexist in a plant and interact with each other. Thus, the associations observed here may influence our knowledge of plant defense and function of the latex proteins. They may also further our understanding of their pharmacology.

The high cytotoxicity of the combination of CmMLP1 and alkaloids for both cancer cell lines (Figure 7b,c) indicates their potential use in cancer therapy. The cell viability of HPV+ cells was twice lower than that of HPV− cells. The biological activity of *C. majus* alkaloids is well described. Cytotoxicity tests demonstrated selective and profound apoptotic effects of a five-alkaloid combination in the mouse melanoma B16F10 cell line [27]. Chelidonine efficiently induced apoptosis in HeLa cells through possible alteration of p38-p53 and AKT/PI3 kinase signaling pathways [28]. Chelidonine was also examined as a potent inducer of cell death in human leukemic and lung carcinoma cells [29], as well as a promising model compound for overcoming multidrug resistance in Caco-2 and CEM/ADR5000 cancer cells together with the alkaloid extract comprising of protoberberine and benzo[c]phenanthridine alkaloids [30]. Our findings report that one of the docking alkaloids to CmMLP1, with high binding affinity, is dihydroberberine (DIH). This alkaloid belongs to the protoberberine alkaloid family and presents strong biological activity including anticancer properties. Recently, it has been shown that the components of the natural plant protoberberine fraction (BBR-F) extracted from *C. majus* may represent promising novel photosensitive agents [6]. Increased cytotoxicity of the combination of CmMLP1 with alkaloids for both cancer cell lines—HeLa, C33A, compared to normal MSU-1.1 fibroblasts (Figure 7, Table 3), is of great importance for the potential use in cancer therapy. The cell viability was the lowest for HeLa HPV positive cells—with less than 10% of living cells—two times lower than for C33A HPV negative cells. This may suggest the joint action of alkaloids and CmMLP1 through the unknown mechanism connected to the HPV genome or its protein products [31,32]. This result suggests the synergistic effect of CmMLP1 and alkaloids against HPV genome or its protein products [32]. The mechanism of this effect, however, remains unknown. Low-molecular-weight latex compounds may act synergistically with proteins and influence their conformation. The proteins, in turn, might facilitate transport of small molecules to the cell or act as their transporters [33].

The presence of MLP-like protein in *C. majus* latex was reported for the first time using proteomic analysis against *C. majus* sequence database, prepared after transcriptome sequencing and annotation [22]. Mass spectrometry analysis allowed the identification of MLP in protein bands with nucleolytic activity as their main constituents (MLP-like protein 28, Table 1). Confirmation of the nucleolytic activity of a particular protein of latex is the significant novelty of this study. Previously, nucleolytic bands were not specifically identified as “nucleic acid binding proteins,” “DNA-binding” or “RNA-binding” [12]

because of the use of the general NCBI plants database (Viridiplantae), which does not consider the various possibilities. Hence, the nucleolytic activity observed by zymography may be a “marker” of the presence of MLP in other samples from *C. majus*. The remaining question still concerns the possible function of the CmMLP1 in association with alkaloids. Previous studies show that the functional role of MLPs is similar to that of the PR-10 proteins [26]. MLPs and PR-10 families both belong to the Bet v 1 superfamily, but the sequence identity between them is rather low (<25%) [16]. Moreover, CaPR-10 protein isolated from hot pepper acts as an antiviral protein inhibiting viral penetration and/or replication. After tobacco mosaic virus (TMV-P0) inoculation CaPR-10 is phosphorylated and functions as a kind of RNase which cleaves viral RNA [27]. The functional role of MLPs is similar to PR-10 proteins, which could possibly explain *C. majus* latex antiviral activities [7,34]. However, this issue needs further studies.

4. Materials and Methods

4.1. Collection of Plant Material

C. majus plants were collected in May 2014 from the neighborhood of Poznan, Poland, in compliance with all Adam Mickiewicz University, Polish state and international guidelines and legislation. Plants were identified by Robert Nawrot and the voucher specimen was deposited in the herbal collection of Faculty of Biology, Adam Mickiewicz University, Poznan, Poland with the number CHM_20140514_001 at Molecular Virology Research Unit. The specimen is fully publicly accessible upon request. Both milky sap and aerial parts (stems, leaves, and flowers) were collected from different adult *C. majus* plants of similar developmental stage (height of the plant was ca. 50 cm).

4.1.1. Whole Plant Extracts

The stems were cut, and the exuding orange milky sap was collected. The samples were directly dissolved in 0.1 M Tris-HCl buffer, pH 8.0, containing 10% glycerol (sap:buffer ratio 1:2). The milky sap (33% *v/v*) samples were separated into a supernatant (referred to as a protein fraction) and a pellet fraction by centrifugation at 12,000 rpm for 20 min at 4 °C. Plant tissue samples stored at –80 °C were frozen in liquid nitrogen and powdered in a grinder. Each sample (200 mg) was directly dissolved in 1 mL of 0.1 M Tris-HCl buffer, pH 8.0, containing 10% glycerol.

4.1.2. Milky Sap

The stems of *C. majus* plants were cut, the surface was dried with a filter paper, and the exuding orange milky sap was collected using plastic micropipettes. Depending on the plant and the sampling site, up to 500 µL sample was collected from one stem by using this method. The samples were dissolved in a buffer in a ratio of 1:2. Both extract and milky sap samples were separated into a supernatant (referred to as a protein extract) and a pellet fraction by centrifugation at 12,000 rpm for 20 min at 4 °C. Supernatants were stored at –20 °C for further analysis.

4.2. Protein Separation

Sodium dodecyl sulfate-polyacrylamide gel electrophoresis (SDS-PAGE) was performed in a slab mini-gel apparatus [35] by using 10% polyacrylamide as a separating gel and 5% polyacrylamide as a stacking gel. The proteins were reduced at 100 °C in the presence of 2-mercaptoethanol for 5 min. The gels were then fixed and stained with silver [36]. In-gel DNase assay (zymography) was applied to crude milky sap and whole plant extract samples. The samples were loaded onto SDS-polyacrylamide gels with embedded DNA, and an in-gel DNase assay was performed [36,37]. Extracts and fractions after purification were dissolved in SDS-PAGE sample buffer without a reducing agent (1:1), incubated at 37 °C for 10 min, and subjected to SDS-PAGE in a 10% polyacrylamide gel containing denatured calf thymus DNA (40 µg/mL). Electrophoresis was run at 100 V and 25 mA at 4 °C for approximately 3 h. To remove SDS, the gels were soaked in 25% isopropanol 2 ×

for 20 min at room temperature. The gels were then washed with a renaturation buffer (10 mM Tris-HCl, pH 8.0, containing 10 mM CaCl₂) 1× for 20 min and 1× for overnight at room temperature. The gels were stained with ethidium bromide (0.5 µg/mL) for 15 min, rinsed with distilled water, and visualized under UV light.

4.3. Affinity Chromatography on a Heparin Column

Protein purification of whole plant extracts was conducted using the ÄKTA Explorer System (Amersham Biosciences). Seven samples showing nucleolytic activity were run over a column filled with heparin (HiTrap Heparin column, 0.7·2.5 cm; GE Healthcare, cat. no. 17-0406-01). Heparin shows high affinity to DNA-binding proteins; hence, it is the best choice for affinity chromatography of nucleic acid binding proteins. Proteins with high affinity for heparin were bound to the resin, while the other components were carried through in buffer A and collected in “flow-through” fraction nos. 1–10. The proteins of interest were returned to solution in buffer B in fractions ~18–40. Absorbance was measured at 280 nm for all fractions, and chromatographs were plotted by UNICORN V3.0 software, Amersham Biosciences UK Limited, Little Chalfont, UK. For each run, 40 to 44 fractions were collected.

To isolate and purify proteins from the milky sap, approximately 0.5 µg protein was loaded onto a HiTrap heparin column equilibrated with 0.1 M Tris-HCl, pH 8.0, containing 10% glycerol. The column was eluted with a linear gradient of 0 to 2 M NaCl in the same buffer. The absorbance at 280 nm and DNase activity of all fractions (volume 1 mL) were determined.

4.4. Identification of Proteins Using LC-ESI-MS/MS

Stained protein bands were analyzed by liquid chromatography coupled to LTQ Orbitrap XL (Thermo Fisher Scientific, Waltham, MA, USA) in the Laboratory of Mass Spectrometry, Institute of Biochemistry and Biophysics, PAS, Warsaw, Poland. Excised gel fragments were placed in 1.5 mL Eppendorf tubes filled with 10% methanol and 2% acetic acid. The proteins were digested using trypsin. The generated peptides were concentrated, desalted on an RP-C18 precolumn (LC Packings, Coventry, UK), and further separated by UltiMate nano-HPLC (LC Packings, San Francisco, CA, USA). The column outlet was directly coupled to a Nanospray ion source operating in a data-dependent MS to MS/MS switch mode. Identification of proteins matching with the *C. majus* CDS database was performed (Cmajus 20150107_1; 209,790 sequences; 74,516,318 residues) [8,10] by using the MASCOT database search engine (Matrix Science, London, UK; www.matrixscience.com; accessed on 28 October 2021).

4.5. Identification of Nonprotein Substances by LC-ESI-MS/MS

Nonprotein substances (small molecules) associated with proteins showing nucleolytic activity were identified by LC-ESI-MS/MS in fractions separated by affinity chromatography on the heparin column.

4.5.1. Sample Preparation

Three hundred microliters of acetonitrile and 100 µL of 2 M Na₂CO₃ were added to 100 µL of samples. The samples were vortexed for 1 min and centrifuged for 5 min at 3500 rpm. Because of the high salt content in the collected fractions, acetonitrile did not mix with the aqueous phase, and the supernatant was directly transferred to a chromatographic vial.

4.5.2. Extracts

LC-ESI-MS/MS consisted of an LC-20 chromatograph (Shimadzu, Duisburg, Germany) and a QTRAP 3200 mass spectrometer (ABSciex, Framingham, MA, USA). Separations were conducted using Luna 5u (C18/2) (4.6 · 250 mm; 5 µm) from Phenomenex (Torrance, CA, USA). Gradient elution was performed using 0.1% aqueous solution of

HCOOH (phase A) and 0.1% acetonitrile solution of HCOOH (phase B). The % phase B was increased from 10% up to 90% at 30 min. Flow was set to 1.0 mL/min, the column was maintained at 30 °C, and the samples were kept at 20 °C. Next, 10 µL of the sample was injected into the column. The samples were screened using ESI (+) with the continuous MS scan mode in the first quadrupole (m/z 100–1000) and scan of product ions in the second quadrupole (m/z 100–1000). We used ESI (+) due to higher signal intensities than ESI (–). Parent ions for fragmentation were selected automatically by the software on the basis of the initial MS scan. Analyst ver. 1.4.2 (Sciex, Washington, DC, USA) was used as the data processing software. Measurements were performed at the Structural Research Laboratory of the Chemistry Department, University of Warsaw, Poland.

4.5.3. Milky Sap

LC-ESI-MS/MS consisted of an Alliance 2695 chromatograph coupled with a Quattro Micro mass spectrometer (Waters, Milford, CT, USA). Gradient elution was performed using a C18 Zorbax column (3.0·150 mm; 3.0 µm) (Agilent Technologies, Santa Clara, CA, USA). The mobile phase consisted of 0.1% HCOOH solution in 9:1 (v/v) H₂O/acetonitrile mixture (phase A) and 0.1% HCOOH solution in 1:9 (v/v) H₂O/acetonitrile mixture (phase B). The % phase B was increased from 0% up to 100% at 50 min. Flow was set to 0.3 mL/min, the column was maintained at 30 °C, and the samples were kept at 20 °C. Next, 10 µL of the sample was injected into the column. The samples were screened using ESI (+) with Single Ion Monitoring (SIM) and a continuous single quadrupole mass scan (m/z 300–400). Twenty-eight values of m/z were monitored based on signals observed in preliminary experiments and the expected analytes. Each value monitored with SIM was microscanned for ±0.1 unit. Additional measurements were performed for each sample with MS scan (m/z 200–400). Data acquisition and processing were performed using MassLynx ver. 4.1 software, Waters Corporation, Milford, MA, USA. The measurements were performed at the Pharmacology Department, Pharmaceutical Research Institute, Warsaw, Poland. A total of 21 signals were selected for indirect comparison on the basis of a peak area's ratio of a given substance to the reference signal. A signal with intensity at m/z 342.2 was used as a reference (no. 21; 100% relative signal intensity).

4.6. Cell Lines

An HPV-positive human epithelial cancer cell line (HeLa) and an HPV-negative human epithelial cancer cell line (C33A) were obtained from American Type Culture Collection (ATCC, Manassas, VA, USA). The normal human fibroblast cell line (MSU-1.1) was provided by Prof. C. Kieda (CBM, CNRS, Orleans, France). All cell lines were grown in Dulbecco's Modified Eagle's Medium (DMEM) with high glucose, GlutaMAX™, and sodium pyruvate (Gibco, Life Technologies). The medium was supplemented with 10% (v/v) fetal bovine serum (Sigma-Aldrich) and 1% (v/v) antibiotics (penicillin and streptomycin, Sigma-Aldrich). All cells were cultivated as a monolayer on sterile culture plates (Sarstedt) at 37 °C in an atmosphere of 95% air and 5% CO₂. When the cell culture reached a confluence of almost 80%, the medium was drained from the cell culture, and the adherent cells were washed with phosphate buffered saline (PBS, Sigma-Aldrich) and trypsinized with 0.25% Trypsin-EDTA (Sigma-Aldrich). After detachment of the cells, fresh medium was added to the culture, and the cells were counted by a TC10 Automated Cell Counter (Bio-Rad) and used to seed onto sterile tissue plates (Sarstedt).

4.7. Cell Viability and Cytotoxicity Test

To assess cell viability, the WST-1 colorimetric assay (Premixed WST-1 Cell Proliferation Reagent, Clontech) was used. The assay is based on the reduction of tetrazolium WST-1 salt (2-(4-iodophenyl)-3-(4-nitrophenyl)-5-(2,4-disulfophenyl)-2H-tetrazolium) to a soluble formazan by metabolically active cells, the concentration of which is directly proportional to the number of viable cells. HeLa, C33A, and normal fibroblasts (MSU-1.1) were seeded onto sterile 96-well tissue culture microplates (Sarstedt) at the concentration of 0.6×10^4

HeLa cells/well, 1.5×10^4 C33A cells/well, and 1×10^4 MSU-1.1 cells/well and incubated overnight in an incubator under standard conditions (at 37 °C and 5 wt% CO₂). The stale medium was removed, cells were gently washed with PBS, and fresh medium with 20 µL of each fraction (protein concentration at 1–2 ng/µL) was added to selected wells to achieve a final volume of 100 µL/well. Untreated cells were used as negative control. Cells treated with 10% solution of DMSO (Sigma-Aldrich) were used as positive control. Next, plates were incubated at 37 °C and 5 wt% CO₂ for 48 h. Then, 10 µL of WST-1 was added to each well and incubated for additional 2 h at 37 °C. The absorbance, which is proportional to cell viability, was measured by a spectrophotometer (Biochrom Anthos Zenyth 340 Microplate Reader) at 450 nm. Each cytotoxicity experiment was repeated at least three times. Cell viability was calculated as follows: Absorbance of treated cells/Absorbance of untreated (control) cells · 100%. Both HeLa and C33A cell lines are derived from cervical cancer samples of women. HeLa cells are HPV-positive (HPV+), while C33A are HPV-negative (HPV–). Statistics. All experiments were performed thrice. Statistical significance was calculated using GraphPad Prism (version 9.0.0), software (GraphPad Software, San Diego, CA, USA) and an unpaired *t* test.

4.8. MLP Structure Prediction and 3D Modeling

Tertiary structure prediction and fold-recognition were performed using the GeneSilico MetaServer gateway [38]. The top-scoring fold-recognition alignments to the structures of the selected template were used as a starting point for homology modeling using “Frankenstein’s Monster” approach [39,40], which comprises cycles of model building, evaluation, realignment in poorly scored regions, and merging of the best scoring fragments. For model evaluation, two Model Quality Assessment Programs (MQAPs) were used: MetaMQAP [41] and PROQ [42]. MQAP scores can only predict the deviation of a model from the real structure (the actual deviation can be calculated only by comparison with the real structures, which are not available). Thus, the scores reported must be interpreted as estimates or predictions and not as ultimate validation of the model quality. However, both PROQ and MetaMQAP performed quite well in independent benchmarks and can be regarded as robust predictors. NCBI CDD [43] and GeneSilico MetaServer [38] predicted the conserved hydrophobic cavity for binding of small molecules in the structure of CmMLP1. The predicted quality of the mature protein structure is illustrated according to Cristobal et al. [44].

4.9. Molecular Docking

Alkaloid structures (ZINC01575028, dihydroberberine; ZINC03872044, 8-hydroxycheilanthrine; ZINC03779067, berberine; ZINC20111233, protopine; ZINC01709414, coptisine; ZINC00000706, sanguinarine; ZINC20470298, stylophine; ZINC30727894, chelidone) were retrieved from the ZINC database (<http://zinc.docking.org/>, accessed on 28 October 2021) and analyzed using Autodock Vina14 (The Scripps Research Institute, La Jolla, CA, USA) implemented in Chimera13 package. AutoDock Vina analysis was performed according to the strength of interaction between hydrophobic amino acids forming “pockets” in the MLP with the respective ligands and visualized by PyMOL (DeLano Scientific, San Carlos, CA, USA). For each of the 8 studied alkaloids, we analyzed 20 possible conformations of the ligand molecule at the active site of the protein. For the conformation with the lowest binding energy, interaction analysis with amino acid residues at the active site of the protein was performed by considering hydrogen bonds and ionic, hydrophobic, and π -electron interactions of aromatic rings (PoseView15) (structures retrieved from ZINC database). The conformational analysis was performed using the Autodock Vina program. It analyzes 20 possible conformations of the ligand molecule at the active site of the protein and calculates binding energy for each conformation.

5. Conclusions

To conclude, we combined biological chemistry and analytical and theoretical techniques to discover the molecular association between CmMLP1 and three alkaloids, namely dihydroberberine, 8-hydroxyceleritrine, and berberine, from *C. majus* milky sap. It was possible with the help of the developed toolbox and the proposed workflow (Figure 1), which may stimulate advanced research that links small molecular and macromolecular biology, botany, and pharmacognosy. The limitation of the work, which was the research using only one plant species, could be also its strength for future research. We isolated the MLP from *C. majus* latex and identified the accompanying low-molecular-weight compounds. We then analyzed their combined cytotoxic activities against cervical cancer cell lines. The cell viability was the lowest for HeLa HPV positive cells—with less than 10% of living cells—twice lower as for C33A HPV negative cells. A significant decrease in the viability of human cervical cancer cells may suggest the synergistic effect of CmMLP1 and alkaloids. Our results suggest conformation-related mechanism of their interaction; however, it still remains unknown and will be an interesting topic for further studies. Resolving these interactions will definitely help to elucidate the mechanism of anti-HPV activity of the *C. majus* latex. Another important topic concerns the function of the CmMLP1 for the plant's latex and for overall plant physiology [34]. The proposed toolbox and workflow may therefore advance pharmacognosy, plant disease resistance research, and agricultural practices [45] to strengthen plant defense and to propose novel bioactive combinations of macro- and low-molecular compounds from different plant species with the advantage to modern pharmacology.

Supplementary Materials: The following are available online at <https://www.mdpi.com/article/10.3390/ijms222111838/s1>.

Author Contributions: Conceptualization, R.N. and A.G.-J.; methodology, R.N.; software, O.M. and K.M.D.; validation, A.W., P.J.R., J.M. and E.U.S.; formal analysis, R.N.; investigation, R.N., A.W., O.M., K.M.D., P.J.R., J.M. and E.U.S.; resources, R.N.; data curation, R.N., A.W., O.M. and K.M.D.; writing—original draft preparation, R.N., A.W. and P.J.R.; writing—review and editing, R.N., A.W., P.J.R., O.M., K.M.D., A.G.-J.; visualization, O.M. and K.M.D.; supervision, A.G.-J.; project administration, R.N.; funding acquisition, R.N. All authors have read and agreed to the published version of the manuscript.

Funding: This research was funded by the National Science Centre, Poland (grant numbers 2012/05/N/NZ9/01337, 2016/21/N/NZ6/00997 and 2019/35/B/NZ9/03851).

Institutional Review Board Statement: Not applicable.

Informed Consent Statement: Not applicable.

Data Availability Statement: Data is contained within the article or Supplementary Materials. The data presented in this study are available in “Supplementary Information” and “Supplementary Data Set” Files.

Acknowledgments: We would like to greatly acknowledge Wojciech Białas from Department of Biotechnology and Food Microbiology, Poznan University of Life Sciences, Poland, for help with chromatographic analyses on heparin column and Anna Czerwoniec from Zylia sp. z o.o. (Zylia Ltd., Poznań, Poland) for 3D modeling and molecular docking analyses. We also thank the Laboratory of Mass Spectrometry, Institute of Biochemistry and Biophysics, PAS, Warsaw, Poland for protein identifications using LC-ESI-MS/MS. The equipment used was sponsored in part by the Centre for Preclinical Research and Technology (CePT), a project co-sponsored by European Regional Development Fund and Innovative Economy, The National Cohesion Strategy of Poland.

Conflicts of Interest: The authors declare no conflict of interest.

References

1. Li, F.-S.; Weng, J.-K. Demystifying Traditional Herbal Medicine with Modern Approach. *Nat. Plants* **2017**, *3*, 17109. [CrossRef]
2. Teixidor-Toneu, I.; Jordan, F.M.; Hawkins, J.A. Comparative Phylogenetic Methods and the Cultural Evolution of Medicinal Plant Use. *Nat. Plants* **2018**, *4*, 754–761. [CrossRef]

3. Musidlak, O.; Baldysz, S.; Krakowiak, M.; Nawrot, R. Plant Latex Proteins and Their Functions. *Adv. Bot. Res.* **2020**, *93*, 55–97.
4. Zielińska, S.; Jezierska-Domaradzka, A.; Wójciak-Kosior, M.; Sowa, I.; Junka, A.; Matkowski, A.M. Greater Celandine's Ups and Downs—21 Centuries of Medicinal Uses of *Chelidonium majus* From the Viewpoint of Today's Pharmacology. *Front. Pharmacol.* **2018**, *9*, 299. [CrossRef]
5. Maji, A.K.; Banerji, P. *Chelidonium Majus* L. (Greater Celandine)—A Review on Its Phytochemical and Therapeutic Perspectives. *Int. J. Herb. Med.* **2015**, *3*, 10–27. [CrossRef]
6. Warowicka, A.; Popena, L.; Bartkowiak, G.; Musidlak, O.; Litowczenko-Cybulska, J.; Kuźma, D.; Nawrot, R.; Jurga, S.; Goździcka-Józefiak, A. Protoberberine Compounds Extracted from *Chelidonium majus* L. as Novel Natural Photosensitizers for Cancer Therapy. *Phytomedicine* **2019**, *64*, 152919. [CrossRef]
7. Nawrot, R. Defense-Related Proteins from *Chelidonium majus* L. as Important Components of Its Latex. *Curr. Protein Pept. Sci.* **2017**, *18*, 864–880. [CrossRef] [PubMed]
8. Konno, K. Plant Latex and Other Exudates as Plant Defense Systems: Roles of Various Defense Chemicals and Proteins Contained Therein. *Phytochemistry* **2011**, *72*, 1510–1530. [CrossRef] [PubMed]
9. Nawrot, J.; Wilk-Jędrusik, M.; Nawrot, S.; Nawrot, K.; Wilk, B.; Dawid-Pač, R.; Urbańska, M.; Micek, I.; Nowak, G.; Gornowicz-Porowska, J. Milky Sap of Greater Celandine (*Chelidonium majus* L.) and Anti-Viral Properties. *Int. J. Environ. Res. Public Health* **2020**, *17*, 1540. [CrossRef] [PubMed]
10. Eid, S.Y.; El-Readi, M.Z.; Wink, M. Synergism of Three-Drug Combinations of Sanguinarine and Other Plant Secondary Metabolites with Digitonin and Doxorubicin in Multi-Drug Resistant Cancer Cells. *Phytomedicine* **2012**, *19*, 1288–1297. [CrossRef]
11. Monavari, S.H.; Shahrabadi, M.S.; Keyvani, H.; Bokharaei-Salim, F. Evaluation of in Vitro Antiviral Activity of *Chelidonium majus* L. against Herpes Simplex Virus Type-1. *Afr. J. Microbiol. Res.* **2012**, *6*, 4360–4364.
12. Nawrot, R.; Lesniewicz, K.; Pienkowska, J.; Goździcka-Jozefiak, A. A Novel Extracellular Peroxidase and Nucleases from a Milky Sap of *Chelidonium Majus*. *Fitoterapia* **2007**, *78*, 496–501. [CrossRef] [PubMed]
13. Nawrot, R.; Wołuń-Cholewa, M.; Goździcka-Józefiak, A. Nucleases Isolated from *Chelidonium majus* L. Milky Sap Can Induce Apoptosis in Human Cervical Carcinoma HeLa Cells but Not in Chinese Hamster Ovary CHO Cells. *Folia Histochem. Cytobiol.* **2008**, *46*, 79–83. [CrossRef] [PubMed]
14. Nawrot, R.; Lippmann, R.; Matros, A.; Musidlak, O.; Nowicki, G.; Mock, H.-P. Proteomic Comparison of *Chelidonium majus* L. Latex in Different Phases of Plant Development. *Plant Physiol. Biochem.* **2017**, *112*, 312–325. [CrossRef] [PubMed]
15. Radauer, C.; Lackner, P.; Breiteneder, H. The Bet v 1 Fold: An Ancient, Versatile Scaffold for Binding of Large, Hydrophobic Ligands. *BMC Evol. Biol.* **2008**, *8*, 286. [CrossRef]
16. Chruszcz, M.; Ciardiello, M.A.; Osinski, T.; Majorek, K.A.; Giangrieco, I.; Font, J.; Breiteneder, H.; Thalassinou, K.; Minor, W. Structural and Bioinformatic Analysis of the Kiwifruit Allergen Act D 11, a Member of the Family of Ripening-Related Proteins. *Mol. Immunol.* **2013**, *56*, 794–803. [CrossRef] [PubMed]
17. Nessler, C.L. Sequence Analysis of Two New Members of the Major Latex Protein Gene Family Supports the Triploid-Hybrid Origin of the Opium Poppy. *Gene* **1994**, *139*, 207–209. [CrossRef]
18. Decker, G.; Wanner, G.; Zenk, M.H.; Lottspeich, F. Characterization of Proteins in Latex of the Opium Poppy (*Papaver Somniferum*) Using Two-Dimensional Gel Electrophoresis and Microsequencing. *Electrophoresis* **2000**, *21*, 3500–3516. [CrossRef]
19. Ruperti, B.; Bonghi, C.; Ziliotto, F.; Pagni, S.; Rasori, A.; Varotto, S.; Tonutti, P.; Giovannoni, J.J.; Ramina, A. Characterization of a Major Latex Protein (MLP) Gene down-Regulated by Ethylene during Peach Fruitlet Abscission. *Plant Sci.* **2002**, *163*, 265–272. [CrossRef]
20. Yang, C.-L.; Liang, S.; Wang, H.-Y.; Han, L.-B.; Wang, F.-X.; Cheng, H.-Q.; Wu, X.-M.; Qu, Z.-L.; Wu, J.-H.; Xia, G.-X. Cotton Major Latex Protein 28 Functions as a Positive Regulator of the Ethylene Responsive Factor 6 in Defense against *Verticillium Dahliae*. *Mol. Plant* **2015**, *8*, 399–411. [CrossRef]
21. Malter, D.; Wolf, S. Melon Phloem-Sap Proteome: Developmental Control and Response to Viral Infection. *Protoplasma* **2011**, *248*, 217–224. [CrossRef] [PubMed]
22. Nawrot, R.; Barylski, J.; Lippmann, R.; Altschmied, L.; Mock, H.-P. Combination of Transcriptomic and Proteomic Approaches Helps to Unravel the Protein Composition of *Chelidonium majus* L. Milky Sap. *Planta* **2016**, *244*, 1055–1064. [CrossRef]
23. Nawrot, R.; Kalinowski, A.; Goździcka-Jozefiak, A. Proteomic Analysis of *Chelidonium majus* Milky Sap Using Two-Dimensional Gel Electrophoresis and Tandem Mass Spectrometry. *Phytochemistry* **2007**, *68*, 1612–1622. [CrossRef]
24. Doorbar, J.; Egawa, N.; Griffin, H.; Kranjec, C.; Murakami, I. Human Papillomavirus Molecular Biology and Disease Association. *Rev. Med. Virol.* **2015**, *25* (Suppl. 1), 2–23. [CrossRef]
25. Song, L.; Wang, J.; Jia, H.; Kamran, A.; Qin, Y.; Liu, Y.; Hao, K.; Han, F.; Zhang, C.; Li, B.; et al. Identification and Functional Characterization of NbMLP28, a Novel MLP-like Protein 28 Enhancing Potato Virus Y Resistance in *Nicotiana Benthiana*. *BMC Microbiol.* **2020**, *20*, 55. [CrossRef] [PubMed]
26. Lytle, B.L.; Song, J.; de la Cruz, N.B.; Peterson, F.C.; Johnson, K.A.; Bingman, C.A.; Phillips, G.N., Jr.; Volkman, B.F. Structures of Two *Arabidopsis Thaliana* Major Latex Proteins Represent Novel Helix-Grip Folds. *Proteins* **2009**, *76*, 237–243. [CrossRef] [PubMed]
27. Park, C.-J.; Kim, K.-J.; Shin, R.; Park, J.M.; Shin, Y.-C.; Paek, K.-H. Pathogenesis-Related Protein 10 Isolated from Hot Pepper Functions as a Ribonuclease in an Antiviral Pathway. *Plant J.* **2004**, *37*, 186–198. [CrossRef] [PubMed]

28. Paul, A.; Bishayee, K.; Ghosh, S.; Mukherjee, A.; Sikdar, S.; Chakraborty, D.; Boujedaini, N.; Khuda-Bukhsh, A.R. Chelidonine Isolated from Ethanolic Extract of *Chelidonium majus* Promotes Apoptosis in HeLa Cells through p38-p53 and PI3K/AKT Signalling Pathways. *Zhong Xi Yi Jie He Xue Bao* **2012**, *10*, 1025–1038. [CrossRef] [PubMed]
29. Havelek, R.; Seifrtova, M.; Kralovec, K.; Krocova, E.; Tejkalova, V.; Novotny, I.; Cahlikova, L.; Safratova, M.; Opletal, L.; Bilkova, Z.; et al. Comparative Cytotoxicity of Chelidonine and Homochelidonine, the Dimethoxy Analogues Isolated from *Chelidonium majus* L.(Papaveraceae), against Human Leukemic and Lung Carcinoma Cells. *Phytomedicine* **2016**, *23*, 253–266. [CrossRef]
30. El-Readi, M.Z.; Eid, S.; Ashour, M.L.; Tahrani, A.; Wink, M. Modulation of Multidrug Resistance in Cancer Cells by Chelidonine and *Chelidonium majus* Alkaloids. *Phytomedicine* **2013**, *20*, 282–294. [CrossRef]
31. Goodwin, E.C.; DiMaio, D. Repression of Human Papillomavirus Oncogenes in HeLa Cervical Carcinoma Cells Causes the Orderly Reactivation of Dormant Tumor Suppressor Pathways. *Proc. Natl. Acad. Sci. USA* **2000**, *97*, 12513–12518. [CrossRef]
32. Xiao, C.-Y.; Fu, B.-B.; Li, Z.-Y.; Mushtaq, G.; Kamal, M.A.; Li, J.-H.; Tang, G.-C.; Xiao, S.-S. Observations on the Expression of Human Papillomavirus Major Capsid Protein in HeLa Cells. *Cancer Cell Int.* **2015**, *15*, 53. [CrossRef]
33. Pang, Y.-N.; Liang, Y.-W.; Feng, T.-S.; Zhao, S.; Wu, H.; Chai, Y.-S.; Lei, F.; Ding, Y.; Xing, D.-M.; Du, L.-J. Transportation of Berberine into HepG2, HeLa and SY5Y Cells: A Correlation to Its Anti-Cancer Effect. *PLoS ONE* **2014**, *9*, e112937. [CrossRef] [PubMed]
34. Fujita, K.; Inui, H. Review: Biological Functions of Major Latex-like Proteins in Plants. *Plant Sci.* **2021**, *306*, 110856. [CrossRef]
35. Laemmli, U.K. Cleavage of Structural Proteins during the Assembly of the Head of Bacteriophage T4. *Nature* **1970**, *227*, 680–685. [CrossRef] [PubMed]
36. Ito, J.; Fukuda, H. ZEN1 Is a Key Enzyme in the Degradation of Nuclear DNA during Programmed Cell Death of Tracheary Elements. *Plant Cell* **2002**, *14*, 3201–3211. [CrossRef] [PubMed]
37. Thelen, M.P.; Northcote, D.H. Identification and Purification of a Nuclease from *Zinnia Elegans* L.: A Potential Molecular Marker for Xylogenesis. *Planta* **1989**, *179*, 181–195. [CrossRef]
38. Kurowski, M.A.; Bujnicki, J.M. GeneSilico Protein Structure Prediction Meta-Server. *Nucleic Acids Res.* **2003**, *31*, 3305–3307. [CrossRef]
39. Kosinski, J.; Cymerman, I.A.; Feder, M.; Kurowski, M.A.; Sasin, J.M.; Bujnicki, J.M. A 'Frankenstein's Monster? Approach to Comparative Modeling: Merging the Finest Fragments of Fold-Recognition Models and Iterative Model Refinement Aided by 3D Structure Evaluation. *Proteins: Struct. Funct. Genet.* **2003**, *53*, 369–379. [CrossRef]
40. Kosinski, J.; Gajda, M.J.; Cymerman, I.A.; Kurowski, M.A.; Pawlowski, M.; Boniecki, M.; Obarska, A.; Papaj, G.; Sroczynska-Obuchowicz, P.; Tkaczuk, K.L.; et al. Frankenstein Becomes a Cyborg: The Automatic Recombination and Realignment of Fold Recognition Models in CASP6. *Proteins* **2005**, *61* (Suppl. 7), 106–113. [CrossRef] [PubMed]
41. Pawlowski, M.; Gajda, M.J.; Matlak, R.; Bujnicki, J.M. MetaMQAP: A Meta-Server for the Quality Assessment of Protein Models. *BMC Bioinform.* **2008**, *9*, 403. [CrossRef] [PubMed]
42. Wallner, B.; Elofsson, A. Can Correct Protein Models Be Identified? *Protein Sci.* **2003**, *12*, 1073–1086. [CrossRef] [PubMed]
43. Marchler-Bauer, A.; Anderson, J.B.; Chitsaz, F.; Derbyshire, M.K.; DeWeese-Scott, C.; Fong, J.H.; Geer, L.Y.; Geer, R.C.; Gonzales, N.R.; Gwadz, M.; et al. CDD: Specific Functional Annotation with the Conserved Domain Database. *Nucleic Acids Res.* **2009**, *37*, D205–D210. [CrossRef] [PubMed]
44. Cristobal, S.; Zemla, A.; Fischer, D.; Rychlewski, L.; Elofsson, A. A Study of Quality Measures for Protein Threading Models. *BMC Bioinform.* **2001**, *2*, 5. [CrossRef] [PubMed]
45. Zhang, H.; Li, Y.; Zhu, J.-K. Developing Naturally Stress-Resistant Crops for a Sustainable Agriculture. *Nat. Plants* **2018**, *4*, 989–996. [CrossRef]



Review

Functional Studies of Plant Latex as a Rich Source of Bioactive Compounds: Focus on Proteins and Alkaloids

Joanna Gracz-Bernaciak , Oliwia Mazur and Robert Nawrot *

Molecular Virology Research Unit, Institute of Experimental Biology, Faculty of Biology, Adam Mickiewicz University, Poznań, Uniwersytetu Poznańskiego 6, 61-614 Poznań, Poland; joanna.gracz-bernaciak@amu.edu.pl (J.G.-B.); oliwia.mazur@amu.edu.pl (O.M.)

* Correspondence: rnawrot@amu.edu.pl; Tel.: +48-61-829-5931

Abstract: Latex, a sticky emulsion produced by specialized cells called laticifers, is a crucial part of a plant's defense system against herbivory and pathogens. It consists of a broad spectrum of active compounds, which are beneficial not only for plants, but for human health as well, enough to mention the use of morphine or codeine from poppy latex. Here, we reviewed latex's general role in plant physiology and the significance of particular compounds (alkaloids and proteins) to its defense system with the example of *Chelidonium majus* L. from the poppy family. We further attempt to present latex chemicals used so far in medicine and then focus on functional studies of proteins and other compounds with potential pharmacological activities using modern techniques such as CRISPR/Cas9 gene editing. Despite the centuries-old tradition of using latex-bearing plants in therapies, there are still a lot of promising molecules waiting to be explored.

Keywords: latex; antiviral proteins; antimicrobial compounds; cytotoxicity; drug discovery; *Chelidonium majus*; CRISPR/Cas9

Citation: Gracz-Bernaciak, J.; Mazur, O.; Nawrot, R. Functional Studies of Plant Latex as a Rich Source of Bioactive Compounds: Focus on Proteins and Alkaloids. *Int. J. Mol. Sci.* **2021**, *22*, 12427. <https://doi.org/10.3390/ijms222212427>

Academic Editor: Gerard Pujadas

Received: 15 October 2021

Accepted: 13 November 2021

Published: 17 November 2021

Publisher's Note: MDPI stays neutral with regard to jurisdictional claims in published maps and institutional affiliations.



Copyright: © 2021 by the authors. Licensee MDPI, Basel, Switzerland. This article is an open access article distributed under the terms and conditions of the Creative Commons Attribution (CC BY) license (<https://creativecommons.org/licenses/by/4.0/>).

1. Introduction

Latex-bearing plants have a long history of benefiting human health and medicinal use in many different regions and cultures all over the world. Recent research suggests that the opium poppy (*Papaver somniferum* L.) was already in the process of domestication at the end of 4th millennium BC [1] and early domesticated ancestors of *Cannabis sativa* L. diverged ~10,000 years BC [2]. Those are two leading examples of laticiferous plant species used for therapies and together with *Hevea brasiliensis* Muli. Arg., which is the main and irreplaceable natural rubber source, have the best known and described latex composition. These complex fluids consist of different secondary metabolites, like terpenes, alkaloids, or phenolics, and jointly with a broad range of proteins are the first line of plant herbivore defense system. Another extensively studied laticiferous medicinal plant is Greater Celandine (*Chelidonium majus* L.), a relative of the opium poppy, which is a rich source of numerous biologically active compounds, used in traditional folk medicine as antiviral, antibacterial, antifungal, choleric, and anticancer agents [3–6]. Many compounds of latex are active in both eukaryotic and prokaryotic organisms [7]. At present, when mankind is running out of antibiotics and other antimicrobial compounds, new cancer therapies are still needed, and to make matters worse, the scale of pest and microbial resistance is increasing. Thus, the exploration of such rich natural deposits of active molecules is a very promising research direction.

This review paper characterizes the main components of latex and summarizes their known potentially therapeutic activities. We focus on two classes of compounds, proteins and alkaloids, which represent complex macromolecules and low-molecular compounds. Both types of molecules co-exist in plant latex and possibly actively cooperate in a synergistic manner to enable and boost their biological activities. We propose a model of antiviral latex activity and present examples of CRISPR/Cas9 editing genomes, which

can shed light on a complex network of specialized metabolites synthesis and interactions or complementation. Despite its long history of use, there is still room for improvement of agronomic traits in domesticated latex-bearing plants and for the exploitation of wild species latex compounds to prepare a range of novel compounds of therapeutic potential, as well as novel drugs and drug carriers.

2. Diversity and Role of Latex in Plant Physiology

Latex is a milky emulsion produced by complex secretory structures called laticifers. It is defined as a suspension of various particles (organic and inorganic) dispersed in a liquid with different refractive index. Depending on prevalent content and plant species studied, it can be milky white or yellowish, orange to brown or even colorless. However, it is more than a liquid. It is identified as a laticifer's protoplast with mitochondria, plastids, endoplasmic reticulum, Golgi bodies, polyribosomes, and vacuoles [8]. Laticifers are latex-producing, highly specialized plant cells or connected cells, which are spread through the whole plant body in the form of linear tubes which can grow and elongate with plant organs. They can be found in almost every part of latescent plants, namely in the root, stem, leaf, sepal, petal, stamen, ovary, and stigma, or they can occur only in some particular organs. Latex occupies the whole volume of the laticifer system [9].

Latex was identified in at least 20,000 plant species belonging to 43 families of vascular plants. Most of them are Angiosperms (41 families), one family belongs to ferns, and one to gymnosperms [8–10]. In a great example of convergent evolution events in the plant kingdom, latex occurrences take place several times in phylogenetically unrelated orders. Laticifers developed in both monocotyledonous and dicotyledonous, in the basal clades (Ana-grade), magnoliids, monocots, basal eudicots, rosids, and asterides [11,12]. One morphotype of laticifers, articulated, which are fused chains of cells with intact, porous, or even absent terminal walls, form laticiferous vessels and were recorded in 27 families. The other main morphotype is called non-articulated, which occurs more rarely and is formed by a single plant cell with almost infinite growth potential. Both types of laticifers can extend not only longitudinally with the growth of organs, but also radically create branched networks of tubes. For the proper classification of the laticifer system, it is essential to use plant material with embryos or meristems. Only based on ontology can articulated and non-articulated morphotypes be distinguished (analysis of number of precursor cells and phase of laticifers development often coupled with analysis of laticifers enzymatic activity of pectinases and chitinases, with the latter active only in articulated laticifers [13]). Previously, cases of incorrect assignment to the appropriate laticifer types were described, e.g., for mulberry [14,15] or for *Ficus montana* Burm.f. and *Maclura tinctoria* L. [13]. Attempts were made to use types of laticifers as a diagnostic tool for some taxa, but it is more likely that different morphotypes will be found in different species within the same family [11].

Nowadays, it is well established that the biological role of latex is plant defense against herbivores and pathogens [10], but in 1989 Webster and Baulk concluded that the function of latex was unknown [16]. Many latex metabolites are stored within large vacuoles and are released after being physically damaged at the site of injury. Some of them act as toxic and dissuasive components. After mechanical disruption of plant tissue, latex is immediately released and is the first line of plant defense. Thanks to its inherent stickiness and coagulation properties, latex forms a barrier against pathogen invasion. Moreover, latex's rapid coagulation and high viscosity can restrict herbivore movements, as well as immobilize mouthparts and other sense organs [17]. This strategy gives an advantage to latescent plants, especially in environments with high a herbivory rate, like tropical or subtropical forests [18].

3. Main Components of Latex-Secondary Metabolites

Taking into consideration the defense role of latex in plant development, it should not be surprising how complex and diverse the latex composition can be. Despite tremendous

variability in latex components, which is dependent on the species, phase of development, external and internal stimuli, and stresses [19], two major groups of biologically active compounds can be distinguished, namely secondary metabolites and proteins. Many of those products are cytotoxic and it was suggested that laticifers evolved as sequestering compartments, which ensure the storage of such substances regardless of the vascular system. This solution provides a unique and preformed defense mechanism with almost immediate response to herbivory attack. The internal pressure of latex causes the secretion of concentrated active substances at the point of damage in a few seconds. In contrast, an inducible defense system needs hours or even days to synthesize and collect sufficient amounts of active substances to act against pathogens [20]. In the context of latex composition, it is worth noticing that a synergetic mode of action was established for some of its constituents, like terpenes associated with phenolic compounds [20,21] or different proteins exhibiting defense functions against insects or fungi [22,23]. Therapeutic properties of selected latex compounds are described in detail in Section 5. Below, we present a short characterization of secondary metabolites common for latex-bearing plants.

Secondary metabolites are a heterogeneous group of chemical compounds not essential to vegetative growth, but for plant adaptation to changes in the external as well as internal environment. As mentioned before, the presence of specific metabolites in latex is a highly species-specific trait, but in general terpenes, phenolics, alkaloids, and cardenolides are present in most of the laticifer types.

One of the most abundant groups of secondary metabolites in plant latex are isoprene-derived compounds, terpenes. Within this group, the most economically important member is rubber (cis-1,4-polyisoprene), which is found in 2500 plant species (300 plant genera from eight families) [7,24], but harvested on global scale from one, *Hevea brasiliensis* species. Rubber particles may constitute up to 50% of *H. brasiliensis* latex volume [25]. It is proposed that the main function of rubber is related to the coagulation process [20], but it was also suggested that rubber biosynthesis accumulate excess of photosynthate and prevent damage to photosynthesis apparatus under stress conditions [26].

Apart from rubber, in latex of *Euphorbia* genus, some triterpenoids (i.e., cycloartenol, 24-methylenecycloartenol, lupeol, lupeol acetate, lanosterol, and 24-methylenelanosterol) are always present in higher concentration than in other organs. Similarly, latex of *Lactuca sativa* L. contains high levels of several sesquiterpene lactones (concentration of lactucopicrin oxalate is 1000 higher than in leaves) [27]. Those terpenoids are often accompanied with steroids. It is presumed that together they can disrupt cell walls of insects or microorganisms, intercalate membranes, and form channels which enable the migration of small, toxic, hydrophilic molecules such as phenolics inside the cell [28].

Phenolics (e.g., tannins, lignans, coumarins, flavonoids), another broad group of secondary metabolites found in latex, have been known for their antioxidant properties and taking part in response to oxidative stress conditions [29]. They are mainly products of shikimate pathways and were found, among others, in latex of sweet potato *Ipomoea batatas* L. The overall concentration of p-coumarate esters exceeded 3% fresh vine latex and 10% root latex of the variety "Jewel". The presence of those phenolics is inversely correlated with the acceptability of sweet potato by weevils [30], which supports the anti-herbivore latex function. Different polyphenol compounds were identified in latex of *H. brasiliensis*, namely gallic acid, naphthoic acid, quercetin, chlorogenic acid, and rutin, which are also postulated to play a role in plant defense system [31]. In common dandelion (*Taraxacum officinale* F.H. Wigg.), phenolic esters, next to sesquiterpene lactones and triterpene acetates, were found in high concentration in the main root. Those active compounds showed a repelling effect in experiments with *Diabrotica balteata* larvae [32].

Another group of secondary metabolites sequestered in laticifers are alkaloids. Those amino acid derivatives, which are highly bioactive and often toxic, serve eco-physiological functions in plants, providing better fitness to specific environmental niches [33]. Alkaloids for thousands of years have been used and abused by humans, even leading to military conflicts (like opium wars in the 19th century or ongoing drug wars in many countries).

Those low molecular compounds were found amongst 35 families, mostly angiosperms, including Apocynaceae, Papaveraceae, and Moraceae [8]. The best known and described example of laticifers rich in alkaloids is opium, namely the dried latex of *P. somniferum* used in folk and traditional medicine, as well as psychedelic drugs. Opium contains at least 20 alkaloids, such as morphine, papaverine, and codeine. Morphine may constitute up to 5% of fresh latex, and codeine up to 1% [34]. Latex of *Chelidonium majus*, a species closely related to *P. somniferum*, is also a rich source of bioactive alkaloids, e.g., chelidoniumine, sanguinarine, berberine or coptisine (chemical structures are depicted on Figure 1). Those isoquinoline alkaloids can reach up to 20% of fresh latex mass [35] and are known for their multiple pharmacological effects (antioxidant, anti-inflammatory, anticancer, anti-neurodegenerative, and antimicrobial). Although *C. majus* is related to *P. somniferum*, its latex does not contain morphine-like alkaloids, such as morphine or codeine, and therefore does not have sedative effects. Yet, some of the *C. majus* secondary metabolites, like berberine and chelidoniumine, as well as protein enriched extracts can have analgesic effects, similar to morphine [36]

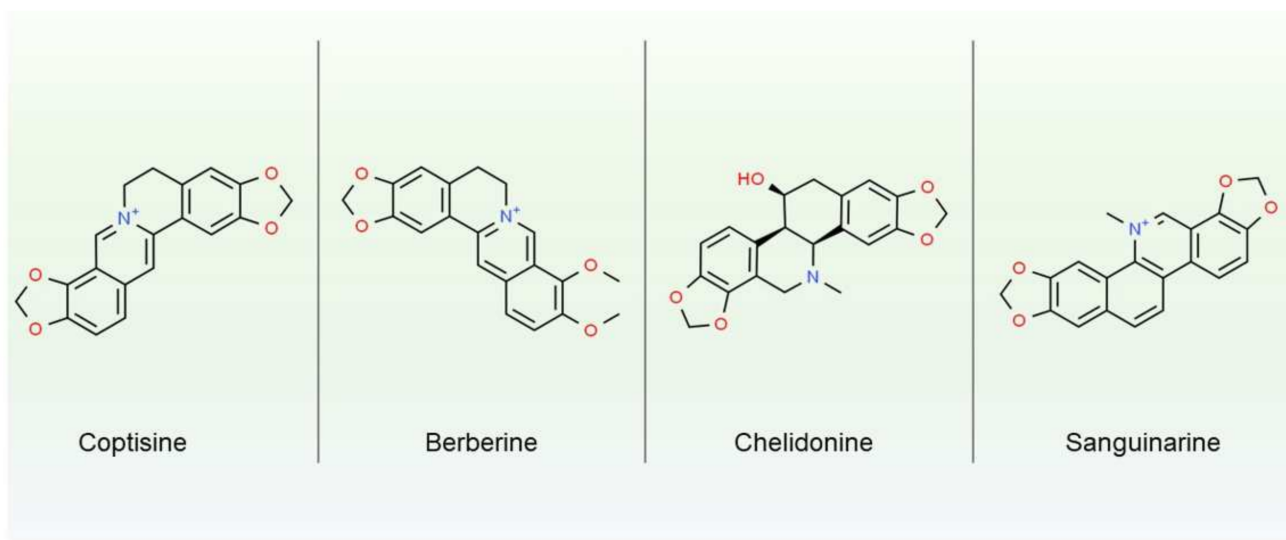


Figure 1. Chemical structure of four most studied alkaloids from *Chelidonium majus*.

Cardenolides, a specific type of steroids (cardiac glycoside) consisting of sugar, steroid, and lactone, are the next group of metabolites commonly occurring in latex. There is no known function of those compounds, other than defense. Cardenolides are inhibitors of Na^+/K^+ -ATPases, which are essential to maintain cell electrical potential, regulate cellular volume, and take part in transmembrane transport. As inhibitors cardiac glycosides are remarkably toxic to most animals, therefore latex of *Antiaris toxicaria* Lesch. (Moraceae) rich in cardenolides, were used by South Asia tribes as a poison on darts during hunting [37]. It is worth mentioning the widely known interaction between cardenolides from *Asclepias* spp. and monarch butterflies (*Danaus plexippus*). Monarch larvae, which feed on plants containing cardenolides, have developed the ability to sequester those compounds, which then cumulate in wings and protect them from bird predators [38,39].

4. Spectrum of Latex Proteins

Laticifers are not only a reservoir system for low-molecular weight defense compounds, but as mentioned earlier, constitute a living cell, and as one, has a distinct proteome. A wide range of both constitutive and inducible proteins are present in latex, with huge diversity between different plant species. Comprehensive studies of 1208 latex proteins from 20 various latex-bearing plants led to the identification of 887 non-redundant proteins from three main species, i.e., *L. sativa*, *H. brasiliensis*, and *P. somniferum*. Only 11 proteins were found in all three species [40], which represents well-illustrated variability within

latex proteomes. In a set of 887 proteins, GO enrichment analysis showed that response to chemical and abiotic stimuli categories were highly overrepresented. Within this category, at least 21 proteins are involved in response to cadmium ion stress, while another 13 proteins were associated with response to high salt conditions. Proteins with function in defense were also identified. Amongst them two proteins, glycosyl hydrolase superfamily proteins (AT4G16260) and the NAD(P)H subunit NDH-N (AT5G58260), were pinpointed for their response to fungi infections. In the category of cellular components, most proteins were located in cytoplasm, but terms related to intracellular membrane-bounded organelles (including plastids and mitochondria) were highly enriched as well. Cho and colleagues also compared latex and phloem proteomes. GO terms common for those two conductive systems were related to metabolic pathways like the metabolism of nitrogen compounds, amine, alcohol, hexose, carboxylic acid, and carbohydrate catabolism. Stress response related terms were shared in laticifers and phloem systems, but for example, osmotic stress GO terms were identified only in latex. On the other hand, GO terms connected with response to zinc were found only in phloem [40]. Despite some similarities with functionally related conduit systems, laticifers present a unique and distinct set of proteins. Nevertheless, we can distinguish some common protein functional groups prevalent in different laticiferous plant species, like proteases, protease inhibitors, lectins, oxidases, chitinases, or defense-related proteins. Below, we survey those common for latex protein's groups.

The most frequently reported latex proteins are proteases. One of the best described examples of protease in laticiferous plants is papain, a cysteine protease in latex of the Papaya tree (*Carica papaya* L.). Papain is an enzyme practically used as a meat tenderizer and in the cosmetic industry. In papaya latex, its concentration is 200 times higher than in leaf tissue, which leads to 20 times higher papain activity [41]. Experiments with protease inhibitors, E-64 and larvae of Eri silkworm, give clear evidence of papain involvement in plant resistance against herbivory (leaf toxicity to Eri silkworm was lost after covering its surface with E-64). Similarly, ficin (cysteine protease from fig) inhibition by E-64 makes fig leaf edible for insects [41]. Nonetheless, the exact site of action and mechanism of protease toxicity remains unclear. Other groups of proteases-serine proteases-were found in Moraceae, Euphorbiaceae, Apocynaceae, and Convolvulaceae families. Rarely are those two protease classes (cysteine and serine) identified in the latex of the same species. More often, one type of peptidases is described for a particular plant. Known exceptions are species from the *Plumeria* genus, where both proteolytic mechanisms have been reported [42].

In the latex of many plants, not only were proteases identified, but protease inhibitors as well. Those compounds bind to proteases and prevent the digestion of proteins, thus causing a shortage of amino acids and impairing the growth and development of aggressors [8]. Protease inhibitors belong to group 6 of Pathogenesis-Related (PR) proteins and their role in plant defense in species without latex is well established [43]. In laticiferous species *Ficus carica* L., the expression level of trypsin inhibitor increases significantly after wounding and jasmonic acid treatment [43,44]. Moreover, in papaya latex, trypsin inhibitor (together with class-II chitinase and a glutaminyl cyclase) was one of the compounds accumulated after mechanical damage [45].

Lectins are proteins with one or more domains which enable them to recognize and bind to specific sugar structure (in free form or as a part of glycoproteins and glycolipids). They are compounds necessary for the perception of possible invasion by recognizing specific glycans at damage sites and from pathogens. Several types of lectins were identified in the families Euphorbiaceae, Moraceae and Apocynaceae. Hevein, the major latex protein from *H. brasiliensis*, is responsible for rubber agglutination, by bridging rubber particles after the recognition of 22 kDa glycoprotein receptor [46]. This small 43 amino acid protein with lectin domain turned out to be the main contact allergen from natural rubber [46,47]. In contrast to indirect mechanisms of latex coagulation, there are studies reporting a straight negative impact of lectins on pests from different families, e.g., Lepidoptera, Coleoptera, Diptera and Hemiptera [18]. It was shown that the expression of exogenous lectins in genetically engineered plants led to various detrimental effects in invading insects, ranging

from a severe delay in development to high mortality rates. Moreover, the introduction of specific lectins to the insect diet negatively affects pest performance, as reviewed in [48]. The toxicity of lectins depends on the presence of specific carbohydrates in the insect body, which, in turn, is correlated with insects' developmental stage [49,50].

Latex from plants belonging to families Euphorbiaceae, Moraceae, and Anacardiaceae shows oxidase activity [51]. Polyphenol oxidase (PPO) and peroxidase (POD) are the most commonly occurring peptides. Both enzymes are known for their role in plant defense, not only in lactiferous plant species. Polyphenol oxidase catalyzes the oxidation of phenols to o-quinones, which are highly reactive and secondary non-enzymatic reactions lead to formation of polymers with protein functional groups. At least three mechanisms of PPO toxicity to insects were proposed: decreased nutritive value of leaf proteins, oxidative burst in insect gut, and direct toxicity of PPO catalyzed products [52]. Products of PPO activity and polymerization are black, brown, or red in color and are responsible for the darkening of latex after contact with air. Peroxidases on the other hand are H₂O₂ scavengers—they catalyze oxidation of phenolic substrates using H₂O₂ as an electron acceptor. Subsequent reactions lead to cross-linking products of phenolic compounds, such as lignin or suberin [52,53]. The ability to reduce ROS makes those enzymes a crucial part of the antioxidant system, which is often triggered in response to both biotic and abiotic stress conditions. As a downstream result of peroxidase activity, the lignification of the plant cell walls occurs, which inhibits, for example, heavy metal entry [54].

Chitinases hydrolyze the β -1,4-glycosidic bonds of chitin, which builds fungi cell walls and insects exoskeletons and peritrophic matrix. Chitinases are classified as pathogenesis related proteins (PR proteins) and are expressed inducible or constitutively in tissues vulnerable to pathogen attack, like laticifers. Several ways of direct chitinase involvement in antifungal defense were established. Plant chitinases can inhibit hyphal growth. The overexpression of those enzymes in transgenic plants increased pathogen resistance in vivo. Meanwhile, products of chitin breakdown, via phytoalexins action, to induce systemic defense response [55]. Insecticidal effects constitute another well documented chitinase activity. For example, after the addition of two chitinases from mulberry (*Morus* sp.) to the *Drosophila melanogaster* larvae diet, 80% were found to be dead [56]. Chitinases identified from *Calotropis procera* (Aiton) W.T.Aiton affected larval survival and weight, mean developmental time and emergence of adults [23]. The mechanism of chitinase's action on insects is not well established. It is postulated that it may involve the hydrolysis of chitin present in their peritrophic membranes, which are responsible for protection against mechanical damage and invasion by microorganisms or parasites. After its destruction, fatal infection can develop [57,58]. Moreover, in latex, chitinases present multiple isoforms. Three isoforms were purified and characterized from *Ficus microcarpa* latex [59], six basic chitinases were identified in *H. brasiliensis* latex [60] and at least 15 isoforms in latex of *C. procera* [61]. Different isoforms exhibit differences in sequences as well as in post-translational modification. Particular isoforms may in consequence differ in structural and biological properties, which need to be included in further studies regarding plant chitinases [61].

As mentioned before, chitinases belong to the group of pathogenesis related proteins. All PR proteins (as the name suggests) take part in plant defense mechanisms, but they are a very diverse group in the context of structures and activities. They were categorized into 17 distinct families (summarized in Table 1). For instance in *C. majus* latex representatives of 12 families were identified [62,63]. Two quantitatively predominant families were PR-9 (peroxidases described previously) and major latex proteins (MLPs), which are homologs of PR-10 proteins (ribonuclease-like/Bet v1 protein family). Similarly, in latex of *P. somniferum*, those two families were also overrepresented. In another well studied laticiferous plant, *H. brasiliensis*, members of 9 PR families were described [8]. PR proteins are low molecular weight and are induced by phytopathogens as well as defense-related signaling molecules, like salicylic and jasmonic acid. Due to their mode of action in biotic and abiotic stress

conditions, they are one of the most promising targets for engineering multiple stress tolerant varieties [8,63].

One of the most interesting latex proteins is a major latex protein (MLP). It was discovered for the first time in the latex of the opium poppy (*P. somniferum*) in 1980's by Nessler et al. Despite its abundance (up to 50% of soluble *P. somniferum* latex sub proteome) shown using SDS-PAGE and the presence of laticifer-specific peptides, its function remained unknown [64–66]. MLPs, being homologs of opium poppy major latex protein, have also been found in other non-latex-bearing plants, namely peach fruits (*Prunus persica* L. Batsch, cv Springcrest) [67], *Arabidopsis thaliana* L. [68], ripening kiwi fruit [69], *Panax ginseng* C.A. Meyer [70], tobacco (*Nicotiana tabacum* L.) [71], pepper (*Capsicum annuum* L.) [72], and cotton [73]. Recent data have shown the functional role of MLPs resembling the function of PR-10 proteins family [67], member of which are involved in the defense of plants against different pathogens and participate in plant metabolism [74–76]. The first proposed ribonuclease activity was demonstrated in major birch pollen allergen, Bet v1 which expresses homology to PR-10-like protein from white lupin (*Lupinus albus* L.) [77]. The most distinctive feature of Bet v1 protein superfamily (Pfam: PF00407) is a large solvent accessible hydrophobic cavity which might potentially function as a site to bind ligands [78]. Both MLPs and PR-10 families are members of Bet v1 superfamily although their sequence similarity is low and is below 25% [68]. Major latex protein/ripening-related proteins (MLP/RRP) subfamily is the second largest subfamily within the plant kingdom. It has 60 members, from which 31 are present in *A. thaliana*. The biological function of MLPs is still unknown, but there are assumptions that they are associated with development of fruit and flower along with response to stress and defense [78]. One of the recent studies has investigated the potential antiviral activity of MLP proteins against potato virus Y (PVY). It is transmitted by aphids and can cause mosaic, dwarfism, mottle, deformities, and even lead to necrosis in tobacco plants. MLP-like protein 28 (NbMLP28) from *Nicotiana benthamiana* Domin. was identified and cloned. Its expression profile has shown responsiveness towards PVY infection and defense-related signaling molecules, such as JA, SA, and ET. Virus-induced silencing of NbMLP28 made plants more susceptible to infection by PVY, though the transient overexpression of NbMLP28 gene improved resistance towards PVY in tobacco plants. The pathway responsible for modulation of the expression of NbMLP28 gene in *N. benthamiana* has also been identified. It showed the cis-acting elements in response to JA, light, auxin, drought, and endosperm expression to be present in the promoter sequence of NbMLP28 [79]. Antiviral properties towards TMV-P0 virus have been proven for CaPR10 proteins from hot pepper which have inhibited the viral penetration and/or replication. This study showed that CaPR10 after inoculation with the virus is phosphorylated and functions as RNase cleaving viral RNA [71]. During the studies on melon phloem-sap proteome, it was also found that major latex protein was present in the sap collected from the cucumber mosaic virus (CMV)-MP-expressing plants and CMV-infected plants [80]. Proteomic studies of *C. majus* latex have shown that MLP is highly overrepresented in *C. majus* latex [78] and can be seen at different stages of plant development till the fruit ripening. It is accumulated early in laticifer development and persists till maturity [78]. *C. majus* MLP (CmMLP) is composed of 147 amino acids, has a molecular weight of 16.77 kDa and theoretical pI 5.88, which corresponds to the typical sizes of MLPs (17 kDa) in other plants [74]. MLPs bind hormones and other metabolites with their conserved hydrophobic cavity during plant growth and development [81]. MLPs from other species, including *A. thaliana*, *N. benthamiana*, or *Cucumis melo* L., as mentioned previously, have also been proved to be involved in antiviral response. This can help to explain the potential antiviral activity of *C. majus* among its other biomedical properties [82] and could serve as a potential molecular target to be used in pharmacology or medicine and to improve the defense potential of agriculturally important crops against viral and non-viral pathogens.

Table 1. Summary of PR proteins previously identified in latex-bearing plants.

PR Proteins	Function	Latex-Bearing Plant Species	Reference
PR 2	β -1,3-glucanases	<i>Chelidonium majus</i> <i>Hevea brasiliensis</i>	[78,83]
PR 3	Class I, II, IV, V, VI, VII Chitinases	<i>Chelidonium majus</i> <i>Hevea brasiliensis</i>	[78,83]
PR 4	Class I, II Chitinases	<i>Chelidonium majus</i> <i>Hevea brasiliensis</i> <i>Carica papaya</i>	[45,78,83]
PR 5	Thaumatococin-like proteins	<i>Chelidonium majus</i> <i>Hevea brasiliensis</i>	[78,83]
PR 6	Proteinase inhibitor	<i>Hevea brasiliensis</i> <i>Ficus carica</i> <i>Carica papaya</i>	[44,45,83]
PR 7	Endoproteinase	<i>Chelidonium majus</i> <i>Hevea brasiliensis</i>	[78,83]
PR 8	Class III Chitinase	<i>Hevea brasiliensis</i>	[83]
PR 9	Peroxidase	<i>Chelidonium majus</i> <i>Hevea brasiliensis</i> <i>Papaver somniferum</i>	[78,83,84]
PR 10	Ribonuclease-like proteins	<i>Chelidonium majus</i> <i>Papaver somniferum</i>	[78,84]
PR 11	Class I Chitinase	<i>Chelidonium majus</i>	[78]
PR 12	Defensin	<i>Chelidonium majus</i> <i>Hevea brasiliensis</i>	[78,83]
PR 14	Lipid-transfer protein	<i>Chelidonium majus</i> <i>Hevea brasiliensis</i>	[78,83]
PR 15	Oxalate oxidase	<i>Chelidonium majus</i>	[78]
PR 16	Oxidase-like	<i>Chelidonium majus</i>	[78]
PR 17	Antifungal and antiviral	<i>Chelidonium majus</i>	[78]

5. Biomedical Properties of Latex from Selected Plants with the Focus on *Chelidonium majus* L.

Nowadays, the demand for complementary therapeutics with herbal medicine including plant latex extracts, is constantly rising. Approximately 40% of drugs available at the market contain herbal active ingredients and the number is still growing [85]. Herbal medicines can act synergistically with currently used therapeutics and have fewer side effects compared to synthetic drugs. Both wild medical plants such as *C. majus* and domesticated species can serve as a source of raw materials (extracts) from which effective remedies can be obtained. *C. majus* is a plant that has been used for centuries to treat warts, papillae, and condylomas which are epidermal symptoms of human papillomavirus (HPV) infection [78]. In North America and Great Britain, it was used as a cure for infantile jaundice and ulcers of the eye. In traditional Chinese medicine, it was also used to fight fever, diminish the cough, promote diuresis in edema and ascites, alleviate the pain and treat blood stasis [86]. To date, it is still exploited in homeopathy and according to Foster et al. it can be used for liver and gallbladder disorders along with rheumatism and respiratory inflammations [87]. Although the molecular mechanism of *C. majus* latex compounds action is largely unknown, its antiparasitic, insecticidal, anti-neoplastic, antiproliferative, antimycotic, immunomodulating, and antiviral properties are well established [4,20,85,88–90].

C. majus belongs to the Papaveraceae family which also includes plants like bloodroot (*Sanguinaria canadensis* L.), persian poppy (*Papaver bracteatum* Lindl.), or opium poppy

(*P. somniferum*). As mentioned before, *P. somniferum* serves as a source of several pharmacologically active substances, such as papaverine with vasodilator activity, noscapine, and sanguinarine with antimicrobial properties [85,91]. So far, it remains the only commercial source for benzyloisoquinoline alkaloids, e.g., codeine, morphine, and its semi-synthetic forms like naltrexone or oxycodone, which are broadly used in medicine worldwide. *C. majus* is also a very important plant concerning its latex with a broad range of different components, connected with its multiple biological activities [3–5]. California poppy (*Eschscholzia californica* Cham.) is used for the production of bioactive compounds in vitro. Similarly to *P. somniferum*, it is involved in synthesis of benzyloisoquinoline alkaloids like chelerythrine or sanguinarine [85]. Biomedical properties of different poppy species with the focus on *P. somniferum* have been already broadly studied and well described in the recent review article of Labanca et al. [92], and therefore it is not necessary to cover in the scope of this article. Another plant whose latex is rich in different molecules with biomedical properties including psychoactive ones is *Cannabis sativa*. It contains phytocannabinoids such as tetrahydrocannabinol (THC) and cannabidiol (CBD). THC has been shown to exhibit anti-cancer, analgesic, muscle relaxing, neuro-antioxidative, anti-inflammatory, and antispasmodic activity [93,94]. CBD also has numerous pharmacological properties and can be used in the case of metabolic syndrome, type I diabetic cardiomyopathy, or inflammatory lung diseases along with many others described in the review article of Burstein S. [95].

Nevertheless, the exact molecular mechanism responsible for many biomedical properties of laticiferous plant species is still not well established. Yet, the research community managed to define some interesting therapeutic activities and latex active compounds responsible for their occurrence. Those examples are presented below.

5.1. Antiviral Activity

In several assays, the ability of latex extracts was confirmed to act not only against plant viruses, but animal and human as well. As previously mentioned, *C. majus* has been effective against skin symptoms of HPV infections and different human viruses (HPV, HSV-1, HIV), although the mechanism of this activity is still undiscovered [96–98]. It is assumed that two groups of proteins are responsible for antiviral properties—peroxidases and nucleic acid binding proteins (see Table 2). Mechanical damage of the plant cell is accompanied by oxidative burst, which prevents any virus from the possible entry [99,100]. Second lines of defense include proteins such as lipoxygenases (LOX) and peroxidases (POX) which generate the H_2O_2 after pathogen attack [78,101]. The third line includes nucleic acid binding proteins, such as MLPs and/or GRPs, which have deoxyribonucleic and ribonucleic activities that allow them to potentially digest the viral RNA and DNA or act in yet not known mechanisms [74,78,102,103]. Another proposed mechanism is based on satellite RNA (satRNA) encapsulation and has been found in plants without significant symptoms of cucumber mosaic virus (CMV) infection. Primary plant defense is based on the silencing of RNA but PTI-based (pattern-triggered immunity-based) innate immune response is connected to antiviral defense. PTI is enabled by conserved pathogen-associated molecular patterns (PAMPs) detected by transmembrane pattern recognition receptors. On the other hand, effector-triggered immunity (ETI) is an “amplified” version of PTI, often associated with hypersensitive response (HR) and programmed cell death (PCD). In this mechanism, proteins from the NBS-LRR family (ETI-based R proteins) could recognize the avirulence (Avr) proteins of RNA viruses, effectors of non-viral origin, and trigger apoptosis in virus-resistant hosts. Avr proteins can function as silencing suppressors, which leads to the statement that innate immunity (both PTI and ETI) can be involved in the mechanism of the fight against plant viruses and can serve as a hint to understanding the activity against animal and human viruses [99,104]. Not only are proteins, but also certain alkaloids crucial to latex antiviral activity. Different secondary metabolites have already shown antiviral properties against herpes simplex virus and human adenoviruses (type 5 and 12) [105,106]. The antiviral activity of *C. majus* against retroviruses has been proven through isolation

of the anti-HIV-1 latex compound named ChM-P2 from its aqueous extract [99]. Analysis has shown the low-sulfated poly-glycosaminoglycan character of the isolated molecule. It prevents infection of human CD4⁺ T-cell lines (AA2, H9) with HIV-1 and subsequent cell death. Virus-induced syncytium formation as well as lower cell-to-cell virus spread were also observed in H9 cells. The anti-retroviral activity of the ChM-P2 substance was also confirmed in vivo in mouse AIDS (MAIDS) model C57Bl/6 [99]. The activity of *C. majus* against herpesvirus, influenza virus, and poxviruses has also been tested on albino mice by Lozjuk et al. The effectiveness of *C. majus* alkaloids was estimated on the median duration of mouse life, degree of pulmonary tissue changes and the differences in median HR titres. All of the used alkaloids have shown an inhibiting effect on the infection [107]. *C. majus* latex was also used in oral form to treat a group of 20 patients suffering from SARS-CoV-2 infection with significant clinical improvement after three days of drug administration [86].

Table 2. Model of antiviral response of *Chelidonium majus* latex based on in vitro studies, which represents preformed immediate defense response with exuding latex. 1st line of defense-after mechanical damage (e.g., herbivore bite) the latex exudes and due its stickiness clots and stops or kills the herbivore. 2nd line of defense-cell wall damage is the prerequisite for the possibility of viral infection. Thereafter it can be stopped by oxidative burst and antiviral response (3rd line of defense). Abbreviations: PPO–polyphenol oxidase; LOX-lipoxygenase; POX-peroxidase; MLP-major latex protein; GRP-glycine-rich protein. According to [74].

Line of Defense	Type of Action	Predominant Proteins and Compounds
1st	Mechanical damage	PPO, LOX (latex stickiness, different chemicals)
2nd	Oxidative burst	POX, LOX et al.
3rd	Antiviral activity	MLP, GRP (RNase/DNase activity, nucleic acid binding)

Antiviral properties of latex ingredients have been also presented in different plant species. A study conducted by Camero et al. showed the in vitro antiviral activity of fig fruit *F. carica* latex against caprine herpesvirus-1 (Cp-HV1) through a reduction of viral titers produced by MDBK cells [108]. Although the Cp-HV1 affects goats, it shares significant similarities with human genital herpes virus (HHV-2), and therefore it can serve as a model in further research. In another study of *F. carica* latex, presented by Houda Lazreg Aref et al., the hexane and ethyl acetate–hexane latex extracts were proven to be active against herpes simplex virus (HSV-1), european catfish virus (ECV-11), and adenovirus [109]. Such activity can be caused by the presence of ferulic acid being the major phenolic compound in the *F. carica* latex extracts. Lyophilized extracts from *Momordica charantia* L. were also shown to be active against HSV-1 virus, along with their antiviral activity towards sindbis virus (SINV) [110]. Other antiviral agents that have been found in latex of medical plants include inophyllum, coumarins, and calanolide A from *Calophyllum teysmannii* Miq., which serves as a unique non-nucleoside reverse transcriptase inhibitor and can be effective against HIV-1 [111]. Oligomeric proanthocyanidin (SP-303) from *Croton lechleri* latex was shown to inhibit respiratory syncytial virus (RSV) and HSV viral absorption and penetration through the plasma membrane [112]. In turn, (+)-pinoresinol-4-O-β-D-glucopyranoside from *Calotropis gigantea* L. latex presented anti-influenza activity towards a panel of human viruses (A/PR/8/34 (H1N1), A/FM/1/47 (H1N1) and A/Aichi/2/68 (H3N2)) [113].

5.2. Cytotoxicity

C. majus along with other medical plants are often studied in the context of cancer treatment and cytotoxicity. In numerous studies, cytotoxicity has already been confirmed towards keratinocytes, cells tightly linked to HPV life cycle [35,114–116]. Sanguinarine, protopine, and less noticeably chelidonine were able to inhibit the growth of keratinocytes as well as apoptosis of MT-4 cells present in acute T lymphoblastic leukemia. Chelidonine from *C. majus* was found to block the cell cycle of MT-4 cells at G2/M phase. Although

it does not bind to DNA directly, it was more successful at apoptosis induction than sanguinarine [117]. Chelidonine was also involved in the apoptosis in HeLa cells by activation of signaling pathways connected to p38–p53 proteins and AKT/PI3 kinase. Morphological analysis has shown the cell shrinkage and blebbing which are typical for apoptosis. Levels of MAPK enzyme p38 responsible for ROS-induced apoptosis in cells were also up-regulated. Chelidonine caused the increase in sub-G1 and G0/G1 cell populations, demonstrating an inhibitory effect. It also led to an increase of mitochondria membrane permeability, thereby allowing for the release of cytochrome c and activation of Apaf-1 involved in apoptosis. The treatment of HeLa cells with *C. majus* extracts also resulted in a decrease of the expression of PI3K, JAK3, AKT, and STAT3 pathways involved in numerous cellular processes, such as apoptosis, survival, proliferation, and cell growth. The down-regulation of oncogenic E6 and E7 HPV proteins was also noticed, further showing its anticancer potential [118]. It was also found to induce expression of telomerase reverse transcriptase (hTERT) and accelerate the senescence of the cells through activation of telomerase in HepG2 cells [117]. In other studies, five alkaloids (sanguinarine, chelidonine, protopine, stylopinine) from *C. majus* latex have been tested against melanoma cells, which led to apoptosis of the cancer cells with only a mild effect on normal cells [119]. The effectiveness of *C. majus* milky sap on dermal tumors has been also tested by Isolde Riede's team. Clinical data have proven the destruction of pathologically altered tissues and eradication of preneoplastic lesions after regular application of the latex [120]. A study conducted by Nawrot et al. has shown the ability of CMN1 and CMN2 nucleases from the milky sap to exert an apoptotic effect after 48 h on neoplastic cell line HeLa with no significant effect on ovarian fibroblast cells of Chinese hamsters. The activity depended on the concentration of nucleases as well as the season time of *C. majus* latex collection. In the case of CMN2, lower pro-apoptotic activity was noticed in October, compared to May. This can be explained by differences in the post-translational modification of proteins as well as by the amount of certain enzyme cofactors [19].

Different plants from the *Ficus* genus have also exhibited cytotoxic activity towards cancer cells. Study conducted by Azza M. Abdel-Aty et al. has shown the cytotoxic activity of phenolic latex extracts from *Ficus sycomorus* L., *F. carica*, and *Euphorbia tirucalli* L. towards the acute myeloid leukemia HL-60, liver HepG2, and breast MCF-7 cancer cell lines. *F. carica* extract exhibited moderate cytotoxic activity towards colon HCT116 cancer cell line and latex extract from *E. tirucalli* had moderate cytotoxic effect on lung A549 cancer cell line. The cytotoxic effect was similar to doxorubicin, which is already used as an anticancer drug. Additional HPLC analysis of latex extracts used in the study helped to distinguish a few bioactive compounds, which include, among others, psoralen, xanthotoxin, phthalic acid, and lanosterol. *F. carica* latex ethanol, dichloromethane, and ethyl acetate extracts were also found moderately cytotoxic towards the HeLa cell line with no significant differences between extracts and crude latex [121]. In a different study conducted by Tulasi et al., the solvent extracts of *Ficus benghalensis* L. and *Ficus religiosa* L. showed an anti-proliferative effect on breast MCF-7 cancer cell line with a 90% inhibition rate at the highest concentration of extract used (200 µg/mL) [122].

Cytotoxic activity towards cancer cell lines has also been proven for other plants from the *Euphorbia* genus. In the study carried out by Livia E.C.Luz et al., the cytotoxic effect of *Euphorbia umbellata* (Pax) Bruyns latex extract was tested on HeLa and HRT-18 cells. Both cell lines were responsive to treatment and morphological analysis demonstrated the presence of apoptotic events and signs of severe toxicity [123]. *E. umbellata* latex was also used on melanoma cells (B16F10) and cytotoxicity in vitro, as well as in vivo were confirmed. Latex application was responsible for lowering the tumor mass in mice. Such activity was linked to the presence of triterpenes in the plants latex [123]. Cytotoxic activity of *Euphorbia* genus latex was also proven by using *Euphorbia helioscopia* L. latex to treat hepatocellular carcinoma in nude mice xenograft. A higher concentration of latex caused the downregulation of cyclin D1 expression, a protein associated with cell cycle regulation (G1 phase), which resulted in cell proliferation inhibition, as well as apoptosis

induction. Another protein whose expression was downregulated was bcl-2 protein, known as an antiapoptotic factor. Latex administration, on the other hand, increased the expression of two proapoptotic factors, bax and caspase-3, which induced cell apoptosis in xenografts. A significant decrease of MMP-9 protein, responsible for degradation of the extracellular matrix, was also confirmed. Together with overexpression of nm23-H1 protein, involved in metastasis inhibition processes, it allowed the suppression of cancer cell invasion and migration [124]. Another species from the *Euphorbia* genus, *Euphorbia macroclada* Boiss. was used against breast cancer cell lines (MDA-MB-468 cell line) with Taxol, an anticancer drug, as a positive control. Dichloromethane and ethyl acetate extracts have shown cytotoxic activity, which resulted in at least 50% growth inhibition of cancerous cells [125]. Another *in vivo* study has been conducted using mice animal model to present *C. procera* dried latex cytotoxic effect on hepatocellular carcinoma cells [126]. For 15 weeks, mice were orally administered with dried latex which resulted in significant decrease of vascular endothelial growth factor (VEGF) levels in the serum. Since VEGF serves as a marker of angiogenesis, the chemopreventive effect of oral administration of *C. procera* latex *in vivo* can be assumed. An *in vitro* assay also confirmed the cytotoxic activity via the increased activity of cellular nucleases, which led to DNA fragmentation. Cytotoxic activity *in vitro* was associated with polar fractions and studies on different cell lines: non-hepatoma (COS-1), hepatoma (Huh-7), and non-cancerous line (AML12). Cytotoxicity was strongly selective for transformed cells.

5.3. Antimicrobial Activity

Because of the rising concern related to antibiotic resistant bacteria, it is crucial to look for alternative antimicrobial compounds. Examples of the use of different plant species latex along with treated bacteria and fungi species are presented in Table 3. Studies by Colombo et. al. have shown the quaternary ammonium groups of isoquinoline alkaloids to be responsible for antibacterial activity since both natural and synthetic compounds lacking those groups had no antimicrobial activity [127]. *C. majus* antimicrobial activity has been confirmed in a few studies, for separated compounds which included different alkaloids and glycoproteins summarized in Table 3 [128–131]. For example, studies conducted by Pavão and Pinto have shown that berberine, coptisine, and sanguinarine had antibacterial effects on *Bacillus subtilis* [132].

Table 3. Examples of antimicrobial activity of latex bearing plants.

Latex-Bearing Plant Species	Examined Bacteria	Examined Fungi	Bioactive Compounds	Reference
<i>Aloe harlana</i> Reynolds	<i>Bacillus pumilus</i> (82)			
	<i>Bacillus subtilis</i> (ATCC 6633)			
	<i>Escherichia coli</i> (CD/99/1, K88, K99, LT37, ROW 7/12, 3:37C, 306, 872)	<i>Aspergillus niger</i> (ATCC 6275)		
	<i>Salmonella typhi</i> (Ty2)	<i>Candida albicans</i> (ATCC 10231)	Anthrone (aloin)	[133]
	<i>Shigella boydii</i> (D13629)	<i>Penicillium funiculosum</i> (NCTC 287)	Chromone (7-O-methylaloesin A)	
	<i>Shigella dysentery</i> 1	<i>Penicillium notatum</i> (ATCC 11625)		
	<i>Shigella dysentery</i> 8			
<i>Shigella flexneri</i> (Type 6)				
<i>Shigella sonnei</i> 1				
<i>Staphylococcus aureus</i> (ML267)				
<i>Aloe weloensis</i> Sebsebe	<i>Vibrio cholerae</i> (85, 293, 1313, 1315)			
	<i>Enterococcus faecalis</i>		Alkaloids	[134]
	<i>Escherichia coli</i>		Anthraquinone	
	<i>Pseudomonas aeruginosa</i>	-	Flavonoids	
	<i>Staphylococcus aureus</i>		Glycosides	
		Tannins Terpenoids		

Table 3. Cont.

Latex-Bearing Plant Species	Examined Bacteria	Examined Fungi	Bioactive Compounds	Reference
<i>Artocarpus heterophyllus</i> Lam.	<i>Bacillus subtilis</i> <i>Klebsiella Pneumoniae</i> <i>Pseudomonas aeruginosa</i> (ATCC 27853) <i>Streptococcus haemolyticus</i> <i>Salmonella typhi</i> <i>Bacillus cereus</i>	<i>Aspergillus niger</i> <i>Candida albicans</i>	48-kDa protease (AMP48)	[135,136]
<i>Calotropis procera</i> (Aiton) W.T.Aiton	<i>Bacillus subtilis</i> <i>Escherichia coli</i> <i>Klebsiella Pneumoniae</i> <i>Pseudomonas aeruginosa</i> <i>Salmonella typhi</i> <i>Staphylococcus aureus</i> <i>Staphylococcus epidermidis</i> <i>Streptococcus haemolyticus</i> <i>Streptococcus pneumoniae</i>	<i>Aspergillus flavus</i> <i>Aspergillus niger</i> <i>Candida albicans</i> <i>Candida tropicalis</i> <i>Penicillium chrysogenum</i> <i>Saccharomyces cerevisiae</i>	-	[137]
<i>Calotropis gigantea</i> L.	<i>Bacillus cereus</i> <i>Escherichia coli</i> <i>Lactobacillus acidophilus</i> <i>Micrococcus luteus</i> <i>Staphylococcus aureus</i> <i>Streptococcus mutans</i> <i>Bacillus subtilis</i>	<i>Candida krusei</i>	Alkaloids Phenolic Steroids Terpenes Cardiac glycoside	[138,139]
<i>Carica papaya</i> L.	<i>Klebsiella Pneumoniae</i> <i>Streptococcus haemolyticus</i> <i>Salmonella typhi</i> <i>Aeromonas hydrophila</i> <i>Agrobacterium tumefaciens</i> <i>Bacillus cereus</i> <i>Bacillus subtilis</i> <i>Candida albicans</i>	<i>Aspergillus niger</i> <i>Candida albicans</i>	-	[136]
<i>Chelidonium majus</i> L.	<i>Escherichia coli</i> <i>Micrococcus luteus</i> <i>Mycobacterium phlei</i> <i>Salmonella enteritidis</i> <i>Sarcina lutea</i> <i>Staphylococcus aureus</i>	<i>Candida albicans</i>		[127–130]
<i>Euphorbia heterophylla</i> L.	<i>Bacillus subtilis</i> <i>Proteus vulgaris</i> <i>Pseudomonas aeruginosa</i> <i>Staphylococcus aureus</i>	<i>Aspergillus niger</i> <i>Fusarium oxysporum</i> <i>Penicillium sp.</i>	Alkaloids Flavonoids Phenols Saponins Steroids Tannins	[140]
<i>Ficus carica</i> L.	<i>Enterobacter cloacae</i> <i>Enterococcus faecalis</i> (ATCC 29212) <i>Escherichia coli</i> <i>Escherichia coli</i> ATCC 25922 <i>Pseudomonas aeruginosa</i> (ATCC 2783, ATCC 27950) <i>Staphylococcus aureus</i> <i>Staphylococcus aureus</i> (ATCC 25923) <i>Staphylococcus epidermidis</i> <i>Staphylococcus saprophyticus</i>	-	alpha-Amyrenyl acetate Aristolone Bornanone-3 Lanosta-8 Olean-12-en-3-ol, acetate Urs-12-en-24-oic acid	[141]
<i>Jatropha gossypifolia</i> L.	<i>Pseudomonas aeruginosa</i> (CRPA) <i>Staphylococcus aureus</i> (MRSA)	-	Flavonoids	[142]
<i>Jatropha multifida</i> L.	<i>Pseudomonas aeruginosa</i> (CRPA) <i>Staphylococcus aureus</i> (MRSA)	-	Flavonoids	[142]

Table 3. Cont.

Latex-Bearing Plant Species	Examined Bacteria	Examined Fungi	Bioactive Compounds	Reference
<i>Jatropha caracas</i> L.	<i>Bacillus subtilis</i> <i>Escherichia coli</i> <i>Klebsiella Pneumoniae</i> <i>Neisseria gonorrhoea</i> <i>Pseudomonas aeruginosa</i> <i>Salmonella typhi</i> <i>Staphylococcus aureus</i> <i>Streptococcus haemolyticus</i>	<i>Aspergillus niger</i> <i>Candida albicans</i>	Alkaloid Glycoside Saponin Steroid Tannin	[136,143,144]
<i>Leptadenia hastata</i> (Pers.) Decne.	<i>Klebsiella Pneumoniae</i> <i>Staphylococcus aureus</i> <i>Staphylococcus aureus</i> (ATCC 29213) <i>Salmonella typhi</i>	-	Alkaloids Flavonoids Glycosides Phenolic Proanthocyanidins Saponins Tannins Triterpene	[145]
<i>Pergularia daemia</i> (Forssk.) Chiov.	<i>Escherichia coli</i> (ATCC 25922) <i>Klebsiella pneumoniae</i> <i>Pseudomonas aeruginosa</i> (ATCC 27853) <i>Staphylococcus aureus</i> <i>Staphylococcus aureus</i> (ATCC 29213) <i>Salmonella typhi</i>	-	Alkaloids Flavonoids Phenols Saponins Steroids Tannins Terpenoids	[145]
<i>Secamone afzelii</i> (Schult.) K.Schum.	<i>Escherichia coli</i> ATCC 25922 <i>Klebsiella pneumoniae</i> <i>Pseudomonas aeruginosa</i> ATCC 27853 <i>Secamone afzelii</i> <i>Staphylococcus aureus</i> <i>Staphylococcus aureus</i> ATCC 29213 <i>Salmonella typhi</i> <i>Bacillus subtilis</i>	-	Alkaloids Cardiac glycosides Saponins Tannins	[145]
<i>Thevetia peruviana</i> L.	<i>Klebsiella Pneumoniae</i> <i>Streptococcus haemolyticus</i> <i>Salmonella typhi</i>	<i>Aspergillus niger</i> <i>Candida albicans</i>	-	[136]

The presence of antimicrobial peptides (AMP) has been noted in latex-bearing plants and is also responsible for antimicrobial characteristics. The majority of AMPs consist of short peptide sequences (between 12 and 50 amino acids) with about 50% of amino acids present being hydrophobic (Val, Ile, Phe, Trp, Leu), therefore allowing AMPs to penetrate cell membranes [146]. They have been proven to act against bacteria and exhibit immunomodulatory properties through suppression of the inflammatory response and stimulation of the host's immune response [147]. They show activity against bacteria, viruses, fungi, and parasites [148,149]. In the study of J. Siritapetawee et al., the activity of 48-kDa protease (AMP48) from *Artocarpus heterophyllus* Lam. latex has been proven to act against *Pseudomonas aeruginosa* and *Candida albicans* (Table 3) [135]. In the case of bacteria, AMP48 was able to alter the morphology of the bacteria cell and therefore significantly reduce its size after the treatment. Other studies have presented the activity of hevein, a small cysteine-rich peptide found in *H. brasiliensis* latex. The inhibition of hyphal growth of fungi by interacting with chitin present in the fungi cell wall was demonstrated [150].

Other examples of antimicrobial latex activity are related to studies on *Aloe harlana*, specifically two latex proteins anthrone (aloin) and chromone (7-O-methylaloesin A), which were tested against 23 bacterial and four fungi strains (Table 3). The antimicrobial activity of those proteins was comparable to the reference drugs. Additional screenings also showed in vitro antioxidant activity (in 2-deoxyribose and DPPH degradation assays), which is probably caused by the phenolic nature of aloin and chromone [133].

It is also crucial to note that plant latex can serve as a support to traditionally used antibiotics or antimicrobial medicines. For example, *C. procera* latex can act synergistically when used with reference drugs. Both Ciprofloxacin and Clotrimazole had better efficacy when used together with crude latex extract of *C. procera*. The modification of therapeutic

doses can help with potential side effects, drug–drug interactions, and the amount of medicine and latex used [137].

5.4. Immunomodulatory Properties

Complexes of proteins and polysaccharides from *C. majus* (CN-Ala) have been shown to have immunomodulatory potential. Such complexes had a mitogenic activity on the bone marrow and spleen cells, along with increasing the levels of granulocytes and macrophage colony stimulating factors (GM-CSF) [151]. Another study has demonstrated the immunomodulatory effect of *C. majus* latex using mouse peritoneal macrophages. The combination of latex and recombinant interferon (γ) led to a significant increase in nitric oxide (NO) production, expression of inducible nitric oxide synthase (iNOS), and increase in TNF- α production. It is important to note that the *C. majus* latex acted synergistically with γ IFN as the combination of two had better effect on NO, iNOS and TNF- α production than the use of separate compounds [152]. Extracts isolated from *C. majus* were also able to increase humoral and cell-mediated immunity and reduce the frequency of relapses in pharyngitis in children with chronic tonsillitis [153]. Such immunomodulatory effects are thought to be connected with cytoprotective effects through the alleviation of oxidative stress and reduction of the proinflammatory cytokines levels (such as TNF- α , IL-6) [6]. The study conducted by Danielle Cristina de Oliveira Nascimento et al. examined the immunomodulatory properties of latex from the *C. procera* plant against the experimental infection of *Listeria monocytogenes*. *C. procera* latex up-regulated the pro-inflammatory cytokines, involved in leukocyte recruitment and activation. It also prompted TNF- α and IL-6 mRNA transcripts after infection which resulted in higher efficacy of intracellular bacterial killing. Additional in vivo studies on Swiss mice have shown that even one administration of *C. procera* latex resulted in higher survival rate, ease of symptoms of infection, and accumulation of leukocytes in bloodstream along with its increased migration into the peritoneal cavity [154].

Other immunomodulatory activities include immunosuppression effect through reduction of antibody titer (delayed type hypersensitivity), which can be used in the treatment of liver disorders, enhancement of activity of Th1 and Th2 helper T cells as well as natural killer (NK) cells [155], enhancement of production of serum lysozyme, total serum proteins, as well as tissue superoxide dismutase (SOD) and immunoglobulins [156]. There are also reports of phagocytosis activity and stimulation of humoral immunity [157–161].

Although medicinal plants carry numerous biomedical benefits to human health, it is also worth noting the potential toxicity of plant extracts. The most important is the hepatotoxic activity which can bring undesirable effects when administering the drug orally. Liver damage after consumption of *C. majus* herb extracts have been noticed. After discontinuation of treatment symptoms resolved and the liver recovered within 2 months [97,162,163]. Due to the hepatotoxic effects, which are assumed to be connected to pharmacological interaction with non-steroidal anti-inflammatory drugs or hormones, caution is needed [6]. Another safety issue is related to phototoxicity. When administering the plant-based drug on skin, patients should be alerted to the potential danger of sun exposure. The efficacy of the treatment is dependent on several factors, which include the need for regular application or oral administration of the drugs, time of plant harvest since the concentration of secondary metabolites, and protein content variability between seasons, as well as the individual profile of the patients since some subsequent hypotheses suggest that there is always a certain percentage of patients resistant to treatment, no matter what kind of drug is tested [164]. Because of still unknown mechanisms underlying the mode of action of certain latex biomedical compounds, the possibility of side effects such as liver issues, and the small number of clinical studies, further experiments must take place in order to successfully introduce more medicines from plant latexes to the drug market.

6. CRISPR/Cas 9 System as Future Direction for Functional Analysis of Proteins

Since 2013, the CRISPR/Cas9 (clustered regularly interspaced short palindromic repeats/CRISPR associated protein 9) genome editing system, with its Cas9 nuclease directed by target-specifying single guide RNA (sgRNA), has emerged as a practical method for the functional analysis of proteins and then as promising tool for the breeding of new varieties [165]. The CRISPR/Cas9 is a naturally occurring mechanism in bacteria and a few Archaea species. It works similarly to human immune systems and enables bacteria to acquire resistance to viruses after infection [166]. Genome editing with the use of CRISPR/Cas9 system is achieved by the induction of site-specific double-strand breaks, which are in turn repaired by either non-homologous end-joining (NHEJ) or homology-directed repair (HDR) machinery of the cell (see Section 6 and Figure 3). Guide RNAs are designed to identify a three-base-pair protospacer adjacent motif (PAM) sequence occurring downstream of the target DNA. Then DNA is cut by Cas9 nuclease leading to gene knock-out [167]. The CRISPR/Cas9 tool has advantages over previously used methods, like zinc-finger nucleases (ZFNs) and transcription activator-like endonucleases (TALENs), in being easier with simple cloning steps needed, high ease of multiplexing (knockout multiple genes), and large-scale library preparation capacity. This method was successfully used in studies of different gene function, regulatory elements, and genetic mechanisms underlying quantitative trait loci (QTLs) in model organisms, as well as major crop species [168–174]. Several attempts of laticiferous plant modifications with CRISPR/Cas9 were also taken and are surveyed below.

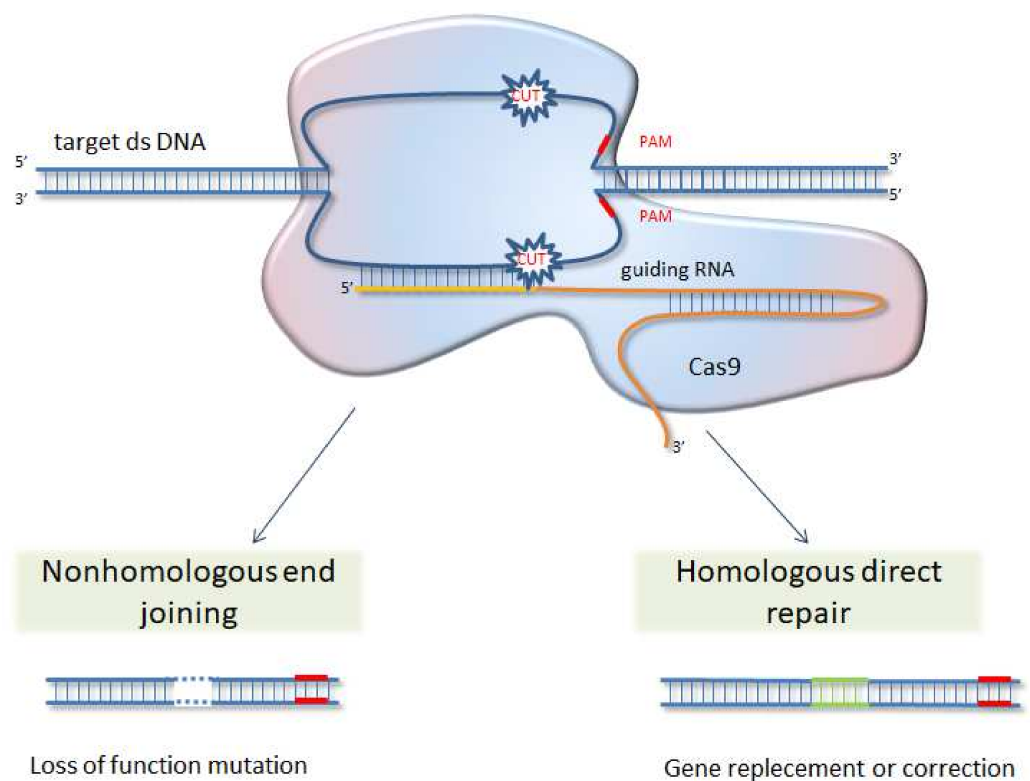


Figure 2. Scheme of CRISPR/Cas9 genome editing technology. Guide RNA, directed by PAM sequences near the targeted gene, lead Cas9 nuclease to altered DNA in desired location. Double strand breaks are repaired either by NHEJ or HDR mechanisms upon the existence of a donor template, which in result lead to deletion or insertion and gene knockout. NHEJ is more efficient than HDR, but may produce indel mutations, whereas HDR can provide a precise gene modification.

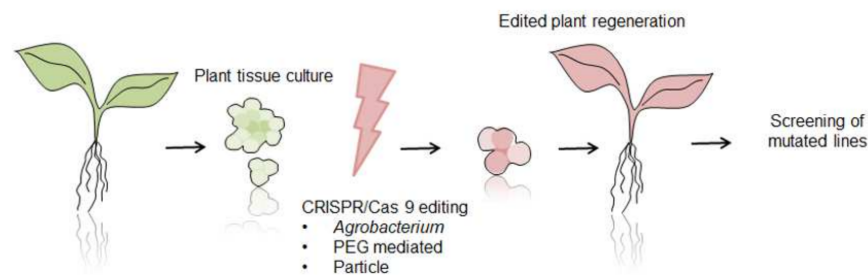


Figure 3. Schematic overview of plant genome editing with CRISPR/Cas9 tool. After obtaining tissue culture from a plant of interest, compounds of CRISPR/Cas9 construct are delivered through *Agrobacterium*, PEG or particle bombardment. In the next step selection of mutated lines, regeneration and screening of mutated plants are performed.

Due to the high importance of natural rubber used to manufacture about 50,000 products, from tires to medical gloves, the Brazilian rubber tree (*H. brasiliensis*), a main source of rubber on a global scale, is subject to modification with CRISPR/Cas9 technology. Five sgRNAs were introduced to *H. brasiliensis* protoplast culture and targeted five different genes involved in flowering regulation—two genes from *FLOWERING LOCUS T* (FT) subfamily and three genes from *TERMINAL FLOWER1* (TFL1) subfamily. Using the RNP-based genome editing system, modifications were introduced in all five genes, from which majority were deletions. The -1 nt deletion of the fourth nucleotide upstream of the PAM sites was the most frequently observed in all cases [175]. The rubber tree is a perennial tree species with a long juvenile phase, so conventional breeding for agronomic trait improvement is time consuming. The creation of early-flowering or delayed-flowering rubber tree plants will undoubtedly push forward studies related to the improvement of yield and quality, along with disease and stress resistance traits of this plant species.

Another example of laticiferous plant modification is the genetic engineering of *Taraxacum kok-saghyz* L.E.Rodin, commonly named Russian dandelion. It is an undomesticated dandelion species which can be a natural rubber source, alternative to *H. brasiliensis*. CRISPR/Cas9 was deployed to knockout gene encoding *fructan:fructan 1-fructosyltransferase* (1-FFT), a key enzyme in inulin biosynthesis [176]. Inulin is considered the main antagonist of rubber production, so the reduction of its synthesis should boost rubber particles formation. Such a modification not only shed lights on rubber biosynthesis mechanisms, but accelerates the domestication of dandelion as a rubber producing crop [177]. The application of *A. rhizogenes*-mediated hairy root induction allows to quickly obtain plants with a mutation rate as high as 80.0% (in regenerated plants).

For the enhancement of *T. kok-saghyz* agronomic performance, the CRISPR/Cas9 system was also used to induce a mutation in a gene called Rapid Alkalinisation Factor 1 (RALF1). In *A. thaliana*, RALF1 has been shown to suppress root growth [178]. As rubber is extracted from dandelion roots, it should be beneficial to change its morphology from branched to taproots, which are easier to harvest, and the wasted yield of lateral roots is minimized. Knockout of gene *TkRALFL1*, achieved using *Agrobacterium tumefaciens*, resulted in introduction of premature stop codon or shortened sequence, which caused the removal of the functionally critical cysteine residues on the protein level. The root volume was 35% higher on average in the heterozygous knockout plants and 60% higher on average in homozygous knockout plants. Moreover, the inulin levels were higher in the knockouts whereas rubber levels were lower. Lower rubber content was compensated for with a higher dry weight of modified roots, such as the total yield per plant of inulin and rubber, which were much higher in knockout plants than in control [179]. It was shown that modification of gene *TkRALFL1* can be used in subsequent breeding of profitable new dandelion varieties.

P. somniferum, as mentioned before, is a rich source of clinically important metabolites, which belongs to a group of benzyloisoquinoline alkaloids (BIAs). For a better understanding of the gene regulation of those compounds synthesis, the CRISPR/Cas9-based

gene knockout system was used to alter BIAs biosynthesis pathway. Enzyme 3'-hydroxy-N-methylcoclaurine 4'-O-methyltransferase (4'OMT), which catalyzes the conversion of central intermediate in BIAs synthesis, was targeted in Agrobacterium-mediated transformation. As a result, decreased total alkaloid content was confirmed. Most dramatic reductions were found in S-reticuline and laudanosine, direct products of 4'OMT [180].

For *Cannabis sativa*, a laticiferous plant species with growing importance in human therapies, a stable transformation protocol for modification with CRISPR/Cas9 strategy has been established recently. In the first step, five genes previously recognized as plant development regulators, were cloned to hypocotyls isolated from the DMG278 variety. Agrobacterium-mediated transformation led to the stimulation of shoot induction, most prominent for the combination of two genes (*CsGRF3-C.*, *sativa* GROWTH-REGULATING FACTOR and *CsGIF1-C.*, *sativa* GRF-INTERACTING FACTOR). After optimization of variety and explant, the constructs expressing sgRNA targeting the *CsPDS1* gene were co-transformed into protoplasts from modified shoot culture. *CsPDS1* encode phytoene desaturase (an enzyme essential for plant carotenoid biosynthesis) and is a common marker gene that can test genetic manipulation tools. Successful knockout of phytoene desaturase results in an easily recognized albino phenotype. Finally, four calli generated white seedlings with the edited *CsPDS1* gene were obtained (account for 2.48% of the generated shoot) [181]. This is the first report of successful gene editing as well as stable transformation in *C. sativa*, which opens new possibilities to improved cannabis varieties production.

7. Conclusions

In the last decades, we have witnessed a huge expansion of demand for herbal medicines, phytonutrients, or nutraceuticals in developing as well as developed countries. They have become a substantial proportion of the global drug market. Moreover, it is estimated that at least four million people rely on herbal medicines as primary sources of healthcare [182]. Therefore, the need for new therapies, but also for plant-derived drugs with a long history of medicinal use (e.g., morphine), is still growing. Laticiferous plant species are a rich source of bioactive compounds (secondary metabolites and proteins), with only partially known medicinal use. The advent of new high throughput sequencing technologies and the fast, efficient genome editing system of CRISPR/Cas9 gives the research community the tools necessary to fulfill the broadened gap between supply and demand for medicines of plant origin. One of the greatest constraints to working with latex-bearing plants is insufficient genome information. Exploration of the genome of the plant of interest enables the precise modification and avoidance of off-target mutations. Nevertheless, the application of CRISPR/Cas9 modification sheds a new light on the function of some genes in laticiferous plant species, as well as sets directions for the improvement of agronomically important traits. Moreover, it provides a modern basis for further exploration and pharmacological utilization of latex compounds.

Author Contributions: Writing—original draft preparation, review and editing, J.G.-B., O.M. and R.N.; visualization, J.G.-B.; supervision, R.N. All authors have read and agreed to the published version of the manuscript.

Funding: This research was funded by the National Science Centre, Poland (grant number 2019/35/B/NZ9/03851).

Institutional Review Board Statement: Not applicable.

Informed Consent Statement: Not applicable.

Data Availability Statement: Data is contained within the article.

Conflicts of Interest: The authors declare no conflict of interest.

References

- Jesus, A.; Bonhomme, V.; Evin, A.; Ivorra, S.; Soteras, R.; Salavert, A.; Antolín, F.; Bouby, L. A Morphometric Approach to Track Opium Poppy Domestication. *Sci. Rep.* **2021**, *11*, 9778. [CrossRef]
- Ren, G.; Zhang, X.; Li, Y.; Ridout, K.; Serrano-Serrano, M.L.; Yang, Y.; Liu, A.; Ravikanth, G.; Nawaz, M.A.; Mumtaz, A.S.; et al. Large-Scale Whole-Genome Resequencing Unravels the Domestication History of *Cannabis sativa*. *Sci. Adv.* **2021**, *7*, eabg2286. [CrossRef]
- Zielińska, S.; Jezierska-Domaradzka, A.; Wójciak-Kosior, M.; Sowa, I.; Junka, A.; Matkowski, A.M. Greater Celandine's Ups and Downs—21 Centuries of Medicinal Uses of *Chelidonium majus* from the Viewpoint of Today's Pharmacology. *Front. Pharmacol.* **2018**, *9*, 299. [CrossRef]
- Gilca, M.; Gaman, L.; Panait, E.; Stoian, I.; Atanasiu, V. *Chelidonium majus*—An Integrative Review: Traditional Knowledge versus Modern Findings. *Complementary Med. Res.* **2010**, *17*, 241–248. [CrossRef] [PubMed]
- Maji, A.K.; Banerji, P. *Chelidonium majus* L. (Greater celandine—A Review on Its Phytochemical and Therapeutic Perspectives. *Int. J. Herb. Med.* **2015**, *3*, 10–27. [CrossRef]
- Nawrot, J.; Wilk-Jędrusik, M.; Nawrot, S.; Nawrot, K.; Wilk, B.; Dawid-Pač, R.; Urbańska, M.; Micek, I.; Nowak, G.; Gornowicz-Porowska, J. Milky Sap of Greater Celandine (*Chelidonium majus* L.) and Anti-Viral Properties. *Int. J. Environ. Res. Public Health* **2020**, *17*, 1540. [CrossRef] [PubMed]
- Salomé Abarca, L.F.; Klinkhamer, P.G.L.; Choi, Y.H. Plant Latex, from Ecological Interests to Bioactive Chemical Resources. *Planta Med.* **2019**, *85*, 856–868. [CrossRef]
- Nawrot, R. (Ed.) *Latex, Laticifers and Their Molecular Components—From Functions to Possible Applications*; Advances in Botanical Research Series; Academic Press: Cambridge, MA, USA, 2020.
- Kekwick, R.G.O. Latex and Laticifers. In *Encyclopedia of Life Sciences 2002*; John Wiley & Sons: London, UK; New York, NY, USA, 2002.
- Ramos, M.V.; Demarco, D.; da Costa Souza, I.C.; de Freitas, C.D.T. Laticifers, Latex, and Their Role in Plant Defense. *Trends Plant Sci.* **2019**, *24*, 553–567. [CrossRef]
- Hagel, J.M.; Yeung, E.C.; Facchini, P.J. Got Milk? The Secret Life of Laticifers. *Trends Plant Sci.* **2008**, *13*, 631–639. [CrossRef]
- Prado, E.; Demarco, D. Laticifers and secretory ducts: Similarities and differences. In *Ecosystem Services and Global Ecology*; InTech: London, UK, 2018; ISBN 9781789237382.
- Marinho, C.R.; Teixeira, S.P. Cellulases and Pectinases Act Together on the Development of Articulated Laticifers in *Ficus montana* and *Maclura tinctoria* (Moraceae). *Protoplasma* **2019**, *256*, 1093–1107. [CrossRef] [PubMed]
- Kitajima, S.; Taira, T.; Oda, K.; Yamato, K.T.; Inukai, Y.; Hori, Y. Comparative Study of Gene Expression and Major Proteins' Function of Laticifers in Lignified and Unlignified Organs of Mulberry. *Planta* **2012**, *235*, 589–601. [CrossRef]
- Van Veenendaal, W.L.H.; Den Outer, R.W. Distribution and Development of the Non-Articulated Branched Laticifers of *Morus nigra* L. (Moraceae). *Acta Bot. Neerl.* **1990**, *39*, 285–296. [CrossRef]
- Webster, C.C. Natural Rubber: Biology, Cultivation and Technology. *Agric. Syst.* **1994**, *45*, 233–235. [CrossRef]
- Dussourd, D.E. Entrapment of Aphids and Whiteflies in Lettuce Latex. *Ann. Entomol. Soc. Am.* **1995**, *88*, 163–172. [CrossRef]
- Agrawal, A.A.; Konno, K. Latex: A Model for Understanding Mechanisms, Ecology, and Evolution of Plant Defense against Herbivory. *Annu. Rev. Ecol. Evol. Syst.* **2009**, *40*, 311–331. [CrossRef]
- Nawrot, R.; Wołń-Cholewa, M.; Goździcka-Józefiak, A. Nucleases Isolated from *Chelidonium majus* L. Milky Sap Can Induce Apoptosis in Human Cervical Carcinoma HeLa Cells but Not in Chinese Hamster Ovary CHO Cells. *Folia Histochem. Cytobiol.* **2008**, *46*, 79–83. [CrossRef]
- Konno, K. Plant Latex and Other Exudates as Plant Defense Systems: Roles of Various Defense Chemicals and Proteins Contained Therein. *Phytochemistry* **2011**, *72*, 1510–1530. [CrossRef] [PubMed]
- Wink, M. Plant Secondary Metabolism: Diversity, Function and Its Evolution. *Nat. Prod. Commun.* **2008**, *3*, 1205–1216. [CrossRef]
- Souza, D.P.; Freitas, C.D.T.; Pereira, D.A.; Nogueira, F.C.; Silva, F.D.A.; Salas, C.E.; Ramos, M.V. Laticifer Proteins Play a Defensive Role against Hemibiotrophic and Necrotrophic Phytopathogens. *Planta* **2011**, *234*, 183–193. [CrossRef]
- Ramos, M.V.; Grangeiro, T.B.; Freire, E.A.; Sales, M.P.; Souza, D.P.; Araújo, E.S.; Freitas, C.D.T. The Defensive Role of Latex in Plants: Detrimental Effects on Insects. *Arthropod-Plant Interact.* **2010**, *4*, 57–67. [CrossRef]
- Men, X.; Wang, F.; Chen, G.-Q.; Zhang, H.-B.; Xian, M. Biosynthesis of Natural Rubber: Current State and Perspectives. *Int. J. Mol. Sci.* **2018**, *20*, 50. [CrossRef]
- Tang, C.; Qi, J.; Li, H.; Zhang, C.; Wang, Y. A Convenient and Efficient Protocol for Isolating High-Quality RNA from Latex of *Hevea brasiliensis* (para Rubber Tree). *J. Biochem. Biophys. Methods* **2007**, *70*, 749–754. [CrossRef]
- Salvucci, M.E.; Barta, C.; Byers, J.A.; Canarini, A. Photosynthesis and Assimilate Partitioning between Carbohydrates and Isoprenoid Products in Vegetatively Active and Dormant Guayule: Physiological and Environmental Constraints on Rubber Accumulation in a Semi-arid Shrub. *Physiol. Plant.* **2010**, *140*, 368–379. [CrossRef]
- Sessa, R.A.; Bennett, M.H.; Lewis, M.J.; Mansfield, J.W.; Beale, M.H. Metabolite Profiling of Sesquiterpene Lactones from Lactuca Species. Major Latex Components Are Novel Oxalate and Sulfate Conjugates of Lactucin and Its Derivatives. *J. Biol. Chem.* **2000**, *275*, 26877–26884. [CrossRef]
- Valitova, J.N.; Sulkarnayeva, A.G.; Minibayeva, F.V. Plant Sterols: Diversity, Biosynthesis, and Physiological Functions. *Biochemistry* **2016**, *81*, 819–834. [CrossRef] [PubMed]

29. Che Sulaiman, I.S.; Basri, M.; Fard Masoumi, H.R.; Chee, W.J.; Ashari, S.E.; Ismail, M. Effects of Temperature, Time, and Solvent Ratio on the Extraction of Phenolic Compounds and the Anti-Radical Activity of Clinacanthus Nutans Lindau Leaves by Response Surface Methodology. *Chem. Cent. J.* **2017**, *11*, 54. [CrossRef]
30. Snook, M.E.; Data, E.S.; Kays, S.J. Characterization and Quantitation of Hexadecyl, Octadecyl, and Eicosyl Esters of P-Coumaric Acid in the Vine and Root Latex of Sweetpotato [*Ipomoea batatas* (L.) Lam.]. *J. Agric. Food Chem.* **1994**, *42*, 2589–2595. [CrossRef]
31. Ismun, A.; Ariffin, M.M.; Razak, S.B.A.; Wei, O.C.; Ahmad, F.T.; Mubarak, A. determination of polyphenol contents in *Hevea brasiliensis* and rubber-processing effluent. *Malays. J. Anal. Sci.* **2018**, *22*, 185–196. [CrossRef]
32. Huber, M.; Triebwasser-Freese, D.; Reichelt, M.; Heiling, S.; Paetz, C.; Chandran, J.N.; Bartram, S.; Schneider, B.; Gershenzon, J.; Erb, M. Identification, Quantification, Spatiotemporal Distribution and Genetic Variation of Major Latex Secondary Metabolites in the Common Dandelion (*Taraxacum officinale* Agg.). *Phytochemistry* **2015**, *115*, 89–98. [CrossRef]
33. Nguyen, T.-D.; Dang, T.-T.T. Cytochrome P450 Enzymes as Key Drivers of Alkaloid Chemical Diversification in Plants. *Front. Plant Sci.* **2021**, *12*, 682181. [CrossRef]
34. Itenov, K.; Mølgaard, P.; Nyman, U. Diurnal Fluctuations of the Alkaloid Concentration in Latex of Poppy Papaver Somniferum Is due to Day–night Fluctuations of the Latex Water Content. *Phytochemistry* **1999**, *52*, 1229–1234. [CrossRef]
35. Tomè, F.; Colombo, M.L. Distribution of Alkaloids in *Chelidonium majus* and Factors Affecting Their Accumulation. *Phytochemistry* **1995**, *40*, 37–39. [CrossRef]
36. Mikołajczak, P.Ł.; Kędzia, B.; Ożarowski, M.; Kujawski, R.; Bogacz, A.; Bartkowiak-Wieczorek, J.; Białas, W.; Gryszczyńska, A.; Buchwald, W.; Szulc, M.; et al. Evaluation of Anti-Inflammatory and Analgesic Activities of Extracts from Herb of *Chelidonium majus* L. *Cent. Eur. J. Immunol.* **2015**, *40*, 400–410. [CrossRef]
37. Kopp, B.; Bauer, W.P.; Bernkop-Schnürch, A. Analysis of Some Malaysian Dart Poisons. *J. Ethnopharmacol.* **1992**, *36*, 57–62. [CrossRef]
38. Agrawal, A.A.; Petschenka, G.; Bingham, R.A.; Weber, M.G.; Rasmann, S. Toxic Cardenolides: Chemical Ecology and Coevolution of Specialized Plant-Herbivore Interactions. *New Phytol.* **2012**, *194*, 28–45. [CrossRef]
39. Malcolm, S.B. Milkweeds, Monarch Butterflies and the Ecological Significance of Cardenolides. *Chemoecology* **1994**, *5–6*, 101–117. [CrossRef]
40. Cho, W.K.; Jo, Y.; Chu, H.; Park, S.-H.; Kim, K.-H. Integration of Latex Protein Sequence Data Provides Comprehensive Functional Overview of Latex Proteins. *Mol. Biol. Rep.* **2014**, *41*, 1469–1481. [CrossRef]
41. Balakireva, A.V.; Zamyatnin, A.A. Indispensable Role of Proteases in Plant Innate Immunity. *Int. J. Mol. Sci.* **2018**, *19*, 629. [CrossRef] [PubMed]
42. Konno, K.; Hirayama, C.; Nakamura, M.; Tateishi, K.; Tamura, Y.; Hattori, M.; Kohno, K. Papain Protects Papaya Trees from Herbivorous Insects: Role of Cysteine Proteases in Latex. *Plant J.* **2004**, *37*, 370–378. [CrossRef]
43. de Freitas, C.D.T.; de Freitas, C.D.T.; de Souza, D.P.; Araújo, E.S.; Cavalheiro, M.G.; Oliveira, L.S.; Ramos, M.V. Anti-Oxidative and Proteolytic Activities and Protein Profile of Laticifer Cells of *Cryptostegia Grandiflora*, *Plumeria Rubra* and *Euphorbia Tirucalli*. *Braz. J. Plant Physiol.* **2010**, *22*, 11–22. [CrossRef]
44. Kim, J.-Y.; Park, S.-C.; Hwang, I.; Cheong, H.; Nah, J.-W.; Hahm, K.-S.; Park, Y. Protease Inhibitors from Plants with Antimicrobial Activity. *Int. J. Mol. Sci.* **2009**, *10*, 2860–2872. [CrossRef] [PubMed]
45. Kim, J.S.; Kim, Y.O.; Ryu, H.J.; Kwak, Y.S.; Lee, J.Y.; Kang, H. Isolation of Stress-Related Genes of Rubber Particles and Latex in Fig Tree (*Ficus Carica*) and Their Expressions by Abiotic Stress or Plant Hormone Treatments. *Plant Cell Physiol.* **2003**, *44*, 412–414. [CrossRef] [PubMed]
46. Azarkan, M.; Wintjens, R.; Looze, Y.; Baeyens-Volant, D. Detection of Three Wound-Induced Proteins in Papaya Latex. *Phytochemistry* **2004**, *65*, 525–534. [CrossRef] [PubMed]
47. Gidrol, X.; Chrestin, H.; Tan, H.L.; Kush, A. Hevein, a Lectin-like Protein from *Hevea Brasiliensis* (rubber Tree) Is Involved in the Coagulation of Latex. *J. Biol. Chem.* **1994**, *269*, 9278–9283. [CrossRef]
48. Barre, A.; Van Damme, E.J.M.; Simplicien, M.; Benoist, H.; Rougé, P. Are Dietary Lectins Relevant Allergens in Plant Food Allergy? *Foods* **2020**, *9*, 1724. [CrossRef]
49. Vandendorre, G.; Smagghe, G.; Van Damme, E.J.M. Plant Lectins as Defense Proteins against Phytophagous Insects. *Phytochemistry* **2011**, *72*, 1538–1550. [CrossRef]
50. Lehrman, A. Does Pea Lectin Expressed Transgenically in Oilseed Rape (*Brassica napus*) Influence Honey Bee (*Apis mellifera*) Larvae? *Environ. Biosafety Res.* **2007**, *6*, 271–278. [CrossRef]
51. John, K.S.; Bhat, S.G.; Prasada Rao, U.J.S. Biochemical Characterization of Sap (latex) of a Few Indian Mango Varieties. *Phytochemistry* **2003**, *62*, 13–19. [CrossRef]
52. Wititsuwannakul, D.; Chareonthiphakorn, N.; Pace, M.; Wititsuwannakul, R. Polyphenol Oxidases from Latex of *Hevea Brasiliensis*: Purification and Characterization. *Phytochemistry* **2002**, *61*, 115–121. [CrossRef]
53. Zhang, J.; Sun, X. Recent Advances in Polyphenol Oxidase-Mediated Plant Stress Responses. *Phytochemistry* **2021**, *181*, 112588. [CrossRef]
54. Rajput, V.D.; Harish; Singh, R.K.; Verma, K.K.; Sharma, L.; Quiroz-Figueroa, F.R.; Meena, M.; Gour, V.S.; Minkina, T.; Sushkova, S.; et al. Recent Developments in Enzymatic Antioxidant Defence Mechanism in Plants with Special Reference to Abiotic Stress. *Biology* **2021**, *10*, 267. [CrossRef]

55. Kidwai, M.; Ahmad, I.Z.; Chakrabarty, D. Class III Peroxidase: An Indispensable Enzyme for Biotic/abiotic Stress Tolerance and a Potent Candidate for Crop Improvement. *Plant Cell Rep.* **2020**, *39*, 1381–1393. [CrossRef]
56. Bishop, J.G.; Dean, A.M.; Mitchell-Olds, T. Rapid Evolution in Plant Chitinases: Molecular Targets of Selection in Plant-Pathogen Coevolution. *Proc. Natl. Acad. Sci. USA* **2000**, *97*, 5322–5327. [CrossRef]
57. Kitajima, S.; Kamei, K.; Taketani, S.; Yamaguchi, M.; Kawai, F.; Komatsu, A.; Inukai, Y. Two Chitinase-like Proteins Abundantly Accumulated in Latex of Mulberry Show Insecticidal Activity. *BMC Biochem.* **2010**, *11*, 6. [CrossRef]
58. Gursharan, S.; Shailendra Kumar, A. Antifungal and Insecticidal Potential of Chitinases: A Credible Choice for the Eco-Friendly Farming. *Biocatal. Agric. Biotechnol.* **2019**, *20*, 101289.
59. Taira, T.; Ohdomari, A.; Nakama, N.; Shimoji, M.; Ishihara, M. Characterization and Antifungal Activity of Gazyumaru (*Ficus Microcarpa*) Latex Chitinases: Both the Chitin-Binding and the Antifungal Activities of Class I Chitinase Are Reinforced with Increasing Ionic Strength. *Biosci. Biotechnol. Biochem.* **2005**, *69*, 811–818. [CrossRef]
60. Martin, M.N. The Latex of *Hevea Brasiliensis* Contains High Levels of Both Chitinases and Chitinases/Lysozymes. *Plant Physiol.* **1991**, *95*, 469–476. [CrossRef]
61. Freitas, C.D.T.; Viana, C.A.; Vasconcelos, I.M.; Moreno, F.B.B.; Lima-Filho, J.V.; Oliveira, H.D.; Moreira, R.A.; Monteiro-Moreira, A.C.O.; Ramos, M.V. First Insights into the Diversity and Functional Properties of Chitinases of the Latex of *Calotropis procera*. *Plant Physiol. Biochem.* **2016**, *108*, 361–371. [CrossRef]
62. Musidlak, O.; Nawrot, R.; Goździcka-Józefiak, A. Which Plant Proteins Are Involved in Antiviral Defense? Review on In Vivo and In Vitro Activities of Selected Plant Proteins against Viruses. *Int. J. Mol. Sci.* **2017**, *18*, 2300. [CrossRef]
63. Ali, S.; Ganai, B.A.; Kamili, A.N.; Bhat, A.A.; Mir, Z.A.; Bhat, J.A.; Tyagi, A.; Islam, S.T.; Mushtaq, M.; Yadav, P.; et al. Pathogenesis-Related Proteins and Peptides as Promising Tools for Engineering Plants with Multiple Stress Tolerance. *Microbiol. Res.* **2018**, *212–213*, 29–37. [CrossRef]
64. Nessler, C.L. Sequence Analysis of Two New Members of the Major Latex Protein Gene Family Supports the Triploid-Hybrid Origin of the Opium Poppy. *Gene* **1994**, *139*, 207–209. [CrossRef]
65. Nessler, C.L.; Allen, R.D.; Galewsky, S. Identification and Characterization of Latex-Specific Proteins in Opium Poppy. *Plant Physiol.* **1985**, *79*, 499–504. [CrossRef] [PubMed]
66. Nessler, C.L.; Vonder Haar, R.A. Cloning and Expression Analysis of DNA Sequences for the Major Latex Protein of Opium Poppy. *Planta* **1990**, *180*, 487–491. [CrossRef] [PubMed]
67. Ruperti, B.; Bonghi, C.; Ziliotto, F.; Pagni, S.; Rasori, A.; Varotto, S.; Tonutti, P.; Giovannoni, J.J.; Ramina, A. Characterization of a Major Latex Protein (MLP) Gene down-Regulated by Ethylene during Peach Fruitlet Abscission. *Plant Sci.* **2002**, *163*, 265–272. [CrossRef]
68. Lytle, B.L.; Song, J.; de la Cruz, N.B.; Peterson, F.C.; Johnson, K.A.; Bingman, C.A.; Phillips, G.N., Jr.; Volkman, B.F. Structures of Two *Arabidopsis thaliana* Major Latex Proteins Represent Novel Helix-Grip Folds. *Proteins* **2009**, *76*, 237–243. [CrossRef] [PubMed]
69. Chruszcz, M.; Ciardiello, M.A.; Osinski, T.; Majorek, K.A.; Giangrieco, I.; Font, J.; Breiteneder, H.; Thalassinou, K.; Minor, W. Structural and Bioinformatic Analysis of the Kiwifruit Allergen Act D 11, a Member of the Family of Ripening-Related Proteins. *Mol. Immunol.* **2013**, *56*, 794–803. [CrossRef]
70. Sun, H.; Kim, M.-K.; Pulla, R.K.; Kim, Y.-J.; Yang, D.-C. Isolation and Expression Analysis of a Novel Major Latex-like Protein (MLP151) Gene from *Panax Ginseng*. *Mol. Biol. Rep.* **2010**, *37*, 2215–2222. [CrossRef] [PubMed]
71. Osmark, P.; Boyle, B.; Brisson, N. Sequential and Structural Homology between Intracellular Pathogenesis-Related Proteins and a Group of Latex Proteins. *Plant Mol. Biol.* **1998**, *38*, 1243–1246. [CrossRef]
72. Park, C.-J.; Kim, K.-J.; Shin, R.; Park, J.M.; Shin, Y.-C.; Paek, K.-H. Pathogenesis-Related Protein 10 Isolated from Hot Pepper Functions as a Ribonuclease in an Antiviral Pathway. *Plant J.* **2004**, *37*, 186–198. [CrossRef]
73. Yang, C.-L.; Liang, S.; Wang, H.-Y.; Han, L.-B.; Wang, F.-X.; Cheng, H.-Q.; Wu, X.-M.; Qu, Z.-L.; Wu, J.-H.; Xia, G.-X. Cotton Major Latex Protein 28 Functions as a Positive Regulator of the Ethylene Responsive Factor 6 in Defense against *Verticillium dahliae*. *Mol. Plant* **2015**, *8*, 399–411. [CrossRef]
74. Nawrot, R. Defense-Related Proteins from *Chelidonium majus* L. as Important Components of Its Latex. *Curr. Protein Pept. Sci.* **2017**, *18*, 864–880. [CrossRef] [PubMed]
75. Chadha, P.; Das, R.H. A Pathogenesis Related Protein, AhPR10 from Peanut: An Insight of Its Mode of Antifungal Activity. *Planta* **2006**, *225*, 213–222. [CrossRef]
76. Michalska, K.; Fernandes, H.; Sikorski, M.; Jaskolski, M. Crystal Structure of Hyp-1, a St. John's Wort Protein Implicated in the Biosynthesis of Hypericin. *J. Struct. Biol.* **2010**, *169*, 161–171. [CrossRef] [PubMed]
77. Bantignies, B.; Séguin, J.; Muzac, I.; Dédaldéchamp, F.; Gulick, P.; Ibrahim, R. Direct Evidence for Ribonucleolytic Activity of a PR-10-like Protein from White Lupin Roots. *Plant Mol. Biol.* **2000**, *42*, 871–881. [CrossRef] [PubMed]
78. Nawrot, R.; Barylski, J.; Lippmann, R.; Altschmied, L.; Mock, H.-P. Combination of Transcriptomic and Proteomic Approaches Helps to Unravel the Protein Composition of *Chelidonium majus* L. Milky Sap. *Planta* **2016**, *244*, 1055–1064. [CrossRef]
79. Song, L.; Wang, J.; Jia, H.; Kamran, A.; Qin, Y.; Liu, Y.; Hao, K.; Han, F.; Zhang, C.; Li, B.; et al. Identification and Functional Characterization of NbMLP28, a Novel MLP-like Protein 28 Enhancing Potato Virus Y Resistance in *Nicotiana glauca*. *BMC Microbiol.* **2020**, *20*, 55. [CrossRef] [PubMed]

80. Malter, D.; Wolf, S. Melon Phloem-Sap Proteome: Developmental Control and Response to Viral Infection. *Protoplasma* **2011**, *248*, 217–224. [CrossRef] [PubMed]
81. Onoyovwe, A.; Hagel, J.M.; Chen, X.; Khan, M.F.; Schriemer, D.C.; Facchini, P.J. Morphine Biosynthesis in Opium Poppy Involves Two Cell Types: Sieve Elements and Laticifers. *Plant Cell* **2013**, *25*, 4110–4122. [CrossRef] [PubMed]
82. Nawrot, R.; Lippmann, R.; Matros, A.; Musidlak, O.; Nowicki, G.; Mock, H.-P. Proteomic Comparison of *Chelidonium majus* L. Latex in Different Phases of Plant Development. *Plant Physiol. Biochem.* **2017**, *112*, 312–325. [CrossRef]
83. D’Amato, A.; Bachi, A.; Fasoli, E.; Boschetti, E.; Peltre, G.; Sénéchal, H.; Sutra, J.P.; Citterio, A.; Righetti, P.G. In-Depth Exploration of *Hevea Brasiliensis* Latex Proteome and “Hidden Allergens” via Combinatorial Peptide Ligand Libraries. *J. Proteom.* **2010**, *73*, 1368–1380. [CrossRef] [PubMed]
84. Zulak, K.G.; Khan, M.F.; Alcantara, J.; Schriemer, D.C.; Facchini, P.J. Plant Defense Responses in Opium Poppy Cell Cultures Revealed by Liquid Chromatography-Tandem Mass Spectrometry Proteomics. *Mol. Cell. Proteom.* **2009**, *8*, 86–98. [CrossRef]
85. Samatadze, T.E.; Zoshchuk, S.A.; Khomik, A.S.; Amosova, A.V.; Svistunova, N.Y.; Suslina, S.N.; Hazieva, F.M.; Yurkevich, O.Y.; Muravenko, O.V. Molecular Cytogenetic Characterization, Leaf Anatomy and Ultrastructure of the Medicinal Plant *Potentilla alba* L. *Genet. Resour. Crop. Evol.* **2018**, *65*, 1637–1647. [CrossRef]
86. Gardin, N.E.; Braga, A.J. Greater Celandine (*Chelidonium majus* L.) for COVID-19: A Twenty-Case Series. *Phytother. Res.* **2021**, *35*, 3792–3798. [CrossRef]
87. Foster, S.; Bradshaw, R.H.; McLanahan, S.; Redwood, D.; Upton, R. Book Reviews: The Complete German Commission E Monographs: Therapeutic Guide to Herbal Medicines. *J. Altern. Complementary Med.* **1998**, *4*, 479–486. [CrossRef]
88. Lee, E.-J.; Hagel, J.M.; Facchini, P.J. Role of the Phloem in the Biochemistry and Ecophysiology of Benzylisoquinoline Alkaloid Metabolism. *Front. Plant Sci.* **2013**, *4*, 182. [CrossRef] [PubMed]
89. Mithöfer, A.; Boland, W. Plant Defense against Herbivores: Chemical Aspects. *Annu. Rev. Plant Biol.* **2012**, *63*, 431–450. [CrossRef]
90. Upadhyay, R.K. Plant Latex: A Natural Source of Pharmaceuticals and Pesticides. *Int. J. Green Pharm. (IJGP)* **2011**, *5*, 169–180. [CrossRef]
91. Gurkok, T.; Turktas, M.; Parmaksiz, I.; Unver, T. Transcriptome Profiling of Alkaloid Biosynthesis in Elicitor Induced Opium Poppy. *Plant Mol. Biol. Rep.* **2015**, *33*, 673–688. [CrossRef]
92. Labanca, F.; Ovesnà, J.; Milella, L. *Papaver Somniferum* L. Taxonomy, Uses and New Insight in Poppy Alkaloid Pathways. *Phytochem. Rev.* **2018**, *17*, 853–871. [CrossRef]
93. De Petrocellis, L.; Ligresti, A.; Moriello, A.S.; Allarà, M.; Bisogno, T.; Petrosino, S.; Stott, C.G.; Di Marzo, V. Effects of Cannabinoids and Cannabinoid-Enriched Cannabis Extracts on TRP Channels and Endocannabinoid Metabolic Enzymes. *Br. J. Pharmacol.* **2011**, *163*, 1479–1494. [CrossRef]
94. Pacher, P.; Bátkai, S.; Kunos, G. The Endocannabinoid System as an Emerging Target of Pharmacotherapy. *Pharmacol. Rev.* **2006**, *58*, 389–462. [CrossRef] [PubMed]
95. Burstein, S. Cannabidiol (CBD) and Its Analogs: A Review of Their Effects on Inflammation. *Bioorg. Med. Chem.* **2015**, *23*, 1377–1385. [CrossRef]
96. Etxenagusia, M.A.; Anda, M.; González-Mahave, I.; Fernández, E.; Fernández de Corrés, L. Contact Dermatitis from *Chelidonium majus* (greater Celandine). *Contact Dermat.* **2000**, *43*, 47.
97. Monavari, S.H.; Shahrabadi, M.S.; Keyvani, H.; Bokharaei-Salim, F. Evaluation of In Vitro Antiviral Activity of *Chelidonium majus* L. against Herpes Simplex Virus Type-1. *Afr. J. Microbiol. Res.* **2012**, *6*, 4360–4364.
98. Horvath, J.; Kery, A.; Kulcsar, G.; Dan, P.; Nasz, J. Antiviral Effect of *Chelidonium* Extracts. In *Spitzky ILH, Karrev K (eds) 13–14 Proc Int Congr Chemother*; Egermann: Vienna, Austria, 1983; Volume 9, pp. 124/106–124/110.
99. Gerencer, M.; Turecek, P.L.; Kistner, O.; Mitterer, A.; Savidis-Dacho, H.; Barrett, N.P. In Vitro and in Vivo Anti-Retroviral Activity of the Substance Purified from the Aqueous Extract of *Chelidonium majus* L. *Antivir. Res.* **2006**, *72*, 153–156. [CrossRef]
100. Mandadi, K.K.; Scholthof, K.-B.G. Plant Immune Responses against Viruses: How Does a Virus Cause Disease? *Plant Cell* **2013**, *25*, 1489–1505. [CrossRef] [PubMed]
101. Wojtaszek, P. Oxidative Burst: An Early Plant Response to Pathogen Infection. *Biochem. J.* **1997**, *322 Pt 3*, 681–692. [CrossRef] [PubMed]
102. Nawrot, R.; Kalinowski, A.; Gozdzicka-Jozefiak, A. Proteomic Analysis of *Chelidonium majus* Milky Sap Using Two-Dimensional Gel Electrophoresis and Tandem Mass Spectrometry. *Phytochemistry* **2007**, *68*, 1612–1622. [CrossRef]
103. Nawrot, R.; Tomaszewski, Ł.; Czerwoniec, A.; Gozdzicka-Józefiak, A. Identification of a Coding Sequence and Structure Modeling of a Glycine-Rich RNA-Binding Protein (CmGRP1) from *Chelidonium majus* L. *Plant Mol. Biol. Report.* **2013**, *31*, 470–476. [CrossRef]
104. Huh, S.U.; Paek, K.-H. Plant RNA Binding Proteins for Control of RNA Virus Infection. *Front. Physiol.* **2013**, *4*, 397. [CrossRef]
105. Zvereva, A.S.; Pooggin, M.M. Silencing and Innate Immunity in Plant Defense against Viral and Non-Viral Pathogens. *Viruses* **2012**, *4*, 2578–2597. [CrossRef]
106. Kéry, A.; Horváth, J.; Nász, I.; Verzár-Petri, G.; Kulcsár, G.; Dán, P. Antiviral Alkaloid in *Chelidonium majus* L. *Acta Pharm. Hung.* **1987**, *57*, 19–25.
107. Lozjuk, R.M.; Lisnyak, O.I.; Lozjuk, L.V. Theoretical Grounds and Experimental Confirmation of the Antiviral Effect of the Preparation Ukrain. *Drugs Exp. Clin. Res.* **1996**, *22*, 213–217. [PubMed]
108. Camero, M.; Marinario, M.; Lovero, A.; Elia, G.; Losurdo, M.; Buonavoglia, C.; Tempesta, M. In Vitroantiviral Activity of *Ficus Caricalatex* against Caprine Herpesvirus-1. *Nat. Prod. Res.* **2014**, *28*, 2031–2035. [CrossRef] [PubMed]

109. Aref, H.L.; Gaaliche, B.; Fekih, A.; Mars, M.; Aouni, M.; Chaumon, J.P.; Said, K. In Vitro Cytotoxic and Antiviral Activities of *Ficus Caricifolia* Extracts. *Nat. Prod. Res.* **2011**, *25*, 310–319. [CrossRef]
110. Beloin, N.; Gbeassor, M.; Akpagana, K.; Hudson, J.; de Souza, K.; Koumaglo, K.; Thor Arnason, J. Ethnomedicinal Uses of *Momordica Charantia* (Cucurbitaceae) in Togo and Relation to Its Phytochemistry and Biological Activity. *J. Ethnopharmacol.* **2005**, *96*, 49–55. [CrossRef]
111. Pengsuparp, T.; Serit, M.; Hughes, S.H.; Soejarto, D.D.; Pezzuto, J.M. Specific Inhibition of Human Immunodeficiency Virus Type 1 Reverse Transcriptase Mediated by Soualattrolide, a Coumarin Isolated from the Latex of *Calophyllum Teysmannii*. *J. Nat. Prod.* **1996**, *59*, 839–842. [CrossRef]
112. Ubillas, R.; Jolad, S.D.; Bruening, R.C.; Kernan, M.R.; King, S.R.; Sesin, D.F.; Barrett, M.; Stoddart, C.A.; Flaster, T.; Kuo, J.; et al. SP-303, an Antiviral Oligomeric Proanthocyanidin from the Latex of *Croton Lechleri* (Sangre de Drago). *Phytomedicine* **1994**, *1*, 77–106. [CrossRef]
113. Parhira, S.; Yang, Z.-F.; Zhu, G.-Y.; Chen, Q.-L.; Zhou, B.-X.; Wang, Y.-T.; Liu, L.; Bai, L.-P.; Jiang, Z.-H. In Vitro Anti-Influenza Virus Activities of a New Lignan Glycoside from the Latex of *Calotropis Gigantea*. *PLoS ONE* **2014**, *9*, e104544. [CrossRef]
114. Kim, H.K.; Farnsworth, N.R.; Blomster, R.N.; Fong, H.H. Biological and Phytochemical Evaluation of Plants. V. Isolation of Two Cytotoxic Alkaloids from *Chelidonium majus*. *J. Pharm. Sci.* **1969**, *58*, 372–374. [CrossRef]
115. Vavrečková, C.; Gawlik, I.; Müller, K. Benzophenanthridine Alkaloids of *Chelidonium majus*; II. Potent Inhibitory Action Against the Growth of Human Keratinocytes. *Planta Med.* **1996**, *62*, 491–494. [CrossRef]
116. Rogelj, B.; Popovic, T.; Ritonja, A.; Strukelj, B.; Brzin, J. Chelidocystatin, a Novel Phytocystatin from *Chelidonium majus*. *Phytochemistry* **1998**, *49*, 1645–1649. [CrossRef]
117. Philchenkov, A.; Kaminskyy, V.; Zavelevich, M.; Stoika, R. Apoptogenic Activity of Two Benzophenanthridine Alkaloids from *Chelidonium majus* L. Does Not Correlate with Their DNA Damaging Effects. *Toxicol. In Vitro* **2008**, *22*, 287–295. [CrossRef]
118. Paul, A.; Bishayee, K.; Ghosh, S.; Mukherjee, A.; Sikdar, S.; Chakraborty, D.; Boujedaini, N.; Khuda-Bukhsh, A.R. Chelidonine Isolated from Ethanolic Extract of *Chelidonium majus* Promotes Apoptosis in HeLa Cells through p38-p53 and PI3K/AKT Signalling Pathways. *Zhong Xi Yi Jie He Xue Bao* **2012**, *10*, 1025–1038. [CrossRef]
119. Kulp, M.; Bragina, O. Capillary Electrophoretic Study of the Synergistic Biological Effects of Alkaloids from *Chelidonium majus* L. in Normal and Cancer Cells. *Anal. Bioanal. Chem.* **2013**, *405*, 3391–3397. [CrossRef]
120. Riede, F.v.D.I. *Chelidonium majus* in der Therapie Prämaligener Hautveränderungen. Available online: https://www.researchgate.net/publication/260197370_Chelidonium_majus_in_der_Therapie_pramaligner_Hautveränderungen (accessed on 15 November 2021).
121. Abdel-Aty, A.M.; Hamed, M.B.; Salama, W.H.; Ali, M.M.; Fahmy, A.S.; Mohamed, S.A. *Ficus Carica*, *Ficus Sycomorus* and *Euphorbia Tirucalli* Latex Extracts: Phytochemical Screening, Antioxidant and Cytotoxic Properties. *Biocatal. Agric. Biotechnol.* **2019**, *20*, 101199. [CrossRef]
122. Tulasi, C.; Lakshmi Narasu, M.; Saida, L. Cytotoxic Effect of *Ficus Religiosa* and *Ficus Benghalensis* Latex Extracts on MCF-7 Cell Line. *Int. J. Sci. Res. Biol. Sci.* **2019**, *5*, 96–100. [CrossRef]
123. Available online: https://www.researchgate.net/profile/Flavio-Beltrame/publication/350549554_TERPENES_OF_EUPHORBIA_UMBELLATA_LATEX_ARE_INVOLVED_IN_CYTOTOXIC_EFFECT_AGAINST_MELANOMA_CELLS/links/60b52790a6fdcc476bda6c8d/TERPENES-OF-EUPHORBIA-UMBELLATA-LATEX-ARE-INVOLVED-IN-CYTOTOXIC-EFFECT-AGAINST-MELANOMA-CELLS.pdf (accessed on 30 September 2021).
124. Cheng, J.; Han, W.; Wang, Z.; Shao, Y.; Wang, Y.; Zhang, Y.; Li, Z.; Xu, X.; Zhang, Y. Hepatocellular Carcinoma Growth Is Inhibited by *Euphorbia Helioscopia* L. Extract in Nude Mice Xenografts. *Biomed Res. Int.* **2015**, *2015*, 601015. [CrossRef]
125. Sadeghi-Aliabadi, H.; Sajjadi, S.E.; Khodamoradi, M. Cytotoxicity of *Euphorbia Macroclada* on MDA-MB-468 Breast Cancer Cell Line. *Iran. J. Pharm. Sci.* **2009**, *5*, 103–108.
126. Choedon, T.; Mathan, G.; Arya, S.; Kumar, V.L.; Kumar, V. Anticancer and Cytotoxic Properties of the Latex of *Calotropis Procera* in a Transgenic Mouse Model of Hepatocellular Carcinoma. *World J. Gastroenterol.* **2006**, *12*, 2517–2522. [CrossRef]
127. Colombo, M.L.; Bosisio, E. Pharmacological Activities of *Chelidonium Majus* L. (Papaveraceae). *Pharmacol. Res.* **1996**, *33*, 127–134. [CrossRef]
128. Ciric, A.; Vinterhalter, B.; Savikin-Fodulovic, K.; Sokovic, M.; Vinterhalter, D. Chemical Analysis and Antimicrobial Activity of Methanol Extracts of Celandine (*Chelidonium majus* L.) Plants Growing in Nature and Cultured in Vitro. *Arch. Biol. Sci.* **2008**, *60*, 7–8. [CrossRef]
129. Kokoska, L.; Polesny, Z.; Rada, V.; Nepovim, A.; Vanek, T. Screening of Some Siberian Medicinal Plants for Antimicrobial Activity. *J. Ethnopharmacol.* **2002**, *82*, 51–53. [CrossRef]
130. Recio, M.C.; Rios, J.L.; Villar, A. Antimicrobial Activity of Selected Plants Employed in the Spanish Mediterranean Area. Part II. *Phytother. Res.* **1989**, *3*, 77–80. [CrossRef]
131. Miao, F.; Yang, X.-J.; Zhou, L.; Hu, H.-J.; Zheng, F.; Ding, X.-D.; Sun, D.-M.; Zhou, C.-D.; Sun, W. Structural Modification of Sanguinarine and Chelerythrine and Their Antibacterial Activity. *Nat. Prod. Res.* **2011**, *25*, 863–875. [CrossRef] [PubMed]
132. Pavão, M.L.; Pinto, R.E. Sensitivity of *Bacillus Subtilis* to Water Soluble Alkaloid Extracts of *Chelidonium majus* L. (Papaveraceae) Roots from Azores. *ARQUIPÉLAGO. Ciências Biológicas e Marinhas (Life Mar. Sci.)* **1995**, *13*, 93–97.
133. Asamenew, G.; Bisrat, D.; Mazumder, A.; Asres, K. In Vitro Antimicrobial and Antioxidant Activities of Anthrone and Chromone from the Latex of *Aloe Harlana* Reynolds. *Phytother. Res.* **2011**, *25*, 1756–1760. [CrossRef]

134. Emiru, Y.K.; Siraj, E.A.; Teklehaimanot, T.T.; Amare, G.G. Antibacterial Potential of *Aloe weloensis* (Aloeacea) Leaf Latex against Gram-Positive and Gram-Negative Bacteria Strains. *Int. J. Microbiol.* **2019**, *2019*, 5328238. [CrossRef] [PubMed]
135. Siritapetawee, J.; Thammasirirak, S.; Samosornsuk, W. Antimicrobial Activity of a 48-kDa Protease (AMP48) from *Artocarpus heterophyllus* Latex. *Eur. Rev. Med. Pharmacol. Sci.* **2012**, *16*, 132–137. [PubMed]
136. Raghavendra, R.; Mahadevan, G.D. In Vitro Antimicrobial Activity of Various Plant Latex against Resistant Human Pathogens. *Int. J. Pharm. Pharm. Sci.* **2011**, *3*, 70–72.
137. Nenaah, E.G.; Ahmed, M.E. Antimicrobial Activity of Extracts and Latex of *Calotropis procera* (Ait.) and Synergistic Effect with Reference Antimicrobials. *J. Med. Plant Res.* **2011**, *5*, 706–716. [CrossRef]
138. Ishnava, K.B.; Chauhan, J.B.; Garg, A.A.; Thakkar, A.M. Antibacterial and Phytochemical Studies on *Calotropis gigantia* (L.) R. Br. Latex against Selected Cariogenic Bacteria. *Saudi J. Biol. Sci.* **2012**, *19*, 87–91. [CrossRef]
139. Kori, P.; Alawa, P. Antimicrobial Activity and Phytochemical Analysis of *Calotropis Gigantea* Root, Latex Extracts. *IOSR J. Pharm. (IOSRPHR)* **2014**, *4*, 7–11. [CrossRef]
140. Ml, P.; Mk, M.; Mary, R.S. Efficacy of Euphorbia Heterophylla Latex against Pathogenic Bacteria and Fungi. *Asian J. Pharm. Clin. Res.* **2020**, *13*, 141–145. [CrossRef]
141. Lazreg-Aref, H.; Mars, M.; Fekih, A.; Aouni, M.; Said, K. Chemical Composition and Antibacterial Activity of a Hexane Extract of Tunisian Caprifig Latex from the Unripe Fruit of *Ficus Carica*. *Pharm. Biol.* **2012**, *50*, 407–412. [CrossRef]
142. Prastiyanto, M.E.; Tama, P.D.; Ananda, N.; Wilson, W.; Mukaromah, A.H. Antibacterial Potential of *Jatropha* Sp. Latex against Multidrug-Resistant Bacteria. *Int. J. Microbiol.* **2020**, *2020*, 8509650. [CrossRef]
143. Arun, K.; Anu, B.; Ruchika, G. A Comparative Study of Antibacterial Activity of Leaves and Latex of *Jatropha Curcas* L. *Int. J. Pharmacogn. Phytochem. Res.* **2012**, *4*, 190–194.
144. Arekemase, M.O.; Kayode, R.M.O.; Ajiboye, A.E. Antimicrobial Activity and Phytochemical Analysis of *Jatropha Curcas* Plant against Some Selected Microorganisms. *Int. J. Biol.* **2011**, *3*, 52. [CrossRef]
145. Hoekou, P.Y.; Tchacondo, T.; Gbogbo, K.A.; Tchelougou, D.; Pissang, P.; Karou, S.D.; Améyapohm, Y.A.; Batawila, K.; Annigoni, P.; Faso, B. Antibacterial Activities of Three Latex Plants of Asclepiadaceae Family Used in Traditional Medicine in South Togo. *Int. J. Curr. Microbiol. App. Sci.* **2015**, *4*, 882–891.
146. Liu, C.-B.; Shan, B.; Bai, H.-M.; Tang, J.; Yan, L.-Z.; Ma, Y.-B. Hydrophilic/hydrophobic Characters of Antimicrobial Peptides Derived from Animals and Their Effects on Multidrug Resistant Clinical Isolates. *Dongwuxue Yanjiu* **2015**, *36*, 41–47.
147. Fox, J.L. Antimicrobial Peptides Stage a Comeback: Better Understanding of the Mechanisms of Action, Modification and Synthesis of Antimicrobial Peptides Is Reigniting Commercial Development. *Nat. Biotechnol.* **2013**, *31*, 379–382. [CrossRef]
148. Bahar, A.A.; Ren, D. Antimicrobial Peptides. *Pharmaceuticals* **2013**, *6*, 1543–1575. [CrossRef] [PubMed]
149. Silva, O.N.; de la Fuente-Núñez, C.; Haney, E.F.; Fensterseifer, I.C.M.; Ribeiro, S.M.; Porto, W.F.; Brown, P.; Faria-Junior, C.; Rezende, T.M.B.; Moreno, S.E.; et al. An Anti-Infective Synthetic Peptide with Dual Antimicrobial and Immunomodulatory Activities. *Sci. Rep.* **2016**, *6*, 35465. [CrossRef] [PubMed]
150. Van Parijs, J.; Broekaert, W.F.; Goldstein, I.J.; Peumans, W.J. Hevein: An Antifungal Protein from Rubber-Tree (*Hevea Brasiliensis*) Latex. *Planta* **1991**, *183*, 258–264. [CrossRef] [PubMed]
151. Song, J.-Y.; Yang, H.-O.; Pyo, S.-N.; Jung, I.-S.; Yi, S.-Y.; Yun, Y.-S. Immunomodulatory Activity of Protein-Bound Polysaccharide Extracted from *Chelidonium majus*. *Arch. Pharm. Res.* **2002**, *25*, 158–164. [CrossRef] [PubMed]
152. Chung, H.-S.; An, H.-J.; Jeong, H.-J.; Won, J.-H.; Hong, S.-H.; Kim, H.-M. Water Extract Isolated from *Chelidonium majus* Enhances Nitric Oxide and Tumour Necrosis Factor- α Production via Nuclear Factor- κ B Activation in Mouse Peritoneal Macrophages. *J. Pharm. Pharmacol.* **2010**, *56*, 129–134. [CrossRef] [PubMed]
153. Khmel'nitskaia, N.M.; Vorob'ev, K.V.; Kliachko, L.L.; Ankhimova, E.S.; Kosenko, V.A.; Tyrnova, E.V.; Mal'tseva, G.S.; Medvedev, E.A. A comparative study of conservative treatment schemes in chronic tonsillitis in children. *Vestn. Otorinolaringol.* **1998**, *4*, 39–42.
154. Nascimento, D.C.d.O.; de Oliveira Nascimento, D.C.; Ralph, M.T.; Batista, J.E.C.; Silva, D.M.F.; Gomes-Filho, M.A.; Alencar, N.M.; Leal, N.C.; Ramos, M.V.; Lima-Filho, J.V. Latex Protein Extracts from *Calotropis Procera* with Immunomodulatory Properties Protect against Experimental Infections with *Listeria Monocytogenes*. *Phytomedicine* **2016**, *23*, 745–753. [CrossRef] [PubMed]
155. Nakano, K.; Kim, D.; Jiang, Z.; Ueno, M.; Okimura, T.; Yamaguchi, K.; Oda, T. Immunostimulatory Activities of the Sulfated Polysaccharide Ascophyllan from *Ascophyllum Nodosum* in in Vivo and in Vitro Systems. *Biosci. Biotechnol. Biochem.* **2012**, *76*, 1573–1576. [CrossRef] [PubMed]
156. Verma, V.K.; Rani, K.V.; Sehgal, N.; Prakash, O. Immunostimulatory Response Induced by Supplementation of *Ficus Benghalensis* Root Powder, in the Artificial Feed the Indian Freshwater Murrel, *Channa Punctatus*. *Fish Shellfish Immunol.* **2012**, *33*, 590–596. [CrossRef]
157. Akram, M.; Hamid, A.; Khalil, A.; Ghaffar, A.; Tayyaba, N.; Saeed, A.; Ali, M.; Naveed, A. Review on Medicinal Uses, Pharmacological, Phytochemistry and Immunomodulatory Activity of Plants. *Int. J. Immunopathol. Pharmacol.* **2014**, *27*, 313–319. [CrossRef] [PubMed]
158. Kukhetpitakwong, R.; Hahnvajanawong, C.; Homchampa, P.; Leelavatcharamas, V.; Satra, J.; Khunkitti, W. Immunological Adjuvant Activities of Saponin Extracts from the Pods of *Acacia Concinna*. *Int. Immunopharmacol.* **2006**, *6*, 1729–1735. [CrossRef] [PubMed]

159. Hueza, I.M.; Gorniak, S.L. The Immunomodulatory Effects of Ipomoea Carnea in Rats Vary Depending on Life Stage. *Hum. Exp. Toxicol.* **2011**, *30*, 1690–1700. [CrossRef] [PubMed]
160. Ramesh, K.V.; Padmavathi, K. Assessment of Immunomodulatory Activity of *Euphorbia hirta* L. *Indian J. Pharm. Sci.* **2010**, *72*, 621–625.
161. Shah, A.S.; Wakade, A.S.; Juvekar, A.R. Immunomodulatory Activity of Methanolic Extract of *Murraya koenigii* (L) Spreng. Leaves. *Indian J. Exp. Biol.* **2008**, *46*, 505–509.
162. Benninger, J.; Thomas Schneider, H.; Schuppan, D.; Kirchner, T.; Hahn, E.G. Acute Hepatitis Induced by Greater Celandine (*Chelidonium majus*). *Gastroenterology* **1999**, *117*, 1234–1237. [CrossRef]
163. Moro, P.A.; Cassetti, F.; Giugliano, G.; Falce, M.T.; Mazzanti, G.; Menniti-Ippolito, F.; Raschetti, R.; Santuccio, C. Hepatitis from Greater Celandine (*Chelidonium majus* L.): Review of Literature and Report of a New Case. *J. Ethnopharmacol.* **2009**, *124*, 328–332. [CrossRef]
164. Jakovljevic, Z.D.; Stankovic, S.M.; Topuzovic, D.M. Seasonal Variability of *Chelidonium majus* L. Secondary Metabolites Content and Antioxidant Activity. *EXCLI J.* **2013**, *12*, 260–268. [PubMed]
165. Rao, M.J.; Wang, L. CRISPR/Cas9 Technology for Improving Agronomic Traits and Future Prospective in Agriculture. *Planta* **2021**, *254*, 68. [CrossRef] [PubMed]
166. Alok, A.; Jain, P.; Kumar, J.; Yajnik, K.; Bhalothia, P. Genome Engineering in Medicinally Important Plants Using CRISPR/Cas9 Tool. In *Genome Engineering via CRISPR-Cas9 System*; Academic Press: Cambridge, MA, USA, 2020; pp. 155–161.
167. Dey, A. CRISPR/Cas Genome Editing to Optimize Pharmacologically Active Plant Natural Products. *Pharmacol. Res.* **2021**, *164*, 105359. [CrossRef]
168. Shen, C.; Que, Z.; Xia, Y.; Tang, N.; Li, D.; He, R.; Cao, M. Knock out of the Annexin Gene OsAnn3 via CRISPR/Cas9-Mediated Genome Editing Decreased Cold Tolerance in Rice. *J. Plant Biol.* **2017**, *60*, 539–547. [CrossRef]
169. Li, J.-F.; Norville, J.E.; Aach, J.; McCormack, M.; Zhang, D.; Bush, J.; Church, G.M.; Sheen, J. Multiplex and Homologous Recombination-Mediated Genome Editing in Arabidopsis and Nicotiana Benthamiana Using Guide RNA and Cas9. *Nat. Biotechnol.* **2013**, *31*, 688–691. [CrossRef] [PubMed]
170. Xu, R.; Wei, P.; Yang, J. Use of CRISPR/Cas Genome Editing Technology for Targeted Mutagenesis in Rice. *Methods Mol. Biol.* **2017**, *1498*, 33–40.
171. Liang, Z.; Zhang, K.; Chen, K.; Gao, C. Targeted Mutagenesis in Zea Mays Using TALENs and the CRISPR/Cas System. *J. Genet. Genom.* **2014**, *41*, 63–68. [CrossRef]
172. Michno, J.-M.; Wang, X.; Liu, J.; Curtin, S.J.; Kono, T.J.; Stupar, R.M. CRISPR/Cas Mutagenesis of Soybean and Medicago Truncatula Using a New Web-Tool and a Modified Cas9 Enzyme. *GM Crops Food* **2015**, *6*, 243–252. [CrossRef] [PubMed]
173. Nekrasov, V.; Staskawicz, B.; Weigel, D.; Jones, J.D.G.; Kamoun, S. Targeted Mutagenesis in the Model Plant Nicotiana Benthamiana Using Cas9 RNA-Guided Endonuclease. *Nat. Biotechnol.* **2013**, *31*, 691–693. [CrossRef]
174. Wang, S.; Zhang, S.; Wang, W.; Xiong, X.; Meng, F.; Cui, X. Efficient Targeted Mutagenesis in Potato by the CRISPR/Cas9 System. *Plant Cell Rep.* **2015**, *34*, 1473–1476. [CrossRef]
175. Fan, Y.; Xin, S.; Dai, X.; Yang, X.; Huang, H.; Hua, Y. Efficient Genome Editing of Rubber Tree (*Hevea brasiliensis*) Protoplasts Using CRISPR/Cas9 Ribonucleoproteins. *Ind. Crops Prod.* **2020**, *146*, 112146. [CrossRef]
176. Van Laere, A.; Van Den Ende, W. Inulin Metabolism in Dicots: Chicory as a Model System. *Plant Cell Environ.* **2002**, *25*, 803–813. [CrossRef]
177. Iaffaldano, B.; Zhang, Y.; Cornish, K. CRISPR/Cas9 Genome Editing of Rubber Producing Dandelion Taraxacum Kok-Saghyz Using Agrobacterium Rhizogenes without Selection. *Ind. Crops Prod.* **2016**, *89*, 356–362. [CrossRef]
178. Bergonci, T.; Ribeiro, B.; Ceciliato, P.H.O.; Guerrero-Abad, J.C.; Silva-Filho, M.C.; Moura, D.S. Arabidopsis Thaliana RALF1 Opposes Brassinosteroid Effects on Root Cell Elongation and Lateral Root Formation. *J. Exp. Bot.* **2014**, *65*, 2219–2230. [CrossRef] [PubMed]
179. Wiegand, A.; Prüfer, D.; Schulze Gronover, C. Loss of Function Mutation of the Rapid Alkalinization Factor (RALF1)-like Peptide in the Dandelion Taraxacum Koksaghyz Entails a High-Biomass Taproot Phenotype. *PLoS ONE* **2019**, *14*, e0217454. [CrossRef]
180. Alagoz, Y.; Gurkok, T.; Zhang, B.; Unver, T. Manipulating the Biosynthesis of Bioactive Compound Alkaloids for Next-Generation Metabolic Engineering in Opium Poppy Using CRISPR-Cas 9 Genome Editing Technology. *Sci. Rep.* **2016**, *6*, 30910. [CrossRef] [PubMed]
181. Zhang, X.; Xu, G.; Cheng, C.; Lei, L.; Sun, J.; Xu, Y.; Deng, C.; Dai, Z.; Yang, Z.; Chen, X.; et al. Establishment of an Agrobacterium-Mediated Genetic Transformation and CRISPR/Cas9-Mediated Targeted Mutagenesis in Hemp (*Cannabis sativa* L.). *Plant Biotechnol. J.* **2021**, *19*, 1979–1987. [CrossRef] [PubMed]
182. Ekor, M. The Growing Use of Herbal Medicines: Issues Relating to Adverse Reactions and Challenges in Monitoring Safety. *Front. Pharmacol.* **2014**, *4*, 177. [CrossRef] [PubMed]



Article

Anti-Cancer and Electrochemical Properties of Thiogenistein—New Biologically Active Compound

Elżbieta U. Stolarczyk ^{1,*}, Weronika Strzempek ^{2,3}, Marta Łaszcz ¹, Andrzej Leś ⁴, Elżbieta Menaszek ³, Katarzyna Sidoryk ⁵ and Krzysztof Stolarczyk ⁴

- ¹ Research Analytics Team, Analytical Department, Łukasiewicz Research Network—Industrial Chemistry Institute, 8 Rydygiera Street, 01-793 Warsaw, Poland; marta.laszcz@ichp.pl
- ² Faculty of Chemistry, Jagiellonian University, 2 Gronostajowa Street, 30-387 Krakow, Poland; weronika.strzempek@doctoral.uj.edu.pl
- ³ Faculty of Pharmacy, Collegium Medicum, Jagiellonian University, 9 Medyczna Street, 30-068 Krakow, Poland; elzbieta.menaszek@uj.edu.pl
- ⁴ Faculty of Chemistry, University of Warsaw, 1 Pasteura Street, 02-093 Warsaw, Poland; ales@chem.uw.edu.pl (A.L.); kstolar@chem.uw.edu.pl (K.S.)
- ⁵ Chemistry Group, Department of Pharmacy, Cosmetic Chemistry and Biotechnology, Łukasiewicz Research Network—Industrial Chemistry Institute, 8 Rydygiera Street, 01-793 Warsaw, Poland; katarzyna.sidoryk@ichp.pl
- * Correspondence: elzbieta.stolarczyk@ichp.pl; Tel.: +48-22-568-25-81

Abstract: Pharmacological and nutraceutical effects of isoflavones, which include genistein (GE), are attributed to their antioxidant activity protecting cells against carcinogenesis. The knowledge of the oxidation mechanisms of an active substance is crucial to determine its pharmacological properties. The aim of the present work was to explain complex oxidation processes that have been simulated during voltammetric experiments for our new thiolated genistein analog (TGE) that formed the self-assembled monolayer (SAM) on the gold electrode. The thiol linker assured a strong interaction of sulfur nucleophiles with the gold surface. The research comprised of the study of TGE oxidative properties, IR-ATR, and MALDI-TOF measurements of SAM before and after electrochemical oxidation. TGE has been shown to be electrochemically active. It undergoes one irreversible oxidation reaction and one quasi-reversible oxidation reaction in PBS buffer at pH 7.4. The oxidation of TGE results in electroactive products composed likely from TGE conjugates (e.g., trimers) as part of polymer. The electroactive centers of TGE and its oxidation mechanism were discussed using IR supported by quantum chemical and molecular mechanics calculations. Preliminary in-vitro studies indicate that TGE exhibits higher cytotoxic activity towards DU145 human prostate cancer cells and is safer for normal prostate epithelial cells (PNT2) than genistein itself.

Keywords: anticancer drugs; nanoparticles; molecular modeling; oxidation mechanisms; electrochemistry; MALDI; spectroscopic data; cytotoxic study; self-assembled monolayer; gold electrode

Citation: Stolarczyk, E.U.; Strzempek, W.; Łaszcz, M.; Leś, A.; Menaszek, E.; Sidoryk, K.; Stolarczyk, K. Anti-Cancer and Electrochemical Properties of Thiogenistein—New Biologically Active Compound. *Int. J. Mol. Sci.* **2021**, *22*, 8783. <https://doi.org/10.3390/ijms22168783>

Academic Editor: Nam Deuk Kim

Received: 4 July 2021

Accepted: 11 August 2021

Published: 16 August 2021

Publisher's Note: MDPI stays neutral with regard to jurisdictional claims in published maps and institutional affiliations.



Copyright: © 2021 by the authors. Licensee MDPI, Basel, Switzerland. This article is an open access article distributed under the terms and conditions of the Creative Commons Attribution (CC BY) license (<https://creativecommons.org/licenses/by/4.0/>).

1. Introduction

Genistein (GE) belongs to the group of isoflavones found mainly in soybeans [1,2]. Some studies suggest that frequent consumption of soy-based products in Asian countries reduces the incidence of breast and prostate cancer compared to Western countries. Genistein also has antioxidant, anti-inflammatory, antiangiogenic, pro-apoptotic, and antiproliferative properties, which gives it great potential for use in anti-cancer therapy. It has been shown that genistein may influence the regulation of apoptosis, angiogenesis, metastasis, and various stages of the cell cycle. In addition to acting on transcription factors, genistein also induces stress on the endoplasmic reticulum, which in turn leads to the apoptosis of neoplastic cells. Additionally, it has been shown to induce apoptosis in cancer cells by targeting the PPAR (peroxisome proliferator-activated receptor) signaling cascade. Various molecular mechanisms of genistein in diverse cancer models were described by

Tuli et al. [3]. However, its low water-solubility and poor oral bioavailability severely hamper its use as an ingredient for food and the pharmaceutical industries [4]. Therefore, there is an urgent need for the study of a new analog of genistein, which additionally can be promising for an economical and feasible delivery system to enhance the solubility and dissolution rates, and bioavailability of genistein while maintaining its chemical stability [4].

Our previous studies showed that genistein interacts electrostatically with gold nanoparticles [5] which turned out to be interesting carriers for active substances. These studies were continued by Vodnik et al. [6], however the authors did not perform a purity study of conjugates in relation to the free GE and stability of new conjugates as well. It is known that electrostatic interactions are not sufficiently stable at extreme pH and in the presence of salt. For example, Dinkel and co-workers [7] described that citrates are only loosely bound to the gold nanoparticles (6.7 kJ/mol). However, sulfur-containing compounds have been used as excellent ligands for binding to flat gold surfaces as well as gold nanoparticles, because of a very strong interaction of sulfur nucleophiles with gold. Therefore, to increase the strength of the interaction, and improve the stability of AuNPs-GE conjugates, we focused on the investigation of an optimal thiol linker as a new derivative—thiolated genistein (TGE, 7-O-[2-(mercaptomethylcarboxy)ethyl-genistein) described by Sidoryk and co-workers [8] (compound No. 26). The structural formula of TGE is presented in Figure 1. TGE is composed of the genistein residue bound at the C7-OH site to the ethyl linker and thioglycolic acid residue. Such a construction assures that the TGE will be bound firmly to the Au surface via the Au-S chemical bond on the gold surface as well as gold nanoparticles.

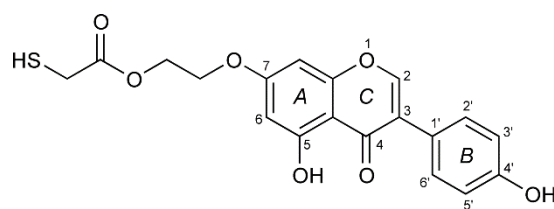


Figure 1. The chemical structure of TGE (the thiolated derivative of genistein). Three rings of the moiety are marked as A, B, and C.

Because pharmacological and nutraceutical effects of isoflavones are attributed to antioxidant mechanisms also, which protect cells against reducing carcinogenesis, the knowledge of the oxidation mechanisms is crucial to ascertain the influence of the redox behavior, on the pharmacological, nutritional, and chemical properties of our new thiolated analog of genistein. TGE was chemically attached to the gold surface as the self-assembled monolayers (SAMs). The study of SAMs of alkanethiol, alkanedithiol, sulphides, and disulfides on the Au surface allowed us to obtain data about processes occurring at the interface, as well as about interactions between molecules in the monolayer [9].

Aromatic molecules create a highly conjugated system that interacts strongly with the metal surface. Additionally, the steric effect of the aromatic ring may also lead to an increase in molecular disorder within the SAM. Generally, aromatic thiols in SAMs are difficult to study, especially in large systems such as drugs. It is known that SAMs have been used for “underpotential polymerization” of aniline and other compounds on gold electrodes [10]. A multitude of experimental approaches is needed for the characterization of SAMs. Attenuated total reflectance spectroscopy (ATR) is a variant of infrared spectroscopy (IR) and is frequently employed to investigate SAMs. The radiation beam is polarized and reinforced in a perpendicular direction to a surface of a substrate. As a consequence, intensities of absorption bands are strictly related to the orientation of dipoles with respect to the substrate surface. Therefore, a band originating from molecules corresponding to vibrations in the plane perpendicular to the surface will show much greater intensity, than the bands associated with vibration parallel to a surface. This dependence

allows for a relatively precise definition of the structure monolayers. Based on the position and intensity of bands, it is possible to obtain information about the degree of monolayer order and the orientation of the molecules that make up the system. In the case of model alkanethiol layers, bands related to stretching vibrations of methyl and methylene groups are used. The ratio of their relative intensities makes it possible to estimate the angle of inclination of the alkyl chains, while their position is closely related to the quasi-crystalline or liquid nature of the monolayer and the presence of gauche defects [11–20].

Our aim is to study the mechanism of the oxidation reaction of a potential new drug with promising biological activity. The selected anticancer drug is thiogenistein—a new analogue of genistein. For the first time, a self-assembled monolayer of such a complex compound attached to the gold electrode is studied. Three instrumental techniques are applied in order to determine products of the TGE oxidation on the Au electrode: electrochemistry, IR-ATR, and MALDI-MS. Selected experimental results are interpreted with the use of molecular modeling and quantum mechanical density functional calculations. We hope that understanding simulated electrochemical reactions will help to determine key molecular fragments involved in the subsequent biochemical processes in living organisms. Apart from these physico-chemical studies, a preliminary evaluation of the anticancer activity of TGE is undertaken based on one human prostate cancer (DU145 line) and safety for normal prostate epithelial cells (PNT2 line).

The topicality of our research is emphasized by the works of Kim and Rizzo [21,22], who confirmed the importance of genistein as an anticancer drug via oxidative processes.

2. Materials and Methods

2.1. Materials

The reagents used in the study were obtained from POCh (Gliwice, Poland) and Sigma-Aldrich (Saint Louis, MO, USA). They were of the highest purity and used without prior purification. All solutions were prepared with deoxidized water, distilled, and cleaned in a “Milli-Q” filter apparatus (Millipore Corporation, Bedford, MA, USA). Its final resistance was 18.2 M Ω /cm.

TGE was manufactured in Łukasiewicz Research Network—Industrial Chemistry Institute (Łukasiewicz-ICHP), Warsaw, Poland. PBS buffer (the phosphate-buffered saline) was obtained from Syngen. The phosphate buffer was prepared from 0.2 M monobasic and dibasic sodium phosphate solution. The pH of the solutions used in the experiments was determined using a commercially available Mettler Toledo (Greifensee, Switzerland) pH meter. The solutions were deoxygenated with argon for 20 min before each experiment, while during the measurements gas was passed over the solution (argon with 99.5% purity from Air Products Kielce, Poland).

The monolayers of the TGE compound on the gold electrodes were prepared in the self-assembly process. First, the monolayers of the TGE compound were prepared on a gold surface by immersing the purified gold electrodes in ethanolic solutions containing 1 mM TGE. After their removal, the electrodes were rinsed thoroughly with ethanol, water, and ethanol to wash off the physically adsorbed molecules and left to dry in the air.

2.2. Electrochemical Measurements

Electrochemical experiments were performed using Autolab potentiostat (Eco Chemie BV, Utrecht, The Netherlands). The potentiostat was controlled using the GPES software. Electrochemical measurements were carried out in a three-electrode system. A silver/silver chloride (Ag/AgCl) electrode with saturated KCl was used as the reference electrode, the platinum plate was used as the auxiliary electrode. The working electrode was a gold electrode (Arrande, Werther, Germany) with a surface area of 0.61 cm². The gold electrodes were 1.1 × 1.1 cm² borosilicate glass plates on which gold was sputtered with a thickness of 200–300 nm. There was a chromium adhesive layer 2–5 nm thick between the gold layer and the glass. The electrolyte solutions were deoxygenated by bubbling argon (99.5% purity, Air Products, Kielce, Poland) through the solutions for 20 min. During the

measurements, gas was passed over the solution. All experiments were performed at the temperature of 22 ± 2 °C.

2.3. IR Measurements

The infrared spectra were recorded on the Nicolet iS10 FT-IR spectrometer (Thermo Scientific, Waltham, MA, USA) using an ATR sampling module, on diamond crystals, in the range from 4000 to 650 cm^{-1} , with the spectral resolution of 4 cm^{-1} . For one spectrum 1000 scans were recorded. IR transmission spectrum of TGE was recorded in the KBr pellet in order to obtain the spectrum of the anisotropic sample.

2.4. Raman Spectroscopy Measurement

The FT Raman spectrum of TGE was recorded on the Nicolet NXR 9650 instrument (Thermo Scientific, Waltham, MA, USA) using a 1064 nm excitation from the Nd:YVO4 laser in the range from 3700 to 150 cm^{-1} with a spectral resolution of 4 cm^{-1} . For one spectrum, 300 scans were recorded with 0.5 W of laser power.

2.5. MS Spectrometry

Mass spectra were acquired in positive reflector mode on Applied Biosystems/MDS SCIEX MALDI 4800 Plus TOF/TOF spectrometer (Matrix-assisted laser desorption/ionization time-of-flight mass spectrometry). 2,5-Dihydroxybenzoic acid (DHB), dissolved in $\text{CH}_3\text{CN}/\text{H}_2\text{O}/\text{TFA}$ (50:50:0.1 ratio) was used as a matrix. Analyte ionization was achieved with 355 nm Nd:YAG laser firing at a 200 Hz rate. Laser fluence was within the 5500–6000 AU range. Typically, 1024 laser shots were accumulated. The acceleration voltage was set to 20 kV, lens to 10 kV, and the delayed extraction time to 250 ns. Raw spectra were analyzed and edited using the Data Explorer software, Version 4.9, Applied Biosystems.

2.6. Quantum Mechanical Modeling

Quantum mechanical modeling was performed using the density functional B3LYP method with medium-size Gaussian basis sets, i.e., 6-31G(d), 6-31G(d,p), and 6-311++G(d,p) for the H, C, N, O, and S atoms depending on the system investigated. Molecular geometry was optimized with the Berny algorithm implemented in the Gaussian G16 program [23]. The minimum was confirmed with all positive harmonic frequencies. For larger molecular systems the UFF molecular mechanics and the semiempirical quantum mechanical PM7 methods were used (also implemented in the G16 program). All calculations were performed on the HPC cluster in the Interdisciplinary Centre for Mathematical and Computational Modelling at the University of Warsaw, Poland.

2.7. In Vitro Study

DU145 (androgen-independent human prostate cancer) cells were grown in DMEM (Dulbecco's modified Eagle's medium, Sigma, Saint Louis, MO, USA), with the addition of 10% (*v/v*) FBS (fetal bovine serum, Sigma, Saint Louis, MO, USA). PNT2 (normal prostate epithelium) cells were maintained in RPMI 1640 medium (Sigma, Saint Louis, MO, USA) with 2 mM glutamine and 10% FBS. Cells were cultured in a humidified atmosphere at 37 °C with 5% CO_2 , incubated until an 80% confluent cell monolayer was developed, and detached from the culture flasks using TrypLE™ Express (ThermoFisher, Waltham, MA, USA). Next, the obtained cell suspension was transferred into a 96-well experimental plate (Nunc, Roskilde, Denmark) at a density of 5×10^3 cells/well. After 24 h, the cancer prostate epithelium was exposed to GE and TGE solutions (maximum content of DMSO was < 1%) which were added to the wells in five final concentrations: 200, 100, 50, 25, 12.5, and 6.25 μM . Cells were incubated for 6, 24, and 72 h in standard conditions, and after that, the viability, cytotoxicity, and morphology were determined. Cell viability was examined by resazurin-based reagent PrestoBlue™ (ThermoFisher, Waltham, MA, USA). The assay was used to determine the mitochondrial metabolic activity by the reduction reaction of non-fluorescent resazurin to fluorescent resorufin. To determine the proliferation rate of DU145

cells and the cytotoxic effect of genistein and thioderivative, the ToxiLight™ BioAssay Kit and the ToxiLight™ 100% Lysis Reagent Set (Lonza, Basel, Switzerland) were used. The kit was used to quantify adenylate kinase (AK) in both the supernatant (representing damaged cells) and lysate (representing intact adherent cells). As a control, cells incubated with the growth medium containing 0.1% DMSO were used. The cell viability and cytotoxicity were evaluated following the manufacturer's protocols for fluorescence or luminescence measurements using a microplate reader POLARstar Omega (BMG Labtech, Ortenberg, Germany). The results were expressed as the mean \pm standard deviation (SD) from six samples for each experimental group.

Cell morphology and rate of proliferation were determined by staining the cells with hematoxylin and eosin solutions (Sigma-Aldrich, St. Louis, MO, USA) and observed under the fluorescence microscope (Olympus CX41, Tokyo, Japan).

3. Results and Discussion

3.1. Electrochemistry

In our previous article [5], we described experiments performed by cyclic voltammetry with free genistein dissolved in PBS buffer pH 7.4 using a glassy carbon electrode (GCE). In the first anode half-cycle, we observed the first peak at approx. 0.4 V which corresponded to the irreversible oxidation of the hydroxyl group on the C4' carbon ring of genistein, while a second peak at approx. 0.8 V corresponded to the oxidation of hydroxyl groups on the C5, C7 carbon ring of genistein. The oxidation peaks decreased in the subsequent CV cycles, which was probably related to the adsorption of genistein oxidation products on the electrode surface.

In this article, the thiolated derivative of genistein, TGE was attached to a gold electrode. The presence of a thiol group allows for the spontaneous organization of TGE molecules in the course of the self-assembly process on the gold surface. As a result, a monolayer of this compound spontaneously forms on the gold electrode. Such systems have plausible advantages because nanomolar amounts of TGE in the monolayer can be studied without further adsorption of the compound in subsequent voltammetric cycles, as it was used in the previous studies with genistein dissolved in solution.

The oxidation of TGE adsorbed on the gold electrode was investigated by cyclic voltammetry in PBS pH 7.4 (Figure 2). When the potential of the modified TGE electrode was varied from -0.3 V to 0.3 V, no Faraday current was observed in the voltammetric curves. If the potential was changed over a wider range of potentials, reaching more positive values, there was an irreversible oxidation peak at 0.59 V (peak a1) and a quasi-reversible pair of peaks at a potential close to 0.17 V (c2 and a2 peaks). After the first cycle, the a1 peak disappeared quickly and only a pair of c2 and a2 peaks was developed. The dependence of the c2 and a2 peak currents on the scan rate of potential was investigated (Figure 3). As the scan rate of potential increased, an increase in the peak current density of oxidation and reduction was observed on the voltammetric curves (Figure 3A). The current of the c2 and a2 peaks depends linearly on the scan rate of the potential in the range of 0.010 – 0.1 V/s, which indicates the presence of a system adsorbed on the gold electrode (Figure 3B). Similar voltammetric curves were recorded by other authors for the compounds 4-aminothiophenol and 4-hydroxythiophenol [24–29], as well as in the recent review from the Oliveira-Brett group [30]. The observed peaks were explained by the formation of dimers in the first stage, and then the formation of the quinone/hydroquinone system.

The properties of the electrode modified with oxidized TGE monolayer were also tested using cyclic voltammetry in solutions of different pH. The tests were carried out in phosphate buffer with different pH ranging from 5.5 to 8.0. The dependence of the a2/c2 peak potential on the solution pH was investigated (Figure 4). On the voltammetric curves, it can be observed that if the pH of the solution decreases, the pair of the a2/c2 peaks shifts to higher potentials, and the density of the peak current becomes smaller (Figure 4A). The relationship between the anode and cathode peak current density was determined and shown in Figure 4B. The slope of the curve for the cathode peak is about 45 mV per pH

unit, which is close to 59 mV. The dependence of the potential of the a2 peak on pH is also linear, with the slope of the curve 74 mV per pH unit, which slightly deviates from the value of 59 mV. This slope indicated a two-electron and two proton redox process. This dependence may confirm the presence of a hydroquinone/quinone system in the B ring of genistein of hydroxyl groups C4' and C3' or C5'.

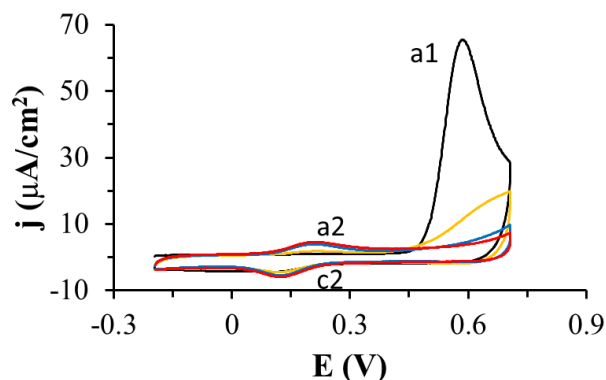


Figure 2. Cyclic voltammograms recorded with the gold electrode coated with thiogenistein in PBS pH 7.4, scan rate of the potential: 0.1 V/s, 1 (black curve), 2 (orange curve), 20 (blue curve), 30 (red curve) denote the cycle number.

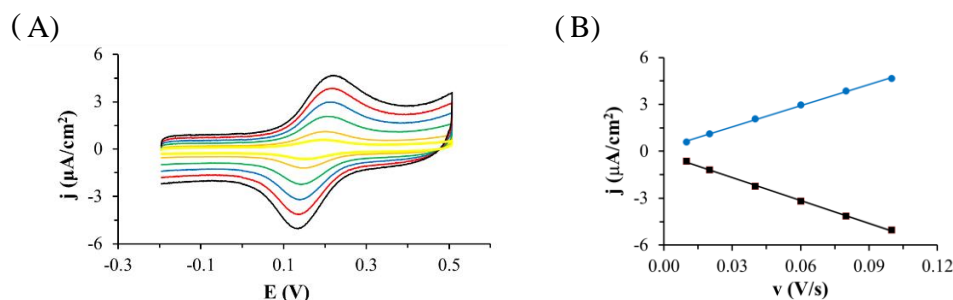


Figure 3. (A) Cyclic voltammograms recorded on the Au electrode modified with oxidized TGE monolayer (TGE_{ox}) in deoxygenated PBS at pH: 7.4, scan rate of the potential 0.1 (black curve), 0.08 (red curve), 0.06 (blue curve), 0.04 (green curve), 0.02 (orange curve), 0.01 (yellow curve) V/s. (B) Dependence of the oxidation (blue dots and line) and reduction (black squares and line) peak current on the scan rate of potential.

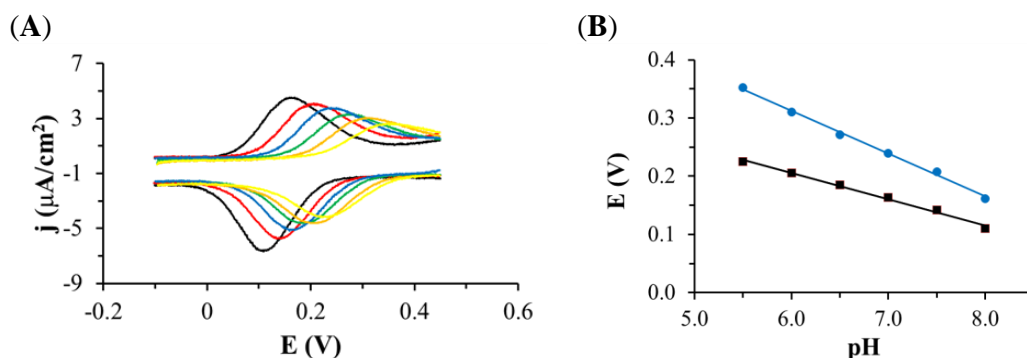


Figure 4. (A) Cyclic voltammograms recorded on the Au electrode modified with TGE in deoxygenated phosphate buffer pH: 8.0 (black curve), 7.5 (red curve), 7.0 (blue curve), 6.5 (green curve), 6.0 (orange curve), 5.5 (yellow curve), scan rate of the potential 0.1 V/s. (B) Dependence of the oxidation (blue dots and line) and reduction (black squares and line) peak potential on pH.

This is a very interesting observation because in this work the c2/a2 peaks appear only after the compound has been oxidized (a1 peak), which means that the hydroxyl

group on the C4' in the B ring of genistein does not oxidize in the first cycle. The a1 peak should be attributed to the oxidation of hydroxyl group on the C5 at the A ring of genistein because group C7 at the A ring of genistein is blocked by the linker with the thiol group. The a1 peak may also be responsible for the attachment of the -OH group in the B ring at C3' or C5' of genistein. In the B ring, a quinone/hydroquinone system is formed, which is manifested by the presence of a pair of a2/c2 peaks, which correspond to the $2e^-/2H^+$ process. Additionally, the a1 peak is very large (peak current, charge under the peak) compared to the a2/c2 peaks which may suggest that more than one process is taking place there. We explain this by the simultaneous process of polymerization and the attachment of the -OH group to the B ring of thiogenistein.

In the next experiment, the quality of the TGE monolayer on gold was assessed in the presence of a fast $[Fe(CN)_6]^{4-}$ redox probe dissolved in the solution. The research was carried out in deoxygenated 0.5 M KCl containing 1 mM $[Fe(CN)_6]^{4-}$. Figure 5 shows cyclic voltammograms recorded with the use of the unmodified and modified TGE gold electrode in the potential range from -0.2 V to 0.6 V at the scan rate of the potential 0.1 V/s. During the recording of the first cycle, only the oxidation peak of the redox probe with a current density of $215 \mu A/cm^2$ and a potential of 0.60 V was observed on the voltammogram curve in the tested potential range. In this cycle, there is also oxidation of the monolayer (a1 peak described in the previous paragraph), which corresponds to the polymerization of TGE molecules and the attachment of the -OH group to the B ring. In the next cycle, the oxidation peak shifts to less positive potentials, and the peak current density decreased, which can be explained by the fact that the monolayer on the electrode is organized and the redox probe penetrates the monolayer less well. This may be due to the presence of a polymer on the electrode. In the third and subsequent cycles, the peak current density slightly decreases, and the peak potential shifts to more positive potentials, which proves that the monolayer is stabilizing.

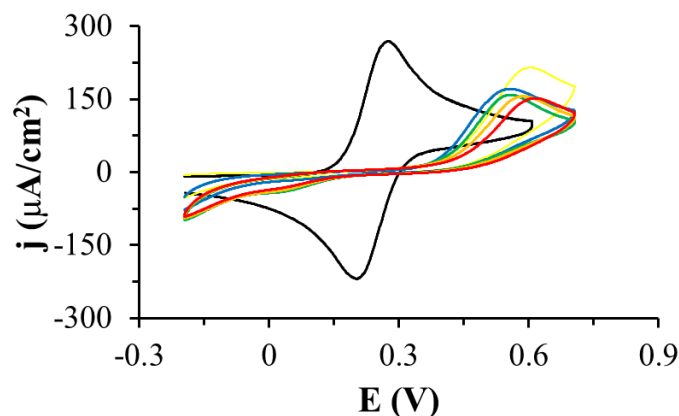


Figure 5. Cyclic voltammograms recorded using gold electrodes unmodified (black curve) and modified with TGE: 1 (yellow curve), 2 (blue curve), 10 (green curve), 20 (orange curve), 30 (red line), in deoxygenated 0.5 M KCl containing 1 mM $Fe(CN)_6^{4-}$, the scan rate of the potential 0.1 V/s.

The desorption of the TGE monolayer adsorbed on the gold electrodes was also performed during the registration of voltammograms in a wide range of potentials in 0.1 M sodium hydroxide solution (Figure 6). Reduction peaks in the potential range from -0.7 V to 1.2 V were observed on the voltammograms. Since there are more than one of these peaks, it suggests that the compound adsorbed on the electrode interacts with the electrode through the S-Au bond and that there are also quite strong intermolecular TGE-TGE interactions. This experiment confirms the presence of the TGE monolayer on the gold electrode.

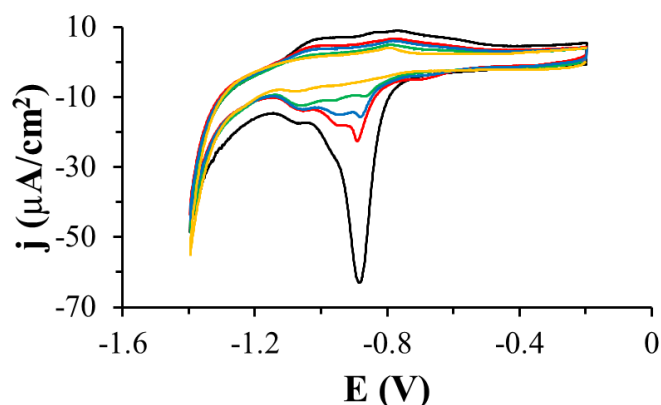


Figure 6. Cyclic voltammetric curves recorded for TGE-modified gold electrodes in a solution of 0.1 M NaOH, scan rate of the potential: 0.05 V/s, 1 (black curve), 2 (red curve), 3 (blue curve), 5 (green curve), 10 (orange curve) cycle.

In the case of studies of thiogenistein on the gold electrode, it is easier to interpret the results compared to the studies conducted with genistein dissolved in a solution, where there is strong adsorption of both the substrates and the products of electrode reactions. In the case of thiogenistein immobilized on the gold electrode, there is a monolayer of this compound on the electrode and redox processes are observed at the molecular level. Our observations and conclusions are consistent with those described by Oliveira-Brett and co-workers [30].

3.2. IR Spectroscopy

The IR spectrum of the anisotropic sample of TGE is shown together with the Raman spectrum in Figure S1. For better clarity, three IR spectra of TGE (KBr) and IR-ATR spectra of TGE on the Au electrode before and after oxidation are collected in Figure 7.

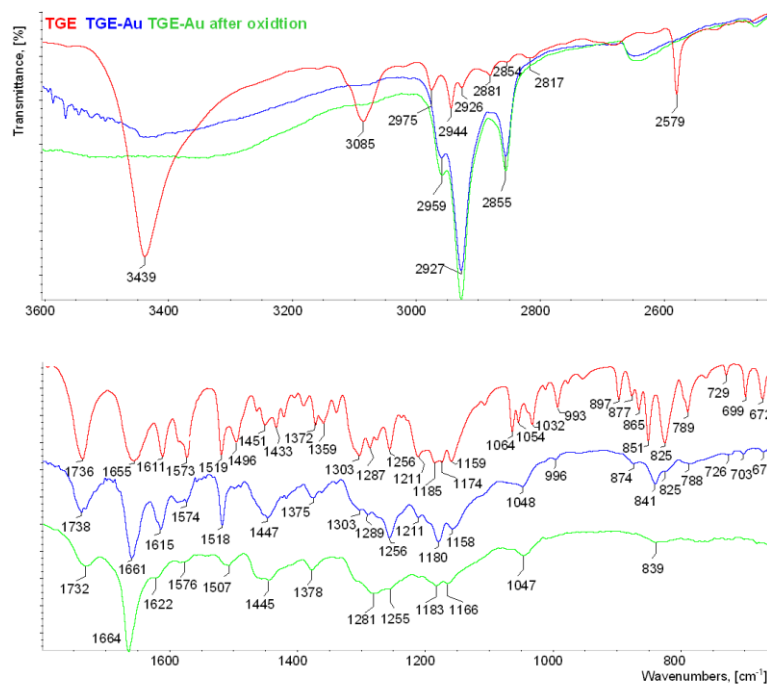


Figure 7. IR spectra of TGE (in KBr pellet), TGE on the Au electrode before and after oxidation (ATR). The upper window is in the range of 3600–400 cm^{-1} ; the lower window is in the range of 1800–650 cm^{-1} .

The presence of hydroxyl groups in the TGE molecule is proven in the IR spectrum by the presence of the band at 3439 cm^{-1} . The first distinctive difference between the TGE spectrum and both spectra of TGE on the Au electrode before and after oxidation is in stretching vibrations of hydroxyl groups. In contrary to the TGE spectrum on other spectra, these vibrations give a broad absorption band from 3600 to 3200 cm^{-1} . Taking into consideration that in the TGE molecule two hydroxyl groups participate in inter- and intra-molecular hydrogen bonding, the broadening of the band is observed in both spectra of TGE on the Au electrode before and after oxidation. This may suggest changes in the nature of these hydrogen bonds.

Bands from C-H stretching vibrations from aromatic rings and the methylene group of the TGE molecule are observed in the range from 3085 to 2817 cm^{-1} . Exact wavenumbers of methylene stretching modes have been used to distinguish between all trans (crystalline-like) and a disordered (gauche rich, liquid-like) conformation of alkyl chains. For alkanethiols containing more than 10 carbons in chains, a generally observed trend is that wavenumbers of the methylene stretching asymmetric and symmetric vibrations increase from about 2918 to 2924 cm^{-1} and from about 2851 to 2855 cm^{-1} respectively when going from a crystalline-like to a disordered conformation of the alkyl chain. However, shorter chains also exhibit a spectral signature characteristic for a disordered conformation [11–20]. In spectra of TGE on Au electrodes before and after oxidation two characteristic, very intensive bands at 2927 and 2855 cm^{-1} resulting from methylene asymmetric and symmetric vibrations are observed, respectively. These bands are shifted 1 cm^{-1} towards higher wavenumbers in reference to their counterparts in the TGE spectrum. This shift does not prove crystalline-like order, like for model alkanethiols, because the TGE molecule is characterized by the short alkyl chain. In order to calculate the twist and tilt angles, the intensity values were used for bands originating from methylene asymmetric and symmetric vibrations as well as from C-O-C asymmetric stretching vibrations from spectra of TGE (in KBr pellet) and TGE on the Au (IR-ATR) [31]. The twist and tilt angles were 43° and 77° , respectively.

In IR and Raman spectra of TGE molecule, the band from stretching vibrations of S-H is observed at 2579 cm^{-1} . The absence of this band in both spectra of TGE on the Au electrode before and after oxidation indicates the formation of a new bond directly via the sulfur atom on the surface of the Au electrode. Two carbonyl groups are present in the TGE molecule, one in the chain and the second in the ring. The comparison of two values 1736 and 1655 cm^{-1} with the reference value of 1647 cm^{-1} for the carbonyl group from GE molecule [5,32] allows assigning the band at 1655 cm^{-1} to the ring and the band 1736 cm^{-1} to the chain. It is supposed that the carbonyl group from the ring participates in the intramolecular hydrogen bonding with a neighboring hydroxyl group [5]. The band from carbonyl stretching vibration from the chain in the spectrum of TGE on the Au electrode is slightly shifted towards higher wavenumbers from 1736 cm^{-1} to 1738 cm^{-1} which may indicate a breaking of the C=O...H-S bond. But in the spectrum of TGE on the Au electrode after oxidation, the carbonyl stretching band is shifted into 1732 cm^{-1} . The band from carbonyl stretching vibration assign to the ring in the spectrum of TGE on the Au electrode is shifted towards higher wavenumbers from 1655 into 1661 cm^{-1} what indicates a weakening of the intramolecular C=O-O-H hydrogen bond that can be caused by an increase in intermolecular interactions with the neighboring molecules. However, an increase in the relative intensity of this band is observed. In the spectrum of TGE on the Au electrode after oxidation, the carbonyl stretching band is observed at 1664 cm^{-1} . It is supposed that this significant shift towards higher wavenumbers is caused by the breaking of the intramolecular C=O-O-H bond during the oxidation reaction. V. Crupi et al. [32] described changes in the Raman and IR spectra of genistein caused by its inclusion into β -cyclodextrins cavity. The changes were analyzed in detail in relation to intra- and intermolecular hydrogen bonds in the wavenumber range 1500 – 1800 cm^{-1} . As a main result, a large high wavenumber shift ($\sim 17\text{ cm}^{-1}$) of the C=O stretching mode has been observed in passing from uncomplexed genistein to inclusion compounds. It has

been ascribed to the breakdown of the intramolecular hydrogen bond of genistein during inclusion phenomena and the formation of intermolecular host–guest H-bonds. This is in agreement with the rearrangement of the H-bond environments revealed by the analysis of the FTIR-ATR spectra of the O–H stretching vibration that is downshifted in with respect to pure genistein.

In IR and Raman spectra of TGE bands from 1611 to 1496 cm^{-1} mainly originate from C=C vibrations. The band at 1611 cm^{-1} in the TGE spectrum is shifted towards higher wavenumbers to 1615 cm^{-1} and 1622 cm^{-1} in spectra of TGE on the Au electrode before and after oxidation, respectively. It is worth observing that a higher shift is for the last spectrum. Moreover, the relative intensity of the band at 1622 cm^{-1} decreased. Similar behavior is observed for bands: 1573 cm^{-1} (TGE), 1574 cm^{-1} (TGE on the Au electrode) and 1576 cm^{-1} (after oxidation) as well as for doublet of bands at 1519 cm^{-1} and 1496 cm^{-1} (TGE). Observations of the whole range of C=C stretching vibrations may indicate profound changes in three rings of oxidized TGE on the Au surface.

In IR and Raman spectra of TGE in ranges of deformation vibrations of methylene and hydroxyl group two separate doublets are observed at 1451 cm^{-1} and 1433 cm^{-1} as well as at 1372 cm^{-1} and 1359 cm^{-1} , respectively. In both spectra of TGE on the Au electrode before and after oxidation, broad bands from deformation vibrations of methylene groups at 1447 cm^{-1} and 1445 cm^{-1} are observed, respectively. Similarly, in these spectra, broad bands from hydroxyl groups at 1375 cm^{-1} and 1378 cm^{-1} are observed.

In IR and Raman spectra of TGE, the doublet at 1174 cm^{-1} and 1159 cm^{-1} originate from C–O–C asymmetric stretching and C–OH stretching vibrations. The symmetric stretching vibrations of the C–O–C group are observed in the Raman spectrum at 993 cm^{-1} and 877 cm^{-1} . In the spectrum of TGE on the Au electrode, the doublet from C–O–C asymmetric vibrations is at 1180 cm^{-1} and 1158 cm^{-1} whereas in the spectrum of TGE after oxidation the doublet is significantly shifted about 10 cm^{-1} into 1183 cm^{-1} and 1166 cm^{-1} .

In the TGE spectrum, bands from C–H deformation out-of-plane vibrations from aromatic rings are at 851 cm^{-1} and 825 cm^{-1} . In the range of these bands in the spectra, TGE on the Au electrode before and after oxidation bands at about 841 cm^{-1} and 839 cm^{-1} are observed, respectively. Moreover, it is worth noting that the band at 839 cm^{-1} is very broad and has smaller intensity than the band at 841 cm^{-1} what may prove that the oxidation of TGE influences rings of the molecule.

3.3. MALDI-TOF MS

The small amounts of molecules are present on gold surfaces, so we use the ultrasensitive method to molecular surface characteristics. MALDI MS was used to characterize TGE SAMs on the gold electrode and the reactions on the monolayers. This technique was used to confirm the structure of the TGE compound, to identify TGE adsorbed on the gold electrode before oxidation and the product after oxidation. Taking into account the signal intensities and the quality of the spectrum, which are influenced by the type of matrix used, disturbing and interfering peaks from the blank (matrix), and the unmodified electrode, the DHB (2,5-dihydroxybenzoic acid) matrix has been turned out to be the best. In Figure 8, the spectrum of the TGE standard on a steel plate is presented. In Figure 9, the spectrum of the electrode with the compound before oxidation (Figure 9A), and the electrode with the compound after oxidation (Figure 9B), and the empty/clean electrode with the matrix (Figure 9C) are presented.

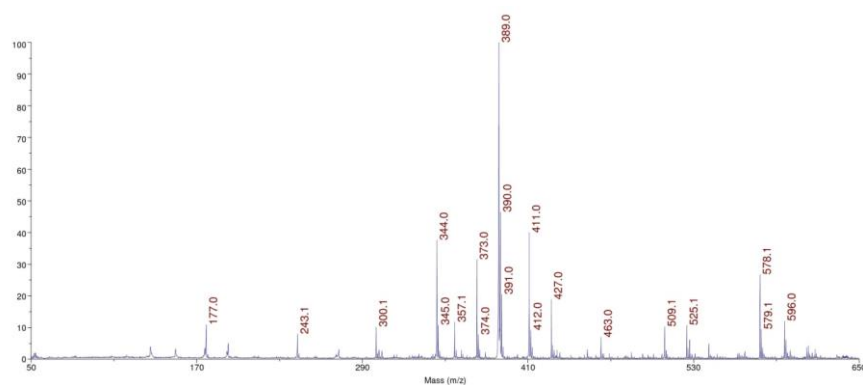


Figure 8. The MALDI-MS spectrum of the TGE compound on a steel plate in the DHB matrix.

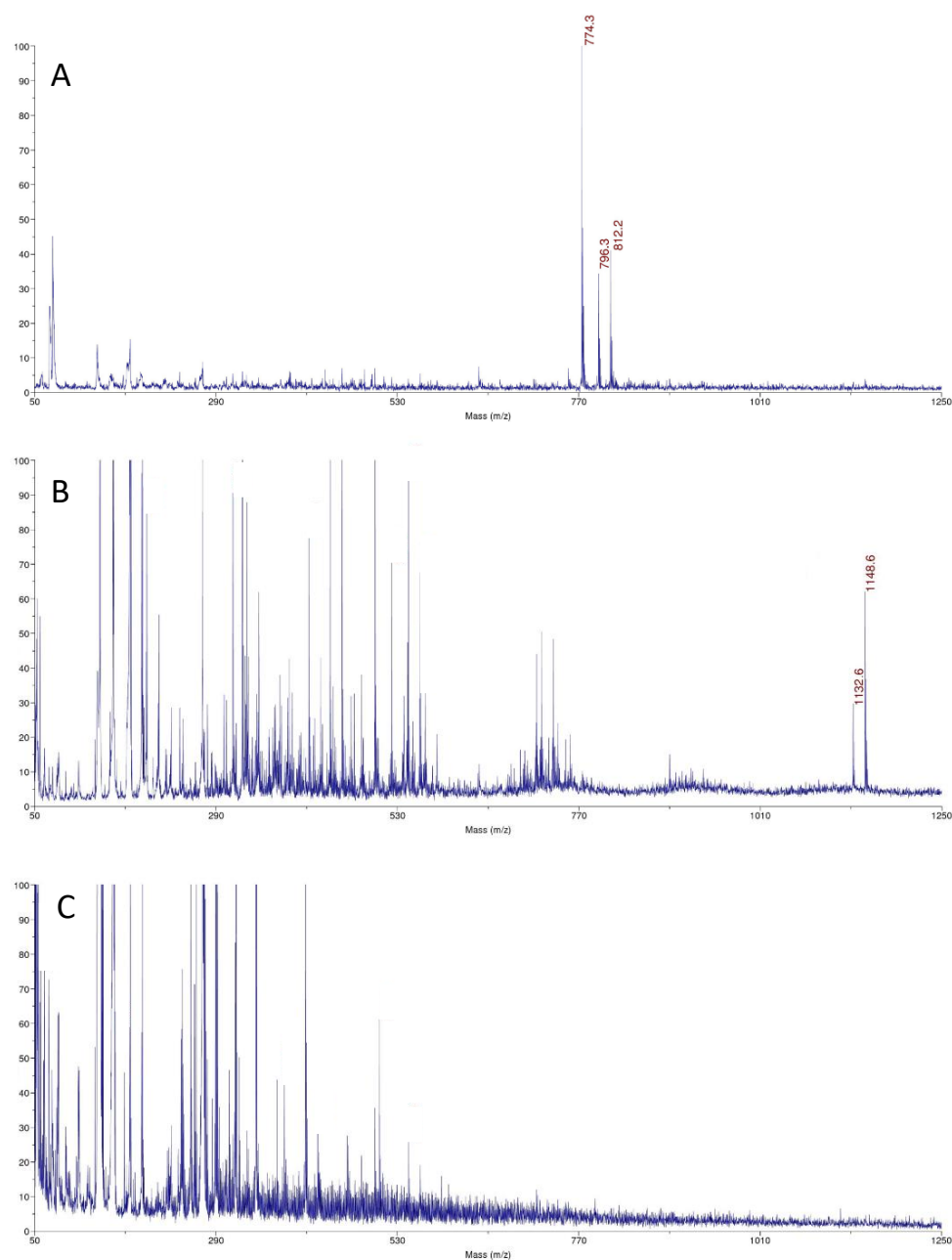


Figure 9. Comparison of MALDI-MS spectra: (A) TGE on the Au electrode before oxidation, (B) the product of oxidation on the Au electrode, (C) the Au electrode.

The TGE compound on the steel plate is observed at m/z 389 Da $[M + H]^+$ ion in a positive ionization. Additionally, adducts with sodium and potassium are observed at m/z 411 Da $[M + Na]^+$, m/z 427 $[M + K]^+$, respectively. The m/z 774 Da ion is observed in the spectrum of TGE on the Au electrode before oxidation. The TGE is stamped from the monolayer on the electrode by the laser as a disulfide (Figure 9A), which agrees with literature data for thiol compounds [33]. The disulfide ions are not necessarily the products of photochemical reactions but may result from solvent extraction, for example during the application of matrix solution to the sample [34].

On the spectrum of TGE on the Au electrode after oxidation, two significant ions, m/z 1148 Da and 1132 Da, differing by 16 Da, are observed. The unexpectedly high molecular weight of the compound can indicate the presence, not only orobol, that was formed by adding an extra -OH group to the B-ring of genistein [35,36]. The mass of 1148 Da indicates the formation of a species which mass corresponds to the TGE trimer with additional modifications in the structure. The obtained results can indicate the formation of the trimer as a complex or condensation, which is known in the literature for tannins [37,38] or species that link the phenolic rings with the neighboring aryl ring via the C-O-C bond [39,40].

3.4. Molecular Modeling and the Quantum Mechanical Density Functional Calculations

A molecular model of the TGE monolayer on the Au electrode plane is visualized in Figure 10. It is composed of 26 TGE molecules and 81 Au atoms. The 81 Au atoms are placed in the geometry corresponding to the fragment of the Au(111) plane. The TGE molecule was first optimized with the B3LYP/6-31G(d,p) method and then cloned over the Au plane and then reoptimized with the semiempirical PM7 method. The closest S-S distance was about 4.6 Å.

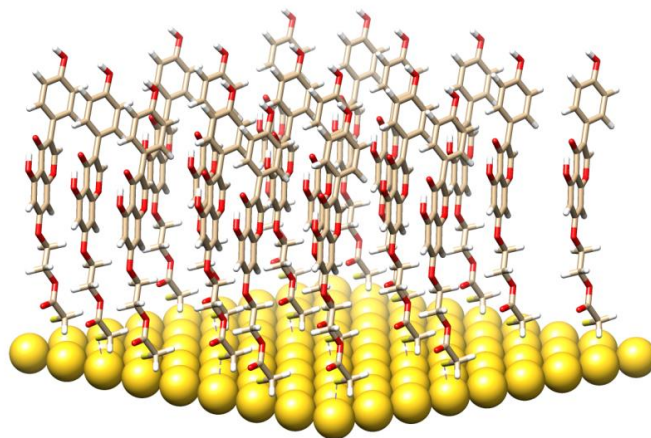


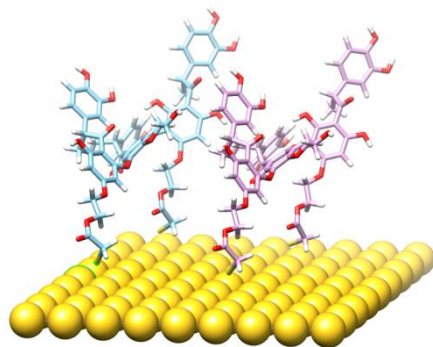
Figure 10. A molecular model of the TGE monolayer.

Selected properties of the TGE monolayer on the Au electrode were investigated with vibrational spectroscopy. The recorded IR and Raman spectra were described earlier in the text. The IR-ATR spectra were supplemented also with the theoretical quantum mechanical calculations of the harmonic frequencies and the intensities of the TGE molecule (Figure S2). The obtained geometry has an internal hydrogen bond between the C(5)-OH and O (at C-4). From a comparison of the IR spectra of the TGE and TGE on the Au electrode, one can deduce an increase of the wavenumber of the C(4)=O bond. To check the reason behind such a wavenumber increase the theoretical IR spectrum for a hypothetical structure without an intramolecular hydrogen bond (Figure S3). In such a structure, the rotated OH bond is characterized by the dihedral angle C(6)-C(5)-O-H equal to 0° in place of about 180° for the structure with the intramolecular H-bond. We found that the C(4)=O frequency increased after H-bond break by about 20 cm^{-1} , i.e., more than twice as large than recorded in the IR spectra (only of about 6 cm^{-1}), Table 1. This suggests that the intramolecular H-bond should be only slightly weakened and that this effect should originate from the intermolecular interactions with the neighboring molecules.

Table 1. Comparison of the IR C(4)=O modes in the TGE and Au-TGE systems, in cm^{-1} .

System	IR	B3LYP	Comments
TGE	1655	1689	B3LYP for H-bonded TGE, Figure S2
Au-TGE	1661	1709	B3LYP for broken H-bond, Figure S3
Difference	6	20	-

A new product is created after TGE monolayer oxidation. Taking into account the results of electrochemical, spectroscopic and MS analyzes, we can propose a hypothetical model of a new product. There are some suggestions from the literature [41,42] that the electrochemical oxidation results in adding the -OH group to the B-ring of the genistein residue. The oxidation can also disintegrate the C-ring of genistein. Moreover, there are known species that link the phenolic rings with the neighboring aryl ring via the C-O-C bond [39,40]. Taking into account these facts, and the mass of the detected species, one can design a model of a hypothetical species possessing the following properties: high molecular weight, extra -OH group in the B-ring, disintegrated the C-ring, disintegrated thiolated linker of TGE, presence of the aryl-O-aryl linkage. The model is presented in the Figure 11 in order to make clear our point of view.

**Figure 11.** The theoretical model of a fragment of the TGE monolayer on the Au plane after oxidation.

The sites suitable for an extra -OH group in the B-ring can be predicted based on the distribution of the spin density after the release of a proton from the 4'-OH group as well as from the 5-OH group, see Table 2.

Table 2. Theoretical prediction of the spin density distribution of the TGE molecule after hydrogen atom removal from the OH group in rings B or A. The calculations were performed with the B3LYP/6-311++G(d,p) density functional theory and the Hartree-Fock/6-311++G(d,p) theory (H-F).

Atom	Ring B		Atom	Ring A	
	B3LYP	H-F		B3LYP	H-F
O(at C4')	0.609	0.899	O(at C5)	0.624	0.928
C4'	-0.089	-0.692	C5	-0.148	-0.673
C3'	0.231	0.784	C5-4 (*)	0.16	0.792
C5'	0.221	0.781	C6	0.311	0.748
C2'	-0.134	-0.819	C7	-0.116	-0.689
C6'	-0.133	-0.833	C8-1	-0.113	-0.722
			C8	0.272	0.729

(*) at the border of the fused A and C rings.

Based on the spin density distribution, one can expect that the molecular positions at C3' and C5' in ring B (when a hydrogen atom is abstracted from the OH group at C4') as well as at the C6 and C8 in ring A (when the hydrogen atom is abstracted from the OH group at C5) are particularly suited for new bond formation with neighboring molecules to form dimeric structure. Although the B3LYP and Hartree-Fock are essentially different theories, they both predict consistently the positions at the TGE rings which are suited for new bond formation.

In the oxidation process on the Au electrode, the TGE molecules in the monolayer can apart from C-ring disintegration also undergo a disintegration of the thiolated linker S-C(=O)O-CH₂-CH₂-(genistein core) from the middle molecule of the trimer which may result in releasing the thioglycolic acid residue. Here, we studied a model system to determine the energy output of such a process. The ΔG (the Gibbs Free Energy) of this model reaction is estimated to be about -5.3 kcal/mol following the B3LYP/6-311++G(d,p) calculations. Thus, one can expect that a split of the ester bond should be considered as one of the possible routes of TGE disintegration under system stress when forming a trimer on a monolayer.

Taking into account the molecular structure of TGE which involves the aromatic rings with the -OH groups as well as numerous cases in the literature [43] presenting the aryl ether linkages we proposed analogical linkages between the TGE molecules in the monolayer. To clarify our doubts on whether the C-C or C-O-C linkage can prevail a simple model was analyzed to compare directly the internal energy of isomers linked by the aryl-O-aryl and the aryl-aryl bond. Two isomeric structures (C₁₂H₁₀O₆) formed by two 1,3,5-hydroxybenzene molecules were calculated with the B3LYP/6-311++G(d,p) method (Figures S4 and S5). Such a theoretical estimation corresponds to the isolated molecules, i.e., non-interacting with the environment. It appeared that the Gibbs free energy of both adducts is comparable.

3.5. In Vitro Study

Genistein is one of the isoflavones whose anti-cancer potential is extensively studied. It modulates various steps of the cell cycle, apoptosis, angiogenesis, and metastasis in different types of cancers. Therefore, the number of studies on the synthesis and biological evaluation of new genistein derivatives is increasing every year [3]. In our research, we focused on a new thioderivative of genistein and its biological properties. A preliminary study of the anti-tumor activity of thiogenistein (TGE) was carried out on DU145 prostate cancer cells to determine the properties of the new derivative and compared to genistein as the base compound. The concentration-dependent cell viability and cytotoxicity effect induced by TGE and GE (as a reference) were measured after 6, 24, and 72-h of incubation (Figure 12). After the addition of 50 μ M TGE solution, the viability of prostate cancer cells is reduced to 81.49% ($\pm 0.73\%$) and 66.12% ($\pm 1.30\%$) after 6 and 24 hours of incubation, respectively. However, in the case of GE, after 6 h, cell viability drops only to 92.91% ($\pm 1.01\%$), and after 24 h to 74.32% ($\pm 0.75\%$). The obtained results suggest that TGE reduces the viability of prostate cancer cells faster compared to GE. No meaningful differences are observed at lower concentrations. However, the most significant differences between cells were observed after 6 h (Figure 12A1). The addition of 100 μ M of the TGE solution reduces the viability of cancer cells to 60.8% ($\pm 0.55\%$), relative to the untreated cells. In contrast, for GE, cell viability remains high at 91.3% ($\pm 0.26\%$). The results achieved by the ToxiLight™ assay are complementary to the analysis described above. The toxicity of TGE is shown in Figure 12B (compared with the effect of GE). The cytotoxicity for the three highest concentrations of TGE increased over time and reached 84% ($\pm 3.41\%$) after 72 h. In the case of the thiol derivative, a significant slow down in the proliferation of DU145 cells is observed (Figure 12B1–B3). The number of cells (estimated by ToxiLight 100% Lysis Control) after 6, 24, and 72 h of incubation with the highest concentrations of TGE did not multiply. Based on these results, it could be concluded that TGE in a short time has far more negative effects on cellular respiration mechanisms and cytochromes of prostate cancer cells compared to GE. Additionally, the incubation of prostate cancer cells with TGE significantly affects their shape (Figure 12D1–D3). After only 6 h, cells become more rounded in contrast to GE-treated cells, which retain their characteristic, elongated shape. Due to early research, we are unable to determine the exact mechanism of TGE activity, which is responsible for reducing the rate of proliferation and reducing the viability of human prostate cancer cells.

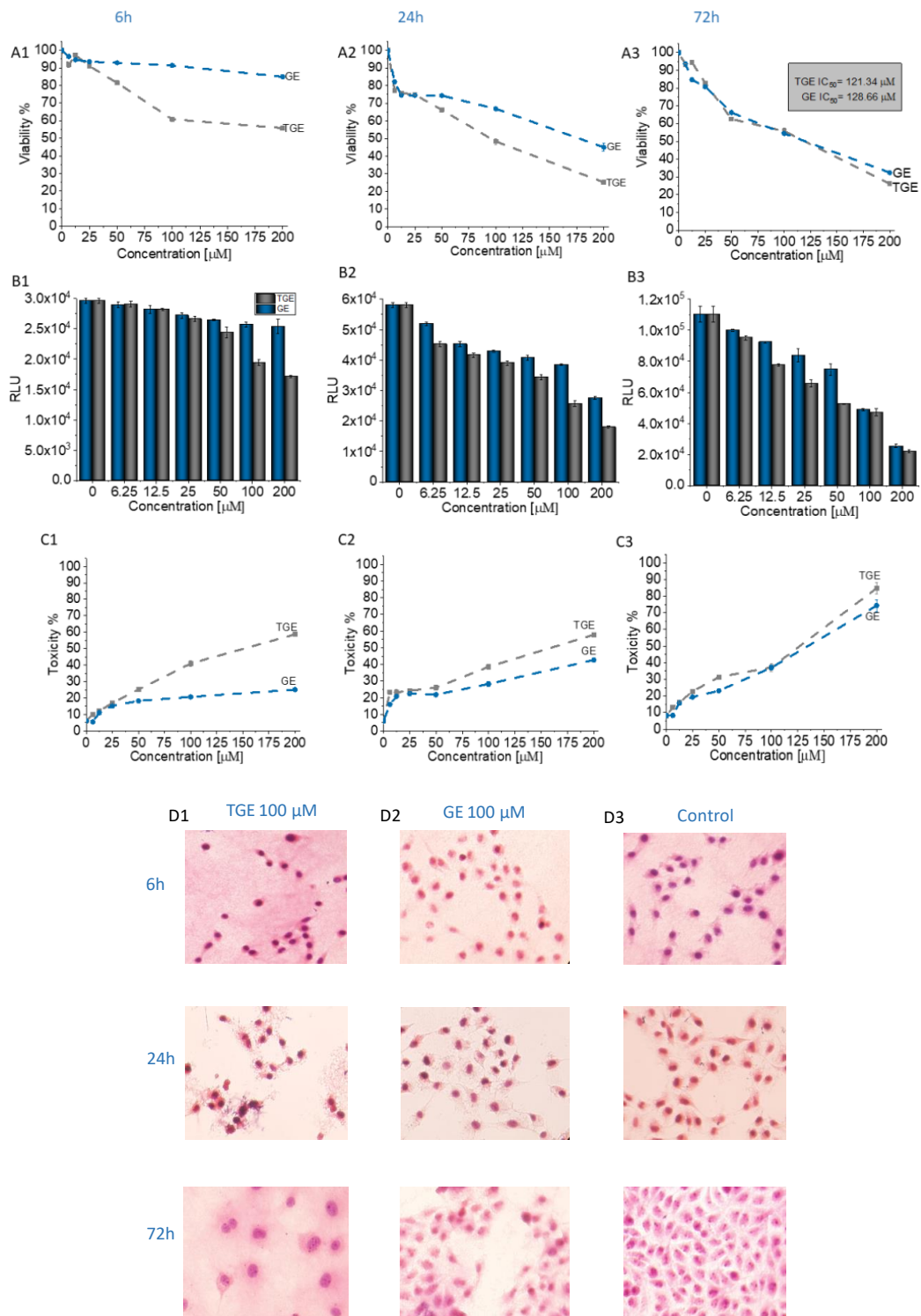


Figure 12. (A1–A3) Dependence of the viability (represented in % regarding control) on the concentration of TGE and GE incubated with DU145 cells for 6, 24, and 72 h. The viability was estimated based on the measurement of fluorescence intensity of the converted nonfluorescent resazurin to resorufin in metabolically active cells. (B1–B3) The luminescence intensity correlates with the adenylate kinase (AK) level obtained from all cells in the samples with ToxiLight 100% Lysate Control. The obtained results are proportional to the cell number of cells. (C1–C3) The cytotoxicity of the drugs was estimated based on the measurements of the AK level in the supernatant (released from the damaged cells) related to the AK level in the lysate (all cells in the samples). The data in (A–C) panels are representative of two independent experiments and are expressed as the mean ± SD. The error bars represent the ± SD. (D1–D3) Photomicrographs of the prostate cancer cells (DU145 line) morphology after 6, 24, and 72 h culture with the addition of 100 μM of TGE and GE as compared with the untreated group (control).

In addition to its anti-tumor properties, the new derivative should also show relative safety concerning healthy cells. Therefore, the initial characterization of TGE was supplemented with studies carried out on the PNT2 cell line—normal prostate epithelial cells. Figure 13 shows the concentration-dependent effect of TGE and GE on prostate epithelial cells. After 72 hours of incubation, the viability of PNT2 incubated with 50 μM GE decreased to 48.35% ($\pm 1.89\%$). With TGE, cell viability only drops to 79.88% ($\pm 0.86\%$). The results achieved by the ToxiLight™ assay are complementary to the analysis described above. The cytotoxicity of TGE against normal prostate epithelial cells is 19.07% ($\pm 0.50\%$), while GE is as high as 45.75% ($\pm 1.09\%$) (Figure 13C). This is clearly visible in the photomicrographs (Figure 13D), which demonstrate the morphology and the number of prostate epithelial cells. After 72 h, cells incubated with 50 μM GE lose the normal epithelial morphology and an arrest of proliferation is evident, relative to the control group. In the case of cells incubated with TGE, the changes in these two parameters are not observed in comparison to untreated cells. Based on the obtained results, we can conclude that TGE shows both a lower cytotoxic effect against normal prostate epithelial cells and an increased antitumor activity. In the case of cancer cells treated with GE and TGE, significant differences in their viability are visible at the dose of 100 μM , while in the case of normal cells, these differences are already visible at the dose of 50 μM .

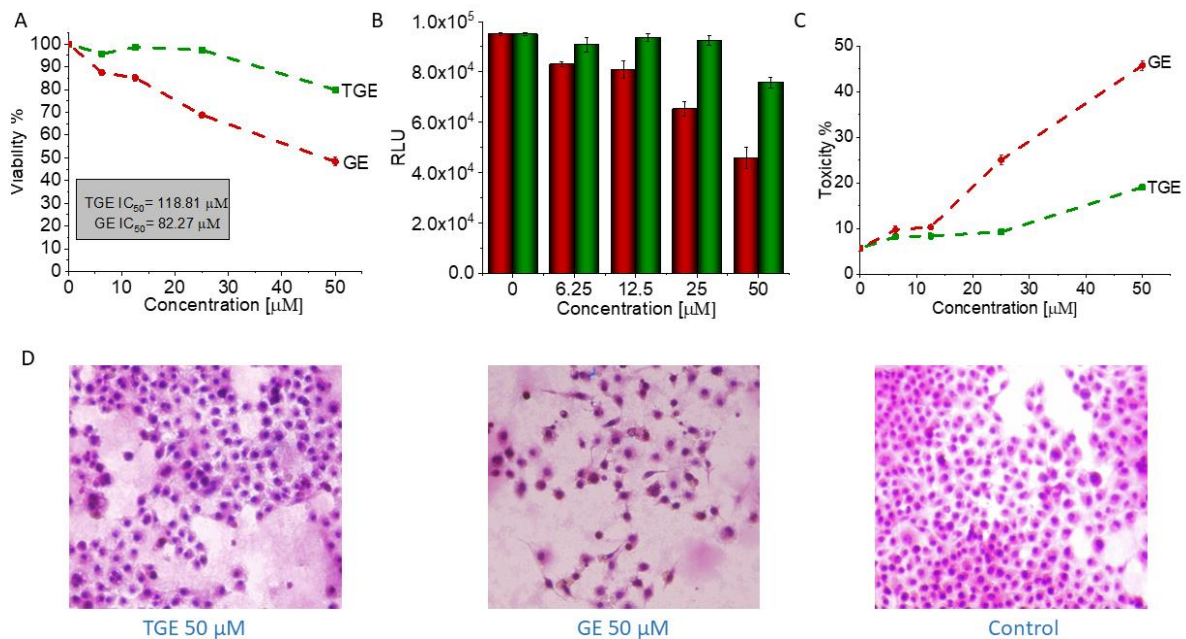


Figure 13. (A) The viability of PNT2 cells treated by different concentrations of GE and TGE for 72 h (determined by PrestoBlue™ test). (B,C) The cytotoxicity effect of TGE and GE was evaluated based on the luminescence intensity of the supernatant and lysate. (D) The morphology of prostate epithelial incubated cells with 50 μM of GE and TGE for 72 h. The data in (A–C) panels are representative of two independent experiments and are expressed as the mean \pm SD. The error bars represent the \pm SD.

According to the literature, genistein is metabolized mainly through oxidation, sulfation, glucuronidation, hydroxylation, or methylation [44]. However, the influence of genistein metabolites on its anti-cancer properties is still not fully understood. Kiriakidis et al. in their work identified two genistein metabolites in T47D cells of the breast epithelium, such as 5,7,39,49-tetrahydroxyisoflavone (THIF)—orobol and 2 glutathinyl conjugates of THI [45]. THIF has also been shown to inhibit angiogenesis and the proliferation of endothelial cells. This suggests that THIF formation during genistein treatment may play a major role in cell cycle arrest, inhibition of cell proliferation, and activation of signaling pathways such as p38 MAPK that have been observed in T47D cells. According to the literature, over time, THIF oxidizes to o-quinone with the formation of hydrogen peroxides and

reactive oxygen, which induces DNA strand breakage [46,47]. The synthetic derivatives, such as genistein glycosides, are also reported to possess anticancer activity when assessed *in vitro*. The anticancer potency of genistein glycosides varies depending on the sugar groups attached. For example, the addition of acetylated sugar hydroxyls to genistein resulted in more selectivity toward tumor cells. It is worthwhile to note that the anticancer potency of genistein and its derivatives differs in various types of cancer, depending on their selectivity toward the target molecule [48].

In vitro studies would suggest that changing the hydroxyl for an ether containing an -SH group on the C7 carbon in ring A may increase the cytotoxic properties of TGE. This effect can be attributed to the presence of a highly reactive -SH group [40]. Additionally, the presence of the -SH group in the new substituent may be responsible for the correct thiol-disulfide balance and the associated oxidation-reduction potential of cells. A similar mechanism is observed for glutathione which is a natural antioxidant [49].

4. Conclusions

This work contributes to the design of a simple and feasible strategy for thio-compounds in nano-drugs for use in oncology. In our previous publication, we described the synthesis of the thiolated genistein analog (TGE). In this work, while continuing the research on this new, promising compound, we examined its properties after oxidation as a process related to the reduction of cancer proliferation. The properties of TGE and its oxidation products were studied on a model system, i.e., the TGE monolayer on the Au electrode. In the course of the voltammetric experiments, it was proven that TGE is electrochemically active. The TGE monolayer undergoes irreversible oxidation reaction of the hydroxyl group in the A ring and the attachment of the -OH group to the B ring in the first stage, and then the quasi-reversible process of the quinone/hydroquinone system in the next stage. The formation of electroactive products that undergo redox reactions were observed. Electroactive centers of TGE were identified and its oxidation mechanisms were analyzed. The structure of TGE with a greater number of hydroxyl groups and additionally in a polymer configuration were discussed through MALDI-TOF MS and IR. Molecular modeling and the quantum mechanical density functional calculations supported this discussion. Our observations from the voltammetric experiments, supported with spectrometric data, are consistent with the literature regarding natural phenolic antioxidants described by the group of Oliveira-Brett [30]. In a preliminary *in-vitro* study, it was recognized that TGE has a higher cytotoxic activity towards DU145 prostate cancer cells and is safer for normal prostate epithelial cells (PNT2) than genistein (GE) itself. Moreover, the formation of TGE trimers upon oxidation deduced from the present study may enhance the biological response than the parent drug due to the synergizing of this response [50–52]. Most often, dimeric/trimeric drugs are not released (or cleaved) within the cell, so they can act as a completely new molecular unit inside the targeted cells [52]. The TGE monolayer firmly bound to the Au surface described in the present work may contribute to the design and development of the carriers of medicines in nanotechnology of biological applications.

Supplementary Materials: The following are available online at <https://www.mdpi.com/article/10.3390/ijms22168783/s1>.

Author Contributions: E.U.S., idea, structure, and design of the paper; MS-Maldi study; analyzed the data; wrote part of the manuscript; W.S., *in vitro* study; wrote part of the paper; M.L., ATR study; wrote part of the manuscript; A.L., molecular modeling; a quantum mechanical density functional calculations; wrote part of the paper; E.M., supervision of biological research; K.S. (Katarzyna Sidoryk), TGE synthesis; K.S. (Krzysztof Stolarczyk), idea for the paper, conceived and designed electrochemical experiments, performed the experiments; analyzed the data; wrote part of the paper. All authors have consulted their results, read, critically reviewed. All authors have read and agreed to the published version of the manuscript.

Funding: The study has been supported by the Polish Ministry of Science and Higher Education grant no. 841343A.

Institutional Review Board Statement: Not applicable.

Informed Consent Statement: Not applicable.

Acknowledgments: The calculations were performed at the Interdisciplinary Centre for Mathematical and Computational Modeling of the University of Warsaw (ICM UW, computer grant G18-6 and g85-962) which is kindly acknowledged for allocating facilities and computer time. The authors would like to thank Renata Bilewicz and Katarzyna Borkowska from the University of Warsaw for their support in this study. We also wish to thank Marta Zezula and Michał Sypniewski for their support in this study.

Conflicts of Interest: The authors declare no conflict of interest.

References

- Xiong, P.; Wang, R.; Zhang, X.; DeLa Torre, E.; Leon, F.; Zhang, Q.; Zheng, S.; Wang, G.; Chen, Q.-H. Design, Synthesis, and Evaluation of Genistein Analogues as Anti-Cancer Agents. *Anti-Cancer Agents Med. Chem.* **2015**, *15*, 1197–1203. [CrossRef]
- Zagórska-Dziok, M.; Kleczkowska, P.; Olędzka, E.; Figat, R.; Sobczak, M. Poly(Chitosan-ester-ether-urethane) hydrogels as highly controlled genistein release systems. *Int. J. Mol. Sci.* **2021**, *22*, 3339. [CrossRef] [PubMed]
- Tuli, H.S.; Tuorkey, M.J.; Thakral, F.; Sak, K.; Kumar, M.; Sharma, A.K.; Sharma, U.; Jain, A.; Aggarwal, V.; Bishayee, A. Molecular mechanisms of action of genistein in cancer: Recent advances. *Front. Pharmacol.* **2019**, *10*, 1–16. [CrossRef]
- Xiao, Y.; Ho, C.-T.; Chen, Y.; Wang, Y.; Wei, Z.; Dong, M.; Huang, Q. Synthesis, Characterization, and Evaluation of Genistein-Loaded Zein/Carboxymethyl Chitosan Nanoparticles with Improved Water Dispersibility, Enhanced Antioxidant Activity, and Controlled Release Property. *Foods* **2020**, *9*, 1604. [CrossRef]
- Stolarczyk, E.U.; Stolarczyk, K.; Łaszcz, M.; Kubiszewski, M.; Maruszak, W.; Olejarz, W.; Bryk, D. Synthesis and characterization of genistein conjugated with gold nanoparticles and the study of their cytotoxic properties. *Eur. J. Pharm. Sci.* **2017**, *96*, 176–185. [CrossRef]
- Vodnik, V.V.; Mojić, M.; Stamenović, U.; Otoničar, M.; Ajdžanović, V.; Maksimović-Ivanić, D.; Mijatović, S.; Marković, M.M.; Barudžija, T.; Filipović, B.; et al. Development of genistein-loaded gold nanoparticles and their antitumor potential against prostate cancer cell lines. *Mater. Sci. Eng. C* **2021**, *124*, 112078. [CrossRef] [PubMed]
- Dinkel, R.; Braunschweig, B.; Peukert, W. Fast and slow ligand exchange at the surface of colloidal gold nanoparticles. *J. Phys. Chem. C* **2016**, *120*, 1673–1682. [CrossRef]
- Sidoryk, K.; Michalak, O.; Kubiszewski, M.; Leś, A.; Cybulski, M.; Stolarczyk, E.U.; Doubsky, J. Synthesis of thiol derivatives of biological active compounds for nanotechnology application. *Molecules* **2020**, *25*, 3470. [CrossRef]
- Jiang, C.; Elliott, J.M.; Cardin, D.J.; Tsang, S.C. An electrochemical study of 4-aminothiophenol/Pt nanoparticle multilayers on gold electrodes. *Langmuir* **2008**, *25*, 534–541. [CrossRef] [PubMed]
- Lukkari, J.; Kleemola, K.; Meretoja, M.; Ollonqvist, T.; Kankare, J. Electrochemical post-self-assembly transformation of 4-aminothiophenol monolayers on gold electrodes. *Langmuir* **1998**, *14*, 1705–1715. [CrossRef]
- Porter, M.D.; Bright, T.B.; Allara, D.L.; Chidsey, C.E. Spontaneously Organized Molecular Assemblies. 4. Structural Characterization of n-Alkyl Thiol Monolayers on Gold by Optical Ellipsometry, Infrared Spectroscopy, and Electrochemistry. *J. Am. Chem. Soc.* **1987**, *109*, 3559–3568. [CrossRef]
- Marshall, G.M.; Bensebaa, F.; Dubowski, J.J. Observation of surface enhanced IR absorption coefficient in alkanethiol based self-assembled monolayers on GaAs(001). *J. Appl. Phys.* **2009**, *105*, 1–8. [CrossRef]
- Peng, D.K.; Lahann, J. Chemical, Electrochemical, and Structural Stability of Low-Density Self-Assembled Monolayers. *Langmuir* **2007**, *23*, 10184–10189. [CrossRef]
- Nuzzo, R.G.; Fusco, F.A.; Allara, D.L. Spontaneously Organized Molecular Assemblies. 3. Preparation and Properties of Solution Adsorbed Monolayers of Organic Disulfides on Gold Surfaces. *J. Am. Chem. Soc.* **1987**, *109*, 2358–2368. [CrossRef]
- Sato, Y.; Mizutani, F. Formation and characterization of aromatic selenol and thiol monolayers on gold: In-situ IR studies and electrochemical measurements. *Phys. Chem. Chem. Phys.* **2004**, *6*, 1328–1331. [CrossRef]
- Skoda, M.W.A.; Jacobs, R.M.J.; Willis, J.; Schreiber, F. Hydration of oligo(ethylene glycol) self-assembled monolayers studied using polarization modulation infrared spectroscopy. *Langmuir* **2007**, *23*, 970–974. [CrossRef] [PubMed]
- Corno, M.; Rimola, A.; Bolis, V.; Ugliengo, P. Hydroxyapatite as a key biomaterial: Quantum-mechanical simulation of its surfaces in interaction with biomolecules. *Phys. Chem. Chem. Phys.* **2010**, *12*, 6309–6329. [CrossRef]
- Stevens, C.A.; Safazadeh, L.; Berron, B.J. Thiol-yne adsorbates for stable, low-density, self-assembled monolayers on gold. *Langmuir* **2014**, *30*, 1949–1956. [CrossRef]
- Tao, Y.T.; Wu, C.C.; Eu, J.Y.; Lin, W.L.; Wu, K.C.; Chen, C.H. Structure evolution of aromatic-derivatized thiol monolayers on evaporated gold. *Langmuir* **1997**, *13*, 4018–4023. [CrossRef]
- Wan, L.J.; Terashima, M.; Noda, H.; Osawa, M. Molecular orientation and ordered structure of benzenethiol adsorbed on gold(111). *J. Phys. Chem. B* **2000**, *104*, 3563–3569. [CrossRef]
- Kim, I. Current Perspectives on the Beneficial Effects of Soybean Isoflavones and Their Metabolites for Humans. *Antioxidants* **2021**, *10*, 1064. [CrossRef]

22. Rizzo, G. The antioxidant role of soy and soy foods in human health. *Antioxidants* **2020**, *9*, 635. [CrossRef]
23. Frisch, M.J.; Trucks, G.W.; Schlegel, H.B.; Scuseria, G.E.; Robb, M.A.; Cheeseman, J.R.; Scalmani, G.; Barone, V.; Petersson, G.A.; Nakatsuji, H.; et al. Gaussian 16, Revision A.03. Available online: <http://gaussian.com> (accessed on 13 August 2021).
24. Hayes, W.A.; Shannon, C. Electrochemistry of surface-confined mixed monolayers of 4-aminothiophenol and thiophenol on Au. *Langmuir* **1996**, *12*, 3688–3694. [CrossRef]
25. Brust, M.; Fink, J.; Bethell, D.; Schiffrin, D.J.; Kiely, C. Synthesis and reactions of functionalised gold nanoparticles. *J. Chem. Soc. Chem. Commun.* **1995**, 1655–1656. [CrossRef]
26. Jin, Q.; Rodriguez, J.A.; Li, C.Z.; Darici, Y.; Tao, N.J. Self-assembly of aromatic thiols on Au(111). *Surf. Sci.* **1999**, *425*, 101–111. [CrossRef]
27. Johnson, S.R.; Evans, S.D.; Mahon, S.W.; Ulman, A. Alkanethiol molecules containing an aromatic moiety self-assembled onto gold clusters. *Langmuir* **1997**, *13*, 51–57. [CrossRef]
28. Stolarczyk, K.; Bilewicz, R. Catalytic oxidation of ascorbic acid on 2D and 3D monolayers of 4-hydroxythiophenol. *Electroanalysis* **2004**, *16*, 1609–1615. [CrossRef]
29. Stolarczyk, K.; Pałys, B.; Bilewicz, R. Catalytic properties of 4-hydroxythiophenol protected gold nanoclusters supported on gold electrodes. *J. Electroanal. Chem.* **2004**, *564*, 93–98. [CrossRef]
30. Chiorcea-Paquim, A.M.; Enache, T.A.; De Souza Gil, E.; Oliveira-Brett, A.M. Natural phenolic antioxidants electrochemistry: Towards a new food science methodology. *Compr. Rev. Food Sci. Food Saf.* **2020**, *19*, 1680–1726. [CrossRef] [PubMed]
31. Sinniah, K.; Cheng, J.; Terrettaz, S.; Reutt-Robey, J.E.; Miller, G.J. Self-assembled ω -hydroxyalkanethiol monolayers with internal functionalities: Electrochemical and infrared structural characterizations of ether-containing monolayers. *J. Phys. Chem.* **1995**, *99*, 14500–14505. [CrossRef]
32. Crupi, V.; Majolino, D.; Paciaroni, A.; Rossi, B.; Stancanelli, R.; Venuti, V.; Viliani, G. The effect of hydrogen bond on the vibrational dynamics of genistein free and complexed with β -cyclodextrins. *J. Raman Spectrosc.* **2010**, *41*, 764–770. [CrossRef]
33. Mrksich, M. Mass spectrometry of self-assembled monolayers: A new tool for molecular surface science. *ACS Nano* **2008**, *2*, 7–18. [CrossRef]
34. Ha, T.K.; Oh, H.B.; Chung, J.; Lee, T.G.; Han, S.Y. Investigation of the MALDI process used to characterize self-assembled monolayers of alkanethiolates on gold. *Langmuir* **2009**, *25*, 3692–3697. [CrossRef] [PubMed]
35. Kulling, S.E.; Honig, D.M.; Metzler, M. Oxidative metabolism of the soy isoflavones daidzein and genistein in humans in vitro and in vivo. *J. Agric. Food Chem.* **2001**, *49*, 3024–3033. [CrossRef] [PubMed]
36. Arora, A.; Valcic, S.; Cornejo, S.; Nair, M.G.; Timmermann, B.N.; Liebler, D.C. Reactions of genistein with alkylperoxyl radicals. *Chem. Res. Toxicol.* **2000**, *13*, 638–645. [CrossRef] [PubMed]
37. Soares, S.; Brandão, E.; Guerreiro, C.; Soares, S.; Mateus, N.; De Freitas, V. Tannins in food: Insights into the molecular perception of astringency and bitter taste. *Molecules* **2020**, *25*, 2590. [CrossRef]
38. Correddu, F.; Lunesu, M.F.; Buffa, G.; Atzori, A.S.; Nudda, A.; Battaccone, G.; Pulina, G. Can agro-industrial by-products rich in polyphenols be advantageously used in the feeding and nutrition of dairy small ruminants? *Animals* **2020**, *10*, 131. [CrossRef]
39. Da Santos, C.C.; Pimenta, T.C.; Thomasini, R.L.; Verly, R.M.; Franco, D.L.; Ferreira, L.F. Electropolymerization of phenol and aniline derivatives: Synthesis, characterization and application as electrochemical transducers. *J. Electroanal. Chem.* **2019**, *846*, 113163. [CrossRef]
40. Zhang, W.; Bao, L.; Zhang, X.; He, J.; Wei, G. Electropolymerization Treatment of Phenol Wastewater and the Reclamation of Phenol. *Water Environ. Res.* **2012**, *84*, 2028–2036. [CrossRef] [PubMed]
41. Khasanov, V.; Kravtsova, S.; Dychko, K.; Khasanov, V. Investigation of intermediate oxidation products of genistein and luteolin generated in aerobic conditions. *Key Eng. Mater.* **2015**, *670*, 171–176. [CrossRef]
42. Niu, L.T.; Li, G.G.; Li, H.F.; Cui, F.; Zhang, J.; Huang, Y.; Chen, K.; Zhang, J.F.; Li, W.F.; Liu, W.L. A Novel Genistein Electrochemical Sensor Based on Molecularly Imprinted Polycarbazole/Carboxylated Multiwalled Carbon Nanotubes Nanocomposite. *Chin. J. Anal. Chem.* **2019**, *47*, e19095–e19103. [CrossRef]
43. Li, F.; Wang, Q.; Ding, Z.; Tao, F. Microwave-assisted synthesis of diaryl ethers without catalyst. *Org. Lett.* **2003**, *5*, 2169–2171. [CrossRef]
44. Nguyen, D.T.; Hernandez-Montes, E.; Vauzour, D.; Schönthal, A.H.; Rice-Evans, C.; Cadenas, E.; Spencer, J.P.E. The intracellular genistein metabolite 5,7,3',4'-tetrahydroxyisoflavone mediates G2-M cell cycle arrest in cancer cells via modulation of the p38 signaling pathway. *Free Radic. Biol. Med.* **2006**, *41*, 1225–1239. [CrossRef] [PubMed]
45. Kiriakidis, S.; Högemeier, O.; Starcke, S.; Dombrowski, F.; Hahne, J.C.; Pepper, M.; Jha, H.C.; Wernert, N. Novel tempeh (fermented soybean) isoflavones inhibit in vivo angiogenesis in the chicken chorioallantoic membrane assay. *Br. J. Nutr.* **2005**, *93*, 317–323. [CrossRef] [PubMed]
46. Akiyama, T.; Ishida, J.; Nakagawa, S.; Ogawara, H.; Watanabe, S.; Itoh, N.; Shibuya, M.; Fukami, Y. Genistein, a specific inhibitor of tyrosine-specific protein kinases. *J. Biol. Chem.* **1987**, *262*, 5592–5595. [CrossRef]
47. Markovits, J.; Linossier, C.; Fossé, P.; Couprie, J.; Pierre, J.; Jacquemin-Sablon, A.; Saucier, J.M.; Le Pecq, J.B.; Larsen, A.K. Inhibitory Effects of the Tyrosine Kinase Inhibitor Genistein on Mammalian DNA Topoisomerase II. *Cancer Res.* **1989**, *49*, 5111–5117.
48. Popiotkiewicz, J.; Polkowski, K.; Skierski, J.S.; Mazurek, A.P. In vitro toxicity evaluation in the development of new anticancer drugs—Genistein glycosides. *Cancer Lett.* **2005**, *229*, 67–75. [CrossRef]
49. Grosso, R.; De-Paz, M.-V. Thiolated-Polymer-Based Nanoparticles as an Avant-Garde Approach for Anticancer Therapies—Reviewing Thiomers from Chitosan and Hyaluronic Acid. *Pharmaceutics* **2021**, *13*, 854. [CrossRef]

50. Berube, G. Natural and Synthetic Biologically Active Dimeric Molecules: Anticancer Agents, Anti-HIV Agents, Steroid Derivatives and Opioid Antagonists. *Curr. Med. Chem.* **2005**, *13*, 131–154. [CrossRef] [PubMed]
51. Fujisawa, S.; Atsumi, T.; Murakami, Y.; Kadoma, Y. Dimerization, ROS formation, and biological activity of o-methoxyphenols. *Arch. Immunol. Ther. Exp.* **2005**, *53*, 28–38.
52. Paquin, A.; Reyes-Moreno, C.; Bérubé, G. Recent advances in the use of the dimerization strategy as a means to increase the biological potential of natural or synthetic molecules. *Molecules* **2021**, *26*, 2340. [CrossRef] [PubMed]



Article

Poly(chitosan-ester-ether-urethane) Hydrogels as Highly Controlled Genistein Release Systems

Martyna Zagórska-Dziok ¹, Patrycja Kleczkowska ^{2,3} , Ewa Olędzka ⁴ , Ramona Figat ⁵ and Marcin Sobczak ^{1,4,*}

¹ Department of Technology of Cosmetic and Pharmaceutical Products, Faculty of Medicine, University of Information Technology and Management in Rzeszow, 2 Sucharskiego St., 35-225 Rzeszow, Poland; mzagorska@wsiz.edu.pl

² Centre for Preclinical Research (CBP), Department of Pharmacodynamics, Medical University of Warsaw, 1B Banacha St., 02-097 Warsaw, Poland; patrycja.kleczkowska@wum.edu.pl

³ Military Institute of Hygiene and Epidemiology, 4 Kozielska St., 01-163 Warsaw, Poland

⁴ Chair of Analytical Chemistry and Biomaterials, Department of Biomaterials Chemistry, Faculty of Pharmacy, Medical University of Warsaw, 1 Banacha St., 02-097 Warsaw, Poland; eoledzka@wum.edu.pl

⁵ Department of Environmental Health Sciences, Faculty of Pharmacy, Medical University of Warsaw, 1 Banacha St., 02-097 Warsaw, Poland; rfigat@wum.edu.pl

* Correspondence: marcin.sobczak@wp.pl; Tel.: +48-22-572-07-55

Abstract: Polymeric hydrogels play an increasingly important role in medicine, pharmacy and cosmetology. They appear to be one of the most promising groups of biomaterials due to their favorable physicochemical properties and biocompatibility. The objective of the presented study was to synthesize new poly(chitosan-ester-ether-urethane) hydrogels and to study the kinetic release of genistein (GEN) from these biomaterials. In view of the above, six non-toxic hydrogels were synthesized via the Ring-Opening Polymerization (ROP) and polyaddition processes. The poly(ester-ether) components of the hydrogels have been produced in the presence of the enzyme as a biocatalyst. In some cases, the in vitro release rate of GEN from the obtained hydrogels was characterized by near-zero-order kinetics, without “burst release” and with non-Fickian transport. It is important to note that developed hydrogels have been shown to possess the desired safety profile due to lack of cytotoxicity to skin cells (keratinocytes and fibroblasts). Taking into account the non-toxicity of hydrogels and the relatively highly controlled release profile of GEN, these results may provide fresh insight into polymeric hydrogels as an effective dermatological and/or cosmetological tool.

Keywords: active substance delivery systems; biomedical hydrogels; active substance-controlled release; genistein; hydrogels for cosmetology; hydrogels for dermatology; transdermal active substance delivery systems

Citation: Zagórska-Dziok, M.; Kleczkowska, P.; Olędzka, E.; Figat, R.; Sobczak, M. Poly(chitosan-ester-ether-urethane) Hydrogels as Highly Controlled Genistein Release Systems. *Int. J. Mol. Sci.* **2021**, *22*, 3339. <https://doi.org/10.3390/ijms22073339>

Academic Editor: Geoffrey Brown

Received: 25 February 2021

Accepted: 22 March 2021

Published: 24 March 2021

Publisher's Note: MDPI stays neutral with regard to jurisdictional claims in published maps and institutional affiliations.



Copyright: © 2021 by the authors. Licensee MDPI, Basel, Switzerland. This article is an open access article distributed under the terms and conditions of the Creative Commons Attribution (CC BY) license (<https://creativecommons.org/licenses/by/4.0/>).

1. Introduction

Hydrogels are a group of biomaterials that are perceived as a valuable tool in both cosmetology and dermatology, as they are efficient carriers of various therapeutic substances used in the treatment of a wide range of skin diseases [1,2]. This is mainly due to their ease of use and minimal range of possible side effects that are often observed in oral or intravenous drug administration. The multitude of hydrogel matrices currently under development enables many active substances, both hydrophilic and hydrophobic, to be incorporated into their structures [3]. This can be achieved through the formation of inclusion complexes, the production of nanoparticles, liposomes, microspheres and/or micelles [1,3–6]. Hydrogels based on natural and synthetic polymers, owing to their high biocompatibility, non-toxicity, biofunctionality, biodegradability, relatively low immunogenicity as well physical properties similar to natural tissues, are used for materials with many biomedical applications [1], namely, for the production of contact lenses, artificial organs and materials for the reconstruction and regeneration of cartilage, for tissue engineering and reconstructive surgery, as dressings for the healing of wounds as well as

release systems for various compounds with therapeutic effects [1,7–13]. In recent years, hydrogel biomaterials that are characterized by static properties or play the role of “smart” hydrogels that can respond to different types of stimuli have been more and more dynamically developed [14]. Furthermore, there is also an increasing interest in this type of material in the treatment of various dermatological diseases and beauty deficiencies. Indeed, the use of hydrogels as carriers of medicinal agents, both local and systemic, may prove to be an effective tool against skin diseases, which has been indicated by numerous scientific reports [15–17].

A number of forms of hydrogels containing numerous pharmacologically active substances in their structures and intended for use in the treatment of numerous skin diseases have been developed. These biomaterials also have a positive effect on the wound healing process and are used as fillers in aesthetic medicine treatments and as scaffolds for tissue regeneration [18–26]. Genistein (GEN) is an isoflavonoid with a wide spectrum of biological activity, which was first isolated from the *Genista tinctoria* L. in 1899, but is also present in many raw materials of plant origin [27]. Being a phytoestrogen makes it interesting as a potent valuable material for cosmetology as well as dermatology [28]. Estrogen receptors are found in various areas of the skin, where they play a specific, well-defined role. The similarity of the chemical structure of GEN to estrogens allows it to bind to estrogen receptors located in the cell nucleus, which results in a change in the expression of many genes that play an important role in many physiological and metabolic processes of the body [29]. Based on the current scientific reports, it can be concluded that the incorporation of GEN into the structure of hydrogels may prove helpful in the context of dermatology and cosmetology, because this phytoestrogen may contribute to the inhibition of skin aging processes [30,31], reduce the appearance of brown “age spots” on the body and improve the elasticity and firmness of our skin [32,33]. Additionally, the possibility of inhibiting the multiplication of many microorganisms by GEN indicates that this compound may also prove to be a useful tool in the fight against various bacterial and fungal diseases of the skin [34–37].

Many research groups have also attempted to evaluate the effects of GEN by conducting both in vitro and in vivo analysis. The obtained results indicate that in vitro GEN can inhibit the excessive growth of fibroblasts, which prevents their excessive proliferation and the formation of unsightly scars [38]. Research also indicates that GEN may counteract the inhibition of collagen biosynthesis by fibroblasts and protect skin cells from the harmful effects of UV radiation [39,40]. In addition, this compound reduces inflammation, improves the wound healing process, reduces oxidative and photodynamic damage and promotes DNA repair processes [32,41,42]. Research on skin ageing has also shown that GEN can inhibit this process by increasing the thickness of collagen fibers, increasing the resistance of the skin to breakage and reducing the levels of TGF- β 1, MMP-2, MMP-9, VEGF, TIMP-1 and TIMP-2 [43,44]. Furthermore, the clinical trials showed that isoflavones, including GEN, have a positive effect on the proliferation of epidermal cells, the production of collagen, the reduction of fine wrinkles and the improvement of skin elasticity [41].

Even though GEN has skin protecting activity, its sustained effect is still limited due to lower stability in cosmeceutical products [45]. In order to enhance stability and prolong activity, delivery technologies have greater impact in cosmeceutical sectors. For example, GEN-loaded nanoemulsions were prepared with 250 nm sized nanoparticles and enhanced delivery of isoflavones to the skin with higher skin protecting activity [46]. In another study, nanosized liposome-encapsulated GEN in nanoparticles the size of about 80 nm was tested on rat skin, with or without hair [47]. In addition to the nanosized liposomes, the hairs on the skin also affect the delivery of the GEN compound to the skin [45]. No commercial hydrogels containing genistein dedicated to cosmetology and dermatology have been yet developed. This is probably due to the unsatisfactory control of the kinetics of genistein release from such carriers. However, there is still intensive work on this type of materials in many scientific and industrial centers.

Given the above, in this work, we have shown for the first time new synthesized poly(chitosan-ester-ether-urethane) hydrogels characterized by highly GEN controlled release. A significant novelty of our findings relies on using biodegradable hydrogels with different structures as an efficient solution for the modification of GEN-release properties. It is important to mention that the obtained hydrogels possess a desired safety profile in terms of lack of cytotoxicity towards skin cells. We believe that such obtained hydrogels could be practically applied for dermatology and cosmetology.

2. Results and Discussion

2.1. Synthesis of CL, LA and PEG Copolymers

The main aim of the present work was the synthesis and characterization of poly(chitosan-ester-ether-urethane) hydrogels as new and potential GEN carriers. Our main intention was to establish a relationship between the composition and physicochemical properties of the synthesized hydrogels and the amount of GEN released from them. As a consequence, the hydrogels were obtained by a three-step method.

In the first step (1), copolymers *rac*-lactide (*rac*-LA) and poly(ethylene glycol) (PEG) (PLA-PEG) or ϵ -caprolactone (CL) and PEG (PCL-PEG) were synthesized via enzyme Ring-Opening Polymerization process (e-ROP) (Table 1). The e-ROP process was carried out at 80 °C during 7 days in toluene as a medium. Immobilized lipase B from *Candida antarctica* (CALB) was used as a biocatalyst. The molar ratio of the monomers (*rac*-LA or CL) to PEG was: 20:1, 25:1, 30:1, 35:1 or 40:1. The chemical structure of the obtained copolymers was confirmed by ¹³C, ¹H NMR and FTIR studies (Experimental section). As shown in Table 1, the synthesized copolymers were characterized by a similar value of Mn (3200–3700 g/mol), but a different content of PEG units in the polymer chain (circa 11, 15 and 20 mol. % PEG). Reaction yields ranged from 69 to 88%.

Table 1. Synthesis of CL, *rac*-LA and PEG copolymers.

Sample	Molar Ratio ^a	Yield [%]	M_n ^b [g/mol]	\bar{D} ^b	% mol CL or LA ^c	% mol PEG ^c
PLA-PEG-1	20:1	77	3200	1.69	79.7	20.3
PLA-PEG-2	25:1	72	3400	1.57	84.9	15.1
PLA-PEG-3	30:1	69	3500	1.62	88.3	11.7
PCL-PEG-1	30:1	88	3400	1.48	80.4	19.6
PCL-PEG-2	35:1	80	3500	1.43	84.3	15.7
PCL-PEG-3	40:1	76	3700	1.52	88.9	11.1

^a *rac*-LA (or CL): PEG 400 molar ratio; ^b average molar mass and dispersity determined by the GPC method; ^c percent of mers molar content in the chain (determined by ¹H NMR); Reaction conditions: temp. 80 °C, time—7days, medium—toluene, CALB (400 mg).

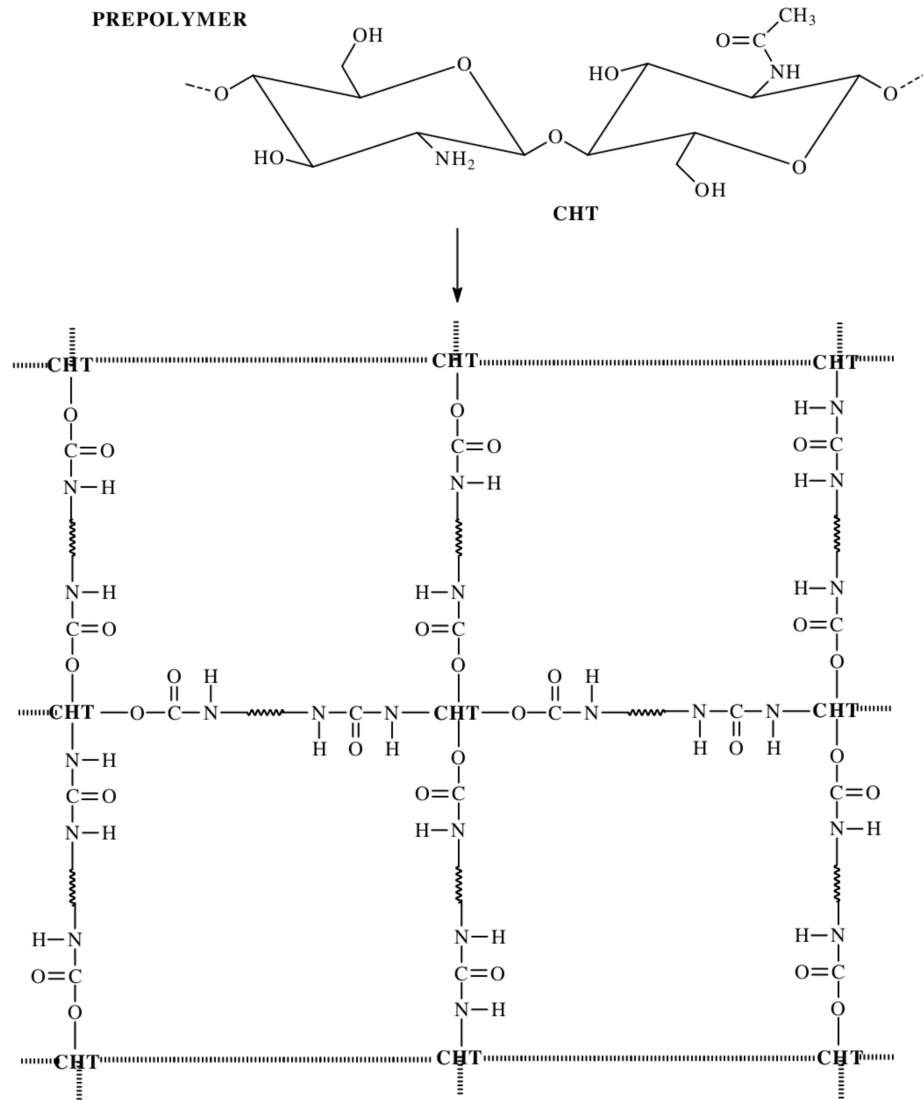
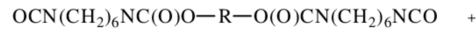
2.2. Swelling and Biodegradation of Hydrogels Studies

In the next stage of this study, the hydrogels were synthesized using prepolymer methods such as: (2) preparation of prepolymers and (3) polyaddition of prepolymers and chitosan (CHT) (Scheme 1). In step (2), various PLA-PEG or PCL-PEG were reacted with hexamethylene diisocyanate (HDI) in a –NCO/–OH molar ratio of 2.05:1. In step (3), the prepolymer was reacted with CHT in a –NCO(prepolymer)/–OH(or NH₂) (CHT) ratio of 1.5:1. The dibutyltin dilaurate (DBDLSn) was used as a polyaddition catalyst (Table 2).

The swelling capacity of the obtained hydrogels was determined (Table 2). The value of the coefficient of the mass swelling ratio (MSR) was 375%, 311%, 284%, 297%, 258% and 211% after 4 h for HPUCHT-1, HPUCHT-2, HPUCHT-3, HPUCHT-4, HPUCHT-5 and HPUCHT-6, respectively. As we can easily see, the value of the MSR depended on the nature of the polyester used and the content of the PEG units in the hydrogel chain. As expected, MSR increases with the growth of hydrophilic fragments—PEG units in the polymer chain.



HDI **PLA-PEG 400** **PREPOLYMER**
PCL-PEG 400



Scheme 1. Hydrogel synthesis.

Table 2. Characterization of hydrogels.

Sample	PLA-PEG	PCL-PEG	MSR [%] ^a	MSR [%] ^b	MSR [%] ^c
HPUCHT-1	PLA-PEG-1 (80:20)	-	375 ± 17	412 ± 18	421 ± 18
HPUCHT-2	PLA-PEG-2 (85:15)	-	311 ± 14	341 ± 15	348 ± 15
HPUCHT-3	PLA-PEG-3 (88:12)	-	284 ± 13	311 ± 13	326 ± 14
HPUCHT-4	-	PCL-PEG-1 (80:20)	297 ± 14	328 ± 15	333 ± 15
HPUCHT-5	-	PCL-PEG-2 (84:16)	258 ± 11	284 ± 13	287 ± 13
HPUCHT-6	-	PCL-PEG-3 (89:11)	211 ± 11	232 ± 11	243 ± 12

Reaction conditions: temperature—80 °C, time—3 h (the first step of the prepolymer process) and 4 h (the second step the of prepolymer process); HDI and PLA-PEG 400 (or PCL-PEG 400) molar ratio: 2.05:1 (in a —NCO/—OH); —NCO(prepolymer)/—OH(or —NH₂) (CHT) molar ratio: 1.5:1; MSR—mass swelling ratio. ^a—after 4 h; ^b—after 24 h; ^c—after 48 h.

2.3. In Vitro Release Studies of GEN from Hydrogels

GEN was loaded into hydrogels using the incorporation method. The mean weight of the devices developed was approximately 200 mg, corresponding to approximately 10 mg of GEN (active substance content was adjusted to about 5%). In vitro studies of the release of GEN from obtained hydrogel materials were determined at pH 7.4 and 37 °C for 80 h (Figure 1). The ordinate of the plot was calculated based on the cumulative amount of GEN released with respect to its initial amount in the hydrogels.

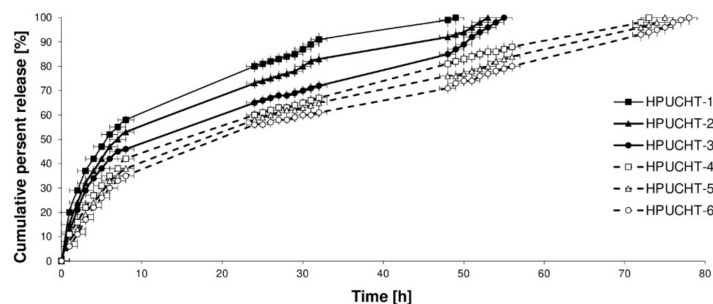


Figure 1. GEN release profiles from the hydrogels.

As mentioned above, our intention in this work was to investigate the influence of two factors on the kinetic release of GEN. The first one was the content of the PEG units in the copolymer; the second was the nature and properties of the polymer forming the copolymer (PLA or PCL).

The rate of the GEN release decreased as follows: HPUCHT-1 (obtained from PLA-PEG-1 (80:20)) > HPUCHT-2 (PLA-PEG-2 (85:15)) > HPUCHT-3 (PLA-PEG-3 (88:12)) > HPUCHT-4 (PCL-PEG-1 (80:20)) > HPUCHT-5 (PCL-PEG-2 (84:16)) > HPUCHT-6 (PCL-PEG-3 (89:11)).

The data points obtained for the drug release studies were subject to zero-order and first-order kinetics as well as to the Korsmeyer–Peppas models for the evaluation of the kinetic and mechanism of GEN release from hydrogels (Table 3). As is known from the literature, according to the Korsmeyer–Peppas model, for the diffusion-degradation-controlled drug release system, the release exponent value n is in the range of 0.45 and 0.89 (anomalous, non-Fickian), whereas when n is close to 0.45, the diffusion (Fickian diffusion) predominates in the process and, in the opposite case, $n > 0.89$, the model corresponds to the super case II transport [48,49].

Table 3. Analysis data of GEN release from the obtained hydrogels.

No.	Zero-Order Model	First-Order Model	Korsmeyer–Peppas Model		GEN Transport Mechanism
	R ²	R ²	R ²	n	
HPUCHT-1	0.847	0.915	0.998	0.516	non-Fickian transport
HPUCHT-2	0.873	0.940	0.995	0.609	non-Fickian transport
HPUCHT-3	0.921	0.868	0.944	0.452	non-Fickian transport
HPUCHT-4	0.923	0.913	0.976	0.488	non-Fickian transport
HPUCHT-5	0.925	0.869	0.968	0.553	non-Fickian transport
HPUCHT-6	0.941	0.831	0.957	0.597	non-Fickian transport

In our study, it was observed that the kinetic release of GEN is mainly influenced by the content of the PEG units in the copolymers used for the preparation of hydrogels. For example, approximately 80.8%, 73.4% and 65.2% of GEN were released after 24 h from the HPUCHT-1, HPUCHT-2 and HPUCHT-3 samples, respectively. This is relatively little, because 60.7%, 58.3% and 56.8% of GEN were released after 24 h from the HPUCHT-4, HPUCHT-5 and HPUCHT-6 materials composed of PCL segments in different molar ratios (Table 2). Thereby, we can conclude that GEN was released more rapidly from materials created of PLA polymers than from PCL segments. After 49, 53 and 55 h, almost 100% of

GEN was released from hydrogels composed of PLA units (Figure 1). In the case of PCL polymer materials, the time for the GEN releasing in 100% was longer and ranged up to 78 h (Figure 1). This is undoubtedly related to the higher hydrophilicity of hydrogels obtained from PLA-PEG copolymers compared with those obtained from PCL-PEG copolymers. The Mn of the PLA-PEG or PCL-PEG copolymers used in the hydrogel synthesis did not appear to affect the amount of GEN released. This could be because the Mn values of all copolymers were similar (3200–3700 g/mol) (which was consistent with the authors' assumptions). It was also discovered that the higher the PEG content in a given matrix composed of PLA or PCL units, the higher the amount of GEN released.

The GEN release kinetic from hydrogels obtained from PCL-PEG copolymers (HPUCHT-4, HPUCHT-5, HPUCHT-6) followed the near-zero-order model (R^2 was 0.923, 0.925 and 0.941, respectively). Furthermore, for the HPUCHT-3 sample (hydrogel containing the lowest percentage of PEG units, but composed of PLA units), the GEN release was also close to the zero-order kinetics ($R^2 = 0.921$). Furthermore, it was noted that GEN was released from the HPUCHT-1 and HPUCHT-2 samples with rather first-order kinetics (R^2 was 0.915 and 0.940 (Table 3). The analysis of GEN release data using the Korsmeyer–Peppas model suggested that all the hydrogels were governed rather by a non-Fickian transport ($n = 0.452–0.609$).

The biodegradation of the blank hydrogels has also been carried out. Hydrolytic degradation test of the resulting carriers was conducted under the same conditions as the GEN release experiments. The degradation process was characterized by the plotting of the weight loss (WL) of hydrogels versus time. The results are shown in Figure 2.

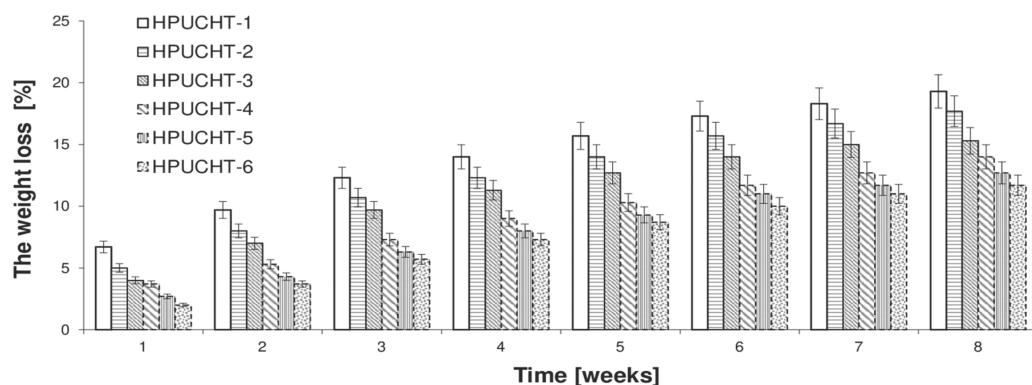


Figure 2. The weight loss (WL) of the obtained hydrogels.

The degradation rate of the hydrogels was found to be similar to that of the GEN release profile (Figure 1). The blank hydrogels degradation rate was as follows: HPUCHT-1 > HPUCHT-2 > HPUCHT-3 > HPUCHT-4 > HPUCHT-5 > HPUCHT-6. Similarly, hydrogels formed of PLA polymer degrade faster than that obtained from PCL segments. Apparently, this corresponds to a higher hydrophilicity of the PLA polymer. In addition, the rate of degradation of the hydrogel has increased with an increase in the content of the PEG units in the copolymer chain. In summary, on the basis of the data obtained from the kinetic release and mathematical models, it can be concluded that in some cases, GEN was released with relatively high control from the synthesized hydrogel materials.

Certain GEN vectors, including nanoparticles, nanocapsules or nanoemulsions, have been developed and thoroughly studied [50–54]. For instance, GEN was released from zein and zein/carboxymethyl CHIT nanoparticles at a rate of about 60% after 24 h. The authors suggest a controlled release, although the “burst release” phenomenon can be observed in the kinetic profiles. Moreover, the authors did not match the obtained release results with any kinetic models [50]. GEN-loaded solid lipid nanoparticles (SLNs) and nanostructured lipid carriers (NLCs) were obtained by Andrade et al. [50]. Skin permeation studies have shown that lipid nanoparticles have increased GEN skin retention but GEN release kinetics have not been fully controlled [50]. GEN-loaded PLA nanocapsules

(GEN-NC) were prepared in paper [52] by interfacial deposition of pre-formed polymers (nanoprecipitation). Permeation experiments have demonstrated that a higher amount of GEN reaches deeper layers of the skin and increased penetration was achieved when GEN-NC was incorporated into a semi-solid gel formulation. It indicated that GEN-NC could be a promising nanocarrier system for GEN skin delivery, but this active substance release kinetics was not fully controlled. Nanoemulsions composed of isopropyl myristate/dioleoylphosphatidylcholine/oleylamine with GEN have also been obtained [53]. The incorporation of GEN into nanoemulsions significantly increased the retention of this isoflavone in epidermis and dermis. These results were supported by confocal images. Such formulations exhibited antiherpetic activity in vitro against herpes simplex virus 1 and herpes simplex virus 2. The results shows that the GEN-loaded nanoemulsions developed in this study are promising options for herpes treatment. Nanoemulsions containing isoflavone aglycone-rich fraction (NE IAF) and derivative semi-solid hydrogels composed of hyaluronic acid have been obtained at work [54]. NE IAF containing GEN has been prepared and, in some formulations, hyaluronic acid has been added to obtain hydrogels. The distribution of GEN in skin layers has been evaluated. These results showed the potential of formulations for topical skin applications. However, the kinetics of GEN release from the above-mentioned carriers have not been investigated.

In the light of the cited literature examples, we are unfortunately of the opinion that the comparison of these biomaterials with the hydrogels produced in our work is quite difficult due to the fact that our materials have been synthesized from a different type of polymer and thus have a different structure. In our view, the developed biodegradable poly(chitosan-ester-ether-urethane) hydrogels (HPUCHT-3, HPUCHT-4, HPUCHT-5, HPUCHT-6) are characterized by relatively high release control and may constitute a potential material for further dermatological applications.

2.4. Genotoxic Test

The umu-test was used to evaluate the genotoxicity of the blank hydrogels (Table 4). In the umu-test, it was found that none of the samples tested were toxic to *S. typhimurium* ($G > 0.5$) (Table 4). None of the tested extracts exhibited a genotoxic effect ($IR < 1.5$) with or without metabolic activation ($IR < 1.5$).

Table 4. The results of the umu-test for the extracts tested.

	−S9 *		+S9 **	
	G ± SD	IR ± SD	G ± SD	IR ± SD
MS H-1	1.00 ± 0.04	0.94 ± 0.07	0.95 ± 0.02	0.96 ± 0.04
MS H-2	1.05 ± 0.05	0.82 ± 0.15	0.98 ± 0.05	0.85 ± 0.20
MS H-3	1.06 ± 0.08	0.81 ± 0.13	1.03 ± 0.06	0.96 ± 0.20
MS H-4	0.99 ± 0.04	0.94 ± 0.08	1.10 ± 0.24	0.85 ± 0.34
MS H-5	1.05 ± 0.08	0.84 ± 0.17	1.07 ± 0.14	0.88 ± 0.26
MS H-6	1.01 ± 0.03	0.93 ± 0.10	1.03 ± 0.15	0.90 ± 0.27
Positive control	0.98 ± 0.01	7.77 ± 0.18	0.88 ± 0.02	4.52 ± 0.13
Negative control	1.01 ± 0.07	1.00 ± 0.13	1.00 ± 0.10	1.02 ± 0.25
Solvent control	1.02 ± 0.04	1.04 ± 0.14	0.74 ± 0.08	1.13 ± 0.20

* without metabolic activation; ** with metabolic activation.

2.5. Cytotoxicity Assessment

2.5.1. Neutral Red Uptake Assay

In order to assess the biocompatibility of the obtained hydrogels and the possibility of their use in the treatment of various skin diseases, cytotoxicity tests were carried out on skin cells located in different layers of the skin—fibroblasts and keratinocytes. For this purpose, these cells were exposed to the tested hydrogels for 2 and 24 h. The cell viability was estimated using the Neutral Red (NR) and Alamar Blue (AB) assays. The obtained results revealed that the hydrogels tested were characterized by high biocompatibility,

as no cytotoxic effects were observed in any of the hydrogels. The analysis conducted showed that the effect of the experiments on keratinocytes (HaCaT) and fibroblasts (BJ) varies depending on the type of hydrogel tested and the time of exposure to hydrogel extracts. The NR assay performed on fibroblasts showed that the extended exposure time to the hydrogels tested had a positive effect on the viability of these cells, which is probably related to the release of GEN from hydrogels and its positive effect on the skin cells of interest. Notably, promising results for HPUCHT-3 and HPUCHT-4 hydrogels were observed after a shorter exposure time. An average cell viability of 188% was recorded for HPUCHT-3 hydrogel at the highest extract concentration (5%). After longer exposure, all the hydrogels tested were found to stimulate an increase in the viability of the fibroblasts. However, in the case of HPUCHT-6 hydrogel, this effect was observed only at the two highest extract concentrations (2.5 and 5.0%) (Figure 3A,B). In the case of keratinocytes, such a significant effect of the prolonged exposure time on the increase in the viability of these cells was unnoted (Figure 4A,B). Increased viability of keratinocytes treated with hydrogels tested was also reported to be lower compared to fibroblasts. The most promising results have, indeed, been achieved for HPUCHT-2, HPUCHT-3 and HPUCHT-4 hydrogels. On the other hand, the remaining hydrogels did not have a positive effect on the viability of HaCaT cells as a response to the extended exposure time, but still had no cytotoxic activity (Figure 4B).

2.5.2. Alamar Blue Assay

In the case of the Alamar Blue assay, no cytotoxicity of the analyzed hydrogels was observed for either types of skin cells. These analyses showed that the longer exposure time (up to 24 h) to the tested hydrogels significantly increased the metabolic activity of the fibroblasts, which reached 165 and 175% for HPUCHT-3 and HPUCHT-4 hydrogels at the highest concentrations (Figure 5A,B). On the other hand, better results were obtained for a shorter incubation time for keratinocytes, indicating a higher sensitivity of these cells to the action of the hydrogels tested.

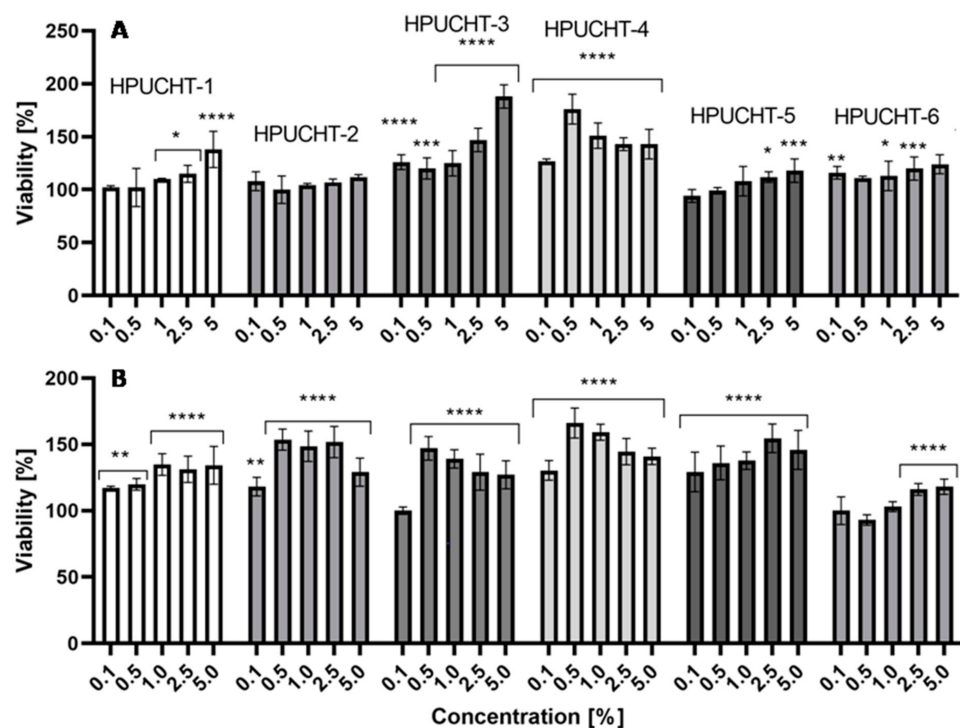


Figure 3. Effect of different concentrations of extracts (0.1–5%) from hydrogels on NR uptake in cultured fibroblasts after 2 h (A) and 24 h (B) of exposure. **** $p < 0.0001$, *** $p < 0.001$, ** $p < 0.01$, * $p < 0.05$ versus the control (100%).

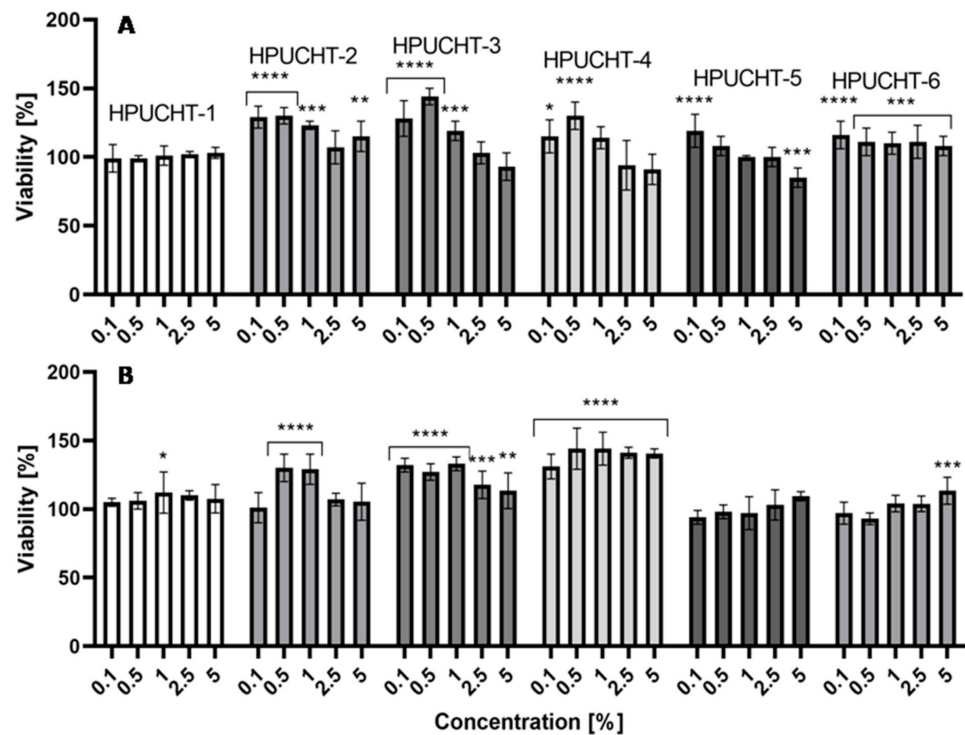


Figure 4. Effect of different concentrations of extracts (0.1–5%) from hydrogels on NR uptake in cultured HaCaT cells after 2 h (A) and 24 h (B) of exposure. **** $p \leq 0.0001$, *** $p \leq 0.001$, ** $p \leq 0.01$, * $p \leq 0.05$ versus the control (100%).

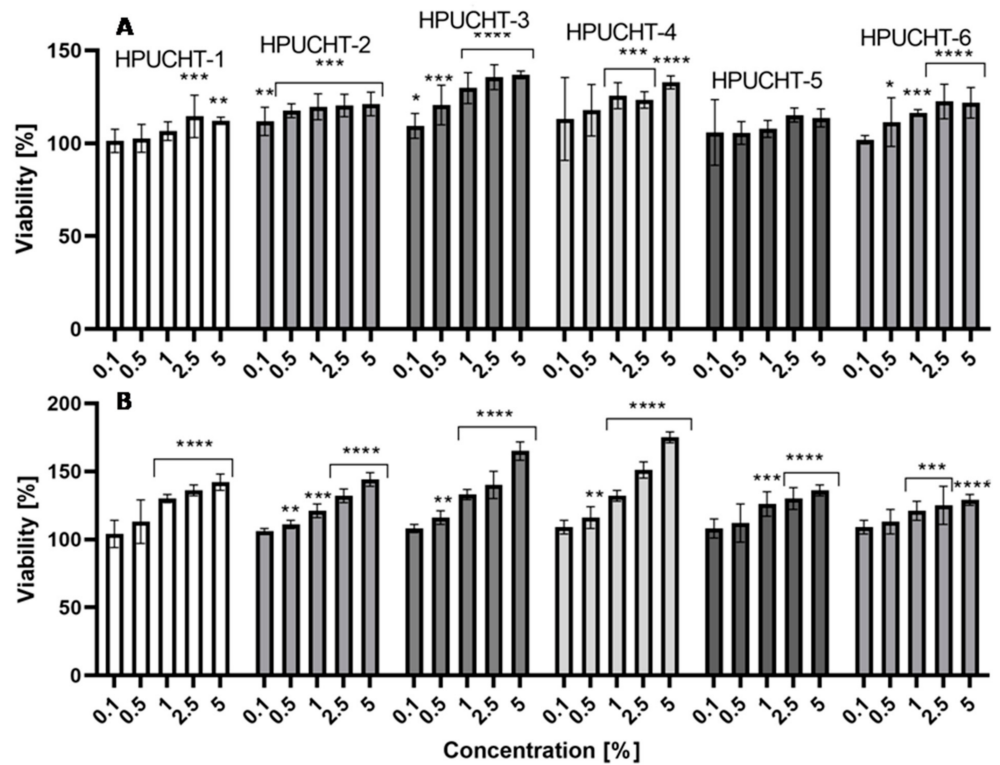


Figure 5. The reduction of resazurin after 2 h (A) and 24 h (B) of exposure to extracts (0.1–5%) from hydrogels in cultured fibroblasts. **** $p \leq 0.0001$, *** $p \leq 0.001$, ** $p \leq 0.01$, * $p \leq 0.05$ versus the control (100%).

It should be noted, however, that no cytotoxic effect was observed after 2 and 24 h of exposure of keratinocytes to the hydrogels tested and most of the hydrogels stimulated the metabolic activity and viability of these cells (Figure 6A,B). The studies carried out, thus, show a lack of in vitro cytotoxicity of the hydrogels tested, which gives hope for the possibility of their potential application after appropriate in vivo analyses and clinical trials.

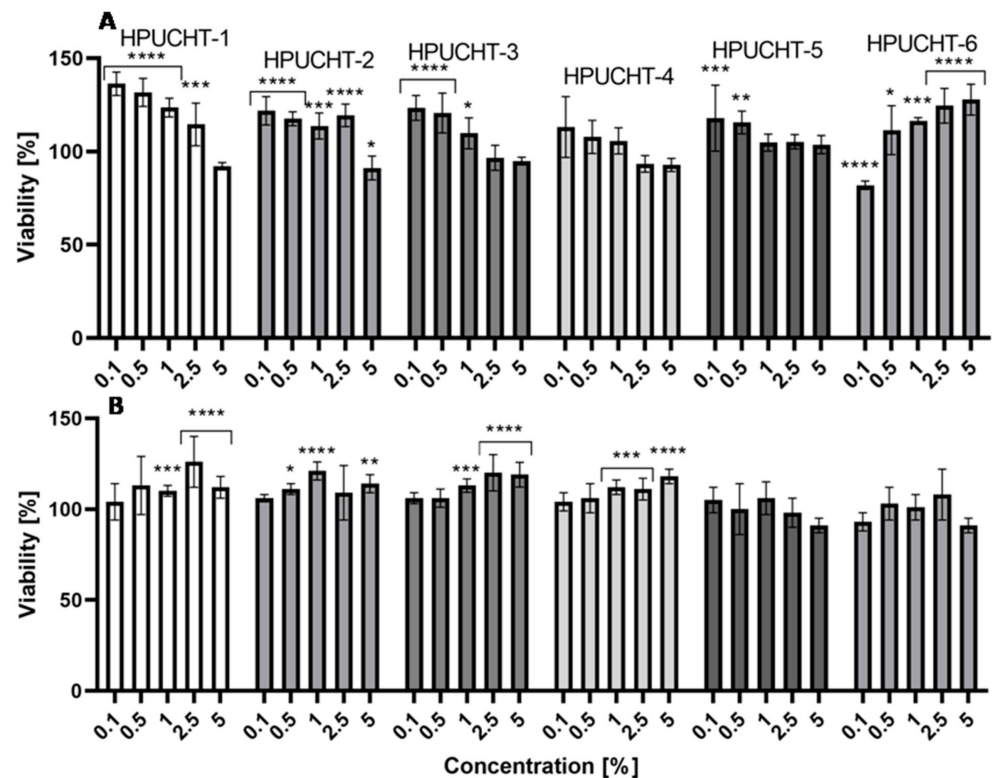


Figure 6. The reduction of resazurin after 2 h (A) and 24 h (B) of exposure to extracts (0.1–5%) from hydrogels in cultured HaCaT cells. **** $p \leq 0.0001$, *** $p \leq 0.001$, ** $p \leq 0.01$, * $p \leq 0.05$ versus the control (100%).

As part of the studies, the effect of GEN on the cell lines tested was also assessed. The obtained results indicate that this compound has no negative effect on both keratinocytes and fibroblasts in the tested concentration range (1–1000 μM). In the case of fibroblasts, it was observed that a 2-h incubation of these cells with GEN causes a statistically significant increase in the metabolic activity of these cells (the concentrations was ranged from 100 to 750 μM), and after 24-h incubation with 100 μM of GEN, the increase in this activity was almost 70% compared to the control cells (untreated with GEN). Concentrations of 250–1000 μM also significantly increased the proliferation of fibroblasts. However, as the concentration of GEN increased, this effect was weaker, which could indicate a cytotoxic effect of GEN at higher concentrations (above 1000 μM) (Figure 7A,B). In the case of keratinocytes, no statistically significant increase in cell proliferation was observed after 2-h incubation, while the longer incubation period resulted in an increase in the metabolic activity of these cells exposed to GEN at concentrations of 1–500 μM . Higher concentrations (750 and 1000 μM) did not cause a decrease in cell proliferation compared to control cells, but, as in the case of fibroblasts, a downward trend in the activity of these cells was observed along with an increase in the GEN concentration (Figure 8A,B).

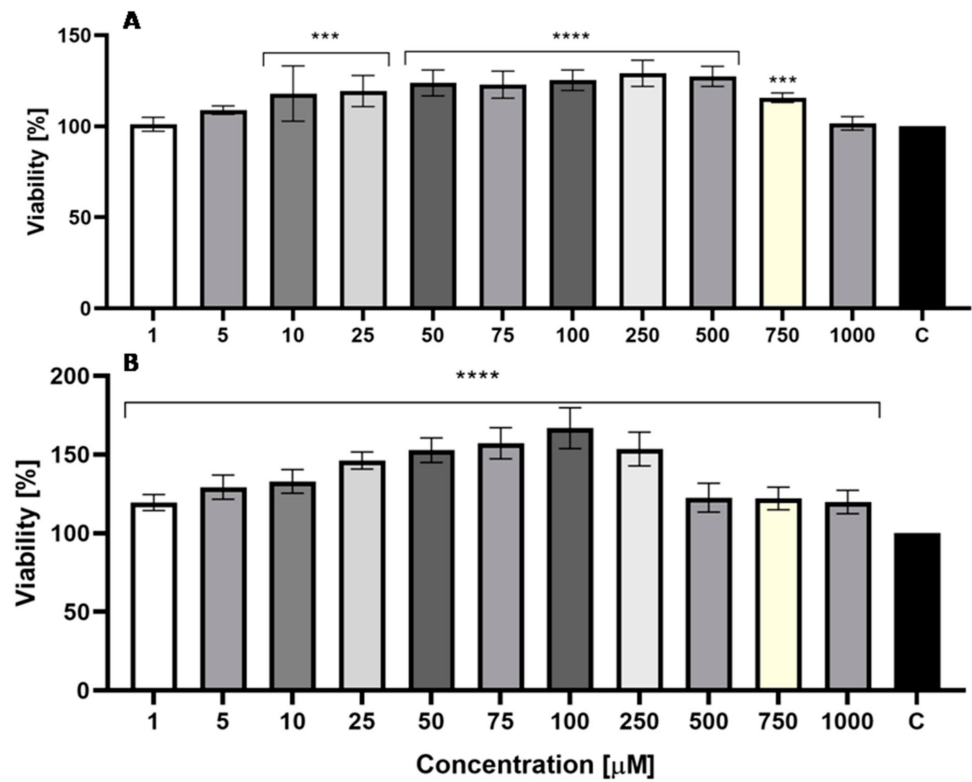


Figure 7. The reduction of resazurin after 2 h (A) and 24 h (B) of exposure to GEN (1–1000 μM) in cultured fibroblasts. **** $p \leq 0.0001$, *** $p \leq 0.001$ versus the control (100%).

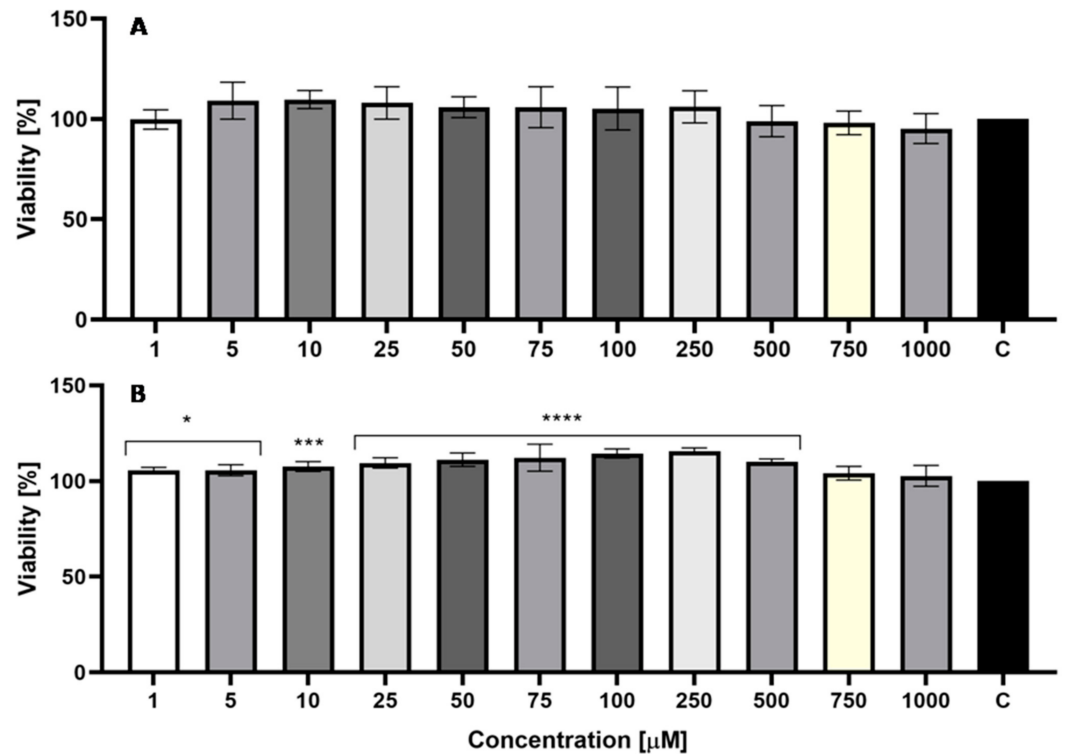


Figure 8. The reduction of resazurin after 2 h (A) and 24 h (B) of exposure to GEN (1–1000 μM) in cultured HaCaT cells. **** $p \leq 0.0001$, *** $p \leq 0.001$, * $p \leq 0.05$ versus the control (100%).

The increase in cell viability and the rate of proliferation following the use of GEN may be due to an improvement in the mitochondrial membrane potential and reduced

release of reactive oxygen species by increasing the glutathione (GSH) level, as indicated by other authors [33]. The use of hydrogel matrices directly to the skin may also prove to be an effective route of administration of this isoflavone, as GEN has low bioavailability and is rapidly metabolized following oral administration, which has a significant effect on the absorption of this compound [55,56]. This is supported by the results obtained by Huang et al., which demonstrate that topical administration may be an effective route for the delivery of soy isoflavones, including GEN [57]. Consequently, the possibility of controlled release of GEN from the biodegradable hydrogels developed in this study, with the simultaneous lack of their cytotoxic effect on skin cells, may suggest the possibility of their potential use in the treatment of dermatological diseases after more detailed in vivo and clinical studies. Taking into account the noticeable lack of effective systems for controlled release of GEN, which has an extremely beneficial effect on the skin described in the introduction to this work, the hydrogels developed may be an opportunity to improve the skin condition of many people currently struggling with common skin diseases.

3. Materials and Methods

3.1. Materials

1,6-diisocyanatohexane (hexamethylene diisocyanate, HDI, 98%, Aldrich, Poznan, Poland), 3,6 dimethyl 1,4 dioxane 2,5 dione (*rac*-lactide, *rac*-LA, 99%, Sigma-Aldrich, Poznan, Poland), acetic acid (CH₃COOH, ≥99%, Sigma-Aldrich, Poznan, Poland), antibiotics (Penicillin-Streptomycin, Life Technologies, Bleiswijk, The Netherlands), ε Caprolactone, (2 Oxepanone, CL, 99%, Aldrich, Poznan, Poland), chitosan (CHT, low molecular weight, 75% deacetylated), dibutyltin dilaurate (DBDLSn, >96%, Sigma-Aldrich, Poznan, Poland), dichloromethane (DCM, CH₂Cl₂, ≥99.8%, POCh, Gliwice, Poland), DMEM (Dulbecco's Modification of Eagle's Medium, Biological Industries, Beit Haemek, Israel), ethyl alcohol (ethanol, C₂H₅OH, 96%, Sigma-Aldrich, Poznan, Poland), FBS (Fetal Bovine Serum, Biological Industries, Genos, Lodz, Poland), genistein (GEN, >98%, Tokyo Chemical Industry Co. LTD., Tokyo, Japan), hydrochloric acid (HCl, ChemPur, Piekary Śląskie, Poland), immobilized lipase B from *Candida antarctica* (CALB) (Sigma-Aldrich, Poznan, Poland), Neutral Red Solution (NR, 0.33%, Sigma-Aldrich, Poznan, Poland), *N,N*-dimethylformamide (DMF, anhydrous, 99.8%, Sigma-Aldrich, Poznan, Poland), phosphate buffered saline (PBS, pH 7.00 ± 0.05, ChemPur, Piekary Śląskie, Poland), poly(ethylene glycol) 400 (PEG 400, Sigma-Aldrich, Poznan, Poland), resazurin sodium salt (RES, Sigma-Aldrich, Poznan, Poland), toluene (99.8%, POCh, Gliwice, Poland) and trypsin-EDTA solution (Sigma-Aldrich, Poznan, Poland) were used as received.

3.2. Synthesis of CL, LA and PEG Copolymers

The polymerization reactions were carried out according to our previously described method with some modifications [58–60]. Before the reaction, monomers (CL or *rac*-LA), PEG and CALB were dried under vacuum at room temperature for 3 h. Next, 0.04 mol CL (or 0.04 mol *rac*-LA) was placed in a three-neck flask equipped with a stirrer and thermometer (under argon atmosphere) and 20 mL of toluene was added. The mixture was stirred at 60 °C for 2 h. Next, an appropriate amount of PEG 400 and CALB (400 mg) was added to the mixture (Table 1). Stirring was continued at 60 °C for 24 h under argon atmosphere. After this time, the enzyme was filtered off. Toluene was removed by evaporation under reduced pressure at room temperature. Next, the cooled product was dissolved in DCM and extracted within cold methanol and distilled water.

3.3. Spectroscopy Data

The ¹H NMR spectrum of *rac*-LA and PEG copolymer (PLA-PEG): 1.57 ppm (-O(O)C-CH(CH₃)-), 3.63 ppm (O CH₂-CH₂-O-), 4.29 ppm (-O(O)C-CH(CH₃)-OH end group) and 5.17 ppm (-O(O)C-CH(CH₃)-).

The ¹³C NMR spectrum of PLA-PEG: 16.7 ppm (-O(O)C-CH(CH₃)-), 69.0 ppm (-O(O)C-CH(CH₃)-), 70.5 ppm (-O-CH₂-CH₂-O) and 169.3 ppm (-O(O)C-CH(CH₃)-).

The FTIR spectrum of PLA-PEG (KBr, cm^{-1}): 2997 ($\nu_{\text{as}}\text{CH}_3$), 2947 ($\nu_{\text{s}}\text{CH}_3$), 2882 (νCH), 1760 ($\nu\text{C}=\text{O}$), 1452 ($\delta_{\text{as}}\text{CH}_3$), 1348–1388 ($\delta_{\text{s}}\text{CH}_3$), 1368–1360 ($\delta_1\text{CH}+\delta_{\text{s}}\text{CH}_3$), 1315–1300 ($\delta_2\text{CH}$), 1270 ($\delta\text{CH} + \nu\text{COC}$), 1215–1185 ($\nu_{\text{as}}\text{COC} + r_{\text{as}}\text{CH}_3$), 1130 ($r_{\text{as}}\text{CH}_3$), 1100–1090 ($\nu_{\text{s}}\text{COC}$), 1045 ($\nu\text{C}-\text{CH}_3$), 960–950 ($r\text{CH}_3 + \nu\text{CC}$), 875–860 ($\nu\text{C}-\text{COO}$), 760–740 ($\delta\text{C}=\text{O}$), 715–695 ($\gamma\text{C}=\text{O}$), 515 ($\delta_1\text{C}-\text{CH}_3 + \delta\text{CCO}$), 415 (δCCO), 350 ($\delta_2\text{C}-\text{CH}_3 + \delta\text{COC}$), 300–295 ($\delta\text{COC} + \delta_2\text{C}-\text{CH}_3$), 240 (τCC).

The ^1H NMR spectrum of CL and PEG copolymer (PCL-PEG): 1.38 ppm ($\text{O}-\text{CH}_2-\text{CH}_2-\text{CH}_2-\text{CH}_2-\text{CH}_2-$), 1.65 ppm ($-\text{O}-\text{CH}_2-\text{CH}_2-\text{CH}_2-\text{CH}_2-\text{CH}_2-$), 2.31 ppm ($-\text{O}(\text{O})\text{C}-\text{CH}_2-\text{CH}_2-\text{CH}_2-\text{CH}_2-\text{CH}_2-$), 3.65 ppm ($-\text{O}-\text{CH}_2-\text{CH}_2-\text{O}-$) from PEG mers and ($\text{CH}_2-\text{CH}_2-\text{CH}_2-\text{CH}_2-\text{OH}$ end groups), 4.06 ppm ($-\text{O}-\text{CH}_2-\text{CH}_2-\text{CH}_2-\text{CH}_2-\text{CH}_2-$) and 4.23 ppm ($-\text{O}-\text{CH}_2-\text{CH}_2-\text{O}(\text{O})\text{C}-\text{CH}_2-\text{CH}_2-\text{CH}_2-\text{CH}_2-\text{CH}_2-$).

The ^{13}C NMR spectrum of PCL-PEG: 24.7 ppm ($-\text{O}(\text{O})\text{C}-\text{CH}_2-\text{CH}_2-\text{CH}_2-\text{CH}_2-\text{CH}_2-$), 25.6 ppm ($-\text{O}(\text{O})\text{C}-\text{CH}_2-\text{CH}_2-\text{CH}_2-\text{CH}_2-\text{CH}_2-$), 28.4 ppm ($-\text{O}-\text{CH}_2-\text{CH}_2-\text{CH}_2-\text{CH}_2-\text{CH}_2-$), 34.2 ppm ($-\text{O}(\text{O})\text{C}-\text{CH}_2-\text{CH}_2-\text{CH}_2-\text{CH}_2-\text{CH}_2-$), 64.2 ppm ($-\text{O}-\text{CH}_2-\text{CH}_2-\text{CH}_2-\text{CH}_2-\text{CH}_2-$), 70.6 ppm ($-\text{O}-\text{CH}_2-\text{CH}_2-\text{O}-$) and 173.6 ppm ($-\text{O}(\text{O})\text{C}-\text{CH}_2-\text{CH}_2-\text{CH}_2-\text{CH}_2-\text{CH}_2-$).

The FTIR spectrum of PCL-PEG (KBr, cm^{-1}): 2944 ($\nu_{\text{as}}\text{CH}_2$), 1722 ($\nu\text{C}=\text{O}$), 1244 ($\nu\text{C}-\text{O}$).

3.4. Hydrogels' Preparation

The hydrogels were obtained according to the described prepolymer method with some modifications [61]. The prepolymers were obtained through a polyaddition reaction between HDI and PLA-PEG (or PCL-PEG) in a $-\text{NCO}/-\text{OH}$ molar ratio of 2.05:1, using 2 drops of 0.1 wt% DBDLSn solution in toluene as catalyst. The reactions were performed at 80 °C for 3 h under argon atmosphere to form an isocyanate terminated prepolymer. Next, the dispersion of CHT into glacial acetic acid/DMF mixture (30 mL) in a volume ratio of 50/50 has been prepared. Next, the obtained prepolymer was added to the dispersion of CHT. The reactions were carried out in a $-\text{NCO}(\text{prepolymer})/-\text{OH}$ (or NH_2) (CHT) molar ratio of 1.5:1 at 80 °C for 4 h under argon atmosphere. The reaction mixture was then transferred to the distilled water. Precipitated products were separated by filtration and washed with DMF, methanol and acetone. The final products were dried under vacuum for one week. The developed hydrogels were denoted as: HPUCHT-1 (formed from PLA-PEG-1, 80:20), HPUCHT-2 (formed from PLA-PEG-2, 85:15), HPUCHT-3 (formed from PLA-PEG-3, 88:12), HPUCHT-4 (formed from PCL-PEG-1, 80:20), HPUCHT-5 (formed from PCL-PEG-2, 84:16) and HPUCHT-3 (formed from PCL-PEG-3, 89:11).

3.5. Swelling and Biodegradation of Hydrogels Studies

The mass swelling ratio (MSR) of hydrogels was determined at 37 °C during 80 h of incubation in PBS. Samples (approximately 0.5 g) in triplicate were submerged in a PBS solution (10 mL) for a given time, and their weights were taken after removing the excessive surface water. The mass swelling ratio was calculated using the following formula:

$$\text{MSR} = ((W_2 - W_1) / W_1) \times 100\%$$

where:

W1 is the weight of the initial hydrogel;

W2 is the weight of the swollen hydrogel.

In order to evaluate the percentage of degradation, the hydrogel samples were immersed in PBS at 37 °C for 4 weeks; most importantly, the medium was replaced with fresh PBS every one week. At the end of the experiment, the samples were dried in a vacuum for 48 h. The degree of degradation of hydrogels (in triplicate) was determined by the weight loss (WL) of the samples according to the equation:

$$\text{WL} = [(W_1 - W_2) / W_1] \times 100\%$$

where:

WL is the weight loss;

W1 is the weight of dry sample before degradation;
W2 is the weight of the dry sample after degradation.

3.6. In Vitro Release Studies of GEN from Hydrogels

GEN was loaded to the hydrogel matrices by physical mixing due to the following procedure. A total of 5.0 % (m/m) of GEN in distilled water/Tween 80 mixture (2% (w/v) was added to six hydrogel samples (HPUCHT-1, HPUCHT-2, HPUCHT-3, HPUCHT-4, HPUCHT-5 and HPUCHT-6). The hydrogels were left sealed for 24 h. The mixtures were dried under vacuum at room temperature to obtain a GEN-loaded hydrogel films. The in vitro release of GEN from the hydrogels was performed in a PBS buffer (pH 7.4 ± 0.05) containing 2% (w/v) Tween 80 at 37 °C under stirring. Vials containing hydrogel films were filled with 5.0 mL of PBS buffer (pH 7.4 ± 0.05), sealed and left in 37 °C for 2 h. The solutions were then removed for further testing and replaced by fresh PBS. Subsequent samples were collected at selected intervals. GEN concentration in the in vitro samples was also determined by HPLC (detected at the wavelength of 262 nm). The mobile phase was composed of 70% methanol and 30% water with 0.1% phosphoric acid [62,63]. The release data points were subjected to zero-order, first-order kinetics and Korsmeyer–Peppas models, respectively. Calculations were made on the basis of formulas mentioned below:

Zero-order model:

$$F=kt$$

First-order model:

$$\log F = \log F_0 - kt/2.303$$

Korsmeyer–Peppas model:

$$F=kt^n \quad (F<0.6)$$

where:

F is the fraction of GEN released up to time (t);

F₀ is the initial concentration of GEN;

k is the constant of the mathematical models;

n is the exponent of the Korsmeyer–Peppas model [48,49].

3.7. Measurements

The structures of synthesized materials were characterized using ¹H and ¹³C NMR techniques (Varian 300 MHz, Palo Alto, CA, USA). The spectra were registered in CDCl₃. The ¹H spectra were recorded under following conditions: 300 MHz, 1 s repetition time, 2 s acquisition time, 32, 64 or 128 scans. The ¹³C spectra: 75.4 MHz, 5 s repetition time, 1.4 s acquisition time, 20,000 scans per each spectrum. Percentage molar value of PEG in a copolymer chain were estimated using the following formulas [64]:

$$\% CL = \frac{\frac{I_{PEG}}{2}}{I_{\epsilon} + \frac{I_{PEG}}{2}} \cdot 100\%$$

$$\% LA = \frac{\frac{I_{PEG}}{4}}{I_{\alpha} + \frac{I_{PEG}}{4}} \cdot 100$$

The FTIR spectra of PLA-PEG and PCL-PEG prepolymers were measured from KBr pellets (PerkinElmer spectrometer, Great Britain). The average molecular weight and molecular weight distribution were determined on the LabAllianceGel Permeation Chromatograph equipped with Jordi Gel DVB mixed bed (250 × 10 mm) column and refractive detector, using chloroform as solvent. The flow rate was 1 mL/min. The average molecular weights were calibrated with polystyrene standards.

3.8. Genotoxic Test

The umu-test is a bioassay to evaluate the genotoxic potential of environmental samples and chemical compounds. The test detects the induction of the SOS system to the strain *Salmonella typhimurium* TA1535/pSK1002. The SOS system is the bacterial response to the DNA-damaging agents. The test strain is genetically modified- the *umuC* gene activity is linked to the synthesis of β -galactosidase, while other DNA regions responsible for the synthesis of this enzyme were deleted. Therefore, β -galactosidase activity strictly depends on the SOS system induction level and the genotoxic activity of the tested sample [65]. Additionally, the bacteria growth (G) is evaluated by a measurement of an optical density to determine the cytotoxicity of tested samples. The genotoxic potential of the sample was presented as the Induction Ratio (IR)-the β -galactosidase activity of the tested sample relative to the negative control. Samples with $IR \geq 1.5$ are considered as genotoxic.

In the present study, the umu-test was carried out in the micro-plate variant according to the ISO guideline, with and without metabolic activation (S9 liver fraction) [66]. Deionized sterile water was used as a negative control, 2-aminoanthracene and 4-nitroquinoline N-oxide were used as positive controls, and phosphate buffered saline (PBS from Gibco, Thermo Fisher Scientific, Darmstadt, Germany) as solvent control. All tested samples were incubated in PBS—100 mg/mL for 24 h, at 37 °C, with shaking. Before the assay, all extracts were sterilized by filtration (0.20 μ m). All samples were tested in two-fold dilution series (four concentrations in three replicates; the highest concentration of 66.6 mg/mL).

3.9. Cell Culture and Preparation of Hydrogel Extracts

Two human skin cell lines were used in the study: HaCaT cells (normal human keratinocytes; CLS Cell Lines Service, Eppelheim, Germany) and BJ cells (fibroblasts, ATCC[®]CRL-2522[™]; the American Type Culture Collection, Manassas, VA, USA). Both cell lines were maintained in DMEM medium supplemented with L-glutamine, 4.5 g/L glucose and sodium pyruvate. In order to achieve optimal results, the culture medium was supplemented with 10% (*v/v*) FBS and 1% (*v/v*) antibiotics (100 U/mL penicillin and 1000 μ g/mL streptomycin). Cells were cultured in an incubator at 37 °C in a humidified atmosphere of 95% air and 5% carbon dioxide (CO₂). After the cultured cells (HaCaT and BJ) had reached proper confluence (about 70–80%), the DMEM culture medium was removed from the culture plate (VWR) and the cells were washed twice with sterile PBS. Subsequently, the cell layer was trypsinized with trypsin/EDTA, and the cells were then resuspended in fresh DMEM medium. In the next step, cells were plated in 96-well flat-bottom plates (separate plates for both cell types) and left for 24 h in the incubator. After HaCaT and fibroblasts were attached to the bottom of the plates, cells were incubated with various concentrations of extracts (0.1, 0.5, 1.0, 2.5 and 5.0%) obtained from six different hydrogels (HPUCHT-1, HPUCHT-2, HPUCHT-3, HPUCHT-4, HPUCHT-5, HPUCHT-6) loaded with GEN. Extracts were obtained by incubating test hydrogels in DMEM culture medium for 24 h on a rocker shaker, after which appropriate dilutions of these extracts were prepared in DMEM. Before the assay started, all extracts were sterilized by filtration (0.20 μ m). The cells were then treated with the hydrogel extracts for 2 and 24 h in an incubator. Control samples were cells grown in the DMEM medium without the addition of hydrogel extracts.

3.10. Cytotoxicity Assays

3.10.1. Neutral Red Uptake Assay

In order to evaluate the cytotoxicity of the tested hydrogels on HaCaT and BJ cells, the Neutral Red Uptake Assay (Sigma Aldrich, Poznan, Poland) was used. This test was performed based on the procedure described previously [67]. After 2 and 24 h of exposure to extracts of the six GEN-loaded hydrogels, cells were incubated for 2 h with a neutral red dye (40 μ g/mL), which was dissolved in serum-free DMEM medium. After incubation with NR, cells were washed with sterile PBS and 150 μ L of decolorizing buffer (C₂H₅OH/CH₃COOH/H₂O, 50%/1%/49%) was added to each well to release cellular dye

into the PBS solution. After shaking the cells for 15 min the absorbance of the dissolved dye at $\lambda = 540$ nm was determined using a FilterMax F5 Multi-Mode microplate reader (Thermo Fisher). The mean absorbance of the control cells (untreated with the extracts) was taken as 100% cell viability and used to calculate the percentage of viable cells in the experimental samples treated with the test hydrogels. As a part of the study, three independent experiments were carried out, in which each concentration of extracts was tested using four replicates.

3.10.2. Alamar Blue Assay

The cytotoxicity assessment of the hydrogels tested on skin cells was also carried out using the Alamar Blue test. The protocol described by Page et al. [68] has been used for this purpose. After 2 and 24 h of exposure of HaCaT and BJ cells (on separate 96-well plates) to individual concentrations of the analyzed hydrogel extracts (0.1 to 5% concentration range), a resazurin solution (with a final concentration of 60 μ M) was added to the well and incubated for 2 h at 37 °C in the dark. The fluorescence of the samples was then measured at $\lambda = 570$ nm using a microplate reader (FilterMax F5, Thermo Fisher). The experiments were performed in three independent experiments, in which the fluorescence of the cells in four wells was measured for each extract concentration. The results were expressed as a percentage of cell viability compared to the control sample (100%), which were cells grown in DMEM medium without any addition of hydrogel extracts. Additionally, in order to assess the effect of GEN (not loaded into hydrogel structures) on the tested cells, fibroblasts and keratinocytes were incubated with GEN in the concentration range of 1–1000 μ M for 2 and 24 h and the cytotoxicity assessment was performed.

3.11. Statistical Analysis

Values of different parameters were expressed as the mean \pm standard deviation (SD). Two-way analysis of variance (ANOVA) and Bonferroni posttest between groups were performed at the level $p < 0.05$ to evaluate the significant differences between values. Statistical analyses were performed using GraphPad Prism 8.4.3 (GraphPad Software, Inc., San Diego, CA, USA).

4. Conclusions

In the present work, new non-toxic and biodegradable hydrogels for controlled release of GEN have been obtained and characterized. The developed materials have been obtained using a three-step method. The poly(ester-ether)s components have been synthesized by an e-ROP process catalyzed by CALB. In the next steps, hydrogels were obtained by a prepolymer method using CHT and HDI, in the presence of DBDLSn as a catalyst. The in vitro release study showed that the release rate of GEN was highly dependent on the composition of newly developed poly(chitosan-ester-ether-urethane) hydrogels. We also found that, in some cases, GEN was released with relatively high control, near-zero-order kinetics. The “burst release” of GEN has not been observed. Importantly, in vitro studies conducted on the skin cells have shown that the hydrogels do not show a cytotoxic effect on both fibroblasts and keratinocytes. In addition, the GEN-loaded hydrogels have a positive effect on the viability and proliferation of these cells. From a broader perspective, this study suggests that synthesized hydrogels may potentially be used in dermatology and cosmetology.

Author Contributions: Conceptualization: M.Z.-D. and M.S.; methodology, M.Z.-D., P.K., E.O., R.F. and M.S.; validation, M.Z.-D., P.K., E.O. and M.S.; formal analysis, M.Z.-D., P.K., E.O. and M.S.; investigation, M.Z.-D., P.K., E.O., R.F. and M.S.; data curation, M.Z.-D., R.F. and M.S.; writing—original draft preparation, M.Z.-D. and M.S.; writing—review and editing, M.Z.-D., P.K., E.O. and M.S.; visualization, M.Z.-D. and M.S.; supervision, M.S.; project administration, M.Z.-D. and M.S.; funding acquisition, M.Z.-D. and M.S. All authors have read and agreed to the published version of the manuscript.

Funding: This work was funded by the 503-07-01-34 Statutory Project of the University of Information Technology and Management in Rzeszow, Poland.

Institutional Review Board Statement: Not applicable.

Informed Consent Statement: Not applicable.

Data Availability Statement: Data are contained within the manuscript.

Conflicts of Interest: The authors declare no conflict of interest. The funders had no role in the design of the study; in the collection, analyses or interpretation of data; in the writing of the manuscript, or in the decision to publish the results.

References

1. Zagórska-Dziok, M.; Sobczak, M. Hydrogel-Based Active Substance Release Systems for Cosmetology and Dermatology Application: A Review. *Pharmaceutics* **2020**, *12*, 396. [CrossRef]
2. Dreno, B.; Araviiskaia, E.; Berardesca, E.; Bieber, T.; Hawk, J.; Sanchez-Viera, M.; Wolkenstein, P. The science of dermocosmetics and its role in dermatology. *J. Eur. Acad. Dermatol. Venereol.* **2014**, *28*, 1409–1417. [CrossRef]
3. Larrañeta, E.; Stewart, S.; Ervine, M.; Al-Kasasbeh, R.; Donnelly, R.F. Hydrogels for Hydrophobic Drug Delivery. *Classification, Synthesis and Applications. J. Funct. Biomater.* **2018**, *9*, 13. [CrossRef]
4. McKenzie, M.; Betts, D.; Suh, A.; Bui, K.; Kim, L.D.; Cho, H. Hydrogel-Based Drug Delivery Systems for Poorly Water-Soluble Drugs. *Molecules* **2015**, *20*, 20397–20408. [CrossRef] [PubMed]
5. Gu, D.; O'Connor, A.J.; Qiao, G.G.; Ladewig, K. Hydrogels with smart systems for delivery of hydrophobic drugs. *Expert Opin Drug Deliv.* **2017**, *14*, 879–895. [CrossRef]
6. Ciobanu, B.C.; Cadinoiu, A.N.; Popa, M.; Desbrieres, J.; Peptu, C.A. Chitosan/Poly(Vinyl Alcohol) Hydrogels For Entrapment of Drug Loaded Liposomes. *Cellulose Chem. Technol.* **2014**, *48*, 485–494.
7. Musgrave, C.S.A.; Fang, F. Contact Lens Materials: A Materials Science Perspective. *Materials* **2019**, *12*, 261. [CrossRef]
8. Li, L.; Yu, F.; Zheng, L.; Wang, R.; Yan, W.; Wang, Z.; Xu, J.; Wu, J.; Shi, D.; Zhu, L.; et al. Natural hydrogels for cartilage regeneration: Modification, preparation and application. *J. Orthop. Translat.* **2018**, *17*, 26–41. [CrossRef] [PubMed]
9. Tavakoli, S.; Klar, A.S. Advanced Hydrogels as Wound Dressings. *Biomolecules* **2020**, *10*, 1169. [CrossRef]
10. Mantha, S.; Pillai, S.; Khayambashi, P.; Upadhyay, A.; Zhang, Y.; Tao, O.; Pham, H.M.; Tran, S.D. Smart Hydrogels in Tissue Engineering and Regenerative Medicine. *Materials* **2019**, *12*, 3323. [CrossRef]
11. Chyzy, A.; Tomczykowa, M.; Plonska-Brzezinska, M.E. Hydrogels as Potential Nano-, Micro- and Macro-Scale Systems for Controlled Drug Delivery. *Materials* **2020**, *13*, 188. [CrossRef] [PubMed]
12. Mihalache, C.; Rata, D.M.; Cadinoiu, A.N.; Patras, X.; Bacaita, S.E.; Popa, M.; Atanase, L.I.; Daraba, O.M. Bupivacaine-loaded chitosan hydrogels for topical anesthesia in dentistry. *Polym. Int.* **2020**, *69*, 1152–1160. [CrossRef]
13. Li, J.; Mooney, D.J. Designing hydrogels for controlled drug delivery. *Nat. Rev. Mater.* **2016**, *1*, 16071. [CrossRef] [PubMed]
14. Soppimath, K.S.; Aminabhavi, T.M.; Dave, A.M.; Kumbar, S.G.; Rudzinski, W.E. Stimulus-responsive “smart” hydrogels as novel drug delivery systems. *Drug Dev. Ind. Pharm.* **2002**, *28*, 957–974. [CrossRef]
15. Trombino, S.; Servidio, C.; Curcio, F.; Cassano, R. Strategies for Hyaluronic Acid-Based Hydrogel Design in Drug Delivery. *Pharmaceutics* **2019**, *11*, 407. [CrossRef] [PubMed]
16. Wechsler, M.E.; Stephenson, R.E.; Murphy, A.C.; Oldenkamp, H.F.; Singh, A.; Peppas, N.A. Engineered microscale hydrogels for drug delivery, cell therapy, and sequencing. *Biomed. Microdevices* **2019**, *21*, 31. [CrossRef]
17. Narayanaswamy, R.; Torchilin, V.P. Hydrogels and Their Applications in Targeted Drug Delivery. *Molecules* **2019**, *24*, 603. [CrossRef]
18. Parente, M.E.; Ochoa Andrade, A.; Ares, G.; Russo, F.; Jiménez-Kairuz, Á. Bioadhesive hydrogels for cosmetic applications. *Int J. Cosmet. Sci.* **2015**, *37*, 511–518. [CrossRef]
19. Lee, T.W.; Kim, J.C.; Hwang, S.J. Hydrogel patches containing triclosan for acne treatment. *Eur. J. Pharm. Biopharm.* **2003**, *56*, 407–412. [CrossRef]
20. Nilforoushzadeh, M.A.; Amirkhani, M.A.; Zarrintaj, P.; Salehi Moghaddam, A.; Mehrabi, T.; Alavi, S.; MollapourSisakht, M. Skin care and rejuvenation by cosmeceutical facial mask. *J. Cosmet. Dermatol.* **2018**, *17*, 693–702. [CrossRef]
21. Huang, D.; Sun, M.; Bu, Y.; Luo, F.; Lin, C.; Lin, Z.; Weng, Z.; Yang, F.; Wu, D. Microcapsule-embedded hydrogel patches for ultrasound responsive and enhanced transdermal delivery of diclofenac sodium. *J. Mater. Chem. B* **2019**, *7*, 2330–2337. [CrossRef]
22. Koehler, J.; Brandl, F.P.; Goepferich, A.M. Hydrogel wound dressings for bioactive treatment of acute and chronic wounds. *Eur. Polym. J.* **2018**, *100*, 1–11. [CrossRef]
23. Monticelli, D.; Martina, V.; Mocchi, R.; Rauso, R.; Zerbinati, U.; Cipolla, G.; Zerbinati, N. Chemical Characterization of Hydrogels Crosslinked with Polyethylene Glycol for Soft Tissue Augmentation. *Open. Access Maced. J. Med. Sci.* **2019**, *7*, 1077–1081. [CrossRef] [PubMed]
24. Vlaia, L.; Coneac, G.; Olariu, I.; Vlaia, V.; Lupuleasa, D. Cellulose-Derivatives-Based Hydrogels as Vehicles for Dermal and Transdermal Drug Delivery. In *Emerging Concepts in Analysis and Applications of Hydrogels*; Majee, S.B., Ed.; IntechOpen: London, UK, 2016.

25. Cen, L.; Liu, W.; Cui, L.; Zhang, W.; Cao, Y. Collagen tissue engineering: Development of novel biomaterials and applications. *Pediatr. Res.* **2008**, *63*, 492–496. [CrossRef]
26. Cheng, L.; Ji, K.; Shih, T.Y.; Haddad, A.; Giatsidis, G.; Mooney, D.J.; Orgill, D.P.; Nabzdyk, C.S. Injectable Shape-Memorizing Three-Dimensional Hyaluronic Acid Cryogels for Skin Sculpting and Soft Tissue Reconstruction. *Tissue Eng. Part A* **2017**, *23*, 243–251. [CrossRef] [PubMed]
27. Yang, Z.; Kulkarni, K.; Zhu, W.; Hu, M. Bioavailability and pharmacokinetics of genistein: Mechanistic studies on its ADME. *Anti-Cancer Agents Med. Chem.* **2012**, *12*, 1264–1280. [CrossRef]
28. Vitale, D.C.; Piazza, C.; Melilli, B.; Drago, F.; Salomone, S. Isoflavones: Estrogenic activity, biological effect and bioavailability. *Eur. J. Drug Metab. Pharmacokinet.* **2013**, *38*, 15–25. [CrossRef]
29. Yuseran, H.; Hartoyo, E.; Nurseta, T.; Kalim, H. Molecular docking of genistein on estrogen receptors, promoter region of BCLX, caspase-3, Ki-67, cyclin D1, and telomere activity. *J. Taibah Univ. Med. Sci.* **2018**, *14*, 79–87. [CrossRef] [PubMed]
30. Thornton, M.J. Estrogens and aging skin. *Dermato-Endocrinology* **2013**, *5*, 264–270. [CrossRef] [PubMed]
31. Horng, H.C.; Chang, W.H.; Yeh, C.C.; Huang, B.S.; Chang, C.P.; Chen, Y.J.; Tsui, K.H.; Wang, P.H. Estrogen Effects on Wound Healing. *Int. J. Mol. Sci.* **2017**, *18*, 2325. [CrossRef]
32. Irrera, N.; Pizzino, G.; D’Anna, R.; Vaccaro, M.; Arcoraci, V.; Squadrito, F.; Altavilla, D.; Bitto, A. Dietary Management of Skin Health: The Role of Genistein. *Nutrients* **2017**, *9*, 622. [CrossRef]
33. Liu, T.; Li, N.; Yan, Y.Q.; Liu, Y.; Xiong, K.; Liu, Y.; Xia, Q.M.; Zhang, H.; Liu, Z.D. Recent advances in the anti-aging effects of phytoestrogens on collagen, water content, and oxidative stress. *Phytother. Res.* **2020**, *34*, 435–447. [CrossRef] [PubMed]
34. Weidenbörner, M.; Hindorf, H.; Jha, H.C.; Tsotsonos, P.; Egge, H. Antifungal activity of isoflavonoids in different reduced stages on *Rhizoctonia solani* and *Sclerotium rolfsii*. *Phytochemistry* **1990**, *29*, 801–803. [CrossRef]
35. Kim, J.W.; Kim, J.G.; Kim, W.G.; Suh, J.W. Talosians A and B: New Isoflavonol Glycosides with Potent Antifungal Activity from *Kitasatosporakifunensine* MJM341. *J. Antibiot.* **2006**, *59*, 633–639. [CrossRef]
36. Hong, H.; Landauer, M.R.; Foriska, M.A.; Ledney, G.D. Antibacterial activity of the soy isoflavone genistein. *J. Basic Microbiol.* **2006**, *46*, 329–335. [CrossRef] [PubMed]
37. Ulanowska, K.; Tkaczyk, A.; Konopa, G.; Węgrzyn, G. Differential antibacterial activity of genistein arising from global inhibition of DNA, RNA and protein synthesis in some bacterial strains. *Arch. Microbiol.* **2006**, *184*, 271–278. [CrossRef]
38. Cao, C.; Li, S.; Dai, X.; Chen, Y.; Feng, Z.; Zhao, Y.; Wu, J. Genistein inhibits proliferation and functions of hypertrophic scar fibroblasts. *Burns* **2009**, *35*, 89–97. [CrossRef]
39. Isoherranen, K.; Punnonen, K.; Jansen, C.; Uotila, P. Ultraviolet irradiation induces cyclooxygenase-2 expression in keratinocytes. *Br. J. Dermatol.* **1999**, *140*, 1017–1022. [CrossRef] [PubMed]
40. Iovine, B.; Iannella, M.L.; Gasparri, F.; Monfrecola, G.; Bevilacqua, M.A. Synergic Effect of Genistein and Daidzein on UVB-Induced DNA Damage: An Effective Photoprotective Combination. *J. Biomed. Biotechnol.* **2011**, *2011*, 692846. [CrossRef]
41. Wei, H.; Saladi, R.; Lu, Y.; Wang, Y.; Palep, S.R.; Moore, J.; Phelps, R.; Shyong, E.; Lebowhl, M.G. Isoflavone genistein: Photoprotection and clinical implications in dermatology. *J. Nutr.* **2003**, *133*, 3811S–3819S. [CrossRef]
42. Terra, V.A.; Souza-Neto, F.P.; Frade, M.A.; Ramalho, L.N.; Andrade, T.A.; Pasta, A.A.; Conchon, A.C.; Guedes, F.A.; Luiz, R.C.; Cecchini, R.; et al. Genistein prevents ultraviolet B radiation-induced nitrosative skin injury and promotes cell proliferation. *J. Photochem. Photobiol. B* **2015**, *144*, 20–27. [CrossRef] [PubMed]
43. Marini, H.; Polito, F.; Altavilla, D.; Irrera, N.; Minutoli, L.; Calò, M.; Adamo, E.B.; Vaccaro, M.; Squadrito, F.; Bitto, A. Genistein aglycone improves skin repair in an incisional model of wound healing: A comparison with raloxifene and oestradiol in ovariectomized rats. *Br. J. Pharmacol.* **2010**, *160*, 1185–1194. [CrossRef] [PubMed]
44. Polito, F.; Marini, H.; Bitto, A.; Irrera, N.; Vaccaro, M.; Adamo, E.B.; Micali, A.; Squadrito, F.; Minutoli, L.; Altavilla, D. Genistein aglycone, a soy-derived isoflavone, improves skin changes induced by ovariectomy in rats. *Br. J. Pharmacol.* **2012**, *165*, 994–1005. [CrossRef]
45. Palanivel, G.; Dong-Kug, C. Current application of phytocompound-based nanocosmeceuticals for beauty and skin therapy. *Int. J. Nanomed.* **2016**, *11*, 1987–2007.
46. de Vargas, B.A.; Bidone, J.; Oliveira, L.K.; Koester, L.S.; Bassani, V.L.; Teixeira, H.F. Development of topical hydrogels containing genistein-loaded nanoemulsions. *J. Biomed. Nanotechnol.* **2012**, *8*, 330–336. [CrossRef] [PubMed]
47. Kang, K.H.; Kang, M.J.; Lee, J.; Choi, Y.W. Influence of liposome type and skin model on skin permeation and accumulation properties of genistein. *J. Disper. Sci. Technol.* **2010**, *31*, 1061–1066. [CrossRef]
48. Siepmann, J.; Göpferich, A. Mathematical modeling of bioerodible, polymeric drug delivery systems. *Adv. Drug Deliv. Rev.* **2001**, *48*, 229–247. [CrossRef]
49. Dash, S.; Murthy, P.N.; Nath, L.; Chowdhury, P. Kinetic modeling on drug release from controlled drug delivery systems. *Acta Pol. Pharm.* **2010**, *67*, 217–223.
50. Xiao, Y.; Ho, C.T.; Chen, Y.; Wang, Y.; Wei, Z.; Dong, M.; Huang, Q. Synthesis, Characterization, and Evaluation of Genistein-Loaded Zein/Carboxymethyl Chitosan Nanoparticles with Improved Water Dispersibility, Enhanced Antioxidant Activity, and Controlled Release Property. *Foods* **2020**, *9*, 1604. [CrossRef] [PubMed]
51. Andrade, L.M.; de Fátima Reis, C.; Maione-Silva, L.; Anjos, J.L.V.; Alonso, A.; Serpa, R.C.; Marreto, R.N.; Lima, E.M.; Taveira, S.F. Impact of lipid dynamic behavior on physical stability, in vitro release and skin permeation of genistein-loaded lipid nanoparticles. *Eur. J. Pharm. Biopharm.* **2014**, *88*, 40–47. [CrossRef] [PubMed]

52. Zampieri, A.L.; Ferreira, F.S.; Resende, E.C.; Gaeti, M.P.; Diniz, D.G.; Taveira, S.F.; Lima, E.M. Biodegradable polymeric nanocapsules based on poly(DL-lactide) for genistein topical delivery: Obtention, characterization and skin permeation studies. *J. Biomed. Nanotechnol.* **2013**, *9*, 527–534. [CrossRef]
53. Argenta, D.F.; de Mattos, C.B.; Misturini, F.D.; Koester, L.S.; Bassani, V.L.; Simões, C.M.; Teixeira, H.F. Factorial design applied to the optimization of lipid composition of topical antiherpetic nanoemulsions containing isoflavone genistein. *Int. J. Nanomed.* **2014**, *9*, 4737–4747. [CrossRef]
54. Nemitz, M.C.; von Poser, G.L.; Teixeira, H.F. In vitro skin permeation/retention of daidzein, genistein and glycitein from a soybean isoflavone rich fraction-loaded nanoemulsions and derived hydrogels. *J. Drug Deliv. Sci. Technol.* **2019**, *51*, 63–69. [CrossRef]
55. Chen, F.; Peng, J.; Lei, D.; Liu, J.; Zhao, G. Optimization of genistein solubilization by κ -carrageenan hydrogel using response surface methodology. *Food Sci. Hum. Well* **2013**, *2*, 124–131. [CrossRef]
56. Zhao, C.; Wang, Y.; Su, Y.; Zhang, H.; Ding, L.; Yan, X.; Zhao, D.; Shao, N.; Ye, X.; Cheng, Y. Inclusion complexes of isoflavones with two commercially available dendrimers: Solubility, stability, structures, release behaviors, cytotoxicity, and anti-oxidant activities. *Int. J. Pharm.* **2011**, *421*, 301–309. [CrossRef] [PubMed]
57. Huang, Z.R.; Hung, C.F.; Lin, Y.K.; Fang, J.Y. In vitro and in vivo evaluation of topical delivery and potential dermal use of soy isoflavones genistein and daidzein. *Int. J. Pharm.* **2008**, *364*, 36–44. [CrossRef] [PubMed]
58. Sobczak, M. Enzyme-Catalyzed Ring-Opening Polymerization of Cyclic Esters in the Presence of Poly(ethylene glycol). *J. Appl. Polym. Sci.* **2012**, *125*, 3602–3609. [CrossRef]
59. Piotrowska, U.; Oledzka, E.; Zgadzaj, A.; Bauer, M.; Sobczak, M. A Novel Delivery System for the Controlled Release of Antimicrobial Peptides: Citropin 1.1 and Temporin A. *Polymers* **2018**, *10*, 489. [CrossRef]
60. Piotrowska, U.; Sobczak, M.; Oledzka, E.; Combes, C. Effect of ionic liquids on the structural, thermal, and in vitro degradation properties of poly(epsilon-caprolactone) synthesized in the presence of *Candida antarctica* lipase B. *J. Appl. Polym. Sci.* **2016**, *133*, 10. [CrossRef]
61. Mahanta, A.K.; Mittal, V.; Singh, N.; Dash, D.; Malik, S.; Kumar, M.; Maiti, P. Polyurethane-grafted chitosan as new biomaterials for controlled drug delivery. *Macromolecules* **2015**, *48*, 2654–2666. [CrossRef]
62. Zhang, T.; Wang, H.; Ye, Y.; Zhang, X.; Wu, B. Micellar emulsions composed of mPEG-PCL/MCT as novel nanocarriers for systemic delivery of genistein: A comparative study with micelles. *Int. J. Nanomed.* **2015**, *10*, 6175–6184. [CrossRef]
63. Cheng, Q.; Qin, W.; Yu, Y.; Li, G.; Wu, J.; Zhuo, L. Preparation and Characterization of PEG-PLA Genistein Micelles Using a Modified Emulsion-Evaporation Method. *J. Nanomater.* **2020**, *2020*, 1–15.
64. Kasiński, A.; Zielińska-Pisklak, M.; Oledzka, E.; Nałęcz-Jawecki, G.; Drobniewska, A.; Sobczak, M. Hydrogels Based on Poly(Ether-Ester)s as Highly Controlled 5-Fluorouracil Delivery Systems—Synthesis and Characterization. *Materials* **2021**, *14*, 98. [CrossRef] [PubMed]
65. Oda, Y.; Nakamura, S.; Oki, I.; Kato, T.; Shinagawa, H. Evaluation of the new system (umu-test) for the detection of environmental mutagens and carcinogens. *Mutat. Res.* **1985**, *147*, 219–229. [CrossRef]
66. International Organization for Standardization. *Water Quality-Determination of the Genotoxicity of Water and Waste Water Using the Umu-Test*; International Standard. ISO/FDIS 13829: 2000; International Organization for Standardization: Geneva, Switzerland, 2000.
67. Zagórska-Dziok, M.; Ziemlewska, A.; Nizioł-Łukaszewska, Z.; Bujak, T. Antioxidant Activity and Cytotoxicity of *Medicago sativa* L. Seeds and Herb Extract on Skin Cells. *Biores. Open Access* **2020**, *9*, 229–242. [CrossRef] [PubMed]
68. Page, B.; Page, M.; Noel, C. A new fluorometric assay for cytotoxicity measurements in-vitro. *Int. J. Oncol.* **1993**, *3*, 473–476. [PubMed]



Communication

Synthesis, Molecular Docking and Antiplasmodial Activities of New Tetrahydro- β -Carbolines

Anna Jaromin ^{1,*}, Beata Gryzłó ², Marek Jamrozik ², Silvia Parapini ³, Nicoletta Basilico ⁴, Marek Cegła ², Donatella Taramelli ⁵ and Agnieszka Zagórska ^{2,*}

- ¹ Department of Lipids and Liposomes, Faculty of Biotechnology, University of Wrocław, Joliot-Curie 14a, 50-383 Wrocław, Poland
- ² Faculty of Pharmacy, Jagiellonian University Medical College, 30-688 Krakow, Poland; beata.gryzlo@uj.edu.pl (B.G.); marek.jamrozik@doctoral.uj.edu.pl (M.J.); marek.cegla@uj.edu.pl (M.C.)
- ³ Dipartimento di Scienze Biomediche per la Salute, Università degli Studi di Milano, 20133 Milan, Italy; silvia.parapini@unimi.it
- ⁴ Dipartimento di Scienze Biomediche, Chirurgiche e Odontoiatriche, Università degli Studi di Milano, 20133 Milan, Italy; nicoletta.basilico@unimi.it
- ⁵ Dipartimento di Scienze Farmacologiche e Biomolecolari, Università degli Studi di Milano, 20133 Milan, Italy; donatella.taramelli@unimi.it
- * Correspondence: anna.jaromin@uwr.edu.pl (A.J.); agnieszka.zagorska@uj.edu.pl (A.Z.)

Abstract: Malaria is still one of the most dangerous infectious diseases and the emergence of drug resistant parasites only worsens the situation. A series of new tetrahydro- β -carbolines were designed, synthesized by the Pictet–Spengler reaction, and characterized. Further, the compounds were screened for their in vitro antiplasmodial activity against chloroquine-sensitive (D10) and chloroquine-resistant (W2) strains of *Plasmodium falciparum*. Moreover, molecular modeling studies were performed to assess the potential action of the designed molecules and toxicity assays were conducted on the human microvascular endothelial (HMEC-1) cell line and human red blood cells. Our studies identified *N*-(3,3-dimethylbutyl)-1-octyl-2,3,4,9-tetrahydro-1H-pyrido[3,4-*b*] indole-3-carboxamide (**7**) (a mixture of diastereomers) as the most promising compound endowed with the highest antiplasmodial activity, highest selectivity, and lack of cytotoxicity. In silico simulations carried out for (1*S*,3*R*)-**7** provided useful insights into its possible interactions with enzymes essential for parasite metabolism. Further studies are underway to develop the optimal nanosized lipid-based delivery system for this compound and to determine its precise mechanism of action.

Keywords: tetrahydro- β -carbolines; *Plasmodium falciparum* (*P. falciparum*); antimalarial; antiparasitic agents; cytotoxicity; hemolysis; molecular docking

Citation: Jaromin, A.; Gryzłó, B.; Jamrozik, M.; Parapini, S.; Basilico, N.; Cegła, M.; Taramelli, D.; Zagórska, A. Synthesis, Molecular Docking and Antiplasmodial Activities of New Tetrahydro- β -Carbolines. *Int. J. Mol. Sci.* **2021**, *22*, 13569. <https://doi.org/10.3390/ijms222413569>

Academic Editors: Geoffrey Brown, Andrzej Kutner and Enikő Kallay

Received: 8 November 2021

Accepted: 13 December 2021

Published: 17 December 2021

Publisher's Note: MDPI stays neutral with regard to jurisdictional claims in published maps and institutional affiliations.



Copyright: © 2021 by the authors. Licensee MDPI, Basel, Switzerland. This article is an open access article distributed under the terms and conditions of the Creative Commons Attribution (CC BY) license (<https://creativecommons.org/licenses/by/4.0/>).

1. Introduction

Malaria is an infectious disease caused by the protozoan parasite of the genus *Plasmodium*, with *Plasmodium falciparum* and *Plasmodium vivax* being predominantly responsible for mortality and morbidity. In 2019, the global tally of malaria cases was 229 million, an annual estimate that has remained virtually unchanged over the last 4 years [1]. Despite the COVID-19 pandemic, an analysis of malaria prevention showed that the 2020 campaigns to control and eradicate malaria were realized as planned. Lastly, in October of 2021, the WHO has recommended Mosquirix, the RTS,S/AS01 malaria vaccine, for the prevention of *P. falciparum* malaria in children living in regions with moderate to high transmission [2]. However, disruptions to continued access to effective antimalarial treatment could lead to considerable loss of life [3].

First-line malaria treatments include several artemisinin-based combination therapies (ACTs), such as artemether-lumefantrine (AL), artesunate-amodiaquine (AS-AQ), artesunate-sulfadoxine-pyrimethamine (AS+SP), artesunate-mefloquine (AS-MQ), and dihydroartemisinin-piperaquine (DHA-PPQ). The malaria problem is evolving, dynamic,

and diverse, mainly due to the intrinsic ability of *P. falciparum* to acquire resistance against drugs. *P. falciparum* has developed resistance to nearly all currently available antimalarial drugs, such as sulfadoxine/pyrimethamine, mefloquine, halofantrine, and quinine [4]. The observed decrease in the effectiveness of artemisinin is correlated with mutation in the *P. falciparum* Kelch13 gene [5]. In addition, there is resistance against artemisinin partner drugs, such as mefloquine and piperazine [6,7]. Thus, there is an urgent need to find a replacement for artemisinin or novel artemisinin partner-drugs active against known-resistant strains. Currently, all new molecules are tested against a wide variety of resistant laboratory strains of *P. falciparum*, and activity in these assays is a key requirement for further evaluation.

The 1,2,3,4-tetrahydro- β -carboline (9H-1,2,3,4-tetrahydropyrido(3,4-b)indole, TH β C) core (Figure 1) is a privileged structure found in many antimalarial drug candidates and represents an important scaffold for the discovery of novel potent antimalarials. Among the TH β C, C1–C3 substituted derivatives were reported as having potent antimalarial activity [8]. Cipargamin (KAE609, NITD609) (Figure 1) is a novel spiroindolone-class drug for the treatment of malaria. The compound displayed low nanomolar 50% inhibitory concentration (IC₅₀) values (range 0.5–1.4 nM), with no evidence of diminished potency against drug-resistant strains. Cipargamin acts on the P-type Na⁺ ATPase (*Pf*ATP4) of *P. falciparum*, disrupting its Na⁺ homeostasis. This mechanism is distinct from that of existing antimalarial drugs. Currently, cipargamin is undergoing a phase 2 clinical trial [9].

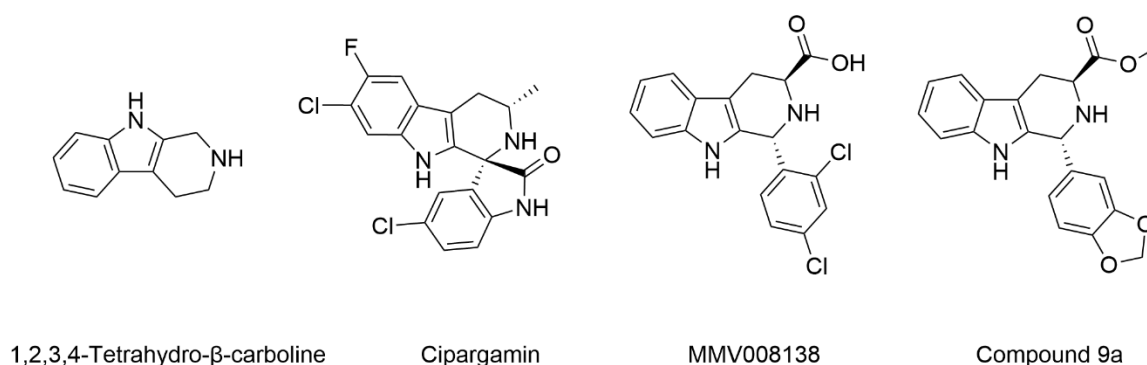


Figure 1. Examples of TH β C derivatives with potent antimalarial activity.

Similarly, compound MMV008138 (Figure 1) exhibits potent antimalarial activity and inhibits the growth of the *P. falciparum* Dd2 strain with an IC₅₀ of 250 nM [10]. Gorki et al. explored the antimalarial activity of a β -carboline derivative, compound 9a (Figure 1), against *P. falciparum*. Compound 9a inhibited both the 3D7 and RKL-9 strains of *P. falciparum* with an IC₅₀ < 2.86 μ M, respectively, was nontoxic to normal dermal fibroblasts, and its selectivity index was >10 against both strains [11]. Further, Gellis et al. reported on a series of 1-phenyl-substituted- β -carboline derivatives with significant antimalarial activity (0.7 < IC₅₀ < 1.7 mM) against the W2 multidrug-resistant strain of *P. falciparum* [12].

Considering these promising antimalarial activities of various TH β C derivatives, we designed and synthesized a new series of compounds with aromatic and/or aliphatic side chains in the 1-position and an amide bond in the 3-position of TH β C (Figure 2). The known TH β C derivatives active against the drug-resistant *P. falciparum* contain mostly bulky aromatic or heteroaromatic substituents (such as piridyl, piperonyl, thiophene, or di-chlorophenyl moieties) at the C1 position and small methyl esters at the C3 position. Consequently, we decided to change the physicochemical properties of the substituents at the C1 and C3 positions, namely, from bulky to small at the C1 position and from small to bulky at the C3 position. The target compounds in the further biological investigations that were conducted, were used as undetermined mixtures of enantiomers and as pure diastereomers or as a mixture of diastereomers.

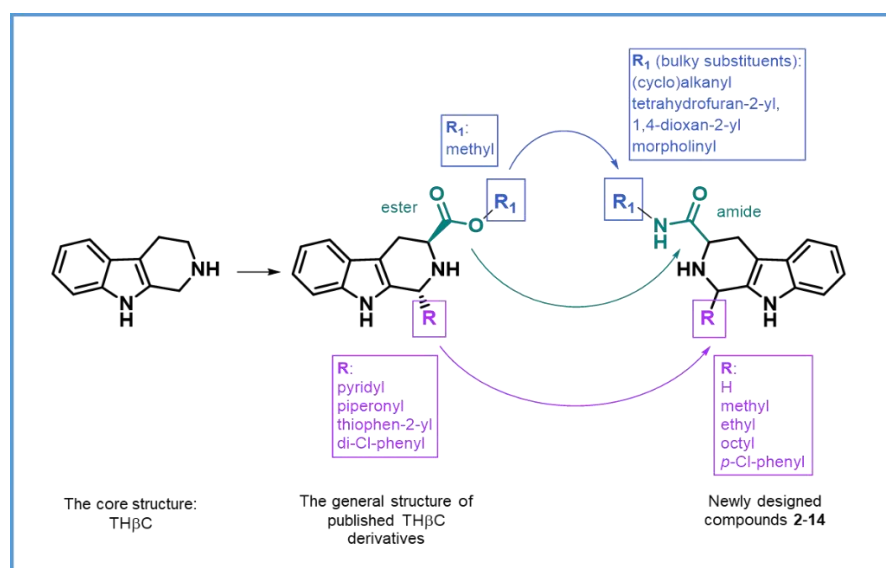


Figure 2. Modification of THβC and general structure of the new compounds (2–14).

The synthesized compounds were evaluated for *in vitro* activity against D10 (CQ-sensitive) and W2 (CQ-resistant) strains of *P. falciparum*. Subsequently, the cytotoxic activity on human microvascular endothelial cells and hemolytic effects on human erythrocytes were also investigated, to obtain more information concerning their safety against mammalian cells. Moreover, compounds 2–14 were also characterized by their physicochemical parameters (Log D). Next, we focused on the probable mechanism of action of the most active compound. Thus, molecular modeling studies were performed to assess the potential binding modes of one enantiomer of compound 7 (that is (1*S*,3*R*)-7) with a series of different enzymes essential for parasite metabolism. Phosphoethanolamine methyltransferase (PMT) plays a critical function in parasite development and differentiation but is absent in mammals. PMT catalyzes the synthesis of phosphatidylcholine—the major phospholipid constituent of the membranes of parasites during the sexual and asexual stages of *Plasmodium* [13]. Lactate dehydrogenase (LDH) is synthesized by parasites in the blood-stage of malaria as the terminal enzyme in the glycolytic pathway of *Plasmodium* [14]. Cytosolic malate dehydrogenase (MDH) converts malate to oxaloacetate and, as a result, generates NADH or NADPH, two reducing equivalents to the respiratory chain of *Plasmodium* [15]. Falcipain-2 (FP2) and falcipain-3 (FP3) are critical hemoglobinasins of *P. falciparum*, which catalyze the degradation of hemoglobin into hemozoin [16].

For this, five different enzymes of *P. falciparum* were selected for docking studies with the view of investigating a possible multitargeting mode of action. Such a strategy would constitute a promising solution to *P. falciparum* drug resistance. To our knowledge, this is the first study describing the syntheses of this type of tetrahydro-β-carboline series as well as their antiplasmodial activities and the *in silico* approach used to study their probable mechanisms of action on this parasite.

2. Results and Discussion

2.1. Chemistry

The synthesis of the designed THβC derivatives (2–14) commenced with the Pictet–Spengler reaction of racemic tryptophan and an appropriate aldehyde in the presence of sulfuric acid (H₂SO₄) in water (Figure 3) [17]. The resultant 1-substituted-tetrahydro-β-carboline-3-carboxylic acids (1a–e) were further reacted with diverse amines in the presence of 4-dimethylaminopyridine (DMAP), 1-ethyl-3-(3-dimethylaminopropyl) carbodiimide (EDC), 1-hydroxybenzotriazole (HOBt), and pyridine. The final compounds were purified by crystallization from hexane or by column chromatography. The structures and purity of the newly synthesized compounds were characterized by ¹H NMR, ¹³C NMR spectroscopy,

and UPLC/MS spectrometry. Compounds were isolated as an undetermined mixture of enantiomers (**3RS-2**, **1RS,3SR** for **8–11** and **14**), pure diastereomers (**1RS,3RS-13**, **1RS,3SR-13**) or as a mixture of diastereomers (**1**, **3–7**, **12**) with various diastereoselectivity (ds) (Sections 3 and 3.1).

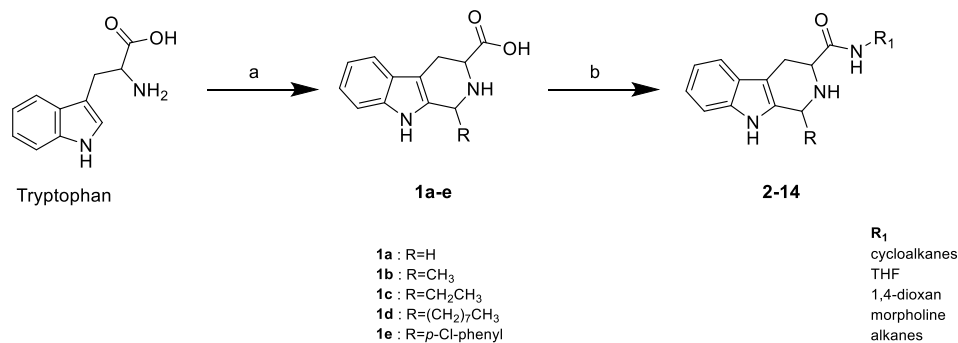


Figure 3. Synthesis of compounds **2–14**. Reagents and conditions: (a) RCHO, H₂SO₄, H₂O, reflux or rt, 20 h; (b) amine, DMAP, EDC, HOBT, pyridine, DCM, reflux, 24 h.

The applied synthetic methods facilitated the synthesis of intermediates (**1a–e**), and compounds (**2–14**), with yields of 15–74% and the purity of the final compounds above 95%.

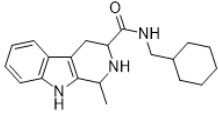
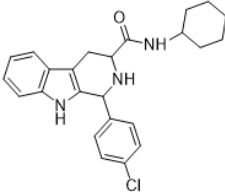
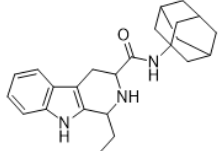
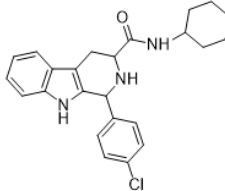
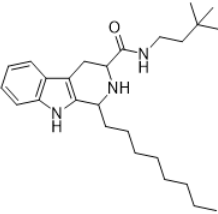
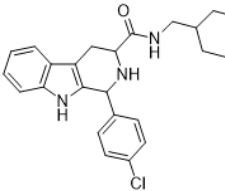
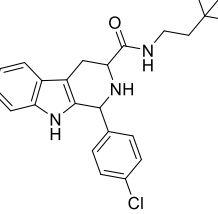
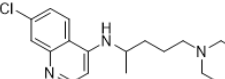
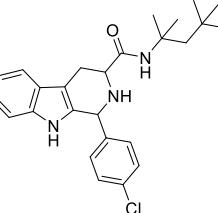
2.2. Log D Calculation

Compounds **2–14** are partially ionized; thus, the distribution coefficients D (Log D) were calculated at fixed pH. The chosen pH (7.4, 7.2, and 5.5) represent the physiological conditions found in the blood, human erythrocyte cytoplasm, and *P. falciparum* food vacuoles. The data in Table 1 show that, for Log D at pH 7.4, the compounds fall in the range 1.73–5.65, and in the range of 1.59–5.53 at pH 7.2, whereas at pH 5.5, the compounds were in the range of 0.05–3.93. Only compound **3** displayed a gradient of Log D similar to CQ, however, the values of Log D for compound **3** were almost twice as large as those for CQ itself.

Table 1. Prediction of Log D for compounds **2–14** and CQ.

Comp	Structure	Log D			Comp	Structure	Log D		
		pH 7.4	pH 7.2	pH 5.5			pH 7.4	pH 7.2	pH 5.5
2		2.53	2.40	0.87	10		3.39	3.34	2.12
3		1.73	1.59	0.05	11		2.77	2.71	1.50
4		2.47	2.33	0.80	12		2.69	2.53	0.05

Table 1. Cont.

Comp	Structure	Log D			Comp	Structure	Log D		
		pH 7.4	pH 7.2	pH 5.5			pH 7.4	pH 7.2	pH 5.5
5		2.79	2.65	1.11	1RS,3RS-13		4.47	4.72	3.50
6		3.18	3.03	1.47	1RS,3SR-13		4.47	4.72	3.50
7		5.65	5.49	3.93	14		5.09	5.03	3.82
8		4.88	4.83	3.61	CQ		0.88	0.64	0.76
9		5.58	5.53	4.31					

2.3. Antiplasmodial Activities

Next, the screening of antiplasmodial activities in in vitro parasite cultures was performed using standard procedures. For this purpose, we tested the susceptibility of two strains of *P. falciparum* differing in resistance to CQ, namely D10 (chloroquine-sensitive) and W2 (chloroquine-resistant). The inhibitory effect on the growth of these strains, expressed as IC_{50} values, is presented in Table 2. The synthesized derivatives have IC_{50} values in the range of 4.00 ± 0.53 – 35.36 ± 4.86 μ M. The highest antiplasmodial activity among the tested series was shown by compound 7, which is also characterized by one of the highest Log D values in the series of compounds. Moreover, many compounds have a similar magnitude of inhibitory activity against the two *P. falciparum* strains, as reported for other tetrahydro- β -carboline derivatives by Eagon et al. [18]. The important fact is also that, except for compound 6, the determined values of IC_{50} are lower for the CQ-resistant strain in comparison to the CQ-sensitive strain, reflected in their RI (resistance index) values. This could suggest superior sensitivity of the designed compounds towards the CQ-resistant parasite strain. The obtained results are very encouraging, especially since malaria control is threatened by the emergence of drug resistance to the artemisinin derivatives [19]. The

data also indicate a different relationship between chemical structure and antiplasmodial activity that is not directly related to Log D values and the types of chemical substituents.

Table 2. The antiplasmodial activity of compounds (2–14) against the D10 (CQ-sensitive) and W2 (CQ-resistant) strains of *P. falciparum* and relevant RI.

Compound	<i>P. falciparum</i> IC ₅₀ (μM)		RI ^a
	D10	W2	
2	21.87 ± 5.82	10.12 ± 2.14	0.46
3	13.17 ± 2.85	9.60 ± 0.78	0.73
4	21.38 ± 4.70	20.10 ± 2.79	0.94
5	33.47 ± 7.58	16.19 ± 4.11	0.48
6	9.73 ± 0.96	11.36 ± 0.82	1.17
7	4.45 ± 0.83	4.00 ± 0.53	0.90
8	10.48 ± 1.53	7.80 ± 1.54	0.74
9	8.41 ± 1.20	6.41 ± 1.05	0.76
10	29.36 ± 7.88	20.54 ± 2.20	0.70
11	35.36 ± 4.86	29.07 ± 4.05	0.82
12	11.45 ± 0.34	6.15 ± 0.46	0.54
1RS,3RS-13	16.05 ± 3.36	13.46 ± 1.99	0.84
1RS,3SR-13	12.53 ± 0.71	9.13 ± 0.83	0.73
14	- ^b	- ^b	-
CQ	0.017 ± 0.006	0.27 ± 0.07	15.88

^a RI = IC₅₀ CQ resistant *P. falciparum* strain/IC₅₀ CQ sensitive *P. falciparum* strain; ^b IC₅₀ > 47.40 μM.

2.4. Biocompatibility Studies

Results from the preliminary antiplasmodial activity screening highlighted the necessity for the evaluation of the safety of these agents to human cells. Hence, we chose two model cell systems: the human microvascular endothelial (HMEC-1) cell line and human erythrocytes, to obtain greater insights into their cell toxicity potential. In these studies, we focused only on derivatives that had exhibited the highest antiplasmodial activities, namely 3, 6, 7, 8, 9, 12, 1RS,3RS-13, and 1RS,3SR-13. The results concerning their cytotoxic effects on HMEC-1 cells as well as their calculated selectivity index (SI), namely the ratio between the IC₅₀ values on the endothelial cells and that on the *Plasmodium* strains, are summarized in Table 3. Based on the analysis of the obtained results, it can be concluded that the determined IC₅₀ values fall within a fairly wide range from 17.95 ± 9.46 to 157.18 ± 42.50 μM, even though they all have their IC₅₀ in the range of low micromolar concentrations against both strains of *Plasmodium*. A similar phenomenon has already been described for methoxy-thiazinoquinones by Imperatore et al. [20]. Interestingly, the most active compound against the parasite (7) is also safe to HMEC-1 cells and is highly selective, also exhibiting the highest SI value of the whole compound series.

Table 3. Cytotoxicity of compounds 3, 6, 7, 8, 9, 12, 1RS,3RS-13, 1RS,3SR-13, and CQ on the HMEC-1 cell line and relevant selectivity indexes (SI).

Compound	IC ₅₀ (μM)	SI ^a	
		D10	W2
3	157.18 ± 42.50	11.93	16.37
6	21.09 ± 8.82	2.17	1.86
7	72.02 ± 22.40	16.18	18.00
8	17.95 ± 9.46	1.71	2.30
9	18.93 ± 10.16	2.25	2.95
12	102.07 ± 14.83	8.91	16.60
1RS,3RS-13	53.78 ± 21.89	3.35	4.00
1RS,3SR-13	- ^b	-	-
CQ	>38 ^c	-	-

^a SI = IC₅₀ HMEC-1/IC₅₀ *P. falciparum* strain; ^b IC₅₀ > 122.57 μM; ^c data from [21].

We also sought to investigate the hemolytic potential of the synthesized compounds. For this experiment, we selected three compounds, namely **3**, **7**, and **12**, which exhibited the highest selectivity. We incubated these compounds at a concentration of 10 μ M, with human erythrocytes, and then, by measuring the released hemoglobin, we assessed their potential harmful effects on these cells. The measured level of hemolysis was less than 5% for all agents, which proves that the compounds are not hemolytic. It is worth emphasizing at this point that this type of test is extremely important to confirm that the observed inhibitory activity against *Plasmodium* is a result of a compound acting directly upon it and not as a result of red blood cell lysis. Taking into account the fact that the tested concentration of **7** in this test was, respectively, 2.2 and 2.5 times higher than the IC_{50} determined for the *Plasmodium* strains, we can conclude that the observed effect on the parasite is not due to activity on erythrocytes. In conclusion, compound **7** is, therefore, biocompatible, since no hemolytic effects were detected in the mammalian cells tested.

2.5. Molecular Modeling

Molecular modeling studies were performed to evaluate the possible mechanism of action of the one enantiomer of compound **7** namely (1*S*,3*R*)-3-[(3,3-dimethylbutyl)carbamoyl]-1-octyl-1*H*,2*H*,3*H*,4*H*,9*H*-pyrido[3,4-*b*]indol-2-ium (*trans*); (compound (1*S*,3*R*)-**7**). The Lig-Prep tool and MarvinSketch software indicated that, at pH 7.4, 73% of compound (1*S*,3*R*)-**7** molecules exist in the form where the 1,2,3,6-tetrahydropyridine ring has a protonated amine group, whereas 27% of molecules remain uncharged. Faced with such a clear disproportion, we assumed that the protonated form is responsible for most of the physiological effect and, consequently, only this form was used in the docking simulations. Compound (1*S*,3*R*)-**7** was docked to the following series of enzymes essential for the functioning of *P. falciparum*: phosphoethanolamine methyltransferase (PMT), falcipain-2 (FP2), falcipain-3 (FP3), lactate dehydrogenase (LDH), and malate dehydrogenase (MDH). Moreover, compound (1*S*,3*R*)-**7** formed molecular interactions with the amino acid residues of these enzymes, as observed in the originally co-crystallized ligands.

In the complex of compound (1*S*,3*R*)-**7** and PMT that was obtained by IFD simulations (Figure 4A), a π -cation interaction between Tyr27 of PMT and the protonated amine group of tetrahydropyridine, as well as hydrogen-bonding between the side chain of Lys247 of PMT and the oxygen in the amide moiety of compound (1*S*,3*R*)-**7** were observed. Moreover, both mentioned amino acid residues participated in forming interactions with phosphocholine in the PMT crystal. In addition, a π - π interaction was observed between Tyr19 of PMT and the aromatic benzene ring from the β -carboline moiety. This additional interaction was not observed in the PMT crystal structure.

The obtained complex of compound (1*S*,3*R*)-**7** and falcipain-2 (Figure 4B) formed H-bonds between the main chain of Gly83 in PMT and the protonated amine group of tetrahydropyridine and the oxygen in the amide moiety of compound (1*S*,3*R*)-**7**. A hydrogen-bond was also observed between the main chain of Asn173 of PMT and the hydrogen on the amide grouping in compound (1*S*,3*R*)-**7**. All the amino acid residues discussed previously formed interactions with epoxysuccinate in the FP2 crystal. However, the H-bond between the side chain of Asp234 and the amine group of the center ring of β -carboline was not observed in the FP3 crystal structure.

The complex of FP3 (Figure 4C) and compound (1*S*,3*R*)-**7** formed H-bonds between the main chain of Asn182 and the protonated amine group of tetrahydropyridine, as well as with hydrogen from the amide of compound (1*S*,3*R*)-**7**. In addition, a hydrogen bond between the main chain of Gly92 of FP3 and the amide's oxygen of compound (1*S*,3*R*)-**7** was observed. It is noteworthy that all the mentioned amino acid residues participated in interactions with leupeptin in the FP3 crystal.

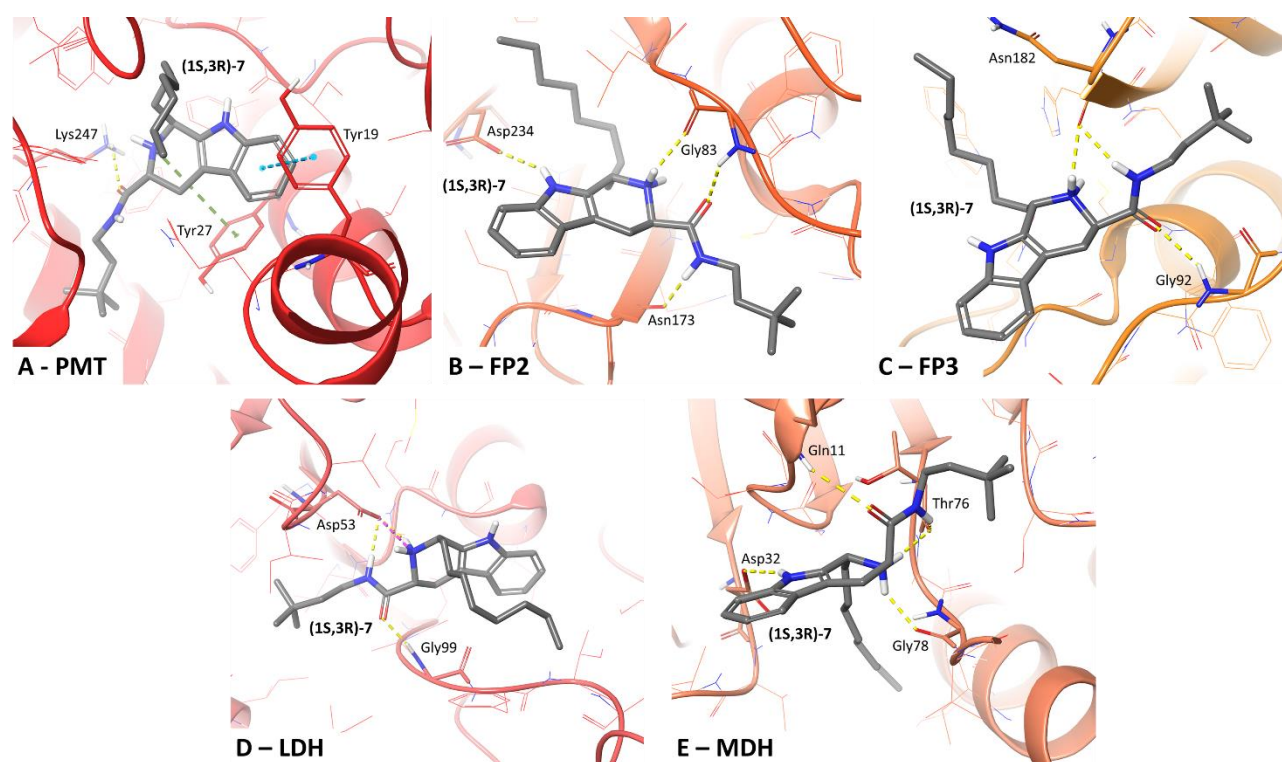


Figure 4. Molecular interactions formed between compound (1*S*,3*R*)-7 and selected molecular targets phosphoethanolamine methyltransferase (PMT) (A); falcipain-2 (FP2) (B); falcipain-3 (FP3) (C); lactate dehydrogenase (LDH) (D); and malate dehydrogenase (MDH) (E). Amino acid residues within 4 Å from the ligand are displayed as thin sticks; amino acid residues engaged in ligand binding by ionic bond (dotted pink lines), H-bond (dotted yellow lines), π -cation interaction (dotted green lines), and π - π interaction (dotted blue lines) are displayed as bold sticks.

An ionic bond (salt bridge) was observed between the side chain of Asp53 in LDH and the protonated amine group of tetrahydropyridine of compound (1*S*,3*R*)-7, as well as a hydrogen bond between the side chain of Asp53 and the hydrogen of the amide group of compounds (1*S*,3*R*)-7, and an additional H-bond identified between the main chain of Gly99 and the oxygen of the amide group of compounds (1*S*,3*R*)-7 (Figure 4D). All the mentioned amino acid residues participated in forming interactions with NADH in the LDH crystal.

Compound (1*S*,3*R*)-7 (Figure 4E) formed a hydrogen bond between the main chain of MDH's Gly78 and the protonated amine group of tetrahydropyridine, along with an H-bond between the main chain of Thr76 and the protonated amine group of tetrahydropyridine and the hydrogen of the amide moiety of compound (1*S*,3*R*)-7. A further H-bond exists between the main chain of Gln11 and the oxygen on the amide moiety of compound (1*S*,3*R*)-7, and an H-bond between the side chain of Asp32 and the amine group of the center ring of β -carboline of compound (1*S*,3*R*)-7. Among the mentioned amino-acid interactions, only Thr76 was not involved in forming interactions with NAD in the 6R8G crystal.

Results from IFD revealed that each H-bond donor/acceptor fragment present in compound (1*S*,3*R*)-7, such as the amine group of the center ring of β -carboline, the protonated amine group on tetrahydropyridine, and the oxygen, nitrogen, and hydrogen atoms of the amide moiety of compound (1*S*,3*R*)-7, were involved in forming an interaction with at least one amino-acid target in the group of enzymes investigated. Moreover, the aliphatic chains of compound (1*S*,3*R*)-7 additionally stabilized the position of the entire molecule within the enzymes. Observations from *in silico* simulations highlight that compound (1*S*,3*R*)-7 has structural features enabling it to interact with five described molecular targets within

sites occupied originally by other ligands (products/inhibitors/cofactors). The results are a good starting point for further in vitro evaluation of compound (1*S*,3*R*)-7.

3. Materials and Methods

3.1. General Remarks

Commercially available reagents were purchased from Merck-Sigma-Aldrich (Poznań, Poland), Acros Organics (Thermo Fisher Scientific, Waltham, MA, USA), or ChemPur (Piekary Śląskie, Poland) and were used without further purification. Purification of chemical compounds by column chromatography was carried out using silica gel mesh: 0.063–0.200 μm (Sigma-Aldrich; Poznań, Poland) as a stationary phase. The reactions were monitored by thin-layer chromatography on aluminum sheets precoated with silica gel 60 F₂₅₄ (Merck; Darmstadt, Germany). Compounds were visualized with UV light (254 nm). In addition, chromatograms were stained in a 0.5% solution of ninhydrin in *n*-propanol or a solution of 5% (NH₄)₆Mo₇O₂₄ and 0.2% Ce(SO₄)₂ in 5% H₂SO₄. The retardation factor R_f was defined using the following solvent systems: S₁ (DCM/methanol/acetic acid, 8:2:0.5 *v/v/v*), S₂ DCM/methanol (95:5, *v/v*), S₃ DCM/EtOAc (9:1, *v/v*), S₄ DCM/MeOH (97.5:2.5 *v/v*), S₅ DCM/EtOAc (14:1 *v/v*). ¹H NMR and ¹³C NMR spectra were recorded using an FT-NMR 500 MHz spectrometer (Joel Ltd., Akishima, Tokyo, Japan). The chemical shifts (δ) are reported in ppm and were calculated concerning the frequency of the deuterium field stabilization signal. The coupling constant J is reported in Hertz. Signal multiplets are represented by the following abbreviations: s (singlet), brs (broad singlet), d (doublet), dd (doublet of doublets), dt (doublet of triplets), t (triplet), q (quintet), m (multiplet). (Supplementary Table S1). Diastereoselectivity was characterized by ds (major/minor) according to ¹H NMR spectra [22]. UPLC separations were carried out according to the procedures described elsewhere [23].

Medium and supplements for *P. falciparum* culture and cell culture (RPMI 1640 Medium, Glutamine, Hepes Buffer, Fetal calf serum) were from EuroClone (Milan, Italy). AlbuMax and MCDD 131 medium were from Invitrogen (Milan, Italy). Unless stated otherwise, all reagents were from Sigma Italia (Milan, Italy).

3.2. Synthetic Procedures

3.2.1. General Method for Synthesis of the 1-Substituted-tetrahydro- β -carboline-3-carboxylic Acids (1a–e)

According to the literature, a mixture of 0.5 N H₂SO₄ (2.5 mL) and H₂O (200 mL), D,L-tryptophan (2.04 g, 10 mmol), and appropriate aldehydes (30 mmol) was stirred at room temperature overnight and the synthesis products detected by TLC. The precipitate was filtered and washed well with H₂O and dried in a vacuum. The material was used without further purification for the following steps.

3.2.2. General Method for Synthesis of the 3-Carboxamide Derivatives of 1-Substituted-tetrahydro- β -carboline-3-carboxylic Acids (2–14)

The appropriate 1-substituted-tetrahydro- β -carboline-3-carboxylic acid (1a–e) (1 equiv) suspensions in dichloromethane (DCM) with EDC (1.3 equiv), DMAP (0.5 equiv), HOBT (1.3 equiv), pyridine (0.05 equiv), and a relevant amine (1 equiv) were refluxed for 18 h. When the reactions were completed, the mixtures were extracted with CHCl₃/isopropanol (3:1 *v/v*; 3 \times 10 mL). The combined organic fractions were dried over Na₂SO₄ and evaporated under vacuum. The crude products were purified by crystallization in hexane or by column chromatography.

- *N*-cyclooctyl-2,3,4,9-tetrahydro-1*H*-pyrido[3,4-*b*]indole-3-carboxamide (2): (3*RS*)

Compound 2 was prepared using 2,3,4,9-tetrahydro-1*H*-pyrido[3,4-*b*]indole-3-carboxylic acid (1a) (0.25 mmol, 0.058 g) and EDC (0.325 mmol, 0.062 g), HOBT (0.325 mmol, 0.043 g), DMAP (0.125 mmol, 0.015 g), pyridine (0.025 mmol, 2 μL) and cyclooctanamine (0.25 mmol, 38 μL) in 8 mL DCM. The product was purified by column chromatography over silica gel and obtained as a crystallized oil with a yield of 40% ($R_f = 0.29$ (S₂)). LC/MS: C₂₀H₂₇N₃O (98%)

m/z : 326.22, found: 326.07. ^1H NMR (500 MHz, CDCl_3) δ 8.05 (br. s., 1H), 7.49 (d, $J = 8.0$ Hz, 1H), 7.32–7.28 (m, 1H), 7.19–7.13 (m, 1H), 7.12–7.08 (m, 1H), 7.04 (d, $J = 8.0$ Hz, 1H), 4.07–3.98 (m, 3H), 3.52 (dd, $J = 4.87$ Hz, 10.60 Hz, 1H), 3.23 (dd, $J = 4.6$ Hz, 15.5 Hz, 1H), 2.82–2.74 (m, 1H), 1.92–1.81 (m, 2H), 1.69 (d, $J = 8.6$ Hz, 2H), 1.61–1.51 (m, 8H). ^{13}C NMR (126 MHz, CDCl_3) δ 171.5, 136.1, 132.3, 127.4, 121.8, 119.6, 118.1, 110.9, 108.6, 57.5, 49.1, 43.0, 32.3, 27.3, 25.5, 24.8, 23.8.

- (1-methyl-2,3,4,9-tetrahydro-1*H*-pyrido[3,4-*b*]indol-3-yl)(piperidin-1-yl)methanone (3): **(1RS,3SR)-3/(1RS,3RS)-3**

Compound **3** was prepared using 1-methyl-2,3,4,9-tetrahydro-1*H*-pyrido[3,4-*b*]indole-3-carboxylic acid (**1b**) (0.25 mmol, 0.058 g) and EDC (0.325 mmol, 0.062 g), HOBT (0.325 mmol, 0.043 g), DMAP (0.125 mmol, 0.015 g), pyridine (0.025 mmol, 2 μL) and piperidine (0.25 mmol, 26 μL) in 8 mL DCM. The product was purified by column chromatography over silica gel and obtained as a yellowish solid with a yield of 72% ($R_f = 0.25$ (S_2)). LC/MS: $\text{C}_{18}\text{H}_{23}\text{N}_3\text{O}$ (95%) m/z : 298.18, found: 298.28. ds: **(1RS,3SR)-3/(1RS,3RS)-3** = 70:3. ^1H NMR (500 MHz, CDCl_3) δ 8.62–8.54 (m, 1H), 7.42 (d, $J = 7.5$ Hz, 1H), 7.31 (s, 1H), 7.10 (d, $J = 7.16$ Hz, 1H), 7.08–7.03 (m, 1H), 4.30–4.23 (m, 1H), 4.08–4.03 (m, 1H), 3.59 (t, $J = 5.3$ Hz, 1H), 3.48–3.43 (m, 1H), 2.88–2.77 (m, 2H), 2.15 (s, 3H), 1.69–1.48 (m, 8H) *NH* proton was not detected. ^{13}C NMR (126 MHz, CDCl_3) δ 171.1, 136.5, 135.9, 126.9, 121.6, 119.4, 117.7, 112.1, 111.0, 107.0, 53.4, 46.5, 42.9, 30.9, 25.4, 24.4, 20.0.

- *N*-cyclohexyl-1-methyl-2,3,4,9-tetrahydro-1*H*-pyrido[3,4-*b*]indole-3-carboxamide (4): **(1RS,3SR)-4/(1RS,3RS)-4**

Compound **4** was prepared using 1-methyl-2,3,4,9-tetrahydro-1*H*-pyrido[3,4-*b*]indole-3-carboxylic acid (**1b**) (0.25 mmol, 0.058 g) and EDC (0.325 mmol, 0.062 g), HOBT (0.325 mmol, 0.043 g), DMAP (0.125 mmol, 0.015 g), pyridine (0.025 mmol, 2 μL) and cyclohexanamine (0.25 mmol, 28 μL) in 8 mL DCM. The product was purified by column chromatography over silica gel and obtained as a yellowish solid with a yield of 74% ($R_f = 0.11$ (S_2)). LC/MS: $\text{C}_{19}\text{H}_{25}\text{N}_3\text{O}$ (96%) m/z : 311.20, found 311.15. ds: **(1RS,3SR)-4/(1RS,3RS)-4** = 10:4. ^1H NMR (500 MHz, CDCl_3) δ 8.40 (s, 1H), 7.47 (d, $J = 8.0$ Hz, 1H), 7.31 (d, $J = 8.0$ Hz, 1H), 7.18–7.08 (m, 2H), 7.07–6.98 (m, 1H), 4.21–4.10 (m, 1H), 3.89–3.77 (m, 1H), 3.54 (dd, $J = 4.6$, 11.5 Hz, 1H), 3.28 (ddd, $J = 2.0$, 4.6, 15.8 Hz, 1H), 2.69 (ddd, $J = 2.9$ Hz, 11.3 Hz, 15.6 Hz, 1H), 2.01–1.90 (m, 2H), 1.78–1.69 (m, 2H), 1.63 (td, $J = 3.6$ Hz, 12.9 Hz, 1H), 1.49 (d, $J = 6.9$ Hz, 3H), 1.45–1.31 (m, 3H), 1.30–1.11 (m, 3H). ^{13}C NMR (126 MHz, CDCl_3) δ 172.1, 137.1, 136.2, 127.4, 121.8, 119.6, 118.3, 111.1, 108.4, 58.0, 49.5, 48.0, 33.2, 25.5, 20.4.

- *N*-(cyclohexylmethyl)-1-methyl-2,3,4,9-tetrahydro-1*H*-pyrido[3,4-*b*]indole-3-carboxamide (5): **(1RS,3SR)-5/(1RS,3RS)-5**

Compound **5** was prepared using 1-methyl-2,3,4,9-tetrahydro-1*H*-pyrido[3,4-*b*]indole-3-carboxylic acid (**1b**) (0.25 mmol, 0.058 g) and EDC (0.325 mmol, 0.062 g), HOBT (0.325 mmol, 0.043 g), DMAP (0.125 mmol, 0.015 g), pyridine (0.025 mmol, 2 μL) and cyclohexylmethanamine (0.25 mmol, 32 μL) in 8 mL DCM. The product was purified by column chromatography over silica gel and obtained as a yellowish solid with a yield of 72% ($R_f = 0.25$ (S_2)). LC/MS: $\text{C}_{20}\text{H}_{27}\text{N}_3\text{O}$ (95%) m/z : 326.22, found 326.05. ds: **(1RS,3SR)-5/(1RS,3RS)-5** = 10:4. ^1H NMR (500 MHz, CDCl_3) δ 8.05 (s, 1H), 7.49 (d, $J = 7.5$ Hz, 1H), 7.27 (s, 1H), 7.19–7.17 (m, 1H), 7.17–7.13 (m, 1H), 7.11–7.07 (m, 1H), 4.23–4.17 (m, 1H), 3.59 (dd, $J = 4.6$ Hz, 11.5 Hz, 1H), 3.33–3.27 (m, 1H), 3.22–3.11 (m, 2H), 2.71 (ddd, $J = 2.6$ Hz, 11.5 Hz, 15.8 Hz, 1H), 1.74 (dd, $J = 3.4$ Hz, 13.1 Hz, 5H), 1.51–1.46 (m, 3H), 1.29–1.12 (m, 4H), 1.01–0.91 (m, 2H) *NH* proton was not detected. ^{13}C NMR (126 MHz, CDCl_3) δ 172.9, 170.6, 137.0, 136.1, 127.4, 121.9, 119.1, 110.9, 108.7, 77.0, 58.1, 49.5, 45.5, 38.1, 31.0, 26.0, 20.4.

- *N*-(Adamantan-1-yl)-1-ethyl-2,3,4,9-tetrahydro-1*H*-pyrido[3,4-*b*]indole-3-carboxamide (6): **(1RS,3SR)-6/(1RS,3RS)-6**

Compound **6** was prepared using 1-ethyl-2,3,4,9-tetrahydro-1*H*-pyrido[3,4-*b*]indole-3-carboxylic acid (**1c**) (0.25 mmol, 0.061 g) and EDC (0.325 mmol, 0.062 g), HOBT (0.325 mmol,

0.037 g), DMAP (0.125 mmol, 0.015 g), pyridine (0.025 mmol, 2 μ L) and adamantan-1-amine (0.25 mmol, 0.27 g) in 8 mL DCM. The product was purified by column chromatography over silica gel and obtained as a white solid with a yield of 60% ($R_f = 0.38$ (S_4)). LC/MS: $C_{24}H_{31}N_3O$ (96%) m/z : 378.25, found 378.30. ds: (1RS,3SR)-6/(1RS,3RS)-6 = 11:4.4. 1H NMR (500 MHz, $CDCl_3$) δ 8.62 (d, $J = 1.7$ Hz, 1H), 8.52 (s, 1H), 7.48–7.44 (m, 1H), 7.32–7.25 (m, 1H), 7.08–7.03 (m, 1H), 6.89 (s, 1H), 4.04 (d, $J = 5.2$ Hz, 1H), 3.44 (dd, $J = 4.6$ Hz, 10.9 Hz, 1H), 3.26 (ddd, $J = 1.7$ Hz, 4.4 Hz, 15.6 Hz, 1H), 2.67 (ddd, $J = 2.3$ Hz, 11.2 Hz, 15.8 Hz, 1H), 2.14–2.01 (m, 9H), 1.80 (ddd, $J = 4.6$ Hz, 7.4 Hz, 14.3 Hz, 1H), 1.74–1.62 (m, 7H), 1.03 (t, $J = 7.2$ Hz, 3H) *NH* indole was not detected. ^{13}C NMR (126 MHz, $CDCl_3$) δ 171.3, 135.0, 128.1, 120.9, 120.0, 119.0, 110.6, 107.1, 70.2, 56.3, 42.0, 36.1, 30.3, 27.2, 25.0, 11.1.

- *N*-(3,3-dimethylbutyl)-1-octyl-2,3,4,9-tetrahydro-1*H*-pyrido[3,4-*b*]indole-3-carboxamide (7): (1RS,3SR)-7/(1RS,3RS)-7

Compound 7 was prepared using 1-octyl-2,3,4,9-tetrahydro-1*H*-pyrido[3,4-*b*]indole-3-carboxylic acid (1d) (0.5 mmol, 0.145 g) and EDC (0.65 mmol, 0.124 g), HOBT (0.65 mmol, 0.086 g), DMAP (0.25 mmol, 0.30 g), pyridine (0.025 mmol, 2 μ L) and 3,3-dimethylbutan-1-amine (0.5 mmol, 56 μ L) in 8 mL DCM. The product was purified by column chromatography over silica gel (DCM/EtOAc = 9:1) and obtained as a dark yellow oil with a yield of 15% ($R_f = 0.22$ (S_3)). LC/MS: $C_{26}H_{41}N_3O$ (96%) m/z 412.32, found 412.28. ds: (1RS,3SR)-7/(1RS,3RS)-7 = 10:4.7. 1H NMR (500 MHz, $CDCl_3$) δ 7.85–7.70 (m, 1H), 7.52 (d, $J = 7.7$ Hz, 1H), 7.32 (dd, $J = 8.0$ Hz, 17.8 Hz, 1H), 7.19–7.14 (m, 1H), 7.17–7.08 (m, 1H), 7.05–7.00 (m, 1H), 4.14 (dd, $J = 2.0$ Hz, 4.9 Hz, 1H), 3.55 (dd, $J = 4.3$ Hz, 11.2 Hz, 1H), 3.40–3.30 (m, 3H), 2.70 (ddd, $J = 2.6$ Hz, 11.5 Hz, 15.5 Hz, 1H), 2.02–1.93 (m, 1H), 1.75 (q, $J = 7.5$ Hz, 1H), 1.67–1.43 (m, 4H), 1.39–1.25 (m, 8H), 1.00–0.95 (m, 9H), 0.90 (t, $J = 6.7$ Hz, 6H). ^{13}C NMR (126 MHz, $CDCl_3$) δ 135.9, 127.5, 121.9, 119.7, 118.4, 110.8, 109.5, 57.8, 53.8, 43.4, 35.9, 31.9, 29.5, 22.7, 14.2.

- 1-(4-chlorophenyl)-*N*-(3,3-dimethylbutyl)-2,3,4,9-tetrahydro-1*H*-pyrido[3,4-*b*]indole-3-carboxamide (8): (1RS,3SR)

Compound 8 was prepared using 1-(4-chlorophenyl)-2,3,4,9-tetrahydro-1*H*-pyrido[3,4-*b*]indole-3-carboxylic acid (1e) (0.25 mmol, 0.081 g) and EDC (0.325 mmol, 0.062 g), HOBT (0.325 mmol, 0.043 g), DMAP (0.125 mmol, 0.015 g), pyridine (0.1 mmol, 8 μ L) and 3,3-dimethylbutan-1-amine (0.25 mmol, 33 μ L) in 15 mL DCM. The product was purified by column chromatography over silica gel and obtained as an off-white solid with a yield of 22% ($R_f = 0.11$ (S_3)). LC/MS: $C_{24}H_{28}ClN_3O$ (97%) m/z : 410.20, found: 410.03. 1H NMR (500 MHz, $CDCl_3$) δ 7.82 (s, 1H), 7.57 (d, $J = 8.0$ Hz, 1H), 7.30–7.24 (m, 4H), 7.18 (dd, $J = 1.2$ Hz, 8.0 Hz, 1H), 7.16–7.11 (m, 3H), 6.80–6.74 (m, 1H), 5.21 (s, 1H), 3.53–3.47 (m, 1H), 3.29 (s, 1H), 3.27–3.15 (m, 1H), 2.90–2.82 (m, 1H), 1.44–1.37 (m, 2H), 1.25 (d, $J = 1.1$ Hz, 2H), 0.91 (s, 9H). ^{13}C NMR (126 MHz, $CDCl_3$) δ 172.4, 139.1, 136.3, 134.2, 129.7, 127.1, 122.4, 119.9, 118.6, 110.7, 110.1, 60.5, 58.2, 43.3, 36.0, 29.8, 24.6, 21.0, 14.3.

- 1-(4-chlorophenyl)-*N*-(2,4,4-trimethylpentan-2-yl)-2,3,4,9-tetrahydro-1*H*-pyrido[3,4-*b*]indole-3-carboxamide (9): (1RS,3SR)

Compound 9 was prepared using 1-(4-chlorophenyl)-2,3,4,9-tetrahydro-1*H*-pyrido[3,4-*b*]indole-3-carboxylic acid (1e) (0.25 mmol, 0.081 g) and EDC (0.325 mmol, 0.062 g), HOBT (0.325 mmol, 0.043 g), DMAP (0.125 mmol, 0.015 g), pyridine (0.1 mmol, 8 μ L) and 7,7-dimethyloctan-1-amine (0.25 mmol, 38 μ L) in 15 mL DCM. The product was purified by column chromatography over silica gel (DCM/EtOAc = 14:1) and obtained as an off-white solid with a yield of 50% ($R_f = 0.33$ (S_5)). LC/MS: $C_{26}H_{32}ClN_3O$ (96%) m/z : 438.22 found 438.05. 1H NMR (500 MHz, $CDCl_3$) δ 7.58 (s, 1H), 7.55–7.52 (m, 1H), 7.38–7.30 (m, 2H), 7.28–7.21 (m, 3H), 7.18–7.09 (m, 2H), 6.84 (s, 1H), 5.14 (t, $J = 2.3$ Hz, 1H), 3.58 (dd, $J = 4.3$ Hz, 11.1 Hz, 1H), 3.38–3.28 (m, 1H), 2.80–2.70 (m, 1H), 1.74 (s, 2H), 1.67–1.60 (m, 1H), 1.43 (s, 6H), 1.00 (s, 9H). ^{13}C NMR (126 MHz, $CDCl_3$) δ 171.4, 139.4, 136.3, 134.0, 129.6, 127.2, 122.3, 119.2, 110.8, 58.2, 52.2, 26.1.

- 1-(4-chlorophenyl)-*N*-((tetrahydrofuran-2-yl)methyl)-2,3,4,9-tetrahydro-1*H*-pyrido[3,4-*b*]indole-3-carboxamide (**10**): (**1RS,3SR**)

Compound **10** was prepared using 1-(4-chlorophenyl)-2,3,4,9-tetrahydro-1*H*-pyrido[3,4-*b*]indole-3-carboxylic acid (**1e**) (2.3 mmol, 0.76 g) and EDC (3.0 mmol, 0.58 g), HOBT (3.0 mmol, 0.4 g), DMAP (1.17 mmol, 0.143 g), pyridine (0.1 mmol, 8 μ L) and (tetrahydrofuran-2-yl)methanamine (2.3 mmol, 0.24 g) in 15 mL DCM. The product was purified by crystallization in hexane and a few drops acetone and obtained as an off-white solid with a yield of 35% ($R_f = 0.09$ (S_3)). LC/MS: $C_{23}H_{24}ClN_3O_2$ (95%) m/z : 410.16, found: 410.10. 1H NMR (500, DMSO- d_6) δ ppm: 10.75 (d, $J = 3.0$ Hz, 1H), 7.97–7.87 (m, 1H), 7.45–7.38 (m, 1H), 7.37–7.28 (m, 2H), 7.25–7.18 (m, 2H), 7.21 (t, $J = 7.4$ Hz, 1H), 7.01 (t, $J = 6.7$ Hz, 1H), 6.97–6.90 (m, 1H), 5.18 (br. s, 1H), 3.85–3.50 (m, 3H), 3.38–2.99 (m, 4H), 2.90 (dd, $J = 4.6$ Hz, $J = 15.1$ Hz, 1H), 2.77–2.56 (m, 1H), 1.85–1.64 (m, 3H), 1.54–1.29 (m, 1H). ^{13}C NMR (126 MHz, DMSO- d_6) δ ppm: 172.7, 142.0, 136.1, 131.6, 130.2, 128.0, 128.0, 126.7, 120.9, 118.4, 117.7, 111.1, 108.1, 108.1, 77.1, 77.0, 67.2, 67.2, 53.2, 42.5, 42.4, 28.5, 28.4, 25.2, 25.2.

- *N*-((1,4-dioxan-2-yl)methyl)-1-(4-chlorophenyl)-2,3,4,9-tetrahydro-1*H*-pyrido[3,4-*b*]indole-3-carboxamide (**11**): (**1RS,3SR**)

Compound **11** was prepared using 1-(4-chlorophenyl)-2,3,4,9-tetrahydro-1*H*-pyrido[3,4-*b*]indole-3-carboxylic acid (**1e**) (2.3 mmol, 0.76 g) and EDC (3.0 mmol, 0.58 g), HOBT (3.0 mmol, 0.4 g), DMAP (1.17 mmol, 0.143 g), pyridine (0.1 mmol, 8 μ L) and (1,4-dioxan-2-yl)methanamine (2.3 mmol, 0.27 g) in 15 mL DCM. The product was purified by crystallization in hexane and obtained as a white solid with a yield of 15% ($R_f = 0.07$ (S_3)). LC/MS: $C_{23}H_{24}ClN_3O_3$ (98%) m/z : 426.15, found 426.04. 1H NMR (500, DMSO- d_6) δ ppm: 10.72 (s, 1H), 7.99–7.85 (m, 1H), 7.44–7.40 (m, 1H), 7.38–7.33 (m, 2H), 7.26–7.17 (m, 3H), 7.04–6.90 (m, 2H), 5.18 (br.s., 1H), 3.71–3.46 (m, 5H), 3.43–3.35 (m, 2H), 3.19–3.02 (m, 4H), 2.90 (dd, $J = 15.5$ Hz, 1H), 2.76–2.61 (m, 1H). ^{13}C NMR (126 MHz, DMSO- d_6) δ ppm: 172.9, 142.0, 136.1, 134.0, 131.7, 130.2, 128.1, 126.7, 121.0, 118.4, 117.7, 111.1, 108.0, 73.6, 73.6, 68.7, 65.9, 65.9, 65.8, 53.2, 51.7, 25.0.

- 1-(4-chlorophenyl)-*N*-(3-morpholinopropyl)-2,3,4,9-tetrahydro-1*H*-pyrido[3,4-*b*]indole-3-carboxamide (**12**): (**1RS,3SR**)-**12**/(**1RS,3RS**)-**12**

Compound **12** was prepared using 1-(4-chlorophenyl)-2,3,4,9-tetrahydro-1*H*-pyrido[3,4-*b*]indole-3-carboxylic acid (**1e**) (1.2 mmol, 0.39 g) and EDC (1.5 mmol, 0.30 g), HOBT (1.5 mmol, 0.20 g), DMAP (0.6 mmol, 0.07 g), pyridine (0.05 mmol, 4 μ L) and (1.2 mmol, 175 μ L) in 10 mL DCM. The obtained crude product was purified by column chromatography over silica gel (DCM/methanol = 95:5) and obtained as pink needlelike crystals with a yield of 45% ($R_f = 0.1$ (S_2)). LC/MS: $C_{25}H_{29}ClN_4O_2$ (96%) m/z : 453.20, found 453.04. ds: (**1RS,3SR**)-**12**/(**1RS,RS**)-**12** = 10:1.5. 1H NMR (500, $CDCl_3$) δ ppm: 8.00–7.89 (m, 1H), 7.70–7.58 (m, 2H), 7.39–7.34 (m, 3H), 7.30–7.19 (m, 4H), 5.34 (s, 1H), 3.68 (t, $J = 4.0$ Hz, 4H), 3.56 (dd, $J = 10.5$ Hz, 1H), 3.50–3.33 (m, 3H), 3.03–2.92 (m, 1H), 2.56–2.44 (m, 6H), 1.76 (quin, $J = 6.5$ Hz, 2H), *NH* proton was not detected. ^{13}C NMR (126 MHz, $CDCl_3$) δ ppm: 172.7, 139.9, 136.2, 133.9, 132.5, 129.9, 129.2, 128.7, 126.9, 122.3, 119.8, 118.5, 110.9, 110.4, 66.7, 66.7, 66.7, 57.3, 54.8, 53.8, 53.6, 52.4, 25.3, 25.0.

- 1-(4-chlorophenyl)-*N*-cyclohexyl-2,3,4,9-tetrahydro-1*H*-pyrido[3,4-*b*]indole-3-carboxamide (**13**)

Compound **13** was prepared using 1-(4-chlorophenyl)-2,3,4,9-tetrahydro-1*H*-pyrido[3,4-*b*]indole-3-carboxylic acid (**1e**) (0.25 mmol, 0.081 g) and EDC (0.325 mmol, 0.062 g), HOBT (0.325 mmol, 0.043 g), DMAP (0.125 mmol, 0.015 g), pyridine (0.1 mmol, 8 μ L) and cyclohexanamine (0.25 mmol, 28 μ L) in 4 mL DCM. The obtained product (mixture of *cis* and *trans* isomers) was purified and diastereoisomers were separated by column chromatography over silica gel ($R_f = 0.3$ and $R_f = 0.29$ (S_5)), overall yield 67%. LC/MS: $C_{24}H_{26}ClN_3O$ (96%) m/z : 408.94, found: 409.01.

- (**1RS,3SR**)-1-(4-chlorophenyl)-*N*-cyclohexyl-2,3,4,9-tetrahydro-1*H*-pyrido[3,4-*b*]indole-3-carboxamide (*trans*-**13**)

^1H NMR (500 MHz, CDCl_3) δ 7.94 (s, 1H), 7.57 (d, $J = 7.4$ Hz, 1H), 7.32–7.28 (m, 3H), 7.20 (dt, $J = 1.1$ Hz, 7.4 Hz, 1H), 7.17–7.13 (m, 3H), 6.75 (d, $J = 8.6$ Hz, 1H), 5.19 (s, 1H), 3.78–3.70 (m, 1H), 3.52 (dd, $J = 4.6$ Hz, 9.7 Hz, 1H), 3.28 (dd, $J = 4.9$ Hz, 15.8 Hz, 1H), 2.88 (ddd, $J = 1.7$ Hz, 9.9 Hz, 15.9 Hz, 1H), 2.10–1.99 (br.s., 1H), 1.93–1.83 (m, 2H), 1.70 (tdd, $J = 4.1$ Hz, 8.6 Hz, 16.5 Hz, 2H), 1.62 (td, $J = 3.7$ Hz, 12.6 Hz, 1H), 1.43–1.30 (m, 2H), 1.25–1.08 (m, 3H) ^{13}C NMR (126 MHz, CDCl_3) δ 171.6, 139.8, 136.2, 133.8, 132.5, 129.9, 128.7, 127.0, 122.3, 119.7, 118.5, 110.9, 110.5, 54.7, 52.3, 47.7, 33.1, 32.9, 25.5, 24.8, 24.7.

- (1SR,3SR)-1-(4-chlorophenyl)-*N*-cyclohexyl-2,3,4,9-tetrahydro-1*H*-pyrido[3,4-*b*]indole-3-carboxamide (*cis*-13)

^1H NMR (500 MHz, CDCl_3) δ 7.58–7.52 (m, 2H), 7.37–7.33 (m, 2H), 7.26–7.24 (m, 2H), 7.23–7.20 (m, 1H), 7.17–7.09 (m, 2H), 6.74 (d, $J = 8.6$ Hz, 1H), 5.15 (t, $J = 2.3$ Hz, 1H), 3.84–3.74 (m, 1H), 3.66 (dd, $J = 4.3$ Hz, 11.1 Hz, 1H), 3.33 (ddd, $J = 1.7$ Hz, 4.4 Hz, 15.6 Hz, 1H), 2.82 (ddd, $J = 2.3$ Hz, 11.1 Hz, 15.8 Hz, 1H), 1.96–1.85 (m, 2H), 1.75–1.65 (m, 2H), 1.61 (td, $J = 3.7$ Hz, 13.1 Hz, 1H), 1.41–1.29 (m, 2H), 1.22–1.09 (m, 3H).

- 1-(4-chlorophenyl)-*N*-(cyclohexylmethyl)-2,3,4,9-tetrahydro-1*H*-pyrido[3,4-*b*]indole-3-carboxamide (14): (1RS,3SR)

Compound **14** was prepared using 1-(4-chlorophenyl)-2,3,4,9-tetrahydro-1*H*-pyrido[3,4-*b*]indole-3-carboxylic acid (**1e**) (0.25 mmol, 0.081 g) and EDC (0.325 mmol, 0.062 g), HOBT (0.325 mmol, 0.043 g), DMAP (0.125 mmol, 0.015 g), pyridine (0.1 mmol, 8 μL) and cyclohexylmethanamine (0.25 mmol, 32 μL) in 8 mL DCM. The product was purified by crystallization in hexane and a few drops of acetone to give a pale yellow solid with a yield of 25% ($R_f = 0.09$ (S_3)). LC/MS: $\text{C}_{25}\text{H}_{28}\text{ClN}_3\text{O}$ (96%) m/z : 422.19 found: 422.10. ^1H NMR (500 MHz, CDCl_3) δ 7.76 (s, 1H), 7.57 (d, $J = 8.0$ Hz, 1H), 7.30–7.26 (m, 3H), 7.21–7.17 (m, 1H), 7.17–7.12 (m, 3H), 6.91 (t, $J = 5.7$ Hz, 1H), 5.23 (s, 1H), 3.56 (dd, $J = 4.6$ Hz, 9.7 Hz, 1H), 3.31 (dd, $J = 5.1$ Hz, 16.0 Hz, 1H), 3.16–3.09 (m, 1H), 3.02 (td, $J = 6.4$ Hz, 13.5 Hz, 1H), 2.89 (ddd, $J = 1.4$ Hz, 10.0 Hz, 16.0 Hz, 1H), 1.74–1.62 (m, 5H), 1.44 (ttd, $J = 3.4$ Hz, 7.3 Hz, 14.5 Hz, 1H), 1.29–1.07 (m, 4H), 0.95–0.85 (m, 2H). ^{13}C NMR (126 MHz, CDCl_3) δ 172.5, 139.3, 136.3, 134.6, 134.0, 130.0, 129.3, 127.2, 122.3, 119.9, 118.6, 111.1, 110.4, 58.4, 45.5, 38.0, 31.0, 26.5, 25.9.

3.3. PKa and Log D Calculation

The decimal logarithm distribution coefficient (Log D) was calculated using the MarvinSketch software (v. 20.12.0, ChemAxon Ltd., Cambridge, MA, USA).

3.4. *P. falciparum* Cultures and Drug Susceptibility Assay

Plasmodium falciparum cultures were established according to the method of Trager and Jensen, with slight modifications [24]. The CQ-susceptible strain, D10, and the CQ-resistant strain, W2, were maintained in human type A-positive red blood cells at 5% hematocrit in RPMI 1640 medium with the addition of 1% AlbuMax, 0.01% hypoxanthine, 20 mM Hepes, and 2 mM glutamine. Cultures were maintained at 37 °C in a gas mixture consisting of 1% O_2 , 5% CO_2 , and 94% N_2 . Compounds were dissolved in DMSO and diluted with medium to achieve the required concentrations (final DMSO concentration <1%, which is non-toxic to the parasite). Drugs were introduced into 96-well flat-bottomed microplates and serial dilutions made. Asynchronous cultures with parasitaemia of 1–1.5% and 1% final hematocrit were aliquoted into the plates and incubated for 72 h at 37 °C. Parasite growth was determined spectrophotometrically (OD_{650}) by measuring the activity of parasite lactate dehydrogenase (pLDH), according to a modified version of the method of Makler, in both control and drug-treated cultures [25]. The antimalarial activity is expressed as 50% inhibitory concentrations (IC_{50}); each IC_{50} value is the mean of at least three separate experiments performed in duplicate.

3.5. Cytotoxicity Assay on HMEC-1 Cell Line

The long-term human microvascular endothelial cell line (HMEC-1) was maintained in MCDB 131 medium supplemented with 10% fetal calf serum, 10 ng/mL of epidermal growth factor, 1 µg/mL of hydrocortisone, 2 mM glutamine and 20 mM Hepes buffer. For the cytotoxicity assays, cells were treated with serial dilutions of test compounds and cell proliferation evaluated using the MTT assay. Plates were incubated for 72 h at 37 °C in 5% CO₂, then 20 µL of a 5 mg/mL solution of 3-(4,5-dimethylthiazol-2-yl)-2,5-diphenyltetrazolium bromide (MTT) in PBS was added for an additional 3 h at 37 °C. The plates were then centrifuged, the supernatants discarded, and the dark blue formazan crystals dissolved using 100 µL of lysing buffer consisting of 20% (*w/v*) of a solution of SDS, 40% of *N,N* dimethylformamide in H₂O, at pH 4.7 adjusted with 80% acetic acid. The plates were then read on a microplate reader (Synergy 4 Bio-Tek Instruments, Thermo Fisher Scientific, Waltham, MA, USA) at a test wavelength of 550 nm and a reference wavelength of 650 nm. All the tests were performed in triplicate at least three times.

3.6. Determination of Hemolytic Activity

The study protocol was approved by the Bioethics Commission at the Lower Silesian Medical Chamber (1/PNHAB/2018, approval date 14 February 2018), and experiments were performed as previously described [26]. Compounds dissolved in DMSO were added in a volume corresponding to a final concentration of 10 µM in the sample. Negative (erythrocytes in PBS buffer), positive (erythrocytes in distilled water), and DMSO controls were also prepared.

3.7. Molecular Modeling

Molecular modeling studies were performed to evaluate the possible mechanism of action of compound (1*S*,3*R*)-7. Crystal structures of five enzymes, whose activities are essential for the functioning of *P. falciparum*, were taken from the Protein Data Bank. These enzymes were: phosphoethanolamine methyltransferase (PMT—code 3UJ9), falcipain-2 (FP2—code 3BPF), falcipain-3 (FP3—code 3BPM), lactate dehydrogenase (LDH—code 1T26), and malate dehydrogenase (MDH—code 6R8G). All simulations were performed using the Small-Molecule Drug Discovery Suite (Schrödinger, Inc, New York, NY, USA). The crystal structure of each enzyme was refined using the Protein Preparation Wizard [27]: system pH was set at 7.4 ± 0.2, all co-crystallized molecules (water molecules, other solvents using in the crystallization process), except a ligand (product/inhibitor/cofactor), were removed, hydrogen atoms were added, and the energy of the whole system was minimized using an OPLS3e force field. The structure of compound (1*S*,3*R*)-7 was optimized using the LigPrep tool (Schrödinger, Inc, New York, NY, USA). The proper protonation state at pH 7.4 was additionally verified using MarvinSketch software (ChemAxon, chemaxon.com accessed on 1st of April 2021, Cambridge, MA, USA). Induced-Fit Docking (IFD) was applied to dock compound (1*S*,3*R*)-7 to the selected enzyme crystal structures and its binding mode within each of the enzymes was evaluated [28]. For each crystal structure, the box centroid was set on the originally co-crystallized ligand: PMT—phosphocholine (product of the enzymatic reaction performed by PMT); FP2—epoxysuccinate (inhibitor); FP3—leupeptin (inhibitor); LDH—1,4-dihydropyridin-2(1*H*)-one adenine dinucleotide (NADH, cofactor); MDH—nicotinamide adenine dinucleotide (NAD, cofactor). No constraints were applied during IFD. Target-ligand complexes, obtained as an IFD output, were analyzed based on the observed molecular interactions. The observed binding modes of compound (1*S*,3*R*)-7 were compared with those captured for the ligands in the original crystal structures.

4. Conclusions

Malaria is still a major life-threatening infectious disease and, unfortunately, drug resistance to commonly used antimalarial drugs has become a serious problem. In this context, the search for new effective and selective agents active against this neglected parasite is obvious. Our studies led to the identification of a promising lead compound

among a series of tetrahydro- β -carboline derivatives that were designed and tested. Compound **7** has the highest activity against *P. falciparum* and is without any toxicity at the tested dose of 10 μ M. Moreover, compound (1*S*,3*R*)-**7** has structural features enabling it to interact with enzymes essential for the functioning of *P. falciparum*, but a thorough explanation of its mechanism of action as well as the optimal delivery system are still required. Interestingly, the chemical structure of compound (1*S*,3*R*)-**7** also appears to aid in its stabilization within the protein crystal co-structures. Our results also provide a basis for further scaffold optimization, that could lead to the design, synthesis, and identification of additional compounds with improved antiplasmodial potency.

Supplementary Materials: The following are available online at <https://www.mdpi.com/article/10.3390/ijms222413569/s1>.

Author Contributions: Conceptualization, A.J. and A.Z.; methodology, A.J., B.G., M.J., A.Z., S.P. and N.B.; software, M.J.; validation, A.J., B.G., M.J., A.Z., S.P. and N.B.; formal analysis, M.C.; investigation, A.J., B.G., M.J., S.P. and N.B.; resources, A.J., B.G., M.J., S.P., N.B. and A.Z.; data curation, A.J., B.G., M.J., A.Z., S.P. and N.B.; writing—original draft preparation, A.J., B.G., M.J. and A.Z.; writing—review and editing, A.J., S.P., N.B., D.T. and A.Z.; visualization, A.J., M.J., S.P., N.B. and A.Z.; supervision, A.J. and A.Z.; project administration, A.J. and N.B.; funding acquisition, A.J. and N.B. All authors have read and agreed to the published version of the manuscript.

Funding: The project is co-financed by the Polish National Agency for Academic Exchange (PPN/BIL/2018/2/00108) and the Italian Ministry of Foreign Affairs and International Cooperation “Executive Programme for Scientific and Technological Cooperation between the Italian Republic and the Republic of Poland” (PO19MO10). Publication of this article was financially supported by the Excellence Initiative—Research University (IDUB) program for the University of Wrocław.

Institutional Review Board Statement: Not applicable.

Informed Consent Statement: Not applicable.

Data Availability Statement: The data presented in this study are available in article or Supplementary Materials.

Conflicts of Interest: The authors declare no conflict of interest.

References

- World Malaria Report 2020. Available online: <https://www.who.int/teams/global-malaria-programme/reports/world-malaria-report-2020> (accessed on 11 October 2021).
- Available online: <https://www.who.int/news/item/06-10-2021-who-recommends-groundbreaking-malaria-vaccine-for-children-at-risk> (accessed on 23 October 2021).
- The “World Malaria Report 2019” at a Glance. Available online: <https://www.who.int/news-room/feature-stories/detail/world-malaria-report-2019> (accessed on 9 November 2020).
- Burrows, J.N.; Duparc, S.; Gutteridge, W.E.; Hooft Van Huijsduijnen, R.; Kaszubska, W.; Macintyre, F.; Mazzuri, S.; Möhrle, J.J.; Wells, T.N.C. New developments in anti-malarial target candidate and product profiles. *Malar. J.* **2017**, *16*, 26. [CrossRef]
- Ariey, F.; Witkowski, B.; Amaratunga, C.; Beghain, J.; Langlois, A.C.; Khim, N.; Kim, S.; Duru, V.; Bouchier, C.; Ma, L.; et al. A molecular marker of artemisinin-resistant *Plasmodium falciparum* malaria. *Nature* **2014**, *505*, 50–55. [CrossRef] [PubMed]
- Amaratunga, C.; Lim, P.; Suon, S.; Sreng, S.; Mao, S.; Sopha, C.; Sam, B.; Dek, D.; Try, V.; Amato, R.; et al. Dihydroartemisinin-piperaquine resistance in *Plasmodium falciparum* malaria in Cambodia: A multisite prospective cohort study. *Lancet Infect. Dis.* **2016**, *16*, 357–365. [CrossRef]
- Leang, R.; Taylor, W.R.J.; Bouth, D.M.; Song, L.; Tarning, J.; Char, M.C.; Kim, S.; Witkowski, B.; Duru, V.; Domergue, A.; et al. Evidence of *Plasmodium falciparum* malaria multidrug resistance to artemisinin and piperaquine in Western Cambodia: Dihydroartemisinin-piperaquine open-label multicenter clinical assessment. *Antimicrob. Agents Chemother.* **2015**, *59*, 4719–4726. [CrossRef] [PubMed]
- Bouwman, S.A.; Zoleko-Manego, R.; Renner, K.C.; Schmitt, E.K.; Mombo-Ngoma, G.; Grobusch, M.P. The early preclinical and clinical development of cipargamin (KAE609), a novel antimalarial compound. *Travel Med. Infect. Dis.* **2020**, *36*, 101765. [CrossRef] [PubMed]
- To Evaluate Efficacy, Safety, Tolerability and PK of Intravenous Cipargamin in Participants with Severe *Plasmodium Falciparum* Malaria-Full Text View-ClinicalTrials.gov. Available online: <https://clinicaltrials.gov/ct2/show/NCT04675931> (accessed on 27 September 2021).

10. Ghavami, M.; Merino, E.F.; Yao, Z.K.; Elahi, R.; Simpson, M.E.; Fernández-Murga, M.L.; Butler, J.H.; Casasanta, M.A.; Krai, P.M.; Totrov, M.M.; et al. Biological Studies and Target Engagement of the 2- C -Methyl- d -Erythritol 4-Phosphate Cytidylyltransferase (IspD)-Targeting Antimalarial Agent (1 R,3 S)-MMV008138 and Analogs. *ACS Infect. Dis.* **2018**, *4*, 549–559. [CrossRef] [PubMed]
11. Gorki, V.; Singh, R.; Walter, N.S.; Bagai, U.; Salunke, D.B. Synthesis and Evaluation of Antiplasmodial Efficacy of β -Carboline Derivatives against Murine Malaria. *ACS Omega* **2018**, *3*, 13200–13210. [CrossRef] [PubMed]
12. Gellis, A.; Dumètre, A.; Lanzada, G.; Hutter, S.; Ollivier, E.; Vanelle, P.; Azas, N. Preparation and antiprotozoal evaluation of promising β -carboline alkaloids. *Biomed. Pharmacother.* **2012**, *66*, 339–347. [CrossRef]
13. Garg, A.; Lukk, T.; Kumar, V.; Choi, J.Y.; Augagneur, Y.; Voelker, D.R.; Nair, S.; Mamoun, C. Ben Structure, Function and Inhibition of the Phosphoethanolamine Methyltransferases of the Human Malaria Parasites Plasmodium vivax and Plasmodium knowlesi. *Sci. Rep.* **2015**, *5*, 1–13. [CrossRef]
14. Makler, M.T.; Piper, R.C.; Milhous, W.K. Lactate Dehydrogenase and the Diagnosis of Malaria. *Parasitol. Today* **1998**, *14*, 376–377. [CrossRef]
15. Chan, M.; Sim, T.S. Functional characterization of an alternative [lactate dehydrogenase-like] malate dehydrogenase in Plasmodium falciparum. *Parasitol. Res.* **2004**, *92*, 43–47. [CrossRef] [PubMed]
16. Kerr, I.D.; Lee, J.H.; Pandey, K.C.; Harrison, A.; Sajid, M.; Rosenthal, P.J.; Brinen, L.S. Structures of Falcipain-2 and Falcipain-3 Bound to Small Molecule Inhibitors: Implications for Substrate Specificity. *J. Med. Chem.* **2009**, *52*, 852–857. [CrossRef]
17. Song, H.J.; Liu, Y.X.; Liu, Y.X.; Huang, Y.Q.; Li, Y.Q.; Wang, Q.M. Design, synthesis, anti-TMV, fungicidal, and insecticidal activity evaluation of 1,2,3,4-tetrahydro- β -carboline-3-carboxylic acid derivatives based on virus inhibitors of plant sources. *Bioorg. Med. Chem. Lett.* **2014**, *24*, 5228–5233. [CrossRef]
18. Eagon, S.; Hammill, J.T.; Bach, J.; Everson, N.; Sisley, T.A.; Walls, M.J.; Durham, S.; Pillai, D.R.; Falade, M.O.; Rice, A.L.; et al. Antimalarial activity of tetrahydro- β -carbolines targeting the ATP binding pocket of the Plasmodium falciparum heat shock 90 protein. *Bioorg. Med. Chem. Lett.* **2020**, *30*, 127502. [CrossRef]
19. Shibeshi, M.A.; Kifle, Z.D.; Atnafie, S.A. Antimalarial Drug Resistance and Novel Targets for Antimalarial Drug Discovery. *Infect. Drug Resist.* **2020**, *13*, 4047–4060. [CrossRef]
20. Imperatore, C.; Persico, M.; Senese, M.; Aiello, A.; Casertano, M.; Luciano, P.; Basilico, N.; Parapini, S.; Paladino, A.; Fattorusso, C.; et al. Exploring the antimalarial potential of the methoxy-thiazinoquinone scaffold: Identification of a new lead candidate. *Bioorg Chem.* **2019**, *85*, 240–252. [CrossRef]
21. Sonawane, D.P.; Persico, M.; Corbett, Y.; Chianese, G.; Di Dato, A.; Fattorusso, C.; Tagliatela-Scafati, O.; Taramelli, D.; Trombini, C.; Dhavale, D.D.; et al. New antimalarial 3-methoxy-1,2-dioxanes: Optimization of cellular pharmacokinetics and pharmacodynamics properties by incorporation of amino and N-heterocyclic moieties at C4. *RSC Adv.* **2015**, *5*, 72995–73010. [CrossRef]
22. Ungemach, F.; Soerens, D.; Weber, R.; DiPierro, M.; Campos, O.; Mokry, P.; Cook, J.M.; Silverton, J.V. General Method for the Assignment of Stereochemistry of 1,3-Disubstituted 1,2,3,4-tetrahydro- β -carbolines by Carbon-13 Spectroscopy. *J. Am. Chem. Soc.* **1980**, *102*, 6976–6984. [CrossRef]
23. Jaromin, A.; Czopek, A.; Parapini, S.; Basilico, N.; Misiak, E.; Gubernator, J.; Zagórska, A. Synthesis and Antiplasmodial Activity of Novel Bioinspired Imidazolidinedione Derivatives. *Biomolecules* **2021**, *11*, 33. [CrossRef]
24. Trager, W.; Jensen, J.B. Human malaria parasites in continuous culture. *Science* **1976**, *193*, 673–675. [CrossRef] [PubMed]
25. Makler, M.T.; Hinrichs, D.J. Measurement of the lactate dehydrogenase activity of Plasmodium falciparum as an assessment of parasitemia. *Am. J. Trop. Med. Hyg.* **1993**, *48*, 205–210. [CrossRef] [PubMed]
26. Jaromin, A.; Korycińska, M.; Piętka-Ottlik, M.; Musiał, W.; Peczyńska-Czoch, W.; Kaczmarek, Ł.; Kozubek, A. Membrane perturbations induced by new analogs of neocryptolepine. *Biol. Pharm. Bull.* **2012**, *35*, 1432–1439. [CrossRef] [PubMed]
27. Sastry, G.M.; Adzhigirey, M.; Day, T.; Annabhimoju, R.; Sherman, W. Protein and ligand preparation: Parameters, protocols, and influence on virtual screening enrichments. *J. Comput. Aided. Mol. Des.* **2013**, *27*, 221–234. [CrossRef] [PubMed]
28. Sherman, W.; Day, T.; Jacobson, M.P.; Friesner, R.A.; Farid, R. Novel procedure for modeling ligand/receptor induced fit effects. *J. Med. Chem.* **2006**, *49*, 534–553. [CrossRef] [PubMed]



Article

Vitamin D Analogs Regulate the Vitamin D System and Cell Viability in Ovarian Cancer Cells

Karina Piatek ¹, Andrzej Kutner ² , Dan Cacsire Castillo-Tong ³, Teresa Manhardt ¹, Nadja Kupper ¹ , Urszula Nowak ⁴ , Michał Chodyński ⁵ , Ewa Marcinkowska ⁴ , Enikő Kallay ¹ and Martin Schepelmann ^{1,*}

- ¹ Institute for Pathophysiology and Allergy Research, Medical University of Vienna, Waehringer Guertel 18-20, 1090 Vienna, Austria; karina.piatek@meduniwien.ac.at (K.P.); teresa.manhardt@meduniwien.ac.at (T.M.); nadja.kupper@meduniwien.ac.at (N.K.); enikoe.kallay@meduniwien.ac.at (E.K.)
 - ² Department of Bioanalysis and Drug Analysis, Faculty of Pharmacy, Medical University of Warsaw, 1 Banacha, 02-097 Warsaw, Poland; andrzej.kutner@wum.edu.pl
 - ³ Translational Gynecology Group, Department of Obstetrics and Gynecology, Comprehensive Cancer Center, Medical University of Vienna, 1090 Vienna, Austria; dan.cacsire-castillo@meduniwien.ac.at
 - ⁴ Faculty of Biotechnology, University of Wrocław, Joliot-Curie 14a, 50-383 Wrocław, Poland; urszula.nowak2@uw.edu.pl (U.N.); ema@cs.uni.wroc.pl (E.M.)
 - ⁵ Łukasiewicz Research Network—Industrial Chemistry Institute, 8 Rydygiera, 01-793 Warsaw, Poland; michal.chodynski@ichp.pl
- * Correspondence: martin.schepelmann@meduniwien.ac.at

Abstract: Background: Ovarian cancer (OC) is one of the most lethal cancers in women. The active form of vitamin D₃, 1,25-dihydroxyvitamin D₃ (1,25D₃, calcitriol) has anticancer activity in several cancers, including ovarian cancer, but the required pharmacological doses may cause hypercalcemia. We hypothesized that newly developed, low calcemic, vitamin D analogs (an1,25Ds) may be used as anticancer agents instead of calcitriol in ovarian cancer cells. Methods: We used two patient-derived high-grade serous ovarian cancer (HGSOC) cell lines with low (13781) and high (14433) mRNA expression levels of the gene encoding 1,25-dihydroxyvitamin D₃ 24-hydroxylase *CYP24A1*, one of the main target genes of calcitriol. We tested the effect of calcitriol and four structurally related series of an1,25Ds (PRI-1906, PRI-1907, PRI-5201, PRI-5202) on cell number, viability, the expression of *CYP24A1*, and the vitamin D receptor (VDR). Results: *CYP24A1* mRNA expression increased in a concentration-dependent manner after treatment with all compounds. In both cell lines, after 4 h, PRI-5202 was the most potent analog (in 13781 cells: EC₅₀ = 2.98 ± 1.10 nmol/L, in 14433 cells: EC₅₀ = 0.92 ± 0.20 nmol/L), while PRI-1907 was the least active one (in 13781 cells: EC₅₀ = n/d, in 14433 cells: EC₅₀ = n/d). This difference among the analogs disappeared after 5 days of treatment. The 13781 cells were more sensitive to the an1,25Ds compared with 14433 cells. The an1,25Ds increased nuclear VDR levels and reduced cell viability, but only in the 13781 cell line. Conclusions: The an1,25Ds had different potencies in the HGSOC cell lines and their efficacy in increasing *CYP24A1* expression was cell line- and chemical structure-dependent. Therefore, choosing sensitive cancer cell lines and further optimization of the analogs' structure might lead to new treatment options against ovarian cancer.

Keywords: vitamin D; vitamin D analogs; 25 vitamin D 24-hydroxylase; *CYP24A1*; proliferation; high-grade serous ovarian cancer cells

Citation: Piatek, K.; Kutner, A.; Cacsire Castillo-Tong, D.; Manhardt, T.; Kupper, N.; Nowak, U.; Chodyński, M.; Marcinkowska, E.; Kallay, E.; Schepelmann, M. Vitamin D Analogs Regulate the Vitamin D System and Cell Viability in Ovarian Cancer Cells. *Int. J. Mol. Sci.* **2022**, *23*, 172. <https://doi.org/10.3390/ijms23010172>

Academic Editor: Luciano Saso

Received: 23 September 2021

Accepted: 21 December 2021

Published: 24 December 2021

Publisher's Note: MDPI stays neutral with regard to jurisdictional claims in published maps and institutional affiliations.



Copyright: © 2021 by the authors. Licensee MDPI, Basel, Switzerland. This article is an open access article distributed under the terms and conditions of the Creative Commons Attribution (CC BY) license (<https://creativecommons.org/licenses/by/4.0/>).

1. Introduction

Ovarian cancer (OC), known as the “silent killer” showing no symptoms at early stages, is the deadliest gynecologic malignancy. Relapse after initial treatment is frequently fatal. Preventing relapse of the tumor is the ultimate, yet still unmet goal in treating OC patients. The standard treatment of OC is cytoreductive surgery and platinum-taxane-based chemotherapy. The use of platinum-based therapeutics is, however, limited in dosage and frequency due to their unspecific mode of action and toxic effects on normal cells,

severely reducing the patients' quality of life [1]. Very often, a small number of cells in the primary tumors escape the toxicity of the drugs. These cells will grow into a life-threatening recurrent disease that finally leads to death [1,2]. Low vitamin D levels were associated with increased risk for various cancers, suggesting a beneficial effect of supplementation or treatment with vitamin D, its active metabolites, or synthetic analogs [3,4].

Vitamin D₃ is produced in the skin by sunlight from 7-dehydrocholesterol [5]. Cytochrome P450 enzymes activate vitamin D in two steps: 25-hydroxylation in the liver, followed by 1 α -hydroxylation in the kidneys [6]. The most active form of vitamin D₃, 1,25-dihydroxyvitamin D₃ (calcitriol) binds to the vitamin D receptor (VDR), which acts as a ligand-activated transcription factor, binding to vitamin D response elements (VDRE) on target genes [7]. Liganded VDR upregulates the transcription of hundreds of target genes. The gene encoding 25-hydroxyvitamin D 24-hydroxylase (*CYP24A1*) is the most strongly upregulated one [8]. Hydroxylation of calcitriol at C-24, catalyzed by *CYP24A1*, initiates its catabolism to the inactive and water-soluble ultimate metabolite, calcitroic acid. *CYP24A1* thus provides negative feedback to the activity of calcitriol [9].

The expression of *CYP24A1* is usually low in the absence of calcitriol [10]. The gene contains multiple *VDRE* sequences and is highly responsive to liganded VDR [8]. *CYP24A1* is present in the inner mitochondrial membrane of all calcitriol responsive cells. After exposure to calcitriol, the expression of *CYP24A1* increases, however, the kinetics of the increase is cell-type specific [11]. Interestingly, several tumors have a high constitutive expression of *CYP24A1*, which may lower the local concentration of calcitriol in the cancer microenvironment [12].

The best-known role of calcitriol is to maintain the calcium-phosphate homeostasis of the organism [13]. It also stimulates other vital processes, such as the differentiation of keratinocytes, the development of immune cells, and the detoxification of the organism [14,15]. In numerous cancer cells, calcitriol inhibits proliferation and induces differentiation or apoptosis [4,16]. Different analogs of calcitriol (an1,25Ds; for simplicity, 1,25D includes both 1,25D₂ and 1,25D₃) were also shown to inhibit proliferation, modulate the immune response of different cancer cells, and reduce tumor growth and metastasis in animal models of various cancers [4,17].

Epidemiological data suggest that persons with low serum levels of the circulating form of vitamin D (25-hydroxyvitamin D, 25D), are at higher risk to develop HGSOC, and therefore, vitamin D supplementation might prevent ovarian carcinogenesis [18]. However, the use of calcitriol in therapeutic, supra-physiological doses is limited by its potent calcemic and phosphatemic activities. Over the years, several an1,25Ds were synthesized [19] with reduced or negligible calcemic and enhanced anticancer activity, as tested in leukemia, breast, prostate, and colon cancer cells [20–24]. However, an1,25Ds have not been extensively studied on OC cells, except for a single study of the 1,25D₃ analog (EB1089) several years ago [25]. Thus, although there are some reports on the activity of calcitriol in commercially available ovarian cancer cells, little is known on the effects of an1,25Ds on HGSOC cells.

We have previously shown that analogs of 1,25-dihydroxyergocalciferol (1,25-dihydroxyvitamin D₂, 1,25D₂) induced differentiation of human acute myeloid leukemia cells [21,26]. As the effect of calcitriol and of different an1,25Ds is very often cell- and tissue-dependent, in this study we tested if these novel, less calcemic an1,25Ds, known to be effective in colorectal and breast cancer models, are also effective in ovarian cancer cells. We compared the effect of a series of structurally related an1,25Ds (PRI-1906, PRI-1907, PRI-5201, PRI-5202, Figure 1) with that of calcitriol in two patient-derived HGSOC cell lines, to investigate if any of these analogs affect ovarian cancer cells and thus to evaluate the possibility of developing an1,25Ds as potential adjuvants for treatment of HGSOC.

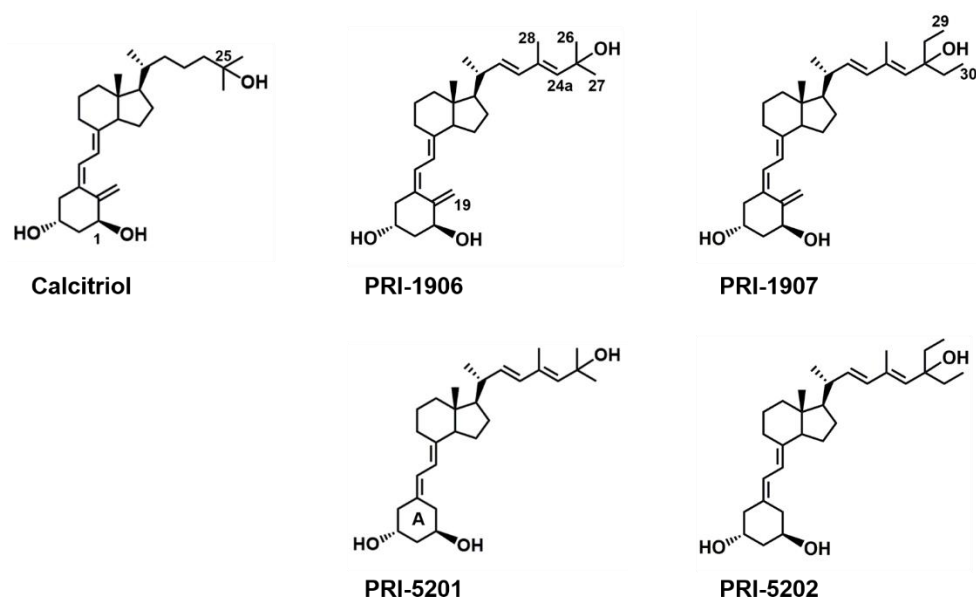


Figure 1. Chemical structures of calcitriol and the tested vitamin D analogs PRI-1906, PRI-1907, PRI-5201, and PRI-5202. Some carbons and rings are specifically labeled due to their structural importance (see discussion section).

2. Results

Synthetic an_{1,25}Ds of the most active forms of vitamin D (1,25D₃ and 1,25D₂) have been tested against several types of cancer [4], however, very little is known about their activity in ovarian cancer cells. We have chosen two cell lines (13781 and 14433) from our previously established patient-derived HGSOC cell line panel [27] and treated them with either calcitriol, as a widely used reference, or four side chain-modified an_{1,25}Ds (PRI-1906, PRI-1907, PRI-5201, and PRI-5202). The side-chain structure and especially the C-26, C-27 alkyls, contribute significantly to the binding affinity of the analog for VDR and thus to its functional activity. They surround the terminal C-25 hydroxyl group and affect the formation of a hydrogen bond with the amino acid residues His397 and His 397 of the ligand-binding pocket of the ligand-binding domain (LBD) of VDR [28].

2.1. Basal Expression of CYP24A1

The main known role of CYP24A1 (the 1,25-dihydroxy vitamin D 24-hydroxylase) enzyme, a mixed-function oxidase cytochrome P450 molecule, is to catabolize both the active form of vitamin D 1,25D and its precursor 25D, in order to prevent hypercalcemia.

Our previous RNA-seq data analysis [27] had already indicated that the 13781 cells have a lower basal level of CYP24A1 mRNA than 14433 cells. To validate the RNA-seq data, we measured the transcript number (Q) of the *CYP24A1* gene using quantitative real-time PCR (RT-qPCR). The results confirmed the data from the RNA-seq analysis. Basal level of CYP24A1 is around 10 times higher in 14433 cells (Q = 221,477 ± 16,629) than in 13781 cells (Q = 22,642 ± 5351) (Figure 2).

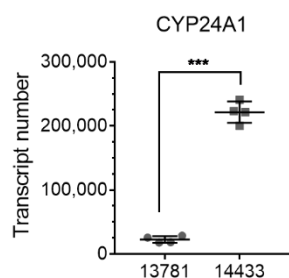


Figure 2. Absolute transcript number of CYP24A1 mRNA in the two cell lines 13781 and 14433 measured by absolute quantification RT-qPCR. Two-tailed *t*-test *** $p < 0.001$, $N = 4$.

2.2. Effect of Treatment with an1,25Ds on CYP24A1 Expression

As CYP24A1 is one of the best-known targets most strongly affected by activation of VDR, we have used its expression as a marker for the activity of the an1,25Ds in the treated cells.

2.2.1. Effect of Short-Term Treatment with an1,25Ds on CYP24A1 Expression

We treated the cells with the an1,25Ds at different concentrations (i.e., 0.1; 0.3; 1; 3; 10; 50; 100 nmol/L) for 4 h and calculated the EC₅₀ (half-maximal effective concentration) for their effect on CYP24A1 gene induction (Figures 3 and 4). In both cell lines, PRI-5202 was the most active analog with the lowest EC₅₀, and PRI-1907 was the least active one. The potency of the analogs was around two times higher in the 14433 cell line, which has a higher CYP24A1 basal expression level than in the 13781 cell line.

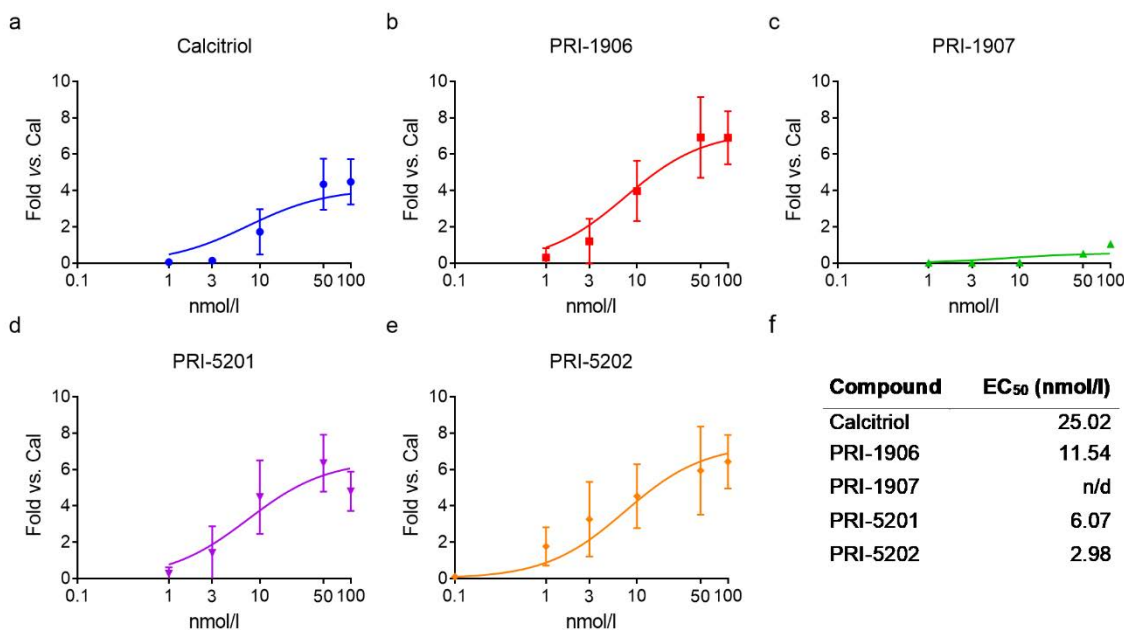


Figure 3. Activity of the compounds in the 13781 cell line. (a–e) Concentration-response curves of CYP24A1 expression after treatment with the an1,25Ds for 4 h. Mean \pm SD, nonlinear regression: sigmoidal three parameter fit with the following constraints: bottom > 0 , EC₅₀ > 0 ; $N = 3–8$. (f) The table shows the calculated EC₅₀ values (n/d = not determined).

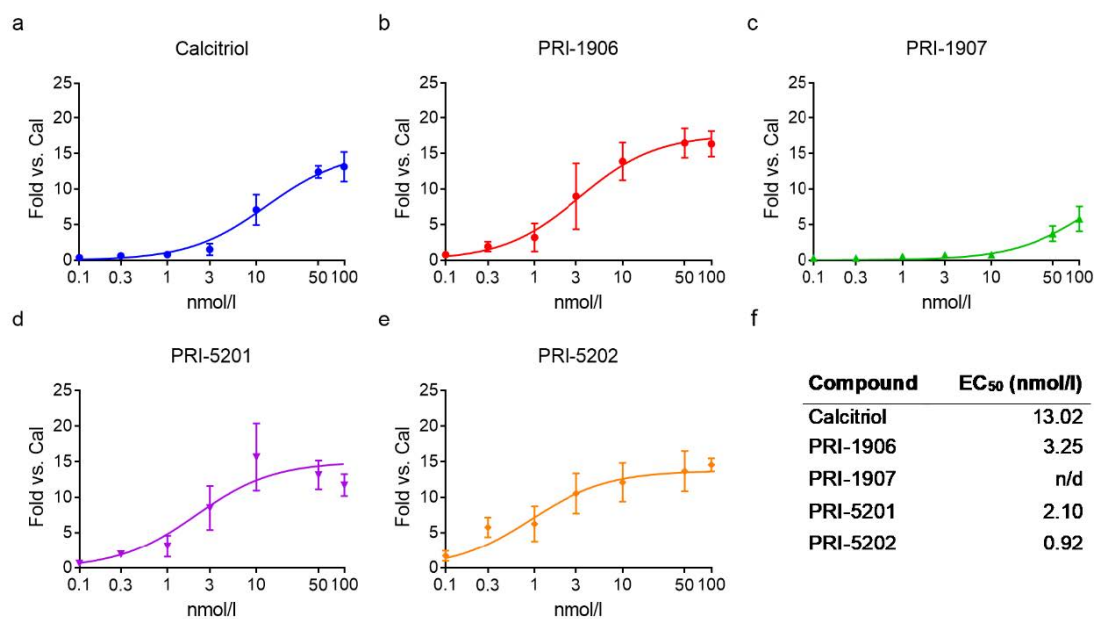


Figure 4. Activity of the compounds in the 14433 cell line. (a–e) Concentration-response curves for *CYP24A1* expression after treatment with the an1,25Ds for 4 h. Mean \pm SD, nonlinear regression: sigmoidal three parameter fit with the following constraints: bottom > 0, EC₅₀ > 0; N = 3–12. (f) The table shows the calculated EC₅₀ values (n/d = not determined).

2.2.2. Effect of Long-Term Treatment with an1,25Ds on Gene Expression

To study the long-term effect of the an1,25Ds, the cells were treated with each compound at 100 nmol/L for 4 h, 1, 3, and 5 days. After 5 days of treatment, the effect was stronger in the 13781 cells (Figure 5a) than in the 14433 cells (Figure 5b). This outcome probably results from the already high basal levels of *CYP24A1* mRNA in the 14433 cells, where an expression plateau is reached earlier.

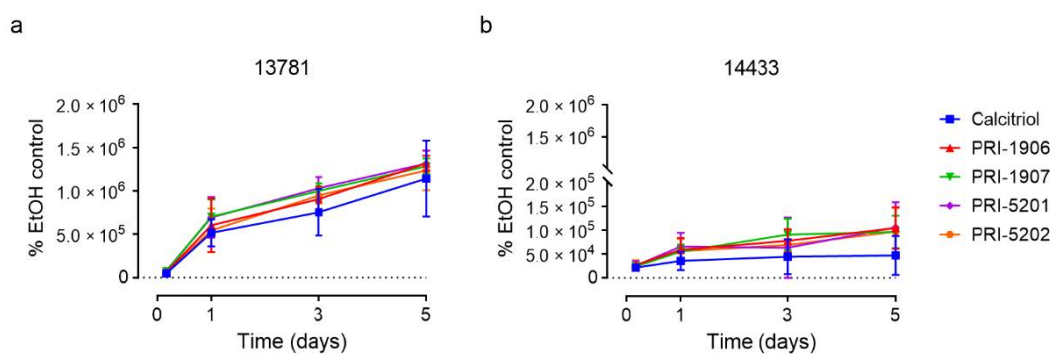


Figure 5. Expression of *CYP24A1* in (a) 13781 and (b) 14433 cells after treatment with an1,25Ds at 100 nmol/L at different time points (4 h, 1 day, 3, and 5 days). The diagrams show the percentage increase compared with the ethanol control. N = 3.

When we compared the effectiveness of the an1,25Ds in the two cell lines, we realized that the increase in *CYP24A1* expression compared to the basal level was always higher in the 13781 cells, compared with the 14433 cells (Table 1, raw values with SD used to calculate these ratios are shown in Supplementary Tables S1 and S2). While we see a stronger effect of PRI-5202 at 1 nmol/L, this difference disappears at a high concentration (100 nmol/L).

Table 1. Increase in *CYP24A1* expression in the 13781 cells relative to the expression increase in the 14433 cells.

13781/14433	1 nmol/L for 4 h ¹	100 nmol/L for 4 h ¹	100 nmol/L for 5 Days ¹
calcitriol	1.54	7.48	24.25
PRI-1906	2.02	8.50	12.58
PRI-1907	0.93	2.50	13.34
PRI-5201	1.79	7.97	12.43
PRI-5202	5.80	8.49	12.71

¹ Values are presented as *CYP24A1* expression increase from the basal level (% ethanol control) in 13781 cells as a fraction of the increase in 14433 cells.

We also tested the effect of an1,25Ds on other genes connected with inflammation and tumorigenesis (Supplementary Figure S1). In the 13781 cells, we observed that at a concentration of 100 nmol/L, all analogs increased the expression of CXCL1, CXCL2, IL-6, and IL-8 after 4 h after which the expression levels returned to the levels of the solvent control. On the other hand, the 14433 cells reacted with initial downregulation of CXCL1 and CXCL2 before returning to baseline levels while IL-6 and IL-8 were not affected by the treatments at all. These results again demonstrated the differential responsiveness of these cells to an1,25Ds.

2.3. Effect of Treatment with an1,25Ds on Nuclear VDR Level

To induce gene expression, the an1,25Ds bind to VDR, which is a transcription factor. In some cells, the ligands of VDR can either upregulate its expression or stabilize the protein. Therefore, our next step was to study the effect of the an1,25Ds on VDR protein level in the nucleus. The cells were treated for 5 days with each compound at a concentration of 100 nmol/L. After the treatment, we stained the cells and analyzed the VDR staining intensity in the nuclei of the cells using single-cell quantitative immunofluorescence. In the 13781 cell line, all compounds except PRI-1906 increased the nuclear intensity for VDR, indicating higher nuclear VDR protein levels (Figure 6a, Supplementary Table S3). In the 14433 cell line, only PRI-5201 increased nuclear VDR protein levels (Figure 6b, Supplementary Table S3).

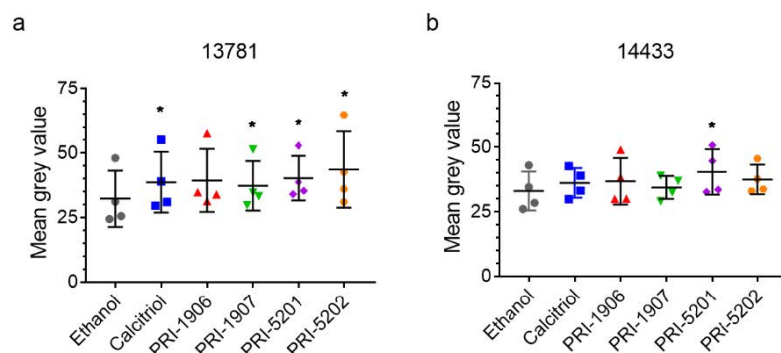


Figure 6. Nuclear VDR protein level in (a) 13781 and (b) 14433 cells after treatment with 100 nmol/L of an1,25Ds for 5 days. RM-ANOVA with Dunnett post-test vs. ethanol control, * $p < 0.05$, $N = 4$.

2.4. Effect of Treatment with an1,25Ds on the Proliferation of Ovarian Cancer Cells

As our previous experiments showed that the compounds affect the vitamin D system of the cells, we investigated the effect of the compounds on different markers of proliferation.

2.4.1. Effect of Treatment with an1,25Ds on Cell Number and Viability

In the 13781 cell line, all tested compounds significantly reduced the cell number (Figure 7a). In contrast, in the 14433 cell line a statistically significant reduction in the

number of cells was observed only after treatment with PRI-1907, PRI-5201, and PRI-5202, but not with calcitriol and PRI-1906 (Figure 7b). In addition to cell number, we measured cell viability directly. In the 13781 cell line, all tested compounds significantly reduced the viability of the cells (Figure 7c). In the 14433 cell line, we observed no significant effects on cell viability (Figure 7d), again highlighting the differences between the individual cell lines.

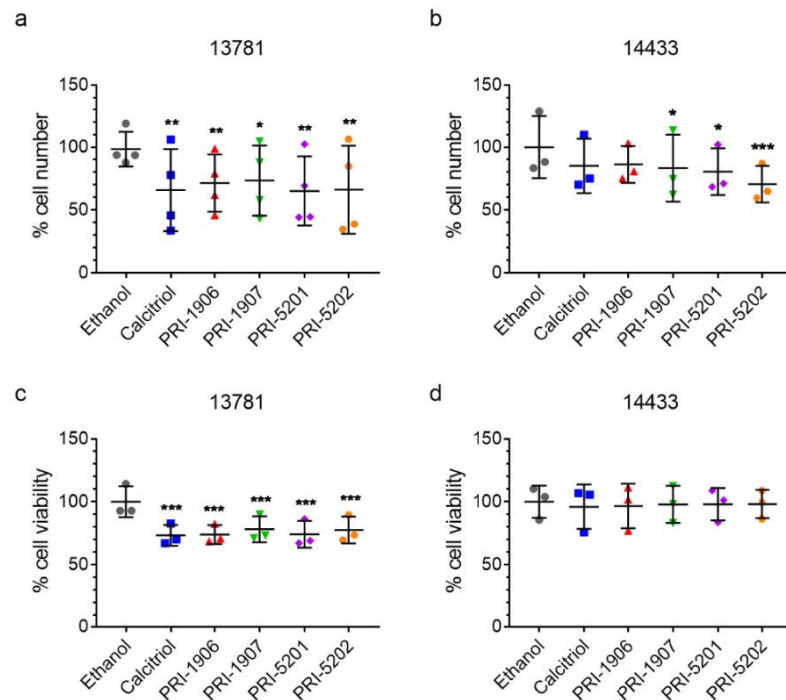


Figure 7. Cell number and viability in (a,c) 13781, and (b,d) 14433 cells after treatment with an1,25Ds at a concentration of 100 nmol/L for 5 days. RM-ANOVA with Dunnett post-test vs. ethanol control, * $p < 0.05$, ** $p < 0.01$, *** $p < 0.001$, N = 4 (a), 3 (b–d).

2.4.2. Effect of Treatment with an1,25Ds on Ki67 Expression

As we had observed a decrease in the cell viability after treatment with the an1,25Ds, we examined how the an1,25Ds affected the expression of the proliferation marker Ki67 in the treated cells. However, there were no significant differences in the percentage of Ki67-positive cells, independent of treatment and cell line (Figure 8, Supplementary Table S3 for values normalized to ethanol control). One explanation for the lack of downregulation could be that in these cells p53 is mutated [27], which might impair its ability to downregulate Ki67 [29].

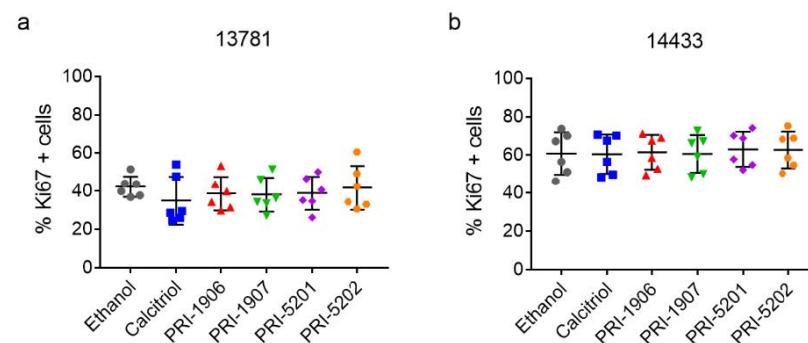


Figure 8. Percentage of Ki67 positive cells in (a) 13781 and (b) 14433 cells after treatment with 100 nmol/L of an1,25Ds for 5 days. RM-ANOVA with Dunnett post-test vs. ethanol control, N = 6.

3. Discussion

Numerous studies have shown that calcitriol had anticancer effects in different models of cancer [4]. However, a major drawback of its use in therapeutic super-physiological doses is the potentially lethal calcemic effect. This led to the development of analogs with lower calcemic effects, but with similar, or stronger anticancer properties [30,31]. In the present study, we have tested for the first time if single- and/or double-point modified analogs of the most active form of vitamin D are effective in HGSOc cells. We demonstrated that our an_{1,25}Ds were able to induce *CYP24A1* expression, suggesting that the vitamin D signaling system is working in these cells. The analogs also increased nuclear VDR levels and reduced cell number—effects which were time-, structure of the analog- and cell line-dependent.

This pilot study is the first paper testing the effectiveness of analogs of active vitamin D in patient-derived high-grade serous ovarian cancer cell lines. Our purpose was to assess if these analogs are able to induce an effect in these cells, and not to understand the whole picture of the functional profile of these compounds. For this purpose, we used two synthetic analogs of vitamin D modified at a single point, PRI-1906 with an extended and rigidified side chain, and its side-chain C-26-, C-27-homolog, PRI-1907. We have also used two double point-modified analogs, PRI-5201 and PRI-5202, additionally depleted of the 19-methylene in their A-ring (see Figure 1) and thus viewed as 19-*nor* variants of the former two [32]. We have compared their activity with calcitriol, as we already knew that the an_{1,25}Ds, except PRI-1907, were less calcemic in mice than calcitriol [33]. In this study, we proved that the response of HGSOc cell lines depends on the structure of the respective an_{1,25}Ds sensitive and the most pronounced activity was found for the double point-modified analogs (modified A-ring and side-chain). Compared to calcitriol, the most active analog PRI-5202 was a 19-*nor* compound extended at both C-26 and C-27.

The activity of the compounds was cell-line dependent, a property already observed earlier in other cell lines [33]. The differences were most pronounced at low concentration (1 nmol/L), while at high concentration (100 nmol/L), the differences leveled out. PRI-5202 was the most potent analog in inducing *CYP24A1* expression in both HGSOc cell lines, while PRI-1907 was the least potent one. Dual activity of PRI-1907 has been observed previously in HL60 cells, where this compound had the highest pro-differentiating effect, while it was least potent in inducing *CYP24A1* mRNA expression when compared with PRI-1906 and calcitriol [34]. This analog, although one of the most active analogs in leukemia and breast cancer models, had also the highest toxicity in animal models [22]. PRI-5202, the 19-*nor* version of PRI-1907 (see Figure 1), was much less toxic in animal models and had the lowest calcemic effect compared with all other an_{1,25}Ds [22,33]. In the tested HGSOc cells, PRI-5202 was the most active in increasing *CYP24A1* expression and reducing cell number even in the less responsive 14433 cells. Except for PRI-1907, all other an_{1,25}Ds were more active than calcitriol, when used at 1 nmol/L. This difference has disappeared when the an_{1,25}Ds were used at 100 nmol/L. The effect of PRI-1906 and PRI-5201 was very similar at all concentrations and treatment times.

Although there are some reports on the activity of calcitriol in ovarian cancer cells little is known about the functioning of an_{1,25}Ds in these cells. Previous studies have shown that calcitriol inhibited the expression of genes involved in proliferation, epithelial-to-mesenchymal transition, the Wnt pathway. However, most of these studies were performed in the commercially available cell lines OVCAR3 or SKOV3 [35–37], which are less reliable models of the most common type of ovarian cancer, the high-grade serous ovarian cancer. This is why we have used two of our patient-derived cell lines, chosen from a whole panel of HGSOc cells. The two tested ovarian cancer cell lines responded differently to the analogs depending on the duration of the treatment, manifesting in differential up- or downregulation of several target genes.

All an_{1,25}Ds, except PRI-1907, were very potent in inducing *CYP24A1* gene expression, as their EC₅₀-s were in the nanomolar range. The potency of the analogs (measured after 4 h treatment) was 2–3 times higher in the 14433 cells than in the 13781 cells; on the other

hand, the efficacy of the compounds (increasing *CYP24A1* expression from basal level) was higher in the 13781 line. This difference between the efficacies of the drugs in the two cell lines increased with the duration of the treatment. We suppose that this difference was due to the differences in the basal expression level of *CYP24A1*: in the 14433 cells, with higher basal levels of *CYP24A1*, the effect of the analogs is lower, because the already existent *CYP24A1* enzyme degrades the analogs, at least partially. The significant accumulation of nuclear VDR in the 13781 cells treated with the analogs might be another explanation for the higher responsiveness of these cells to the treatment with the an1,25Ds. These cells were also significantly less viable after treatment with the an1,25Ds than the 14433 cells.

In this study, we showed that the single- and double-point modified analogs of 1,25D₂ are active in HGSOC cells, and their activity depends on the cell-line and the chemical structure of the an1,25Ds. Next, we need to explore whether these compounds have anti-cancer effects in ovarian cancer cells. There is also an urgent need for new an1,25Ds which would be effective also in cell lines like 14433 and to discover what makes some HGSOCs responsive to an1,25Ds and others not. Based on these considerations, our results underline the necessity of testing more patient-derived cell lines, to understand the biological activity of the an1,25Ds in ovarian cancer. Understanding what makes these cells responsive to the analogs could help in designing analogs that have even higher anticancer activity and retain low toxicity.

4. Materials and Methods

4.1. Compounds

Calcitriol and the analogs (PRI-1906, PRI-1907, PRI-5201, PRI-5202) were obtained and handled as previously described [19,32]. All an1,25Ds were dissolved in ethanol, which was used as vehicle control at a maximum concentration of 0.1%.

4.2. Cell Culture

The patient-derived high-grade serous ovarian cancer cell lines (13781 and 14433) were selected from a panel of 34 cell lines [27]. Informed consent was obtained from all patients with HGSOC included in this study in the Department of Obstetrics and Gynecology, Medical University of Vienna. The study protocol was approved by the relevant ethics committees (EK No. 366/2003 and 260/2003). The cells were cultured in DMEM/F-12 (1:1) + GlutaMAX containing 10% fetal calf serum (FCS), 100 U/mL Pen-Strep (all Thermo Fisher Scientific, MA, USA). For the treatments with an1,25Ds, the cells were cultured for 2 days and then washed with phosphate-buffered saline (PBS) and cultured in the same medium containing only 2% FCS for the whole duration of the treatment.

4.3. Cell Number & Cell Viability

To measure cell number and viability, the cells were treated with 100 nmol/L of each compound for 5 days. For cell number, the cells were washed with PBS, detached using Trypsin-EDTA (Thermo Fisher Scientific) and the number of cells was determined using an automated cell counter TC10™ (Biorad, CA, USA). Cell viability was measured using CellTiter-Blue® Cell Viability Assay (Promega, WI, USA) according to the manufacturer's protocol. Fluorescence was measured in black-well plates from the bottom using a Tecan Infinite M200 PRO (Tecan AG, CH) with the following parameters: excitation 550 nm, emission 600 nm.

4.4. RT-qPCR

4.4.1. mRNA Expression Analysis

RNA was isolated using EXTRAzol Reagent (Blirt, PL) according to the manufacturer's protocol. cDNA was synthesized using a High Capacity cDNA Reverse Transcription Kit (Thermo Fisher Scientific). *CYP24A1* gene expression was analyzed in a quantitative polymerase chain reaction (qPCR) using Power SYBR Green PCR Master Mix (Thermo Fisher Scientific). Primers used for the reactions were *GAPDH*: fwd: 5'-

TCCTCTGACTTCAACAGCGAC-3', rev: 5'-TGCTGTAGCCAAATTCGTTGTC-3'; *CYP24A1*: fwd: 5'-CAAACCGTGGAAGGCTATC-3', rev: 5'-AGTCTTCCCCTTCCAGGATCA-3'; *CXCL1*: fwd: 5'-GAAAGCTTGCCTCAATCCTG-3', rev: 5'-CTTCTCCTCCCCTTCTGGT-3'; *CXCL2*: fwd: 5'-GGGCAGAAAGCTTGTCTCAA-3', rev: 5'-GCTTCTCCTTCCCTTCTGGT-3'; *IL-6*: fwd: 5'-AATTCGGTACATCCTCGACGG-3', rev: 5'-GGTTGTTTTCTGCCAGTGCC-3'; *IL-8*: fwd: 5'-GTTGGCAGCCTTCTGATTT-3', rev: 5'-TTCTTTAGCACTCCTTGGCAA-3'. Acquired data were analyzed using the $2^{-\Delta\Delta CT}$ method, [38] using *GAPDH* as the housekeeping gene and total human RNA (Takara, JP) as calibrator.

4.4.2. Quantitative Assessment of *CYP24A1* Transcript

To measure *CYP24A1* transcripts quantitatively, the following primers were used: fwd: 5'-CTCATGCTAAATACCCAGGTG-3', rev: 5'-TCGCTGGCAAACGCGATGGG-3'. The standard curve obtained using the amplicon of a known quantity, with the sequence matching the one produced from cDNA using these primers, was obtained in RT-qPCR. Constitutive expression of *CYP24A1* in 14433 and 13781 cells was measured from the cDNA, and the number of transcripts was read out from the standard curve.

4.5. Immunofluorescence

For immunofluorescence staining, cells were cultured on 8-chamber slides (Thermo Fisher Scientific). Cells were treated with 100 nmol/L of each compound for 5 days. After treatment, cells were fixed using 3.6% formaldehyde in PBS for 15 min. The fixed cells were incubated for 20 min in 0.2% Triton-X in PBS at room temperature (RT) for permeabilization followed by incubation with 50 mmol/L NH_4Cl for 15 min and 30 min in 3% BSA in PBS at RT for blocking. Cells were incubated with primary VDR (1:200) antibody (Merck Darmstadt, DE) for 1 h at RT or Ki67 (1:500) (Thermo Fisher Scientific) antibodies for 1 h at RT. An Alexa Fluor 647 conjugated anti-rabbit secondary antibody was used at a concentration of 1:500 in PBS for VDR staining visualization. Next cells were incubated with Ki67 (1:500) antibody (Thermo Fisher Scientific) for 1 h at RT. The Ki67 antibody had a fluorescence marker. Cells were counterstained using DAPI (Thermo Fisher Scientific) and mounted using Fluoromount G (Southern Biotech, Birmingham, AL, USA). Images of the stained cells were acquired using TissueFAXS hard- and software (TissueGnostics GmbH, Vienna, Austria) equipped with a Zeiss AxioImager Z1 using a Zeiss NeoFluar 20 \times /0.5 objective (Zeiss, Oberkochen, Germany).

4.6. Image Analysis

The acquired images were automatically analyzed using TissueQuest 6.0 software (TissueGnostics GmbH) using individual cell detection based on nuclear segmentation. A nuclear mask was used to detect the levels of Ki67 and VDR. Thresholds were set manually based on visual inspection to discriminate Ki67 positive from Ki67 negative cells and propagated to all samples. For VDR, mean pixel-intensities for each cell were used to determine the average grey value (=staining intensity) for each cell.

4.7. Data Analysis

Data analysis was performed using Microsoft Excel (Microsoft, Redmond, WA, USA) and statistical analysis was performed using GraphPad Prism 7.0 (Graphpad Software, San Diego, CA, USA). Employed statistical tests are described in the respective figure legends.

Supplementary Materials: All data are available online at <https://www.mdpi.com/article/10.3390/ijms23010172/s1>.

Author Contributions: Conceptualization, A.K., E.K., M.S., E.M.; methodology, E.K., E.M., K.P., M.S.; validation, K.P.; formal analysis, K.P., M.S.; investigation, K.P., N.K., T.M., U.N.; resources, D.C.C.-T., E.K., E.M., M.C., M.S.; data curation, K.P.; writing—original draft preparation, E.K., K.P., M.S.; writing—review and editing, A.K., D.C.C.-T., E.K., E.M., K.P., M.S., M.C.; visualization, K.P.,

M.S.; supervision, E.K., M.S.; project administration, E.K., M.S.; funding acquisition, E.K., E.M., M.S. All authors have read and agreed to the published version of the manuscript.

Funding: This research was funded by: the Austrian Science Fund (FWF) and the Herzfelder'sche Familienstiftung, grant number P 32840-B (to M.S.); the Austrian Science Fund (FWF), grant number P 29948-B28 (to E.K.); The National Science Centre of Poland, grant OPUS 2015/17/B/NZ4/02632 (to E.M.).

Institutional Review Board Statement: Informed consent was obtained from all patients with HG-SOC included in this study in the Department of Obstetrics and Gynecology, Medical University of Vienna. The study protocol was approved by the relevant ethics committees (EK No. 366/2003 and 260/2003).

Informed Consent Statement: Informed consent was obtained from all subjects involved in the study.

Conflicts of Interest: The authors declare no conflict of interest.

References

1. Mikula-Pietrasik, J.; Witucka, A.; Pakula, M.; Uruski, P.; Begier-Krasinska, B.; Niklas, A.; Tykarski, A.; Ksiazek, K. Comprehensive review on how platinum- and taxane-based chemotherapy of ovarian cancer affects biology of normal cells. *Cell. Mol. Life Sci.* **2019**, *76*, 681–697. [CrossRef] [PubMed]
2. Charkhchi, P.; Cybulski, C.; Gronwald, J.; Wong, F.O.; Narod, S.A.; Akbari, M.R. CA125 and Ovarian Cancer: A Comprehensive Review. *Cancers* **2020**, *12*, 3730. [CrossRef] [PubMed]
3. Guo, H.; Guo, J.; Xie, W.; Yuan, L.; Sheng, X. The role of vitamin D in ovarian cancer: Epidemiology, molecular mechanism and prevention. *J. Ovarian Res.* **2018**, *11*, 71. [CrossRef] [PubMed]
4. Carlberg, C.; Munoz, A. An update on vitamin D signaling and cancer. In *Seminars in Cancer Biology*; Academic Press: Cambridge, MA, USA, 2020. [CrossRef]
5. Holick, M.; MacLaughlin, J.; Clark, M.; Holick, S.; Potts, J.J.; Anderson, R.; Blank, I.; Parrish, J.; Elias, P. Photosynthesis of previtamin D₃ in human skin and the physiologic consequences. *Science* **1980**, *210*, 203–205. [CrossRef] [PubMed]
6. Prosser, D.; Jones, G. Enzymes involved in the activation and inactivation of vitamin D. *Trends Biochem. Sci.* **2004**, *29*, 664–673. [CrossRef]
7. Carlberg, C.; Seuter, S.; de Mello, V.; Schwab, U.; Voutilainen, S.; Pulkki, K.; Nurmi, T.; Virtanen, J.; Tuomainen, T.; Uusitupa, M. Primary vitamin D target genes allow a categorization of possible benefits of vitamin D₃ supplementation. *PLoS ONE* **2013**, *8*, e71042.
8. Vaisanen, S.; Dunlop, T.; Sinkkonen, L.; Frank, C.; Carlberg, C. Spatio-temporal activation of chromatin on the human CYP24 gene promoter in the presence of 1 α ,25-dihydroxyvitamin D₃. *J. Mol. Biol.* **2005**, *350*, 65–77. [CrossRef]
9. Christakos, S.; Dhawan, P.; Verstuyf, A.; Verlinden, L.; Carmeliet, G. Vitamin D: Metabolism, Molecular Mechanism of Action, and Pleiotropic Effects. *Physiol. Rev.* **2016**, *96*, 365–408. [CrossRef]
10. Roff, A.; Wilson, R.T. A novel SNP in a vitamin D response element of the CYP24A1 promoter reduces protein binding, transactivation, and gene expression. *J. Steroid Biochem. Mol. Biol.* **2008**, *112*, 47–54. [CrossRef]
11. Berkowska, K.; Corcoran, A.; Grudzień, M.; Jakuszek, A.; Chodyński, M.; Kutner, A.; Marcinkowska, E. Investigating the role of megalin in semi-selectivity 2 of side-chain modified 19-nor analogs of vitamin D. *Int. J. Mol. Sci.* **2019**, *20*, 4183. [CrossRef]
12. Höbaus, J.; Hummel, D.; Thiem, U.; Fetahu, I.; Aggarwal, A.; Müllauer, L.; Heller, G.; Egger, G.; Mesteri, I.; Baumgartner-Parzer, S.; et al. Increased copy-number and not DNA hypomethylation causes overexpression of the candidate proto-oncogene CYP24A1 in colorectal cancer. *Int. J. Cancer* **2013**, *133*, 1380–1388. [CrossRef] [PubMed]
13. Holick, M.F. Vitamin D and bone health. *J. Nutr.* **1996**, *126*, 1159S–1164S. [CrossRef] [PubMed]
14. Feldman, D.; Krishnan, A.V.; Swami, S.; Giovannucci, E.; Feldman, B.J. The role of vitamin D in reducing cancer risk and progression. *Nat. Rev. Cancer* **2014**, *14*, 342–357. [CrossRef] [PubMed]
15. Makishima, M.; Lu, T.T.; Xie, W.; Whitfield, G.K.; Domoto, H.; Evans, R.M.; Haussler, M.R.; Mangelsdorf, D.J. Vitamin D receptor as an intestinal bile acid sensor. *Science* **2002**, *296*, 1313–1316. [CrossRef]
16. Trump, D.L.; Deeb, K.K.; Johnson, C.S. Vitamin D: Considerations in the continued development as an agent for cancer prevention and therapy. *Cancer J.* **2010**, *16*, 1–9. [CrossRef] [PubMed]
17. Fernandez-Barral, A.; Bustamante-Madrid, P.; Ferrer-Mayorga, G.; Barbachano, A.; Larriba, M.J.; Munoz, A. Vitamin D Effects on Cell Differentiation and Stemness in Cancer. *Cancers* **2020**, *12*, 2413. [CrossRef] [PubMed]
18. Ong, J.S.; Cuellar-Partida, G.; Lu, Y.; Australian Ovarian Cancer Study; Fasching, P.A.; Hein, A.; Burghaus, S.; Beckmann, M.W.; Lambrechts, D.; Van Nieuwenhuysen, E.; et al. Association of vitamin D levels and risk of ovarian cancer: A Mendelian randomization study. *Int. J. Epidemiol.* **2016**, *45*, 1619–1630. [CrossRef] [PubMed]
19. Nadkarni, S.; Chodynski, M.; Corcoran, A.; Marcinkowska, E.; Brown, G.; Kutner, A. Double point modified analogs of vitamin D as potent activators of vitamin D receptor. *Curr. Pharm. Des.* **2015**, *21*, 1741–1763. [CrossRef]

20. Baurka, H.; Kielbinski, M.; Biecek, P.; Haus, O.; Jazwiec, B.; Kutner, A.; Marcinkowska, E. Monocytic differentiation induced by side-chain modified analogs of vitamin D in ex vivo cells from patients with acute myeloid leukemia. *Leuk. Res.* **2014**, *38*, 638–647. [CrossRef]
21. Nachliely, M.; Trachtenberg, A.; Khalfin, B.; Nalbandyan, K.; Cohen-Lahav, M.; Yasuda, K.; Sakaki, T.; Kutner, A.; Danilenko, M. Dimethyl fumarate and vitamin D derivatives cooperatively enhance VDR and Nrf2 signaling in differentiating AML cells in vitro and inhibit leukemia progression in a xenograft mouse model. *J. Steroid Biochem. Mol. Biol.* **2019**, *188*, 8–16. [CrossRef]
22. Wietrzyk, J.; Nevozhay, D.; Milczarek, M.; Filip, B.; Kutner, A. Toxicity and antitumor activity of the vitamin D analogs PRI-1906 and PRI-1907 in combined treatment with cyclophosphamide in a mouse mammary cancer model. *Cancer Chemother. Pharmacol.* **2008**, *62*, 787–797. [CrossRef]
23. Milczarek, M.; Chodynski, M.; Pietraszek, A.; Stachowicz-Suhs, M.; Yasuda, K.; Sakaki, T.; Wietrzyk, J.; Kutner, A. Synthesis, CYP24A1-Dependent Metabolism and Antiproliferative Potential against Colorectal Cancer Cells of 1,25-Dihydroxyvitamin D₂ Derivatives Modified at the Side Chain and the A-Ring. *Int. J. Mol. Sci.* **2020**, *21*, 642. [CrossRef] [PubMed]
24. Baurka, H.; Klopot, A.; Kielbinski, M.; Chrobak, A.; Wijas, E.; Kutner, A.; Marcinkowska, E. Structure-function analysis of vitamin D₂ analogs as potential inducers of leukemia differentiation and inhibitors of prostate cancer proliferation. *J. Steroid Biochem. Mol. Biol.* **2011**, *126*, 46–54. [CrossRef] [PubMed]
25. Zhang, X.; Jiang, F.; Li, P.; Li, C.; Ma, Q.; Nicosia, S.V.; Bai, W. Growth suppression of ovarian cancer xenografts in nude mice by vitamin D analogue EB1089. *Clin. Cancer Res.* **2005**, *11*, 323–328.
26. Nachliely, M.; Sharony, E.; Kutner, A.; Danilenko, M. Novel analogs of 1,25-dihydroxyvitamin D₂ combined with a plant polyphenol as highly efficient inducers of differentiation in human acute myeloid leukemia cells. *J. Steroid Biochem. Mol. Biol.* **2016**, *164*, 59–65. [CrossRef] [PubMed]
27. Kreuzinger, C.; von der Decken, I.; Wolf, A.; Gamperl, M.; Koller, J.; Karacs, J.; Pfaffinger, S.; Bartl, T.; Reinhaller, A.; Grimm, C.; et al. Patient-derived cell line models revealed therapeutic targets and molecular mechanisms underlying disease progression of high grade serous ovarian cancer. *Cancer Lett.* **2019**, *459*, 1–12. [CrossRef] [PubMed]
28. Wanat, M.; Malinska, M.; Kutner, A.; Wozniak, K. Effect of Vitamin D Conformation on Interactions and Packing in the Crystal Lattice. *Cryst. Growth Des.* **2018**, *18*, 3385–3396. [CrossRef]
29. Engeland, K. Cell cycle arrest through indirect transcriptional repression by p53: I have a DREAM. *Cell Death Differ.* **2018**, *25*, 114–132. [CrossRef] [PubMed]
30. Arai, M.A.; Kittaka, A. Novel 2-alkyl-1 α ,25-dihydroxy-19-norvitamin D₃: Efficient synthesis with Julia olefination, evaluation of biological activity and development of new analyzing system for co-activator recruitment. *Anticancer Res.* **2006**, *26*, 2621–2631.
31. Yang, S.W.; Tsai, C.Y.; Pan, Y.C.; Yeh, C.N.; Pang, J.H.; Takano, M.; Kittaka, A.; Juang, H.H.; Chen, T.C.; Chiang, K.C. MART-10, a newly synthesized vitamin D analog, represses metastatic potential of head and neck squamous carcinoma cells. *Drug Des. Dev. Ther.* **2016**, *10*, 1995–2002. [CrossRef]
32. Pietraszek, A.; Malinska, M.; Chodynski, M.; Krupa, M.; Krajewski, K.; Cmoch, P.; Wozniak, K.; Kutner, A. Synthesis and crystallographic study of 1,25-dihydroxyergocalciferol analogs. *Steroids* **2013**, *78*, 1003–1014. [CrossRef] [PubMed]
33. Trynda, J.; Turlej, E.; Milczarek, M.; Pietraszek, A.; Chodynski, M.; Kutner, A.; Wietrzyk, J. Antiproliferative Activity and in Vivo Toxicity of Double-Point Modified Analogs of 1,25-Dihydroxyergocalciferol. *Int. J. Mol. Sci.* **2015**, *16*, 24873–24894. [CrossRef]
34. Baurka, H.; Marchwicka, A.; Klopot, A.; Kutner, A.; Marcinkowska, E. Studies on the mechanisms of superagonistic pro-differentiating activities of side-chain modified analogs of vitamin D₂. *Oncol. Rep.* **2012**, *28*, 1110–1116. [CrossRef] [PubMed]
35. Li, P.; Li, C.; Zhao, X.; Zhang, X.; Nicosia, S.V.; Bai, W. p27(Kip1) stabilization and G(1) arrest by 1,25-dihydroxyvitamin D(3) in ovarian cancer cells mediated through down-regulation of cyclin E/cyclin-dependent kinase 2 and Skp1-Cullin-F-box protein/Skp2 ubiquitin ligase. *J. Biol. Chem.* **2004**, *279*, 25260–25267. [CrossRef]
36. Shen, Z.; Zhang, X.; Tang, J.; Kasiappan, R.; Jinwal, U.; Li, P.; Hann, S.; Nicosia, S.V.; Wu, J.; Zhang, X.; et al. The coupling of epidermal growth factor receptor down regulation by 1 α ,25-dihydroxyvitamin D₃ to the hormone-induced cell cycle arrest at the G1-S checkpoint in ovarian cancer cells. *Mol. Cell. Endocrinol.* **2011**, *338*, 58–67. [CrossRef] [PubMed]
37. Hou, Y.F.; Gao, S.H.; Wang, P.; Zhang, H.M.; Liu, L.Z.; Ye, M.X.; Zhou, G.M.; Zhang, Z.L.; Li, B.Y. 1 α ,25(OH)₂D₃ Suppresses the Migration of Ovarian Cancer SKOV-3 Cells through the Inhibition of Epithelial-Mesenchymal Transition. *Int. J. Mol. Sci.* **2016**, *17*, 1285. [CrossRef]
38. Livak, K.J.; Schmittgen, T.D. Analysis of relative gene expression data using real-time quantitative PCR and the 2^{(-Delta Delta C(T))} Method. *Methods* **2001**, *25*, 402–408. [CrossRef]



Article

Differential Response of Lung Cancer Cells, with Various Driver Mutations, to Plant Polyphenol Resveratrol and Vitamin D Active Metabolite PRI-2191

Ewa Maj ^{1,*} , Beata Maj ¹, Klaudia Bobak ¹, Michalina Gos ¹, Michał Chodyński ² , Andrzej Kutner ³ and Joanna Wietrzyk ¹

¹ Hirszfeld Institute of Immunology and Experimental Therapy, Polish Academy of Sciences, 12 Weigla, 53-114 Wrocław, Poland; maj.beata9@gmail.com (B.M.); klaudia.bobak13@gmail.com (K.B.); michalina.gos104@gmail.com (M.G.); joanna.wietrzyk@hirszfeld.pl (J.W.)

² Łukasiewicz Research Network—Industrial Chemistry Institute, 8 Rydygiera, 01-793 Warsaw, Poland; m.chodynski@ifarm.eu

³ Faculty of Mathematics and Natural Sciences, School of Sciences, Institute of Chemical Sciences, Cardinal Stefan Wyszyński University in Warsaw, 1/3 Wóycickiego, 01-938 Warsaw, Poland; a.kutner@uksw.edu.pl

* Correspondence: ewa.maj@hirszfeld.pl; Tel.: +48-71-370-9942

Citation: Maj, E.; Maj, B.; Bobak, K.; Gos, M.; Chodyński, M.; Kutner, A.; Wietrzyk, J. Differential Response of Lung Cancer Cells, with Various Driver Mutations, to Plant Polyphenol Resveratrol and Vitamin D Active Metabolite PRI-2191. *Int. J. Mol. Sci.* **2021**, *22*, 2354. <https://doi.org/10.3390/ijms22052354>

Academic Editor:
Alexander Schramm

Received: 1 February 2021
Accepted: 22 February 2021
Published: 26 February 2021

Publisher's Note: MDPI stays neutral with regard to jurisdictional claims in published maps and institutional affiliations.



Copyright: © 2021 by the authors. Licensee MDPI, Basel, Switzerland. This article is an open access article distributed under the terms and conditions of the Creative Commons Attribution (CC BY) license (<https://creativecommons.org/licenses/by/4.0/>).

Abstract: Plant polyphenols and vitamins D exhibit chemopreventive and therapeutic anticancer effects. We first evaluated the biological effects of the plant polyphenol resveratrol (RESV) and vitamin D active metabolite PRI-2191 on lung cancer cells having different genetic backgrounds. RESV and PRI-2191 showed divergent responses depending on the genetic profile of cells. Antiproliferative activity of PRI-2191 was noticeable in EGFRmut cells, while RESV showed the highest antiproliferative and caspase-3-inducing activity in KRASmut cells. RESV upregulated p53 expression in wtp53 cells, while downregulated it in mutp53 cells with simultaneous upregulation of p21 expression in both cases. The effect of PRI-2191 on the induction of CYP24A1 expression was enhanced by RESV in two KRASmut cell lines. The effect of RESV combined with PRI-2191 on cytokine production was pronounced and modulated. RESV cooperated with PRI-2191 in regulating the expression of IL-8 in EGFRmut cells, while OPN in KRASmut cells and PD-L1 in both cell subtypes. We hypothesize that the differences in response to RESV and PRI-2191 between EGFRmut and KRASmut cell lines result from the differences in epigenetic modifications since both cell subtypes are associated with the divergent smoking history that can induce epigenetic alterations.

Keywords: anticancer activity; lung cancer; resveratrol; PRI-2191; vitamin D

1. Introduction

Accumulating evidence has demonstrated the chemopreventive and therapeutic potential of polyphenolic antioxidants derived from plants in various preclinical models of human cardiovascular, metabolic, neurodegenerative, and cancer diseases. The chemopreventive and therapeutic effects of these compounds are believed to involve the regulation of signaling pathways like mitogen-activated protein kinases, p53-MDM2 (MDM—ubiquitin E3 ligase of the tumor suppressor p53), nuclear factor-kappaB (NFκB). By modulating these cell signaling pathways, polyphenols activate the cell death signals and induce apoptosis of precancerous or malignant cells, thereby inhibiting the development or progression of cancer [1–3]. In addition, the antiangiogenic activity of these compounds was under investigation. Studies showed that this activity of the plant polyphenols involves the inhibition of endothelial cell proliferation and migration, prevention of sprout formation, inhibition of matrix metalloproteinases, and modulation of angiogenic signaling pathways [4]. Commonly studied polyphenols, such as curcumin, quercetin, and resveratrol (RESV; Figure 1), interact with multiple protein targets and thus modulate the signaling pathways related to various diseases [5].

Plant-originated substances demonstrated synergism when used in combination with different anticancer agents. For example, RESV, a natural stilbenoid phenol, which is produced by plants in response to injury or attack of pathogens, was tested in combination with other substances, including anticancer drugs. Although there is a lack of randomized controlled trials analyzing the effect of this substance on humans, RESV sensitized tumor cells in neuroblastoma, glioma, breast cancer, prostate cancer, pancreatic cancer, and leukemia to the proapoptotic effects of cytostatics such as doxorubicin, 5-fluorouracil, or cisplatin [6]. Kubota et al. studied the activity of RESV and paclitaxel, one of the primary cytostatics used in the treatment of lung cancer. The authors reported the antiproliferative effect and pro-apoptotic properties of this cytostatic potentiated by RESV in lung A549 cells [7]. Baatout et al. demonstrated high-dose RESV sensitizing chronic myeloid leukemia or cervical cancer cells to X-rays [8]. Beneficial role of polyphenols in the prevention and management of lung cancer in vitro have been already described [9,10].

Moreover, 1,25-dihydroxycholecalciferol (1,25(OH)₂D₃, calcitriol; Figure 1), the most active hormonal form of vitamin D₃, exerts anticancer effects by regulating proliferation, differentiation, apoptosis, and angiogenesis [11]. The antiproliferative activity of vitamin D compounds was therefore tested in different cancer models, including leukemia and lymphoma, breast cancer, prostate cancer, colon cancer, and lung cancer [12–15]. Studies on animal cancer models have also indicated several vitamin D analogs as potent agents, especially when used in combination with chemotherapeutics [16–20]. However, not all types of cancer cells are equally sensitive to the anticancer properties of vitamins D. Therefore, several studies were performed to understand why cancer cells vary in their response to vitamins D and what is the mechanism of the resistance of certain cancer cells to the antiproliferative activity of 1,25(OH)₂D₃ and other vitamin D compounds [21].

A number of oncogenic driver mutations have been identified in lung cancer with the EGFR and KRAS mutations as the most prevalent and with significant clinical implications. Briefly, EGFR mutations are common in never smokers and respond to targeted therapy with the use of tyrosine kinase inhibitors (erlotinib and gefitinib), while KRAS mutations are associated with smoking history and are difficult to target. What is more, EGFR and KRAS mutations are mutually exclusive [22,23]. Additionally, among genetic abnormalities responsible for tumorigenesis of lung cancer are mutations of tumor suppressor gene TP53 [22,24,25].

In our previous study, we analyzed the antiproliferative activity of vitamin D₃ active metabolite ((24R)-1,24-dihydroxycholecalciferol ((24R)-1,24(OH)₂D₃, PRI-2191, tacalcitol; Figure 1)) alone and in combination with anticancer drugs (tyrosine kinase inhibitors and cytostatics) in in vivo A549 lung cancer model and showed that PRI-2191 enhanced anticancer activity of the drugs [18,19]. Following, we evaluated the antiproliferative activity of PRI-2191 in a panel of lung cancer cell lines and found that the cells having different genetic backgrounds revealed differential responses to this metabolite. The most vulnerable to antiproliferative activity of PRI-2191 was EGFR-mutant HCC827 lung cancer cell line, while KRAS-mutant cell lines were less sensitive. However, despite the effect of vitamin D compounds on cell proliferation was weak in some cell lines, vitamin D compounds were transcriptionally active as assessed on increased CYP24A1 expression [14]. Thus, EGFR-mutant lung cancer cells are more sensitive to the anti-proliferative effects of vitamin D in contrast to KRAS-mutant lung cancer cells. Although no significant antiproliferative effect of vitamin D was observed in KRAS mutations, induction of CYP24 expression, typical of vitamin D, is observed in these cells. This suggests that VDR is active in these cells, but does not show antiproliferative activity. Probably VDR is not able to activate the expression of these genes, which could contribute to the antiproliferative effect. Therefore, we decided to find out what is the difference in the response of both subtypes of lung cancer cells to the anti-cancer effects of vitamin D. We assume that, first, some other genes may also be expressed in KRASmut cells after vitamin D treatment, and second, the use of vitamin D when combined with another active substance like RESV, will respond differently to vitamin D, because some additional signaling mechanism or pathway will

be activated. In the AML model, vitamin D induction of leukemia cell differentiation was shown to be potentiated by plant polyphenols. So, we decided to investigate the interaction of the active vitamin D metabolite with RESV as a plant polyphenol. Since these two cell subtypes responded differently to the vitamin D metabolite used, we were also interested in whether the response of the cells would be similar or different when RESV worked alone, and whether any relationship could be observed. Here, we asked the question, whether lung cancer cell lines of different origin respond similarly to anticancer properties of RESV and whether any correlation can be found between the mode of RESV action and the lung cancer cell type. Therefore, in this study, we aimed to analyze the influence of RESV on cell proliferation inhibition, cell cycle, apoptosis, and expression of some cytokines and proteins. Additionally, the activity of natural compounds can be modulated when used in combinations. The study on acute myeloid leukemia (AML) cell lines, representing different stages of myeloid maturation, showed that the differentiation-inducing activity of vitamin D analogs can be enhanced by combination with plant polyphenol carnosic acid [26]. Therefore, we decided to examine the activity of the combination of plant polyphenol RESV with an active metabolite of vitamin D PRI-2191 in a lung cancer model, that we previously tested in lung cancer cell lines [14], to see whether the activity of both compounds influences one another.

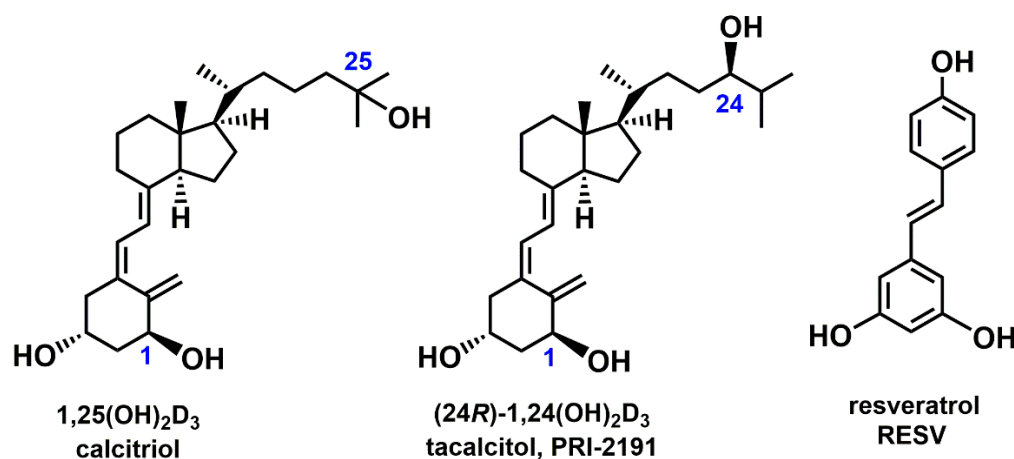


Figure 1. The chemical structure of 1,25(OH)₂D₃ (calcitriol), (24R)-1,24(OH)₂D₃ (PRI-2191, tacalcitol), and resveratrol (RESV).

2. Results

2.1. Antiproliferative Activity of RESV and PRI-2191 in Lung Cancer Cell Lines

First, we determined the antiproliferative activity of RESV and PRI-2191 used alone on a panel of lung cancer cell lines briefly characterized in Materials and Methods. Cells were incubated with RESV and PRI-2191 by 72 h, and after that time, antiproliferative activity was assessed and inhibitory concentration 50 (IC₅₀) was calculated. RESV showed antiproliferative activity against all the lung cancer cell lines tested in the study, but with differential potency. The highest activity was observed against NCI-H1581 and NCI-H1703 (IC₅₀ 15–32 μM) and moderate activity against A549, NCI-H358, NCI-H1299, HCC827, and A-427 (IC₅₀ 40–60 μM), while the weakest activity was observed against Calu-3 cells (IC₅₀ above 200 μM) (Table 1). Treatment with PRI-2191 alone caused proliferation inhibition by 20.47% and 7.52% of HCC827 cells and by 11.5% and 8.82% in NCI-H1703 cells at the concentrations of 1000 and 100 nM, respectively. Cell proliferation was stimulated by 10.63% and 12.83% in NCI-H358 cells at the concentrations of 1000 and 100 nM, respectively (Table 2). However, PRI-2191 added at the concentration of 100 nM did not significantly improve the cytotoxic activity of RESV. Only in NCI-H1703 cells, a slight increase in the antiproliferative activity was observed after treatment with RESV in combination with PRI-2191 compared to that observed with RESV alone. On the contrary, in the case of NCI-H358, a decrease in the antiproliferative activity was observed when PRI-2191 was used together

with RESV (Table 1). The dose-response curves of RESV used alone and RESV used in combination with PRI-2191 are presented in the Supplementary Material (Figure S1).

Table 1. Antiproliferative activity of resveratrol (RESV) alone and in combination with (24R)-1,24-dihydroxycholecalciferol, (24R)-1,24(OH)₂D₃ (PRI-2191) on lung cancer cell lines expressed as inhibitory concentration 50 (IC₅₀).

	RESV	RESV + PRI-2191 ¹
NCI-H1703	21.6 ± 5.9	17.8 ± 3.3
NCI-H1581	31.9 ± 10.1	34.3 ± 11.8
NCI-H358	39.8 ± 1.6	47.4 ± 2.9
A549	43.9 ± 3.2	36.5 ± 7.4
NCI-H1299	52.2 ± 7.0	48.8 ± 8.5
HCC827	60.6 ± 12.0	51.9 ± 13.2
A-427	60.8 ± 25.0	71.6 ± 35.0
Calu-3	231.8 ± 110.3	184.1 ± 64.6

¹ PRI-2191 in combination with RESV was used at a concentration of 100 nM. Results are expressed as the mean ± standard deviation of at least three independent experiments.

Table 2. Proliferation inhibition (%) caused by PRI-2191 on lung cancer cell lines.

	PRI-2191	
	1000 nM	100 nM
A-427	3.37 ± 4.91	2.57 ± 3.36
A549	2.09 ± 1.38	0.55 ± 1.82
Calu-3	0.70 ± 0.99	1.28 ± 0.10
HCC827	20.47 ± 6.88	7.52 ± 4.63
NCI-H1299	0.61 ± 0.44	0.45 ± 0.54
NCI-H1581	3.11 ± 1.50	0.60 ± 0.24
NCI-H1703	11.50 ± 5.74	8.82 ± 1.72
NCI-H358	* 10.63 ± 0.91	* 12.83 ± 2.69

* The numbers indicate proliferation stimulation.

2.2. Cell Cycle Analysis of Lung Cancer Cells Treated with RESV and PRI-2191

Next, we performed cell cycle analysis in lung cancer cells of different genetic backgrounds treated with RESV to check whether RESV activity is cell cycle dependent and whether it arrests cells in a given phase of cell cycle depending on the cell type or not. For this purpose, tested lung cancer cells were treated with RESV at the concentration of IC₂₅–IC₃₅ averaged to 20 μM. As shown in Figure 2, treatment with RESV resulted in diverse effects on cell cycle depending on the cell line. For instance, a decrease in the percentage of cells in the G₀/G₁ phase was observed for A-427, A549, HCC827, NCI-H1299, NCI-H1581, and NCI-H358. A simultaneous increase in cell percentage in the S phase was observed for HCC827 (the highest percentage of cells in S phase for these cells), A-427, NCI-H1581, and NCI-H358 cell lines (statistically significant), while a simultaneous increase in the percentage of cells in the G₂/M phase was noticed for A-427, NCI-H1581, and NCI-H358. However, no changes in the percentage of cells in the G₀/G₁ phase were observed for NCI-H1703, but a small increase in the cell percentage in the S phase (not statistically significant) with a simultaneous significant decrease in the G₂/M phase was noticed. Only for Calu-3 cells, RESV treatment resulted in an increase in the cell percentage in the G₀/G₁ phase with a concomitant significant decrease in the S and G₂/M phase (Figure 2). The representative histograms of this analysis are presented in the Supplementary Material (Figure S2). The treatment with RESV alone or in combination with PRI-2191 caused a significant increase in the percentage of cells with fractional DNA content (sub-G₁ cells) in the case of NCI-H1299, NCI-H1581, NCI-H1703, and NCI-H358 cell lines (for NCI-H1703, only the difference caused by treatment with RESV plus PRI-2191 was statistically significant) (Figure 2 and Figure S3).

When used alone, PRI-2191 did not influence the cell cycle of lung cancer cell lines. The exception was the cell line HCC827, for which PRI-2191 treatment resulted in an increased percentage of cells in the G0/G1 phase of the cell cycle compared to the non-treated cells (data showed in the Supplementary Material, Figure S3). A small reversal trend was noted in the effect of RESV with the addition of PRI-2191 in A549 and NCI-H358 cell lines. With the use of RESV alone, the increase observed in the percentage of cells in the S phase for NCI-H358 and the decrease observed in the G0/G1 phase for A549 were statistically significant, while the changes observed with the combination of RESV and PRI-2191 were not significant. In addition, a significant difference in the percentage of cells in the G0/G1 phase was observed for NCI-H358 cells treated with RESV combined with PRI-2191 compared to treatment with RESV alone (Figure S3).

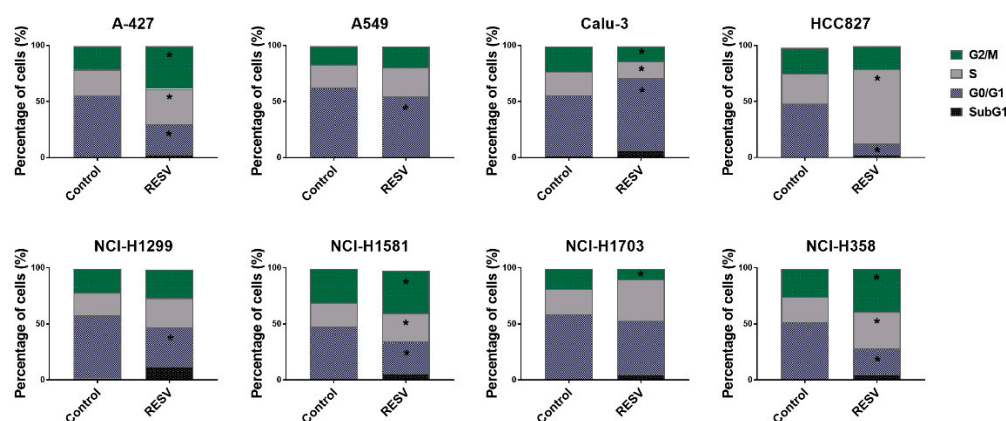


Figure 2. Flow cytometry cell cycle analysis of lung cancer cells after treatment with resveratrol (RESV) (20 μ M). Data were analyzed using the Flowing Software v2.5.1. * Compared to control (untreated cells) ($p < 0.05$, Student's t -test).

2.3. Induction of Caspase-3 Activity by RESV and PRI-2191

We analyzed also the activity of caspase-3 in lung cancer cells treated with RESV to check whether proliferation inhibition of lung cancer cells was a result of caspase-3-dependent cell death and to see if the ability of RESV to induce caspase activity was similar or not in tested lung cancer cells. Caspase-3 is a key executioner of caspases, which, in addition to caspase-7, is necessary for apoptosis. We used a method based on the enzyme's ability to hydrolyze the synthetic Ac-DEVD-ACC substrate, upon treatment with RESV or PRI-2191 or both, which leads to the release of 7-amino-coumarin fluorochrome. Following the treatment, we measured the increase of fluorescence with time. RESV most effectively induced caspase-3 activity in NCI-H1703 cells ($V_{max} = \sim 1000$), while its activity was mild in A-427, Calu-3, and NCI-H1581 ($V_{max} = \sim 400$) and moderate in A549, NCI-H1299, and NCI-H358 ($V_{max} = 100\text{--}200$ in a concentration-dependent manner). The least caspase-inducing effect was found in EGFR-mutant HCC827 cells ($V_{max} = 10\text{--}20$) (Figure 3), which suggests that EGFR-mutant lung cancer cells are possibly the least vulnerable to caspase induction by RESV. It was also observed that PRI-2191 decreased both the basal caspase-3 activity (significantly in NCI-H1581, NCI-H1703, and NCI-H358) and the RESV-induced caspase-3 activity (significantly in Calu-3 and HCC827 at the indicated concentrations) (Figure S4).

2.4. Changes in p53 and p21 Expression in Lung Cancer Cells after RESV and PRI-2191 Treatment

Even though we did not observe the robust effect of combining RESV and PRI-2191, on anti-proliferative activity of lung cancer cells, in the following experiments, the impact of both RESV and PRI-2191, as well as their combination, on the expression of some proteins was tested. It could not be ruled out that some changes have taken place at the molecular level. Therefore, we have made an attempt to check this possibility on a few examples.

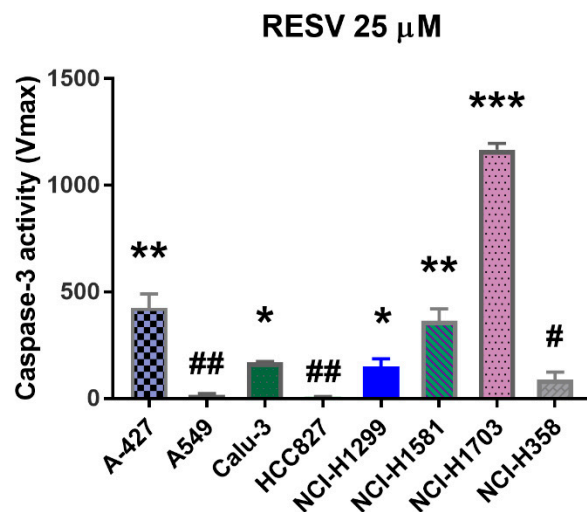


Figure 3. Induction of caspase-3 activity in lung cancer cells by RESV. RESV was used at a concentration of 0–75 μ M and PRI-2191 at 100 nM. The above chart shows only the results for RESV at the concentration of 25 μ M, while the remaining data (for 0–75 μ M and 100 nM of PRI-2191) are presented in Supplementary material, Figure S4. Cells were lysed and the substrate (Ac-DEVD-ACC) was added to cell lysates. Fluorescence was measured with time, and kinetics was calculated as RFU/min. Data were analyzed using Gen5 2.09 software. * compared to A-427, A549, HCC827, and NCI-H1581, NCI-H1703; ** compared to A549, Calu-3, HCC827, NCI-H1299, NCI-H1703, and NCI-H358; *** compared to all other cell lines; # compared to A-427, NCI-H1581, and NCI-H1703; ## compared to A-427, Calu-3, NCI-H1299, NCI-H1581, and NCI-H1703 ($p < 0.05$, one-way ANOVA with Tukey's post hoc with multiple comparisons).

We analyzed the expression of p53 and p21 proteins, which regulate the cell cycle progression and apoptosis, using the Western blot analysis. p53 is known also as the guardian of the genome and is more frequently mutated in human cancers than any other gene [25]. Here, the results revealed that RESV significantly induced the expression of p53 in A-427 and A549 cells (Figure 4), but only slightly in NCI-H1703 cells (not statistically significant in the latter) (Figure S6). Furthermore, the combination of PRI-2191 and RESV significantly augmented the upregulation of p53 in A549 cells compared to that observed with RESV alone (Figure 4). In Calu-3, the level of p53 was found to be significantly lowered after RESV treatment, while a decrease was also noted in HCC827, but it was not statistically significant (Figure 4). The expression of p21, which is regulated by p53, was upregulated simultaneously with p53 expression in A-427 and A549 cells. In addition, the level of p21 was found to be also increased in Calu-3 and HCC827 cells after treatment with RESV, although p53 expression was not upregulated. Similarly, the level of p21 in Calu-3 cells was also significantly upregulated with PRI-2191–RESV combination compared to that observed with PRI-2191 alone (Figure 4). Furthermore, RESV lowered the level of p21 in NCI-H1581 cells (Figure S6). No significant changes in p53 and p21 expression were observed for other tested cell lines (Figure S6).

RESV is mainly known to modulate the activity of SIRT1, a NAD⁺-dependent histone deacetylase [27,28]. However, SIRT1 is also responsible for the deacetylation of nonhistone proteins, such as p53 and VDR, and thus impact their activity [29,30]. Therefore, we estimated the level of SIRT1 expression to analyze whether it could be modulated by RESV and/or PRI-2191 in lung cancer cells. Western blot revealed the expression of SIRT1 in all lung cancer cell lines, but the treatment of cells with RESV and/or PRI-2191 did not significantly influence the level of expression (Figure S5).

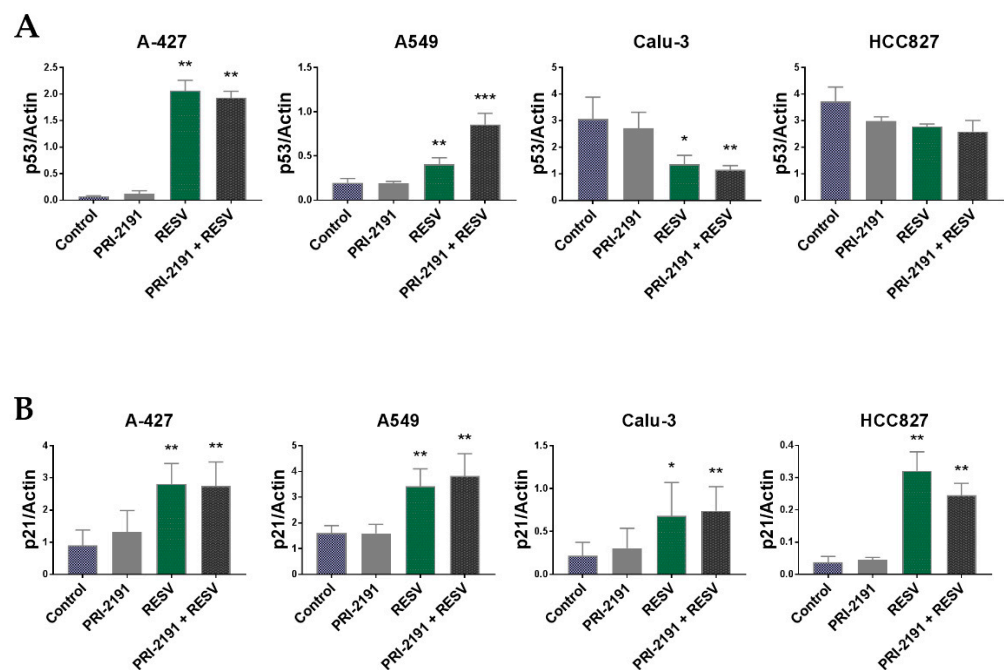


Figure 4. Western blot analysis of lung cancer cells treated with PRI-2191 (100 nM) and RESV (20 μ M). Effect of PRI-2191 and RESV on (A) p53 and (B) p21 expression in lung cancer cells (all blots and statistical analysis for other cell lines are presented in Figure S6). Cell lysates were subjected to SDS-polyacrylamide gel electrophoresis and analyzed by Western blotting. Actin was used as a normalization control. * Compared to control (untreated cells); ** compared to control and PRI-2191; *** compared to control, PRI-2191, and RESV ($p < 0.05$, one-way ANOVA with Tukey's post hoc with multiple comparisons).

2.5. Differential Expression of CYP24A1, RXR α , and VDR in Lung Cancer Cells after PRI-2191 and RESV Treatment

Afterwards, we analyzed the expression of the following key proteins that regulate the activity of vitamin D: VDR, CYP24A1 (24-hydroxylase, the enzyme responsible for vitamin D deactivation and the strongest known vitamin D-responsive gene), and RXR α (retinoid X receptor α , which together with VDR forms a heterodimer binding, e.g., to the promoter sequence of the CYP24A1) [31], to check whether their expression was modulated by RESV and PRI-2191 in lung cancer cells. Western blot analysis showed that the expression of CYP24A1 was significantly upregulated upon PRI-2191 treatment in Calu-3, HCC827, NCI-H358 cells, and only slightly and not statistically significantly in A-427 (also in RESV-treated cells), A549, and NCI-H1299 cells (Figure 5 and Figure S7). CYP24A1 expression was also significantly augmented by the PRI-2191–RESV combination in A549, HCC827, and NCI-H358 cells, compared to control cells and RESV-treated cells, and the expression was also significantly increased in NCI-H358 cells compared to PRI-2191-treated cells (Figure 5). The analysis of RXR α expression showed that treatment with RESV, either alone or in combination with PRI-2191, significantly upregulated the expression of this receptor only in A-427 (Figure S7), but downregulated the expression in A549, HCC827, NCI-H1703, and NCI-H358 cells. The expression was also downregulated in Calu-3 cells, but the difference was significant only when RESV was used with PRI-2191 (Figure 5 and Figure S7). The analysis of VDR expression showed a significant increase in the level only in NCI-H1299 lung cancer cells after treatment with PRI-2191 and when PRI-2191 was used with RESV (Figure S7). In addition, VDR expression was slightly upregulated in Calu-3 and HCC827 cells treated with PRI-2191 alone, but the increase was not statistically significant (Figure 5 and Figure S7). However, when PRI-2191 was used in combination with RESV, the level of VDR in the cells was increased in a statistically significant manner. Furthermore, the use of RESV also upregulated VDR expression to some extent in A549 cells, but the increase

was not statistically significant in the replicates (Figure 5). Taken together, although in some cell lines the RESV treatment caused a decrease in the expression of RXR α , which cooperates with VDR in gene regulation, it did not influence the ability of PRI-2191 to induce CYP24A1 expression when both compounds were used together. Moreover, some improvement was observed in the ability of PRI-2191 to influence CYP24A1 expression with the addition of RESV.

2.6. Impact of RESV and -2191 on VEGF, PD-L1, IL-8, and OPN Expression

We analyzed the impact of RESV and PRI-2191 on the expression (at mRNA and protein level) of the following proteins regulating the processes responsible for cancer development: (a) vascular endothelial growth factor (VEGF) engaged in angiogenesis; (b) PD-L1 (also known as CD274 or B7-H1) responsible for tumor immune escape; (c) interleukin 8 (IL-8, also known as CXCL8), which is a multifunctional inflammatory chemokine produced by many cell types; and d) osteopontin (OPN, also known as SPP1), a multifunctional protein, highly expressed in bone, but also regulates immune cell functions, and whose expression is stimulated by 1,25(OH) $_2$ D $_3$. The following cell lines were used for this analysis: A549 (KRASmut, p53wt), HCC827 (EGFRmut, p53mut), and NCI-H358 (KRASmut, p53null) in order to compare the activity of RESV and PRI-2191 on cells representing two main molecular subtype of lung cancer: EGFR mutant and KRAS mutant. Of the three, HCC827 was the most sensitive to the antiproliferative activity of PRI-2191, while the proliferation of NCI-H358 was stimulated by PRI-2191. In all three cell lines, CYP24A1 expression was found to be induced when PRI-2191 was used alone or in combination with RESV. The effect of RESV, PRI-2191, and their combination on the secretion of VEGF, OPN, and IL-8 by A549, HCC827, and NCI-H358 tumor cells was tested using enzyme-linked immunosorbent assay (ELISA) in conditioned medium, while the level of PD-L1 was analyzed in cell lysates.

RESV, when used alone or in combination with PRI-2191, caused a significant decrease in the secretion of VEGF by A549 and NCI-H358 cells. Besides, a significant reduction in VEGF secretion was noted in NCI-H358 cells after treatment with PRI-2191 alone. By contrast, RESV did not affect the secretion of VEGF by HCC827 cells (Figure 6). Also, RESV appear to reveal antiangiogenic activity in KRAS-mutant lung cancer, but not in EGFR mutant. No significant changes in the expression of VEGF mRNA were observed between the treatment groups (Figure S9).

Analysis of OPN secretion by lung cancer cells showed that RESV, when used either alone or in combination with PRI-2191, significantly increased the level of this protein in conditioned medium of A549 and NCI-H358 cells, while this effect was observed only with RESV–PRI-2191 combination in HCC827 cells. On the other hand, the addition of PRI-2191 to RESV caused an opposite effect on A549 and NCI-H358 cells; a significantly lower level of OPN was found in A549 cells compared to those treated with RESV alone, while the OPN level was significantly higher in NCI-H358 cells (Figure 7). Quantitative polymerase chain reaction (qPCR) revealed that the expression of OPN was significantly upregulated in lung cancer cells treated with RESV alone and RESV in combination with PRI-2191, and also in HCC827 cells treated with PRI-2191 alone (Figure S10). Therefore, we concluded that KRAS-mutant lung cancer cells were more receptive to modulation of OPN expression by RESV than EGFR-mutant lung cancer cells.

Treatment with RESV resulted in a significant increase in the level of IL-8 of HCC827 cells compared to control cells, but the combination of PRI-2191 and RESV caused a significant reduction in the IL-8 level compared to cells treated with RESV alone (Figure 8). At the mRNA level, a significant increase in IL-8 expression was observed in HCC827 cells when they were treated with RESV alone (Figure S11). In the case of NCI-H358 cells, an increase in IL-8 level was observed using RESV, either alone or in combination with PRI-2191, but the difference was statistically significant compared to cells treated with PRI-2191 alone. A549 cells secreted a small basal amount of IL-8 compared to the other two cell lines. After treatment with RESV combined with PRI-2191, a slight decrease in IL-8

level was observed, but the difference was not statistically significant (Figure 8). Therefore, RESV treatment impacts IL-8 expression only in EGFR-mutant lung cancer cells.

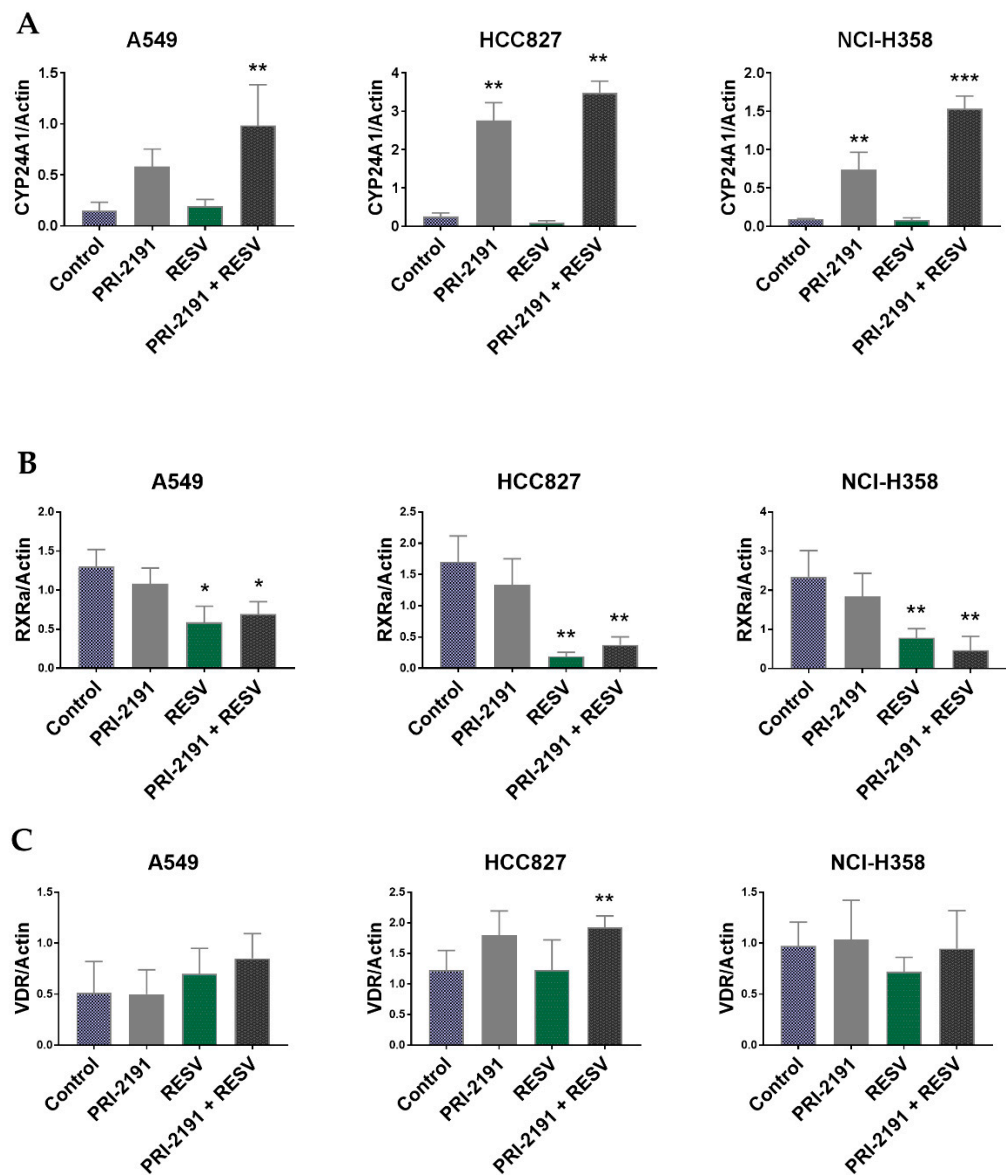


Figure 5. Western blot analysis of lung cancer cells treated with PRI-2191 (100 nM) and RESV (20 μ M). Effect of PRI-2191 and RESV on (A) CYP24A1, (B) RXR α , and (C) vitamin D receptor (VDR) expression in lung cancer cells (all blots and statistical analysis for other cell lines are presented in Figure S7). Cell lysates were subjected to SDS-polyacrylamide gel electrophoresis and analyzed by Western blotting. Actin was used as a normalization control. * Compared to control (untreated cells); ** compared to control and RESV (for RXR α compared to control and PRI-2191); *** compared to control, RESV, and PRI-2191 ($p < 0.05$, one-way ANOVA with Tukey's post hoc with multiple comparisons).

Analysis of PD-L1 expression in lung cancer cells showed that PRI-2191 significantly upregulated the expression of this molecule in HCC827 and NCI-H358 cells, while in A549 cells, an expression was increased only when PRI-2191 was used with RESV. Additionally, PRI-2191 combined with RESV caused a significant increase in PD-L1 expression in NCI-H358 cells compared to PRI-2191 used alone. RESV used alone also induced the expression of PD-L1 in HCC827 cells, but the increase was not statistically significant (Figure 9). Treatment with PRI-2191 and PRI-2191 in combination with RESV also significantly induced PD-L1 mRNA expression in HCC827 and NCI-H358 cells, while a significant induction in

expression was observed for RESV alone or in combination with PRI-2191 in A549 cells (Figure S12).

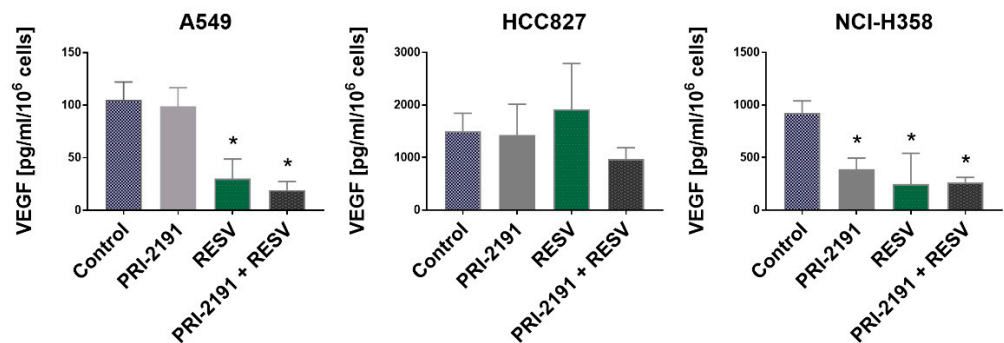


Figure 6. Effect of PRI-2191 and RESV on vascular endothelial growth factor (VEGF) secretion by lung cancer cells. RESV was used at a concentration of 20 μ M and PRI-2191 at 100 nM. Cells were exposed to tested compounds for 72 h, then washed with PBS, and cultured in a serum-free medium for the next 24 h. Conditioned medium was collected, and the level of VEGF secreted by lung cancer cells was measured by ELISA. A549: * compared to control (untreated cells) and PRI-2191; NCI-H358: * compared to control ($p < 0.05$, one-way ANOVA with Tukey’s post hoc with multiple comparisons).

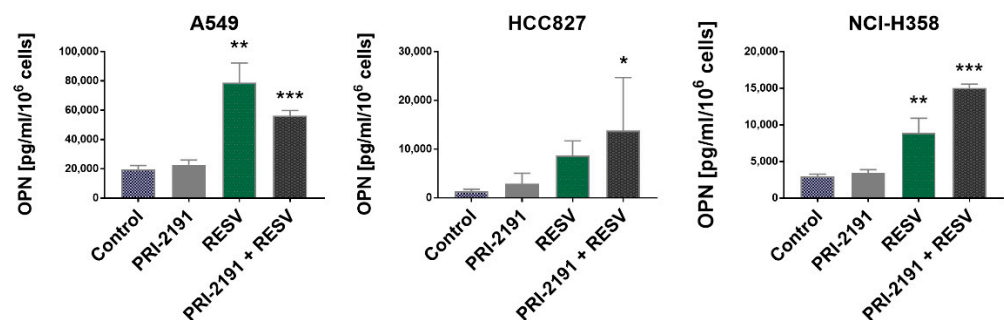


Figure 7. Effect of PRI-2191 and RESV on osteopontin (OPN) secretion by lung cancer cells. RESV was used at a concentration of 20 μ M and PRI-2191 at 100 nM. Cells were exposed to tested compounds for 72 h, then washed with PBS, and cultured in a serum-free medium for the next 24 h. Conditioned medium was collected, and the level of OPN secreted by lung cancer cells was measured by ELISA. * Compared to control; ** compared to control (untreated cells) and PRI-2191; *** compared to control, PRI-2191, and RESV ($p < 0.05$, one-way ANOVA with Tukey’s post hoc with multiple comparisons).

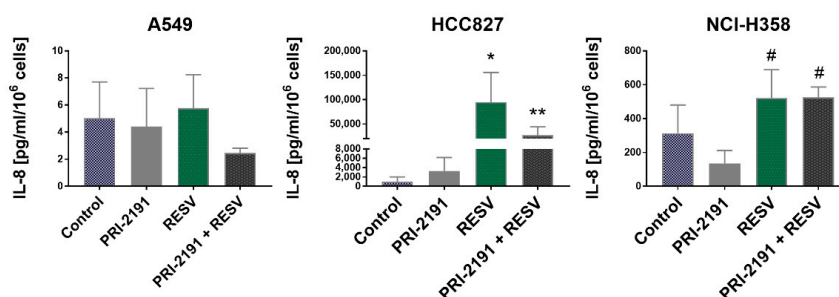


Figure 8. Effect of PRI-2191 and RESV on interleukin (IL-8) (CXCL8) secretion by lung cancer cells. RESV was used at a concentration of 20 μ M and PRI-2191 at 100 nM. Cells were exposed to tested compounds for 72 h, then washed with PBS, and cultured in a serum-free medium for the next 24 h. Conditioned medium was collected, and the level of IL-8 secreted by lung cancer cells was measured by ELISA. * Compared to control (untreated cells) and PRI-2191; ** compared to RESV; # compared to PRI-2191 ($p < 0.05$, one-way ANOVA with Tukey’s post hoc with multiple comparisons).

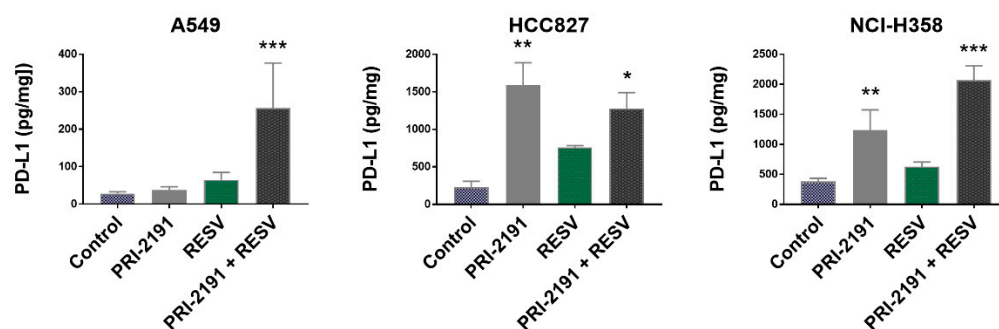


Figure 9. Effect of PRI-2191 and RESV on programmed death-ligand 1 (PD-L1) expression by lung cancer cells. RESV was used at a concentration of 20 μ M and PRI-2191 at 100 nM. Cells were exposed to tested compounds for 72 h, then washed with PBS, and cultured in a serum-free medium for the next 24 h. Cells were collected, and the level of PD-L1 in lung cancer cells was measured by ELISA. * Compared to control (untreated cells); ** compared to control and RESV; *** compared to control, PRI-2191, and RESV ($p < 0.05$, one-way ANOVA with Tukey's post hoc with multiple comparisons).

Furthermore, the expression of SIRT1, VDR, and RXR α was analyzed at the mRNA level in all the chosen cell lines (A549, HCC827, and NCI-H358) utilizing qPCR, but no significant changes were observed after treatment with PRI-2191 and RESV (Figure S8).

3. Discussion

We evaluated the biological activity of RESV against lung cancer cells with different genetic background. The cell lines were chosen based on key mutations driving lung cancer: EGFR, KRAS, and additionally TP53 mutation status, in order to evaluate whether lung cancer cell lines of different origin respond similarly to anticancer properties of RESV and whether there is any correlation between the mode of RESV action and the lung cancer cell type. We also first combined the vitamin D active metabolite PRI-2191 with the plant polyphenol RESV and evaluated their biological effects on these lung cancer cell lines. This idea came out from the cross-talk between these two nutrients and also from observations that different plant polyphenols and vitamins D may advantageously cooperate in anticancer activity [26,32–37].

Initial in vitro antiproliferative activity assay of plant polyphenol RESV against lung cancer cells showed that RESV revealed the highest antiproliferative activity against NCI-H1703 cells and the activity was weakest against Calu-3 (the lowest and the highest IC₅₀, respectively). However, when RESV and PRI-2191 were used in combination, no improvement in proliferation inhibition was found. On the other hand, in NCI-H358 cells, the addition of PRI-2191 to RESV caused a reduction in the antiproliferative activity of RESV.

Next, we tested the influence of RESV on cell cycle and the activity of caspase-3, an indicator of apoptosis and compared achieved results between tested cells. The ability of RESV to arrest the progression of cell cycle depending on the cancer cell line origin was reported. For example, the impact of RESV on cell cycle progression varied in prostate cancer cell lines, depending on their molecular subtype: androgen vs. estrogen receptor-expressing cells (LNCaP and PC-3, respectively) [38]. A cell-specific mechanism of cell cycle modulation and apoptosis induction by RESV was also reported in breast cancer cell lines MCF-7 and MDA-MB-231, which represent two molecular subtypes: estrogen receptor-positive and triple-negative, respectively [39]. In our study, we found that RESV, when used alone, promoted the accumulation of cells in the G0/G1 phase and S or G2/M phase depending on the lung cancer cell lines, with the most significant arrest in G2/M phase for HCC827 cell line, which is the representative of EGFR-mutant lung cancer. A small reversal trend was noted in the effect of RESV on cell cycle progression when PRI-2191 was added. The strongest induction of caspase-3 by RESV was observed in TP53-mutant lung squamous cell carcinoma NCI-H1703 cells, which may explain that these cells were the most sensitive

ones to the antiproliferative activity of RESV (the lowest IC₅₀ of RESV). The weakest ability of RESV to induce caspase-3 was noticed for EGFR-mutant lung adenocarcinoma HCC827 cells. In addition, PRI-2191 did not significantly inhibit the activation of caspase-3 induced by RESV, and only a decrease of this activity was observed. Taken together, the impact of RESV on proliferation inhibition, cell cycle progression, and apoptosis induction was different depending on the target lung cancer cells, but was not significantly or strongly modulated by the addition of PRI-2191.

RESV and vitamin D are known to regulate signaling molecules including p53 protein, which contribute to cell cycle arrest as well as programmed cell death and DNA repair. In our study, we observed that RESV upregulated the expression of p53 in A-427 and A549 cells (both cell lines carry wtp53). The addition of PRI-2191 to RESV significantly augmented the upregulation of p53 only in A549 cells, which indicates the cooperative action of these two compounds in this cell line. On the other hand, a decline in the level of p53 was observed after RESV treatment in Calu-3 and HCC827 cells, both of which carry mutant p53 (M237I and V218del, respectively) according to the IARC TP53 Database. Ferraz da Costa et al. showed that RESV decreased the level of p53 mutant R248Q in HCC70, a highly invasive human breast ductal carcinoma cell line. By contrast, in MCF-7 cells, carrying wild-type p53, RESV increased the level of the protein [40]. It is already known that mutant p53 frequently loses its tumor-suppressive effect and gains new, undesirable oncogenic properties [41]. M237I, a mutant form of p53, has been shown to form amyloid oligomers in glioblastoma cells, which presented a chemoresistant gain-of-function phenotype [42]. Therefore, the downregulation of mutant p53 expression by RESV may be considered beneficial. Furthermore, Yi et al. showed that a 4-h treatment with the boronic acid chalcone analog of combretastatin A-4, YK-3-237, caused deacetylation of the mutant M237I-p53 at lysine 382 (K382) by activating the expression of SIRT1 in a triple-negative breast cancer. Deacetylation resulted in the depletion of the mutant p53 protein while upregulating the expression of the wild-type p53 target genes, such as PUMA and NOXA, which suggests that deacetylation leads to the reactivation of the wild-type p53 activity [43]. In this study, after treatment of Calu-3 and HCC827 cells with RESV alone or in combination with PRI-2191, we observed that p21 expression was reactivated. Willis et al. showed that mutant p53 exhibited a dominant-negative effect by preventing the wild-type p53 from inducing p21 expression [44]. Furthermore, by reducing the level of mutant p53 through treatment with RESV, the diminished induction of p21 was restored in lung cancer cells carrying mutant p53. On the other hand, it was speculated that acetylation of p53 at K120, K373, and K382 is crucial for the induction of p21 and the suppression of Ras-mediated tumorigenesis [45,46]. If we assume that RESV treatment deacetylated wild-type p53 through SIRT1 induction, then according to the reported data it can be expected that p53 was inactivated and its transcriptional activation of target genes, such as p21, was prevented. As shown here, in two RAS-mutant/p53-wild-type cell lines A-427 and A549 RESV treatment upregulated the expression of wild-type p53 and p21. Brochier et al. identified that K382 acetylation prevented the association of p53 with the proapoptotic gene promoter PUMA in mouse cortical neurons, highlighting that the consequence of p53 acetylation/deacetylation may be context-dependent [47]. Therefore, analyzing the acetylation status of p53 in lung cancer cells following RESV treatment could explain these differences in RESV activity on wild-type vs. mutant p53.

It was revealed that RESV and SIRT1 cooperate with vitamin D to enhance VDR signaling. Sabir et al. showed that SIRT1 and RESV potentiated the vitamin D-stimulated expression of CYP24A1 in HEK293 embryonic, kidney-derived cells [30]. On the other hand, we have previously shown that in lung cancer cells that were either sensitive or resistant to the antiproliferative activity of vitamin D, vitamin D signaling was active as revealed by the upregulated expression of CYP24A1 after treatment with vitamin D compounds [14]. In the present study, CYP24A1 expression was significantly upregulated upon PRI-2191 treatment in Calu-3, HCC827, and NCI-H358 cells, and when PRI-2191 was combined with RESV, a significant upregulation of expression was also noticed in A-427

and A549 cells. Further potentiation of CYP24A1 expression by RESV, when used with PRI-2191, was seen in NCI-H358. Therefore, in those cells, RESV cooperated with PRI-2191 in CYP24A1 expression. It should be noted that vitamin D itself directly influences the expression levels of VDR, increasing the mRNA level and stability of VDR, thus protecting against its degradation [48]. In this study, PRI-2191 used alone significantly induced VDR expression only in NCI-H1299 cells, but when combined with RESV, the receptor expression was significantly enhanced in Calu-3 and HCC827 cells while it was moderate in A549 cells. Thus, it may be concluded that depending on the cell line, RESV may influence vitamin D signaling in lung cancer cells, increasing the activity of vitamin D when combined with PRI-2191.

The effect of vitamin D is mainly mediated by VDR, which is a member of the steroid nuclear receptor superfamily. Vitamin D binds and activates VDR that functions as a transcription factor modulating the transcriptional activity of the vitamin D target genes. The binding of vitamin D results in conformational changes in VDR, facilitating the recruitment of its co-receptor, RXR. Vitamin D-liganded VDR–RXR heterodimer binds to vitamin D-responsive elements (VDREs) and regulates the expression of the target genes [49]. RESV potentiates the actions of $1,25(\text{OH})_2\text{D}_3$ by facilitating the heterodimerization of VDR with RXR, thus causing a cooperative effect on gene transactivation [50]. In our study, we observed that treatment with RESV resulted in the downregulation of RXR α expression in four out of eight cell lines and its upregulation in only one cell line. Wassermann et al. reported similar findings in the acute myeloid leukemia model for carnosic acid and silibinin. However, the study showed the opposite effect of silibinin on the prodifferentiation activity of vitamin D in myeloblastic HL60 and promonocytic U937 cells, accompanied by the upregulation of RXR α expression in HL60 cells and downregulation in U937 cells. This indicated that the modulation of RXR α by plant polyphenols is cell type specific [35]. A study on E12 embryos of diabetic dams showed that RESV modulated the expression of RXR in diabetic embryopathy and normalized the diabetes-induced suppression of the receptor level [51]. What is more, as it was showed in this study, although RESV decreased RXR α expression, it did not affect the ability of the PRI-2191 to induce CYP24A1 expression.

Several studies have examined the dual-anticancer effects of phytochemicals such as RESV and curcumin, combined with $1,25(\text{OH})_2\text{D}_3$. One example is the inhibition of tumor angiogenesis and augmentation of the antiproliferative and prodifferentiation activity of $1,25(\text{OH})_2\text{D}_3$. In the triple-negative breast cancer in vivo model, it was shown that RESV with $1,25(\text{OH})_2\text{D}_3$ reduced the vessel diameter of the tumor, and blood vessels of the combinatorial treatment group showed normal vessel morphology indicating vessel normalization unlike the groups receiving each agent alone. RESV also significantly induced endothelial cell death in vitro, which probably might be the reason for the reduced number of tumor microvessels found in the group receiving RESV and $1,25(\text{OH})_2\text{D}_3$ [52]. In the present study, we evaluated the ability of RESV and PRI-2191 to modulate the expression of VEGF in lung cancer cells. We found that only in both the KRAS-mutant lung cancer cell lines tested, RESV (alone or in combination with PRI-2191) decreased the level of secreted VEGF. Similarly, inhibition of VEGF production by RESV was also observed in human leukemia U937 cells, in stimulated human gingival fibroblasts, in A549 cells cocultured with adipose-derived mesenchymal stem cells, and c-FLIP-overexpressing H460 lung cancer cells [53–56]. Reinmuth et al. reported that VEGF expression correlated with EGFR mutational status in clinical specimens obtained from lung cancer patients. It was also shown that EGFR-mutant lung tumors showed a significantly higher VEGF expression than EGFR-wild-type tumors [57]. In HCC827, a lung cancer cell line with EGFR mutation, RESV either alone or in combination with PRI-2191 did not affect the level of VEGF secreted by the cells. Therefore, it may be concluded that RESV normalizes tumor angiogenesis in KRAS-mutant lung cancer but not in EGFR-mutant ones.

OPN is a protein that plays a key role in the progression and metastasis of several tumors, including lung, breast, prostate, or liver [58]. Overexpression of this protein in lung cancer has been shown to correlate with poor prognosis [59]. OPN promotes the epithelial–

mesenchymal transition (EMT) in many types of cancer, such as breast or prostate cancer, as well as non-small cell lung cancer. In the present study, we tested the cooperative activity of RESV and PRI-2191 on the secretion of OPN, the expression of which is known to be regulated by $1,25(\text{OH})_2\text{D}_3$ [60,61]. We found that RESV increased the secretion of OPN in all three lung cancer cell lines examined. In particular, a significant increase in OPN secretion was noted for A549 and NCI-H358 cells, after incubation with RESV. RESV was also shown to induce OPN expression in mesenchymal bone marrow cells or human periodontal ligament cells. Furthermore, RESV synergized with $1,25(\text{OH})_2\text{D}_3$ in the induction of OPN expression in bone marrow osteoblast precursors [62,63]. Additionally, it was revealed that the incubation of periodontal ligament cells with the SIRT1 activator RESV increased the expression of differentiation markers, namely, alkaline phosphatase, OPN, and osteocalcin. It was also confirmed using siSIRT1 that SIRT1 stimulated osteoblastic differentiation [63]. Li et al. studied the role of SIRT1 in OPN-induced EMT in lung cancer cells A549 and NCI-H358 and revealed that the overexpression of SIRT1 attenuated EMT induction by OPN. While OPN decreased the expression of E-cadherin, upregulated the expression of N-cadherin and vimentin, and induced cell migration and invasion, SIRT1 overexpression prevented these effects. Moreover, exogenously added OPN caused the downregulation of SIRT1 expression in A549 and NCI-H358 cells [64]. Therefore, despite the induction of OPN expression by RESV, it could be expected that by activating SIRT1, RESV may counteract the protumorigenic effects of OPN. The opposite effects were noticed with the addition of PRI-2191 to RESV on OPN expression in A549 and NCI-H358 cells. PRI-2191 counteracted the induction of OPN expression in A549 cells but augmented the induction in NCI-H358 cells. The promoter region of the OPN gene contains a VDRE [60], and it is known that $1,25(\text{OH})_2\text{D}_3$ strongly induces OPN expression [62,65]. These together may explain the increase in OPN secretion by the addition of PRI-2191 to RESV in NCI-H358 cells. An interesting observation, however, is the lower level of OPN after treatment with RESV in combination with PRI-2191 observed in A549 cells, but the explanation of the mechanism responsible for it requires additional research.

RESV is also known for its anti-inflammatory properties since it inhibits the NF κ B pathway. The activation of this pathway is required for the expression of many proteins involved in the inflammatory response, such as granulocyte-macrophage colony-stimulating factor, cyclooxygenase 2, inducible nitric oxide synthase, and IL-8 [66]. In the present study, we noticed a strong induction of IL-8 expression by RESV in the HCC827 cell line. Similar observations were made by Tino et al. in their study on the effect of RESV on VEGF and IL-8 expression in ovarian cancer cells [67]. Pastore et al. also showed that keratinocytes exposed to RESV displayed increased IL-8 expression. In addition, they noticed that RESV caused continuous activation of the EGFR signaling pathway. Therefore, the authors concluded that RESV induces delayed IL-8 expression through continuous activation of the EGFR-ERK pathway [68]. HCC827 cells tested in this study have an EGFR-activating mutation, which explains why these cells secreted the highest level of IL-8 compared to the other tested cell lines. In turn, Fan et al. showed that RESV inhibited EGFR phosphorylation only in gefitinib-resistant lung cancer cells (NCI-H1975), but not in the cells with wild-type EGFR (A549, NCI-H358). The authors suggested that the RESV analog studied exhibited selectivity in affecting the EGFR pathway depending on whether EGFR is mutated or wild-type [69]. These data suggest that RESV may have a divergent effect on the EGFR pathway and either activate or inhibit it. However, this leads to the questions: What mechanism is responsible for the increase of IL-8 level observed in HCC827 cells after incubation with RESV? Did RESV in these cells alone inhibit the EGFR pathway or enhance its activation, and consequently cause the increase of IL-8 level? To clarify these, some additional studies assessing the activity of the EGFR pathway in the RESV-treated cells are required. Pastore et al. also observed a decrease in IL-8 levels with the use of the EGFR inhibitor PD168393 [69]. In the present study, after using RESV together with PRI-2191, HCC827 cells showed less IL-8 compared to the cells incubated with RESV alone. It is known that $1,25(\text{OH})_2\text{D}_3$ inhibits the EGFR signaling pathway in cancer cells, and

perhaps, PRI-2191 could contribute to a decrease in IL-8 levels by inhibiting this pathway in HCC827 cells [70–72].

The discovery of mechanisms behind the cancer-immune escape has revolutionized the research on new approaches of anticancer treatments, while the use of immune checkpoint inhibitors has brought new hopes for successful treatment of various cancers. One such immune checkpoint is the PD-1 (programmed death-1) pathway involving the receptor PD-1 (CD279) and ligands PD-L1 (programmed death ligand-1; also known as B7 homolog 1 (B7-H1) or CD274) and PD-L2 (B7-DC or CD273). The binding of PD-L1 to the inhibitory checkpoint molecule PD-1, found on activated T cells, B cells, and myeloid cells, results in anergy and apoptosis of T cells and thus helps the tumor cells to evade the antitumor immunity [73]. It is known that PD-L1 is highly expressed in cancer cells of different origins, including lung cancer cells [74]. Therefore, we analyzed the impact of PRI-2191 in combination with RESV on PD-L1 expression in lung cancer cells. As presented here, PRI-2191 caused significant upregulation of the PD-L1 expression in HCC827 and NCI-H358 cells, while a significant increase in PD-L1 expression was seen in A549 cells only when PRI-2191 was used together with RESV. Moreover, PRI-2191 in combination with RESV significantly increased PD-L1 expression compared to PRI-2191 alone in NCI-H358 cells. Dimitrov et al. showed that vitamin D acts as a direct inducer of the PD-L1 and PD-L2 expression in epithelial and myeloid cells (PD-L2 expression only in myeloid cells). They also characterized VDREs present in both genes and showed that pretreatment of epithelial cells with vitamin D inhibited the activation of CD4+ and CD8+ T cells. Based on these findings, the authors concluded that vitamin D may represent a double-edged sword in controlling the inflammatory immune response [75]. In Crohn's disease patients, vitamin D treatment also increased PD-1 expression in CD4+CD25+int T cells and reduced T cell activation. On the other hand, *in vitro* treatment with vitamin D reduced PD-1 expression, thus indicating that the response of T cells to vitamin D stimulation may differ depending on the environmental conditions [76]. In turn, an increase in PD-L1 expression was observed followed by RESV treatment in breast and colorectal cancer cell lines. The authors suggested that the increase of PD-L1 expression caused by priming with or coexposure to stilbenoids, such as RESV, may sensitize the cancer cells to anti-PD-L1 therapy; however, this approach seems controversial [77]. On the other hand, Verdura et al. recently published very interesting results concerning the immunomodulatory properties of RESV. They showed that RESV disrupted N-glycan branching and promoted PD-L1 dimerization, thereby impeding the correct localization of PD-L1 to the plasma membrane and preventing the surface interaction of PD-L1 with PD-1, and as a consequence, the compound increased the susceptibility of cancer cells to T cell-mediated cell death [78]. In a study on ovarian carcinoma, RESV was shown to stimulate immunogenic cell death and cause an increase in the number of mature dendritic cells and cytotoxic T cells, while the combinatorial treatment with PD-1 antibody and RESV markedly inhibited tumor growth *in vivo* [79]. In the present study, we analyzed the level of PD-L1 expression in the total cell lysates of RESV- and PRI-2191-treated lung cancer cells. Therefore, the question is whether, despite the enhanced upregulation of PD-L1 in the tested lung cancer cells, PD-L1 was retained in the cytoplasmic compartments and not found on the plasma membrane.

4. Materials and Methods

4.1. Cell Lines and Culturing Conditions

The following cell lines (mutation status of the main genes is indicated in brackets, according to: https://cancer.sanger.ac.uk/cell_lines, accessed on 28 May 2020) were used in this study: A-427 (wtEGFR, mutKRAS, wtp53), A549 (wtEGFR, mutKRAS, wtp53), Calu-3 (wtEGFR, wtKRAS, mutp53), HCC827 (mutEGFR, wtKRAS, mutp53), NCI-H1299 (wtEGFR, mutNRAS, nullp53), NCI-H1581 (wtEGFR, wtKRAS, mutp53), NCI-H1703 (wtEGFR, wtKRAS, mutp53), and NCI-H358 (wtEGFR, mutKRAS, nullp53).

A549 cell line was obtained from the European Collection of Authenticated Cell Cultures (Salisbury, UK); A-427, Calu-3, HCC827, NCI-H1581, NCI-H1703, and NCI-H358

cell lines were purchased from the American Type Culture Collection (Manassas, VA, USA); and NCI-H1299 cell line was provided by Professor Zdzisław Krawczyk from Cancer Center and Institute of Oncology (Gliwice, Poland). A-427 cells were cultured in Eagle's medium (PChO IIET PAS, Wrocław, Poland), supplemented with 10% fetal bovine serum (FBS), 2 mM L-glutamine, 1% amino acid, and 1 mM sodium pyruvate (Sigma-Aldrich, Steinheim, Germany). A549 cells were cultured in Ham's F-12K (Kaighn's) Medium (Life Technologies Limited, Paisley, UK), supplemented with 10% FBS (GE Healthcare, Logan, UT, USA). Calu-3 cells were cultured in Dulbecco's Modified Eagle's Medium (Life Technologies Limited, Paisley, UK), supplemented with 10% FBS (GE Healthcare, Logan, UT, USA) and 2 mM L-glutamine (Sigma-Aldrich, Steinheim, Germany). HCC827, NCI-H1299, NCI-H1703, and NCI-H358 cells were cultured in RPMI 1640 + GlutaMAX-I medium (Life Technologies Limited, Paisley, UK), supplemented with 10% FBS (GE Healthcare, Logan, UT, USA). All culture media contained 0.1 mg/mL streptomycin (Sigma-Aldrich, Steinheim, Germany) and 100 U/mL penicillin (Polfa Tarchomin, Warsaw, Poland). Cells were cultured in the AutoFlow Water Jacket Laboratory CO₂ incubator (NU-5510 E; NuAire, Plymouth, MN, USA) at +37 °C, in a humidified atmosphere saturated with 5% CO₂.

4.2. Compounds

The vitamin D metabolite (24*R*)-1,24-dihydroxycholecalciferol, (24*R*)-1,24(OH)₂D₃, coded as PRI-2191, was synthesized in the Department of Chemistry at the Pharmaceutical Research Institute (PRI) in Warsaw, Poland. Samples of PRI-2191, dried down at PRI from methanol solutions under argon in amber vials, were dissolved in 99.8% ethanol (POCH, Gliwice, Poland) and stored at −20 °C for further analysis. RESV was purchased from Selleck Chemicals (Houston, TX, USA).

4.3. Antiproliferative Activity

To determine the antiproliferative activity, the lung cancer cell lines were seeded onto 96-well plates at different densities as follows: 0.5×10^3 cells per well for A549 and NCI-H1299 cell lines and 2.5×10^3 cells per well for the remaining cell lines. After 24 h, PRI-2191 was added to the wells at concentrations of 1000, 100, 10, and 1 nM, and RESV was added at concentrations of 625, 125, 25, and 1 μM for 72 h either alone or in combination with PRI-2191 at a concentration of 100 nM. The antiproliferative activity of the tested compounds was evaluated using the sulforhodamine B (SRB) assay, as described previously [14]. The experiment was repeated at least three times independently. Proliferation inhibition and inhibitory concentration (IC₅₀) in each repeat were analyzed using Cheburator 0.4, Dmitry Nevozhay software [80].

4.4. Cell Cycle Analysis

For analyzing the progression of the cell cycle, the lung cancer cells were seeded in six-well plates (Corning Inc., Corning, NY, USA) in the culture medium. After incubating the plates for 24 h, the test compounds were added alone and in combination and the cells were exposed to these compounds for 72 h. RESV was used at the concentration of IC₂₅–IC₃₅ averaged to 20 μM, and PRI-2191 at 100 nM. Then, the cells were collected, washed in phosphate-buffered saline (PBS) (PChO, IIET PAS, Wrocław, Poland), and fixed in 70% ethanol (POCH, Gliwice, Poland) at −20 °C for at least 24 h. Later, the cells were washed in PBS and incubated at +37 °C for 1 h with RNase (Thermo Fisher Scientific, Waltham, MA, USA). Subsequently, they were incubated with propidium iodide for 30 min (Sigma-Aldrich, Steinheim, Germany) and analyzed using the BD LSR Fortessa flow cytometer with FACS Diva Software (Becton-Dickinson, San Jose, CA, USA) and then using Flowing Software v2.5.1 (University of Turku, Finland). The experiment was done in triplicate.

4.5. Caspase-3 Activity

The activity of caspase-3 was analyzed based on its ability to hydrolyze the synthetic substrate Ac-DEVD-ACC, leading to the release of 7-amino-coumarin fluorochrome. The

analysis was carried out by measuring the fluorescence intensity with time. Briefly, the lung cancer cell lines were seeded in 24-well plates, and 24 h later, the test compounds were added to the cells, either alone or in different combinations. RESV was used at a concentration of 0–75 μM and PRI-2191 at 100 nM. After incubating the cells for 72 h, caspase-3 activity was measured as described in [19].

4.6. Western Blot

For Western blot analysis, the human lung cancer cells treated with PRI-2191 (100 nM) and RESV (100 μM for Calu-3, 20 μM for the remaining cells) for 72 h were collected and lysed in RIPA buffer supplemented with cocktails of protease and phosphatase inhibitors (Sigma-Aldrich, Steinheim, Germany). Protein concentration was determined using the DC Protein Assay (Bio-Rad Laboratories Inc., Hercules, CA, USA). For this purpose, equal amounts of protein in Laemmli sample buffer were first separated in sodium dodecyl sulfate (SDS)-polyacrylamide gels (Bio-Rad Laboratories Inc., Hercules, CA, USA) and transferred to polyvinylidene difluoride membranes (GE Healthcare Europe GmbH, Freiburg, Germany). The membranes were then blocked in 5% nonfat dried milk in Tris-buffered saline (PChO, IJET PAS, Wroclaw, Poland) for 1 h at room temperature. Next, the membranes were incubated overnight at +4 °C with the following primary antibodies in 0.1% PBS-Tween 20 (Tween 20 from Sigma-Aldrich (Steinheim, Germany)): anti-p21, SIRT1 (Cell Signaling Technology, Beverly, MA, USA), anti-CYP24A1, p53, RXR α , VDR, and β -actin (loading control) (Santa Cruz Biotechnology Inc., Dallas, TX, USA). Then, the membranes were incubated with secondary antibodies conjugated with horseradish peroxidase (Santa Cruz Biotechnology Inc., Dallas, TX, USA). Finally, the results were visualized by applying the chemiluminescence method using the ChemiDoc MP Imaging System (Bio-Rad Laboratories Inc., Hercules, CA, USA). The analyses were repeated in triplicates. Densitometric analysis of the Western blots was performed using ImageJ 1.48v software (National Institutes of Health, Bethesda, MA, USA).

4.7. qPCR Analysis

For qPCR, the lung cancer cells were first seeded in Petri dishes, and after 24 h, they were exposed to PRI-2191 and RESV, either alone or in combination. After 72 h, the cells were collected from the Petri dishes with TRI Reagent (Sigma-Aldrich, Steinheim, Germany) and kept at -80 °C until further analysis. After thawing, RNA was isolated from all the cell samples using phenol-chloroform extraction [19]. Then, 2 μg RNA of each cell sample was cleaned from genomic DNA using DNase (Thermo Scientific, Vilnius, Lithuania), following which cDNA was synthesized using GoScript kit (Promega, Madison, WI, USA). Four most stable endogenous control genes were chosen from 16 endogenous control candidates by a screening analysis using TaqMan Array Human Endogenous Control Panel array (Life Technologies, Carlsbad, CA, USA). The expression of the chosen genes was analyzed using real-time PCR using TaqMan probes and Master Mix (Life Technologies, Carlsbad, CA, USA) in Viia 7 with Viia 7 Software v 1.1. The following TaqMan probes were used for the study: *18SrRNA* (Hs99999901_s1), *GAPDH* (cat. 4352665), *HPRT1* (Hs99999909_m1), *RPLP0* (Hs99999902_m1), *CD274* (Hs01125301_m1), *CXCL8* (Hs00174103_m1), *RXRA* (Hs01067640_m1), *SIRT1* (Hs01009006_m1), *SPP1* (Hs00959010_m1), *VDR* (Hs01045840_m1), and *VEGFA* (Hs00900055_m1). The $\Delta\Delta\text{CT}$ method was used for determining the relative changes in gene expression. The results were analyzed using Expression Suite Software v1.0.3 (Life Technologies, Carlsbad, CA, USA), and the level of gene expression was normalized to the most stable endogenous control.

4.8. ELISA Analysis

The secretion of cytokines IL-8, OPN, and VEGF by the lung cancer cell lines treated with PRI-2191 and RESV in conditioned medium was analyzed using ELISA (R&D Systems, Minneapolis, MN, USA). In addition, B7-H1 expression in the tested lung cancer cell lysates was also analyzed using ELISA (R&D Systems, Minneapolis, MN, USA). First, cells were

seeded onto culture dishes, and after 24 h, they were exposed to RESV and PRI-2191. After 72 h, the culture media were discarded and the cells were washed with saline, followed by the addition of serum-free and phenol red-free culture medium supplemented with 2 mM L-glutamine (Sigma-Aldrich, Steinheim, Germany) to each well. After incubating the cells for 24 h, the conditioned media were collected and frozen, and the cell number was counted. The concentration of the given growth factors was measured by ELISA, following the manufacturer's instructions. Then, the level of cytokines in each sample was normalized to the cell number. For ELISA analysis of PD-L1, the lung cancer cell lysates obtained as described in 4.6 were used. The level of PD-L1 in each sample was normalized to the total protein concentration.

4.9. Statistical Analysis

Statistical analysis and graph preparation was done using GraphPad Prism 7 (GraphPad Software, Inc., San Diego, CA, USA). Where applicable, one-way ANOVA, and unpaired *t*-test were applied. A *p*-value < 0.05 was considered statistically significant.

5. Conclusions

We found that RESV and/or vitamin D derivative may exert a divergent effect on the progression of the cell cycle, the activity of caspase-3, and the expression of several proteins, including p53, VEGF, IL-8, OPN, and PD-L1, depending on the type and genetic profile of cells. RESV augmented VDR expression in a few lung cancer cell lines, which suggests that this compound may influence the vitamin D signaling in lung cancer cells, leading to an increase in vitamin D activity when used in the combination regimens. In addition, when PRI-2191 was combined with RESV, significant upregulation of CYP24A1 expression was noticed in some lung cancer cells, confirming the ability of RESV to modulate the action of vitamin D in these cells. Furthermore, opposite effects were observed on OPN expression in two KRAS-mutant lung cancer cell lines when PRI-2191 was added to RESV. PRI-2191 counteracted the induction of OPN expression in A549 cells but augmented the induction in NCI-H358 cells. On the other hand, only the EGFR-mutant HCC827 cells produced less IL-8 after exposure to RESV together with PRI-2191, compared to the cells incubated with RESV alone. Moreover, PRI-2191 caused significant upregulation of PD-L1 expression in HCC827 and NCI-H358 cells, while a significant increase in PD-L1 expression was seen in A549 cells only when PRI-2191 was used together with RESV. Additionally, PRI-2191 in combination with RESV caused an increase in the level of PD-L1 expression in NCI-H358 cells, compared to PRI-2191 alone. Thus, the study showed that although the impact of vitamin D on cell proliferation or cell cycle was not very significant, it was more pronounced at the molecular level, through the modulation of the expression of several proteins engaged in the regulation of angiogenesis, immune response, and other functions, varied depending on the genetic background of the cancer cells when vitamin D was combined with RESV. We speculate that the differences in response to RESV and PRI-2191 between EGFRmut and KRASmut cell lines may result from the differences in epigenetic modifications since both subtypes are associated with divergent smoking history and smoking can induce epigenetic machinery alterations. In turn, epigenetic changes affect the access of transcription factors, such as VDR, to the genes they regulate. Therefore, the impact of epigenetic changes on divergent activity of RESV and PRI-2191 in lung cancer cells requires additional study.

Supplementary Materials: The following data are available online at <https://www.mdpi.com/1422-0067/22/5/2354/s1>. Figure S1: Inhibition of cell proliferation in lung cancer cell lines treated with resveratrol (RESV) alone (green) or in combination with (24R)-1,24-dihydroxycholecalciferol, (24R)-1,24(OH)₂D₃ (PRI-2191) (100 nM) (black), Figure S2: Representative histograms of cell cycle analysis of lung cancer cells treated with PRI-2191 (100 nM) and RESV (20 μM), Figure S3: Flow cytometry cell cycle analysis of lung cancer cells after treatment with PRI-2191 and RESV, Figure S4: Induction of caspase-3 activity in lung cancer cells by PRI-2191 and RESV, Figure S5: Western blot analysis of SIRT1 expression in lung cancer cells treated with PRI-2191 (100 nM) and RESV (20 μM),

Figure S6: Western blot analysis of (A) p53 and (B) p21 expression in lung cancer cells treated with PRI-2191 (100 nM) and RESV (20 μ M), Figure S7: Western blot analysis of (A) CYP24A1, (B) RXR α , and (C) vitamin D receptor (VDR) expression in lung cancer cells treated with PRI-2191 (100 nM) and RESV (20 μ M), Figure S8: Analysis of SIRT1, RXR α , and VDR expression in lung cancer cells treated with PRI-2191 (100 nM) and RESV (20 μ M) using qPCR, Figure S9: Analysis of vascular endothelial growth factor A (VEGFA) expression in lung cancer cells treated with PRI-2191 (100 nM) and RESV (20 μ M) using PCR, Figure S10: Analysis of osteopontin (OPN) expression in lung cancer cells treated with PRI-2191 (100 nM) and RESV (20 μ M) using PCR, Figure S11: Analysis of interleukin 8 (CXCL8) (IL-8) expression in lung cancer cells treated with PRI-2191 (100 nM) and RESV (20 μ M) using PCR, Figure S12: Analysis of PD-L1 expression in lung cancer cells treated with PRI-2191 (100 nM) and RESV (20 μ M) using PCR.

Author Contributions: Conceptualization, E.M.; methodology, E.M., B.M., and M.C.; software, E.M.; validation, E.M., A.K., and J.W.; formal analysis, E.M. and B.M.; investigation, E.M., B.M., K.B., and M.G.; resources, E.M., M.C., and A.K.; data curation, E.M., and B.M.; writing—original draft preparation, E.M. and B.M.; writing—review and editing, A.K. and J.W.; visualization, E.M.; supervision, A.K. and J.W.; project administration, E.M.; funding acquisition, E.M. All authors have read and agreed to the published version of the manuscript.

Funding: This research was funded by the National Science Centre (NCN), grant number 2018/31/D/NZ3/01739.

Institutional Review Board Statement: Not applicable.

Informed Consent Statement: Not applicable.

Data Availability Statement: Not applicable.

Acknowledgments: We thank Professor Zdzisław Krawczyk from Cancer Center and Institute of Oncology in Gliwice, Poland, for providing us with NCI-H1299 lung cancer cells.

Conflicts of Interest: The authors declare no conflict of interest. The funders had no role in the design of the study; in the collection, analyses, or interpretation of the data; in the writing of the manuscript; or in the decision to publish the results.

References

1. Fresco, P.; Borges, F.I.G.M.; Diniz, C.G.; Marques, M. New insights on the anticancer properties of dietary polyphenols. *Med. Res. Rev.* **2006**, *26*, 747–766. [CrossRef]
2. Li, M.; Zhang, Z.; Hill, D.L.; Wang, H.; Zhang, R. Curcumin, a Dietary Component, Has Anticancer, Chemosensitization, and Radiosensitization Effects by Down-regulating the MDM2 Oncogene through the PI3K/mTOR/ETS2 Pathway. *Cancer Res.* **2007**, *67*, 1988–1996. [CrossRef]
3. Pesakhov, S.; Khanin, M.; Studzinski, G.P.; Danilenko, M. Distinct Combinatorial Effects of the Plant Polyphenols Curcumin, Carnosic Acid, and Silibinin on Proliferation and Apoptosis in Acute Myeloid Leukemia Cells. *Nutr. Cancer* **2010**, *62*, 811–824. [CrossRef]
4. Wang, Z.; Dabrosin, C.; Yin, X.; Fuster, M.M.; Arreola, A.; Rathmell, W.K.; Generali, D.; Nagaraju, G.P.; El-Rayes, B.; Ribatti, D.; et al. Broad targeting of angiogenesis for cancer prevention and therapy. *Semin. Cancer Biol.* **2015**, *35*, S224–S243. [CrossRef] [PubMed]
5. Lacroix, S.; Badoux, J.K.; Scott-Boyer, M.-P.; Parolo, S.; Matone, A.; Priami, C.; Morine, M.J.; Kaput, J.; Moco, S. A computationally driven analysis of the polyphenol-protein interactome. *Sci. Rep.* **2018**, *8*, 1–13. [CrossRef]
6. Fulda, S.; Debatin, K.-M. Sensitization for anticancer drug-induced apoptosis by the chemopreventive agent resveratrol. *Oncogene* **2004**, *23*, 6702–6711. [CrossRef]
7. Kubota, T.; Uemura, Y.; Kobayashi, M.; Taguchi, H. Combined effects of resveratrol and paclitaxel on lung cancer cells. *Anticancer. Res.* **2003**, *23*, 4039–4046.
8. Baatout, S.; Derradji, H.; Jacquet, P.; Ooms, D.; Michaux, A.; Mergeay, M. Enhanced radiation-induced apoptosis of cancer cell lines after treatment with resveratrol. *Int. J. Mol. Med.* **2004**, *13*, 895–902. [CrossRef]
9. Niedzwiecki, A.; Roomi, M.W.; Kalinovsky, T.; Rath, M. Anticancer Efficacy of Polyphenols and Their Combinations. *Nutrients* **2016**, *8*, 552. [CrossRef] [PubMed]
10. Amararathna, M.; Johnston, M.R.; Rupasinghe, H.P.V. Plant Polyphenols as Chemopreventive Agents for Lung Cancer. *Int. J. Mol. Sci.* **2016**, *17*, 1352. [CrossRef] [PubMed]
11. Feldman, D.; Krishnan, A.V.; Swami, S.; Giovannucci, E.; Feldman, B.J. The role of vitamin D in reducing cancer risk and progression. *Nat. Rev. Cancer* **2014**, *14*, 342–357. [CrossRef]

12. Okamoto, R.; Delansorne, R.; Wakimoto, N.; Doan, N.B.; Akagi, T.; Shen, M.; Ho, Q.H.; Said, J.W.; Koeffler, H.P. Inecalcitol, an analog of $1\alpha,25(\text{OH})_2\text{D}_3$, induces growth arrest of androgen-dependent prostate cancer cells. *Int. J. Cancer* **2012**, *130*, 2464–2473. [CrossRef]
13. Trynda, J.; Turlej, E.; Milczarek, M.; Pietraszek, A.; Chodyński, M.; Kutner, A.; Wietrzyk, J. Antiproliferative Activity and in Vivo Toxicity of Double-Point Modified Analogs of 1,25-Dihydroxyergocalciferol. *Int. J. Mol. Sci.* **2015**, *16*, 24873–24894. [CrossRef] [PubMed]
14. Maj, E.; Trynda, J.; Maj, B.; Gebura, K.; Bogunia-Kubik, K.; Chodyński, M.; Kutner, A.; Wietrzyk, J. Differential response of lung cancer cell lines to vitamin D derivatives depending on EGFR, KRAS, p53 mutation status and VDR polymorphism. *J. Steroid Biochem. Mol. Biol.* **2019**, *193*, 105431. [CrossRef] [PubMed]
15. Milczarek, M.; Rossowska, J.; Kłopotowska, D.; Stachowicz, M.; Kutner, A.; Wietrzyk, J. Tacalcitol increases the sensitivity of colorectal cancer cells to 5-fluorouracil by downregulating the thymidylate synthase. *J. Steroid Biochem. Mol. Biol.* **2019**, *190*, 139–151. [CrossRef]
16. Milczarek, M.; Psurski, M.; Kutner, A.; Wietrzyk, J. Vitamin D analogs enhance the anticancer activity of 5-fluorouracil in an in vivomouse colon cancer model. *BMC Cancer* **2013**, *13*, 294. [CrossRef] [PubMed]
17. Leyssens, C.; Verlinden, L.; Verstuyf, A. The future of vitamin D analogs. *Front. Physiol.* **2014**, *5*, 18. [CrossRef]
18. Maj, E.; Filip-Psurska, B.; Świtalska, M.; Kutner, A.; Wietrzyk, J. Vitamin D Analogs Potentiate the Antitumor Effect of Imatinib Mesylate in a Human A549 Lung Tumor Model. *Int. J. Mol. Sci.* **2015**, *16*, 27191–27207. [CrossRef]
19. Maj, E.; Filip-Psurska, B.; Milczarek, M.; Psurski, M.; Kutner, A.; Wietrzyk, J. Vitamin D derivatives potentiate the anticancer and anti-angiogenic activity of tyrosine kinase inhibitors in combination with cytostatic drugs in an A549 non-small cell lung cancer model. *Int. J. Oncol.* **2017**, *52*, 337–366. [CrossRef] [PubMed]
20. Pawlik, A.; Anisiewicz, A.; Filip-Psurska, B.; Kłopotowska, D.; Maciejewska, M.; Mazur, A.; Wietrzyk, J. Divergent Effect of Tacalcitol (PRI-2191) on Th17 Cells in 4T1 Tumor Bearing Young and Old Ovariectomized Mice. *Aging Dis.* **2020**, *11*, 241–253. [CrossRef] [PubMed]
21. Campbell, M.J.; Trump, D.L. Vitamin D Receptor Signaling and Cancer. *Endocrinol. Metab. Clin. North Am.* **2017**, *46*, 1009–1038. [CrossRef] [PubMed]
22. Ding, L.; Getz, G.; Wheeler, D.A.; Mardis, E.R.; McLellan, M.D.; Cibulskis, K.; Sougnez, C.; Greulich, H.; Muzny, D.M.; Morgan, M.B.; et al. Somatic mutations affect key pathways in lung adenocarcinoma. *Nat. Cell Biol.* **2008**, *455*, 1069–1075. [CrossRef]
23. Bacchi, C.E.; Ciol, H.; Queiroga, E.M.; Benine, L.C.; Silva, L.H.; Ojopi, E.B. Epidermal growth factor receptor and KRAS mutations in Brazilian lung cancer patients. *Clinics* **2012**, *67*, 419–424. [CrossRef]
24. Robles, A.I.; Linke, S.P.; Harris, C.C. The p53 network in lung carcinogenesis. *Oncogene* **2002**, *21*, 6898–6907. [CrossRef] [PubMed]
25. Vogelstein, B.; Sur, S.; Prives, C. p53: The Most Frequently Altered Gene in Human Cancers. *Nat. Educ.* **2010**, *3*, 6.
26. Nachliely, M.; Sharony, E.; Bolla, N.R.; Kutner, A.; Danilenko, M. Prodifferentiation Activity of Novel Vitamin D2 Analogs PRI-1916 and PRI-1917 and Their Combinations with a Plant Polyphenol in Acute Myeloid Leukemia Cells. *Int. J. Mol. Sci.* **2016**, *17*, 1068. [CrossRef] [PubMed]
27. Howitz, K.T.; Bitterman, K.J.; Cohen, H.Y.; Lamming, D.W.; Lavu, S.; Wood, J.G.; Zipkin, R.E.; Chung, P.; Kisielewski, A.; Zhang, L.-L.; et al. Small molecule activators of sirtuins extend *Saccharomyces cerevisiae* lifespan. *Nature* **2003**, *425*, 191–196. [CrossRef] [PubMed]
28. Carafa, V.; Rotili, D.; Forgione, M.; Cuomo, F.; Serretiello, E.; Hailu, G.S.; Jarho, E.; Lahtela-Kakkonen, M.; Maija, L.-K.; Altucci, L. Sirtuin functions and modulation: from chemistry to the clinic. *Clin. Epigenet.* **2016**, *8*, 1–21. [CrossRef]
29. Langley, E.; Pearson, M.; Faretta, M.; Bauer, U.; Frye, R.A.; Minucci, S.; Pelicci, P.G.; Kouzarides, T. Human SIR2 deacetylates p53 and antagonizes PML/p53-induced cellular senescence. *EMBO J.* **2002**, *21*, 2383–2396. [CrossRef]
30. Sabir, M.S.; Khan, Z.; Hu, C.; Galligan, M.A.; Dussik, C.M.; Mallick, S.; Stone, A.D.; Batie, S.F.; Jacobs, E.T.; Whitfield, G.K.; et al. SIRT1 enzymatically potentiates 1,25-dihydroxyvitamin D3 signaling via vitamin D receptor deacetylation. *J. Steroid Biochem. Mol. Biol.* **2017**, *172*, 117–129. [CrossRef]
31. Ohyama, Y.; Ozono, K.; Uchida, M.; Shinki, T.; Kato, S.; Suda, T.; Yamamoto, O.; Noshiro, M.; Kato, Y. Identification of a vitamin D-responsive element in the 5′-flanking region of the rat 25-hydroxyvitamin D3 24-hydroxylase gene. *J. Biol. Chem.* **1994**, *269*, 10545–10550. [CrossRef]
32. Sharabani, H.; Izumchenko, E.; Wang, Q.; Kreinin, R.; Steiner, M.; Barvish, Z.; Kafka, M.; Sharoni, Y.; Levy, J.; Uskokovic, M.; et al. Cooperative antitumor effects of vitamin D3 derivatives and rosemary preparations in a mouse model of myeloid leukemia. *Int. J. Cancer* **2006**, *118*, 3012–3021. [CrossRef]
33. Bobilev, I.; Novik, V.; Levi, I.; Shpilberg, O.; Levy, J.; Sharoni, Y.; Studzinski, G.P.; Danilenko, M. The Nrf2 transcription factor is a positive regulator of myeloid differentiation of acute myeloid leukemia cells. *Cancer Biol. Ther.* **2011**, *11*, 317–329. [CrossRef]
34. Bhatia, V.; Falzon, M. Restoration of the anti-proliferative and anti-migratory effects of 1,25-dihydroxyvitamin D by silibinin in vitamin D-resistant colon cancer cells. *Cancer Lett.* **2015**, *362*, 199–207. [CrossRef] [PubMed]
35. Wassermann, R.; Novik, V.; Danilenko, M. Cell-Type-Specific Effects of Silibinin on Vitamin D-Induced Differentiation of Acute Myeloid Leukemia Cells Are Associated with Differential Modulation of RXR α Levels. *Leuk. Res. Treat.* **2012**, *2012*, 401784. [CrossRef]
36. Inoue, J.; Choi, J.-M.; Yoshidomi, T.; Yashiro, T.; Sato, R. Quercetin enhances VDR activity, leading to stimulation of its target gene expression in Caco-2 cells. *J. Nutr. Sci. Vitaminol.* **2010**, *56*, 326–330. [CrossRef] [PubMed]

37. Haussler, M.R.; Saini, R.K.; Sabir, M.S.; Dussik, C.M.; Khan, Z.; Whitfield, G.K.; Griffin, K.P.; Kaneko, I.; Jurutka, P.W. Vitamin D Nutrient-Gene Interactions and Healthful Aging. In *Molecular Basis of Nutrition and Aging*; Elsevier: Amsterdam, The Netherlands, 2016; pp. 449–471.
38. Benitez, D.A.; Pozo-Guisado, E.; Alvarez-Barrientos, A.; Fernandez-Salguero, P.M.; Castellón, E.A. Mechanisms Involved in Resveratrol-Induced Apoptosis and Cell Cycle Arrest in Prostate Cancer-Derived Cell Lines. *J. Androl.* **2006**, *28*, 282–293. [CrossRef]
39. Pozo-Guisado, E.; Alvarez-Barrientos, A.; Mulero-Navarro, S.; Santiago-Josefat, B.; Fernandez-Salguero, P.M. The antiproliferative activity of resveratrol results in apoptosis in MCF-7 but not in MDA-MB-231 human breast cancer cells: cell-specific alteration of the cell cycle. *Biochem. Pharmacol.* **2002**, *64*, 1375–1386. [CrossRef]
40. Da Costa, D.C.F.; Campos, N.P.C.; Santos, R.A.; Guedes-Da-Silva, F.H.; Martins-Dinis, M.M.D.C.; Zanphorlin, L.; Ramos, C.; Rangel, L.P.; Silva, J.L. Resveratrol prevents p53 aggregation in vitro and in breast cancer cells. *Oncotarget* **2018**, *9*, 29112–29122. [CrossRef]
41. Oren, M.; Rotter, V. Mutant p53 Gain-of-Function in Cancer. *Cold Spring Harb. Perspect. Biol.* **2009**, *2*, a001107. [CrossRef]
42. Pedrote, M.M.; Motta, M.F.; Ferretti, G.D.; Norberto, D.R.; Spohr, T.C.; Lima, F.R.; Gratton, E.; Silva, J.L.; de Oliveira, G.A. Oncogenic Gain of Function in Glioblastoma Is Linked to Mutant p53 Amyloid Oligomers. *iScience* **2020**, *23*, 100820. [CrossRef] [PubMed]
43. Yi, Y.W.; Kang, H.J.; Kim, H.J.; Kong, Y.; Brown, M.L.; Bae, I. Targeting Mutant p53 by a SIRT1 Activator YK-3-237 Inhibits the Proliferation of Triple-Negative Breast Cancer Cells. *Oncotarget* **2013**, *4*, 984–994. [CrossRef]
44. Willis, A.; Jung, E.J.; Wakefield, T.; Chen, X. Mutant p53 exerts a dominant negative effect by preventing wild-type p53 from binding to the promoter of its target genes. *Oncogene* **2004**, *23*, 2330–2338. [CrossRef]
45. Zhao, Y.; Lu, S.; Wu, L.; Chai, G.; Wang, H.; Chen, Y.; Sun, J.; Yu, Y.; Zhou, W.; Zheng, Q.; et al. Acetylation of p53 at Lysine 373/382 by the Histone Deacetylase Inhibitor Depsipeptide Induces Expression of p21Waf1/Cip1. *Mol. Cell. Biol.* **2006**, *26*, 2782–2790. [CrossRef] [PubMed]
46. Rokudai, S.; Laptenko, O.; Arnal, S.M.; Taya, Y.; Kitabayashi, I.; Prives, C. MOZ increases p53 acetylation and premature senescence through its complex formation with PML. *PNAS* **2013**, *110*, 3895–3900. [CrossRef]
47. Brochier, C.; Dennis, G.; Riviaccio, M.A.; McLaughlin, K.; Coppola, G.; Ratan, R.R.; Langley, B. Specific Acetylation of p53 by HDAC Inhibition Prevents DNA Damage-Induced Apoptosis in Neurons. *J. Neurosci.* **2013**, *33*, 8621–8632. [CrossRef]
48. Ekongsbak, M.; Levring, T.B.; Egeisler, C.; Von Essen, M.R. The Vitamin D Receptor and T Cell Function. *Front. Immunol.* **2013**, *4*, 148. [CrossRef]
49. Haussler, M.R.; Whitfield, G.K.; Kaneko, I.; Haussler, C.A.; Hsieh, D.; Hsieh, J.-C.; Jurutka, P.W. Molecular Mechanisms of Vitamin D Action. *Calcif. Tissue Int.* **2013**, *92*, 77–98. [CrossRef] [PubMed]
50. Dampf-Stone, A.; Batie, S.F.; Sabir, M.S.; Jacobs, E.T.; Lee, J.H.; Whitfield, G.K.; Haussler, M.R.; Jurutka, P.W. Resveratrol Potentiates Vitamin D and Nuclear Receptor Signaling. *J. Cell. Biochem.* **2015**, *116*, 1130–1143. [CrossRef]
51. Singh, C.K.; Kumar, A.; Lavoie, H.A.; DiPette, D.J.; Singh, U.S. Resveratrol Prevents Impairment in Activation of Retinoic Acid Receptors and MAP Kinases in the Embryos of a Rodent Model of Diabetic Embryopathy. *Reprod. Sci.* **2012**, *19*, 949–961. [CrossRef]
52. García-Quiroz, J.; García-Becerra, R.; Santos-Cuevas, C.; Ramírez-Nava, G.J.; Morales-Guadarrama, G.; Cárdenas-Ochoa, N.; Segovia-Mendoza, M.; Prado-Garcia, H.; Ordaz-Rosado, D.; Avila, E.; et al. Synergistic Antitumorigenic Activity of Calcitriol with Curcumin or Resveratrol is Mediated by Angiogenesis Inhibition in Triple Negative Breast Cancer Xenografts. *Cancers* **2019**, *11*, 1739. [CrossRef]
53. Tang, Z.; Liu, X.-Y.; Zou, P. Resveratrol inhibits the secretion of vascular endothelial growth factor and subsequent proliferation in human leukemia U937 cells. *Acta Acad. Med. Wuhan* **2007**, *27*, 508–512. [CrossRef]
54. Núñez, M.J.; Novío, S.; Balboa, J.; Seoane, J.; Suárez, J.A.; Freire-Garabal, M. Effects of resveratrol on expression of vascular endothelial growth factor in human gingival fibroblasts stimulated by periodontal pathogens. *Acta Odontol. Scand.* **2010**, *68*, 239–247. [CrossRef]
55. Sahin, E.; Bayçu, C.; Kopal, A.T.; Donmez, D.B.; Bektur, E. Resveratrol reduces IL-6 and VEGF secretion from co-cultured A549 lung cancer cells and adipose-derived mesenchymal stem cells. *Tumor Biol.* **2015**, *37*, 7573–7582. [CrossRef] [PubMed]
56. Wright, C.; Iyer, A.K.V.; Yakisich, J.S.; Azad, N. Anti-Tumorigenic Effects of Resveratrol in Lung Cancer Cells Through Modulation of c-FLIP. *Curr. Cancer Drug Targets* **2017**, *17*, 669–680. [CrossRef]
57. Reinmuth, N.; Jauch, A.; Xu, E.C.; Muley, T.; Granzow, M.; Hoffmann, H.; Dienemann, H.; Herpel, E.; Schnabel, P.A.; Herth, F.J.; et al. Correlation of EGFR mutations with chromosomal alterations and expression of EGFR, ErbB3 and VEGF in tumor samples of lung adenocarcinoma patients. *Lung Cancer* **2008**, *62*, 193–201. [CrossRef] [PubMed]
58. Wei, R.; Wong, J.P.C.; Kwok, H.F. Osteopontin—A promising biomarker for cancer therapy. *J. Cancer* **2017**, *8*, 2173–2183. [CrossRef]
59. Jin, Y.; Tong, D.-Y.; Chen, J.-N.; Feng, Z.-Y.; Yang, J.-Y.; Shao, C.-K.; Li, J.-P. Overexpression of Osteopontin, $\alpha\beta3$ and Pim-1 Associated with Prognostically Important Clinicopathologic Variables in Non-Small Cell Lung Cancer. *PLoS ONE* **2012**, *7*, e48575. [CrossRef]
60. Noda, M.; Vogel, R.L.; Craig, A.M.; Prah, J.; DeLuca, H.F.; Denhardt, D.T. Identification of a DNA sequence responsible for binding of the 1,25-dihydroxyvitamin D3 receptor and 1,25-dihydroxyvitamin D3 enhancement of mouse secreted phosphoprotein 1 (SPP-1 or osteopontin) gene expression. *PNAS* **1990**, *87*, 9995–9999. [CrossRef]

61. Shen, Q.; Christakos, S. The Vitamin D Receptor, Runx2, and the Notch Signaling Pathway Cooperate in the Transcriptional Regulation of Osteopontin. *J. Biol. Chem.* **2005**, *280*, 40589–40598. [CrossRef] [PubMed]
62. Boissy, P.; Andersen, T.L.; Abdallah, B.M.; Kassem, M.; Plesner, T.; Delaissé, J.-M. Resveratrol Inhibits Myeloma Cell Growth, Prevents Osteoclast Formation, and Promotes Osteoblast Differentiation. *Cancer Res.* **2005**, *65*, 9943–9952. [CrossRef]
63. Lee, Y.-M.; Shin, S.-I.; Shin, K.-S.; Park, B.-H.; Kim, E.-C. The role of sirtuin 1 in osteoblastic differentiation in human periodontal ligament cells. *J. Periodontol Res.* **2011**, *46*, 712–721. [CrossRef] [PubMed]
64. Li, X.; Jiang, Z.; Li, X.; Zhang, X. SIRT1 overexpression protects non-small cell lung cancer cells against osteopontin-induced epithelial-mesenchymal transition by suppressing NF- κ B signaling. *Oncotargets Ther.* **2018**, *11*, 1157–1171. [CrossRef] [PubMed]
65. Rangaswami, H.; Bulbule, A.; Kundu, G.C. Osteopontin: role in cell signaling and cancer progression. *Trends Cell Biol.* **2006**, *16*, 79–87. [CrossRef] [PubMed]
66. Donnelly, L.E.; Newton, R.; Kennedy, G.E.; Fenwick, P.S.; Leung, R.H.F.; Ito, K.; Russell, R.E.K.; Barnes, P.J. Anti-inflammatory effects of resveratrol in lung epithelial cells: molecular mechanisms. *Am. J. Physiol. Cell. Mol. Physiol.* **2004**, *287*, L774–L783. [CrossRef]
67. Tino, A.B.; Chitcholtan, K.; Sykes, P.H.; Garrill, A. Resveratrol and acetyl-resveratrol modulate activity of VEGF and IL-8 in ovarian cancer cell aggregates via attenuation of the NF- κ B protein. *J. Ovarian Res.* **2016**, *9*, 1–12. [CrossRef]
68. Pastore, S.; Lulli, D.; Maurelli, R.; Dellambra, E.; De Luca, C.; Korkina, L.G. Resveratrol Induces Long-Lasting IL-8 Expression and Peculiar EGFR Activation/Distribution in Human Keratinocytes: Mechanisms and Implications for Skin Administration. *PLoS ONE* **2013**, *8*, e59632. [CrossRef]
69. Fan, X.-X.; Yao, X.-J.; Xu, S.W.; Wong, V.K.-W.; He, J.-X.; Ding, J.; Xue, W.-W.; Mujtaba, T.; Michelangeli, F.; Huang, M.; et al. (Z) 3,4,5,4'-trans-tetramethoxystilbene, a new analogue of resveratrol, inhibits gefitinb-resistant non-small cell lung cancer via selectively elevating intracellular calcium level. *Sci. Rep.* **2015**, *5*, 16348. [CrossRef]
70. Cordero, J.B.; Cozzolino, M.; Lu, Y.; Vidal, M.; Slatopolsky, E.; Stahl, P.D.; Barbieri, M.A.; Dusso, A. 1,25-Dihydroxyvitamin D Down-regulates Cell Membrane Growth- and Nuclear Growth-promoting Signals by the Epidermal Growth Factor Receptor. *J. Biol. Chem.* **2002**, *277*, 38965–38971. [CrossRef]
71. McGaffin, K.R.; A Chrysogelos, S. Identification and characterization of a response element in the EGFR promoter that mediates transcriptional repression by 1,25-dihydroxyvitamin D₃ in breast cancer cells. *J. Mol. Endocrinol.* **2005**, *35*, 117–133. [CrossRef]
72. Shen, Z.; Zhang, X.; Tang, J.; Kasiappan, R.; Jinwal, U.; Li, P.; Hann, S.; Nicosia, S.V.; Wu, J.; Zhang, X.; et al. The coupling of epidermal growth factor receptor down regulation by 1 α ,25-dihydroxyvitamin D₃ to the hormone-induced cell cycle arrest at the G1-S checkpoint in ovarian cancer cells. *Mol. Cell. Endocrinol.* **2011**, *338*, 58–67. [CrossRef] [PubMed]
73. Ostrand-Rosenberg, S.; Horn, L.A.; Haile, S.T. The Programmed Death-1 Immune-Suppressive Pathway: Barrier to Antitumor Immunity. *J. Immunol.* **2014**, *193*, 3835–3841. [CrossRef]
74. Dong, H.; Strome, S.E.; Salomao, D.R.; Tamura, H.; Hirano, F.; Flies, D.B.; Roche, P.C.; Lu, J.; Zhu, G.; Tamada, K.; et al. Tumor-associated B7-H1 promotes T-cell apoptosis: A potential mechanism of immune evasion. *Nat. Med.* **2002**, *8*, 793–800. [CrossRef]
75. Dimitrov, V.; Bouttier, M.; Boukhaled, G.; Salehi-Tabar, R.; Avramescu, R.G.; Memari, B.; Hasaj, B.; Lukacs, G.L.; Krawczyk, C.M.; White, J.H. Hormonal vitamin D up-regulates tissue-specific PD-L1 and PD-L2 surface glycoprotein expression in humans but not mice. *J. Biol. Chem.* **2017**, *292*, 20657–20668. [CrossRef] [PubMed]
76. Bendix, M.; Greisen, S.; Dige, A.; Hvas, C.L.; Bak, N.; Jørgensen, S.P.; Dahlerup, J.F.; Deleuran, B.; Agnholt, J. Vitamin D increases programmed death receptor-1 expression in Crohn's disease. *Oncotarget* **2017**, *8*, 24177–24186. [CrossRef]
77. Lucas, J.; Hsieh, T.-C.; Halicka, H.D.; Darzynkiewicz, Z.; Wu, J.M. Upregulation of PD-L1 expression by resveratrol and piceatannol in breast and colorectal cancer cells occurs via HDAC3/p300-mediated NF- κ B signaling. *Int. J. Oncol.* **2018**, *53*, 1469–1480. [CrossRef]
78. Verdura, S.; Cuyàs, E.; Cortada, E.; Brunet, J.; Lopez-Bonet, E.; Martin-Castillo, B.; Bosch-Barrera, J.; Encinar, J.A.; Menendez, J.A. Resveratrol targets PD-L1 glycosylation and dimerization to enhance antitumor T-cell immunity. *Aging* **2020**, *12*, 8–34. [CrossRef]
79. Zhang, Y.; Yang, S.; Yang, Y.; Liu, T. Resveratrol induces immunogenic cell death of human and murine ovarian carcinoma cells. *Infect. Agents Cancer* **2019**, *14*, 1–9. [CrossRef] [PubMed]
80. Nevozhay, D. Cheburator Software for Automatically Calculating Drug Inhibitory Concentrations from In Vitro Screening Assays. *PLoS ONE* **2014**, *9*, e106186. [CrossRef] [PubMed]



Review

New Approaches to Assess Mechanisms of Action of Selective Vitamin D Analogues

John Wesley Pike * and Mark B. Meyer

Department of Biochemistry, University of Wisconsin-Madison, 433 Babcock Drive, Madison, WI 53706, USA; markmeyer@wisc.edu

* Correspondence: jpikew@wisc.edu; Tel.: +1-(608)-262-8229; Fax: +1-(608)-263-7609

Abstract: Recent studies of transcription have revealed an advanced set of overarching principles that govern vitamin D action on a genome-wide scale. These tenets of vitamin D transcription have emerged as a result of the application of now well-established techniques of chromatin immunoprecipitation coupled to next-generation DNA sequencing that have now been linked directly to CRISPR-Cas9 genomic editing in culture cells and in mouse tissues *in vivo*. Accordingly, these techniques have established that the vitamin D hormone modulates sets of cell-type specific genes via an initial action that involves rapid binding of the VDR–ligand complex to multiple enhancer elements at open chromatin sites that drive the expression of individual genes. Importantly, a sequential set of downstream events follows this initial binding that results in rapid histone acetylation at these sites, the recruitment of additional histone modifiers across the gene locus, and in many cases, the appearance of H3K36me3 and RNA polymerase II across gene bodies. The measured recruitment of these factors and/or activities and their presence at specific regions in the gene locus correlate with the emerging presence of cognate transcripts, thereby highlighting sequential molecular events that occur during activation of most genes both *in vitro* and *in vivo*. These features provide a novel approach to the study of vitamin D analogs and their actions *in vivo* and suggest that they can be used for synthetic compound evaluation and to select for novel tissue- and gene-specific features. This may be particularly useful for ligand activation of nuclear receptors given the targeting of these factors directly to genetic sites in the nucleus.

Keywords: vitamin D biology and action; transcription; ChIP-chip analysis; distal enhancers; histone H3 acetylation; RNA polymerase II; analogue actions at genes; vitamin D hormone (1,25(OH)₂D₃)

Citation: Pike, J.W.; Meyer, M.B. New Approaches to Assess Mechanisms of Action of Selective Vitamin D Analogues. *Int. J. Mol. Sci.* **2021**, *22*, 12352. <https://doi.org/10.3390/ijms222212352>

Academic Editors: Andrzej Kutner, Geoffrey Brown and Enikő Kallay

Received: 14 October 2021

Accepted: 11 November 2021

Published: 16 November 2021

Publisher's Note: MDPI stays neutral with regard to jurisdictional claims in published maps and institutional affiliations.



Copyright: © 2021 by the authors. Licensee MDPI, Basel, Switzerland. This article is an open access article distributed under the terms and conditions of the Creative Commons Attribution (CC BY) license (<https://creativecommons.org/licenses/by/4.0/>).

1. Background and Review Rationale

The fundamental actions of the steroid hormone 1,25-dihydroxyvitamin D₃ (1,25(OH)₂D₃) are to contribute to the maintenance of calcium (Ca) and phosphorus (P) homeostasis in vertebrate organisms [1]. This activity is achieved through direct actions of the hormone in the intestine, kidney, and bone, and through feedback inhibition of PTH production at the parathyroid glands and induction of FGF23 production in mature osteoblasts and osteocytes. In the intestine, the transepithelial uptake of Ca is known to be upregulated by 1,25(OH)₂D₃ via induction of the apical Ca ion channel gene *TRPV6*, genes encoding the soluble cytosolic Ca binding calbindins, and genes that include the basolateral ATPase driven Ca pump *PMCA2b*. P uptake, on the other hand, is regulated in the intestine by induction of the P transporter gene *SLC34A2* [2]. In the kidney, Ca levels are controlled directly via the induction of TRPV5, the calbindins, and the sodium/Ca exchanger *NCX1*, while P is regulated by *SLC34A1* and *SLC34A3* and indirectly via 1,25(OH)₂D₃'s regulatory control of hormonal PTH and FGF23 [3–6]. FGF23 is dominant with regard to P regulation, although PTH has similar yet more modest actions [7,8]. Activity in the skeleton is driven via 1,25(OH)₂D₃ and PTH, primarily via RANKL expression, a TNF-like factor that is produced in stroma, osteoblastic cells, and osteocytes and is essential to the formation, activation,

and survival of bone-resorbing osteoclasts [9–11]. Recent studies suggest that the osteocyte plays a fundamental role in lacunar bone formation and resorption within cortical bone as well [12]. The vitamin D hormone also contributes to the regulation of many additional genes that are involved not only in osteocyte function, as above, but also in osteoblast differentiation, bone formation, and biomineralization [13–15]. This hormone also contributes to the transcriptional regulation of *FGF23*, a primarily osteocyte-produced hormone [16–18]. While the function of the vitamin D hormone in the kidney (we use $1,25(\text{OH})_2\text{D}_3$ and the vitamin D hormone interchangeably) involves genetic control of Ca and P reabsorption, as described above, its actions also extend to many additional genes [19,20]. Indeed, a primary function of $1,25(\text{OH})_2\text{D}_3$ is to regulate the expression of renal *Cyp27b1* and *Cyp24a1*, two genes that, in the kidney, are responsible for the synthesis as well as turnover of $1,25(\text{OH})_2\text{D}_3$ [21]. This regulation occurs by not only $1,25(\text{OH})_2\text{D}_3$ but also by *FGF23*, both of which suppress *Cyp27b1* expression and induce *Cyp24a1*. These two genes are also regulated by PTH, which induces *Cyp27b1* while suppressing *Cyp24a1* [22]. These three hormones represent the primary determinants of circulating $1,25(\text{OH})_2\text{D}_3$ in the blood. Individual disruption or loss of expression of any of these hormones, either via genetic manipulation, altered hormonal metabolism, or through disease, results in a significant impact on extracellular Ca and/or P levels in vivo, supporting their essential role in the regulation of mineral homeostasis.

In the past decade or more, however, the actions of vitamin D have also been increasingly linked to a diverse set of important biological activities in non-renal tissues that appear to be separate from those that are involved in mineral regulation [23]. In many of these targets and specific cell types within, the actions of vitamin D in vitro appear to contribute to differentiation and/or maturation and to the regulation of genes involved in those processes. Cell types include those of the immune system, but also those in skin, the cardiovascular system, including smooth muscle cells and cardiac cells, striated muscle cells, and diverse reproductive and placental tissue targets, to name only a few [24–26]. Consistent with the validity of these assertions, these cell types retain the molecular machinery essential for mediating $1,25(\text{OH})_2\text{D}_3$ regulation through genes that are essential for unique biological responses (see below). It has also been suggested that many of these cell types may also synthesize and catabolically degrade $1,25(\text{OH})_2\text{D}_3$ locally via *Cyp27b1* and *Cyp24a1*, respectively [27]. Despite the very low levels of expression of these two genes in non-renal tissues, the observations suggest a secondary pathway as an entrée into an additional sphere of vitamin D biology that could potentially be independent of that which maintains circulating endocrine $1,25(\text{OH})_2\text{D}_3$. In support of this concept, the regulation of *Cyp27b1* in non-renal cell types differs substantially from that in kidney. Accordingly, this gene is regulated not by PTH, *FGF23*, or $1,25(\text{OH})_2\text{D}_3$, as in kidney, but rather by a variety of inflammatory cytokine modulators [28–30]. *Cyp24a1*, on the other hand, is not regulated in these tissues by either PTH or *FGF23* as in the kidney but remains sensitive to $1,25(\text{OH})_2\text{D}_3$ [30]. This suggests that the primary functional role for *Cyp24a1* in these cells may be to prevent $1,25(\text{OH})_2\text{D}_3$ toxicity. These differences in regulation support the idea that local production of $1,25(\text{OH})_2\text{D}_3$ may function in these cell types in a fashion distinct from those involved in mineral metabolism. While much needs to be learned about the impact of the local production of $1,25(\text{OH})_2\text{D}_3$, the diverse actions of the vitamin D hormone in this broad array of tissue/cellular targets supports the concept that vitamin D may play a contributory role in biological processes that extend beyond mineral metabolism. They also imply that vitamin D deficiency could have a unique impact on these numerous biological processes. Thus, restoration of the parent vitamin or the addition of $1,25(\text{OH})_2\text{D}_3$ and/or a selective analogue of $1,25(\text{OH})_2\text{D}_3$ could be particularly useful therapeutically in diseases such as those of altered immune function or in cancer, where vitamin D may exert beneficial actions. Indeed, by promoting differentiation, $1,25(\text{OH})_2\text{D}_3$ not only reduces tumor cell growth but may also function to reduce inflammation through the down-regulation of inflammatory mediators [31]. While attractive conceptually, validation of these hypotheses in human disease requires further confirmation.

Considering the possibility that analogues of vitamin D and/or $1,25(\text{OH})_2\text{D}_3$ might be designed to selectively target tissues involved in these secondary biology activities of vitamin D, chemists have synthesized and examined hundreds of biologically active vitamin D-like compounds for tissue-selective activity over several decades or more. The identification of compounds potentially useful therapeutically has, however, met with generally limited success. We posit that this may be due to the lack of rigorous structure/function assays in vivo that are necessary for guiding the efforts of synthetic chemists. In this article, we suggest that advances in our understanding of vitamin D action at the transcriptional level in vivo may provide not only useful structure/function relationships, but also detailed genomic analyses that could well identify the underlying mechanisms through which a novel analog might operate to manifest tissue, cell, and gene selectivity. Thus, this article represents a combination of transcriptional review, opinion piece, and proposal for incorporating new methods into the analysis of both existing as well as de novo synthesized new vitamin D chemical entities.

2. Transcriptional Mechanism of Action of $1,25(\text{OH})_2\text{D}_3$

Early studies using radioactive ligands served to both identify the existence of the VDR and to facilitate preliminary characterization and purification of the protein itself, an approach that also led similarly to the characterization of nuclear receptors (NR) for other soluble endocrine hormones [32]. It was the cloning of the VDR, however, that placed it unequivocally within the emerging family of concurrently cloned NRs [33–35]. It also precipitated the field's move towards true molecular studies that eventually identified the protein's structural organization, key functional domains, and ultimately, its 3D crystallographic structure [36–38]. As these discoveries evolved, however, additional research led to the realization that, in contrast to the true steroid receptors, the VDR formed a $1,25(\text{OH})_2\text{D}_3$ -dependent heterodimer with a nuclear accessory factor (NAF) that was required for DNA binding; subsequent experiments proved that this factor was RXR, a member of the NR family composed of three isoforms [39–43]. These studies also identified the first DNA response element (VDRE) that served as a binding site for the VDR; this site was located near the promoter within the human osteocalcin gene [41–43]. While many VDREs have been identified since, initially through traditional transfection methods and currently through genome-wide VDR/RXR DNA binding studies using ChIP-seq analysis, this single promoter-proximal element in the osteocalcin gene has been repeatedly confirmed [15]. In total, this collection of early molecular biological studies revealed that NRs including the VDR function largely facilitate the formation of complex multi-protein structures at VDRE-containing sites on vitamin D target genes. These protein complexes contain distinct members of several classes of transcriptional co-regulators capable of modifying chromatin structure and/or directing functions that are necessary for either the induction or the suppression of transcriptional output [44,45]. Many of these latter factors do not bind to DNA directly, however, but establish contact via protein–protein interactions. Thus, similarly to other NRs and most DNA binding transcription factors, the VDR serves as an initial site-specific DNA adaptor, although there are hints that it may also sub-serve a non-DNA binding role by interacting with proteins previously bound to DNA as well.

3. Analogues of Vitamin D

The biological actions of vitamin D to control mineral metabolism prompted the early synthesis of $1,25(\text{OH})_2\text{D}_3$ and initial investigations into the utility of this hormone as a therapeutic for multiple diseases. Many of these maladies altered vitamin D metabolism and thus provoked crucial deficiencies in extracellular Ca and/or P that resulted in loss of bone mineral density and skeletal abnormalities. Classic genetic diseases included vitamin D dependent rickets type 1, later identified as arising from a mutation in the renal *Cyp27b1* gene that causes crippling $1,25(\text{OH})_2\text{D}_3$ deficiency due to an inability to hydroxylate $25(\text{OH})\text{D}_3$ at the 1α position, and vitamin D-resistant rickets due to mutations

in the VDR [46]. Much of this discovery work was prompted early on by the development of clinically relevant assays for blood $1,25(\text{OH})_2\text{D}_3$, pioneered initially by Haussler and his colleagues [47]. The therapeutic utility of $1,25(\text{OH})_2\text{D}_3$ was limited in many instances, however, by its potency and narrow therapeutic window, which frequently prompted hypercalcemia through predictable actions in intestine, kidney, and bone. These clinical difficulties prompted strong efforts by chemists to synthesize analogues of vitamin D and/or $1,25(\text{OH})_2\text{D}_3$ that were of greater practical utility, and perhaps to identify analogues with reduced “side-effects” relative to hypercalcemia. Reviews of these efforts and the many analogues that were synthesized have been documented extensively over several decades [48]. While they will not be discussed here, synthesis is ongoing in many laboratories. As biological effects of $1,25(\text{OH})_2\text{D}_3$ that were separate from those influencing mineral metabolism (growth, differentiation, immune effects) became evident, chemists attempted to home in on the creation of analogues with preferential biological activities that lacked calcemic activity. These selective disease targets included those related to chronic kidney disease and its eventual consequences on the skeleton and the cardiovascular system, as well as on hyperproliferative disorders that included cancer [49–53]. In retrospect, however, while numerous analogues appeared to retain a subset of these properties, the analyses that supported them were frequently misinterpreted. Consequently, vitamin D analogues have not proven to be particularly effective in targeted, non-calcemic biology, and no real understanding has emerged as to the mechanisms that might underpin the purported actions of these “non-calcemic” compounds. The absence of key assays for these analogues, based upon rigorous structure/function/activity relationships (SAR) either *in vitro* or *in vivo*, has exacerbated the efforts expended over the years to synthesize analogues with these properties. Indeed, basic and clinical scientists now have thousands of vitamin D analogues available for study. However, a rather limited understanding of the structural basis for any of the functional properties ascribed to these analogues has emerged, and no real insight has been gained as to their mechanisms. Consequently, only a few of the many analogues synthesized by chemists have become useful therapeutics, and those that have emerged have frequently exploited unique approaches to their administration. Interestingly, even the basic tenant that vitamin D supplementation in clinical trials should result in improved metabolite levels in patients deficient in vitamin D, and where additional $1,25(\text{OH})_2\text{D}_3$ was predicted to ameliorate disease onset (cancer, cardiovascular disease, prediabetes, and tuberculosis to name a few) has not been particularly effective in clinical trials [54–58]. A most recent example is the utility of vitamin D supplementation in the prevention of SARS-CoV2 disease, despite the fact that vitamin D has been shown in basic studies to impact the very molecular targets that facilitate viral cellular entry [59]. One might imagine that, until vitamin D analogues can be developed based upon rational SAR and their mechanisms firmly established *in vivo*, an entry point for their therapeutic use is not likely to emerge.

4. Pharmacology of Vitamin D Analogues

How might analogues operate mechanistically? The possibilities are enormous and include such features as the individual pharmacologic, pharmacokinetic, and/or pharmacodynamic properties of the compounds themselves. Speculatively, these also include parameters impacting the distribution of the compounds based upon their interaction affinity with vitamin D binding protein (DBP) and other serum-interacting factors, requirements for activation by residual renal and non-renal enzymes, and metabolic outcomes that could lead to retention of residual vitamin D-like activity. They also include the potential for selective tissue distribution and localization, relative rates of tissue uptake, as well as unique metabolic degradation rates determined either through catabolic vitamin D enzymes or by novel degradative enzymes not known routinely to degrade vitamin D compounds. With regard to the VDR, the relative biological activity of an analogue is almost certain to be affected by its affinity for the receptor, the longevity of the ligand receptor complex at its sites of action on DNA, and/or the compound’s novel impact on VDR structure. The latter

could uniquely alter receptor function at numerous downstream mechanistic levels prior to or while bound to DNA at target gene loci, thereby altering the transcriptional outcome in a potentially selective manner. While the impact of ligand-dependent pharmacodynamic issues has only briefly been considered, the impact of novel ligands on VDR structure has been an attractive hypothesis for years, and has garnered much attention, largely due to the possibility that altered VDR structure mirrors that seen for several other steroid receptors, particularly the estrogen receptor [60–68]. Indeed, the structure of this receptor has been the focus of much attention, since it displays differential activity depending upon the tissue involved, and this appears to correlate with altered 3D crystal structures of ER. It is noteworthy, however, that this type of differential activity of the VDR on vitamin D biology has not been identified. Accordingly, the evidence supporting the impact of novel vitamin D analogues on the VDR protein is indirect, modest at best, and based largely upon techniques and data generated exclusively *in vitro* almost three decades ago [69,70]. While additional efforts have been made to identify novel ligand-induced anomalies at the VDR protein utilizing 3D crystallography, the results of these studies have been limited to the utilization of the ligand-binding portion of the VDR, which together with crystal structure elucidation may or may not reflect true structural changes in the holoprotein [71,72]. In addition, analogue-based studies have not been conducted in combination with RXR in the presence of appropriate DNA or in the presence of additional cofactors required for transcriptional regulation. Perhaps most importantly, with the exception of antagonist-induced loss of function, none of these structural differences have been linked directly to any selective differences in vitamin D biology at genes *in vivo*. Indeed, early attempts at linking VDR activity to transcription was limited to molecular biologic studies that are now viewed as generally inconsistent with concepts that have emerged over the past decade and that occur at the level of endogenous genes in a natural genomic environment. Finally, it is also not clear whether ligand affinity measurements determined in *in vitro* biochemical assays to assess analogue interaction relative to $1,25(\text{OH})_2\text{D}_3$ are impacted upon the formation of active VDR complexes on DNA within the nucleus of cells. We will discuss new ways below, wherein altered or disrupted actions of the VDR at individual genes and in different tissues might be determined not only *in vitro* but also *in vivo*.

5. New Insights into Transcriptional Activation of Vitamin D

The development of chromatin-immunoprecipitation and other genomic procedures coupled to next-generation DNA sequencing technics (ChIP-seq analysis) and their applications have fully changed the way in which gene regulation is evaluated. This technique has widespread applications, including the capacity to identify and characterize ligand-induced transcription factor binding activity, coregulator recruitment to specific genomic sites, and to assess downstream actions such as RNA polymerase II recruitment in a generally unbiased, genome-wide fashion [73]. These studies have also revealed a multitude of new details inherent to transcriptional processes at a genome-wide scale; some of these principles confirm what has previously been determined, while others identify modifications of those already known to exist. These methods have also revealed entirely new principles of gene regulation at both genome-wide as well as single-gene levels that need to be considered. Perhaps just as important, they have also revealed how inherent technical bias now disqualifies many of the conclusions drawn from over three decades of analyses using *in vitro* molecular biological methods involving transfection. With regard to the molecular actions of vitamin D, genome-wide analyses using chromatin immunoprecipitation, as summarized in Table 1, has revealed many relevant findings. As can be seen, these analyses in both human and mouse cultured cells as well as tissues *in vivo* indicate between 2000 and 8000 VDR binding sites; the number and location of these sites are affected by the quality of the analyses, but within a single laboratory, can be species and cell type specific [45,74–77]. Most of, but not all, these sites are highly dependent upon $1,25(\text{OH})_2\text{D}_3$ pretreatment, indicating that VDR represents a ligand-dependent DNA binding factor. RXR DNA binding is also modestly induced by $1,25(\text{OH})_2\text{D}_3$ at these VDR occupied sites as well, although RXR

can be residually present even in the absence of ligand. This has suggested that prebound RXR may serve an initial role, perhaps to facilitate (affinity) and/or mark specific DNA sites for subsequent VDR binding that is dependent upon DNA half-site configuration. As RXR interacts with numerous additional NRs, it is also possible that RXR may exist at some of these sites with an alternative partner [78]. Nevertheless, the bioinformatically determined close proximity of VDR and RXR at most genomic sites reinforces the idea that the active transcription factor complex is indeed the VDR/RXR heterodimer [14,15]. De novo sequence analysis across these VDR sites confirms the presence of at least one and often multiple motifs, each composed of a typical VDRE of two hexameric DNA half-sites separated by three base pairs. This DNA structure represents a typical VDRE currently at hundreds of genes and in all species examined, although one of the half-sites in a VDRE is frequently highly degenerate, making it difficult in some cases to identify this motif. Additional DNA motifs with dissimilar nucleotide arrangements are also evident at some sites and may represent additional VDR/RXR interacting sequences yet to be explored. In addition, VDR binding at sites known to function in repression often contain novel DNA motifs, suggesting that the VDR may be bound to these sites indirectly via association with other DNA or non-DNA binding proteins that serve additional regulatory functions. These observations at genome-wide levels both confirm and extend our understanding of several key features of vitamin D action via the VDR at target genes. Perhaps the most important discovery arising from unbiased genome-wide analyses of VDR/RXR binding sites and, indeed, most other transcription factor-binding sites is the observation that these regulatory sites are not located exclusively near target gene promoters as previously suspected [22,74,79]. Rather, they can be found at sites that are commonly distributed within intergenic regions both upstream and downstream of the genes they regulate, often with unregulated genes interspersed, as well as commonly within the introns of the target gene itself or in unregulated genes located adjacent to the regulated gene or both. These can also be located 10s if not 100s of kilobases distal to a gene's promoter as well, the locations of which may have an impact on their function [80–83]. Perhaps even more interestingly, this regulatory capacity is frequently composed of multiple interacting components, often 2 to 10 or more regulatory regions, each representing an individual and perhaps unique enhancer function. Finally, these individual enhancers are also modular in nature, serving to bind multiple factors that can span a kilobase or less to more complex segments that can span many kilobases; super-enhancers and other large regulatory regions to which the VDR binds, appear to represent consolidated collections of multiple enhancers that can span over 20 kilobases [84].

Since multiple enhancers may control a single gene, and the localization of transcription factors at sites on the genome does not identify the gene or genes they regulate, it is certain that enhancer location near a gene cannot be used to determine a gene target. Accordingly, the genome-wide number of VDR binding sites in a cell, for example, is not useful in determining the number or identity of genes that are regulated by the hormone. Indeed, the repeated suggestion that the VDR regulates a high percent of genes in the genome is highly misleading, since the VDR binds in a cell-specific manner to only small, although overlapping, subsets of genes in any given cell type. Furthermore, temporal delays in regulation suggest that many if not most purported target genes for vitamin D likely result from indirect secondary and tertiary activity. These evolve from vitamin D's traditional capacity to induce autocrine and paracrine growth factors and/or endocrine hormones as well as other components that influence in turn the activity of multiple cellular signaling pathways. It would also appear that the activation of some rapidly induced genes are temporally consistent with a direct action, yet represent activities of a secondary nature as well, as appears to be the case for FGF23 [13]. Details of this type of activity remain unclear. Importantly, current knowledge also indicates that the functional outcomes of transcription factor binding and coregulator recruitment can be evaluated via epigenetic modifications that are now measurable at genes via current techniques [85,86]. Some of these epigenetic modifications are linked directly to the facilitation of transcriptional output [85].

Mechanistically, it is also worth noting that, although linear arrangements of binding sites at a gene locus are often schematically displayed, the actual arrangement *in vivo* is almost certainly a 3D complex of all or subsets of these regulatory units via looping. Interestingly, these enhancer regions are also characterized by an open chromatin structure that is assembled ultimately near target genes and serves in an integrative fashion to control the transcriptional output of the gene itself. These enhancers may also retain a unique historical, temporal, and spatial function, conferring regulatory capacity on a subset of cell types in a timely manner. This complexity also indicates why earlier studies using cell lines transfected with biased gene promoter plasmid constructs with or without transcription factor or coregulator cotransfection has resulted in numerous conclusions about the regulation of individual genes that fails to confirm at endogenous genes with newly devised, unbiased ChIP-seq methods [29,30,74]. Finally, as indicated earlier, it is noteworthy that binding sites for transcription factors such as the VDR are not fixed, but are dynamic, even within a cell type. Thus, they can be altered via epigenetic modification to accommodate the cell's differentiation and/or maturation status, physiological environment, or perhaps more importantly, the host's state of health or disease [87].

Table 1. Overarching Principles of Vitamin D Action in Target Cells (Ref. [45]).

Active Transcription Unit for Induction: The VDR/RXR heterodimer
VDR Binding Sites (The VDR Cistrome): 2000–8000 1,25(OH)₂D₃-sensitive binding sites/genome whose number and location are chromatin dependent and a function of cell-type
Mode of DNA Binding: Predominantly, but not exclusively, 1,25(OH)₂D₃-dependent
VDR/RXR Binding Site Sequence (VDRE): Induction mediated by classic hexameric half-sites (AGGTCA) separated by 3 base pairs; Repression mediated by divergent sites
Distal Binding Site Locations: Dispersed in <i>cis</i>-regulatory modules (CRMs or enhancers) across the genome; located in a cell-type specific manner near promoters, but predominantly within introns and distal intergenic regions; frequently located in clusters of elements
Epigenetic CRM Signatures: Defined by the dynamically regulated post-translational histone H3 and H4 modifications
Modular Features of CRMs: Contain binding sites for multiple transcription factors that facilitate either independent or synergistic interaction
VDR Cistromes: Dynamic alterations in the cellular epigenome during differentiation, maturation, and disease provoke changes to the VDR cistrome that qualitatively and quantitatively affect the vitamin D regulated transcriptome

6. Current Advances in Transcriptional Regulation

The discovery of novel pathways, as well as insights into the mechanisms of existing and now well-described regulators of transcription, provide reliable avenues through which mechanistic advances can be made and new compounds with drug potential can be synthesized and assessed. Certainly, the overarching principles described in Table 1 that now describe transcriptional regulation by vitamin D are also applicable to regulation by additional small molecules. Accordingly, they have led to new methods to characterize the details of gene regulation both *in vitro* and *in vivo*, the latter at molecular levels almost equivalent to those heretofore achievable only in cultured cells. Indeed, many of the details from these studies have been enhanced *in vivo* through recent analyses of selected cell populations from complex tissues and from the development of genome-wide techniques with increased sensitivity [88]. Organoids created from embryonic stem cells have also provided new *in vitro* insight as well, although cellular mass for analysis is frequently limited. Details now extend to the coupling of changing epigenetic architecture in response to genetic and epigenetic action at regulatory loci to the recruitment of additional transcription factors that play direct roles in promoting or inhibiting transcriptional output. These include detection of epigenetic readers that affect the distribution and release of

RNA polymerase II across the transcription unit to those that influence the downstream mechanisms essential for transcription of the gene per se, resulting in the production of RNA transcripts [85,89]. The capacity to detect the presence and activity of many of these factors at genes and to assess the potential consequences of these factors at both genetic and epigenetic levels is important. It suggests that transcriptional mechanisms for $1,25(\text{OH})_2\text{D}_3$ that result from the binding of the VDR to its site(s) of action can be assessed, and that detailed consequences arising from the activity of prospective vitamin D analogs may also be determined in an endogenous gene context. Thus, temporal relationships, tissue and cellular specificity, and gene selectivity and coregulator recruitment specificity (or lack thereof) can all be determined directly at this endogenous level. Of additional advantage is the fact that these studies can frequently benefit through an assessment of the overarching functional roles of specific enhancers deleted at the genes of interest using CRISPR/Cas9 methods in cells and in animals in vivo [90,91]. Thus, new actionable opportunities have now emerged to determine the mechanisms through which existing as well as newly synthesized vitamin D analogues operate as compared to $1,25(\text{OH})_2\text{D}_3$. These assays might now provide a rational SAR approach for driving the synthesis of new vitamin D analogues with directed tissue activities as well.

7. Recent Work at the Frontier for Enhancing Vitamin D Analogue SAR Potential

We have taken a pragmatic approach to the study of gene expression and its regulation by $1,25(\text{OH})_2\text{D}_3$. This effort focused initially upon a variety of cell types in vitro, where we identified many of the principles enumerated in Table 1. Subsequently, however, we have focused on unique cell types in culture using the above approach and then transitioned to parallel studies in vivo using rodents. Insights gained from the initial studies in cells facilitated this transition, providing baseline insight that has enabled in vivo studies to commence at a mechanistic level equivalent to those conducted in vitro. The advantages of in vivo studies are numerous, but first and foremost, they are free of the bias that has limited those conducted in cultured cells. Secondly, they enable concurrent analyses of molecular mechanisms at multiple genes that are potentially regulated and expressed uniquely in different target tissues. This advantage facilitated the study of the differential regulation of specific genes, the influence of cellular background, and the identification of mechanisms that underlie these differences as well. Most recently, this approach has been strengthened through the ability to exploit emerging methodologies. These techniques can also be used on a genome-wide basis to isolate specific cell types and single cells in order to delineate the sources and molecular features of the cells that are involved in the expression of genes of interest [92–94]. Finally, loss of function/regulation studies utilizing CRISPR/Cas9 mediated gene-editing methods can be employed in vivo to determine the regulatory impact of removing key enhancer regions as well as specific DNA sequences within the loci of genes of interest in order to map regulatory regions in response to specific systemic regulators [29,30,90].

Bone genes: We first explored the genome-wide DNA binding site profile (termed a cistrome) for VDR and RXR in osteoblastic and osteocytic cell lines. These initial studies as well as others highlighted the interaction of the VDR at multiple sites near many genes involved in bone cell maturation, bone formation, biomineralization, and osteoclast-mediated bone resorption. As an example, we initially explored the effects of $1,25(\text{OH})_2\text{D}_3$ on the *Tnfrsf11* gene for RANKL in both cell types [13,95,96]. As can be seen in the ChIP-seq tracks in Figure 1, $1,25(\text{OH})_2\text{D}_3$ induced the localization of both VDR and RXR to four regulatory regions that extended upstream of the gene to 76 kb. Neither VDR nor RXR bound to regions near the *Tnfrsf11* gene promoter. Additional factors bound to a subset of these enhancers including a master bone regulator RUNX2 and a potential pioneering factor CEBP β [97]. These factors, as well as others, frequently colocalized to VDR/RXR binding sites at numerous additional genes as well. Importantly, deletion of several of these enhancers, including the distal 75 kb *Tnfrsf11* segment in mice in vivo, resulted in a blunting of both $1,25(\text{OH})_2\text{D}_3$ and PTH induction [98]. Deletion of a region immediately upstream

of the *Tnfsf11* promoter had no effect, confirming that this gene was not induced through promoter-proximal sequences [74]. Thus, the regulation of *Tnfsf11* by these two hormones is achieved through multiple distal enhancers. Many additional genes have been explored in bone cells in this manner including the *VDR* itself, *Mmp13*, *Lrp5*, and *Enpp1* to name a few. These and other studies therefore reveal roles for not only VDR and RXR, but other factors that are essential to $1,25(\text{OH})_2\text{D}_3$ action as well.

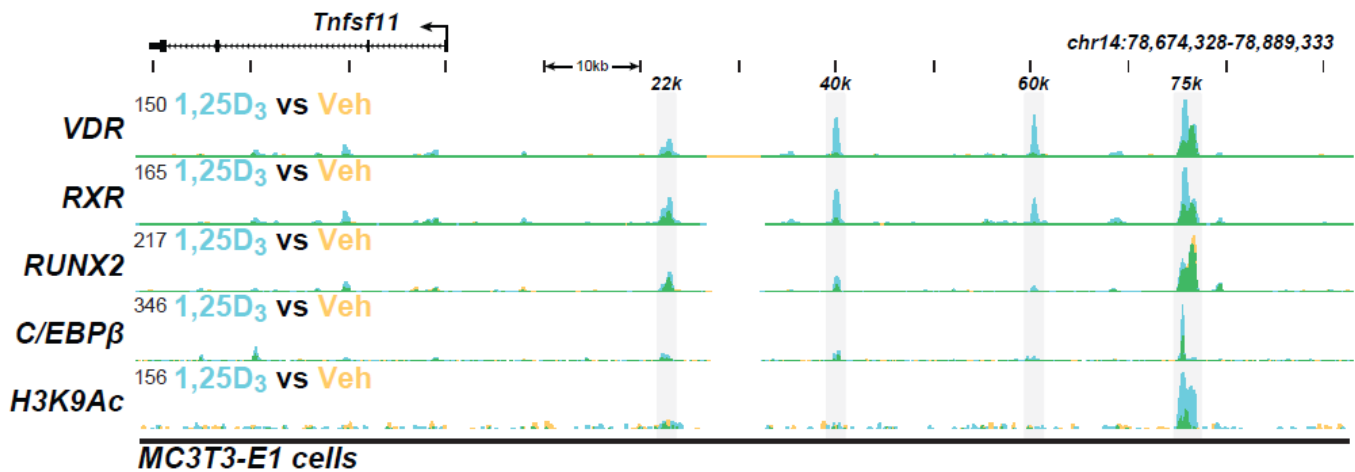


Figure 1. The ChIP-seq tracts for *Tnfsf11* gene were derived from a previous genome-wide analysis of the IDG-SW3 osteocyte cell line in Ref. [13].

In osteocytes, the activity of $1,25(\text{OH})_2\text{D}_3$ was also linked to those regulated by PTH through the frequent presence CREB at VDR/RXR binding sites [96]. These studies also revealed a role for $1,25(\text{OH})_2\text{D}_3$ in enhancing the expression of two co-receptors essential to the Hedgehog pathway activity. This latter observation illuminated an example of the crosstalk that is provoked by $1,25(\text{OH})_2\text{D}_3$ and that is likely to initiate transcriptional effects secondary to those that are direct. Sites of VDR action were also characterized by the presence of active VDREs and classic epigenetic histone signatures that were indicative of dynamic regulatory chromatin architecture. At the *Tnfsf11* gene, as seen in Figure 1, the activity of the VDR/RXR heterodimer-induced histone H3K9 acetylation at the 75 kb region, indicating that VDR binding was active at this site for *Tnfsf11* expression. In many genes, all the above events, including co-localization of coregulators, the presence of RNA polymerase II, and enrichment of H3K36me3, a histone mark present at the gene body itself and reflective of the induction of transcripts, were also seen. These features are linked directly to the transcriptional output of genes themselves. Thus, they provide direct evidence for rapid $1,25(\text{OH})_2\text{D}_3$ modulated transcript output that can be detected at the genomic level and correlated via RNA analysis. Finally, the impact of many of the regulatory features identified for some of the bone genes listed above were explored in the mouse in vivo through loss of expression studies, wherein regulation of the expression of the gene of interest was eliminated entirely upon deletion of the specific enhancer region. These results show that the identified enhancers and the activities they engender are linked directly to specific genetic output in vivo. This demonstration is essential, since, as indicated earlier, enhancers may be located many kilobases (kb) distal to the genes they regulate. It also provides additional opportunities to understand how non-vitamin D regulators participate with $1,25(\text{OH})_2\text{D}_3$ in the expression of specific bone genes. We would anticipate that vitamin D analogues would show alteration in one or more of these progressive events during activation in vivo, perhaps in a tissue-specific manner.

Interestingly, the successful study of VDR/RXR binding across several bone cell genomes failed to identify the presence of either VDR or RXR across the extended locus that surrounds the *Fgf23* gene, despite the fact that $1,25(\text{OH})_2\text{D}_3$ induces *Fgf23* transcripts in these cells [13]. This observation provides significant evidence that the induction of

Fgf23 by $1,25(\text{OH})_2\text{D}_3$ may be indirect, perhaps through a primary DNA binding factor(s). One approach is to conduct enhancer deletion experiments in the mouse in vivo. Thus, an enhancer region that plays an extended role in $1,25(\text{OH})_2\text{D}_3$ induction of *Fgf23*, as established in vivo, could be dissected via loss of regulation studies to identify a more restricted genomic segment capable of mediating $1,25(\text{OH})_2\text{D}_3$ induction [99]. This approach extends the utility of in vivo studies to the level of fine genomic dissection of existing enhancer regions based upon DNA sequence. This functional approach can also reveal motifs that might lead to the identification of mediators of secondary actions of $1,25(\text{OH})_2\text{D}_3$.

Intestinal epithelial genes: Aside from functional studies, it has been the use of ChIP-seq analyses that has enabled a complete transition to the evaluation of gene regulation in vivo. Indeed, in addition to the advantages listed earlier, this approach provides opportunities for study at both tissue/cell- and genome-wide levels that are unparalleled. It may also facilitate a detailed study of regulation at genes of therapeutic interest using mouse disease models. $1,25(\text{OH})_2\text{D}_3$ action in vivo has been explored at different mechanistic levels in intestinal epithelia and in kidney cortex (enriched in proximal tubules). In intestinal epithelial cells isolated from mice pre-injected with $1,25(\text{OH})_2\text{D}_3$, the VDR is bound to multiple genes across the mouse genome; its binding is enhanced by prior treatment with $1,25(\text{OH})_2\text{D}_3$ [100–102]. More recent studies have revealed differences in VDR binding in enterocytes vs. crypt cells, suggesting differential roles for vitamin D in these two cells [101,102]. Enhancer regions at key genes in epithelial cells that are involved in calcium absorption are highlighted in the ChIP-seq tracks documented in Figure 2A,B, for *S100g* (calbindins D9k) and *Trpv6*; others are linked to intracellular Ca regulation and to the transport of elements such as manganese. The enhancers for *Trpv6* were validated previously in a human intestinal cell line. VDR/RXR also induced the intestinal P transporter *Slc34A2* (Figure 2C) as well. Contemporary knowledge of the sites of action of the VDR will now facilitate an up-to-date discovery that could reveal the identities of additional factors that regulate the transcriptional output of these genes and the role of epigenetic histone modifications in this process. This would enable mechanistic study of vitamin D analogues in vivo, purported to be deficient in their capacity to promote intestinal Ca and P uptake. In these cases, we might anticipate that certain “non-calcemic” analogues might exhibit reduced cofactor recruitment and perhaps histone acetylation.

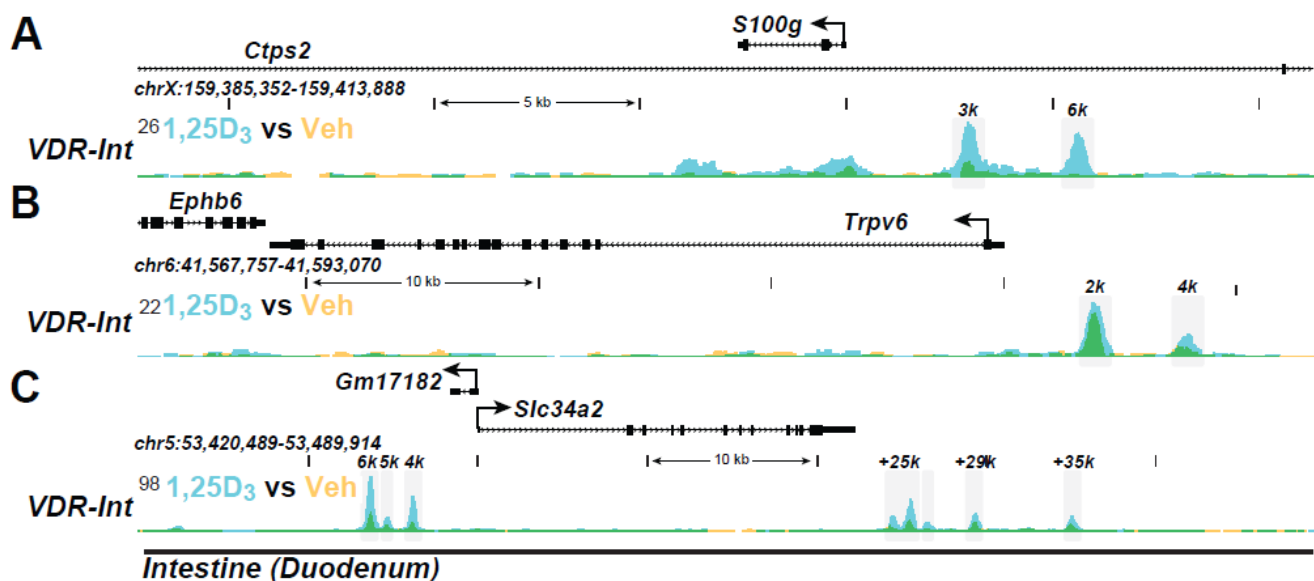


Figure 2. The ChIP-seq tracks for the intestinal genes (A) *Trpv5*, (B) *Trpv6*, and (C) *S100g* were derived from a previous genome-wide analysis of mouse intestinal epithelial cells in vivo as in Ref. [95].

Kidney Genes: Perhaps the most extensive analysis of the mechanistic actions underpinning $1,25(\text{OH})_2\text{D}_3$ action in vivo have been conducted recently in the kidney. Multiple

genes represent targets of vitamin D action in this organ. Indeed, multiple VDR and RXR binding sites are evident at *Trpv5*, *Trpv6*, and *S100g*, as seen in the ChIP-seq tracks in Figure 3A–C, supporting $1,25(\text{OH})_2\text{D}_3$ actions that are involved in Ca regulation in the kidney. Epigenetic chromatin activity is also seen at these sites for H3K27ac modification. VDR binding sites are also present upstream of the *Slc34a1* and *Slc34a3* genes that encode transporters involved in P reabsorption. *Fgf23* displays actions in the kidney to regulate P transporter location, thus controlling P diuresis. These actions involve specific isoforms of the FGFRs, whose ability to bind *Fgf23* is influenced by *Klotho*. The ability to dissect the many players involved in the regulation of genes in the kidney, bone, and intestine that are involved in the maintenance of Ca and P homeostasis is important. It suggests that they may prove useful in identifying unusual features of vitamin D analogs that have direct non-calcemic and/or P diuretic properties that may occur in a tissue-selective manner.

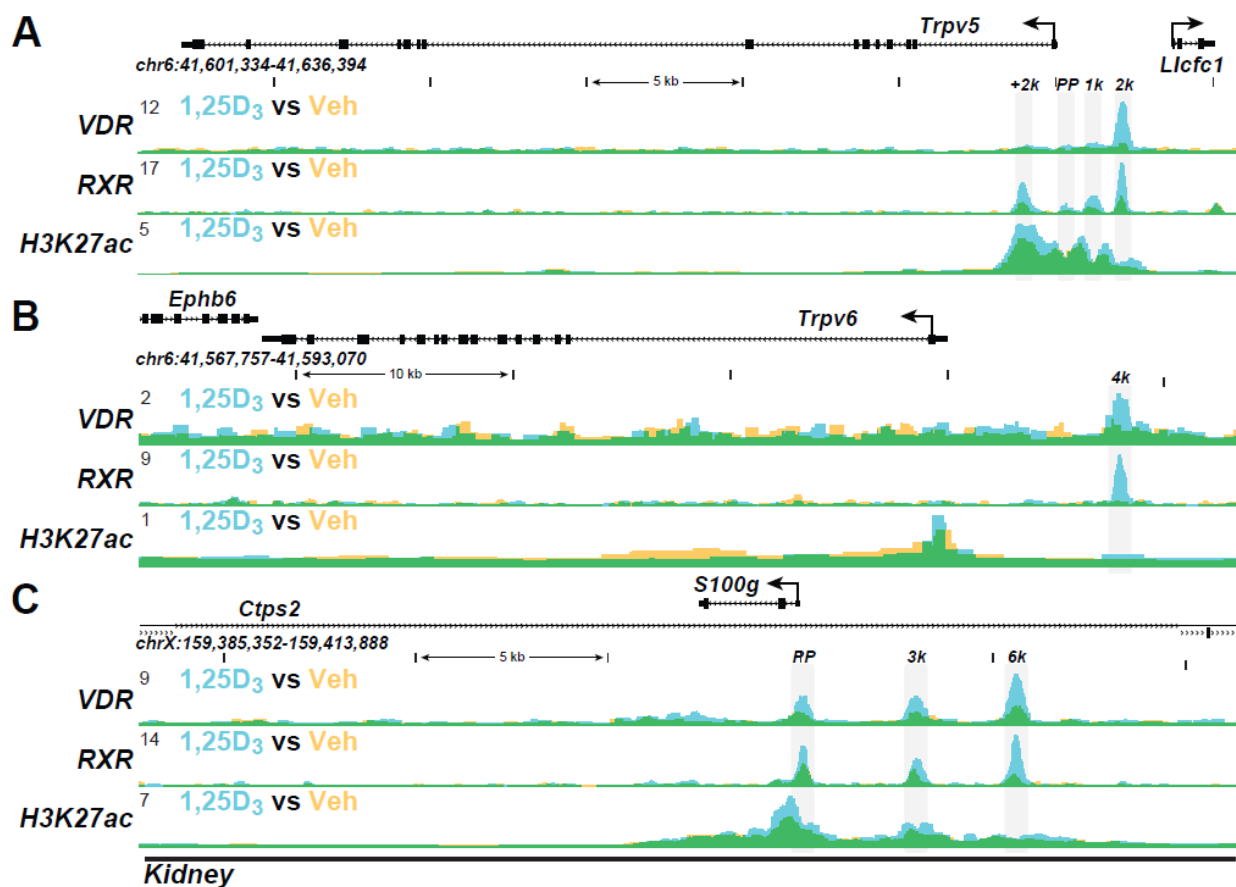


Figure 3. The ChIP-seq tracks for the kidney genes (A) *Trpv5*, (B) *Trpv6*, and (C) *S100g* were derived from a previous genome-wide analyses of mouse kidney cortex in vivo as in Ref. [29].

As discussed in the Introduction, $1,25(\text{OH})_2\text{D}_3$ also plays a striking role together with PTH and FGF23 in modulating the expression of *Cyp27b1* and *Cyp24a1* in the kidney. The *Cyp27b1* gene is induced by PTH but suppressed by $1,25(\text{OH})_2\text{D}_3$ and FGF23, while the *Cyp24a1* gene is reciprocally regulated by each of these three hormones [29,90]. This reciprocal regulation enables the activities of these two genes to acutely and dynamically control the levels of $1,25(\text{OH})_2\text{D}_3$ secretion into the blood. The basal and regulated expression of *Cyp27b1* and *Cyp24a1* is mediated by each of the three hormones via a complex regulatory module located within introns of two upstream genes adjacent to the *Cyp27b1* locus and in an intergenic location downstream of *Cyp24a1*, as seen in Figure 4A,B [29,30,90]. These regulatory sites at both gene loci bind both CREB and VDR and mediate the actions of PTH and $1,25(\text{OH})_2\text{D}_3$, respectively. These same enhancers also mediate the actions of FGF23, although the factor responsible for this hormone's activity is still unidentified.

Most importantly, the entire intronic regulatory module at *Cyp27b1* and some segments of the intergenic regulatory complex downstream of *Cyp24a1* are unique to the kidney due to the presence of novel open chromatin structures. These open chromatin modules are absent in non-renal tissues, with the exception that several components of the *Cyp24a1* module that mediates $1,25(\text{OH})_2\text{D}_3$ action are retained across all tissues [30]. Accordingly, removal of the intronic *Cyp27b1* regulatory module eliminates basal and regulated *Cyp27b1* expression selectively in the kidney, while removal of the downstream *Cyp24a1* regulatory module eliminates basal, PTH, and FGF23-regulated expression selectively in the kidney. $1,25(\text{OH})_2\text{D}_3$ regulation of *Cyp24a1* is retained in all tissues. Interestingly, treatment by PTH also leads to a striking enhancement of H3K27 acetylation (H3K27ac) at CREB-binding sites in the *Cyp27b1* gene locus in the kidney but suppresses H3K27ac at CREB-binding sites in the *Cyp24a1* locus (Figure 4A,B). Thus, H3K27ac levels track uniquely with the upregulation of *Cyp27b1* RNA transcripts and the downregulation of *Cyp24a1* RNA transcripts in the kidney. Treatment with $1,25(\text{OH})_2\text{D}_3$, in contrast, leads to a striking suppression of H3K27ac at VDR binding sites in the *Cyp27b1* gene locus in the kidney, but strongly induces H3K27ac at VDR binding sites in the *Cyp24a1* locus. Thus, again, H3K27ac levels correlate uniquely with *Cyp27b1* and *Cyp24a1* RNA transcript regulation in the kidney. As a suppressor of *Cyp27b1* and an inducer of *Cyp24a1*, FGF23 actions on H3K27ac mimic that of $1,25(\text{OH})_2\text{D}_3$ at the genes for both *Cyp27b1* and *Cyp24a1*. Therefore, similarly to $1,25(\text{OH})_2\text{D}_3$, FGF23-regulated H3K27ac levels track uniquely with the downregulation of *Cyp27b1* and the upregulation of *Cyp24a1* transcripts as well. Consistent with the absence of these modules in *Cyp27b1*, no changes in H3K27ac are seen in non-renal tissues. However, $1,25(\text{OH})_2\text{D}_3$ does induce H3K27ac at selected sites in the *Cyp24a1* gene in both renal and non-renal tissues. Finally, detection of H3K36 tri-methylation (H3K36me3) levels increase in response to PTH across the *Cyp27b1* gene body but are suppressed in response to $1,25(\text{OH})_2\text{D}_3$ and FGF23, while detection of this same histone modification decreases in response to PTH but is increased in response to $1,25(\text{OH})_2\text{D}_3$ and FGF23 across the *Cyp24a1* gene body. Additional factors linked to the induction or suppression of these two genes are also detected at each of the sites of regulation in both genes.

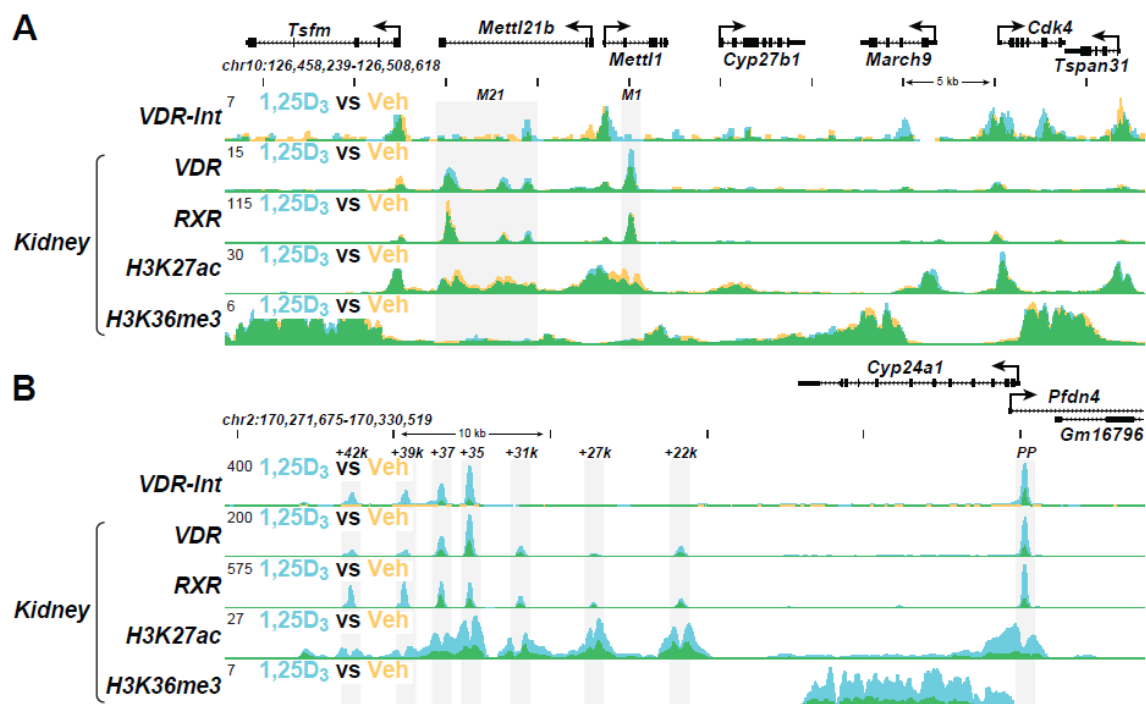


Figure 4. The ChIP-seq tracks for the kidney genes (A) *Cyp27b1* and (B) *Cyp24a1* were derived from a previous genome-wide analyses of mouse kidney cortex in vivo as in Reference [29].

8. Vitamin D Analogues

Exploring the effects of synthetic analogues of vitamin D using this combination of *in vitro* and *in vivo* approaches has the clear potential of revealing molecular differences relevant to unique analogue action. These differences could emerge with authentic interacting factors such as coregulators specific for individual gene targets under investigation if an analogue exerts its actions via a structural alteration that provokes a functional change in the VDR. It is now clear that many of the original hypotheses regarding the basis for coregulator recruitment at genes derived from traditional transfection methods have not been entirely correct. Since current studies are routinely conducted on a genome-wide basis, genes selected for their specific function in Ca and P homeostasis in bone could provide a focus for designing (SAR), identifying and understanding analogues that exhibit non-calcemic actions in an endogenous context relative to 1,25(OH)₂D₃. It seems likely that a vitamin D antagonist would reveal itself rapidly under this type of molecular scrutiny as well.

9. Conclusions

The purpose of this manuscript has been to delineate new approaches to the study of mechanisms related to the transcriptional regulation of genes by 1,25(OH)₂D₃ and their potential application to the analysis of the vitamin D mediated mechanisms *in vitro* and *in vivo*. Based on new techniques that involve ChIP-seq analysis, sites of action of the vitamin D hormone can be identified via the co-localization of the VDR and its partner RXR on endogenous DNA on a genome-wide basis in both culture cells and in tissues *in vivo*. Detection of gene-specific coregulators as well as the activities of these factors via epigenetic changes to histones may also be assessed. The identity of facilitator proteins that initiate the recruitment and/or distribution of RNA polymerase II across the gene body that result in nascent transcripts could also be examined. The ability to detect each of these component proteins and their activities at early time points in a largely gene-specific manner using the vitamin D hormone, as a one-time control suggests that similar studies could be used to characterize the actions of novel vitamin D analogues. This could readily be accomplished to conduct SAR based on newly synthesized compounds as well as to assess the unique mechanistic bases for unusual vitamin D analogue specificities. Indeed, this process could facilitate either the detection and/or mechanisms through which an analogue might retain a non-calcemic activity directly *in vivo*.

Author Contributions: J.W.P. contributed to the conceptualization and original draft preparation, J.W.P. and M.B.M. to writing—review and editing, M.B.M. to figure creation, and J.W.P. to funding acquisition. All authors have read and agreed to the published version of the manuscript.

Funding: This work was supported by National Institutes of Health Grants DK-072281, DK-073995, DK-074993 and AR-045173 at J.W.P.

Acknowledgments: The authors also acknowledge the contributions of collaborators including Seong Min Lee and Nancy A. Benkusky within the Pike laboratory as well as those that contributed to the described work outside this laboratory. The latter include our most recent collaborators, Glenville Jones and Martin Kaufmann of the Department of Biochemistry and Molecular Sciences at Queens University, Kingston, ON, Canada.

Conflicts of Interest: The authors declare no conflict of interest in preparation of this manuscript.

References

1. DeLuca, H.F. Overview of general physiologic features and functions of vitamin D. *Am. J. Clin. Nutr.* **2004**, *80*, 1689S–1696S. [CrossRef]
2. Song, Y.; Peng, X.; Porta, A.; Takanaga, H.; Peng, J.-B.; Hediger, M.A.; Fleet, J.C.; Christakos, S. Calcium Transporter 1 and Epithelial Calcium Channel Messenger Ribonucleic Acid Are Differentially Regulated by 1,25 Dihydroxyvitamin D₃ in the Intestine and Kidney of Mice. *Endocrinology* **2003**, *144*, 3885–3894. [CrossRef]
3. Hoenderop, J.G.J.; Nilius, B.; Bindels, R.J.M. Calcium Absorption across Epithelia. *Physiol. Rev.* **2005**, *85*, 373–422. [CrossRef] [PubMed]

4. Van Cromphaut, S.J.; Dewerchin, M.; Hoenderop, J.G.J.; Stockmans, I.; Van Herck, E.; Kato, S.; Bindels, R.J.M.; Collen, D.; Carmeliet, P.; Bouillon, R.; et al. Duodenal calcium absorption in vitamin D receptor-knockout mice: Functional and molecular aspects. *Proc. Natl. Acad. Sci. USA* **2001**, *98*, 13324–13329. [CrossRef]
5. Van Abel, M.; Hoenderop, J.G.J.; Bindels, R.J. The epithelial calcium channels TRPV5 and TRPV6: Regulation and implications for disease. *Naunyn-Schmiedeberg's Arch. Pharmacol.* **2005**, *371*, 295–306. [CrossRef]
6. Nijenhuis, T.; Hoenderop, J.G.J.; Bindels, R.J.M. TRPV5 and TRPV6 in Ca²⁺ (re)absorption: Regulating Ca²⁺ entry at the gate. *Pflug. Arch.* **2005**, *451*, 181–192. [CrossRef] [PubMed]
7. Shimada, T.; Hasegawa, H.; Yamazaki, Y.; Muto, T.; Hino, R.; Takeuchi, Y.; Fujita, T.; Nakahara, K.; Fukumoto, S.; Yamashita, T. FGF-23 Is a Potent Regulator of Vitamin D Metabolism and Phosphate Homeostasis. *J. Bone Miner. Res.* **2004**, *19*, 429–435. [CrossRef]
8. Hu, M.C.; Shiizaki, K.; Kuro-O, M.; Moe, O.W. Fibroblast Growth Factor 23 and Klotho: Physiology and Pathophysiology of an Endocrine Network of Mineral Metabolism. *Annu. Rev. Physiol.* **2013**, *75*, 503–533. [CrossRef] [PubMed]
9. Suda, T.; Takahashi, N.; Udagawa, N.; Jimi, E.; Gillespie, M.; Martin, T. Modulation of osteoclast differentiation and function by the new members of the tumor necrosis factor receptor and ligand families. *Endocr. Rev.* **1999**, *20*, 345–357. [CrossRef]
10. Kondo, M.; Yamaoka, K.; Sakata, K.; Sonomoto, K.; Lin, L.; Nakano, K.; Tanaka, Y. Contribution of the Interleukin-6/STAT-3 Signaling Pathway to Chondrogenic Differentiation of Human Mesenchymal Stem Cells. *Arthritis Rheumatol.* **2015**, *67*, 1250–1260. [CrossRef]
11. Kim, S.; Shevde, N.K.; Pike, J.W. 1,25-Dihydroxyvitamin D3 Stimulates Cyclic Vitamin D Receptor/Retinoid X Receptor DNA-Binding, Co-activator Recruitment, and Histone Acetylation in Intact Osteoblasts. *J. Bone Miner. Res.* **2004**, *20*, 305–317. [CrossRef] [PubMed]
12. Yuan, Y.; Jagga, S.; Martins, J.S.; Rana, R.; Pajevic, P.D.; Liu, E.S. Impaired 1,25 dihydroxyvitamin D3 action and hypophosphatemia underlie the altered lacuno-canalicular remodeling observed in the Hyp mouse model of XLH. *PLoS ONE* **2021**, *16*, e0252348. [CrossRef]
13. St John, H.C.; Bishop, K.A.; Meyer, M.B.; Benkusky, N.A.; Leng, N.; Kendzierski, C.; Bonewald, L.F.; Pike, J.W. The osteoblast to osteocyte transition: Epigenetic changes and response to the vitamin D3 hormone. *Mol. Endocrinol.* **2014**, *28*, 1150–1165. [CrossRef] [PubMed]
14. Meyer, M.B.; Goetsch, P.D.; Pike, J.W. Genome-wide analysis of the VDR/RXR cistrome in osteoblast cells provides new mechanistic insight into the actions of the vitamin D hormone. *J. Steroid Biochem. Mol. Biol.* **2010**, *121*, 136–141. [CrossRef]
15. Meyer, M.B.; Benkusky, N.A.; Lee, C.-H.; Pike, J. Genomic Determinants of Gene Regulation by 1,25-Dihydroxyvitamin D3 during Osteoblast-lineage Cell Differentiation. *J. Biol. Chem.* **2014**, *289*, 19539–19554. [CrossRef]
16. Martin, A.; Quarles, L.D. Evidence for FGF23 Involvement in a Bone-Kidney Axis Regulating Bone Mineralization and Systemic Phosphate and Vitamin D Homeostasis. *Adv. Exp. Med. Biol.* **2012**, *728*, 65–83. [CrossRef]
17. Quarles, L.D. Role of FGF23 in vitamin D and phosphate metabolism: Implications in chronic kidney disease. *Exp. Cell Res.* **2012**, *318*, 1040–1048. [CrossRef]
18. Saini, R.K.; Kaneko, I.; Jurutka, P.; Forster, R.; Hsieh, A.; Hsieh, J.-C.; Haussler, M.R.; Whitfield, G.K. 1,25-Dihydroxyvitamin D3 Regulation of Fibroblast Growth Factor-23 Expression in Bone Cells: Evidence for Primary and Secondary Mechanisms Modulated by Leptin and Interleukin-6. *Calcif. Tissue Int.* **2012**, *92*, 339–353. [CrossRef]
19. Andrukhova, O.; Zeitz, U.; Goetz, R.; Mohammadi, M.; Lanske, B.; Erben, R.G. FGF23 acts directly on renal proximal tubules to induce phosphaturia through activation of the ERK1/2-SGK1 signaling pathway. *Bone* **2012**, *51*, 621–628. [CrossRef] [PubMed]
20. Andrukhova, O.; Slavic, S.; Smorodchenko, A.; Zeitz, U.; Shalhoub, V.; Lanske, B.; Pohl, E.E.; Erben, R.G. FGF 23 regulates renal sodium handling and blood pressure. *EMBO Mol. Med.* **2014**, *6*, 744–759. [CrossRef]
21. Jones, G.; Prosser, D.E.; Kaufmann, M. Cytochrome P450-mediated metabolism of vitamin D. *J. Lipid Res.* **2014**, *55*, 13–31. [CrossRef]
22. Meyer, M.B.; Pike, J.W. Mechanistic homeostasis of vitamin D metabolism in the kidney through reciprocal modulation of Cyp27b1 and Cyp24a1 expression. *J. Steroid Biochem. Mol. Biol.* **2019**, *196*, 105500. [CrossRef] [PubMed]
23. Adams, J.S.; Hewison, M. Extrarenal expression of the 25-hydroxyvitamin D-1-hydroxylase. *Arch. Biochem. Biophys.* **2012**, *523*, 95–102. [CrossRef] [PubMed]
24. Hewison, M.; Burke, F.; Evans, K.N.; Lammas, D.A.; Sansom, D.; Liu, P.; Modlin, R.; Adams, J. Extra-renal 25-hydroxyvitamin D3-1 α -hydroxylase in human health and disease. *J. Steroid Biochem. Mol. Biol.* **2007**, *103*, 316–321. [CrossRef]
25. Chun, R.; Liu, P.T.; Modlin, R.L.; Adams, J.S.; Hewison, M. Impact of vitamin D on immune function: Lessons learned from genome-wide analysis. *Front. Physiol.* **2014**, *5*, 151. [CrossRef] [PubMed]
26. Bikle, D.D. Vitamin D and the skin. *J. Bone Min. Metab.* **2010**, *28*, 117–130. [CrossRef]
27. Hewison, M.; Adams, J.S. *Extrarenal 1 α -Hydroxylase*, 3rd ed.; Academic Press: San Diego, CA, USA, 2018; Volume 1.
28. Adams, J.S.; Rafison, B.; Witzel, S.; Reyes, R.E.; Shieh, A.; Chun, R.; Zavala, K.; Hewison, M.; Liu, P.T. Regulation of the extrarenal CYP27B1-hydroxylase. *J. Steroid Biochem. Mol. Biol.* **2014**, *144 Pt A*, 22–27. [CrossRef]
29. Meyer, M.B.; Benkusky, N.A.; Kaufmann, M.; Lee, S.M.; Onal, M.; Jones, G.; Pike, J.W. A kidney-specific genetic control module in mice governs endocrine regulation of the cytochrome P450 gene Cyp27b1 essential for vitamin D3 activation. *J. Biol. Chem.* **2017**, *292*, 17541–17558. [CrossRef]

30. Meyer, M.B.; Lee, S.M.; Carlson, A.H.; Benkusky, N.A.; Kaufmann, M.; Jones, G.; Pike, J.W. A chromatin-based mechanism controls differential regulation of the cytochrome P450 gene *Cyp24a1* in renal and non-renal tissues. *J. Biol. Chem.* **2019**, *294*, 14467–14481. [CrossRef]
31. Welsh, J. Vitamin D and breast cancer: Insights from animal models. *Am. J. Clin. Nutr.* **2004**, *80*, 1721S–1724S. [CrossRef]
32. Pike, J.; Haussler, M. Characteristics and purification of the intestinal receptor for 1,25-dihydroxyvitamin D. *Methods Enzymol.* **1980**, *67*, 508–522.
33. McDonnell, D.P.; Mangelsdorf, D.J.; Pike, J.W.; Haussler, M.R.; O'Malley, B.W. Molecular Cloning of Complementary DNA Encoding the Avian Receptor for Vitamin, D. *Science* **1987**, *235*, 1214–1217. [CrossRef]
34. Baker, A.R.; McDonnell, D.P.; Hughes, M.; Crisp, T.M.; Mangelsdorf, D.; Haussler, M.R.; Pike, J.W.; Shine, J.; O'Malley, B.W. Cloning and expression of full-length cDNA encoding human vitamin D receptor. *Proc. Natl. Acad. Sci. USA* **1988**, *85*, 3294–3298. [CrossRef]
35. Mangelsdorf, D.J.; Thummel, C.; Beato, M.; Herrlich, P.; Schütz, G.; Umesono, K.; Blumberg, B.; Kastner, P.; Mark, M.; Chambon, P.; et al. The nuclear receptor superfamily: The second decade. *Cell* **1995**, *83*, 835–839. [CrossRef]
36. Rochel, N.; Wurtz, J.-M.; Mitschler, A.; Klaholz, B.; Moras, D. The Crystal Structure of the Nuclear Receptor for Vitamin D Bound to Its Natural Ligand. *Mol. Cell* **2000**, *5*, 173–179. [CrossRef]
37. Vanhooke, J.L.; Prahl, J.M.; Kimmel-Jehan, C.; Mendelsohn, M.; Danielson, E.W.; Healy, K.D.; DeLuca, H.F. CYP27B1 null mice with LacZ reporter gene display no 25-hydroxyvitamin D3-1-hydroxylase promoter activity in the skin. *Proc. Natl. Acad. Sci. USA* **2005**, *103*, 75–80. [CrossRef] [PubMed]
38. Rochel, N.; Ciesielski, F.; Godet, J.; Moman, E.; Rössle, M.; Peluso-Iltis, C.; Moulin, M.; Haertlein, M.; Callow, P.; Mély, Y.; et al. Common architecture of nuclear receptor heterodimers on DNA direct repeat elements with different spacings. *Nat. Struct. Mol. Biol.* **2011**, *18*, 564–570. [CrossRef]
39. Liao, J.; Ozono, K.; Sone, T.; McDonnell, D.P.; Pike, J.W. Vitamin D receptor interaction with specific DNA requires a nuclear protein and 1,25-dihydroxyvitamin D3. *Proc. Natl. Acad. Sci. USA* **1990**, *87*, 9751–9755. [CrossRef] [PubMed]
40. Kliewer, S.A.; Umesono, K.; Mangelsdorf, D.; Evans, R. Retinoid X receptor interacts with nuclear receptors in retinoic acid, thyroid hormone and vitamin D3 signalling. *Nature* **1992**, *355*, 446–449. [CrossRef] [PubMed]
41. Kerner, S.A.; Scott, R.A.; Pike, J.W. Sequence elements in the human osteocalcin gene confer basal activation and inducible response to hormonal vitamin D3. *Proc. Natl. Acad. Sci. USA* **1989**, *86*, 4455–4459. [CrossRef]
42. Sone, T.; Kerner, S.; Pike, J. Vitamin D receptor interaction with specific DNA. Association as a 1,25-dihydroxyvitamin D3-modulated heterodimer. *J. Biol. Chem.* **1991**, *266*, 23296–23305. [CrossRef]
43. Ozono, K.; Liao, J.; Kerner, S.A.; Scott, R.A.; Pike, J.W. The vitamin D-responsive element in the human osteocalcin gene. Association with a nuclear proto-oncogene enhancer. *J. Biol. Chem.* **1990**, *265*, 21881–21888. [CrossRef]
44. Meyer, M.B.; Pike, J.W. Corepressors (NCoR and SMRT) as well as coactivators are recruited to positively regulated 1 α ,25-dihydroxyvitamin D3-responsive genes. *J. Steroid Biochem. Mol. Biol.* **2013**, *136*, 120–124. [CrossRef]
45. Pike, J.W.; Lee, S.M.; Meyer, M.B. Regulation of gene expression by 1,25-dihydroxyvitamin D3 in bone cells: Exploiting new approaches and defining new mechanisms. *BoneKey Rep.* **2014**, *3*, 482. [CrossRef] [PubMed]
46. St-Arnaud, R.; Messerlian, S.; Moir, J.M.; Omdahl, J.L.; Glorieux, F.H. The 25-Hydroxyvitamin D 1-Alpha-Hydroxylase Gene Maps to the Pseudovitamin D-Deficiency Rickets (PDDR) Disease Locus. *J. Bone Miner. Res.* **1997**, *12*, 1552–1559. [CrossRef]
47. Haussler, M.R.; McCain, T.A. Basic and clinical concepts related to vitamin D metabolism and action (first of two parts). *N. Engl. J. Med.* **1977**, *297*, 974–983. [CrossRef] [PubMed]
48. Verstuyf, A.; Segaert, S.; Verlinden, L.; Bouillon, R.; Mathieu, C. Recent developments in the use of vitamin D analogues. *Expert Opin. Investig. Drugs* **2000**, *9*, 443–455. [CrossRef]
49. Bouillon, R.; Eelen, G.; Verlinden, L.; Mathieu, C.; Carmeliet, G.; Verstuyf, A. Vitamin D and cancer. *J. Steroid Biochem. Mol. Biol.* **2006**, *102*, 156–162. [CrossRef]
50. Eelen, G.; Verlinden, L.; Meyer, M.; Gijssbers, R.; Pike, J.W.; Bouillon, R.; Verstuyf, A. 1,25-Dihydroxyvitamin D3 and the aging-related Forkhead Box O and Sestrin proteins in osteoblasts. *J. Steroid Biochem. Mol. Biol.* **2013**, *136*, 112–119. [CrossRef] [PubMed]
51. Nigwekar, S.U.; Thadhani, R.I. Shining light on vitamin D trials in chronic kidney disease. *Kidney Int.* **2013**, *83*, 198–200. [CrossRef] [PubMed]
52. Nigwekar, S.U.; Tamez, H.; Thadhani, R.I. Vitamin D and chronic kidney disease-mineral bone disease (CKD-MBD). *Bonekey Rep.* **2014**, *3*, 498. [CrossRef]
53. Nigwekar, S.U.; Thadhani, R. Vitamin D receptor activation: Cardiovascular and renal implications. *Kidney Int. Suppl.* **2013**, *3*, 427–430. [CrossRef] [PubMed]
54. Pittas, A.G.; Jorde, R.; Kawahara, T.; Dawson-Hughes, B. Vitamin D Supplementation for Prevention of Type 2 Diabetes Mellitus: To D or Not to D? *J. Clin. Endocrinol. Metab.* **2020**, *105*, 3721–3733. [CrossRef] [PubMed]
55. Kim, S.H.; Brodsky, I.G.; Chatterjee, R.; Kashyap, S.R.; Knowler, W.C.; Liao, E.; Nelson, J.; Pratley, R.; Rasouli, N.; Vickery, E.M.; et al. Effect of Vitamin D Supplementation on Kidney Function in Adults with Prediabetes: A Secondary Analysis of a Randomized Trial. *Clin. J. Am. Soc. Nephrol.* **2021**, *16*, 1201–1209. [CrossRef] [PubMed]

56. Rasouli, N.; Brodsky, I.G.; Chatterjee, R.; Kim, S.H.; Pratley, R.E.; Staten, M.A.; Pittas, A.G.; Ceglia, L.; Chadha, C.; Dawson-Hughes, B.; et al. Effects of Vitamin D Supplementation on Insulin Sensitivity and Secretion in Prediabetes. *J. Clin. Endocrinol. Metab.* **2021**. [CrossRef] [PubMed]
57. Pittas, A.G.; Dawson-Hughes, B.; Sheehan, P.R.; Rosen, C.J.; Ware, J.H.; Knowler, W.C.; Staten, M.A.; The D2d Research Group. Rationale and Design of the Vitamin D and Type 2 Diabetes (D2d) Study: A Diabetes Prevention Trial. *Diabetes Care* **2014**, *37*, 3227–3234. [CrossRef]
58. Pittas, A.G.; Dawson-Hughes, B.; Sheehan, P.; Ware, J.H.; Knowler, W.C.; Aroda, V.R.; Brodsky, I.; Ceglia, L.; Chadha, C.; Chatterjee, R. Vitamin D Supplementation and Prevention of Type 2 Diabetes. *N. Engl. J. Med.* **2019**, *381*, 520–530. [CrossRef]
59. Arroyo-Díaz, J.A.; Julve, J.; Vlachos, B.; Corcoy, R.; Ponte, P.; Román, E.; Navas-Méndez, E.; Llauradó, G.; Franch-Nadal, J.; Domingo, P. Previous Vitamin D Supplementation and Morbidity and Mortality Outcomes in People Hospitalised for COVID-19: A Cross-Sectional Study. *Front. Public Health* **2021**, *9*, 758347. [CrossRef]
60. Sato, Y.; Ramalanjaona, N.; Huet, T.; Potier, N.; Osz, J.; Antony, P.; Peluso-Ilitis, C.; Poussin-Courmontagne, P.; Ennifar, E.; Mély, Y.; et al. The “Phantom Effect” of the Rexinoid LG100754: Structural and Functional Insights. *PLoS ONE* **2010**, *5*, e15119. [CrossRef]
61. Tocchini-Valentini, G.; Rochel, N.; Wurtz, J.-M.; Moras, D. Crystal Structures of the Vitamin D Nuclear Receptor Liganded with the Vitamin D Side Chain Analogues Calcipotriol and Seocalcitol, Receptor Agonists of Clinical Importance. Insights into a Structural Basis for the Switching of Calcipotriol to a Receptor Antagonist by Further Side Chain Modification. *J. Med. Chem.* **2004**, *47*, 1956–1961. [CrossRef]
62. Tocchini-Valentini, G.; Rochel, N.; Wurtz, J.-M.; Mitschler, A.; Moras, D. Crystal structures of the vitamin D receptor complexed to superagonist 20-epi ligands. *Proc. Natl. Acad. Sci. USA* **2001**, *98*, 5491–5496. [CrossRef]
63. Orlov, I.; Rochel, N.; Moras, D.; Klaholz, B.P. Structure of the full human RXR/VDR nuclear receptor heterodimer complex with its DR3 target DNA. *EMBO J.* **2011**, *31*, 291–300. [CrossRef] [PubMed]
64. Hourai, S.; Rodrigues, L.C.; Antony, P.; Reina-San-Martin, B.; Ciesielski, F.; Magnier, B.C.; Schoonjans, K.; Mouriño, A.; Rochel, N.; Moras, D. Structure-Based Design of a Superagonist Ligand for the Vitamin D Nuclear Receptor. *Chem. Biol.* **2008**, *15*, 383–392. [CrossRef]
65. Cherepanova, O.A.; Gomez, D.; Shankman, L.S.; Swiatlowska, P.; Williams, J.; Sarmiento, O.F.; Alencar, G.F.; Hess, D.L.; Bevard, M.H.; Greene, E.S.; et al. Activation of the pluripotency factor OCT4 in smooth muscle cells is atheroprotective. *Nat. Med.* **2016**, *22*, 657–665. [CrossRef] [PubMed]
66. Nettles, K.W.; Greene, G.L. Ligand control of coregulator recruitment to nuclear receptors. *Annu. Rev. Physiol.* **2005**, *67*, 309–333. [CrossRef]
67. Brzozowski, A.M.; Pike, A.C.W.; Dauter, Z.; Hubbard, R.E.; Bonn, T.; Engström, O.; Öhman, L.; Greene, G.L.; Gustafsson, J.A.; Carlquist, M. Molecular basis of agonism and antagonism in the oestrogen receptor. *Nature* **1997**, *389*, 753–758. [CrossRef]
68. Wu, Y.-L.; Yang, X.; Ren, Z.; McDonnell, D.P.; Norris, J.; Willson, T.M.; Greene, G.L. Structural Basis for an Unexpected Mode of SERM-Mediated ER Antagonism. *Mol. Cell* **2005**, *18*, 413–424. [CrossRef] [PubMed]
69. Peleg, S.; Sastry, M.; Collins, E.D.; Bishop, J.E.; Norman, A.W. Distinct Conformational Changes Induced by 20-epi Analogues of 1 α ,25-Dihydroxyvitamin D₃ Are Associated with Enhanced Activation of the Vitamin D Receptor. *J. Biol. Chem.* **1995**, *270*, 10551–10558. [CrossRef]
70. Posner, G.H.; Crawford, K.R.; Peleg, S.; Welsh, J.E.; Romu, S.; Gewirtz, D.A.; Gupta, M.S.; Dolan, P.; Kensler, T.W. A non-calcemic sulfone version of the vitamin D(3) analogue seocalcitol (EB 1089): Chemical synthesis, biological evaluation and potency enhancement of the anticancer drug adriamycin. *Bioorgan. Med. Chem.* **2001**, *9*, 2365–2371. [CrossRef]
71. Igarashi, M.; Yoshimoto, N.; Yamamoto, K.; Shimizu, M.; Ishizawa, M.; Makishima, M.; DeLuca, H.F.; Yamada, S. Identification of a highly potent vitamin D receptor antagonist: (25S)-26-Adamantyl-25-hydroxy-2-methylene-22,23-didehydro-19,27-dinor-20-epi-vitamin D₃ (ADMI3). *Arch. Biochem. Biophys.* **2007**, *460*, 240–253. [CrossRef]
72. Choi, M.; Yamamoto, K.; Itoh, T.; Makishima, M.; Mangelsdorf, D.; Moras, D.; DeLuca, H.F.; Yamada, S. Interaction between Vitamin D Receptor and Vitamin D Ligands: Two-Dimensional Alanine Scanning Mutational Analysis. *Chem. Biol.* **2003**, *10*, 261–270. [CrossRef]
73. Meyer, M.B.; Benkusky, N.A.; Pike, J.W. 1,25-Dihydroxyvitamin D₃ induced histone profiles guide discovery of VDR action sites. *J. Steroid Biochem. Mol. Biol.* **2013**, *144*, 19–21. [CrossRef] [PubMed]
74. MacLeod, R.S.; Meyer, M.B.; Xiong, J.; Cawley, K.M.; Liu, Y.; Onal, M.; Benkusky, N.A.; Thostenson, J.D.; Pike, J.W.; O'Brien, C.A. Deletion of a putative promoter-proximal Tnfsf11 regulatory region in mice does not alter bone mass or Tnfsf11 expression in vivo. *PLoS ONE* **2021**, *16*, e0250974. [CrossRef]
75. Onal, M.; John, H.C.S.; Danielson, A.L.; Pike, J.W. Deletion of the Distal Tnfsf11 RL-D2 Enhancer That Contributes to PTH-Mediated RANKL Expression in Osteoblast Lineage Cells Results in a High Bone Mass Phenotype in Mice. *J. Bone Miner. Res.* **2015**, *31*, 416–429. [CrossRef]
76. Onal, M.; Bishop, K.A.; John, H.C.S.; Danielson, A.L.; Riley, E.M.; Piemontese, M.; Xiong, J.; Goellner, J.J.; O'Brien, C.A.; Pike, J.W. A DNA Segment Spanning the Mouse Tnfsf11 Transcription Unit and Its Upstream Regulatory Domain Rescues the Pleiotropic Biologic Phenotype of the RANKL Null Mouse. *J. Bone Miner. Res.* **2014**, *30*, 855–868. [CrossRef]
77. Pike, J.W.; Meyer, M.B.; Benkusky, N.A.; Lee, S.M.; John, H.S.; Carlson, A.; Onal, M.; Shamsuzzaman, S. Genomic Determinants of Vitamin D-Regulated Gene Expression. *Vitam Horm.* **2015**, *100*, 21–44. [CrossRef]

78. Mangelsdorf, D.; Umesono, K.; Kliewer, S.A.; Borgmeyer, U.; Ong, E.S.; Evans, R. A direct repeat in the cellular retinoid-binding protein type II gene confers differential regulation by RXR and RAR. *Cell* **1991**, *66*, 555–561. [CrossRef]
79. Kaneko, I.; Sabir, M.S.; Dussik, C.M.; Whitfield, G.K.; Karrys, A.; Hsieh, J.-C.; Haussler, M.R.; Meyer, M.B.; Pike, J.W.; Jurutka, P.W. 1,25-Dihydroxyvitamin D regulates expression of the tryptophan hydroxylase 2 and leptin genes: Implication for behavioral influences of vitamin D. *FASEB J.* **2015**, *29*, 4023–4035. [CrossRef]
80. Gerstein, M.B.; Kundaje, A.; Hariharan, M.; Landt, S.G.; Yan, K.-K.; Cheng, C.; Mu, X.J.; Khurana, E.; Rozowsky, J.; Alexander, R.P.; et al. Architecture of the human regulatory network derived from ENCODE data. *Nature* **2012**, *489*, 91–100. [CrossRef]
81. Lan, X.; Witt, H.; Katsumura, K.; Ye, Z.; Wang, Q.; Bresnick, E.H.; Farnham, P.J.; Jin, V.X. Integration of Hi-C and ChIP-seq data reveals distinct types of chromatin linkages. *Nucleic Acids Res.* **2012**, *40*, 7690–7704. [CrossRef] [PubMed]
82. Mouse ENCODE Consortium; Stamatoyannopoulos, J.A.; Snyder, M.; Hardison, R.; Ren, B.; Gingeras, T.; Gilbert, D.M.; Groudine, M.; Bender, M.; Kaul, R.; et al. An encyclopedia of mouse DNA elements (Mouse ENCODE). *Genome Biol.* **2012**, *13*, 1–5. [CrossRef]
83. Thurman, R.E.; Day, N.; Noble, W.S.; Stamatoyannopoulos, J.A. Identification of higher-order functional domains in the human ENCODE regions. *Genome Res.* **2007**, *17*, 917–927. [CrossRef] [PubMed]
84. Bikle, D.D. Vitamin D: Newer Concepts of Its Metabolism and Function at the Basic and Clinical Level. *J. Endocr. Soc.* **2020**, *4*, bvz038. [CrossRef]
85. Yoon, Y.S.; Tsai, W.W.; Van de Velde, S.; Chen, Z.; Lee, K.F.; Morgan, D.A.; Rahmouni, K.; Matsumura, S.; Wiater, E.; Song, Y.; et al. cAMP-inducible coactivator CRT3 attenuates brown adipose tissue thermogenesis. *Proc. Natl. Acad. Sci. USA* **2018**, *115*, E5289–E5297. [CrossRef]
86. Montminy, M.R.; Gonzalez, G.A.; Yamamoto, K.K. Characteristics of the cAMP response unit. *Metabolism* **1990**, *39*, 6–12. [CrossRef]
87. Meyer, M.B.; Benkusky, N.A.; Sen, B.; Rubin, J.; Pike, J.W. Epigenetic Plasticity Drives Adipogenic and Osteogenic Differentiation of Marrow-derived Mesenchymal Stem Cells. *J. Biol. Chem.* **2016**, *291*, 17829–17847. [CrossRef] [PubMed]
88. Pike, J.W.; Lee, S.M.; Benkusky, N.A.; Meyer, M.B. Genomic Mechanisms Governing Mineral Homeostasis and the Regulation and Maintenance of Vitamin D Metabolism. *JBMR Plus* **2020**, *5*, e10433. [CrossRef]
89. Van de Velde, S.; Wiater, E.; Tran, M.; Hwang, Y.; Cole, P.A.; Montminy, M. CREB Promotes Beta Cell Gene Expression by Targeting Its Coactivators to Tissue-Specific Enhancers. *Mol. Cell. Biol.* **2019**, *39*, e00200-19. [CrossRef] [PubMed]
90. Meyer, M.B.; Benkusky, N.A.; Kaufmann, M.; Lee, S.M.; Redfield, R.R.; Jones, G.; Pike, J.W. Targeted genomic deletions identify diverse enhancer functions and generate a kidney-specific, endocrine-deficient Cyp27b1 pseudo-null mouse. *J. Biol. Chem.* **2019**, *294*, 9518–9535. [CrossRef]
91. Meyer, M.B.; Benkusky, N.A.; Pike, J.W. Selective Distal Enhancer Control of the Mmp13 Gene Identified through Clustered Regularly Interspaced Short Palindromic Repeat (CRISPR) Genomic Deletions. *J. Biol. Chem.* **2015**, *290*, 11093–11107. [CrossRef]
92. Domcke, S.; Hill, A.J.; Daza, R.M.; Cao, J.; O’Day, D.R.; Pliner, H.A.; Aldinger, K.A.; Pokholok, D.; Zhang, F.; Milbank, J.H.; et al. A human cell atlas of fetal chromatin accessibility. *Science* **2020**, *370*. [CrossRef] [PubMed]
93. Cao, J.; Cusanovich, D.A.; Ramani, V.; Aghamirzaie, D.; Pliner, H.A.; Hill, A.J.; Daza, R.M.; McFaline-Figueroa, J.L.; Packer, J.S.; Christiansen, L.; et al. Joint profiling of chromatin accessibility and gene expression in thousands of single cells. *Science* **2018**, *361*, 1380–1385. [CrossRef]
94. Cusanovich, D.; Hill, A.J.; Aghamirzaie, D.; Daza, R.M.; Pliner, H.; Berletch, J.B.; Filippova, G.N.; Huang, X.; Christiansen, L.; DeWitt, W.S.; et al. A Single-Cell Atlas of In Vivo Mammalian Chromatin Accessibility. *Cell* **2018**, *174*, 1309–1324.e18. [CrossRef] [PubMed]
95. Swarthout, J.T.; D’Alonzo, R.C.; Selvamurugan, N.; Partridge, N.C. Parathyroid hormone-dependent signaling pathways regulating genes in bone cells. *Gene* **2001**, *282*, 1–17. [CrossRef]
96. St John, H.C.; Meyer, M.B.; Benkusky, N.A.; Carlson, A.H.; Prideaux, M.; Bonewald, L.F.; Wesley Pike, J. The parathyroid hormone-regulated transcriptome in osteocytes: Parallel actions with 1,25-dihydroxyvitamin D3 to oppose gene expression changes during differentiation and to promote mature cell function. *Bone* **2014**, *72*, 81–91. [CrossRef]
97. Meyer, M.B.; Benkusky, N.A.; Pike, J.W. The RUNX2 cistrome in osteoblasts: Characterization, down-regulation following differentiation, and relationship to gene expression. *J. Biol. Chem.* **2014**, *289*, 16016–16031. [CrossRef]
98. Galli, C.; Zella, L.A.; Fretz, J.A.; Fu, Q.; Pike, J.W.; Weinstein, R.S.; Manolagas, S.C.; O’Brien, C.A. Targeted deletion of a distant transcriptional enhancer of the receptor activator of nuclear factor-kappaB ligand gene reduces bone remodeling and increases bone mass. *Endocrinology* **2008**, *149*, 146–153. [CrossRef] [PubMed]
99. Lee, S.M.; Carlson, A.H.; Onal, M.; Benkusky, N.A.; Meyer, M.B.; Pike, J.W. A Control Region Near the Fibroblast Growth Factor 23 Gene Mediates Response to Phosphate, 1,25(OH)2D3, and LPS In Vivo. *Endocrinology* **2019**, *160*, 2877–2891. [CrossRef] [PubMed]
100. Lee, S.M.; Riley, E.M.; Meyer, M.B.; Benkusky, N.A.; Plum, L.A.; DeLuca, H.F.; Pike, J.W. 1,25-Dihydroxyvitamin D3 Controls a Cohort of Vitamin D Receptor Target Genes in the Proximal Intestine That Is Enriched for Calcium-regulating Components. *J. Biol. Chem.* **2015**, *290*, 18199–18215. [CrossRef] [PubMed]
101. Ii, Z.K.C.; Bhasin, N.; Di Rienzi, S.C.; Rajan, A.; Deans-Fielder, K.; Swaminathan, G.; Kamyabi, N.; Zeng, X.-L.; Doddapaneni, H.; Menon, V.K.; et al. Drivers of Transcriptional Variance in Human Intestinal Epithelial Organoids. *Physiol. Genom.* **2021**. [CrossRef]
102. Christakos, S.; Li, S.; De La Cruz, J.; Shroyer, N.F.; Criss, Z.K.; Verzi, M.P.; Fleet, J.C. Vitamin D and the intestine: Review and update. *J. Steroid Biochem. Mol. Biol.* **2020**, *196*, 105501. [CrossRef] [PubMed]



Review

Development of In Vitro and In Vivo Evaluation Systems for Vitamin D Derivatives and Their Application to Drug Discovery

Kaori Yasuda¹, Miyu Nishikawa², Hiroki Mano¹, Masashi Takano³, Atsushi Kittaka³ , Shinichi Ikushiro² and Toshiyuki Sakaki^{1,*}

¹ Department of Pharmaceutical Engineering, Faculty of Engineering, Toyama Prefectural University, 5180 Kurokawa, Imizu 939-0398, Toyama, Japan; kyasuda@pu-toyama.ac.jp (K.Y.); z16003@st.pu-toyama.ac.jp (H.M.)

² Department of Biotechnology, Faculty of Engineering, Toyama Prefectural University, 5180 Kurokawa, Imizu 939-0398, Toyama, Japan; m-nishikawa@pu-toyama.ac.jp (M.N.); ikushiro@pu-toyama.ac.jp (S.I.)

³ Faculty of Pharmaceutical Sciences, Teikyo University, Tokyo 173-8605, Japan; mtakano@pharm.teikyo-u.ac.jp (M.T.); akittaka@pharm.teikyo-u.ac.jp (A.K.)

* Correspondence: tsakaki@pu-toyama.ac.jp

Abstract: We have developed an in vitro system to easily examine the affinity for vitamin D receptor (VDR) and CYP24A1-mediated metabolism as two methods of assessing vitamin D derivatives. Vitamin D derivatives with high VDR affinity and resistance to CYP24A1-mediated metabolism could be good therapeutic agents. This system can effectively select vitamin D derivatives with these useful properties. We have also developed an in vivo system including a *Cyp27b1*-gene-deficient rat (a type I rickets model), a *Vdr*-gene-deficient rat (a type II rickets model), and a rat with a mutant *Vdr* (R270L) (another type II rickets model) using a genome editing method. For *Cyp27b1*-gene-deficient and *Vdr* mutant (R270L) rats, amelioration of rickets symptoms can be used as an index of the efficacy of vitamin D derivatives. *Vdr*-gene-deficient rats can be used to assess the activities of vitamin D derivatives specialized for actions not mediated by VDR. One of our original vitamin D derivatives, which displays high affinity VDR binding and resistance to CYP24A1-dependent metabolism, has shown good therapeutic effects in *Vdr* (R270L) rats, although further analysis is needed.

Keywords: vitamin D; vitamin D receptor; split luciferase-based biosensor; CYP24A1-dependent metabolism; CYP27B1; rickets; genome editing

Citation: Yasuda, K.; Nishikawa, M.; Mano, H.; Takano, M.; Kittaka, A.; Ikushiro, S.; Sakaki, T. Development of In Vitro and In Vivo Evaluation Systems for Vitamin D Derivatives and Their Application to Drug Discovery. *Int. J. Mol. Sci.* **2021**, *22*, 11839. <https://doi.org/10.3390/ijms222111839>

Academic Editor: Enikő Kallay

Received: 1 September 2021

Accepted: 26 October 2021

Published: 31 October 2021

Publisher's Note: MDPI stays neutral with regard to jurisdictional claims in published maps and institutional affiliations.



Copyright: © 2021 by the authors. Licensee MDPI, Basel, Switzerland. This article is an open access article distributed under the terms and conditions of the Creative Commons Attribution (CC BY) license (<https://creativecommons.org/licenses/by/4.0/>).

1. Introduction

The active form of vitamin D₃ (1 α ,25(OH)₂D₃) plays essential roles in calcium and phosphate homeostasis, cellular proliferation and differentiation, and immune responses. Since it could cause hypercalcemia and hypercalciuria, its clinical utility is limited [1,2]. A huge number of vitamin D derivatives have been synthesized. Many of them have been studied in clinical trials for the treatment of type I rickets, osteoporosis, psoriasis, renal osteodystrophy, and also leukemia, pancreatic, prostate, and breast cancers [3–9]. A number of vitamin D derivatives have been approved by the FDA for clinical use in a variety of disorders, for example, 22-oxacalcitriol (Maxacalcitol) and calcipotriol (Dovonex) for treatment of psoriasis, 19-nor-1 α ,25(OH)₂D₂ (Zemlar), 26,26,26,27,27,27-hexafluoro-1 α ,25(OH)₂D₃ (Falcacalcitriol), and doxercalciferol (Hectorol) for secondary hyperparathyroidism, and 1 α (OH)D₃ (alfacalcidol) and eldecacitriol (Edirol) for osteoporosis. Although many vitamin D derivatives have antiproliferative activity, none have been approved for cancer treatment. So far, only a small number of clinical studies have taken place, such as EB1089 in a phase II study for pancreatic cancer [6,10], and Hectorol and Zemlar in phase I/II advanced androgen-insensitive prostate cancer trials [7,11,12]. Unfortunately, neither have produced any significant objective responses. However, a new 1 α ,25(OH)₂D₃ analog, 19-nor-14-epi-23-yne-1 α ,25(OH)₂D₃ (inecalcitol), is being developed for prostate cancers and chronic leukemia [13,14].

The active form of vitamin D₃ (1 α ,25(OH)₂D₃) plays essential roles in calcium and phosphate homeostasis, cellular proliferation and differentiation, and immune responses. Its clinical utility is limited because it can cause hypercalcemia and hypercalciuria. [1,2]. Several thousand vitamin D derivatives have been synthesized, and many have been studied in clinical trials to treat conditions, including type I rickets, osteoporosis, leukemia, psoriasis, renal osteodystrophy, and pancreatic, prostate, and breast cancers. [3–9]. A number of vitamin D derivatives have been approved by the FDA for clinical use in a variety of disorders. These derivatives include calcipotriol (Dovonex; Leo Pharmaceuticals) and 22-oxacalcitriol (Maxacalcitol; Chugai Pharmaceuticals) for treatment of psoriasis; 19-nor-1 α ,25(OH)₂D₂ (Zemplar; Abbot Laboratories; Chicago, IL, USA), 26,26,26,27,27,27-hexafluoro- (Falecalcitriol; Sumitomo Pharmaceuticals and Taisho Pharmaceuticals), and doxercalciferol (Hectorol; Bone Care Int.; Middleton, WI, USA) for secondary hyperparathyroidism; and 1 α (OH)D₃ (alfacalcidol; Chugai Pharmaceuticals Co., Ltd.; Tokyo, Japan) and eldecalcitol (Chugai Pharmaceuticals Co., Ltd.; Tokyo, Japan) for osteoporosis. Although many vitamin D derivatives, including those approved by the FDA for treating secondary hyperparathyroidism and renal osteodystrophy, have displayed antiproliferative activity, none have been approved for cancer treatment. To date, only a limited number of clinical studies have taken place, including a phase II study of EB1089 in pancreatic cancer. [6,10]. Hectorol and Zemplar have been studied in phase I/II advanced androgen-insensitive prostate cancer trials [7,11,12]. Unfortunately, neither produced any significant objective responses. Recently, a new 1 α ,25(OH)₂D₃ analog, inecalcitol, is being developed for prostate cancers and chronic leukemia [13,14].

In evaluating these vitamin D derivatives, (1) affinity for vitamin D receptor, (2) affinity for vitamin-D-binding protein (DBP), (3) resistance to metabolism by CYP24A1, and (4) ability to differentiate leukemia-derived HL-60 cells into macrophages are considered to be essential properties. In addition, they must show therapeutic efficacy in animal studies. In the case of derivatives under development for cancer treatment, therapeutic efficacy will be evaluated using tumor-bearing animals. Construction of appropriate evaluation models is indispensable for developing vitamin D derivatives for pharmaceutical use. We have developed *in vitro* systems that can easily measure vitamin D receptor (VDR) affinity [15–19] and CYP24A1-mediated metabolism [20–24]. We have also generated genetically modified rats using genome editing as follows: *Cyp27b1*-gene-deficient rats (a type 1 rickets model animal), vitamin D receptor-gene-deficient rats, and rats harboring a mutant vitamin D receptor (R270L) gene (type II rickets model animals) [25]. We have also generated *Cyp24a1*-gene-deficient rats to elucidate enzymes and metabolic pathways responsible for vitamin D derivative metabolism [26]. In this review, we describe the *in vitro* and *in vivo* systems we have developed for evaluation of vitamin D derivatives, and discuss the derivatives we have synthesized to date.

2. In Vitro System to Easily Examine the Affinity for VDR of Vitamin D Derivatives

2.1. Measurement of Binding Affinity of Vitamin D Derivatives for VDR

The widely used method for evaluating the binding ability of vitamin D derivatives for VDR in a cell-based assay system is a reporter assay that induces expression of luciferase (Luc) under the control of a promoter containing a vitamin D response element (VDRE) [27–29]. It is noted that it takes more than 12 h for the reporter protein to be expressed, and the direct binding between the receptor and the ligand cannot be evaluated. Although a competitive system using native VDR and tritium-labeled 1 α ,25(OH)₂D₃ was widely used, it is no longer commercially available. Thus, we tried to develop a new detection system that easily evaluates the affinity of vitamin D derivatives for VDR in a short time. We focused on the split-type luciferase technology [15–19,30–37]. This system can evaluate the affinity of the ligand by increasing or decreasing the luminescence of the split-type luciferase.

2.2. Development of a Novel Bioluminescent Sensor to Detect and Discriminate between Vitamin D Receptor Agonists and Antagonists in Living Cells (1st Generation)

Two chimeric fusion proteins that contained both split-luciferase and the ligand binding domain (LBD) of the VDR were constructed. This fusion protein was labeled as LucN–LBD–LucC. It contained the N-terminal domain taken from luciferase (LucN), LBD, and C-terminal domain from luciferase (LucC) from N-terminus to C-terminus. LucC–LBD–LucN has the C-terminal domain of luciferase at the N-terminus of the fusion protein (Figure 1) [15]. Unexpectedly, the LucC–LBD–LucN worked better than LucN–LBD–LucC. Luciferase activity was significantly diminished by the addition of the VDR agonists to COS-7 cells that expressed LucC–LBD–LucN. On the other hand, the VDR antagonist notably enhanced the activity of the chimeric luciferase in a dose- and time-dependent manner. Our novel model for detecting and discriminating between VDR agonists and antagonists is very useful for testing synthetic analogs of vitamin D that show reasonable affinity for normal or mutant VDRs.

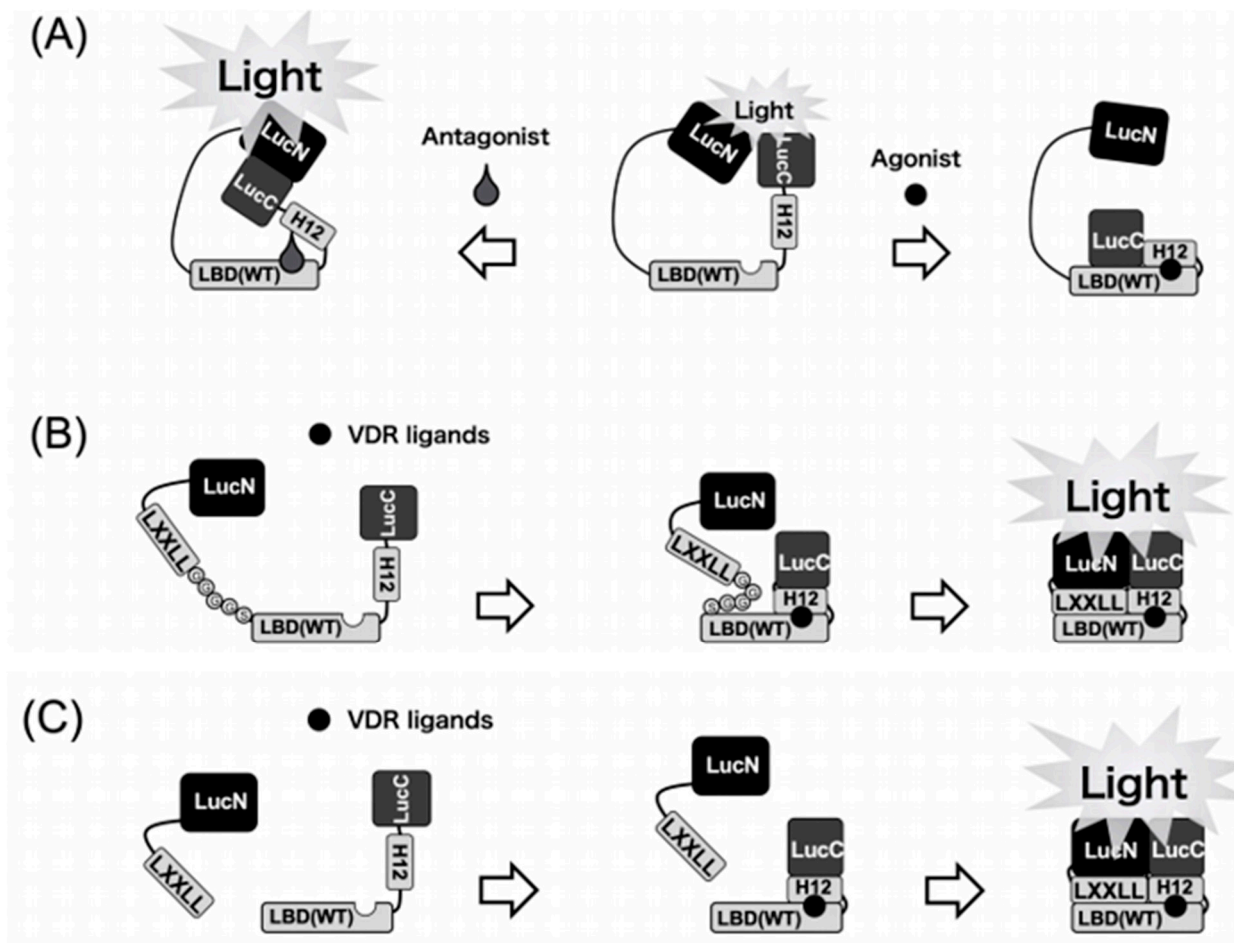


Figure 1. Schematic diagrams of the biosensors to detect VDR ligands. (A) 1st generation. Binding of the VDR agonists to the LBD may cause a conformational change of the LBD that leads to disruption of the functional complex between N-terminal and C-terminal domains of the luciferase. In contrast, binding of the antagonist leads to the reassembly of N-terminal and C-terminal domains of the luciferase to increase the activity. (B) 2nd generation. Binding of VDR ligands to the biosensor may cause a conformational change of helix12 (H12) in LBD. After conformational change of LBD, the LXXLL motif interacts with LBD in the biosensor. Then, this intramolecular dynamic change of the WT biosensor leads to reconstitution of the functional complex between LucN and LucC fragments of the split luciferase. (C) 3rd generation. Binding of the VDR ligands to the LBD–LucC may cause a positional change of helix12 in LBD. Then, the LucN–LXXLL and LBD–LucC forms a functional complex to exhibit the luciferase activity.

Patients with type II rickets showing the R274L mutation caused a 1000-fold reduction in the binding activity for $1\alpha,25(\text{OH})_2\text{D}_3$ and remarkably lowered vitamin-D-related gene expression [38]. It is Arg274, located in LBD of VDR, that is responsible for attaching $1\alpha,25(\text{OH})_2\text{D}_3$. This happens by a formation of an additional hydrogen bond with 1α -hydroxyl of $1\alpha,25(\text{OH})_2\text{D}_3$. LucC–LBD (R274L)–LucN was constructed to investigate vitamin D ligands of high affinity for the mutant VDR (R274L). A total of 5 out of the 33 vitamin D analogs tested showed much higher binding for the mutant VDR (R274L) than the vitamin D hormone. The highest binding activity was shown by 2α -(2-(tetrazol-2-yl)ethyl)-(AH-1). These analogs might be considered as future drug candidates against HVDRR that is caused by the mutant VDR (R274L) [16].

2.3. Development of a Highly Sensitive In Vitro System to Detect and Discriminate between Vitamin D Receptor Agonists and Antagonists

We have established an in vitro screening system for VDR ligands using the LucC–LBD–LucN proteins expressed in *Escherichia coli* (*E. coli*) cells [17]. It should be noted that this system could be completed within 30 min, and its activity was unchanged after 10 freeze–thaw cycles. This highly sensitive and convenient system would be quite useful to screen VDR ligands with therapeutic potential for osteoporosis, renal osteodystrophy, cancers, and immune disorders.

2.4. Design of a Biosensor Based on Split Luciferase for Detection of VDR Ligands (2nd Generation)

The model we developed is very useful for a fast investigation of VDR ligands. However, the sensitivity of our biosensor (LucC–LBD–LucN) is not as high as expected. LBD is known to interact via the LXXLL motif with transcription coactivators, such as SRC-1, TIF-2, or DRIP-205 to initiate vitamin-D-related gene expression, when binding natural VDR ligands. This is why we anticipated that it is the LXXLL motif that changes the enzymatic profile of luciferase–LBD biosensors. This is why LucN–LBD–LucC and not LucC–LBD–LucN was used as a basing fragment. We created a new biosensor consisting of the LBD (121–427 aa) of VDR, N- and C-terminal of firefly luciferase fragments (LucN (1–415 aa) and LucC (416–550 aa)), the LXXLL peptide sequence, and peptide sequence (Gly–Gly–Gly–Gly–Ser (GGGGS)) \times 3 as the flexible linker [18]. This construct we labeled as LucN–LXXLL–(GGGGS) \times 3–LBD–LucC WT biosensor and WT means the wild-type of LBD (Figure 1). Light intensity of luciferase is low when natural VDR ligands are absent. The luciferase light intensity is immediately and remarkably increased when the ligand is bound to the WT biosensor. To sum up, we have successfully created a very sensitive biosensor which shows the increase in light intensity when binding VDR agonists.

To this end, we developed a novel and WT biosensor of high sensitivity by examining three types of LXXLL peptides (NHPMLMNLKDN, LTEMHPILTSLLQNGVDHV, and LSETHPLLWTLSSSTEGDSM) that interact with the LBD in response to $1\alpha,25(\text{OH})_2\text{D}_3$ or synthetic VDR agonists. The COS-7 cells that expressed each type of biosensor were treated with $1\alpha,25(\text{OH})_2\text{D}_3$ (100 nM) and then the luminescence was measured 90 min later. Among the 10 biosensors we constructed, one showed a reduction in intensity of light in response to $1\alpha,25(\text{OH})_2\text{D}_3$. Seven biosensors showed an excellent increase in light intensity. Our best biosensor showed the light intensity ca. one-third of that of full-length native luciferase of firefly. Quite unexpectedly, $25(\text{OH})\text{D}_3$, as the low-affinity VDR ligand, also enhanced the intensity of light in a concentration-dependent manner. The half maximal relative intensity of light was recorded at 1 nM of $1\alpha,25(\text{OH})_2\text{D}_3$ and at 20 nM of $25(\text{OH})\text{D}_3$, respectively. We then compared the binding activity of $1\alpha,25(\text{OH})_2\text{D}_3$ and $25(\text{OH})\text{D}_3$ for the mutant VDR (R274L). As previously mentioned, the substitution of Arg274 to Leu causes a 1000-fold decrease in affinity of $1\alpha,25(\text{OH})_2\text{D}_3$. As expected, in the R274L biosensor the concentration–response curve of $1\alpha,25(\text{OH})_2\text{D}_3$ was very similar to that of $25(\text{OH})\text{D}_3$. Thus, the biosensor system we developed may be very useful in elucidating novel vitamin D analogs as drug candidates against type II rickets resulting from VDR mutation, such as R274L.

2.5. Development of a Novel Two-Molecule System with a Highly Sensitive Biosensor (3rd Generation)

In the next step, we developed a two-molecule system named LXXLL + LBD biosensor, as shown in Figure 1, with a combination of two components [19]. The two plasmids were co-transfected and two proteins were co-expressed in COS-7 cells. The LXXLL + LBD biosensor-expressing COS-7 cells were treated with 100 nM of $1\alpha,25(\text{OH})_2\text{D}_3$, and luciferase light intensity was measured at 90 min after treatment. Among all combinations of LXXLL + LBD biosensor, relative light intensity of A1 + B1 [19] was the highest in all combinations. The relative light intensity of combination A1 + B1 was approximately a 90- to 100-fold increase in response to 100 nM of $1\alpha,25(\text{OH})_2\text{D}_3$. It should be noted that the detection limit was 0.005 nM (5 pM) of $1\alpha,25(\text{OH})_2\text{D}_3$, indicating that the sensitivity of LXXLL + LBD biosensor is higher than that of our previous biosensors. [15–18]. Our LXXLL + LBD biosensor might be used for the measurement of $1\alpha,25(\text{OH})_2\text{D}_3$ and $25(\text{OH})\text{D}_3$ in the plasma.

3. In Vitro Evaluation of CYP24A1-mediated Metabolism of Vitamin D Derivatives

3.1. Expression of Rat or Human CYP24A1 in E. coli Cells

The rat *Cyp24a1* cDNA was cloned from the rat kidney cDNA library [39], and the isolated cDNA clone contained the open reading frame consisting of 514 amino acids. Since the amino acid sequence showed less than 40 % homology with already known CYPs, the new CYP family name, CYP24, was given to this vitamin-D-24-hydroxylase.

The molecular mechanism of *CYP24A1* gene regulation is quite complicated, and many factors are tissue-specifically involved in the expression of *CYP24A1* [40–44]. These facts strongly suggest that *CYP24A1* is a physiologically essential enzyme that regulates the level of the active form of vitamin D.

When the deduced amino acid sequence from its cDNA was compared to that amino-terminal amino acid sequence of the *CYP24A1* purified from rat kidney, it was found that the mature form of rat *CYP24A1* lacks amino-terminal 32 amino acids. These results suggest that amino-terminal 32 amino acids function as a mitochondrial targeting signal, which is removed after translocation of *CYP24A1* to mitochondria. We have successfully expressed the mature forms of rat and human *CYP24A1* in *E. coli* cells to reveal their enzymatic properties [20–24].

3.2. Construction of a CYP24A1 Enzyme System Containing Adrenodoxin (ADX) and NADPH-Adrenodoxin Reductase (ADR)

The mitochondrial P450 system consists of three components: CYP, ADX, and ADR. Electrons are sequentially transferred from NADPH through ADR and ADX to *CYP24A1* (Figure 2). Thus, *CYP24A1*-dependent activity was measured in an in vitro reconstituted system containing purified ADX and ADR proteins. On the other hand, in a whole-cell system, co-expression of mature forms of *CYP24A1*, ADX, and ADR in *E. coli* is required. We have demonstrated that the *E. coli* expression system is quite useful to investigate enzymatic properties of *CYP24A1*. Using this *E. coli* expression system, we have determined kinetic parameters of *CYP24A1* in the metabolism of the native vitamin D and various vitamin D derivatives, and revealed their metabolic pathways [45–58].

3.3. CYP24A1-Dependent Multi-Step Reaction toward the Active form of Vitamin D₃

CYP24A1 plays central roles in vitamin D metabolism and produces a wide variety of metabolites. We revealed that rat or human *CYP24A1* catalyzes a six-step reaction, starting with hydroxylation at the 24R position of $1\alpha,25(\text{OH})_2\text{D}_3$ to produce the final metabolite, calcitric acid (Figure 3). In addition, human *CYP24A1* catalyzes a four-step reaction, starting with hydroxylation at the 23S position to produce the 26,23-lactone form (Figure 3). In the reaction of P450, it is often seen that the reaction product is not released from the substrate binding pocket and the reaction proceeds further. Thus, the two- or three-step reaction is not special in the P450 reaction; however, there is no other P450 that catalyzes

such a multi-step reaction for one substrate. Moreover, it is noted that the reaction by human CYP24A1 proceeds in a dual pathway, the C-24 pathway and the C-23 pathway. Interestingly, the ratio of the C-24 to C-23 pathways varies among animal species. In human CYP24A1, it is about 4:1, but, in rat CYP24A1, about 25:1; however, in animal species such as guinea pig and opossum, the C-23 pathway is major. In rat and human CYP24A1, the 326th amino acid residue from the N-terminus is Ala, whereas it is Gly in guinea pigs and opossum, and, when the Ala326 in rat and human CYP24A1 is replaced by Gly, it changes to the guinea pig type [59]. Given that inactivating the active form of vitamin D is the physiological role of CYP24A1, it may be less important whether the C-24 or C-23 pathway is predominant.

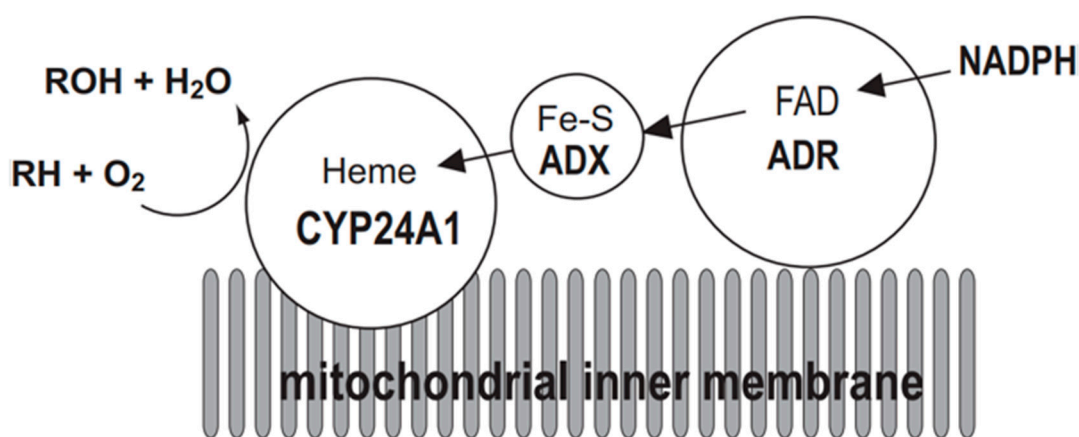


Figure 2. Mitochondrial electron transport chain of CYP24A1. CYP24A1-dependent mono-oxygenase activity requires the electron transfer from NADPH via NADPH-adrenodoxin oxidoreductase (ADR) and adrenodoxin (ADX) to the heme iron of CYP24A1 situated on the inner membrane of mitochondria. RH represents substrate of CYP24A1.

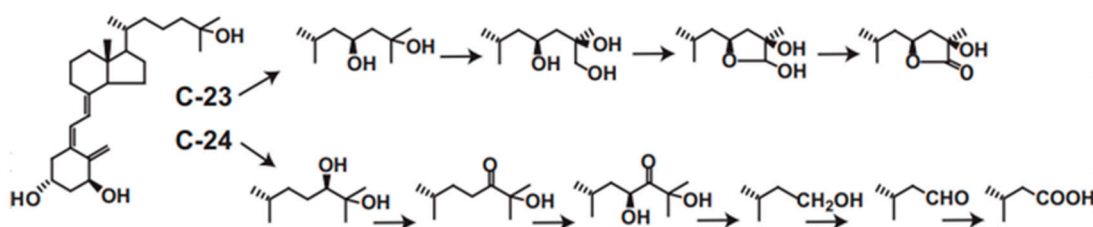


Figure 3. C-23 and C-24 oxidative pathways of $1\alpha,25(\text{OH})_2\text{D}_3$ catalyzed by human CYP24A1. Human CYP24A1 catalyzes 6-step mono-oxygenation from C-24 hydroxylation to produce calcitroic acid, and 4-step mono-oxygenation from C-23 hydroxylation to the lactone formation.

3.4. Metabolism of Vitamin D Derivatives by CYP24A1

The CYP24A1 gene has two VDREs in the promoter region [40,41,60] and, when the active form of vitamin D binds to VDR, remarkable transcriptional induction of CYP24A1 occurs. When a large amount of CYP24A1 protein is expressed in the cell, the active form of vitamin D is inactivated via the metabolic pathways described above. This mechanism appears to be crucial for keeping the level of the active form of vitamin D. However, when a vitamin D derivative with a high affinity for VDR is developed as a drug, the drug binds to VDR to induce CYP24A1. Therefore, vitamin D derivatives that are not easily metabolized by CYP24A1 could be excellent drugs with long-lasting efficacy. Eldecalcitol, an osteoporosis treatment drug developed by Chugai Pharmaceutical Co., Ltd., has a 3-hydroxy-propyloxy group at the 2β position of $1\alpha,25(\text{OH})_2\text{D}_3$ (Figure 4). We revealed that CYP24A1 hardly metabolizes Eldecalcitol [53] and suggest that the resistance to CYP24A1-dependent metabolism may be a key factor that keeps its efficacy for a long time [53,61–63]. We have investigated the metabolism of many vitamin D deriva-

tives by CYP24A1 and have clearly demonstrated the importance of CYP24A1-dependent metabolism. In addition, as mentioned above, the fact that there are animal species differences in the metabolic mode of $1\alpha,25(\text{OH})_2\text{D}_3$ by CYP24A1 suggests that there are also animal species differences in the metabolism of vitamin D derivatives. Therefore, the development of vitamin D derivatives requires not only animal studies, but also metabolic studies using human CYP24A1 enzyme.

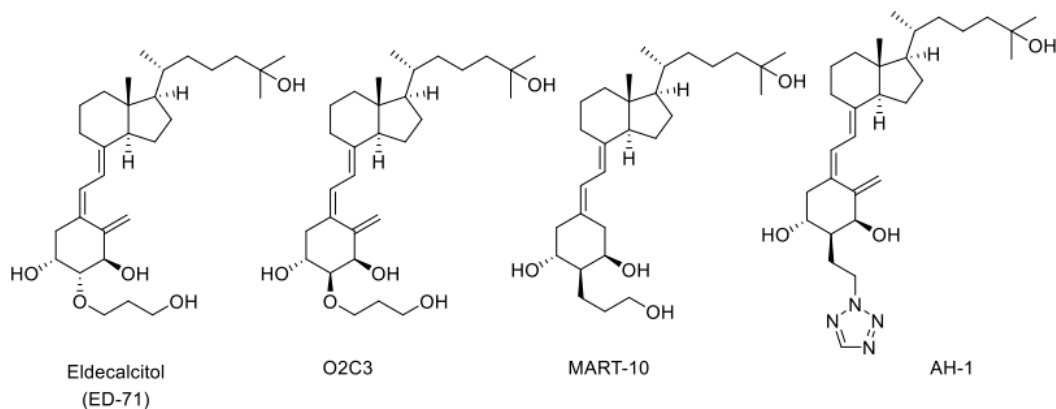


Figure 4. Structures of three CYP24A1-resistant VDR agonists: Eldecalcitol (ED-71), O2C3, MART-10, and AH-1.

3.5. CYP24A1-Resistant Vitamin D Derivatives with a Substituent at C2 α Position

We have synthesized many of A-ring-modified derivatives with a substituent at the C2 α position, which have unique biological activities [64–68]. Of these derivatives, 2 α -(3-hydroxypropoxy)- $1\alpha,25(\text{OH})_2\text{D}_3$ (O2C3), which is a C2-epimer of Eldecalcitol, was examined for the metabolism by CYP24A1. Five metabolites were detected in its metabolism by human CYP24A1, including both C-23 and C-24 oxidation pathways [48]. The K_m and k_{cat} values of human CYP24A1 for O2C3 were estimated to be approximately 16 times greater and 3 times lower than those for $1\alpha,25(\text{OH})_2\text{D}_3$, respectively [48]. Accordingly, the catalytic efficiency (k_{cat}/K_m) of human CYP24A1 for O2C3 is only about 3% of $1\alpha,25(\text{OH})_2\text{D}_3$. These results strongly suggest that O2C3 is much more resistant to CYP24A1-dependent metabolism than $1\alpha,25(\text{OH})_2\text{D}_3$. It is noted that another C-2-substituted derivative, 19-nor-2 α -(3-hydroxypropyl)- $1\alpha,25(\text{OH})_2\text{D}_3$ (MART-10) (Figure 4), was more resistant to CYP24A1-dependent degradation than O2C3 [69–74]. The k_{cat}/K_m values of human CYP24A1 for MART-10 were about 0.3 % of those for $1\alpha,25(\text{OH})_2\text{D}_3$.

Our *in vivo* studies using rats revealed that MART-10 had a potent anticancer effect, with a low calcemic effect, which is a suitable property as an anticancer drug. The resistance to CYP24A1 is also a suitable property of MART-10 as an anticancer drug.

4. In Vivo Evaluation System for Vitamin D Derivatives Using Genetically Modified Rats Generated by Genome Editing

4.1. Appearance and Growth of Genetically Modified (GM) Rats

Figure 5A shows WT, *Vdr* (R270L), and *Vdr*-KO rats fed an F-2 diet containing 0.75% Ca, and *Cyp27b1*-KO rats fed a diet containing 1.15% Ca at 15 weeks after birth. Although *Cyp27b1*-KO rats were much smaller than WT rats, body sizes of *Vdr* (R270L) and *Vdr*-KO rats were not so different from that of the WT rats. Figure 5A shows the *Vdr*-abnormal skin and alopecia of KO rats. Elasticity and softness of the skin of *Vdr*-KO rats were substantially lowered and the wavy skin was formed [25]. Keratinization was elevated and follicles decreased, and formation of cysts appeared in the dorsal skin of *Vdr*-KO rats [25].

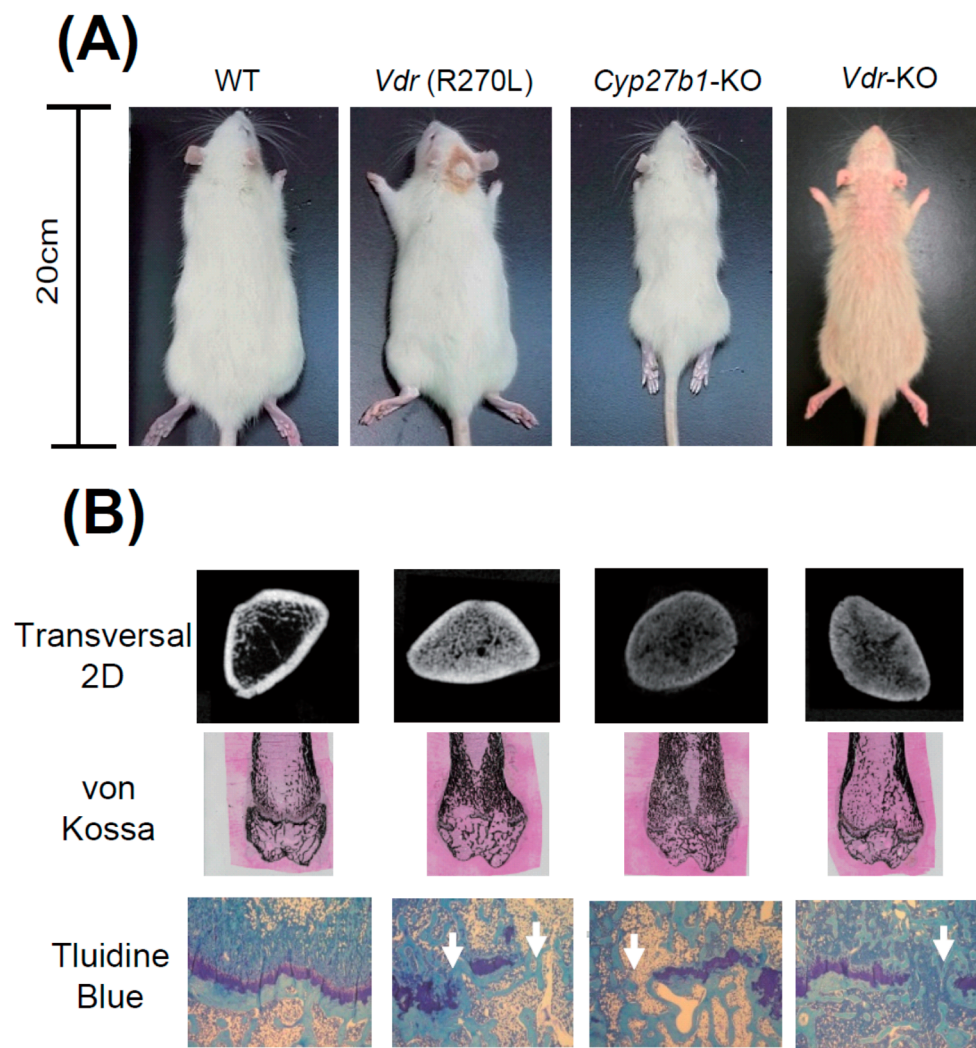


Figure 5. The appearance of GM rats and their abnormal bone formation [25]. (A) Comparison of body size and skin phenotype at 15 weeks of age. (B) First panels, 2D μ -CT images of horizontal section at distal femur; second panels, von Kossa staining of distal femur; bottom panels, toluidine blue staining of epiphyseal cartilage.

Figure 5A shows that growth was substantially diminished in *Cyp27b1*-KO rats compared to WT rats. However, only a slight decrease was observed in *Vdr* (R270L) and *Vdr*-KO rats. It was noted that approximately a half of male *Cyp27b1*-KO rats fed with the diet containing 0.75 % Ca died prior to 9 weeks of age, and none survived to 10 weeks of age (data not shown), whereas no animals had died at 15 weeks of age in the *Cyp27b1*-KO rats fed with the diet containing 1.15% Ca. Thus, the diet that contained 0.75% Ca was used for mutant *Vdr* (R270L) and *Vdr*-KO rats, while the diet containing 1.15 % Ca was used for *Cyp27b1*-KO rats.

4.2. Osteogenesis and Plasma Ca, PTH, and $1\alpha,25(\text{OH})_2\text{D}_3$ Levels in the GM Rats

It is noted that *Cyp27b1*-KO rats are remarkably smaller than other rats. Figure 5B shows the middle region of the femur in 2D μ CT scan images. The femur lengths of *Cyp27b1*-KO, *Vdr* (R270L), and *Vdr*-KO rats were found to be remarkably shorter than those of WT rats. The μ CT scanning and von Kossa staining of femurs showed hyperplasia of calcified trabecular bones with a narrow medullary cavity in all the *Vdr* (R270L), *Cyp27b1*-KO, and *Vdr*-KO rats (Figure 5B). The *Vdr* (R270L) and *Vdr*-KO rats expressed no clear differences

in total bone mineral density (BMD). In contrast, the BMD of cortical bone in *Cyp27b1*-KO rats was substantially diminished [25].

Histological analysis of the epiphyseal cartilage demonstrated structural disorder of the growth plate in all the *Vdr* (R270L), *Cyp27b1*-KO, and *Vdr*-KO rats. Whereas WT growth plates contained aligned cartilage cells in the layered structure, growth plates in all three GM rats lost the sequential plate structure and cartilage cell alignment (Figure 5). Thus, the morphology of bone was abnormal in all three GM rats, and, in *Cyp27b1*-KO rats, the most significant disorders of bone were observed.

It is well known that rickets type I model *Cyp27b1*-KO mice, and rickets type II model *Vdr*-KO mice, have significantly lower plasma Ca levels than WT mice [75,76]. Expectedly, the plasma Ca level was substantially reduced, and the level of parathyroid hormone (PTH) in plasma was greatly increased in *Vdr* (R270L) rats and *Cyp27b1*-KO rats [25]. Unexpectedly, the plasma Ca level in *Vdr*-KO rats was normal at 15 weeks. In *Vdr*-KO rats, until 10 weeks, the plasma level of Ca was significantly lower than that in WT rats, and PTH level was substantially higher than that in WT rats [25]. Plasma PTH level in *Vdr*-KO rats was remarkably higher than that in WT rats; although, at 15 weeks, the level of Ca in plasma in *Vdr*-KO rats returns to normal. These findings might indicate that hyperparathyroidism occurred in *Vdr*-KO rats [25]. In addition, the putative incomplete formation of intercellular barriers in epithelial tissues, including the small intestine, in *VDR*-KO rats might cause the increased calcium permeability to result in the normal level of plasma Ca concentration [77].

Although plasma $1\alpha,25(\text{OH})_2\text{D}_3$ level was significantly increased in *Vdr* (R270L) and *Vdr*-KO rats, it was significantly decreased in *Cyp27b1*-KO rats (8.0 ± 3.2 pg/mL (mean \pm SEM, $n = 7$)) compared to WT rats (24.8 ± 5.2 pg/mL, (mean \pm SEM, $n = 7$)) [25].

4.3. Effects of $25(\text{OH})\text{D}_3$ Administration on *Cyp27b1*-KO Rats

As described previously [76], dietary administration of $25(\text{OH})\text{D}_3$ recovered growth failure, skeletal disorders, and hypocalcemia of *Cyp27b1*-KO mice. Dietary administration of $25(\text{OH})\text{D}_3$ to *Cyp27b1*-KO rats at $200 \mu\text{g}\cdot\text{kg}^{-1}\cdot\text{day}^{-1}$ also significantly reversed growth failure [25]. The $25(\text{OH})\text{D}_3$ administration normalized BMD of the cortex and trabecular bone of *Cyp27b1*-KO rats. Histological analysis of the femur clearly indicated a normal structure of the cortex and trabecular bone in *Cyp27b1*-KO rats [25]. The growth plate and chondrocytes were also normalized, and the plasma Ca and PTH levels of *Cyp27b1*-KO rats were fully normalized after $25(\text{OH})\text{D}_3$ administration [25].

Plasma $1\alpha,25(\text{OH})_2\text{D}_3$ level in *Cyp27b1*-KO rats was normalized by $25(\text{OH})\text{D}_3$ administration. The 1α -hydroxylation activity toward $25(\text{OH})\text{D}_3$ was observed in the liver mitochondrial fraction prepared from *Cyp27b1*-KO rats. It is noted that these results were similar to those obtained in our previous study using *Cyp27b1*-KO mice [76]. Because hepatic *Cyp27a1* has a weak 1α -hydroxylation activity toward $25(\text{OH})\text{D}_3$, *Cyp27a1* is the most probable candidate to produce $1\alpha,25(\text{OH})_2\text{D}_3$ from $25(\text{OH})\text{D}_3$ in *Cyp27b1*-KO rats.

It is noted that $25(\text{OH})\text{D}_3$ administration is highly effective in type I rickets model mice and rats. Because human *CYP27A1* can convert $25(\text{OH})\text{D}_3$ into $1\alpha,25(\text{OH})_2\text{D}_3$, similar effects might be expected in humans.

4.4. Effects of $25(\text{OH})\text{D}_3$ Administration on *Vdr* (R270L) Rats

The $25(\text{OH})\text{D}_3$ administration also normalized bone disorders with increased cortical BMD of *Vdr* (R270L) rats [25]. The reduced plasma Ca level in *Vdr* (R270L) rats was normalized by $25(\text{OH})\text{D}_3$ diet, and the elevated plasma PTH and $1\alpha,25(\text{OH})_2\text{D}_3$ levels observed before $25(\text{OH})\text{D}_3$ administration were reduced to the normal levels.

The plasma concentration of $25(\text{OH})\text{D}_3$ in *Vdr* (R270L) rats fed a $25(\text{OH})\text{D}_3$ -containing diet was about 500 nM. This concentration was 20 times higher than that in WT rats. It is noted that the affinity of $1\alpha,25(\text{OH})_2\text{D}_3$ for *Vdr* (R270L) is nearly the same as that of $25(\text{OH})\text{D}_3$. Thus, $25(\text{OH})\text{D}_3$ is thought to be a leading ligand of *Vdr* (R270L) in these rats, because plasma $1\alpha,25(\text{OH})_2\text{D}_3$ level in the *Vdr* (R270L) rats after the $25(\text{OH})\text{D}_3$ treatment

was much lower than that of 25(OH)D₃ [25]. The remarkably higher levels of 24,25(OH)₂D₃ and 24-oxo-25(OH)D₃ were consistent with the induction of *Cyp24a1* expression, which indicates the “*Vdr* (R270L)-dependent effects of 25(OH)D₃”. The remarkable effects of 25(OH)D₃ administration on rickets symptoms in *Vdr* (R270L) rats indicate that 25(OH)D₃ might be efficacious in the treatment of patients with type II rickets caused by the human VDR mutant (R274L).

4.5. Predicted Effects of the Vitamin D Derivative AH-1 towards Patients with Type II Rickets Harboring VDR (R274L) cDNA

As described in the previous sections, AH-1 showed a high binding ability to VDR (R274L) and a high resistance to CYP24A1-dependent metabolism. These results suggest that AH-1 could demonstrate therapeutic effects on type II rickets caused by VDR (R274L). Currently, we administered AH-1 to VDR (R270L) rats, and the expected results have been obtained (data not shown).

4.6. Elucidation of Molecular Mechanism Vitamin D Actions by Comparison among the GM Rats

Various vitamin D actions could be elucidated by comparing physiological conditions, such as bone and skin formation, and multiple serum parameters, such as Ca, P, 25(OH)D₃, and PTH, in the GM rats generated in this study (Figure 6). Previous studies have showed genomic and nongenomic actions of vitamin D mediated by VDR [78,79], and VDR-independent actions of vitamin D [80]. The VDR-independent effect of 25(OH)D₃ on lipid metabolism by inducing degradation of SREBP/SCAP was recently reported. In addition, ligand-independent effects of VDR have been reported [81]. Thus, at least five types of effects of vitamin D and/or the VDR should be considered, namely: (1) VDR-dependent effects of 1 α ,25(OH)₂D₃ [19,20], (2) VDR-independent effects of 1 α ,25(OH)₂D₃ [80], (3) VDR-dependent effects of 25(OH)D₃ (VDR-25(OH)D₃) [82], (4) VDR-independent effects of 25(OH)D₃ [83], and (5) ligand-independent effects of VDR (Table 1) [81].

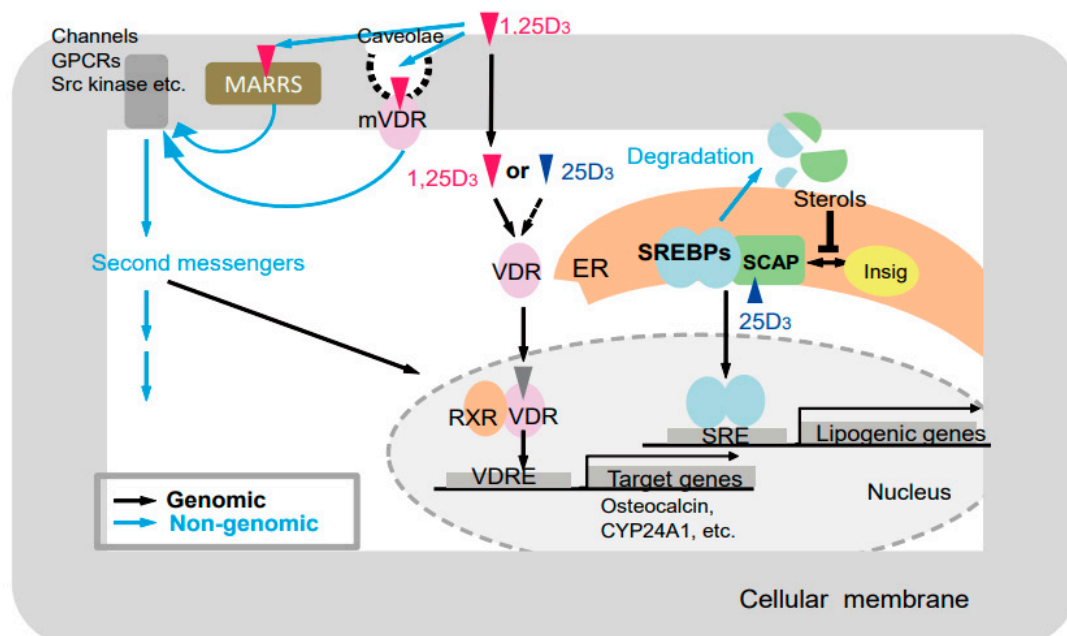


Figure 6. Putative modes of action of vitamin D [25]. Black and blue arrows indicate genomic and nongenomic pathways, respectively. GPCRs, G-protein-coupled receptor; MARRS, (membrane-associated, rapid response steroid-binding) receptor; VDR, vitamin D receptor; mVDR, membrane-bound vitamin D receptor; RXR, retinoid X receptor; VDRE, vitamin D response element; ER, endoplasmic reticulum; SREBPs, sterol regulatory-element-binding proteins; SCAP, SREBP cleavage-activating protein; SRE, sterol regulatory element.

Table 1. Vitamin D and/or VDR actions observed in WT and GM rats [25].

Rat Strain	Mode of Action of Vitamin D				
	(1) Vdr-1,25D3	(2) non Vdr-1,25D3	(3) Vdr-25D3	(4) non Vdr-25D3	(5) Vdr-no ligand
WT	+	+	+	+	+
<i>Vdr</i> (R270L)	–	+	+	+	+
<i>Cyp27b1</i> -KO	–	–	+	+	+
<i>Vdr</i> -KO	–	+	–	+	–

Vdr-1,25D3; Vdr-dependent action of: non-Vdr-1,25D3; Vdr-independent action of: Vdr-25D3; Vdr-dependent action of 25(OH)D3: non-Vdr-25D3; Vdr-independent action of 25(OH)D3: Vdr-no ligand; ligand-independent action of Vdr.

Comparison between wild-type and *Vdr* (R270L) rats could reveal (1) VDR-dependent $1\alpha,25(\text{OH})_2\text{D}_3$ effects (Table 1). Comparison between *Vdr* (R270L) and *Cyp27b1*-KO rats may reveal (2) VDR-independent effects of $1\alpha,25(\text{OH})_2\text{D}_3$. In addition, comparison between *Vdr* (R270L) and *Vdr*-KO rats may reveal (3) VDR-dependent effects of $25(\text{OH})\text{D}_3$ or (5) ligand-independent effects of the VDR. Thus, our GM rats appear to be useful for the elucidation of molecular mechanism vitamin D actions and the development of vitamin D derivatives for clinical treatment.

5. Conclusions

The vitamin D derivative evaluation systems we have developed in this study are quite useful. They can readily measure VDR affinity and CYP24A1-mediated metabolism. In addition, the GM rats we have generated by genome editing are highly useful for evaluating the efficacy, safety, and pharmacokinetics of vitamin D derivatives. The reasons rats were used in this study instead of mice include their much larger body size and greater blood volume relative to mice, rendering rats more suitable for pharmacokinetic studies. We hope these evaluation systems will contribute to the near-future development of drugs with excellent therapeutic potential.

Author Contributions: Conceptualization, T.S.; methodology, K.Y., M.N., H.M., M.T., A.K.; validation, K.Y., M.N., H.M., A.K. formal analysis, K.Y., T.S.; investigation, K.Y., M.N., H.M., M.T., A.K.; data curation, K.Y., T.S.; writing—original draft preparation, K.Y., T.S.; writing—review and editing, S.I., T.S.; funding acquisition, T.S. All authors have read and agreed to the published version of the manuscript.

Funding: Japan Society for the Promotion of Science: 16K14904, 16H04912, 19H02889.

Institutional Review Board Statement: The study was conducted according to the guidelines of the Declaration of Helsinki, and approved by the Institutional Review Board of Toyama Prefectural University.

Conflicts of Interest: The authors declare no conflict of interest.

References

- Osborn, J.L.; Schwartz, G.G.; Smith, D.; Bahnson, R.; Day, R.; Trump, D.L. Phase II trial of oral $1,25$ -dihydroxyvitamin D (calcitriol) in hormone refractory prostate cancer. *Urol. Oncol. Semin. Orig. Investig.* **1995**, *1*, 195–198. [CrossRef]
- Gross, C.; Stamey, T.; Hancock, S.; Feldman, D. Treatment of early recurrent prostate cancer with $1,25$ -dihydroxyvitamin D3 (calcitriol). *J. Urol.* **1998**, *15*, 2035–2039. [CrossRef]
- Binderup, L.; Latini, S.; Bretting, C.; Calverley, M.; Hansen, K. 20 -EPI-vitamin D3 analogues: A novel class of potent regulators of cell growth and immune responses. *Biochem. Pharmacol.* **1991**, *42*, 1569–1575. [CrossRef]
- Bishop, J.E.; Collins, E.D.; Okamura, W.H.; Norman, A.W. Profile of ligand specificity of the vitamin D binding protein for $1\alpha,25$ -dihydroxyvitamin d3 and its analogs. *J. Bone Miner. Res.* **2009**, *9*, 1277–1288. [CrossRef] [PubMed]
- Bouillon, R.; Okamura, W.H.; Norman, A.W. Structure-function relationships in the vitamin D endocrine system. *Endocr. Rev.* **1995**, *16*, 200–257. [PubMed]
- Evans, T.R.; Colston, K.W.; Lofts, F.J.; Cunningham, D.; Anthoney, D.A.; Gogas, H.; de Bono, J.S.; Hamberg, K.J.; Skov, T.; Mansi, J.L. A phase II trial of the vitamin D analogue Seocalcitol (EB1089) in patients with inoperable pancreatic cancer. *Br. J. Cancer* **2002**, *86*, 680–685. [CrossRef] [PubMed]

7. Liu, G.; Oettel, K.; Ripple, G.; Staab, M.J.; Horvath, D.; Alberti, D.; Arzoomanian, R.; Marnocha, R.; Bruskewitz, R.; Mazess, R.; et al. Phase I trial of 1alpha-hydroxyvitamin D(2) in patients with hormone refractory prostate cancer. *Clin. Cancer Res.* **2002**, *8*, 2820–2827. [PubMed]
8. Yamada, S.; Shimizu, M.; Yamamoto, K. Structure-function relationships of vitamin D including ligand recognition by the vitamin D receptor. *Med. Res. Rev.* **2003**, *23*, 89–115. [CrossRef]
9. Masuda, S.; Jones, G. Promise of vitamin D analogues in the treatment of hyperproliferative conditions. *Mol. Cancer Ther.* **2006**, *5*, 797–808. [CrossRef]
10. Lin, R.; Nagai, Y.; Sladek, R.; Bastien, Y.; Ho, J.; Petrecca, K.; Sotiropoulou, G.; Diamandis, E.P.; Hudson, T.J.; White, J.H. Expression profiling in squamous carcinoma cells reveals pleiotropic effects of vitamin D3 analog EB1089 signaling on cell proliferation, differentiation, and immune system regulation. *Mol. Endocrinol.* **2002**, *16*, 1243–1256. [CrossRef]
11. Liu, G.; Wilding, G.; Staab, M.J.; Horvath, D.; Miller, K.; Dresen, A.; Alberti, N.; Arzoomanian, R.; Chappell, R.; Bailey, H.H. Phase II study of 1alpha-hydroxyvitamin D(2) in the treatment of advanced androgen-independent prostate cancer. *Clin. Cancer Res.* **2003**, *9*, 4077–4083.
12. Schwartz, G.G.; Hall, M.C.; Stindt, D.; Patton, S.; Lovato, J.; Torti, F.M. Phase I/II study of 19-nor-1alpha-25-dihydroxyvitamin D2 (paricalcitol) in advanced, androgen-insensitive prostate cancer. *Clin. Cancer Res.* **2005**, *11*, 8680–8685. [CrossRef] [PubMed]
13. Medioni, J.; Deplanque, G.; Ferrero, J.M.; Maurina, T.; Rodier, J.M.; Raymond, E.; Allyon, J.; Maruani, G.; Houillier, P.; Mackenzie, S.; et al. Phase I safety and pharmacodynamic of inecalcitol, a novel VDR agonist with docetaxel in metastatic castration-resistant prostate cancer patients. *Clin. Cancer Res.* **2014**, *20*, 4471–4477. [CrossRef] [PubMed]
14. Studzinski, G.P.; Gocek, E.; Coffman, F.; Danilenko, M. Effects of Vitamin D Derivatives on Differentiation, Cell Cycle, and Apoptosis in Hematological Malignancies. *Vitamin. D (Forth Edition)* **2018**, *2*, 761–799.
15. Mano, H.; Nishikawa, M.; Yasuda, K.; Ikushiro, S.; Saito, N.; Takano, M.; Kittaka, A.; Sakaki, T. Development of Novel Bioluminescent Sensor to Detect and Discriminate between Vitamin D Receptor Agonists and Antagonists in Living Cells. *Bioconjug. Chem.* **2015**, *26*, 2038–2045. [CrossRef] [PubMed]
16. Mano, H.; Nishikawa, M.; Yasuda, K.; Ikushiro, S.; Saito, N.; Sawada, D.; Honzawa, S.; Takano, M.; Kittaka, A.; Sakaki, T. Novel screening system for high-affinity ligand of hereditary vitamin D-resistant rickets-associated vitamin D receptor mutant R274L using bioluminescent sensor. *J. Steroid Biochem. Mol. Biol.* **2017**, *167*, 61–66. [CrossRef]
17. Mano, H.; Ikushiro, S.; Saito, N.; Kittaka, A.; Sakaki, T. Development of a highly sensitive in vitro system to detect and discriminate between vitamin D receptor agonists and antagonists based on split-luciferase technique. *J. Steroid Biochem. Mol. Biol.* **2018**, *178*, 55–59. [CrossRef]
18. Mano, H.; Ikushiro, S.; Sakaki, T. Novel split luciferase-based biosensors for evaluation of vitamin D receptor ligands and their application to estimate CYP27B1 activity in living cells. *J. Steroid Biochem. Mol. Biol.* **2018**, *183*, 221–227. [CrossRef]
19. Mano, H.; Takano, M.; Ikushiro, S.; Kittaka, A.; Sakaki, T. Novel biosensor using split-luciferase for detecting vitamin D receptor ligands based on the interaction between vitamin D receptor and coactivator. *Biochem. Biophys. Res. Commun.* **2018**, *505*, 460–465. [CrossRef] [PubMed]
20. Akiyoshi-Shibata, M.; Sakaki, T.; Ohyama, Y.; Noshiro, M.; Okuda, K.; Yabusaki, Y. Further Oxidation of 24,25-Dihydroxyvitamin D₃ by 25-Hydroxyvitamin D₃ 24-Hydroxylase Itself. *Eur. J. Biochem.* **1994**, *224*, 335–343. [CrossRef]
21. Sakaki, T.; Sawada, N.; Nonaka, Y.; Ohyama, Y.; Inouye, K. Metabolic studies using recombinant Escherichia coli cells producing rat mitochondrial CYP24: CYP24 can convert 1 α ,25-dihydroxyvitamin D₃ to calcitric acid. *JBIC J. Biol. Inorg. Chem.* **1999**, *262*, 43–48. [CrossRef]
22. Sakaki, T.; Sawada, N.; Komai, K.; Shiozawa, S.; Yamada, S.; Yamamoto, K.; Ohyama, Y.; Inouye, K. Dual metabolic pathway of 25-hydroxyvitamin D₃ catalyzed by human CYP24. *Eur. J. Biochem.* **2000**, *267*, 6158–6165. [CrossRef]
23. Sawada, N.; Kusudo, T.; Sakaki, T.; Hatakeyama, S.; Hanada, M.; Abe, D.; Kamao, M.; Okano, T.; Ohta, M.; Inouye, K. Novel metabolism of 1 α ,25-dihydroxyvitamin D₃ with C₂₄–C₂₅ bond cleavage catalyzed by human CYP24A1. *Biochemistry* **2004**, *43*, 4530–4537. [CrossRef]
24. Hamamoto, H.; Kusudo, T.; Urushino, N.; Masuno, H.; Yamamoto, K.; Yamada, S.; Kamakura, M.; Ohta, M.; Inouye, K.; Sakaki, T. Structure-function analysis of vitamin D 24-hydroxylase (CYP24A1) by site-directed mutagenesis: Amino acid residues responsible for species-based difference of CYP24A1 between humans and rats. *Mol. Pharmacol.* **2006**, *70*, 120–128. [CrossRef] [PubMed]
25. Nishikawa, M.; Yasuda, K.; Takamatsu, M.; Abe, K.; Okamoto, K.; Horibe, K.; Mano, H.; Nakagawa, K.; Tsugawa, N.; Hirota, Y.; et al. Generation of novel genetically modified rats to reveal the molecular mechanisms of vitamin D actions. *Sci. Rep.* **2020**, *10*, 5677. [CrossRef]
26. Yasuda, K.; Nishikawa, M.; Okamoto, K.; Horibe, K.; Mano, H.; Yamaguchi, M.; Okon, R.; Nakagawa, K.; Tsugawa, N.; Okano, T.; Kawagoe, F.; et al. Elucidation of metabolic pathways of 25-hydroxyvitamin D₃ mediated by CYP24A1 and Cyp3A using Cyp24a1 knockout rats generated by CRISPR/Cas9 System. *J. Biol. Chem.* **2021**, *296*, 100668. [CrossRef] [PubMed]
27. Nakabayashi, M.; Tsukahara, Y.; Iwasaki-Miyamoto, Y.; Mihori-Shimazaki, M.; Yamada, S.; Inaba, S.; Oda, M.; Shimizu, M.; Makishima, M.; Tokiwa, H.; et al. Crystal structures of hereditary vitamin D-resistant rickets-associated vitamin D receptor mutants R270L and W282R bound to 1,25-dihydroxyvitamin D₃ and synthetic ligands. *J. Med. Chem.* **2013**, *56*, 6745–6760. [CrossRef] [PubMed]
28. Tashiro, K.; Ishii, C.; Ryoji, M. Role of distal upstream sequence in vitamin D-induced expression of human CYP24 gene. *Biochem. Biophys. Res. Commun.* **2007**, *358*, 259–265. [CrossRef] [PubMed]

29. Yamamoto, K.; Masuno, H.; Choi, M.; Nakashima, K.; Taga, T.; Ooizumi, H.; Umesono, K.; Sicinska, W.; VanHooke, J.; DeLuca, H.F.; et al. Three-dimensional modeling of and ligand docking to vitamin D receptor ligand binding domain. *Proc. Natl. Acad. Sci. USA* **2000**, *97*, 1467–1472. [CrossRef]
30. Kim, H.K.; Cho, E.J.; Jo, S.m.; Sung, B.R.; Lee, S.; Yun, S.H. A split luciferase complementation assay for studying in vivo protein-protein interactions in filamentous ascomycetes. *Curr. Genet.* **2012**, *58*, 179–189. [CrossRef] [PubMed]
31. Azad, T.; Tashakor, A.; Hosseinkhani, S. Split-luciferase complementary assay: Applications, recent developments, and future perspectives. *Anal. Bioanal. Chem.* **2014**, *406*, 5541–5560. [CrossRef]
32. Shavkunov, A.S.; Ali, S.R.; Panova-Elektronova, N.I.; Laezza, F. Split-luciferase complementation assay to detect channel-protein interactions in live cells. *Methods Mol. Biol.* **2015**, *1278*, 497–514. [PubMed]
33. Varnum, M.M.; Clayton, K.A.; Yoshii-Kitahara, A.; Yonemoto, G.; Koro, L.; Ikezu, S.; Ikezu, T. A split-luciferase complementation, real-time reporting assay enables monitoring of the disease-associated transmembrane protein TREM2 in live cells. *J. Biol. Chem.* **2017**, *292*, 10651–10663. [CrossRef] [PubMed]
34. Moustaqil, M.; Bhumkar, A.; Gonzalez, L.; Raoul, L.; Hunter, D.J.B.; Carrive, P.; Sierceki, E.; Gambin, Y. A Split-Luciferase Reporter Recognizing GFP and mCherry Tags to Facilitate Studies of Protein-Protein Interactions. *Int. J. Mol. Sci.* **2017**, *18*, 2681. [CrossRef]
35. Forster, L.; Grätz, L.; Mönnich, D.; Bernhardt, G.; Pockes, S. A Split Luciferase Complementation Assay for the Quantification of beta-Arrestin2 Recruitment to Dopamine D(2)-Like Receptors. *Int. J. Mol. Sci.* **2020**, *21*, 6103. [CrossRef] [PubMed]
36. Spillmann, M.; Thurner, L.; Romantini, N.; Zimmermann, M.; Meger, B.; Behe, M.; Waldhoer, M.; Schertler, G.F.X.; Berger, P. New Insights into Arrestin Recruitment to GPCRs. *Int. J. Mol. Sci.* **2020**, *21*, 4949. [CrossRef] [PubMed]
37. Li, Y.C.; Lytle, N.K.; Gammon, S.T.; Wang, L.; Hayes, T.K.; Sutton, M.N.; Bast, R.C., Jr.; Der, C.J.; Piwnica-Worms, D.; McCormick, F.; et al. Analysis of RAS protein interactions in living cells reveals a mechanism for pan-RAS depletion by membrane-targeted RAS binders. *Proc. Natl. Acad. Sci. USA* **2020**, *117*, 12121–12130. [CrossRef] [PubMed]
38. Malloy, P.J.; Pike, J.W.; Feldman, D. The vitamin D receptor and the syndrome of hereditary 1,25-dihydroxyvitamin D-resistant rickets. *Endocr. Rev.* **1999**, *20*, 156–188. [PubMed]
39. Ohya, Y.; Noshiro, M.; Okuda, K. Cloning and expression of cDNA encoding 25-hydroxyvitamin D₃ 24-hydroxylase. *FEBS Lett.* **1991**, *278*, 195–198. [CrossRef]
40. Ohya, Y.; Ozono, K.; Uchida, M.; Shinki, T.; Kato, S.; Suda, T.; Yamamoto, O.; Noshiro, M.; Kato, Y. Identification of a vitamin D-responsive element in the 5'-flanking region of the rat 25-hydroxyvitamin D₃ 24-hydroxylase gene. *J. Biol. Chem.* **1994**, *269*, 10545–10550. [CrossRef]
41. Zierold, C.; Mings, J.A.; DeLuca, H.F. Parathyroid hormone regulates 25-hydroxyvitamin D₃-24-hydroxylase mRNA by altering its stability. *Proc. Natl. Acad. Sci. USA* **2001**, *98*, 13572–13576. [CrossRef] [PubMed]
42. Dhawan, P.; Peng, X.; Sutton, A.L.; MacDonald, P.N.; Croniger, C.M.; Trautwein, C.; Centrella, M.; McCarthy, T.L.; Christakos, S. Functional cooperation between CCAAT/enhancer-binding proteins and the vitamin D receptor in regulation of 25-hydroxyvitamin D₃ 24-hydroxylase. *Mol. Cell Biol.* **2005**, *25*, 472–487. [CrossRef] [PubMed]
43. Meyer, M.B.; Goetsch, P.D.; Pike, J.W. A downstream intergenic cluster of regulatory enhancers contributes to the induction of CYP24A1 expression by 1 α ,25-dihydroxyvitamin D₃. *J. Biol. Chem.* **2010**, *285*, 15599–15610. [CrossRef] [PubMed]
44. Meyer, M.B.; Lee, S.M.; Carlson, A.H.; Benkusky, N.A.; Kaufmann, M.; Jones, G.; Pike, J.W. A chromatin-based mechanism controls differential regulation of the cytochrome P450 gene Cyp24a1 in renal and non-renal tissues. *J. Biol. Chem.* **2019**, *294*, 14467–14481. [CrossRef]
45. Sakaki, T.; Sawada, N.; Abe, D.; Komai, K.; Shiozawa, S.; Nonaka, Y.; Nakagawa, K.; Okano, T.; Ohta, M.; Inouye, K. Metabolism of 26,26,27,27-F₆-1 α ,25-dihydroxyvitamin D₃ by CYP24: Species-based difference between humans and rats. *Biochem. Pharmacol.* **2003**, *65*, 1957–1965. [CrossRef]
46. Kusudo, T.; Sakaki, T.; Abe, D.; Fujishima, T.; Kittaka, A.; Takayama, H.; Ohta, M.; Inouye, K. Metabolism of 20-epimer of 1 α ,25-dihydroxyvitamin D₃ by CYP24: Species-based difference between humans and rats. *Biochem. Biophys. Res. Commun.* **2003**, *309*, 885–892. [CrossRef]
47. Kusudo, T.; Sakaki, T.; Abe, D.; Fujishima, T.; Kittaka, A.; Takayama, H.; Hatakeyama, S.; Ohta, M.; Inouye, K. Metabolism of A-ring diastereomers of 1 α ,25-dihydroxyvitamin D₃ by CYP24A1. *Biochem. Biophys. Res. Commun.* **2004**, *321*, 774–782. [CrossRef] [PubMed]
48. Abe, D.; Sakaki, T.; Kusudo, T.; Kittaka, A.; Saito, N.; Suhara, Y.; Fujishima, T.; Takayama, H.; Hamamoto, H.; Kamakura, M.; et al. Metabolism of 2 α -propoxy-1 α ,25-dihydroxyvitamin D₃ and 2 α -(3-hydroxypropoxy)-1 α ,25-dihydroxyvitamin D₃ by human CYP27A1 and CYP24A1. *Drug Metab. Dispos.* **2005**, *33*, 778–784. [CrossRef]
49. Urushino, N.; Nakabayashi, S.; Arai, M.A.; Kittaka, A.; Chen, T.C.; Yamamoto, K.; Hayashi, K.; Kato, S.; Ohta, M.; Kamakura, M.; et al. Kinetic Studies of 25-Hydroxy-19-Nor-Vitamin D₃ and 1 α ,25-Dihydroxy-19-Nor-Vitamin D₃ Hydroxylation by CYP27B1 and CYP24A1. *Drug Metab. Dispos.* **2007**, *35*, 1482–1488. [CrossRef]
50. Saito, N.; Suhara, Y.; Abe, D.; Kusudo, T.; Ohta, M.; Yasuda, K.; Sakaki, T.; Honzawa, S.; Fujishima, T.; Kittaka, A. Synthesis of 2 α -propoxy-1 α ,25-dihydroxyvitamin D₃ and comparison of its metabolism by human CYP24A1 and rat CYP24A1. *Bioorg. Med. Chem.* **2009**, *17*, 4296–4301. [CrossRef]
51. Sawada, D.; Tsukuda, Y.; Yasuda, K.; Sakaki, T.; Saito, H.; Takagi, K.-I.; Takenouchi, K.; Chen, T.; Reddy, G.S.; Kittaka, A. Synthesis and Biological Activities of 1 α ,4 α ,25- and 1 α ,4 β ,25-Trihydroxyvitamin D₃ and Their Metabolism by Human CYP24A1 and UDP-Glucuronosyltransferase. *Chem. Pharm. Bull.* **2012**, *60*, 1343–1346. [CrossRef]

52. Yasuda, K.; Ikushiro, S.; Kamakura, M.; Takano, M.; Saito, N.; Kittaka, A.; Chen, T.; Ohta, M.; Sakaki, T. Human cytochrome P450-dependent differential metabolism among three 2 α -substituted-1 α ,25-dihydroxyvitamin D₃ analogs. *J. Steroid Biochem. Mol. Biol.* **2013**, *133*, 84–92. [CrossRef]
53. Yasuda, K.; Iwanaga, Y.; Ogawa, K.; Mano, H.; Ueno, S.; Kimoto, S.; Ohta, M.; Kamakura, M.; Ikushiro, S.; Sakaki, T. Human hepatic metabolism of the anti-osteoporosis drug eldcalcitol (ED-71) involves sterol C4-methyl oxidase. *Pharmacol. Res. Prospect.* **2015**, *3*, e00120.
54. Takano, M.; Yasuda, K.; Higuchi, E.; Tohyama, E.; Takeuchi, A.; Sakaki, T.; Kittaka, A. Synthesis, metabolism, and biological activity of 2-[3-(tetrazolyl) propyl]-1 α ,25-dihydroxy-19-norvitamin D₃. *J. Steroid Biochem. Mol. Biol.* **2016**, *164*, 40–44. [CrossRef] [PubMed]
55. Kawagoe, F.; Sugiyama, T.; Yasuda, K.; Uesugi, M.; Sakaki, T.; Kittaka, A. Concise synthesis of 23-hydroxylated vitamin D₃ metabolites. *J. Steroid Biochem. Mol. Biol.* **2018**, *186*, 161–168. [CrossRef] [PubMed]
56. Kawagoe, F.; Yasuda, K.; Mototani, S.; Sugiyama, T.; Uesugi, M.; Sakaki, T.; Kittaka, A. Synthesis and CYP24A1-Dependent Metabolism of 23-Fluorinated Vitamin D₃ Analogues. *ACS Omega* **2019**, *4*, 11332–11337. [CrossRef] [PubMed]
57. Kawagoe, F.; Mototani, S.; Yasuda, K.; Nagasawa, K.; Uesugi, M.; Sakaki, T.; Kittaka, A. Introduction of Fluorine Atoms to Vitamin D₃ Side-chain and Synthesis of 24,24-Difluoro-25-hydroxyvitamin D₃. *J. Steroid Biochem. Mol. Biol.* **2019**, *195*, 105477. [CrossRef]
58. Milczarek, M.; Chodyński, M.; Pietraszek, A.; Stachowicz-Suhs, M.; Yasuda, K.; Sakaki, T.; Wietrzyk, J.; Kutner, A. Synthesis, CYP24A1-Dependent Metabolism and Antiproliferative Potential against Colorectal Cancer Cells of 1,25-Dihydroxyvitamin D₂ Derivatives Modified at the Side Chain and the A-Ring. *Int. J. Mol. Sci.* **2020**, *21*, 642. [CrossRef]
59. Prosser, D.E.; Kaufmann, M.; O'Leary, B.; Byford, V.; Jones, G. Single A326G mutation converts human CYP24A1 from 25-OH-D₃-24-hydroxylase into -23-hydroxylase, generating 1,25-(OH)₂D₃-26,23-lactone. *Proc. Natl. Acad. Sci. USA* **2007**, *104*, 12673–12678. [CrossRef]
60. Ohyama, Y.; Ozono, K.; Uchida, M.; Yoshimura, M.; Shinki, T.; Suda, T.; Yamamoto, O. Functional assessment of two vitamin D-responsive elements in the rat 25-hydroxyvitamin D₃ 24-hydroxylase gene. *J. Biol. Chem.* **1996**, *271*, 30381–30385. [CrossRef]
61. Shankar, V.N.; Dilworth, F.J.; Makin, H.L.; Schroeder, N.J.; Trafford, D.J.; Kissmeyer, A.M.; Calverley, M.J.; Binderup, E.; Jones, G. Metabolism of the vitamin D analog EB1089 by cultured human cells: Redirection of hydroxylation site to distal carbons of the side-chain. *Biochem. Pharmacol.* **1997**, *53*, 783–793. [CrossRef]
62. Lechner, D.; Manhardt, T.; Bajna, E.; Posner, G.H.; Cross, H.S. A 24-phenylsulfone analog of vitamin D inhibits 1 α ,25-dihydroxyvitamin D(3) degradation in vitamin D metabolism-competent cells. *J. Pharmacol. Exp. Ther.* **2007**, *320*, 1119–1126. [CrossRef] [PubMed]
63. Schuster, I.; Egger, H.; Astecker, N.; Herzig, G.; Schüssler, M.; Vorisek, G. Selective inhibitors of CYP24: Mechanistic tools to explore vitamin D metabolism in human keratinocytes. *Steroids* **2001**, *66*, 451–462. [CrossRef]
64. Kittaka, A.; Suhara, Y.; Takayanagi, H.; Fujishima, T.; Kurihara, M.; Takayama, H. A concise and efficient route to 2 α -(omega-hydroxyalkoxy)-1 α ,25-dihydroxy vitamin D₃: Remarkably high affinity to vitamin D receptor. *Org. Lett.* **2000**, *2*, 2619–2622. [CrossRef] [PubMed]
65. Suhara, Y.; Nihei, K.I.; Tanigawa, H.; Fujishima, T.; Konno, K.; Nakagawa, K.; Okano, T.; Takayama, H. Syntheses and biological evaluation of novel 2 α -substituted 1 α ,25-dihydroxyvitamin D₃ analogues. *Bioorg. Med. Chem. Lett.* **2000**, *10*, 1129–1132. [CrossRef]
66. Suhara, Y.; Nihei, K.I.; Kurihara, M.; Kittaka, A.; Yamaguchi, K.; Fujishima, T.; Konno, K.; Miyata, N.; Takayama, H. Efficient and versatile synthesis of novel 2 α -substituted 1 α ,25-dihydroxyvitamin D(3) analogues and their docking to vitamin D receptors. *J. Org. Chem.* **2001**, *66*, 8760–8771. [CrossRef] [PubMed]
67. Saito, N.; Suhara, Y.; Kurihara, M.; Fujishima, T.; Honzawa, S.; Takayanagi, H.; Kozono, T.; Matsumoto, M.; Ohmori, M.; Miyata, N.; et al. Design and efficient synthesis of 2 α -(omega-hydroxyalkoxy)-1 α ,25-dihydroxyvitamin D₃ Analogues, including 2-epi-ED-71 and their 20-epimers with HL-60 cell differentiation activity. *J. Org. Chem.* **2004**, *69*, 7463–7471. [CrossRef] [PubMed]
68. Takahashi, E.; Nakagawa, K.; Suhara, Y.; Kittaka, A.; Nihei, K.; Konno, K.; Takayama, H.; Ozono, K.; Okano, T. Biological activities of 2 α -substituted analogues of 1 α ,25-dihydroxyvitamin D₃ in transcriptional regulation and human promyelocytic leukemia (HL-60) cell proliferation and differentiation. *Biol. Pharm. Bull.* **2006**, *29*, 2246–2250. [CrossRef]
69. Ono, K.; Yoshida, A.; Saito, N.; Fujishima, T.; Honzawa, S.; Suhara, Y.; Kishimoto, S.; Sugiura, T.; Waku, K.; Takayama, H.; et al. Efficient synthesis of 2-modified 1 α ,25-dihydroxy-19-norvitamin D₃ with Julia olefination: High potency in induction of differentiation on HL-60 cells. *J. Org. Chem.* **2003**, *68*, 7407–7415. [CrossRef]
70. Arai, M.A.; Takeyama, K.; Ito, S.; Kato, S.; Chen, T.C.; Kittaka, A. High-throughput system for analyzing ligand-induced cofactor recruitment by vitamin D receptor. *Bioconjug. Chem.* **2007**, *18*, 614–620. [CrossRef]
71. Chen, T.; Persons, K.; Zheng, S.; Mathieu, J.; Holick, M.; Lee, Y.; Bao, B.; Arai, M.; Kittaka, A. Evaluation of C-2-substituted 19-nor-1 α ,25-dihydroxyvitamin D₃ analogs as therapeutic agents for prostate cancer. *J. Steroid Biochem. Mol. Biol.* **2007**, *103*, 717–720. [CrossRef]
72. Flanagan, J.N.; Zheng, S.; Chiang, K.C.; Kittaka, A.; Sakaki, T.; Nakabayashi, S.; Zhao, X.; Spanjaard, R.A.; Persons, K.S.; Mathieu, J.S.; et al. Evaluation of 19-nor-2 α -(3-hydroxypropyl)-1 α ,25-dihydroxyvitamin D₃ as a therapeutic agent for androgen-dependent prostate cancer. *Anticancer Res.* **2009**, *29*, 3547–3553.
73. Chen, T.C.; Kittaka, A. Novel vitamin d analogs for prostate cancer therapy. *Int. Sch. Res. Not.* **2011**, *2011*, 301490. [CrossRef]

74. Chiang, K.C.; Yeh, C.N.; Chen, H.Y.; Lee, J.M.; Juang, H.H.; Chen, M.F.; Takano, M.; Kittaka, A.; Chen, T.C. 19-Nor-2 α -(3-hydroxypropyl)-1 α ,25-dihydroxyvitamin D₃ (MART-10) is a potent cell growth regulator with enhanced chemotherapeutic potency in liver cancer cells. *Steroids* **2011**, *76*, 1513–1519. [CrossRef] [PubMed]
75. Hirota, Y.; Nakagawa, K.; Mimatsu, S.; Sawada, N.; Sakaki, T.; Kubodera, N.; Kamao, M.; Tsugawa, N.; Suhara, Y.; Okano, T. Nongenomic effects of 1 α ,25-dihydroxyvitamin D₃ on cartilage formation deduced from comparisons between Cyp27b1 and Vdr knockout mice. *Biochem. Biophys. Res. Commun.* **2017**, *483*, 359–365. [CrossRef]
76. Nishikawa, M.; Kaori Yasuda, K.; Takamatsu, M.; Abe, K.; Nakagawa, K.; Tsugawa, N.; Hirota, Y.; Tanaka, K.; Yamashita, S.; Ikushiro, S.; et al. Generation of 1,25-dihydroxyvitamin D₃ in Cyp27b1 knockout mice by treatment with 25-hydroxyvitamin D₃ rescued their rachitic phenotypes. *J. Steroid Biochem. Mol. Biol.* **2019**, *185*, 71–79. [CrossRef] [PubMed]
77. Zhang, Y.G.; Wu, S.; Lu, R.; Zhou, D.; Zhou, J.; Carmeliet, G.; Petrof, E.; Claud, E.C.; Sun, J. Tight junction CLDN2 gene is a direct target of the vitamin D receptor. *Sci. Rep.* **2015**, *5*, 10642. [CrossRef]
78. Norman, A.W.; Bishop, J.E.; Collins, E.D.; Seo, E.G.; Satchell, D.P.; Dormanen, M.C.; Zanello, S.B.; Farach-Carson, M.C.; Bouillon, R.; Okamura, W.H. Differing shapes of 1 alpha,25-dihydroxyvitamin D₃ function as ligands for the D-binding protein, nuclear receptor and membrane receptor: A status report. *J. Steroid Biochem. Mol. Biol.* **1996**, *56*, 13–22. [CrossRef]
79. Mizwicki, M.T.; Norman, A.W. The vitamin D sterol-vitamin D receptor ensemble model offers unique insights into both genomic and rapid-response signaling. *Sci. Signal.* **2009**, *2*, re4. [CrossRef]
80. Hii, C.S.; Ferrante, A. The Non-Genomic Actions of Vitamin D. *Nutrients* **2016**, *8*, 135. [CrossRef] [PubMed]
81. Skorija, K.; Cox, M.; Sisk, J.M.; Dowd, D.R.; MacDonald, P.N.; Thompson, C.C.; Demay, M.B. Ligand-independent actions of the vitamin D receptor maintain hair follicle homeostasis. *Mol. Endocrinol.* **2005**, *19*, 855–862. [CrossRef] [PubMed]
82. Munetsuna, E.; Kawanami, R.; Nishikawa, M.; Ikeda, S.; Nakabayashi, S.; Ohta, M.; Kamakura, M.; Ikushiro, S.; Sakaki, T. Anti-proliferative activity of 25-hydroxyvitamin D₃ in human prostate cells. *Mol. Cell Endocrinol.* **2014**, *382*, 960–970. [CrossRef] [PubMed]
83. Asano, L.; Watanabe, M.; Ryoden, Y.; Usuda, K.; Yamaguchi, T.; Khambu, B.; Takashima, M.; Sato, S.I.; Sakai, J.; Nagasawa, K.; et al. Vitamin D Metabolite, 25-Hydroxyvitamin D, Regulates Lipid Metabolism by Inducing Degradation of SREBP/SCAP. *Cell Chem. Biol.* **2017**, *24*, 207–217. [CrossRef] [PubMed]



Review

Design and Synthesis of Fluoro Analogues of Vitamin D

Fumihiko Kawagoe , Sayuri Mototani and Atsushi Kittaka *

Faculty of Pharmaceutical Sciences, Teikyo University, 2-11-1 Kaga, Itabashi, Tokyo 173-8605, Japan; fkawagoe@pharm.teikyo-u.ac.jp (F.K.); 19dy10003vu@stu.teikyo-u.ac.jp (S.M.)

* Correspondence: akittaka@pharm.teikyo-u.ac.jp; Tel.: +81-3-3964-8109; Fax: +81-3-3964-8117

Abstract: The discovery of a large variety of functions of vitamin D₃ and its metabolites has led to the design and synthesis of a vast amount of vitamin D₃ analogues in order to increase the potency and reduce toxicity. The introduction of highly electronegative fluorine atom(s) into vitamin D₃ skeletons alters their physical and chemical properties. To date, many fluorinated vitamin D₃ analogues have been designed and synthesized. This review summarizes the molecular structures of fluoro-containing vitamin D₃ analogues and their synthetic methodologies.

Keywords: synthesis; fluorine; vitamin D₃; metabolite; A-ring; CD-ring; side-chain

Citation: Kawagoe, F.; Mototani, S.; Kittaka, A. Design and Synthesis of Fluoro Analogues of Vitamin D. *Int. J. Mol. Sci.* **2021**, *22*, 8191. <https://doi.org/10.3390/ijms22158191>

Academic Editors: Geoffrey Brown, Andrzej Kutner and Enikő Kallay

Received: 8 July 2021

Accepted: 27 July 2021

Published: 30 July 2021

Publisher's Note: MDPI stays neutral with regard to jurisdictional claims in published maps and institutional affiliations.

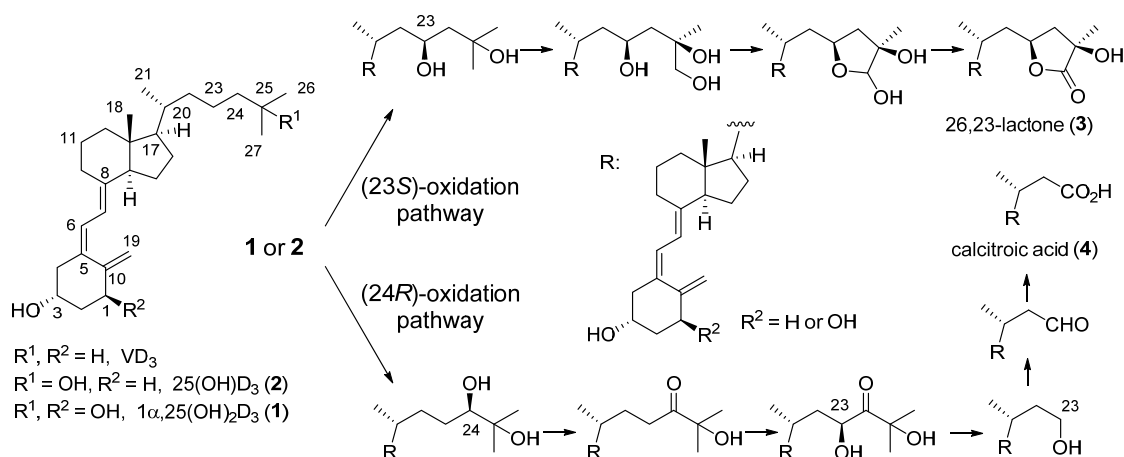


Copyright: © 2021 by the authors. Licensee MDPI, Basel, Switzerland. This article is an open access article distributed under the terms and conditions of the Creative Commons Attribution (CC BY) license (<https://creativecommons.org/licenses/by/4.0/>).

1. Introduction

Fluorine is one of the halogens, known as a small and the most electronegative element. Fluorine substitution offers a variety of advantages, such as changing the pKa and dipole moment of the molecule, improving the chemical or metabolic stability, and enhancing the binding affinity to the target protein. Furthermore, it has a small atomic radius, similar to that of a hydrogen atom. Due to their unique properties, fluorine atoms have been incorporated into many drugs, drug candidates, and agricultural chemicals [1–12]. The contribution of fluorine to drug development and medicinal chemistry, and the life science as well as material science fields, is widely recognized around the world [13–17]. Many scientists have been engaged in the practical synthesis of organofluorine compounds, including fluorinated vitamin D₃ analogues. Vitamin D₃ (VD₃) is a fat-soluble vitamin whose biological function depends on metabolic activation by CYP enzymes [18]. Bioactivation of VD₃ requires sequential oxidation steps at C-25 and C-1 catalyzed by vitamin D 25-hydroxylase (CYP2R1) and 25-hydroxyvitamin D₃-1 α -hydroxylase (CYP27B1), respectively. The resulting B-secosterol, 1 α ,25-dihydroxyvitamin D₃ [1 α ,25(OH)₂D₃ (**1**)], is the fully active and hormonal form of VD₃. Moreover, 1 α ,25(OH)₂D₃ (**1**) and 25-hydroxyvitamin D₃ [25(OH)D₃ (**2**)] are degraded via hydroxylation at C23 or C24 catalyzed by 1 α ,25-dihydroxyvitamin D₃-24-hydroxylase (CYP24A1) [19]. C23 hydroxylation and subsequent three-step oxidation lead to vitamin D₃-26,23-lactone (**3**). On the other hand, C24 hydroxylation and subsequent five-step oxidation lead to calcitric acid (**4**) (Scheme 1) [19,20].

For slowing or preventing the biological degradation of the VD₃ side chain, replacing C-H with C-F bond(s) at appropriate positions should prolong their half-life in vivo, since a C-F bond is stronger than a C-H bond chemically. The introduction of fluorine atoms into VD₃ analogues can also alter electron distribution, which can confer lower pKa at the hydroxy group(s), change the dipole moment, and influence the conformation because of their marked electron-withdrawing properties. Because of these unique properties, both academic institutions and industries have designed and synthesized numerous fluorinated VD₃ analogues, similarly to other bioactive compounds with fluorine atoms. Most of them show fluorination at the main metabolic site(s) and/or neighboring hydroxy group of the VD₃ molecule, namely either an A-ring or a side-chain moiety or both. This review introduces fluorinated VD₃ analogues and their synthetic methodologies, including some basic biological activities.



Scheme 1. Deactivation metabolic pathways of $25(OH)D_3$ (2) and $1\alpha,25(OH)_2D_3$ (1).

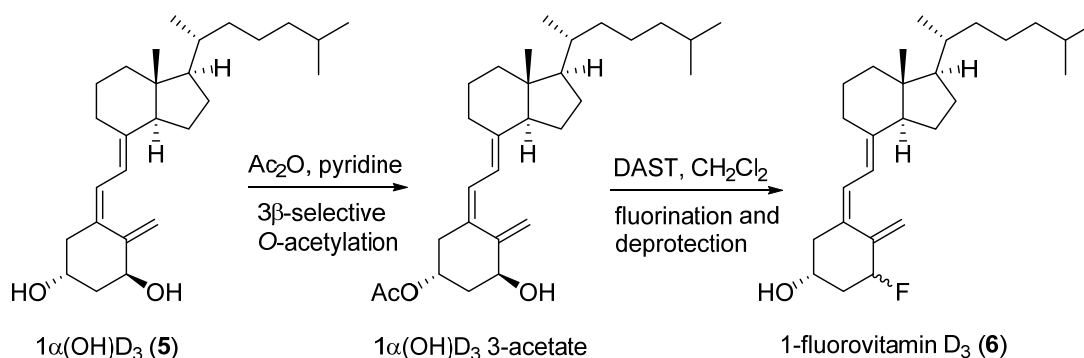
2. A-Ring Fluorinated VD_3 Analogues

On the VD_3 A-ring, 1α -hydroxylation is the final and essential step to produce the hormonal form of VD_3 from $25(OH)D_3$ (2), and $1\alpha,25(OH)_2D_3$ (1) exerts a range of physiological activities by binding to the vitamin D receptor (VDR). The A-ring moiety is anchored in the VDR ligand-binding pocket through four hydrogen-bonding interactions, i.e., the 1α -hydroxy group to Ser233 and Arg270, and the 3β -hydroxy group to Tyr143 and Ser274 [21]. As expected, based on the importance of the A-ring moiety, many A-ring fluorinated VD_3 analogues have been synthesized and evaluated regarding their biological activities.

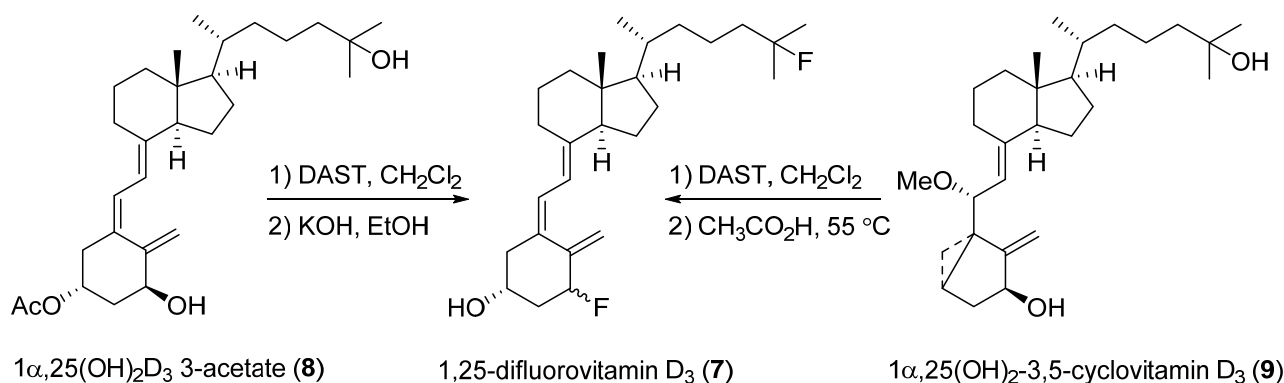
2.1. 1-Fluorinated VD_3 Analogues

DeLuca and coworkers described the first synthesis of 1-fluoro- VD_3 for the purpose of studying the possibility of using it as a kind of VD_3 antagonist against 1α -hydroxylase in 1979 [22]. They prepared 1α -hydroxyvitamin D_3 -3-acetate by the selective acetylation of 1α -hydroxyvitamin D_3 [$1\alpha(OH)D_3$ (5)] and used it as a starting material. The fluorination step was achieved by *N,N*-(diethylamino)sulfur trifluoride (DAST) to afford 1-fluorovitamin D_3 (6) (Scheme 2). The authors did not assign its C1 configuration in the report. The biological evaluation revealed that 6 demonstrated a relative preference for stimulating bone calcium mobilization with respect to intestinal calcium transport after metabolism *in vivo*, and 6 was a weak agonist that could not be used as an anti-vitamin D agent.

Next, DeLuca et al. designed and synthesized $1\alpha,25$ -difluorovitamin D_3 (7) in 1981 [23]. As shown in Scheme 3, it was synthesized from either $1\alpha,25(OH)_2D_3$ 3-acetate (8) or $1\alpha,25(OH)_2$ -3,5-cyclovitamin D_3 (9) using DAST as a fluorination reagent. The authors explained that the stereochemistry at C1 was 1α in the report, but they revised it to 1β in 1984 [24].



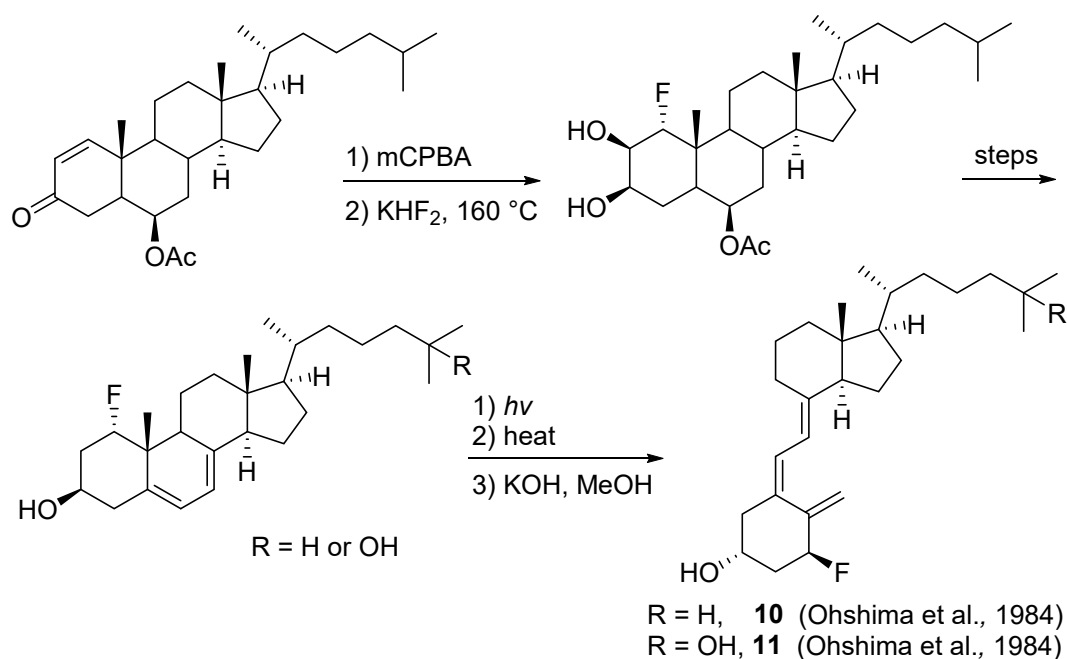
Scheme 2. DeLuca's direct fluorination approach to 1-fluorovitamin D_3 (6).



Scheme 3. Direct C1 and C25 fluorination approach to 1 α ,25-difluorovitamin D₃ (7).

The authors evaluated the biological properties of 1 α ,25-difluorovitamin D₃ (7) and demonstrated that it had essentially no vitamin D activity. These results strongly supported the idea that C1 and C25 hydroxylation are essential aspects of vitamin D function. Initially, since both the C1 and C25 positions of VD₃ were blocked with fluorine atoms, it might have shown the anti-vitamin D activity of 25-hydroxylation of VD₃ in vivo. However, 7 did not exhibit the expected inhibitory activity against the 25-hydroxylation of VD₃.

In 1984, 1 α -fluorovitamin D₃ (10) and 1 α -fluoro-25(OH)D₃ (11) were synthesized utilizing a steroid A-ring epoxide as the starting material in order to confirm the stereochemistry at C1 (Scheme 4) [24,25].

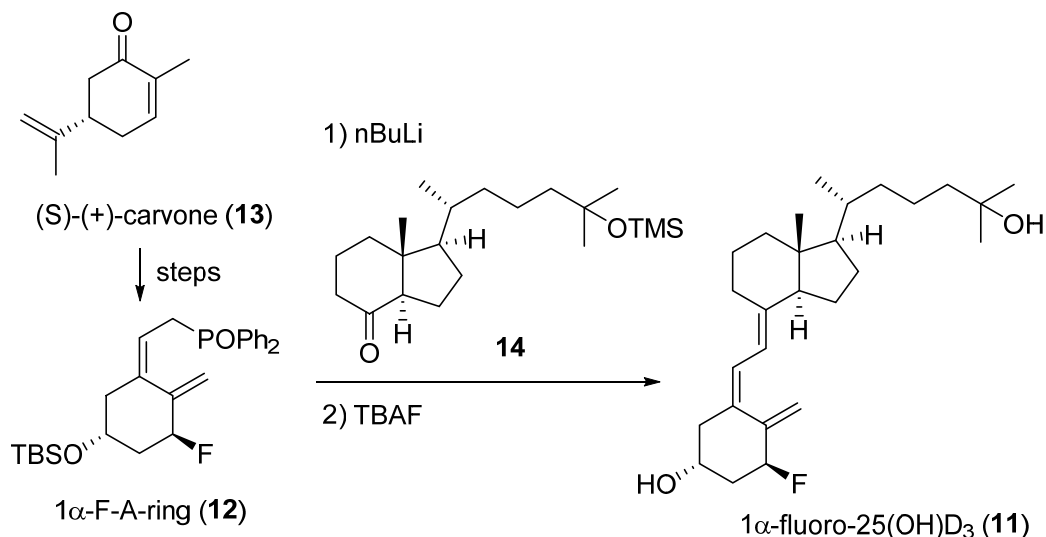


Scheme 4. Synthesis of 1 α -fluoro-VD₃ (10) and 1 α -fluoro-25(OH)D₃ (11) from sterols.

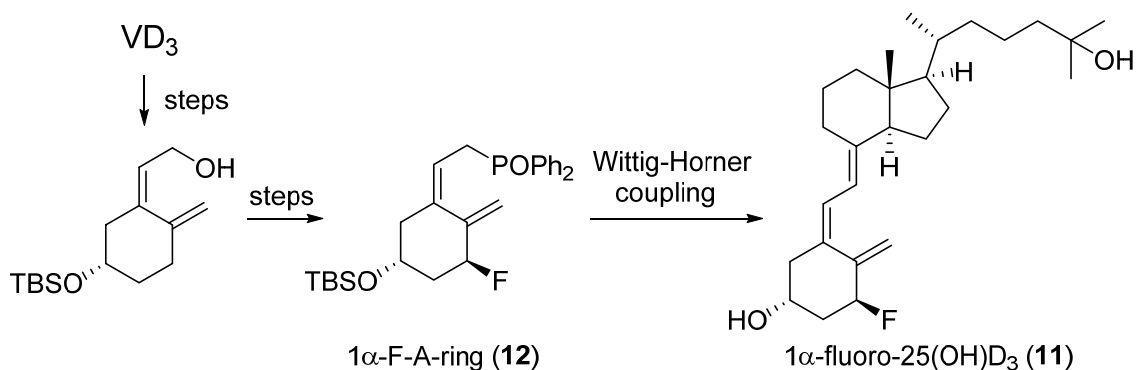
A comparison of the spectral data of the report [24] and previous ones [22,23] revealed that the reported 1 α -fluorovitamin D₃ in 1979 [22] and 1 α ,25-difluorovitamin D₃ in 1981 [23] were, in fact, 1 β -fluorovitamin D₃ and 1 β ,25-difluorovitamin D₃, respectively.

On the other hand, although 1 α -fluoro-25(OH)D₃ (11) showed no stimulation of intestinal calcium transport or bone calcium mobilization activities at a dosage level of 1.3 μ g, its binding affinity to chick intestine VDR was 30 times greater than that of 25(OH)D₃.

A convergent synthetic route to 1-fluoro-VD₃ analogues was described by Uskoković and coworkers using an A-ring key fragment, a 1 α -fluorinated A-ring precursor (**12**), which was prepared from (*S*)-(+)-carvone (**13**), in 1990 (17 steps in 4%) (Scheme 5) [26], as well as an A ring from VD₃ in 1991 (12 steps) (Scheme 6) [27]. A lithium anion of the A-ring phosphine oxide (**12**) underwent a Wittig–Horner coupling reaction with the 8-keto-CD-ring (**14**) to afford the desired 1 α -fluoro-25(OH)D₃ (**11**).

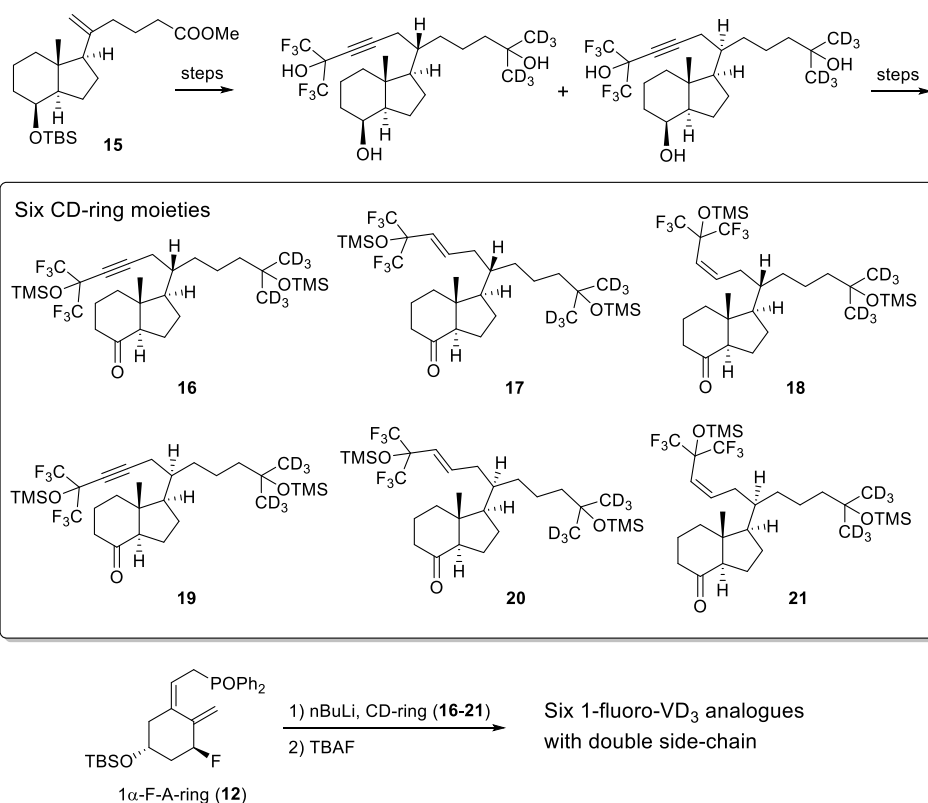


Scheme 5. Uskoković's approach to 1 α -fluoro-25(OH)D₃ (**11**) using the Wittig–Horner reaction.



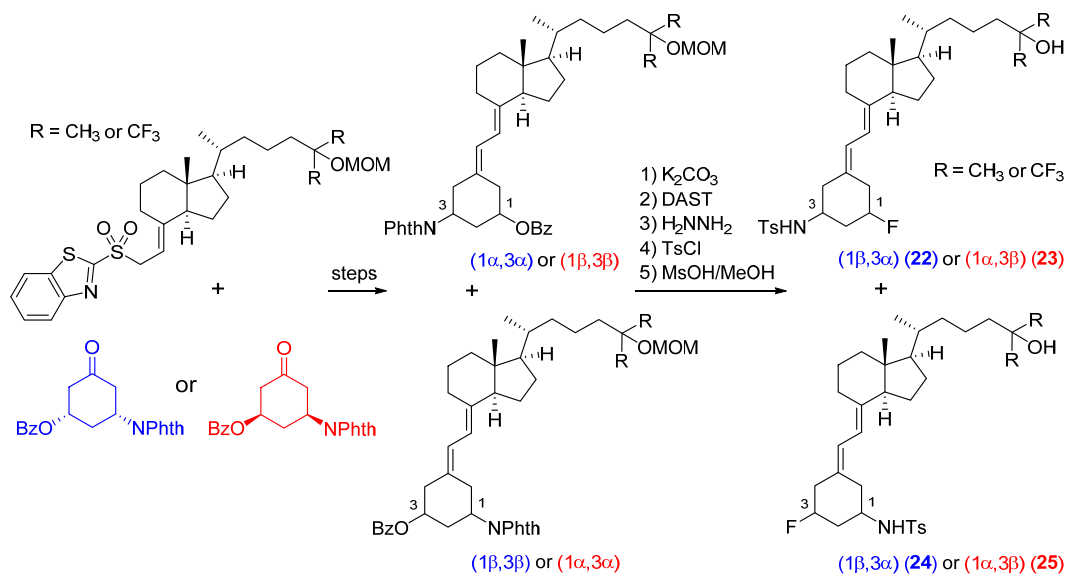
Scheme 6. Alternative convergent synthetic approach to 1 α -fluoro-25(OH)D₃ (**11**) using the A-ring moiety (**12**), available from the A-ring of VD₃.

Later, Uskoković's group utilized the 1 α -fluoro-A-ring (**12**) to synthesize six 1 α -fluoro-VD₃ analogues with two different side chains at C20 (Gemini analogues). They prepared six 8-keto-CD-rings (**16–21**) starting from the methyl ester (**15**) and coupled it with **12** under basic conditions (Scheme 7) [28]. The anticancer activity of these compounds was tested, but 1 α -fluorination did not effectively promote the activity.



Scheme 7. Various 1 α -fluoro-VD₃ analogues with six different double side chains were synthesized using the Wittig–Horner olefination at the coupling stage with the 1 α -fluoro-A-ring part (12).

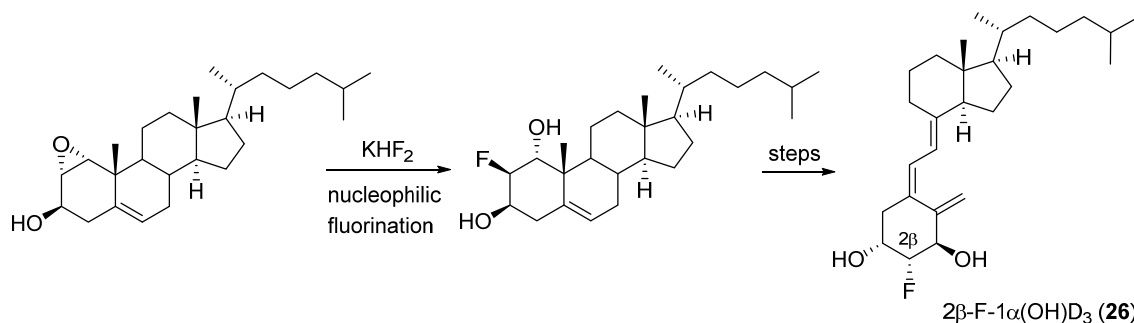
In 2019, Uesugi and colleagues published the first synthesis of 1-fluoro-19-norVD₃ analogues [29]. They constructed 1-hydroxy-19-norvitamin D₃ structures with a modified Julia olefination method [30], and the direct deoxyfluorination of C1 yielded the corresponding 1-fluorinated analogues (22,23). In this reaction sequence, shown in Scheme 8, they also obtained 3-fluoro-19-norVD₃ analogues (24,25). Some of these analogues were poor VDR binders but showed potent sterol regulatory element-binding protein (SREBP) inhibitory activity via inducing SREBP cleavage-activating protein (SCAP) degradation [29].



Scheme 8. Synthesis of 1- and 3-fluoro-19-norvitamin D₃ analogues (22–25) using direct deoxyfluorination reactions.

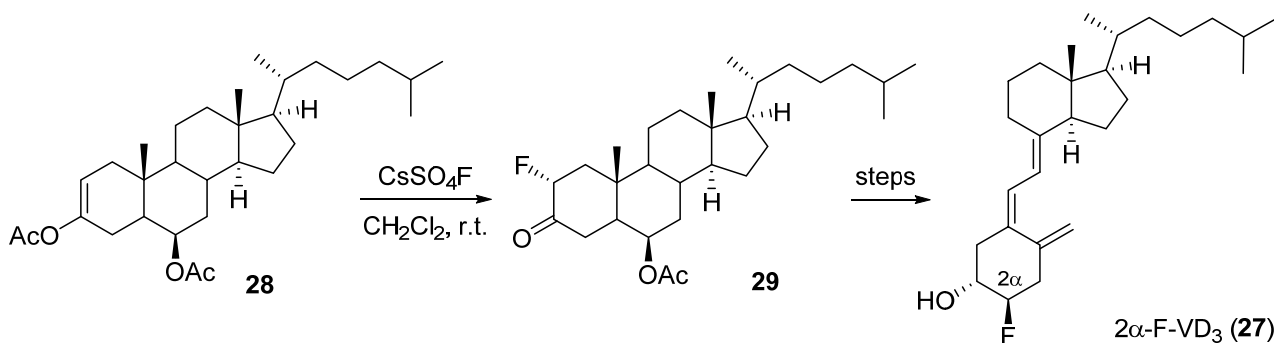
2.2. 2-Fluorinated VD₃ Analogues

Several 2-fluorinated VD₃ analogues have been reported to date, because fluorine substitution at this position can change the A-ring conformation and pK_a value of the neighboring 1 α - and 3 β -hydroxy groups. The first synthesis of 2 β -fluoro-VD₃ was reported by Ikekawa and coworkers in 1980, in which nucleophilic fluorination using KHF₂ to 1,2 α -epoxycholesterol gave 2 β -fluoro-1 α (OH)D₃ (**26**), (Scheme 9) [31]. It was noted that the biological activity of **26** was increased [32].



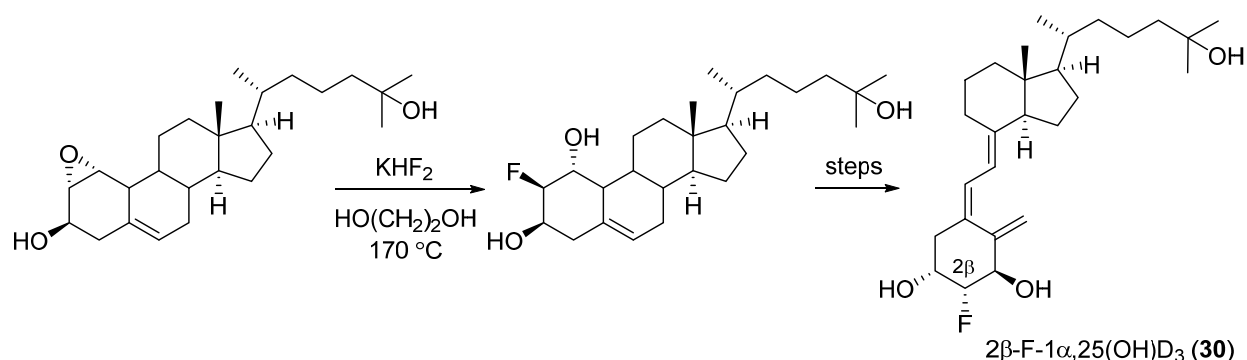
Scheme 9. Ikekawa's approach to 2 β -fluoro-1 α (OH)D₃ (**26**) via 2 β -fluorination of A-ring epoxide using a nucleophilic fluorination reaction.

Next, 2 α -fluorovitamin D₃ (**27**) was also synthesized, and its biological activity was tested in 1986 [32]. Electrophilic 2 α -fluorination of 3,6 β -diacetoxycholest-2-ene (**28**) using CsSO₄F gave 2 α -fluoroketone (**29**). To construct the B-secosteroidal structure, conventional photochemical conversion and subsequent thermal isomerization were applied (Scheme 10) [32]. The biological effects of **27** on intestinal calcium transport and bone calcium mobilization as well as the serum calcium concentration at a dosage level of 500 ng for rats were measured, and the activities were found to be essentially equivalent to those of VD₃ itself.



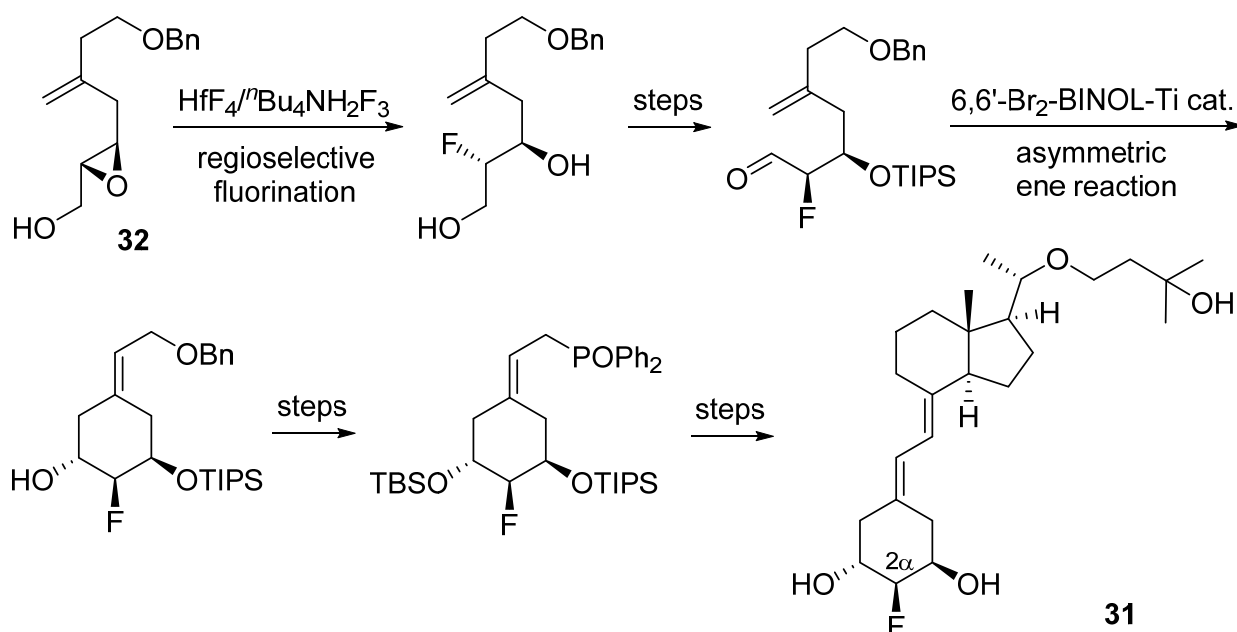
Scheme 10. Introduction of the 2 α -fluoro group to VD₃ using an electrophilic fluorination reaction.

The synthesis and biological activities of 2 β -fluoro-1 α ,25-dihydroxyvitamin D₃ (**30**) were reported by Scheddin et al. in 1998 [33]. The synthetic route was similar to Ikekawa's [31], as shown in Scheme 11, and the biological evaluation revealed that the synthetic 2 β -fluoro-1 α ,25-(OH)₂D₃ (**30**) exhibited greater potency in vitro, for example, six-times higher affinity for VDR, nearly identical affinity for the vitamin D-binding protein (DBP), and 90-times higher antiproliferative activity toward C3H10T1/2 cells under serum-containing conditions, as well as five-times greater adipogenesis inhibitory activity than the natural hormone 1 α ,25(OH)₂D₃ (**1**).



Scheme 11. Synthesis of 2 β -fluoro-1 α ,25-(OH)₂D₃ (**30**).

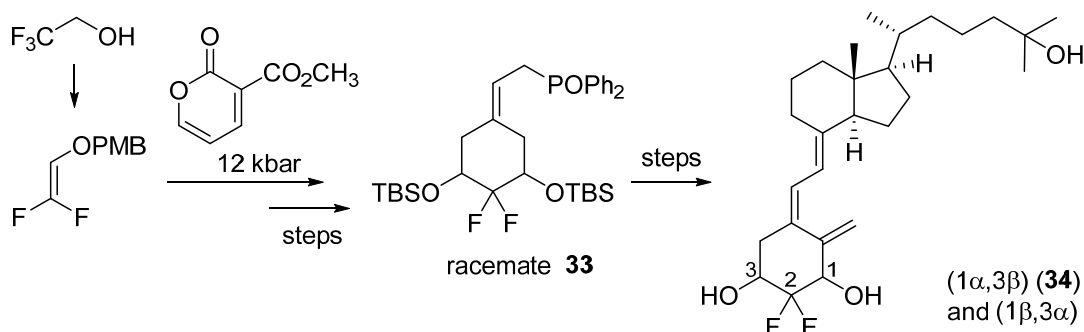
The catalytic asymmetric stereoselective synthesis of the A-ring precursor of the 19-nor type 2 α -fluorovitamin D₃ analogue (**31**) and its synthesis were reported by Mikami et al. [34,35]. The regio- and stereo-selective 2 α -fluorination was achieved via a ring opening reaction of chiral epoxide (**32**) mediated by HfF₄/Bu₄NH₂F₃, the asymmetric catalytic carbonyl-ene cyclization was used to construct the 6-membered A-ring precursor, and the subsequent coupling reaction with the CD ring afforded 2 α -fluoro-19-normaxacalcitol (**31**) (Scheme 12). This 2 α -fluoro-22-oxa-19-nor analogue (**31**) had very low DBP-binding affinity but four-times stronger VDR-binding potency than its 22-oxa-19-nor counterpart and also showed significant transactivation activity [34]. It was also shown that **31** was highly effective in inhibiting metastatic tumor growth in vivo without toxicity in terms of hypercalcemia and weight loss [35].



Scheme 12. Mikami's group synthesized 2 α -fluoro-19-normaxacalcitol (**31**) using a convergent coupling method between the 2 α -fluoro-A-ring part, prepared from regio- and stereoselective fluorination to **32**, followed by asymmetric catalytic carbonyl-ene cyclization, and the appropriate 8-keto-CD-ring.

Posner's group showed the first example of synthesis of the 2,2-difluorovitamin D₃ analogue in 2002 [36]. They synthesized the racemic 2,2-difluoro substituted A-ring phosphine oxide (**33**) from trifluoroethanol (7% in 13 steps). A coupling reaction of **33** with the 8-keto-CD-ring and subsequent deprotection yielded the 2,2-difluoro-1,25-dihydroxyvitamin D₃ analogues in the ratio of 5:1 (1 α ,3 β (**34**):1 β ,3 α) (Scheme 13). The diastereomers were

separated with reversed-phase HPLC to afford the target 2,2-difluoro-1 α ,25(OH) $_2$ D $_3$ (**34**). Biological evaluation revealed that **34** exhibited antiproliferative activity similar to that of 1 α ,25(OH) $_2$ D $_3$ (**1**) and was 2-3 times more transcriptionally active than **1** in rat osteosarcoma cells, even though the human VDR-binding affinity was 9.6% relative to that of **1**. Compound **34** showed strong calcemic activity in vivo.

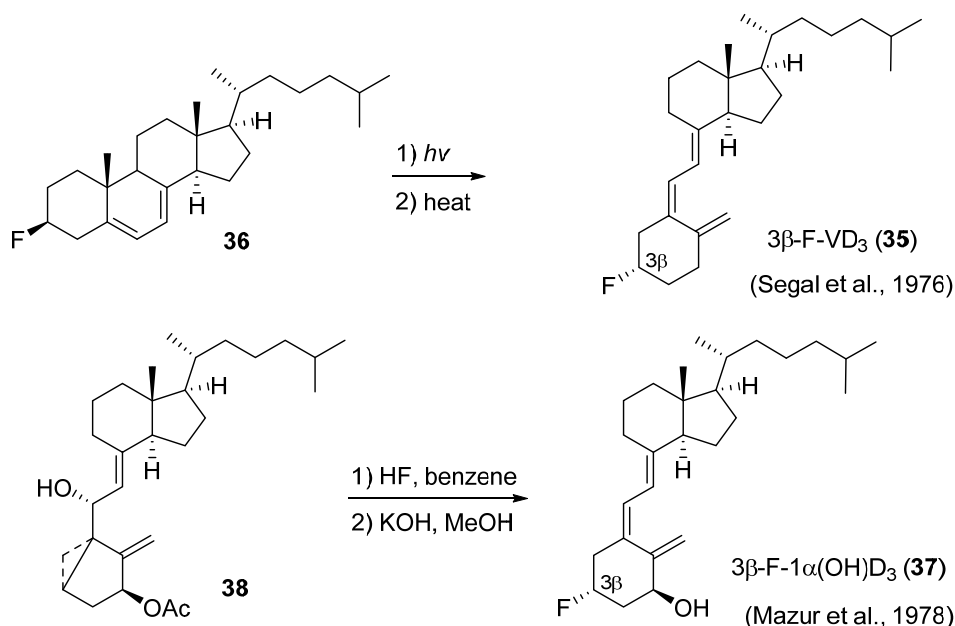


Scheme 13. Posner's synthetic route to 2,2-difluoro-1 α ,25-dihydroxyvitamin D $_3$ (**34**) from 2,2-difluoro-A-ring (**33**) via an inverse-electron-demand Diels–Alder reaction between a pyrone diene and difluorovinyl ether.

2.3. 3-Fluorinated VD $_3$ Analogues

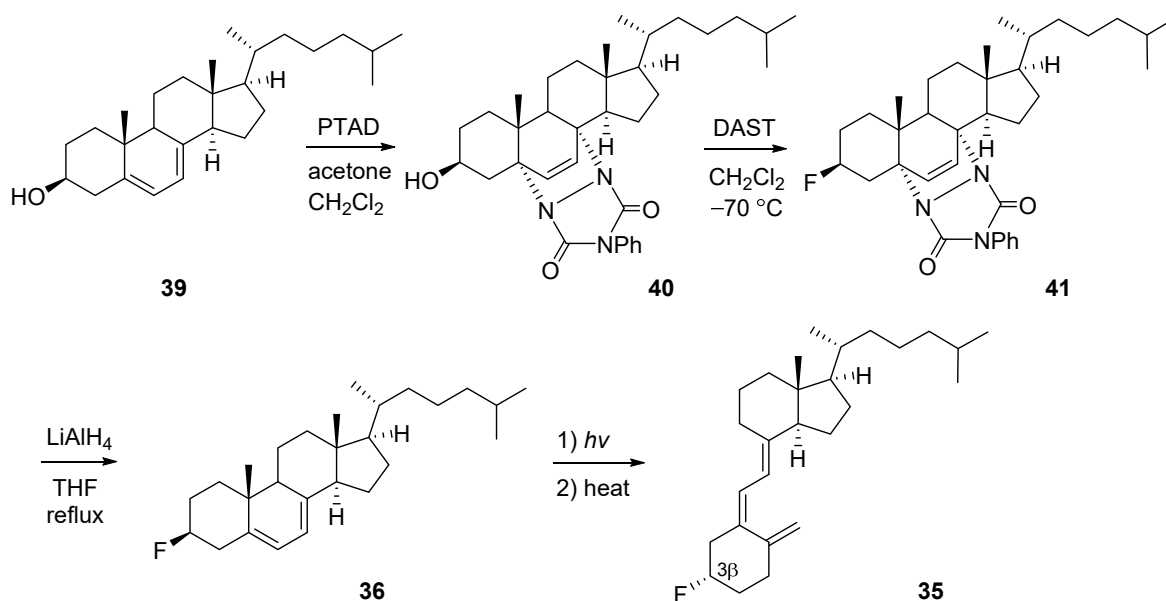
The C3 position of VD $_3$ has a β -hydroxy group, and substitution of the hydroxy with a fluorine atom is of fundamental interest. There are several reports of replacing the C3-hydroxy group with a fluorine atom in order to demonstrate the expected positive effects on biological activity.

The synthesis of 3 β -fluoro-3-deoxyvitamin D $_3$ (**35**) from 3 β -fluorocholesta-5,7-diene (**36**) via photochemical transformation followed by thermal isomerization was described by Segal et al. in 1976 [37]. It was found that 3 β -fluoro-3-deoxyvitamin D $_3$ (**35**) had an antirachitic effect analogous to VD $_3$. On the other hand, in 1978, Mazur and coworkers designed and synthesized 3 β -fluoro-3-deoxy-1 α -hydroxyvitamin D $_3$ (**37**) to elicit VD $_3$ activity. The 3 β -fluoro group was constructed from (6*R*)-hydroxy-3,5-cyclovitamin D $_3$ (**38**) by treatment with HF (Scheme 14) [38]. The biological activities of the newly synthesized analogue were tested, and the fluoro-analogue (**37**) could actively induce the formation of a calcium-binding protein and stimulate intestinal calcium absorption in rachitic chicks.



Scheme 14. Segal's and Mazur's 3 β -fluoro-3-deoxyvitamin D $_3$ syntheses.

Later, in 1985, Kumar and coworkers reported the synthetic route to 3β -fluoro-3-deoxyvitamin D₃ (**35**) starting from 7-dehydrocholesterol (**39**) via 3-deoxy-3-fluoro-7-dehydrocholesterol (**36**) [39]. The B-ring protected PTAD (4-phenyl-1,2,4-triazoline-3,5-dione) adduct (**40**) was reacted with DAST to yield a fluorinated product (**41**), and subsequent deprotection of **41** gave 3-deoxy-3-fluoro-7-dehydrocholesterol (**36**) (Scheme 15). To investigate the influence of the replacement of the C3-hydroxy group with fluorine, they compared the biological activities of VD₃, 3-deoxyvitamin D₃, and 3β -fluoro-3-deoxyvitamin D₃ (**35**) and revealed that **35** was less active than VD₃ and more active than 3-deoxyvitamin D₃ in terms of intestinal calcium transport and bone calcium mobilization in vivo.

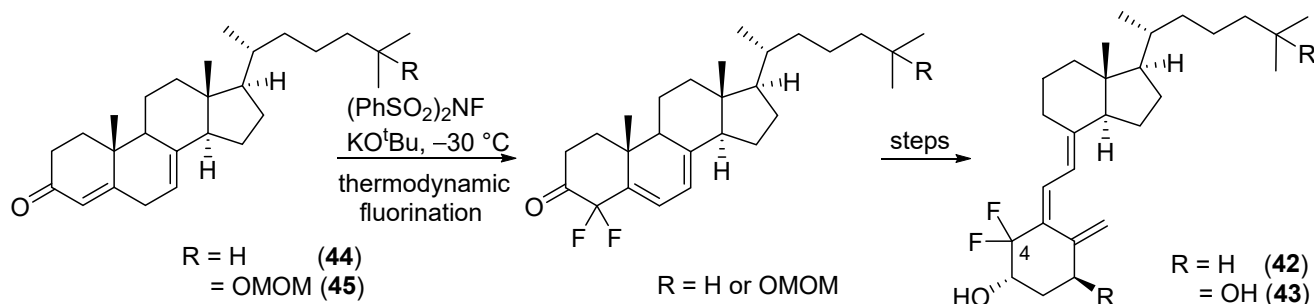


Scheme 15. Synthesis of 3β -fluoro-3-deoxyvitamin D₃ (**35**) starting from 7-dehydrocholesterol (**39**).

As mentioned in Section 2.1, Uesugi and colleagues reported the first synthesis of 3-fluoro-19-norVD₃ analogues and evaluated their SREBP inhibitory activity vs. VDR activity (see Scheme 8) [29].

2.4. 4-Fluorinated VD₃ Analogues

Yamada and coworkers reported 4,4-difluorovitamin D₃ (**42**) and 4,4-difluoro-1 α ,25(OH)₂D₃ (**43**) in an A-ring conformational study in 1999, and these analogues were synthesized starting with enones (**44**,**45**), which were constructed from ergosterol, respectively [40]. The difluorination step was achieved by electrophilic fluorination under thermodynamic conditions (Scheme 16). The binding affinity of 4,4-difluoro-1 α ,25(OH)₂D₃ (**43**) for VDR was only ca. 1% of that of the natural hormone, 1 α ,25(OH)₂D₃ (**1**).

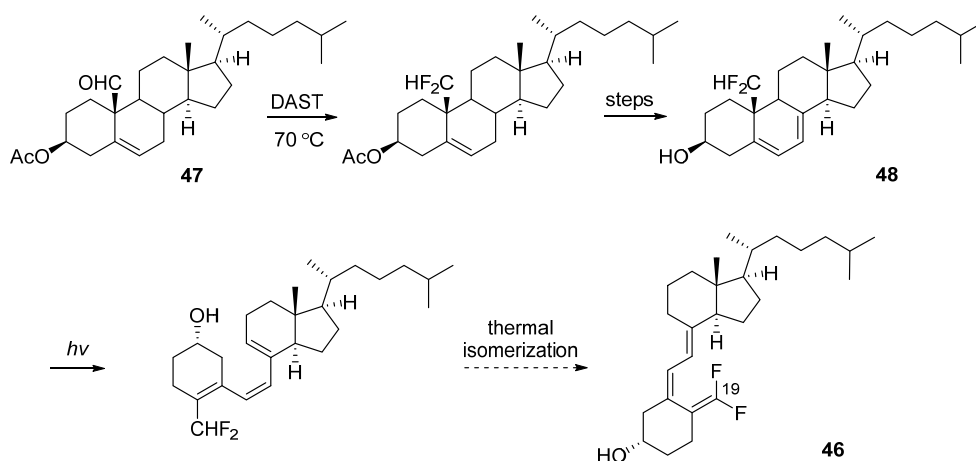


Scheme 16. Yamada's approach to 4,4-difluorovitamin D₃ (**42**,**43**) using a thermodynamic fluorination reaction.

3. Introduction of a Fluorine Atom into the Triene Part of VD₃

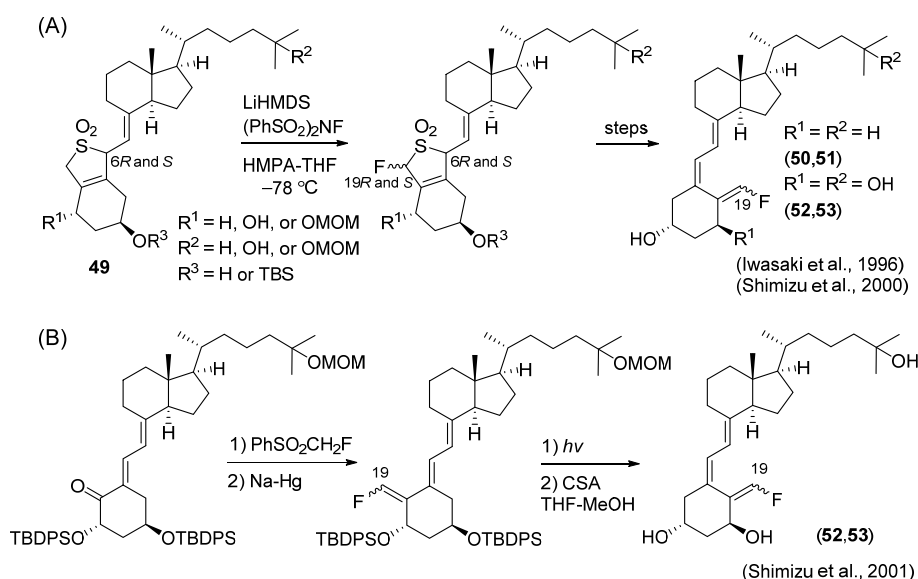
3.1. 19-Fluorinated VD₃ Analogues

In 1980, the first attempt to synthesize 19,19-difluorovitamin D₃ (**46**) starting from 19-oxocholesteryl acetate (**47**) via photoirradiation and thermal isomerization reactions using diene (**48**) failed, because the final thermal isomerization step by [1,7]-sigmatropic rearrangement did not proceed in the presence of the difluoromethyl group at the C10 position (Scheme 17) [41].



Scheme 17. Mazur's trial to synthesize 19,19-difluorovitamin D₃ (**46**).

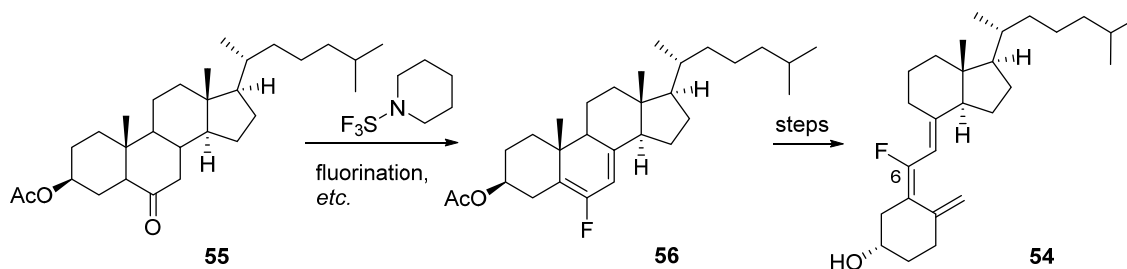
Later, in 1996, Yamada and coworkers showed a novel synthetic route to the first (10*E*)- and (10*Z*)-19-fluorovitamin D₃ (**50,51**) [42]. They prepared VD₃-SO₂ adducts (**49**) from VD₃, and fluorination at the C19 position was achieved by electrophilic fluorination using (PhSO₂)₂NF in the presence of LiHMDS (Scheme 18A). In 2000, the same group showed the regioselective introduction of a fluorine atom to the C19 position and synthesized both (10*E*)- and (10*Z*)-19-fluoro-1α,25(OH)₂D₃ (**52,53**) [43]. The binding affinity of (10*Z*)-19-fluoro-1α,25(OH)₂D₃ for VDR was ca. 10% compared with that of 1α,25(OH)₂D₃ (**1**). The alternative synthetic route to **52** and **53** from a 10-oxo-19-norVD₃ derivative was also established by the same group in 2001 (Scheme 18B) [44].



Scheme 18. Yamada's approach to (10*E*)- and (10*Z*)-19-fluorovitamin D₃ (**50,51**) in (A) and (10*E*)- and (10*Z*)-19-fluoro-1α,25(OH)₂D₃ (**52,53**) analogues in (A,B).

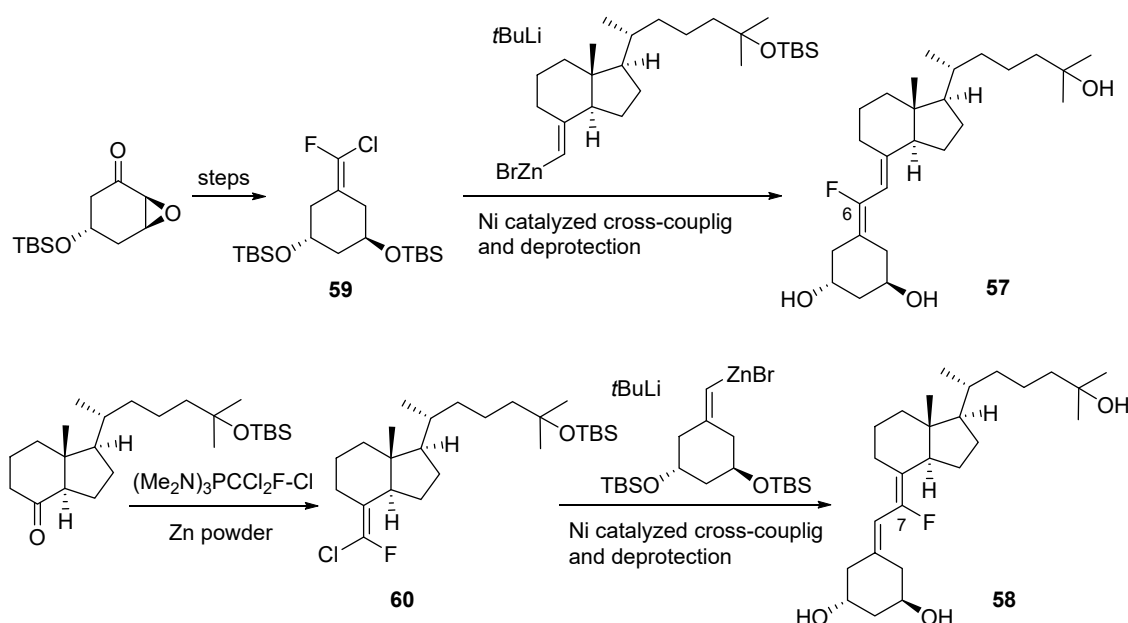
3.2. 6- and 7-Fluorinated VD₃ Analogues

The synthesis of 6-fluorovitamin D₃ (**54**) was described by Dauben et al. in 1985, and the synthetic route started from 6-oxo-cholestanyl acetate (**55**) [45]. The key intermediate, 6-fluoro-7-dehydrocholesteryl acetate (**56**), was synthesized by allowing **55** to react with piperidinosulfur trifluoride in the presence of sulfuric acid. To construct the triene system, 6-fluoro-7-dehydrocholesterol was irradiated, followed by thermal [1,7]-sigmatropic hydrogen rearrangement, to give the desired 6-fluorovitamin D₃ (**54**) (Scheme 19). The obtained 6-fluorovitamin D₃ (**54**) was air-sensitive, and decomposition proceeded. The biological profile of the analogue was evaluated *in vivo*, revealing that **54** had no biological effect on either intestinal calcium absorption or bone calcium mobilization. However, it significantly inhibited both VD₃- and 1 α ,25(OH)₂D₃-mediated intestinal calcium absorption through a direct interaction with VDR [46].



Scheme 19. Synthesis of 6-fluorovitamin D₃ (**54**) using piperidinosulfur trifluoride as a fluorination reagent.

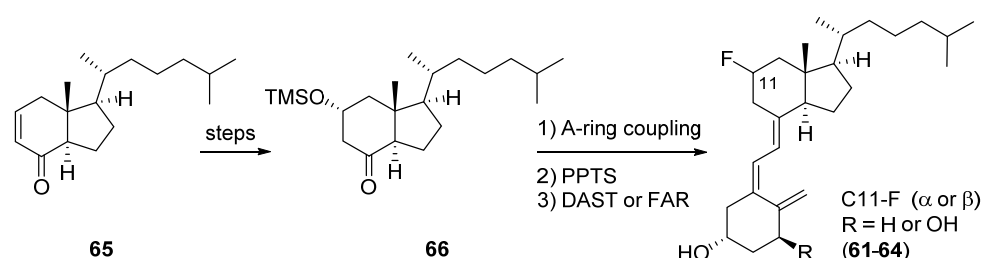
Furthermore, 6-fluoro-1 α ,25-dihydroxy-19-norvitamin D₃ (**57**) and 7-fluoro-1 α ,25-dihydroxy-19-norvitamin D₃ (**58**) were synthesized by the Teijin research group in 2004 [47]. Takenouchi et al. prepared a C6-fluorinated A-ring (**59**) and C7-fluorinated CD-ring (**60**), respectively. A Ni-catalyzed cross-coupling reaction with each CD-ring- or A-ring-activated alkene counterpart was used to construct the diene structures of **57** and **58** (Scheme 20). These compounds possessed 10–70% VDR binding affinity of that of 1 α ,25(OH)₂D₃ and potential activity to induce HL-60 cell differentiation.



Scheme 20. Efficient introduction of the C6- and C7-fluorovinyl unit to the A-ring or CD-ring followed by construction of the diene structures using a Ni-catalyzed cross-coupling reaction.

4. CD-Ring Fluorinated VD₃ Analogues: 11-Fluorinated VD₃ Analogues

To our knowledge, only one report has been published on the synthesis of CD-ring fluoro-VD₃ analogues. In 1994, De Clercq and coworkers designed and synthesized 11 α - and 11 β -fluorovitamin D₃ analogues (**61–64**) with the aim of inducing a conformational change from *s-trans* to *s-cis* at the C6-C7 single bond via expected hydrogen bond formation between the C11-F and C1 α -OH groups [48]. Enone (**65**), readily available from Grundmann's ketone, was used as a starting material. Epoxidation of **65**, followed by reductive opening with lithium dimethylcuprate, gave the C11 α -OH functional group (**66**). After coupling with A-ring phosphine oxides, the C11 α -OH group was treated with *N*-(2-chloro-1,1,2-trifluoroethyl)diethylamine (FAR) to give C11 α -F and C11 β -F isomers as well as an elimination product at a ratio of 3:1:1 (Scheme 21). NMR spectra analyses of the 11-fluoro-1 α (OH)D₃ showed that all analogues had a large J_{6-7} coupling constant, reflecting an almost exclusive *s-trans* extended geometry without intramolecular hydrogen bonding between C11-F and 1 α -OH.



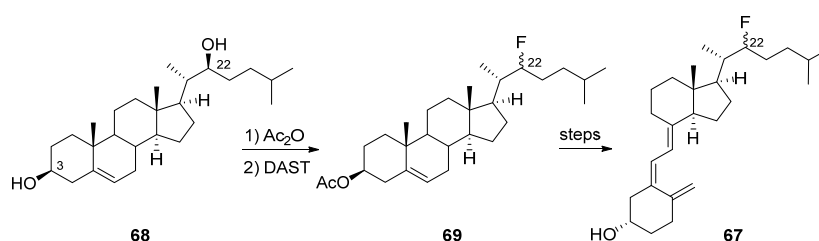
Scheme 21. Stereoselective hydroxylation, coupling with the A-ring precursor, and subsequent fluorination at the C11 position.

5. Side-Chain Fluorinated VD₃ Analogues

The CYP24A1 pathway is well-known as the deactivation pathway of both 25(OH)D₃ (**2**) and 1 α ,25(OH)₂D₃ (**1**) [19]. Varieties of side-chain-fluorinated VD₃ analogues have been actively synthesized because of the expected slower catabolism resulting from the presence of fluorine atoms at the oxidation site or adjacent area.

5.1. 22-Fluorinated VD₃ Analogues

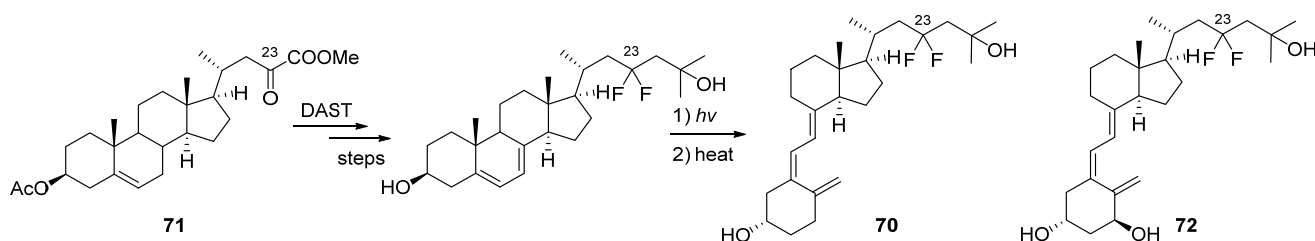
In 1986, Kumar and coworkers described the synthesis of 22-fluorovitamin D₃ (**67**) starting from (22*S*)-cholest-5-ene-3 β ,22-diol (**68**) [49]. Selective protection of the C3 hydroxy group as an acetate, followed by fluorination at the C22 position by DAST, gave 22-fluorocholest-5-en-3 β -acetate (**69**). After forming the C5-7 diene unit in the B ring, photolysis and thermal isomerization yielded the target 22-fluorovitamin D₃ (**67**) without assigning C22 stereochemistry (Scheme 22). They tested the biological activities of the analogue *in vitro* and *in vivo*, referring to the potency of intestinal calcium transport, serum calcium level, calcium-binding protein induction, plasma vitamin D-binding protein (DBP), and VDR affinities, and concluded that the introduction of a fluorine atom to C22 resulted in the compound, with weak biological activities and poor binding to DBP compared with VD₃ itself.



Scheme 22. Synthesis of 22-fluorovitamin D₃ (**67**) from (22*S*)-22-hydroxycholesterol (**68**).

5.2. 23-Fluorinated VD₃ Analogues

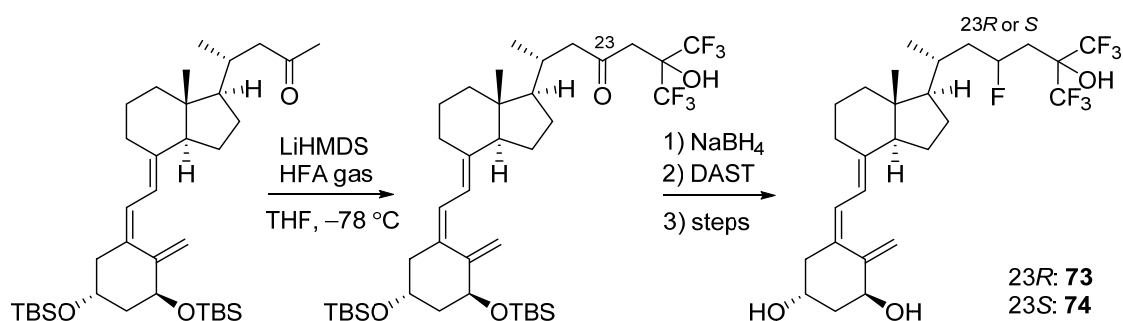
As mentioned in the Introduction, the C23 position of VD₃ is one of the essential metabolic sites of CYP24A1; therefore, C23-fluorinated VD₃ analogues have been designed and synthesized based on the idea of blocking the oxidative position. Ikekawa and colleagues achieved the first synthesis of a C23-fluoro-VD₃ analogue, 23,23-difluoro-25(OH)D₃ (**70**), in 1984 [50]. For the synthesis of **70**, the triene structure was constructed by applying the well-established route through 5,7-diene steroids, and the difluoro unit was introduced using DAST into a reactive α -ketoester (**71**) (Scheme 23).



Scheme 23. Synthesis of 23,23-difluoro-25(OH)D₃ (**70**) using α -ketoester (**71**) as a key intermediate, and the structure of 23,23-difluoro-1 α ,25(OH)₂D₃ (**72**) is also shown.

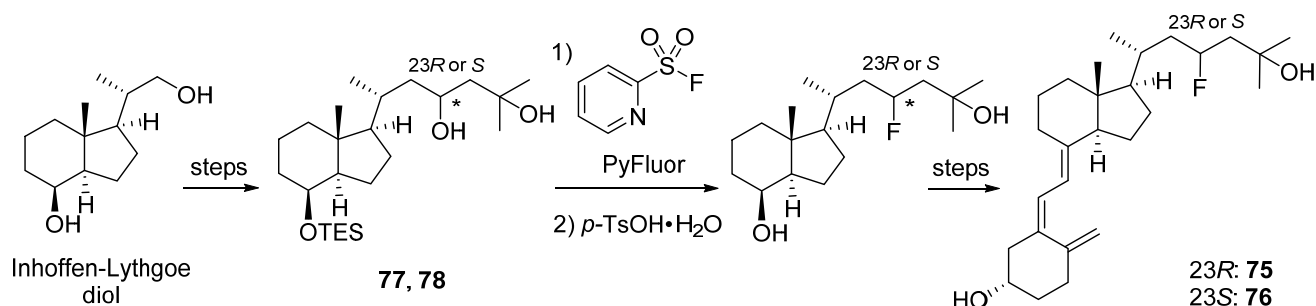
The same group continued to report 23,23-difluoro-1 α ,25(OH)₂D₃ (**72**) by the enzymatic 1 α -hydroxylation of **70** in 1985 [51]. Their biological activities were evaluated, and 23,23-difluoro-25(OH)D₃ (**70**) was 5–10 times less active than 25(OH)D₃ in stimulating intestinal calcium transport, bone calcium mobilization, mineralization of rachitic bone, etc., and 23,23-difluoro-1 α ,25(OH)₂D₃ (**72**) was one-seventh as active as 1 α ,25(OH)₂D₃ in binding to VDR.

Ikeda and coworkers of the Sumitomo research group reported the synthesis of (23*R*)-23,26,26,26,27,27,27-heptafluoro-1 α ,25(OH)₂D₃ (**73**) and its 23*S* isomer (**74**) in 2000 [52]. The starting methyl ketone was available from VD₂, and a subsequent hexafluoroacetone (HFA) aldol reaction gave a 23-oxo derivative, which was reduced to 23*R*- and 23*S*-secondary alcohols that could be separated and subjected to deoxyfluorination using DAST to afford **73** and **74** (Scheme 24). Both analogues showed higher VDR-binding affinity and HL-60 cell differentiation activity than calcitriol.



Scheme 24. Synthesis of 23,26,26,26,27,27,27-heptafluoro-1 α ,25(OH)₂D₃ using DAST for the seventh fluorine introduction.

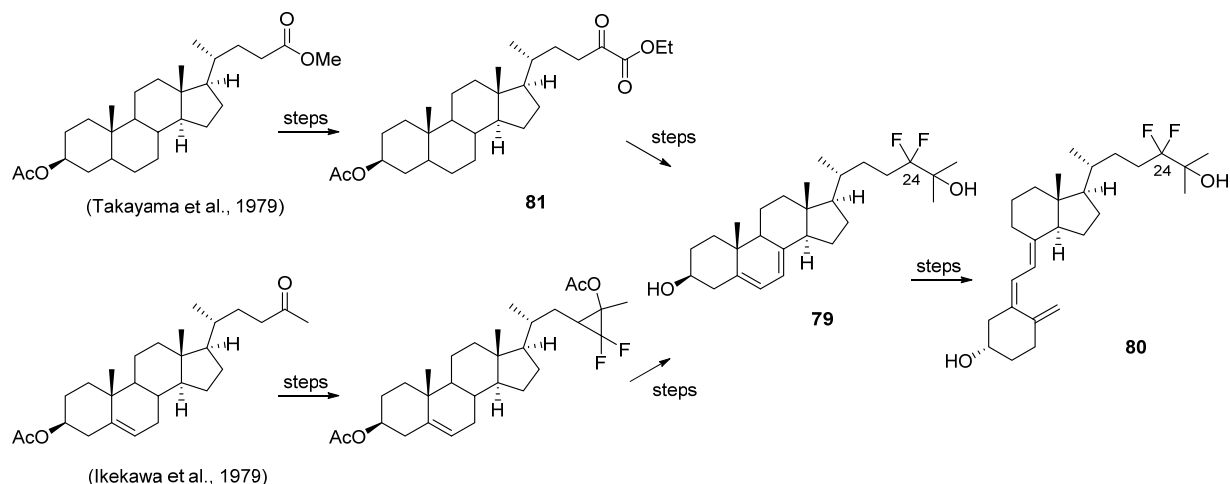
Later, in 2019, our group synthesized (23*R*)-23-fluoro-25(OH)D₃ (**75**) and its 23*S*-isomer (**76**) starting from the Inhoffen–Lythgoe diol via the key intermediate 23-hydroxy-CD-rings (**77**,**78**) (Scheme 25) [53]. The preliminary biological evaluation revealed that the 23*S*-isomer (**76**) showed higher resistance to CYP24A1 metabolism than its 23*R*-isomer (**75**).



Scheme 25. Stereoselective C23-fluorination of 23-hydroxy-CD-rings using PyFluor.

5.3. 24-Fluorinated VD_3 Analogues

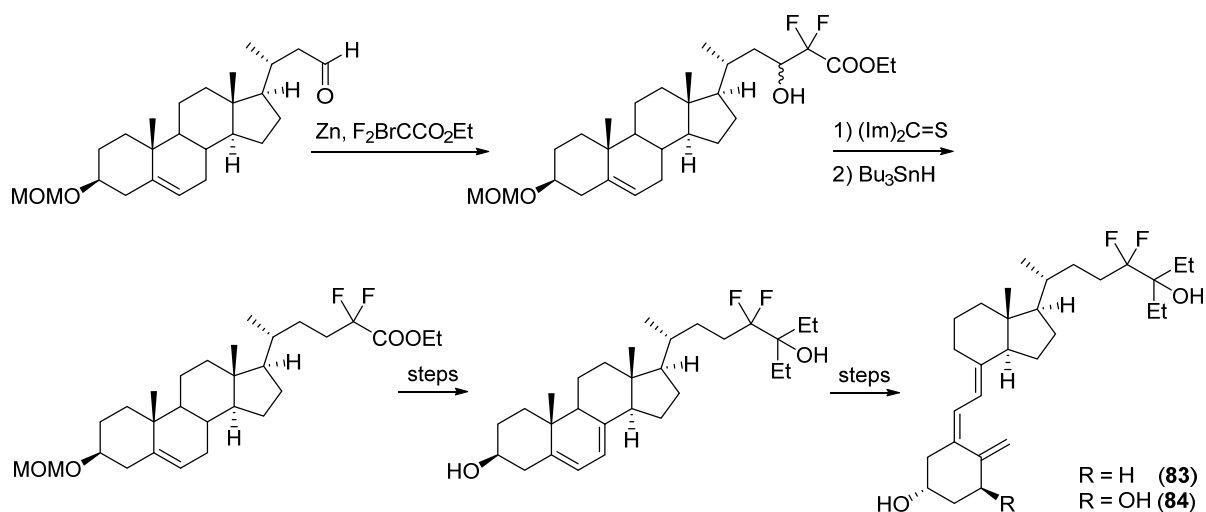
Since oxidation of the hydroxy function at the C24 position catalyzed by CYP24A1 is one of the important pathways to deactivate both $25(OH)D_3$ and $1\alpha,25(OH)_2D_3$, developing practical methods to construct the C24-fluoro unit on the VD_3 skeleton has been pursued since 1979. The first synthesis of the 24,24-difluorovitamin D_3 analogue was reported independently by Takayama's group [54] and Kobayashi-Ikekawa's group [55]. Both synthetic routes involved the key intermediate (**79**), and the two groups synthesized the same analogue, 24,24-difluoro- $25(OH)D_3$ (**80**). For the construction of the 24,24-difluoro unit, Takayama and coworkers utilized the reaction of α -ketoester (**81**), which was derived from lithocholic acid, with DAST. On the other hand, Kobayashi et al. used the reaction of steroidal enol ether, derived from cholic acid, with difluorocarbene (Scheme 26).



Scheme 26. Takayama's and Kobayashi-Ikekawa's synthetic routes to 24,24-difluoro- $25(OH)D_3$ (**80**).

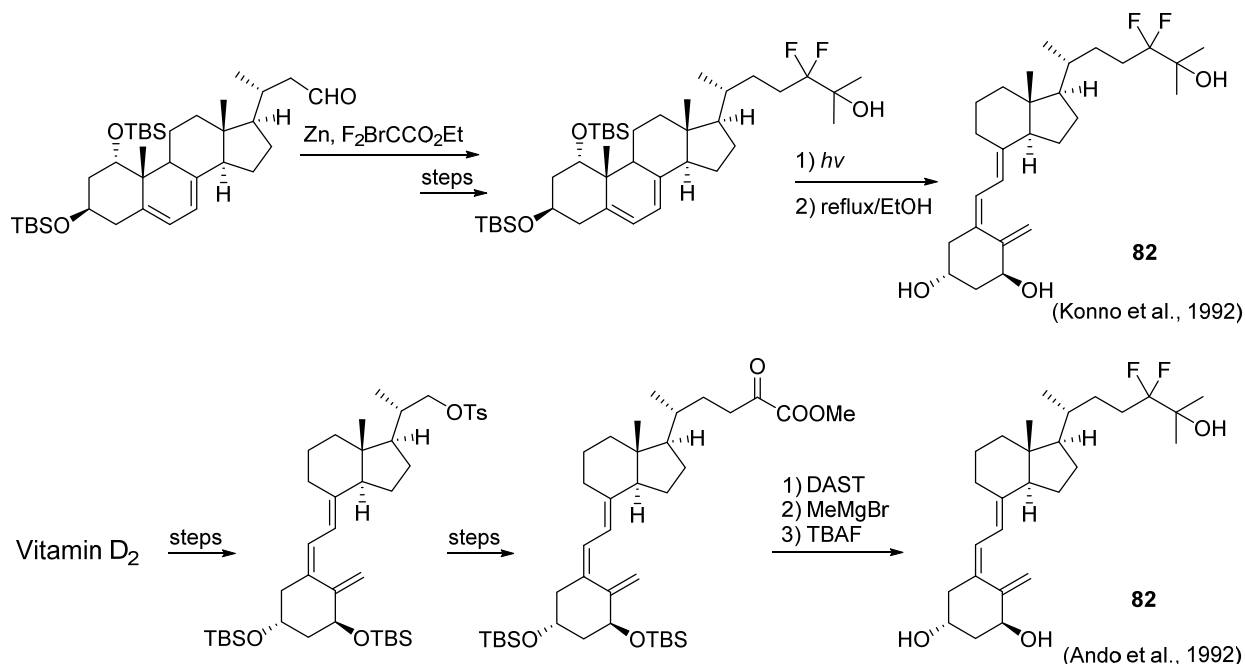
In 1980, Kobayashi-DeLuca's group subsequently demonstrated that kidney homogenates from the chicken converted 24,24-difluoro- $25(OH)D_3$ (**80**) to 24,24-difluoro- $1\alpha,25(OH)_2D_3$ (**82**) [56]. The results of the biological evaluation revealed that **82** and its nonfluorinated counterpart $1\alpha,25(OH)_2D_3$ (**1**) equipotently stimulate intestinal calcium transport and bone calcium mobilization in vivo, while in another in vitro system, **82** was found to be four times more potent than $1\alpha,25(OH)_2D_3$ (**1**).

In 1990, Kumar's group synthesized 24,24-difluoro- 25 -hydroxy- $26,27$ -dihomovitamin D_3 (**83**) and its 1α -hydroxy analogue (**84**) from 3β -hydroxy- $22,23$ -dinorcholenic acid using a Reformatsky reaction in their synthetic route (Scheme 27) [57]. Both analogues showed similar biological activities, such as intestinal calcium transport and bone calcium mobilization in vivo, to those of the respective nonfluorinated counterparts and also $25(OH)D_3$ or $1\alpha,25(OH)_2D_3$.



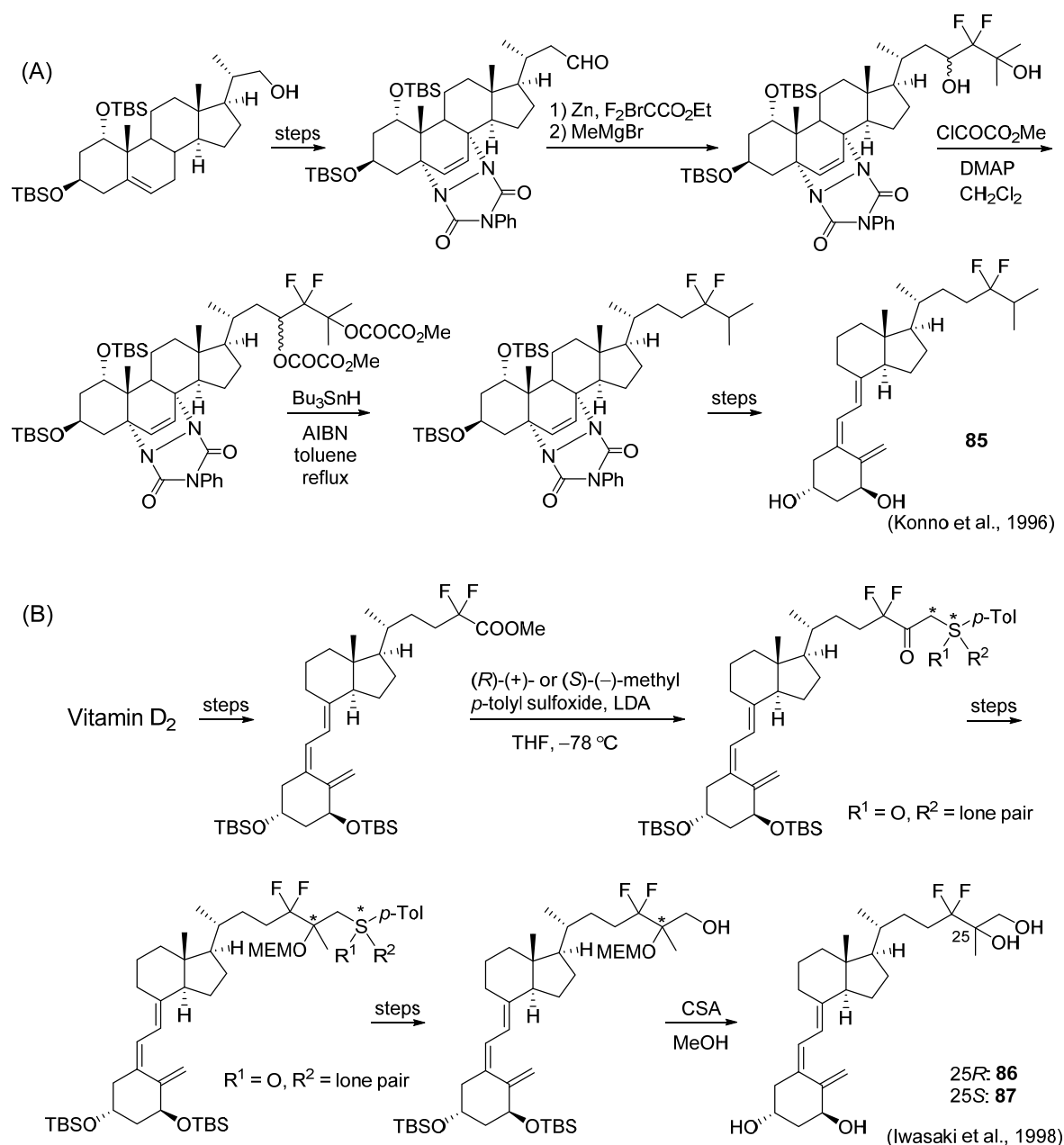
Scheme 27. Kumar's synthetic approach to 24,24-difluorovitamin D homologues (**83,84**) using the Reformatsky reaction.

In 1992, two alternative linear synthetic routes to 24,24-difluoro-1 α ,25(OH)₂D₃ (**82**) were reported by Takayama et al. using the Reformatsky reaction with ethyl bromodifluoroacetate or Horner–Emmons reaction as the key step, respectively (Scheme 28) [58,59]. The starting material of the former was 1 α -hydroxydehydroepiandrosterone, with a 3.8% overall yield of **82** [58], and that of the latter was vitamin D₂, with a 9.3% overall yield of **82** [59].



Scheme 28. Takayama's two improved synthetic approaches to 24,24-difluoro-1 α ,25(OH)₂D₃ (**82**).

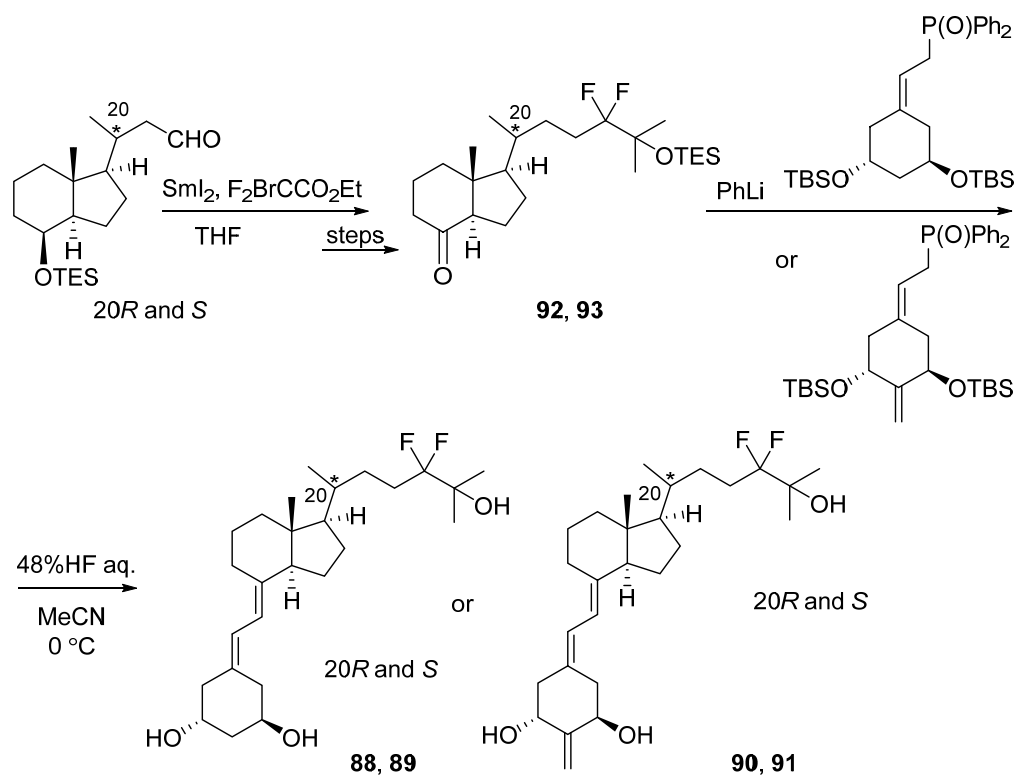
As shown in Scheme 29A, the same group synthesized 24,24-difluoro-1 α (OH)D₃ (**85**) from a steroidal skeleton in 1996 [60]. This compound showed higher activity than 24,24-difluoro-1 α ,25(OH)₂D₃ (**82**) in intestinal calcium absorption. In 1998, Iwasaki-Takayama's group reported the synthesis of (25*R*)- and (25*S*)-24,24-difluoro-1 α ,25,26-trihydroxyvitamin D₃ (**86,87**), including the X-ray crystallographic analysis of a synthetic intermediate to determine C25-stereochemistry, and proved that the 25*S*-isomer (**87**) was the main CYP24-metabolite of **82** (Scheme 29B) [61].



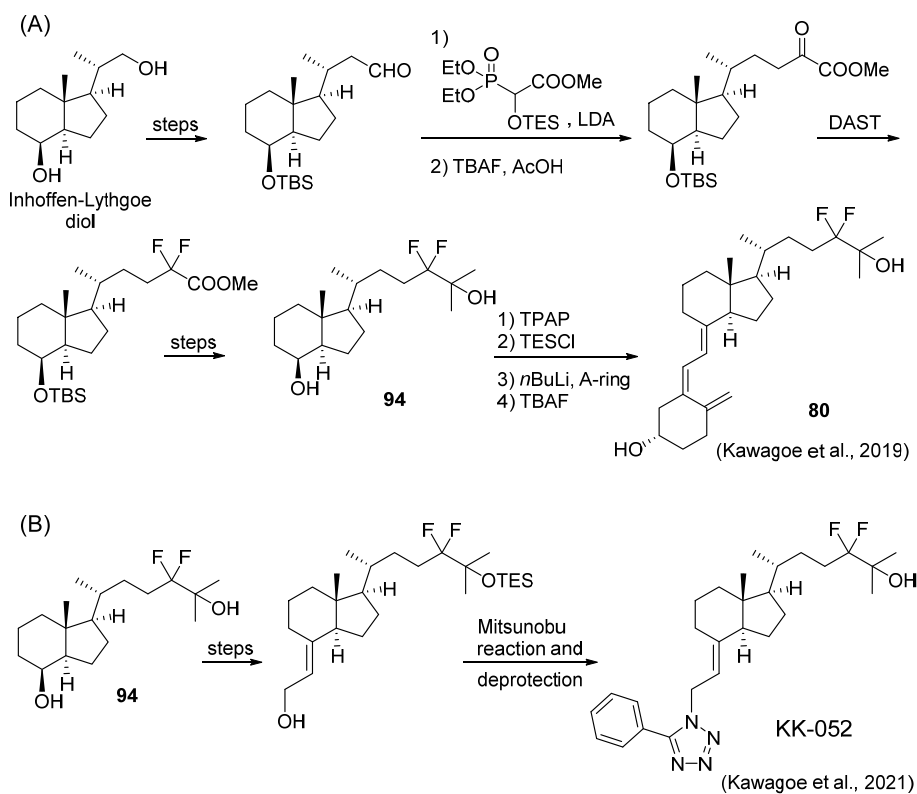
Scheme 29. Synthetic routes to 24,24-difluoro-1 α (OH)D₃ (85) (A) and its CYP24-metabolite (87) (B) by the Takayama group.

The 24,24-difluoro-19-norVD₃ analogues including 20-*epi*-versions (88–91) were reported by DeLuca et al. in 2015 [62]. In contrast to the previous synthetic methods starting from steroid skeletons, they demonstrated a convergent method utilizing the Wittig–Horner reaction between 24,24-difluoro-CD-rings (92,93) and a lithium salt of a phosphine oxide anion from A-ring precursors (Scheme 30). The 20S-derivatives showed marked bone-mobilizing activity *in vivo*; however, 2-methylene substitution was required for such elevated activity in the 20R series.

In 2019, our group developed the convergent synthesis of 24,24-difluoro-25(OH)D₃ (80) using a coupling reaction between the 24,24-difluoro-CD ring ketone derived from the Inhoffen–Lythgoe diol via 94 and an A-ring phosphine oxide (Scheme 31A) [63]. We subsequently synthesized a novel vitamin D-based VDR-silent SREBP inhibitor, KK-052, from 94 (Scheme 31B) [64].

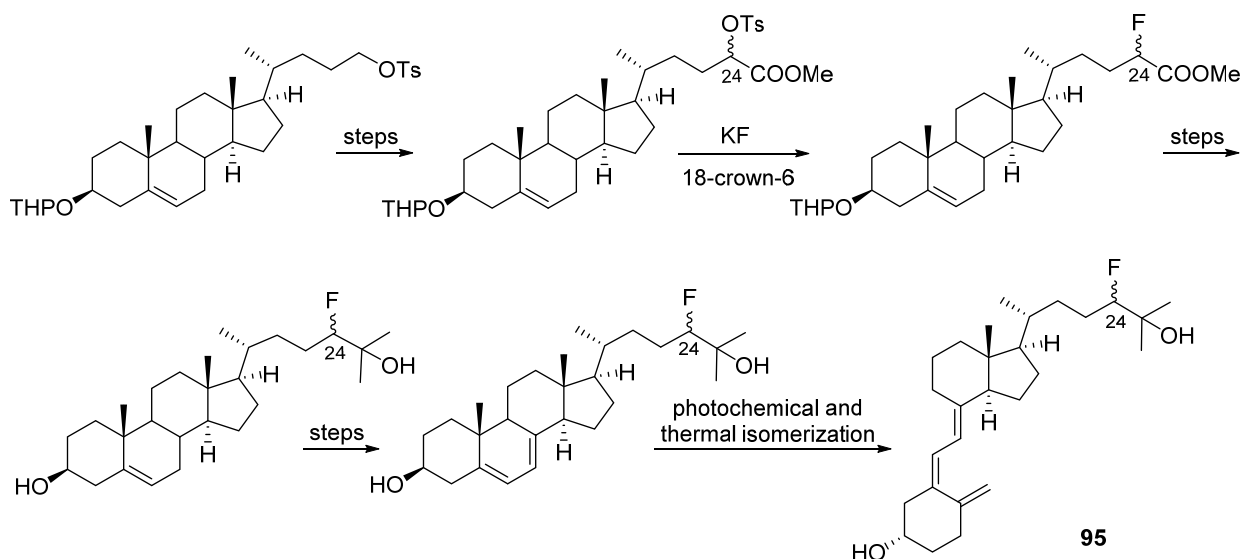


Scheme 30. DeLuca's convergent approach to 24,24-difluoro-1 α ,25(OH)₂-19-norVD₃ (88,89) and the 2-exomethylene analogues (90,91) including their 20-*epi* versions using the Wittig–Horner reaction.



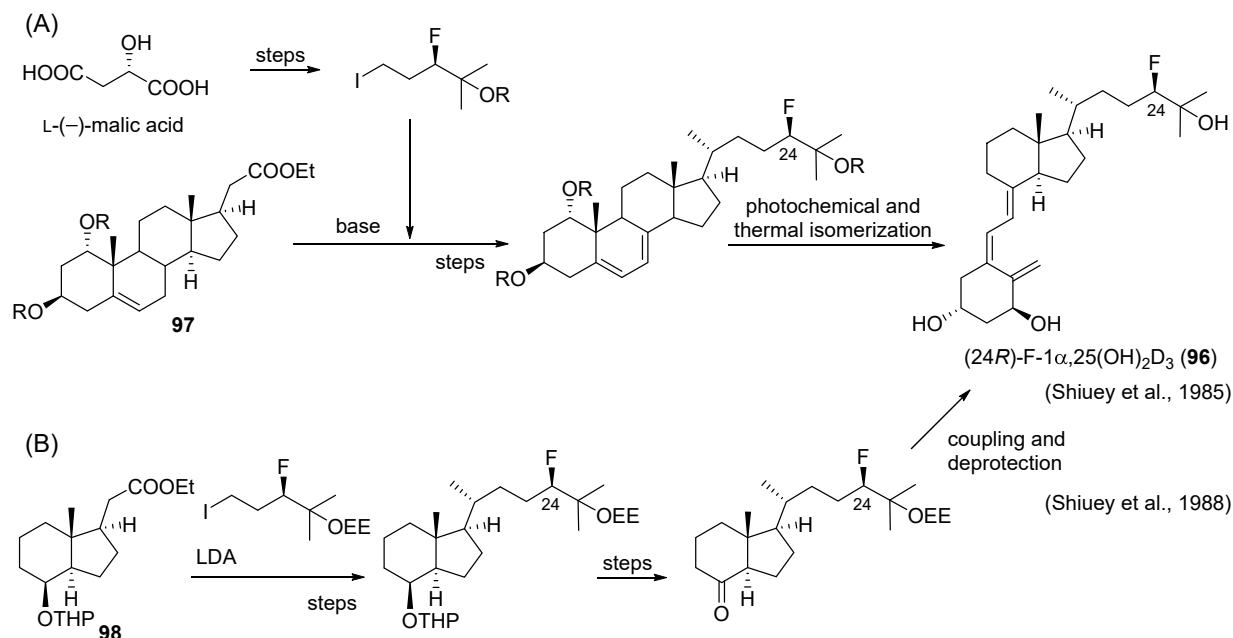
Scheme 31. Efficient construction of the 24,24-difluorinated CD-ring unit (94) and the subsequent A-ring coupling reaction (A). Synthesis of the novel SREBP-specific inhibitor KK-052 (B).

Ikekawa's group reported in 1979 the first synthesis of C₂₄-monofluoro-25(OH)D₃ (**95**) from cholenic acid without assigning the C₂₄ stereochemistry (Scheme 32) [55].



Scheme 32. Synthesis of 24-monofluoro-25(OH)D₃ (**95**) using nucleophilic fluorination as a key step.

After this, (24*R*)-24-fluoro-1 α ,25(OH)₂D₃ (**96**) was synthesized by Uskoković's group through linear (Scheme 33A) and convergent (Scheme 33B) synthetic routes in 1985 [65] and 1988 [66], respectively. In this case, (24*R*)-24-fluoro-1 α ,25(OH)₂D₃ (**96**) showed a longer plasma half-life and higher anti-rachitogenic activity than 1 α ,25(OH)₂D₃ in vivo.

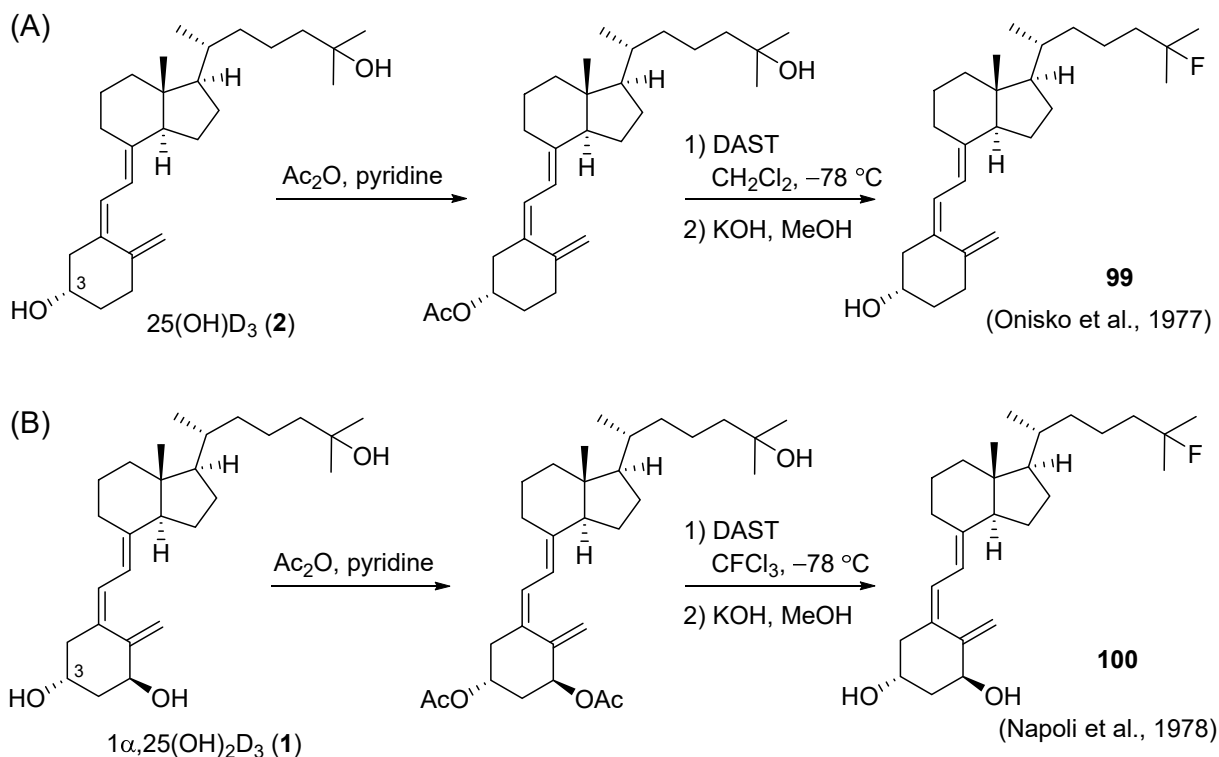


Scheme 33. (24*R*)-Fluoro-1 α ,25(OH)₂D₃ (**96**) was synthesized by Uskoković et al. through a linear synthetic route using **97** and optically active L-(-)-malic acid as a chiral synthon (A) and an alternative convergent route starting from a CD-ring part, **98** (B).

5.4. 25-Fluorinated VD₃ Analogues

The 25-hydroxylation is the initial metabolic conversion of VD₃ by CYP2R1 or CYP27A1 [18], and 25(OH)D₃ (**2**) is known as the major circulating metabolite in the human body.

The first introduction of fluorine to C25, i.e., the synthesis of 25-fluoro-VD₃, was reported by DeLuca et al. in 1977 (Scheme 34A) [67]. C3-Selective O-acetylation of 25(OH)D₃ (**2**) and subsequent direct fluorination at the C25 position using DAST, followed by deacetylation, gave 25-fluorovitamin D₃ (**99**). In 1978, Stern and coworkers synthesized 25-fluoro-1 α (OH)D₃ (**100**) using the same approach (Scheme 34B) [68]. The results of the biological evaluation indicated that 25-fluoro-1 α (OH)D₃ (**100**) was approximately equipotent to 1 α (OH)D₃ (**5**) in VDR binding and stimulating bone resorption in vitro, and the C25-fluoro substituent behaved similarly to hydrogen, without elevating its biological potency.



Scheme 34. Synthesis of 25-fluoro-VD₃ analogues via direct C25 fluorination from 25(OH)D₃ (A) and 1 α ,25(OH)₂D₃ (B) using DAST as a fluorinating reagent.

As described in Section 2.1, DeLuca's group also synthesized 1,25-difluorovitamin D₃ in 1981, and this compound was devoid of any biological activity [21].

5.5. 26,27-Hexafluorinated VD₃ Analogues

Falecalcitriol (**101**) is 26,26,26,27,27,27-hexafluorinated VD₃ and has been approved for therapeutic use against secondary hyperparathyroidism in Japan [69,70]. Falecalcitriol (**101**) was ca. 10 times more active in increasing bone calcium mobilization than the natural hormone (**1**) in vivo [71]. Similarly to other fluorinated VD₃ analogues, it was metabolized more slowly than 1 α ,25(OH)₂D₃ (**1**) by CYP24A1, and interestingly, its major metabolite (23S)-23-hydroxyfalecalcitriol (**102**) was equipotent to the parent compound **101** in its biological activity (Figure 1) [72–74]. The 23-hydroxylated **102** was specifically glucuronidated by UGT1A3 [75].

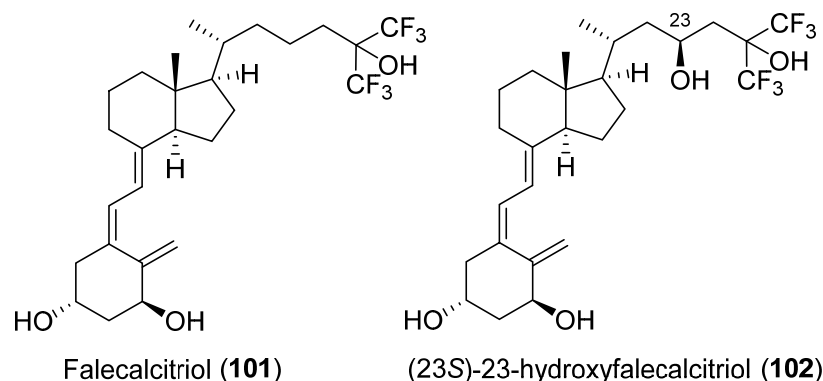
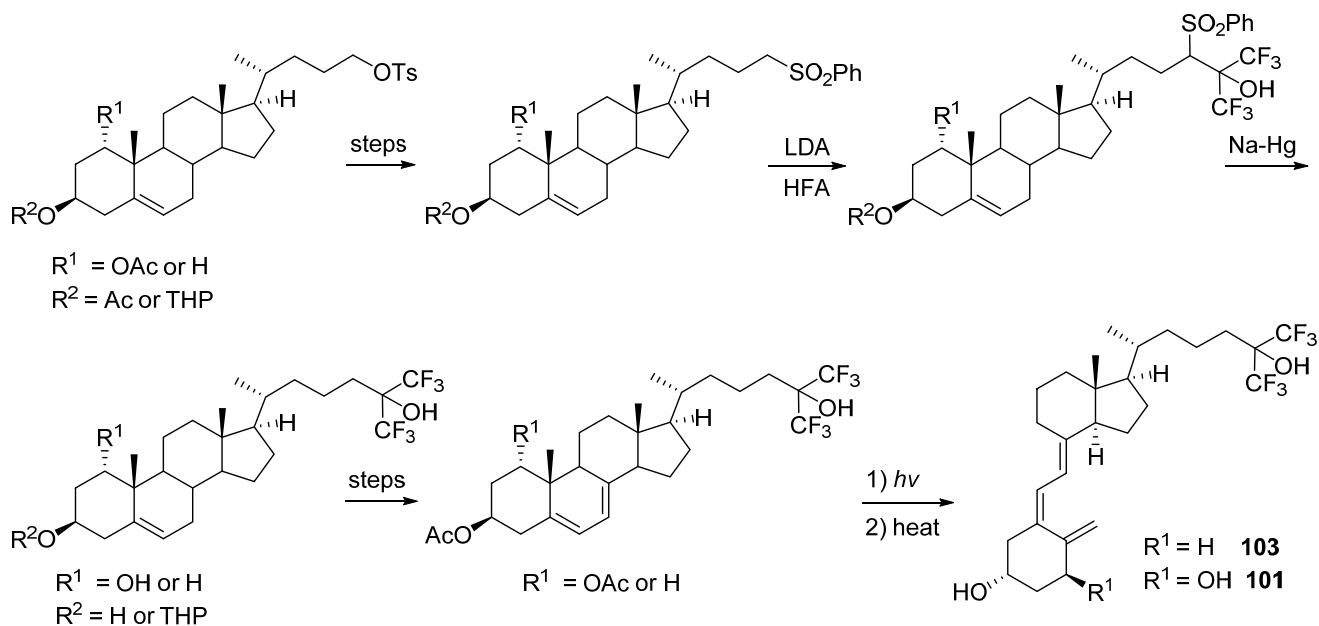


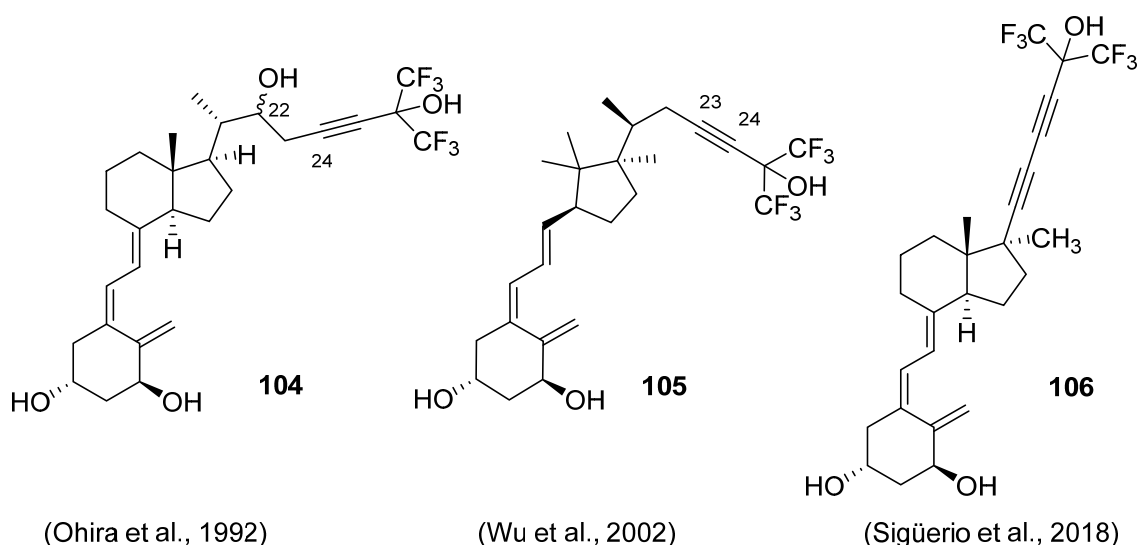
Figure 1. Structures of falcacitriol (**101**) and its major metabolite (23S)-23-hydroxyfalcacitriol (**102**).

The first synthesis of 26,26,26,27,27,27-hexafluoro-25(OH)D₃ (**103**) was reported by Kobayashi et al. in 1980 [76], and the same group subsequently synthesized 26,26,26,27,27,27-hexafluoro-1 α ,25(OH)₂D₃ (**101**) in 1982 [77]. In this case, 3 β -Tetrahydropyranoloxychol-5-en-24-ol tosylate was used as a starting material, and hexafluoroacetone (HFA) was utilized for construction of the 26,26,26,27,27,27-hexafluoro unit (Scheme 35). The biological evaluation revealed that **101** was approximately 5-10-fold more active than 1 α ,25(OH)₂D₃ (**1**) without inducing severe hypercalcemia.



Scheme 35. Synthesis of 26,26,26,27,27,27-hexafluoro-25(OH)D₃ (**103**) and 26,26,26,27,27,27-hexafluoro-1 α ,25(OH)₂D₃ (**101**) using hexafluoroacetone as a fluorine source.

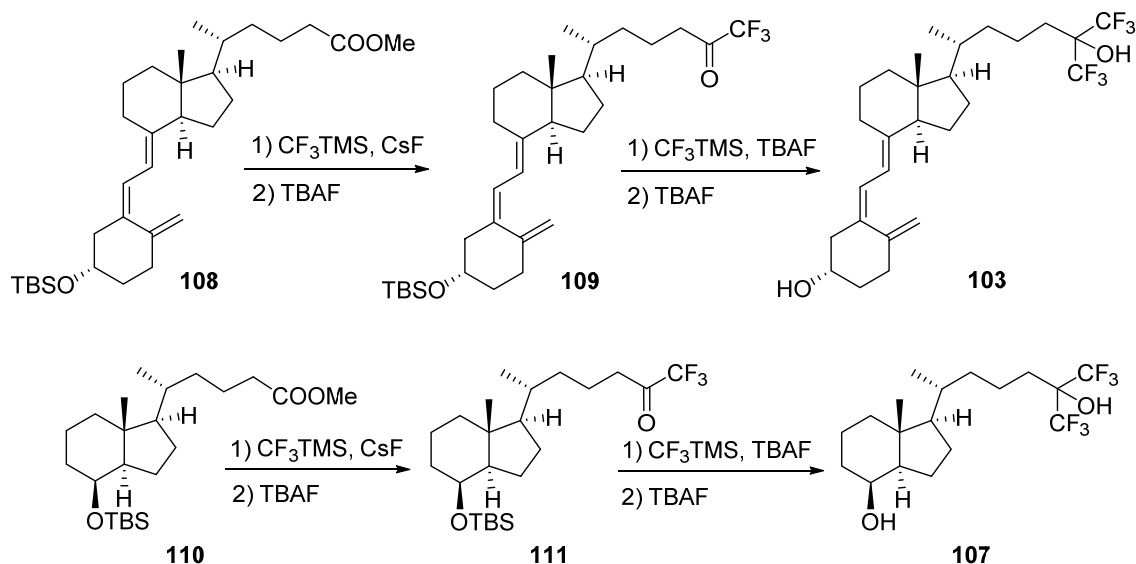
Using the reaction of acetylides with excess HFA gas as the key step, syntheses of the hexafluoroalkynyl-VD₃ analogue (**104**), *C-seco*-hexafluoroalkynyl-VD₃ analogue (**105**), and the previously mentioned two-side-chain analogues **17-22** including alkene side chains (Section 2.1) were reported by Ohira et al. in 1992 [78], by Wu et al. in 2002 [79], and by Maehr et al. in 2009 [28], respectively (Scheme 36). Compound **104** had a potent inducing effect on the differentiation of cancer cells, with little calcium mobilization activity. Compound **105** showed comparable VDR-binding affinity to the natural hormone **1** and had strong antiproliferative activity against four cancer cell lines in vitro, with 1% calcemic activity compared with **1** in vivo. More recently, Sigüeiro et al. synthesized C22-diyne analogues with a C17-methyl group, including the hexafluoropropanol unit at the terminal (**106**), which showed potent VDR-binding affinity [80].



Scheme 36. Combination of the hexafluoroisopropanol unit derived from hexafluoroacetone (HFA) and triple bond(s), which brought conformational rigidity to the side chain.

Hayashi and colleagues described the introduction of the 26,26,26,27,27,27-hexafluoro unit utilizing an aldol reaction [52]. The C23 ketone was treated with HFA in the presence of LiHMDS to afford the HFA adduct (see Scheme 24 in Section 5.2).

As an alternative path to construct the hexafluoro unit, the nucleophilic trifluoromethylation of methyl esters with Ruppert–Prakash reagent (CF_3TMS) can be utilized. In our group, 26,26,26,27,27,27-hexafluoro-25(OH) D_3 (**103**) and 26,26,26,27,27,27-hexafluoro-CD ring (**107**) were synthesized in 2018 starting from the methyl esters (**108,110**) through trifluoromethylketones (**109,111**) as the intermediates (Scheme 37) [81].



Scheme 37. Synthesis of 26,26,26,27,27,27-hexafluoro-25(OH) D_3 (**103**) and synthetically useful 26,26,26,27,27,27-hexafluoro-CD-ring precursor (**107**) using efficient two-step trifluoromethylation method.

6. Summary

This review summarized the historical fluorinated VD_3 analogues with modification from the A-ring to the end of the side-chain, including their synthetic methods. With the aim of preventing or slowing their activation or degradation by CYPs, the A-ring and side-chain have been mainly focused on, and numerous VD_3 analogues containing the

fluorine atom(s) have been synthesized. Hydroxylation at the C25 and C1 α positions of VD₃ is necessary for the activation process of the molecule by CYP2R1/CYP27A1 and CYP27B1, respectively; therefore, in general, the introduction of fluorine to these positions decreases the biological activity through VDR if compared to non-fluorinated 25(OH)D₃ or 1 α ,25(OH)₂D₃ as each parent VDR ligand. On the other hand, fluorination at the side chain C23, C24, and C26(27) of VD₃, where deactivating hydroxylation occurs based on CYP24A1 metabolism, produces strong VDR agonists that have a long half-life in vivo. Among them, falecalcitriol was successfully approved for the treatment of secondary hyperparathyroidism in Japan. Discovery of the new functions of VD₃ continues; for example, the potent SREBP-inhibitory activity of 25(OH)D₃ [82] and the new fluorinated analogues with their efficient synthetic methods may contribute to the treatment of patients with VD₃-function-related disease in the future.

Author Contributions: Conceptualization, F.K. and A.K.; writing—original draft preparation, F.K. and S.M.; writing—review and editing, A.K.; supervision, A.K.; funding acquisition, A.K. All authors have read and agreed to the published version of the manuscript.

Funding: This work was supported by a Grant-in-Aid from the Japan Society for the Promotion of Science (No. 18K06556 to A.K.).

Institutional Review Board Statement: Not applicable.

Informed Consent Statement: Not applicable.

Conflicts of Interest: The authors declare no conflict of interest.

References

- Müller, K.; Faeh, C.; Diederich, F. Fluorine in pharmaceuticals: Looking beyond intuition. *Science* **2007**, *317*, 1881–1886. [CrossRef]
- Johnson, B.M.; Shu, Y.Z.; Zhuo, X.; Meanwell, N.A. Metabolic and pharmaceutical aspects of fluorinated compounds. *J. Med. Chem.* **2020**, *63*, 6315–6386. [CrossRef] [PubMed]
- Böhm, H.-J.; Banner, D.; Bendels, S.; Kansy, M.; Kuhn, B.; Müller, K.; Obst-Sander, U.; Stahl, M. Fluorine in medicinal chemistry. *Chembiochem* **2004**, *5*, 637–643. [CrossRef]
- Kirk, K.L. Fluorine in medicinal chemistry: Recent therapeutic applications of fluorinated small molecules. *J. Fluor. Chem.* **2006**, *127*, 1013–1029. [CrossRef]
- Purser, S.; Moore, P.R.; Swallow, S.; Gouverneur, V. Fluorine in medicinal chemistry. *Chem. Soc. Rev.* **2008**, *37*, 320–330. [CrossRef] [PubMed]
- Wang, J.; Sánchez-Roselló, M.; Aceña, J.L.; Del Pozo, C.; Sorochinsky, A.E.; Fustero, S.; Soloshonok, V.A.; Liu, H. Fluorine in pharmaceutical industry: Fluorine-containing drugs introduced to the market in the last decade (2001–2011). *Chem. Rev.* **2014**, *114*, 2432–2506. [CrossRef] [PubMed]
- Mei, H.; Han, J.; Fustero, S.; Medio-Simon, M.; Sedgwick, D.M.; Santi, C.; Ruzziconi, R.; Soloshonok, V.A. Fluorine-containing drugs approved by the FDA in 2018. *Chemistry* **2019**, *25*, 11797–11819. [CrossRef]
- Bégué, J.-P.; Bonnet-Delpon, D. Recent advances (1995–2005) in fluorinated pharmaceuticals based on natural products. *J. Fluor. Chem.* **2006**, *127*, 992–1012. [CrossRef]
- Shah, P.; Westwell, A.D. The role of fluorine in medicinal chemistry. *J. Enzym. Inhib. Med. Chem.* **2007**, *22*, 527–540. [CrossRef]
- Berkowitz, D.B.; Karukurichi, K.R.; De La Salud-Bea, R.; Nelson, D.L.; McCune, C.D. Use of fluorinated functionality in enzyme inhibitor development: Mechanistic and analytical advantages. *J. Fluor. Chem.* **2008**, *129*, 731–742. [CrossRef]
- Maienfisch, P.; Hall, R.G. The importance of fluorine in the life science industry. *Chimia* **2004**, *58*, 93–98. [CrossRef]
- Prchalová, E.; Štěpánek, O.; Smrček, S.; Kotora, M. Medicinal applications of perfluoroalkylated chain-containing compounds. *Future Med. Chem.* **2014**, *6*, 1201–1229. [CrossRef]
- Kukhar', V.P.; Soloshonok, V.A. Aliphatic fluorine-containing amino acids. *Russ. Chem. Rev.* **1991**, *60*, 850–864. [CrossRef]
- Liu, P.; Sharon, A.; Chu, C.K. Fluorinated nucleosides: Synthesis and biological implication. *J. Fluor. Chem.* **2008**, *129*, 743–766. [CrossRef]
- Isanbor, C.; O'Hagan, D. Fluorine in medicinal chemistry: A review of anti-cancer agents. *J. Fluor. Chem.* **2006**, *127*, 303–319. [CrossRef]
- Al-Harthy, T.; Zoghaib, W.; Abdel-Jalil, R. Importance of fluorine in benzazole compounds. *Molecules* **2020**, *25*, 4677. [CrossRef]
- Krafft, M.P. Fluorocarbons and fluorinated amphiphiles in drug delivery and biomedical research. *Adv. Drug Deliv. Rev.* **2001**, *47*, 209–228. [CrossRef]
- Sakaki, T.; Kagawa, N.; Yamamoto, K.; Inouye, K. Metabolism of vitamin D₃ by cytochromes P450. *Front. Biosci.* **2005**, *10*, 119–134.
- Sakaki, T.; Sawada, N.; Komai, K.; Shiozawa, S.; Yamada, S.; Yamamoto, K.; Ohyama, Y.; Inouye, K. Dual metabolic pathway of 25-hydroxyvitamin D₃ catalyzed by human CYP24. *Eur. J. Biochem.* **2000**, *267*, 6158–6165. [CrossRef]

20. Yasuda, K.; Nishikawa, M.; Okamoto, K.; Horibe, K.; Mano, H.; Yamaguchi, M.; Okon, R.; Nakagawa, K.; Tsugawa, N.; Okano, T.; et al. Elucidation of metabolic pathways of 25-hydroxyvitamin D₃ mediated by Cyp24A1 and Cyp3A using Cyp24a1 knockout rats generated by CRISPR/Cas9 system. *J. Biol. Chem.* **2021**, *296*, 100668. [CrossRef]
21. Rochel, N.; Wurtz, J.M.; Mitschler, A.; Klaholz, B.; Moras, D. The crystal structure of the nuclear receptor for vitamin D bound to its natural ligand. *Mol. Cell* **2000**, *5*, 173–179. [CrossRef]
22. Napoli, J.L.; Fivizzani, M.A.; Schnoes, H.K.; DeLuca, H.F. 1-Fluorovitamin D₃, a vitamin D₃ analogue more active on bone-calcium mobilization than on intestinal-calcium transport. *Biochemistry* **1979**, *18*, 1641–1646. [CrossRef]
23. Paaren, H.E.; Fivizzani, M.A.; Schnoes, H.K.; DeLuca, H.F. 1 α ,25-Difluorovitamin D₃: An inert vitamin D analog. *Arch. Biochem. Biophys.* **1981**, *209*, 579–583. [CrossRef]
24. Ohshima, E.; Takatsuto, S.; Ikekawa, N.; De Luca, H.F. Synthesis of 1 α -fluorovitamin D₃. *Chem. Pharm. Bull.* **1984**, *32*, 3518–3524. [CrossRef]
25. Ohshima, E.; Sai, H.; Takatsuto, S.; Ikekawa, N.; Kobayashi, Y.; Tanaka, Y.; DeLuca, H.F. Synthesis and biological activity of 1 α -fluoro-25-hydroxyvitamin D₃. *Chem. Pharm. Bull.* **1984**, *32*, 3525–3531. [CrossRef]
26. Shiuey, S.-J.; Kulesha, I.; Baggolini, E.G.; Uskoković, M.R. Total synthesis of 1 α -fluoro-25-hydroxycholecalciferol and -ergocalciferol. *J. Org. Chem.* **1990**, *55*, 243–247. [CrossRef]
27. Kiegiel, J.; Wovkulich, P.M.; Uskoković, M.R. Chemical conversion of vitamin D₃ to its 1,25-dihydroxy metabolite. *Tetrahedron Lett.* **1991**, *32*, 6057–6060. [CrossRef]
28. Maehr, H.; Lee, H.J.; Perry, B.; Suh, N.; Uskoković, M.R. Calcitriol derivatives with two different side chains at C-20. V. Potent inhibitors of mammary carcinogenesis and inducers of leukemia differentiation. *J. Med. Chem.* **2009**, *52*, 5505–5519. [CrossRef]
29. Nagata, A.; Akagi, Y.; Asano, L.; Kotake, K.; Kawagoe, F.; Mendoza, A.; Masoud, S.S.; Usuda, K.; Yasui, K.; Takemoto, Y.; et al. Synthetic chemical probes that dissect vitamin D activities. *ACS Chem. Biol.* **2019**, *14*, 2851–2858. [CrossRef]
30. Ono, K.; Yoshida, A.; Saito, N.; Fujishima, T.; Honzawa, S.; Suhara, Y.; Kishimoto, S.; Sugiura, T.; Waku, K.; Takayama, H.; et al. Efficient synthesis of 2-modified 1 α ,25-dihydroxy-19-norvitamin D₃ with Julia olefination: High potency in induction of differentiation on HL-60 cells. *J. Org. Chem.* **2003**, *68*, 7407–7415. [CrossRef]
31. Oshida, J.-I.; Morisaki, M.; Ikekawa, N. Synthesis of 2 β -fluoro-1 α -hydroxyvitamin D₃. *Tetrahedron Lett.* **1980**, *21*, 1755–1756. [CrossRef]
32. Kobayashi, Y.; Nakazawa, M.; Kumadaki, I.; Taguchi, T.; Ohshima, E.; Ikekawa, N.; Tanaka, Y.; DeLuca, H.F. Studies on organic fluorine compounds. L. Synthesis and biological activity of 2 α -fluorovitamin D₃. *Chem. Pharm. Bull.* **1986**, *34*, 1568–1572. [CrossRef]
33. Scheddin, D.; Mayer, H.; Schönecker, B.; Gliesing, S.; Reichenbacher, M. Synthesis and biological activities of 2 β -chloro-, 2 β -fluoro-, and 2 β -methoxy-1 α ,25-dihydroxyvitamin D₃. *Steroids* **1998**, *63*, 633–643. [CrossRef]
34. Mikami, K.; Ohba, S.; Ohmura, H.; Kubodera, N.; Nakagawa, K.; Okano, T. Asymmetric catalytic ene-cyclization approach to 2-fluoro-19-nor-1,25-dihydroxyvitamin D₃ A-ring analog with significant transactivation activity. *Chirality* **2001**, *13*, 366–371. [CrossRef] [PubMed]
35. Nakagawa, K.; Okano, T.; Ozono, K.; Kato, S.; Kubodera, N.; Ohba, S.; Itoh, Y.; Mikami, K. Catalytic asymmetric synthesis and anticancer effects of the novel non-calcemic analog of vitamin D, 2 α -fluoro-19-nor-22-oxa-1 α ,25-dihydroxyvitamin D₃ in metastatic lung carcinoma. *J. Fluor. Chem.* **2007**, *128*, 654–667. [CrossRef]
36. Posner, G.H.; Woodard, B.T.; Crawford, K.R.; Peleg, S.; Brown, A.J.; Dolan, P.; Kensler, T.W. 2,2-Disubstituted analogues of the natural hormone 1 α ,25-dihydroxyvitamin D₃: Chemistry and biology. *Bioorg. Med. Chem.* **2002**, *10*, 2353–2365. [CrossRef]
37. Yakhimovich, R.I.; Klimashevskii, V.M.; Segal, G.M. Synthesis and biological activity of 3 α -fluoro-9,10-secocholesta-5,7,10(19)-triene, the fluoro derivative of vitamin D₃. *Khimiko-Farmatsevticheskii Zhurnal* **1976**, *10*, 58–64. [CrossRef]
38. Sheves, M.; Sialom, B.; Mazur, Y. Stereoselective conversion of vitamin D₃ into its 3 β -halogenated derivatives. The synthesis of a 1 α -hydroxy-3 β -fluorovitamin D₃ analogue. *J. Chem. Soc. Chem. Commun.* **1978**, 554–555. [CrossRef]
39. Revelle, L.K.; Londowski, J.M.; Kost, S.B.; Corradino, R.A.; Kumar, R. Synthesis and biological activity of 3 β -fluorovitamin D₃: Comparison of the biological activity of 3 β -fluorovitamin D₃ and 3-deoxyvitamin D₃. *J. Steroid Biochem.* **1985**, *22*, 469–474. [CrossRef]
40. Shimizu, M.; Iwasaki, Y.; Yamada, S. 4,4-Difluoro-1 α ,25-dihydroxyvitamin D₃: Analog to probe A-ring conformation in vitamin D-receptor complex. *Tetrahedron Lett.* **1999**, *40*, 1697–1700. [CrossRef]
41. Sialom, B.; Mazur, Y. Influence of fluorine and oxygen atoms at C-19 on the previtamin D-vitamin D interconversion. *J. Org. Chem.* **1980**, *45*, 2201–2204. [CrossRef]
42. Iwasaki, Y.; Shimizu, M.; Hirosawa, T.; Yamada, S. Regioselective synthesis of 19-fluorovitamin D via fluorination of vitamin D-sulfur dioxide adducts. *Tetrahedron Lett.* **1996**, *37*, 6753–6754. [CrossRef]
43. Shimizu, M.; Iwasaki, Y.; Ohno, A.; Yamada, S. Synthesis of (10Z)- and (10E)-19-fluoro-1 α ,25-dihydroxyvitamin D₃: Compounds to probe vitamin D conformation in receptor complex by 19F-NMR. *Chem. Pharm. Bull.* **2000**, *48*, 1484–1493. [CrossRef] [PubMed]
44. Shimizu, M.; Ohno, A.; Yamada, S. (10Z)- and (10E)-19-fluoro-1 α ,25-dihydroxyvitamin D₃: An improved synthesis via 19-nor-10-oxo-vitamin D. *Chem. Pharm. Bull.* **2001**, *49*, 312–317. [CrossRef] [PubMed]
45. Dauben, W.G.; Kohler, B.; Roesle, A. Synthesis of 6-fluorovitamin D₃. *J. Org. Chem.* **1985**, *50*, 2007–2010. [CrossRef]

46. Wilhelm, F.; Dauben, W.G.; Kohler, B.; Roesle, A.; Norman, A.W. 6-Fluoro-vitamin D₃: A new antagonist of the biological actions of vitamin D₃ and its metabolites which interacts with the intestinal receptor for 1 α ,25(OH)₂-vitamin D₃. *Arch. Biochem. Biophys.* **1984**, *233*, 127–132. [CrossRef]
47. Takenouchi, K.; Ishizuka, S.; Miura, D.; Sato, F.; Hanazawa, T. 6,7-Substituted 19-norvitamin D₃ derivatives and pharmaceuticals containing them. *Jpn. Kokai Tokkyo Koho*. JP 2004-175763. 2004. Available online: <https://patents.google.com/patent/US7530024> (accessed on 26 July 2021).
48. Zhu, G.-D.; Haver, D.V.; Jurriaans, H.; De Clercq, P.J. 11-Fluoro-1 α -hydroxyvitamin D₃: The quest for experimental evidence of the folded vitamin D conformation. *Tetrahedron* **1994**, *50*, 7049–7060. [CrossRef]
49. Gill, H.S.; Londowski, J.M.; Corradino, R.A.; Kumar, R. The synthesis and biological activity of 22-fluorovitamin D₃: A new vitamin D analog. *Steroids* **1986**, *48*, 93–108. [CrossRef]
50. Taguchi, T.; Mitsuhashi, S.; Yamanouchi, A.; Kobayashi, Y.; Sai, H.; Ikekawa, N. Synthesis of 23,23-difluoro-25-hydroxyvitamin D₃. *Tetrahedron Lett.* **1984**, *25*, 4933–4936. [CrossRef]
51. Nakada, M.; Tanaka, Y.; DeLuca, H.F.; Kobayashi, Y.; Ikekawa, N. Biological activities and binding properties of 23,23-difluoro-25-hydroxyvitamin D₃ and its 1 α -hydroxy derivative. *Arch. Biochem. Biophys.* **1985**, *241*, 173–178. [CrossRef]
52. Ikeda, M.; Matsumura, H.; Sawada, N.; Hashimoto, K.; Tanaka, T.; Noguchi, T.; Hayashi, M. Synthesis and biological evaluations of C-23-modified 26,26,27,27-F₆-vitamin D₃ analogues. *Bioorg. Med. Chem.* **2000**, *8*, 1809–1817. [CrossRef]
53. Kawagoe, F.; Yasuda, K.; Mototani, S.; Sugiyama, T.; Uesugi, M.; Sakaki, T.; Kittaka, A. Synthesis and CYP24A1-dependent metabolism of 23-fluorinated vitamin D₃ analogues. *ACS Omega* **2019**, *4*, 11332–11337. [CrossRef]
54. Yamada, S.; Ohmori, M.; Takayama, H. Synthesis of 24,24-difluoro-25-hydroxyvitamin D₃. *Tetrahedron Lett.* **1979**, *20*, 1859–1862. [CrossRef]
55. Kobayashi, Y.; Taguchi, T.; Terada, T.; Oshida, J.-I.; Morisaki, M.; Ikekawa, N. Synthesis of 24,24-difluoro- and 24 ξ -fluoro-25-hydroxyvitamin D₃. *Tetrahedron Lett.* **1979**, *20*, 2023–2026. [CrossRef]
56. Tanaka, Y.; DeLuca, H.F.; Schnoes, H.K.; Ikekawa, N.; Kobayashi, Y. 24,24-difluoro-1,25-dihydroxyvitamin D₃: In vitro production, isolation, and biological activity. *Arch. Biochem. Biophys.* **1980**, *199*, 473–478. [CrossRef]
57. Gill, H.S.; Londowski, J.M.; Corradino, R.A.; Zinsmeister, A.R.; Kumar, R. Synthesis and biological activity of novel vitamin D analogues: 24,24-difluoro-25-hydroxy-26,27-dimethylvitamin D₃ and 24,24-difluoro-1 α ,25-dihydroxy-26,27-dimethylvitamin D₃. *J. Med. Chem.* **1990**, *33*, 480–490. [CrossRef]
58. Konno, K.; Ojima, K.; Hayashi, T.; Takayama, H. An alternative and efficient synthesis of 24,24-difluoro-1 α ,25-dihydroxyvitamin D₃. *Chem. Pharm. Bull.* **1992**, *40*, 1120–1124. [CrossRef]
59. Ando, K.; Kondo, F.; Koike, F.; Takayama, H. An improved synthesis of 24,24-difluoro-1 α ,25-dihydroxyvitamin D₃ from vitamin D₂. *Chem. Pharm. Bull.* **1992**, *40*, 1662–1664. [CrossRef]
60. Kondo, F.; Maki, S.; Konno, K.; Takayama, H. The first synthesis of 24,24-difluoro-1 α -hydroxyvitamin D₃ by means of radical deoxygenation of alcohols. *Chem. Pharm. Bull.* **1996**, *44*, 62–66. [CrossRef]
61. Iwasaki, H.; Hosotani, R.; Miyamoto, Y.; Nakano, Y.; Yamamoto, K.; Yamada, S.; Shinki, T.; Suda, T.; Yamaguchi, K.; Konno, K.; et al. Stereoselective synthesis and structural establishment of (25S)-24,24-difluoro-1 α ,25,26-trihydroxyvitamin D₃, a major metabolite of 24,24-difluoro-1 α ,25-dihydroxyvitamin D₃. *Tetrahedron* **1998**, *54*, 14705–14724. [CrossRef]
62. Flores, A.; Massarelli, I.; Thoden, J.B.; Plum, L.A.; DeLuca, H.F. A methylene group on C-2 of 24,24-difluoro-19-nor-1 α ,25-dihydroxyvitamin D₃ markedly increases bone calcium mobilization in vivo. *J. Med. Chem.* **2015**, *58*, 9731–9741. [CrossRef] [PubMed]
63. Kawagoe, F.; Mototani, S.; Yasuda, K.; Nagasawa, K.; Uesugi, M.; Sakaki, T.; Kittaka, A. Introduction of fluorine atoms to vitamin D₃ side-chain and synthesis of 24,24-difluoro-25-hydroxyvitamin D₃. *J. Steroid Biochem. Mol. Biol.* **2019**, *195*, 105477. [CrossRef]
64. Kawagoe, F.; Mendoza, A.; Hayata, Y.; Asano, L.; Kotake, K.; Mototani, S.; Kawamura, S.; Kurosaki, S.; Akagi, Y.; Takemoto, Y.; et al. Discovery of a vitamin D receptor-silent vitamin D derivative that impairs sterol regulatory element-binding protein in vivo. *J. Med. Chem.* **2021**, *64*, 5689–5709. [CrossRef]
65. Shiuey, S.-J.; Partridge, J.J.; Chadha, N.K.; Boris, A.; Uskoković, M.R. Stereospecific synthesis of 1 α ,25-dihydroxy-24R-fluorocholecalciferol (Ro23-0233). In *Vitamin D, Chemical, Biochemical and Clinical Update*; Walter De Gruyter: Berlin, Germany, 1985; pp. 765–766.
66. Shiuey, S.-J.; Partridge, J.J.; Uskoković, M.R. Triply convergent synthesis of 1 α ,25-dihydroxy-24(R)-fluorocholecalciferol. *J. Org. Chem.* **1988**, *53*, 1040–1046. [CrossRef]
67. Onisko, B.L.; Schnoes, H.K.; DeLuca, H.F. Synthesis of potential vitamin D antagonists. *Tetrahedron Lett.* **1977**, *18*, 1107–1108. [CrossRef]
68. Napoli, J.L.; Fivizzani, M.A.; Hamstra, A.H.; Schnoes, H.K.; DeLuca, H.F.; Stern, P.H. The synthesis and activity in vitro of 25-masked 1 α -hydroxylated vitamin D₃ analogs. *Steroids* **1978**, *32*, 453–466. [CrossRef]
69. Leyssens, C.; Verlinden, L.; Verstuyf, A. The future of vitamin D analogs. *Front. Physiol.* **2014**, *5*, 122. [CrossRef] [PubMed]
70. Maestro, M.A.; Molnár, F.; Carlberg, C. Vitamin D and its synthetic analogs. *J. Med. Chem.* **2019**, *62*, 6854–6875. [CrossRef]
71. Tanaka, Y.; DeLuca, H.F.; Kobayashi, Y.; Ikekawa, N. 26,26,26,27,27,27-Hexafluoro-1,25-dihydroxyvitamin D₃: A highly potent, long-lasting analog of 1,25-dihydroxyvitamin D₃. *Arch. Biochem. Biophys.* **1984**, *229*, 348–354. [CrossRef]

72. Harada, M.; Miyahara, T.; Miyata, M.; Tomita, I.; Okayachi, H.; Ikemoto, Y.; Higuchi, S.; Otomo, S.; Kozuka, H.; Ikekawa, N. Effects on cultured neonatal mouse calvaria of $1\alpha,25$ -dihydroxyvitamin D₃, 26,26,26,27,27,27-hexafluoro- $1\alpha,25$ -dihydroxyvitamin D₃ and 26,26,26,27,27,27-hexafluoro- $1\alpha,23S,25$ -trihydroxyvitamin D₃. *Bone Miner.* **1992**, *18*, 41–49. [CrossRef]
73. Inaba, M.; Okuno, S.; Nishizawa, Y.; Imanishi, Y.; Katsumata, T.; Sugata, I.; Morii, H. Effect of substituting fluorine for hydrogen at C-26 and C-27 on the side chain of $1,25$ -dihydroxyvitamin D₃. *Biochem. Pharmacol.* **1993**, *45*, 2331–2336. [CrossRef]
74. Sakaki, T.; Sawada, N.; Abe, D.; Komai, K.; Shiozawa, S.; Nonaka, Y.; Nakagawa, K.; Okano, T.; Ohta, M.; Inouye, K. Metabolism of 26,26,26,27,27,27-F₆- $1\alpha,25$ -dihydroxyvitamin D₃ by CYP24: Species-based difference between humans and rats. *Biochem. Pharmacol.* **2003**, *65*, 1957–1965. [CrossRef]
75. Kasai, N.; Sakaki, T.; Shinkyō, R.; Ikushiro, S.; Iyanagi, T.; Ohta, M.; Inouye, K. Metabolism of 26,26,26,27,27,27-F₆- $1\alpha,23S,25$ -trihydroxyvitamin D₃ by human UDP-glucuronosyltransferase 1A₃*. *Drug Metab. Dispos.* **2005**, *33*, 102–107. [CrossRef]
76. Kobayashi, Y.; Taguchi, T.; Kanuma, N. Synthesis of 26,26,26,27,27,27-hexafluoro-25-hydroxyvitamin D₃. *J. Chem. Soc. Chem. Commun.* **1980**, 459–460. [CrossRef]
77. Kobayashi, Y.; Taguchi, T.; Mitsunashi, S.; Eguchi, T.; Ohshima, E.; Ikekawa, N. Studies on organic fluorine compounds. XXXIX. Studies on steroids. LXXIX. Synthesis of $1\alpha,25$ -dihydroxy-26,26,26,27,27,27-hexafluorovitamin D₃. *Chem. Pharm. Bull.* **1982**, *30*, 4297–4304. [CrossRef]
78. Ohira, Y.; Taguchi, T.; Iseki, K.; Kobayashi, Y. Preparation of (22S)- and (22R)-24-homo-26, 26, 26, 27, 27, 27-hexafluoro- $1,22,25$ -trihydroxy-24-yne-vitamin D₃. *Chem. Pharm. Bull.* **1992**, *40*, 1647–1649. [CrossRef]
79. Wu, Y.; Sabbe, K.; De Clercq, P.; Vandewalle, M.; Bouillon, R.; Verstuyf, A. Vitamin D₃: Synthesis of seco C-9,11,21-trisnor-17-methyl- $1\alpha,25$ -dihydroxyvitamin D₃ analogues. *Bioorg. Med. Chem. Lett.* **2002**, *12*, 1629–1632. [CrossRef]
80. Sigüeiro, R.; Maestro, M.A.; Mouriño, A. Synthesis of side-chain locked analogs of $1\alpha,25$ -dihydroxyvitamin D₃ bearing a C17 methyl group. *Org. Lett.* **2018**, *20*, 2641–2644. [CrossRef]
81. Kawagoe, F.; Sugiyama, T.; Uesugi, M.; Kittaka, A. Recent developments for introducing a hexafluoroisopropanol unit into the vitamin D side chain. *J. Steroid Biochem. Mol. Biol.* **2018**, *177*, 250–254. [CrossRef]
82. Asano, L.; Watanabe, M.; Ryoden, Y.; Usuda, K.; Yamaguchi, T.; Khambu, B.; Takashima, M.; Sato, S.; Sakai, J.; Nagasawa, K.; et al. Vitamin D metabolite, 25-hydroxyvitamin D, regulates lipid metabolism by inducing degradation of SREBP/SCAP. *Cell Chem. Biol.* **2017**, *24*, 207–217. [CrossRef] [PubMed]



Article

The Cytotoxic Effect of Copper (II) Complexes with Halogenated 1,3-Disubstituted Arylthioureas on Cancer and Bacterial Cells

Alicja Chrzanowska ¹, Aleksandra Drzewiecka-Antonik ², Katarzyna Dobrzyńska ³, Joanna Stefańska ⁴, Piotr Pietrzyk ⁵, Marta Struga ¹ and Anna Bielenica ^{1,*}

- ¹ Chair and Department of Biochemistry, Medical University of Warsaw, 02-097 Warszawa, Poland; achrzanowska@wum.edu.pl (A.C.); mstruga@wum.edu.pl (M.S.)
² Laboratory of X-ray and Electron Microscopy Research, Institute of Physics, Polish Academy of Sciences, 02-668 Warszawa, Poland; adrzew@ifpan.edu.pl
³ Students' Scientific Society at Department of Pharmaceutical Microbiology, Faculty of Pharmacy, Warsaw Medical University, 02-097 Warszawa, Poland; k-dobrzynska@o2.pl
⁴ Department of Pharmaceutical Microbiology, Centre for Preclinical Research, Medical University of Warsaw, 02-097 Warszawa, Poland; jstefanska@wum.edu.pl
⁵ Inorganic Chemistry Department, Faculty of Chemistry, Jagiellonian University, 30-387 Kraków, Poland; pietrzyk@chemia.uj.edu.pl
* Correspondence: abielenica@wum.edu.pl; Tel.: +48-022-572-0693; Fax: +48-022-572-0679

Citation: Chrzanowska, A.; Drzewiecka-Antonik, A.; Dobrzyńska, K.; Stefańska, J.; Pietrzyk, P.; Struga, M.; Bielenica, A. The Cytotoxic Effect of Copper (II) Complexes with Halogenated 1,3-Disubstituted Arylthioureas on Cancer and Bacterial Cells. *Int. J. Mol. Sci.* **2021**, *22*, 11415. <https://doi.org/10.3390/ijms222111415>

Academic Editor: Valentina Gandin

Received: 14 September 2021

Accepted: 19 October 2021

Published: 22 October 2021

Publisher's Note: MDPI stays neutral with regard to jurisdictional claims in published maps and institutional affiliations.



Copyright: © 2021 by the authors. Licensee MDPI, Basel, Switzerland. This article is an open access article distributed under the terms and conditions of the Creative Commons Attribution (CC BY) license (<https://creativecommons.org/licenses/by/4.0/>).

Abstract: A series of eight copper (II) complexes with 3-(4-chloro-3-nitrophenyl)thiourea were designed and synthesized. The cytotoxic activity of all compounds was assessed in three human cancer cell lines (SW480, SW620, PC3) and human normal keratinocytes (HaCaT). The complexes **1**, **3**, **5**, **7** and **8** were cytotoxic to the studied tumor cells in the low micromolar range, without affecting the normal cells. The complexes **1**, **3**, **7** and **8** induced lactate dehydrogenase (LDH) release in all cancer cell lines, but not in the HaCaT cells. They provoked early apoptosis in pathological cells, especially in SW480 and PC3 cells. The ability of compounds **1**, **3**, **7** and **8** to diminish interleukin-6 (IL-6) concentration in a cell was established. For the first time, the influence of the most promising Cu (II) complexes on intensities of detoxifying and reactive oxygen species (ROS) scavenging the enzymes of tumor cells was studied. The cytotoxic effect of all copper (II) conjugates against standard and hospital bacterial strains was also proved.

Keywords: copper (II) complexes; thiourea; cytotoxic activity; proteome analysis; antimicrobial activity

1. Introduction

Enzymes incorporate transition metal cofactors to perform a wide range of metabolic reactions. Among metal cations, copper (II) ions play an essential function in the human organism, being a structural component of several enzymatic proteins, such as ascorbate oxidase, ceruloplasmin, amine oxidase, cytochrome C oxidase, nitrite reductase and superoxide dismutase Cu–Zn (SODC) [1,2]. Complexes of organic chelators with Cu (II) have been receiving increased attention due to their potential biomedical applications, such as cytotoxic or antibacterial activities. Within a group of acylthiourea ligands, those containing electron-withdrawing chloro- and nitro-substituents were effective against adenocarcinoma cell lines [3]. Intercalating properties of N-(2-hydroxyethyl)-N'-benzoylthiourea-Cu (II) complexes with strong deoxyribonucleic acid (DNA) binding and cleavage abilities were denoted [4]. Chelates with orthophenanthroline units studied by Pivetta et al. exerted high cytotoxic affect against acute leukemia and other carcinomas [5]. Moreover, a wide antibacterial profile of copper-based thiourea coordinates of 4-azatricyclo-3,5-dione [6] and 3-(trifluoromethyl)aniline was also studied. Their inhibitory effect on bacterial topoisomerases was also established [7].

Requirements for safer, more active and more selective chemotherapeutics have stimulated the search for other metal-based antitumor candidates. First of all, investigations in the treatment of cancer diseases are oriented to synthesize new analogues of cisplatin, a platinum (II) coordinate and chemotherapeutic drug effective against various types of tumors. Recently published Pd (II) and Pt (II) complexes of *N*-allylthioureas containing morpholine and *tert*-butylamine moieties showed proapoptotic and cytostatic influence on HeLa (Henrietta Lacks) cell culture stronger or comparable with cisplatin [8]. Antitumor properties of structurally similar coordinates based on pyrazol-3-ylpyridine fragments were connected with their inducing effect on cell accumulations in the S phase (HeLa cells) and a reduction of cell subpopulations in G₂/M and G₀/G₁ phases (pancreatic cancer cells) [9]. Among tested palladium complexes of *N*, *N*-disubstituted thioureas, those endowed with furoyl and ethyl groups were the most effective against human breast cancer cells, as compared to the platinum-derived standard drug [10]. On the other hand, Marverti et al. [11] introduced a series of thiourea-Pd (II) compounds that acted as productive growth inhibitors of cisplatin-sensitive ovarian cancer cell lines and their resistant counterparts. Coordinates altered malignant cell metabolism via inhibition of thymidylate synthase and dihydrofolate reductase expression. Interestingly, photoactivated platinum (IV) azide dipyrindine complexes bonded strongly to the nuclear DNA of tumor cells and blocked ribonucleic acid (RNA) polymerase II more efficiently than conventional adducts of cisplatin [12]. Platinum (II)-acridine hybrids linked to the amidine group [13] have shown inhibition of lung cancer cell proliferation and a promising antitumor potency in mouse xenograft models. In contrast, cationic gold (I) complexes of thiourea containing an acridine core are devoid of cytotoxic properties. However, they exert remarkable activity against *M. tuberculosis* [14]. Gold (I) complexes of cyclic disubstituted 4-chlorophenylthiourea ligand severely affected mitochondrial respiration by inhibition of complexes II and IV of the respiratory chain and induced mitochondrial swelling, resulting in enhanced permeability of a membrane and its declined fluidity [15]. An alternative class of anticancer drugs has been identified within ruthenium (II)-arene compounds. The Ru (II)-acylthiourea organometallic complexes were found to be significantly cytotoxic towards lung [16–18], prostate [16] and breast [18] tumor cell cultures, inducing their apoptosis and reducing migration by interaction with human serum albumin. What is more, other results showed that silver (I) chelates of 2-benzimidazolylurea mediate a strong cytotoxic response to the tested breast cancer cell lines (MCF-7) and normal cells, but with better parameters than metallodrug cisplatin [19].

Reactive oxygen species (ROS), produced in the mitochondria, peroxisomes and endoplasmic reticulum, include highly reactive species such as hydroxyl and superoxide free radicals, singlet oxygen or less reactive hydrogen peroxide molecules. Regulation of ROS levels is crucial for cellular life, cell proliferation and differentiation. Under oxidative stress states, accumulation of ROS causes the damage of proteins, lipids and DNA, which contributes to carcinogenesis [20]. The expanded scavenging system of a cell is based on superoxide dismutases (SODs), glutathione peroxidase (GPX), glutathione reductase (GR), peroxiredoxins (PRDXs), thioredoxin and catalase (CAT), which neutralize reactive species or recover antioxidants to their reduced state [21]. In comparison with normal cells, an extent of ROS in cancer counterparts is higher, as they keep an improved antioxidant system [22]. What is more, expanded levels of GPX, CAT, glutathione and thioredoxin proteins are correlated with tumor aggression and its resistance to chemotherapy [22]. It was proved that a decline of ROS-scavenging capacity leads to apoptosis of malignant cells, especially when it is used in combination with ROS-increasing chemotherapeutics, such as 5-fluorouracil (therapy of colon cancer), celecoxib (prostate tumor) or doxorubicin (breast, liver cancers) [21,23–26]. Numerous organic complexes with transition metals are reported to induce autophagy and/or apoptosis by regulation of ROS. This group includes complexes of gold (I) with thiourea [15,27], ruthenium (II) coordinates with β -carboline [28], copper (II) complexes with 2-hydroxy-1-naphthaldehyde [29] and with the derivative of bipyridine-acetylacetonate (Casiopaina III-ia) [30]. The antioxidant abilities of coordi-

nates evaluated by the diphenyl-2,2-picrylhydrazyl/ N, N-diethyl-p-phenylenediamine (DPPH/DPD) method were also confirmed for ruthenium (III) chelates with 1-ethyl-3-phenylthiourea ligands [31] and copper (II) complexes with biuret or urea [32], as well as with auxin [33] or N-ethylpiperazine [34].

As a part of our research on developing biologically active 1,3-disubstituted thioureas [7,35–37], we have synthesized a series of halogenated copper (II) complexes of (4-chloro-3-nitrophenyl) thiourea and reported their cytotoxic, prooxidant and antimicrobial properties.

2. Results and Discussion

2.1. Synthesis of Complexes

Thiourea–Cu (II) coordination compounds **1–8** were prepared by the reaction of copper (II) chloride with 3-(4-chloro-3-nitrophenyl)thiourea compounds (Figure 1). The complexes were obtained with satisfactory yields (45–61%). The identification of the parent ligands **L1–L8**, using nuclear magnetic resonance (NMR) and mass spectroscopy, was described previously [37,38]. The derivatives chosen for complexation reactions came from a series of mono- (**L4–L6**) or di-halogenated (**L1–L3**, **L7**, **L8**) 1-phenylthioureas with the most promising bioactivity. The presented selection of the phenyl ring substituents in their structures allow for the analysis of the influence of the substitution isomerism, as well as the impact of electron-withdrawing elements on the biological properties of newly synthesized metal–organic compounds.

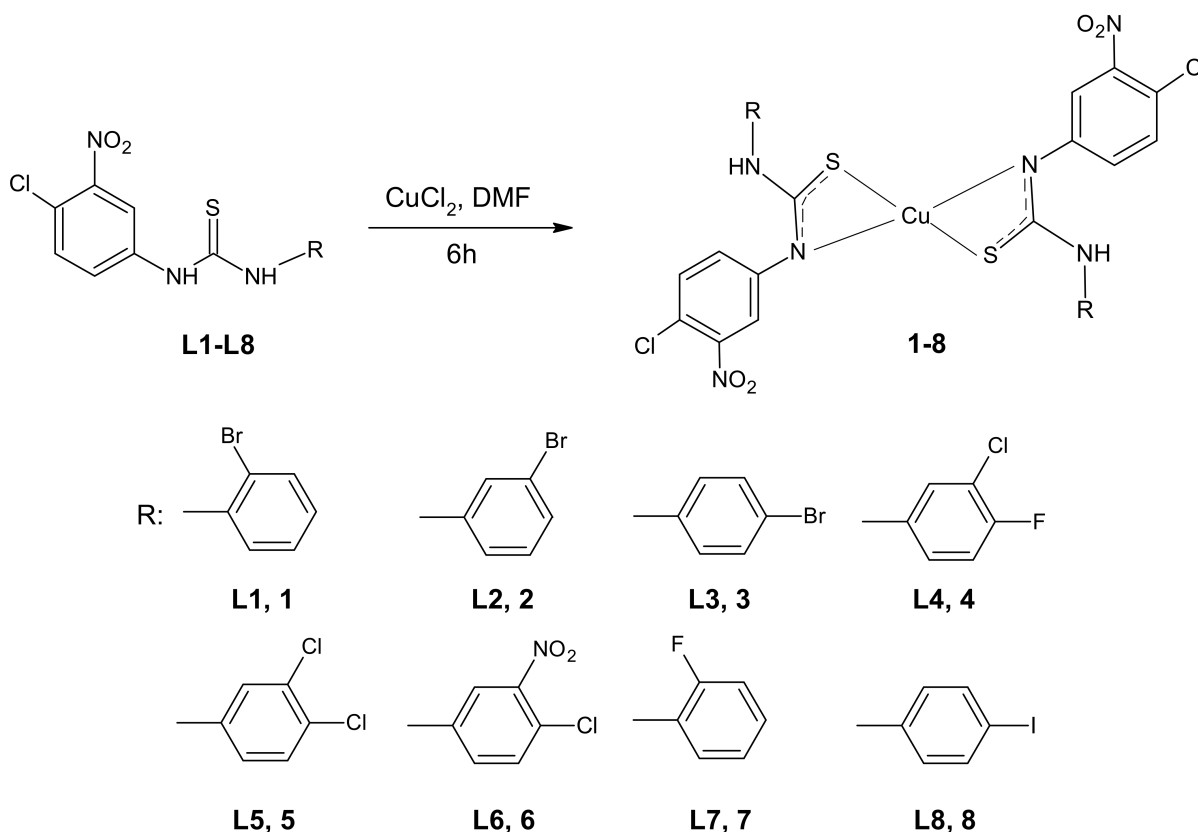


Figure 1. Scheme of the complexation reaction of the respective arylthiourea ligands **L1–L8** with proposed molecular structures of complexes **1–8** (DMF—dimethylformamide).

2.2. Structural Characterization of Complexes

The complexes were initially characterized by elemental analysis and infrared spectroscopy. During all complexation reactions, disubstituted thiourea acts as bidentate ligand (L), forming a hydrated complex of the type CuL_2 . In order to determine the geometry of

metal–organic ligand complexes, ultraviolet–visible (UV–Vis) and electron paramagnetic resonance (EPR) spectroscopies have been applied.

The infrared spectra of ligands (L1–L8) exhibit a broad band with several maxima in the high-energy part (Figure 2), corresponding to the stretching vibrations of the N–H and C–H groups. In the spectra of Cu (II) complexes (1–8), this band widens (Figure 2), which confirms the presence of water molecules in the product of the complexation reactions. The molecules of the initial ligands (L1–L8) and their complexes (1–8) contain two N–H groups (Figure 1), which are reflected in two infrared absorption bands. These bands are in different positions in the spectra of a pair of free and bonded ligands (Figure 2, Table 1). This confirms deprotonation of one N-atom from the ligand's molecules and suggests different intermolecular interactions (N–H... X; X=O, Br, Cl, F, I hydrogen bonding patterns) in the crystal structure of free and bonded thioureas. The region of 1600–1400 cm^{-1} in the spectra of ligands (L1–L8) is dominated by the stretching vibrations of the C–C and C–N bonds. In the spectra of complexes (1–8), this feature is extended towards the higher frequencies (around 1700 cm^{-1} , Figure 2) as the consequence of increased intensities of asymmetric ring stretching modes within the molecules of complexes [7]. The spectral ranges: 1550–1500 cm^{-1} (NO_2 asymmetric stretching vibrations), 1360–1330 cm^{-1} (NO_2 symmetric stretching vibrations) and 1240–1040 cm^{-1} (C–halogen stretching modes) are quite similar for parent ligands and their Cu (II) complexes (Table 1), which excludes the interaction of the nitro group or the halogen atom with the metal cation. The bands corresponding to the C=S stretching vibrations are found around 1333 cm^{-1} and in the 854–832 cm^{-1} range in the uncomplexed ligand's spectra (Table 1). In the spectra of complexes, they are red shifted and observed at 1313–1300 cm^{-1} and 785–771 cm^{-1} regions (Table 1). This indicates that the ligands coordinate to the Cu (II) through the sulfur atom [39–41].

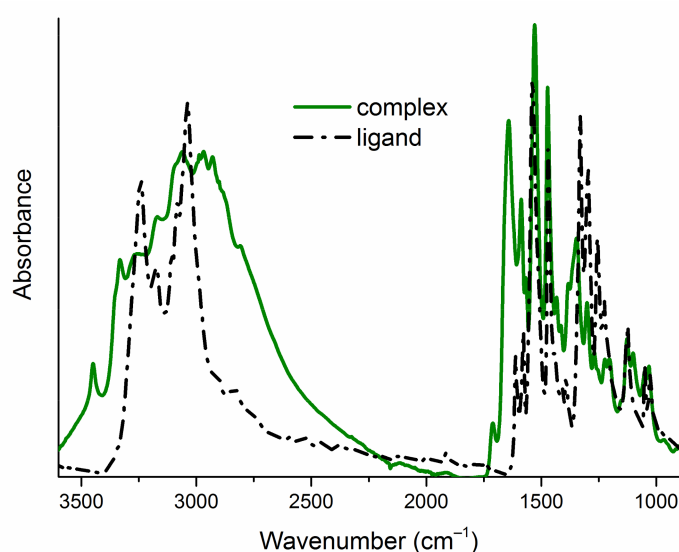
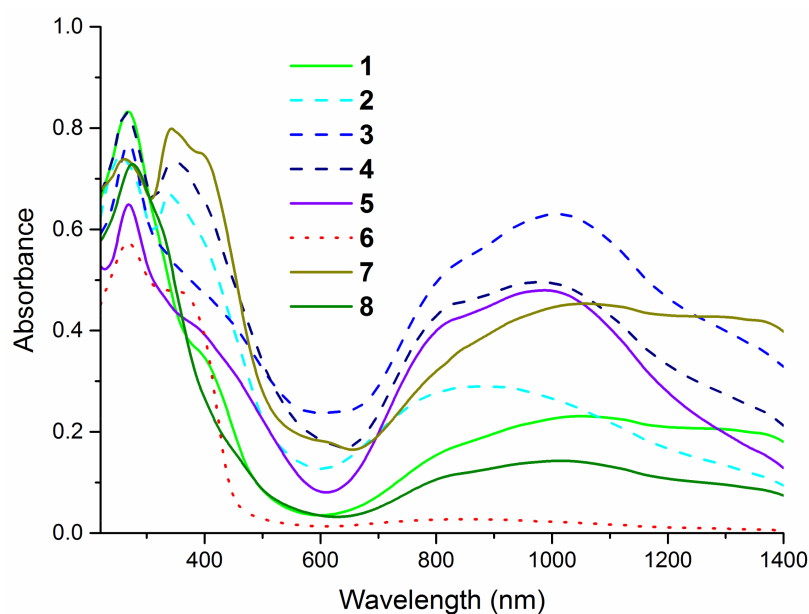


Figure 2. Attenuated total reflection infrared (ATR-IR) spectra of one exemplary pair of a free ligand (L5) and a complex (5) in the range of 3600–900 cm^{-1} . ATR-IR spectra of all studied compounds are gathered in the Supplementary Materials (Figure S1).

The electronic spectra of the complexes (Figure 3) exhibit the intense absorption bands in the region 230–300 nm corresponding to the $\pi \rightarrow \pi^*$ and $n \rightarrow \pi^*$ intra-ligand transitions. The presence of S \rightarrow Cu (II) ligand-to-metal charge transfer (LMCT band) around 400 nm is additional evidence of the coordination of thiourea ligands to the metal cation via sulfur atom [39,40,42]. All presented compounds show the $d-d$ bands in a wide region 650–1400 nm, which confirms the formation of four-coordinate complexes with copper in +2 oxidation state [41].

Table 1. Characteristic infrared absorption bands of N–H, NO₂, C=S and C–X (X = Br, Cl, F, I) groups. Band position in cm⁻¹, intensity: w is weak, m is medium, s is strong, vs is very strong, sh is shoulder, ^{as} is asymmetric, ^s is symmetric, * is broad band.

Compound	ν N–H	ν^{as} NO ₂	ν^s NO ₂	ν C=S	ν C–X
1	3470 w, 3372 m	1529 m *	1347 m *	1301 m, 782 w	1047 w
L1	3340 w, 3209 m	1537 sh, 1526 vs	1347 sh	1332 m, 832 m	1044 m
2	3444 w, 3395 w	1531 m *	1344 m *	1306 w, 776 w	1070 w
L2	3334 sh, 3250 m	1547 m, 1526 m	1352 m, 1333 s	1332 m, 834 w	1067 m
3	3448 w, 3333 w	1530 m *	1351 m *	1305 w, 774 sh	1071 w
L3	3361 w, 3317 s	1537 sh, 1525 s	1355 m *	–, 839 w	1070 m
4	3449 w, 3335 m	1531vs *	1344 m *	1311 m, 781 w	1051 m
L4	3365 sh, 3244 s	1546 m, 1525 s	1353 m, 1335 s	1335 m, 840 m	1049 m
5	3449 w, 3333 m	1529 vs *	1344 m *	1300 m, 779 sh	1050 m
L5	3348 sh, 3243 s	1539 vs, 1509 sh	1347 sh, 1331 s	1331 m, 835 m	1050 m
6	3449 w, 3340 m	1539 sh, 1519 vs	1341 m *	1313 m, 784 w	1044 m
L6	3327 s, 3243 m	1542 m, 1515 s	1353 w, 1333 m	1333 m, 837 sh	1047 m
7	3446 w, 3341 m	1532 m *	1346 m *	1313 m, 785 w	1236 w
L7	3325 s, 3242 m	1539 s, 1518 vs	1356 s, 1335 s	1335 m, 854 w	1232 w
8	3448 w, 3336 w	1532 m *	1350 m *	1307 w, 771 w	1057 w
L8	3364 s, 3314 m	1538 s, 1525 s	1350 s *	1331 sh, 833 sh	1059 m

**Figure 3.** Solid state ultraviolet–visible (UV–Vis) spectra of complexes in the range of 220–1400 nm.

EPR spectra of the investigated complexes **1–8** (Figure 4) are in agreement with the conjectures drawn based on the infrared (IR) and UV–Vis results. The obtained spectra indicate clearly the divalent state of copper upon complexation and are very characteristic of typical Cu (II) complexes. The signals were simulated assuming rhombic symmetry with the z component (parallel) split into four lines due to the hyperfine interaction between the unpaired electron and nuclear magnetic moment of copper ($I = 3/2$, ^{63,65}Cu). The splitting of the perpendicular line (x and y components) remains unresolved, yet it was necessary for obtaining the correct shape of the simulated spectra. Slight rhombicity of the spectra with $g_{zz} \gg g_{xx} > g_{yy}$ confirms dominant contribution of a single d-orbital ($3d_{x^2-y^2}$) in the semi-occupied molecular orbital. Exemplary parameters obtained for compound **5** are: $g_{xx} = 2.086$, $g_{yy} = 2.054$, $g_{zz} = 2.357$, A_{xx} and A_{yy} unresolved, $|A_{zz}| = 12.8$ mT. Similar parameters were recently reported for Cu (II) thiourea complexes [6,7]. The EPR parameters obtained for other complexes are very similar (12.6 mT $< |A_{zz}| < 12.8$ mT, $2.353 < g_{zz} < 2.358$), which strongly indicates very similar coordination around the copper

center. It is in agreement with the molecular structure of the complexes (with two thiourea ligands chelated to the Cu (II) cation via deprotonated N and thiocarbonyl S atoms), which differ only in the substituents of thiourea ligands (Figure 1). Such modification has only a minute effect on the first coordination sphere of copper, to which continuous wave EPR is sensitive. No features characteristic of Cu dimer in solution were observed, e.g., a forbidden magnetic dipolar transition at half-field with $g = 4$ value.

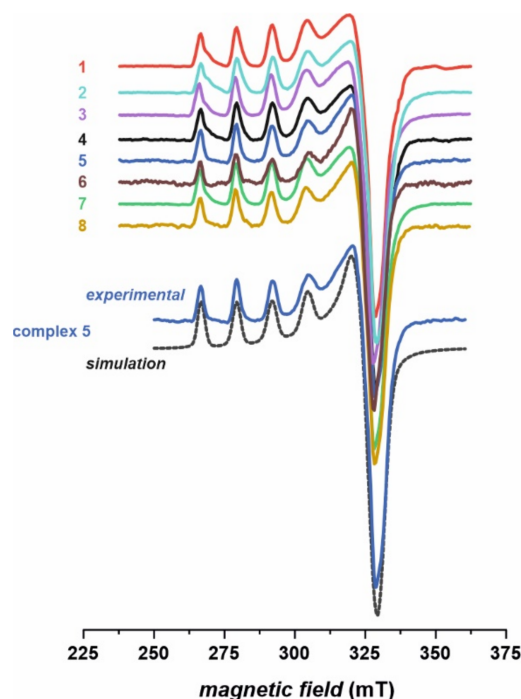


Figure 4. Frozen solution (77 K) X-band electron paramagnetic resonance (EPR) spectra of complexes 1–8, along with exemplary computer simulation of spectrum for the complex 5.

The molecular structure proposed for compounds 1–8, in which the Cu (II) cation is the part of two four-membered rings (Cu-S-C-N, see Figure 1), is quite unusual for copper. However, this type of coordination was reported for one crystal structure determined by Singh et al. [43]. They found Cu (II) ions being chelated by two thiourea ligands in a trans manner and the distorted square-planar geometry of the complex was stabilized by electron delocalization in chelate rings. Moreover, such coordination was postulated by some of the authors of the current study for another series of Cu (II) complexes, namely for 3-(trifluoromethyl)phenylthiourea derivatives [7] and thioureas containing tricyclic imide's part [6,41]. Structural characterization of those complexes, possibly owing to the combination of several experimental laboratory and synchrotron techniques (including X-ray absorption spectroscopy) and molecular modelling, indicated that 1,3-disubstituted thiourea ligands coordinate to Cu (II) cation in bidentate fashion through S and N atoms, forming a four membered 1,3-N, S chelate ring (as presented in Figure 1 for compounds 1–8).

2.3. Biological Studies

2.3.1. Anticancer Activity

MTT Assay

In vitro cytotoxicity studies of synthesized thiourea complexes 1–8 were assessed by standard 3-(4,5-dimethylthiazol-2-yl)-2,5-diphenyltetrazolium bromide (MTT) bioassay in different cancer cells at 72 h of drug exposure (Table 2). The ability of compounds to inhibit cell proliferation was established by means of their half-maximal inhibitory concentration (IC₅₀) values towards the human tumor cell lines, such as SW480 (primary colon cancer),

SW620 (metastatic colon cancer) and PC3 (metastatic prostate cancer), as well as against the non-tumor cell line HaCaT (immortal keratinocytes).

Table 2. Cytotoxic activity (IC_{50} , μM) of studied compounds estimated by the MTT assay ^a.

Compound	R	Cancer Cells						Normal Cells
		SW480 ^d		SW620 ^e		PC3 ^f		HaCaT ^g
		IC_{50} ^b	SI ^c	IC_{50}	SI	IC_{50}	SI	IC_{50}
1	2-Br-Ph	4.7 ± 0.3	23.2	3.3 ± 0.2	33.2	9.7 ± 0.1	11.5	109.6 ± 3.4
2	3-Br-Ph	24.3 ± 2.6	6.8	22.3 ± 1.8	7.5	19.2 ± 2.2	8.7	167.2 ± 2.3
3	4-Br-Ph	11.9 ± 2.1	8.6	19.2 ± 2.3	5.3	8.8 ± 0.8	11.7	103.2 ± 3.2
4	3-Cl,4-F-Ph	19.2 ± 1.1	6.3	21.6 ± 2.9	5.7	23.2 ± 1.6	5.2	120.9 ± 5.2
5	3-Cl,4-Cl-Ph	20.6 ± 2.1	8.1	10.8 ± 2.6	15.2	11.4 ± 2.4	14.4	164.9 ± 4.7
6	3-NO ₂ ,4-Cl-Ph	26.8 ± 2.3	4.6	21.5 ± 1.4	5.7	20.3 ± 3.1	6.1	123.2 ± 2.1
7	2-F-Ph	15.5 ± 2.6	8.9	9.1 ± 0.8	12.8	10.8 ± 1.3	5.5	138.3 ± 4.4
8	4-I-Ph	3.9 ± 0.8	26.3	17.8 ± 1.3	5.7	4.3 ± 0.5	23.8	102.7 ± 3.4
Doxorubicin ^h		0.75 ± 0.1	0.4	0.26 ± 0.1	1.1	0.31 ± 0.1	0.9	0.29 ± 0.1
Cisplatin ⁱ		10.4 ± 0.9	0.6	6.7 ± 1.1	0.9	13.2 ± 2.1	0.5	6.3 ± 0.7
CuCl ₂ ^j		109.4 ± 7.6	1.0	96.3 ± 5.2	1.2	106.5 ± 6.3	1.1	114.3 ± 4.8

^a MTT: 3-(4,5-dimethylthiazol-2-yl)-2,5-diphenyltetrazolium bromide. Data are expressed as mean standard deviation (SD);

^b IC_{50} (half-maximal inhibitory concentration, μM): the concentration of the compound that corresponds to a 50% growth inhibition of the cell line (as compared to the control) after culturing the cells for 72 h with the individual compound; ^c the SI (selectivity index) was calculated using the formula $SI = IC_{50}$ for normal cell line/ IC_{50} cancer cell line; ^d human primary colon cancer (SW480); ^e human metastatic colon cancer (SW620); ^f human metastatic prostate cancer (PC3); ^g human immortal keratinocyte cell line from adult human skin (HaCaT);

^{h,i,j} the reference compounds.

The 1,3-disubstituted arylthiourea complexes **1**, **3**, **5**, **7** and **8** were cytotoxic to studied cancer cells at concentration $\leq 10 \mu M$. The monohalogen derivatives **1** and **8** showed cytotoxic activity in the low micromolar range in all tested pathological cell lines. Their IC_{50} values ranged from 3.3 ± 0.2 to $9.7 \pm 0.1 \mu M$ (compound **1**) and between 3.9 ± 0.8 and $17.8 \pm 1.3 \mu M$ for compound **8**. In particular, they both were strongly potent towards SW480 cells (at 3.9 ± 0.8 and $4.7 \pm 0.3 \mu M$), whereas derivative **1** was against SW620 (at $3.3 \pm 0.2 \mu M$) and derivative **8** towards the PC3 cell line (with IC_{50} of $4.3 \pm 0.5 \mu M$).

The 4-bromophenyl compound (**3**) exerted remarkable growth-inhibiting activity mainly against PC3 cells ($8.8 \pm 0.8 \mu M$). On the other hand, the 2-fluorophenyl-containing molecule **7** exerted the highest IC_{50} values for SW480 and PC3 cell lines (9.1 ± 0.8 and $10.8 \pm 1.3 \mu M$, respectively). Dichlorophenyl derivative **5** was potent against SW620 cancer cells at $10.8 \pm 2.6 \mu M$.

In general, the PC3 cell line was the most sensitive to the presence of new complexes, and substances **1**, **3** and **8** appeared the most effective in the inhibition of their rise. The same set of compounds acted the strongest against primary cancerous SW480 cells. In contrast, for substances **1**, **5** and **7**, the lowest IC_{50} indexes for metastatic SW620 cells were denoted. The cytotoxicity of other tested derivatives (**2**, **4**, **6**) towards pathological cell lines was moderate, with IC_{50} values from 19.2 ± 1.1 to $26.8 \pm 2.3 \mu M$.

The studied thiourea complexes were non-cytotoxic against normal HaCaT cell lines ($IC_{50} > 100 \mu M$). The highest selectivity indexes (SI) were observed for the most promising derivatives: **1** (33.2 vs. SW620; 23.3 for SW480) and **8** (26.3 vs. SW480; 23.8 vs. PC3 cells). The selectivity factors of other complexes **2–7** were in the range of $4.6–8.9$ (SW480), $5.3–15.2$ (SW620) and $5.2–14.4$ (PC3 cell line). These indexes were incomparably greater than those of the reference doxorubicin and cisplatin (SI between 0.4 and 1.1), which proves a low toxicity of tested complexes towards health cells.

As compared to cisplatin, the cytotoxic properties of the synthesized diarylthiourea derivatives were considerably stronger. Complexes **1**, **3**, **5**, **7** and **8** were 1.2–3.1-fold more active against human PC3 cell lines. Additionally, both studied colon cancer cell lines appeared to be 2–2.7 times more sensitive to the presence of coordination compounds **1** and **8** than cisplatin, one of the most frequently used chemotherapy drugs.

The present study reveals that monohalogen substituted phenylthiourea complexes (**1–3**, **7**, **8**) possess stronger cytotoxic properties in human cancer cell lines, when compared to disub-

stituted derivatives (4–6). The moderately electronegative atom, such as bromine or iodide at the ortho (1,7) or para (3, 8) position of the aromatic ring, was responsible for enhanced cytotoxicity in the MTT model. The location of an element at meta position (2) resulted in a severalfold reduction in anticancer activity. Among disubstituted halogen coordinates, the 3,4-dichlorophenyl derivative (5) appeared to be the most effective towards SW620 and PC3 cells. The substitution of the benzene with chlorine and nitro group together provided a less promising drug candidate (6), with IC_{50} at least $20.3 \pm 3.1 \mu\text{M}$ against all tested cancer cells. Comparing pairs 7 (2-fluorophenyl-) and 4 (4-fluoro-3-chlorophenylthiourea), an introduction of the second halogen to the molecule led to the twofold decrease in cytotoxic activity vs. metastatic SW620 and PC3 cell lines. In fact, the location of two different groups in both third and fourth position of the ring was not beneficial on biological activity (4,6). Only 3,4-dichlorophenyl complex (5) restrained the potency in the low micromolar range, as compared to its monohalogen analogs 3 and 7. To sum up, the phenyl ring substituents can be arranged in order of their decreasing impact on bioactivity as follows: 2-bromo > 4-iodo > 2-fluoro > 4-bromo > 3,4-dichloro >> 3-chloro-4-fluoro > 3-bromo > 3-nitro-4-chloro. It is worth noting that all of them were at least 350 times less toxic for normal HaCaT cell lines than reference doxorubicin.

As reported, the cytotoxicity of standard copper (II) chloride towards cancer cells was negligible in comparison with thiourea derivatives. Its C_{50} ranged between 96.3 and 109.4 μM , and the salt was nontoxic for normal cells ($IC_{50} > 100 \mu\text{M}$). DMF, an organic solvent that contaminates synthesized complexes, has already been tested on various cells and appears to be nontoxic at the concentrations used in our synthesis (see in the Supplementary Material section). Considering an influence of starting ligands L1–L8 on studied cell lines, the derivative L5, at the concentration 8 μM , caused an approximately 20% decrease in HaCaT cell viability, which indicated its weak cytotoxic impact against normal cells [36]. In contrast, new complexes are devoid of visible influence on keratinocytes. In preliminary tests published previously, ligands L1, L3–L5 and L8 influenced the growth of other cancer cells, such as human leukemia and solid (melanoma, prostate) tumors, as well as normal tissue foreskin fibroblasts [36]. These results encouraged us to proceed with deeper investigations on the cytotoxicity mechanism of complexes 1–8.

LDH Assay

The lactate dehydrogenase (LDH) release assay was used to determine the level of plasma membrane damage of the most distinctive derivatives 1, 3, 7, 8. They were studied at concentrations of 10–60 μM against cancer cell lines and 60–120 μM towards normal HaCaT cells.

The LDH release curve results (Figure 5) demonstrated that the applied amounts of complexes did not affect the normal keratinocytes viability, as the secretion of LDH in their presence varied from 1.3% to 5.7%. The 4-iodophenylthiourea complex 8 exerted the highest cytotoxicity against all three tumor cell lines. This effect was the most evident in PC3 and SW480 cells, compared to SW620. When used at 60 μM , the derivative 8 achieved 64% LDH release in PC3 cells and 58% in SW480 cell lines. LDH secretion in these cells accounted for other complexes, used at the highest concentrations, ranging from 19% to 32%. The compound 8, applied in a dose of 40 and 20 μM , also expressed an increased response against SW480 cells (LDH release was 46.4% and 42%, respectively). Similarly, the LDH leakage induced in PC3 cells by this derivative used at lower concentrations differed from 56.4% (40 μM) to 27.2% (10 μM). On the other hand, the number of lysed SW620 cells evoked by the presence of the 2-bromophenylthiourea complex 1 ranged from 48% (at 60 μM) to 22% (10 μM applied), and incubation of these cell lines with the derivative 8 expressed similar enzyme releases of 42.4% and 23%, respectively. 2-fluorophenyl compound 7, studied at its highest dose, was less cytotoxic and achieved 30.2% LDH secretion.

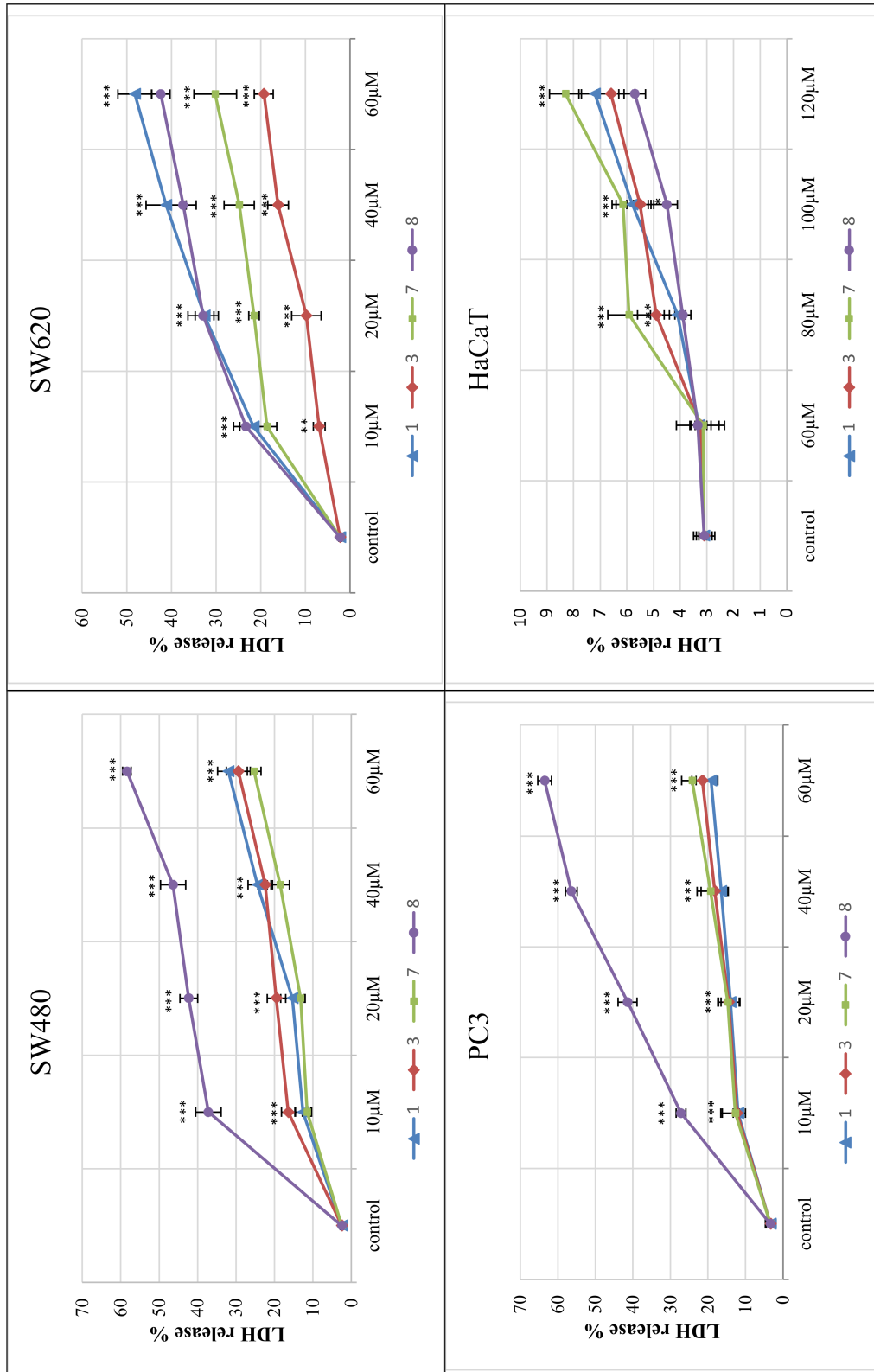


Figure 5. Lactate dehydrogenase (LDH) release as a marker of cell death in the SW480, SW620, PC3 and HaCaT cells, treated for 72 h with different concentrations of compounds **1**, **3**, **7** and **8**. LDH release in the HaCaT was analyzed after treatment with higher doses of compounds. *** $p \leq 0.001$ as compared to the control.

The reference cancer chemotherapeutic doxorubicin showed very high LDH release in all studied cancer cell lines, even when applied in lower doses. The LDH percentage for this compound at 1.5 μ M varied from 70% to 98%. However, its toxicity against normal HaCaT cells was significantly higher than examined complexes and accounted for 80%.

The data gained by the LDH activity assay are in an agreement with the results obtained for derivatives **1**, **3**, **7** and **8** by the MTT method.

Apoptotic Activity

To establish the anticancer mechanism of activity, SW480, SW620 and PC3 cells were incubated for 72 h in the presence of the most promising monohalogeno complexes **1**, **3**, **7** and **8**, after which annexin content was measured by flow cytometry analysis. The apoptotic effect is shown in Figure 6 and Figure S2.

All studied compounds, applied in their IC_{50} doses, induced early apoptosis in pathological cells, especially in SW480 and PC3 cell lines, as compared to untreated cancerous controls. Derivatives of 2-bromophenyl- (**1**) and 4-iodophenylthiourea (**8**) revealed the most significant early-apoptosis-activating effect in primary colon cancer cell lines ($45.18\% \pm 3.9\%$ and $48.9\% \pm 3.4\%$, respectively). The influence of complexes bearing 4-bromophenyl (**3**) and 2-fluorophenyl (**7**) moieties in these cells was not so evident and did not exceed 40%. The most potent activators of apoptosis in metastatic PC3 cells were both para-substituted coordination compounds **3** and **8**, as they promoted the process in $45.5\% \pm 3.5\%$ and $45.7\% \pm 3.3\%$ of cells. On the other hand, complexes containing a halogen atom in ortho position of the benzene ring (**1** and **7**) induced the early apoptosis in one third of tested PC3 cells. The similar pro-apoptotic inducing effect of these two compounds was observed in metastatic colon cancer cells ($38.4\% \pm 2.4\%$ and $35.4\% \pm 2.8\%$). The incubation of these cells with derivatives **3** or **8** increased early apoptosis in only approximately 20%.

The studied set of thiourea complexes did not considerably promote the process of late apoptosis of cells, as compared to controls. Only the most cytotoxic derivative **8** had the late apoptosis activating property, in $20.7\% \pm 2.8\%$ of SW480 cells. It is also worth noting that tested coordination compounds **1**, **3**, **7** and **8** did not affect the level of early/late apoptosis in normal human keratinocytes (HaCaT), giving the result from 1.6% to 9.2% only.

In addition, conducted studies revealed that the referential doxorubicin was only a necrosis inducer. The number of SW480, SW620 and PC3 cells at the necrotic stage was 86%, 51% and 50%, respectively. Only in the case of PC3 cells, it induced late apoptosis as well (23%). HaCaT cells were considerably sensitive to doxorubicin, which produced a necrotic stage in 42% of cells, without affecting early and late apoptosis.

The obtained data comply with IC_{50} results found for mentioned cancer cells, particularly indicating the pro-apoptotic promoting role of complexes **1** and **8** in SW480 cells, as well as substances **3** and **8** in the prostate cancer cell line.

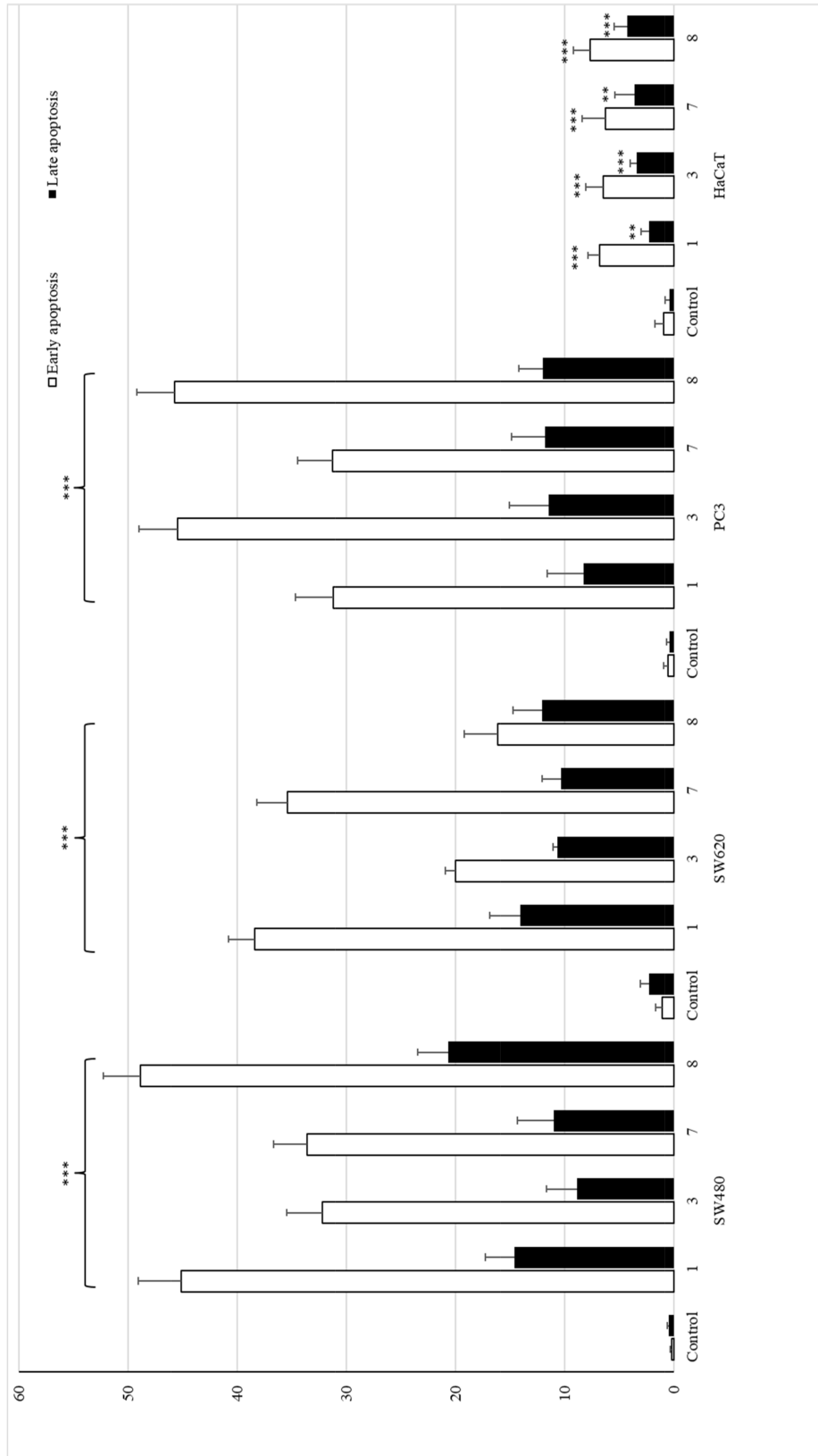


Figure 6. The effect of complexes 1, 3, 7 and 8 on early and late apoptosis, or necrosis in SW480, SW620, PC3 and HaCaT cells. Cells were incubated for 72 h with tested compounds used in their IC₅₀ concentrations. Then, cells were harvested, stained with annexin V-FITC and PI (fluorescein isothiocyanate and propidium iodide) and analyzed using flow cytometry. *** $p \leq 0.001$, ** $p \leq 0.01$ as compared to the control.

IL-6 Assay

Human interleukin-6 (IL-6) is a pro-inflammatory cytokine, involved in numerous biological processes such as inflammation, cell growth, apoptosis, aging or bone remodeling. The ability of compounds to diminish IL-6 concentration in a cell, as a measure of their anti-inflammatory properties, was established for the most cytotoxic copper (II) complexes of thiourea derivatives (1, 3, 7, 8).

As shown in Figure 7, tested derivatives applied in their IC₅₀ doses inhibited interleukin release in all evaluated cancer cell lines. Among them, the SW480 line was the most susceptible for the inhibition of the IL-6 secretion, elicited by the presence of evaluated substances. The 4-iodophenyl-containing complex (8) diminished the IL-6 level in these cells twofold. Similarly, the treatment of the primary colon cancer cells with 2-bromophenylthiourea coordinate (1) reduced the cytokine amount 1.9 times. However, the other complexes (3 and 7) decreased that level not more than by 30%, as compared to the controls. The effectiveness of the complex 1 in metastatic SW620 cells equaled to the referential doxorubicin. Both substances inhibited the concentration of IL-6 2.4 times, while other tested derivatives diminished its secretion by an average of 23%. The strongest effect in PC3 cells was denoted for the 4-iodophenylthiourea complex (8), which, just as doxorubicin, diminished the IL-6 secretion almost twofold. On the other hand, the incubation of PC3 cells with the 2-bromophenyl compound (1) lowered the IL-6 concentration 1.5 times, with weaker effect of other complexes (3 and 7).

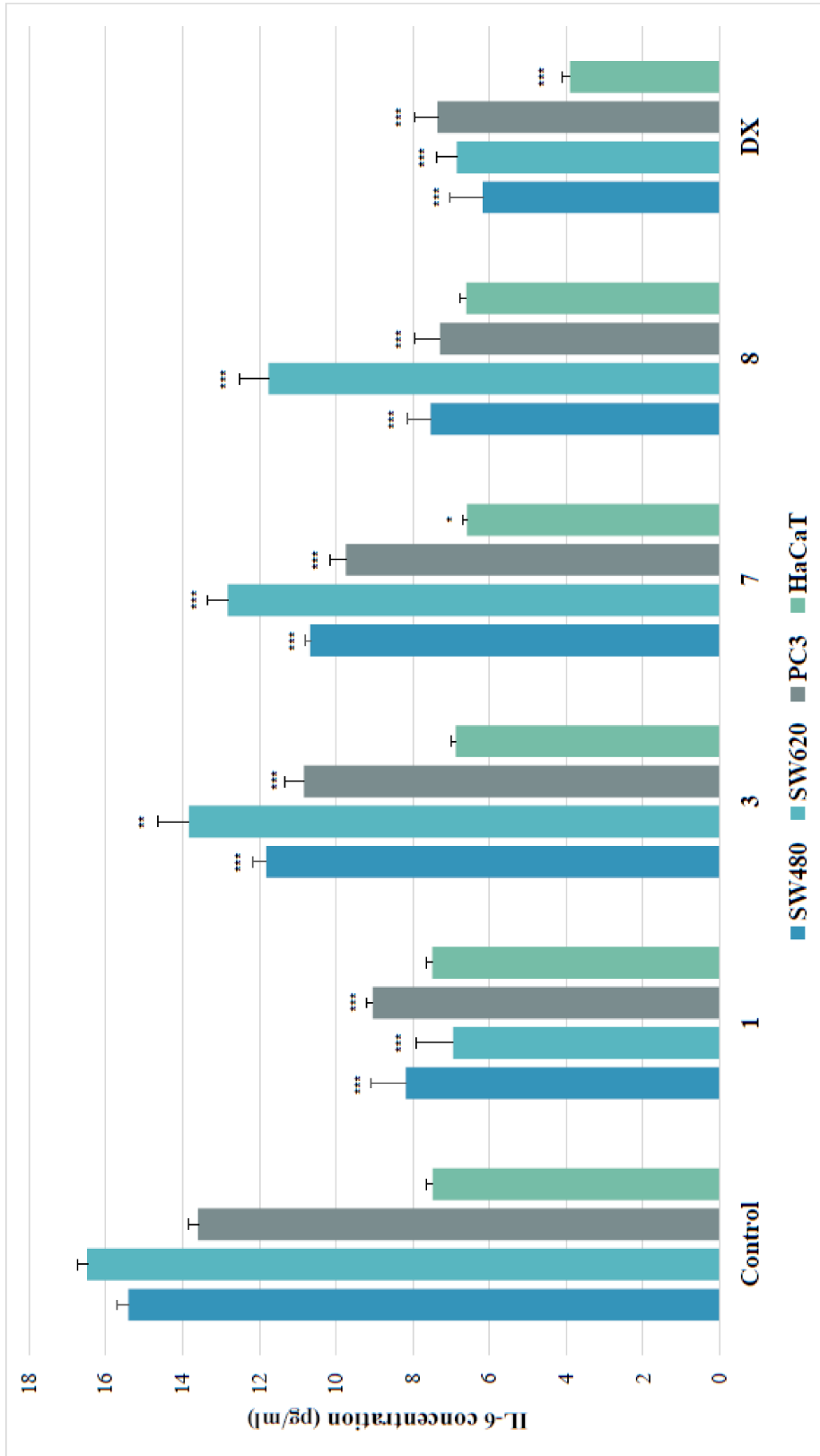


Figure 7. Effects of thiourea complexes **1**, **3**, **7** and **8** on IL-6 levels, measured by enzyme-linked immunosorbent assay (ELISA) test. Data are expressed as the mean \pm SD from three independent experiments performed in triplicate. *** $p \leq 0.001$, ** $p \leq 0.01$, * $p \leq 0.05$, as compared to the control. DX (doxorubicin) is the reference compound.

Proteomic Analysis of Antioxidant and Detoxifying Enzymes

To evaluate the impact of the tested compounds on antioxidant status, they were screened for their influence on intensities of selected detoxifying and ROS-scavenging enzymes, occurring in human cancer cell lines such as glutathione S-transferase (GST), glutathione reductase (GR), superoxide dismutase (SOD) and peroxiredoxin (PRDX) (Table 3 and Table S1).

All tested complex compounds, applied in their IC_{50} concentrations, reduced intensities of colon and prostate cancer enzymatic proteins, in most cases by at least 30% of a control. The types of studied thiourea terminal moieties can be arranged in order of their decreasing influence, as shown: 2-fluoro- (7), 4-bromo- (3), 4-iodo- (8) and 2-bromophenyl (1). The most susceptible for the presence of tested coordinates were the proteins of metastatic PC3 cells. The level of all tested enzymes in the PC3 cell was diminished, while simultaneously superoxide dismutase [Cu-Zn] (SODC), mitochondrial superoxide dismutase (Mn) (SODM) and the majority of PRDXs belonged to the most sensitive. The 2-fluorophenyl derivative (7) reduced the intensity of 12 prostatic enzymes by 20.8–87.6%. Among them, both types of SOD and mitochondrial PRDX3 were the most vulnerable; their intensities were reduced by at least 75%. The compound 3 diminished the amount of all tested proteins in the PC3 cells by 29.4–69.1%, affecting most significantly the levels of both SODs. Similarly, after treatment of the cells with the complex 8, the amount of 12 enzymes was reduced by 31.5–75.2%, including glutathione S-transferase A1 (GSTA1), SODs, PRDX3 and PRDX4, which intensities equaled about 30% of a control. After incubation with the coordinate 1, quantities of SODM and PRDX5 were diminished up to 29% of the initial level.

On the other hand, GSTA1, glutathione S-transferase P (GSTP1) and PRDX3 of metastatic SW620 cells were the most susceptible to the treatment with copper (II) complexes. The derivative 7 appeared to be the most powerful. It reduced intensities of all tested colon proteins by 32.5–63.9%, most heavily both GSTs (up to 63.6%) and SODs (55.3%). Other analogs (1, 3, 8) affected considerably mainly on GSTA1, leading to a 45.7% (compound 8) and 54.8% (complex 3) decrease in the amount of this protein, respectively.

The impact of the tested compounds on enzymes of the primary SW480 cells was also evident, but weaker than that observed for both metastatic lines. The quantitative changes affected mainly GSTA1, SODC and PRDX4. The derivative 7 exerted the strongest effect, reducing their intensities by 54.9%, 59.4% and 41.7%, respectively. Additionally, it diminished the amount of five other proteins by 28.4% or more. Complexes 1 and 3 acted similarly to their analogs, but they also affected smaller group of enzymes, most significantly mitochondrial glutathione reductase (GSHR) (compound 1) and PRDX4 (compound 3). The thiourea coordination compound 8 had the greatest relevance for GSTA1, giving 47.6% inhibition of its intensity.

Obtained results confirmed the cytotoxic effect of tested complexes by the decreasing of antioxidant influence on cytoplasmic and mitochondrial proteins of malignant cells, especially observed for derivatives 7 and 3.

According to the literature data, there are few evidences that suggest GSTs function in the cancer development and resistance of colon and prostate tumor cells to anticancer agents. Colon cancers reflected elevated levels of GST expression compared with normal mucosa [44]. It was observed that GST overexpression was related to a doxorubicin-resistance phenomenon [45]. Similarly, the high level of glutathione-S-transferase pi (GST-pi) was detected in prostate cancer cells, and it contributed to the development of drug resistance and a significant increase in the cell proliferation rate of androgen independent PC3 cells [46].

Likewise, an increased GR expression and activity was shown in colon tumors, where it was involved in cellular defense against ROS by producing a reduced form of GSH. This activity may favor tumor development [47]. It was also shown that this enzyme may protect PC3 cells under persistent ROS production induced by radiotherapy and chemotherapy. Therefore, GR activity depletion could lead to the intensified H_2O_2 toxicity in metastatic prostate cancer cells [48].

There are contradictory reports indicating the function of SOD enzymes on primary tumor proliferation and metastasis activity. It was shown that overexpression of SOD could increase cell differentiation, decrease proliferation and turn back a malignant phenotype [49]. Other studies demonstrated that high SOD expression correlates with colon tumor aggressiveness and with resistance to cytotoxic drugs and radiotherapy [50]. The loss of SOD1 expression by siRNA knockdown significantly increased prostate cell sensitivity to cytotoxic agents, confirming SOD1 participation in cellular response and resistance [51]. Some evidence has indicated SOD1 overexpression in cancers maintaining cellular ROS below the crucial threshold [52]. Suddenly, down-regulation of SOD2 itself was reported in breast cancer cell lines [53].

Table 3. Liquid chromatography–mass spectrometry (LC–MS) proteome analysis provided in the SW480, SW620 and PC3 cells treated for 24 h with IC₅₀ concentrations of complexes 1, 3, 7 and 8. Protein intensities were expressed as percentage of a control.

Accession	Name of Enzyme	Protein Intensity, %														
		SW480				SW620				PC3						
		Control	1	3	7	8	Control	1	3	7	8	Control	1	3	7	8
GSTA1_HUMAN	Glutathione S-transferase A1 OS = Homo sapiens OX = 9606 GN = GSTA1 PE = 1 SV = 3	100	78.3	86.6	75.6	91.6	100	50.2	45.2	36.4	54.3	100	84.4	70.6	79.2	73.5
GSTO1_HUMAN	Glutathione S-transferase omega-1 OS = Homo sapiens OX = 9606 GN = GSTO1 PE = 1 SV = 2	100	70.9	66.0	45.1	52.4	100	85.5	77.0	52.5	65.0	100	65.0	64.0	68.6	31.6
GSTP1_HUMAN	Glutathione S-transferase P OS = Homo sapiens OX = 9606 GN = GSTP1 PE = 1 SV = 2	100	84.8	75.9	80.9	83.0	100	74.4	64.5	67.3	57.5	100	95.0	51.1	35.8	64.1
GSHR_HUMAN	Glutathione reductase, mitochondrial OS = Homo sapiens OX = 9606 GN = GSR PE = 1 SV = 2	100	58.1	63.1	91.7	74.3	100	69.1	79.2	67.3	79.3	100	71.1	58.9	61.2	68.5
SODC_HUMAN	Superoxide dismutase [Cu-Zn] OS = Homo sapiens OX = 9606 GN = SOD1 PE = 1 SV = 2	100	68.2	75.3	40.6	88.2	100	72.7	78.2	44.7	64.5	100	58.5	30.9	15.4	33.0
SODM_HUMAN	Superoxide dismutase [Mn], mitochondrial OS = Homo sapiens OX = 9606 GN = SOD2 PE = 1 SV = 3	100	67.8	77.7	65.1	94.3	100	88.8	77.1	45.3	92.7	100	29.1	31.2	25.2	29.4
PRDX1_HUMAN	Peroxiredoxin-1 OS = Homo sapiens OX = 9606 GN = PRDX1 PE = 1 SV = 1	100	95.9	88.5	71.6	84.4	100	96.1	89.0	83.2	93.5	100	73.9	47.8	46.5	52.3
PRDX2_HUMAN	Peroxiredoxin-2 OS = Homo sapiens OX = 9606 GN = PRDX2 PE = 1 SV = 5	100	95.5	93.7	69.4	78.3	100	92.1	71.6	58.6	88.6	100	42.3	47.3	32.2	39.9
PRDX4_HUMAN	Peroxiredoxin-4 OS = Homo sapiens OX = 9606 GN = PRDX4 PE = 1 SV = 1	100	67.6	60.1	58.3	78.2	100	79.4	76.4	73.0	93.9	100	72.6	61.1	35.7	30.8
PRDX5_HUMAN	Peroxiredoxin-5, mitochondrial OS = Homo sapiens OX = 9606 GN = PRDX5 PE = 1 SV = 4	100	77.3	84.8	91.0	81.7	100	88.3	82.4	81.4	74.4	100	29.3	40.9	36.7	42.0
PRDX6_HUMAN	Peroxiredoxin-6 OS = Homo sapiens OX = 9606 GN = PRDX6 PE = 1 SV = 3	100	75.1	81.3	68.3	71.1	100	83.2	66.4	67.5	77.6	100	66.6	71.1	35.0	53.7
PRDX3_HUMAN	Thioredoxin-dependent peroxide reductase, mitochondrial OS = Homo sapiens OX = 9606 GN = PRDX3 PE = 1 SV = 3	100	95.2	85.4	90.4	96.3	100	69.9	67.5	61.2	95.2	100	69.5	57.3	12.4	24.8

Beyond the PRDX family protein's regulatory function on cytokine-induced hydrogen peroxide concentration, some members can act independently during their peroxidase activity on cell proliferation, differentiation, apoptosis and gene expression [54]. Recent studies highlight dual catalytic activities of PRDX1, because besides antioxidant activity it has a physiologically significant overoxidation site [55,56]. The positive PRDX1 immunohistochemical staining was strongly associated with a poor response to neoadjuvant chemoradiotherapy and a worse prognosis in rectal cancer patients [57]. The PRDX3 protein in antiandrogen resistant prostate cancer cell lines is responsible for increased tolerance to oxidative stress and a lack of activation of pro-apoptotic pathways. Therefore,

the knockdown of PRDX3 leads to an increased tendency to oxidative stress [58]. In vivo studies showed the up-regulation of both PRDX3 and PRDX4 in prostate tumors. It could be an attempt at adaptation of the cancer cells to the microenvironment in a way favorable for survival and proliferation rate, while maintaining their tumor's aggressiveness [59]

2.3.2. In Vitro Antimicrobial Activity

To assess the antimicrobial profile of coordination compounds 1–8, we assembled a panel of isolates, which included Gram-positive and Gram-negative organisms of clinical importance, as well as strains of fungal pathogens. The synthesized derivatives displayed significant to weak inhibitory effects towards standard staphylococci, as shown in Table 4. Derivatives of 3-chloro-4-fluorophenyl- (4) and 4-iodophenylthiourea (8) appeared to be the most active, with MIC values of 4 µg/mL. Bromophenyl compounds (1 and 3) and 3-nitro-4-chlorophenyl-containing complex (6) moderately inhibited the growth of *S. aureus* isolates, at concentrations from 4 to 8 µg/mL. The least potent monohalogen derivatives 2, 7 and dichlorophenyl complex 5 in doses of 16–32 µg/mL suppress the rise of staphylococcal rods. On the other hand, Gram-negative strains were weakly susceptible to the presence of tested thiourea coordinates (minimal inhibitory concentration, MIC ≥ 128 µg/mL). No evident antifungal properties were also observed; compounds 2, 3, 6 and 8, applied only at a dose of 64 µg/mL, exerted growth inhibitory properties towards studied *Candida* species

Table 4. In vitro activity of complexes 1–8 against standard bacterial and fungal strains—minimal inhibitory concentrations (MIC, µg/mL).

Strain	1	2	3	4	5	6	7	8	Ref. *	Ref. **
<i>S. aureus</i> NCTC 4163	8	16	8	4	32	8	32	4	0.25	-
<i>S. aureus</i> ATCC 25923	8	16	8	4	32	8	32	4	0.5	-
<i>S. aureus</i> ATCC 6538	8	16	8	4	32	8	32	4	0.25	-
<i>S. aureus</i> ATCC 29213	8	16	16	4	32	8	32	4	0.25	-
<i>S. epidermidis</i> ATCC 12228	16	16	16	4	32	8	32	8	0.25	-
<i>S. epidermidis</i> ATCC 35984	8	16	16	4	32	8	32	4	≤0.125	-
<i>E. coli</i> NCTC 10538	128	128	128	128	128	128	128	128	≤0.125	-
<i>E. coli</i> ATCC 25922	256	128	>256	128	128	128	256	128	≤0.125	-
<i>P. aeruginosa</i> ATCC 15442	128	128	128	128	128	128	>256	128	0.5	-
<i>P. aeruginosa</i> ATCC 27853	128	128	128	128	128	128	128	128	0.5	-
<i>C. albicans</i> ATCC 10231	≥256	64	64	128	128	64	128	64	-	0.5
<i>C. albicans</i> ATCC 90028	≥256	64	64	128	128	64	128	128	-	0.5
<i>C. parapsilosis</i> ATCC 22019	≥256	64	64	64	64	64	128	64	-	0.5

Ref. *—Ciprofloxacin, Ref. **—Fluconazole.

On extended testing, a series of copper (II) complexes showed activity against 30 clinical methicillin-resistant strains of *S. aureus* (MRSA) and *S. epidermidis* (MRSE) (Table 5), and their potency against most of above-mentioned cocci was severalfold higher than the reference ciprofloxacin. The derivative 3, possessing 4-bromophenyl substituent at the thiourea branch, exhibited its growth-inhibitory effect towards all evaluated hospital *S. aureus* rods with MIC of 4 µg/mL, whereas against most of *S. epidermidis* species at a dose of 4–8 µg/mL. The similar sensitivity of clinical isolates of *S. aureus* to the presence of 3-chloro-4-fluorophenyl complex (4) was observed. Monosubstituted compounds, containing bromine (1, 2), fluorine (7) and iodide (8) on the phenyl ring, also possessed a moderate antibacterial potency (MIC 4–8 µg/mL). However, complexes 3, 4, 7 and 8 were 64 times more active towards *S. aureus* 572 and 481 strains than ciprofloxacin, while the bioactivity of coordinates 1–4, 7 and 8 against six clinical *S. aureus* rods was 16–64 times stronger than the reference drug. Disubstituted derivatives 5 and 6 acted with lesser strength than their analogues incorporating one halogen in a molecule, but they were still 4–16 times more potent as compared to ciprofloxacin.

Table 5. In vitro activity of complexes 1–8 against hospital methicillin-resistant strains of *Staphylococcus aureus* (MRSA) and *Staphylococcus epidermidis* (MRSE)—minimal inhibitory concentrations (MIC, µg/mL).

Strain	1	2	3	4	5	6	7	8	Ref. *
<i>S. aureus</i> 498	8	8	4	4	16	32	4	8	0.5
<i>S. aureus</i> 537	8	8	4	4	16	32	8	8	256
<i>S. aureus</i> 567	8	8	4	4	16	32	4	8	0.5
<i>S. aureus</i> 568	8	8	4	4	16	32	8	8	0.5
<i>S. aureus</i> 573	8	8	4	4	16	32	8	8	128
<i>S. aureus</i> 585	8	8	4	4	16	32	8	8	256
<i>S. aureus</i> 586	4	8	4	4	16	32	8	8	0.5
<i>S. aureus</i> 495	8	8	4	4	16	32	8	4	0.5
<i>S. aureus</i> 496	8	8	4	8	32	32	8	8	0.25
<i>S. aureus</i> 497	8	8	4	8	16	32	8	8	256
<i>S. aureus</i> 514	8	8	4	4	32	32	8	4	128
<i>S. aureus</i> 522	8	8	4	4	16	32	8	4	256
<i>S. aureus</i> 572	8	8	4	4	16	32	4	4	256
<i>S. aureus</i> 481	8	8	4	4	16	32	4	4	256
<i>S. epidermidis</i> 420	4	8	8	4	32	64	8	8	0.5
<i>S. epidermidis</i> 423	8	8	4	4	32	64	8	8	0.5
<i>S. epidermidis</i> 424	8	8	4	8	32	64	8	8	16
<i>S. epidermidis</i> 469	8	8	4	4	32	64	8	8	0.5
<i>S. epidermidis</i> 471	8	8	8	8	32	64	8	8	32
<i>S. epidermidis</i> 510	8	8	4	8	16	64	8	8	0.5
<i>S. epidermidis</i> 511	8	8	4	4	32	64	8	8	32
<i>S. epidermidis</i> 515	4	8	8	4	32	64	8	8	32
<i>S. epidermidis</i> 431	8	8	4	8	16	64	8	8	8
<i>S. epidermidis</i> 432	8	8	4	8	32	64	8	8	64
<i>S. epidermidis</i> 433	4	8	4	4	32	64	8	4	64
<i>S. epidermidis</i> 435	8	8	4	8	32	128	8	8	0.25
<i>S. epidermidis</i> 436	8	8	4	8	32	128	8	8	≤ 0.125
<i>S. epidermidis</i> 437	8	8	8	8	32	128	8	8	0.5
<i>S. epidermidis</i> 438	8	8	4	8	32	128	8	8	≤ 0.125
<i>S. epidermidis</i> 513	8	8	4	8	16	64	8	8	0.5

Ref. *—Ciprofloxacin.

Most of the clinical strains of *S. epidermidis* were less susceptible to the presence of the synthesized complexes. However, derivatives **1**, **2**, **4**, **7** and **8** appeared to be 2–16 times more effective against *S. epidermidis* 424, 471, 511, 515 and 431–433 isolates than the reference chemotherapeutic. Similarly, weak antimicrobials, such as disubstituted compounds **5** and **6**, were still equally or more potent towards these cocci, as compared to ciprofloxacin.

To sum up, thiourea complexes incorporating a copper (II) ion expressed higher inhibitory growth properties against hospital than standard bacterial rods. What is more, their efficiency depended on the type of electronegative functionalities attached to the benzene ring. Derivatives incorporating 3-chloro-4-fluorophenyl- (**4**) and 4-iodophenyl substituents (**8**) showed the strongest effect towards both types of strains, while their 4-bromosubstituted analog (**3**) was powerful distinctly against clinical isolates. Ortho-substituted compounds, bearing bromine (**1**) or fluorine (**7**) atoms, shared a similar inhibitory activity when incubated with *Staphylococci*, but were weaker than the mentioned para-substituted. Comparing dihalogeno derivatives **4** and **5**, the replacement of the fluorine atom by chlorine led to a severalfold decrease of the antimicrobial potency. On the other hand, the compound possessing both chlorine and nitro group (**6**) was much more active against standard than hospital *S. aureus* species.

As proved by *Bacillus subtilis* rec-assay test, newly synthesized complexes 1–8 exerted no mutagenic and carcinogenic activities (Table S2). Thus, their antimicrobial effects were not linked with DNA-damaging potency.

As compared to results obtained for complexes, the antimicrobial activities of parental ligands were considerably higher [37]. MIC values of the most active ligands **L1–L5**, **L7** and **L8** against standard Staphylococcal strains ranged from 0.5 to 2 µg/mL. As expected, new copper (II) complexes were much more potent than copper (II) chloride itself (MIC ≥ 128 µg/mL for all strains). Although the complexation of halogen-containing

4-chloro-3-nitrophenylthioureas with copper (II) ion diminished their antibacterial properties [36,37], it incomparably increased their cytotoxicity towards various cancer cell lines, without influencing on normal keratinocytes.

Antimicrobial activity of the close analogs of the title complexes was previously described [6,7]. The formerly tested copper (II) complex of 1-(3-chloro-4-fluorophenyl)-3-[3-(trifluoromethyl)phenylthiourea, an analog of the complex 4 described in this paper, exerted comparable growth-inhibitory activity towards standard bacterial strains (MIC 4–256 µg/mL) [7]. The same level of activities of both compounds was observed for clinical strains (MIC 4–8 µg/mL). However, for the derivative of 3,4-dichlorophenylthiourea, the observed differences in bioactivity were considerable. The complex of 3-(trifluoromethyl)phenylthiourea inhibited the growth of Staphylococcal strains at 2 µg, whereas the coordinate of 1-(4-chloro-3-nitrophenyl)-3-(3,4-dichlorophenyl)thiourea (5) was only at 32 µg/mL. Variabilities in antibacterial actions were even higher when hospital strains were considered. The 3-(trifluoromethyl)phenylthiourea analog was 16–64 times more potent than its 4-chloro-3-nitrophenylthiourea counterpart (5). On the other hand, copper (II) complexes with 2-bromo- and 3-bromophenylthiourea derivatives of 4-azatricyclo[5.2.1.0 2,6]dec-8-ene-3,5-dione were poorly active in comparison with the 4-chloro-3-nitrophenyl thioureas published in this paper [6]. The only exception was the 4-bromophenylthiourea with an azatricyclodione terminal fragment, which was four times more active against standard Staphylococcal isolates than its 3-chloro-4-fluorophenylthiourea analog (3). To conclude, derivatives of substituted phenylthioureas, mainly 3-trifluoromethylphenylthiourea complexes, revealed higher antimicrobial activity in comparison with coordinates of cyclic imides.

3. Materials and Methods

3.1. General Procedure

All chemicals were of analytical grade and were purchased from Sigma-Aldrich. The melting point (m.p.) was determined on a Boetius (HMK65/ 1360) microscope. Elemental analysis of all complexes was carried out using elemental analyzer CHNS (Vario Micro Cube) with an electronic microbalance. The copper content for complex 5 was determined using the energy dispersive X-ray fluorescence spectrometer EDX-7000 from Shimadzu.

3.1.1. Synthesis of Cu (II) Complexes of 3-(4-Chloro-3-nitrophenyl)thiourea (1–8)

The appropriate 3-(4-chloro-3-nitrophenyl)thiourea L1–L8 (1 mmol) was stirred in dimethylformamide (DMF) (2 mL) until its dissolution. Next, anhydrous copper (II) chloride (1 mmol) was added to the solution. After stirring for 6 h, the solvent was evaporated. The solid residue was collected, washed several times with cold distilled water and dried in vacuo over anhydrous calcium chloride at room temperature to yield complexes 1–8.

1. Copper (II) complex with 1-(2-bromophenyl)-3-(4-chloro-3-nitrophenyl)thiourea.
Yield 53%; dark brown solid; m.p. 93–95 °C; Anal. Calc for $\text{Cu(L1)}_2 \cdot 0.75\text{DMF} \cdot 0.5\text{H}_2\text{O}$; Calc. C 37.76, H 2.50, N 10.52, Found C 37.92, H 2.28, N 10.57 (%).
2. Copper (II) complex with 1-(3-bromophenyl)-3-(4-chloro-3-nitrophenyl)thiourea.
Yield 61%; dark brown solid; m.p. 80–82 °C; Anal. Calc for $\text{Cu(L2)}_2 \cdot 0.25\text{DMF} \cdot 1.25\text{H}_2\text{O}$, Calc. C 36.69, H 2.23, N 10.00, Found C 36.28, H 2.39, N 10.40 (%).
3. Copper (II) complex with 1-(4-bromophenyl)-3-(4-chloro-3-nitrophenyl)thiourea.
Yield 58%; dark brown solid; m.p. 88–90 °C; Anal. Calc for $\text{Cu(L3)}_2 \cdot 0.75\text{DMF} \cdot 0.5\text{H}_2\text{O}$, Calc. C 37.76, H 2.50, N 10.52, Found C 38.04, H 2.24, N 10.30 (%).
4. Copper (II) complex with 1-(3-chloro-4-fluorophenyl)-3-(4-chloro-3-nitrophenyl)thiourea.
Yield 55%; dark brown solid; m.p. 95–97 °C; Anal. Calc for $\text{Cu(L4)}_2 \cdot 0.75\text{DMF} \cdot 0.5\text{H}_2\text{O}$, Calc. C 40.12, H 2.41, N 11.18, Found C 40.26, H 2.18, N 11.30 (%).

5. Copper (II) complex with 1-(4-chloro-3-nitrophenyl)-3-(3,4-dichlorophenyl)thiourea.
Yield 57%; brown solid; m.p. 76–78 °C; Anal. Calc for $\text{Cu(L5)}_2 \cdot 3.25\text{H}_2\text{O}$, Calc. C 35.76, H 2.37, N 9.62, Cu 7.28, Found C 35.76, H 2.20, N 9.88, Cu 7.74 (%).
6. Copper (II) complex with 1,3-bis(4-chloro-3-nitrophenyl)thiourea.
Yield 45%; light yellow solid; m.p. 107–108 °C; Anal. Calc for $\text{Cu(L6)}_2 \cdot 0.75\text{DMF} \cdot 0.75\text{H}_2\text{O}$, Calc. C 37.52, H 2.31, N 13.55, Found C 37.41, H 2.22, N 13.41 (%).
7. Copper (II) complex with 1-(2-fluorophenyl)-3-(4-chloro-3-nitrophenyl)thiourea.
Yield 57%; yellow-green solid; m.p. 97–99 °C; Anal. Calc for $\text{Cu(L7)}_2 \cdot 0.5\text{DMF} \cdot 0.25\text{H}_2\text{O}$, Calc. C 43.8, H 2.67, N 12.07, Found C 43.82, H 2.47, N 12.22 (%).
8. Copper (II) complex with 1-(4-iodophenyl)-3-(4-chloro-3-nitrophenyl)thiourea.
Yield 47%; orange brown solid; m.p. 99–101 °C; Anal. Calc for $\text{Cu(L8)}_2 \cdot 3.5\text{H}_2\text{O}$, Calc. C 31.48, H 2.32, N 8.47, Found C 31.20, H 2.08, N 8.50 (%).

3.1.2. Instrumentation

Infrared spectra were performed on Nicolet iS5 FTIR spectrometer (Thermo Scientific) with diamond ATR sample accessory. The complexes **1–8** as well as organic ligands **L1–L8** were recorded in the range of 400–4000 cm^{-1} . The solid state electronic reflectance spectra of complexes **1–8** were collected on SHIMADZU UV-2600 spectrophotometer with UV-2600Plus Integrating Sphere in the range of 220–1400 nm. Electron paramagnetic resonance (EPR) spectra were recorded with a Bruker ELEXSYS-E580 X-band spectrometer (100 kHz field modulation). The microwave power of 5 mW and the modulation amplitude of 0.1–0.5 mT were applied. Prior, the measurements of the samples were dissolved in a mixture of ethanol–toluene solvent (1:1 *v/v*) to form solution of ca. 0.1 mM. The EPR measurements of frozen solutions were carried out at 77 K. The EPR parameters of the copper complexes were determined by computer simulation of the experimental spectra using the EPRsim32 package [60].

3.2. Cell Culture

The human primary (SW480), metastatic (SW620) colon cancer, metastatic prostate cancer (PC3) and human immortal keratinocyte (HaCaT) cell lines were purchased from the American Type Culture Collection (ATCC, Rockville, USA). The cells were cultured in medium according to protocols (MEM for SW480 and SW620, RPMI 1640 for PC3 and DMEM for HaCaT cells) supplemented with 10% fetal bovine serum (FBS), penicillin (100 U/mL) and streptomycin (100 $\mu\text{g/mL}$) and cultured in 37 °C / 5% CO_2 humidified incubator. The cells were cultured until appropriate confluence was achieved (80–90%). Next, they were harvested by treatment with 0.25% trypsin (Gibco Life Technologies, USA) and used for studies.

3.3. MTT Assay

To determine IC_{50} of the thiourea complexes, cells were seeded in 96-well plates (1×10^4 cells per well) and treated for 72 h with different concentrations of compounds. Cells without studied compounds in medium were used as a control.

The cell viability was assessed by determination of MTT salt (3-(4,5-dimethylthiazol-2-yl)-2,5-diphenyltetrazolium bromide) conversion by mitochondrial dehydrogenase. MTT assay was performed as previously described [61]. Experiments were repeated three times. Cell viability was presented as a percentage of MTT reduction in the treated cells versus the control cells. Number of viable cells cultured without studied compounds was assumed to be 100%. Decreased relative MTT level means decreased cell viability. Thiourea complexes with the highest cytotoxic potential assessed by MTT determination (with the lowest IC_{50}) were chosen for subsequent assessments of cytotoxicity mechanisms.

3.4. LDH Assay

The presence of lactate dehydrogenase (LDH) in culture medium indicates a disturbance of the integrity of the cellular membrane. The LDH activity was performed after 72 h incubation of cells (1×10^4 cells per well) in 96-well plates with selected compounds according to manufacturer's protocol (Roche Diagnostics, Germany), as was described by Chrzanowska et al. [61]. Compound mediated cytotoxicity was determined using equation: $((A \text{ test sample} - A \text{ low control}) / (A \text{ high control} - A \text{ low control})) \times 100\%$ (A-absorbance), where "low control" means cells in medium with 2% FBS without tested compounds, and "high control" means cells incubated in medium with 2% FBS and 1% Triton X-100 (100% LDH release). The cytotoxicity was expressed as percentage of LDH release as compared with the maximum release of LDH from Triton-X-100-treated cells.

3.5. Annexin V Binding Assay

The cells were cultured and harvested under the conditions described in the cell culture section. Then, they were seeded in six-well plates (2×10^5 cells per well) and treated with selected thioureas complexes at their IC_{50} concentration for 72 h. The effect of these compounds on the process of early and late apoptosis and necrosis was determined, as described previously [61], by dual staining with annexin V-FITC and propidium iodide according to manufacturer's protocol (Becton Dickinson). The cells that were annexin V-FITC positive and PI-negative were identified as early apoptotic and annexin V-FITC and PI-positive as late apoptotic or necrotic.

3.6. IL-6 Level Assay

IL-6 concentration at all studied cancer cells and normal HaCaT cell lines was measured by ELISA kit (Diaclon SAS Besancon Cedex, France). Cells were seeded in twelve-well plates (1×10^5 cells per well) and treated with IC_{50} concentration of selected studied complexes for 72 h. IL-6 in cell culture supernatant was measured using enzyme-linked immunosorbent assay in accordance with the manufacturer's protocol.

3.7. LC-MS Proteome Analysis

Enzymes involved in oxidoreductive potential were analyzed in the cell lysates obtained after treatment cells with selected conjugates for 24 h. Cells were washed with phosphate-buffered saline (PBS) and harvested, then centrifuged at $1000 \times g$ for 10 min. Then, lysis buffer (containing protease inhibitor, 1% RIPA Lysis and Extraction Buffer (ThermoFisher)) and cold PBS were added, and samples were sonicated three times in ice bath. Next, the cell lysates were centrifuged at $14,000 \times g$ at $4^\circ C$ for 15 min, and then supernatants were stored at $70^\circ C$ before use. Protein concentration was measured by the Bradford method.

Normalized protein concentrations (5 μg) from cell lysate were precipitated by ice cold ($-20^\circ C$) acetonitrile (ACN, Merck, in ratio 1:4). Then, samples were centrifuged ($-9^\circ C$, 30 min., $18,000 \times g$), the supernatant was discarded and ACN excess was evaporated using a vacuum centrifuge (5 min., room temp.). Protein pellet was dissolved in 40 mM ammonium bicarbonate. An amount of 500 mM dithiothreitol (DTT, with final concentration 20 mM) and 1 M iodoacetamide (IAA, with final concentration 40 mM) were used for reduction and alkylation processes. After 16 h of incubation in $37^\circ C$ with Trypsin Gold (Promega), digested protein samples were diluted with 0.1% formic acid (ThermoFisher) and centrifuged ($+2^\circ C$, 30 min, $18,000 \times g$).

LC-MS analysis was carried out with the use of nanoUHPLC (nanoElute, Bruker) coupled by CaptiveSpray (Bruker) to ESI-Q-TOF mass spectrometer (Compact, Bruker). Two-column separation method was used, i.e., pre-column ($300 \mu m \times 5 mm$, C18 PepMap 100, $5 \mu m$, 100 \AA , Thermo Scientific) and Aurora separation column with CSI fitting ($75 \mu m \times 250 mm$, C18 $1.6 \mu m$) in gradient 2% B to 35% B in 90 min with the 300 nL/min flow rate. Mobile phases (A) 0.1% formic acid in water and (B) 0.1% formic acid in ACN were used.

Sample ionizations were performed at a gas flow of 3.0 L/min, temperature of 150 °C and voltage of the capillary at 1600 V. The quadrupole energy was fixed to 5.0 eV and collision chamber energy 7.0 eV, with an ion transfer time of 90 µs. The ions were analyzed in the positive polarity mode in the range 150–2200 *m/z*, with the acquisition frequency of the 1 Hz spectrum, as well as with the autoMS/MS system.

The collected spectra were analyzed and calibrated using DataAnalysis software (Bruker) and then identified in ProteinScape (Bruker) by the MASCOT server. Protein identification was conducted using the online SwissProt and NCBIprot databases, and their references and biological significance were identified using Reactome.org, String.org and KEGG.

3.8. In Vitro Evaluation of Antimicrobial Activity

The antimicrobial activity of the compounds was tested on Gram-positive bacteria (*Staphylococcus aureus* NCTC 4163, *Staphylococcus aureus* ATCC 25923, *Staphylococcus aureus* ATCC 6538, *Staphylococcus aureus* ATCC 29213, *Staphylococcus epidermidis* ATCC 12228, *Staphylococcus epidermidis* ATCC 35984), Gram-negative rods (*Escherichia coli* ATCC 10538, *Escherichia coli* ATCC 25922, *Pseudomonas aeruginosa* ATCC 15442, *Pseudomonas aeruginosa* ATCC 27863) and yeasts (*Candida albicans* ATCC 10231, *Candida albicans* ATCC 90028, *Candida parapsilosis* ATCC 22019). Hospital methicillin-resistant strains of *Staphylococcus aureus* and *Staphylococcus epidermidis* were obtained from the collection of the Department of Pharmaceutical Microbiology, Medical University of Warsaw, Poland.

Antibacterial activity was examined by the disc-diffusion method under standard conditions using Mueller–Hinton II agar medium (Becton Dickinson) according to CLSI (previously NCCLS) guidelines [62]. Antifungal activities were assessed using Mueller–Hinton agar + 2% glucose and 0.5 µg/mL methylene blue dye medium [63]. Sterile filter paper discs (9 mm diameter, Whatman Number 3 chromatography paper) were dripped with tested compound solutions (in dimethylsulfoxide, DMSO) to load 400 µg of a given compound per disc. Dry discs were placed on the surface of appropriate agar medium. The results (diameter of the growth inhibition zone) were read after 18 h of incubation at 35 °C. Minimal inhibitory concentration (MIC) was tested by the twofold serial microdilution method (in 96-well microtiter plates) using Mueller–Hinton broth medium (Beckton Dickinson) for bacteria or RPMI-1640 medium for *Candida* species, according to CLSI guidelines [64,65]. The stock solution of tested agent was prepared in DMSO and diluted in sterile water. Concentrations of tested agents ranged from 0.125 to 512 µg/mL. The final inoculum of all studied microorganisms was 10⁵ CFU/ mL⁻¹ (colony forming units per ml). Minimal inhibitory concentrations (the lowest concentration of a tested agent that prevents visible growth of a microorganism) were read after 18 h (bacteria) or 24 h (yeasts) of incubation at 35 °C.

3.9. Genotoxicity Studies

DNA-damaging activity of compounds was tested by rec-assay using two genetically modified *Bacillus subtilis* strains: M45 (rec⁻) and H17 (rec⁺) [66,67]. Tested compounds were dissolved in DMSO, and 10 µL of each solution was dripped onto sterile cotton discs (Rotilabo) to load 256 µg of a given compound per 9 mm disc. Discs were placed on the surface nutrient agar plates (Difco), inoculated with 100 µL of bacterial overnight culture and incubated 24 h at 35 °C. After incubation, the growth inhibition zones were measured. 4-nitroquinoline N-oxide (NOQ) was used as reference genotoxin (concentration 2 µg per disc). Results of the genotoxicity test were estimated after 18 h of incubation at 35 °C by comparing the diameter of the inhibition zone on the *B. subtilis* M45 (rec⁻) strain with that on the *B. subtilis* H17 (rec⁺) strain.

3.10. Statistical Analyses

Statistical analyses were performed using GraphPad Prism 9 software (GraphPad Software). Statistical significance was assessed by ANOVA with Dunnett's post hoc test.

p values below 0.05 were considered statistically significant. Data were presented as the mean \pm SD from at least three independent experiments.

4. Conclusions

To conclude, we have presented the cytotoxic influences of four-coordinate Cu (II) complexes with 3-(4-chloro-3-nitrophenyl)thiourea derivatives on a panel of human cancer and normal cell lines, as well as on bacterial isolates. In contrast to initial ligands, the complexation with metal ions has revealed the cytotoxic profile of synthesized compounds towards tumor cells and to a lesser extent to bacterial strains. Diversity of a type, a position and quantity of halogen substituents on the phenyl ring of the thiourea branch allowed for the examination of the impact of the structure of synthesized complexes on their bioactivity. Studied coordination compounds did not express cytotoxic effects in normal cells (HaCaT) at clinically achievable concentrations, and they were also proven to be non-genotoxic. The most active halogen phenylthiourea complexes (**1**, **3**, **7**, **8**) showed stronger anticancer potential against PC3 compared to colon cancer cell lines. They were also more effective than the tested disubstituted derivatives (**4–6**). Compound **8** achieved the highest percentage of LDH release from PC3 and SW480 cells. Studied complexes, especially **3** and **8**, induced early apoptosis in the above-mentioned pathological cells. Additionally, all coordination compounds, with emphasis on derivatives **1** and **8**, reduced the secretion of IL-6 by tumor cell lines. Their interleukin-inhibitory properties in the selected cells were equally as strong as doxorubicin. Moreover, new compounds were active against selected strains of Staphylococci of clinical importance, being up to 2–64 times more potent in comparison to the reference antibiotic, ciprofloxacin. Our preliminary studies also showed the general tendency of tested compounds to disturb the antioxidant and detoxifying systems in cancer cells, especially evident for complexes **3**, **7** and **8**. This is an initial signal that this may be one of the cytotoxicity mechanisms. Such a diminishing effect of compounds on the antioxidant defense of cancer cells may support the action of other pro-oxidative agents, including drug resistance as well as support radiotherapy treatment.

Supplementary Materials: The following are available online at <https://www.mdpi.com/article/10.3390/ijms222111415/s1>.

Author Contributions: Conceptualization, A.B.; methodology, A.C. and A.D.-A.; software, P.P.; validation, A.C.; formal analysis, J.S.; investigation, A.C., A.D.-A., K.D. and P.P.; resources, A.B.; data curation, A.C.; writing—original draft preparation, A.B.; writing—review and editing, M.S.; visualization, A.D.-A. and K.D.; supervision, J.S.; project administration, A.B.; funding acquisition, M.S. All authors have read and agreed to the published version of the manuscript.

Funding: This research received no external funding.

Institutional Review Board Statement: Not applicable.

Informed Consent Statement: Not applicable.

Conflicts of Interest: The authors declare that they have no known competing financial interests or personal relationships that have or could be perceived to have influenced the work reported in this article.

References

- Solomon, E.I.; Heppner, D.E.; Johnston, E.M.; Ginsbach, J.W.; Cirera, J.; Qayyum, M.; Kieber-Emmons, M.T.; Kjaergaard, C.H.; Hadt, R.G.; Tian, L. Copper active sites in biology. *Chem. Rev.* **2014**, *114*, 3659–3853. [CrossRef] [PubMed]
- MacPherson, I.S.; Murphy, M.E.P. Type-2 copper-containing enzymes. *Cell. Mol. Life Sci.* **2007**, *64*, 2887–2899. [CrossRef] [PubMed]
- Hernández-Gorriti, W.-R.; Spodine-Spirinova, E.; Beyler, L.; Schröder, U.; Richter, R.; Ferreira, J.; Pavani, M. Synthesis, characterization and antitumor activity of copper (II) complexes, [CuL₂] [HL1-3 = N,N-Diethyl-N'-(R-Benzoyl)Thiourea (R = H, o-Cl and p-NO₂)]. *Bioinorg. Chem. Appl.* **2005**, *3*, 299–316. [CrossRef] [PubMed]
- Peng, B.; Gao, Z.; Li, X.; Li, T.; Chen, G.; Zhou, M.; Zhang, J. DNA binding, DNA cleavage and HSA interaction of several metal complexes containing N-(2-hydroxyethyl)-N'-benzoylthiourea and 1,10-phenanthroline ligands. *JBC J. Biol. Inorg. Chem.* **2016**, *21*, 903–916. [CrossRef] [PubMed]

5. Pivetta, T.; Isaia, F.; Verani, G.; Cannas, C.; Serra, L.; Castellano, C.; Demartin, F.; Pilla, F.; Manca, M.; Pani, A. Mixed-1,10-phenanthroline–Cu(II) complexes: Synthesis, cytotoxic activity versus hematological and solid tumor cells and complex formation equilibria with glutathione. *J. Inorg. Biochem.* **2012**, *114*, 28–37. [CrossRef] [PubMed]
6. Drzewiecka-Antonik, A.; Rejmak, P.; Klepka, M.; Wolska, A.; Pietrzyk, P.; Stępień, K.; Sanna, G.; Struga, M. Synthesis, structural studies and biological activity of novel Cu (II) complexes with thiourea derivatives of 4-azatricyclo [5.2.1.0 2,6] dec-8-ene-3,5-dione. *J. Inorg. Biochem.* **2017**, *176*, 8–16. [CrossRef] [PubMed]
7. Bielenica, A.; Drzewiecka-Antonik, A.; Rejmak, P.; Stefańska, J.; Koliński, M.; Kmiecik, S.; Lesyng, B.; Włodarczyk, M.; Pietrzyk, P.; Struga, M. Synthesis, structural and antimicrobial studies of type II topoisomerase-targeted copper (II) complexes of 1,3-disubstituted thiourea ligands. *J. Inorg. Biochem.* **2018**, *182*, 61–70. [CrossRef] [PubMed]
8. Repich, H.; Orysyk, V.; Palchykovska, L.; Orysyk, S.; Zborovskii, Y.L.; Vasylychenko, O.; Storozhuk, O.; Biluk, A.; Nikulina, V.; Garmanchuk, L.; et al. Synthesis, spectral characterization of novel Pd (II), Pt (II) π -coordination compounds based on N-allylthioureas. Cytotoxic properties and DNA binding ability. *J. Inorg. Biochem.* **2017**, *168*, 98–106. [CrossRef]
9. Čočić, D.; Jovanovic, S.; Radisavljević, S.; Korzekwa, J.; Scheurer, A.; Puchta, R.; Baskić, D.; Todorovic, D.; Popovic, S.; Matić, S.; et al. New monofunctional platinum (II) and palladium (II) complexes: Studies of the nucleophilic substitution reactions, DNA/BSA interaction, and cytotoxic activity. *J. Inorg. Biochem.* **2018**, *189*, 91–102. [CrossRef] [PubMed]
10. Plutín, A.M.; Mocolo, R.; Alvarez, A.; Ramos, R.; Castellano, E.E.; Cominetti, M.R.; Graminha, A.E.; Ferreira, A.G.; Batista, A.A. On the cytotoxic activity of Pd (II) complexes of N,N-disubstituted-N'-acyl thioureas. *J. Inorg. Biochem.* **2014**, *134*, 76–82. [CrossRef] [PubMed]
11. Marverti, G.; Gozzi, G.; Lauriola, A.; Ponterini, G.; Belluti, S.; Imbriano, C.; Costi, M.P.; D'Arca, D. The 1,10-phenanthroline ligand enhances the antiproliferative activity of DNA-intercalating thiourea-Pd (II) and -Pt (II) complexes against cisplatin-sensitive and-resistant human ovarian cancer cell lines. *Int. J. Mol. Sci.* **2019**, *20*, 6122. [CrossRef] [PubMed]
12. Pracharova, J.; Zerkankova, L.; Stepankova, J.; Novakova, O.; Farrer, N.J.; Sadler, P.J.; Brabec, V.; Kasparkova, J. Interactions of DNA with a new platinum (IV) azide dipyridine complex activated by UVA and visible light: Relationship to toxicity in tumor cells. *Chem. Res. Toxicol.* **2012**, *25*, 1099–1111. [CrossRef]
13. Ma, Z.; Choudhury, J.R.; Wright, M.W.; Day, C.S.; Saluta, G.; Kucera, G.L.; Bierbach, U. A non-cross-linking platinum–acridine agent with potent activity in non-small-cell lung cancer. *J. Med. Chem.* **2008**, *51*, 7574–7580. [CrossRef] [PubMed]
14. Eiter, L.C.; Hall, N.W.; Day, C.S.; Saluta, G.; Kucera, G.L.; Bierbach, U. Gold (I) analogues of a platinum–acridine antitumor agent are only moderately cytotoxic but show potent activity against mycobacterium tuberculosis. *J. Med. Chem.* **2009**, *52*, 6519–6522. [CrossRef] [PubMed]
15. Yu, B.; Ma, L.; Jin, J.; Jiang, F.; Zhou, G.; Yan, K.; Liu, Y. Mitochondrial toxicity induced by a thiourea gold (I) complex: Mitochondrial permeability transition and respiratory deficit. *Toxicol. Res.* **2018**, *7*, 1081–1090. [CrossRef] [PubMed]
16. Correa, R.; de Oliveira, K.M.; Delolo, F.G.; Alvarez, A.; Mocolo, R.; Plutín, A.M.; Cominetti, M.R.; Castellano, E.E.; Batista, A.A. Ru (II)-based complexes with N-(acyl)-N',N'-(disubstituted)thiourea ligands: Synthesis, characterization, BSA- and DNA-binding studies of new cytotoxic agents against lung and prostate tumour cells. *J. Inorg. Biochem.* **2015**, *150*, 63–71. [CrossRef] [PubMed]
17. Cunha, B.N.; Colina-Vegas, L.; Plutín, A.M.; da Silveira, R.G.; Honorato, J.; de Oliveira, K.M.; Cominetti, M.R.; Ferreira, A.G.; Castellano, E.E.; Batista, A.A. Hydrolysis reaction promotes changes in coordination mode of Ru (II)/acylthiourea organometallic complexes with cytotoxicity against human lung tumor cell lines. *J. Inorg. Biochem.* **2018**, *186*, 147–156. [CrossRef] [PubMed]
18. De Oliveira, T.D.; Plutín, A.M.; Luna-Dulcey, L.; Castellano, E.E.; Cominetti, M.R.; Batista, A.A. Cytotoxicity of ruthenium-N, N-disubstituted-N'-acylthioureas complexes. *Mater. Sci. Eng. C* **2020**, *115*, 111106. [CrossRef] [PubMed]
19. Poyraz, M.; Berber, H.; Banti, C.N.; Kourkoumelis, N.; Manos, M.J.; Hadjidakou, S.K. Synthesis characterization and biological activity of mixed ligand silver (I) complex of 2-benzimidazolylurea and triphenylphosphine. *Polyhedron* **2017**, *128*, 95–103. [CrossRef]
20. Perillo, B.; di Donato, M.; Pezone, A.; di Zazzo, E.; Giovannelli, P.; Galasso, G.; Castoria, G.; Migliaccio, A. ROS in cancer therapy: The bright side of the moon. *Exp. Mol. Med.* **2020**, *52*, 192–203. [CrossRef] [PubMed]
21. Arfin, S.; Jha, N.; Jha, S.; Kesari, K.; Ruokolainen, J.; Roychoudhury, S.; Rath, B.; Kumar, D. Oxidative stress in cancer cell metabolism. *Antioxidants* **2021**, *10*, 642. [CrossRef]
22. Bułdak, R.; Buldak, L.; Kukla, M.; Gabriel, A.; Żwirska-Korczala, K. Significance of selected antioxidant enzymes in cancer cell progression. *Pol. J. Pathol.* **2014**, *3*, 167–175. [CrossRef]
23. Hwang, P.M.; Bunz, F.; Yu, J.; Rago, C.; Chan, T.A.; Murphy, M.P.; Kelso, G.F.; Smith, R.A.J.; Kinzler, K.W.; Vogelstein, B. Ferredoxin reductase affects p53-dependent, 5-fluorouracil-induced apoptosis in colorectal cancer cells. *Nat. Med.* **2001**, *7*, 1111–1117. [CrossRef]
24. Longley, D.B.; Harkin, D.P.; Johnston, P.G. 5-fluorouracil: Mechanisms of action and clinical strategies. *Nat. Rev. Cancer* **2003**, *3*, 330–338. [CrossRef] [PubMed]
25. Zhu, J. Using cyclooxygenase-2 inhibitors as molecular platforms to develop a new class of apoptosis-inducing agents. *J. Natl. Cancer Inst.* **2002**, *94*, 1745–1757. [CrossRef]
26. Zhou, W.; Liotta, L.A.; Petricoin, E.F. Cancer metabolism: What we can learn from proteomic analysis by mass spectrometry. *Cancer Genom.-Proteom.* **2012**, *9*, 373–381.
27. Yu, B.; Liu, Y.; Peng, X.; Hua, S.; Zhou, G.; Yan, K.; Liu, Y. Synthesis, characterization, and antitumor properties of Au (I)–thiourea complexes. *Metallomics* **2020**, *12*, 104–113. [CrossRef] [PubMed]

28. Tan, C.-P.; Lai, S.; Wu, S.; Hu, S.; Zhou, L.; Chen, Y.; Wang, M.; Zhu, Y.; Lian, W.; Peng, W.; et al. Nuclear permeable ruthenium (II) β -carboline complexes induce autophagy to antagonize mitochondrial-mediated apoptosis. *J. Med. Chem.* **2010**, *53*, 7613–7624. [CrossRef] [PubMed]
29. Khan, M.H.; Cai, M.; Deng, J.; Yu, P.; Liang, H.; Yang, F. Anticancer function and ROS-mediated multi-targeting anticancer mechanisms of copper (II) 2-hydroxy-1-naphthaldehyde complexes. *Molecules* **2019**, *24*, 2544. [CrossRef]
30. Trejo-Solís, C.; Jimenez-Farfan, D.; Rodriguez-Enriquez, S.; Fernandez-Valverde, F.; Cruz-Salgado, A.; Ruiz-Azuara, L.; Sotelo, J. Copper compound induces autophagy and apoptosis of glioma cells by reactive oxygen species and JNK activation. *BMC Cancer* **2012**, *12*, 156. [CrossRef]
31. Terbouche, A.; Ramdane-Terbouche, C.A.; Bendjilali, Z.; Berriah, H.; Lakhdri, H.; Lerari, D.; Bachari, K.; Mezaoui, D.; Bensiradj, N.E.H.; Guegan, J.-P.; et al. Synthesis, spectral characterization, molecular modeling, antibacterial and antioxidant activities and stability study of binuclear Pd (II) and Ru (III) complexes with novel bis-[1-(2-[(2-hydroxynaphthalen-1-yl)methylidene]amino)ethyl]-1-ethyl-3-phenylthiourea] ligand: Application to detection of cholesterol. *Spectrochim. Acta Part A Mol. Biomol. Spectrosc.* **2018**, *205*, 146–159. [CrossRef]
32. Esmaili, L.; Perez, M.G.; Jafari, M.; Paquin, J.; Ispas-Szabo, P.; Pop, V.; Andruh, M.; Byers, J.; Mateescu, M.A. Copper complexes for biomedical applications: Structural insights, antioxidant activity and neuron compatibility. *J. Inorg. Biochem.* **2019**, *192*, 87–97. [CrossRef] [PubMed]
33. Inci, D.; Aydın, R.; Zorlu, Y. Cu (II) complex with auxin (3-indoleacetic acid) and an aromatic planar ligand: Synthesis, crystal structure, biomolecular interactions and radical scavenging activity. *Eur. Biophys. J.* **2021**, *50*, 1–15. [CrossRef] [PubMed]
34. Karagoz, Z.; Genc, M.; Yilmaz, E.; Keser, S. Synthesis and antitumor, antioxidant effects studies of N-ethylpiperazine substitute thiourea ligands and their copper (II) complexes. *Spectrosc. Lett.* **2013**, *46*, 182–190. [CrossRef]
35. Bielenica, A.; Stefańska, J.; Stepień, K.; Napiórkowska, A.; Augustynowicz-Kopeć, E.; Sanna, G.; Madeddu, S.; Boi, S.; Giliberti, G.; Wrzosek, M.; et al. Synthesis, cytotoxicity and antimicrobial activity of thiourea derivatives incorporating 3-(trifluoromethyl)phenyl moiety. *Eur. J. Med. Chem.* **2015**, *101*, 111–125. [CrossRef]
36. Bielenica, A.; Sanna, G.; Madeddu, S.; Giliberti, G.; Stefańska, J.; Koziol, A.E.; Savchenko, O.; Strzyga-Lach, P.; Chrzanowska, A.; Kubiak-Tomaszewska, G.; et al. Disubstituted 4-chloro-3-nitrophenylthiourea derivatives: Antimicrobial and cytotoxic studies. *Molecules* **2018**, *23*, 2428. [CrossRef]
37. Bielenica, A.; Stepień, K.; Napiórkowska, A.; Augustynowicz-Kopeć, E.; Krukowski, S.; Włodarczyk, M.; Struga, M. Synthesis and antimicrobial activity of 4-chloro-3-nitrophenylthiourea derivatives targeting bacterial type II topoisomerases. *Chem. Biol. Drug Des.* **2016**, *87*, 905–917. [CrossRef]
38. Stefańska, J.; Stepień, K.; Bielenica, A.; Wrzosek, M.; Struga, M. Antistaphylococcal activity of selected thiourea derivatives. *Pol. J. Microbiol.* **2016**, *65*, 451–460. [CrossRef]
39. John, R.P.; Sreekanth, A.; Kurup, M.R.P.; Usman, A.; Ibrahim, A.R.; Fun, H.K. Spectral studies and structure of a 2-hydroxyacetophenone 3-hexamethyleneiminy l thiosemicarbazone (–2) copper (II) complex containing 1,10-phenanthroline. *Spectrochim. Acta Part A Mol. Biomol. Spectrosc.* **2003**, *59*, 1349–1358. [CrossRef]
40. Sreekanth, A.; Kurup, M.R.P. Structural and spectral studies on four coordinate copper (II) complexes of 2-benzoylpyridine N(4), N(4)-(butane-1,4-diyl) thiosemicarbazone. *Polyhedron* **2003**, *22*, 3321–3332. [CrossRef]
41. Drzewiecka-Antonik, A.; Rejmak, P.; Klepka, M.; Wolska, A.; Chrzanowska, A.; Struga, M. Structure and anticancer activity of Cu (II) complexes with (bromophenyl) thiourea moiety attached to the polycyclic imide. *J. Inorg. Biochem.* **2020**, *212*, 111234. [CrossRef] [PubMed]
42. Low, M.L.; Maigre, L.; Tahir, M.I.M.; Tiekink, E.R.; Dorlet, P.; Guillot, R.; Ravoof, T.B.; Rosli, R.; Pagès, J.-M.; Polcar, C.; et al. New insight into the structural, electrochemical and biological aspects of macrocyclic Cu (II) complexes derived from S-substituted dithiocarbamate schiff bases. *Eur. J. Med. Chem.* **2016**, *120*, 1–12. [CrossRef]
43. Singh, D.P.; Pratap, S.; Shukla, M. Solvent induced geometry transformation of trigonal planar Cu (I) complexes of N-((2/4-methoxy carbonyl) phenyl)-N'-(ethoxy/methoxy carbonyl) thiocarbamides to square-planar Cu (II) complexes: Synthesis, spectral, single crystal, DFT and in vitro cytotoxic study. *Inorg. Chim. Acta* **2014**, *423*, 386–396. [CrossRef]
44. Singh, S. Cytoprotective and regulatory functions of glutathione S-transferases in cancer cell proliferation and cell death. *Cancer Chemother. Pharmacol.* **2014**, *75*, 1–15. [CrossRef]
45. Beaumont, P.; Moore, M.J.; Ahmad, K.; Payne, M.M.; Lee, C.; Riddick, D.S. Role of glutathione S-transferases in the resistance of human colon cancer cell lines to doxorubicin. *Cancer Res.* **1998**, *58*, 947–955. [PubMed]
46. Hasegawa, N.; Mizutani, K.; Suzuki, T.; Deguchi, T.; Nozawa, Y. A comparative study of protein profiling by proteomic analysis in camptothecin-resistant PC3 and camptothecin-sensitive LNCaP human prostate cancer cells. *Urol. Int.* **2006**, *77*, 347–354. [CrossRef] [PubMed]
47. Lorestani, S.; Hashemy, S.I.; Mojarad, M.; Shahrestanaki, M.K.; Bahari, A.; Asadi, M.; Avval, F.Z. Increased glutathione reductase expression and activity in colorectal cancer tissue samples: An investigational study in Mashhad, Iran. *Middle East J. Cancer* **2018**, *9*, 99–104.
48. Freitas, M.; Baldeiras, I.; Proença, T.; Alves, V.; Mota-Pinto, A.; Sarmiento-Ribeiro, A. Oxidative stress adaptation in aggressive prostate cancer may be counteracted by the reduction of glutathione reductase. *FEBS Open Bio* **2012**, *2*, 119–128. [CrossRef] [PubMed]
49. Zhang, Y.; Zhao, W.; Zhang, H.J.; Domann, F.E.; Oberley, L.W. Overexpression of copper zinc superoxide dismutase suppresses human glioma cell growth. *Cancer Res.* **2002**, *62*, 1205–1212. [PubMed]

50. Satomi, A.; Murakami, S.; Hashimoto, T.; Ishida, K.; Matsuki, M.; Sonoda, M. Significance of superoxide dismutase (SOD) in human colorectal cancer tissue: Correlation with malignant intensity. *J. Gastroenterol.* **1995**, *30*, 177–182. [CrossRef]
51. Martino, T.; Kudrolli, T.A.; Kumar, B.; Salviano, I.; Mencialha, A.L.; Coelho, M.G.P.; Justo, G.; Costa, P.R.R.; Sabino, K.C.C.; Lupold, S.E. The orally active pterocarpanquinone LQB-118 exhibits cytotoxicity in prostate cancer cell and tumor models through cellular redox stress. *Prostate* **2018**, *78*, 140–151. [CrossRef]
52. Papa, L.; Manfredi, G.; Germain, D. SOD1, an unexpected novel target for cancer therapy. *Genes Cancer* **2014**, *5*, 15–21. [CrossRef] [PubMed]
53. Papa, L.; Hahn, M.; Marsh, E.L.; Evans, B.S.; Germain, D. SOD2 to SOD1 switch in breast cancer. *J. Biol. Chem.* **2014**, *289*, 5412–5416. [CrossRef] [PubMed]
54. Zhang, B.; Wang, Y.; Su, Y. Peroxiredoxins, a novel target in cancer radiotherapy. *Cancer Lett.* **2009**, *286*, 154–160. [CrossRef]
55. Kim, Y.-J.; Lee, W.-S.; Ip, C.; Chae, H.-Z.; Park, E.-M.; Park, Y.-M. Prx1 suppresses radiation-induced c-Jun NH2-terminal kinase signaling in lung cancer cells through interaction with the glutathione S-transferase Pi/c-Jun NH2-terminal kinase complex. *Cancer Res.* **2006**, *66*, 7136–7142. [CrossRef] [PubMed]
56. Jang, H.H.; Kim, S.Y.; Park, S.K.; Jeon, H.S.; Lee, Y.M.; Jung, J.H.; Lee, S.Y.; Chae, H.B.; Jung, Y.J.; Lee, K.O.; et al. Phosphorylation and concomitant structural changes in human 2-Cys peroxiredoxin isotype I differentially regulate its peroxidase and molecular chaperone functions. *FEBS Lett.* **2005**, *580*, 351–355. [CrossRef] [PubMed]
57. Chen, M.-F.; Lee, K.-D.; Yeh, C.-H.; Chen, W.-C.; Huang, W.-S.; Chin, C.-C.; Lin, P.-Y.; Wang, J.-Y. Role of peroxiredoxin I in rectal cancer and related to p53 status. *Int. J. Radiat. Oncol.* **2010**, *78*, 868–878. [CrossRef]
58. Whitaker, H.C.; Patel, D.J.; Howat, W.J.; Warren, A.Y.; Kay, J.; Sangan, T.; Marioni, J.; Mitchell, J.F.B.; Aldridge, S.; Luxton, H.J.; et al. Peroxiredoxin-3 is overexpressed in prostate cancer and promotes cancer cell survival by protecting cells from oxidative stress. *Br. J. Cancer* **2013**, *109*, 983–993. [CrossRef]
59. Basu, A.; Banerjee, H.; Rojas, H.; Martinez, S.R.; Roy, S.; Jia, Z.; Lilly, M.B.; de Leon, M.; Casiano, C.A. Differential expression of peroxiredoxins in prostate cancer: Consistent upregulation of PRDX3 and PRDX4. *Prostate* **2011**, *71*, 755–765. [CrossRef]
60. Spałek, T.; Pietrzyk, P.; Sojka, Z. Application of the genetic algorithm joint with the powell method to nonlinear least-squares fitting of powder EPR spectra. *J. Chem. Inf. Model.* **2005**, *45*, 18–29. [CrossRef] [PubMed]
61. Clinical and Laboratory Standards Institute. *Methods for Dilution Antimicrobial Susceptibility Tests for Bacteria that Grow Aerobically. Approved Standard M7-A9*; Clinical and Laboratory Standards Institute: Wayne, PA, USA, 2012.
62. Clinical and Laboratory Standards Institute. *Methods for Determining Bactericidal Activity of Antimicrobial Agents. Approved Guideline M26-A*; Clinical and Laboratory Standards Institute: Wayne, PA, USA, 1999.
63. Clinical and Laboratory Standards Institute. *Methods for Dilution Antimicrobial Susceptibility Tests for Bacteria that Grow Aerobically. Approved Standard M7-A*; Clinical and Laboratory Standards Institute: Wayne, PA, USA, 2006.
64. Clinical and Laboratory Standards Institute. Reference method for broth dilution antifungal susceptibility testing of yeasts. Approved standard. In *CLSI Document M27-A3*, 3rd ed.; Clinical and Laboratory Standards Institute: Wayne, PA, USA, 2008; pp. 1–25.
65. Kada, T.; Hirano, K.; Shirasu, Y. Bacillus subtilis rec-assay test. In *Chemical Mutagens*; de Sevres, F.E., Hollaende, A., Eds.; Plenum Press: New York, NY, USA, 1980; Volume 6, p. 149.
66. Sadaie, Y.; Kada, T. Recombination-deficient mutants of *Bacillus subtilis*. *J. Bacteriol.* **1976**, *125*, 489–500. [CrossRef] [PubMed]
67. Chrzanowska, A.; Roszkowski, P.; Bielenica, A.; Olejarz, W.; Stępień, K.; Struga, M. Anticancer and antimicrobial effects of novel ciprofloxacin fatty acids conjugates. *Eur. J. Med. Chem.* **2020**, *185*, 111810. [CrossRef] [PubMed]



Article

In Vitro and In Vivo Efficacy of a Novel Glucose–Methotrexate Conjugate in Targeted Cancer Treatment

Marta Woźniak ¹, Gabriela Pastuch-Gawolek ^{2,3} , Sebastian Makuch ¹ , Jerzy Wiśniewski ^{4,5} , Tibor Krenács ⁶, Peter Hamar ⁷, Andrzej Gamian ⁵, Wiesław Szeja ², Danuta Szkudlarek ¹, Monika Krawczyk ^{2,3,*} and Siddarth Agrawal ^{1,8,*}

- ¹ Department of Pathology, Wrocław Medical University, 50-367 Wrocław, Poland; marta.wozniak@umed.wroc.pl (M.W.); sebastian.makuch@student.umed.wroc.pl (S.M.); danuta.szkudlarek@umed.wroc.pl (D.S.)
- ² Department of Organic Chemistry, Bioorganic Chemistry and Biotechnology, Faculty of Chemistry, 44-100 Gliwice, Poland; gabriela.pastuch-gawolek@polsl.pl (G.P.-G.); wieslaw.szeja@polsl.pl (W.S.)
- ³ Biotechnology Centre, Silesian University of Technology, 44-100 Gliwice, Poland
- ⁴ Department of Medical Biochemistry, Wrocław Medical University, 50-367 Wrocław, Poland; jerzy.wisniewski@hirszweld.pl
- ⁵ Department of Immunology of Infectious Diseases, Hirsfeld Institute of Immunology and Experimental Therapy, Polish Academy of Sciences, 53-114 Wrocław, Poland; andrzej.gamian@hirsfeld.pl
- ⁶ Department of Pathology and Experimental Cancer Research, Semmelweis University, 1085 Budapest, Hungary; krenacst@gmail.com
- ⁷ Institute of Translational Medicine, Semmelweis University, 1085 Budapest, Hungary; hamar.peter@med.semmelweis-univ.hu
- ⁸ Department and Clinic of Internal Medicine, Occupational Diseases, Hypertension and Clinical Oncology, Wrocław Medical University, 50-367 Wrocław, Poland
- * Correspondence: monika.krawczyk@polsl.pl (M.K.); siddarth@agrawal.pl (S.A.)

Citation: Woźniak, M.;

Pastuch-Gawolek, G.; Makuch, S.; Wiśniewski, J.; Krenács, T.; Hamar, P.; Gamian, A.; Szeja, W.; Szkudlarek, D.; Krawczyk, M.; et al. In Vitro and In Vivo Efficacy of a Novel Glucose–Methotrexate Conjugate in Targeted Cancer Treatment. *Int. J. Mol. Sci.* **2021**, *22*, 1748. <https://doi.org/10.3390/ijms22041748>

Academic Editor: Andrzej Kutner

Received: 8 January 2021

Accepted: 4 February 2021

Published: 9 February 2021

Publisher's Note: MDPI stays neutral with regard to jurisdictional claims in published maps and institutional affiliations.



Copyright: © 2021 by the authors. Licensee MDPI, Basel, Switzerland. This article is an open access article distributed under the terms and conditions of the Creative Commons Attribution (CC BY) license (<https://creativecommons.org/licenses/by/4.0/>).

Abstract: Methotrexate (MTX) is a commonly used antimetabolite, which inhibits folate and DNA synthesis to be effective in the treatment of various malignancies. However, MTX therapy is hindered by the lack of target tumor selectivity. We have designed, synthesized and evaluated a novel glucose–methotrexate conjugate (GLU–MTX) both in vitro and in vivo, in which a cleavable linkage allows intracellular MTX release after selective uptake through glucose transporter–1 (GLUT1). GLU–MTX inhibited the growth of colorectal (DLD-1), breast (MCF-7) and lung (A427) adenocarcinomas, squamous cell carcinoma (SCC-25), osteosarcoma (MG63) cell lines, but not in WI-38 healthy fibroblasts. In tumor cells, GLU–MTX uptake increased 17-fold compared to unconjugated MTX. 4,6-O-ethylidene- α -D-glucose (EDG), a GLUT1 inhibitor, significantly interfered with GLU–MTX induced growth inhibition, suggesting a glucose-mediated drug uptake. Glu-MTX also caused significant tumor growth delay in vivo in breast cancer-bearing mice. These results show that our GLUT-MTX conjugate can be selectively uptake by a range of tumor cells to cause their significant growth inhibition in vitro, which was also confirmed in a breast cancer model in vivo. GLUT1 inhibitor EDG interfered with these effects verifying the selective drug uptake. Accordingly, GLU–MTX offers a considerable tumor selectivity and may offer cancer growth inhibition at reduced toxicity.

Keywords: glycoconjugates; methotrexate; cancer treatment; glucose metabolism; drug design and discovery; anticancer drugs; targeted therapy; Warburg effect

1. Introduction

Methotrexate (MTX) is among the most widely applied and effective therapeutic agents available to treat various cancers, including breast cancer, lung cancer, bladder carcinoma, and osteogenic sarcoma, as well as autoimmune diseases [1]. However, MTX has a number of deficiencies that arise from a lack of tumor selectivity [2,3]. The pharmacokinetic parameters of MTX are unsatisfactory and frequently result in an insufficient

clinical response. Increasing the dose of MTX may result in higher therapeutic efficacy, but it also leads to a greater risk of side effects [4]. In general, the principal reason for the discontinuation of MTX is not the lack of efficacy but life-threatening toxicity. We addressed these limitations by designing a next-generation tumor-targeting MTX delivery system for improved safety and efficacy.

One of the attractive strategies to achieve the desired specificity is to connect a therapeutic agent with a ligand that selectively interacts with the pathological cell. To increase the safety and efficacy of the therapy, the synthesis of a prodrug in which the chemotherapeutic is bound to a ligand with a high-affinity for diseased cells is required. To achieve this, the diseased cells must overexpress the ligand-specific receptor that could facilitate the targeted uptake of the therapeutic agent. Examples of such prodrugs include peptide-drug, antibody-drug, aptamer-drug, and folic acid-drug conjugates [5].

In order to sustain the growth and proliferation, malignant cells significantly increase glucose uptake and the flux of substrates through glycolysis even under oxidative conditions. This abnormality, termed “the Warburg effect,” originates from mitochondrial metabolic changes and is one of cancer’s most common traits [6]. The elevated glucose intake requires the overexpression of glucose transporters (GLUTs), which is frequent in neo-plasms and provide clinical targets for therapy [7,8]. Therefore, glycoconjugation, in which cytotoxic agents or targeted anticancer therapeutics have been linked to glucose, can improve the selective uptake of anticancer drugs [9–14]. Since the introduction of glufosfamide [15], the potential of this strategy in diagnosis and therapy has already been realized, yet there is tremendous scope for improvement [7].

These ligand-targeting drugs (LTD) are constructed by conjugating a cleavable linker to the payload. The efficacy of such conjugate is primarily determined by the therapeutic agent activity, while the safety of the conjugate is dictated by the ligand specificity on the tumor cell. Separating the diseased cell selectivity and therapeutic drug activity is the most critical step which can be independently optimized. Therefore, we first focused on determining the optimal structure of the glucoside, through which the sugar is locked to the linker, then the transfer of the conjugate to tumor cells and its uptake mediated by GLUT1 protein. Based on these considerations, we designed, synthesized, and biologically evaluated a novel glucose–methotrexate conjugate (GLU–MTX), in which MTX, D-Glucose, and the linker are connected via a cleavable linkage susceptible to the action of hydrolytic enzymes. To the best of our knowledge, no one has previously synthesized or evaluated the conjugation of glucose to MTX. In our recent study, we showed that GLU–MTX exerts a strong cytotoxic effect on breast and colon cancer cells and displays an increased selectivity in the tumor microenvironment [16]. These findings conclusively prove the potential of glycoconjugation for the selective destruction of cancer cells by MTX. In view of this, the objective of this study was to further evaluate the efficacy of GLU–MTX on a wide variety of cancer cell lines as well as in vivo and examine the mechanisms underlying the cellular transport of glucose–methotrexate conjugate. The present study revealed that GLU–MTX is a potent therapeutic agent that preferentially accumulates in and annihilates cancer cells at reduced toxicity in the noncancerous tissues (Figure 1).

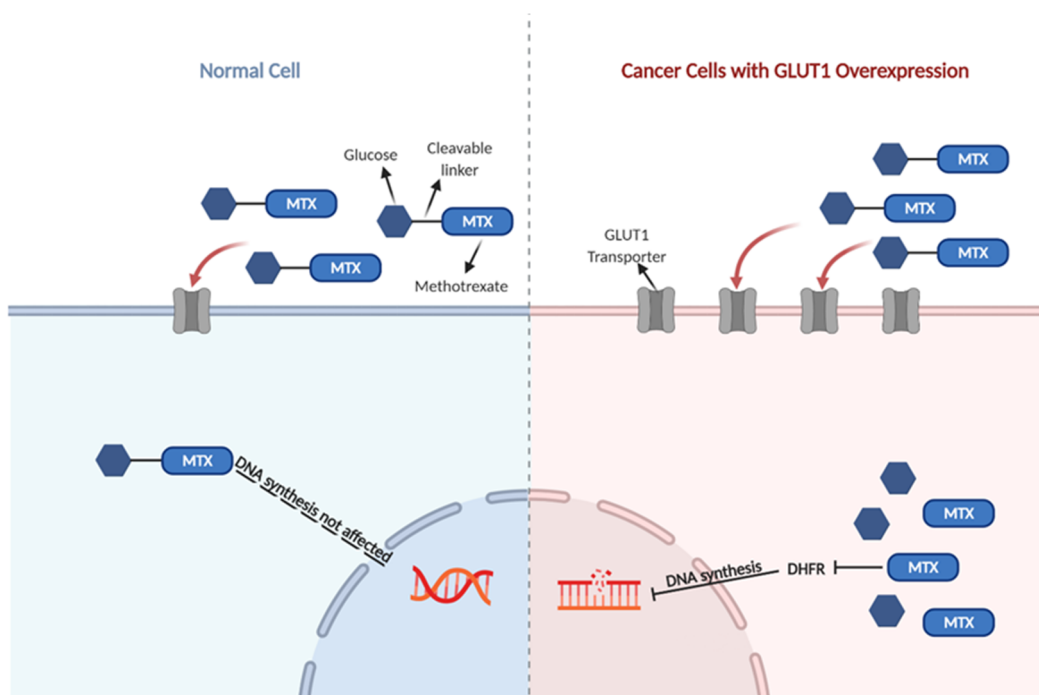
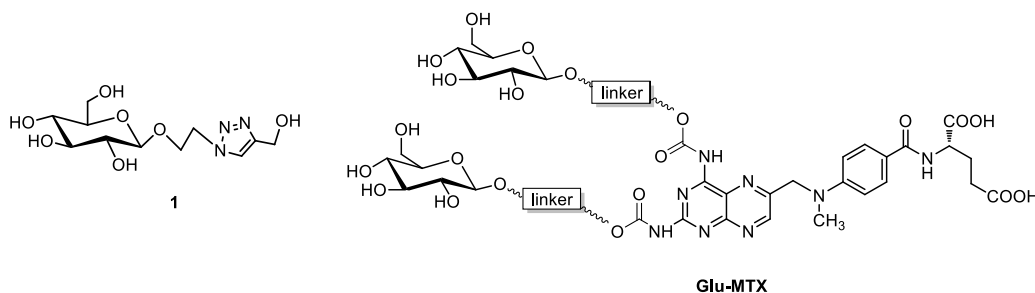


Figure 1. Cellular transport of glucose–methotrexate conjugate (GLU–MTX) in healthy and cancer cells with GLUT1 overexpression. The intracellular cleavage of acid-labile bonds in the acidic environment of cancer cells results in controlled release of MTX, which inhibits dihydrofolate reductase (DHFR) and leads to cell death. In healthy cells, no major effect in DNA synthesis is observed.

2. Results

2.1. Synthesis of Sugar Derivative Emerging from GLU–MTX Conjugate Hydrolysis in Tumor Cells

The initial stage of the research was the synthesis of a glucoconjugate **1** containing a D-glucose- unit linked via a glycosidic bond with a linker (Scheme 1). The conjugate **1** was prepared by the 1,3-dipolar cycloaddition reaction of 2-azidoethyl β -D-O-glucopyranoside and propargyl alcohol. As indicated in the experimental section, the results suggest that the uptake of the glucoconjugate **1** is mediated by the GLUT1 transporter. During these studies, it was also noticed that this compound has a weak cytotoxic effect. Based on the encouraging result that glucoconjugate **1** was transferred into the tumor cells, we synthesized prodrug GLU–MTX in the cycloaddition reaction according to the method developed by Sharpless. The substrates for this reaction were 2-azidoethyl β -D-O-glucopyranoside and MTX di-propargylcarbamide derivatives, obtained by reacting the propargyl chloroformate with an antibiotic (MTX) in the presence of *N*-methylimidazole (NMI) and tertiary amine such as *N,N*-diisopropylethylamine in methylene chloride as a solvent [16].



Scheme 1. Structures of the glucoconjugate **1** and GLU–MTX glycoconjugate.

GLU–MTX exhibits comparable antiproliferative activity to MTX against different cancer cell lines and has higher selectivity for cancer cells over normal cells in vitro.

GLU–MTX and MTX were first tested for their in vitro cytotoxicity with the use of the MTT assay. Six cell lines representing five types of human malignancies (breast, colon, skin, lung, bone) were cultured with test compounds at concentrations in the range of 10 to 50 μM for 48 h; then, cell viability was determined. The findings demonstrated that GLU–MTX had a similar cytotoxic effect compared to MTX on the SCC-25 skin cancer cell line (Figure 2A). Cell viability of the other MTX-treated cell lines was slightly lower (16–19% depending on the cell line) (Figure 2B–E) than the viability of the same dose of GLU–MTX-treated cells. We compared the selectivity of GLU–MTX and MTX using various cancer cell lines to match the results with a healthy fibroblast WI38 cell line. As shown in Figure 2F, we found that the cellular viability of WI-38 was significantly higher in GLU–MTX-treated cells compared to MTX-treated cells. This result indicates that GLU–MTX is less cytotoxic to healthy cells than MTX.

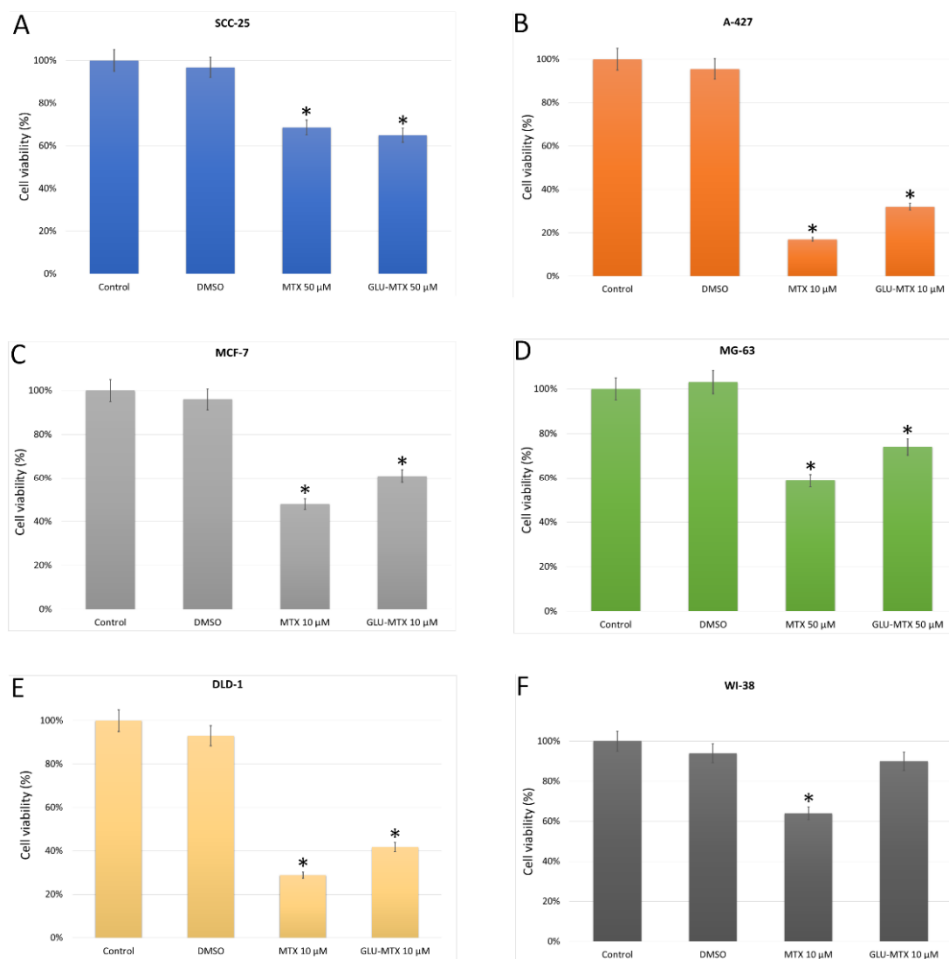


Figure 2. Cell viability of various human cancer cell lines: squamous cell carcinoma SCC-25, lung carcinoma A-427, human colon adenocarcinoma DLD-1, breast carcinoma MCF-7, osteosarcoma MG-63 (A–E) and normal human fibroblast WI-38 (F) after MTX and GLU–MTX treatment for 48 h at doses 10–50 μM . Results are presented as means \pm standard deviations from three independent experiments. * $p < 0.05$ vs. control.

2.2. The Cytotoxic Effect of GLU–MTX Is Reversed by GLUT1 Inhibitor

The cytotoxicity assay was carried out in the absence and presence of an exofacial GLUT1 competitive inhibitor 4,6-O-ethylidene- α -D-glucose (EDG). Cells preincubated with EDG and then with conjugated MTX had a lower cell death ratio in comparison to cells incubated with free MTX in both cell lines. MCF-7 and A-427 cells viability after EDG + MTX treatment was 35% and 15%, respectively, whereas following EDG + GLU–MTX was 70% and 50%, respectively (Figure 3). The MTT assay results support the hypothesis that glucose transporter GLUT1 is involved in the cellular uptake of glucose conjugate MTX.

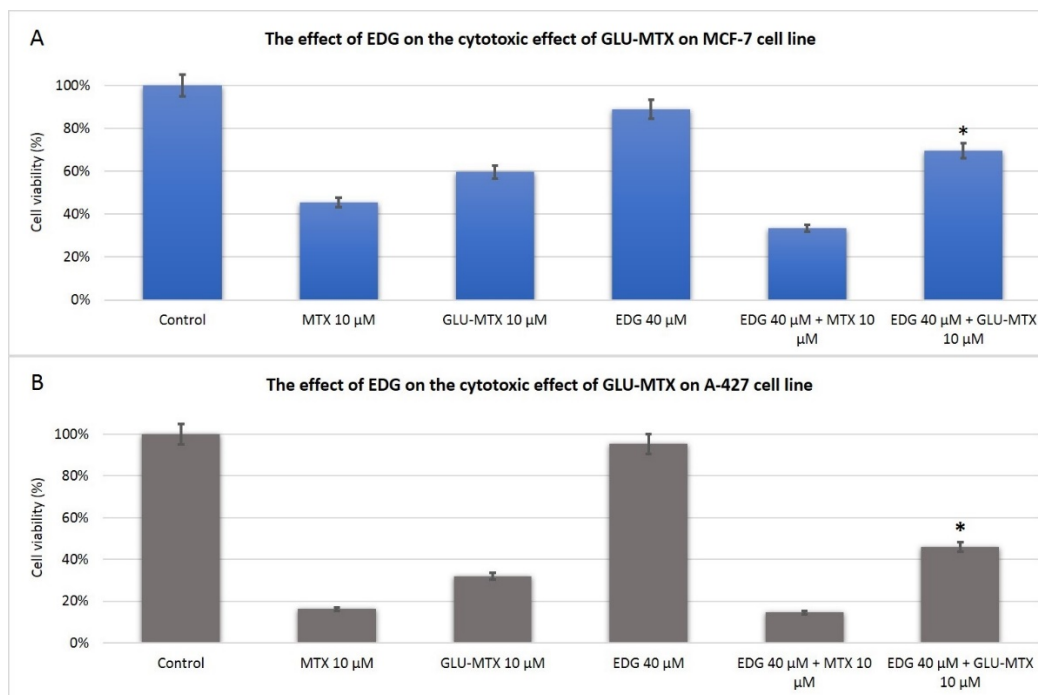


Figure 3. The effect of glucose transporter–1 (GLUT1) inhibitor 4,6-O-ethylidene- α -D-glucose (EDG) on the efficacy of free MTX and GLU–MTX treatment of (A) breast cancer cell line MCF-7 and (B) lung cancer cell line A-427. Cells were preincubated with EDG for 4 h and then incubated for 48 h with MTX or GLU–MTX. Results are presented as means \pm standard deviations from two independent experiments. * $p < 0.05$ vs. GLU–MTX 10 μ M.

2.3. Cellular Uptake of GLU–MTX Is Significantly Higher in SW-480 Colon Cancer Cells Compared to Free MTX

GLU–MTX is transported by facilitated diffusion exploiting overexpressed GLUT1 transporters [17] and is approximately 17-times more preferentially accumulated in cancer cells compared to free MTX (Figure 4). In the intracellular compartment, the cleavage of acid-labile bonds occurs, which results in the controlled release of free MTX.

2.4. Both MTX and GLU–MTX Lead to Cell Cycle Arrest in S Phase

To investigate whether MTX and GLU–MTX display the same mode of action, their effect on cell cycle progression was examined on the MCF-7 cell line. The results showed that cell populations in the S phase were significantly higher in MTX and GLU–MTX-treated cells after 24 h, in contradistinction with untreated cells (Figure 5, Table 1). This result proves that both compounds affect the cell cycle in a similar way, indicating the presence of free MTX originated from GLU–MTX in the intracellular compartment.

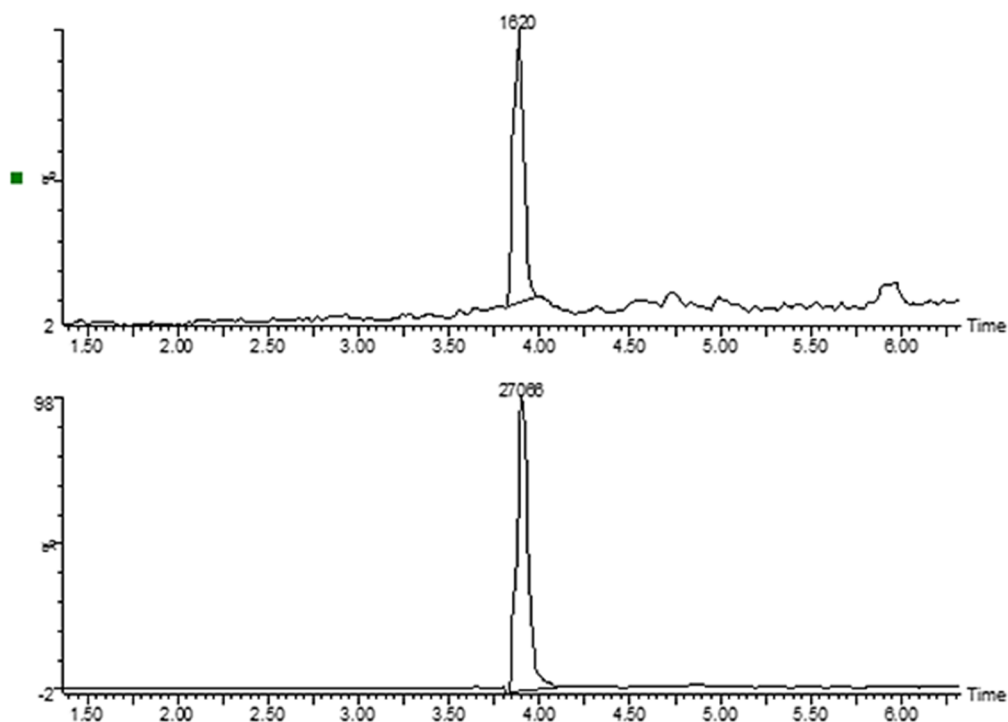


Figure 4. Mass chromatograms for m/z 455.18 ions in extracts from colon cancer SW-480 cell line—upper chromatogram MTX, lower GLU-MTX.

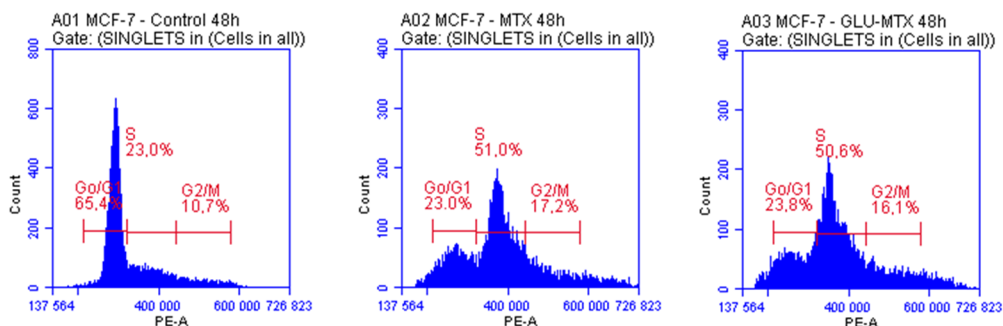


Figure 5. The effect of MTX and GLU-MTX on MFC-7 cell cycle progression.

Table 1. Cell cycle progression data presented as mean ± standard deviation (SD).

	G0/G1	S	G2/M
Control	65.4 ± 2.1	22.99 ± 0.8	10.7 ± 0.6
MTX	23.05 ± 1.4	50.97 ± 2.3	17.17 ± 1.3
GLU-MTX	23.83 ± 1.7	50.61 ± 1.9	16.11 ± 1.8

2.5. *In Vivo* Efficacy of GLU-MTX

After our observations of its potent *in vitro* effects, GLU-MTX and MTX were evaluated on 4T1 breast tumor-bearing mice, which are characterized by GLUT1 overexpression [18]. The compounds were injected *i.v.* in a single dose (day 0). MTX was given at 120 mg/kg, and GLU-MTX was given at a corresponding dose of 300 mg/kg. GLU-MTX significantly inhibited 4T1 allograft tumor growth by about 74.4% on day 18 ($p < 0.01$), whereas MTX led to tumor growth inhibition by 16.2% (Figure 6A). There was no significant loss of body weight in neither of the treatment groups (Figure 6B).

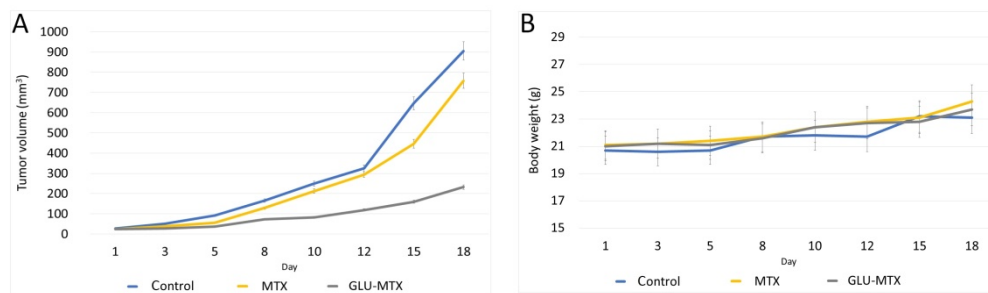


Figure 6. Results of the in vivo study. (A) The average tumor volume after 18 days in 3 groups (1—control, 2—MTX-treated and 3—GLU-MTX treated). In group 3, the tumor volume was significantly lower compared to other groups, as analyzed by one-way ANOVA followed by Bartlett's test ($p < 0.001$). (B) The effect of the therapy on body weight. No significant loss of body weight has been observed.

Histopathological analyses of the liver and lungs excised from MTX and GLU-MTX-treated mice showed differences in tissue morphology (Figure 7). Liver sections after MTX-treatment indicate visible periportal inflammation, while lung sections show lymphocytic and plasmacytic infiltration. Livers and lungs from GLU-MTX treated mice were without any morphological changes. Thus, the results indicate that GLU-MTX significantly inhibited tumor growth without affection of livers and lungs compared to free MTX.

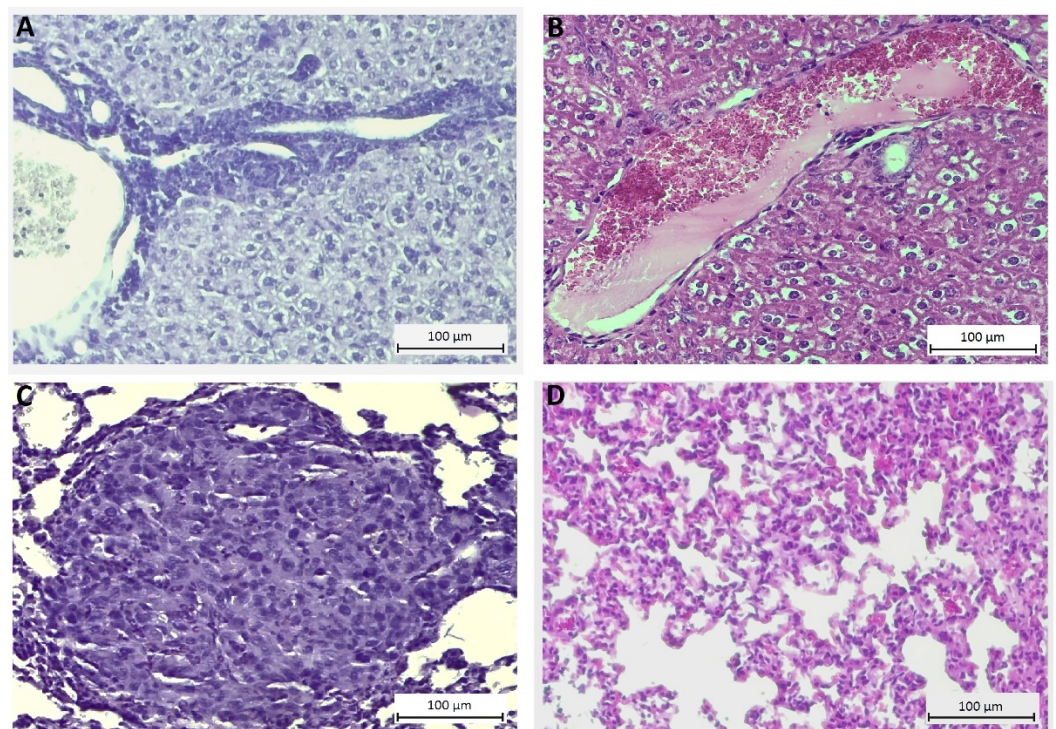


Figure 7. Representative images of liver and lung sections stained with hematoxylin-eosin (HE) to evaluate the cytotoxic impact of the MTX and GLU-MTX on the mice tissues. (A) Liver with typical for MTX therapy periportal inflammation. (B) The liver without pathological changes after GLU-MTX treatment. (C) The lung section shows lymphocytic and plasmacytic infiltration in mice treated with MTX. (D) Lung section without significant changes in the morphology from mice after treatment of GLU-MTX. Optical magnification: 200 \times . Scale bars 100 μ m.

3. Discussion

The “Warburg effect,” the increased aerobic glycolysis in many malignancies, has been extensively scrutinized and is now suggested to be the reason for most of the hallmarks of cancer [19,20]. Metabolic differences between normal and cancer provide an environment that often results in drug resistance. However, these characteristic features may also provide an opportunity to design appropriately tailored molecular targeted oncology interventions.

This study represents the first attempt to systematically evaluate the anticancer activities of a novel glucose–methotrexate conjugate in vitro and in vivo. We have shown several essential characteristics of this drug: (a) GLU–MTX exhibits potent anticancer activity against a range of solid tumor cell lines with IC₅₀ values similar to free MTX; (b) GLU–MTX preferentially annihilates cancer cells while showing low toxicity in noncancerous cells in vitro; (c) cellular uptake of GLU–MTX is glucose-transporter-specific; (d) the uptake of GLU–MTX in cancer cells is 17 times more efficient than that of MTX; (e) GLU–MTX caused significant tumor growth delay in breast tumor-bearing mice compared to MTX-treated and control mice.

Our results indicate that GLU–MTX may be used against a broad spectrum of cancers. GLU–MTX cytotoxicity consistently had IC₅₀ values in the $\mu\text{mol/L}$ range. The compound exerted higher selectivity for cancer cells over normal cells. The translocation efficiency and subsequent cellular accumulation were significantly higher in GLU–MTX-treated cells than in MTX. Notably, our results indicate that glucose transporter GLUT1 is involved in the cellular uptake of glucose conjugates. The viability of MTX-treated cells did not change significantly in the presence of an exofacial GLUT1 inhibitor. However, the GLUT1 inhibitor decreased the activity of GLU–MTX, which suggests that the reduced uptake of the compound resulted in lower cellular accumulation and weaker anticancer action. We cannot univocally state that the cellular transport of glucose conjugate is facilitated solely via the GLUT1 transporter. However, knowing that the glycoconjugates are highly hydrophilic, it is rather unlikely that their transport occurs via passive diffusion. Evidence has been found that the cellular uptake of some glycoconjugates may also be mediated by other receptors such as OCT2, SGLT, SWEET, and asialoglycoprotein receptor (ASGPR) [21,22]. These findings are corroborated by other studies showing that glucose conjugates exploit glucose transporters of cancer cells [9,17]. The uptake analysis showed that in the intracellular compartment, the payload was quickly detached from the conjugate. This suggests that the cleavable linkage allows the release of the cytotoxic payload inside the malignant cells, possibly through enzymatic hydrolysis. This finding is particularly significant as the spacer arm must be designed in such a way as to ensure its stability in the extracellular compartment while also allowing the action of the active cytotoxic payload addressed to tumor cells. The nature of the spacer thus influences how favorable drug delivery is and its outcome. Over-stable linkers can curb the activity of the associated pharmacophore, resulting in a low-potency compound. Conversely, an understable spacer can provoke poor target specificity and high systemic toxicity [23].

Our study bears several limitations. First, the synthesis is multi-staged and requires more delicate control of the experimental parameters. Hence, a limited amount of the compound was obtained for biological assays. Second, we were able to perform in vitro and in vivo analysis only on selected cancer cell models; hence the results may not be generalizable. Third, the in vivo study did not include multiple administrations of the tested compounds. Further analyses are required to examine these effects on an animal model.

4. Materials and Methods

4.1. Chemistry

NMR spectra were recorded with an Agilent spectrometer 400 MHz using TMS as internal standard and CDCl₃ or DMSO-d₆ as a solvent. NMR solvents were purchased from ACROS Organics (Geel, Belgium). Chemical shifts (δ) were expressed in ppm and coupling constants (J) in Hz. Optical rotations were measured with a JASCO P-2000 polarimeter

using a sodium lamp (589.3 nm) at room temperature. Melting point measurements were performed on a Stanford Research Systems OptiMelt (MPA 100). Electrospray ionization mass spectrometry was performed on the Xevo G2 Q-TOF mass spectrometer. Reactions were monitored by TLC on precoated plates of silica gel 60 F254 (Merck Millipore, Burlington, MA, USA). The TLC plates were inspected under UV light ($\lambda = 254$ nm) or charring after spraying with 10% sulfuric acid in ethanol. Crude products were purified using column chromatography performed on silica gel 60 (70–230 mesh, Fluka, St. Louis, MI, USA) developed with toluene/EtOAc and $\text{CHCl}_3/\text{MeOH}$ as solvent systems. Organic solvents were evaporated on a rotary evaporator under diminished pressure at 40 °C. All of the chemicals used in the experiments were purchased from Sig-ma-Aldrich (Saint Louis, Missouri, USA), ACROS Organics (Geel, Belgium), and Avantor Performance Materials Poland S.A (Gliwice, Poland) and were used without purification. Methotrexate, propargyl chloroformate, propargyl alcohol, and D-glucose are commercially available. 2-Azidoethyl β -D-O-glucopyranoside [24,25] and GLU–MTX [16] was prepared according to the respective published procedures.

Synthesis of Glycoconjugate

2-Azidoethyl β -D-O-glucopyranoside (82 mg, 0.33 mmol) and propargyl alcohol (20 μL , 0.33 mmol) were dissolved in a dry solvent system: THF (3 mL) and *i*-PrOH (3 mL). The solutions of sodium ascorbate (27 mg, 0.13 mmol) in H_2O (1.5 mL) and $\text{CuSO}_4 \cdot 5\text{H}_2\text{O}$ (16 mg, 0.06 mmol) in H_2O (1.5 mL), mixed and immediately added to the reaction mixture. The reaction mixture was stirred for 24 h at room temperature. Then, the solvents were evaporated in vacuo, and the crude products were purified by column chromatography (dry loading: $\text{CHCl}_3:\text{MeOH}$, gradient: 50:1 to 2:1) to give products 1 (69 mg, 70% yield): m.p. 60–63 °C; $[\alpha]_{\text{D}}^{22} = -5$ ($c = 1.0$, DMSO).

^1H NMR (400 MHz, DMSO- d_6): δ 2.97 (m, 1H, H-2_{Glu}), 3.04 (m, 1H, H-4_{Glu}), 3.09–3.16 (m, 2H, H-3_{Glu}, H-5_{Glu}), 3.43 (m, 1H, H-6a_{Glu}), 3.68 (m, 1H, H-6b_{Glu}), 3.89 (m, 1H, CH), 4.07 (m, 1H, CH), 4.23 (d, 1H, $J = 7.8$ Hz, H-1_{Glu}), 4.47–4.58 (m, 5H, 2xCH₂, OH), 4.91 (d, 1H, $J = 5.1$ Hz, OH), 4.95 (d, 1H, $J = 4.7$ Hz, OH), 5.06 (d, 1H, $J = 5.1$ Hz, OH), 5.15 (dd, 1H, $J = 5.5$ Hz, $J = 5.9$ Hz, OH), 8.01 (s, 1H, H-5_{triaz}).

^{13}C NMR (100 MHz, DMSO- d_6): δ 49.54, 54.99, 61.05, 67.41, 69.99, 73.29, 76.60, 76.97, 102.93, 123.45, 147.68.

HRMS (ESI-TOF): calcd for $\text{C}_{11}\text{H}_{20}\text{N}_3\text{O}_7$ ($[\text{M} + \text{H}]^+$): m/z 306.1301; found m/z 306.1300.

4.2. Cell Culture

The panel of different human cell lines was used to evaluate the effectiveness of the novel compound, human colon adenocarcinoma SW-480 and DLD-1, breast carcinoma MCF-7, squamous cell carcinoma SCC-25 purchased from the Leibniz Institute DSMZ-German Collection of Microorganisms and Cell Cultures, (DSMZ, Braunschweig, Germany), lung carcinoma A427, osteosarcoma MG63, normal fibroblasts WI-38 kindly provided by Institute of Immunology and Experimental Therapy, the Polish Academy of Sciences, Poland, and obtained from American Type Culture Collection. Cell lines A427, MG63, WI-38 cells were maintained in Eagle's minimum essential medium, MCF-7, DLD-1 in RPMI 1640, SCC-25 in DMEM/F12 medium. To make the complete growth medium, fetal bovine serum (FBS) to a final concentration of 10% and 100 U/mL penicillin, 100lg/mL streptomycin were added. Cells were grown in a humidified incubator with 5% CO_2 at 37 °C. The fresh culture medium was changed every 2–3 days. Cell culture media, FBS, trypsin, and antibiotics were used from Gibco (Thermo Fisher Scientific Inc., Waltham, MA, USA).

4.3. *In Vitro* Cytotoxicity of MTX and GLU–MTX

For MTT experiments, cell lines were seeded in 96-well plates ($5-8 \times 10^3$ cells/well). The following day cells were treated with an appropriate complete culture medium (control) and different doses of methotrexate and glucose conjugated MTX (10, 50 μ M) for 48 h.

After the incubation, an MTT assay was performed. Cell viability was evaluated by the conversion of the yellow tetrazolium salt (MTT) into violet formazan insoluble crystals in mitochondria of active cells. Following 4 h, the medium was removed, and the dye was dissolved by dimethyl sulfoxide (DMSO, Sigma-Aldrich, Munich Germany), creating the color, which intensity is proportional to the viable cells. The absorbance rate was measured at 490 nm, and the reference wavelength was 570 nm (Bio-TekBioTek ELX800 multi-well reader, BioTek, Winooski, VT, USA). The viable cells (VC) were calculated as $VC (100\%) = (\text{absorbance of experimental group} / \text{absorbance of the control group}) \times 100\%$. MTT experiments were repeated, and figures represent the mean with standard deviation.

4.4. Measurement of Cellular Uptake of MTX and GLU–MTX by Mass Spectrometry

To measure differences in cellular uptake of Glu-Met and methotrexate, MCF-7 and SW480 cells were seeded in density 3×10^5 /well on 6 well plates. When cells reached 80% confluence, the medium was replaced with 1 mL/well fresh medium with or without tested compounds in dose 50 μ M. Following 6 h of incubation, the medium was centrifuged, collected and stored immediately at -80 °C. Then adherent cells were washed once with 1 mL PBS at room temperature (RT). Next, the plate was placed on ice and washed with 500 μ L ice-cold methanol: H₂O (3:1) twice. The collected supernatant was centrifuged and stored at -80 °C until the analysis.

4.5. LC/MS Analysis

4.5.1. Equipment

The UPLC system consisted of the Acquity UPLC binary pump, cooled sample manager and column oven (Waters, Milford, MA, USA). The mass spectrometer was a Xevo G2 Q-TOF MS equipped with an electrospray ionization interface (Waters, Milford, MA, USA). The data were acquired by using MassLynx software (version 4.0, Waters, Milford, MA, USA).

4.5.2. LC Conditions

Chromatographic separation was performed using a Waters BEH Shield (1.7 μ m, 2.1×100 mm) analytical column. The oven temperature was set at 45 °C. The mobile phases containing 0.1% formic acid in water (mobile phase A) and 0.1% formic acid in methanol (mobile phase B) were used at a flow rate of 0.2 mL/min. Gradient elution was performed according to the following steps: 1.0 min—5% B, 5.0 min—40% B, 7.5 min—65% B, 10 min—90% B, 11 min—90% B, 11.1 min—5% B, 13 min—5% B. The autosampler temperature was kept at 5 °C.

4.5.3. MS Conditions

A mass spectrometer was interfaced with an electrospray ionization (ESI) probe. Mass spectra acquisition parameters were optimized using electrospray ionization (ESI) in the positive ionization mode. The temperatures were maintained at 120 °C and 450 °C for the source and desolvation line, respectively. The voltages were set at 0.5 kV and 40 V for the capillary and sampling cone, respectively. The desolvation gas and the cone gas (N₂) flow rate was set at 800 L/h and 80 L/h, respectively.

4.6. Cell Cycle Analysis

After treatment, control cells, MTX and GLU–MTX-treated cells were harvested, collected and washed in PBS. Then, the cells were resuspended at $1-2 \times 10^6$ cells/mL, and 5 mL of cold 70% ethanol was carefully added. Afterward, the cells were fixed for at least 1 h at 4 °C. Following washing twice in PBS, 0.5 mL of FxCycle™ PI/RNase staining

solution (Life Technologies, Carlsbad, USA) to cell pellet was added and mixed well. The samples were incubated for 15–30 min at room temperature, protected from light and then analyzed by flow cytometry to determine the cell cycle profile.

4.7. Mouse Allograft Model of Human Breast Cancer

The animal use and care protocol were approved by the local ethical committee for animal experiments. The female BALB/c mice with a weight of 17–20 g (6–8 weeks old) were provided and maintained on free access to food and water. Then female BALB/c mice were injected subcutaneously with 4T1 breast cancer cell. The cells were suspended in 50 μ L of Hanks' solution: Matrigel (9:1) and implanted in the second right mammary gland (10^5 – 10^6 cells per mouse).

All animals were monitored for activity, physical condition, body weight, and tumor growth. Tumor size was determined every other day by caliper measurement of two perpendicular diameters of the implant. Tumor weight (in grams) was calculated by the formula $TV = 1/2 \times a^2 \times b$, in which a is the long diameter, and b is the short diameter (in millimeters).

4.8. In Vivo Chemotherapy

The animals bearing breast cancer allograft tumors were randomly divided into two treatment groups and a control group (5–7 mice per group). Test animals received a single i.v. injection via the tail vein of GLU–MTX and MTX at a dose of 300 mg/kg, and 120 mg/kg, respectively. The treatment was started one day after the transplantation of tumor cells. The control animals received an injection of 0.2 mL of the vehicle only. The tumor volume and weight of each mouse were measured over a period of 18 days. The body weights of 4T1 tumor-bearing mice treated with GLU–MTX, MTX, and vehicle (DMSO) only were recorded simultaneously every 2 to 3 days during the study. No mice were lost during the experiment.

4.9. Histological Evaluation of Toxicity

Formalin-fixed and paraffin-embedded tissue sections of livers and lungs were stained with hematoxylin–eosin (HE) to evaluate the impact of the therapeutics on the tissues and 4T1 cells metastasis.

4.10. Statistical Analysis

In vivo data were analyzed by one-way analysis of variance (ANOVA). $p < 0.05$ was considered statistically significant. Data from in vitro experiments were expressed as means \pm standard deviation (SD), and the statistical analysis was performed using Mann–Whitney U test in the PAST 4.03 program. The differences between groups were considered significant at $p < 0.05$.

5. Conclusions

In conclusion, we have synthesized a novel GLU–MTX conjugate and have shown that it has broad-spectrum anticancer activity. The compound preferentially accumulates in and annihilates malignant cells while showing reduced accumulation and low toxicity in normal fibroblasts. These results collectively represent a critical step forward in developing molecular tumor-targeting properties into established therapeutic drugs for improved safety and efficacy of anticancer therapies. These studies are essential for further preclinical and clinical development of a glucose-based class of compounds.

6. Patents

The authors are inventors on submitted patent applications (serial number P.426731).

Author Contributions: Conceptualization, M.W. and S.A.; methodology, M.W., G.P.-G., J.W., M.K.; validation, G.P.-G., T.K.; formal analysis, S.M., W.S.; investigation, M.W., S.M., T.K., P.H., D.S., M.K.; writing—original draft preparation, M.W., G.P.-G., S.A.; writing—review and editing, S.M., T.K., P.H., M.K.; supervision, A.G., W.S.; project administration, S.A.; funding acquisition, S.A. All authors have read and agreed to the published version of the manuscript.

Funding: This research was funded by the National Centre for Research and Development, grant number TANGO3/426098/NCBR/2019, and by Wroclaw Medical University, grant number STM.A010.20.135.

Institutional Review Board Statement: The study was conducted according to the guidelines of the EU Directive 2010/63/EU on the protection of animals used for scientific purposes and approved by the Ethics Committee of the Local Ethical Committee for Animal Experiments, Wroclaw, Poland (no. 51/2018 issued on 16/05/2018).

Informed Consent Statement: Not applicable.

Data Availability Statement: Data are contained within the article.

Conflicts of Interest: The authors declare no conflict of interest.

References

1. Khan, Z.A.; Tripathi, R.; Mishra, B. Methotrexate: A detailed review on drug delivery and clinical aspects. *Expert Opin. Drug Deliv.* **2012**, *9*, 151–169. [CrossRef]
2. Howard, S.C.; McCormick, J.; Pui, C.; Buddington, R.K.; Harvey, R.D. Preventing and Managing Toxicities of High-Dose Methotrexate. *Oncologist* **2016**, *21*, 1471–1482. [CrossRef] [PubMed]
3. Świerkot, J. Toxicity of low dose methotrexate in rheumatoid arthritis. *Adv. Clin. Exp. Med.* **2007**, *16*, 287–295.
4. Abolmaali, S.S.; Tamaddon, A.M.; Dinarvand, R. A review of therapeutic challenges and achievements of methotrexate delivery systems for treatment of cancer and rheumatoid arthritis. *Cancer Chemother. Pharmacol.* **2013**, *71*, 1115–1130. [CrossRef] [PubMed]
5. Mahato, R.; Tai, W.; Cheng, K. Prodrugs for improving tumor targetability and efficiency. *Adv. Drug Deliv. Rev.* **2011**, *63*, 659–670. [CrossRef]
6. Liberti, M.V.; Locasale, J.W. The Warburg Effect: How Does it Benefit Cancer Cells? *Trends Biochem. Sci.* **2016**, *41*, 211–218. [CrossRef]
7. Calvaresi, E.C.; Hergenrother, P.J. Glucose conjugation for the specific targeting and treatment of cancer. *Chem. Sci.* **2013**, *4*, 2319–2333. [CrossRef]
8. Makuch, S.; Wozniak, M.; Krawczyk, M.; Pastuch-Gawolek, G.; Szeja, W.; Agrawal, S. Glycoconjugation as a promising treatment strategy for psoriasis. *J. Pharmacol. Exp. Ther.* **2020**, *373*, 204–212. [CrossRef]
9. Patra, M.; Awuah, S.G.; Lippard, S.J. Chemical Approach to Positional Isomers of Glucose-Platinum Conjugates Reveals Specific Cancer Targeting through Glucose-Transporter-Mediated Uptake in Vitro and in Vivo. *J. Am. Chem. Soc.* **2016**, *138*, 12541–12551. [CrossRef]
10. Agrawal, S.; Wozniak, M.; Luc, M.; Walaszek, K.; Pielka, E.; Szeja, W.; Pastuch-Gawolek, G.; Gamian, A.; Ziolkowski, P. Insulin and novel thioglycosides exert suppressive effect on human breast and colon carcinoma cells. *Oncotarget* **2017**, *8*, 114173–114182. [CrossRef]
11. Ma, Y.; Wang, W.; Idowu, M.O.; Oh, U.; Wang, X.Y.; Temkin, S.M.; Fang, X. Ovarian cancer relies on glucose transporter 1 to fuel glycolysis and growth: Anti-tumor activity of BAY-876. *Cancers* **2019**, *11*, 33. [CrossRef] [PubMed]
12. Dyshlovoy, S.A.; Pelageev, D.N.; Hauschild, J.; Borisova, K.L.; Kaune, M.; Krisp, C.; Venz, S.; Sabutskii, Y.E.; Khmelevskaya, E.A.; Busenbender, T.; et al. Successful targeting of the warburg effect in prostate cancer by glucose-conjugated 1,4-naphthoquinones. *Cancers* **2019**, *11*, 1609. [CrossRef] [PubMed]
13. Barbosa, A.M.; Martel, F. Targeting glucose transporters for breast cancer therapy: The effect of natural and synthetic compounds. *Cancers* **2020**, *12*, 154. [CrossRef] [PubMed]
14. Tomaszowski, K.-H.; Hellmann, N.; Ponath, V.; Takatsu, H.; Shin, H.-W.; Kaina, B. Uptake of glucose-conjugated MGMT inhibitors in cancer cells: Role of flippases and type IV P-type ATPases. *Sci. Rep.* **2017**, *7*, 13925. [CrossRef]
15. Pohl, J.; Bertram, B.; Hilgard, P.; Nowrousian, M.R.; Stüben, J.; Wießler, M. D-19575-a sugar-linked isophosphoramidate mustard derivative exploiting transmembrane glucose transport. *Cancer Chemother. Pharmacol.* **1995**, *35*, 364–370. [CrossRef] [PubMed]
16. Woźniak, M.; Pastuch-Gawolek, G.; Makuch, S.; Wiśniewski, J.; Ziolkowski, P.; Szeja, W.; Krawczyk, M.; Agrawal, S. Overcoming hypoxia-induced chemoresistance in cancer using a novel glycoconjugate of methotrexate. *Pharmaceuticals* **2021**, *14*, 13. [CrossRef]
17. Patra, M.; Johnstone, T.C.; Suntharalingam, K.; Lippard, S.J. A Potent Glucose-Platinum Conjugate Exploits Glucose Transporters and Preferentially Accumulates in Cancer Cells. *Angew. Chem. Int. Ed.* **2016**, *55*, 2550–2554. [CrossRef]
18. Young, C.D.; Lewis, A.S.; Rudolph, M.C.; Ruehle, M.D.; Jackman, M.R.; Yun, U.J.; Ilkun, O.; Pereira, R.; Abel, E.D.; Anderson, S.M. Modulation of glucose transporter 1 (GLUT1) expression levels alters mouse mammary tumor cell growth in vitro and in vivo. *PLoS ONE* **2011**, *6*, e23205. [CrossRef] [PubMed]

19. Schwartz, L.; Supuran, C.; Alfarouk, K. The Warburg Effect and the Hallmarks of Cancer. *Anticancer Agents Med. Chem.* **2017**, *17*, 164–170. [CrossRef]
20. Hanahan, D.; Weinberg, R.A. Hallmarks of cancer: The next generation. *Cell* **2011**, *144*, 646–674. [CrossRef] [PubMed]
21. Fu, J.; Yang, J.; Seeberger, P.H.; Yin, J. Glycoconjugates for glucose transporter-mediated cancer-specific targeting and treatment. *Carbohydr. Res.* **2020**, *498*, 108195. [CrossRef] [PubMed]
22. Deng, D.; Yan, N. GLUT, SGLT, and SWEET: Structural and mechanistic investigations of the glucose transporters. *Protein Sci.* **2016**, *25*, 546–558. [CrossRef] [PubMed]
23. El Hilali, M.; Reux, B.; Debiton, E.; Leal, F.; Galmier, M.J.; Vivier, M.; Chezal, J.M.; Miot-Noirault, E.; Coudert, P.; Weber, V. Linker structure-activity relationships in fluorodeoxyglucose chlorambucil conjugates for tumor-targeted chemotherapy. *Bioorg. Med. Chem.* **2017**, *25*, 5692–5708. [CrossRef] [PubMed]
24. Krawczyk, M.; Pastuch-Gawolek, G.; Pluta, A.; Erfurt, K.; Domiński, A.; Kurcok, P. 8-hydroxyquinoline glycoconjugates: Modifications in the linker structure and their effect on the cytotoxicity of the obtained compounds. *Molecules* **2019**, *24*, 4181. [CrossRef] [PubMed]
25. Zemplén, G.; Pacsu, E. Über die Verseifung acetylierter Zucker und verwandter Substanzen. *Ber. Dtsch. Chem. Ges. (A B Ser.)* **1929**, *62*, 1613–1614. [CrossRef]



Article

Alpha Ketoglutarate Exerts In Vitro Anti-Osteosarcoma Effects through Inhibition of Cell Proliferation, Induction of Apoptosis via the JNK and Caspase 9-Dependent Mechanism, and Suppression of TGF- β and VEGF Production and Metastatic Potential of Cells

Katarzyna Kaławaj ¹, Adrianna Sławińska-Brych ², Magdalena Mizerska-Kowalska ¹ , Aleksandra Żurek ¹, Agnieszka Bojarska-Junak ³ , Martyna Kandefer-Szerszeń ¹ and Barbara Zdzisińska ^{1,*}

¹ Department of Virology and Immunology, Maria Curie-Skłodowska University, Akademicka 19, 20-033 Lublin, Poland; katarzyna.kalawaj@op.pl (K.K.); magdalena.mizerska-dudka@poczta.umcs.lublin.pl (M.M.-K.); zurekaleksandra@wp.pl (A.Ż.); kandem@poczta.umcs.lublin.pl (M.K.-S.)

² Department of Cell Biology, Maria Curie-Skłodowska University, Akademicka 19, 20-033 Lublin, Poland; adrianna.slawska-brych@poczta.umcs.lublin.pl

³ Chair and Department of Clinical Immunology, Medical University of Lublin, Chodźki 4a, 20-093 Lublin, Poland; agnieszka.bojarska-junak@umlub.pl

* Correspondence: basiaz@poczta.umcs.lublin.pl

Received: 10 November 2020; Accepted: 8 December 2020; Published: 10 December 2020

Abstract: Osteosarcoma (OS) is the most common type of primary bone tumor. Currently, there are limited treatment options for metastatic OS. Alpha-ketoglutarate (AKG), i.e., a multifunctional intermediate of the Krebs cycle, is one of the central metabolic regulators of tumor fate and plays an important role in cancerogenesis and tumor progression. There is growing evidence suggesting that AKG may represent a novel adjuvant therapeutic opportunity in anti-cancer therapy. The present study was intended to check whether supplementation of Saos-2 and HOS osteosarcoma cell lines (harboring a TP53 mutation) with exogenous AKG exerted an anti-cancer effect. The results revealed that AKG inhibited the proliferation of both OS cell lines in a concentration-dependent manner. As evidenced by flow cytometry, AKG blocked cell cycle progression at the G₁ stage in both cell lines, which was accompanied by a decreased level of cyclin D1 in HOS and increased expression of p21^{Waf1/Cip1} protein in Saos-2 cells (evaluated with the ELISA method). Moreover, AKG induced apoptotic cell death and caspase-3 activation in both OS cell lines (determined by cytometric analysis). Both the immunoblotting and cytometric analysis revealed that the AKG-induced apoptosis proceeded predominantly through activation of an intrinsic caspase 9-dependent apoptotic pathway and an increased Bax/Bcl-2 ratio. The apoptotic process in the AKG-treated cells was mediated via c-Jun N-terminal protein kinase (JNK) activation, as the specific inhibitor of this kinase partially rescued the cells from apoptotic death. In addition, the AKG treatment led to reduced activation of extracellular signal-regulated kinase (ERK1/2) and significant inhibition of cell migration and invasion in vitro concomitantly with decreased production of pro-metastatic transforming growth factor β (TGF- β) and pro-angiogenic vascular endothelial growth factor (VEGF) in both OS cell lines suggesting the anti-metastatic potential of this compound. In conclusion, we showed the anti-osteosarcoma potential of AKG and provided a rationale for a further study of the possible application of AKG in OS therapy.

Keywords: alpha-ketoglutarate; cell cycle; apoptosis; JNK; cell migration; cell invasion; TGF- β ; VEGF

1. Introduction

Osteosarcoma (OS) is a malignant mesenchymal-origin primary tumor of bone. Its histological hallmark is the production of osteoid or immature bone by neoplastic cells [1]. Although bone tumors are relatively rare overall (less than 1% and 3–5% of all newly diagnosed malignant cancers in adults and children, respectively), OS is the most common bone cancer in children and adolescents [2]. OS has a bimodal age incidence distribution worldwide with the first peak in teenagers (at the age of 10–14 in females and 15–19 in males) and the second peak in the elderly [3]. The survival rates may vary depending on various factors (e.g., age, sex, disease stage, localization, country); in children and adolescents, they are similar in most countries, ranging from 55% to 75% [4]. However, the 5-year overall survival rates of OS patients with distant metastasis and/or relapsed OS is low, i.e., approximately 30% in individuals with lung metastasis [5]. The current OS treatment combines surgery with chemotherapy, which was introduced in the 1980s and resulted in significant improvement in OS patients' survival rates over the 1990s [4]. Most importantly, for the past 20 years, the survival rates in OS patients did not change essentially and no successful targeted therapies of this cancer have been developed so far [6]. Therefore, there is still a need for novel OS treatment strategies.

Alpha-ketoglutarate (AKG) or 2-oxoglutarate is known mainly as an intermediate of the tricarboxylic acid (TCA) cycle that serves the production of the energetic molecule ATP [7], although it can also be synthesized via other biosynthetic pathways in cells [8]. In the TCA cycle, AKG is formed as a product of isocitrate oxidative decarboxylation catalyzed by NADP-dependent isocitrate dehydrogenase isoforms (IDH1-3) [9]. AKG is characterized as a metabolite with pleiotropic activity due to its metabolic and non-metabolic functions associated with direct involvement in different cellular processes as a biosynthetic substrate, a co-substrate of 2-oxoglutarate-dependent dioxygenases (2-OGDDs), or a signaling molecule [8]. Mounting evidence suggests that AKG is one of the central metabolic regulators of tumor fate and plays an important role in cancerogenesis and tumor development [10]. Most importantly, it is involved in the regulation of hypoxic response and epigenetic modifications, i.e., two main phenomena that drive oncogenic transformation. AKG is a co-substrate for prolyl hydroxylases (PHDs) belonging to the 2-OGDD family, which regulate the stability of the hypoxia-inducible factor (HIF-1), i.e., an important transcription factor in cancer development and progression. Thus, the abundance of AKG may be a determinant of the HIF-1 stabilization/activity through the regulation of PHD activity [11,12]. Moreover, other AKG-dependent enzymes from the OGDD family, namely ten-eleven translocation hydroxylases (TET1-3) and Jumonji C domain-containing lysine demethylases (KDM2-7), are involved in DNA and histone demethylation, respectively, and take part in shaping the cellular epigenetic landscape that is important in cancerogenesis [13]. What is more, mutations in genes encoding TCA cycle enzymes, such as succinate dehydrogenase (SDH), fumarate hydratase (FH), and IDHs, may be present in several cancers, leading to the accumulation of appropriate metabolites, i.e., succinate, fumarate, and D-2-hydroxyglutarate, respectively, inside cells. All these metabolites may act as competitive inhibitors of 2-OGDD enzymes (including PHDs, TETs, and KDMs), and they have been termed "oncometabolites" due to their role in the metabolic reprogramming of cells and progression toward malignancy [14]. It is suggested that an increase in the level of AKG in cells may result in the reverse of 2-OGDD inhibition by oncometabolites and exert an anticancer effect [11,15–19].

Recent *in vitro* and *in vivo* experiments suggest that an increase in the intracellular level of AKG through different strategies, e.g., exogenous supplementation, alpha-ketoglutarate dehydrogenase (KGD; an enzyme that catalyses the oxidative decarboxylation of AKG to succinyl-Co-A in the TCA cycle) inactivation or even IDH overexpression, may lead to downregulation of HIF-1 or upregulation of

epigenetic enzymes and prevent/inhibit tumor progression or show direct anticancer effects [17,19–24]. A more recent study has also proposed therapeutic strategies to increase AKG intracellular levels as a mechanism of engagement of latent tumor-suppressive pathways in p53-deficient cancers. It has been shown that AKG is an effector molecule of p53-mediated tumor suppression and its accumulation in p53-deficient tumors can antagonize malignant progression [25].

OS is a cancer with numerous chromosomal abnormalities, gene mutations, and epigenetic defects, e.g., hypermethylation at promoter CpG islands of the key (Rb and p53) tumor suppressor pathways [26]. However, no mutations in the TCA enzymes have been identified so far [27,28] except for one study that has demonstrated IDH2 mutations in OS tissues [29]. Nevertheless, a few studies have shown that IDH1/IDH2 expression inversely correlated with the pathological grade and metastasis in OS [30,31], and the expression of IDH1 was lower in OS than normal bone tissue [24], suggesting that interference in the level of AKG abundance-regulating enzymes may represent a potential target in the OS therapy. Given these reports, our present study was intended to check whether supplementation of OS cells with exogenous AKG exerted an anti-osteosarcoma effect.

2. Results

2.1. AKG Inhibits Proliferation of OS Cells

Since AKG (supplemented as an alpha-ketoglutarate disodium salt dihydrate) was described to exhibit direct antiproliferative activity [22], we evaluated its influence on cell proliferation in two OS cell lines, i.e., Saos-2 (p53-null cell line) and HOS (p53 mutant). The OS cells were cultured in a complete growth medium with AKG, which was used at concentrations ranging from 2.5 to 200 mM established on the basis of research carried out by other authors [20–22]. The results showed a concentration-dependent ability of AKG to inhibit proliferation in both cell lines. Incubation of the Saos-2 and HOS cells in a growth medium with increasing concentrations of AKG for 96 h resulted in a similar degree of inhibition of proliferation of both types of OS cells evaluated by the MTT assay (Figure 1A,B). To verify the antiproliferative effect of AKG against OS cells, measurement of DNA synthesis (with the BrdU assay) was additionally performed after 48-h incubation with AKG. As shown in Figure 1C,D, AKG induced a concentration-dependent decrease in OS cell proliferation. The lowest concentrations inducing significant inhibition of the BrdU incorporation into the DNA of dividing cells were 5 mM and 10 mM of AKG for Saos-2 and HOS, respectively. However, the IC₅₀ values for both cell lines were very similar and amounted to 35.41 ± 0.17 mM and 35.37 ± 0.19 mM for the Saos-2 and HOS cells, respectively.

2.2. AKG Induces Cell Cycle Arrest in the G₁ Phase in OS Cells through Modulation of the Expression of Cell Cycle-Associated Proteins

To further explore the antiproliferative activity of AKG, the influence of the selected concentrations (10, 25, and 50 mM) of this compound on the distribution of cell cycle phases in both OS cell lines after 48-h incubation was analyzed by flow cytometry. As shown in Figure 2A–D, the AKG treatment at all the concentrations used resulted in accumulation of Saos-2 (Figure 2A,B) and HOS (Figure 2C,D) cells in the G₁ phase with a concomitant reduction of the cell number in the S and G₂ phases. Compared to the control, the highest AKG concentration of 50 mM significantly elevated the G₁-fraction from $60.02 \pm 0.92\%$ to $72.81 \pm 1.58\%$ in the Saos-2 cell culture and from 67.51 ± 0.29 to $74.37 \pm 0.61\%$ in the HOS cell culture.

Since AKG caused the cell cycle arrest in the G₁ phase, further studies were conducted to investigate the effect of AKG on the expression of proteins responsible for the transition from the G₁ phase to the S phase of the cell cycle, i.e., cyclin D1 and the cyclin-dependent p21^{Waf1/Cip1} inhibitor. Changes in the expression of these proteins were evaluated by means of immunoassay methods. Only trace amounts of cyclin D1 were detected in the Saos-2 cells (which is in agreement with a previous study [32]), and its expression did not change significantly after the AKG treatment [data not shown].

In contrast, the HOS cells expressed cyclin D1 and its level was downregulated in the AKG-treated cells in a concentration-dependent manner. The 24-h AKG treatment at the concentrations of 25 and 50 mM decreased its expression by approx. 9% and 33%, respectively (Figure 2E). In turn, the expression of the cyclin-dependent p21^{Waf1/Cip1} inhibitor in the AKG-treated Saos-2 cells was significantly upregulated in a concentration- and time-dependent manner. After the 6-h AKG treatment at the concentrations of 10, 25, and 50 mM, the expression of p21^{Waf1/Cip1} increased by 7%, 14%, and 42%, respectively. The 24-h treatment with the same concentrations of AKG resulted in a greater increase in the expression of this protein by 19%, 39%, and 57% respectively, in comparison with the control levels (Figure 2F). In the case of the HOS cells, only the 6-h incubation with AKG at the concentrations of 25 and 50 mM induced a statistically significant increase in p21^{Waf1/Cip1} protein expression by 17% and 57%, respectively, compared to the control. In turn, the longer AKG treatment (24 h) resulted in a decrease in the expression of this protein (Figure 2G).

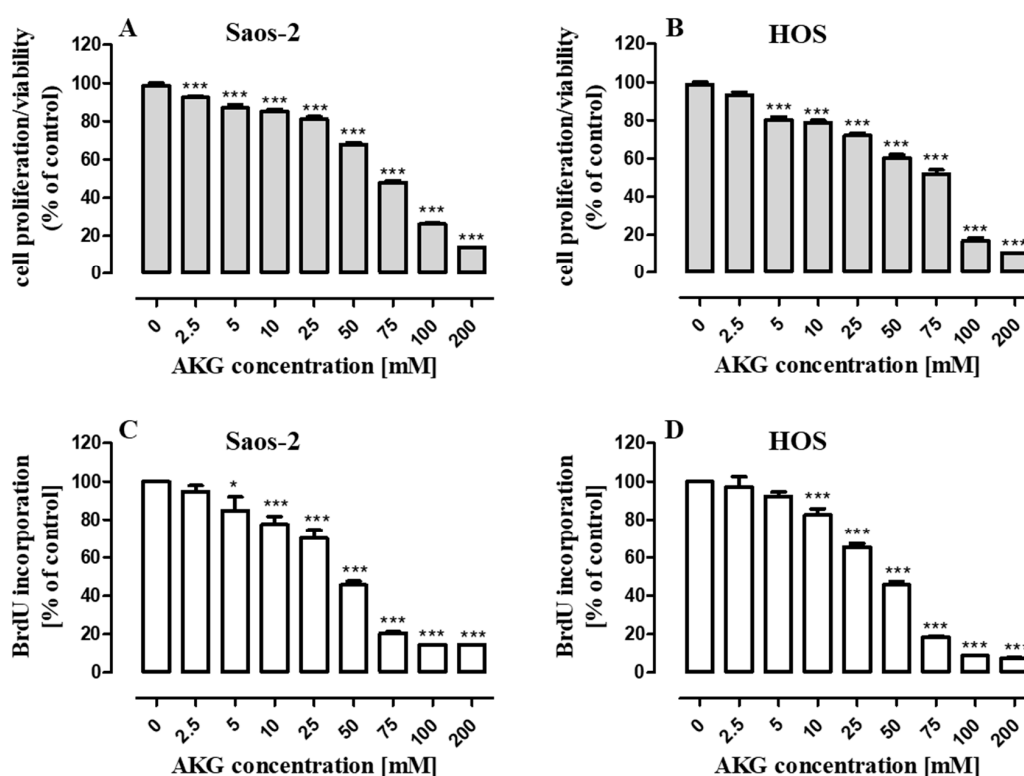


Figure 1. Effect of alpha-ketoglutarate (AKG) on Saos-2 and HOS cell proliferation. The osteosarcoma (OS) cells were treated with increasing concentrations of the compound. Cell proliferation was assessed with the MTT assay after 96 h (A,B) and the levels of BrdU incorporated into the cells after the 48-h AKG treatment were determined (C,D). All experiments were repeated independently at least three times, and data ($n = 24$ for each concentration) are expressed as the mean \pm SD; * $p < 0.05$ and *** $p < 0.001$ in comparison to the control; one-way ANOVA test.

2.3. AKG Induces Cell Death in OS Cells through Apoptosis via an Intrinsic Caspase-Dependent Pathway

Since the cell growth inhibition by AKG may have been also a result of the induction of cell death via apoptosis and/or necrosis, the cells were analyzed using Annexin V-FITC/PI double staining and flow cytometry. As shown in Figure 3A–D, after 72-h treatment, AKG was found to induce apoptosis in both Saos-2 and HOS cells, whereas necrosis was only slightly increased when the Saos-2 cells were incubated with 50 mM of AKG (Figure 3B). Significant induction of apoptosis was observed even at 5 mM of AKG. The percentage of Saos-2 cells undergoing apoptosis increased significantly from $0.5 \pm 0.01\%$ in the control to $7.5 \pm 0.29\%$, 8.2 ± 0.28 , $9.6 \pm 0.22\%$, and $12.1 \pm 0.22\%$ after the incubation with 5, 10, 25, or 50 mM of the AKG, respectively (Figure 3B). Similarly, the percentage of HOS cells

undergoing apoptosis increased from $1.0 \pm 0.16\%$ in the control to $5.0 \pm 0.58\%$, $5.8 \pm 0.16\%$, $8.3 \pm 0.30\%$, and $12.0 \pm 0.28\%$ after the incubation with 5, 10, 25, or 50 mM of the compound, respectively (Figure 3D).

Moreover, to identify the mechanism of AKG-induced apoptosis in OS cells, the activation of effector caspase-3 was evaluated by flow cytometry. As shown in Figure 4A–D, in both OS cell lines, the 72-h AKG treatment resulted in a concentration-dependent increase in the number of cells with active caspase 3.

A further study was undertaken to resolve which pathway, receptor- or mitochondria-dependent, was involved in the AKG-induced caspase 3 activation in the OS cells. Since a higher number of cells with activated caspase 3 was observed in the Saos-2 culture, this cell line was chosen to examine the activation of initiator caspase-8 (extrinsic pathway) and caspase-9 (intrinsic pathway) with the use of immunoblotting and flow cytometry methods. As shown in Figure 5A–C, AKG caused a slight increase in the active forms of caspase-8, in comparison with the control, after the 72-h treatment, although only in a small percentage of cells. In contrast, an AKG concentration-dependent decrease in the procaspase-9 levels and an increase in its active form were observed in the Saos-2 cells (Figure 5D), and a large number of cells exhibited the presence of the active form of this caspase (Figure 5E,F). Since these results indicated that the AKG-treatment activated predominantly the intrinsic apoptotic pathway, the expression of pro-apoptotic and anti-apoptotic proteins associated with mitochondrial membrane integrity were further assessed by Western blot analysis at 72 h. As shown in Figure 5G,H, the exposure to AKG triggered a significant increase in the amount of the pro-apoptotic Bax protein and a decrease (although to a lesser extent) in the expression of Bcl-2 (apoptosis inhibitor) in the Saos-2 cells. This suggests that the AKG treatment may result in the predominance of pro-apoptotic signals through an increase in the Bax/Bcl-2 ratio.

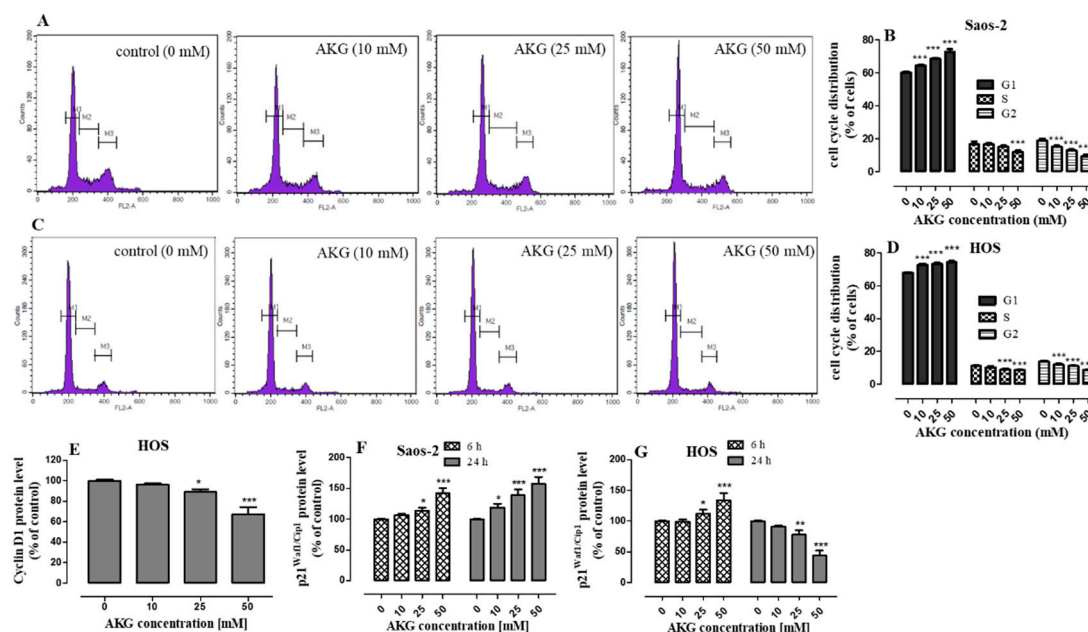


Figure 2. Effect of AKG on cell cycle distribution and expression of cell cycle-associated proteins in Saos-2 and HOS cultures. After the treatment with various concentrations of AKG for 48 h, the cells were stained with propidium iodide and analyzed by flow cytometry. Representative DNA histograms for Saos-2 (A) and HOS (C) cell lines with statistical analysis of the percentages of cells in the G1, S, and G2 phases in Saos-2 (B) and HOS (D) cultures. The levels of cyclin D1 in HOS cells (E) were measured after 24-h, while p21^{Waf1/Cip1} in the Saos-2 (F) and HOS (G) cells after 6-h and 24-h incubation without or with AKG (10, 25, and 50 mM) (with the ELISA assay). Data are expressed as means \pm SD for at least three independent experiments. ($n = 3$), * $p < 0.05$, ** $p < 0.01$ and *** $p < 0.001$ in comparison to the control; one-way ANOVA test.

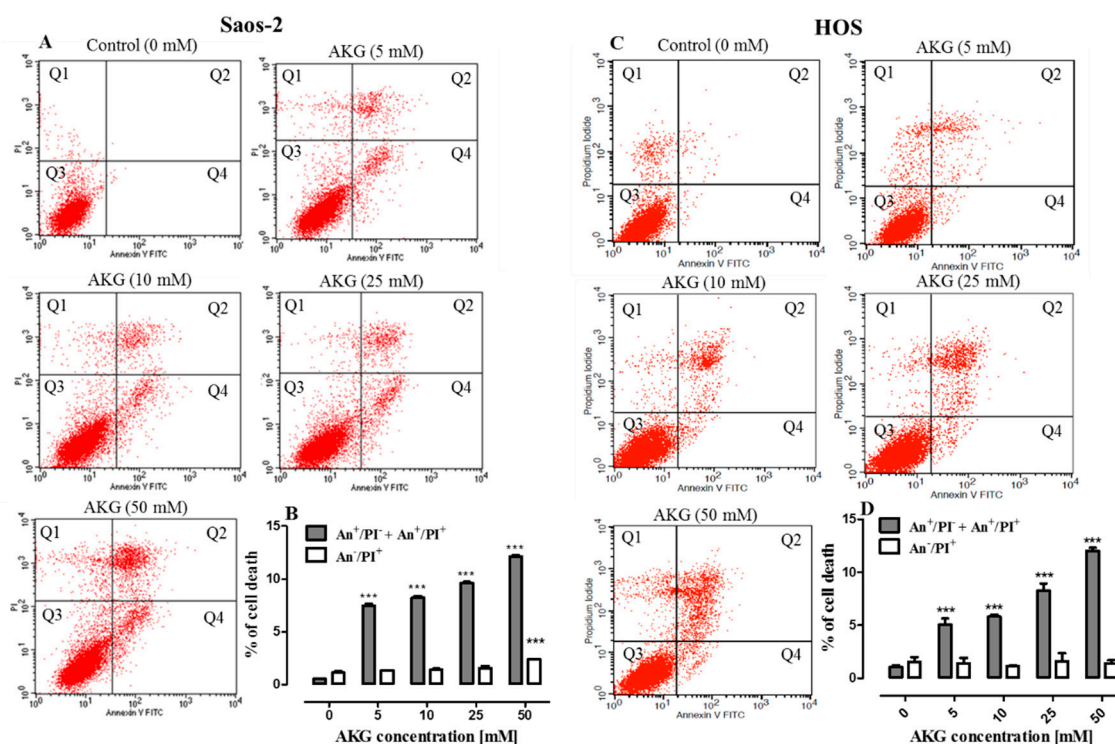


Figure 3. Effect of AKG on apoptosis induction in Saos-2 and HOS cell lines. After the 72-h exposure to the different concentrations of AKG, the cells were stained with annexin (An) V-FITC/propidium iodide (PI) and examined with flow cytometry. The representative dot plots indicate the percentage of An⁻/PI⁺ necrotic cells (Q1), An⁺/PI⁺ late apoptotic cells (Q2), An⁻/PI⁻ viable cells (Q3), and An⁺/PI⁻ early apoptotic cells (Q4) in AKG-treated Saos-2 (A) and HOS (C) cell cultures. Histogram representation of the quantitative percentage of total apoptotic cells (early + late apoptosis) and necrotic cells in the control and AKG-treated Saos-2 (B) and HOS (D) cell cultures. All experiments presented in this figure were repeated independently at least three times, and data ($n = 12$ for each concentration) are expressed as mean \pm SD; *** $p < 0.001$ in comparison to the control; one-way ANOVA test.

2.4. AKG Modulates the Phosphorylation of Mitogen-Activated Protein Kinases and Induces Apoptosis in OS Cells through a c-Jun N-Terminal Protein Kinase (JNK)-Dependent Mechanism

To explore the involvement of mitogen-activated protein kinases (MAPKs) in AKG-induced OS cell apoptosis, phosphorylation of JNK, extracellular signal-regulated kinase (ERK1/2), and p38 was examined with the quantitative ELISA method. As shown in Figure 6A, the AKG treatment reduced ERK1/2 phosphorylation in a concentration-dependent manner within 6 and 24 h in the Saos-2 cells. In contrast, AKG remarkably augmented the level of phospho-JNK in a concentration-dependent manner, but not phospho-p38 (Figure 6B,C).

JNK is a stress-activated kinase, and a signaling pathway with the participation of this kinase regulates e.g., apoptosis [33]. To clarify whether the AKG-activated JNK signaling pathway was engaged in the apoptotic process, the Saos-2 cells were cultured with AKG in the presence of a specific inhibitor of JNK (SP600125). After 72 h, the percentage of apoptotic cells was measured with FACS, whereas the JNK phosphorylation status was evaluated after 24 h with ELISA. As shown in Figure 6D, the percentage of apoptotic cells declined from $22.52 \pm 1.8\%$ after the treatment with 50 mM AKG alone to $13.1 \pm 1.2\%$ when the cells were co-treated with AKG and 5 μ M of SP600125. It was found that the inhibition of JNK phosphorylation by SP600125 completely inhibited the activation of JNK induced by this compound (Figure 6E) and partially reduced the level of AKG-induced apoptosis in the Saos-2 cells (Figure 6F). These data may therefore support the observation that the AKG-induced apoptosis in the Saos-2 cells was mediated partially through the activation of the JNK signaling pathway.

2.5. AKG Inhibits the Migration and Invasiveness of OS Cells and Decreases the Production of VEGF and TGF- β in These Cells

Since OS is classified as a strong tumor metastatic disease, the effect of AKG (5, 10, 25, 50 mM) on the migration (evaluated in a wound-healing assay) and invasion (evaluated in a transwell chamber assay with a basement membrane extract (BME)-coated membrane) of the Saos-2 and HOS cells was assessed. As shown in Figure 7A–D, the AKG treatment suppressed cell migration in both cell lines in a concentration-dependent manner. The inhibition of the migration of Saos-2 and HOS cells after the 24-h AKG treatment at a concentration of 50 mM increased approx. 2.3 and 2.5 times, respectively, in comparison with the migratory potential of control cells. At the same time, the AKG treatment decreased the invasiveness of both cell lines in a concentration-dependent manner (Figure 8A,B). The lowest AKG concentration used, i.e., 5 mM decreased the invasive activity of the Saos-2 and HOS cells by $14 \pm 0.87\%$ and $17 \pm 2.71\%$, respectively, in comparison with the control cells. In turn, at the highest AKG concentration, i.e., 50 mM, the invasiveness of the Saos-2 and HOS cells decreased markedly by $43 \pm 1.37\%$ and $60.5 \pm 3.53\%$, respectively.

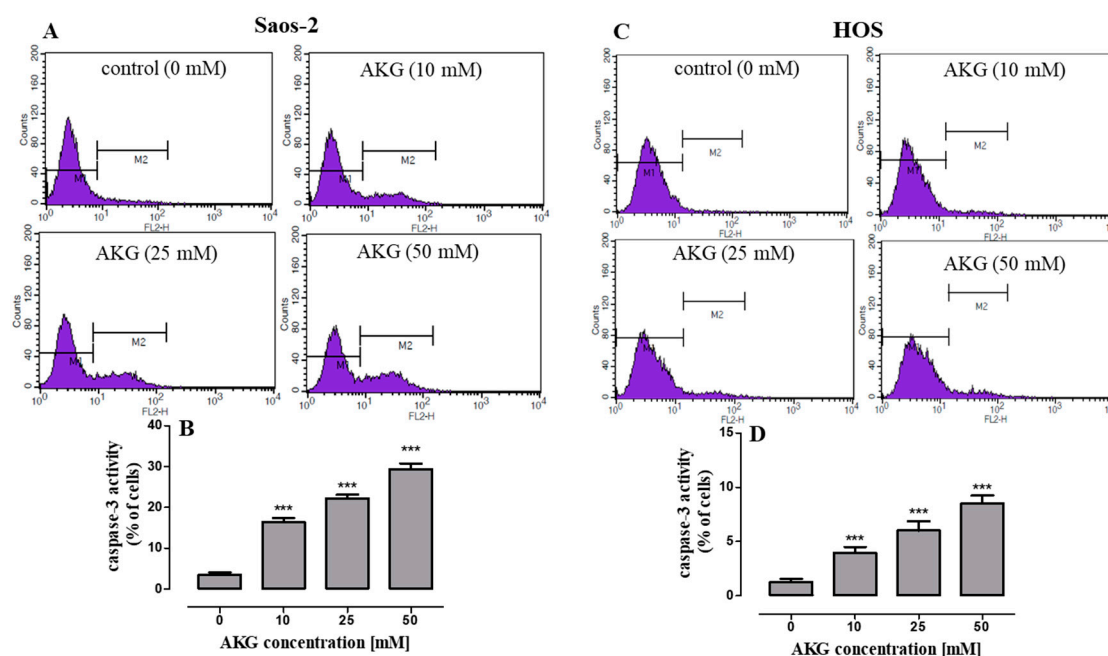


Figure 4. Flow cytometry analysis of active caspase-3 in Saos-2 and HOS cells treated with AKG for 72 h. Representative histograms of Saos-2 (A) and HOS (C) cell cultures. Symbols M1 and M2 represent peaks for viable (caspase-3 negative cells) and apoptotic cell fractions (caspase-3 positive cells), respectively. Quantification of caspase-3 activity in Saos-2 (B) and HOS (D) cell cultures. Mean \pm SD of 3 measurements in three independent experiments ($n = 12$ for each concentration); statistically significant at $p < 0.001$ *** in comparison to the control; one-way ANOVA test.

In addition, the production of some cell migration-, invasion- and angiogenesis-associated growth factors such as transforming growth factor β (TGF- β) and vascular endothelial growth factor (VEGF) was examined by ELISA. As shown in Figure 8C,D, both OS cell lines constitutively produced significant amounts of TGF- β , although the Saos-2 cells secreted almost two-fold higher levels of this cytokine than the HOS cells. The level of TGF- β produced by the control Saos-2 and HOS cultures was 5570 ± 27.85 pg/mL and 2851 ± 55.70 pg/mL, respectively. The 72-h treatment of the Saos-2 and HOS cells with AKG suppressed the production of TGF- β in a concentration-dependent manner in both OS cell types (Figure 8C,D). At the highest concentration tested, i.e., 50 mM, AKG decreased the production of TGF- β in the Saos-2 and HOS cells by approx. 29% and 43%, respectively. Similarly, both OS cell lines secreted constitutively significant amounts of VEGF, although also in this case the

control Saos-2 cells produced substantially higher quantities of this growth factor than the HOS cells ($29\,670 \pm 35$ pg/mL vs. 1985 ± 14 pg/mL, respectively). The 72-h treatment of the Saos-2 and HOS cells with AKG suppressed the production of VEGF in a concentration-dependent manner in both OS cell lines (Figure 8E,F); however, this effect was stronger in the HOS cells. In this cell line, all the AKG concentrations tested, i.e., 5, 10, 25, and 50 mM, inhibited significantly VEGF production by approx. 21%, 33%, 74%, and 94%, respectively (Figure 8F). After the treatment of the Saos-2 cells with AKG at a concentration of 10, 25, and 50 mM, the production of VEGF decreased by approx. 9%, 17%, and 39%, respectively (Figure 8E).

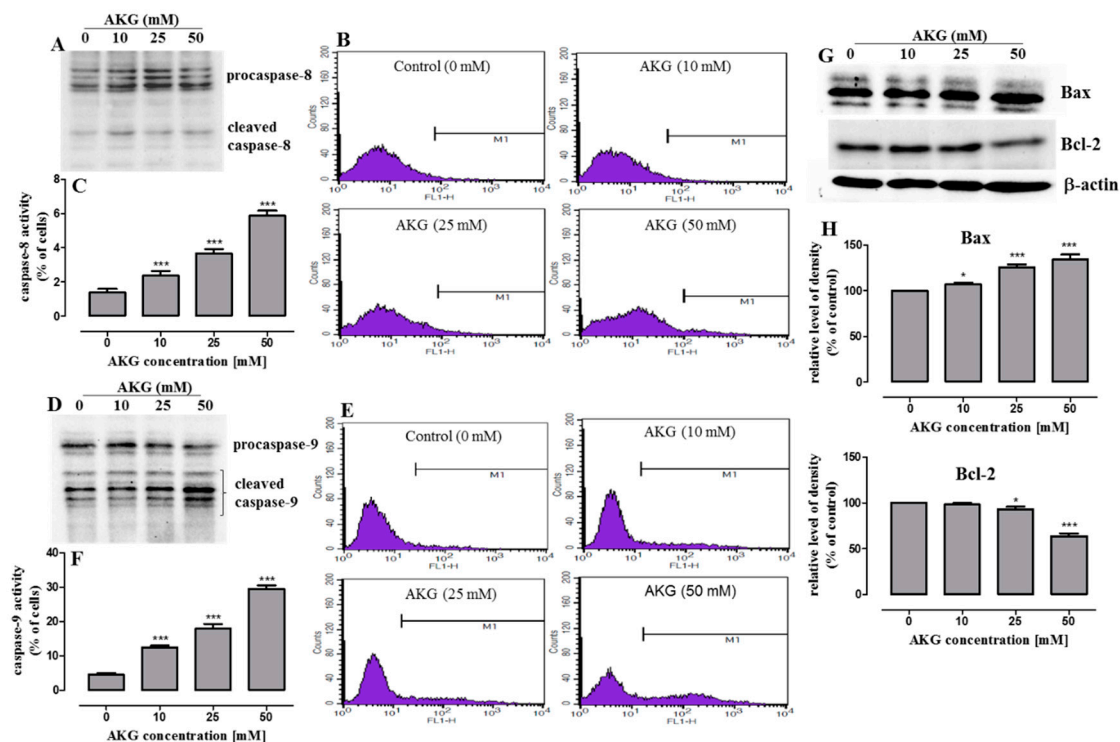


Figure 5. Analysis of the expression of apoptosis-related proteins in Saos-2 cells treated with AKG. After 72-h incubation with AKG, the expressions of procaspases-8 and -9 and cleaved forms of these caspases were examined by Western blotting, and active caspase-8 and -9 were analyzed by flow cytometric analysis. Representative blots from three independent experiments (A,D). Representative histograms of Saos-2 cell culture (B,E). Symbol M1 represents peaks for active caspase-8 or -9 positive cells. Quantification of caspase-8 (C) and -9 (F) activity in Saos-2 cell cultures. Mean \pm SD of 3 measurements in three independent experiments ($n = 12$ for each concentration); statistically significant at $*** p < 0.001$ in comparison to the control; one-way ANOVA test. Western blotting of Bax and Bcl-2 expression after 72-h treatment with AKG (G) Equal loading was confirmed by immunodetection of β -actin. Densitometry analysis of Bax and Bcl-2 bands with ImageLab™ Software (H). Data are expressed as means \pm SD for at least three independent experiments; ($n = 3$), $* p < 0.05$ and $*** p < 0.001$ in comparison to the control; one-way ANOVA test.

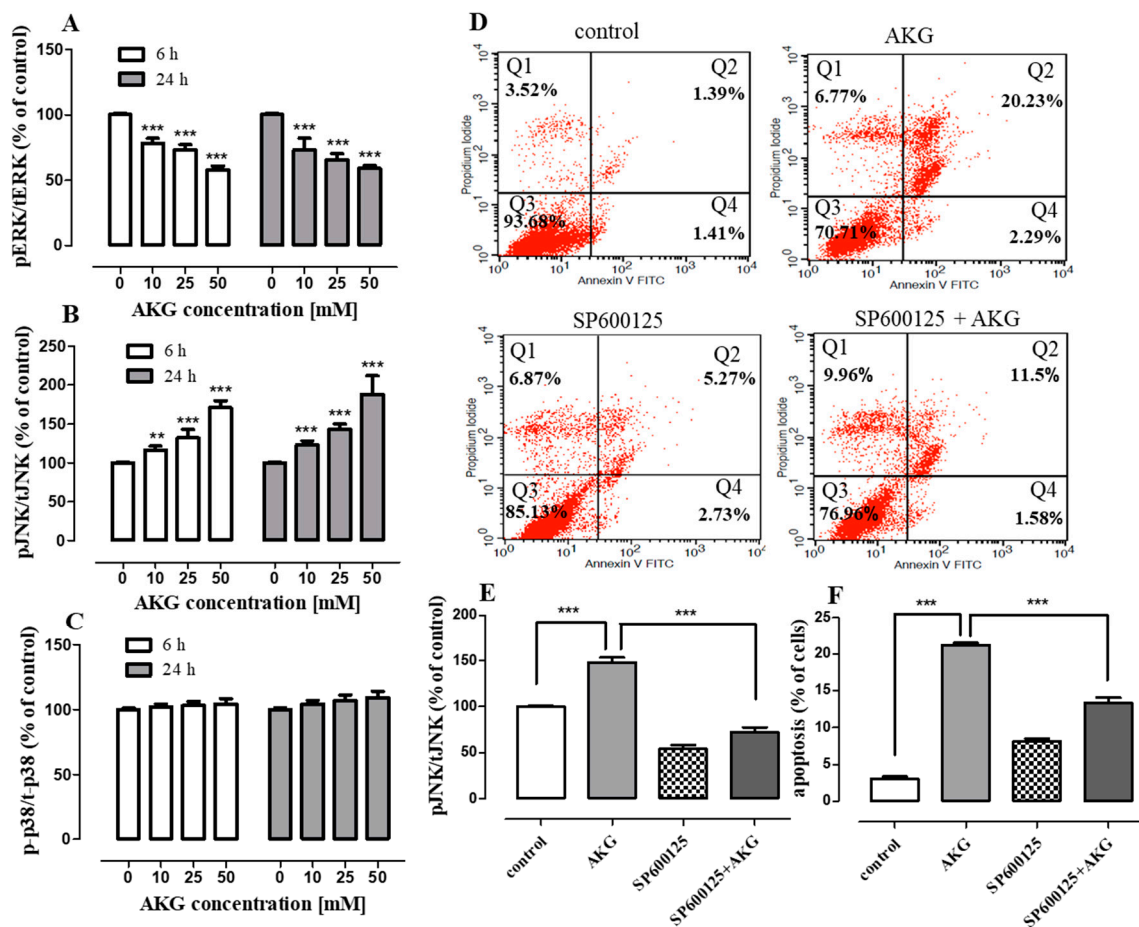


Figure 6. Effect of AKG on phosphorylation of MAP kinases and the influence of the selective JNK inhibitor (SP600125) on AKG-induced apoptosis in Saos-2 cells. The cells were incubated without or with AKG for 6 h and 24 h, and phosphorylated and total ERK1/2, JNK and p38 levels were determined with the ELISA assay. Quantification of the amounts of phosphorylated to total MAP kinases (A–C). The cells were treated with 50 mM AKG without or with SP600125 (5 μ M) and harvested after 72 h of treatment for apoptosis analysis. The representative dot plots indicate the percentage of An⁻/PI⁺ necrotic cells (Q1), An⁺/PI⁺ late apoptotic cells (Q2), An⁻/PI⁻ viable cells (Q3), and An⁺/PI⁻ early apoptotic cells (Q4) in the AKG or/and SP600125-treated Saos-2 cell cultures (D). Quantification of the amounts of phosphorylated to total JKN kinase (E) and histogram representation of the quantitative percentage of apoptotic (early + late apoptosis) cells (F) in the control, SP600125, AKG, and SP600125 + AKG-treated Saos-2 cell cultures. Data are expressed as means \pm SD for three independent experiments. ** $p < 0.01$, *** $p < 0.001$ in comparison to the control; one-way ANOVA test.

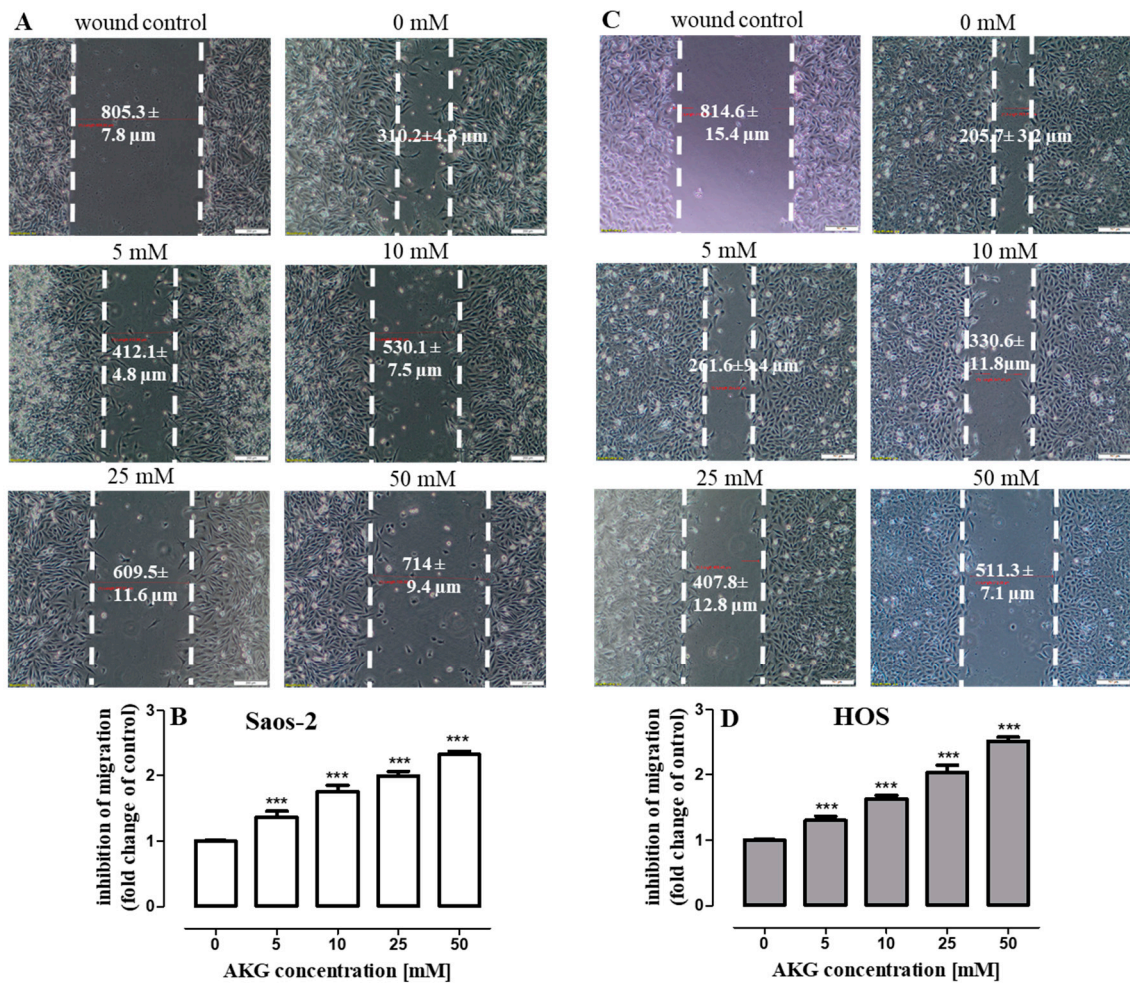


Figure 7. Effect of AKG on migration of Saos-2 and HOS cells in the wound healing assay. Cells were scraped and cultured without or with AKG for 24 h. Saos-2 (A) and HOS (C) cultures were imaged under a contrast-phase light microscope (magnification $\times 40$) before and after injury. Cell migration was quantified by measuring the gap width of wounds. Quantitative data (B,D) are presented as a relative fold change in the inhibition of migration in comparison to the control. Data are expressed as means \pm SD for three independent experiments. scale bar = 200 μm , *** $p < 0.001$ in comparison to the control; one-way ANOVA test.

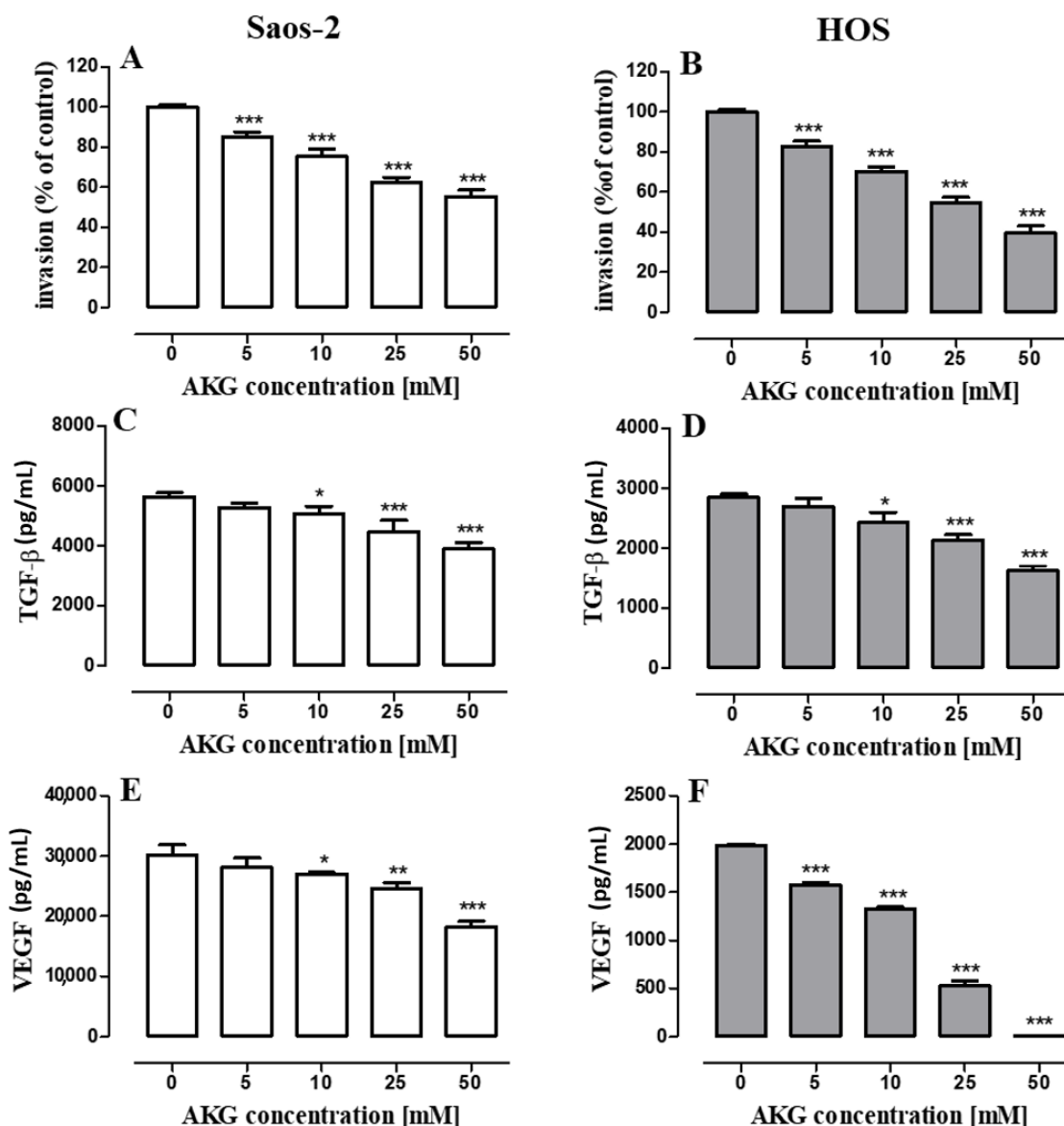


Figure 8. Effect of AKG on cell invasion and production of transforming growth factor β (TGF- β) and vascular endothelial growth factor (VEGF) in Saos-2 and HOS cells. Cell invasion was evaluated in a transwell chamber assay with a basement membrane extract (BME)-coated membrane (8 μ M) after 24 h. Invaded Saos-2 (A) and HOS (B) cells were quantified by measuring calcein-AM fluorescence. Following the 72-h AKG treatment, the conditioned media from the Saos-2 and HOS cell cultures were collected and the levels of TGF- β (C,D) and VEGF (E,F) were assayed with ELISA. Representative results of three independent experiments are shown. ($n = 9$); statistically significant at $p < 0.05$ *, at $p < 0.01$ ** or at $p < 0.001$ *** in comparison to the control; one-way ANOVA test.

3. Discussion

OS is the most common type of primary bone cancer, often associated with a high degree of malignancy, early metastasis, and rapid progression. There are different molecular types of OS; however, the tumor suppressor *TP53* is the most frequently altered gene in OS [6,26]. Although the survival rate in the case of non-metastatic patients is quite high, distant metastases (mainly to lungs) are found in about 20% of OS patients and the prognosis for these patients is still poor due to strong resistance of OS to chemotherapy [34]. Given the high rates of recurrence after tumor resection, resistance to chemotherapy and stagnation in the survival rates of OS patients during the last years, an intensive search for novel agents and alternative strategies to combat this malignancy is suggested [35].

Evidence from recent studies suggests that exogenous supplementation of AKG may exert anti-cancer effects against colorectal carcinoma or breast cancer [19,22]. Moreover, our recent study has revealed that exogenous AKG can inhibit cell proliferation and stimulate differentiation of normal osteoblasts [36]. However, the influence of AKG on osteosarcoma cell lines has not been studied so far. In the present study, to assess the anti-osteosarcoma potential of exogenous AKG, two primary osteosarcoma cell lines harboring *TP53* mutations were used, i.e., Saos-2 (p53-null cell line) and HOS (p53 mutant). The AKG treatment resulted in significantly reduced OS cell proliferation with IC₅₀ values of approx. 35 mM for both cell lines (in the BrdU assay). In the study conducted by other authors [22], AKG inhibited DNA synthesis in colon carcinoma cell lines such as Caco-2, HT-29, and LS-150 with IC₅₀ values of approx. 55 mM, 64 mM, and 67 mM, respectively. In turn, AKG was able to inhibit slightly the growth of MDA-MB-231 breast cancer cells at a concentration of 1 mM [19], while OS cell proliferation was inhibited by AKG at a concentration of 2.5 and 5 mM (in the Saos-2 and HOS cell lines, respectively). These data suggest a cell type-specific effect of AKG, probably related to different oncogenic pathways in the tested tumor cell lines. It is worth mentioning that exogenous AKG does not easily penetrate into the cell (although this occurs via simple diffusion), thus the intracellular level of this metabolite depends on the extracellular concentration [8] in an in vitro study and probably on the time required for its consumption by the cell. Nevertheless, even cell-permeable AKG derivatives (e.g., dimethyl alpha-ketoglutarate), which are often used to increase the intracellular AKG level, were applied at a concentration of 4 mM [25].

Previous studies conducted by other authors have shown that exogenous AKG (25 and 50 mM) can modulate the expression of cell cycle-related proteins such as cyclin D1 and the inhibitor of cyclin-dependent kinases p21^{Waf1/Cip1} [22]. Cyclin D1 is well known for its role in the response to mitogenic signals and regulation of the G₁ to S phase transition in the cell cycle. This protein activates cyclin-dependent kinases CDK4 and CDK6, which form active complexes with cyclin D1 and phosphorylate the RB protein, leading to transcriptional activation of genes required for cell division [37]. Cyclin D1 and CDK4 have also been reported to be overexpressed in osteosarcoma and related to its occurrence and development [38,39]. In turn, the p21 protein can function as a regulator of cell cycle progression at the G₁ checkpoint through binding to cyclin/CDK2 complexes and inhibition of RB phosphorylation or direct interaction with PCNA (proliferating cell nuclear antigen), which both trigger inhibition of DNA replication [40]. P21 has been shown to be involved in both p53-dependent and p53-independent control of cell proliferation, differentiation, and cell death [40]. Recently, p21 has been found to be significantly downregulated in osteosarcoma tissue, compared to their matched adjacent non-tumor tissues [41], and upregulation of this protein has been shown to inhibit proliferation of OS cells [42,43]. In our study, AKG (25 and 50 mM) was able to decrease cyclin D1 expression in the HOS cells but not in the Saos-2 cells, which do not express cyclin D1 [32]. On the other hand, AKG remarkably upregulated p21 only in the p53 null OS cells, but not in HOS cells harboring a *TP53* mutation. The results of our study suggest that AKG can disturb cell cycle progression through different mechanisms depending on the distinct genetic characteristics of OS cells.

A successful OS therapy requires, among others, effective agents that promote apoptotic cell death [44]. Drug-induced apoptosis can often occur through extrinsic or intrinsic pathways involving the activation of initiator caspase-8 and -9, respectively. The initiation of the mitochondrial pathway is under the control of the Bcl-2 family members, such as pro-apoptotic Bax and anti-apoptotic Bcl-2, and the Bax/Bcl-2 ratio is a critical determinant of the cell's apoptotic threshold. Bax insertion into the outer mitochondrial membrane leads to its permeabilization and release of various apoptotic proteins, which trigger the activation of caspase 9/3 signaling cascade [45]. In the present study, the AKG treatment induced apoptosis in both OS cell lines through activation of caspase 3. The further study revealed that the AKG-treatment of the Saos-2 cells resulted mainly in the upregulation of Bax, suggesting that changes in the ratio of Bax/Bcl-2 proteins could contribute to the subsequent activation of caspases-9 and -3. Surprisingly, a similar mechanism associated with the induction of apoptotic death was mediated by upregulation of IDH1 in osteosarcoma cell lines [24].

Mitogen-activated protein kinases (MAPKs), such as extracellular signal-regulated kinases (ERK1/2), c-Jun N-terminal protein kinases (JNKs), and p38, have been identified as key proteins of the signaling pathways that transmit mitogenic signals into the nucleus in response to various extracellular stimuli [46]. The ERK pathway is usually identified as a key mediator of cell proliferation and survival [47]. In turn, JNK may play a dual role in cancer cell survival, but preferentially exerts a pro-apoptotic effect [33,46,48]. Mounting evidence indicates that activation of JNK kinase in response to various anti-cancer agents may contribute to OS cell death [49,50]. In our study, AKG induced phosphorylation of JNK in the Saos-2 cells. Moreover, the pretreatment of the OS cells with the JNK inhibitor abolished the AKG-induced increase in the phosphorylation of this kinase and partially inhibited the AKG treatment-induced apoptosis. These data suggest an essential role of the JNK signaling pathway in AKG-induced apoptotic death of OS cells. It is well known that activated JNK promotes an intrinsic apoptotic pathway and cytochrome c release from the mitochondrion via multiple mechanisms, including Bax and Bcl-2 regulation [33]. More importantly, it phosphorylates cytoplasmic Bax-anchor proteins, which triggers dissociation of Bax from the complexes, its translocation to mitochondria, and induction of outer mitochondrial membrane permeabilization [51]. Moreover, JNK may increase the expression of Bax through transcriptional activation of c-Jun [52]. Furthermore, it may induce apoptosis through direct Bcl-2 phosphorylation and inhibition of its anti-apoptotic activity [33]. Since the AKG treatment of the Saos-2 cells resulted in both JNK activation and reduction of the Bax/Bcl-2 ratio, we can suppose that the caspase-9 and caspase-3 activation observed was linked with the mechanisms above mentioned.

The present study also revealed that AKG decreased ERK1/2 phosphorylation in the Saos-2 cells. The ERK pathway mediates several upstream signals from growth factors (e.g., vascular endothelial growth factor, VEGF) or proinflammatory stimulants, and regulates cell proliferation, migration, and metastasis in most cancers, including osteosarcoma [53]. It has been shown that overexpression and abnormal activation of the ERK signaling pathway are implicated in the pathogenesis of OS; therefore, this pathway is an attractive molecular target in OS [53–56]. Many studies have shown that suppression of this pathway by anticancer agents results in increased apoptosis and decreased metastasis in OS [53,57,58]. Therefore, besides the JNK pathway, inhibition of ERK1/2 activation may also be implicated in the AKG-mediated inhibition of cell cycle progression and programmed OS cell death observed in our study. However, this issue needs further investigations, to confirm these suggestions. On the other hand, the decrease in the ERK1/2 activation may be also implicated in the anti-migratory and anti-invasive effects of AKG observed in the OS cells.

Earlier studies have shown that exogenous AKG has the ability to reduce the level of the HIF-1 α subunit, resulting in downregulation of HIF-1 downstream targets, including the production of VEGF, and inhibition of angiogenesis [20,21]. Moreover, a recent study has shown that exogenous supplementation of AKG prevented tumor growth and metastasis of breast cancer cells through stabilization of PHD2 and decreasing HIF-1 α [19]. Furthermore, other strategies associated with intracellular AKG accumulation resulted in anti-metastatic effects [17,24]. In the present study, the AKG supplementation also markedly inhibited cell motility and invasion of both OS cell lines in a concentration-dependent manner, which confirms the anti-metastatic potential of this compound. Moreover, AKG was able to decrease the production of TGF- β and VEGF by the OS cells, i.e., growth factors that are implicated in osteosarcoma progression and metastasis.

Although TGF- β acts in most cancers both as a tumor suppressor in premalignant stages and a tumor promoter in advanced stages of the disease, in OS it exerts only pro-tumoral effects through the promotion of metastasis [59]. It has been shown that the level of TGF- β in sera of OS patients is higher compared to those of healthy donors, which is correlated with a high grade of disease and associated with chemoresistance and presence of metastases in lungs and other sites [60]. Moreover, *in vitro* studies have revealed that TGF- β is implicated in the EMT-like phenomenon, stimulates proliferation of OS cells, and exerts pro-angiogenic properties in OS [60,61]. In addition, the secretion of TGF- β by OS cells or stromal cells can regulate the phenotype and function of the microenvironment in order

to stimulate switching its function to pro-tumoral [59]. Since TGF- β plays a pro-tumoral role in OS, the downregulation of TGF- β by AKG seems to be an important feature of this compound in terms of anti-cancer activity.

In the present study, AKG was also able to inhibit the VEGF production in both OS cell lines, which is in agreement with the results of previous studies conducted by Matsumoto et al. [20,21] in the Hep3B hepatocellular carcinoma cell line and LCC (Lewis lung carcinoma) cell line. In their study, AKG decreased VEGF production at a concentration of 7.5 mM and 5 mM, respectively. Similarly, in our study, the lowest concentrations inducing significant inhibition of VEGF production were 5 mM and 10 mM of AKG for HOS and Saos-2 cells, respectively. VEGF is a key potent tumor-derived pro-angiogenic factor influencing both the tumor microenvironment and cancer cells. It acts in a paracrine manner on endothelial cells which leads to the promotion of angiogenesis [62]. Moreover, VEGF can act in an autocrine manner on several cancer cells, including aggressive osteosarcoma phenotypes, which leads to activation of various signaling pathways in these cells (e.g., PI3K/Akt and MEK/ERK), ultimately supporting tumor growth [63]. VEGF plays an important role in the pathogenesis of OS [64]. VEGF serum levels in OS patients are elevated and associated with poor prognosis [65]. Moreover, overexpression of VEGF is a predictor of pulmonary OS metastasis [66,67]. Recently, it has been shown that silencing of VEGF in Saos-2 cells inhibited cell proliferation and promoted apoptosis in vitro [68]. Therefore, the inhibition of VEGF production in osteosarcoma cells by AKG treatment may have therapeutic value.

As mentioned earlier, we used cell lines with p53 function deficiency in our study; however, the *TP53* gene mutation does not occur in all OS cases. Early studies reported that the rate of the *TP53* gene mutation in OS is around 20% [69]; however, recent studies have shown that more than 90% of osteosarcomas have either missense mutations in this gene or structural variation in p53 [70]. Nevertheless, some percentages of osteosarcomas have functional p53, which raises a question of whether AKG would act in these cases in a similar way as in cells harboring the *TP53* mutation. A recent study has shown that AKG is an effector molecule of p53-mediated tumor suppression, and its accumulation in p53-deficient tumors can partially recapitulate the p53 action linked with the remodeling of cancer cell metabolism through epigenetic modifications and alterations of gene expression [25]. It has also been shown that exogenous AKG can switch metabolism from glycolytic to oxidative, which can prevent the growth and metastasis of breast cancer cells [19]. Based on the analysis of cell lines in which AKG exhibited anti-cancer activity [19–22], we identified that all these cell lines, except the LS-180 colon cancer cell line, have *TP53* mutations; nevertheless, AKG also inhibited the proliferation of LS-180 cells with the wild type of p53. Therefore, we can speculate that AKG would similarly affect OS lines with functional p53, and that more than one mechanism of AKG activity may operate in cancer cells, depending on the distinct genetic/epigenetic characteristics of these cells. However, further studies of the AKG influence on OS cell lines with functional p53 and their metabolism are needed to confirm this hypothesis.

4. Materials and Methods

4.1. Cell Culture and AKG

Human osteosarcoma cell lines Saos-2 (HTB-85TM) and HOS (CRL-1543TM) were purchased from the American Type Culture Collection (ATCC, Manassas, VA, USA). The Saos-2 cells were maintained in McCoy's 5A Modified Medium (Sigma-Aldrich Chemicals, St. Louis, MO, USA) supplemented with an antibiotic/antimycotic solution (a/a; Sigma-Aldrich) and 10% fetal bovine serum (FBS; Sigma-Aldrich) in a 5% CO₂ humidified atmosphere at a temperature of 37 °C. The HOS cells were grown in Eagle's Minimum Essential Medium (Sigma-Aldrich) supplemented with 10% FBS and a/a. The cells were maintained in a humidified incubator with 5% CO₂ in air at 37 °C.

Alpha-ketoglutarate disodium salt dihydrate (Na₂AKG × 2H₂O; (Sigma-Aldrich) was used in the experiments. Before each experiment, the stock solution of AKG (1 M) was prepared by dissolving

the compound in the culture medium. The stock solution was filtered through a sterile syringe filter Millex-GV (Merck Millipore Corporation, Burlington, MA, USA) and diluted in an appropriate culture medium to obtain the required concentrations.

4.2. Cell Proliferation Assays

The influence of AKG on the proliferation of OS cells was estimated with the MTT (3-(4,5-dimethylthiazol-2-yl)-2,5-diphenyltetrazolium bromide solution) assay as described previously [71]. Briefly, 4×10^3 cells/well were seeded into 96-well plates in growth medium. After 24 h, the culture medium was removed and the cells were exposed to the dilutions of AKG (2.5–200 mM) prepared in the growth medium with 10% FBS. Following 96-h exposure, the cells were incubated for 3 h with an MTT (Sigma-Aldrich) solution (5 mg/mL) and then formazan crystals were solubilized overnight by adding SDS buffer (10% SDS in 0.01 N HCl). The absorbance was determined at a wavelength of 570 nm using an EL800 Microplate Reader (BioTek Instruments, Winooski, VT, USA).

The anti-proliferative activity of AKG was also assessed with the BrdU assay, in which DNA synthesis in proliferating cells was determined after 48 h by measuring bromodeoxyuridine incorporation using a commercial Cell Proliferation ELISA BrdU kit (Roche Molecular Biochemicals, Mannheim, Germany) according to the manufacturer's instructions.

The absorbance of the control wells was taken as 100% and the results were expressed as a percentage of the control. IC₅₀ values were defined as drug concentrations necessary to inhibit 50% of growth, compared to untreated control cells. IC₅₀ was obtained using the non-linear regression program GraphPad Prism v5 software (GraphPad Software Inc., San Diego, CA, USA).

4.3. Cell Cycle Analysis

The Saos-2 or HOS cells were seeded into 6-well plates in medium containing 10% FBS without or with AKG (10, 25, or 50 mM). After 48-h treatment, the cell cycle analysis consisting of determination of DNA contents on the basis of PI staining was performed using a flow cytometer (BD FACSCalibur, BD Biosciences, San Jose, CA, USA) and the Cell Quest Pro Version 6.0. for the Macintosh operating system as described previously [72]. Briefly, the cells were washed with PBS and fixed overnight with 80% ethanol at -20 °C. Next, the cells were washed with PBS and stained with PI using PI/RNase Staining Buffer (BD Biosciences, BD Pharmingen™, San Jose, CA, USA) for 30 min in darkness at RT. Next, the stained cells were analyzed using FACS Calibur. In total, 10,000 events were measured per sample. The data were analyzed to determine the percentage of cells at each phase of the cell cycle (G1, S, and G2/M).

4.4. Flow Cytometry

The quantitative analysis of AKG-induced cell death was performed using an Annexin V-fluorescein isothiocyanate (FITC)/propidium iodide (PI) apoptosis kit (BD Biosciences, BD Pharmingen™, San Jose, CA, USA) and the flow cytometry method as described previously [73]. Briefly, the Saos-2 or HOS cells were seeded into 6-well plates at a density of 7×10^5 cells/well. The next day, the growth medium was replaced with a fresh one containing 2% of FBS supplemented with AKG (5, 10, 25, or 50 mM). In some experiments, the Saos-2 cells were exposed to AKG (50 mM), SP600125 (a selective inhibitor of JNK, 5 μ M, Sigma-Aldrich), or a combination of these two compounds. After 72-h incubation, the samples were harvested, washed with PBS, and resuspended in $1 \times$ binding buffer. The cells (1×10^5) were then stained with 5 mM of FITC-Annexin V and 5 mM of PI. After 15-min incubation in the dark at room temperature, the cells were immediately analyzed using a flow cytometer (BD FACSCalibur) with CellQuest Pro Version 6.0 software. All experiments were performed in triplicate and yielded similar results.

The fluorescence-activated cell sorting (FACS) technique was also employed to determine the active form of caspase-3, caspase-9, and caspase-8 in the AKG-treated or untreated OS cells. After 72-h exposure to AKG, a phycoerythrin (PE) Active Caspase-3 Apoptosis Kit (BD Biosciences, San Jose, CA,

USA)) and a fluorescein CaspaTag Caspase 9 In Situ Assay kit (Sigma-Aldrich) or a CaspaTag Caspase 8 In Situ Assay kit (Sigma-Aldrich) were used according to the manufacturer's instructions.

4.5. Immunoblotting Analysis

The immunoblotting analysis was carried out as described previously [72]. Briefly, the Saos-2 cells (3×10^5 cells/mL) were seeded into 6-well plates and, after attachment, cultured in medium with 2% FBS without AKG or with AKG for 72 h. The cells were harvested and lysed for 40 min on ice in RIPA buffer (Sigma-Aldrich) supplemented with protease and phosphatase inhibitor cocktail (Sigma-Aldrich) and centrifuged ($10,000 \times g$ for 10 min at 4 °C). The total protein concentrations were determined using a BCA protein assay kit (Pierce® BCA Protein Assay Kit, Thermo Scientific, Rockford, IL, USA). For Western blot analysis, supernatants of RIPA cell lysates were solubilized in 4 x Laemmli sample buffer (Bio-rad Laboratories Inc., Hercules, CA, USA) and denatured (for 5 min at 100 °C). Equal amounts of the protein extracts (40 micrograms) were electrophoresed on SDS-PAGE (Bio-Rad Laboratories Inc., Hercules, CA, USA, Mini-Protean® Tetra Cell) and transferred onto a PVDF membrane (Merck Millipore Corporation, Burlington, MA, USA). After blocking with 5% non-fat dry milk/TBS/0.1% Tween (Sigma-Aldrich) for 1h at RT and washing, the membranes were incubated overnight at 4 °C with the following primary antibodies: anti-caspase-8 and anti-caspase-9 (1:400) as well as anti-Bcl-2 and anti-Bax (1:1000) (all antibodies from Santa Cruz Biotechnology Inc. CA, USA). Next, primary antibodies were detected by horseradish peroxidase (HRP)-conjugated rat, mouse, or goat secondary antibodies (1:2000, Santa Cruz Biotechnology Inc. CA, USA), and protein-antibody complexes were visualized with the ECL™ Western Blotting Analysis System (Amersham™ GE Healthcare, Buckinghamshire, UK) and Molecular Imager® ChemiDoc™ XRS+ (Bio-rad Laboratories Inc., Hercules, CA, USA) equipped with ImageLab™ Version 3.0 Software. The blots were reprobated with antibodies against β -actin (1:500, Santa Cruz Biotechnology Inc., CA, USA) used as a load control. Additionally, protein molecular markers (Precision Plus Protein™ Dual Color Standards, Bio-rad Laboratories Inc., Hercules, CA, USA) were loaded onto electrophoretic gels to control the molecular weight of protein bands. Densitometric measurement of chemiluminescent signals was performed using software ImageLab™ Version 3.0. The optical density of the bands was normalized to β -actin levels.

4.6. ELISA Assays

The Saos-2 or HOS cells (3.3×10^5 cells/mL) were incubated for 72 h without or with AKG (5, 10, 25, 50 mM) in 24-well plates containing appropriate culture medium with 2% FBS at 37 °C in an atmosphere of 5% CO₂. Enzyme-linked immunosorbent assay (ELISA) kits were used to measure the levels of TGF- β (DRG International Inc., Springfield, NJ, USA) and VEGF (Diaclone Besançon, France) in the culture media according to the manufacturer's instructions.

4.7. PathScan ELISA Assays

The quantification of the intracellular levels of total and phosphorylated JNK, ERK1/2, p38, and AKT kinases and the contents of cyclin D1 and p21 proteins in the treated cells was carried out using the PathScan® ELISA kits: Total SAPK/JNK Sandwich ELISA Kit, Phospho-SAPK/JNK (Thr183/Tyr185) Sandwich ELISA Kit, Total p44/42 MAPK (Erk1/2) Sandwich ELISA Kit, Phospho-p44/42 MAPK (Thr202/Tyr204) Sandwich ELISA Kit, Phospho-p38 MAPK (Thr180/Tyr182) Sandwich ELISA Kit, Total Cyclin D1 Sandwich ELISA Kit, Total p21^{Waf1/Cip1} Sandwich ELISA Kit (Cell Signaling Technology Danvers, MA, USA), and p38 MAPK alpha ELISA Kit (Abcam, Cambridge, UK) according to the manufacturer's instructions as described previously [36]. Briefly, the Saos-2 cells (1×10^6 cells/mL) were incubated in culture medium (2% FBS) without or with the selected concentrations of AKG (10, 25, and 50 mM) in 10-cm diameter plastic plates. In some experiments, the cells were pre-treated with SP600125 (a selective inhibitor of JNK1/2, Sigma-Aldrich) at a concentration of 5 μ M for 1 h. After 6, 24, or 48 h of incubation, the media were removed and the cells were rinsed with ice-cold PBS

(Sigma-Aldrich). Then, the cells were lysed in lysis buffer (included in the kits) supplemented with PMSF (Sigma-Aldrich) and protease and phosphatase inhibitor cocktail (Sigma-Aldrich) according to the manufacturer's protocol. Total cell lysates were centrifuged at $14,000\times g$ rpm, 5 min at $4\text{ }^{\circ}\text{C}$, and kept at $-80\text{ }^{\circ}\text{C}$ until analysis. Before the assay, the total protein concentrations in the cell lysates were determined with a Pierce BCA Protein Assay Kit (Thermo Fisher Scientific, Waltham, MA, USA), and samples containing equal amounts of total proteins per $100\text{ }\mu\text{L}$ of the sample diluent were subjected to ELISA. The optical density was measured using an E-max Microplate Reader (Molecular Devices Corporation, Menlo Park, CA, USA).

4.8. Cell Migration Assay

The wound-healing assay was used to evaluate the influence of AKG on the migration of osteosarcoma cells *in vitro*. The Saos-2 (3×10^5 cells/mL) and HOS (2.5×10^5 cells/mL) cells were seeded into 3-cm diameter plastic plates and cultured until confluence. Afterwards, wounds were made in the monolayers with a sterile $100\text{-}\mu\text{L}$ pipette tip. The cells were washed twice with PBS to remove cell debris, and fresh growth media without or with AKG (5, 10, 25, and 50 mM) were added. The gap width of the wound in one dish (wound control) was measured and recorded immediately after wounding. After 24-h incubation, the gap width of the wounds in the other plates was measured and contrast-phase images were taken using an inverted microscope Olympus CKX41 (Olympus Optical Co, LTD, Tokyo, Japan) and analyzed with Image Processing (CellSens) software. The inhibition of migration (fold change of the control) was calculated as the quotient of the mean width of the gap in the AKG-treated culture and the mean width of the gap in the control culture.

4.9. Cell Invasion Assay

The OS cell invasion was estimated with the CultureCoat[®] 24 Well Low BME Cell Invasion Assay (Trevigen, Inc., Gaithersburg, MD, USA) according to the manufacturer's instructions. The Saos-2 or HOS cells (both 1.0×10^6 cells/mL) suspended in medium with 1% of FBS and supplemented with AKG (5, 10, 25, or 50 mM) or without AKG (control) were seeded into BME-coated inserts ($8\text{ }\mu\text{m}$) in the wells of a 24-well plate. Medium with 10% FBS (as a chemoattractant) was added into the bottom chamber. After 24 h of incubation, the number of OS cells invading the bottom surface of the insert membrane was quantified based on the amount of free Calcein generated from Calcein AM by migrating cells, as indicated in the manufacturer's instructions. The Calcein fluorescence level was measured by means of a Perkin Elmer Victor[™] plate reader (PerkinElmer, Waltham, MA, USA)

4.10. Statistical Analysis

Each experiment was repeated at least three times. Statistical analyses were performed using GraphPAD Prism 5 (GraphPAD Software Inc., San Diego, CA, USA). The data were analyzed by one-way ANOVA followed by Dunnett's or Tukey's multiple comparison tests. Values were expressed as means \pm SD, and *p* values < 0.05 were considered significant.

5. Conclusions

In conclusion, our data demonstrated the anti-osteosarcoma effects of AKG supplementation in an *in vitro* study. AKG was able to modulate the expression of cell cycle-associated proteins (cyclin D1, p21^{Waf1/Cip1}) and arrest cell cycle progression at the G_1 phase, which resulted in inhibition of OS cell proliferation. Moreover, the AKG-induced activation of the JNK pathway, augmentation of the Bax/Bcl-2 ratio, and activation of caspase-9 and -3 led to the induction of apoptotic cell death in the OS cells. The inhibition of the ERK pathway by AKG may also be involved both in the pro-apoptotic effect of AKG and in the anti-metastatic potential of AKG linked with inhibition of OS cell motility and invasion by this compound. The anti-osteosarcoma potential of AKG was also attributed to its inhibitory influence on the production and release of cytokines such as pro-metastatic TGF- β and

pro-angiogenic VEGF. These results may thus provide a rationale for further in vivo study of the possible application of AKG in osteosarcoma therapy.

Author Contributions: Conceptualization, B.Z.; methodology and investigations, K.K., A.S.-B., M.M.-K., A.Ż., A.B.-J. and B.Z.; data analysis and interpretation, K.K., A.S.-B. and B.Z.; writing—original draft preparation, B.Z.; writing—review & editing, B.Z. and M.K.-S.; founding acquisition, M.K.-S.; project administration, B.Z. All authors have read and agreed to the published version of the manuscript.

Funding: This work was supported by research Grant No. 2013/11/B/NZ4/04557 from the State Funds for Scientific Research National Science Centre, Poland.

Conflicts of Interest: The authors declare no conflict of interest.

References

1. Klein, M.J.; Siegal, G.P. Osteosarcoma. *Am. J. Clin. Pathol.* **2006**, *125*, 555–581. [CrossRef] [PubMed]
2. Damron, T.A.; Ward, W.G.; Stewart, A. Osteosarcoma, chondrosarcoma, and Ewing's sarcoma: National cancer data base report. *Clin. Orthop. Relat. Res.* **2007**, *459*, 40–47. [CrossRef] [PubMed]
3. Mirabello, L.; Troisi, R.J.; Savage, S.A. International osteosarcoma incidence patterns in children and adolescents, middle ages and elderly persons. *Int. J. Cancer* **2009**, *125*, 229–234. [CrossRef] [PubMed]
4. Savage, S.A.; Mirabello, L. Using epidemiology and genomics to understand osteosarcoma etiology. *Sarcoma* **2011**, *2011*, 548151. [CrossRef]
5. Gill, J.; Ahluwalia, M.K.; Geller, D.; Gorlick, R. New targets and approaches in osteosarcoma. *Pharmacol. Ther.* **2013**, *137*, 89–99. [CrossRef]
6. Czarnecka, A.M.; Synoradzki, K.; Firlej, W.; Bartnik, E.; Sobczuk, P.; Fiedorowicz, M.; Grieb, P.; Rutkowski, P. Molecular biology of osteosarcoma. *Cancers* **2020**, *12*, 2130. [CrossRef]
7. Akram, M. Citric Acid Cycle and Role of its Intermediates in Metabolism. *Cell Biochem. Biophys.* **2014**, *68*, 475–478. [CrossRef]
8. Zdzisińska, B.; Żurek, A.; Kandefer-Szerszeń, M. Alpha-Ketoglutarate as a Molecule with Pleiotropic Activity: Well-Known and Novel Possibilities of Therapeutic Use. *Arch. Immunol. Ther. Exp. (Warsz.)* **2017**, *65*, 21–36. [CrossRef]
9. Dalziel, K. Isocitrate dehydrogenase and related oxidative decarboxylases. *FEBS Lett.* **1980**, *117*, K45–K55. [CrossRef]
10. Abła, H.; Sollazzo, M.; Gasparre, G.; Iommarini, L.; Porcelli, A.M. The multifaceted contribution of α -ketoglutarate to tumor progression: An opportunity to exploit? *Semin. Cell Dev. Biol.* **2020**, *98*, 26–33. [CrossRef]
11. Tennant, D.A.; Frezza, C.; MacKenzie, E.D.; Nguyen, Q.D.; Zheng, L.; Selak, M.A.; Roberts, D.L.; Dive, C.; Watson, D.G.; Aboagye, E.O.; et al. Reactivating HIF prolyl hydroxylases under hypoxia results in metabolic catastrophe and cell death. *Oncogene* **2009**, *28*, 4009–4021. [CrossRef] [PubMed]
12. MacKenzie, E.D.; Selak, M.A.; Tennant, D.A.; Payne, L.J.; Crosby, S.; Frederiksen, C.M.; Watson, D.G.; Gottlieb, E. Cell-Permeating α -Ketoglutarate Derivatives Alleviate Pseudohypoxia in Succinate Dehydrogenase-Deficient Cells. *Mol. Cell. Biol.* **2007**, *27*, 3282–3289. [CrossRef] [PubMed]
13. Blanquart, C.; Linot, C.; Cartron, P.-F.; Tomaselli, D.; Mai, A.; Bertrand, P. Epigenetic Metalloenzymes. *Curr. Med. Chem.* **2018**, *26*, 2748–2785. [CrossRef] [PubMed]
14. Zhou, Z.; Ibekwe, E.; Chornenky, Y. Metabolic alterations in cancer cells and the emerging role of oncometabolites as drivers of neoplastic change. *Antioxidants* **2018**, *7*, 16. [CrossRef]
15. Xu, W.; Yang, H.; Liu, Y.; Yang, Y.; Wang, P.; Kim, S.H.; Ito, S.; Yang, C.; Wang, P.; Xiao, M.T.; et al. Oncometabolite 2-hydroxyglutarate is a competitive inhibitor of α -ketoglutarate-dependent dioxygenases. *Cancer Cell* **2011**, *19*, 17–30. [CrossRef]
16. Letouzé, E.; Martinelli, C.; Lorient, C.; Burnichon, N.; Abermil, N.; Ottolenghi, C.; Janin, M.; Menara, M.; Nguyen, A.T.; Benit, P.; et al. SDH Mutations Establish a Hypermethylator Phenotype in Paraganglioma. *Cancer Cell* **2013**, *23*, 739–752. [CrossRef]
17. Atlante, S.; Visintin, A.; Marini, E.; Savoia, M.; Dianzani, C.; Giorgis, M.; Sürün, D.; Maione, F.; Schnütgen, F.; Farsetti, A.; et al. α -ketoglutarate dehydrogenase inhibition counteracts breast cancer-associated lung metastasis article. *Cell Death Dis.* **2018**, *9*, 1–18. [CrossRef]

18. Sun, X.; Zhu, M.J. Butyrate Inhibits Indices of Colorectal Carcinogenesis via Enhancing α -Ketoglutarate-Dependent DNA Demethylation of Mismatch Repair Genes. *Mol. Nutr. Food Res.* **2018**, *62*, e1700932. [CrossRef]
19. Tseng, C.W.; Kuo, W.H.; Chan, S.H.; Chan, H.L.; Chang, K.J.; Wang, L.H. Transketolase Regulates the Metabolic Switch to Control Breast Cancer Cell Metastasis via the α -Ketoglutarate Signaling Pathway. *Cancer Res.* **2018**, *78*, 2799–2812. [CrossRef]
20. Matsumoto, K.; Imagawa, S.; Obara, N.; Suzuki, N.; Takahashi, S.; Nagasawa, T.; Yamamoto, M. 2-Oxoglutarate downregulates expression of vascular endothelial growth factor and erythropoietin through decreasing hypoxia-inducible factor-1 α and inhibits angiogenesis. *J. Cell. Physiol.* **2006**, *209*, 333–340. [CrossRef]
21. Matsumoto, K.; Obara, N.; Ema, M.; Horie, M.; Naka, A.; Takahashi, S.; Imagawa, S. Antitumor effects of 2-oxoglutarate through inhibition of angiogenesis in a murine tumor model. *Cancer Sci.* **2009**, *100*, 1639–1647. [CrossRef] [PubMed]
22. Rzeski, W.; Walczak, K.; Juszczak, M.; Langner, E.; Pożarowski, P.; Kandefer-Szerszeń, M.; Pierzynowski, S.G. Alpha-ketoglutarate (AKG) inhibits proliferation of colon adenocarcinoma cells in normoxic conditions. *Scand. J. Gastroenterol.* **2012**, *47*, 565–571. [CrossRef] [PubMed]
23. Tennant, D.A.; Gottlieb, E. HIF prolyl hydroxylase-3 mediates alpha-ketoglutarate-induced apoptosis and tumor suppression. *J. Mol. Med.* **2010**, *88*, 839–849. [CrossRef] [PubMed]
24. Hu, X.; Liu, Y.; Qin, C.; Pan, Z.; Luo, J.; Yu, A.; Cheng, Z. Up-regulated isocitrate dehydrogenase 1 suppresses proliferation, migration and invasion in osteosarcoma: In vitro and in vivo. *Cancer Lett.* **2014**, *346*, 114–121. [CrossRef] [PubMed]
25. Morris, J.P.; Yashinskie, J.J.; Koche, R.; Chandwani, R.; Tian, S.; Chen, C.C.; Baslan, T.; Marinkovic, Z.S.; Sánchez-Rivera, F.J.; Leach, S.D.; et al. α -Ketoglutarate links p53 to cell fate during tumour suppression. *Nature* **2019**, *573*, 595–599. [CrossRef]
26. Morrow, J.J.; Khanna, C. Osteosarcoma genetics and epigenetics: Emerging biology and candidate therapies. *Crit. Rev. Oncog.* **2015**, *20*, 173–197. [CrossRef]
27. Amary, M.F.; Bacsı, K.; Maggiani, F.; Damato, S.; Halai, D.; Berisha, F.; Pollock, R.; O'Donnell, P.; Grigoriadis, A.; Diss, T.; et al. IDH1 and IDH2 mutations are frequent events in central chondrosarcoma and central and periosteal chondromas but not in other mesenchymal tumours. *J. Pathol.* **2011**, *224*, 334–343. [CrossRef]
28. Anderson, N.M.; Mucka, P.; Kern, J.G.; Feng, H. The emerging role and targetability of the TCA cycle in cancer metabolism. *Protein Cell* **2018**, *9*, 216–237. [CrossRef]
29. Liu, X.; Kato, Y.; Kaneko, M.K.; Sugawara, M.; Ogasawara, S.; Tsujimoto, Y.; Naganuma, Y.; Yamakawa, M.; Tsuchiya, T.; Takagi, M. Isocitrate dehydrogenase 2 mutation is a frequent event in osteosarcoma detected by a multi-specific monoclonal antibody MsMab-1. *Cancer Med.* **2013**, *2*, 803–814. [CrossRef]
30. Hu, X.; Yu, A.-X.; Qi, B.-W.; Fu, T.; Wu, G.; Zhou, M.; Luo, J.; Xu, J.-H. The expression and significance of IDH1 and p53 in osteosarcoma. *J. Exp. Clin. Cancer Res.* **2010**, *29*, 43. [CrossRef]
31. Yi, W.R.; Li, Z.H.; Qi, B.W.; Hu, X.; Yu, A.X. Downregulation of IDH2 exacerbates the malignant progression of osteosarcoma cells via increased NF- κ B and MMP-9 activation. *Oncol. Rep.* **2016**, *35*, 2277–2285. [CrossRef] [PubMed]
32. Ewen, M.E.; Sluss, H.K.; Sherr, C.J.; Matsushima, H.; Kato, J.Y.; Livingston, D.M. Functional interactions of the retinoblastoma protein with mammalian D-type cyclins. *Cell* **1993**, *73*, 487–497. [CrossRef]
33. Dhanasekaran, D.N.; Premkumar Reddy, E. JNK-signaling: A multiplexing hub in programmed cell death. *Genes Cancer* **2017**, *8*, 682–694. [CrossRef] [PubMed]
34. Huang, X.; Zhao, J.; Bai, J.; Shen, H.; Zhang, B.; Deng, L.; Sun, C.; Liu, Y.; Zhang, J.; Zheng, J. Risk and clinicopathological features of osteosarcoma metastasis to the lung: A population-based study. *J. Bone Oncol.* **2019**, *16*, 100230. [CrossRef] [PubMed]
35. Zhang, Y.; Yang, J.; Zhao, N.; Wang, C.; Kamar, S.; Zhou, Y.; He, Z.; Yang, J.; Sun, B.; Shi, X.; et al. Progress in the chemotherapeutic treatment of osteosarcoma. *Oncol. Lett.* **2018**, *16*, 6228–6237. [CrossRef] [PubMed]
36. Żurek, A.; Mizerska-Kowalska, M.; Sławińska-Brych, A.; Kaławaj, K.; Bojarska-Junak, A.; Kandefer-Szerszeń, M.; Zdzisińska, B. Alpha ketoglutarate exerts a pro-osteogenic effect in osteoblast cell lines through activation of JNK and mTOR/S6K1/S6 signaling pathways. *Toxicol. Appl. Pharmacol.* **2019**, *374*, 53–64. [CrossRef]
37. Qie, S.; Diehl, J.A. Cyclin D1, cancer progression, and opportunities in cancer treatment. *J. Mol. Med.* **2016**, *94*, 1313–1326. [CrossRef]
38. Si, X.H.; Liu, Z. Expression of cyclin D1 and CDK4 in osteosarcoma of the jaws. *Chin. J. Cancer Res.* **2001**, *13*, 140–143. [CrossRef]

39. Zhou, Y.; Shen, J.K.; Yu, Z.; Hornicek, F.J.; Kan, Q.; Duan, Z. Expression and therapeutic implications of cyclin-dependent kinase 4 (CDK4) in osteosarcoma. *Biochim. Biophys. Acta-Mol. Basis Dis.* **2018**, *1864*, 1573–1582. [CrossRef]
40. Abbas, T.; Dutta, A. P21 in cancer: Intricate networks and multiple activities. *Nat. Rev. Cancer* **2009**, *9*, 400–414. [CrossRef]
41. He, Y.; Yu, B. MicroRNA-93 promotes cell proliferation by directly targeting P21 in osteosarcoma cells. *Exp. Ther. Med.* **2017**, *13*, 2003–2011. [CrossRef] [PubMed]
42. Chen, X.; Deng, M.; Ma, L.; Zhou, J.; Xiao, Y.; Zhou, X.; Zhang, C.; Wu, M. Inhibitory effects of forkhead box L1 gene on osteosarcoma growth through the induction of cell cycle arrest and apoptosis. *Oncol. Rep.* **2015**, *34*, 265–271. [CrossRef] [PubMed]
43. Chen, J.M.; Zhang, J.; Xia, Y.M.; Wang, X.X.; Li, J. The natural sweetener metabolite steviol inhibits the proliferation of human osteosarcoma U2OS cell line. *Oncol. Lett.* **2018**, *15*, 5250–5256. [CrossRef] [PubMed]
44. Li, J.; Yang, Z.; Li, Y.; Xia, J.; Li, D.; Li, H.; Ren, M.; Liao, Y.; Yu, S.; Chen, Y.; et al. Cell apoptosis, autophagy and necroptosis in osteosarcoma treatment. *Oncotarget* **2016**, *7*, 44763–44778. [CrossRef]
45. Redza-Dutordoir, M.; Averill-Bates, D.A. Activation of apoptosis signalling pathways by reactive oxygen species. *Biochim. Biophys. Acta-Mol. Cell Res.* **2016**, *1863*, 2977–2992. [CrossRef]
46. Boutros, T.; Chevet, E.; Metrakos, P. Mitogen-Activated Protein (MAP) kinase/MAP kinase phosphatase regulation: Roles in cell growth, death, and cancer. *Pharmacol. Rev.* **2008**, *60*, 261–310. [CrossRef]
47. Guo, Y.; Pan, W.; Liu, S.; Shen, Z.; Xu, Y.; Hu, L. ERK/MAPK signalling pathway and tumorigenesis (Review). *Exp. Ther. Med.* **2020**, *19*, 1997–2007. [CrossRef]
48. Wu, Q.; Wu, W.; Fu, B.; Shi, L.; Wang, X.; Kuca, K. JNK signaling in cancer cell survival. *Med. Res. Rev.* **2019**, *39*, 2082–2104. [CrossRef]
49. Zhang, Y.; Chen, P.; Hong, H.; Wang, L.; Zhou, Y.; Lang, Y. JNK pathway mediates curcumin-induced apoptosis and autophagy in osteosarcoma MG63 cells. *Exp. Ther. Med.* **2017**, *14*, 593–599. [CrossRef]
50. Wang, S.; Li, H.; Chen, S.; Wang, Z.; Yao, Y.; Chen, T.; Ye, Z.; Lin, P. Andrographolide induces apoptosis in human osteosarcoma cells via the ROS/JNK pathway. *Int. J. Oncol.* **2020**, *56*, 1417–1428. [CrossRef]
51. Tsuruta, F.; Sunayama, J.; Mori, Y.; Hattori, S.; Shimizu, S.; Tsujimoto, Y.; Yoshioka, K.; Masuyama, N.; Gotoh, Y. JNK promotes Bax translocation to mitochondria through phosphorylation of 14-3-3 proteins. *EMBO J.* **2004**, *23*, 1889–1899. [CrossRef] [PubMed]
52. Papadakis, E.S.; Finegan, K.G.; Wang, X.; Robinson, A.C.; Guo, C.; Kayahara, M.; Tournier, C. The regulation of Bax by c-Jun N-terminal protein kinase (JNK) is a prerequisite to the mitochondrial-induced apoptotic pathway. *FEBS Lett.* **2006**, *580*, 1320–1326. [CrossRef] [PubMed]
53. Chandhanayingyong, C.; Kim, Y.; Staples, J.R.; Hahn, C.; Lee, F.Y. MAPK/ERK signaling in osteosarcomas, Ewing sarcomas and chondrosarcomas: Therapeutic implications and future directions. *Sarcoma* **2012**, *2012*, 404810. [CrossRef] [PubMed]
54. Noh, K.; Kim, K.O.; Patel, N.R.; Staples, J.R.; Minematsu, H.; Nair, K.; Lee, F.Y.I. Targeting inflammatory kinase as an adjuvant treatment for osteosarcomas. *J. Bone Jt. Surg.-Ser. A* **2011**, *93*, 723–732. [CrossRef]
55. Sasaki, K.; Hitora, T.; Nakamura, O.; Kono, R.; Yamamoto, T. The role of MAPK pathway in bone and soft tissue tumors. *Anticancer Res.* **2011**, *31*, 549–553.
56. Yu, Y.; Luk, F.; Yang, J.-L.; Walsh, W.R. Ras/Raf/MEK/ERK pathway is associated with lung metastasis of osteosarcoma in an orthotopic mouse model. *Anticancer Res.* **2011**, *31*, 1147–1152.
57. Salas, S.; Jiguet-Jiglaire, C.; Champion, L.; Bartoli, C.; Frassinetti, F.; Deville, J.L.; Maues De Paula, A.; Forest, F.; Jézéquel, P.; Gentet, J.C.; et al. Correlation between ERK1 and STAT3 expression and chemoresistance in patients with conventional osteosarcoma. *BMC Cancer* **2014**, *14*, 606. [CrossRef]
58. Pan, P.-J.; Liu, Y.-C.; Hsu, F.-T. Protein Kinase B and Extracellular Signal-Regulated Kinase Inactivation is Associated with Regorafenib-Induced Inhibition of Osteosarcoma Progression In Vitro and In Vivo. *J. Clin. Med.* **2019**, *8*, 900. [CrossRef]
59. Verrecchia, F.; Rédini, F. Transforming growth factor- β signaling plays a pivotal role in the interplay between osteosarcoma cells and their microenvironment. *Front. Oncol.* **2018**, *8*, 133. [CrossRef]
60. Lamora, A.; Talbot, J.; Mullard, M.; Brounais-Le Royer, B.; Redini, F.; Verrecchia, F. TGF- β Signaling in Bone Remodeling and Osteosarcoma Progression. *J. Clin. Med.* **2016**, *5*, 96. [CrossRef]

61. Sung, J.Y.; Park, S.Y.; Kim, J.H.; Kang, H.G.; Yoon, J.H.; Na, Y.S.; Kim, Y.N.; Park, B.K. Interferon consensus sequence-binding protein (ICSBP) promotes epithelial-to-mesenchymal transition (EMT)-like phenomena, cell-motility, and invasion via TGF- β signaling in U2OS cells. *Cell Death Dis.* **2014**, *5*, e1224. [CrossRef]
62. Lee, S.H.; Jeong, D.; Han, Y.S.; Baek, M.J. Pivotal role of vascular endothelial growth factor pathway in tumor angiogenesis. *Ann. Surg. Treat. Res.* **2015**, *89*, 1–8. [CrossRef]
63. Ohba, T.; Cates, J.M.M.; Cole, H.A.; Slosky, D.A.; Haro, H.; Ando, T.; Schwartz, H.S.; Schoenecker, J.G. Autocrine VEGF/VEGFR1 signaling in a subpopulation of cells associates with aggressive osteosarcoma. *Mol. Cancer Res.* **2014**, *12*, 1100–1111. [CrossRef]
64. Yang, J.; Yang, D.; Sun, Y.; Sun, B.; Wang, G.; Trent, J.C.; Araujo, D.M.; Chen, K.; Zhang, W. Genetic amplification of the vascular endothelial growth factor (VEGF) pathway genes, including VEGFA, in human osteosarcoma. *Cancer* **2011**, *117*, 4925–4938. [CrossRef] [PubMed]
65. Chen, D.; Zhang, Y.J.; Zhu, K.W.; Wang, W.C. A systematic review of vascular endothelial growth factor expression as a biomarker of prognosis in patients with osteosarcoma. *Tumor Biol.* **2013**, *34*, 1895–1899. [CrossRef] [PubMed]
66. Kaya, M.; Wada, T.; Akatsuka, T.; Kawaguchi, S.; Nagoya, S.; Shindoh, M.; Higashino, F.; Mezawa, F.; Okada, F.; Ishii, S. Vascular endothelial growth factor expression in untreated osteosarcoma is predictive of pulmonary metastasis and poor prognosis. *Clin. Cancer Res.* **2000**, *6*, 572–577.
67. Bajpai, J.; Sharma, M.; Sreenivas, V.; Kumar, R.; Gamnagatti, S.; Khan, S.A.; Rastogi, S.; Malhotra, A.; Bakhshi, S. VEGF expression as a prognostic marker in osteosarcoma. *Pediatr. Blood Cancer* **2009**, *53*, 1035–1039. [CrossRef] [PubMed]
68. Peng, N.; Gao, S.; Guo, X.; Wang, G.; Cheng, C.; Li, M.; Liu, K. Silencing of VEGF inhibits human osteosarcoma angiogenesis and promotes cell apoptosis via VEGF/PI3K/AKT signaling pathway. *Am. J. Transl. Res.* **2016**, *8*, 1005–1015.
69. Wunder, J.S.; Gokgoz, N.; Parkes, R.; Bull, S.B.; Eskandarian, S.; Davis, A.M.; Beauchamp, C.P.; Conrad, E.U.; Grimer, R.J.; Healey, J.H.; et al. TP53 mutations and outcome in osteosarcoma: A prospective, multicenter study. *J. Clin. Oncol.* **2005**, *23*, 1483–1490. [CrossRef]
70. Chen, X.; Bahrami, A.; Pappo, A.; Easton, J.; Dalton, J.; Hedlund, E.; Ellison, D.; Shurtleff, S.; Wu, G.; Wei, L.; et al. Recurrent somatic structural variations contribute to tumorigenesis in pediatric osteosarcoma. *Cell Rep.* **2014**, *7*, 104–112. [CrossRef] [PubMed]
71. Sławinska-Brych, A.; Zdzisinska, B.; Mizerska-Dudka, M.; Kandefer-Szerszen, M. Induction of apoptosis in multiple myeloma cells by a statin-thalidomide combination can be enhanced by p38 MAPK inhibition. *Leuk. Res.* **2013**, *37*, 586–594. [CrossRef] [PubMed]
72. Sławinska-Brych, A.; Król, S.K.; Dmoszyńska-Graniczka, M.; Zdzisińska, B.; Stepulak, A.; Gagoś, M. Xanthohumol inhibits cell cycle progression and proliferation of larynx cancer cells in vitro. *Chem. Biol. Interact.* **2015**, *240*, 110–118. [CrossRef] [PubMed]
73. Bartnik, M.; Sławinska-Brych, A.; Żurek, A.; Kandefer-Szerszeń, M.; Zdzisińska, B. 8-methoxypsoralen reduces AKT phosphorylation, induces intrinsic and extrinsic apoptotic pathways, and suppresses cell growth of SK-N-AS neuroblastoma and SW620 metastatic colon cancer cells. *J. Ethnopharmacol.* **2017**, *207*, 19–29. [CrossRef] [PubMed]

Publisher's Note: MDPI stays neutral with regard to jurisdictional claims in published maps and institutional affiliations.



© 2020 by the authors. Licensee MDPI, Basel, Switzerland. This article is an open access article distributed under the terms and conditions of the Creative Commons Attribution (CC BY) license (<http://creativecommons.org/licenses/by/4.0/>).



Review

Gold (III) Derivatives in Colon Cancer Treatment

Agata Gurba ^{1,*}, Przemysław Taciak ¹, Mariusz Sacharczuk ^{1,2}, Izabela Młynarczuk-Biały ³,
Magdalena Bujalska-Zadrożny ¹ and Jakub Fichna ⁴

- ¹ Department of Pharmacodynamics, Faculty of Pharmacy, Medical University of Warsaw, 02-097 Warsaw, Poland; przemyslaw.taciak@wum.edu.pl (P.T.); mariusz.sacharczuk@wum.edu.pl (M.S.); magdalena.bujalska@wum.edu.pl (M.B.-Z.)
- ² Department of Genomics, Institute of Genetics and Animal Breeding, Polish Academy of Sciences, Jastrzebiec, 05-552 Magdalenka, Poland
- ³ Department for Histology and Embryology, Medical University of Warsaw, Chalubinskiego 5, 02-004 Warsaw, Poland; imlynarczuk@wum.edu.pl
- ⁴ Department of Biochemistry, Faculty of Medicine, Medical University of Lodz, 92-215 Lodz, Poland; jakub.fichna@umed.lodz.pl
- * Correspondence: agata.grabowska@wum.edu.pl

Abstract: Cancer is one of the leading causes of morbidity and mortality worldwide. Colorectal cancer (CRC) is the third most frequently diagnosed cancer in men and the second in women. Standard patterns of antitumor therapy, including cisplatin, are ineffective due to their lack of specificity for tumor cells, development of drug resistance, and severe side effects. For this reason, new methods and strategies for CRC treatment are urgently needed. Current research includes novel platinum (Pt)- and other metal-based drugs such as gold (Au), silver (Ag), iridium (Ir), or ruthenium (Ru). Au(III) compounds are promising drug candidates for CRC treatment due to their structural similarity to Pt(II). Their advantage is their relatively good solubility in water, but their disadvantage is an unsatisfactory stability under physiological conditions. Due to these limitations, work is still underway to improve the formula of Au(III) complexes by combining with various types of ligands capable of stabilizing the Au(III) cation and preventing its reduction under physiological conditions. This review summarizes the achievements in the field of stable Au(III) complexes with potential cytotoxic activity restricted to cancer cells. Moreover, it has been shown that not nucleic acids but various protein structures such as thioredoxin reductase (TrxR) mediate the antitumor effects of Au derivatives. The state of the art of the in vivo studies so far conducted is also described.

Keywords: gold; Au(III) complex; colorectal cancer; anticancer drugs; organometallic; cancer therapy; cytotoxicity; metallodrugs

Citation: Gurba, A.; Taciak, P.; Sacharczuk, M.; Młynarczuk-Biały, I.; Bujalska-Zadrożny, M.; Fichna, J. Gold (III) Derivatives in Colon Cancer Treatment. *Int. J. Mol. Sci.* **2022**, *23*, 724. <https://doi.org/10.3390/ijms23020724>

Academic Editors: Enikő Kallay, Andrzej Kutner and Geoffrey Brown

Received: 16 December 2021

Accepted: 4 January 2022

Published: 10 January 2022

Publisher's Note: MDPI stays neutral with regard to jurisdictional claims in published maps and institutional affiliations.



Copyright: © 2022 by the authors. Licensee MDPI, Basel, Switzerland. This article is an open access article distributed under the terms and conditions of the Creative Commons Attribution (CC BY) license (<https://creativecommons.org/licenses/by/4.0/>).

1. Introduction

Cancer is one of the leading causes of morbidity and mortality in the world, being responsible for approximately 9.6 million deaths in 2018 [1] and almost 10.0 million in 2020 [2]. According to global epidemiological data, colorectal cancer (CRC) is the third most frequently diagnosed cancer in men and the second in women. The worldwide burden of the disease is estimated to rise by 60% to over 2.2 million new cases and 1.1 million deaths by 2030. As reported in National Registry of Cancers, there has been a continuous increase in colon cancer incidence rate in Poland, with 4720 newly diagnosed cases [3,4].

Colon cancer develops as a result of the change of normal colonic epithelium including dysplasia and metaplasia to cancerous tumor, both polyposis and nonpolyposis, as a result of genetic alterations and the functional impact of these changes [5]. Colorectal tumors are driven by a wide range of spontaneous or induced mutations by mutagens, which is why they constitute a very heterogeneous group of cancers that are difficult to treat [6,7]. In the natural history of CRC development, a sequence of mutations accumulates, including antioncogene APC that becomes inactive and drives uncontrolled cell divisions.

Further, K-Ras hyperactivity quickens cell divisions, and finally p53 becomes inactive. The accumulation of mutations in nonhereditary forms of CRC lasts about three decades [8].

It has been observed that median age at diagnosis with invasive cancer is about 70 years in developed countries [9]. The relationship between the aging and cancer is linked to the aging of lymphocytes (immunosenescence) [10] and with DNA defects that accumulate with age as well as with hormonal changes [11]. The development of CRC in a large number of cases begins decades before its detection through the adenoma–carcinoma sequence. By that time, it reaches a late stage, which complicates the treatment [12]. The risk for developing CRC is associated with personal features or habits [13] such as age [14], chronic diseases history including inflammatory bowel disease [15], Crohn’s disease [16] and sedentary lifestyle, obesity [17], unhealthy nutritional habits [18], smoking and alcohol consumption [19]. Therefore, a continuous increase in the incidence of CRC in developed countries can be attributed to an increasingly aging population, unfavorable modern eating habits and an increase in risk factors such as smoking, low physical activity and obesity [20].

In the case of early diagnosis, the basic treatment is surgery, but this is already ineffective in advanced cases with metastases, which constitute about 25% of diagnoses [21,22]. The effectiveness of a standard neoadjuvant cytotoxic therapy in these patients, based on oxaliplatin and other cisplatin analogues, has been drastically reduced by the lack of specificity towards cancer cells, rapid development of drug resistance and cancer recurrence [23].

Thus, current research has been focused on developing new metallodrugs based on other nonplatinum transition metals, such as gold (Au), silver (Ag), iridium (Ir) or ruthenium (Ru) [24]. Another approach is the substitution of a ligand and the modification of existing chemical structures that led to the synthesis of a wide range of metal-based compounds, some of which have shown improved cytotoxic and pharmacokinetic profiles [25]. Furthermore, nanoparticles, through their enhanced permeability and retention (EPR) effect, preferentially accumulate in tumors [26], which also makes them an attractive research topic. Despite an abundant literature on gold nanoparticles in experimental cancer biology, only a few of the gold-based nanodevices are currently being tested in clinical trials [27], and none of them are approved by health agencies. In recent years, the field of cytotoxicity of Au complexes has been rapidly developing, which is reflected in numerous reviews. Au(III) compounds seem to be a particularly promising and good alternative for platinum-based anticancer drugs due to their structural similarity to platinum (Pt)(II) [28]. However, most of the described compounds have an unclear mode of action and a lack of clinical relevance. That is why we are constantly looking for new and fully characterized Au(III) derivatives. In this review, we summarize the previous work and describe the most recent advances in the use of Au(III) derivatives in CRC treatment.

1.1. Colorectal Cancer Treatment

CRC can be divided into five stages: 0, I, II, III and IV, depending on the involvement of lymph nodes, formation of metastases and the grade of local invasion depth. The most advanced stage with the worst prognosis is stage IV. The therapeutic approach depends on the stage of the disease. Thus, tumors at stage 0 are surgically removed while patients with stage II and above (invasive cancer crossing the basement membrane) require more complex treatment methods that include surgery, chemotherapy and/or radiotherapy [12,29,30].

The standard therapy for CRC currently involves various medicines, either in combination or as single agents, such as: 5-fluorouracil/leucovorin (5-FU/LV), capecitabine, irinotecan, oxaliplatin, bevacizumab, cetuximab, panitumumab, ziv-aflibercept, ramucirumab, regorafenib, trifluridine-tipiracil, pembrolizumab and nivolumab. The described mechanisms of action of cytostatics are varied and include interference in DNA replication and inhibition of the activities of vascular endothelial growth factor (VEGF) and epidermal growth factors (EGF) [31–34].

In surgical treatment of CRC that crosses the basement membrane, adjuvant and neoadjuvant therapy is proposed to be the gold standard. These terms (adjuvant and

neoadjuvant) refer to the pairing of sequential steps of therapy, that is, chemotherapy followed by surgery, or surgery followed by chemotherapy, respectively.

In context of CRC therapy, the clinical prospective data on neoadjuvant therapy is limited—patients can benefit from these treatments [35], however the limitations are side effects such as neuropathy induced by oxaliplatin—that force for the invention of better and safer alternatives, such as other metallodrugs, including gold complexes [29].

The main reason for the low effectiveness of CRC treatment is the limited bioavailability and the lack of specificity towards cancer cells of conventional chemotherapeutic agents, which contributes to the destruction not only of cancerous cells but also of normal cells, and consequently leads to serious side effects. In addition, the development of drug resistance is observed [26,36–39].

In order to optimize anticancer therapy and reduce side effects, new alternative therapies in CRC are being investigated [13]. The most promising trends of research are the use of agarose tumor macrobeads [40–42], anti-inflammatory drugs [43–45], probiotics [46–48] and metal-based drugs [29,49–52].

1.2. Metallodrugs

Laboratories and scientific institutions around the world have researched many derivatives of metals such as Pt, Au and other metals for the treatment of tumors. Moreover, some of them have been patented or even implemented. A well-known drug is cisplatin, whose potent anticancer effect is derived from the interaction with DNA and impaired processes of replication, transcription and translation [53,54]. Unfortunately, the use of cisplatin may lead to neuro- and nephron-toxicity, along with evidence of either induced or intrinsic resistance to the treatment in some tumors [55,56]. Thus, development of both novel Pt- and other metal-based compounds is needed in order to obtain complexes with higher effectiveness, increased selectivity for tumor tissue, reduced toxicity, wider spectrum of activity, and ability to overcome tumor resistance often arising from cisplatin treatment [57].

Currently, the most abundant group of non-Pt, metal-based anticancer preparations are those incorporating Au. In fact, the group of reported compounds exhibiting anticancer activity based on Pt is less numerous than the group with same activity based on Au. Further down, medicinal preparations based on metallic Au (Au⁰), also known as—depending on the size of particles—colloidal or nanoparticle Au, are by far the largest group among all therapeutic Au-based compounds [39,58,59].

Metallic Au particles are insoluble in blood and plasma, but the tumor cells exhibit the ability to greater accumulation of Au particles in relation to normal cells according to the EPR effect [60,61]. Despite the promising results of preclinical studies, low bioavailability and very rapid excretion from the body discourage further attempts to use metallic Au in the clinical setting [62,63]. Moreover, indicated accumulation of such compounds of Au in the liver and spleen is an important side effect [64–67].

The low bioavailability of Au(0)-based drugs has initiated research into Au complexes that are characterized by better bioavailability and solubility. During the last two decades, a large variety of Au(I) and Au(III) compounds are reported to possess relevant antiproliferative properties *in vitro* against selected human tumor cell lines, qualifying them as excellent candidates for further pharmacological evaluation. The unique chemical properties of the Au center confer very interesting and innovative pharmacological profiles to Au-based metallodrugs [68]. As previously described, Au(I) and Au(III) compounds are widely used in research as anticancer agents, however, most of them display limitations concerning solution stability under physiological conditions [24,25,29,69–76]. Au(III) compounds seem to be particularly promising and a good alternative for Pt-based anticancer drugs, due to their structural similarity [28]. Currently, researchers aim to develop different types of ligands able to stabilize the Au(III) cation and prevent its reduction under physiological conditions.

1.3. Perspectives for Gold-Based Compounds against Colorectal Cancer

There are several properties of Au that make it a potential anticancer agent in CRC. Since Au compounds have been used for centuries in the treatment of rheumatoid arthritis; their well-known anti-inflammatory and immunosuppressing properties made them promising drug candidates for CRC treatment [77].

Moreover, there is evidence that not nucleic acids, as in the case of cisplatin, but some selected protein targets, for example, thioredoxin reductase (TrxR), mediate the antitumor effects of Au derivatives [29,78–80]. This is particularly important as Trx-1 expression is upregulated in several human cancers, including CRC. The Trx/TrxR redox pathway is an attractive target for the development of new anticancer drugs, as elevated Trx-1 levels result in rapid tumor growth, inhibition of apoptosis, and reduced patient survival [81,82]. Gold complexes have multimodal mechanisms of action, and examples of them are listed below.

Direct DNA interaction—platin-derived compounds such as oxaliplatin are standard DNA-binding therapeutics applied in CRC—it was shown that some gold complexes cause DNA fragmentation rather than cross-linkage as a result of reversible and noncovalent DNA interaction [83–86].

Gold complexes can induce apoptosis by intrinsic mechanisms involving caspase 9 and 3 activation, cytochrome C release, and PARP cleavage [80,87–89].

Protein kinase C (PKC) is involved in cell proliferation, differentiation, migration, and survival. Hyperactivation of PKC signaling can be observed in cancers including CRC. Some gold complexes including aurothioglucose and aurothiomalate can inhibit PKC and consequently inhibit proliferation of cancer cells [90,91].

MEK/ERK (Ras) pathway—this pathway is necessary for proper cell divisions, and if hyperactivated it drives unhampered divisions of the cancer cell, its motility, mobility and insensitivity to induction of apoptosis. Ras hyperactivation is often involved in CRC development, but all signaling elements including growth receptors and downstream kinases (Raf, MEK, ERK) might participate in cancer progression [92].

The proteasome–ubiquitin pathway (UPS)—this cellular protein destination and degradation system was shown to be a good anticancer drug target, since proteasome inhibitors are applied in cancer treatment. Tumor cells with deregulated cell divisions are more sensitive to inhibition of UPS than normal cells that can enter the cell cycle, and block and escape death by proteasome inhibition. Particular gold complexes such as the Au(III) dithiocarbamate compound turned out to inhibit proteasome activity and induce accumulation of polyubiquitin complexes, both in vitro in tumor cell lines, as well as in xenografts resected from experimental animals [83,93].

Thus, the advantage of Au complexes is their multimodal mechanism of action targeting various elements crucial for cancer progression.

2. In Vitro Studies

Au(III) compounds, due to their similarity to cisplatin, were among the first metal complexes tested for anticancer activity. It was initially assumed that the mechanism of action of these compounds would be the same as Pt-based drugs, and based mainly on interactions with DNA [94,95]. However, subsequent studies revealed that the cytostatic effect of Au derivatives is rather multifaceted, and may include some selected proteins such as TrxR or deubiquitinases [78–80,96,97]. It is also known that these proteins are overexpressed in cancer cells, and inhibition of their activity is lethal to cancer cells, although with a much lower effect on noncancerous cells. Therefore, it is believed that the systemic toxicity of Au complexes will be significantly reduced compared to conventional therapy [29]. Notwithstanding, most of them display limitations concerning solution stability under physiological conditions and are easily reduced to Au(I) or Au(0), thus losing their activity. However, as the following examples show, it is possible to synthesize stable, resilient-to-reduction, organogold(III) complexes, which is the main goal in this field. To

date, according to our knowledge, inorganic Au(III) complexes have not been described as cytostatic agents in CRC.

2.1. Organogold Derivatives

One of the first studies of Au(III) compounds on colon cancer cell lines was not satisfactory. In 1996, four analogues of the Au(III) complex [AuCl₂(damp)] (damp = 2-[(dimethylamino)methyl]-phenyl) (**2a–e**) were evaluated for antitumor activity. The compounds have structural features in common with cisplatin, which was included as a comparison in the study (Figure 1). The derivatives have been tested on a panel of cell lines, among others made from human colorectal cancer such as: SW620, SW1116, SW403, HT29/219. The comparison of results for Au(III) compounds and cisplatin showed broadly similar growth-inhibiting properties and differential cytotoxicity, and the SW620 and SW1116 lines were the least sensitive to the compounds (Table 1). Therefore, these complexes might have the potential as an antitumor agent but in selected cancer types. In addition, although some compounds had some structural similarity to cisplatin, their mode of action seemed different [98]. Furthermore, the organogold compounds studied exhibit good stability within a physiological-like environment. Subsequent chemical and biological studies of **2a–e** derivatives also confirmed the same properties [99].

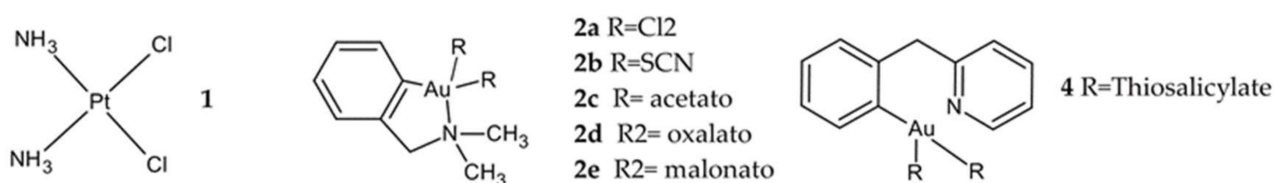


Figure 1. Structural comparison of organogold derivatives **2a–e**, **4** with cisplatin (**1**).

Table 1. Comparison of IC₅₀ (μM) for complexes **2a–2e** and cisplatin (**1**) against selected human cell lines [98].

Symbol	Cell Line					
	SW620 (Colon)	SW1116 (Colon)	HT29/219 (Rectum)	ZR-75-1 (Breast)	HT-1376 (Bladder)	SK-OV-3 (Ovary)
1	167	163	17	27	23	23
2a	124	119	55	34	30	45
2b	51	47	25	45	6,7	20
2c	281	238	67	41	13	13
2d	205	215	19	36	10	10
2e	67	80	36	27	11	11

Calamai et al. designed, synthesized and evaluated for cytotoxicity four complexes (**3a–3d**, Figure 2) with a square-planar geometry, like cisplatin. The experiment was performed on a panel of five tumor cell lines, composed mainly of cell lines sensitive to cisplatin, e.g., HCT-8 with cisplatin and sodium tetrachloroaurate (NaAuCl₃) as control. In a colon cancer cell line, all four investigated derivatives exhibited less cytotoxic effect (with IC₅₀ ranging from 8 to 29 μM) than cisplatin (IC₅₀ value 3.9 μM). On the contrary, their antitumor potency against other tumor cell lines was comparable to or even greater than cisplatin (Table 2) [84].

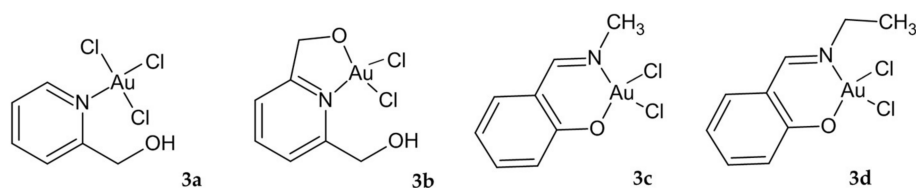


Figure 2. Au complexes **3a–d** with a square-planar geometry.

Table 2. Characterization of the anticancer properties of new organogold compounds.

Symbol	Proposed Mechanism of Action	Cell Line	IC ₅₀ Range (μM)
3a–d	Bind to DNA	HCT8	8.0 ± 2.5 (3a) 11.6 ± 2.0 (3b) 29 (3c) 28.5 (3d) 3.9 ± 0.6 (cisplatin)
4	Inhibition of cathepsins B and K	DLD-1 HCT-116 HT-29	3.5 (DLD-1) 5.7 (HCT-116) 11.7 (HT-29)
5a,b	Undetermined	Caco-2 HT-29	>120 (5a,b) 39.8 (5a) >120 (5b)
6	Intercalation of DNA, inhibition of topoisomerase I, II	SW620	15
7	Undetermined	LS-174T	74.0
8a–d	Undetermined	HT-29	5.2 ± 0.4 (8a) 18.1 ± 0.6 (8b) 17.7 ± 0.4 (8c) 33.7 ± 2.2 (8d)
8e,g	Induction of apoptosis, G0/G1 cell cycle arrest	HCT-116	47.0 ± 3.1 (8e) 67.0 ± 4.8 (8f) 14.9 ± 0.6 (8g)
9a–d	Undetermined	LoVo	(2.40 ± 0.04) × 10 ⁻² (9a) 3.8 ± 0.1 (9b) 7.6 ± 0.2 (9c) 7.9 ± 0.1 (9d)
10a,b	Induction of ROS-dependent opening of the PTP.	HCT-116	15.8 ± 2.1 (10a) 43.6 ± 5.4 (10b)
11	Modification of MtMP, release of cytochrome C to the cytoplasm, caspase-3 activation; inhibition of proteasome.	Caco-2/TC7	1.00 ± 0.06 (11) 45.6 ± 8.08 (cisplatin) 2.1 ± 0.4 (auranorfin)
12	Distortion of DNA double helix	HCT-116	
13	Inhibition of the zinc-finger protein PARP-1	HCT116 p53+/+ HCT116 p53-/-	2.1 ± 0.7 14.0 ± 1.1
14a,b	14a proapoptotic activation, 14b pronecrotic actions	HCT116 HCT116p53-/-	0.48 ± 0.57 (14a) 0.33 ± 0.14 (14b) 0.23 ± 0.20 (14a) 0.27 ± 0.12 (14b)
15	Molecular target: sulfur-containing proteins	WiDr	9.8 ± 1.2
16	Undetermined	HCT116	>50

Cytostatic activity for square-planar cycloaurated Au(III) compounds on HCT-116 and HT29 cell lines was also studied. The most active thiosalicylate derivative **4** (Figure 1), with IC_{50} value 11.7 μ M for HT29, was further tested in vivo. Additionally, it was proposed that the molecular targets of these compounds are thiol-containing biological molecules such as the cathepsin cysteine proteases, and it was found that they are able to inhibit both cathepsins B and K [100].

The cytotoxicity of two sterically different bithiazole Au(III) complexes, regular square-planar compound **5a** and disordered square-pyramidal geometry in **5b** (Figure 3), was also investigated. Of the three cancer cell lines studied, derivative **5a** showed no cytotoxicity in Caco-2, but its toxicity in HT29 was similar to cisplatin (Table 2). Compound **5b** had no anticancer value because it exhibited very little toxicity on the studied cell lines. This lack of activity might be due to steric construction [101].

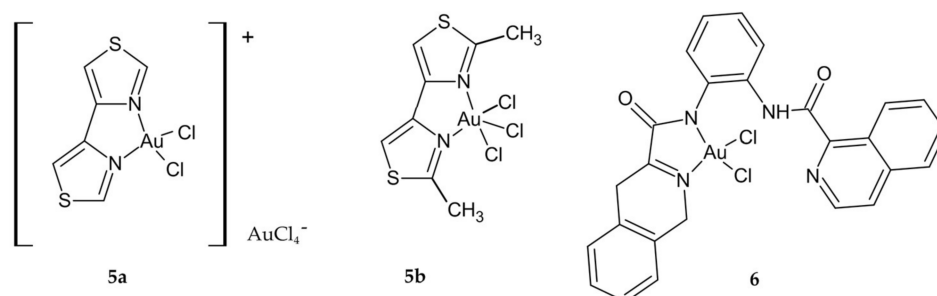


Figure 3. Au derivatives **5a**, **b** and **6**.

Wilson et al. reported that out of a series of four square-planar Au(III) chelates, only isoquinolylamidogold(III) chelate **6** (Figure 3) was sufficiently cytotoxic in the single-dose assay and promising for further studies. The data indicate that seven different colon cell lines were among the most susceptible to the Au(III) complex, with IC_{50} values below 20 μ M. The lowest IC_{50} value was for the colon cancer cell line SW-620 (Table 2). The cytotoxicity of the investigated compound compares favorably with that of cisplatin and etoposide (a nonintercalating topoisomerase II inhibitor). Dual topoisomerase I and II inhibitors were given as the mechanism of action of the compounds. However, there is a need to improve the structure of the chelates so that they are less susceptible to precipitation from aqueous solutions, which may increase their cytotoxicity and thus the chances of further development [85].

Another approach was presented by researchers who synthesized a new bile acid cholyglycinato Au(III) complex **7** (Figure 4) based on the ability of bile acids for vectorializing the cytostatic activity of other agents. Cytostatic effect of the investigated compound was mild against human colon adenocarcinoma LS-174T in vitro, but **7** had a significantly higher IC_{50} value than cisplatin (Table 2). The appearance of colloidal Au during the process of hydrolysis under physiological conditions may explain the low cytostatic activity [102].

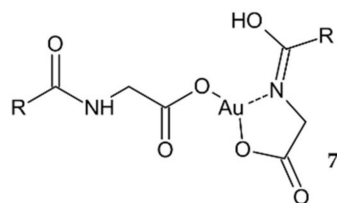


Figure 4. A new bile acid cholyglycinato Au(III) complex **7**.

Investigations of the cytotoxicity scores of novel organogold (III) compounds **8a–d** (Figure 5) revealed that all of these compounds, except for **8d**, are generally stable under physiological conditions and exhibit significant cytotoxic properties on a limited panel of

human tumor cell lines. However, negligible anticancer effects (Table 2) were generally measured on the HT29 line compared to those of cisplatin and oxaliplatin [103]. Massai et al. published further work on derivatives of these cyclometallated complexes **8e,g** (Figure 5). All three compounds, especially **8g**, cause moderate, but still significant, antiproliferative effects toward HCT-116 cancer cells, accompanied by a strong induction of apoptosis and a G0/G1 cell cycle arrest (Table 2). Given the fact that all these effects were greater on CRC cell line HCT-116 compared to the normal L-929 fibroblast cell line, there is a possibility to further investigate and characterize **8g** as a potential anticancer agent on a larger and more complex panel of cancer cell lines, as well as to evaluate the mechanisms of its different toxicity effects between in vitro models of tumoral and healthy tissue [104].

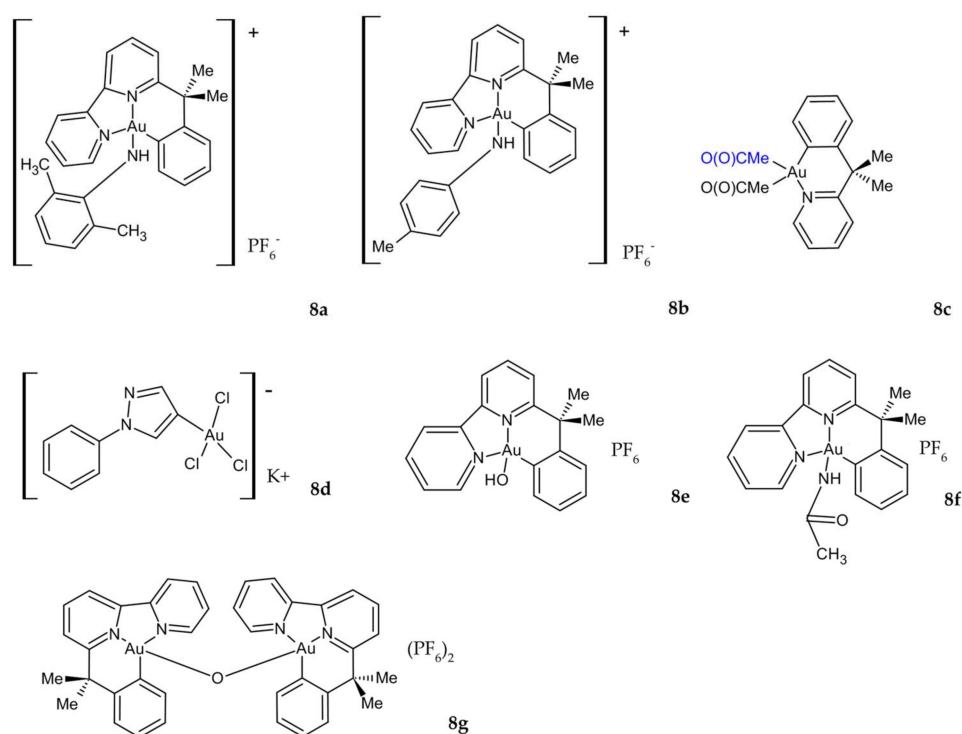


Figure 5. Novel organogold (III) compounds **8a–g**.

Considering the ability of dithiocarbamates to act as chelating ligands, many examples of Au(III) dithiocarbamate derivatives have been reported. The first more promising studies on the cytotoxic activity of Au(III) compounds in CRC were published by Ronconi et al., which described some of Au(I) and Au(III) complexes with dithiocarbamate ligands (DMDT = N,N-dimethyldithiocarbamate; DMDTM = S-methyl-N,N-dimethyldithiocarbamate; ESDT = thylsarcosinedithiocarbamate). Their preliminary studies have shown that the biological activity of the compounds should generally be attributed to the presence of the Au(III) metal center, and that the Au(I) compounds produce a less pronounced inhibition of cell growth compared to Au(III) analogues. Four complexes **9a–d** (Figure 6) were selected for further in vitro cytotoxicity testing. Data regarding their in vitro antiproliferative activity against colon adenocarcinoma cell lines (LoVo), which are notoriously not very sensitive to cisplatin, are extremely interesting, because these new Au(III) complexes seem to also be cytotoxic against tumor cell lines resistant to cisplatin, overcoming their intrinsic resistance and supporting the hypothesis of a different mechanism of action. The IC₅₀ values of investigated compounds ranged from 2.4 nM to 7.9 μM (Table 2), while cisplatin's IC₅₀ value was 56 μM [105,106].

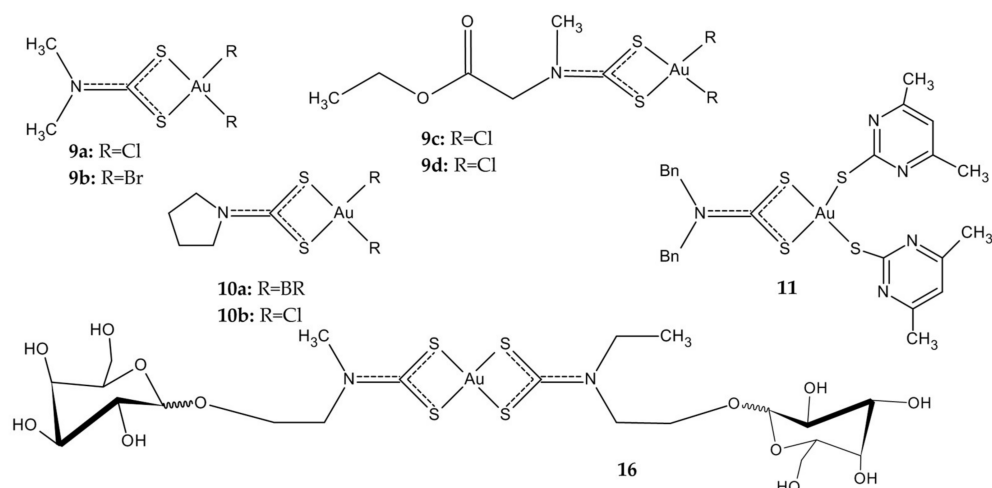


Figure 6. Au(III) dithiocarbamate derivatives **9a–d**, **10a,b**, **11**, **16**.

Treatment with the other two Au(III) compounds based on the pyrrolidinedithiocarbamates (PDT), **10a,b** (Figure 6), showed a rapid (three-hour) dose-dependent decrease in cell viability in the HCT-116 colorectal carcinoma cells. It was found that the bromide derivative **10a** was more effective than the chloride one **10b** in inducing cell death and acting via elicited oxidative stress, with effects on the permeability transition pore, a mitochondrial channel whose opening leads to cell death (Table 2). Cisplatin did not show any cytotoxicity under the same experimental conditions [107]. Greater cytotoxicity of bromides is in agreement with the findings reported by Casini et al. [108] for other Au(III) anticancer agents.

Mixed thiolate–dithiocarbamate Au(III) complexes display high antiproliferative activity against colon cancer cell line Caco-2/TC7, without affecting differentiated enterocytes. The most promising derivative **11** (Figure 6) is characterized by a much higher cytotoxicity compared to cisplatin, and slightly higher than auranofin (Table 2). Although it was assumed that TrxR was a potential target of the dithiocarbamate Au complexes, this was not supported, as reactive oxygen species (ROS) levels and TrxR activity remained unchanged during the experiment. Cell death studies showed that the complexes induced changes in mitochondrial membrane potential, cytochrome C release and caspase-3 activation. The complexes are characterized by high stability under physiological conditions, which gives the opportunity to develop new cytostatics in the treatment of colorectal cancer with the proteasome as a possible target [88].

Another study showing high cytotoxicity against the colon cancer cell line was reported by Shi et al. Compared to cisplatin, Au(III) compound **12** (Figure 7) has demonstrated higher cytotoxicity for HCT-116 cell lines at all the concentrations used in the studies. At the concentration of 106 M, the compound showed 30% inhibition against the HCT-116 cell line, while at the same concentration, cisplatin shows 20% inhibition. Additionally, it has been shown that the compound **12** can induce DNA double helix distortion in its mechanism of action [86].

The new Au(III) cyclometallated phosphine derivative **13**, with PTA = 1,3,5-triazaphosphaadamantane ligand (Figure 7), which is not cytotoxic but is known in general to improve water solubility, has been proposed as a new antineoplastic agent in colorectal cancer. The derivative **13** was the most active of all investigated complexes in the study, twice as toxic as cisplatin against HCT-116 p53+/+ cells, and poorly effective on HCT-116 p53−/− (Table 2). This result suggests a similar dependence on p53 pathways for Au(III) complex as for cisplatin. Interestingly, compound **13** inhibited the zinc finger enzyme PARP-1 in nM concentrations, suggesting the possible design of selective inhibitors and the use of organometallic Au compounds in combination therapies with other anticancer drugs [89].

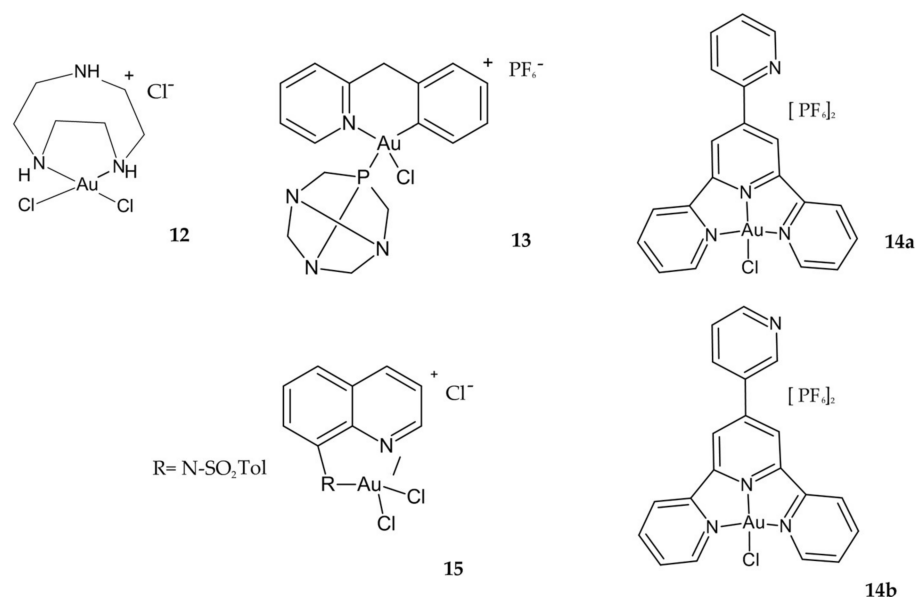


Figure 7. Au(III) complexes **12**, **13**, **14a,b**, **15**.

Both Au(III) complexes **14a** and **14b** incorporating 2,2':6',2''-terpyridine ligand (Figure 7), showed excellent antiproliferative activities against HCT-116, higher than the free ligands and cisplatin. Additionally, compound **14a** showed high selectivity against HCT-116 and HCT-116p53 – / – cells, confirmed by the selectivity index (SI). Most interestingly, the complex **14a** exhibited proapoptotic activation, while **14b** displayed pronecrotic actions [109].

Au(III) complexes containing quinoline ligands at position 8 with different groups arose due to the broad spectrum of medical applications of 8-hydroxyquinoline. It was found that compound **15** with an N-tosyl-8-aminoquinoline ligand (Figure 7) is the most active of the synthesized complexes in all cancer cell lines tested, including the cisplatin-resistant WiDr cell line, and acts by interacting with proteins. Moreover, this complex has proved to be the most stable compound in DMSO and saline solution, even after several hours [110].

The latest available work in this area describes Au(III) complexes with glycoconjugated dithiocarbamate ligands (among others **16**, Figure 6). To improve the selective accumulation of an anticancer metal payload in malignant cells, carbohydrates (D-glucose, D-galactose, and D-mannose) were chosen as targeting agents exploiting the Warburg effect that accounts for the overexpression of glucose-transporter proteins (in particular GLUTs) in the phospholipid bilayer of most cancer cells. Unfortunately, the collected results indicate that the Au(III) complexes are not good substrates for GLUT and are inactive toward HCT-116 cells, with IC₅₀ values higher than 50 μM (Table 2) [111].

2.2. Porphyrin Complexes

More comprehensive and promising results were presented by using porphyrin ligand, which can stabilize the Au(III) ion against demetallation and reduction by the biological reductant glutathione [112].

Preliminary studies of a series of Au(III) tetraarylporphyrin (TPP) derivatives confirmed their stability in the presence of glutathione and demonstrated a much greater potency than cisplatin in killing human cancer cells, including drug-resistant variants [113]. The **17** complex (Figure 8) was selected for further study of its antitumor activity and its mechanism against colon cancer. The investigated compound exhibited marked cytotoxicity against different colon cancer cell lines and IC₅₀ values with 9-fold to 21-fold greater potency than that of cisplatin (Table 3). Furthermore, the **17** complex significantly induced apoptosis and cell cycle arrest and cleaved caspase 3, caspase 7, and poly(ADP-ribose) polymerase; released cytochrome C, and upregulated p53, p21, p27, and Bax. Further-

more, in vivo tests were also carried out [114]. The same complex was further studied by Altaf et al. with promising results. Compound **17** showed very high activity compared to Au(III) complexes of meso-1,2-di(1-naphthyl)-1,2-diaminoethane and cisplatin. It was about 7–8 times more potent than cisplatin against the HCT-15 cancer cell [115].

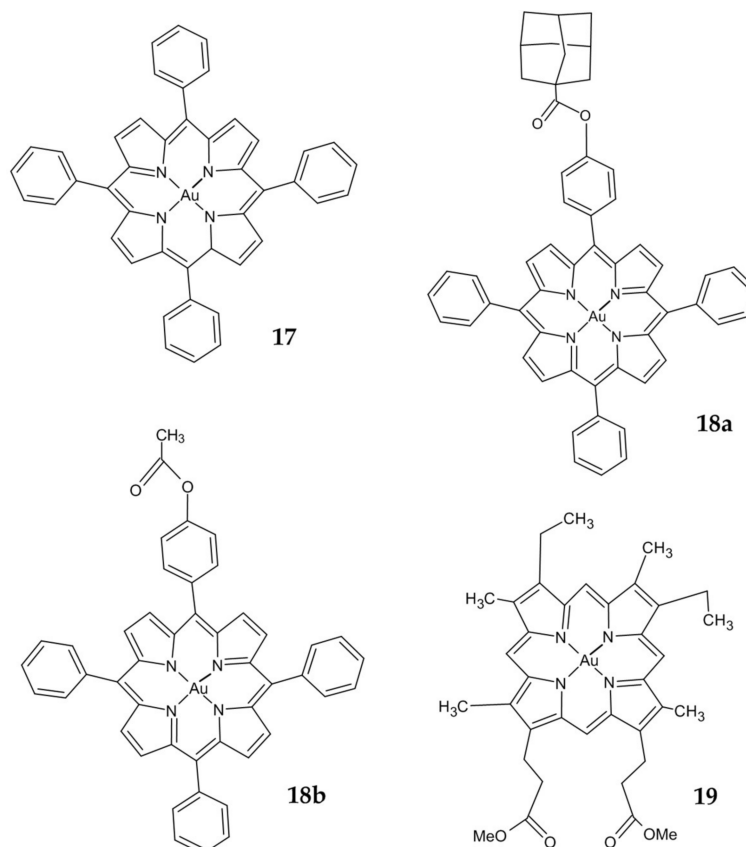


Figure 8. Au(III) porphyrin complexes **17**, **18a,b**, **19**.

Table 3. Characterization of the anticancer properties of porphyrin complexes.

Symbol	Proposed Mechanism of Action	Cell Line	IC ₅₀ Range (μM)
17a–e	Inducing apoptosis by a mitochondrial death pathway	SW1116	0.20 ± 0.02
		Colo 205	0.27 ± 0.02
		CRL-238	1.41 ± 0.20
		CCL-2134	0.65 ± 0.13
		HCT-15	0.86 ± 0.15
		HCT-15A2	3.43 ± 0.46
18a,b	Inducing apoptosis by intrinsic pathway	HT-29	17.0 (18a)
			3.5 (18b)
		HCT-116	16.0 (18a)
			3.0 (18b)
19	Inhibition the Trx, peroxiredoxin and deubiquitinases	HCT-116	0.06 ± 0.01
		NCM460	1.5 ± 0.15

A novel Au(III) porphyrin analogs **18a** and **18b** (Figure 8) were prepared by modifying one of the peripheral phenyl groups of **17**. Results revealed that **18b** was more cytotoxic to the colon cancer line than **18a** (Table 3). The investigated complexes reduced the survival of human CRC HT-29 and HCT-116 cell lines, caused cell cycle arrest in the G2/M phase,

and decreased expression of cyclin B1 and cyclin-dependent kinase 1 (Cdk1) was observed with an increase in regulation of the active form of p53, p21, and Bcl-2 associated with X (Bax) [87]. Furthermore, they induced apoptosis by the intrinsic pathway, as previously described [114].

Tong et al. demonstrate an anticancer activity of Au(III) mesoporphyrin IX dimethyl ester (**19**) (Figure 8). This compound displayed a higher cytotoxicity in HCT-116 colon cancer cells compared to noncancerous colon epithelial cells (NCM460) with 25-fold differences in IC₅₀ values (Table 3). Promising results from in vivo studies were also reported. The mechanism of action involves modification of the reactive cysteine residues and inhibiting the activity of thioredoxin, peroxiredoxin and deubiquitinases. Crucially, this study revealed that Au(III) induced ligand scaffold reactivity to target the thiol, which could be a useful tool in oncology [93].

2.3. N-Heterocyclic Carbenes (NHCs) Derivatives

A large part of the reviewed papers concerns research on N-heterocyclic carbenes (NHCs) Au complexes. It is widely accepted that the replacement of phosphine ligands by the isolobal NHC ligands frequently improves the properties of the new compounds for practical applications, which are them being water- and air-stable and easier to handle. Moreover, the imidazolium salts as the ligand precursor can be functionalized with almost any substituent, a rarely accessible feature in phosphines [116].

Lemke et al. described the synthesis and antiproliferative activity of a new halide, amino acid and dipeptide NHC Au(I) and NHC Au(III) complexes. In vitro cytostatic effect of compound **20** (Figure 9) was only mild against human colon adenocarcinoma HT-29, with an IC₅₀ value higher than most active complexes and slightly higher compared to cisplatin (Table 4) [116].

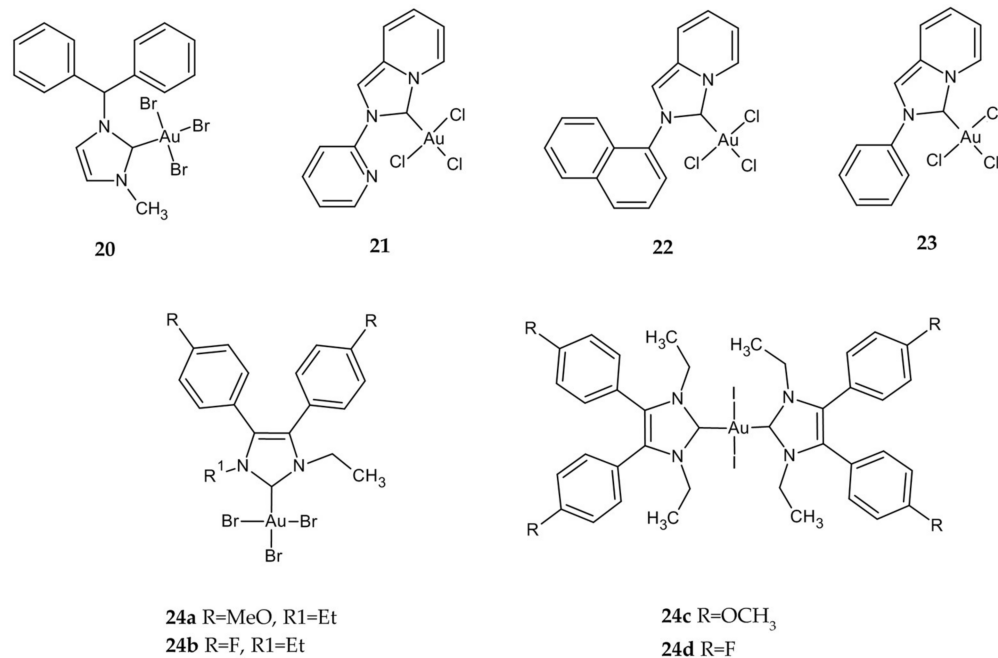


Figure 9. NHCs Au(III) derivatives 20–24.

Other groups were evaluated in vitro for the cytotoxicities of Au and Ag NHCs complexes supported by a pyridine, annulated imidazole-2-ylidene (**21**) [117,118], imidazolium salt 1-naphthyl-2-pyridin-2-yl-2H-imidazo[1,5-a]pyridin-4-ylidene hexafluorophosphate (**22**) [119], pyridyl[1,2-a][2-acetylphenylimidazol]-3-ylidene (**23**) [120] (Figure 9). All complexes of Au(III)–NHC exhibited lower cytotoxicity than Ag(I) and Au(I) complexes for nearly all cell lines tested. Despite that, compounds **21**, **22**, and **23** were more potent

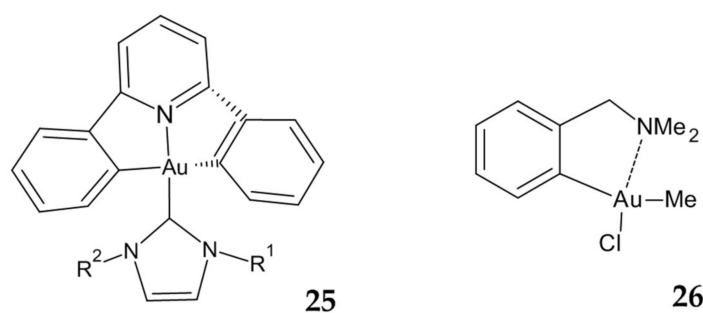
than cisplatin against the HCT-116 cell line (Table 4). Unfortunately, due to the lower cytotoxicity of Au(III)–NHC, studies involving the mechanism of action have not been performed for this complex.

Table 4. Characterization of the anticancer properties of N-heterocyclic carbenes (NHCs).

Symbol	Proposed Mechanism of Action	Cell Line	IC ₅₀ Range (μM)
20	Undetermined	HT-29	12.7 ± 1.2
21	Undetermined	HCT-116	5.9 ± 3.6
22	Undetermined	HCT-116	6.78 ± 2.01
23	Undetermined	HCT-116	21.25 ± 1.37
24a,b	Inhibition of TrxR	HT-29	6.2 ± 1.0 (24a) 7.5 ± 2.9 (24b)
24c,d	Undetermined	HT-29	0.26 ± 0.03 (24c) 0.30 ± 0.01 (24d)
25a–g	Multiple molecular targets	HCT-116	4.40 ± 1.50 (25a) 1.10 ± 0.28 (25b) 0.49 ± 0.12 (25c) 0.23 ± 0.11 (25d) 0.25 ± 0.10 (25e) 0.52 ± 0.34 (25f) 0.20 ± 0.06 (25g)

Liu et al. have proposed NHC–Au halide complexes derived from 4,5-diarylimidazoles. The influence of the oxidation state of the metal (Au(I) or Au(III)) is relatively low in general, however, on the HT-29 cell line, the Au(III) complexes **24a** and **24b** (Figure 9) were less active than their Au(I) congeners, which coincides with earlier papers. All complexes inhibit TrxR with different IC₅₀ values, nevertheless, other targets should be considered as part of the mode of action [121]. Researchers, encouraged by these promising results, have investigated the effect of halide exchange in Au–NHC complexes on their pharmacological properties. The growth-inhibitory effect against HT-29 cells was more than 10-fold higher for complexes **24c** and **24d** (Figure 9) than that of cisplatin or 5-FU. Moreover, this effect was independent of the oxidation state of Au and type of halides. Although the investigated complexes were successfully accumulated in the neoplastic tissue and localized in large amounts in the cell nucleus, their mode of action has not been clearly defined [122].

Fung et al. described the identification of multiple molecular targets for cyclometalated Au(III) complexes containing NHC ligands using photoaffinity groups. The IC₅₀ values for complexes **25a–g** (Figure 10) ranged from 4.4 μM to 0.2 μM in comparison to cisplatin with an IC₅₀ value 11.8 μM (Table 4). Importantly, all the compounds showed much higher cytotoxicity to HCT-116 than to immortalized normal human hepatocyte (MIHA) cells, which may indicate their selectivity. Numerous tests showed the ability of complexes to bind to intracellular proteins such as mitochondrial heat shock protein 60 (HSP60), vimentin (VIM), nucleoside diphosphate kinase A (NDKA), nucleophosmin (NPM), nuclease-sensitive element binding protein (Y box binding protein, YB-1), and peroxiredoxin 1 (PRDX1). The fact that the complexes have multiple molecular targets can minimize the occurrence of drug resistance that is usually encountered with single-target anticancer agents due to naturally occurring genetic mutations [123].



	25a	25b	25c	25d	25e	25f	25g
R ¹	CH ₃	C ₂ H ₅	nC ₃ H ₇	nC ₄ H ₉	nC ₅ H ₁₁	benzyl	nC ₄ H ₉
R ²	CH ₃	C ₂ H ₅	nC ₃ H ₇	nC ₄ H ₉	nC ₅ H ₁₁	benzyl	benzyl

Figure 10. Cyclometalated Au(III) complexes **25**, **26**.

2.4. Chlorite–Cyanide Complex of Gold (III)

Recently we characterized the synthesis, *in vitro* safety as well as anticancer activity of a novel chlorite–cyanide complex of gold (III) named TGS121 (patent no: PL422125A1). The compound was prepared as described by Krajewska et al. The obtained Au(III) complex with the formula [Au(CN)₄]₂ (ClO₂)Na is a sodium salt of chloride dioxide associated with Au(III)–cyanide group complex. This complex is water soluble, stable in a neutral pH and can be kept at room temperature. This complex turned out to be stable in cell culture medium and serum. Its relatively low molecular mass (692.5 g/mol) and the form of sodium salt makes it stable in physiological fluids and enables the passage through biological membranes such as the cell membrane. The novel Au(III) compound turned out to exert cytostatic/cytotoxic effects in cancer Ha-Ras transfected NIH3T3 fibroblasts selectively in comparison to the noncancer NIH3T3 cells (Table 5). Since Ras isoforms share 80% identity and share similar activity—one can conclude that in CRC with Ras hyperactivation (mostly K-Ras) (like HCT116), the compound TGS121 would also be effective [124,125].

Table 5. Characterization of the anticancer properties of TGS121.

Symbol	Proposed Mechanism of Action	Cell line	IC ₅₀ Range (μM)
TGS121	Apoptosis induction, inhibition of Ras-mediated pathway, cell cycle arrest at G2/M	Ras-3T3 NIH3T3	0.231 ± 1.2 5.05 ± 2.6

3. In Vivo Studies

Promising cytotoxicity of many Au(III) complexes has been observed against tumor cells *in vitro* however, to our knowledge, there has been very little evaluation of these compounds on *in vivo* tumor models.

Thiosalicylate derivative of cycloaurated Au(III) **4** was tested *in vivo* against the colon HT29 tumor xenograft. Its cytotoxicity did not translate into *in vivo* pharmacological activity, with only modest inhibition of tumor growth. The lack of activity could in part be explained by the poor solubility of this complex, indicating that further work is necessary to improve both solubility and lipophilicity in order to improve biodistribution [100].

The second compound tested *in vivo* was an organogold(III) complex **26** (Figure 10), which exhibits promising *in vitro* cytotoxicity, but it failed to inhibit *in vivo* tumor growth in HT29 colon cancer xenografts [126].

Only two described Au(III) compounds exhibited favorable antitumor properties both *in vitro* and *in vivo*. The tetraarylporphyrin Au(III) complex **17**, after intraperitoneal injection

tion in mice at doses of 1.5 mg/kg and 3.0 mg/kg, significantly inhibited the proliferation of Colo205 tumor cells, induced apoptosis and inhibited colon cancer tumor growth [114]. The second one, Au(III) mesoporphyrin IX dimethyl ester **19**, after intravenous injection twice per week for 21 days in nude mice bearing human colon cancer HCT-116 at doses 2 mg/kg, resulted in suppression of tumor growth by 72% compared to mice treated with vehicle control [93]. Acute toxicity studies have confirmed that the test compounds, in therapeutic concentrations, do not exhibit additional side effects in mice. Compound **19**, after being transiently present in the liver and kidneys, was completely excreted in the urine. In contrast, complex **17** accumulated in the liver and kidneys with low urinary excretion [93]. The presented results suggest that these complexes may be a new potential therapeutic drug for colorectal cancer.

4. Scope and Limitations

This article is limited to gold compounds acting on human CRC cell lines, which might poorly represent the clinical disease. However, especially in CRC surgical treatment, neoadjuvant and adjuvant therapy is applied to reduce the micrometastatic area, and in this context, cell-based assays, especially clonogenic assays, can mimic the *in vivo* situation [35]. We are observing a significant increase in publications on gold complexes. This indicates a great interest in this subject. Review work is also needed to systematize and summarize knowledge about this group of compounds.

5. Conclusions

Metallotherapeutics are very promising due to the fact that, depending on the choice of metal, its oxidation state, type, and number of coordinated ligands, we obtain a unique mechanism of drug action [72]. Therapies based on Au(III) compounds are particularly interesting and are currently being intensively developed due to their structural similarity to Pt(II) [28].

Colorectal cancer was shown to arise as a result of multiple genetic alternations in both oncogenes and tumor suppressor genes. If the initiated colon epithelium cells bearing mutations in APC or k-Ras can still control the DNA repair due to presence of active and functional p53, we talk about early and late adenoma—that is, nonmalignant and not-yet invasive. However, after genetic alternations that render the p53 pathway inactive, the initiated cells continue their unhampered divisions, despite DNA errors, and become malignant colon cancer cells [8]. That is why in colon cancer therapy, metal-based chemotherapeutics such as platinum derivatives are used. Such drugs interfere with DNA, initiating cell-division catastrophe and subsequently cancer-cell death. The effectiveness of established metallotherapeutics is not always good due to resistance development in genetically instable cancer cells. In this context, novel drugs are needed.

The efficacy of Au(III) in the treatment of CRC has been proven in many *in vitro* assays using various colon cancer cell lines such as HT29, HT-116, COLO 205, and many others. Au(III) complexes are characterized by high efficiency, selectivity towards cancer cells, and compared to cisplatin display reduced toxicity, a broader spectrum of activity and the ability to overcome tumor resistance [57].

Given the structural and electronic similarity of Au(III) complexes to cisplatin and Pt-related anticancer drugs, it was assumed that their mechanism of action involves binding to DNA. However, it appears that DNA may not be the primary biological target of Au(III) complexes due to studies reporting low DNA binding affinity [115]. Although TrxR inhibition was found to be the main pathway of potent antitumor activity of many Au-NHC complexes [127], the reviewed studies on Au(III)-NHC complexes do not support this mode of action. Notwithstanding the fact that we observe a great deal of scientific interest in Au compounds as drug candidates, we still have insufficient data to describe modes of action and the mechanisms they involve [128].

So far, only two Au(III) derivatives are characterized by high cytotoxicity for colon cancer cells, confirmed by both *in vitro* and *in vivo* assays. More advances in metallotherapeutic

studies are expected to improve the therapeutic potential of Au(III) in colorectal cancer treatment.

Author Contributions: Conceptualization, A.G. and P.T.; writing—original draft preparation, A.G.; writing—review and editing, P.T., I.M.-B. and M.S.; supervision, M.B.-Z.; funding acquisition, P.T. and J.F. All authors have read and agreed to the published version of the manuscript.

Funding: This research was supported by the grant from the National Science Center (2017/25/B/NZ5/02848 to J.F.) and the Medical University of Lodz (#503/1-156-04/503-11-001-19 to J.F.). The research was funded by grant No. 1M15/3/M/MG/N/20 to P.T. The grant was supervised by I.M.-B. and was funded by a subsidy for science received by the Medical University of Warsaw.

Institutional Review Board Statement: Not applicable.

Informed Consent Statement: Not applicable.

Data Availability Statement: Data are contained within the article.

Conflicts of Interest: The authors declare no conflict of interest.

References

1. Bray, F.; Ferlay, J.; Soerjomataram, I.; Siegel, R.L.; Torre, L.A.; Jemal, A. Global cancer statistics 2018: GLOBOCAN estimates of incidence and mortality worldwide for 36 cancers in 185 countries. *CA Cancer J. Clin.* **2018**, *68*, 394–424. [CrossRef]
2. Sung, H.; Ferlay, J.; Siegel, R.L.; Laversanne, M.; Soerjomataram, I.; Jemal, A.; Bray, F. Global Cancer Statistics 2020: GLOBOCAN Estimates of Incidence and Mortality Worldwide for 36 Cancers in 185 Countries. *CA Cancer J. Clin.* **2021**, *71*, 209–249. [CrossRef]
3. Stewart, B.; Wild, C.P. *World Cancer Report 2014*; WHO: Geneva, Switzerland, 2014.
4. Parkin, D.M.; Bray, F.; Ferlay, J.; Pisani, P. Global Cancer Statistics, 2002. *CA Cancer J. Clin.* **2005**, *55*, 74–108. [CrossRef]
5. Ilyas, M.; Straub, J.; Tomlinson, I.P.M.; Bodmer, W.F. Genetic pathways in colorectal and other cancers. *Eur. J. Cancer* **1999**, *35*, 1986–2002. [CrossRef]
6. Rawla, P.; Sunkara, T.; Barsouk, A. Epidemiology of colorectal cancer: Incidence, mortality, survival, and risk factors. *Prz. Gastroenterol.* **2019**, *14*, 89–103. [CrossRef]
7. Sideris, M.; Papagrigroriadis, S. Molecular Biomarkers and Classification Models in the Evaluation of the Prognosis of Colorectal Cancer. *Anticancer Res.* **2014**, *34*, 2061–2068. [PubMed]
8. Fearon, E.R.; Vogelstein, B. A genetic model for colorectal tumorigenesis. *Cell* **1990**, *61*, 759–767. [CrossRef]
9. Siegel, R.; DeSantis, C.; Virgo, K.; Stein, K.; Mariotto, A.; Smith, T.; Cooper, D.; Gansler, T.; Lerro, C.; Fedewa, S.; et al. Cancer treatment and survivorship statistics, 2012. *CA: A Cancer J. Clin.* **2012**, *62*, 220–241. [CrossRef] [PubMed]
10. Pawelec, G. Immunosenescence and cancer. *Biogerontology* **2017**, *18*, 717–721. [CrossRef]
11. Anisimov, V.N.; Sikora, E.; Pawelec, G. Relationships between cancer and aging: A multilevel approach. *Biogerontology* **2009**, *10*, 323–338. [CrossRef] [PubMed]
12. Brenner, H.; Kloor, M.; Pox, C.P. Colorectal cancer. *Lancet* **2014**, *383*, 1490–1502. [CrossRef]
13. Mármol, I.; Sánchez-De-Diego, C.; Pradilla Dieste, A.; Cerrada, E.; Rodríguez Yoldi, M. Colorectal Carcinoma: A General Overview and Future Perspectives in Colorectal Cancer. *Int. J. Mol. Sci.* **2017**, *18*, 197. [CrossRef]
14. Levin, B.; Lieberman, D.A.; McFarland, B.; Andrews, K.S.; Brooks, D.; Bond, J.; Dash, C.; Giardiello, F.M.; Glick, S.; Johnson, D.; et al. Screening and Surveillance for the Early Detection of Colorectal Cancer and Adenomatous Polyps, 2008: A Joint Guideline from the American Cancer Society, the US Multi-Society Task Force on Colorectal Cancer, and the American College of Radiology. *CA Cancer J. Clin.* **2008**, *58*, 130–160. [CrossRef] [PubMed]
15. Eaden, J.A.; Abrams, K.R.; Mayberry, J.F. The risk of colorectal cancer in ulcerative colitis: A meta-analysis. *Gut* **2001**, *48*, 526–535. [CrossRef] [PubMed]
16. Canavan, C.; Abrams, K.; Mayberry, J. Meta-analysis: Colorectal and small bowel cancer risk in patients with Crohn's disease. *Aliment. Pharmacol. Ther.* **2006**, *23*, 1097–1104. [CrossRef] [PubMed]
17. Martinez-Useros, J.; Garcia-Foncillas, J. Obesity and colorectal cancer: Molecular features of adipose tissue. *J. Transl. Med.* **2016**, *14*, 1–12. [CrossRef] [PubMed]
18. Willett, W.C. Diet and Cancer: An Evolving Picture. *JAMA* **2005**, *293*, 233–234. [CrossRef]
19. Pöschl, G.; Seitz, H.K. Alcohol and Cancer. *Alcohol. Alcohol.* **2004**, *39*, 155–165. [CrossRef] [PubMed]
20. Kuipers, E.J.; Grady, W.M.; Lieberman, D.; Seufferlein, T.; Sung, J.J.; Boelens, P.G.; Van De Velde, C.J.H.; Watanabe, T. Colorectal cancer. *Nat. Rev. Dis. Primers* **2015**, *1*, 15065. [CrossRef]
21. Singhal, S.; Nie, S.; Wang, M.D. Nanotechnology Applications in Surgical Oncology. *Annu. Rev. Med.* **2010**, *61*, 359–373. [CrossRef]
22. Kekelidze, M.; D'Errico, L.; Pansini, M.; Tyndall, A.; Hohmann, J. Colorectal Cancer: Current Imaging Methods and Future Perspectives for the Diagnosis, Staging and Therapeutic Response Evaluation. *World J. Gastroenterol.* **2013**, *19*, 8502. [CrossRef] [PubMed]

23. Colussi, D.; Brandi, G.; Bazzoli, F.; Ricciardiello, L. Molecular Pathways Involved in Colorectal Cancer: Implications for Disease Behavior and Prevention. *Int. J. Mol. Sci.* **2013**, *14*, 16365–16385. [CrossRef]
24. Markowska, A.; Kasprzak, B.; Jaszczyńska-Nowinka, K.; Lubin, J.; Markowska, J. Noble Metals in Oncology. *Contemp. Oncol.* **2015**, *19*, 271. [CrossRef] [PubMed]
25. Ndagi, U.; Mhlongo, N.; Soliman, M.E. Metal Complexes in Cancer Therapy—an Update from Drug Design Perspective. *Drug Des. Devel. Ther.* **2017**, *11*, 599. [CrossRef] [PubMed]
26. Wang, A.Z.; Langer, R.; Farokhzad, O.C. Nanoparticle Delivery of Cancer Drugs. *Annu. Rev. Med.* **2012**, *63*, 185–198. [CrossRef] [PubMed]
27. Nanospectra Biosciences, Inc. A Pilot Study of AuroLase(Tm) Therapy in Patients with Refractory and/or Recurrent Tumors of the Head and Neck. 2016. Available online: clinicaltrials.gov (accessed on 15 December 2021).
28. Shaw, C.F. Gold-Based Therapeutic Agents. *Chem. Rev.* **1999**, *99*, 2589–2600. [CrossRef] [PubMed]
29. Mármol, I.; Quero, J.; Rodríguez-Yoldi, M.J.; Cerrada, E. Gold as a Possible Alternative to Platinum-Based Chemotherapy for Colon Cancer Treatment. *Cancers* **2019**, *11*, 780. [CrossRef]
30. Lee, M.M.; MacKinlay, A.; Semira, C.; Schieber, C.; Yepes, A.J.J.; Lee, B.; Wong, R.; Hettiarachchige, C.K.H.; Gunn, N.; Tie, J.; et al. Stage-based Variation in the Effect of Primary Tumor Side on All Stages of Colorectal Cancer Recurrence and Survival. *Clin. Colorectal Cancer* **2018**, *17*, e569–e577. [CrossRef]
31. Benson, A.B.; Venook, A.P.; Cederquist, L.; Chan, E.; Chen, Y.-J.; Cooper, H.S.; Deming, D.; Engstrom, P.F.; Enzinger, P.C.; Fichera, A.; et al. Colon Cancer, Version 1.2017, NCCN Clinical Practice Guidelines in Oncology. *J. Natl. Compr. Cancer Netw.* **2017**, *15*, 370–398. [CrossRef]
32. Van Cutsem, E.; Cervantes, A.; Nordlinger, B.; Arnold, D.; ESMO Guidelines Working Group. Metastatic colorectal cancer: ESMO Clinical Practice Guidelines for diagnosis, treatment and follow-up. *Ann. Oncol.* **2014**, *25*, iii1–iii9. [CrossRef]
33. Van Cutsem, E.; Nordlinger, B.; Cervantes, A. Advanced colorectal cancer: ESMO Clinical Practice Guidelines for treatment. *Ann. Oncol.* **2010**, *21*, v93–v97. [CrossRef]
34. Venook, A. Critical Evaluation of Current Treatments in Metastatic Colorectal Cancer. *Oncol.* **2005**, *10*, 250–261. [CrossRef]
35. Roth, M.T.; Zheng, S. Neoadjuvant Chemotherapy for Colon Cancer. *Cancers* **2020**, *12*, 2368. [CrossRef]
36. Cho, K.; Wang, X.; Nie, S.; Chen, Z.; Shin, D.M. Therapeutic Nanoparticles for Drug Delivery in Cancer. *Clin. Cancer Res.* **2008**, *14*, 1310–1316. [CrossRef]
37. Parveen, S.; Sahoo, S.K. Polymeric nanoparticles for cancer therapy. *J. Drug Target.* **2008**, *16*, 108–123. [CrossRef]
38. Balducci, L.; Ades, S. Faculty Opinions recommendation of Adjuvant chemotherapy for colon cancer in the elderly: Moving from evidence to practice. *Oncology* **2009**, *23*, 162. [CrossRef]
39. Banerjee, A.; Pathak, S.; Subramaniam, V.D.; Dharanivasan, G.; Murugesan, R.; Verma, R.S. Strategies for targeted drug delivery in treatment of colon cancer: Current trends and future perspectives. *Drug Discov. Today* **2017**, *22*, 1224–1232. [CrossRef] [PubMed]
40. Prehn, R.T. The inhibition of tumor growth by tumor mass. *Cancer Res.* **1991**, *51*, 2–4. [PubMed]
41. Smith, B.H.; Gazda, L.S.; Conn, B.L.; Jain, K.; Asina, S.; Levine, D.M.; Parker, T.S.; Laramore, M.A.; Martis, P.C.; Vinerean, H.V.; et al. Hydrophilic Agarose Macrobead Cultures Select for Outgrowth of Carcinoma Cell Populations That Can Restrict Tumor Growth. *Cancer Res.* **2011**, *71*, 725–735. [CrossRef] [PubMed]
42. Ocean, A.J.; Parikh, T.; Berman, N.; Escalon, J.; Shah, M.A.; Andrada, Z.; Akahoho, E.; Pogoda, J.M.; Stoms, G.B.; Escobias, V.B. *Phase I/II Trial of Intraperitoneal Implantation of Agarose-Agarose Macrobeads (MB) Containing Mouse Renal Adenocarcinoma Cells (RENCA) in Patients (Pts) with Advanced Colorectal Cancer (CRC)*; American Society of Clinical Oncology: Alexandria, VA, USA, 2013.
43. Suh, O.; Mettlin, C.; Petrelli, N.J. Aspirin use, cancer, and polyps of the large bowel. *Cancer* **1993**, *72*, 1171–1177. [CrossRef]
44. McDonald, B.F.; Quinn, A.M.; Devers, T.; Cullen, A.; Coulter, I.S.; Marison, I.W.; Loughran, S. In-vitro characterisation of a novel celecoxib microbead formulation for the treatment and prevention of colorectal cancer. *J. Pharm. Pharmacol.* **2015**, *67*, 685–695. [CrossRef]
45. Lev-Ari, S.; Strier, L.; Kazanov, D.; Madar-Shapiro, L.; Dvory-Sobol, H.; Pinchuk, I.; Marian, B.; Lichtenberg, D.; Arber, N. Celecoxib and Curcumin Synergistically Inhibit the Growth of Colorectal Cancer Cells. *Clin. Cancer Res.* **2005**, *11*, 6738–6744. [CrossRef] [PubMed]
46. Sah, B.; Vasiljevic, T.; McKechnie, S.; Donkor, O. Effect of probiotics on antioxidant and antimutagenic activities of crude peptide extract from yogurt. *Food Chem.* **2014**, *156*, 264–270. [CrossRef] [PubMed]
47. Choi, S.S.; Kim, Y.; Han, K.S.; You, S.; Oh, S.; Kim, S.H. Effects of Lactobacillus Strains on Cancer Cell Proliferation and Oxidative Stress in Vitro. *Lett. Appl. Microbiol.* **2006**, *42*, 452–458. [CrossRef] [PubMed]
48. Chong, E.S.L. A potential role of probiotics in colorectal cancer prevention: Review of possible mechanisms of action. *World J. Microbiol. Biotechnol.* **2013**, *30*, 351–374. [CrossRef] [PubMed]
49. Dasari, S.; Tchounwou, P.B. Cisplatin in cancer therapy: Molecular mechanisms of action. *Eur. J. Pharmacol.* **2014**, *740*, 364–378. [CrossRef]
50. Muhammad, N.; Guo, Z. Metal-based anticancer chemotherapeutic agents. *Curr. Opin. Chem. Biol.* **2014**, *19*, 144–153. [CrossRef]
51. Komeda, S.; Casini, A. Next-Generation Anticancer Metallodrugs. *Curr. Top. Med. Chem.* **2012**, *12*, 219–235. [CrossRef]
52. Frezza, M.; Hindo, S.; Chen, D.; Davenport, A.; Schmitt, S.; Tomco, D.; Dou, Q.P. Novel Metals and Metal Complexes as Platforms for Cancer Therapy. *Curr. Pharm. Des.* **2010**, *16*, 1813–1825. [CrossRef]

53. Arnesano, F.; Natile, G. Mechanistic insight into the cellular uptake and processing of cisplatin 30 years after its approval by FDA. *Coord. Chem. Rev.* **2009**, *253*, 2070–2081. [CrossRef]
54. Wheate, N.J.; Walker, S.; Craig, G.E.; Oun, R. The status of platinum anticancer drugs in the clinic and in clinical trials. *Dalton Trans.* **2010**, *39*, 8113–8127. [CrossRef] [PubMed]
55. Kelland, L. The resurgence of platinum-based cancer chemotherapy. *Nat. Rev. Cancer* **2007**, *7*, 573–584. [CrossRef] [PubMed]
56. Shen, D.-W.; Pouliot, L.M.; Hall, M.D.; Gottesman, M.M. Cisplatin Resistance: A Cellular Self-Defense Mechanism Resulting from Multiple Epigenetic and Genetic Changes. *Pharmacol. Rev.* **2012**, *64*, 706–721. [CrossRef]
57. Timerbaev, A.R.; Hartinger, C.G.; Aleksenko, S.S.; Keppler, B.K. Interactions of Antitumor Metallo drugs with Serum Proteins: Advances in Characterization Using Modern Analytical Methodology. *Chem. Rev.* **2006**, *106*, 2224–2248. [CrossRef]
58. De Araújo, R.F.; de Araújo, A.A.; Pessoa, J.B.; Neto, F.P.F.; da Silva, G.R.; Oliveira, A.L.C.L.; Carvalho, T.G.; Silva, H.F.O.; Eugênio, M.; Sant’Anna, C.; et al. Anti-inflammatory, analgesic and anti-tumor properties of gold nanoparticles. *Pharmacol. Rep.* **2017**, *69*, 119–129. [CrossRef]
59. Aminabad, N.S.; Farshbaf, M.; Akbarzadeh, A. Recent Advances of Gold Nanoparticles in Biomedical Applications: State of the Art. *Cell Biochem. Biophys.* **2018**, *77*, 123–137. [CrossRef]
60. Upreti, M.; Jyoti, A.; Sethi, P. Tumor microenvironment and nanotherapeutics. *Transl. Cancer Res.* **2013**, *2*, 309–319. [CrossRef]
61. Kalaydina, R.-V.; Bajwa, K.; Qorri, B.; DeCarlo, A.; Szewczuk, M.R. Recent advances in “smart” delivery systems for extended drug release in cancer therapy. *Int. J. Nanomed.* **2018**, *ume 13*, 4727–4745. [CrossRef]
62. Pérez-Herrero, E.; Fernández-Medarde, A. Advanced targeted therapies in cancer: Drug nanocarriers, the future of chemotherapy. *Eur. J. Pharm. Biopharm.* **2015**, *93*, 52–79. [CrossRef]
63. Blanco, E.; Shen, H.; Ferrari, M. Principles of nanoparticle design for overcoming biological barriers to drug delivery. *Nat. Biotechnol.* **2015**, *33*, 941–951. [CrossRef] [PubMed]
64. Zaki, A.A.; Hui, J.Z.; Higbee, E.; Tsourkas, A. Biodistribution, Clearance, and Toxicology of Polymeric Micelles Loaded with 0.9 or 5 Nm Gold Nanoparticles. *J. Biomed. Nanotechnol.* **2015**, *11*, 1836–1846. [CrossRef]
65. Balasubramanian, S.K.; Jittiwat, J.; Manikandan, J.; Ong, C.N.; Yu, L.; Ong, W.-Y. Biodistribution of gold nanoparticles and gene expression changes in the liver and spleen after intravenous administration in rats. *Biomaterials* **2010**, *31*, 2034–2042. [CrossRef] [PubMed]
66. Bednarski, M.; Dudek, M.; Knutelska, J.; Nowiński, L.; Sapa, J.; Zygmunt, M.; Nowak, G.; Luty-Błocho, M.; Wojnicki, M.; Fitzner, K. The Influence of the Route of Administration of Gold Nanoparticles on Their Tissue Distribution and Basic Bio-chemical Parameters: In Vivo Studies. *Pharmacol. Rep.* **2015**, *67*, 405–409. [CrossRef] [PubMed]
67. Wojnicki, M.; Luty-Błocho, M.; Bednarski, M.; Dudek, M.; Knutelska, J.; Sapa, J.; Zygmunt, M.; Nowak, G.; Fitzner, K. Tissue distribution of gold nanoparticles after single intravenous administration in mice. *Pharmacol. Rep.* **2013**, *65*, 1033–1038. [CrossRef]
68. Nobili, S.; Mini, E.; Landini, I.; Gabbiani, C.; Casini, A.; Messori, L. Gold compounds as anticancer agents: Chemistry, cellular pharmacology, and preclinical studies. *Med. Res. Rev.* **2009**, *30*, 550–580. [CrossRef] [PubMed]
69. Bertrand, B.; Williams, M.R.M.; Bochmann, M. Gold(III) Complexes for Antitumor Applications: An Overview. *Chem.-A Eur. J.* **2018**, *24*, 11840–11851. [CrossRef]
70. Casini, A.; Sun, R.W.-Y.; Ott, I. Medicinal Chemistry of Gold Anticancer Metallo drugs. *Met. Ions Life Sci.* **2018**, *18*. [CrossRef]
71. Jurgens, S.; Kuhn, F.E.; Casini, A. Cyclometalated Complexes of Platinum and Gold with Biological Properties: State-of-the-Art and Future Perspectives. *Curr. Med. Chem.* **2018**, *25*, 437–461. [CrossRef]
72. Lazarevic, T.; Rilak, A.; Bugarčić, Ž.D. Platinum, palladium, gold and ruthenium complexes as anticancer agents: Current clinical uses, cytotoxicity studies and future perspectives. *Eur. J. Med. Chem.* **2017**, *142*, 8–31. [CrossRef]
73. Parveen, S.; Arjmand, F.; Tabassum, S. Development and future prospects of selective organometallic compounds as anticancer drug candidates exhibiting novel modes of action. *Eur. J. Med. Chem.* **2019**, *175*, 269–286. [CrossRef]
74. Porchia, M.; Pelli, M.; Marinelli, M.; Tisato, F.; Del Bello, F.; Santini, C. New insights in Au-NHCs complexes as anticancer agents. *Eur. J. Med. Chem.* **2018**, *146*, 709–746. [CrossRef]
75. Yeo, C.; Ooi, K.; Tiekink, E. Gold-Based Medicine: A Paradigm Shift in Anti-Cancer Therapy? *Molecules* **2018**, *23*, 1410. [CrossRef]
76. Zou, T.; Lum, C.T.; Lok, C.-N.; Zhang, J.-J.; Che, C.-M. Chemical biology of anticancer gold(III) and gold(I) complexes. *Chem. Soc. Rev.* **2015**, *44*, 8786–8801. [CrossRef]
77. Ott, I. On the medicinal chemistry of gold complexes as anticancer drugs. *Coord. Chem. Rev.* **2009**, *253*, 1670–1681. [CrossRef]
78. Casini, A. Exploring the mechanisms of metalbased pharmacological agents via an integrated approach. *J. Inorg. Biochem.* **2012**, *109*, 97–106. [CrossRef]
79. Chen, X.; Yang, Q.; Xiao, L.; Tang, D.; Dou, Q.P.; Liu, J. Metal-Based Proteasomal Deubiquitinase Inhibitors as Potential Anti-cancer Agents. *Cancer Metastasis Rev.* **2017**, *36*, 655–668. [CrossRef] [PubMed]
80. Casini, A.; Messori, L. Molecular Mechanisms and Proposed Targets for Selected Anticancer Gold Compounds. *Curr. Top. Med. Chem.* **2011**, *11*, 2647–2660. [CrossRef] [PubMed]
81. Powis, G.; Montfort, W.R. Properties and Biological Activities of Thioredoxins. *Annu. Rev. Pharmacol. Toxicol.* **2001**, *41*, 261–295. [CrossRef] [PubMed]
82. Raffel, J.; Bhattacharyya, A.K.; Gallegos, A.; Cui, H.; Einspahr, J.G.; Alberts, D.S.; Powis, G. Increased expression of thioredoxin-1 in human colorectal cancer is associated with decreased patient survival. *J. Lab. Clin. Med.* **2003**, *142*, 46–51. [CrossRef]

83. Arsenijevic, M.; Milovanovic, M.; Volarevic, V.; Djekovic, A.; Kanjevac, T.; Arsenijevic, N.; Dukic, S.; Bugarcic, Z.D. Cytotoxicity of gold(III) Complexes on A549 Human Lung Carcinoma Epithelial Cell Line. *Med. Chem.* **2012**, *8*, 2–8. [CrossRef] [PubMed]
84. Calamai, P.; Carotti, S.; Guerri, A.; Mazzei, T.; Messori, L.; Mini, E.; Orioli, P.; Speroni, G.P. Cytotoxic effects of gold(III) complexes on established human tumor cell lines sensitive and resistant to cisplatin. *Anti-Cancer Drug Des.* **1998**, *13*, 67–80.
85. Wilson, C.R.; Fagenson, A.M.; Ruangpradit, W.; Muller, M.T.; Munro, O.Q. Gold (III) Complexes of Pyridyl-and Iso-quinolylamido Ligands: Structural, Spectroscopic, and Biological Studies of a New Class of Dual Topoisomerase I and II In-hibitors. *Inorg. Chem.* **2013**, *52*, 7889–7906. [CrossRef]
86. Shi, P.; Jiang, Q.; Lin, J.; Zhao, Y.; Lin, L.; Guo, Z. Gold(III) compounds of 1,4,7-triazacyclononane showing high cytotoxicity against A-549 and HCT-116 tumor cell lines. *J. Inorg. Biochem.* **2006**, *100*, 939–945. [CrossRef]
87. Dandash, F.; Léger, D.Y.; Fidanzi-Dugas, C.; Nasri, S.; Brégier, F.; Granet, R.; Karam, W.; Diab-Assaf, M.; Sol, V.; Liagre, B. In vitro anticancer activity of new gold(III) porphyrin complexes in colon cancer cells. *J. Inorg. Biochem.* **2017**, *177*, 27–38. [CrossRef]
88. Quero, J.; Cabello, S.; Fuertes, T.; Mármol, I.; Laplaza, R.; Polo, V.; Gimeno, M.C.; Rodriguez-Yoldi, M.J.; Cerrada, E. Proteasome versus Thioredoxin Reductase Competition as Possible Biological Targets in Antitumor Mixed Thiolate-Dithiocarbamate Gold(III) Complexes. *Inorg. Chem.* **2018**, *57*, 10832–10845. [CrossRef]
89. Bertrand, B.; Spreckelmeyer, S.; Bodio, E.; Cocco, F.; Picquet, M.; Richard, P.; Le Gendre, P.; Orvig, C.; Cinellu, M.A.; Casini, A. Exploring the potential of gold(III) cyclometallated compounds as cytotoxic agents: Variations on the C^N theme. *Dalton Trans. Camb. Engl.* **2015**, *44*, 11911–11918. [CrossRef]
90. Erdogan, E.; Lamark, T.; Stallings-Mann, M.; Jamieson, L.; Pellechia, M.; Thompson, E.A.; Johansen, T.; Fields, A.P. Aurothiomalate Inhibits Transformed Growth by Targeting the PB1 Domain of Protein Kinase C α . *J. Biol. Chem.* **2006**, *281*, 28450–28459. [CrossRef] [PubMed]
91. Islam, S.M.A.; Patel, R.; Acevedo-Duncan, M. Protein Kinase C- ζ stimulates colorectal cancer cell carcinogenesis via PKC- ζ /Rac1/Pak1/ β -Catenin signaling cascade. *Biochim. Biophys. Acta Mol. Cell Res.* **2018**, *1865*, 650–664. [CrossRef]
92. Wang, Y.; He, Q.-Y.; Che, C.M.; Tsao, S.W.; Sun, R.W.-Y.; Chiu, J.-F. Modulation of gold(III) porphyrin 1a-induced apoptosis by mitogen-activated protein kinase signaling pathways. *Biochem. Pharmacol.* **2008**, *75*, 1282–1291. [CrossRef] [PubMed]
93. Tong, K.-C.; Lok, C.-N.; Wan, P.-K.; Hu, D.; Fung, Y.M.E.; Chang, X.-Y.; Huang, S.; Jiang, H.; Che, C.-M. An anticancer gold(III)-activated porphyrin scaffold that covalently modifies protein cysteine thiols. *Proc. Natl. Acad. Sci. USA* **2020**, *117*, 1321–1329. [CrossRef] [PubMed]
94. Mirabelli, C.K.; Sung, C.-M.; Zimmerman, J.P.; Hill, D.T.; Mong, S.; Crooke, S.T. Interactions of gold coordination complexes with DNA. *Biochem. Pharmacol.* **1986**, *35*, 1427–1433. [CrossRef]
95. Mirabelli, C.K.; Zimmerman, J.P.; Bartus, H.R.; Chiu-Mei, S.; Crooke, S.T. Inter-strand cross-links and single-strand breaks produced by gold(I) and gold(III) coordination complexes. *Biochem. Pharmacol.* **1986**, *35*, 1435–1443. [CrossRef]
96. Bindoli, A.; Rigobello, M.P.; Scutari, G.; Gabbiani, C.; Casini, A.; Messori, L. Thioredoxin reductase: A target for gold compounds acting as potential anticancer drugs. *Coord. Chem. Rev.* **2009**, *253*, 1692–1707. [CrossRef]
97. Nardon, C.; Boscutti, G.; Fregona, D. Beyond platinum: Gold complexes as anticancer agents. *Anticancer. Res.* **2014**, *34*, 487–492.
98. Buckley, R.G.; Elsome, A.M.; Fricker, S.P.; Henderson, G.R.; Theobald, B.R.C.; Parish, R.V.; Howe, A.B.P.; Kelland, L.R. Antitumor Properties of Some 2-[(Dimethylamino)methyl]phenylgold(III) Complexes. *J. Med. Chem.* **1996**, *39*, 5208–5214. [CrossRef]
99. Parish, R.V.; Howe, B.P.; Wright, J.P.; Mack, J.; Pritchard, R.G.; Buckley, R.G.; Elsome, A.M.; Fricker, S.P. Chemical and Bio-logical Studies of Dichloro (2-((Dimethylamino) Methyl) Phenyl) Gold (III). *Inorg. Chem.* **1996**, *35*, 1659–1666. [CrossRef]
100. Zhu, Y.; Cameron, B.R.; Mosi, R.; Anastassov, V.; Cox, J.; Qin, L.; Santucci, Z.; Metz, M.; Skerlj, R.T.; Fricker, S.P. Inhibition of the Cathepsin Cysteine Proteases B and K by Square-Planar Cycloaurated Gold (III) Compounds and Investigation of Their Anti-Cancer Activity. *J. Inorg. Biochem.* **2011**, *105*, 754–762. [CrossRef]
101. Notash, B.; Amani, V.; Safari, N.; Ostad, S.N.; Abedi, A.; Dehnavi, M.Z. The Influence of Steric Effects on Intramolecular Secondary Bonding Interactions; Cytotoxicity in Gold (III) Bithiazole Complexes. *Dalton Trans.* **2013**, *42*, 6852–6858. [CrossRef]
102. Carrasco, J.; Criado, J.J.; Macias, R.; Manzano, J.L.; Marin, J.; Medarde, M.; Rodríguez, E. Structural characterization and cytostatic activity of chlorobis(cholylglycinato)gold(III). *J. Inorg. Biochem.* **2001**, *84*, 287–292. [CrossRef]
103. Messori, L.; Marcon, G.; Cinellu, M.A.; Coronello, M.; Mini, E.; Gabbiani, O.; Orioli, P. Solution chemistry and cytotoxic properties of novel organogold(III) compounds. *Bioorganic Med. Chem.* **2004**, *12*, 6039–6043. [CrossRef]
104. Massai, L.; Cirri, D.; Michelucci, E.; Bartoli, G.; Guerri, A.; Cinellu, M.A.; Cocco, F.; Gabbiani, C.; Messori, L. Organogold(III) compounds as experimental anticancer agents: Chemical and biological profiles. *BioMetals* **2016**, *29*, 863–872. [CrossRef] [PubMed]
105. Ronconi, L.; Giovagnini, L.; Marzano, C.; Bettio, F.; Graziani, R.; Piloni, G.; Fregona, D. Gold Dithiocarbamate Derivatives as Potential Antineoplastic Agents: Design, Spectroscopic Properties, and in Vitro Antitumor Activity. *Inorg. Chem.* **2005**, *44*, 1867–1881. [CrossRef]
106. Ronconi, L.; Fregona, D. The Midas touch in cancer chemotherapy: From platinum- to gold-dithiocarbamate complexes. *Dalton Trans.* **2009**, 10670–10680. [CrossRef] [PubMed]
107. Nardon, C.; Chiara, F.; Brustolin, L.; Gambalunga, A.; Ciscato, F.; Rasola, A.; Trevisan, A.; Fregona, D. Gold(III)-pyrrolidinedithiocarbamate Derivatives as Antineoplastic Agents. *ChemistryOpen* **2015**, *4*, 183–191. [CrossRef]
108. Casini, A.; Kelter, G.; Gabbiani, C.; Cinellu, M.A.; Minghetti, G.; Fregona, D.; Fiebig, H.-H.; Messori, L. Chemistry, antiproliferative properties, tumor selectivity, and molecular mechanisms of novel gold(III) compounds for cancer treatment: A systematic study. *JBC J. Biol. Inorg. Chem.* **2009**, *14*, 1139–1149. [CrossRef] [PubMed]

109. Czerwińska, K.; Golec, M.; Skonieczna, M.; Palion-Gazda, J.; Zygadło, D.; Szlapa-Kula, A.; Krompiec, S.; Machura, B.; Szurko, A. Cytotoxic gold(III) complexes incorporating a 2,2':6',2''-terpyridine ligand framework—The impact of the substituent in the 4'-position of a terpy ring. *Dalton Trans.* **2017**, *46*, 3381–3392. [CrossRef] [PubMed]
110. Casado-Sánchez, A.; Martín-Santos, C.; Padrón, J.M.; Mas-Ballesté, R.; Navarro-Ranninger, C.; Alemán, J.; Cabrera, S. Effect of Electronic and Steric Properties of 8-Substituted Quinolines in Gold (III) Complexes: Synthesis, Electrochemistry, Stability, Interactions and Antiproliferative Studies. *J. Inorg. Biochem.* **2017**, *174*, 111–118. [CrossRef] [PubMed]
111. Pettenuzzo, N.; Brustolin, L.; Coltri, E.; Gambalunga, A.; Chiara, F.; Trevisan, A.; Biondi, B.; Nardon, C.; Fregona, D. CuI- and AuIII-Complexes with Glycoconjugated Dithiocarbamate Ligands for Potential Applications in Targeted Chemotherapy. *ChemMedChem* **2019**, *14*, 1162–1172. [CrossRef] [PubMed]
112. Sun, R.W.-Y.; Li, C.K.-L.; Ma, D.-L.; Yan, J.J.; Lok, C.-N.; Leung, C.-H.; Zhu, N.; Che, C.-M. Stable Anticancer Gold(III)-Porphyrin Complexes: Effects of Porphyrin Structure. *Chem.-A Eur. J.* **2010**, *16*, 3097–3113. [CrossRef]
113. Che, C.-M.; Sun, R.W.-Y.; Yu, W.-Y.; Ko, C.-B.; Zhu, N.; Sun, H. Gold(III) porphyrins as a new class of anticancer drugs: Cytotoxicity, DNA binding and induction of apoptosis in human cervix epitheloid cancer cells. Electronic supplementary information (ESI) available: Further experimental and crystallographic details. *Chem. Commun.* **2003**, 1718–1719. [CrossRef]
114. Tu, S.; Sun, R.W.-Y.; Lin, M.C.M.; Cui, J.T.; Zou, B.; Gu, Q.; Kung, H.-F.; Che, C.M.; Wong, B.C.Y. Gold (III) porphyrin complexes induce apoptosis and cell cycle arrest and inhibit tumor growth in colon cancer. *Cancer* **2009**, *115*, 4459–4469. [CrossRef]
115. Altaf, M.; Ahmad, S.; Kawde, A.-N.; Baig, N.; Alawad, A.; Altuwaijri, S.; Stoeckli-Evans, H.; Isab, A.A. Synthesis, Structural Characterization, Electrochemical Behavior and Anticancer Activity of Gold (III) Complexes of Meso-1, 2-Di (1-Naphthyl)-1, 2-Diaminoethane and Tetraphenylporphyrin. *New J. Chem.* **2016**, *40*, 8288–8295. [CrossRef]
116. Lemke, J.; Pinto, A.; Niehoff, P.; Vasylyeva, V.; Metzler-Nolte, N. Synthesis, structural characterisation and anti-proliferative activity of NHC gold amino acid and peptide conjugates. *Dalton Trans.* **2009**, 7063–7070. [CrossRef]
117. Dinda, J.; Samanta, T.; Nandy, A.; Saha, K.D.; Seth, S.K.; Chattopadhyay, S.K.; Bielawski, C.W. N-Heterocyclic Carbene Supported Au (I) and Au(III) Complexes: A Comparison of Cytotoxicities. *New J. Chem.* **2014**, *38*, 1218–1224. [CrossRef]
118. Rana, B.K.; Nandy, A.; Bertolasi, V.; Bielawski, C.W.; Saha, K.D.; Dinda, J. Novel Gold(I)- and Gold(III)-N-Heterocyclic Carbene Complexes: Synthesis and Evaluation of Their Anticancer Properties. *Organometallics* **2014**, *33*, 2544–2548. [CrossRef]
119. Samanta, T.; Munda, R.N.; Roymahapatra, G.; Nandy, A.; Saha, K.D.; Al-Deyab, S.S.; Dinda, J. Silver (I), Gold (I) and Gold (III)-N-Heterocyclic Carbene Complexes of Naphthyl Substituted Annelated Ligand: Synthesis, Structure and Cytotoxicity. *J. Organomet. Chem.* **2015**, *791*, 183–191. [CrossRef]
120. Jhulki, L.; Dutta, P.; Santra, M.K.; Cardoso, M.H.; Oshiro, K.G.; Franco, O.L.; Bertolasi, V.; Isab, A.A.; Bielawski, C.W.; Dinda, J. Synthesis and Cytotoxic Characteristics Displayed by a Series of Ag(i)-, Au(i)- and Au(III)-Complexes Supported by a Common N-Heterocyclic Carbene. *New J. Chem.* **2018**, *42*, 13948–13956. [CrossRef]
121. Liu, W.; Bendorf, K.; Proetto, M.; Abram, U.; Hagenbach, A.; Gust, R. NHC Gold Halide Complexes Derived from 4,5-Diarylimidazoles: Synthesis, Structural Analysis, and Pharmacological Investigations as Potential Antitumor Agents. *J. Med. Chem.* **2011**, *54*, 8605–8615. [CrossRef] [PubMed]
122. Liu, W.; Bendorf, K.; Proetto, M.; Hagenbach, A.; Abram, U.; Gust, R. Synthesis, Characterization, and in Vitro Studies of Bis [1,3-Diethyl-4, 5-Diarylimidazol-2-Ylidene] Gold (I/III) Complexes. *J. Med. Chem.* **2012**, *55*, 3713–3724. [CrossRef]
123. Fung, S.K.; Zou, T.; Cao, B.; Lee, P.-Y.; Fung, Y.M.E.; Hu, D.; Lok, C.-N.; Che, C.-M. Cyclometalated Gold(III) Complexes Containing N-Heterocyclic Carbene Ligands Engage Multiple Anti-Cancer Molecular Targets. *Angew. Chem. Int. Ed.* **2017**, *56*, 3892–3896. [CrossRef]
124. Krajewska, J.; Włodarczyk, J.; Jacenik, D.; Kordek, R.; Taciak, P.; Szczepaniak, R.; Fichna, J. New Class of Anti-Inflammatory Therapeutics Based on Gold (III) Complexes in Intestinal Inflammation—Proof of Concept Based on In Vitro and In Vivo Studies. *Int. J. Mol. Sci.* **2021**, *22*, 3121. [CrossRef]
125. Lipiec, S.; Szymański, P.; Gurba, A.; Szeleszczuk, Ł.; Taciak, P.; Fichna, J.; Młynarczuk-Biały, I. Innovative Gold Complexes with CN Group as Anticancer Agents—Possible Mechanisms of Action. In *Advances in Biomedical Research—Cancer and Miscellaneous*; Młynarczuk-Biały, I., Biały, Ł., Eds.; Wydawnictwo Naukowe Tygiel Sp. z o. o.: Lubin, Poland, 2021; pp. 9–22. ISBN 978-83-67104-12-8. Available online: <https://bc.wydawnictwo-tygiel.pl/publikacja/AA60CB34-1A06-4ECD-748B-83D6A9A5B19C> (accessed on 15 December 2021).
126. Engman, L.; McNaughton, M.; Gajewska, M.; Kumar, S.; Birmingham, A.; Powis, G. Thioredoxin reductase and cancer cell growth inhibition by organogold(III) compounds. *Anti-Cancer Drugs* **2006**, *17*, 539–544. [CrossRef] [PubMed]
127. Karaaslan, M.G.; Aktaş, A.; Gürses, C.; Gök, Y.; Ateş, B. Chemistry, structure, and biological roles of Au-NHC complexes as TrxR inhibitors. *Bioorganic Chem.* **2019**, *95*, 103552. [CrossRef] [PubMed]
128. Massai, L.; Grguric-Sipka, S.; Liu, W.; Bertrand, B.; Pratesi, A. Editorial: The Golden Future in Medicinal Chemistry: Perspectives and Resources from Old and New Gold-Based Drug Candidates. *Front. Chem.* **2021**, *9*. [CrossRef] [PubMed]



Article

New *N*-Substituted-1,2,4-triazole Derivatives of Pyrrolo[3,4-*d*]pyridazinone with Significant Anti-Inflammatory Activity—Design, Synthesis and Complementary In Vitro, Computational and Spectroscopic Studies

Lukasz Szczukowski ^{1,*}, Edward Krzyżak ², Benita Wiatrak ³, Paulina Jawień ³, Aleksandra Marciniak ², Aleksandra Kotynia ² and Piotr Świątek ^{1,*}

- ¹ Department of Medicinal Chemistry, Wrocław Medical University, Borowska 211, 50-556 Wrocław, Poland
- ² Department of Inorganic Chemistry, Wrocław Medical University, Borowska 211a, 50-556 Wrocław, Poland; edward.krzyzak@umed.wroc.pl (E.K.); aleksandra.marciniak@umed.wroc.pl (A.M.); aleksandra.kotynia@umed.wroc.pl (A.K.)
- ³ Department of Pharmacology, Wrocław Medical University, Mikulicza-Radeckiego 2, 50-345 Wrocław, Poland; benita.wiatrak@umed.wroc.pl (B.W.); paulina.jawien@umed.wroc.pl (P.J.)
- * Correspondence: lukasz.szczukowski@umed.wroc.pl (Ł.S.); piotr.swiatek@umed.wroc.pl (P.Ś.); Tel.: +48-71-784-0391 (P.Ś.)

Citation: Szczukowski, Ł.; Krzyżak, E.; Wiatrak, B.; Jawień, P.; Marciniak, A.; Kotynia, A.; Świątek, P. New *N*-Substituted-1,2,4-Triazole Derivatives of Pyrrolo[3,4-*d*]pyridazinone with Significant Anti-Inflammatory Activity—Design, Synthesis and Complementary In Vitro, Computational and Spectroscopic Studies. *Int. J. Mol. Sci.* **2021**, *22*, 11235. <https://doi.org/10.3390/ijms222011235>

Academic Editors: Andrzej Kutner, Geoffrey Brown and Enikő Kallay

Received: 23 September 2021
Accepted: 14 October 2021
Published: 18 October 2021

Publisher's Note: MDPI stays neutral with regard to jurisdictional claims in published maps and institutional affiliations.

Abstract: Regarding that the chronic use of commonly available non-steroidal and anti-inflammatory drugs (NSAIDs) is often restricted by their adverse effects, there is still a current need to search for and develop new, safe and effective anti-inflammatory agents. As a continuation of our previous work, we designed and synthesized a series of 18 novel *N*-substituted-1,2,4-triazole-based derivatives of pyrrolo[3,4-*d*]pyridazinone **4a-c-9a-c**. The target compounds were afforded via a convenient way of synthesis, with good yields. The executed cell viability assay revealed that molecules **4a-7a**, **9a**, **4b-7b**, **4c-7c** do not exert a cytotoxic effect and were qualified for further investigations. According to the performed in vitro test, compounds **4a-7a**, **9a**, **4b**, **7b**, **4c** show significant cyclooxygenase-2 (COX-2) inhibitory activity and a promising COX-2/COX-1 selectivity ratio. These findings are supported by a molecular docking study which demonstrates that new derivatives take position in the active site of COX-2 very similar to *Meloxicam*. Moreover, in the carried out in vitro evaluation within cells, the title molecules increase the viability of cells pre-incubated with the pro-inflammatory lipopolysaccharide and reduce the level of reactive oxygen and nitrogen species (RONS) in induced oxidative stress. The spectroscopic and molecular modeling study discloses that new compounds bind favorably to site II(m) of bovine serum albumin. Finally, we have also performed some in silico pharmacokinetic and drug-likeness predictions. Taking all of the results into consideration, the molecules belonging to series **a** (**4a-7a**, **9a**) show the most promising biological profile.

Keywords: cyclooxygenase; 1,2,4-triazole; pyridazinone; SAR; molecular docking; anti-inflammatory activity; antioxidant activity; ADME



Copyright: © 2021 by the authors. Licensee MDPI, Basel, Switzerland. This article is an open access article distributed under the terms and conditions of the Creative Commons Attribution (CC BY) license (<https://creativecommons.org/licenses/by/4.0/>).

1. Introduction

The inflammatory response that leads to homeostasis restoration is provoked by various exogenous and endogenous harmful stimuli and inducers, such as injury, tissue malfunctioning or infection. Its course, purpose and aftermath depend on the trigger. Characteristic symptoms that occur in inflamed areas are edema, reddening, hypersensitivity and often pain, which plays an important warning and protective role and promotes the organism's reflex and behavioral response to minimize the effects of tissue damage. The inflammation is a complicated process coordinated by a great variety of mediators whose expression and complex network of relationships are still not satisfactorily understood. Numerous proinflammatory mediators of different origins could be divided into the following

groups: vasoactive amines, vasoactive peptides, fragments of complement components and lipid mediators, such as eicosanoids, cytokines, chemokines and proteolytic enzymes. A lot of those aforementioned agents, besides affecting the target cells and tissues, could also induce the production of other elements. The best possible understanding and explanation of the mechanisms responsible for inflammatory mediators' expression, action and mutual dependence is essential in the effective management of different inflammatory diseases. Suitable pharmacological treatment and natural tissue healing processes cause acute pain and inflammation to disappear after some days. Nevertheless, the lack of or ineffective pharmacotherapy may trigger dangerous pathophysiological changes, which lead to the evolution of chronic inflammation and pain syndrome [1–5].

Most drugs commonly used in the treatment of pain and inflammatory disorders act as, mainly non-selective, inhibitors of both isoforms of cyclooxygenase (COX) and belong to a varied and spacious group of medicines named as non-steroidal and anti-inflammatory drugs (NSAIDs) [6–10]. The analgesic, antipyretic and anti-inflammatory effects associated with the administration of these medicaments are related to the reduction of COX-dependent prostaglandins (PGs) production, which belong, alongside with leukotrienes and lipoxins, to the above-mentioned group of eicosanoids [4–10]. Because PGs, except for the mediation of inflammation, play a crucial role in homeostasis maintenance and exert a protective effect, e.g., in the gastrointestinal and cardiovascular system, such decreased COX activity may also lead to dangerous side effects [6,7,11–15]. Usually, in patients receiving NSAIDs, adverse effects related to the gastroduodenal tract, such as heartburn, dyspepsia, stomach ache or even ulceration, may occur [11–14]. Initially, it was believed that a constitutive isoform named COX-1 is engaged in various physiological processes, while the development of pain and inflammation is under control of the mediators produced by the inducible form—COX-2 [6–10,13,15]. However, the introduction of selective COX-2 inhibitors—COXIBs, which were supposed to spare gastric mucosa, have quickly disproved this theory. Although any significant harmful impact of COXIBs on the gastrointestinal tract has not been noticed, the therapy with those drugs has been shown to carry a serious risk of hazardous cardiovascular incidents, which can even lead to patient death. Consequently, some COXIBs have been withdrawn from the market, and among them, the case of *Rofecoxib* became the most shameful [11–17].

Therefore, there is still a current need to search for and develop new, safe and efficient analgesic and anti-inflammatory compounds, since severe adverse effects often restrict the long-term usage of already known and available NSAIDs [11–14]. New drug candidates with potential application in the treatment of various inflammatory disorders can be received either through the structural alteration of already known NSAIDs, such as *Diclofenac* [18], *Naproxen* [19], *Celecoxib* [20], *Ibuprofen* [21], or by developing fully novel classes of cyclooxygenase inhibitors. When considering the design of new anti-inflammatory agents, one of the most popular and effective synthetic approaches in contemporary medicinal chemistry relies on replacing the free carboxylic group with different bioisosteric five-membered heterocyclic rings, such as 1,3,4-oxadiazole [18–22], 1,3-thiazole [23–25], pyrazole [26,27] or 1,2,4-triazole [28–33]. According to the leading investigations, such a strategy can be successfully applied to modify widespread used NSAIDs and other promising compounds not introduced in the market yet. As a result, potent cyclooxygenase inhibitors with an improved affinity towards COX-2 isoform and reduced gastrototoxicity can be received [18,19,22,23,30,31].

In our former studies, we have reported the synthesis and comprehensive biological evaluation of new 1,3,4-oxadiazole-based derivatives of pyrrolo [3,4-*d*]pyridazinone designed as a new class of COX inhibitor. The investigated compounds exerted promising in vitro cyclooxygenase inhibitory activity and acted as specific or selective COX-2 inhibitors. It is worth emphasizing that each examined molecule showed a superior COX-2/COX-1 selectivity ratio than *Meloxicam*, which was used as a reference drug. These findings were supported by the results of molecular docking studies, which revealed that tested 1,3,4-oxadiazole derivatives of pyrrolo[3,4-*d*]pyridazinone take place in the

active site of cyclooxygenase very similar to that of *Meloxicam* [34,35]. Subsequently, the most potent molecules have been investigated in vivo. It has been demonstrated by the enzyme-linked immunosorbent assay (ELISA) tests that the measured concentrations of inflammatory mediators—prostaglandin E₂ (PGE₂) and myeloperoxidase (MPO) in mice serum—were decreased after the application of our derivatives. Moreover, the macro- and microscopic histopathological assessment of gastric mucosa proved that novel compounds caused negligible stomach lesions and no histopathological changes were observed. These results confirmed the safe gastric profile of investigated molecules [36].

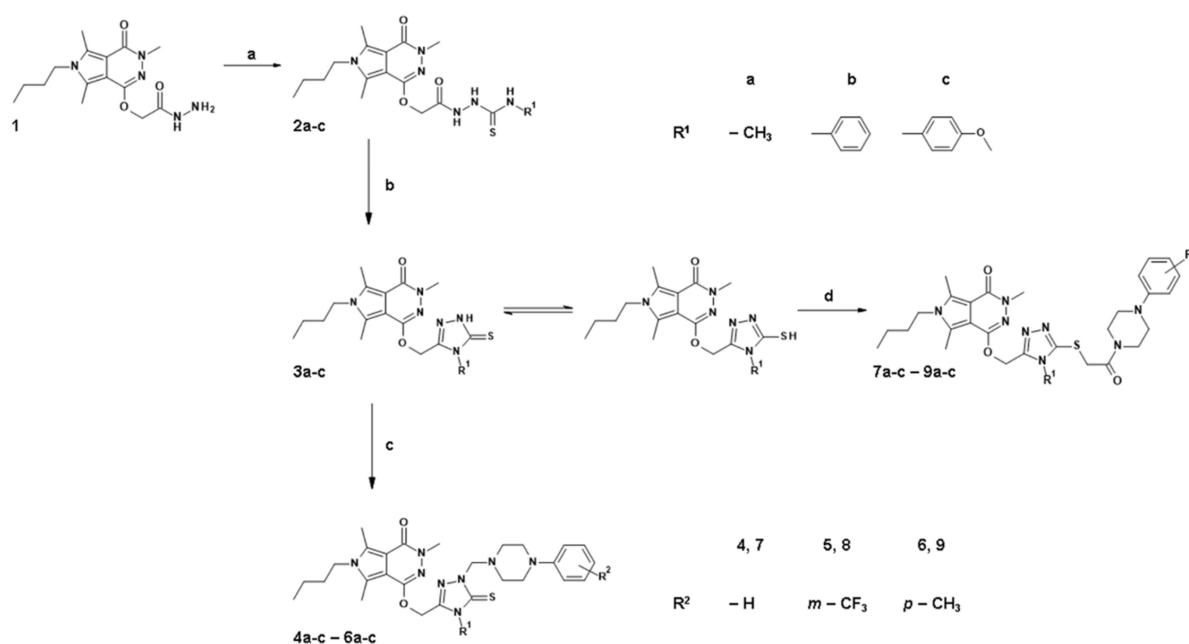
Encouraged by those promising results, we have decided to modify the structure of the above-mentioned derivatives by replacing the 1,3,4-oxadiazole with 4-substituted-1,2,4-triazole pharmacophore to obtain even more effective compounds. The introduction of this five-membered ring was inspired by the leading research described in the most recent literature [28–33]. The 1,2,4-triazole is an important moiety present in numerous potent bioactive molecules with a wide range of therapeutic applications [28–32]. It also acts as a valuable building block used in the design and synthesis of promising analgesic and anti-inflammatory agents, especially those with a good affinity towards an inducible COX-2 isoform [28,30–32]. Needless to say, different five-membered heterocycles serve as the structural core of the previously mentioned selective COX-2 inhibitors—COXIBs [17,20,25]. Considering that the binding pocket of COX-2 isoenzyme is bigger than that of COX-1 [6–10], we expect that the presence of expanded 4-substituted-1,2,4-triazole residues will enhance the COX-2 selectivity of titled compounds.

In summing up, here we report herein the design, synthesis and complex in vitro and in silico investigations of a new series of 4-substituted-1,2,4-triazole-based derivatives of pyrrolo[3,4-*d*]pyridazinone. First of all, we have determined the cytotoxic effect of the new compounds. After excluding toxic derivatives from further studies, we have defined the potential affinity and binding mode of the novel structures to both isoforms of cyclooxygenase. The investigations were carried out using in vitro enzymatic assay and computational studies, as well. Afterwards, we have estimated the antioxidant activity of the title compounds. Finally, the interaction binding manner of novel 1,2,4-triazole-based derivatives of pyrrolo[3,4-*d*]pyridazinone with bovine serum albumin (BSA) has been established. All of the performed experiments focused on the most precise determination of the possible mechanism of action and pharmacokinetic properties of new molecules and their potential application in the treatment of inflammatory disorders.

2. Results

2.1. Chemistry

The aim of the present study was the design and synthesis of a new series of *N*-substituted-1,2,4-triazole derivatives of pyrrolo[3,4-*d*]pyridazinone. Scheme 1 presents all of the performed chemical modifications and structures of novel molecules (each new compounds' structural formula is also presented in Table S1 in Supplementary Data). The thin layer chromatography (TLC) technique was used to monitor the progress of the reaction. The structure and purity of all of the new derivatives were established and confirmed based on the spectra analysis: ¹H and ¹³C nuclear magnetic resonance (NMR), Fourier transform infrared (FT-IR), electrospray ionization mass spectrometry (ESI-MS). All of the analytical and spectroscopic properties of every newly obtained compound were in good agreement with their predicted structures. The Experimental Section and Supplementary Data provide detailed information concerning the analytical and spectroscopic data, reactants, solvents and reactions environment. The synthetic pathway and structure of the starting molecule 2-(6-butyl-3,5,7-trimethyl-4-oxo-pyrrolo[3,4-*d*]pyridazin-1-yl)oxyacetohydrazide 1 has already been published in our previous paper [34].



Scheme 1. Synthesis of the intermediates **2a-c-3a-c** and the title compounds **4a-c-9a-c**. Reagents and reaction conditions: (a) *N* substituted isothiocyanate, ethanol, reflux, 0.5–2 h; (b) I. 5% NaOH (aq), reflux, 2 h; II. Cooling, crushed ice, stirring, acidification with 7.5% HCl; (c) 37% HCHO, 4 aryl piperazine derivative, methanol, RT 5 h; (d) C₂H₅ONa, 1 (2-chloro-1-oxoethyl)-4-aryl piperazine derivative, ethanol, reflux, 5 h.

The first step of the current synthesis relied on forming adequate *N*-substituted-(aminothioxomethyl)hydrazides **2a-c**. The aforementioned hydrazide **1** was refluxed in ethanol in the presence of the appropriate *N*-substituted isothiocyanate for 30 to 120 min. The mixture was then cooled down, and the formed precipitate was filtered off, washed thoroughly with ethanol and purified by crystallization from this solvent. Compounds **2a-c** were obtained with a good to excellent yield (up to 94%). Their formation was confirmed by spectral analysis. When considering the ¹H NMR spectra of molecules **2a-c**, a characteristic peak of protons linked to *N*1, *N*2 and *N*3 nitrogens of thiosemicarbazide moiety were recorded as three singlets in the range of δ 7.89–10.18 ppm. The methylene group connecting the pyrrolo[3,4-*d*]pyridazinone core and hydrazine residue appears as two proton singlets within δ 4.70–4.76 ppm in the ¹H NMR and as a signal about δ 63.74–63.84 ppm in the ¹³C NMR spectra, respectively. Moreover, in the ¹³C NMR spectra of compounds **2a-c**, a signal near δ 182 ppm is assigned to the carbon atom forming the C=S bond. Finally, in both the ¹H and ¹³C NMR spectra of structures **2a-c**, new peaks characteristic for the methyl group in series **a** and phenyl or 4-methoxyphenyl substituent in series **b** and **c** can be distinguished.

Subsequently, the synthesis of key 1,2,4-triazole derivatives of pyrrolo[3,4-*d*]pyridazinone **3a-c** was carried out. First, compounds **2a-c** underwent alkaline cyclization by refluxing in a 5% aqueous sodium hydroxide solution for about 2 h. Then, the reaction mixture was poured onto crushed ice and acidified with 7.5% hydrochloric acid solution, affording the corresponding *N*-substituted-1,2,4-triazoles **3a-c**. Finally, the formed white or yellowish precipitate of compounds **3a-c** was filtered off, washed with cold water and recrystallized from a proper solvent. In reference to the NMR spectra of structures **3a-c**, the change in the chemical shift of the signal of methylene linker can be easily observed. The signal of the protons of this group is shown at δ 5.12–5.30 ppm in the ¹H NMR, while the signal of a carbon atom is recorded about δ 57.85–58.09 ppm in the ¹³C NMR spectra, accordingly. Moreover, the presence of the distinctive peak near δ 168.04–169.12 ppm in the ¹³C NMR spectra, which is identified with the triazole carbon forming C=S bond, alongside with the signal characteristic for a NH proton observed in the range of δ 13.82–14.04 ppm in the ¹H NMR spectra may suggest that derivatives **3a-c** occur in the thione form.

The final stage of the planned synthesis relied on the formation of titled *N*-substituted-1,2,4-triazole derivatives of pyrrolo[3,4-*d*]pyridazinone **4a-c-9a-c**. As it has already been mentioned, the concept of their structure was inspired by the leading literature data and our own previous investigations. As it was depicted on Scheme 1, the final molecules **4a-c-9a-c** could be divided into two series.

Compounds **4a-c-6a-c** are the new Mannich base-type derivatives of pyrrolo[3,4-*d*]pyridazinone based 1,2,4-triazoles. These molecules were obtained via an effective and convenient one-step reaction, carried out at room temperature. The corresponding derivative **3a-c** was stirred with the appropriate 4-aryl piperazine derivative and formaldehyde in methanol for several hours and left overnight. The distinctive two-proton singlet in the ¹H NMR spectrum observed about δ 5.15–5.29 ppm. The signal at around δ 69.39–69.66 ppm in the ¹³C NMR spectrum clearly indicates the creation of the methylene linker, characteristic for Mannich bases. What is obvious, in both the ¹H and ¹³C NMR spectra of compounds **4a-c-6a-c**, are the signals assigned to aryl piperazine pharmacophore have been recorded.

On the other hand, the structure of the final compounds **7a-c-9a-c** was inspired by the pharmacophore theory featured by Dogruer [37]. Therefore, in the case of these derivatives, the 4-aryl piperazine moiety is connected with a five-membered 1,2,4-triazole ring via a flexible 2-oxoethylene linker. First of all, suitable 2-chloro-1-oxoethylaryl piperazine derivatives were afforded according to the synthetic protocols which have already been reported [38]. Due to the occurrence of possible tautomerism in the mentioned five-membered ring, the alkylation of 1,2,4-triazole analogue of pyrrolo[3,4-*d*]pyridazinone **3a-c** with 2-chloro-1-oxoethylaryl piperazine derivative may result in the formation of a mixture of *N*- and *S*-isoforms. Based on our former study, we have engaged the same synthetic conditions [35]. Therefore, the title compounds **7a-c-9a-c** were obtained by refluxing the 4-substituted-1,2,4-triazole derivatives of pyrrolo[3,4-*d*]pyridazinone **3a-c** with the appropriate 2-chloro-1-oxoethylaryl piperazine for several hours in ethanol in the presence of sodium ethoxide (Scheme 1). The crude products were filtered off, washed thoroughly with ethanol and purified by crystallization from this solvent. The lack of characteristic peak in the ¹³C NMR spectra observed about δ 169.72–170.78 ppm, which was assigned to a carbon atom, forming a C=S bond (Experimental Section, Supplementary Data), strongly suggests that the final compounds **7a-c-9a-c** were formed via *S*-alkylation of 1,2,4-triazole derivatives of pyrrolo[3,4-*d*]pyridazinone **3a-b** (Scheme 1). This claim is supported by the presence of a distinctive signal shown near δ 152.25–152.62 ppm in the ¹³C NMR spectra of **7a-c-9a-c**, which can be identified with carbon atom C3 in 1,2,4-triazole ring binding sulphur atom via a single bond (Ar-C-S-CH₂). Furthermore, a peak recorded about δ 165.49–165.72 ppm is typical for carbon atoms in carbonyl moiety (C=O). On the other hand, the signal which occurs near δ 41.98–42.23 ppm is assigned to carbon atom C1 (-CH₂-) of the 2-oxoethylene linker. Moreover, the two-proton singlet in the range of δ 4.37–4.42 ppm in the ¹H NMR spectra of **7a-c-9a-c** is assigned with the protons of carbon atom C1 in the mentioned linker. More detailed information is provided in the Experimental Section and Supplementary Data.

2.2. Evaluation of Viability

To estimate the effect of the new compounds on normal cells, a 3-(4, 5-Dimethylthiazol-2-yl)-2, 5-diphenyltetrazolium bromide (MTT) test was performed according to ISO 10993 part 5 Appendix C. The percentage of survival and the assessment of changes in the morphology of normal human dermal fibroblasts (NHDF) after contact with the tested compounds are presented in Table 1. The derivatives with 4-phenylpiperazine moiety, **4a-c** and **7a-c** and compounds **5a**, **6a**, **9a**, did not reduce the viability of NHDF cells below 70% in the tested concentration ranges. In the case of these molecules, no significant differences in cell survival were observed at a concentration of 100 μM. However, NHDF cell survival after 24-hour incubation was less than 50% for compounds **8a**, **8b**, **8c**, **9b** and **9c**, and the concentration at which 50% cell survival was observed has been calculated for these molecules. Therefore, these derivatives were excluded from further experiments.

Furthermore, due to the low level of cytotoxicity (less than 30% of dead cells compared to the control—culture without test compounds in a complete medium only), the theoretical IC₅₀ values for compounds **5b**, **6b**, **5c** and **6c** were calculated. In all of the cases, it was noted that an increase in cell viability was observed at the reduced concentration (10 and 50 µM).

Table 1. The cell viability [IC₅₀ (SEM) n = 3] and the evaluation of the morphology of cells treated with the tested compounds.

	IC ₅₀ [µM]	Cell Morphology in Culture
4a	Non-toxic	normal morphology for fibroblasts—elongated cells, single granular cells in 1 of 10 assessed fields of view
5a	Non-toxic	normal morphology for fibroblasts—elongated cells, single granular cells in 1 of 10 assessed fields of view
6a	Non-toxic	normal morphology for fibroblasts—elongated cells, single granular cells in 1 of 10 assessed fields of view
7a	Non-toxic	normal morphology for fibroblasts—elongated cells, single granular cells in 1 of 10 assessed fields of view
8a	35.60 (4.46)	many granules, cells shrunken, cell lysis was observed
9a	Non-toxic	normal morphology for fibroblasts—elongated cells, single granular cells in 1 of 10 assessed fields of view
4b	Non-toxic	normal morphology for fibroblasts—elongated cells, single granular cells in 1 of 10 assessed fields of view
5b	200.00 (7.05)	granularities were observed in 3–5 fields of view from 10 analyzed fields, cells with an elongated shape characteristic of fibroblasts
6b	156.25 (6.70)	granularities were observed in 3–5 fields of view from 10 analyzed fields, cells with an elongated shape characteristic of fibroblasts
7b	Non-toxic	normal morphology for fibroblasts—elongated cells, single granular cells in 1 of 10 assessed fields of view
8b	22.72 (2.25)	many granules, cells shrunken, cell lysis was observed
9b	30.80 (3.04)	many granules, cells shrunken, cell lysis was observed
4c	Non-toxic	normal morphology for fibroblasts—elongated cells, single granular cells in 1 of 10 assessed fields of view
5c	166.67 (3.35)	granularities were observed in 3–5 fields of view from 10 analyzed fields, cells with an elongated shape characteristic of fibroblasts
6c	103.89 (2.75)	granularities were observed in 3–5 fields of view from 10 analyzed fields, cells with an elongated shape characteristic of fibroblasts
7c	Non-toxic	normal morphology for fibroblasts—elongated cells, single granular cells in 1 of 10 assessed fields of view
8c	18.97 (1.84)	many granules, cells shrunken, cell lysis was observed
9c	28.56 (4.59)	many granules, cells shrunken, cell lysis was observed

Note: Cytotoxic compounds which were excluded from further investigations are marked in red.

On the microscopic image, few granules were observed in the NHDF cells in the tested concentration range for the compounds **4a–7a**, **9a**, **4b**, **7b**, **4c** and **7c**. Cell shrinkage and separation from the surface of the culture wells were not observed. These changes were classified according to the criterion of grade 1—low toxicity. Similar changes in the cell morphology were observed in the systems containing 100 µM for **5b**, **6b** and **5c**. In this case, a slightly greater number of endoplasmic granules were observed without any effect on the cell contraction. In this case, low toxicity was considered as well.

With reference to derivative **6c** at a concentration of 100 µM, the cells in the range of 10–15% contracted and detached from the medium. The appearance of fine granules inside the cytoplasmic cells was observed. However, at the reduced concentration of the tested compounds from individual endoplasmic pellets, a culture density comparable to that of the control culture was observed. Cell lysis was not observed. Regardless of the tested derivatives, there was no significant change in the NHDF cells compared to the control.

2.3. Cyclooxygenase (COX-1, COX-2) Inhibition Studies

2.3.1. In Vitro COX Inhibition Assay

Inhibition of COX-1 and COX-2 activity of the tested compounds was assessed after 2 min incubation at 100 µM concentration using the Cayman's COX Colorimetric Inhibitor Screening Assay Kit (Cat # 701050). The IC₅₀ values and the COX-2/COX-1 selectivity ratios were calculated for each investigated and reference compound (*Meloxicam*, *Celecoxib* and *Diclofenac*). The results are shown in Table 2. The derivatives **4a–7a**, **9a**, **4b**, **7b** and **4c** revealed COX-2 inhibitory activity comparable to *Meloxicam*. Four of the studied molecules: **5a**, **7a**, **4b** and **7b**, also inhibited the constitutive isoform COX-1, but this activity was significantly lower. Compounds **5b**, **6b**, **5c–7c** did not exert any cyclooxygenase inhibition

profile in the performed in vitro investigations. The analysis of these data allows us to conclude that the derivatives of series **a**, with methyl substituent in the 1,2,4-triazole ring, demonstrate possibly the best COX inhibitory activity. Better affinity towards COX-2 can be explained by the bigger binding pocket of that isoenzyme. Large and expanded molecules, like those from series **b** and **c**, with aryl substituent in the 1,2,4-triazole moiety, revealed poor or no inhibitory activity towards COX.

2.3.2. Molecular Docking Study

The molecular docking analysis was carried out to explore the binding interactions of the tested compounds inside the active site of cyclooxygenase. The binding free energy (ΔG°) for the interaction with COX-1 for all of the studied compounds showed positive value. The energies obtained for the interactions with COX-2 are presented in Table 3. The ΔG° is negative for all of the compounds from series **a**, and for **4b**, **7b** and **4c**. The lowest value was found for compounds number **4** in each series (**4a-c**). The energies ΔE_2 , ΔE_3 indicate that the main interactions are van der Waals and hydrogen bonding. The size of the COX-2 pocket is bigger than COX-1, which allows for the selective binding of larger molecules. However, the analyzed compounds are relatively large, especially the compounds from the **b** and **c** series, with phenyl and 4-methoxyphenyl rings. It can make some difficulties in the efficient docking to even COX-2.

Table 2. The IC_{50} [μM] values determined for COX-1 and COX-2.

Compound	IC_{50} [μM] (SD)		COX-2/COX-1 Selectivity Ratio
	COX-1	COX-2	
4a	NA	45.24 (0.018)	-
5a	95.75 (0.1)	48.24 (0.04)	0.50
6a	NA	43.85 (0.035)	-
7a	70.96 (0.2)	48.48 (0.037)	0.68
9a	NA	42.64 (0.015)	-
4b	79.47 (0.06)	47.83 (0.039)	0.60
5b	NA	NA	-
6b	NA	NA	-
7b	86.30 (0.005)	49.79 (0.001)	0.58
4c	NA	48.50 (0.027)	-
5c	NA	NA	-
6c	NA	NA	-
7c	NA	NA	-
<i>Meloxicam</i>	83.7 (0.03)	59.2 (0.06)	0.71
<i>Celecoxib</i>	56 (0.1)	0.30 (0.08)	0.005
<i>Diclofenac</i>	3.5 (0.04)	16.6 (0.03)	4.74

Note: Data are shown as standard deviation (SD), NA stands for “not applicable”.

Inside the COX-2 active site, some hydrogen bonds interactions were found, especially for the compounds belonging to series **a**: SER530, TYR355, ARG120, SER120. Moreover, various kinds of π interactions are observed. The details are presented in Figures 1–3. In addition, the position of the studied compounds was found very similar to *Meloxicam* (Figure 4).

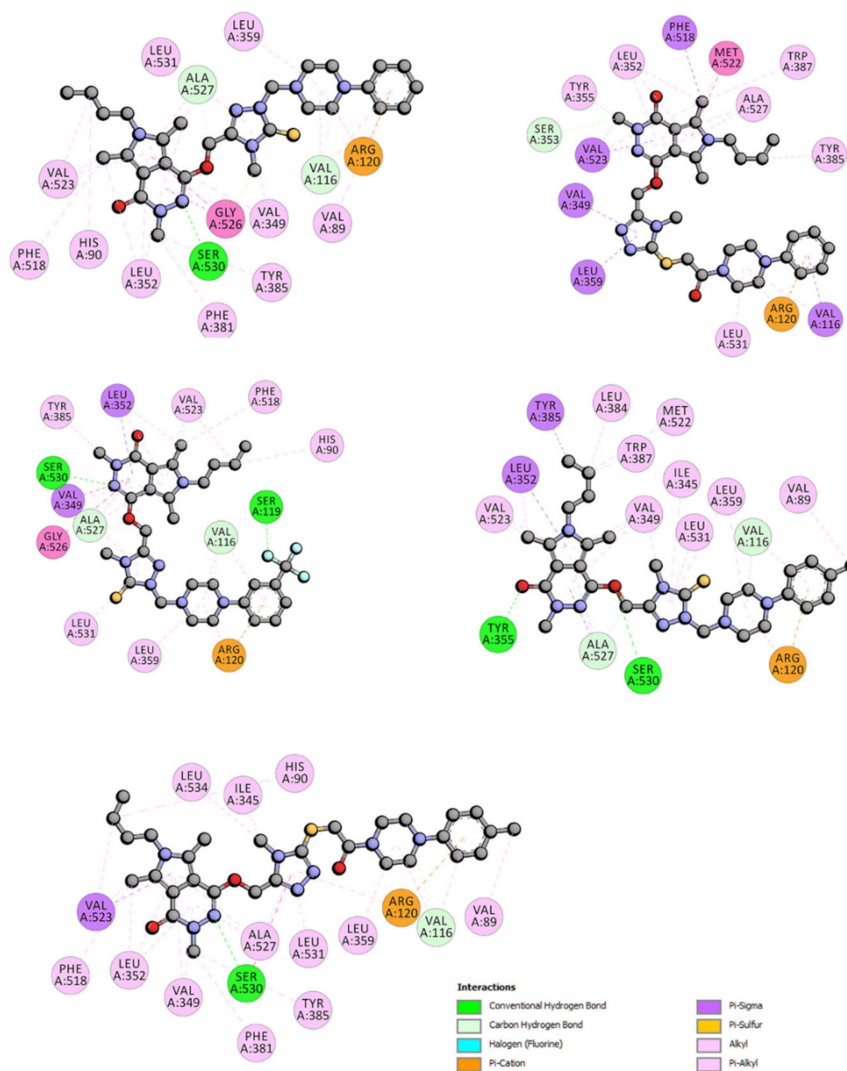


Figure 1. Two-dimensional interaction plot of 4a-7a, 9a with COX-2.

2.4. Anti-Inflammatory and Antioxidant Activity within Cells

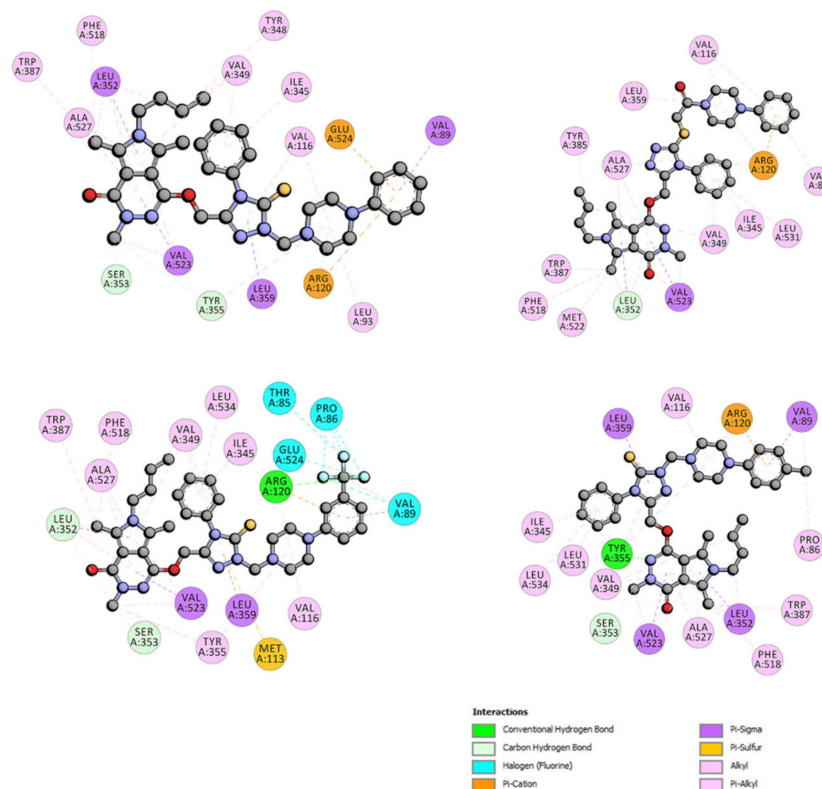
The titled *N*-substituted-1,2,4-triazole derivatives of pyrrolo[3,4-*d*]pyridazinone were further evaluated for their anti-inflammatory potential in NHDF cells pre-incubated with the proinflammatory agent lipopolysaccharide (LPS) at a concentration of 50 µg/mL.

The NHDF cell line was firstly treated with LPS for 24 h to induce inflammation. Then, the culture was washed and incubated with the test compounds for 24 h at a concentration range of 10–100 µM. All of the tested molecules increased the cell viability compared to the positive control (except 5c and 6c in the concentration range of 50–100 µM). This fact can suggest that the investigated derivatives could probably exert a good ability to reduce cell inflammation (Figure 5). For the remaining tested compounds, the increase in the activity of mitochondria was statistically significantly higher than in the positive control. At the same time, compounds 6a and 9a showed a greater increase in mitochondrial activity than the negative control in the entire range of the tested concentrations.

Table 3. Energies of the interactions of the tested compounds with COX-2 were obtained from the molecular study.

	ΔG° [kJmol ⁻¹]	ΔE_1 [kJmol ⁻¹]	ΔE_2 [kJmol ⁻¹]	ΔE_3 [kJmol ⁻¹]	K_i [μ M]
4a	-22.57	-33.81	-34.52	0.75	109
5a	-15.38	-27.84	-28.67	0.84	2010
6a	-23.28	-34.48	-35.44	0.96	83
7a	-11.32	-23.83	-23.83	0.00	10,250
9a	-21.02	-33.48	-33.41	-0.16	206
4b	-20.40	-32.85	-34.36	1.50	226
5b	11.60	-2.17	-3.89	1.76	-
6b	13.29	-0.83	-0.25	1.08	-
7b	-5.93	-19.64	-19.10	-0.84	90,800
4c	-8.07	-21.82	-23.24	1.42	38,200
5c	29.63	14.67	11.87	2.71	-
6c	52.36	36.65	35.44	1.21	-
7c	6.18	-8.78	-8.66	-0.12	-
Meloxicam	-34.02	-37.74	-37.32	-0.42	1.09
Celecoxib	-30.17	-36.40	-36.11	-0.08	5.13
Diclofenac	-29.59	-35.82	-30.18	-5.63	6.50

Notes: ΔG° —binding free energy; ΔE_1 —intermolecular interaction energy, which is the sum of van der Waals energy, hydrogen bonding energy, desolvation free energy and electrostatic energy; ΔE_2 —the sum of van der Waals energy, hydrogen bonding energy and desolvation free energy; ΔE_3 —electrostatic energy, K_i —inhibit constants.

**Figure 2.** Two-dimensional interaction plot of 4b-7b with COX-2.

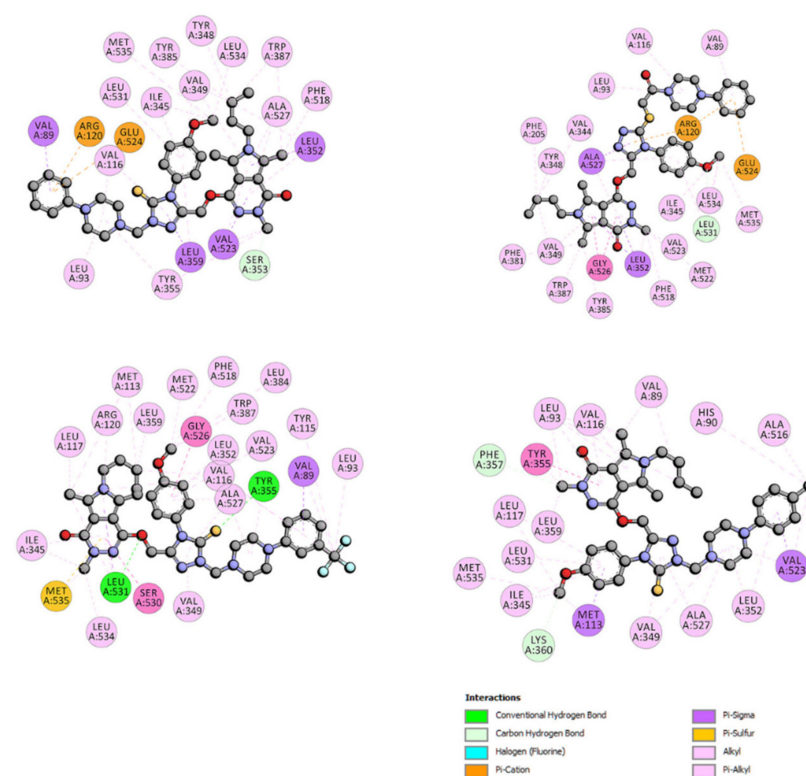


Figure 3. Two-dimensional interaction plot of 4c-7c with COX-2.

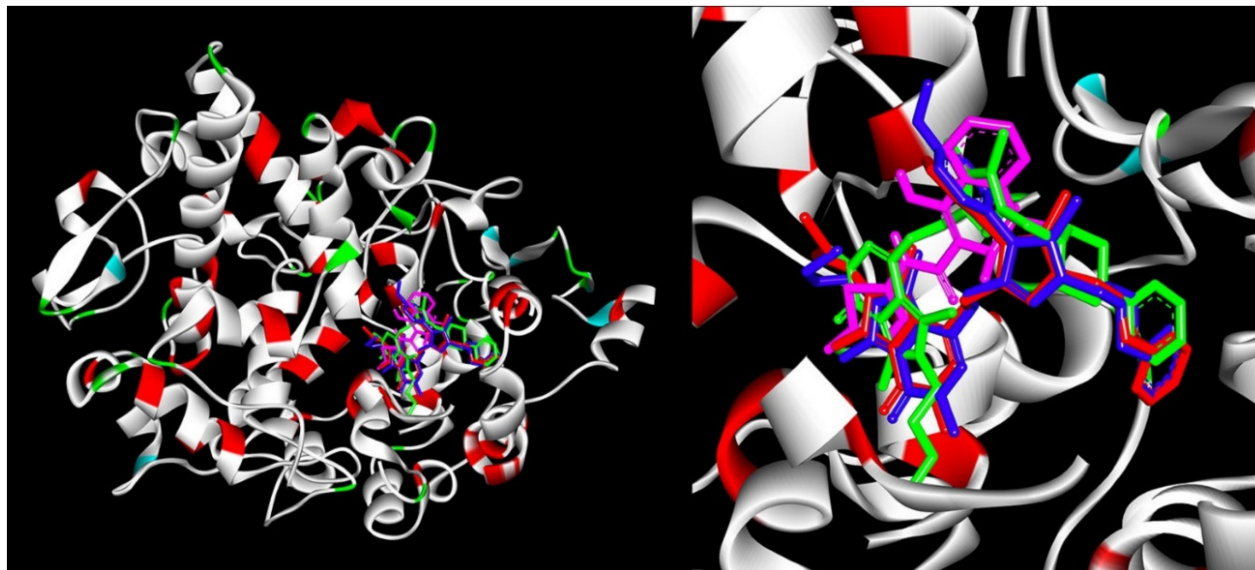


Figure 4. Docking poses of 4a (green), 4b (red), 4c (blue) and Meloxicam (pink) inside COX-2.

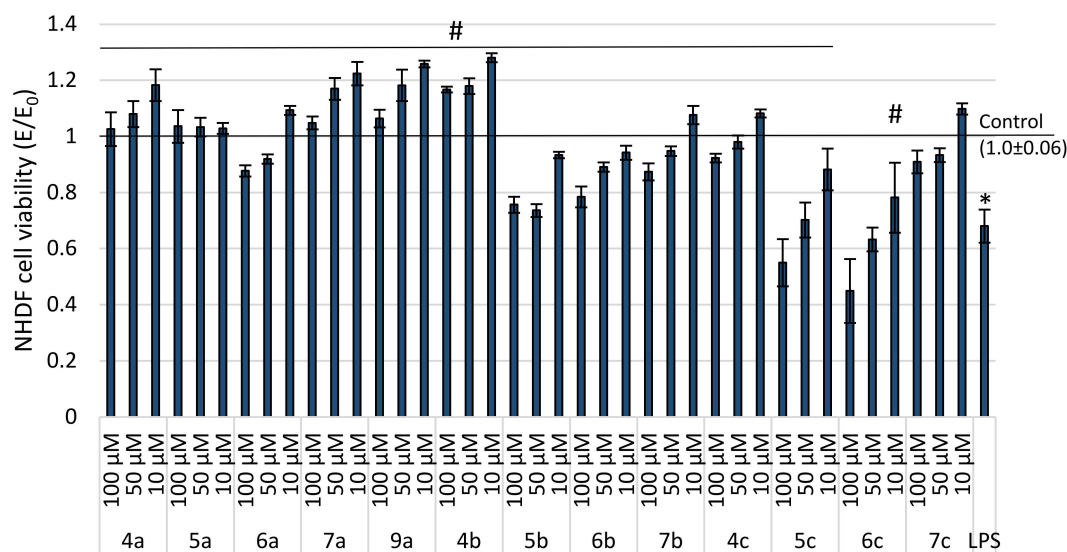


Figure 5. Impact of investigated compounds on NHDF cells after incubation with 50 $\mu\text{g/mL}$ LPS measured through MTT assay; # $p < 0.05$ —significant difference compared to the control with 50 $\mu\text{g/mL}$ LPS and without compounds; * $p < 0.05$ —significant difference compared to a negative control without 50 $\mu\text{g/mL}$ LPS and compounds.

Needless to say, such factors like hypoxia or inflammation can increase the intracellular level of reactive oxygen and nitrogen species (RONS). As a consequence, oxidative and/or nitrosative stress can develop in inflamed tissue [39]. According to many studies, the aforementioned processes often co-exist and potentiate one another [39,40]. Being aware that there is an increased level of free oxygen radicals and nitric oxide (NO) in inflammation, we evaluated whether the tested compounds exhibit antiradical activity in the dichlorofluorescein diacetate (DCF-DA) and Griess assays and assessed the levels of reactive oxygen species (ROS) and NO, respectively (Figure 6A,B).

The dependence on the concentration of the new derivatives of pyrrolo[3,4-*d*]pyridazinone and their antioxidant activity has been demonstrated in the executed experiments (Figure 6). The higher the concentration of the tested compound, the stronger the scavenging of oxygen free radicals has been noticed. All of the tested compounds statistically significantly decreased the level of ROS as compared to the positive control. Moreover, the derivatives **6a** and **9a** scavenged oxygen free radicals to the level of the negative control in the whole range of the tested concentrations. At the same time, all of the examined molecules showed a statistically significant reduction in the NO level, as compared to the positive control. Compound **9a** was the only one that lowered NO levels to negative control levels over the whole range of the investigated concentrations.

2.5. Structure-Activity Relationship Study

When considering the composition of 18 title compounds reported in this paper, we can point out three characteristic and variable structural elements which could have the impact on the toxicity and the biological activity of the investigated derivatives (Figure 7). The first one is the substituent in position 4 in the 1,2,4-triazole ring. We have introduced there residues of a different size and character. Based on this structural element, we have divided title compounds into three main series: (a) with methyl group, (b) with phenyl ring and (c) with 4-methoxyphenyl moiety. The second one is the aryl piperazine pharmacophore—being more precise, the substituent or its lack in its phenyl ring. In this case, we can also demonstrate three groups of compounds. The first one is those with unsubstituted phenylpiperazine moiety (**4a-c**, **7a-c**). In the second class (**5a-c**, **8a-c**) we can distinguish the derivatives with the trifluoromethyl group in position 3. On the other hand, compounds **6a-c**, **9a-c** possess a substituent completely different in the size and electronic character—a methyl residue in position 4 of phenyl ring. Finally, when taking

into consideration the way in which the aryl piperazine pharmacophore is linked with 1,2,4-triazole moiety, we can divide the target compounds into two groups. Mannich base-type derivatives are the first one (4a-c-6a-c), while the second one consists of structures with flexible oxoethylene linker (7a-c-9a-c) received via S-alkylation of 1,2,4-triazole.

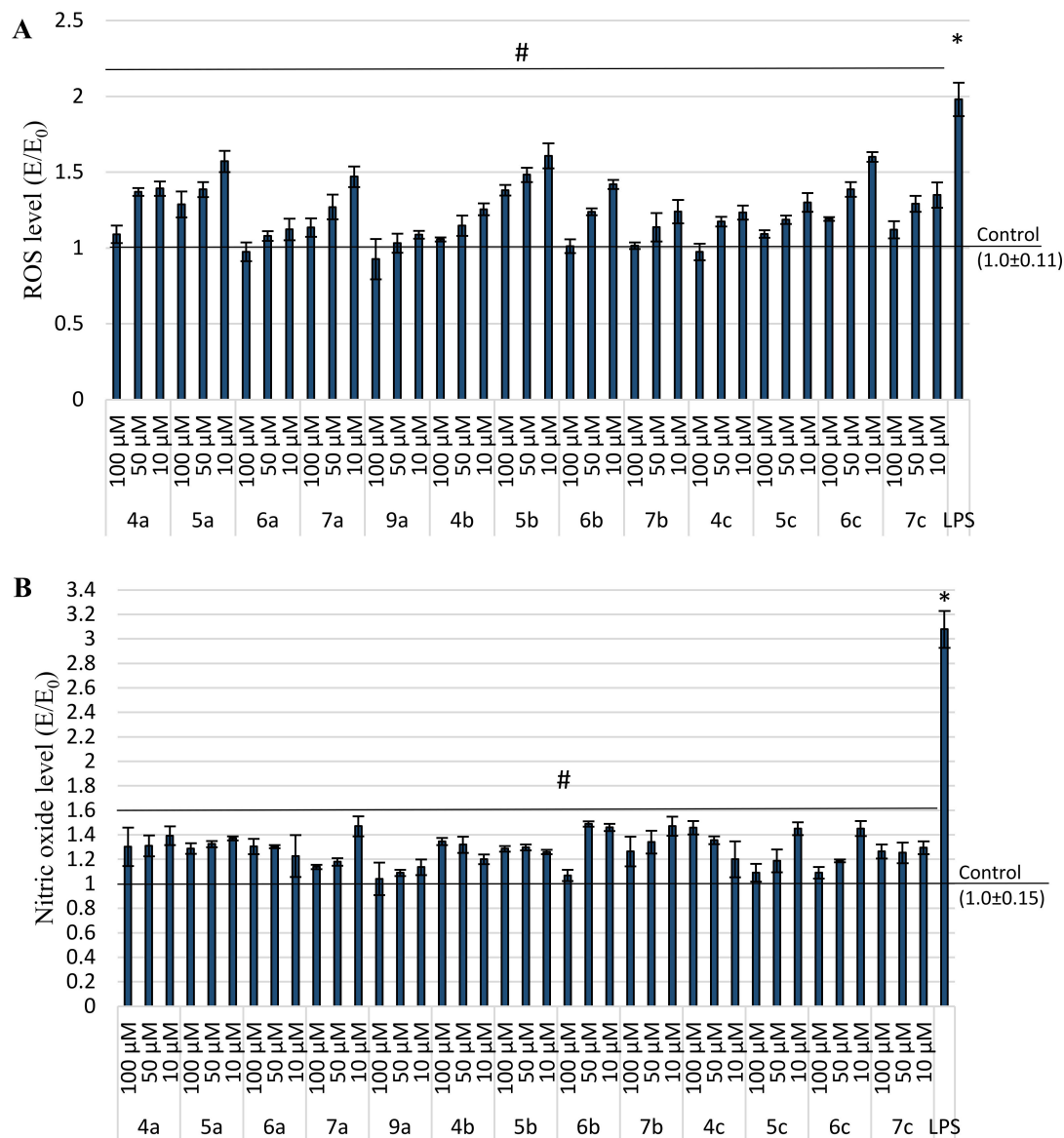


Figure 6. Impact of investigated compounds on NHDF cells after incubation with 50 µg/mL LPS; (A) DCF-DA assay and (B) Griess assay; # $p < 0.05$ —significant difference compared to the control with 50 µg/mL LPS and without compounds; * $p < 0.05$ —significant difference compared to a negative control without 50 µg/mL LPS and compounds.

When analyzing the results of the cell viability evaluation, we can see that there is a significant relationship between the structure and cytotoxicity of the titled compounds. First of all, in every series, a, b and c molecules with unsubstituted phenylpiperazine, that is 4 and 7, appeared to be non-toxic. On the contrary, all of the derivatives with both the trifluoromethyl group and oxoethylene linker (8a-c) caused cell lysis. Such an effect was also observed in the case of compounds possessing 4-methylphenylpiperazine pharmacophore connected via the oxoethylene group with 1,2,4-triazole, which are 9b and 9c. Continuing our considerations, it is worth noticing that the data shown in the Table 1 clearly indicate that out of six compounds from series a (methyl residue in 1,2,4-triazole), as many as five derivatives (4a-7a, 9a) did not reveal a cytotoxic effect at all. Therefore, the

presence of a small substituent in that place appear to be the most favorable. Moreover, Mannich base derivatives (**4a-c-6a-c**) were found to be less toxic than compounds with oxoethylene linker (**7a-c-9a-c**).

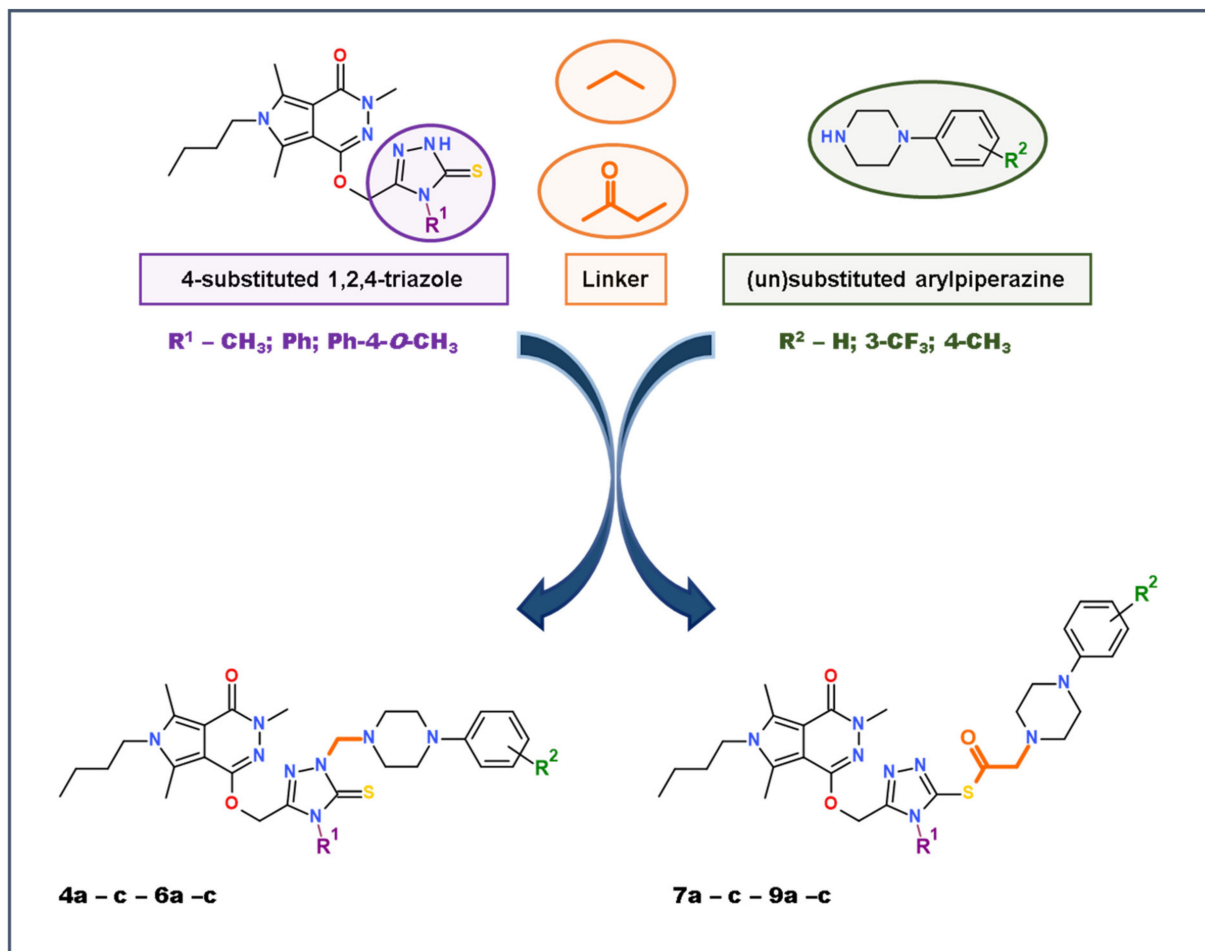


Figure 7. The concept of design and synthesis of target *N*-substituted-1,2,4-triazole-based derivatives of pyrrolo[3,4-*d*]pyridazinone.

We can assume that the introduction of a large substituent into position 4 of 1,2,4-triazole ring, with the simultaneous presence of substituted aryl piperazine pharmacophore, leads to an increase of cytotoxicity, which may be caused by large molecular weight. In this case, the nature and size of the residue in the triazole ring seems to be substantial. The compounds with a small methyl group in the position 4 of 1,2,4-triazole ring and/or unsubstituted phenylpiperazine pharmacophore did not affect the cell viability at all (except **8a**). Summing up, the cytotoxic effect grew up alongside with increased molecular weight and the size of molecule. Derivatives **8a-c**, **9b-c** were excluded from further investigations.

Considering COX inhibition studies, derivatives **5b**, **6b**, **5c-7c**, did not show any activity in in vitro assay and their binding free energy (ΔG°) for interaction with both of the isoenzymes presented positive values. Thus, a large substituent in 1,2,4-triazole ring led to a decrease in the biological activity. From series **b** and **c** only **4b**, **7b** and **4c** revealed potential COX inhibition. Compounds **4a-7a**, **9a** demonstrated good cyclooxygenase inhibitory activity, especially towards COX-2 isoform (Table 2). It is worth to mention, that **5a**, **7a**, **4b** and **7b** inhibited also COX-1 isoform in vitro, but it was not confirmed by the results of the molecular docking studies. Moreover, the IC_{50} values of active compounds determined for both COX-1 and COX-2 were very similar to that defined for *Meloxicam*. Taking into

consideration the results obtained in in vitro COX inhibition assay and in the molecular docking studies, the most promising appeared to be derivatives from series a.

Analyzing the result of performed in vitro anti-inflammatory and antioxidant activity evaluation within cells, we did not notice such meaningful differences between the investigated compounds. All of the derivatives exerted a good ability to reduce induced inflammation, except 5c and 6c. Once more, structures which belong to series a turned out to be the most potent.

Taking all of the above into account, we can suppose that the nature of aryl piperazine pharmacophore and the linker had the main impact on the compounds' toxicity. On the other hand, the substituent in the position 4 of 1,2,4-triazole had the influence on both the cytotoxicity and the COX inhibitory activity.

Our consideration concerning the structure-activity relationships in the group of the investigated target molecules are summarized in Figure 8.

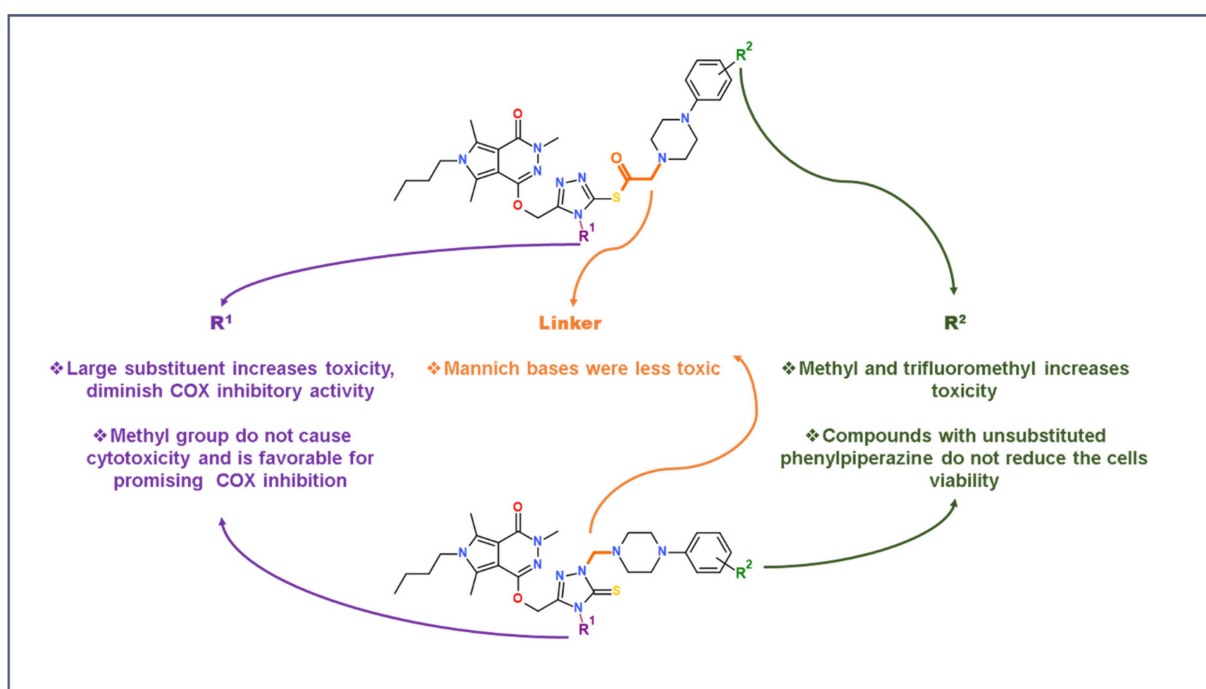


Figure 8. The structure-activity relationships in the group of investigated molecules.

2.6. Bovine Serum Albumin (BSA) Ligand-Binding Assay

The interaction of new compounds with blood proteins affects their pharmacokinetics in vivo. Therefore, we have performed experiments which were aimed at the estimation of the binding mode of the target compounds with the bovine serum albumin (BSA). Its structure is very similar to human serum albumin (HSA), and therefore can be used instead of human protein, especially since the costs of the application of bovine protein are significantly lower [41,42]. The mature BSA protein consists of 583 amino acids and is formed by 3 homologous domains, I, II and III, which in turn are composed of 2 subdomains: A and B [42]. Aromatic and heterocyclic ligands can bind to hydrophobic cavities in the subdomains IIA and IIIA [41]. The molecular interaction between new ligands and bovine serum albumin can be monitored by optical techniques such as circular dichroism (CD), FT-IR, ultraviolet-visible (UV-vis) or fluorescence spectroscopy [43].

2.6.1. Fluorescence Quenching of BSA, Binding Constants, Thermodynamic Studies

In this study, we checked the binding properties of the analyzed compounds to bovine serum albumin (BSA). Due to this, the fluorescence spectra were recorded in the range of 300–500 nm upon excitation at 280 nm, where both Trp and Tyr residues are excited,

and concentration range 0.0–2.0 μM (Figure 9). After the addition of each portion of the analyzed compound, the fluorescence intensity of BSA decreased. It suggests that all compounds could interact with BSA. The analyzed compounds can interact with BSA in two ways: forming a complex (what means static quenching) or due to collisions between molecules (dynamic quenching). The analysis by the Stern–Volmer equation, in dependence on temperature, can explain which way of interaction is observed in the case of our compounds [44].

The Stern–Volmer Equation (1) [45] at three different temperatures 297, 303, 308 K, was used for all of the fluorescence data after correction due to the infer filter effect (2):

$$F_{\text{corr}} = F_{\text{obs}} 10^{\frac{(A_{\text{ex}} + A_{\text{em}})}{2}} \quad (1)$$

where, F_{corr} and F_{obs} are the corrected and observed fluorescence intensities, respectively. A_{ex} and A_{em} are the absorbance values at excitation and emission wavelengths, respectively.

$$\frac{F_0}{F} = 1 + k_q \tau [Q] = 1 + K_{\text{SV}} \quad (2)$$

where F_0 and F are the steady-state fluorescence intensities at the maximum wavelength in the absence and presence of quencher, respectively, k_q the quenching rate constant of the biomolecule, τ_0 the average lifetime of the biomolecule, $[Q]$ is the quencher concentration and K_{SV} is the Stern–Volmer constant.

The Stern–Volmer (K_{SV}) constant was determined by linear fitting. The calculated results are collected in Table 4. When the temperature increases, the K_{SV} values also decrease. Furthermore, the quenching rate constant (k_q) values are much greater than the value of the maximum scatter collision quenching constant equal to $2 \times 10^{10} \text{ dm}^3 \cdot \text{mol}^{-1} \cdot \text{s}^{-1}$ [46]. Thus, all of the above indicate that the static quenching mechanism is more probable than dynamic and suggests forming the ground–state complex.

A double logarithm regression curve (3) was used to calculate the binding constants and the number of binding sites:

$$\log \frac{F_0 - F}{F} = \log K_b + n \log [Q] \quad (3)$$

where F_0 and F are the steady-state fluorescence intensities at the maximum wavelength in the absence and presence of quencher, respectively, $[Q]$ is the quencher concentration.

Figure 10 shows a good linear fit for all of the studied compounds. The results listed in Table 4 made visible that the binding constants indicate values of about $10^5 \text{ dm}^3 \cdot \text{mol}^{-1}$ at 297 K and decrease in higher temperatures. Similar values were obtained for many biologically active compounds [44,47–51]. Thus, the number of binding sites is close to 1 for all of the studied compounds, which means a one-to-one interaction.

Small molecules can interact with proteins in various ways, such as a hydrogen bond, van der Waals force, electrostatic and hydrophobic interactions, etc. [52]. The values of the thermodynamic parameters, enthalpy change (ΔH°), the entropic change (ΔS°) and free energy change (ΔG°), indicate the manners of these interactions.

The thermodynamic parameters were calculated from Equations (4) and (5):

$$\log K_b = -\frac{\Delta H^\circ}{RT} + \frac{\Delta S^\circ}{R} \quad (4)$$

$$\Delta G^\circ = \Delta H^\circ - T\Delta S^\circ = -RT \ln K_b \quad (5)$$

where K_b is the binding constant, R is the universal gas constant.

The results are listed in Table 4. The negative ΔG° values indicate that the interaction between BSA and the analyzed compounds was spontaneous. Simultaneously, the ΔH° and ΔS° also had negative values. Due to this, it can be concluded that van der Waals forces and/or hydrogen bonds were the main interaction types in the binding process.

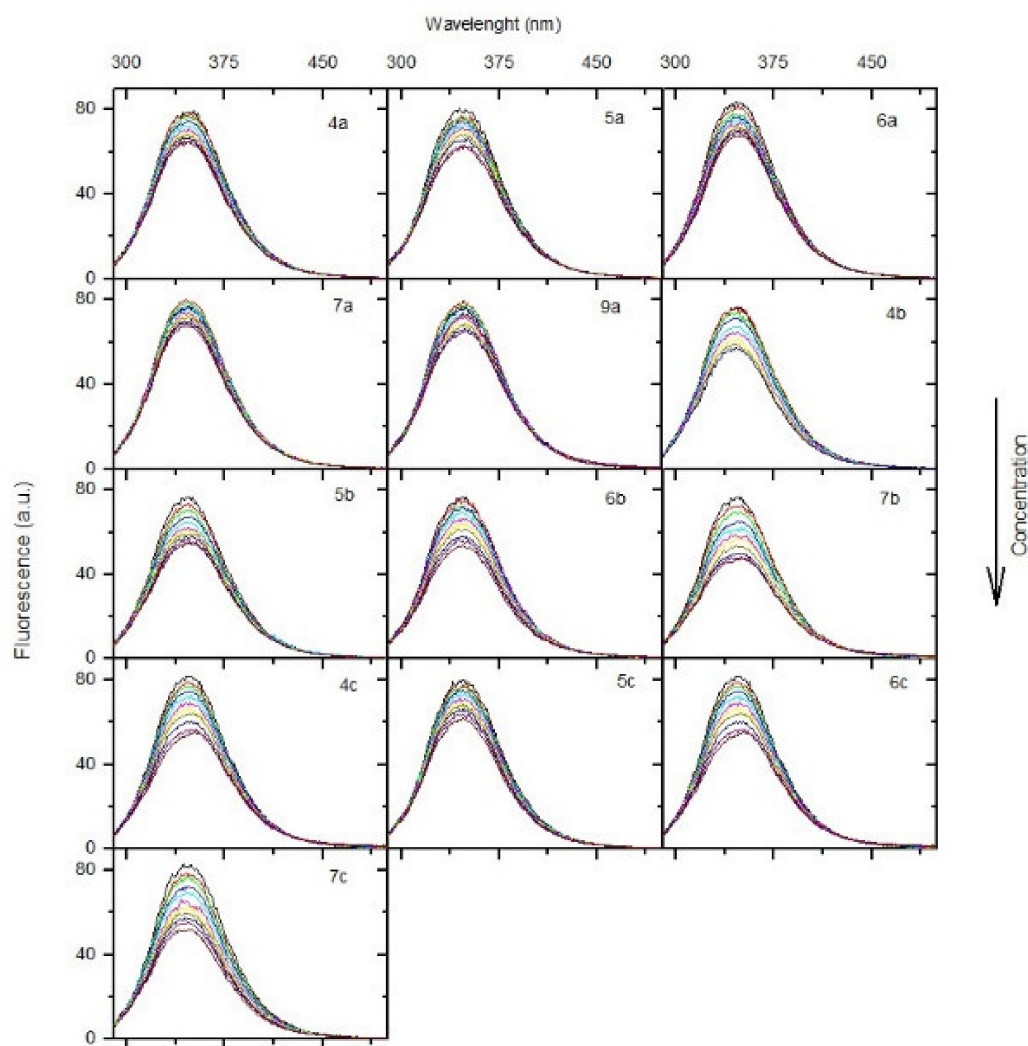


Figure 9. Fluorescence spectra of BSA solution in the presence of studied compounds (T-297 K, $\lambda_{\text{ex}} = 280$ nm). The concentration of derivatives from series a, b and c increased gradually as follows: 0, 0.2, 0.4, 0.6, 0.8, 1.0, 1.2, 1.4, 1.6, 1.8, 2.0 μM .

2.6.2. Circular Dichroism Spectra

Circular dichroism spectroscopy is a good method to determine the changes in the secondary structure in the conformation of proteins and to check if the analyzed compounds can interact with protein molecules [53]. In this study, we investigated the changes in the structure of BSA when all of the analyzed compounds were absent or present in solutions. Two negative bands characteristic for BSA, at near 208 nm and 222 nm, were observed in all of the CD spectra (Table S6 in Supplementary Data), which is typical for the α -helical structure of the protein. Any changes in this region mean conformational changes in protein molecules [54]. On the CD spectra shown in Table S6, a reduction of ellipticity values at 208 nm and 222 nm after adding every portion of the analyzed compounds can be seen. The loss in the α -helix(%) was observed. The content of the α -helix was calculated using Equations (6) and (7):

$$\alpha - \text{helix}(\%) = \frac{-\text{MRE}_{208} - 4000}{33000 - 4000} 100\% \quad (6)$$

where MRE_{208} is the MRE value observed at 208 nm, 4000 and 33,000 is the MRE value of the β -form and random coil conformation cross at 208 nm value of pure α -helix at 208 nm, respectively.

$$MRE = \frac{\text{ObservedCD[mdeg]}}{10Cnl} \quad (7)$$

where C is the molar concentration of BSA, n is the number of amino acid residues, which is 583 for BSA, l is the path length in cm [55].

Table 4. The Stern–Volmer constant K_{sv} and the quenching rate constant k_q , the binding constants K_b and number of binding sites n and the thermodynamic parameters for the interaction of BSA with studied compounds at different temperatures.

	T [K]	Quenching		$\log K_b$	Binding		Thermodynamic		
		$K_{sv} \times 10^5$ [$\text{dm}^3\text{mol}^{-1}$]	$k_q \times 10^{13}$ [$\text{dm}^3\text{mol}^{-1}\cdot\text{s}^{-1}$]		$K_b \times 10^4$ [$\text{dm}^3\text{mol}^{-1}$]	n	ΔG° [kJmol^{-1}]	ΔH° [kJmol^{-1}]	ΔS° [$\text{Jmol}^{-1}\text{K}^{-1}$]
4a	297	0.82	0.82	4.95 ± 0.09	8.91	1.00 ± 0.02	−28.20	−95.14	−225.40
	303	0.56	0.56	4.65 ± 0.09	4.47	0.98 ± 0.02			
	308	0.24	0.24	4.35 ± 0.27	2.24	0.99 ± 0.05			
5a	297	0.89	0.89	4.91 ± 0.14	8.13	0.99 ± 0.02	−28.20	−95.17	−225.50
	303	0.97	0.97	4.74 ± 0.04	5.50	0.96 ± 0.01			
	308	0.80	0.80	4.30 ± 0.07	2.00	0.89 ± 0.01			
6a	297	0.51	0.51	4.69 ± 0.13	4.90	0.99 ± 0.02	−27.07	−186.69	−537.43
	303	0.40	0.40	4.27 ± 0.14	1.86	0.94 ± 0.02			
	308	0.14	0.14	3.51 ± 0.22	0.33	0.89 ± 0.04			
7a	297	0.66	0.66	4.67 ± 0.07	4.68	0.97 ± 0.01	−26.89	−222.14	−657.43
	303	0.27	0.27	4.09 ± 0.20	1.23	0.94 ± 0.03			
	308	0.10	0.10	3.26 ± 0.21	0.99	0.87 ± 0.04			
9a	297	1.71	1.71	4.91 ± 0.05	4.90	0.94 ± 0.01	−27.89	−108.40	−271.08
	303	0.48	0.48	4.52 ± 0.09	1.86	0.97 ± 0.02			
	308	0.20	0.20	4.23 ± 0.18	0.33	0.98 ± 0.03			
4b	297	1.76	1.76	4.82 ± 0.20	6.61	0.92 ± 0.03	−27.75	−156.84	−434.67
	303	0.97	0.97	4.47 ± 0.22	2.95	0.91 ± 0.03			
	308	0.42	0.42	3.82 ± 0.20	0.61	0.86 ± 0.02			
5b	297	1.72	1.72	4.76 ± 0.12	5.75	0.92 ± 0.02	−26.92	−131.53	−352.20
	303	0.97	0.97	4.22 ± 0.13	1.66	0.93 ± 0.02			
	308	0.25	0.25	3.94 ± 0.17	0.87	0.92 ± 0.03			
6b	297	1.78	1.78	4.91 ± 0.15	8.13	0.95 ± 0.02	−27.90	−167.25	−469.18
	303	0.52	0.52	4.32 ± 0.12	2.09	0.93 ± 0.02			
	308	0.48	0.48	3.86 ± 0.06	0.72	0.90 ± 0.01			
7b	297	3.07	3.07	4.97 ± 0.17	9.33	0.91 ± 0.03	−28.36	−142.60	−384.65
	303	1.95	1.95	4.53 ± 0.16	3.39	0.87 ± 0.02			
	308	0.78	0.78	4.07 ± 0.10	1.17	0.86 ± 0.02			
4c	297	0.59	0.59	4.82 ± 0.19	5.61	1.01 ± 0.03	−27.44	−135.07	−362.40
	303	0.24	0.24	4.37 ± 0.40	2.34	0.99 ± 0.08			
	308	0.37	0.37	3.97 ± 0.12	0.93	0.90 ± 0.02			
5c	297	0.81	0.81	4.97 ± 0.18	9.33	1.01 ± 0.03	−28.29	−136.72	−365.09
	303	0.60	0.60	4.51 ± 0.10	3.24	0.95 ± 0.02			
	308	0.36	0.36	4.11 ± 0.13	1.29	0.92 ± 0.02			
6c	297	2.68	2.68	4.98 ± 0.12	9.55	0.92 ± 0.02	−28.34	−111.23	−279.08
	303	0.76	0.76	4.61 ± 0.03	4.07	0.95 ± 0.01			
	308	0.31	0.31	4.28 ± 0.12	1.91	0.96 ± 0.02			
7c	297	2.37	2.37	4.97 ± 0.20	9.33	0.93 ± 0.03	−28.48	−162.47	−451.14
	303	1.03	1.03	4.53 ± 0.10	3.39	0.92 ± 0.02			
	308	0.41	0.41	3.94 ± 0.18	0.87	0.88 ± 0.03			

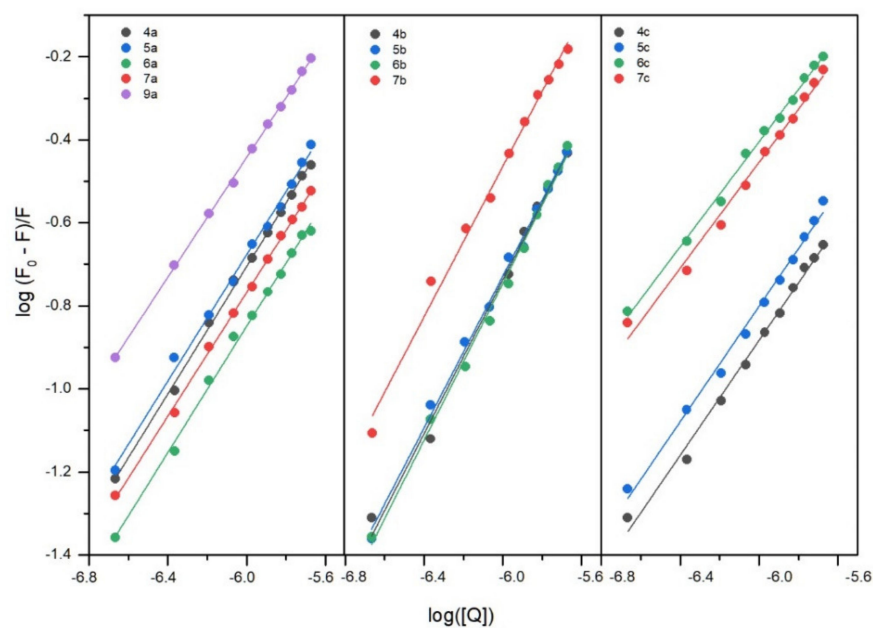


Figure 10. Fluorescence spectra of BSA solution in presence of studied compounds (T-297 K, $\lambda_{\text{ex}} = 280$ nm). The concentration of a, b and c was as follows: 0, 0.2, 0.4, 0.6, 0.8, 1.0, 1.2, 1.4, 1.6, 1.8, 2.0 μM .

The reduction in the α -helical contents of BSA is observed in the presence of all of the analyzed compounds. The changes after adding every portion of analyzed ligands are presented in Table 5. The observed changes ranged from 2.72% for **7a** to 5.88% for **7b** (Figure 11). Thus, CD studies showed that all of the analyzed compounds could interact with BSA, which agrees with the fluorescence spectroscopy.

Table 5. The values of the calculated α -helix(%) for BSA with the absence and presence of all analyzed compounds.

BSA/Analyzed Compound Molar Ratio	α -Helix [%]												
	4a	5a	6a	7a	9a	4b	5b	6b	7b	4c	5c	6c	7c
1:0	51.83	52.15	51.93	51.59	51.90	51.08	52.80	52.44	52.87	52.70	53.10	53.49	52.77
1:0.5	51.35	51.52	51.28	50.49	50.79	51.40	51.05	51.89	51.78	52.64	52.24	52.41	52.07
1:1	51.16	50.62	50.74	49.99	50.74	50.48	50.86	49.81	51.75	51.66	52.49	51.81	51.22
1:5	49.80	50.26	49.59	48.79	49.76	49.74	51.21	49.15	49.92	51.10	50.36	50.74	50.31
1:10	48.09	47.56	47.45	48.87	46.94	47.00	48.53	47.66	46.99	47.45	50.12	48.01	48.19

2.6.3. Fourier Transform Infrared Spectroscopic Measurements

The interaction of BSA with a series of investigated compounds was evaluated by analyzing changes in the protein secondary structure. The backbone conformation of BSA is related to the shape and intensity variation of the Amide I bond (C=O—stretching) and Amide II bond (C—N—stretching coupled with N—H bending) detected in the range 1700–1600 cm^{-1} [56]. Shi et al. mention that the Amide I bond is more sensitive than the Amide II bond for changes in the secondary structure [42]. The major signals found for free BSA: 1658 cm^{-1} and 1550 cm^{-1} are related to the α -helix structure and contribution of 53.8% (Table 6). It corresponds well with the CD measurements. The second large share has the β -sheet structure, which accounts for 29.2% and manifests as 1638 cm^{-1} , 1630 cm^{-1} and 1618 cm^{-1} peaks (Table 6, Table S7a). For all of the measurement BSA-compound complexes, it was observed that there was a tendency to decrease the intensity of the 1650 cm^{-1} and 1545 cm^{-1} signals with an increase of the compound concentration

(Table S8 in Supplementary Data). This clearly proves that all of the presented compounds interact with BSA, and binding to a protein is demonstrated by changing its secondary structure. A reduction in the α -helix structures in BSA was observed for all of the studied compounds after binding them to the protein. These results are in good agreement with fluorescence and CD spectroscopy. The majority of the changes were exhibited in It is with good correspondence the **5b**, **5c**, **6b**, **6c** and **7c** compounds. Moreover, the certain losing β -sheet structure occurred, especially for the **5c**, **6c** and **7c**. These findings correspond to a rise in the percentage of β -turn and β -antiparallel in the secondary structure of BSA. Moreover, the higher contribution of disordered random coil stood out in the samples containing **5c**, **6c** and **7c**.

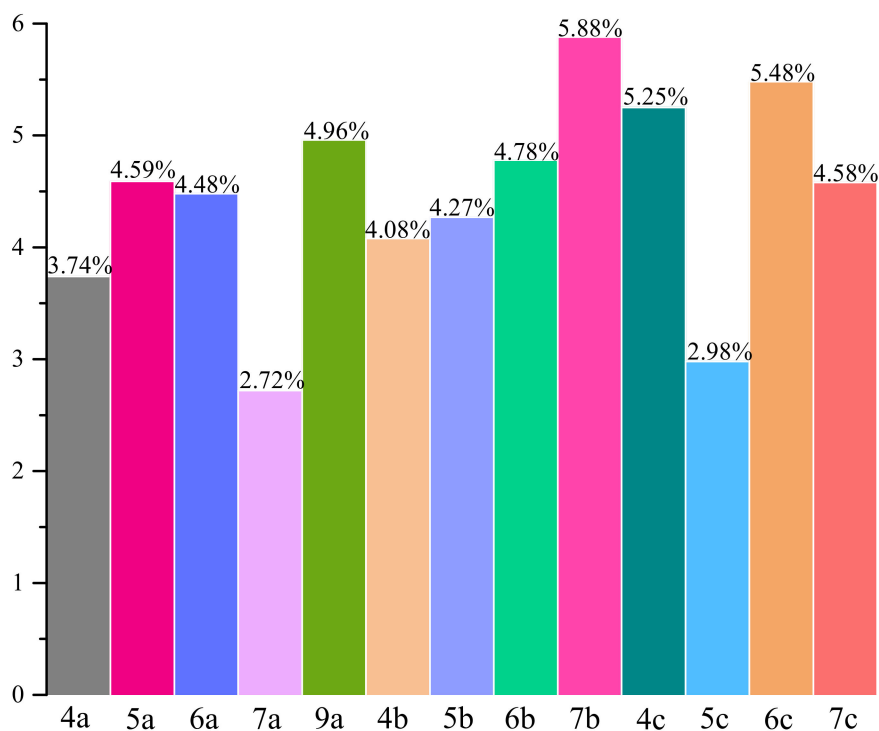


Figure 11. The comparison of changes in the α -helix(%) of BSA after adding 10 portions of each analyzed compound.

2.6.4. Site Markers Studies and Molecular Docking

In the BSA molecule, there are two binding sites situated in subdomains IIA and IIIA [57]. To confirm the binding sites where the analyzed compounds can be bound, *Phenylbutazone* (PHB) and *Ibuprofen* (IBP) were used as site probes [58]. Equation (3) was used to analyze the results here. The obtained results are collected in Table 7. The values of K_b of all of the tested compounds with BSA in the presence of IBP and PHB decline compared to compounds without BSA (Table 7). However, in the case of the values with PHB, the differences are smaller than in the case of IBP. Therefore, the results suggest that all of the studied compounds mainly bind to subdomain IIIA of BSA.

Table 6. Secondary structure of free BSA and BSA-drug complexes at pH = 7.5 calculated from Amide I bond obtained by FT-IR.

Compound	α -Helix [%]	β -Sheet [%]	β -Turn [%]	β -Anti [%]	Random-Coil [%]
Free—BSA	53.8	29.2	6.6	1.6	8.8
4a —BSA	50.2	16.5	11.8	11.8	9.7
5a —BSA	50.4	16.5	8.9	15.4	8.8
6a —BSA	50.3	17.8	4.9	19.5	7.5
7a —BSA	51.7	17.1	8.5	15.6	7.1
9a —BSA	51.8	16.2	5.8	18.4	7.8
4b —BSA	50.2	14.3	11.7	16.4	7.4
5b —BSA	49.7	13.8	13.7	12.5	10.3
6b —BSA	49.8	12.4	12.3	13.4	12.1
7b —BSA	51.5	14.2	15.6	9.9	8.8
4c —BSA	50.1	17.3	13.2	8.3	11.1
5c —BSA	49.1	6.1	16.4	3.6	24.8
6c —BSA	49.9	5.6	18.8	4.1	21.6
7c —BSA	48.3	6.6	18.6	4.2	22.3

Table 7. The binding constant of the studied compounds with BSA in the presence of site markers *Phenylbutazone* (PHB) and *Ibuprofen* (IBP) at 297 K.

	Site Marker	$\log K_b$		Site Marker	$\log K_b$		Site Marker	$\log K_b$
4a	-	4.95 ± 0.09	4b	-	4.82 ± 0.20	4c	-	4.82 ± 0.19
	BSA + IBP	3.50 ± 0.07		BSA + IBP	3.55 ± 0.19		BSA + IBP	3.30 ± 0.08
	BSA + PHP	4.54 ± 0.05		BSA + PHP	4.55 ± 0.07		BSA + PHP	4.57 ± 0.12
5a	-	4.91 ± 0.14	5b	-	4.76 ± 0.12	5c	-	4.97 ± 0.18
	BSA + IBP	3.60 ± 0.09		BSA + IBP	3.45 ± 0.05		BSA + IBP	3.27 ± 0.09
	BSA + PHP	4.36 ± 0.07		BSA + PHP	4.25 ± 0.13		BSA + PHP	4.58 ± 0.05
6a	-	4.69 ± 0.13	6b	-	4.91 ± 0.15	6c	-	4.98 ± 0.12
	BSA + IBP	3.40 ± 0.11		BSA + IBP	3.60 ± 0.12		BSA + IBP	3.68 ± 0.06
	BSA + PHP	4.10 ± 0.09		BSA + PHP	4.46 ± 0.15		BSA + PHP	4.63 ± 0.05
7a	-	4.67 ± 0.07	7b	-	4.97 ± 0.17	7c	-	4.97 ± 0.20
	BSA + IBP	3.37 ± 0.09		BSA + IBP	3.20 ± 0.08		BSA + IBP	3.50 ± 0.14
	BSA + PHP	4.20 ± 0.11		BSA + PHP	4.39 ± 0.07		BSA + PHP	4.58 ± 0.09
9a	-	4.91 ± 0.05						
	BSA + IBP	3.50 ± 0.09						
	BSA + PHP	4.55 ± 0.10						

The binding interactions between the tested compounds and BSA were studied by the molecular docking method. The simulated results were listed in Table 8. The results revealed that the binding free energy for all of the compounds within the hydrophobic cavity in site II (m) of BSA was more negative than that within the hydrophobic cavity in site I and site II(l). This indicates that site II (m) is favorable. The value of electrostatic energy (ΔE_3) is much less than ΔE_2 . It can indicate that the main interactions are van der Waals and hydrogen bonding interactions. The position of the compounds with the lowest binding free energy from all of the studied series in site II (m) compared to *Ibuprofen* is shown in Figure 12. The compounds are surrounded by various kinds of residues (Figure 13). Hydrogen bonds with Arg208, Leu326, Leu346 are formed. The π -sigma and other hydrophobic interactions are observed.

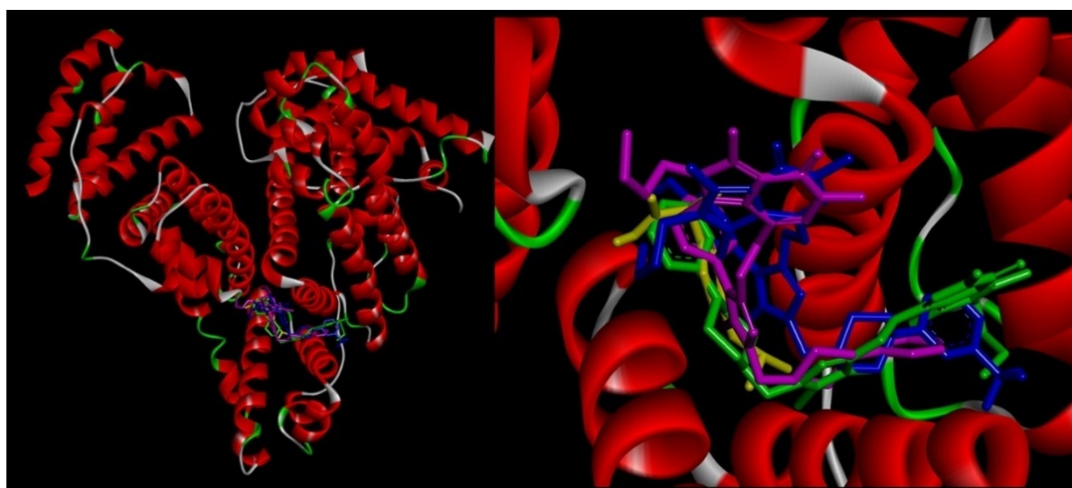


Figure 12. Docking poses of 4a (pink), 4b (green), 5c (blue) and *Ibuprofen* (yellow) inside BSA site II (m).

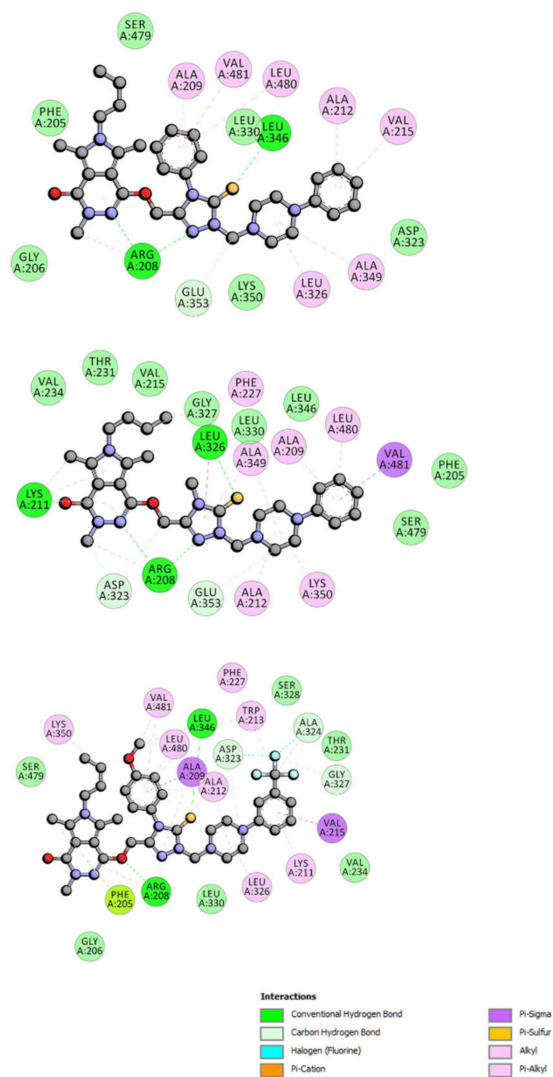


Figure 13. Two-dimensional interaction plot of 4b, 4a, and 5c with BSA in site 2 (m).

Table 8. Energies of the binding complexes BSA with studied compounds obtained from molecular docking.

	Binding Site	ΔG° [kJmol ⁻¹]	ΔE_1 [kJmol ⁻¹]	ΔE_2 [kJmol ⁻¹]	ΔE_3 [kJmol ⁻¹]
4a	site I	-31.02	-42.22	-37.66	-4.56
	site II(m)	-40.08	-51.33	-46.73	-4.60
	site II(l)	-27.42	-38.66	-39.88	1.21
5a	site I	-29.93	-42.38	-39.00	-3.38
	site II(m)	-38.22	-50.74	-46.89	-3.85
	site II(l)	-28.88	-41.38	-42.38	1.00
6a	site I	-30.18	-42.79	-38.67	-4.10
	site II(m)	-38.03	-49.28	-46.48	-2.80
	site II(l)	-31.30	-42.55	-43.72	1.17
7a	site I	-30.51	-43.01	-42.93	-0.04
	site II(m)	-35.69	-48.20	-47.36	-0.84
	site II(l)	-28.55	-41.04	-40.38	-0.67
9a	site I	-31.06	-43.55	-43.35	-0.21
	site II(m)	-35.44	-47.95	-47.19	-0.76
	site II(l)	-25.16	-37.62	-37.12	-0.50
4b	site I	-35.53	-47.98	-44.02	-4.01
	site II(m)	-41.17	-53.62	-50.20	-3.43
	site II(l)	-25.37	-37.87	-38.03	0.20
5b	site I	-32.02	-45.73	-41.05	-4.68
	site II(m)	-39.54	-53.30	-50.95	-2.30
	site II(l)	-30.47	-44.18	-45.06	0.84
6b	site I	-33.56	-46.02	-41.08	-4.22
	site II(m)	-41.17	-53.63	-51.00	-2.63
	site II(l)	-28.30	-40.76	-39.67	-1.08
7b	site I	-29.30	-43.01	-42.64	-0.37
	site II(m)	-39.67	-53.38	-52.83	-0.55
	site II(l)	-23.57	-37.28	-37.57	0.29
4c	site I	-34.48	-48.19	-43.76	-4.43
	site II(m)	-38.79	-52.50	-49.87	-2.63
	site II(l)	-28.34	-45.01	-43.09	1.08
5c	site I	-31.51	-46.48	-42.18	-4.26
	site II(m)	-42.48	-57.81	-54.88	-2.93
	site II(l)	-22.40	-37.37	-39.17	1.80
6c	site I	-31.77	-45.48	-42.39	-3.09
	site II(m)	-37.20	-50.91	-47.82	-3.09
	site II(l)	-24.03	-37.75	-36.12	-1.63
7c	site I	-27.21	-42.17	-41.08	-1.09
	site II(m)	-38.12	-53.08	-52.37	-0.71
	site II(l)	-33.89	-48.86	-48.91	0.05

ΔG° —binding free energy; ΔE_1 —intermolecular interaction energy, which is the sum of van der Waals energy, hydrogen bonding energy, desolvation free energy and electrostatic energy; ΔE_2 —the sum of van der Waals energy, hydrogen bonding energy and desolvation free energy; ΔE_3 —electrostatic energy.

2.7. In Silico Pharmacokinetic and Druglikeness Prediction

The derivatives **4a-7a**, **9a**, **4b-7b**, **4c-7c** were predicted for their possible pharmacokinetic (absorption distribution metabolism excretion; ADME) and drug-likeness properties using the SWISSADME server (<http://www.swissadme.ch/index.php>, accessed on 9 September 2021). The simulated results concerning the physicochemical features in the context of the Lipinski's rule of five (Ro5) [59] are presented in the Table 9. The compounds **4a-6a**, **4b** and **6b** meet the conditions of the Ro5, and therefore are supposed to show good oral bioavailability and membrane permeability. These findings are supported by the

results collected in Table 10. Most of the investigated molecules are predicted to be highly absorbed through the gastrointestinal (GI) tract. On the other hand, none of them are expected to cross blood–brain barrier (BBB). The water solubility was found to be rather poor (Table 10).

Table 9. Predicted physicochemical properties of studied compounds using SWISSADME server.

Compound	Physicochemical Properties—Lipinski's Rule of Five (Ro5)				
	#H-Bond Acceptors	#H-Bond Donors	Log $P_{o/w}$ (MLOGP)	MW [g/mol]	#Violations
4a	5	0	2.88	550.72	1
5a	8	0	3.36	618.72	1
6a	5	0	3.07	564.75	1
7a	6	0	2.99	578.73	2
9a	6	0	3.18	592.76	2
4b	5	0	3.89	612.79	1
5b	8	0	4.35	680.79	2
6b	5	0	4.08	626.81	1
7b	5	0	3.99	640.80	2
4c	6	0	3.58	642.81	2
5c	9	0	4.03	710.81	2
6c	6	0	3.76	656.84	2
7c	7	0	3.68	670.82	2

Table 10. Predicted ADME parameters of studied compounds using SWISSADME server.

Compound	Pharmacokinetics			
	GI Absorption	BBB Permeant	P-gp Substrate	Water Solubility
4a	High	No	Yes	Moderately soluble
5a	High	No	Yes	Poorly soluble
6a	High	No	Yes	Moderately soluble
7a	High	No	Yes	Poorly soluble
9a	High	No	Yes	Poorly soluble
4b	High	No	Yes	Poorly soluble
5b	Low	No	Yes	Poorly soluble
6b	High	No	Yes	Poorly soluble
7b	Low	No	Yes	Poorly soluble
4c	High	No	Yes	Poorly soluble
5c	Low	No	Yes	Poorly soluble
6c	High	No	Yes	Poorly soluble
7c	Low	No	Yes	Poorly soluble

According to the results presented in Table 11, the derivatives **4a-6a**, **4b**, **6b** not only do not violate the Lipinski's rule of five, but also fulfill the descriptors of Veber's rule [59,60]. This factors, alongside with the promising bioavailability score and calculated values of topological polar surface area (TPSA) ($<140 \text{ \AA}^2$) [61], can suggest that our compounds could be easily transported through biological membranes.

Table 11. Predicted drug-likeness properties of studied compounds using SWISSADME server.

Compound	Drug-Likeness			
	Lipinski	Veber	Bioavailability Score	TPSA [Å ²]
4a	Yes, 1 violation	Yes	0.55	110.37
5a	Yes, 1 violation	Yes	0.55	110.37
6a	Yes, 1 violation	Yes	0.55	110.37
7a	No, 2 violations	No, 1 violation	0.17	128.61
9a	No, 2 violations	No, 1 violation	0.17	128.61
4b	Yes, 1 violation	Yes	0.55	110.37
5b	No, 2 violations	No, 1 violation	0.17	110.37
6b	Yes, 1 violation	Yes	0.55	110.37
7b	No, 2 violations	No, 1 violation	0.17	128.61
4c	No, 2 violations	No, 1 violation	0.17	119.60
5c	No, 2 violations	No, 1 violation	0.17	119.60
6c	No, 2 violations	No, 1 violation	0.17	119.60
7c	No, 2 violations	No, 1 violation	0.17	137.84

3. Materials and Methods

3.1. Chemistry

3.1.1. Instrumentation and Chemicals

All of the chemicals, solvents and reagents used during chemical synthesis, purification and other experiments were delivered by commercially available suppliers (Alchem, Wrocław, Poland; Chemat, Gdańsk, Poland; Archem, Łany, Poland) and were used without further purification. Dry solvents were received according to the standard procedures. The reaction progress was monitored using the thin-layer chromatography (TLC) technique on silica-gel-60-F254-coated TLC plates, which were observed in UV light at 254 or 366 nm. The melting points of all of the new compounds were determined on the Electrothermal Mel-Temp 1101D apparatus (Cole-Parmer, Vernon Hills, IL, USA) using the open capillary method and were uncorrected. The ¹H NMR (300 MHz) and ¹³C NMR (75 MHz) spectra were recorded on the Bruker 300 MHz NMR spectrometer (Bruker Analytische Messtechnik GmbH, Rheinstetten, Germany). The samples were dissolved in CDCl₃ or DMSO-*d*₆, and tetramethylsilane (TMS) was used as an internal reference. Chemical shifts (δ) were reported in ppm. The infrared (IR) spectra were determined on the Nicolet iS50 FT-IR Spectrometer (Thermo Fisher Scientific, Waltham, MA, USA). The samples were applied as solids, and the frequencies were reported in cm⁻¹. Mass spectra (MS) were recorded using the Bruker Daltonics Compact ESI-Mass Spectrometer (Bruker Daltonik, GmbH, Bremen, Germany), operating in the positive ion mode. The analyzed compounds were dissolved in a methanol–chloroform mixture. All of the new reported derivatives were determined to have purities of >95% by the above-mentioned methods, unless stated otherwise.

3.1.2. Chemical Synthesis

The synthesis protocols and experimental data for compound **1** and all of the intermediates have already been reported [34].

General Procedure for Preparation of *N*-Substituted(aminothioxomethyl)hydrazide Derivatives of Pyrrolo[3,4-*d*]pyridazinone (**2a-c**)

The 2-(6-butyl-3,5,7-trimethyl-4-oxo-pyrrolo[3,4-*d*]pyridazin-1-yl)oxyacetohydrazide **1** (0.001 mol) was suspended in anhydrous ethanol (25 mL), and the mixture was heated under reflux until the hydrazide dissolved completely. Then, the appropriate *N*-substituted isothiocyanate (0.0011 mol) was added, and the reflux was continued for a further 0.5–2 h till the product precipitated. Finally, the mixture was cooled down, and the solid was filtered off, thoroughly washed with ethanol and purified by crystallization from this solvent.

2a:1-[[2-(6-butyl-3,5,7-trimethyl-4-oxo-pyrrolo[3,4-*d*]pyridazin-1-yl)oxyacetyl]amino]-3-methyl-thiourea

Yield: 87.56%; m.p.: 207–209 °C;

FT-IR (selected lines, γ_{\max} , cm^{-1}): 3263 (N-H), 2960, 2937, 2875 (C-H aliph.), 1698 (C=O), 1372 (C=S), 1231 (C-O), ^1H NMR (300 MHz, DMSO- d_6) δ : 0.88–0.93 (m, 3H, -CH₂-CH₂-CH₂-CH₃), 1.27–1.35 (m, 2H, -CH₂-CH₂-CH₂-CH₃), 1.57 (m, 2H, -CH₂-CH₂-CH₂-CH₃), 2.51 (s, 3H, 7-CH₃), 2.58 (s, 3H, 5-CH₃), 2.85 (s, 3H, *N*-CH₃), 3.38 (s, 3H, 3-CH₃), 3.94–3.99 (m, 2H, -CH₂-CH₂-CH₂-CH₃), 4.70 (s, 2H, O-CH₂-); 7.88 (s, 1H, NH), 9.31 (s, 1H, NH), 9.96 (s, 1H, NH); ^{13}C NMR (75 MHz, DMSO- d_6) δ : 10.65, 11.33, 13.99, 19.91, 31.27, 32.06, 37.04, 63.74, 108.00, 111.23, 123.58, 129.07, 148.57, 158.46, 167.62, 182.59; MS (ESI-MS) (m/z): calcd. for C₁₇H₂₆N₆O₃S [L+H]⁺: 395.1860; found: 395.1839.

2b:1-[[2-(6-butyl-3,5,7-trimethyl-4-oxo-pyrrolo[3,4-*d*]pyridazin-1-yl)oxyacetyl]amino]-3-phenyl-thiourea

Yield: 89.88%; m.p.: 214–216 °C;

FT-IR (selected lines, γ_{\max} , cm^{-1}): 3323, 3237 (N-H), 3049 (C-H arom.), 2961, 2938, 2876 (C-H aliph.), 1689 (C=O), 1360 (C=S); ^1H NMR (300 MHz, DMSO- d_6) δ : 0.88–0.93 (m, 3H, -CH₂-CH₂-CH₂-CH₃), 1.28–1.35 (m, 2H, -CH₂-CH₂-CH₂-CH₃), 1.58 (m, 2H, -CH₂-CH₂-CH₂-CH₃), 2.53 (s, 3H, 7-CH₃), 2.58 (s, 3H, 5-CH₃), 3.36 (s, 3H, 3-CH₃), 3.94–3.99 (m, 2H, -CH₂-CH₂-CH₂-CH₃), 4.77 (s, 2H, O-CH₂-); 7.16–7.18 (m, 1H, Ar-H), 7.30–7.42 (m, 4H, Ar-H), 9.56 (s, 1H, NH), 9.71 (s, 1H, NH), 10.18 (s, 1H, NH); ^{13}C NMR (75 MHz, DMSO- d_6) δ : 10.65, 11.36, 13.99, 19.91, 32.06, 37.03, 63.84, 108.01, 111.25, 123.57, 125.64, 128.56, 129.09, 139.50, 148.57, 158.46; MS (ESI-MS) (m/z): calcd. for C₂₂H₂₈N₆O₃S [L+H]⁺: 457.2016; found: 457.1985.

2c:1-[[2-(6-butyl-3,5,7-trimethyl-4-oxo-pyrrolo[3,4-*d*]pyridazin-1-yl)oxyacetyl]amino]-3-(4-methoxyphenyl)-thiourea

Yield: 94.12%; m.p.: 217–219 °C;

FT-IR (selected lines, γ_{\max} , cm^{-1}): 3321, 3219 (N-H), 3051 (C-H arom.), 2957, 2872, 2836 (C-H aliph.), 1678 (C=O), 1348 (C=S); ^1H NMR (300 MHz, DMSO- d_6) δ : 0.88–0.93 (m, 3H, -CH₂-CH₂-CH₂-CH₃), 1.28–1.35 (m, 2H, -CH₂-CH₂-CH₂-CH₃), 1.58 (m, 2H, -CH₂-CH₂-CH₂-CH₃), 2.53 (s, 3H, 7-CH₃), 2.58 (s, 3H, 5-CH₃), 3.36 (s, 3H, 3-CH₃), 3.73 (s, 3H, O-CH₃), 3.94–3.97 (m, 2H, -CH₂-CH₂-CH₂-CH₃), 4.76 (s, 2H, O-CH₂-); 6.87–6.90 (m, 2H, Ar-H), 7.22–7.25 (m, 2H, Ar-H), 9.44 (s, 1H, NH), 9.61 (s, 1H, NH), 10.14 (s, 1H, NH); ^{13}C NMR (75 MHz, DMSO- d_6) δ : 10.65, 11.35, 13.99, 19.91, 32.06, 37.03, 55.67, 63.84, 108.02, 111.25, 113.78, 123.57, 127.77, 129.08, 132.31, 148.59, 157.32, 158.46, 167.69; MS (ESI-MS) (m/z): calcd. for C₂₃H₃₀N₆O₄S [L+H]⁺: 487.2122; found: 487.2087.

General Procedure for Preparation of 4-Substituted-2*H*-1,2,4-triazole Derivatives of Pyrrolo[3,4-*d*]pyridazinone (**3a-c**)

The appropriate *N*-substituted-(aminothioxomethyl)hydrazide derivative of pyrrolo[3,4-*d*]pyridazinone (**2a-c**) (0.0001 mol) was dissolved in a 5% aqueous solution of sodium hydroxide (25 mL), and the mixture was stirred and refluxed for about 2–3 h. Afterward, it was poured onto crushed ice and carefully acidified to pH 2–3 with 7.5% hydrochloric acid (aq), resulting in the formation of a white or yellowish solid of adequate 4-substituted-1,2,4-triazole derivative (**3a-c**). Finally, the afforded precipitate was filtered off, washed with ice-cold water and recrystallized from ethanol.

3a:6-butyl-3,5,7-trimethyl-1-(4-methyl-3-thioxo-2*H*-1,2,4-triazol-5-yl)methoxy]pyrrolo[3,4-*d*]pyridazin-4-one

Yield: 83.12%; m.p.: 117–120 °C;

FT-IR (selected lines, γ_{\max} , cm^{-1}): 3425 (N-H), 3120, 3050 (C-H arom.), 2935, 2871 (C-H aliph.), 1544 (C=N), 1340 (C=S); ^1H NMR (300 MHz, DMSO- d_6) δ : 0.86–0.91 (m, 3H, -CH₂-CH₂-CH₂-CH₃), 1.26–1.33 (m, 2H, -CH₂-CH₂-CH₂-CH₃), 1.56 (m, 2H, -CH₂-CH₂-CH₂-CH₃), 2.42 (s, 3H, 7-CH₃), 2.57 (s, 3H, 5-CH₃), 3.40 (s, 3H, 3-CH₃), 3.50 (s, 3H, triazole-*N*-CH₃),

3.92–3.97 (m, 2H, $-\text{CH}_2-\text{CH}_2-\text{CH}_2-\text{CH}_3$), 5.30 (s, 2H, $\text{O}-\text{CH}_2-$), 13.82 (s, 1H, NH); ^{13}C NMR (75 MHz, $\text{DMSO}-d_6$) δ : 10.64, 11.18, 13.97, 19.89, 30.65, 32.01, 37.03, 43.83, 58.09, 107.62, 111.18, 123.42, 129.38, 148.07, 148.89, 158.40, 168.05; HR-MS (ESI-MS) (m/z): calcd. for $\text{C}_{17}\text{H}_{24}\text{N}_6\text{O}_2\text{S}$ $[\text{L}+\text{H}]^+$: 377.1754; found: 377.1736.

3b: 6-butyl-3,5,7-trimethyl-1-[(4-phenyl-3-thioxo-2H-1,2,4-triazol-5-yl)methoxy]pyrrolo[3,4-*d*]pyridazin-4-one

Yield: 81.69%; m.p.: 123–125 °C;

FT-IR (selected lines, γ_{max} , cm^{-1}): 3414 (N-H), 3037 (C-H arom.), 2957, 2928, 2871 (C-H aliph.), 1543 (C=N); ^1H NMR (300 MHz, $\text{DMSO}-d_6$) δ : 0.86–0.91 (m, 3H, $-\text{CH}_2-\text{CH}_2-\text{CH}_2-\text{CH}_3$), 1.24–1.31 (m, 2H, $-\text{CH}_2-\text{CH}_2-\text{CH}_2-\text{CH}_3$), 1.53 (m, 2H, $-\text{CH}_2-\text{CH}_2-\text{CH}_2-\text{CH}_3$), 2.25 (s, 3H, 7- CH_3), 2.53 (s, 3H, 5- CH_3), 3.32 (s, 3H, 3- CH_3), 3.88–3.93 (m, 2H, $-\text{CH}_2-\text{CH}_2-\text{CH}_2-\text{CH}_3$), 5.12 (s, 2H, $\text{O}-\text{CH}_2-$); 7.45 (m, 5H, Ar-H), 14.04 (s, 1H, NH); ^{13}C NMR (75 MHz, $\text{DMSO}-d_6$) δ : 10.59, 11.20, 13.97, 19.86, 31.97, 36.95, 43.76, 57.85, 107.38, 111.05, 123.31, 128.28, 129.19, 129.69, 129.91, 133.86, 147.76, 148.60, 158.28, 168.90; MS (ESI-MS) (m/z): calcd. for $\text{C}_{22}\text{H}_{26}\text{N}_6\text{O}_2\text{S}$ $[\text{L}+\text{H}]^+$: 439.1911; found: 439.1874.

3c: 6-butyl-3,5,7-trimethyl-1-[[4-(4-methoxy)phenyl-3-thioxo-2H-1,2,4-triazol-5-yl]methoxy]pyrrolo[3,4-*d*]pyridazin-4-one

Yield: 84.49%; m.p.: 129–131 °C;

FT-IR (selected lines, γ_{max} , cm^{-1}): 3414 (N-H), 3041 (C-H arom.), 2956, 2931, 2872 (C-H aliph.), 1543 (C=N); ^1H NMR (300 MHz, $\text{DMSO}-d_6$) δ : 0.87–0.92 (m, 3H, $-\text{CH}_2-\text{CH}_2-\text{CH}_2-\text{CH}_3$), 1.31 (m, 2H, $-\text{CH}_2-\text{CH}_2-\text{CH}_2-\text{CH}_3$), 1.54 (m, 2H, $-\text{CH}_2-\text{CH}_2-\text{CH}_2-\text{CH}_3$), 2.29 (s, 3H, 7- CH_3), 2.54 (s, 3H, 5- CH_3), 3.31 (s, 3H, 3- CH_3), 3.74 (s, 3H, Ar-O- CH_3), 3.92 (m, 2H, $-\text{CH}_2-\text{CH}_2-\text{CH}_2-\text{CH}_3$), 5.12 (s, 2H, $\text{O}-\text{CH}_2-$); 6.96–6.99 (m, 2H, Ar-H), 7.31–7.34 (m, 2H, Ar-H), 13.99 (s, 1H, NH); ^{13}C NMR (75 MHz, $\text{DMSO}-d_6$) δ : 10.59, 11.20, 13.98, 19.88, 31.99, 36.95, 43.78, 55.84, 57.85, 107.46, 111.06, 114.79, 115.18, 123.34, 126.32, 129.19, 129.54, 129.97, 147.83, 148.88, 158.29, 160.13, 169.12; MS (ESI-MS) (m/z): calcd. for $\text{C}_{13}\text{H}_{28}\text{N}_6\text{O}_3\text{S}$ $[\text{L}+\text{H}]^+$: 469.2016; found: 469.1976.

General Procedure for Preparation of Mannich Base-Type Derivatives of Pyrrolo[3,4-*d*]pyridazinone (**4a-c-6a-c**)

Aqueous formaldehyde of 37% (0.01 mol, ~1 mL) was added to the solution of adequate 4-substituted-1,2,4-triazole derivative of pyrrolo[3,4-*d*]pyridazinone (**3a**, **3b** or **3c**) (0.001 mol) in methanol (30 mL). The mixture was stirred at room temperature (RT) for 30 min. Subsequently, a corresponding aryl piperazine derivative (0.0015 mol) was added, and the stirring was continued for a further several hours at RT. The mixture was left overnight. The formed precipitate was filtered off, thoroughly washed with cold methanol and purified by crystallization from methanol.

4a: 6-butyl-3,5,7-trimethyl-1-[[4-methyl-2-[(4-phenyl)piperazin-1-yl)methyl]-3-thioxo-2H-1,2,4-triazol-5-yl]methoxy]pyrrolo[3,4-*d*]pyridazin-4-one

Yield: 72.35%; m.p.: 186–188 °C;

FT-IR (selected lines, γ_{max} , cm^{-1}): 3019 (C-H arom.), 2962, 2937, 2874 (C-H aliph.), 1549 (C=N) 1272 (C=S); ^1H NMR (300 MHz, CDCl_3) δ : 0.94–0.99 (m, 3H, $-\text{CH}_2-\text{CH}_2-\text{CH}_2-\text{CH}_3$), 1.34–1.41 (m, 2H, $-\text{CH}_2-\text{CH}_2-\text{CH}_2-\text{CH}_3$), 1.60–1.66 (m, 2H, $-\text{CH}_2-\text{CH}_2-\text{CH}_2-\text{CH}_3$), 2.43 (s, 3H, 7- CH_3), 2.68 (s, 3H, 5- CH_3), 2.98–2.99 (m, 4H, CH_2 —piperazine), 3.18–3.19 (m, 4H, CH_2 —piperazine), 3.57 (s, 3H, 3- CH_3), 3.67 (s, 3H, triazole-*N*- CH_3), 3.94–3.97 (m, 2H, $-\text{CH}_2-\text{CH}_2-\text{CH}_2-\text{CH}_3$), 5.21 (s, 2H, *N*- CH_2 -*N*), 5.31 (s, 2H, $\text{O}-\text{CH}_2-$); 6.82–6.91 (m, 3H, Ar-H), 7.22–7.27 (m, 2H, Ar-H); ^{13}C NMR (75 MHz, CDCl_3) δ : 10.65, 11.30, 13.69, 20.04, 31.69, 32.32, 37.05, 43.99, 49.29, 50.42, 57.54, 69.49, 108.05, 111.84, 116.32, 119.89, 122.24, 129.10, 129.43, 146.76, 147.95, 151.28, 159.17, 169.74; HRMS (ESI-MS) (m/z): calcd. for $\text{C}_{28}\text{H}_{38}\text{N}_8\text{O}_2\text{S}$ $[\text{L}+\text{H}]^+$: 551.2911; found: 551.2894.

5a:6-butyl-3,5,7-trimethyl-1-[[4-methyl-2-[[4-[3-(trifluoromethyl)phenyl]piperazin-1-yl]methyl]-3-thioxo-2H-1,2,4-triazol-5-yl]methoxy]pyrrolo[3,4-d]pyridazin-4-one

Yield: 64.84%; m.p.: 198–200 °C;

FT-IR (selected lines, γ_{\max} , cm^{-1}): 2963, 2935, 2876, 3843 (C-H aliph.), 1650 (C=N), 1242 (C=S); ^1H NMR (300 MHz, CDCl_3) δ : 0.94–0.98 (m, 3H, $-\text{CH}_2-\text{CH}_2-\text{CH}_2-\text{CH}_3$), 1.34–1.41 (m, 2H, $-\text{CH}_2-\text{CH}_2-\text{CH}_2-\text{CH}_3$), 1.60–1.63 (m, 2H, $-\text{CH}_2-\text{CH}_2-\text{CH}_2-\text{CH}_3$), 2.42 (s, 3H, 7- CH_3), 2.68 (s, 3H, 5- CH_3), 2.96–2.99 (m, 4H, CH_2 —piperazine), 3.22–3.25 (m, 4H, CH_2 —piperazine), 3.57 (s, 3H, 3- CH_3), 3.67 (s, 3H, triazole- N - CH_3), 3.87–3.92 (m, 2H, $-\text{CH}_2-\text{CH}_2-\text{CH}_2-\text{CH}_3$), 5.21 (s, 2H, N - CH_2 - N) 5.31 (s, 2H, O - CH_2 -); 7.01–7.07 (m, 3H, Ar-H), 7.30–7.35 (m, 1H, Ar-H); ^{13}C NMR (75 MHz, CDCl_3) δ : 10.65, 11.27, 13.67, 20.04, 31.71, 32.32, 37.04, 43.99, 48.77, 50.23, 57.51, 69.39, 108.05, 111.83, 112.39, 115.99, 118.93, 122.21, 129.45, 129.56, 131.22, 131.64, 146.84, 147.91, 151.32, 159.16, 169.78; MS (ESI-MS) (m/z): calcd. for $\text{C}_{29}\text{H}_{37}\text{F}_3\text{N}_8\text{O}_2\text{S}$ [$\text{L}+\text{H}$] $^+$: 619.2785; found: 619.2748.**6a:**6-butyl-3,5,7-trimethyl-1-[[4-methyl-2-[[4-(4-methyl)phenyl]piperazin-1-yl]methyl]-3-thioxo-2H-1,2,4-triazol-5-yl]methoxy]pyrrolo[3,4-d]pyridazin-4-one

Yield: 68.98%; m.p.: 181–183 °C;

FT-IR (selected lines, γ_{\max} , cm^{-1}): 2962, 2933, 2878, 2855, 2826 (C-H aliph.), 1633 (C=N), 1248 (C=S); ^1H NMR (300 MHz, CDCl_3) δ : 0.94–0.98 (m, 3H, $-\text{CH}_2-\text{CH}_2-\text{CH}_2-\text{CH}_3$), 1.34–1.42 (m, 2H, $-\text{CH}_2-\text{CH}_2-\text{CH}_2-\text{CH}_3$), 1.63 (m, 2H, $-\text{CH}_2-\text{CH}_2-\text{CH}_2-\text{CH}_3$), 2.26 (s, 3H, Ar- CH_3), 2.43 (s, 3H, 7- CH_3), 2.67 (s, 3H, 5- CH_3), 2.99 (m, 4H, CH_2 —piperazine), 3.15 (m, 4H, CH_2 —piperazine), 3.57 (s, 3H, 3- CH_3), 3.67 (s, 3H, triazole- N - CH_3), 3.87–3.92 (m, 2H, $-\text{CH}_2-\text{CH}_2-\text{CH}_2-\text{CH}_3$), 5.21 (s, 2H, N - CH_2 - N) 5.31 (s, 2H, O - CH_2 -); 6.85 (m, 2H, Ar-H), 7.05–7.08 (m, 2H, Ar-H); ^{13}C NMR (75 MHz, CDCl_3) δ : 10.66, 11.33, 13.70, 20.05, 20.44, 31.70, 32.33, 37.06, 43.99, 50.34, 57.54, 69.43, 108.04, 111.82, 112.26, 116.81, 122.26, 129.41, 129.67, 146.77, 147.95, 159.18, 169.72; MS (ESI-MS) (m/z): calcd. for $\text{C}_{29}\text{H}_{40}\text{N}_8\text{O}_2\text{S}$ [$\text{L}+\text{H}$] $^+$: 565.3068; found: 565.3019.**4b:**6-butyl-3,5,7-trimethyl-1-[[4-phenyl-2-[(4-phenyl)piperazin-1-yl]methyl]-3-thioxo-2H-1,2,4-triazol-5-yl]methoxy]pyrrolo[3,4-d]pyridazin-4-one

Yield: 69.02%; m.p.: 129–131 °C;

FT-IR (selected lines, γ_{\max} , cm^{-1}): 2932, 2828 (C-H aliph.), 1543 (C=N), 1269 (C=S); ^1H NMR (300 MHz, CDCl_3) δ : 0.94–0.99 (m, 3H, $-\text{CH}_2-\text{CH}_2-\text{CH}_2-\text{CH}_3$), 1.36–1.38 (m, 2H, $-\text{CH}_2-\text{CH}_2-\text{CH}_2-\text{CH}_3$), 1.61 (m, 2H, $-\text{CH}_2-\text{CH}_2-\text{CH}_2-\text{CH}_3$), 2.34 (s, 3H, 7- CH_3), 2.65 (s, 3H, 5- CH_3), 3.06 (m, 4H, CH_2 —piperazine), 3.22 (m, 4H, CH_2 —piperazine), 3.46 (s, 3H, 3- CH_3), 3.84–3.89 (m, 2H, $-\text{CH}_2-\text{CH}_2-\text{CH}_2-\text{CH}_3$), 5.16 (s, 2H, N - CH_2 - N) 5.30 (s, 2H, O - CH_2 -); 6.87–6.94 (m, 3H, Ar-H), 7.24–7.29 (m, 2H, Ar-H) 7.39 (m, 2H, Ar-H); 7.45–7.46 (m, 3H, Ar-H); ^{13}C NMR (75 MHz, CDCl_3) δ : 10.62, 11.23, 13.71, 20.03, 32.31, 36.97, 43.92, 49.36, 50.52, 57.09, 69.64, 108.05, 111.74, 116.39, 119.98, 122.18, 127.67, 129.13, 129.63, 130.03, 133.80, 146.79, 147.81, 151.31, 159.11, 170.52; MS (ESI-MS) (m/z): calcd. for $\text{C}_{33}\text{H}_{40}\text{N}_8\text{O}_2\text{S}$ [$\text{L}+\text{H}$] $^+$: 613.3068; found: 613.2995.**5b:**6-butyl-3,5,7-trimethyl-1-[[4-phenyl-2-[[4-[3-(trifluoromethyl)phenyl]piperazin-1-yl]methyl]-3-thioxo-2H-1,2,4-triazol-5-yl]methoxy]pyrrolo[3,4-d]pyridazin-4-one

Yield: 65.29%; m.p.: 118–120 °C;

FT-IR (selected lines, γ_{\max} , cm^{-1}): 2935, 2872, 2850 (C-H aliph.), 1268 (C=S); ^1H NMR (300 MHz, CDCl_3) δ : 0.94–0.99 (m, 3H, $-\text{CH}_2-\text{CH}_2-\text{CH}_2-\text{CH}_3$), 1.33–1.40 (m, 2H, $-\text{CH}_2-\text{CH}_2-\text{CH}_2-\text{CH}_3$), 1.59–1.61 (m, 2H, $-\text{CH}_2-\text{CH}_2-\text{CH}_2-\text{CH}_3$), 2.33 (s, 3H, 7- CH_3), 2.65 (s, 3H, 5- CH_3), 3.05–3.07 (m, 4H, CH_2 —piperazine), 3.24–3.26 (m, 4H, CH_2 —piperazine), 3.46 (s, 3H, 3- CH_3), 3.84–3.89 (m, 2H, $-\text{CH}_2-\text{CH}_2-\text{CH}_2-\text{CH}_3$), 5.16 (s, 2H, N - CH_2 - N) 5.30 (s, 2H, O - CH_2 -); 7.04–7.09 (m, 3H, Ar-H), 7.32–7.39 (m, 3H, Ar-H); 7.46–7.48 (m, 3H, Ar-H); ^{13}C NMR (75 MHz, CDCl_3) δ : 10.62, 11.20, 13.69, 20.02, 32.31, 36.96, 43.92, 48.84, 50.34, 57.08, 69.54, 108.01, 111.72, 112.44, 116.01, 119.00, 122.15, 126.08, 127.65, 129.15, 129.60, 129.66, 130.07, 131.23, 131.65, 133.75, 146.87, 147.78, 151.37, 159.09, 170.52; MS (ESI-MS) (m/z): calcd. for $\text{C}_{34}\text{H}_{39}\text{F}_3\text{N}_8\text{O}_2\text{S}$ [$\text{L}+\text{H}$] $^+$: 681.2942; found: 681.2864.

6b: 6-butyl-3,5,7-trimethyl-1-[[4-phenyl-2-[[4-[(4-methyl)phenyl]piperazin-1-yl]methyl]-3-thioxo-2H-1,2,4-triazol-5-yl]methoxy]pyrrolo[3,4-d]pyridazin-4-one

Yield: 61.74%; m.p.: 108–111 °C;

FT-IR (selected lines, γ_{\max} , cm^{-1}): 2959, 2935, 2860, 2832 (C-H aliph.), 1618 (C=N), 1234 (C=S); ^1H NMR (300 MHz, CDCl_3) δ : 0.94–0.99 (m, 3H, $-\text{CH}_2-\text{CH}_2-\text{CH}_2-\text{CH}_3$), 1.36–1.38 (m, 2H, $-\text{CH}_2-\text{CH}_2-\text{CH}_2-\text{CH}_3$), 1.61 (m, 2H, $-\text{CH}_2-\text{CH}_2-\text{CH}_2-\text{CH}_3$), 2.27 (s, 3H, Ar-CH₃), 2.34 (s, 3H, 7-CH₃), 2.66 (s, 3H, 5-CH₃), 3.07 (m, 4H, CH_2 —piperazine), 3.18 (m, 4H, CH_2 —piperazine), 3.46 (s, 3H, 3-CH₃), 3.84–3.90 (m, 2H, $-\text{CH}_2-\text{CH}_2-\text{CH}_2-\text{CH}_3$), 5.16 (s, 2H, N-CH₂-N) 5.30 (s, 2H, O-CH₂-); 6.86 (m, 2H, Ar-H), 7.06–7.09 (m, 2H, Ar-H); 7.39 (m, 2H, Ar-H), 7.45–7.46 (m, 3H, Ar-H); ^{13}C NMR (75 MHz, CDCl_3) δ : 10.63, 11.26, 13.71, 20.04, 32.32, 36.97, 43.92, 50.47, 57.09, 69.60, 108.02, 111.74, 116.84, 122.20, 127.68, 129.11, 129.64, 129.69, 130.02, 133.80, 146.80, 147.81, 159.11, 170.52; MS (ESI-MS) (m/z): calcd. for $\text{C}_{34}\text{H}_{42}\text{N}_8\text{O}_2\text{S}$ [$\text{L}+\text{H}$]⁺: 627.3224; found: 627.3176.

4c: 6-butyl-1-[[4-(4-methoxyphenyl)-2-[(4-phenylpiperazin-1-yl)methyl]-3-thioxo-2H-1,2,4-triazol-5-yl]methoxy]-3,5,7-trimethyl-pyrrolo[3,4-d]pyridazin-4-one

Yield: 71.07%; m.p.: 169–170 °C;

FT-IR (selected lines, γ_{\max} , cm^{-1}): 2961, 2933, 2860, 2838 (C-H aliph.), 1651 (C=N); ^1H NMR (300 MHz, CDCl_3) δ : 0.94–0.99 (m, 3H, $-\text{CH}_2-\text{CH}_2-\text{CH}_2-\text{CH}_3$), 1.34–1.41 (m, 2H, $-\text{CH}_2-\text{CH}_2-\text{CH}_2-\text{CH}_3$), 1.62 (m, 2H, $-\text{CH}_2-\text{CH}_2-\text{CH}_2-\text{CH}_3$), 2.36 (s, 3H, 7-CH₃), 2.66 (s, 3H, 5-CH₃), 3.05–3.07 (m, 4H, CH_2 —piperazine), 3.20–3.22 (m, 4H, CH_2 —piperazine), 3.47 (s, 3H, 3-CH₃), 3.81 (s, 3H, O-CH₃), 3.85–3.90 (m, 2H, $-\text{CH}_2-\text{CH}_2-\text{CH}_2-\text{CH}_3$), 5.15 (s, 2H, N-CH₂-N) 5.29 (s, 2H, O-CH₂-); 6.84–6.95 (m, 5H, Ar-H), 7.24–7.28 (m, 4H, Ar-H); ^{13}C NMR (75 MHz, CDCl_3) δ : 10.62, 11.26, 13.72, 20.05, 32.33, 36.97, 43.94, 49.36, 50.52, 55.51, 57.11, 69.66, 108.08, 111.74, 114.83, 116.39, 119.97, 122.19, 126.21, 129.13, 147.11, 147.88, 151.31, 159.11, 160.48, 170.75; HRMS (ESI-MS) (m/z): calcd. for $\text{C}_{34}\text{H}_{42}\text{N}_8\text{O}_3\text{S}$ [$\text{L}+\text{H}$]⁺: 643.3173; found: 643.3194.

5c: 6-butyl-1-[[4-(4-methoxyphenyl)-2-[[4-[3-(trifluoromethyl)phenyl]piperazin-1-yl]methyl]-3-thioxo-2H-1,2,4-triazol-5-yl]methoxy]-3,5,7-trimethyl-pyrrolo[3,4-d]pyridazin-4-one

Yield: 59.73%; m.p.: 163–165 °C;

FT-IR (selected lines, γ_{\max} , cm^{-1}): 2964, 2935, 2870, 2840 (C-H aliph.), 1650 (C=N), 1248 (C=S); ^1H NMR (300 MHz, CDCl_3) δ : 0.94–0.99 (m, 3H, $-\text{CH}_2-\text{CH}_2-\text{CH}_2-\text{CH}_3$), 1.34–1.41 (m, 2H, $-\text{CH}_2-\text{CH}_2-\text{CH}_2-\text{CH}_3$), 1.62 (m, 2H, $-\text{CH}_2-\text{CH}_2-\text{CH}_2-\text{CH}_3$), 2.36 (s, 3H, 7-CH₃), 2.66 (s, 3H, 5-CH₃), 3.04 (m, 4H, CH_2 —piperazine), 3.24–3.26 (m, 4H, CH_2 —piperazine), 3.47 (s, 3H, 3-CH₃), 3.81 (s, 3H, O-CH₃), 3.85–3.90 (m, 2H, $-\text{CH}_2-\text{CH}_2-\text{CH}_2-\text{CH}_3$), 5.15 (s, 2H, N-CH₂-N) 5.29 (s, 2H, O-CH₂-); 6.92–6.95 (m, 2H, Ar-H), 7.04–7.09 (m, 3H, Ar-H), 7.29–7.37 (m, 3H, Ar-H); ^{13}C NMR (75 MHz, CDCl_3) δ : 10.61, 11.20, 13.68, 20.03, 32.32, 36.95, 43.93, 48.83, 50.34, 55.51, 57.10, 69.57, 108.09, 111.75, 112.42, 114.84, 116.04, 118.98, 122.15, 126.18, 128.83, 129.14, 129.59, 131.24, 147.18, 147.85, 151.37, 159.09, 160.51, 170.78; HRMS (ESI-MS) (m/z): calcd. for $\text{C}_{35}\text{H}_{41}\text{F}_3\text{N}_8\text{O}_3\text{S}$ [$\text{L}+\text{H}$]⁺: 711.3047; found: 711.3031.

6c: 6-butyl-1-[[4-(4-methoxyphenyl)-2-[[4-[(4-methyl)phenyl]piperazin-1-yl]methyl]-3-thioxo-2H-1,2,4-triazol-5-yl]methoxy]-3,5,7-trimethyl-pyrrolo[3,4-d]pyridazin-4-one

Yield: 74.21%; m.p.: 151–153 °C;

FT-IR (selected lines, γ_{\max} , cm^{-1}): 2958, 2934, 2860, 2837 (C-H aliph.), 1651 (C=N), 1247 (C=S); ^1H NMR (300 MHz, CDCl_3) δ : 0.94–0.99 (m, 3H, $-\text{CH}_2-\text{CH}_2-\text{CH}_2-\text{CH}_3$), 1.36–1.41 (m, 2H, $-\text{CH}_2-\text{CH}_2-\text{CH}_2-\text{CH}_3$), 1.62 (m, 2H, $-\text{CH}_2-\text{CH}_2-\text{CH}_2-\text{CH}_3$), 2.27 (s, 3H, Ar-CH₃), 2.37 (s, 3H, 7-CH₃), 2.66 (s, 3H, 5-CH₃), 3.07 (m, 4H, CH_2 —piperazine), 3.17 (m, 4H, CH_2 —piperazine), 3.47 (s, 3H, 3-CH₃), 3.81 (s, 3H, O-CH₃), 3.85–3.90 (m, 2H, $-\text{CH}_2-\text{CH}_2-\text{CH}_2-\text{CH}_3$), 5.15 (s, 2H, N-CH₂-N) 5.29 (s, 2H, O-CH₂-); 6.85 (m, 2H, Ar-H), 6.92–6.95 (m, 2H, Ar-H), 7.07–7.09 (m, 2H, Ar-H), 7.25–7.29 (m, 2H, Ar-H); ^{13}C NMR (75 MHz, CDCl_3) δ : 10.63, 11.28, 13.72, 20.05, 20.46, 32.33, 36.97, 43.94, 50.43, 55.51, 57.11, 69.61, 108.08, 111.74, 114.82, 116.86,

117.24, 122.21, 126.22, 128.85, 129.10, 129.71, 147.12, 147.88, 159.11, 160.48, 170.75; HRMS (ESI-MS) (m/z): calcd. for $C_{35}H_{44}N_8O_3S$ [L+H]⁺: 657.3330; found: 657.3316.

General Procedure for Preparation of S-Substituted Derivatives of Pyrrolo[3,4-*d*]pyridazinone (7a-c-9a-c)

The appropriate 4-substituted-1,2,4-triazole derivative of pyrrolo[3,4-*d*]pyridazinone (3a, 3b or 3c) (0.001 mol) was suspended in 30 mL of anhydrous ethanol in a round bottom flask. Next, the 1 mL of 1M sodium ethoxide (0.001 mol) and the appropriate 2-chloro-1-oxoethyl aryl piperazine derivative was added, and the mixture was refluxed for 4–6 h. TLC monitored the reaction progress. After the completion of synthesis, the mixture was cooled, and the precipitate was formed. Finally, the solid was filtered off, washed thoroughly with ethanol and, afterward, purified by crystallization from this solvent.

7a:6-butyl-3,5,7-trimethyl-1-[[4-methyl-3-[2-oxo-2-(4-phenylpiperazin-1-yl)ethyl]sulfanyl-2*H*-1,2,4-triazol-5-yl]methoxy]pyrrolo[3,4-*d*]pyridazin-4-one

Yield: 62.52%; m.p.: 183–184 °C;

FT-IR (selected lines, γ_{max} , cm^{-1}): 3054 (C-H arom.), 2961, 2922, 2873 (C-H aliph.), 1639 (C=O), 1268 (C=S); ¹H NMR (300 MHz, CDCl₃) δ : 0.93–0.98 (m, 3H, -CH₂-CH₂ CH₂-CH₃), 1.33–1.41 (m, 2H, -CH₂-CH₂ CH₂-CH₃), 1.59–1.62 (m, 2H, -CH₂-CH₂ CH₂-CH₃), 2.41 (s, 3H, 7-CH₃), 2.68 (s, 3H, 5-CH₃), 3.17–3.19 (m, 2H, CH₂—piperazine), 3.23 (m, 2H, CH₂—piperazine), 3.57 (s, 3H, 3-CH₃), 3.66 (s, 3H, triazole-*N*-CH₃), 3.78 (m, 4H, CH₂—piperazine), 3.86–3.91 (m, 2H, -CH₂-CH₂ CH₂-CH₃), 4.38 (s, 2H, S-CH₂) 5.44 (s, 2H, O-CH₂-); 6.92–6.94 (m, 3H, Ar-H), 7.28–7.31 (m, 2H, Ar-H); ¹³C NMR (75 MHz, CDCl₃) δ : 10.64, 11.21, 13.68, 20.04, 30.54, 32.32, 36.57, 37.02, 42.21, 43.93, 46.11, 49.33, 49.74, 57.45, 108.27, 111.86, 116.80, 120.80, 122.29, 129.19, 129.29, 148.33, 151.80, 152.30, 159.19, 165.55; HRMS (ESI-MS) (m/z): calcd. for $C_{29}H_{38}N_8O_3S$ [L+H]⁺: 579.2860; found: 579.2843.

8a:6-butyl-3,5,7-trimethyl-1-[[4-methyl-3-[2-oxo-2-[4-[3-(trifluoromethyl)phenyl]piperazin-1-yl]ethyl]sulfanyl-2*H*-1,2,4-triazol-5-yl]methoxy]pyrrolo[3,4-*d*]pyridazin-4-one

Yield: 56.41%; m.p.: 201–202 °C;

FT-IR (selected lines, γ_{max} , cm^{-1}): 2964, 2934, 2919 (C-H aliph.) 1226 (C=S); ¹H NMR (300 MHz, CDCl₃) δ : 0.93–0.98 (m, 3H, -CH₂-CH₂ CH₂-CH₃), 1.33–1.41 (m, 2H, -CH₂-CH₂ CH₂-CH₃), 1.59–1.62 (m, 2H, -CH₂-CH₂ CH₂-CH₃), 2.42 (s, 3H, 7-CH₃), 2.68 (s, 3H, 5-CH₃), 3.23 (m, 2H, CH₂—piperazine), 3.31 (m, 2H, CH₂—piperazine), 3.57 (s, 3H, 3-CH₃), 3.68 (s, 3H, triazole-*N*-CH₃), 3.80–3.84 (m, 4H, CH₂—piperazine), 3.86–3.91 (m, 2H, -CH₂-CH₂ CH₂-CH₃), 4.41 (s, 2H, S-CH₂) 5.44 (s, 2H, O-CH₂-); 7.08–7.16 (m, 3H, Ar-H), 7.35–7.41 (m, 1H, Ar-H); ¹³C NMR (75 MHz, CDCl₃) δ : 10.64, 11.22, 13.68, 20.04, 30.68, 32.32, 36.56, 37.02, 42.01, 43.94, 45.90, 48.85, 49.21, 57.33, 108.21, 111.83, 112.97, 117.10, 119.54, 122.29, 129.25, 129.79, 131.43, 131.85, 148.26, 150.69, 151.83, 152.31, 159.17, 165.51; MS (ESI-MS) (m/z): calcd. for $C_{30}H_{37}F_3N_8O_3S$ [L+H]⁺: 647.2734; found: 647.2680.

9a:6-butyl-3,5,7-trimethyl-1-[[4-methyl-3-[2-oxo-2-[4-[4-(methyl)phenyl]piperazin-1-yl]ethyl]sulfanyl-2*H*-1,2,4-triazol-5-yl]methoxy]pyrrolo[3,4-*d*]pyridazin-4-one

Yield: 59.49%; m.p.: 190–191 °C;

FT-IR (selected lines, γ_{max} , cm^{-1}): 2960, 2919, 2851 (C-H aliph.), 1643 (C=O) 1227 (C=S); ¹H NMR (300 MHz, CDCl₃) δ : 0.93–0.98 (m, 3H, -CH₂-CH₂ CH₂-CH₃), 1.34–1.41 (m, 2H, -CH₂-CH₂ CH₂-CH₃), 1.62 (m, 2H, -CH₂-CH₂ CH₂-CH₃), 2.27 (s, 3H, Ar-CH₃), 2.41 (s, 3H, 7-CH₃), 2.68 (s, 3H, 5-CH₃), 3.11 (m, 4H, CH₂—piperazine), 3.57 (s, 3H, 3-CH₃), 3.66 (s, 3H, triazole-*N*-CH₃), 3.78 (m, 4H, CH₂—piperazine), 3.86–3.91 (m, 2H, -CH₂-CH₂ CH₂-CH₃), 4.38 (s, 2H, S-CH₂) 5.44 (s, 2H, O-CH₂-); 6.86 (m, 2H, Ar-H), 7.08–7.11 (m, 2H, Ar-H); ¹³C NMR (75 MHz, CDCl₃) δ : 10.64, 11.22, 13.68, 20.04, 20.45 30.54, 32.32, 36.67, 37.03, 42.26, 43.93, 46.16, 49.88, 50.27, 57.46, 108.28, 111.87, 117.14, 122.29, 129.19, 129.81, 148.33, 151.84, 152.29, 159.19, 165.50; MS (ESI-MS) (m/z): calcd. for $C_{30}H_{40}N_8O_3S$ [L+H]⁺: 593.3017; found: 593.3092.

7b:6-butyl-3,5,7-trimethyl-1-[[4-phenyl-3-[2-oxo-2-(4-phenylpiperazin-1-yl)ethyl]sulfanyl-2H-1,2,4-triazol-5-yl]methoxy]pyrrolo[3,4-d]pyridazin-4-one

Yield: 53.83%; m.p.: 126–128 °C;

FT-IR (selected lines, γ_{\max} , cm^{-1}): 3053 (C-H arom.), 2929, 2871 (C-H aliph.), 1636 (C=O); ^1H NMR (300 MHz, CDCl_3) δ : 0.94–0.99 (m, 3H, $-\text{CH}_2-\text{CH}_2-\text{CH}_2-\text{CH}_3$), 1.33–1.41 (m, 2H, $-\text{CH}_2-\text{CH}_2-\text{CH}_2-\text{CH}_3$), 1.59–1.61 (m, 2H, $-\text{CH}_2-\text{CH}_2-\text{CH}_2-\text{CH}_3$), 2.33 (s, 3H, 7- CH_3), 2.66 (s, 3H, 5- CH_3), 3.17 (m, 2H, CH_2 —piperazine), 3.23 (m, 2H, CH_2 —piperazine), 3.46 (s, 3H, 3- CH_3), 3.78 (m, 4H, CH_2 —piperazine), 3.84–3.89 (m, 2H, $-\text{CH}_2-\text{CH}_2-\text{CH}_2-\text{CH}_3$), 4.42 (s, 2H, S- CH_2) 5.31 (s, 2H, O- CH_2 -); 6.89–6.94 (m, 3H, Ar-H), 7.29–7.34 (m, 4H, Ar-H), 7.44–7.46 (m, 3H, Ar-H); ^{13}C NMR (75 MHz, CDCl_3) δ : 10.61, 11.19, 13.70, 20.04, 32.32, 36.32, 42.18, 43.87, 46.13, 49.26, 49.72, 56.94, 108.24, 111.78, 116.76, 120.72, 122.21, 126.65, 129.27, 129.91, 130.21, 132.60, 148.15, 150.76, 152.28, 159.13, 165.54; MS (ESI-MS) (m/z): calcd. for $\text{C}_{34}\text{H}_{40}\text{N}_8\text{O}_3\text{S}$ [$\text{L}+\text{H}$] $^+$: 641.3017; found: 641.2935.

8b:6-butyl-3,5,7-trimethyl-1-[[4-phenyl-3-[2-oxo-2-[4-[3-(trifluoromethyl)phenyl]piperazin-1-yl]ethyl]sulfanyl-2H-1,2,4-triazol-5-yl]methoxy]pyrrolo[3,4-d]pyridazin-4-one

Yield: 60.84%; m.p.: 141–143 °C;

FT-IR (selected lines, γ_{\max} , cm^{-1}): 3053 (C-H arom.), 2959, 2930, 2872 (C-H aliph.), 1635 (C=O); ^1H NMR (300 MHz, CDCl_3) δ : 0.94–0.99 (m, 3H, $-\text{CH}_2-\text{CH}_2-\text{CH}_2-\text{CH}_3$), 1.33–1.40 (m, 2H, $-\text{CH}_2-\text{CH}_2-\text{CH}_2-\text{CH}_3$), 1.59–1.61 (m, 2H, $-\text{CH}_2-\text{CH}_2-\text{CH}_2-\text{CH}_3$), 2.33 (s, 3H, 7- CH_3), 2.65 (s, 3H, 5- CH_3), 3.22 (m, 2H, CH_2 —piperazine), 3.30 (m, 2H, CH_2 —piperazine), 3.45 (s, 3H, 3- CH_3), 3.81–3.84 (m, 4H, CH_2 —piperazine), 3.86–3.89 (m, 2H, $-\text{CH}_2-\text{CH}_2-\text{CH}_2-\text{CH}_3$), 4.39 (s, 2H, S- CH_2) 5.31 (s, 2H, O- CH_2 -); 7.06–7.15 (m, 3H, Ar-H), 7.31–7.35 (m, 2H, Ar-H), 7.37–7.40 (m, 1H, Ar-H), 7.44–7.46 (m, 3H, Ar-H); ^{13}C NMR (75 MHz, CDCl_3) δ : 10.61, 11.18, 13.69, 20.03, 32.31, 36.02, 36.94, 41.98, 43.87, 45.92, 48.76, 49.17, 56.92, 108.21, 108.23, 111.78, 112.93, 116.94, 119.44, 122.20, 125.95, 126.64, 128.92, 129.76, 129.92, 130.25, 131.43, 131.86, 132.57, 148.13, 150.85, 152.34, 152.34, 159.13, 165.65; MS (ESI-MS) (m/z): calcd. for $\text{C}_{35}\text{H}_{39}\text{F}_3\text{N}_8\text{O}_3\text{S}$ [$\text{L}+\text{H}$] $^+$: 708.2891; found: 708.2827.

9b:6-butyl-3,5,7-trimethyl-1-[[4-phenyl-3-[2-oxo-2-[4-[4-(methyl)phenyl]piperazin-1-yl]ethyl]sulfanyl-2H-1,2,4-triazol-5-yl]methoxy]pyrrolo[3,4-d]pyridazin-4-one

Yield: 55.89%; m.p.: 129–131 °C;

FT-IR (selected lines, γ_{\max} , cm^{-1}): 2958, 2925, 2870 (C-H aliph.), 1639 (C=O); ^1H NMR (300 MHz, CDCl_3) δ : 0.94–0.99 (m, 3H, $-\text{CH}_2-\text{CH}_2-\text{CH}_2-\text{CH}_3$), 1.35–1.38 (m, 2H, $-\text{CH}_2-\text{CH}_2-\text{CH}_2-\text{CH}_3$), 1.61 (m, 2H, $-\text{CH}_2-\text{CH}_2-\text{CH}_2-\text{CH}_3$), 2.28 (s, 3H, Ar- CH_3), 2.33 (s, 3H, 7- CH_3), 2.65 (s, 3H, 5- CH_3), 3.11–3.16 (m, 4H, CH_2 —piperazine), 3.45 (s, 3H, 3- CH_3), 3.76 (m, 4H, CH_2 —piperazine), 3.84–3.89 (m, 2H, $-\text{CH}_2-\text{CH}_2-\text{CH}_2-\text{CH}_3$), 4.41 (s, 2H, S- CH_2) 5.31 (s, 2H, O- CH_2 -); 6.83–6.86 (m, 2H, Ar-H), 7.08–7.11 (m, 2H, Ar-H), 7.33–7.34 (m, 2H, Ar-H), 7.43–7.46 (m, 3H, Ar-H); ^{13}C NMR (75 MHz, CDCl_3) δ : 10.60, 10.98, 11.19, 13.69, 20.02, 20.43, 32.31, 36.39, 36.94, 42.23, 43.87, 46.17, 49.81, 50.28, 56.94, 108.25, 111.78, 117.111, 122.21, 126.76, 127.16, 128.89, 129.78, 129.90, 130.19, 130.36, 132.61, 133.46, 148.16, 148.65, 152.25, 159.13, 165.49; MS (ESI-MS) (m/z): calcd. for $\text{C}_{35}\text{H}_{42}\text{N}_8\text{O}_3\text{S}$ [$\text{L}+\text{Na}$] $^+$: 677.2993; found: 677.2945.

7c:6-butyl-3,5,7-trimethyl-1-[[4-(4-methoxy)phenyl-3-[2-oxo-2-(4-phenylpiperazin-1-yl)ethyl]sulfanyl-2H-1,2,4-triazol-5-yl]methoxy]pyrrolo[3,4-d]pyridazin-4-one

Yield: 59.71%; m.p.: 150–152 °C;

FT-IR (selected lines, γ_{\max} , cm^{-1}): 3060, (C-H arom.), 2957, 2929, 2871 (C-H aliph.), 1640 (C=O), 1271 (C=S); ^1H NMR (300 MHz, CDCl_3) δ : 0.94–0.99 (m, 3H, $-\text{CH}_2-\text{CH}_2-\text{CH}_2-\text{CH}_3$), 1.36–1.39 (m, 2H, $-\text{CH}_2-\text{CH}_2-\text{CH}_2-\text{CH}_3$), 1.61 (m, 2H, $-\text{CH}_2-\text{CH}_2-\text{CH}_2-\text{CH}_3$), 2.36 (s, 3H, 7- CH_3), 2.66 (s, 3H, 5- CH_3), 3.16 (m, 2H, CH_2 —piperazine), 3.23 (m, 2H, CH_2 —piperazine), 3.47 (s, 3H, 3- CH_3), 3.78 (m, 4H, CH_2 —piperazine), 3.81 (s, 3H, O- CH_3), 3.84–3.89 (m, 2H, $-\text{CH}_2-\text{CH}_2-\text{CH}_2-\text{CH}_3$), 4.40 (s, 2H, S- CH_2) 5.28 (s, 2H, O- CH_2 -); 6.89–6.94 (m, 5H, Ar-H), 7.21–7.31 (m, 4H, Ar-H); ^{13}C NMR (75 MHz, CDCl_3) δ : 10.62, 11.23, 13.71, 20.05, 32.32, 36.22, 36.95, 42.16, 43.89, 46.12, 49.25, 49.72, 55.59, 56.94, 108.29, 111.78, 114.99,

116.75, 120.71, 122.23, 124.91, 127.97, 128.87, 129.28, 148.24, 150.76, 152.55, 153.09, 159.13, 160.71, 165.58; HRMS (ESI-MS) (m/z): calcd. for $C_{35}H_{42}N_8O_4S [L+Na]^+$: 693.2942; found: 693.2956.

8c: 6-butyl-3,5,7-trimethyl-1-[[4-(4-methoxy)phenyl-3-[2-oxo-2-[4-[3-(trifluoromethyl)phenyl]piperazin-1-yl]ethyl]sulfanyl-2H-1,2,4-triazol-5-yl]methoxy]pyrrolo[3,4-*d*]pyridazin-4-one

Yield: 69.10%; m.p.: 114–117 °C;

FT-IR (selected lines, γ_{max} , cm^{-1}): 2959, 2929, 2871 (C-H aliph.), 1644 (C=O); 1H NMR (300 MHz, $CDCl_3$) δ : 0.94–0.99 (m, 3H, $-CH_2-CH_2-CH_2-CH_3$), 1.33–1.41 (m, 2H, $-CH_2-CH_2-CH_2-CH_3$), 1.62 (m, 2H, $-CH_2-CH_2-CH_2-CH_3$), 2.36 (s, 3H, $7-CH_3$), 2.66 (s, 3H, 5- CH_3), 3.22 (m, 2H, CH_2 —piperazine), 3.29 (m, 2H, CH_2 —piperazine), 3.46 (s, 3H, 3- CH_3), 3.81 (s, 3H, O- CH_3), 3.84 (m, 4H, CH_2 —piperazine), 3.86–3.89 (m, 2H, $-CH_2-CH_2-CH_2-CH_3$), 4.37 (s, 2H, S- CH_2), 5.28 (s, 2H, O- CH_2 -); 7.89–6.92 (m, 2H, Ar-H), 7.05–7.14 (m, 3H, Ar-H), 7.21–7.24 (m, 2H, Ar-H), 7.35–7.40 (m, 1H, Ar-H); ^{13}C NMR (75 MHz, $CDCl_3$) δ : 10.59, 11.21, 13.69, 20.03, 32.32, 35.86, 36.94, 41.98, 43.88, 45.92, 48.72, 49.14, 55.57, 56.92, 108.30, 111.79, 112.88, 114.99, 116.87, 119.39, 122.21, 124.91, 127.97, 128.90, 129.75, 131.42, 131.84, 148.22, 150.89, 152.62, 152.91, 159.12, 160.74, 165.72; HRMS (ESI-MS) (m/z): calcd. for $C_{36}H_{41}F_3N_8O_4S [L+Na]^+$: 761.2816; found: 761.2812.

9c: 6-butyl-3,5,7-trimethyl-1-[[4-(4-methoxy)phenyl-3-[2-oxo-2-[4-[4-(methyl)phenyl]piperazin-1-yl]ethyl]sulfanyl-2H-1,2,4-triazol-5-yl]methoxy]pyrrolo[3,4-*d*]pyridazin-4-one

Yield: 67.44%; m.p.: 119–121 °C;

FT-IR (selected lines, γ_{max} , cm^{-1}): 3052, 3002 (C-H arom.), 2957, 2922, 2871 (C-H aliph.), 1643 (C=O); 1H NMR (300 MHz, $CDCl_3$) δ : 0.94–0.99 (m, 3H, $-CH_2-CH_2-CH_2-CH_3$), 1.34–1.41 (m, 2H, $-CH_2-CH_2-CH_2-CH_3$), 1.59–1.61 (m, 2H, $-CH_2-CH_2-CH_2-CH_3$), 2.28 (s, 3H, Ar- CH_3), 2.36 (s, 3H, 7- CH_3), 2.66 (s, 3H, 5- CH_3), 3.10 (m, 2H, CH_2 —piperazine), 3.16 (m, 2H, CH_2 —piperazine), 3.46 (s, 3H, 3- CH_3), 3.78 (m, 4H, CH_2 —piperazine), 3.81 (s, 3H, O- CH_3), 3.84–3.89 (m, 2H, $-CH_2-CH_2-CH_2-CH_3$), 4.40 (s, 2H, S- CH_2), 5.28 (s, 2H, O- CH_2 -); 6.83–6.2 (m, 4H, Ar-H), 7.08–7.11 (m, 2H, Ar-H), 7.21–7.24 (m, 2H, Ar-H); ^{13}C NMR (75 MHz, $CDCl_3$) δ : 10.61, 11.22, 13.69, 20.04, 20.44, 32.32, 36.28, 36.95, 42.22, 43.88, 46.18, 49.81, 50.29, 55.58, 56.94, 108.30, 111.79, 114.99, 117.10, 122.22, 124.94, 127.97, 128.87, 129.79, 130.35, 148.24, 148.66, 152.54, 153.11, 159.13, 160.72, 165.54; HRMS (ESI-MS) (m/z): calcd. for $C_{36}H_{44}N_8O_4S [L+H]^+$: 685.3279; found: 685.3246.

3.2. Biological Evaluation

3.2.1. Cell Line and Conditions

Normal human dermal fibroblasts (NHDF) were purchased from Lonza and used in bioassays between 7–12 passages. The cells were incubated in 5% CO_2 , 95% humidity at 37 °C with morphology and confluence assessments twice weekly using EVOS FL microscopy. The cells were passaged with TrypLE solution when the cell confluence was greater than 70%. The cells were transferred to a tube and centrifuged at $1000 \times g$ for 5 min. Then, the supernatant was removed, and the cells were resuspended in a fresh medium, and the number of cells was counted using the Burcher chamber. Finally, the cells were plated on the assay plates or reduced by about half and placed back in the culture flasks. The NHDF cells were grown in Dulbecco's modified Eagle's medium (DMEM) without phenol red supplemented with 10% fetal bovine serum (FBS), 2 mM ultra-glutamine and 2 $\mu g/mL$ gentamicin and streptomycin. The medium was stored at 4–8 °C for one month or until used.

3.2.2. Tested Compounds

The tested compounds were dissolved in dimethyl sulfoxide (DMSO) to form 10 mM stock solutions which were stored at -20 °C. These compounds were thawed immediately before the preparation of the bioassay concentrations. The concentration range of 10–100 μM was used, so the DMSO concentration did not exceed 1% at the higher concen-

tration tested. The bioassay concentrations were prepared in DMEM without phenol red, which was supplemented as a medium for traditional cultures, but with a reduced amount of FBS to 5%.

3.2.3. Cyclooxygenase Inhibition Assay

The cyclooxygenase (COX) inhibition was evaluated using a ready-to-used test from the Cayman company. In this study, the only 100 μ M concentrations that were tested, each in triplicate, for the obtained results were calculated IC_{50} —concentration, which inhibited activity of COX-1 or COX-2 about 50% compared to 100% activity of these enzymes. In these studies, *Meloxicam*, *Diclofenac* and *Celecoxib* were used as reference compounds.

3.2.4. MTT Assay

The assessment of cell viability after 24-hour incubation with the test compounds was performed according to ISO 10993 Part 5 Appendix C. The cells were seeded at 10,000 cells per well and left in a CO₂ incubator overnight to allow the cells to adhere. Non-adherent cells were removed with the medium, and freshly prepared concentrations of test compounds were added for 24 h. During the last hour of 24-hour incubation, the cells were assessed microscopically according to the ISO 10,993 scale for cytotoxicity. The medium with the compounds was replaced with a 1 mg/mL MTT in phosphate buffered saline (PBS) for 2 h at 37 °C. The solution was then gently removed and the purple crystals dissolved in isopropanol, and the absorbance was measured at 570 nm with a VirusScan microplate reader.

3.2.5. Anti-Inflammatory and Antioxidant Activity

To evaluate the anti-inflammatory and antioxidant activity of the tested compounds, the MTT, DCF-DA and Griess assays were performed. In the first assay, the NHDF cells were seeded at a density of 10,000 cells per well, and in the other assay, 40,000 cells per well. After the cells adhered overnight, the supernatant with the non-adherent cells was replaced with 50 μ g/mL lipopolysaccharide (LPS) for 24 h. Next, the cells were washed, and freshly prepared concentrations of the test compounds were added for 24 h. Then, the culture plate was washed for MTT assay, and the procedure described in Section 3.2.4. was used. To evaluate the free radicals scavenging of tested the compounds, the 50 μ L supernatant was transferred to a new plate. The rest of the supernatant was removed and 25 μ M of DCF-DA solution in MEM without phenol red was added for 1 h at 37 °C to measure the reactive oxygen species (ROS) and into collected supernatant 50 μ M mixture reagent A and reagent B in a volume ratio 1:1 for 20 min at RT in the dark to measure the nitric oxide (NO). The ROS was measured at 498 nm excitation and 535 nm emission, and NO at 548 nm using a VirusScan microplate reader.

3.3. Molecular Docking

The structure optimization was performed using the DFT/B3LYP method combined with the 6-311+G (d,p) basis set. From the Protein Data Bank (<http://www.rcsb.org>, accessed on 1 May 2021), the following crystal structure was selected for the docking studies: 4O1Z, 4M11, 3V03. The ligand and receptor files were prepared using AutoDock 4.2.6 software and AutoDock Tools 1.5.6. All of the ligands and water molecules were removed, and then polar hydrogen atoms and Kollman charges were added to the protein structure. To prepare the ligand molecules, the partial charges were calculated, non-polar hydrogens were merged, and rotatable bonds were assigned. The interactions with COX-1, COX-2 and BSA were performed using AutoDock Script downloaded from The Scripps Research Institute (TSRI). The centers of the grid boxes for COX-1 and COX-2 were set according to the *Meloxicam* binding site in the crystal structure 4O1Z, 4M11. The centers of the grid boxes for BSA were set according to the binding site I phenylbutazone (PDB ID: 2BXC) and site II *Ibuprofen* (PDB ID: 2BXG) on HSA [58]. The Lamarckian genetic algorithm was selected for the conformational search. The running times of the genetic algorithm

and the evaluation times were set to 100 and 2.5million, respectively. After the molecular docking, the ligand–receptor complexes were further analyzed using Discovery Studio software (<http://accelrys.com/>, accessed on 1 May 2021).

3.4. Spectroscopic Studies

3.4.1. Fluorescence

The spectroscopic fluorescence studies were performed using a Cary Eclipse 500 spectrophotometer (Agilent, Santa Clara, CA, USA). A concentration of BSA was $1.0 \times 10^{-6} \text{ mol}\cdot\text{dm}^{-3}$. A solution of BSA was titrated by successive additions of $1.0 \times 10^{-3} \text{ mol}\cdot\text{dm}^{-3}$ solution of the studied compounds to give a final concentration of 0.2×10^{-6} – $2.0 \times 10^{-6} \text{ mol}\cdot\text{dm}^{-3}$. Experiments were carried out at three temperatures: 297, 303, and 308 K in pH = 7.4. The quenching spectra were recorded at excitation and an emission wavelength of 280 nm and 300–500 nm. The molar ratio compound/BSA was 0.1–2.0 with 0.2 steps. Binding site identification studies were indicated in the presence of the two site markers, *Phenylbutazone* (PHB) and *Ibuprofen* (IBP), as sites I and II markers, respectively. Concentrations of BSA and site markers were set at 1.0×10^{-6} and $3.0 \times 10^{-6} \text{ mol}\cdot\text{dm}^{-3}$, respectively.

3.4.2. Circular Dichroism

Circular dichroism (CD) spectra were measured on the Jasco J-1500 magnetic circular dichroism spectrometer. All of the measurements for the BSA solutions in the absence and presence of the analyzed compounds were made at room temperature under simulated physiological conditions in pH 7.4, in phosphate buffer as a solvent. The CD spectra were collected in the range of 205–250 nm at a scan rate speed of 50 nm min^{-1} , with a response time of 1 s, 10 mm path length, and were baseline corrected. The concentrations of BSA and the analyzed compounds were $1 \times 10^{-6} \text{ mol}\cdot\text{dm}^{-3}$ and $1 \times 10^{-3} \text{ mol}\cdot\text{dm}^{-3}$, respectively. BSA performed experiments on each analyzed compound in molar ratios: 1:0, 1:0.5, 1:1, 1:5 and 1:10.

3.4.3. FT-IR Measurement

Infrared spectra were recorded on the Nicolet iS50 FT-IR (Thermo Fisher Scientific, Waltham, MA, USA) equipped with a deuterated triglycine sulphate (DTGS) detector and KBr beam splitter. The spectra were obtained at room temperature using the attenuated total reflectance (ATR) method. The spectral data were recorded within 4000 to 600 cm^{-1} with resolution 4 cm^{-1} and 100 scans were averaged for each spectrum.

Bovine serum albumin (Sigma Aldrich) was dissolved in an aqueous solution containing phosphate buffer (pH = 7.5) (Sigma Aldrich) to obtain $0.02 \text{ mol}\cdot\text{dm}^{-1}$ concentration. The concentration of the studied compounds was $0.01 \text{ mol}\cdot\text{dm}^{-1}$ and solutions were prepared in methanol (Chempur). The $200 \mu\text{L}$ solution of BSA was mixed with the appropriate amount of the compounds solution to achieve 0.25, 0.50, 0.75 and 1.0 molar ratio and $10 \mu\text{L}$ of mixture was dropped on the crystal to register a spectrum.

The analysis of the secondary structure was proceeded by Omnic 9.3.30 (Thermo Fisher Scientific Inc.) software. The analysis of the FT-IR spectra was evaluated by the Byler and Susi procedure [56]. After normalization of each spectrum, the fragment with the peak 1650 cm^{-1} was extracted, and a second derivate was made. The major peaks are characteristic for the α -helix (1660 – 1650 cm^{-1}), β -sheet (1640 – 1610 cm^{-1}), β -turn (1691 – 1680 cm^{-1}), β -antiparallel (1660 – 1650 cm^{-1}) and random coil (1650 – 1640 cm^{-1}) [56,62–64]. The self-deconvolution and curve-fitting by Gaussian function allowed for us to determine the intensity and total area under peaks. The calculation of the percentage of area peaks corresponds with the contribution of the type of structure.

3.5. Statistical Analysis

The biological results are shown again as the mean \pm SD of the IC_{50} in the cyclooxygenase inhibition assay and the E/E_0 ratio in the remaining assays. E is the mean result for

the compounds tested, and E_0 is the mean result for the controls. For the viability assay, E_0 cells were incubated only with a medium without the test compounds. In assessing the anti-inflammatory activity of the tested compounds, cells treated with only 50 $\mu\text{g}/\text{mL}$ LPS were controls. The statistical analyses were performed using the Statistica program. One-way ANOVA and Tukey post-hoc analysis were calculated. The p -value was set at 0.05.

4. Conclusions

The present paper describes the design, synthesis and complex biological, computational and also spectroscopic studies of novel, three series of N -substituted-1,2,4-triazole-based derivatives of pyrrolo[3,4- d]pyridazinone. The structures of the title compounds were inspired by the results of our previous investigations and most recent literature reports. Their formation relied on the molecular hybridization of the biheterocyclic scaffold of pyrrolo[3,4- d]pyridazinone, N -substituted-1,2,4-triazole moiety and aryl piperazine pharmacophore (Scheme 1, Figure 7). Our goal was to receive potent anti-inflammatory agents with possibly the best affinity towards an inducible COX-2 isoform. The evaluation of the viability revealed that five compounds **8a-c**, **9b**, **9c** cause cell lysis and were excluded from further examination. The results of in vitro COX inhibition assay indicate that molecules **4a-7a**, **9a**, **4b**, **7b** and **4c** have good, comparable to *Meloxicam*, inhibitory activity towards COX-2 isoenzyme and are characterized by a promising COX-2/COX-1 selectivity ratio. Moreover, derivatives **4a**, **6a**, **9a** and **4c** acted as selective COX-2 inhibitors. These findings were supported by the results of the molecular docking studies, according to which, new molecules take position in the active site of COX-2 very similar to *Meloxicam* and did not show an affinity to COX-1 isoform. What is more, the potential good anti-inflammatory and antioxidant activity of the examined derivatives was confirmed in the performed in vitro evaluation within cells. As it has already been stated, all molecules bind and interact with serum albumin, which is the most abundant protein in blood. Some of them, especially those belonging to series **a**, exert promising and beneficial properties in the executed in silico ADME prediction.

Taking the above information into account, we can summarize that title N -substituted-1,2,4-triazole-based derivatives of pyrrolo[3,4- d]pyridazinone can serve as promising and valuable structures in the development of novel anti-inflammatory agents. Undoubtedly, further, extended investigations, especially in vivo experiments, concerning these compounds are necessary. Moreover, based on the described biological, computational, structure–activity relationship (SAR) and ADME study, we are going to perform rational structural modifications of the reported derivatives in order to receive a new series of potent and effective molecules.

Supplementary Materials: The following are available online at <https://www.mdpi.com/article/10.3390/ijms222011235/s1>: The structures of all reported compounds **2a-c-9a-c** (Table S1), the ^1H and ^{13}C NMR (Table S2), ESI-MS (Table S3), FT-IR (Table S4), spectra of reported derivatives. Molecular formula strings (CSV) (Table S5). BSA binding interactions—CD spectra (Table S6), FT-IR spectra (Tables S7 and S8).

Author Contributions: Conceptualization, Ł.S. and P.Ś.; methodology, Ł.S., P.Ś., E.K., B.W., A.M. and A.K.; software, E.K.; formal analysis, Ł.S., E.K., B.W., A.M. and A.K.; investigation, Ł.S., E.K., B.W., P.J., A.M. and A.K.; resources, P.Ś.; data curation, Ł.S.; writing—original draft preparation, Ł.S., E.K., B.W., A.M., A.K. and P.Ś.; writing—review and editing, Ł.S., E.K., B.W., P.J., A.M., A.K. and P.Ś.; visualization, Ł.S., E.K., B.W., A.M. and A.K.; supervision, Ł.S. and P.Ś.; project administration, Ł.S. and P.Ś.; funding acquisition, P.Ś. All authors have read and agreed to the published version of the manuscript.

Funding: This study was financially supported by the Ministry of Health subvention according to the number SUB.D070.21.094 from the IT Simple system of Wrocław Medical University.

Institutional Review Board Statement: Not applicable.

Informed Consent Statement: Not applicable.

Data Availability Statement: Calculations have been carried out in Wroclaw Centre for Networking and Supercomputing (<http://www.wcss.wroc.pl>, accessed on 1 May 2021).

Conflicts of Interest: The authors declare no conflict of interest.

Abbreviations

ADME, Absorption Distribution Metabolism Excretion; Arg, Arginine; ATR, Attenuated Total Reflectance; BBB, Blood Brain Barrier, BSA, Bovine Serum Albumin; CD, Circular Dichroism; COX, Cyclooxygenase; DCF-DA, Dichlorofluorescein Diacetate; DMEM, Dulbecco's Modified Eagle's Medium; DMSO, Dimethyl Sulfoxide; ELISA, Enzyme-Linked Immunosorbent Assay; ESI-MS, Electrospray Ionization Mass Spectrometry; FBS, Fetal Bovine Serum; FT-IR, Fourier Transform Infrared; GI, Gastrointestinal; HSA, Human Serum Albumine; IBP, *Ibuprofen*; IC, Inhibitory Concentration; Leu, Leucine; LPS, Lipopolysaccharide; MPO, Myeloperoxidase; MTT 3-(4,5-dimethylthiazol-2-yl)-2,5-diphenyltetrazolium bromide; MW, Molecular Weight; NA, Not Applicable; NHDF, Normal Human Dermal Fibroblasts; NMR, Nuclear Magnetic Resonance; NO, Nitric Oxide; NSAIDs, Non-Steroidal Anti-Inflammatory Drugs; PBS, Phosphate Buffered Saline; PGE₂, Prostaglandin E₂; PGs, Prostaglandins; PHB, *Phenylbutazone*; RONS, Reactive Oxygen and Nitrogen Species; Ro5, Rule of Five; ROS, Reactive Oxygen Species; RT, Room Temperature; SAR, Structure-Activity Relationship; SD, Standard Deviation; Ser, Serine; TLC, Thin Layer Chromatography; TMS, Tetramethylsilane; TPSA, Topological Polar Surface Area; Trp, Tryptophan; Tyr, Tyrosine.

References

- Nathan, C. Points of control in inflammation. *Nature* **2002**, *420*, 846–852. [CrossRef] [PubMed]
- Serhan, C.N.; Savill, J. Resolution of inflammation: The beginning programs the end. *Nat. Immunol.* **2005**, *6*, 1191–1197. [CrossRef] [PubMed]
- Negus, S.S.; Vanderah, T.W.; Brandt, M.R.; Bilsky, E.J.; Becerra, L.; Borsook, D. Preclinical Assessment of Candidate Analgesic Drugs: Recent Advances and Future Challenges. *J. Pharmacol. Exp. Ther.* **2006**, *319*, 507–514. [CrossRef] [PubMed]
- Medzhitov, R. Origin and physiological roles of inflammation. *Nature* **2008**, *454*, 428–435. [CrossRef] [PubMed]
- Leuti, A.; Fazio, D.; Fava, M.; Piccoli, A.; Oddi, S.; Maccarrone, M. Bioactive lipids, inflammation and chronic diseases. *Adv. Drug Deliv. Rev.* **2020**, *159*, 133–169. [CrossRef] [PubMed]
- Cashman, J.N. The Mechanisms of Action of NSAIDs in Analgesia. *Drugs* **1996**, *52*, 13–23. [CrossRef]
- Vane, J.R.; Botting, R.M. Mechanism of action of nonsteroidal anti-inflammatory drugs. *Am. J. Med.* **1998**, *104*, 25–85. [CrossRef]
- Marnett, L.J. Cyclooxygenase mechanisms. *Curr. Opin. Chem. Biol.* **2000**, *4*, 545–552. [CrossRef]
- Blobaum, A.L.; Marnett, L.J.; Hancock, A.B. Perspective Structural and Functional Basis of Cyclooxygenase Inhibition. *J. Med. Chem.* **2006**, *50*, 1425–1441. [CrossRef]
- Soliva, R.; Almansa, C.; Kalko, S.G.; Luque, J.; Orozco, M. Theoretical Studies on the Inhibition Mechanism of Cyclooxygenase-2. Is There a Unique Recognition Site? *J. Med. Chem.* **2003**, *46*, 1372–1382. [CrossRef]
- Sostres, C.; Gargallo, C.J.; Arroyo, M.T.; Lanás, A. Adverse effects of non-steroidal anti-inflammatory drugs (NSAIDs, aspirin and coxibs) on upper gastrointestinal tract. *Best Pract. Res. Clin. Gastroenterol.* **2010**, *24*, 121–132. [CrossRef]
- Soll, A.H.; McCarthy, D. NSAID-related gastrointestinal complications. *Clin. Cornerstone* **1999**, *1*, 42–56. [CrossRef]
- Wallace, J.L. NSAID gastropathy and enteropathy: Distinct pathogenesis likely necessitates distinct prevention strategies. *Br. J. Pharmacol.* **2012**, *165*, 67–74. [CrossRef]
- Laine, L. Gastrointestinal effects of NSAIDs and coxibs. *J. Pain Symptom Manag.* **2003**, *25*, 32–40. [CrossRef]
- Wallace, J.L.; Devchand, P.R. Emerging roles for cyclooxygenase-2 in gastrointestinal mucosal defense. *Br. J. Pharmacol.* **2005**, *145*, 275–282. [CrossRef]
- Cannon, C.P.; Cannon, P.J. Physiology. COX-2 inhibitors and cardiovascular risk. *Science* **2012**, *336*, 1386–1387. [CrossRef]
- Dogné, J.-M.; Supuran, C.T.; Pratico, D. Adverse Cardiovascular Effects of the Coxibs. *J. Med. Chem.* **2005**, *48*, 2251–2257. [CrossRef] [PubMed]
- Palkar, M.B.; Singhai, A.S.; Ronad, P.M.; Vishwanathswamy, A.H.M.; Boreddy, T.S.; Veerapur, V.P.; Shaikh, M.S.; Rane, R.A.; Karpoomath, R. Synthesis, pharmacological screening and in silico studies of new class of Diclofenac analogues as a promising anti-inflammatory agents. *Bioorganic Med. Chem.* **2014**, *22*, 2855–2866. [CrossRef] [PubMed]
- Avci, A.; Taşci, H.; Kandemir, Ü.; Can, Ö.D.; Gökhan-Kelekçi, N.; Tozkoparan, B. Synthesis, characterization, and in vivo pharmacological evaluation of novel mannich bases derived from 1,2,4-triazole containing a naproxen moiety. *Bioorg. Chem.* **2020**, *100*, 103892. [CrossRef]
- Alsayed, S.S.R.; Elshemy, H.A.H.; Abdelgawad, M.A.; Abdel-Latif, M.S.; Abdellatif, K.R.A. Design, synthesis and biological screening of some novel celecoxib and etoricoxib analogs with promising COX-2 selectivity, anti-inflammatory activity and gastric safety profile. *Bioorg. Chem.* **2017**, *70*, 173–183. [CrossRef] [PubMed]

21. Manjunatha, K.; Poojary, B.; Lobo, P.L.; Fernandes, J.; Kumari, N.S. Synthesis and biological evaluation of some 1,3,4-oxadiazole derivatives. *Eur. J. Med. Chem.* **2010**, *45*, 5225–5233. [CrossRef] [PubMed]
22. El-Sayed, N.A.; Nour, M.S.; Salem, M.A.; Arafa, R.K. New oxadiazoles with selective-COX-2 and EGFR dual inhibitory activity: Design, synthesis, cytotoxicity evaluation and in silico studies. *Eur. J. Med. Chem.* **2019**, *183*, 111693. [CrossRef]
23. Sağlık, B.N.; Osmaniye, D.; Levent, S.; Çevik, U.A.; Çavuşoğlu, B.K.; Özkay, Y.; Kaplancıklı, Z.A. Design, synthesis and biological assessment of new selective COX-2 inhibitors including methyl sulfonyl moiety. *Eur. J. Med. Chem.* **2021**, *209*, 112918. [CrossRef]
24. Jacob, P.J.; Manju, S.L. Identification and development of thiazole leads as COX-2/5-LOX inhibitors through in-vitro and in-vivo biological evaluation for anti-inflammatory activity. *Bioorg. Chem.* **2020**, *100*, 103882. [CrossRef] [PubMed]
25. Abdel-Aziz, S.A.; Taher, E.S.; Lan, P.; Asaad, G.F.; Gomaa, H.A.M.; El-Koussi, N.A.; Youssif, B.G.M. Design, synthesis, and biological evaluation of new pyrimidine-5-carbonitrile derivatives bearing 1,3-thiazole moiety as novel anti-inflammatory EGFR inhibitors with cardiac safety profile. *Bioorg. Chem.* **2021**, *111*, 104890. [CrossRef] [PubMed]
26. Abdellatif, K.R.A.; Abdelall, E.K.A.; Lamie, P.F.; Labib, M.B.; El-Nahaas, E.S.; Abdelhakeem, M.M. New pyrazole derivatives possessing amino/methanesulphonyl pharmacophore with good gastric safety profile: Design, synthesis, cyclooxygenase inhibition, anti-inflammatory activity and histopathological studies. *Bioorg. Chem.* **2020**, *95*, 103540. [CrossRef] [PubMed]
27. Abdellatif, K.R.; Abdelall, E.K.; Elshemy, H.A.; Lamie, P.F.; Elnahaas, E.; Amin, D.M. Design, synthesis of new anti-inflammatory agents with a pyrazole core: COX-1/COX-2 inhibition assays, anti-inflammatory, ulcerogenic, histopathological, molecular Modeling, and ADME studies. *J. Mol. Struct.* **2021**, *1240*, 130554. [CrossRef]
28. Abu-Rahma, G.E.D.A.A.; Abdel-Aziz, M.; Farag, N.A.; Kaoud, T.S. Novel 1-[4-(Aminosulfonyl)phenyl]-1H-1,2,4-triazole derivatives with remarkable selective COX-2 inhibition: Design, synthesis, molecular docking, anti-inflammatory and ulcerogenicity studies. *Eur. J. Med. Chem.* **2014**, *83*, 398–408. [CrossRef]
29. Abdel-Aziz, M.; Beshr, E.A.; Abdel-Rahman, I.M.; Ozadali, K.; Tan, O.U.; Aly, O.M. 1-(4-Methoxyphenyl)-5-(3,4,5-trimethoxyphenyl)-1H-1,2,4-triazole-3-carboxamides: Synthesis, molecular modeling, evaluation of their anti-inflammatory activity and ulcerogenicity. *Eur. J. Med. Chem.* **2014**, *77*, 155–165. [CrossRef]
30. Abdelazeem, A.H.; El-Din, A.G.S.; Arab, H.H.; El-Saadi, M.T.; El-Moghazy, S.M.; Amin, N.H. Design, synthesis and anti-inflammatory/analgesic evaluation of novel di-substituted urea derivatives bearing diaryl-1,2,4-triazole with dual COX-2/sEH inhibitory activities. *J. Mol. Struct.* **2021**, *1240*, 130565. [CrossRef]
31. Abdellatif, K.R.A.; Abdelall, E.K.A.; Elshemy, H.A.H.; Philoppes, J.N.; Hassanein, E.H.M.; Kahk, N.M. Optimization of pyrazole-based compounds with 1,2,4-triazole-3-thiol moiety as selective COX-2 inhibitors cardioprotective drug candidates: Design, synthesis, cyclooxygenase inhibition, anti-inflammatory, ulcerogenicity, cardiovascular evaluation, and molecular modeling studies. *Bioorg. Chem.* **2021**, *114*, 105122.
32. Mohassab, A.M.; Hassan, H.A.; Abdelhamid, D.; Gouda, A.M.; Gomaa, H.A.M.; Youssif, B.G.M.; Radwan, M.O.; Fujita, M.; Otsuka, M.; Abdel-Aziz, M. New quinoline/1,2,4-triazole hybrids as dual inhibitors of COX-2/5-LOX and inflammatory cytokines: Design, synthesis, and docking study. *J. Mol. Struct.* **2021**, *1244*, 130948. [CrossRef]
33. Cai, H.; Huang, X.; Xu, S.; Shen, H.; Zhang, P.; Huang, Y.; Jiang, J.; Sun, Y.; Jiang, B.; Wu, X.; et al. Discovery of novel hybrids of diaryl-1,2,4-triazoles and caffeic acid as dual inhibitors of cyclooxygenase-2 and 5-lipoxygenase for cancer therapy. *Eur. J. Med. Chem.* **2016**, *108*, 89–103. [CrossRef]
34. Szczukowski, Ł.; Redzicka, A.; Wiatrak, B.; Krzyżak, E.; Marciniak, A.; Gębczak, K.; Gębarowski, T.; Świątek, P. Design, synthesis, biological evaluation and in silico studies of novel pyrrolo[3,4-*d*]pyridazinone derivatives with promising anti-inflammatory and antioxidant activity. *Bioorg. Chem.* **2020**, *102*, 104035. [CrossRef]
35. Szczukowski, Ł.; Krzyżak, E.; Zborowska, A.; Zajac, P.; Potyrak, K.; Peregrym, K.; Wiatrak, B.; Marciniak, A.; Świątek, P. Design, Synthesis and Comprehensive Investigations of Pyrrolo[3,4-*d*]pyridazinone-Based 1,3,4-Oxadiazole as New Class of Selective COX-2 Inhibitors. *Int. J. Mol. Sci.* **2020**, *21*, 9623. [CrossRef]
36. Szandruk-Bender, M.; Wiatrak, B.; Szczukowski, Ł.; Świątek, P.; Rutkowska, M.; Dzimira, S.; Merwid-Łąd, A.; Danielewski, M.; Szela, A. Oxadiazole Derivatives of Pyrrolo[3,4-*d*]pyridazinone Exert Antinociceptive Activity in the Tail-Flick and Formalin Test in Rodents and Reveal Reduced Gastrotoxicity. *Int. J. Mol. Sci.* **2020**, *21*, 9685. [CrossRef] [PubMed]
37. Dogruer, D.S.; Kupeli, E.; Yesilada, E.; Sahin, M.F. Synthesis of New 2-[1(2H)-Phthalazinon-2-yl]acetamide and 3-[1(2H)-Phthalazinon-2-yl]propanamide Derivatives as Antinociceptive and Anti-inflammatory Agents. *Arch. Pharm. (Weinheim)* **2004**, *337*, 303–310. [CrossRef]
38. Gupta, S.; Pandey, D.; Mandalapu, D.; Bala, V.; Sharma, V.; Shukla, M.; Yadav, S.K.; Singh, N.; Jaiswal, S.; Maikhuri, J.P.; et al. Design, synthesis and biological profiling of aryl piperazine based scaffolds for the management of androgen sensitive prostatic disorders. *Medchemcomm* **2016**, *7*, 2111–2121. [CrossRef]
39. McGarry, T.; Binięcka, M.; Veale, D.J.; Fearon, U. Hypoxia, oxidative stress and inflammation. *Free Radic. Biol. Med.* **2018**, *125*, 15–24. [CrossRef]
40. Burdon, C.; Mann, C.; Cindrova-Davies, T.; Ferguson-Smith, A.C.; Burton, G.J. Oxidative Stress and the Induction of Cyclooxygenase Enzymes and Apoptosis in the Murine Placenta. *Placenta* **2007**, *28*, 724–733. [CrossRef] [PubMed]
41. Li, D.; Zhu, M.; Xu, C.; Ji, B. Characterization of the baicalein-bovine serum albumin complex without or with Cu²⁺ or Fe³⁺ by spectroscopic approaches. *Eur. J. Med. Chem.* **2011**, *46*, 588–599. [CrossRef] [PubMed]

42. Shi, J.H.; Pan, D.Q.; Wang, X.X.; Liu, T.T.; Jiang, M.; Wang, Q. Characterizing the binding interaction between antimalarial artemether (AMT) and bovine serum albumin (BSA): Spectroscopic and molecular docking methods. *J. Photochem. Photobiol. B Biol.* **2016**, *162*, 14–23. [CrossRef] [PubMed]
43. Li, Y.; He, W.; Liu, J.; Sheng, F.; Hu, Z.; Chen, X. Binding of the bioactive component Jatrorrhizine to human serum albumin. *Biochim. Biophys. Acta—Gen. Subj.* **2005**, *1722*, 15–21. [CrossRef]
44. Wani, T.A.; Bakheit, A.H.; Zargar, S.; Bhat, M.A.; Al-Majed, A.A. Molecular docking and experimental investigation of new indole derivative cyclooxygenase inhibitor to probe its binding mechanism with bovine serum albumin. *Bioorg. Chem.* **2019**, *89*, 103010. [CrossRef]
45. Lakowicz, J.R. *Principles of Fluorescence Spectroscopy*, 3rd ed.; Springer: Boston, MA, USA, 2006; ISBN 978-0-387-31278-1.
46. Ware, W.R. Oxygen quenching of fluorescence in solution: An experimental study of the diffusion process. *J. Phys. Chem.* **1962**, *66*, 455–458. [CrossRef]
47. Dufour, C.; Dangles, O. Flavonoid-serum albumin complexation: Determination of binding constants and binding sites by fluorescence spectroscopy. *Biochim. Biophys. Acta—Gen. Subj.* **2005**, *1721*, 164–173. [CrossRef]
48. Abdelhameed, A.S.; Bakheit, A.H.; Mohamed, M.S.; Eldehna, W.M.; Abdel-Aziz, H.A.; Attia, M.I. Synthesis and biophysical insights into the binding of a potent anti-proliferative non-symmetric bis-isatin derivative with bovine serum albumin: Spectroscopic and molecular docking approaches. *Appl. Sci.* **2017**, *7*, 617. [CrossRef]
49. Suryawanshi, V.D.; Walekar, L.S.; Gore, A.H.; Anbhule, P.V.; Kolekar, G.B. Spectroscopic analysis on the binding interaction of biologically active pyrimidine derivative with bovine serum albumin. *J. Pharm. Anal.* **2016**, *6*, 56–63. [CrossRef]
50. Wani, T.A.; Bakheit, A.H.; Al-Majed, A.R.A.; Bhat, M.A.; Zargar, S. Study of the interactions of bovine serum albumin with the new anti-inflammatory agent 4-(1,3-dioxo-1,3-dihydro-2H-isoindol-2-yl)-N-[(4-ethoxy-phenyl) methylidene]benzohydrazide using a multi-spectroscopic approach and molecular docking. *Molecules* **2017**, *22*, 1258. [CrossRef]
51. Mohammadnia, F.; Fatemi, M.H.; Taghizadeh, S.M. Study on the interaction of anti-inflammatory drugs with human serum albumin using molecular docking, quantitative structure–activity relationship, and fluorescence spectroscopy. *Luminescence* **2020**, *35*, 266–273. [CrossRef] [PubMed]
52. Klotz, I.M.; Urquhart, J.M. The Binding of Organic Ions by Proteins. Effect of Temperature. *J. Am. Chem. Soc.* **1949**, *71*, 847–851. [CrossRef]
53. Kelly, S.M.; Jess, T.J.; Price, N.C. How to study proteins by circular dichroism. *Biochim. Biophys. Acta—Proteins Proteom.* **2005**, *1751*, 119–139. [CrossRef]
54. Kelly, S.; Price, N. The Use of Circular Dichroism in the Investigation of Protein Structure and Function. *Curr. Protein Pept. Sci.* **2005**, *1*, 349–384. [CrossRef]
55. Lu, Z.X.; Cui, T.; Shi, Q.L. *Applications of Circular Dichroism (CD) and Optical Rotatory Dispersion (ORD) in Molecular Biology*, 1st ed.; Science Press: Beijing, China, 1987.
56. Byler, D.M.; Susi, H. Examination of the secondary structure of proteins by deconvolved FTIR spectra. *Biopolymers* **1986**, *25*, 469–487. [CrossRef]
57. Sudlow, G.; Birkett, D.J.; Wade, D.N. The Characterization of Two Specific Drug Binding Sites on Human Serum Albumin. *Mol. Pharmacol.* **1975**, *11*, 824–832.
58. Ghuman, J.; Zunszain, P.A.; Petitpas, I.; Bhattacharya, A.A.; Otagiri, M.; Curry, S. Structural basis of the drug-binding specificity of human serum albumin. *J. Mol. Biol.* **2005**, *353*, 38–52. [CrossRef] [PubMed]
59. Lipinski, C.A.; Lombardo, F.; Dominy, B.W.; Feeney, P.J. Experimental and computational approaches to estimate solubility and permeability in drug discovery and development settings. *Adv. Drug Deliv. Rev.* **2001**, *46*, 3–26. [CrossRef]
60. FVEber, D.F.; Johnson, S.R.; Cheng, H.-Y.; Smith, B.R.; Ward, K.W.; Kopple, K.D. Molecular Properties That Influence the Oral Bioavailability of Drug Candidates. *J. Med. Chem.* **2002**, *45*, 2615–2623.
61. Ertl, P.; Rohde, B.; Selzer, P. Fast calculation of molecular polar surface area as a sum of fragment-based contributions and its application to the prediction of drug transport properties. *J. Med. Chem.* **2000**, *43*, 3714–3717. [CrossRef]
62. Ahmed, A.; Tajmir-Riahi, H.A.; Carpentier, R. A quantitative secondary structure analysis of the 33 kDa extrinsic polypeptide of photosystem II by FTIR spectroscopy. *FEBS Lett.* **1995**, *363*, 65–68. [CrossRef]
63. Liu, Y.; Xie, M.X.; Kang, J.; Zheng, D. Studies on the interaction of total saponins of panax notoginseng and human serum albumin by Fourier transform infrared spectroscopy. *Spectrochim. Acta Part A Mol. Biomol. Spectrosc.* **2003**, *59*, 2747–2758. [CrossRef]
64. Kong, J.; Yu, S. Fourier Transform Infrared Spectroscopic Analysis of Protein Secondary Structures. *Acta Biochim. Biophys. Sin. (Shanghai)* **2007**, *39*, 549–559. [CrossRef] [PubMed]



Article

Synthesis of Novel Pyrido[1,2-*c*]pyrimidine Derivatives with 6-Fluoro-3-(4-piperidynyl)-1,2-benzisoxazole Moiety as Potential SSRI and 5-HT_{1A} Receptor Ligands

Marek Król¹, Grzegorz Ślifirski^{1,*}, Jerzy Kleps¹, Szymon Ulenberg², Mariusz Belka², Tomasz Bączek², Agata Siwek³, Katarzyna Stachowicz⁴, Bernadeta Szewczyk⁴, Gabriel Nowak^{3,4}, Beata Duszyńska⁴ and Franciszek Herold¹

¹ Department of Drug Technology and Pharmaceutical Biotechnology, Faculty of Pharmacy, Medical University of Warsaw, 1, Banacha Street, 02-097 Warsaw, Poland; mkrol@wum.edu.pl (M.K.); jkleps@wum.edu.pl (J.K.); fherold@wum.edu.pl (F.H.)

² Department of Pharmaceutical Chemistry, Medical University of Gdańsk, 107, J. Hallera Street, 80-416 Gdańsk, Poland; szymon.ulenberg@gmail.com (S.U.); mariusz.belka@gumed.edu.pl (M.B.); tomasz.baczek@gumed.edu.pl (T.B.)

³ Department of Pharmacobiology, Faculty of Pharmacy, Jagiellonian University Medical College, 9, Medyczna Street, 30-688 Kraków, Poland; agat.siwek@uj.edu.pl (A.S.); nowak@if-pan.krakow.pl (G.N.)

⁴ Maj Institute of Pharmacology, Polish Academy of Sciences, 12, Smetna Street, 31-343 Kraków, Poland; stachow@if-pan.krakow.pl (K.S.); szewczyk@if-pan.krakow.pl (B.S.); duszyn@if-pan.krakow.pl (B.D.)

* Correspondence: gslifirski@wum.edu.pl

Citation: Król, M.; Ślifirski, G.; Kleps, J.; Ulenberg, S.; Belka, M.; Bączek, T.; Siwek, A.; Stachowicz, K.; Szewczyk, B.; Nowak, G.; et al. Synthesis of Novel Pyrido[1,2-*c*]pyrimidine Derivatives with 6-Fluoro-3-(4-piperidynyl)-1,2-benzisoxazole Moiety as Potential SSRI and 5-HT_{1A} Receptor Ligands. *Int. J. Mol. Sci.* **2021**, *22*, 2329. <https://doi.org/10.3390/ijms22052329>

Academic Editor: Geoffrey Brown

Received: 20 January 2021

Accepted: 22 February 2021

Published: 26 February 2021

Publisher's Note: MDPI stays neutral with regard to jurisdictional claims in published maps and institutional affiliations.



Copyright: © 2021 by the authors. Licensee MDPI, Basel, Switzerland. This article is an open access article distributed under the terms and conditions of the Creative Commons Attribution (CC BY) license (<https://creativecommons.org/licenses/by/4.0/>).

Abstract: Two series of novel 4-aryl-2H-pyrido[1,2-*c*]pyrimidine (**6a–i**) and 4-aryl-5,6,7,8-tetrahydropyrido[1,2-*c*]pyrimidine (**7a–i**) derivatives were synthesized. The chemical structures of the new compounds were confirmed by ¹H and ¹³C NMR spectroscopy and ESI-HRMS spectrometry. The affinities of all compounds for the 5-HT_{1A} receptor and serotonin transporter protein (SERT) were determined by in vitro radioligand binding assays. The test compounds demonstrated very high binding affinities for the 5-HT_{1A} receptor of all derivatives in the series (**6a–i** and **7a–i**) and generally low binding affinities for the SERT protein, with the exception of compounds **6a** and **7g**. Extended affinity tests for the receptors D₂, 5-HT_{2A}, 5-HT₆ and 5-HT₇ were conducted with regard to selected compounds (**6a**, **7g**, **6d** and **7i**). All four compounds demonstrated very high affinities for the D₂ and 5-HT_{2A} receptors. Compounds **6a** and **7g** also had high affinities for 5-HT₇, while **6d** and **7i** held moderate affinities for this receptor. Compounds **6a** and **7g** were also tested in vivo to identify their functional activity profiles with regard to the 5-HT_{1A} receptor, with **6a** demonstrating the activity profile of a presynaptic agonist. Metabolic stability tests were also conducted for **6a** and **6d**.

Keywords: antidepressants; pyrido[1,2-*c*]pyrimidines; dual 5-HT_{1A}/SERT activity; drug design

1. Introduction

The serotonergic nervous system plays a substantial role in regulating mood, diurnal rhythm, cognitive functions, memory, thermoregulation and anxiety, while also contributing to many other vital functions [1]. Numerous studies in recent years have confirmed that disturbances in serotonergic neurotransmission are closely related to central nervous system (CNS) disorders such as depression, anxiety, schizophrenia or obsessive compulsive disorder (OCD) [2,3]. There is an increase in patients with these depressive disorders, which represent the fourth most common class of medical conditions and affect approximately 20% of the population. Consequently, there is a growing interest in novel modulators of the serotonergic system [4]. The World Health Organization predicts that by 2030, unipolar depression will be the primary reason for inability to work worldwide, with depression

and anxiety affecting approximately 100 million people in Europe alone [5]. At the same time, drugs currently used to treat depression are far from satisfactory [2].

The introduction of selective serotonin reuptake inhibitors (SSRIs) such as fluoxetine or citalopram in the 1980s marked a turning point in the pharmacotherapy of depression (Figure 1) [6]. SSRIs demonstrate low affinities for adrenergic, histaminic and muscarinic receptors, contributing to their limited adverse effects, better tolerability and higher therapeutic index than tricyclic antidepressants or monoamine oxidase inhibitors [6–8]. Therapeutic efficacy of SSRIs has been documented for unipolar depression, anxiety disorder, posttraumatic stress disorder, OCD and negative symptoms of schizophrenia [9]. However, SSRIs are not free from adverse effects, which include insomnia, nausea, sexual dysfunction and a possible effect on myocardial ion channels [9,10]. One serious drawback of SSRIs is their long therapeutic latency (therapeutic effects become evident two to three weeks after administration) and limited efficacy (visible effects are only seen in approximately 60% of patients) [7]. Given the high probability of suicide in depressive patients, drugs without a latency period are extremely important [1,4].

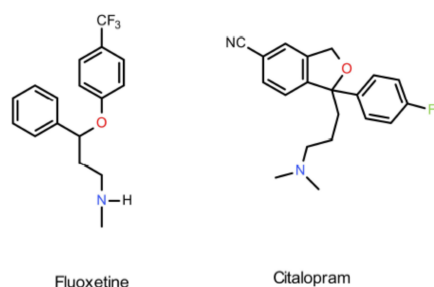


Figure 1. Chemical structures of fluoxetine and citalopram.

5-HT_{1A} receptors play an important role in the self-regulation of the serotonergic system [2]. They may function both as presynaptic (autoreceptors) or postsynaptic receptors. The 5-HT_{1A} presynaptic receptors are found in the neurons and dendrites of brainstem raphe nuclei. Upon stimulation, they release endogenous serotonin into the synaptic cleft, reducing transmission across serotonergic neurons. On the other hand, postsynaptic 5-HT_{1A} neurons are stimulated in somatodendritic nerve endings in the cortico-limbic area of the CNS, increasing transmission via serotonergic neurons [7,11,12]. In fact, a number of 5-HT_{1A} agonists are currently undergoing various phases of clinical studies or have already been approved for marketing. Their pharmacological activity is not limited to the treatment of depression, but may also be used in the treatment of anxiety (osemozotan, phase II), schizophrenia (bifeprunox, phase III) or pain (befiradol, phase II) (Figure 2) [13].

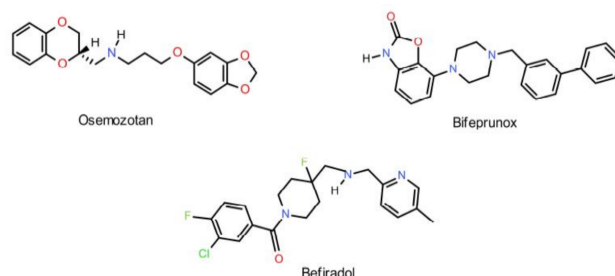


Figure 2. Chemical structures of osemozotan, bifeprunox and befiradol.

The aforementioned SSRI latency period is associated with changes in adaptive processes within the CNS that result in increased serotonergic neurotransmission via postsynaptic 5-HT_{1A} receptors [8,14]. The therapeutic effects seen during SSRI administration are the combined result of neurochemical changes in the brain, including desensitization of 5-HT_{1A} autoreceptors, downregulation of receptor responsivity to neurotransmitters,

changes in signal transmission, neurotropism and hippocampal neurogenesis [15]. One key consequence of desensitization of somatodendritic 5-HT_{1A} autoreceptors on brainstem raphe nuclei is increasing serotonin levels in synaptic clefts [7,16].

In 1993, Artigas proposed that coadministration of a 5-HT_{1A} receptor antagonist with SSRIs should potentiate the antidepressant effect through accelerating the desensitization of 5-HT_{1A} autoreceptors, thus strengthening their function [17]. This hypothesis was confirmed upon coadministration of an SSRI with the partial 5-HT_{1A} antagonist pindolol [7]. Unfortunately, 5-HT_{1A} antagonists were nonselective and simultaneously blocked pre- and postsynaptic receptors, an undesirable effect when treating depression [9]. A more promising direction in the search for next-generation antidepressants looks at agonists of both the 5-HT_{1A} receptor and SSRI. Such compounds have a potential for accelerating desensitization and downregulation of autoreceptors, while directly stimulating postsynaptic serotonergic neurons. As a result of this process, the concentration of endogenous serotonin in the synaptic cleft increases [18]. Most importantly, the sensitivity of postsynaptic receptors does not decrease with prolonged administration [18,19]. This approach was positively verified by the introduction of vilazodone (Viibryd) to treat depression (Figure 3). Vilazodone was the first of several SSRI+ drugs whose mechanism of action involves both agonism towards the 5-HT_{1A} receptors and serotonin transporter protein (SERT) inhibition [20–22]. In 2013, the Food and Drug Administration approved vortioxetine as another SSRI+ agent with an extended receptor activity profile for pharmacotherapy of depression (Figure 3). Vortioxetine acts as an SSRI, an agonist of the 5-HT_{1A} receptor, a partial agonist of the 5-HT_{1B} and an antagonist of the 5-HT₃ and 5-HT₇ receptors [23].

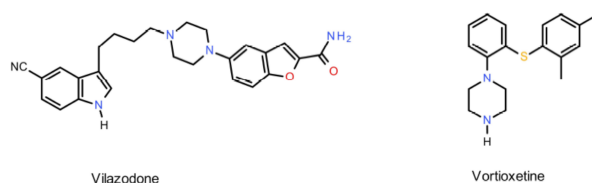


Figure 3. Chemical structures of vilazodone and vortioxetine.

This work describes the synthesis and results of pharmacological testing of a series of novel derivatives of 4-aryl-2H-pyrido[1,2-*c*]pyrimidine, characterized by double binding for the 5-HT_{1A} receptor and SERT protein. Selected compounds were tested further to determine their activity towards other molecular targets, such as the 5-HT_{2A}, 5-HT₆, 5-HT₇ and D₂ receptors.

The research presented in this paper is a continuation of a long-term research project conducted in our department, where ligands are tested for a double binding affinity for both the SERT protein and 5-HT_{1A} receptors [24–28]. Two series of novel derivatives of 4-aryl-2H-pyrido[1,2-*c*]pyrimidine and 4-aryl-5,6,7,8-tetrahydropyrido[1,2-*c*]pyrimidine were designed, based on lead compounds (I–IV) that had been synthesized previously by the same research group and had demonstrated a high affinity for both the 5-HT_{1A} receptors and SERT protein (Figure 4) [26,27].

Modifications of lead compounds involved a change in the pharmacophore part via the introduction of a 6-fluoro-3-(4-piperidinyl)-1,2-benzisoxazole residue. This addition should increase affinity for the 5-HT_{1A} receptors and SERT protein, and thus these new compounds would potentially demonstrate dual binding affinity, appropriate functional activity and affinity for other molecular targets (e.g., 5-HT_{2A}, 5-HT₆, 5-HT₇ and D₂).

This study aimed to investigate the effect of (i.) introducing a 6-fluoro-3-(4-piperidinyl)-1,2-benzisoxazole residue to the pharmacophore, (ii.) the degree of saturation of the pyrido[1,2-*c*]pyrimidine residue in the terminal segment and (iii.) substituents in the 4-aryl-pyrido[1,2-*c*]pyrimidine moiety on affinity for both the 5-HT_{1A} receptor and SERT protein and other receptors (5-HT_{2A}, 5-HT₆, 5-HT₇, D₂) in extended receptor profile tests. Further testing probed the effect of these modifications on the functional activity (agonism-antagonism) and metabolic stability of the compounds of interest.

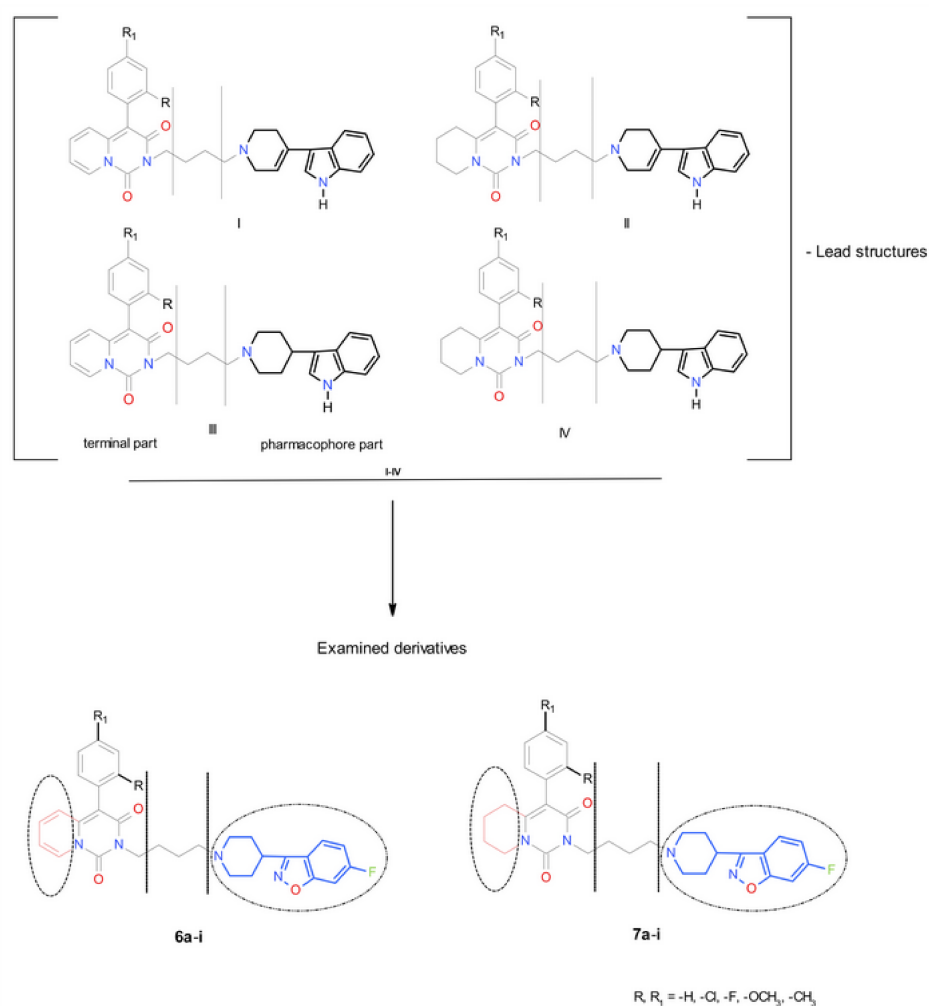
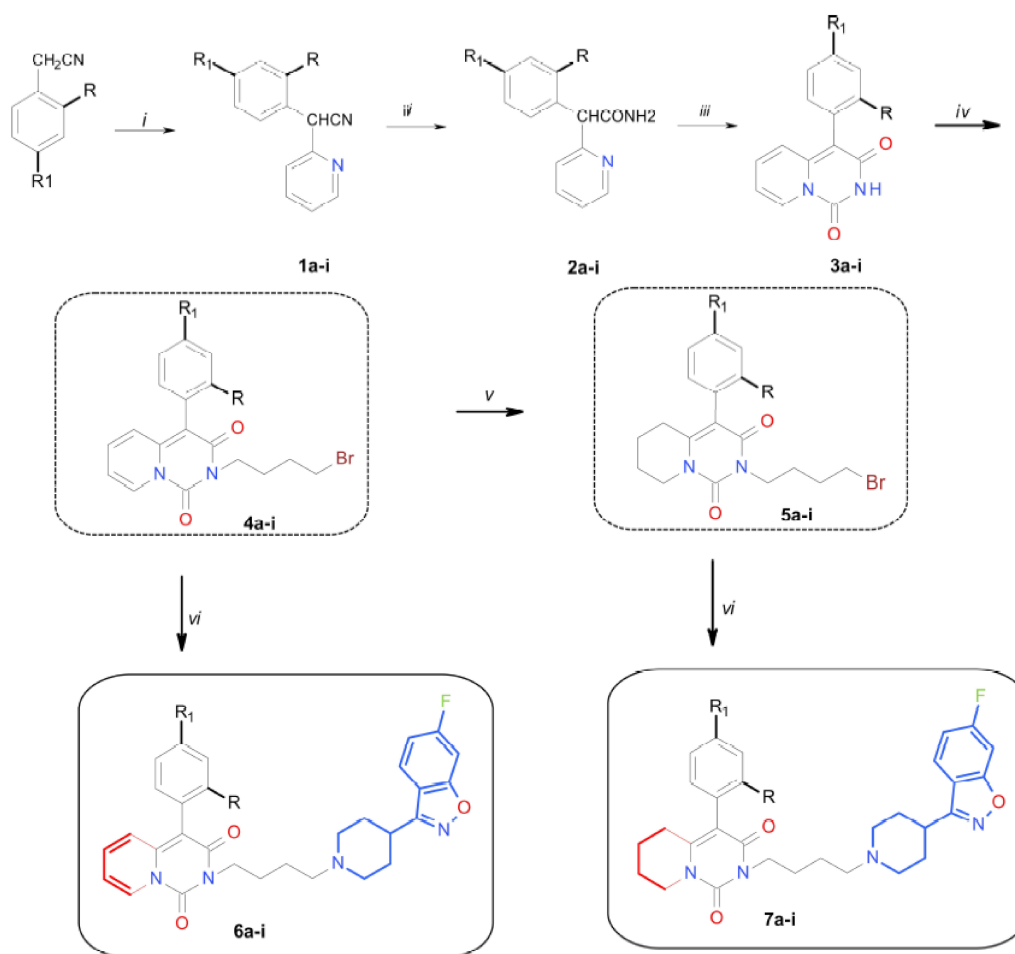


Figure 4. Comparison of the novel derivatives of 4-aryl-2H-pyrido[1,2-c]pyrimidine (**6a-i**) and 4-aryl-5,6,7,8-tetrahydropyrido[1,2-c]pyrimidine (**7a-i**), designed in this paper with lead compounds (I-IV).

2. Results and Discussion

2.1. Chemistry

The designed target compounds (**6a-i**) and (**7a-i**) were obtained in a multistage synthesis process (Figure 5). The starting materials were phenylacetone nitrile derivatives subjected to C-arylation with 2-bromopyridine over KOH. This reaction yielded respective derivatives of α -(2-pyridyl)- α -(aryl)-acetone nitriles (**1a-i**), which were subsequently hydrolyzed in an acidic environment to obtain respective α -(2-pyridyl)- α -(aryl)-acetamides (**2a-i**). These amides were then reacted with diethyl carbonate via a cyclocondensation process, producing derivatives of 4-aryl-2H-pyrido[1,2-c]pyrimidine-1,3-dione (**3a-i**). All the compounds (**1a-i**), (**2a-i**), (**3a-i**) were obtained according to an original method. The imides (**3a-i**) were then *N*-alkylated with 1,4-dibromobutane to produce *N*-bromobutyl derivatives of 4-aryl-2H-pyrido[1,2-c]pyrimidine-1,3-dione (**4a-i**). Some of the 2-(4-bromobutyl)-4-aryl-pyrido[1,2-c]pyrimidine-1,3-dione (**4a-i**) derivatives were subjected to catalytic reduction over 10% Pd/C, yielding 2-(4-bromobutyl)-4-aryl-5,6,7,8-tetrahydropyrido[1,2-c]pyrimidine-1,3-dione (**5a-i**) derivatives. The target compounds (**6a-i**) and (**7a-i**) were obtained by reacting the bromobutyl derivatives of (**4a-i**) and (**5a-i**) with 6-fluoro-3-(4-piperidinyl)-1,2-benzisoxazole. The chemical structures and purity of the newly synthesized compounds (**6a-i**) and (**7a-i**) were confirmed by ^1H and ^{13}C NMR spectroscopy, as well as LC/MS and HRMS spectrometry. The investigated compounds were subsequently tested in vitro and in vivo as free bases.



6 and 7: a. R, R₁ = -H; b. R = -CH₃, R₁ = -H; c. R = -OCH₃, R₁ = -H; d. R = -Cl, R₁ = -H;
 e. R = -F, R₁ = -H; f. R = -H, R₁ = -CH₃; g. R = -H, R₁ = -OCH₃; h. R = -H, R₁ = -Cl; i. R = -H, R₁ = -F

Figure 5. Schematic of the syntheses of compounds **6a–i** and **7a–i**. Reagents and conditions: (i) 2-bromopyridine, KOH, DMSO, 50 °C; (ii) H₂SO₄, CH₃COOH, 100 °C; (iii) (C₂H₅)₂CO₃, EtONa, EtOH reflux; (iv) 1,4-dibromobutane, acetone, K₂CO₃, reflux; (v) H₂, 10% Pd/C, EtOH, 60 atm., 50 °C; (vi) 6-fluoro-3-(4-piperidinyl)-1,2-benzisoxazole, K₂CO₃, CH₃CN, 45 °C.

2.2. Biological Evaluation

2.2.1. Radioligand Binding Assay for 5-HT_{1A} and SERT

The target compounds (**6a–i**) and (**7a–i**) were assessed for in vitro affinity for the 5-HT_{1A} receptor and SERT protein by radioligand binding assays [26,29,30]. The results, which were subsequently used for structure–activity relationship (SAR) analysis, can be found in Table 1. Various substituents at the ortho or para position of the benzene ring—as well as the degree of saturation of the pyrido[1,2-*c*]pyrimidine residue—were investigated with regard to their effect on the binding affinity of the compounds (**6a–i**) and (**7a–i**). The resulting data on 5-HT_{1A}R binding affinity indicated very high affinity of the following ligands: **6c** ($K_i = 7.0$ nM), **6g** ($K_i = 10.0$ nM), **6d** ($K_i = 11.0$ nM), **6e** ($K_i = 15.0$ nM), **6i** ($K_i = 17.0$ nM), **6h** ($K_i = 21.0$ nM), **6a** ($K_i = 23.0$ nM) and **6b** ($K_i = 30$ nM), with **6f** being the only compound with a binding affinity at the level of $K_i = 74$ nM (Table 1). The compounds (**7a–i**) (4-aryl-5,6,7,8-tetrahydropyrido[1,2-*c*]pyrimidine derivatives) demonstrated slightly lower binding affinity for the 5-HT_{1A}R compared to (**6a–i**). Very high binding affinity was noted for **7g** ($K_i = 5.0$ nM), **7i** ($K_i = 9.5$ nM), **7h** ($K_i = 25.0$ nM), **7a** ($K_i = 27.0$ nM), **7b** ($K_i = 35.0$ nM) and **7e** ($K_i = 36.0$ nM); the other three derivatives demonstrated high binding affinity, viz., **7f** ($K_i = 52.0$ nM), **7c** ($K_i = 62.0$ nM) and **7d** ($K_i = 71.0$ nM). A comparison of

binding affinity data for the ligands (**6a–i**) and (**7a–i**) indicated that the degree of saturation had little effect, with the 4-aryl-2H-pyrido[1,2-*c*]pyrimidine derivatives (**6a–i**) being slightly superior to the 4-aryl-5,6,7,8-tetrahydropyrido[1,2-*c*]pyrimidine derivatives (**7a–i**).

Table 1. 5-HT_{1A} receptor and SERT binding affinities, as well as cLogP [31] of 4-aryl-2H-pyrido[1,2-*c*]pyrimidine derivatives 4-aryl-2H-pyrido[1,2-*c*]pyrimidine (**6a–i**) and 4-aryl-5,6,7,8-tetrahydropyrido[1,2-*c*]pyrimidine derivatives (**7a–i**).

Compound	R	R ₁	K _i [nM]		
			5-HT _{1A}	SERT	cLogP
6a	–H	–H	23.0 ± 1.0	32.0 ± 3.6	4.32
6b	–CH ₃	–H	30.0 ± 3.5	>5000	4.81
6c	–OCH ₃	–H	7.0 ± 1.0	>5000	4.30
6d	–Cl	–H	11.0 ± 1.4	373.0 ± 32.0	4.98
6e	–F	–H	15.0 ± 0.6	>1000	4.52
6f	–H	–CH ₃	74.0 ± 4.0	772.0 ± 36.0	4.81
6g	–H	–OCH ₃	10.0 ± 1.1	730.0 ± 79.0	4.98
6h	–H	–Cl	21.0 ± 1.5	310.0 ± 1.0	4.98
6i	–H	–F	17.0 ± 2.0	342.0 ± 28.8	4.55
7a	–H	–H	27.0 ± 2.0	520.0 ± 58.8	5.02
7b	–CH ₃	–H	35.0 ± 3.5	>1000	5.51
7c	–OCH ₃	–H	62.0 ± 6.0	878.0 ± 88.0	5.00
7d	–Cl	–H	71.0 ± 6.9	310.0 ± 34.5	5.68
7e	–F	–H	36.0 ± 4.1	>1000	5.22
7f	–H	–CH ₃	52.0 ± 2.5	1773.0 ± 180.0	5.90
7g	–H	–OCH ₃	5.0 ± 0.5	48.0 ± 2.4	5.00
7h	–H	–Cl	25.0 ± 3.0	290.0 ± 22.7	5.68
7i	–H	–F	9.5 ± 1.1	311.0 ± 35.0	5.22
Reference compound					
Serotonin			3.6 ± 0.4		
Methiotepin			4.8 ± 0.5		
Imipramine				17.0 ± 1.3	

An analysis of the effect of the substituents in the benzene ring of the 4-aryl-2H-pyrido[1,2-*c*]pyrimidine residue on 5-HT_{1A}R affinity of the ligands (**6a–i**) showed that the presence of a substituent at the ortho position generally increased binding affinity, compared to ligands with a substituent at the para position. The most marked effect on affinity was exerted by substituents in the compounds (**6a–i**) in the following order: **6c** (*o*-OCH₃) > **6g** (*p*-OCH₃) > **6d** (*o*-Cl) > **6e** (*o*-F) > **6i** (*p*-F) > **6h** (*p*-Cl) > **6a** (–H) > **6b** (*o*-CH₃) > **6f** (*p*-CH₃). Analysis of the effect of substituents on the binding affinity of the derivatives of the 4-aryl-5,6,7,8-tetrahydro-pyrido[1,2-*c*]pyrimidine (**7a–i**) series revealed the most marked effect on binding affinity of substituents at the para position in the following order: **7g** (*p*-OCH₃) > **7i** (*p*-F) > **7h** (*p*-Cl) > **7a** (–H) > **7b** (*o*-CH₃) > **7e** (*o*-F) > **7f** (*p*-CH₃) > **7c** (*o*-OCH₃) > **7d** (*o*-Cl).

Data on the affinity of the ligands (**6a–i**) and (**7a–i**) for SERT protein generally indicated poor binding affinity of most of the compounds. Consequently, it is difficult to determine the effect of the degree of saturation and substituents of the 4-aryl-pyrido[1,2-*c*]pyrimidine residue in the test compounds on their binding affinity. High binding affinity was only demonstrated for **6a** ($K_i = 32.0$ nM) and **7g** ($K_i = 48.0$ nM). The binding affinity values for the other ligands in both series are low ($K_i =$ from 310 to > 5000 nM for series **6** and $K_i = 290–1773$ nM for series **7**).

The compounds **6a**, **6d**, **7g** and **7i** were selected for in vitro studies. The compounds **6a** and **7g** showed very high affinity for the 5-HT_{1A} receptor and SERT protein, while the compounds **6d** and **7i** demonstrated very high affinity for the 5-HT_{1A} receptor and poor affinity for SERT. The compounds were tested for their multiple receptor binding affinity,

with special regard to their affinity for the receptors 5-HT_{2A}, 5-HT₆, 5-HT₇ and D₂, whose role in the pathomechanism of depression has been well documented [15,32] (Table 2). It has been confirmed that disturbed dopaminergic neurotransmission in the mesolimbic and nigrostriatal regions also contributes significantly to the development of depression [32]. Consequently, intensive research is under way on a new class of potential drugs which exert their effects through interaction with D₂/5-HT_{1A}[33]; where the ligand would be a partial agonist of the 5-HT_{1A} receptor and would induce postsynaptic serotonergic neurotransmission, which would increase dopamine levels in the mPFC (medial prefrontal cortex) [34]. The role of 5-HT_{2A} receptors in the treatment of schizophrenia has also been well documented in numerous publications. Accordingly, multireceptor studies of the selected ligands **6a**, **6d**, **7g** and **7i**—including this molecular target—appear well justified. The role of the serotonergic receptors 5-HT₆ and 5-HT₇ in the pathomechanism of CNS disorders, including depression, has been well documented and presented in numerous papers [15], and so have the satisfactory results of treatment with multireceptor drugs, such as Aripiprazole, Clozapine[35] or Vortioxetine[23]. This encouraged us to investigate the extended affinity profile of selected compounds [36], targeting 5-HT_{2A}, 5-HT₆, 5-HT₇ and D₂ receptors.

Table 2. Binding affinity data on serotonin 5-HT_{1A}, 5-HT_{2A}, 5-HT₆, 5-HT₇ receptors, SERT protein, and dopamine D₂ receptor of the investigated 4-aryl-2H-pyrido[1,2-*c*]pyrimidine (**6a**, **6d**) and 4-aryl-5,6,7,8-tetrahydro-pyrido[1,2-*c*]pyrimidine (**7g**, **7i**) derivatives.

Compound	R ₁	R ₂	K _i [nM]					
			5-HT _{1A}	SERT	5-HT _{2A}	5-HT ₆	5-HT ₇	D ₂
6a	–H	–H	23.0 ± 1.0	32.0 ± 3.6	17 ± 3	376 ± 58	62 ± 5	7 ± 2
6d	–Cl	–H	11.0 ± 1.4	373.0 ± 32.0	20 ± 4	709 ± 135	109 ± 14	9 ± 2
7g	–H	–OCH ₃	5.0 ± 0.5	48.0 ± 2.4	16 ± 2	400 ± 32	94 ± 11	10 ± 1
7i	–H	–F	9.5 ± 1.1	311.0 ± 35.0	44 ± 6	740 ± 183	161 ± 27	17 ± 2
Reference Compound								
Olanzapine [37]					4.6 ± 0.9	7 ± 1	n.d.	n.d.
Mianserin [37]					2.8 ± 0.5	n.d.	n.d.	n.d.
Clozapine [37]					n.d.	n.d.	18 ± 2	n.d.
Haloperidol [37]					n.d.	n.d.	n.d.	4.5 ± 0.7
Apomorphine [37]					n.d.	n.d.	n.d.	42 ± 6
Chlorpromazine [37]					n.d.	n.d.	n.d.	1.8 ± 0.3

n.d. = not determined.

Table 2 presents binding affinities of the compounds **6a** and **7g**, which exhibited very high binding affinity for the receptors 5-HT_{1A}, 5-HT_{2A}, SERT and D₂, and high binding affinity for 5-HT₇. The compounds **6d** and **7i**, in turn, demonstrated very high affinity for the receptors 5-HT_{1A}, 5-HT_{2A} and D₂ and moderate affinity for the receptor 5-HT₇, with low affinity for the receptors 5-HT₆ and SERT. The in vitro data for both groups of compounds can be seen as a good starting point for further research on multireceptor ligands in the treatment of depressive disorder or schizophrenia. Additionally, cLogP values for the compounds in the 4-aryl-2H-pyrido[1,2-*c*]pyrimidine (**6a–i**) series ranged from 4.30 to 4.98, while cLogP values for the series of 4-aryl-5,6,7,8-tetrahydro-pyrido[1,2-*c*]pyrimidine (**7a–i**) derivatives ranged from 5.00–5.90. These values are given in Table 1. A comparison of cLogP values for both ligand series shows that all cLogP values for the (**6a–i**) series do not exceed 5.00—which, according to Lipiński [38,39] is a cut-off value for transmembrane penetration required of candidate drugs. The derivatives **6a** (R = –H, R₁ = –H) and **6c** (R = –OCH₃, R₁ = H) had a cLogP value of 4.32 and 4.30, respectively, which can be compared to the cLogP value of 4.26 [30] of Vortioxetine, a well-known antidepressant of the SSRI/5-HT_{1A} class. At the same time, ligands of the (**7a–i**) series

demonstrated cLogP values >5, which is not pharmacologically desirable, according to Lipiński's rule [38].

2.2.2. In Vivo Studies

To determine the profile of functional activity of the selected ligands, behavioral tests were performed. It is known that 8-OH-DPAT, a 5-HT_{1A} receptor agonist, can induce hypothermia in mice, through 5-HT_{1A} somatodendritic receptors [30,40]. Moreover, this effect can be abolished by WAY-100635 [41], a 5-HT_{1A} receptor antagonist. Based on this knowledge, we tested compounds **6a** (R = -H, R₁ = -H) and **7g** (R = -H, R₁ = -OCH₃) in a commonly used in vivo panel of tests, to assess their functional 5-HT_{1A} receptor activity. Test compounds **6a** and **7g**, like 8-OH-DPAT, induced hypothermia in mice (Table 3).

Table 3. The effect of compounds **6a** and **7g** on body temperature in mice.

Treatment	Dose (mg/kg)	$\Delta t \pm \text{SEM} (^{\circ}\text{C})$			
		30 min	60 min	90 min	120 min
Vehicle 6a	-	-0.2 ± 0.2	-0.0 ± 0.2	-0.1 ± 0.1	-0.0 ± 0.1
	5	-2.0 ± 0.2 ^b	-3.2 ± 0.5 ^b	-3.1 ± 0.5 ^b	-2.8 ± 0.5 ^b
	2.5	-1.6 ± 0.2 ^b	-2.5 ± 0.3 ^b	-2.4 ± 0.3 ^b	-2.0 ± 0.2 ^b
	1.25	-1.7 ± 0.3 ^b	-1.7 ± 0.3 ^b	-1.6 ± 0.2 ^b	-1.6 ± 0.3 ^b
	0.6	-1.0 ± 0.2 ^b	-1.2 ± 0.1 ^b	-0.9 ± 0.1 ^a	-0.8 ± 0.2 ^a
		$p < 0.0001$	$p < 0.0001$	$p < 0.0001$	$p < 0.0001$
Vehicle 7g	-	-0.0 ± 0.2	0.0 ± 0.1	-0.1 ± 0.1	-0.1 ± 0.1
	5	-2.1 ± 0.1 ^b	-3.4 ± 0.3 ^b	-3.9 ± 0.5 ^b	-4.2 ± 0.8 ^b
	2.5	-2.2 ± 0.2 ^b	-2.8 ± 0.3 ^b	-2.9 ± 0.3 ^b	-3.0 ± 0.4 ^b
	1.25	-1.5 ± 0.3 ^b	-1.7 ± 0.3 ^b	-1.3 ± 0.4 ^b	-1.0 ± 0.3
		$p < 0.0001$	$p < 0.0001$	$p < 0.0001$	$p < 0.0001$
Vehicle	-	0.2 ± 0.1	0.1 ± 0.2	0.1 ± 0.2	0.1 ± 0.2
WAY-100635	0.1	0.1 ± 0.2	0.1 ± 0.2	-0.1 ± 0.2	-0.2 ± 0.1
8-OH-DPAT	5	-1.7 ± 0.2 ^b	-1.1 ± 0.2 ^b	-0.1 ± 0.1	0.3 ± 0.3
		$p < 0.0001$	$p < 0.005$	ns	ns

The investigated compounds were administered 30 min before the test, ^a $p < 0.05$ vs vehicle, ^b $p < 0.001$ vs vehicle, ns = non-significant.

WAY-100635 (0.1 mg/kg) diminished hypothermia induced by compound **6a** (0.6 mg/kg) by 50% (Table 4).

Table 4. The effect of WAY-100635 (0.1 mg/kg sc) on the hypothermia induced by compounds **6a** and **7g**.

Treatment and Dose (mg/kg)	$\Delta t \pm \text{SEM} (^{\circ}\text{C})$	
	30 min	60 min
Vehicle	0.0 ± 0.1	0.0 ± 0.0
Vehicle + 6a (0.6)	-1.0 ± 0.2 ^c	-1.2 ± 0.1 ^c
WAY-100635 + 6a	-0.5 ± 0.2 ^{b,d}	-0.4 ± 0.2 ^{a,e}
	$p < 0.0001$	$p < 0.0001$
Vehicle	-0.3 ± 0.1	-0.2 ± 0.1
Vehicle + 7g (1.25)	-1.5 ± 0.3 ^c	-1.7 ± 0.3 ^c
WAY-100635 + 7g	-1.2 ± 0.2 ^b	-0.7 ± 0.3 ^d
	$p < 0.0001$	$p < 0.0005$
Vehicle	0.1 ± 0.1	-0.0 ± 0.1
WAY-100635	0.3 ± 0.3	0.2 ± 0.3
	ns	ns

WAY-100635 was administered 15 min before the tested compounds, ^a $p < 0.05$ vs vehicle, ^b $p < 0.01$ vs vehicle, ^c $p < 0.001$ vs vehicle, ^d $p < 0.05$ vs compound group, ^e $p < 0.001$ vs compound group, ns = non-significant.

In conclusion, the decrease in mouse body temperature produced by compound **6a** can be accounted as a measure of its presynaptic 5-HT_{1A} agonistic activity. Tested compound **6a** was ineffective in the forced swimming test in mice (Figure 6), so we can conclude lack of postsynaptic 5-HT_{1A} receptor activity [40].

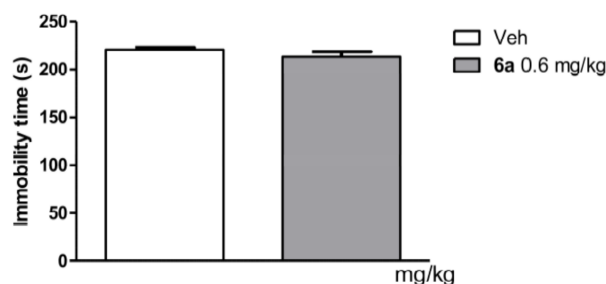


Figure 6. Effect of compound **6a** on forced swimming test in CD-1 mice.

2.2.3. Metabolic Stability Evaluation

We decided to carry out preliminary tests of metabolic stability for selected compounds, as metabolic stability is an important index of a compound's pharmacokinetics. Such studies are routinely performed at earlier stages of studies of potential new drugs. They are extremely important, as many known valuable compounds possessing high desirable pharmacological activity are disqualified at later clinical stages on account of an undesirable pharmacokinetic profile with regard to metabolic stability. Thus, the preliminary studies in this regard performed by us appeared advisable.

A compound with poor metabolic stability will not reach appropriate therapeutic levels for a given molecular target. High metabolic stability of a candidate drug or its metabolite can, in turn, potentially cause higher toxicity or adverse effects. On the other hand, the identification of inhibition or induction of cytochrome P-450 isoenzymes, which mediate the metabolism of most drugs, allows for predicting potential drug-drug interactions [42,43]. The results of a metabolic stability study in the presence of pooled human liver microsomes (HLMs) and nicotinamide adenine dinucleotide phosphate (NADPH) are shown in Table 5. Metabolic stability is presented in the form of biological half-life value, which allows for easy comparison of compounds' structure and their susceptibility to phase 1 biotransformation reactions (the result of incubation on the presence of human liver microsomes). Results presented in Table 5 allow for the quick assessment of metabolic stability.

Table 5. Experimental $t_{1/2}$ values along with corresponding SD and RSD%.

Compound	Average $t_{1/2}$ [min] (<i>n</i> = 2)	SD [min]	RSD%
6a	3.61	0.43	11.18
6d	3.20	0.09	2.81

Table legend: SD—standard deviation, RSD%—relative standard deviation, expressed as $SD/average \times 100\%$.

Even though the biological half-life values for studied compounds were far from high, it is worth noticing that biological half-life value depends on the compound's initial concentration in the incubation mix. As the initial studied compound concentration was 1 μ M, such values were to be expected. Of the studied pyrido[1,2-*c*]pyrimidine derivatives, compounds **6a** (R = -H, R₁ = -H) and **6d** (R = -Cl, R₁ = -H) were most susceptible to phase 1 biotransformation reactions. The metabolic stability investigations for the compounds **6a** and **6d** showed their sensitivity to the activity of human liver microsomes, which is most likely associated with the presence of a 6-fluoro-3-(4-piperidiny)-1,2-benzisoxazole residue in the pharmacophore part. These results will prompt further studies in search of compounds with greater metabolic stability in this group of derivatives. The justification

for further research stems from the fact that the novel compounds revealed very high affinity for a number of receptors and were also characterized by appropriate cLogP values.

3. Materials and Methods

3.1. General Remarks

Reagents and solvents were purchased from commercial suppliers: Sigma-Aldrich, TCI, Alfa Aesar and Chempur. The purity of the obtained samples was routinely confirmed by TLC using Merck plates (Kieselgel 60 F₂₅₄). Melting points (m.p.) were determined using the Electrothermal IA 9200 apparatus with open capillary tubes and were not corrected. ¹H and ¹³C NMR spectra were recorded on a Bruker AVANCE III HD (500 MHz) instrument in CDCl₃ (chemical shifts are reported in δ units), with the use of TMS as the internal reference. The following abbreviations were used to describe peak patterns when appropriate: s (singlet), 2s (double singlet), d (doublet), dd (double doublet), dt (double triplet), t (triplet), td (triple doublet), 4d (quartet of doublets), m (multiplet), q (quartet), qu (quintet). Coupling constants (J) are in hertz (Hz). Numbering system, which was used in NMR spectra interpretation is shown in Figure 7. ESI-HRMS spectra were obtained on a Thermo Q-Exactive instrument. Flash column chromatography was carried out using Merck Silicagel (40–63 μm) Geduran[®] Si 60 and a mixture of toluene:ethylacetate:methanol (10:4:3 v/v), methylene chloride:methanol:triethylamine (64:2:0.4 v/v), chloroform:methanol (9:1 v/v) as an eluent. Thin layer chromatography was performed on Merck Silicagel (Kieselgel 60 F₂₅₄) plates, where the mobile phase was composed of toluene, dioxane, ethanol, and 25% ammonia (9.0:5.0:1.0:0.3 v/v) or methylene chloride, methanol, triethylamine (16.0:1.0:0.2 v/v). Plates were visualized by UV light (254 nm).

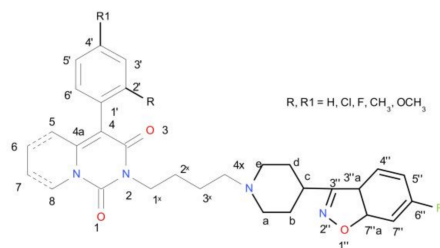


Figure 7. Numbering system for NMR spectra interpretation of compounds (6a–i) and (7a–i).

3.2. Synthesis of Compounds

3.2.1. Procedure for the Synthesis of

2-(4-Bromobutyl)-4-aryl-pyrido[1,2-c]pyrimidine-1,3-diones (4a–i) and
2-(4-bromobutyl)-4-aryl-5,6,7,8-tetrahydropyrido[1,2-c]pyrimidine-1,3-diones (5a–i)

Compounds (4a–i) and (5a–i) were obtained according to the previously described procedures [26,37,44].

3.2.2. General Procedure for the Synthesis of Derivatives of

4-Aryl-2H-pyrido[1,2-c]pyrimidine-1,3-dione (6a–i) and
4-aryl-5,6,7,8-tetrahydropyrido[1,2-c]pyrimidine-1,3-dione (7a–i)

The appropriate bromobutyl derivatives (4a–i) or (5a–i) (0.75 mmol), 6-fluoro-3-(4-piperidinyl)-1,2-benzisoxazole (0.75 mmol) and K₂CO₃ (2 mmol) were suspended in acetonitrile (25 mL). The reaction mixture was carried out at 45 °C and stirred for 8–12 h. The reaction time was determined using TLC. The mixture was filtered to remove inorganic salts, and the solvent was removed from the filtrate under vacuum. The residue was purified by column chromatography (flash or gravity technique) using toluene:ethylacetate:methanol (10:4:3 v/v), methylene chloride:methanol:triethylamine (64:2:0.4 v/v), chloroform:methanol (9:1 v/v) as an eluent. Appropriate fractions were identified by TLC and evaporated to give compounds (6a–i) or (7a–i).

4-Phenyl-2-[4-[4-(6-fluoro-1,2-benzoxazol-3-yl)-1-piperidyl]butyl]-pyrido[1,2-c]pyrimidine-1,3-dione **6a**

The title compound was isolated as a yellow powder. Yield: 20.5%; m.p. 132–133 °C.

¹H NMR (500 MHz, CDCl₃): δ 8.33 (C8H, dt, ³J = 7.5, ⁴J = ⁵J = 1.5), 7.75 (C4''H, dd, ³J = 8.5, ⁴J_{H-F} = 5.0), 7.42–7.47 (C2'H, C6'H, m), 7.35 (C4'H, tt, ³J = 7.5, ⁴J = 1.5), 7.30–7.33 (C3'H, C5'H, m), 7.22 (C7''H, 4d, ³J_{H-F} = 8.5, ⁴J = 2.5, ⁵J = 0.5), 7.04 (C5''H, td, ³J = 9.0, ⁴J = 2.0), 6.89–6.91 (C5H, C6H, m), 6.38 (C7H, m, ³J₁ = 8.0, ³J₂ = 4.5, ⁴J = 3.5), 4.20 (C1^xH₂, t, ³J = 7.5), 3.11 (CaH(E), CeH(E), CcH, m), 2.52 (C4^xH₂, t, ³J = 7.0), 2.02–2.30 (CaH(A), CeH(A), CbH(A), CdH(A), CbH(E), CdH(E), m), 1.81 (C2^xH₂, q, ³J = 7.5), 1.68 (C3^xH₂, q, ³J = 7.5).

¹³C NMR (125 MHz, CDCl₃): δ 164.1 (C6'', d, ¹J = 250.6*), 163.9 (C7''a, d, ³J = 13.6*), 160.9 (C3, s), 160.1 (C3'', s), 148.9 (C1, s), 143.5 (C4a, s), 132.8 (C1', s), 132.4 (C6, s), 131.2 (C2', C6', s), 128.8 (C3', C5', s), 127.9 (C4', s), 127.8 (C8, s), 122.8 (C4'', d, ³J = 10.2*), 121.4 (C5, s), 117.2 (C3''a, s), 112.3 (C5'', d, ²J = 25.3*), 110.7 (C7, s), 104.9 (C4, s), 97.3 (C7'', d, ²J = 26.7*), 58.3 (C4^x, s), 53.4 i 53.4 (Ca i/lub Ce, 2s), 42.3 (C1^x, s), 34.4 (Cc, s), 30.1 (Cb, Cd, s), 25.4 (C2^x, s), 24.1 (C3^x, s).

ESI-HRMS m/z: Calcd for C₃₀H₃₀FN₄O₃ [M + H]⁺ 513.2296. Found: 513.2304

4-(2-Methylphenyl)-2-[4-[4-(6-fluoro-1,2-benzoxazol)-1-piperidyl]butyl]-pyrido[1,2-c]pyrimidine-1,3-dione **6b**

The title compound was isolated as a yellow powder. Yield: 59.7%; m.p. 120–122 °C.

¹H NMR (500 MHz, CDCl₃): δ 8.33 (C8H, dt, ³J = 7.5, ⁴J = ⁵J = 1.0), 7.78 (C4''H, dd, ³J = 8.5, ⁴J_{H-F} = 5.0), 7.21–7.33 (C4'-6'H, C7''H, [4H], m), 7.14 (C3'H, dd, ³J = 8.0, ⁴J = 1.5), 7.05 (C5''H, td, ³J = 9.0, ⁴J = 2.0), 6.88 (C6H, 4d, ³J₁ = 9.5, ³J₂ = 6.0, ⁴J = 1.5), 6.56 (C5H, dt, ³J = 9.5, ⁴J = ⁵J = 1.0), 6.38 (C7H, m, ³J₁ = 7.5, ³J₂ = 6.0, ⁴J = 1.0), 4.20 (C1^xH₂, t, ³J = 7.5), 3.08 (CaH(E), CeH(E), CcH, m), 2.48 (C4^xH₂, t, ³J = 7.5), 2.15 (CH₃, s), 2.0–2.2 (Ca(A), Ce(A), CbH₂, CdH₂, m), 1.80 (C2^xH₂, q, ³J = 7.5), 1.65 (C3^xH₂, q, ³J = 7.5).

¹³C NMR (125 MHz, CDCl₃): δ 164.0 (C6'', d, ¹J = 250.6*), 163.8 (C7''a, d, ³J = 13.6*), 161.0 (C3'', s), 159.6 (C3, s), 149.1 (C1, s), 143.4 (C4a, s), 138.4 (C2', s), 132.4 (C1', s), 132.1 (C6, s), 131.5 (C6', s), 130.5 (C3', s), 128.4 (C4', s), 128.0 (C8, s), 126.4 (C5', s), 122.7 (C4'', d, ³J = 11.1*), 121.4 (C5, s), 117.2 (C3''a, s), 112.3 (C5'', d, ²J = 25.3*), 110.5 (C7, s), 104.1 (C4, s), 97.4 (C7'', d, ²J = 26.7*), 58.4 (C4^x, s), 53.4 (Ca, Ce, s), 42.2 (C1^x, s), 34.5 (Cc, s), 30.3 (Cb, Cd, s), 25.5 (C2^x, s), 24.2 (C3^x, s), 19.6 (CH₃, s).

ESI-HRMS m/z: Calcd for C₃₁H₃₂FN₄O₃ [M + H]⁺ 527.2453. Found: 527.2461

4-(2-Methoxyphenyl)-2-[4-[4-(6-fluoro-1,2-benzoxazol)-1-piperidyl]butyl]-pyrido[1,2-c]pyrimidine-1,3-dione **6c**

The title compound was isolated as a yellow powder. Yield: 71.1%; m.p. 65–70 °C.

¹H NMR (500 MHz, CDCl₃): δ 8.32 (C8H, dt, ³J = 7.5, ⁴J = ⁵J = 1.0), 7.73 (C4''H, dd, ³J = 8.5, ⁴J_{H-F} = 5.0), 7.37 (C4'H, 4d, ³J₁ = 8.0, ³J₂ = 7.5, ⁴J = 1.5), 7.22 (C6'H, C7''H, m), 7.01–7.07 (C5'H, C5''H, m), 6.88 (C6H, 4d, ³J₁ = 9.5, ³J₂ = 6.5, ⁴J = 1.5), 6.63 (C5H, dt, ³J = 9.0, ⁴J = ⁵J = 1.5), 6.37 (C7H, m, ³J₁ = 7.5, ³J₂ = 6.5, ⁴J = 1.5), 4.19 (C1^xH₂, t, ³J = 7.5), 3.76 (OCH₃, s), 3.08 (CaH(E), CeH(E), CcH, m), 2.48 (C4^xH₂, t, ³J = 7.5), 2.0–2.2 (Ca(A), Ce(A), CbH₂, CdH₂, m), 1.80 (C2^xH₂, q, ³J = 7.0), 1.66 (C3^xH₂, q, ³J = 7.0).

¹³C NMR (125 MHz, CDCl₃): δ 164.0 (C6'', d, ¹J = 250.4*), 163.8 (C7''a, d, ³J = 13.6*), 161.1 (C3'', s), 159.9 (C3, s), 157.8 (C2', s), 149.1 (C1, s), 143.6 (C4a, s), 133.0 (C6', s), 131.9 (C6, s), 129.6 (C4', s), 127.8 (C8, s), 122.8 (C4'', d, ³J = 11.1*), 121.9 (C1', s), 121.4 (C5, s), 120.9 (C5', s), 117.2 (C3''a, s), 112.3 (C5'', d, ²J = 25.1*), 111.4 (C3', s), 110.5 (C7, s), 101.2 (C4, s), 97.3 (C7'', d, ²J = 26.7*), 58.4 (C4^x, s), 55.6 (OCH₃, s), 53.5 (Ca, Ce, s), 42.3 (C1^x, s), 34.5 (Cc, s), 30.3 (Cb, Cd, s), 25.5 (C2^x, s), 24.2 (C3^x, s).

ESI-HRMS m/z: Calcd for C₃₁H₃₂FN₄O₄ [M + H]⁺ 543.2402. Found: 543.2410

4-(2-Chlorophenyl)-2-{4-[4-(6-fluoro-1,2-benzoxazol)-1-piperidyl]butyl}-pyrido[1,2-c]pyrimidine-1,3-dione **6d**

The title compound was isolated as a yellow powder. Yield: 71.7%; m.p. 69–74 °C.

¹H NMR (500 MHz, CDCl₃): δ 8.37 (C8H, dt, ³J = 7.5, ⁴J = ⁵J = 1.0), 7.75 (C4''H, bs), 7.52 (C3'H, m), 7.29–7.37 (C4'H, C5'H, C6'H, m), 7.23 (C7''H, 4d, ³J_{H-F} = 8.5, ⁴J = 2.5, ⁵J = 0.5), 7.05 (C5''H, td, ³J = 8.5, ⁴J = 2.0), 6.97 (C6H, 4d, ³J₁ = 9.5, ³J₂ = 6.0, ⁴J = 1.0), 6.56 (C5H, dt, ³J = 9.0, ⁴J = ⁵J = 1.0), 6.43 (C7H, m, ³J₁ = 7.5, ³J₂ = 6.5, ⁴J = 1.5), 4.21 (C1^xH₂, m), 3.10 (CaH(E), CeH(E), CcH, bs), 2.51 (C4^xH₂, bs), 2.0–2.3 (CaH(A), CeH(A), CbH₂, CdH₂), 1.81 (C2^xH₂, m), 1.67 (C3^xH₂, m).

¹³C NMR (125 MHz, CDCl₃): δ 164.1 (C6'', d, ¹J = 250.6*), 163.9 (C7''a, d, ³J = 13.6*), 161.0 (C3'', s), 159.5 (C3, s), 149.0 (C1, s), 143.8 (C4a, s), 135.7 (C2', s), 133.4 (C6', s), 133.1 (C1', s), 131.7 (C6, s), 130.0 (C3', s), 129.7 (C4', s), 128.1 (C8, s), 127.3 (C5', s), 122.8 (C4'', d, ³J = 10.7*), 121.1 (C5, s), 117.2 (C3''a, s), 122.3 (C5'', d, ²J = 25.1*), 110.8 (C7, s), 102.2 (C4, s), 97.4 (C7'', d, ²J = 26.7*), 58.3 (C4^x, s), 53.4 (Ca, Ce, s), 42.2 (C1^x, s), 34.4 (Cc, s), 30.2 (Cb, Cd, s), 25.4 (C2^x, s), 24.0 (C2^x, s).

ESI-HRMS m/z: Calcd for C₃₀H₂₉ClFN₄O₃ [M + H]⁺ 547.1907. Found: 547.1915

4-(2-Fluorophenyl)-2-{4-[4-(6-fluoro-1,2-benzoxazol)-1-piperidyl]butyl}-pyrido[1,2-c]pyrimidine-1,3-dione **6e**

The title compound was isolated as a yellow powder. Yield: 63.2%; m.p. 58–62 °C.

¹H NMR (500 MHz, CDCl₃): δ 8.37 (C8H, dt, ³J = 7.5, ⁴J = ⁵J = 1.0), 7.74 (C4''H, m), 7.35–7.43 (C4'H, m), 7.33 (C5'H, td, ³J = 7.5, ⁴J = 2.0), 7.23 (C6'H, C7''H, m), 7.17 (C3'H, m, ³J_{H-F} = 10.0, ³J = 8.5, ⁴J = 1.0), 7.04 (C5''H, td, ³J = 8.5, ⁴J = 2.5), 6.98 (C6H, 4d, ³J₁ = 9.5, ³J₂ = 6.5, ⁴J = 1.5), 6.74 (dt) i 6.74 (dt) (C5H, ³J = 9.0, ⁴J = ⁵J = 1.5**), 6.43 (C7H, m, ³J₁ = 7.5, ³J₂ = 6.5, ⁴J = 1.5), 4.20 (C1^xH₂, t, ³J = 7.5), 3.09 (CaH(E), CeH(E), CcH, pd), 2.49 (C4^xH₂, bs), 2.00–2.30 (CaH(A), CeH(A), CbH₂, CdH₂, m), 1.81 (C2^xH₂, q, ³J = 7.5), 1.66 (C3^xH₂, q, ³J = 7.5).

¹³C NMR (125 MHz, CDCl₃): δ 164.1 (C6'', d, ¹J = 250.4*), 163.9 (C7''a, d, ³J = 13.5*), 161.1 (C3'', s), 160.9 (C2', d, ¹J = 246.9*), 159.6 (C3, s), 148.9 (C1, s), 144.0 (C4a, s), 133.4 (C6', d, ³J = 3.0*), 133.1 (C6, s), 130.1 (C4', d, ³J = 8.2*), 128.2 (C8, s), 124.4 (C5', d, ⁴J = 3.5*), 122.8 (C4'', d, ³J = 11.1*), 121.2 (C5, s), 120.3 (C1', d, ²J = 16.0*), 117.2 (C3''a, s), 116.1 (C3', d, ²J = 22.3*), 112.3 (C5'', d, ²J = 25.1*), 110.8 (C7, s), 98.4 (C4, s), 97.4 (C7'', d, ²J = 26.8*), 58.4 (C4^x, s), 53.5 (Ca, Ce, s), 42.4 (C1^x, s), 34.5 (Cc, s), 30.3 (Cb, Cd, s), 25.5 (C2^x, s), 24.2 (C3^x, s).

ESI-HRMS m/z: Calcd for C₃₀H₂₉F₂N₄O₃ [M + H]⁺ 531.2202. Found: 531.2212

4-(4-Methylphenyl)-2-{4-[4-(6-fluoro-1,2-benzoxazol)-1-piperidyl]butyl}-pyrido[1,2-c]pyrimidine-1,3-dione **6f**

The title compound was isolated as a yellow powder. Yield: 71.1%; m.p. 158–159 °C.

¹H NMR (500 MHz, CDCl₃): δ 8.32 (C8H, dt, ³J = 7.5, ⁴J = ⁵J = 1.0), 7.78 (C4''H, bs), 7.18–7.26 (C2'H, C3'H, C5'H, C6'H, C7''H, m), 7.05 (C5''H, td, ³J = 9.0, ⁴J = 2.0), 6.86–6.93 (C5H, C6H, m), 6.37 (C7H, m, ³J₁ = 7.5, ³J₂ = 5.5, ⁴J = 1.5), 4.19 (C1^xH₂, t, ³J = 7.5), 3.14 (CaH(E), CeH(E), Cc, bs), 2.57 (C4^xH₂, bs), 2.39 (CH₃, s), 2.03–2.35 (CaH(A), CeH(A), CbH₂, CdH₂, m), 1.81 (C2^xH₂, q, ³J = 7.5), 1.70 (C3^xH₂, bs).

¹³C NMR (125 MHz, CDCl₃): δ 164.1 (C6'', d, ¹J = 250.7*), 163.9 (C7''a, d, ³J = 13.6*), 160.8 (C3'', s), 160.3 (C3, s), 149.0 (C1, s), 143.5 (C4a, s), 137.6 (C6, s), 132.2 (C4', s), 131.0 (C2', C6', s), 129.7 (C1', s), 129.5 (C3', C5', s), 127.9 (C8, s), 122.8 (C4'', d*), 121.6 (C5, s), 117.1 (C3''a, bs), 112.4 (C5'', d, ²J = 25.1*), 110.6 (C7H, s), 104.9 (C4, s), 97.4 (C7'', d, ²J = 26.8*), 58.2 (C4^x, s), 53.2 (Ca, Ce, s), 42.1 (C1^x, s), 34.2 (Cc, s), 30.0 (Cb, Cd, s), 25.4 (C2^x, s), 23.7 (C3^x, s), 21.3 (CH₃, s).

ESI-HRMS m/z: Calcd for C₃₁H₃₂FN₄O₃ [M + H]⁺ 527.2453. Found: 527.2459

4-(4-Methoxyphenyl)-2-{4-[4-(6-fluoro-1,2-benzoxazol)-1-piperidyl]butyl}-pyrido[1,2-c]pyrimidine-1,3-dione **6g**

The title compound was isolated as a yellow powder. Yield: 78.9%; m.p. 163–166 °C.

¹H NMR (500 MHz, CDCl₃): δ 8.31 (C8H, dt, ³J = 7.5, ⁴J = ⁵J = 1.0), 7.73 (C4''H, dd, ³J = 8.5, ⁴J_{H-F} = 5.0), 7.24 (C2'H, C6'H, dt, ³J = 8.5, ⁴J = 3.0), 7.21–7.24 (C7''H, m**), 7.04 (C5''H, td, ³J = 9.0, ⁴J = 2.0), 6.98 (C3'H, C5'H, dt, ³J = 8.5, ⁴J = 3.0), 6.86–6.94 (C5H, C6H, m), 6.37 (C7H, m, ³J₁ = 8.0, ³J₂ = 6.0, ⁴J = 1.5), 4.19 (C1^xH₂, t, ³J = 7.5), 3.84 (OCH₃, s), 3.09 (Ca(E), Ce(E), Cc, 3.09, m), 2.47 (C4^xH₂, t, ³J = 7.5), 2.00–2.20 (Ca(A), Ce(A), CbH₂, CdH₂, m), 1.80 (C2^xH₂, q, ³J = 7.5), 1.65 (C3^xH₂, q, ³J = 7.7).

¹³C NMR (125 MHz, CDCl₃): δ 164.1 (C6'', d, ¹J = 250.4*), 163.8 (C7''a, d, ³J = 13.6*), 161.1 (C3'', s), 160.4 (C3, s), 159.1 (C4', s), 149.0 (C1, s), 143.5 (C4a, s), 132.3 (C2', C6', s), 132.1 (C6, s), 127.9 (C8, s), 124.8 (C1', s), 122.7 (C4'', d, ³J = 11.1*), 121.6 (C5, s), 117.2 (C3''a, s), 114.3 (C3', C5', s), 112.3 (C5'', d, ²J = 25.3*), 110.6 (C7, s), 104.6 (C4, s), 97.4, d, ²J = 26.8*), 58.4 (C4^x, s), 55.3 (OCH₃, s), 53.5 (Ca, Ce, s), 42.4 (C1^x, s), 34.5 (Cc, s), 30.4 (Cb, Cd, s), 25.5 (C2^x, s), 24.3 (C3^x, s).

ESI-HRMS m/z: Calcd for C₃₁H₃₂FN₄O₄ [M + H]⁺ 543.2402. Found: 543.2411

4-(4-Chlorophenyl)-2-{4-[4-(6-fluoro-1,2-benzoxazol)-1-piperidyl]butyl}-pyrido[1,2-c]pyrimidine-1,3-dione **6h**

The title compound was isolated as a yellow powder. Yield: 63.2%; m.p. 152–155 °C.

¹H NMR (500 MHz, CDCl₃): δ 8.35 (C8H, dt, ³J = 7.5, ⁴J = ⁵J = 1.0), 7.76 (C4''H, bs), 7.25–7.29 (C3'H, C5'H, dt, ³J = 8.5, ⁴J = 2.5), 7.23 (C7''H, 4d, ³J_{H-F} = 8.5, ⁴J = 2.0, ⁵J = 0.5), 7.40–7.44 (C2'H, C6'H, dt, ³J = 8.5, ⁴J = 2.5), 7.05 (C5''H, td, ³J = 8.5, ⁴J = 2.0), 6.95 (C6H, 4d, ³J₁ = 9.5, ³J₂ = 6.0, ⁴J = 1.0), 6.88 (C5H, m, ³J = 9.0, ⁴J = ⁵J = 1.5), 6.42 (C7H, m, ³J₁ = 7.5, ³J₂ = 6.0, ⁴J = 1.0), 4.19 (C1^x H₂, t, ³J = 7.5), 3.13 (CaH(E), CeH(E), CcH, bs), 2.55 (C4^xH₂, bs), 2.0–2.4 (CaH(A), CeH(A), CbH₂, CdH₂, m), 1.80 (C2^xH₂, q, ³J = 7.0), 1.70 (C3^xH₂, bs).

¹³C NMR (125 MHz, CDCl₃): δ 164.1 (C6'', d, ¹J = 250.7*), 163.9 (C7''a, d, ³J = 13.7*), 160.8 (C3'', s), 160.0 (C3, s), 148.8 (C1, s), 143.7 (C4a, s), 133.7 (C4', s), 132.9 (C6, s), 132.6 (C3', C5', s), 131.2 (C1', s), 129.0 (C2', C6', s), 128.1 (C8, s), 122.8 (C4'', d, ³J = 9.4*), 121.1 (C5, s), 117.1 (C3''a, s), 112.4 (C5'', d, ²J = 24.9*), 110.9 (C7, s), 103.5 (C4, s), 97.4 (C7'', d, ²J = 26.8*), 58.2 (C4^x, s), 53.3 (Ca, Ce, s), 42.3 (C1^x, s), 34.3 (Cc, s), 29.9 (Cb, Cd, s), 25.4 (C2^x, s), 23.8 (C3^x, s).

ESI-HRMS m/z: Calcd for C₃₀H₂₉ClFN₄O₃ [M + H]⁺ 547.1907. Found: 547.1916

4-(4-Fluorophenyl)-2-{4-[4-(6-fluoro-1,2-benzoxazol)-1-piperidyl]butyl}-pyrido[1,2-c]pyrimidine-1,3-dione **6i**

The title compound was isolated as a yellow powder. Yield: 17.6%; m.p. 102–107 °C.

¹H NMR (500 MHz, CDCl₃): δ 8.34 (C8H, dt, ³J = 7.0, ⁴J = ⁵J = 1.5), 7.75 (C4''H, bs), 7.29 (C2'H, C6'H, m), 7.23 (C7''H, 4d, ³J_{H-F} = 8.5, ⁴J = 2.0, ⁵J = 0.5), 7.14 (C3'H, C5'H, tt, ³J = 8.5), 7.052 (C5''H, td, ³J = 8.5, ⁴J = 2.0), 6.94 (C6H, 4d, ³J₁ = 9.0, ³J₂ = 6.0, ⁴J = 1.5), 6.87 (C5H, dt, ³J = 9.0, ⁴J = ⁵J = 1.5), 6.41 (C7H, m, ³J₁ = 7.5, ³J₂ = 6.0, ⁴J = 1.5), 4.19 (C1^xH₂, t, ³J = 7.5), 3.12 (CaH(E), CeH(E)C₆H₅, bs), 2.53 (C4^xH₂, bs), 2.0–2.3 (CaH(A), CeH(A), CbH₂, CdH₂, m), 1.81 (C2^xH₂, q, ³J = 7.5), C3^xH₂, bs).

¹³C NMR (125 MHz, CDCl₃): δ 164.1 (C6'', d, ¹J = 250.8*), 163.9 (C7''a, d, ³J = 13.5*), 162.3 (C4'H, d, ¹J = 247.2*), ~161.0 (C3'', s), 160.2 (C3, s), 148.9 (C1, s), 143.7 (C4a, s), 133.0 (C2', C6', d, ³J = 8.2*), 132.8 (C6, s), 128.6 (C1', d, ⁴J = 3.5*), 128.1 (C8, s), 122.8 (C4'', d, ³J = 10.8*), 121.2 (C5, s), 117.2 (C3''a, s), 115.8 (C3', C5', d, ²J = 21.5*), 112.4 (C5'', d, ²J = 24.9*), 110.8 (C7, s), 103.8 (C4, s), 97.4 (C7'', d, ²J = 26.8*), 58.4 (C4^x, s), 53.4 (Ca, Ce, s), 42.3 (C1^x, s), 34.4 (Cc, s), 30.1 (Cb, Cd, s), 25.4 (C2^x, s), 24.1 (C3^x, s).

ESI-HRMS m/z: Calcd for C₃₀H₂₉F₂N₄O₃ [M + H]⁺ 531.2202. Found: 531.2211

4-Phenyl-2-{4-[4-(6-fluoro-1,2-benzoxazol-3-yl)-1-piperidyl]butyl}-5,6,7,8-tetrahydro-pyrido[1,2-c]pyrimidine-1,3-dione **7a**

The title compound was isolated as a white powder. Yield: 81.6%; m.p. 110–113 °C.

¹H NMR (500 MHz, CDCl₃): δ 7.78 (C4''H, bs), 7.40 (C3'H, C5'H, tt, ³J = 7.5), 7.33 (C4'H, tt, ³J = 7.5), 7.23 (C7''H, dd, ³J_{H-F} = 8.0, ⁴J = 2.0), 7.19 (C2'H, C6'H, dt, ³J = 7.5), 7.05 (C5''H, td, ³J = 9.0, ⁴J = 2.0), 4.05 (C1^xH₂, t, ³J = 7.5), 3.95 (C8H₂, t, ³J = 6.5), 3.14 (CaH(E), CeH(E), CcH, bs), 2.54 (C4^xH₂, C5H₂, m), 2.05–2.35 (CaH(A), CeH(A), CdH₂, m), 1.93 (C7H₂, q, ³J = 6.5), 1.71 (C2^xH₂, C3^xH₂, C6H₂, m).

¹³C NMR (125 MHz, CDCl₃): δ 164.1 (C6'', d, ¹J = 250.6*), 163.9 (C7''a, d, ³J = 13.4*), 162.0 (C3, s), 160.8 (C3'', s), 151.7 (C1, s), 149.8 (C4a, s), 133.3 (C1', s), 130.7 (C2', C6', s), 128.5 (C3', C5', s), 127.7 (C4', s), 122.9 (C4'', d*), 117.1 (C3''a, s), 112.4 (C5'', d, ²J = 25.2*), 112.4 (C4, s), 97.4 (C7'', d, ²J = 26.7*), 58.3 (C4^x, s), 53.3 (Ca, Ce, s), 42.7 (C8, s), 41.3 (C1^x, s), 34.1 (Cc, s), 29.8 (Cb, Cd, s), 26.7 (C5, s), 25.6 (C2^x, s), 23.9 (C3^x, s), 21.8 (C7, s), 18.6 (C6, s).

ESI-HRMS m/z: Calcd for C₃₀H₃₄FN₄O₃ [M + H]⁺ 517.2609. Found: 517.2617

4-(2-Methylphenyl)-2-{4-[4-(6-fluoro-1,2-benzoxazol)-1-piperidyl]butyl}-5,6,7,8-tetrahydro-pyrido[1,2-c]pyrimidine-1,3-dione **7b**

The title compound was isolated as an oil. Yield: 97.4%.

¹H NMR (500 MHz, CDCl₃): δ 7.75 (C4''H, bs), 7.18–7.26 (C4'-6'H, C7''H, m), 7.05 (C3'H, C5'H, m), 4.05 (C1^xH₂, t, ³J = 7.0), 3.93 (C8H₂, m), 3.09 (CaH(E), CeH(E), CcH, pd), 2.49 (C4^xH₂, bs), 2.45 (C5H(1), m), 2.27 (C5(2), m), 2.00–2.23 (CaH(A), CeH(A), CbH₂, CdH₂, m), 2.14 (OCH₃, s), 1.93 (C7H₂, m), 1.60–1.78 (C2^xH₂, C3^xH₂, C6H₂, m).

¹³C NMR (125 MHz, CDCl₃): δ 164.1 (C6'', d, ¹J = 250.4*), 163.9 (C7''a, d, ³J = 13.6*), 161.4 (C3, s), 161.0 (C3'', s), 151.9 (C1, s), 149.6 (C4a, s), 137.6 (C2', s), 132.9 (C1', s), 130.7 (C6', s), 130.3 (C3', s), 128.2 (C4', s), 126.2 (C5', s), 122.8 (C4'', d, ³J = 10.8*), 117.2 (C3''a, s), 112.4 (C5'', d, ²J = 25.3*), 111.8 (C4, s), 97.4 (C7'', d, ²J = 26.7*), 58.4 (C4^x, s), 53.4 (Ca, Ce, s), 42.9 (C8, s), 41.3 (C1^x, s), 34.5 (Cc, s), 30.2 (cb, Cd, s), 26.5 (C5, s), 25.7 (C2^x, s), 24.1 (C3^x, s), 21.9 (C7, s), 19.7 (CH₃, s), 18.6 (C6, s).

ESI-HRMS m/z: Calcd for C₃₁H₃₆FN₄O₃ [M + H]⁺ 531.2766. Found: 531.2774

4-(2-Methoxyphenyl)-2-{4-[4-(6-fluoro-1,2-benzoxazol)-1-piperidyl]butyl}-5,6,7,8-tetrahydro-pyrido[1,2-c]pyrimidine-1,3-dione **7c**

The title compound was isolated as an oil. Yield: 71.1%.

¹H NMR (500 MHz, CDCl₃): δ 7.79 (C4''H, bs), 7.33 (C4'H, 4d, ³J₁ = 8.5, ³J₂ = 7.5, ⁴J = 1.5), 7.23 (C7''H, 4d, ³J_{H-F} = 8.5, ⁴J = 2.0, ⁵J = 0.5), 7.11 (C6'H, dd, ³J = 7.5, ⁴J = 1.5), 7.06 (C5''H, td, ³J = 9.0, ⁴J = 2.0), 6.99 (C5'H, td, ³J = 7.5, ⁴J = 1.0), 6.94 (C3'H, dd, ³J = 8.5, ⁴J = 1.0), 4.03 (C1^xH₂, t, ³J = 7.0), 3.95 (C8H(1), dt, ²J = 13.5, ³J = 7.0), 3.90 (C8H(2), dt, ²J = 13.5, ³J = 7.0), 3.78 (OCH₃, s), 3.14 (CaH(E), CeH(E), CcH, bs), 2.56 (C4^xH₂, bs), 2.43 (C5H₂, m), 2.00–2.35 (CaH(A), CeH(A), CbH₂, CdH₂, m), 1.92 (C7H₂, q, ³J = 6.5), 1.61–1.80 (C2^xH₂, C3^xH₂, C6H₂, m).

¹³C NMR (125 MHz, CDCl₃): δ 164.1 (C6'', d, ¹J = 250.8*), 163.9 (C7''a, d, ³J = 13.3*), 161.8 (C3, s), 160.8 (C3'', s), 157.3 (C2', s), 151.9 (C1, s), 150.2 (C4a, s), 132.3 (C6', s), 129.5 (C4', s), 122.9 (C4'', s), 122.0 (C1', s), 120.8 (C5', s), 117.1 (C3''a, s), 112.5 (C5'', d, ²J = 25.5*), 111.1 (C3', s), 108.5 (C4, s), 97.4 (C7'', d, ²J = 26.8*), 58.3 (C4^x, s), 55.5 (OCH₃, s), 53.3 (Ca, Ce, s), 42.9 (C8, s), 41.1 (C1^x, s), 34.2 (Cc, s), 29.9 (Cb, Cd, s), 26.3 (C5, s), 25.5 (C2^x, s), ~23.8 (C3^x, s), 21.8 (C7, s), 18.5 (C6, s).

ESI-HRMS m/z: Calcd for C₃₁H₃₆FN₄O₄ [M + H]⁺ 547.2715. Found: 547.2726

4-(2-Chlorophenyl)-2-{4-[4-(6-fluoro-1,2-benzoxazol)-1-piperidyl]butyl}-5,6,7,8-tetrahydro-pyrido[1,2-c]pyrimidine-1,3-dione **7d**

The title compound was isolated as an oil. Yield: 51.4%.

^1H NMR (500 MHz, CDCl_3): δ 7.71 (C4''H, pt), 7.46 (C3'H, m), 7.28–7.33 (C5'H, C6'H, m), 7.23 (C7''H, 4d, $^3J_{\text{H-F}} = 8.5$, $^4J = 2.0$, $^5J = 0.5$), 7.18–7.21 (C4'H, m), 7.04 (C5''H, td, $^3J = 9.0$, $^4J = 2.0$), 4.05 (C1 \times H₂, t, $^3J = 7.0$), 3.98 (C8H(1), dt, $^2J = 13.5$, $^3J = 6.5$), 3.90 (C8H(2), dt, $^2J = 13.5$, $^3J = 6.5$), 3.06 (CaH(E), CeH(E), CcH, pd), 2.44 (C4 \times H₂, pt), 2.41 (C5H₂, m), 2.00–2.20 (CaH(A), CeH(A), CbH₂, CdH₂, m), 1.93 (C7H₂, m), 1.67–1.79 (C2 \times H₂, C6H₂ m), 1.61 (C3 \times H₂, q, $^3J = 7.0$).

^{13}C NMR (125 MHz, CDCl_3): δ 164.1 (C6'', d, $^1J = 250.4^*$), 163.9 (C7''a, d, $^3J = 13.6^*$), 161.2 (C3, C3'', pd), 151.8 (C1, s), 150.4 (C4a, s), 135.1 (C2', s), 132.6 (C6', s), 132.5 (C1', s), 129.7 (C3', s), 129.5 (C4', s), 127.1 (C5', s), 122.7 (C4'', d, $^3J = 10.9^*$), 117.3 (C3''a, s), 112.3 (C5'', d, $^2J = 25.3^*$), 110.1 (C4, s), 97.4 (C7'', d, $^2J = 26.7^*$), 58.5 (C4 \times , s), 53.5 (Ca, Ce, s), 43.0 (C8, s), 41.5 (C1 \times , s), 34.7 (Cc, s), 30.5 (Cb, Cd, s), 26.4 (C5, s), 25.7 (C2 \times , s), 24.4 (C3 \times , s), 21.8 (C7, s), 18.5 (C6, s).

ESI-HRMS m/z : Calcd for $\text{C}_{30}\text{H}_{33}\text{ClFN}_4\text{O}_3$ $[\text{M} + \text{H}]^+$ 551.2220. Found: 551.2230

4-(2-Fluorophenyl)-2-{4-[4-(6-fluoro-1,2-benzoxazol)-1-piperidyl]butyl}-5,6,7,8-tetrahydro-pyrido[1,2-c]pyrimidine-1,3-dione **7e**

The title compound was isolated as an oil. Yield: 76.3%.

^1H NMR (500 MHz, CDCl_3): δ 7.72 (C4''H, dd, $^3J = 9.0$, $^4J_{\text{H-F}} = 5.5$), 7.31–7.37 (C4'H, m), 7.20–7.25 (C6'H, C7''H, m), 7.19 (C5'H, td, $^3J = 7.5$, $^4J = 1.0$), 7.12 (C3'H, m, $^3J_{\text{H-F}} = 9.5$, $^3J = 8.0$, $^4J = 1.0$), 7.04 (C5''H, td, $^3J = 9.0$, $^4J = 2.0$), 4.04 (C1 \times H₂, t, $^3J = 7.5$), 3.97 (C8H(1), dt, $^2J = 14.0$, $^3J = 7.0$ **), 3.92 (C8H(2), dt, $^2J = 14.0$, $^3J = 7.0$ **), 3.07 (CaH(E), CeH(E), CcH, pd), 2.47–2.57 (C5H₂, m**), 2.45 (C4 \times H₂ t, $^3J = 7.0$), 2.00–2.19 (CaH(A), CeH(A), CbH₂, CdH₂, m), 1.94 (C7H₂, q, $^3J = 7.0$), 1.65–1.81 (C2 \times H₂, C6H₂, m), 1.61 (C3 \times H₂, q, $^3J = 7.5$).

^{13}C NMR (125 MHz, CDCl_3): δ 164.1 (C6'', d, $^1J = 250.4^*$), 163.9 (C7''a, d, $^3J = 13.4^*$), 161.4 (C3, s), 161.1 (C3'', s), 160.4 (C2', d, $^1J = 245.8^*$), 151.7 (C1, s), 150.9 (C4a, s), 132.9 (C6', d, $^3J = 3.1^*$), 130.0 (C4', d, $^3J = 8.3^*$), 124.2 (C5', d, $^4J = 3.6^*$), 122.7 (C4'', d, $^3J = 11.2^*$), 120.8 (C1', d, $^2J = 16.2^*$), 117.3 (C3''a, s), 115.8 (C3', d, $^2J = 22.4^*$), 112.3 (C5'', d, $^2J = 25.1^*$), 106.1 (C4, s), 97.4 (C7'', d, $^2J = 26.7^*$), 58.5 (C4 \times , s), 53.5 (Ca, Ce, s), 42.8 (C8, s), 34.6 (Cc, s), 30.5 (Cb, Cd, s), 26.5 (C5, s), 25.7 (C2 \times , s), 24.4 (C3 \times , s), 21.8 (C7, s), 18.4 (C6, s).

ESI-HRMS m/z : Calcd for $\text{C}_{30}\text{H}_{33}\text{F}_2\text{N}_4\text{O}_3$ $[\text{M} + \text{H}]^+$ 535.2515. Found: 535.2522

4-(4-Methylphenyl)-2-{4-[4-(6-fluoro-1,2-benzoxazol)-1-piperidyl]butyl}-5,6,7,8-tetrahydro-pyrido[1,2-c]pyrimidine-1,3-dione **7f**

The title compound was isolated as a white powder. Yield: 55.3%; m.p. 107–110 °C.

^1H NMR (500 MHz, CDCl_3): δ 7.71 (C4''H, pt), 7.23 (C7''H, dd, $^3J_{\text{H-F}} = 8.5$, $^4J = 2.0$), 7.20 (C2'H, C6'H, d, $^3J = 8.0$), 7.08 (C3'H, C5'H, d, $^3J = 8.0$), 7.04 (C5''H, td, $^3J = 9.0$, $^4J = 2.0$), 4.04 (C1 \times H₂, t, $^3J = 7.0$), 3.94 (C8H₂, t, $^3J = 6.0$), 3.06 (CaH(E), CeH(E), CcH, pd), 2.54 (C5H₂, t, $^3J = 6.5$), 2.440 (C4 \times H₂, pt), 2.36 (CH₃, s), 2.00–2.17 (CaH(A), CeH(A), CbH₂, CdH₂, m), 1.92 (C7H₂, q, $^3J = 6.5$), 1.65–1.77 (C2 \times H₂, C6H₂, m), 1.605 (C3 \times H₂, q, $^3J = 6.5$).

^{13}C NMR (125 MHz, CDCl_3): δ 164.1 (C6'', d, $^1J = 250.4^*$), 163.9 (C7''a, d, $^3J = 13.4^*$), 162.1 (C3, s), 161.1 (C3'', s), 151.7 (C1, s), 149.5 (C4a, s), 137.4 (C4', s), 130.6 (C2', C6', s), 130.3 (C1', s), 129.2 (C3', C5', s), 122.7 (C4'', d, $^3J = 10.9^*$), 117.3 (C3''a, s), 112.4 (C4, s), 112.3 (C5'', d, $^2J = 25.1^*$), 97.4 (C7'', d, $^2J = 26.7^*$), 58.6 (C4 \times , s), 53.6 (Ca, Ce, s), 42.6 (C8, s), 41.5 (C1 \times , s), 34.7 (Cc, s), 30.5 (Cb, Cd, s), 26.7 (C5, s), 25.7 (C2 \times , s), 24.4 (C3 \times , s), 21.8 (C7, s), 21.3 (CH₃, s), 18.6 (C6, s).

ESI-HRMS m/z : Calcd for $\text{C}_{31}\text{H}_{36}\text{FN}_4\text{O}_3$ $[\text{M} + \text{H}]^+$ 531.2766. Found: 531.2775

4-(4-Methoxyphenyl)-2-{4-[4-(6-fluoro-1,2-benzoxazol)-1-piperidyl]butyl}-5,6,7,8-tetrahydro-pyrido[1,2-c]pyrimidine-1,3-dione **7g**

The title compound was isolated as a white powder. Yield: 78.9%; m.p. 108–109 °C.

^1H NMR (500 MHz, CDCl_3): δ 7.75 (C4''H, bs), 7.23 (C7''H, dd, $^3J_{\text{H-F}} = 8.5$, $^4J = 2.0$), 7.12 (C2'H, C6'H, dt, $^3J = 8.5$, $^4J = 3.0$), 7.05 (C5''H, td, $^3J = 9.0$, $^4J = 2.0$), 6.93 (C3'H, C5'H,

dt, $^3J = 9.0$, $^4J = 2.5$), 4.04 (C1^xH₂, t, $^3J = 7.5$), 3.94 (C8H₂, t, $^3J = 6.5$), 3.82 (OCH₃, s), 3.10 (CaH(E), CeH(E), CcH, bs), 2.55 (C5H₂, t, $^3J = 7.0$), 2.49 (C4^xH₂, bs), 2.00–2.25 (CaH(A), CeH(A), CbH₂, CdH₂, m), 1.93 (C7H₂, q, $^3J = 7.0$), 1.60–1.80 (C2^xH₂, C3^xH₂, C6H₂, m).

¹³C NMR (125 MHz, CDCl₃): δ 164.1 (C6^{''}, d, $^1J = 250.5^*$), 163.9 (C7^{''}a, d, $^3J = 13.6^*$), 162.2 (C3, s), 161.0 (C3^{''}, s), 151.7 (C1, s), 149.7 (C4a, s), 131.8 (C2', C6', s), 125.5 (C1', s), 122.8 (C4^{''}, d, $^3J = 11.2^*$), 117.2 (C3^{''}a, s), 114.0 (C3', C5', s), 112.4 (C5^{''}, d, $^2J = 25.1^*$), 112.0 (C4, s), 97.4 (C7^{''}, d, $^2J = 26.7^*$), 58.5 (C4^x, s), 55.3 (OCH₃, s), 53.4 (Ca, Ce, s), 42.7 (C8, s), 41.4 (C1^x, s), 34.5 (Cc, s), 30.2 (Cb, Cd, s), 26.8 (C5, s), 25.7 (C2^x, s), 24.2 (C3^x, s), 21.8 (C7, s), 18.6 (C6, s).

ESI-HRMS m/z: Calcd for C₃₁H₃₆FN₄O₄ [M + H]⁺ 547.2715. Found: 547.2724

4-(4-Chlorophenyl)-2-{4-[4-(6-fluoro-1,2-benzoxazol)-1-piperidyl]butyl}-5,6,7,8-tetrahydro-pyrido[1,2-c]pyrimidine-1,3-dione **7h**

The title compound was isolated as a white powder. Yield: 89.2%; m.p. 116–120 °C.

¹H NMR (500 MHz, CDCl₃): δ 7.77 (C4^{''}H, bs), 7.37 (C2'H, C6'H, dt, $^3J = 9.0$, $^4J = 2.5$), 7.23 (C7^{''}H, 4d, $^3J_{H-F} = 8.5$, $^4J = 2.0$, $^5J = 0.5$), 7.15 (C3'H, C5'H, dt, $^3J = 8.5$, $^4J = 2.5$), 7.06 (C5^{''}H, td, $^3J = 9.0$, $^4J = 2.0$), 4.04 (C1^xH₂, t, $^3J = 7.5$), 3.94 (C8H₂, t, $^3J = 6.5$), 3.14 (CaH(E), CeH(E), CcH, bs), 2.52 (C4^xH₂, C5H₂, m), 2.02–2.40 (CaH(A), CeH(A), CbH₂, CdH₂, m), 1.94 (C7H₂, q, $^3J = 6.5$), 1.72 (C2^xH₂, C3^xH₂, C6H₂, m).

¹³C NMR (125 MHz, CDCl₃): δ 164.1 (C6^{''}, d, $^1J = 250.8^*$), 163.9 (C7^{''}a, d, $^3J = 13.6^*$), 161.8 (C3, s), 160.8 (C3^{''}, s), 151.6 (C1, s), 150.0 (C4a, s), 133.715 (C4', s), 132.176 (C3', C5', s), 131.776 (C1', s), 128.731 (C2', C6', s), 122.8 (C4^{''}, d, $^3J = 10.3^*$), 117.1 (C3^{''}a, s), 112.5 (C5^{''}, d, $^2J = 25.7^*$), 111.2 (C4, s), 97.4 (C7^{''}, d, $^2J = 26.8^*$), 58.3 (C4^x, s), 53.2 (Ca, Ce, s), 42.7 (C8, s), 41.3 (C1^x, s), 34.2 (Cc, s), 29.8 (Cb, Cd, s), 26.8 (C5, s), 25.5 (C2^x, s), 23.8 (C3^x, s), 21.7 (C7, s), 18.5 (C6, s).

ESI-HRMS m/z: Calcd for C₃₀H₃₃ClFN₄O₃ [M + H]⁺ 551.2220. Found: 551.2227

4-(4-Fluorophenyl)-2-{4-[4-(6-fluoro-1,2-benzoxazol)-1-piperidyl]butyl}-5,6,7,8-tetrahydro-pyrido[1,2-c]pyrimidine-1,3-dione **7i**

The title compound was isolated as a white powder. Yield: 71.1%; m.p. 57–60 °C.

¹H NMR (500 MHz, CDCl₃): δ 7.71 (C4^{''}H, pt), 7.23 (C7^{''}H, 4d, $^3J_{H-F} = 8.5$, $^4J = 2.0$, $^5J = 0.5$), 7.17 (C2'H, C6'H, kt, $^3J = 9.0$, $^4J_{H-F} = 5.5$, $^4J = 2.0$), 7.09 (C3'H, C5'H, tt, $^3J = 8.5$, $^4J = 2.0$), 7.04 (C5^{''}H, td, $^3J = 8.5$, $^4J = 2.0$), 4.04 (C1^xH₂, t, $^3J = 7.5$), 3.94 (C8H₂, t, $^3J = 6.5$), 3.07 (CaH(E), CeH(E), CcH, pd), 2.52 (C5H₂, t, $^3J = 6.5$), 2.44 (C4^xH₂, bs), 2.20–2.22 (CaH(A), CeH(A), CbH₂, CdH₂, pd), 1.93 (C7H₂, q, $^3J = 7.0$), 1.72 (C2^xH₂, C6H₂, m), 1.61 (C3^xH₂, q, $^3J = 7.0$).

¹³C NMR (125 MHz, CDCl₃): δ 164.1 (C6^{''}, d, $^1J = 250.6^*$), 163.9 (C7^{''}a, d, $^3J = 13.6^*$), 162.3 (C4', d, $^1J = 246.9^*$), 162.0 (C3, s), 161.1 (C3^{''}, s), 151.6 (C1, s), 149.9 (C4a, s), 132.5 (C2', C6', d, $^3J = 8.0^*$), 129.2 (C1', d, $^4J = 3.5^*$), 122.7 (C4^{''}, d, $^3J = 11.3^*$), 117.3 (C3^{''}a, s), 115.5 (C3', C5', d, $^2J = 21.5^*$), 112.3 (C5^{''}, d, $^2J = 25.5^*$), 111.4 (C4, s), 97.4 (C7^{''}, d, $^2J = 26.7^*$), 58.5 (C4^x, s), 53.6 (Ca, Ce, s), 42.7 (C8, s), 41.6 (C1^x, s), 34.6 (Cc, s), 30.5 (Cb, Cd, s), 26.8 (C5, s), 25.7 (C2^x, s), 24.4 (C3^x, s), 21.7 (C7, s), 18.6 (C6, s).

ESI-HRMS m/z: Calcd for C₃₀H₃₃F₂N₄O₃ [M + H]⁺ 535.2515. Found: 535.2523

3.3. Biological Tests

3.3.1. In Vitro Tests

5-HT_{1A} Binding Assay

Radioligand binding was performed using membranes from CHO-K1 cells stably transfected with the human 5-HT_{1A} receptor (PerkinElmer, Fremont, CA, USA). All assays were carried out in duplicate. Then, 50 μL working solution of the tested compounds, 50 μL [³H]-8-OH-DPAT (final concentration 1 nM) and 150 μL diluted membranes (20 μg protein per well) prepared in assay buffer (50 mM Tris, pH 7.4, 10 mM MgSO₄, 0.5 mM EDTA, 0.1% ascorbic acid) were transferred to a polypropylene 96-well microplate

using 96-wells pipetting station Rainin Liquidator (MettlerToledo, Columbus, OH, USA). Serotonin (10 μ M) was used to define nonspecific binding. The microplate was covered with a sealing tape, mixed and incubated for 60 min at 27 °C. The reaction was terminated by rapid filtration through GF/B filter mate, presoaked with 0.5% polyethyleneimine for 30 min. Ten rapid washes with 200 μ L 50 mM Tris buffer (4 °C, pH 7.4) were performed using an automated harvester system—Harvester-96 MACH III FM (Tomtec, Hamden, CT, USA). The filter mates were dried at 37 °C in a forced-air fan incubator, and then solid scintillator Meltilex was melted on filter mates at 90 °C for 6 min. The radioactivity on the filter was measured in a MicroBeta TriLux 1450 scintillation counter (PerkinElmer, Waltham, MA, USA). Data were fitted to a one-site curve-fitting equation with Prism 6 (GraphPad Software, San Diego, CA, USA) and K_i values were estimated from the Cheng–Prusoff equation.

SERT Binding Assay

Radioligand binding was performed using rat cortex tissue. All assays were carried out in duplicate. First, 50 μ L working solution of the tested compounds, 50 μ L [3 H]-citalopram (final concentration 1.0 nM) and 150 μ L tissue suspension, prepared in assay buffer (50 mM Tris, pH 7.7; 150 mM NaCl; 5 mM KCl), were transferred to a polypropylene 96-well microplate using 96-wells pipetting station Rainin Liquidator (MettlerToledo). Imipramine (10 μ M) was used to define nonspecific binding. The microplate was covered with sealing tape, mixed and incubated for 60 min at 24 °C. The reaction was terminated by rapid filtration through GF/B filter mate presoaked with 0.3% polyethyleneimine for 30 min. Ten rapid washes with 200 μ L 50 mM Tris buffer (4 °C, pH 7.7) were performed using an automated harvester system—Harvester-96 MACH III FM (Tomtec). The filter mates were dried at 37 °C in a forced-air fan incubator and then solid scintillator MeltiLex was melted on filter mates at 90 °C for 6 min. The radioactivity on the filter was measured in MicroBeta TriLux 1450 scintillation counter (PerkinElmer, USA). Data were fitted to a one-site curve-fitting equation with Prism 6 (GraphPad Software) and K_i values were estimated from the Cheng–Prusoff equation.

5-HT_{2A}, 5-HT₆, 5-HT₇ and D₂ Binding Assay

In vitro radioligand binding assays for 5-HT_{2A}, 5-HT₆, 5-HT₇ and D₂ receptors were carried out using methods published by Zajdel et al. [45]. For the assays, HEK293 cell cultures stably expressing the investigated human receptors were used. Cell pellets were thawed and homogenized in 20 vol of assay buffer using an Ultra Turrax tissue homogenizer, then centrifuged twice at 35000 g for 20 min at 4 °C, with incubation for 15 min at 37 °C in between. The composition of the assay buffers was as follows: for 5-HT_{2A} receptors—50 mM Tris-HCl, 0.1 mM EDTA, 4 mM MgCl₂ and 0.1% ascorbate; for 5-HT₆ receptors—50 mM Tris-HCl, 0.5 mM EDTA, 4 mM MgCl₂; for 5-HT₇ receptors—50 mM Tris-HCl, 4 mM MgCl₂, 10 μ M pargyline and 0.1% ascorbate; for D₂ receptors—50 mM Tris-HCl, 1 mM EDTA, 4 mM MgCl₂, 120 mM NaCl, 5 mM KCl, 1.5 mM CaCl₂ and 0.1% ascorbate. All assays were incubated in total volume of 200 μ L in 96-well microtitre plates for 1 h at 37 °C, except for 5-HT_{2A} receptors which were incubated at room temperature for 1.5 h. The process of equilibration was terminated by rapid filtration through Unifilter plates with a 96-well cell harvester, and radioactivity retained on the filters was quantified on a Microbeta plate reader (PerkinElmer, USA). For displacement studies, the assay samples contained as radioligands (PerkinElmer): 2 nM [3 H]-ketanserin (spec. act. 53.4 Ci/mmol) for 5-HT_{2A} receptors; 2 nM [3 H]-LSD (spec. act. 83.6 Ci/mmol) for 5-HT₆ receptors; 0.6 nM [3 H]-5-CT (spec. act. 39.2 Ci/mmol) for 5-HT₇ receptors and [3 H]-raclopride (spec. act. 76.0 Ci/mmol) for D₂ receptors. Nonspecific binding was defined with 10 μ M chlorpromazine, 10 μ M methiotepine, or 1 μ M (+) butaclamol used in 5-HT_{2A}, 5-HT₆ and D₂ receptors assays, respectively. Each compound was tested in triplicate at 7–8 concentrations (10⁻¹¹–10⁻⁴ M). The inhibition constants (K_i) were calculated from the Cheng–Prusoff equation [46]. Results were expressed as means of at least two separate experiments.

3.3.2. In Vivo Tests

All studies were performed according to the guidelines of the European Community Council (Directive 86/609/EEC) and were approved by the Ethical Committee of the Institute of Pharmacology (88/2016, 05/31/2016). The experiments were performed on male CD-1 mice (23–40 g). The animals were kept at room temperature (21 ± 2 °C) on a natural day-night cycle (March–October) and housed under standard laboratory conditions. They had free access to food and tap water before the experiment. Each experimental group consisted of 6–8 animals/dose. All the animals were used only once. 8-Hydroxy-2-(di-*n*-propylamino)tetralin hydro-bromide (8-OH-DPAT, Research Biochemical Inc.) was used as aqueous solution. Compounds **6a** and **7g** were suspended in a 10% aqueous solution of dimethyl sulphoxide (DMSO). Vehicle group was administered as 10% aqueous solution of dimethyl sulphoxide (DMSO). 8-OH-DPAT was injected subcutaneously (sc); **6a** and **7g** were given intraperitoneally (ip) in a volume of 10 mL/kg/mice. The obtained data were analyzed by Dunnett's test (one drug administration) or by the Newman-Keuls test (two drugs administrations). Forced swim test: the obtained data was evaluated by one-way analysis of variance (ANOVA) followed by the Dunnett's multiple comparisons test: $p < 0.05$ was considered significant.

Body Temperature in Mice

The effects of the tested compounds **6a** and **7g** given alone, on the rectal body temperature in mice (measured with an Ellab thermometer) were recorded 30, 60, 90 and 120 min after their administration. In a separate experiment the effect of WAY-100635 (0.1 mg/kg s.c.) on the hypothermia induced by tested compounds was measured. WAY-100635 was administered 15 min before the tested compounds and the rectal body temperature was recorded 30 min and 60 min after injection. The absolute mean body temperatures were within a range 36.7 ± 0.5 °C. The results were expressed as a change in body temperature (Δt) with respect to the basal body temperature, as measured at the beginning of the experiment.

Forced Swim Test in Mice

The forced swim test (FST) was carried out according to the method of Porsolt et al. [47]. Mice were placed individually into glass cylinders (height 25 cm, diameter 10 cm) containing 20 cm of water and maintained at 23 ± 1 °C. The animals were left in the cylinder for 6 min. After the first 2 min adaptation period, the total duration of immobility was measured during the last 4 min test. The mouse was judged to be immobile when it remained floating passively, performing slow motions to keep its head above the water. Tested compounds were administered 30 min before test.

Metabolic Stability

Stock solutions of studied compounds were prepared at concentration of 100 μ M in 1:1 acetonitrile/water mixture. Incubation mixes consisted 1 μ M of a studied compound, 100 μ M of NADPH in phosphate buffer and 1 mg/mL of pooled HLMs (Sigma-Aldrich, St. Louis, MO, USA) in potassium phosphate buffer (0.1 M, pH 7.4). Incubation was carried out in 96-well plates at 37 °C. Incubation mixtures (excluding compound solution) were subjected to 5 min preincubations, and started by addition of 10 μ L of compound stock solution. After 0, 5, 10, 15, and 30 min, 25 μ L samples of incubation reaction were added to the equal volume of ice-cold acetonitrile containing 1 μ M of IS (buspirone hydrochloride). Control incubations were performed without NADPH to assess possible chemical instability. All samples were immediately centrifuged (10 min, 10,000 rpm) and the resulting supernatant was directly subjected to LC-MS analysis.

LC-MS analysis was performed on an Agilent 1260 system coupled to SingleQuad 6120 mass spectrometer (Agilent Technologies, Santa Clara, CA, USA). A Poroshell C18 EC120 column (3.0×100 mm², 2.7 μ m, Agilent Technologies, Santa Clara, CA, USA) was used in reversed-phase mode with gradient elution starting with 90% of phase A (0.1%

formic acid in deionised water) and 10% of phase B (0.1% formic acid in acetonitrile). The gradient elution program was: 0.00–10.00 min, 10–95% B; 10.01 min–10.02 min, 95–10% B; 10.02–15.00 min, 10% B. Total analysis time was 15 min at 40 °C, flow rate was 0.4 mL/min and the injection volume was 5 µL. The mass spectrometer was equipped with an electrospray ionization source and was in positive ionization mode. The mass analyzer was set individually to each derivative to detect pseudomolecular ions $[M + H]^+$. Mass spectrometry detector (MSD) parameters of the ESI source were as follows: nebulizer pressure—35 psig (N_2); drying gas 12 L/min (N_2); drying gas temperature—300 °C; capillary voltage—3.0 kV; fragmenter voltage—70 V.

4. Conclusions

The use of antidepressants or neuroleptic drugs acting through an extended receptor profile is now becoming a widely used therapeutic approach. The paper describes the synthesis and biological studies in vitro and in vivo (binding affinity for receptor, functional profile and metabolic stability) of new 4-aryl-2H-pyrido[1,2-c]pyrimidine derivatives (**6a–i**), as well as 4-aryl-5,6,7,8-tetrahydro-pyrido[1,2-c]pyrimidines (**7a–i**), having a 6-fluoro-3-(4-piperidinyl)-1,2-benzisoxazole residue in the pharmacophore ligand part. Receptor studies of derivatives **6a** (5-HT_{1A} K_i = 23.0 nM; SERT K_i = 32.0 nM) and **7g** (5-HT_{1A} K_i = 5.0 nM; SERT K_i = 48.0 nM) showed their desirable very high binding to both molecular targets.

Analyses of the obtained results of affinities of the derivatives (**6a–i**) and (**7a–i**) for the 5-HT_{1A} receptor, showed that the derivatives of both series have very high bindings (**6a–i** 5-HT_{1A} K_i = 7.0–30.0 nM, and for **7a–i** K_i = 5.0–52.0 nM), where the series (**6a–i**) showed higher (more active derivatives) activity against compounds of the series (**7a–i**).

Thus, when examining the effect of the degree of hydrogenation of the terminal part of ligands on the affinity for the 5-HT_{1A} receptor for both series (**6a–i**) and (**7a–i**), it can be concluded that it was low. Derivatives of both series (**6a–i**) and (**7a–i**) generally showed low affinity for SERT protein with the exception of **6a** (SERT K_i = 32.0 nM) and **7g** (SERT K_i = 48.0 nM). Analysis of the effect of substituents (R, R₁) bound to the benzene ring of 4-aryl-2H-pyrido[1,2-c]pyrimidine residue, (**6a–i**) derivatives on affinity for the 5-HT_{1A} receptor, showed a significant effect in the ortho position. However, in the case of 4-aryl-5,6,7,8-tetrahydro-pyrido[1,2-c]pyrimidine derivatives, compounds (**7a–i**), an increase in affinity for the 5-HT_{1A} receptor was observed for derivatives having substituents in the para position.

Functional profile study for compound **6a** in induced hypothermia tests showed that it is a presynaptic agonist of the 5-HT_{1A} receptor. In turn, studies of the **6a** compound in the FST showed its inactivity, which indicated the lack of postsynaptic activity to the 5-HT_{1A} receptor.

Metabolic stability studies were performed for the **6a** and **6d** derivatives, which showed their sensitivity to the action of human liver microsomes. Low stability may be due to the introduction of the 6-fluoro-3-(4-piperidinyl)-1,2-benzisoxazole residue into the pharmacophore part.

For the selected compounds **6a**, **6d**, **7g** and **7i**, further in vitro studies were performed. In vitro affinity studies in an extended receptor profile (D₂, 5-HT_{2A}, 5-HT₆ and 5-HT₇) indicated that derivatives **6a** and **7g** have very high binding affinity to the 5-HT_{1A}, 5-HT_{2A}, SERT, D₂ receptors, high binding affinity to the 5-HT₇ receptor and low binding affinity to 5-HT₆. For compounds **6d** and **7i**, ligands showed very high affinity for 5-HT_{1A}, 5-HT_{2A}, D₂ receptors, medium affinity for 5-HT₇ and low affinity for 5-HT₆ and SERT. By analyzing the results, it can be concluded that they are a good starting point for further research on ligands with a multireceptor profile.

The obtained study results encourage further optimization of the obtained ligand structures in the search for new pyrido[1,2-c]pyrimidine derivatives with potential antidepressant activity from the SSRI+ group.

Author Contributions: Conceptualization, M.K.; synthesis of compounds M.K., G.Ś. and F.H.; methodology, investigation, and data analysis, M.K., G.Ś., J.K., S.U., M.B., T.B., A.S., K.S., B.S., G.N., B.D. and F.H.; writing—original draft preparation, M.K.; writing—review and editing, F.H. and G.Ś. All authors have read and agreed to the published version of the manuscript.

Funding: This research was funded by the Polish National Science Center, grant OPUS 6, No. UMO-2013/11/B/NZ7/01638.

Institutional Review Board Statement: In vivo studies were performed according to the guidelines of the European Community Council (Directive 86/609/EEC) and were approved by the Ethical Committee of Maj Institute of Pharmacology (88/2016, 05/31/2016).

Informed Consent Statement: Not applicable.

Data Availability Statement: Data is contained within the article.

Conflicts of Interest: The authors declare no conflict of interest.

References

1. Akimova, E.; Lanzenberger, R.; Kasper, S. The Serotonin-1A Receptor in Anxiety Disorders. *Biol. Psychiatry* **2009**, *66*, 627–635. [CrossRef] [PubMed]
2. Artigas, F. Serotonin receptors involved in antidepressant effects. *Pharmacol. Ther.* **2013**, *137*, 119–131. [CrossRef] [PubMed]
3. Breier, A. Serotonin, schizophrenia and antipsychotic drug action. *Schizophr. Res.* **1995**, *14*, 187–202. [CrossRef]
4. Pacher, P.; Kohegyi, E.; Kecskemeti, V.; Furst, S. Current Trends in the Development of New Antidepressants. *Curr. Med. Chem.* **2001**, *8*, 89–100. [CrossRef]
5. Doucet, M.V.; Harkin, A.; Dev, K.K. The PSD-95/nNOS complex: New drugs for depression? *Pharmacol. Ther.* **2012**, *133*, 218–229. [CrossRef] [PubMed]
6. Romero, L.; Celada, P.; Martin-Ruiz, R.; Diaz-Mataix, L.; Mourelle, M.; Delgado, J.; Hervas, I.; Artigas, F. Modulation of serotonergic function in rat brain by VN2222, a serotonin reuptake inhibitor and 5-HT_{1A} receptor agonist. *Neuropsychopharmacology* **2003**, *28*, 445–456. [CrossRef]
7. Artigas, F.; Adell, A.; Celada, P. Pindolol Augmentation of Antidepressant Response. *Curr. Drug Targets* **2006**, *7*, 139–147. [CrossRef] [PubMed]
8. Blier, P. The pharmacology of putative early-onset antidepressant strategies. *Eur. Neuropsychopharmacol.* **2003**, *13*, 57–66. [CrossRef]
9. Spinks, D.; Spinks, G. Serotonin Reuptake Inhibition: An Update on Current Research Strategies. *Curr. Med. Chem.* **2002**, *9*, 799–810. [CrossRef]
10. Pacher, P.; Kecskemeti, V.; Pal Pacher, V.K. Trends in the development of new antidepressants. Is there a light at the end of the tunnel? *Curr. Med. Chem.* **2004**, *11*, 925–943. [CrossRef]
11. Nichols, D.E.; Nichols, C.D. Serotonin Receptors. *Chem. Rev.* **2008**, *108*, 1614–1641. [CrossRef]
12. Ohno, Y. Therapeutic Role of 5-HT_{1A} Receptors in The Treatment of Schizophrenia and Parkinson's Disease. *CNS Neurosci. Ther.* **2011**, *17*, 58–65. [CrossRef]
13. Newman-Tancredi, A. Biased agonism at serotonin 5-HT_{1A} receptors: Preferential postsynaptic activity for improved therapy of CNS disorders. *Neuropsychiatry* **2011**, *1*, 149–164. [CrossRef]
14. Adell, A.; Castro, E.; Celada, P.; Bortolozzi, A.; Pazos, A.; Artigas, F. Strategies for producing faster acting antidepressants. *Drug Discov. Today* **2005**, *10*, 578–585. [CrossRef]
15. Carr, G.V.; Lucki, I. The role of serotonin receptor subtypes in treating depression: A review of animal studies. *Psychopharmacology* **2011**, *213*, 265–287. [CrossRef]
16. Lacivita, E.; Leopoldo, M.; Berardi, F.; Perrone, R. 5-HT_{1A} receptor, an old target for new therapeutic agents. *Curr. Top. Med. Chem.* **2008**, *8*, 1024–1034. [CrossRef] [PubMed]
17. Artigas, F.; Bramwell, S.R.; Grahame-Smith, D.G.; Probst, A.; Palacios, J.M. 5-HT and antidepressants: New views from microdialysis studies. *Trends Pharmacol. Sci.* **1993**, *14*, 262. [CrossRef]
18. Blier, P.; Ward, N.M. Is there a role for 5-HT_{1A} agonists in the treatment of depression? *Biol. Psychiatry* **2003**, *53*, 193–203. [CrossRef]
19. Blier, P.; De Montigny, C. Modification of 5-HT neuron properties by sustained administration of the 5-HT_{1A} agonist gepirone: Electrophysiological studies in the rat brain. *Synapse* **1987**, *1*, 470–480. [CrossRef] [PubMed]
20. Rickels, K.; Athanasiou, M.; Reed, C. Vilazodone, a novel, dual-acting antidepressant: Current status, future promise and potential for individualized treatment of depression. *Per. Med.* **2009**, *6*, 217–224. [CrossRef] [PubMed]
21. Howland, R.H. Vilazodone: Another novel atypical antidepressant drug. *J. Psychosoc. Nurs. Ment. Health Serv.* **2011**, *49*, 19–22. [CrossRef] [PubMed]
22. Frampton, J.E. Vilazodone: In major depressive disorder. *CNS Drugs* **2011**, *25*, 615–627. [CrossRef] [PubMed]

23. Bang-Andersen, B.; Ruhland, T.; Jørgensen, M.; Smith, G.; Frederiksen, K.; Jensen, K.G.; Zhong, H.; Nielsen, S.M.; Hogg, S.; Mørk, A.; et al. Discovery of 1-[2-(2,4-Dimethylphenylsulfanyl)phenyl]piperazine (Lu AA21004): A Novel Multimodal Compound for the Treatment of Major Depressive Disorder. *J. Med. Chem.* **2011**, *54*, 3206–3221. [CrossRef] [PubMed]
24. Herold, F.; Chodkowski, A.; Izbicki, Ł.; Król, M.; Kleps, J.; Turło, J.; Nowak, G.; Stachowicz, K.; Dybała, M.; Siwek, A. Novel 4-aryl-pyrido[1,2-c]pyrimidines with dual SSRI and 5-HT_{1A} activity, Part 1. *Eur. J. Med. Chem.* **2009**, *44*, 1710–1717. [CrossRef]
25. Herold, F.; Izbicki, Ł.; Chodkowski, A.; Dawidowski, M.; Król, M.; Kleps, J.; Turło, J.; Wolska, I.; Nowak, G.; Stachowicz, K. Novel 4-aryl-pyrido[1,2-c]pyrimidines with dual SSRI and 5-HT_{1A} activity: Part 2. *Eur. J. Med. Chem.* **2009**, *44*, 4702–4715. [CrossRef] [PubMed]
26. Herold, F.; Chodkowski, A.; Izbicki, Ł.; Turło, J.; Dawidowski, M.; Kleps, J.; Nowak, G.; Stachowicz, K.; Dybała, M.; Siwek, A.; et al. Novel 4-aryl-pyrido[1,2-c]pyrimidines with dual SSRI and 5-HT_{1A} activity. Part 3. *Eur. J. Med. Chem.* **2011**, *46*, 142–149. [CrossRef]
27. Chodkowski, A.; Wróbel, M.Z.; Turło, J.; Kleps, J.; Siwek, A.; Nowak, G.; Belka, M.; Bączek, T.; Mazurek, A.P.; Herold, F. Novel 4-aryl-pyrido[1,2-c]pyrimidines with dual SSRI and 5-HT_{1A} activity. Part 4. *Eur. J. Med. Chem.* **2015**, *90*, 21–32. [CrossRef]
28. Gomolka, A.; Ciesielska, A.; Wróbel, M.Z.; Chodkowski, A.; Kleps, J.; Dawidowski, M.; Siwek, A.; Wolak, M.; Stachowicz, K.; Slawinska, A.; et al. Novel 4-aryl-pyrido[1,2-c]pyrimidines with dual SSRI and 5-HT_{1A} activity. Part 5. *Eur. J. Med. Chem.* **2015**, *98*, 221–236. [CrossRef]
29. Wróbel, M.Z.; Chodkowski, A.; Herold, F.; Gomółka, A.; Kleps, J.; Mazurek, A.P.; Pluciński, F.; Mazurek, A.; Nowak, G.; Siwek, A.; et al. Synthesis and biological evaluation of novel pyrrolidine-2,5-dione derivatives as potential antidepressant agents. Part 1. *Eur. J. Med. Chem.* **2013**, *63*, 484–500. [CrossRef]
30. Martin, K.F.; Heal, D.J. 8-OH-DPAT-Induced Hypothermia in Rodents. A Specific Model of 5-HT_{1A} Autoreceptor Function. In *Serotonin: Molecular Biology, Receptors and Functional Effects*; Birkhäuser Basel: Basel, Switzerland, 1991; pp. 483–490. ISBN 9783034872614.
31. *ACD/ChemSketch 2017*; Version 2017.1.2; Advanced Chemistry Development, Inc.: Toronto, ON, Canada, 2017.
32. Di Giovanni, G.; Esposito, E.; Di Matteo, V. Role of Serotonin in Central Dopamine Dysfunction. *CNS Neurosci. Ther.* **2010**, *16*, 179–194. [CrossRef]
33. Etievant, A.; Bétry, C.; Haddjeri, N. Partial Dopamine D₂/Serotonin 5-HT_{1A} Receptor Agonists as New Therapeutic Agents. *Open Neuropharmacol. J.* **2010**, *3*, 1–12. [CrossRef]
34. Sakaue, M.; Somboonthum, P.; Nishihara, B.; Koyama, Y.; Hashimoto, H.; Baba, A.; Matsuda, T. Postsynaptic 5-hydroxytryptamine 1A receptor activation increases in vivo dopamine release in rat prefrontal cortex. *Br. J. Pharmacol.* **2000**, *129*, 1028–1034. [CrossRef]
35. Fountoulakis, K.N.; Kelsoe, J.R.; Akiskal, H. Receptor targets for antidepressant therapy in bipolar disorder: An overview. *J. Affect. Disord.* **2012**, *138*, 222–238. [CrossRef] [PubMed]
36. Millan, M.J. Multi-target strategies for the improved treatment of depressive states: Conceptual foundations and neuronal substrates, drug discovery and therapeutic application. *Pharmacol. Ther.* **2006**, *110*, 135–370. [CrossRef]
37. Ślifirski, G.; Król, M.; Kleps, J.; Podsadni, P.; Belka, M.; Bączek, T.; Siwek, A.; Stachowicz, K.; Szewczyk, B.; Nowak, G.; et al. Synthesis of new 5,6,7,8-tetrahydropyrido[1,2-c]pyrimidine derivatives with rigidized tryptamine moiety as potential SSRI and 5-HT_{1A} receptor ligands. *Eur. J. Med. Chem.* **2019**, *180*, 383–397. [CrossRef] [PubMed]
38. Lipinski, C.A.; Lombardo, F.; Dominy, B.W.; Feeney, P.J. Experimental and computational approaches to estimate solubility and permeability in drug discovery and development settings. *Adv. Drug Deliv. Rev.* **1997**, *23*, 3–25. [CrossRef]
39. Chang, Y.; Pi, W.; Ang, W.; Liu, Y.; Li, C.; Zheng, J.; Xiong, L.; Yang, T.; Luo, Y. Synthesis and evaluation of amide side-chain modified Agomelatine analogues as potential antidepressant-like agents. *Bioorg. Med. Chem. Lett.* **2014**, *24*, 1672–1676. [CrossRef]
40. Goodwin, G.M.; De Souza, R.J.; Green, A.R. The pharmacology of the hypothermic response in mice to 8-hydroxy-2-(DI-n-propylamino)tetralin (8-OH-DPAT). *Neuropharmacology* **1985**, *24*, 1187–1194. [CrossRef]
41. Forster, E.A.; Cliffe, I.A.; Bill, D.J.; Dover, G.M.; Jones, D.; Reilly, Y.; Fletcher, A. A pharmacological profile of the selective silent 5-HT_{1A} receptor antagonist, WAY-100635. *Eur. J. Pharmacol.* **1995**, *281*, 81–88. [CrossRef]
42. Yap, C.; Xue, Y.; Chen, Y. Application of Support Vector Machines to In Silico Prediction of Cytochrome P450 Enzyme Substrates and Inhibitors. *Curr. Top. Med. Chem.* **2006**, *6*, 1593–1607. [CrossRef] [PubMed]
43. Ulenberg, S.; Belka, M.; Georgiev, P.; Król, M.; Herold, F.; Bączek, T. In Vitro approach for identification of a leading cytochrome P450 isoenzyme responsible for biotransformation of novel arylpiperazine drug candidates and their inhibition potency towards CYP3A4. *Acta Pol. Pharm. Drug Res.* **2020**, *77*, 69–76. [CrossRef]
44. Ślifirski, G.; Król, M.; Kleps, J.; Ulenberg, S.; Belka, M.; Bączek, T.; Siwek, A.; Stachowicz, K.; Szewczyk, B.; Nowak, G.; et al. Synthesis of novel pyrido[1,2-c]pyrimidine derivatives with rigidized tryptamine moiety as potential SSRI and 5-HT_{1A} receptor ligands. *Eur. J. Med. Chem.* **2019**, *166*, 144–158. [CrossRef] [PubMed]
45. Zajdel, P.; Kos, T.; Marciniak, K.; Satała, G.; Canale, V.; Kamiński, K.; Hołuj, M.; Lenda, T.; Koralewski, R.; Bednarski, M.; et al. Novel multi-target azinesulfonamides of cyclic amine derivatives as potential antipsychotics with pro-social and pro-cognitive effects. *Eur. J. Med. Chem.* **2018**, *145*, 790–804. [CrossRef]
46. Yung-Chi, C.; Prusoff, W.H. Relationship between the inhibition constant (KI) and the concentration of inhibitor which causes 50 per cent inhibition (I₅₀) of an enzymatic reaction. *Biochem. Pharmacol.* **1973**, *22*, 3099–3108. [CrossRef]
47. Porsolt, R.D.; Bertin, A.; Jalfre, M. Behavioral despair in mice: A primary screening test for antidepressants. *Arch. Int. Pharmacodyn. Ther.* **1977**, *229*, 327–336.



Review

5-HT Receptors and the Development of New Antidepressants

Grzegorz Ślifirski , Marek Król * and Jadwiga Turło

Department of Drug Technology and Pharmaceutical Biotechnology, Faculty of Pharmacy, Medical University of Warsaw, 1 Banacha Street, 02-097 Warsaw, Poland; gslifirski@wum.edu.pl (G.Ś.); jturlo@wum.edu.pl (J.T.)

* Correspondence: mkrol@wum.edu.pl

Abstract: Serotonin modulates several physiological and cognitive pathways throughout the human body that affect emotions, memory, sleep, and thermal regulation. The complex nature of the serotonergic system and interactions with other neurochemical systems indicate that the development of depression may be mediated by various pathomechanisms, the common denominator of which is undoubtedly the disturbed transmission in central 5-HT synapses. Therefore, the deliberate pharmacological modulation of serotonergic transmission in the brain seems to be one of the most appropriate strategies for the search for new antidepressants. As discussed in this review, the serotonergic system offers great potential for the development of new antidepressant therapies based on the combination of SERT inhibition with different pharmacological activity towards the 5-HT system. The aim of this article is to summarize the search for new antidepressants in recent years, focusing primarily on the possibility of benefiting from interactions with various 5-HT receptors in the pharmacotherapy of depression.

Keywords: antidepressants; drug design; dual 5-HT_{1A}/SERT activity; multimodal activity

Citation: Ślifirski, G.; Król, M.; Turło, J. 5-HT Receptors and the Development of New Antidepressants. *Int. J. Mol. Sci.* **2021**, *22*, 9015. <https://doi.org/10.3390/ijms22169015>

Academic Editor: Philippe De
Deurwaerdère

Received: 26 July 2021

Accepted: 19 August 2021

Published: 20 August 2021

Publisher's Note: MDPI stays neutral with regard to jurisdictional claims in published maps and institutional affiliations.



Copyright: © 2021 by the authors. Licensee MDPI, Basel, Switzerland. This article is an open access article distributed under the terms and conditions of the Creative Commons Attribution (CC BY) license (<https://creativecommons.org/licenses/by/4.0/>).

1. Introduction

Depression is a mental illness that affects over 250 million people worldwide [1]. Emotional (depressed mood, irritability, anhedonia), somatic (sleep, appetite, libido), and functional disorders (suicidal thoughts, slowed speech and movement, learning, memory and attention deficits) [2] make this disease the main cause of disabilities in the general population [3,4].

An important step in the treatment of depressive disorders is the introduction of SSRIs (serotonin reuptake inhibitors), which are currently first-line antidepressants (e.g., fluoxetine, sertraline, escitalopram). Their mechanism of action is based on the serotonergic system, and the molecular target is the serotonin transporter protein (SERT). The effectiveness of these therapeutics, unfortunately, leaves much to be desired; 60–70% of patients do not experience a remission of symptoms, and 30–40% do not respond to the treatment at all [5]. A serious drawback of selective serotonin reuptake inhibitors is their latency period, i.e., a delay in the therapeutic response by 2–6 weeks. Common side effects for SSRIs are sexual dysfunction, anxiety, and food intolerances.

Apart from SSRIs, other selective monoamine reuptake inhibitors are also used in pharmacotherapy. Reboxetine, a selective norepinephrine reuptake inhibitor, appears to be less effective than the SSRIs. These observations may, however, result from its relatively low tolerance [6]. Bupropion, on the other hand, is a norepinephrine and dopamine reuptake inhibitor and, therefore, has a more activating profile than SSRI drugs. Two drugs, venlafaxine and duloxetine, are classified as dual serotonin-norepinephrine reuptake inhibitors (SNRIs). However, the efficacy of the norepinephrine reuptake blocking at clinical doses of duloxetine is unclear [7]. Clinical guidelines often recommend the use of SNRIs in patients who do not respond to SSRIs [8–10].

There is a need for the further exploration of the neurochemical causes of depression. Recent studies report the influence of many various types of neurosignaling on

the mechanism of depression [11–14]. The search for new generations of antidepressants using the triple reuptake inhibition mechanism (SSRI/SNRI/SDARI), or the combination of serotonin reuptake inhibition with affinities for various 5-hydroxytryptamine (5-HT) receptor subtypes, broadens the knowledge in this field [15–17].

A significant part of recent studies proves that serotonergic dysfunction, especially related to the postsynaptic 5-HT_{1A} receptor, plays an important role in the pathomechanism of Major Depressive Disorder (MDD) [18–24]. Clinical trials show that the combination of SSRIs with both partial agonism and antagonism of the 5-HT_{1A} receptor may result in an improvement in the speed and efficacy of the antidepressant effect [23,25,26]. This can be confirmed by the drugs recently introduced into the pharmacotherapy of depression—vilazodone and vortioxetine (Figure 1). Vilazodone exhibits partial agonist activity at the 5-HT_{1A} receptor, while vortioxetine binds to several 5-HT receptor subtypes (5-HT_{1A}, 5-HT_{1B}, 5-HT_{1D}, 5-HT₃, and 5-HT₇). For example, the degree of sexual dysfunction associated with the use of vilazodone has been found to be relatively low [27]. Vortioxetine, on the other hand, positively influences cognitive impairment related to depression [10,28].

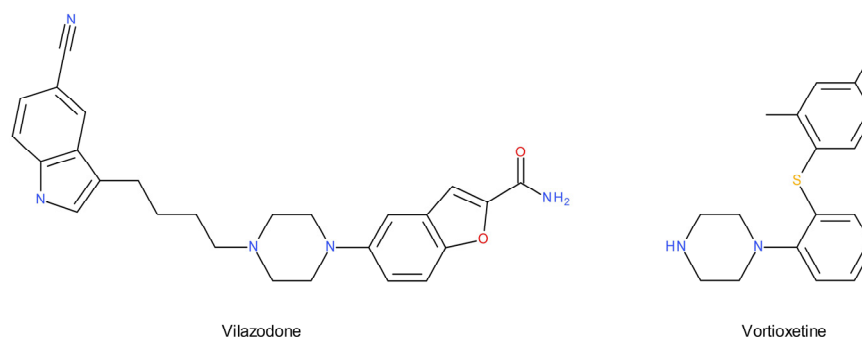


Figure 1. Novel antidepressants: vilazodone and vortioxetine.

The targeted pharmacological modulation of serotonergic transmission in the brain continues to be a leading strategy in the search for new antidepressants. The careful selection of molecular targets for the proper use of the mechanisms of serotonergic modulation, which influences other neurotransmission systems, seems to be the most effective strategy for supplementing the activity of “serotonin-enhancing” drugs in the near future. A better understanding of the receptors and receptor signaling responsible for the effects of serotonin on neurogenesis can also help in the development of new and more effective drugs. The aim of this article is to summarize the search for new antidepressants in recent years, focusing primarily on the possibility of benefiting from interactions with various 5-HT receptors in the pharmacotherapy of depression.

2. The Serotonergic System and Depression

Serotonin, or 5-hydroxytryptamine (5-HT), is a monoamine neurotransmitter found throughout the human body [19,29]. Serotonin is synthesized in the midbrain in a small population of raphe nucleus neurons where tryptophan hydroxylase is expressed [30]. However, serotonin synthesis is not limited to the central nervous system (CNS), as tryptophan hydroxylase is also found in enterochromaffin cells in the gastrointestinal tract [31]. In fact, it should be noted that most of the serotonin in the human body is produced by this cell type [32]. Serotonin binds to more than 14 receptor proteins, most of which are G-protein coupled receptors [30,33]. This molecule mediates the transmission of several physiological and cognitive systems throughout the body that affect emotions, memory, sleep, and thermal regulation [34].

Serotonin is synthesized in the body from an essential amino acid—L-tryptophan. Ingested with food, L-tryptophan is converted into serotonin through a series of reactions. The first step, which simultaneously limits the rate of serotonin synthesis, is the hydroxylation of L-tryptophan to 5-hydroxy-L-tryptophan (5-HTP) by tryptophan hydroxylase

(TPH) using oxygen and tetrahydropteridine as co-factors. There are two isoforms of TPH that can participate in this reaction: TPH1, expressed predominantly peripherally; and TPH2, expressed only in the brain. L-aromatic amino acid decarboxylase (AADC) then converts 5-HTP to serotonin [19,31].

The crossing of the blood–brain barrier (BBB) by serotonin is impossible due to its acid dissociation [35]; therefore, the amount of serotonin present in the CNS depends on the amount of centrally present L-tryptophan. The L-tryptophan present in the systemic circulation is actively transported by the BBB to the CNS using a carrier protein, where it is then converted into serotonin. Serotonin synthesized in the central nervous system is stored in secretory vesicles, where it remains until neuronal depolarization triggers its release into the synaptic cleft, allowing postsynaptic binding. Once released into the synapse, the serotonin molecules are eventually taken up by the serotonin transporter (5-HTT), which is located on the presynaptic axonal membrane. After the above-mentioned reuptake occurs, serotonin molecules are metabolized by monoamine oxidase (MAO) to 5-hydroxyindole acetic acid (5-HIAA) [29]. There are two isoforms of MAO (MAO-A and MAO-B), and both break down serotonin into neurons through oxidative deamination. The serotonin metabolite (5-HIAA) is actively transported from the CNS to the periphery and then excreted in the urine [19].

Already by the 1950s, it was noted that several mental illnesses showed abnormalities in the serotonergic system. The relationship between the serotonergic system and depression has been confirmed in clinical trials. They showed that an acute, transient relapse of depressive symptoms can be produced in subjects in remission using p-chlorophenylalanine (an irreversible inhibitor of serotonin synthesis). L-tryptophan depletion, causing a temporary reduction in central serotonin levels, had similar consequences. These findings have shown that the clinical efficacy of antidepressants depends on the presynaptic serotonergic function. Other studies have demonstrated a reduced concentration of the major metabolite of serotonin (5-HIAA) in the cerebrospinal fluid of untreated depressed patients and a reduced concentration of 5-HT and its major metabolite (5-HIAA) in the postmortem brain tissue of depressed and/or suicidal patients [20].

The serotonergic neurons of the mammalian brain constitute the most extensive and complex neurochemical network in the CNS after the glutamatergic system, which is the brain's primary transmission network. It has been estimated that the human brain contains approximately 250,000 5-HT neurons. For comparison, the total number of all neurons is around 10^{11} [36]. While serotonergic neurons originate mainly in the brainstem dorsal and median raphe nuclei, they arborise over large areas such that they innervate almost every area of the brain with high densities of axonal varicosities. Some serotonergic projections create classical chemical synapses, but many release 5-HT in a paracrine manner (sometimes referred to as “volumetric transmission”). In addition, serotonin neurons exhibit slow (~1 Hz) and regular tonic activity that ceases during the rapid eye movement sleep phase (REM-off neurons). This activity is parallel to the noradrenergic neurons of the locus coeruleus [34]. Under normal conditions, the activity of serotonergic neurons is tightly controlled by a number of mechanisms, including: (i.) glutamatergic inputs from the forebrain (mainly the prefrontal cortex) [37], (ii.) the tonic noradrenergic input from the pontine nuclei [38], (iii.) inhibitory GABAergic signals from local interneurons [39], and (iv.) dopamine signals from the dopaminergic nuclei of the midbrain [40]. Moreover, the serotonin system is, in a way, self-regulating. The key control mechanism of 5-HT neurons is negative feedback through the 5-HT_{1A} autoreceptors [20]. This mechanism is currently being studied in great detail in the context of the treatment of CNS diseases.

The aforementioned anatomical and electrophysiological picture shows that changes in the activity of serotonergic neurons affect a large population of target neurons in the forebrain. The complex nature of the serotonergic system and interactions with other neurochemical systems indicate that the development of MDD may be mediated by various pathomechanisms. Currently suggested mechanisms include: (i.) low neuronal production of serotonin or of postsynaptic receptors, (ii.) decreased excitatory inputs or excessive

system self-control, and (iii.) decreased 5-HT synthesis and/or tryptophan deficiency. The common denominator of these phenomena in depression is undoubtedly the disturbed transmission in the central 5-HT synapses. Therefore, the deliberate pharmacological modulation of serotonergic transmission in the brain seems to be one of the appropriate strategies for the search for new antidepressants.

3. The 5-HT Receptors

The serotonergic system affects various physiological functions, including psychoemotional expression, sensorimotor integration, and the regulation of the autonomic, cardiovascular, respiratory, and digestive systems. Within the CNS, 5-HT is involved in the regulation of higher mental functions and emotions, extrapyramidal motor functions, and cognitive functions (e.g., learning and memory).

At least 14 different serotonin receptors have been identified. These receptors can be divided into distinct families, which are labelled 1, 2, 3, 4, 5, 6, and 7, and the subtypes in each family are labelled with letters (e.g., a, b, c). Many of these receptors are thought to be involved in the pathogenesis of various CNS disorders [41].

3.1. The 5-HT_{1A} Receptors

The 5-HT_{1A} receptors are located primarily in the following populations: (i.) presynaptic neurons of the raphe nuclei of the midbrain and (ii.) postsynaptic neurons, mainly in the hippocampus, septum, amygdala, and corticolimbic regions [42]. Autoreceptors are located within the bodies and dendrites of serotonin neurons. Their activation inhibits neuronal discharges and reduces the release of serotonin [43]. Thus, 5-HT_{1A} autoreceptors play an important role in the self-regulation of the serotonergic system; they partially inhibit the activity of adenylate cyclase [44] and activate G protein-dependent rectifying potassium channels (GIRK) with the use of the $\beta\gamma$ subunit of G protein [45]. This causes membrane hyperpolarization, a reduction in neuronal excitability, and the inhibition of potential-dependent calcium channels, reducing the influx of calcium ions. The consequence is a reduction in the neural discharge rate. Given the significant influence of these neuronal discharges on the overall activity of the entire serotonergic system, it can be concluded that the reduction in the firing rate evoked by serotonin and other 5-HT_{1A} agonists immediately translates into an overall reduction in 5-HT release in most areas of the brain, particularly in regions innervated by the dorsal raphe [20].

The activation of 5-HT_{1A} autoreceptors by endogenous serotonin, therefore, plays an essential role in the physiological control of the activity of the 5-HT ascending neurons. The 5-HT neurons during waking periods show a slow and regular rate of discharge [36]. Under conditions of excessive excitatory input (e.g., stress), there is an increased release of serotonin in the vicinity of neuronal bodies. It activates 5-HT_{1A} autoreceptors, which allow low and regular neuronal activity to be maintained [40]. Thus, 5-HT_{1A} autoreceptors act as negative feedback physiological “safety valves” to maintain homeostasis.

The expression of 5-HT_{1A} heteroreceptors, in turn, takes place in populations of non-serotonin receptors, mainly in the limbic system within: (i.) bodies and dendrites of glutamatergic neurons [43] or (ii.) axons of GABA-ergic [46], and (iii.) cholinergic neurons [47]. These receptors are involved in regulating the release of various neurotransmitters: acetylcholine in the medial septum [48], glutamate in the prefrontal cortex [49], and dopamine in the ventral tegmental area [50]. In most regions of the brain, the inhibition of adenylate cyclase occurs due to the activation of the G α i protein. The GIRK channels in the hippocampus are activated by the $\beta\gamma$ subunits of the G α o isoform [51]. The 5-HT_{1A} receptors in the cortex and hypothalamus bind to both the G α i and G α o subunits, while their preferential binding to the G α i3 protein occurs within the raphe nucleus.

The differences in the properties of 5-HT_{1A} auto- and hetero-receptors are manifested in their different functional selectivity [52]: 5-HT_{1A} heteroreceptors stimulate [53], while 5-HT_{1A} autoreceptors inhibit ERK1/2 transmission [54]. The 5-HT_{1A}-biased agonism appears to result in the preferential activation of a specific signaling pathway without

affecting or even blocking other pathways associated with this receptor subtype [55]. It has also been shown that there is an agonist-dependent modulation of G-protein coupling and a transduction of 5-HT_{1A} receptors in rat dorsal raphe nucleus. Moreover, 8-hydroxy-2-(di-n-propylamino)tetralin (8-OH-DPAT, a full 5-HT_{1A} receptor agonist) compared with buspirone (a partial 5-HT_{1A} receptor agonist) fails to modify forskolin-stimulated cAMP accumulation [56].

In general, 5-HT_{1A} receptor-deficient mice show a shorter immobility time in the forced swim test than wild-type control animals [57]. The lack of functional 5-HT_{1A} autoreceptors may, therefore, favor a less-depressed phenotype. The whole-life suppression of 5-HT_{1A} heteroreceptor expression in adolescence results in a broad depression-like phenotype. In addition, the group showed physiological and cellular changes within medial prefrontal cortex–dorsal raphe proper circuitry: (i.) increased basal serotonin levels in the medial prefrontal cortex, which is hyporeactive to stress and (ii.) decreased basal serotonin levels and firing rates in a dorsal raphe hyperactivated by the same stressor [57].

Animal studies show that both the stimulation and blockade of 5-HT_{1A} receptors can cause or accelerate the antidepressant effect [17]. It is difficult not to associate this with the above-described functional differences of 5-HT_{1A} auto- and hetero-receptors and the phenomenon of the biased 5-HT_{1A} agonism. Many studies have demonstrated the antidepressant effect of 8-OH-DPAT reversed by 5-HT_{1A} receptor antagonists [58]. Moreover, 5-HT_{1A} receptor-deficient mice showed no increase in adult neurogenesis in the hippocampus after chronic treatment with fluoxetine (SSRI) and not with imipramine (TCA) [59]. The preferential activation of postsynaptic 5-HT_{1A} receptors by F15599 (Figure 2), a biased 5-HT_{1A} agonist, resulted in an antidepressant-like effect [60]. Similar activity was shown by F13714, a non-selective agonist of 5-HT_{1A} receptors, but it induced a deeper “serotonin syndrome”, hypothermia, and corticosterone release in rats. Elevated corticosterone levels accompany chronic stress in animals, leading to depression [61]. Moreover, the activation of 5-HT_{1A} receptors in the prefrontal cortex (PFC) by F15599 produces strong antidepressant-like effects in the forced swim test (FST) in rats, with a distinctive bimodal dose–response pattern. These data suggest that F15599 may target specific 5-HT_{1A} receptor subpopulations in the PFC, possibly located on the GABAergic and/or glutamergic neurons [62].

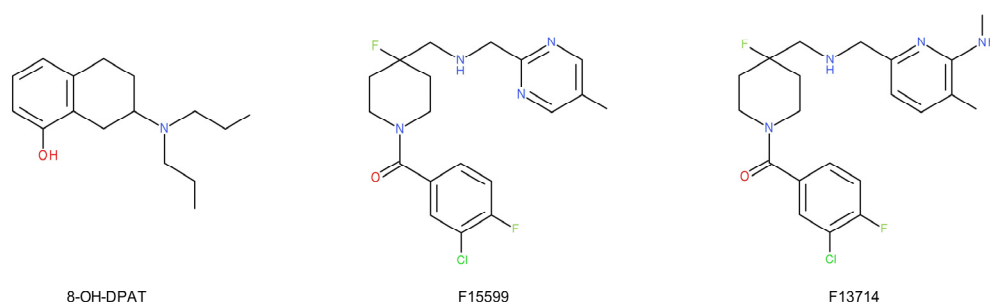


Figure 2. 5-HT_{1A} receptor agonists: 8-OH-DPAT, F15599, and F13714.

The previously described physiological function of 5-HT_{1A} autoreceptors and their regulation of depressive behavior seem to be unfavorable in the context of the mechanism of action of antidepressants [20,63]. The negative feedback pathway through 5-HT_{1A} autoreceptors may decrease the efficacy of the SSRI as the dose increases, thus creating a second, anomalous part of the dose–response curve. This effect may also be responsible for the so-called therapeutic window for such antidepressants [64]. The prolonged use of SSRIs translates into significantly higher levels of extracellular 5-HT than after a single administration [65]. The negative feedback loop is believed to be the cause of the slow and delayed clinical efficacy of antidepressant drugs [66]. Administration of antidepressants (tricyclic drugs, monoamine oxidase inhibitors, and SSRIs) significantly increases the level of extracellular 5-HT in the midbrain raphe [67]. This leads to: (i.) the activation of 5-HT_{1A} receptors, (ii.) the reduction in 5-HT cell firing [68], and (iii.) the terminal release of

5-HT [69]. The inhibition of SSRIs in the negative feedback pathway clearly decreases with the duration of treatment. This is most likely due to the serotonin-induced desensitization of raphe 5-HT_{1A} autoreceptors discussed earlier [70]. Thus, the desensitization of 5-HT_{1A} autoreceptors may accelerate the onset and/or enhance the antidepressant effect [71]. Mice with higher levels of 5-HT_{1A} autoreceptors showed a blunted physiological response to acute stress, increased behavioral despair, and no behavioral response to fluoxetine [72]. Moreover, mice with lower autoreceptor levels showed a strong behavioral response to fluoxetine after both chronic and subchronic administration [72]. Thus, lowering the level of 5-HT_{1A} autoreceptors prior to antidepressant treatment may accelerate and increase the effectiveness of antidepressant therapy. Combining SSRI treatment with the 5-HT_{1A} receptor antagonist pindolol significantly reduces the latency of the antidepressant response and improves the clinical response in previously untreated MDD patients (Table 1) [20,21,73]. The above data indicate that the stimulation of postsynaptic 5-HT_{1A} receptors or the blockade of presynaptic 5-HT_{1A} receptors results in antidepressant-like activity. (-)-pindolol may also stimulate somatodendritic 5-HT_{1A} receptors. Then, its accelerating antidepressant effect might stem from the accelerated adaptive changes like autoreceptor desensitization in response to both serotonin and pindolol. This mechanism can also be achieved by initiating the treatment with high-dose SSRI when a patient is suicidal. The antidepressant action of pindolol may also be related to its agonistic activity at the β_1 -adrenoreceptor as this drug possesses the strongest intrinsic sympathicomimetic activity among other β -blockers [74].

Table 1. Clinical effects of augmentation of SERT inhibition with different activities towards 5-HT receptors.

Clinical Intervention	Mechanism of Action	Effect	References
SSRI + pindolol	SERT inhibition + 5-HT _{1A} agonism	Reduced latency of the antidepressant response and improved the clinical response in previously untreated MDD patients	[21]
SSRI + buspirone	SERT inhibition + 5-HT _{1A} partial agonism	Symptom remission in patients unsuccessfully treated with SSRIs	[75]
SSRI + mirtazapine	SERT inhibition + 5-HT _{2A} antagonism	Augmentation of the clinical response to SSRIs in treatment-resistant patients	[76]
Vilazodone	SERT inhibition + 5-HT _{1A} partial agonism	In contrast to prototypical SSRIs, vilazodone has not been associated with treatment-emergent sexual difficulties or dysfunction	[27]
Vortioxetine	SERT, 5-HT ₃ and 5-HT ₇ receptors inhibition, 5-HT _{1A} agonism	Potential rapid onset of action	[77]

According to the neurotrophic hypothesis of depression, decreased neurotrophic support causes neuronal atrophy, which in turn reduces hippocampal neurogenesis and leads to depression. Clinical data support this theory: postmortem analysis has shown reduced volumes of the hippocampus and prefrontal cortex in depressed patients [78,79]. Persons diagnosed with MDD showed decreased levels of BDNF (brain-derived neurotrophic factor) and NGF (nerve growth factor) in the hippocampus. A deficit of these neurotrophins may promote neuronal loss [80,81]. This phenomenon was confirmed by *in vivo* studies [82–85], which showed that antidepressants reversed these changes [86]. Chronic treatment with 8-OH-DPAT, in turn reduced the feeding delay in the novelty-suppressed feeding test and increased adult hippocampal neurogenesis in wild-type mice, but showed no effect in the 5-HT_{1A} receptor knockout group [59]. Thus, 5-HT_{1A} receptors mediate the action of 8-OH-DPAT, from which it can be concluded that the postsynaptic 5-HT_{1A} receptors mediate the antidepressant-like action of 8-OH-DPAT [87]. The specific deletion of the 5-HT_{1A} heteroreceptors from mature granular cells in the dentate gyrus of

the hippocampus has also been found to abolish the effects of SSRIs in various behavioral tests [88]. It also attenuated the effects of SSRIs on adult neurogenesis and the expression of hippocampal neurotrophic factors: BDNF and VEGF (vascular endothelial growth factor). Whole-life 5-HT_{1A} heteroreceptor-knockout (but not autoreceptor-knockout) mice showed decreased mobility in the forced swim test [89]. Such a depression-like phenotype was not observed when the suppression of heteroreceptors was initiated in adulthood. Therefore, serotonergic signaling in the forebrain during development may stably influence the circuits underlying the behavioral response to the FST [89].

The STAR*D clinical trial shows that in patients unsuccessfully treated with SSRIs, the augmentation with buspirone resulted in symptom remission [75]. Buspirone (a partial agonist of the 5-HT_{1A} receptor) enhances the desensitization of 5-HT_{1A} autoreceptors, increasing the effectiveness of the SSRI treatment. Recently, a single transcription factor, Freud-1, has been found to be crucial for the expression of the 5-HT_{1A} autoreceptor [90]. Mice with a conditional knockout of Freud-1 in serotonin neurons were shown to have elevated levels of 5-HT_{1A} autoreceptors and exhibited the enhanced anxiety and depressive behavior in adulthood that was refractory to chronic SSRI treatment [90]. Interestingly, the double knockout of the Freud-1/5-HT_{1A} gene did not produce such effects. In this case, the depressive-like behavior was even reduced [90]. The study suggests that targeting specific transcription factors may increase the response to antidepressant treatment. These reports indicated the need to search for compounds targeting only the population of 5-HT_{1A} auto- or heteroreceptors.

The results of postmortem and neuroimaging studies suggest an increased density of 5-HT_{1A} autoreceptors in patients with MDD compared to the control group [91–93]. Genetic studies have shown that individuals with an increased density or activity of 5-HT_{1A} autoreceptors are more prone to mood disorders and respond poorly to antidepressant treatment [94,95]. However, the number and density of postsynaptic 5-HT_{1A} receptors have been shown to be unaltered or reduced in depressed patients, and this alteration is not sensitive to antidepressant treatment [96]. Long-term antidepressant therapy causes the tonic activation of 5-HT_{1A} receptors in the dorsal hippocampus [97], and activation of 5-HT_{1A} receptors in the dentate gyrus increases hippocampal neurogenesis [98]. In light of the cited reports, the use of 5-HT_{1A} agonists as antidepressants seems natural [99]. Some agents possessing such activity (e.g., buspirone and gepirone) show antidepressant efficacy in placebo-controlled trials, but their potency is lower than that of SSRIs. Most 5-HT_{1A} agonists (especially azapirones, Figure 3) show the preferential activation of presynaptic 5-HT_{1A} receptors. Moreover, these agents tend to have a reduced efficacy at postsynaptic 5-HT_{1A} receptors. Thus, endogenous serotonin competes in the postsynaptic sites with an exogenous substance (with lower agonism), which causes a paradoxical reduction in the tone at the postsynaptic 5-HT_{1A} receptors. Higher doses of 5-HT_{1A} agonists (such as those used in experimental animals) are likely to result in the greater activation of postsynaptic 5-HT_{1A} receptors, which may explain the positive results of efficacy studies in animal models. Conversely, the administration of the selective 5-HT_{1A} receptor antagonist DU125530 with fluoxetine did not accelerate or increase the efficacy of fluoxetine in a double-blind, randomized, placebo-controlled clinical trial. DU125530 had similar binding to pre- and post-synaptic 5-HT_{1A} receptors [100], and the blockade of postsynaptic 5-HT_{1A} receptors likely offset the benefits of enhancing presynaptic serotonergic function [101]. This may show the importance of the activation of postsynaptic 5-HT_{1A} receptors in the mechanism of antidepressant action.

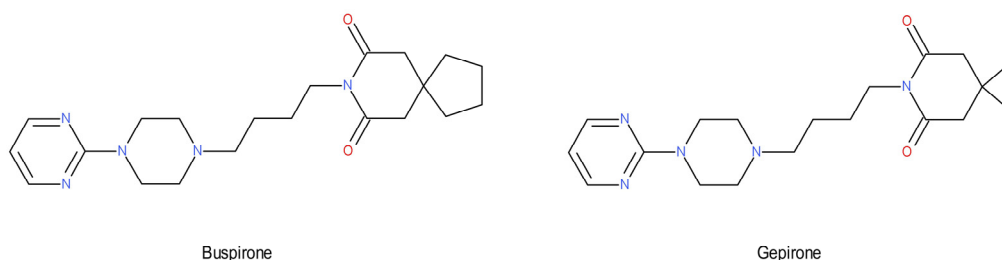


Figure 3. Azapirones: buspirone and gepirone.

Observations on the 5-HT_{1A} receptor population contributed to a fruitful search for potential multimodal antidepressants that incorporate 5-HT_{1A} receptor activity into their mechanism of action [102]. Recently developed compounds seem to overcome the aforementioned therapeutic problems of azapirones and other first-generation 5-HT_{1A} agonists. Two new antidepressants, vilazodone [27,103] and vortioxetine [104,105], inhibit 5-HT reuptake and show the partial agonism at 5-HT_{1A} receptors.

The 5-HT_{1A} receptor ligands also possess their own potentially therapeutic activity. The 5-HT_{1A} partial agonists show antianxiety [106,107], antidepressant [108], antiaggressive [109], anticraving [110], and anticataleptic properties [111]:

- Animal studies show that both the stimulation and blockade of 5-HT_{1A} receptors can cause or accelerate the antidepressant effect. It is difficult not to associate this with the functional differences of 5-HT_{1A} auto- and hetero-receptors and the phenomenon of a biased 5-HT_{1A} agonism;
- A single transcription factor, Freud-1, has been found to be crucial for the expression of the 5-HT_{1A} autoreceptor. Targeting it may increase the response to antidepressant treatment;
- Observations on the 5-HT_{1A} receptor population contributed to a fruitful search for potential multimodal antidepressants (vilazodone and vortioxetine) that incorporate 5-HT_{1A} receptor activity into their mechanism of action.

3.2. The 5-HT_{1B} Receptors

The 5-HT_{1B} receptors, like 5-HT_{1A} receptors, are located pre- and post-synaptically and are also negatively coupled to adenylate cyclase. Their highest densities are in the striatum, pallidum, nucleus accumbens, substantia nigra, and ventral tegmental area. Lower levels of 5-HT_{1B} receptors are found in the hippocampus, amygdala, and cingulate cortex [112].

Unlike somatodendritic 5-HT_{1A} autoreceptors, 5-HT_{1B} autoreceptors are located on serotonergic axons, where they regulate the synthesis and release of 5-HT locally. The 5-HT_{1B} postsynaptic receptors are located mainly in the centers of motor control (such as the basal ganglia), where they control the synaptic transmission of other neurotransmitters [112]. Studies have shown that 5-HT_{1B} receptors play a role in depression, anxiety, migraines, locomotor activity, aggressive behavior, and the potentiation of the action of other drugs [112–114].

Animal studies show that the involvement of 5-HT_{1B} receptors in the pathophysiology of depression is partly related to their responsiveness to environmental stress as well as their exposure to antidepressants [115]. The 5-HT_{1B} heteroreceptors are involved in hippocampal neurogenesis, which may explain their importance for the antidepressant-like effect [116]. Mice lacking 5-HT_{1B} autoreceptors showed an increased mobility in the FST as well as an increased preference for lower-sucrose concentrations in the sucrose preference test compared to the control group. After SSRI administration, elevated levels of serotonin in the hippocampus were observed [117]. Moreover, two common genetic polymorphisms of 5-HT_{1B} receptors, G861C [118] and C129T [119], were associated with MDD and affective disorders. The 5-HT_{1B} receptor gene knockout mice showed increased aggression [120].

The p11 protein, which colocalizes with 5-HT_{1B} and 5-HT₄ receptors [121], plays a key role in modulating the function of the 5-HT_{1B} receptor. Its dysregulation has been reported

in preclinical models of depression and in postmortem samples from MDD patients [122]. The p11 protein improves 5-HT_{1B} receptor function in various regions of the brain and contributes to an antidepressant-like effect in animal behavioral tests [123]. P11 knockout mice showed depression-like behavior and demonstrated a reduced responsiveness to 5-HT_{1B} receptor agonists and tricyclic antidepressants [123].

Studies in the learned helplessness model showed that 5-HT_{1B} receptors were up-regulated in various regions of the brain following stress exposure. A reduced 5-HT_{1B} autoreceptor function and, thus, increased serotonin release, has also been demonstrated after chronic antidepressant treatment [124]. Moreover, chronic treatment with SSRIs induced a negative regulation and/or desensitization of 5-HT_{1B} autoreceptors [125] and facilitated the effect of SSRIs in serotonin neurotransmission [126]. Compounds exhibiting 5-HT_{1B} antagonism, administered alone or with antidepressants, have been shown to be effective in preclinical models of depression [127]. The pretreatment with 5-HT_{1B} receptor antagonists [128] or the genetic inactivation of the 5-HT_{1B} receptor [129] increased the SSRI-induced effect in mice. Therefore, the blockade of 5-HT_{1B} autoreceptors may promote the antidepressant effect. It has been suggested that the 5-HT_{1B} receptor antagonists themselves may be attributed to an antidepressant-like effect. SB-616234-A, a 5-HT_{1B} receptor antagonist, decreased immobility in a forced swim test in mice (Figure 4) [130]. The selective 5-HT_{1B} receptor inverse agonist, SB236057A, increased, in turn, the extracellular concentration of serotonin in the dentate gyrus of a guinea pig. This effect was comparable to that of 14 days of paroxetine therapy [131]. The acute blockade of the 5-HT_{1B} receptor might cause a rapid antidepressant effect [131]. It appears that the agonist activation of 5-HT_{1B} heteroreceptors may also induce antidepressant-like effects [132]. CP94253, a selective 5-HT_{1B} receptor agonist, showed an antidepressant-like activity in a forced swimming test in mice [133]. Anpirtoline, as a selective 5-HT_{1B} receptor agonist, also reduced immobility in control mice but had no effect in 5-HT_{1B} knockout mice [132]. The effect of this compound in the FST was, therefore, due to the activation of the 5-HT_{1B} receptor. The above studies suggest that 5-HT_{1B} receptors play a role in antidepressant-like activity. Their stimulation of postsynaptic receptors and the inhibition of presynaptic 5-HT_{1B} receptors may be beneficial in the treatment of depression [134].

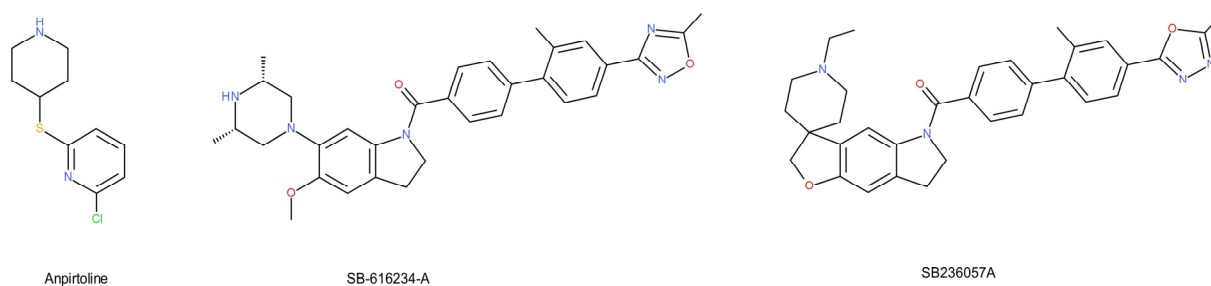


Figure 4. 5-HT_{1B} receptor ligands: anpirtoline, SB-616234-A, and SB236057A.

As with 5-HT_{1A} receptors, acute SSRI therapy activates terminally localized 5-HT_{1B} receptors, thus reducing 5-HT synthesis and release. The long-term administration of SSRIs desensitizes terminal 5-HT_{1B} autoreceptors [135], suggesting that the plasticity of the autoregulatory function of both 5-HT_{1A} and 5-HT_{1B} receptors may be important with respect to the therapeutic profile of SSRIs. Again, as with 5-HT_{1A} receptor antagonists, the administration of 5-HT_{1B} receptor antagonists increases the neurochemical and behavioral effects of SSRIs [128,136]. Interestingly, the co-administration of the selective 5-HT_{1A} antagonist WAY-100635 and the 5-HT_{1B} receptor antagonist SB-224289 has an additive effect, enhancing the neurochemical effects of fluoxetine. This has led to the suggestion that the combination of the 5-HT_{1A} and 5-HT_{1B} receptor antagonism may increase CNS serotonin levels and, therefore, potentially be an effective treatment strategy for depression [20]:

- Animal studies show that the involvement of 5-HT_{1B} receptors in the pathophysiology of depression is partly related to their responsiveness to environmental stress as well as an exposure to antidepressants;
- The p11 protein improves 5-HT_{1B} receptor function in various regions of the brain and contributes to an antidepressant-like effect in animal behavioral tests;
- The 5-HT_{1B} heteroreceptors are involved in hippocampal neurogenesis, which may explain their importance for the antidepressant-like effect. The stimulation of postsynaptic receptors and the inhibition of presynaptic 5-HT_{1B} receptors may be beneficial in the treatment of depression.

3.3. The 5-HT_{1D}, 5-HT_{1E}, and 5-HT_{1F} Receptors

The clinical significance of the remaining 5-HT₁ receptors (5-HT_{1D}, 5-HT_{1E}, 5-HT_{1F}) is less clear. There is limited preclinical evidence linking some of the receptors with depressive states. The sensitivity of postsynaptic 5-HT_{1D} receptors in patients after treatment with SSRIs has been found to be impaired [137]. On the other hand, a postmortem study of untreated suicidal victims with a confirmed history of depression showed a much higher density of 5-HT_{1D} receptors in the globus pallidus [138]. The observed high expression of the 5-HT_{1E} receptor in the frontal cortex and hippocampus may indicate the relationship between 5-HT_{1E} receptors and cognitive functions and memory [20,139].

3.4. The 5-HT_{2A} Receptors

The 5-HT_{2A} receptors, like the others of the 5-HT₂ family, are preferentially coupled to the G protein of the Gq/11 type, so their activation increases the cellular level of inositol phosphate and, consequently, the cytosolic concentration of calcium ions. The 5-HT_{2A} receptors are distributed postsynaptically and presynaptically throughout the brain at serotonergic terminals, with the greatest concentration in the neocortex [140–142]. Recent anatomical and functional studies suggest that 5-HT_{2A} receptors are also present presynaptically as heteroreceptors, where they may enhance glutamatergic neurotransmission and participate in memory processes [143]. It has also been demonstrated that the 5-HT_{2A} receptors of the cerebral cortex are located on GABAergic interneurons as well as glutamatergic projection neurons in the brains of humans and rodents [42,144].

Many antidepressants and antipsychotic drugs possess a relatively high binding to 5-HT_{2A} receptors [145]. Although there is no direct correlation between the affinity of these drugs for 5-HT_{2A} receptors and clinically effective doses, there is ample evidence that the 5-HT_{2A} receptor plays a role in the pathomechanism of depression [20,146]. Some antidepressants mediate their action partly via the antagonism of 5-HT_{2A} receptors [147]. In addition, chronic treatment with antidepressants, such as tricyclic antidepressants, monoamine oxidase inhibitors, mianserin, mirtazapine, or sertraline, decreased the number of 5-HT_{2A} receptors in rodents [148]. Chronic electroconvulsive shock treatment resulted in the upregulation of cortical 5-HT_{2A} receptors in rodents [149].

Several clinical trials have shown that atypical antipsychotics [150] and the antidepressant mirtazapine with an affinity for α_2 -adrenoceptors and 5-HT_{2A} receptors [151] augment the clinical response to SSRIs in treatment-resistant patients [76]. A common feature of these substances is their ability, at clinical doses, to block responses to signals mediated by 5-HT_{2A} receptors [152]. Such downregulation could, inter alia, explain why the side effects of SSRIs diminish after 2 or 3 weeks. The high co-expression of 5-HT_{1A} and 5-HT_{2A} receptors in the neocortex [153] may indicate that the blockade of 5-HT_{2A} receptors enhances 5-HT_{1A} receptor-mediated neurotransmission in the cortical and limbic regions, an activity associated with antidepressant efficacy. The chronic administration of 5-HT_{2A} receptor antagonists has been shown to result in a paradoxically negative regulation of 5-HT_{2A} receptors [154,155], which may be beneficial in the treatment of depression. Moreover, preclinical studies indicate that 5-HT_{2A} antagonists have anxiolytic properties, as demonstrated by ritanserin, a 5-HT_{2A} antagonist with anxiolytic effects in humans [156].

Another issue is the relationship between the 5-HT_{2A} receptor and the noradrenergic system in relation to depression [157]. Studies have shown that the activation of 5-HT_{2A} receptors as a result of treatment with SSRIs causes an increase in serotonin levels in GABA neurons. This inhibits the neuronal activity of norepinephrine through the prolonged release of GABA [158–160]. In turn, citalopram, in addition to reducing norepinephrine firing, also has the effect of lowering basal and evoked extracellular norepinephrine levels in the amygdala [161]. This may underlie SSRI ineffectiveness in resistant depression. The co-administration of an SSRI and a 5-HT_{2A} receptor antagonist trazodone (as well as atypical antipsychotics, such as quetiapine, risperidone, olanzapine, and aripiprazole) reversed this inhibitory effect in noradrenergic neurons in rats and might be beneficial in the treatment of resistant depression [160,162–164]. Increasing evidence shows that 5-HT_{2A} receptor antagonists display antidepressant effects. EMD 281014 (Figure 5), a 5-HT_{2A} receptor antagonist, showed significant activity in the FST in congenital learned helpless rats [165]. A similar effect was shown by another 5-HT_{2A} receptor antagonist, FG5893, which significantly shortened the immobility time in the FST [166]. The selective 5-HT_{2A} receptor antagonist, M100907, enhanced the antidepressant-like behavioral effects of fluoxetine [167], suggesting that a selective 5-HT_{2A} receptor blockade may complement the behavioral effects of serotonin transporter inhibition. In contrast, recent studies in rats have shown that the functional disturbance of the 5-HT_{2A} receptor in the medial prefrontal cortex may contribute to postpartum mental disorders, including depression and psychosis [168]. In addition, prefrontal 5-HT_{2A} receptors may both have beneficial and negative effects on cognition, which might explain the aggravation of cognitive deficits after the onset of SSRI treatment in depressed patients, as well as the limited efficacy of second-generation antipsychotics that act as 5-HT_{2A} receptor antagonists against the strongly debilitating cognitive symptoms of schizophrenia and other psychiatric disorders [169]. A deficiency in 5-HT_{2A} receptors has also been shown to alter the metabolic and transcriptional, but not behavioral, consequences of chronic unpredictable stress in mice [170]. The 5-HT_{2A} blockade or SSRI-induced downregulation of 5-HT_{2A} may lead to emotional blunting in patients. It is, therefore, very likely that 5-HT_{2A} receptors may have different functions depending on the region of the brain:

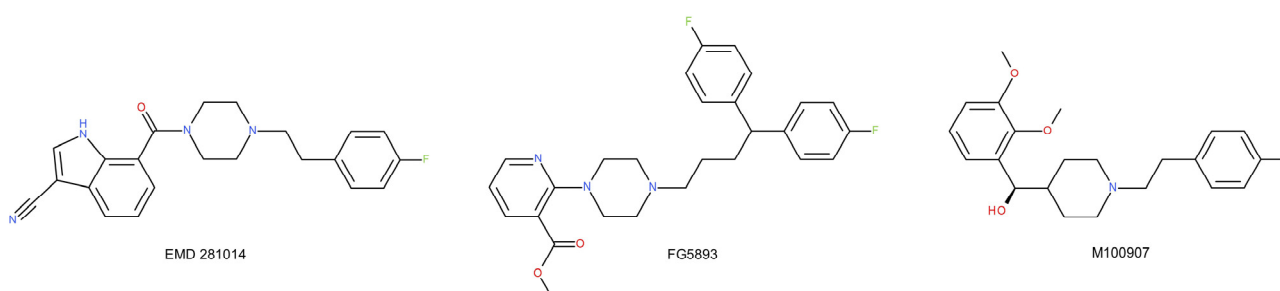


Figure 5. 5-HT_{2A} receptor antagonists: EMD 281014, FG5893 and M100907.

- Many antidepressants and antipsychotic drugs have relatively high binding to 5-HT_{2A} receptors;
- The high co-expression of 5-HT_{1A} and 5-HT_{2A} receptors in the neocortex may indicate that the blockade of 5-HT_{2A} receptors enhances 5-HT_{1A} receptor-mediated neurotransmission in the cortical and limbic regions, an activity associated with antidepressant efficacy;
- Increasing evidence shows that 5-HT_{2A} receptor antagonists display antidepressant effects. A selective 5-HT_{2A} receptor blockade may complement the behavioral effects of serotonin transporter inhibition.

3.5. The 5-HT_{2B} Receptors

The 5-HT_{2B} receptor is expressed mainly in peripheral tissues, especially in the liver, kidneys, and heart, and its distribution in the brain is low [171]. In the central nervous system, the 5-HT_{2B} receptor is present in septal nuclei, the dorsal hypothalamus, and the medial amygdala at levels similar to those found in the stomach [171]. The 5-HT_{2B} receptor, mRNA, is found in the dorsal raphe nucleus, suggesting a potential autoreceptor role [172]. The 5-HT_{2B} receptors are coupled to the Gq protein, which activates PLC (phospholipase C)/PKC (protein kinase C) and increases the concentration of calcium ions in the cytosol.

The knowledge about the function of the 5-HT_{2B} receptor in the CNS is limited; however, there are reports of the antidepressant properties of selective 5-HT_{2B} receptor agonists [173]. The presence of 5-HT_{2B} receptors in the dorsal raphe and their stimulatory role in 5-HT release has been demonstrated [173]. The pharmacological or genetic inactivation of the 5-HT_{2B} receptor abolished the effects of chronic treatment with SSRIs, and the stimulation of 5-HT_{2B} receptors induced an SSRI-like response in behavioral and neurogenic tests. In turn, the genetic inactivation of 5-HT_{2B} receptors in serotonergic neurons eliminated the neurogenic effects of fluoxetine [173]. It has recently been confirmed that 5-HT_{2B} receptors directly and positively regulated the activity of serotonin neurons [174]. In addition, the stimulation of the 5-HT_{2B} receptor via fluoxetine in astrocyte cell cultures resulted in the phosphorylation of extracellular signal-regulated kinases and the transactivation of the EGF (epidermal growth factor) receptor [175]. A reduced level of astroglial (but not neuronal) 5-HT_{2B} receptors in a mouse model of Parkinson's disease was also reported, which paralleled the development of the depression-like phenotype [176]. The stimulation of astroglial 5-HT_{2B} receptors may, therefore, be beneficial in treating depressive disorders [177].

Considering the role of peripherally located 5-HT_{2B} receptors, potential new antidepressants acting on 5-HT_{2B} receptors may adversely affect the function of the respiratory and circulatory systems [17,20]:

- 5-HT_{2B} receptors directly and positively regulate the activity of serotonin neurons;
- There are reports of the antidepressant properties of selective 5-HT_{2B} receptor agonists;
- Potential new antidepressants acting on 5-HT_{2B} receptors may adversely affect the function of the respiratory and circulatory systems.

3.6. The 5-HT_{2C} Receptors

The 5-HT_{2C} receptors are mainly located in the choroid plexuses, cerebral cortex, hippocampus, substantia nigra, and cerebellum. They bind preferentially with Gq/11 and increase the concentrations of inositol phosphates and cytosolic Ca²⁺. Like 5-HT_{2A} receptors, they are involved in the regulation of mood, motor behavior, and appetite [178].

Several classes of antidepressants have an affinity for 5-HT_{2C} receptors. Although these receptors are usually somatodendritic, in some regions they are also present on axon terminals [179]. The location of 5-HT_{2C} receptors in relation to serotonergic and GABAergic neurons in the anterior raphe nuclei demonstrates complex systemic relationships in the brain. It has been shown that 5-HT_{2C} receptors are preferentially located on GABAergic interneurons (and not on serotonergic neurons). This suggests that the stimulation of GABAergic interneurons by 5-HT_{2C} receptors plays an important role in the suppression of serotonergic cell firing in the dorsal raphe and surrounding areas [180]. The immunoreactivity of the 5-HT_{2C} receptor has also been described in GABAergic cells in the PFC [181] and in the dopaminergic and GABAergic neurons of the mesolimbic pathway [182].

A potent 5-HT_{2C} receptor antagonist, S32006 (Figure 6), showed antidepressant activity in rodent behavioral tests and increased dopamine and norepinephrine levels in the frontal cortex [183]. This compound reduced immobility in the FST in mice, suppressed anhedonia in a chronic mild stress model, and increased cell proliferation and BDNF expression in the dentate gyri of rats [183]. In contrast, the inverse agonist of the 5-HT_{2C} receptor,

S32212, showed an antidepressant effect in the FST in rats after both acute and chronic treatment [184].

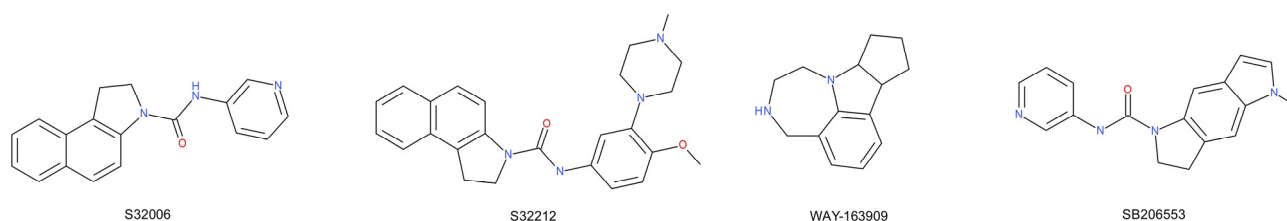


Figure 6. 5-HT_{2C} receptor ligands: S32006, S32212, WAY-163909 and SB206553.

On the other hand, some studies report that 5-HT_{2C} agonists have been shown to be active in animal models of depression, suggesting an antidepressant-like effect [185,186]. WAY-163909, a selective 5-HT_{2C} receptor agonist, elicited a rapid antidepressant effect in a rat FST that was blocked by the 5-HT_{2C/2B} receptor antagonist, SB206553 [186]. Moreover, after chronic treatment, WAY163909 reduced the hyperactivity associated with olfactory bulbectomy in rats [186,187]. It is possible that the mediated antidepressant effects of these compounds were due to the stimulation of 5-HT_{2C} receptors and the resulting activation of postsynaptic serotonin receptors [188]. Other selective 5-HT_{2C} receptor agonists have also been effective in animal models of depression and obsessive–compulsive disorder [189].

Preclinical data show that the antagonism of 5-HT_{2C} receptors increases the neurochemical and behavioral effects of SSRIs. Examples include: the increase in the effect of SSRIs on extracellular 5-HT concentrations in the hippocampus and cortex [190,191], or a significant increase in the effect of SSRIs in behavioral models of depression by selective and non-selective 5-HT_{2C} antagonists [190].

Additionally, 5-HT_{2C} receptors have been shown to be involved in the anti-immobility effect of antidepressants in the FST, increasing the serotonin level in the synapse [192]. Few studies suggest that 5-HT_{2C} receptor antagonists alone may also exhibit antidepressant-like properties. The inactivation of 5-HT_{2C} receptors has been shown to potentiate SSRI-induced serotonin release in rodents [190]. However, 5-HT_{2C} receptor antagonists administered separately had no effect on serotonin levels [191].

An altered editing of the mRNA-encoding 5-HT_{2C} receptors has been reported in the PFC of depressed suicide victims [193]. The desensitization of these receptors has been observed in patients after chronic treatment with SSRIs [194].

The 5-HT_{2C} receptors are also involved in the tonic modulation of dopaminergic activity [195]. The role of the dopaminergic system in schizophrenia, along with the antagonism of atypical antipsychotics towards the 5-HT_{2C} receptors, has aroused interest in this receptor for the treatment of schizophrenia [196]. Conversely, the ineffectiveness of SSRIs in some patients may be due to the serotonin-related inhibition of the neuronal activity of dopamine in the ventral capping region via 5-HT_{2C} receptors [157]. Escitalopram has been shown to reduce the stimulation of dopamine neurons by activating 5-HT_{2C} receptors located on GABA neurons. Some studies indicate that the co-administration of SSRIs with 5-HT_{2C} receptor antagonists (including atypical antipsychotics, such as aripiprazole) may eliminate the inhibitory effects on dopaminergic neurons in rat brains and restore the effect of the SSRI [163]. The aforementioned 5-HT_{2C} receptor antagonist S32006, with a potential antidepressant- and anxiolytic-like effect, increased dopamine levels in the frontal cortex of rats and enhanced dopaminergic neuron firing [183]. The modulation of dopaminergic activity may, therefore, be beneficial in the development of antidepressants due to the above-mentioned activity of 5-HT_{2C} receptor ligands. Recent studies demonstrate the contradictory effect of 5-HT_{2C} receptors on the effects of SSRIs on motor function and affective behavior, highlighting the potential benefits of 5-HT_{2C} receptor antagonists both for reducing SSRI motor side effects and enhancing the therapeutic antidepressant and anxiolytic effects [197].

Both 5-HT_{2C} receptor agonists and antagonists exhibit antidepressant-like activity, and there is still a need to further define the role of this receptor subtype in depression:

- Several classes of antidepressants have an affinity for 5-HT_{2C} receptors. Alterations in their functional status have been observed in depressive and anxiety states;
- Both 5-HT_{2C} agonists and antagonists have been shown to be active in animal models of depression. Preclinical data show that the antagonism of 5-HT_{2C} receptors increases the neurochemical and behavioral effects of SSRIs;
- There is still a need to further define the role of 5-HT_{2C} receptor subtype in depression.

3.7. The 5-HT₃ Receptors

The activation of the 5-HT₃ receptor leads to a rapid opening of the transmembrane channel, resulting in an increase in the conductivity of Na⁺/K⁺ ions and an immediate influx of extracellular Ca²⁺ ions. This, in turn, triggers the release of neurotransmitters and/or peptides. The 5-HT₃ receptors are found throughout the brain and CNS and the highest density of 5-HT₃ receptors was found in the spinal cord and brainstem. The 5-HT₃ receptors present in the dorsal vagal complex are involved in the control of the emetic mechanism [142]. Many 5-HT₃ receptor antagonists have been developed as antiemetics for use in cancer chemotherapy. In the 1990s, lithoxetine, an antidepressant combining serotonin reuptake and 5-HT₃ receptor antagonism, was developed to prevent SSRI-induced gastrointestinal side effects [198]. In the forebrain, on the other hand, 5-HT₃ receptors were present mainly in structures of the limbic system, such as the hippocampus, amygdala, and entorhinal cortex [199].

The 5-HT₃ receptors are involved in the control of dopamine and acetylcholine release. They also control the functioning of the GABAergic system. Activity towards other neurotransmission systems is the main mechanism of action for 5-HT₃ receptor ligands. The 5-HT₃ receptors are expressed on different types of GABAergic interneurons in the forebrain [200,201]. The physiological stimulation of serotonergic neurons stimulates cortical (and possibly hippocampal) GABAergic neurons. This likely results in the inhibition of neighboring excitatory neurons by GABA_A and GABA_B receptors [201].

Preclinical studies suggest that the 5-HT₃ receptor plays a role in mental disorders [17]. The 5-HT₃ antagonists show antidepressant-like activity in various animal models [202]. The systemic administration of tropisetron (a 5-HT₃ receptor antagonist) prevented restraint stress-induced dopamine release in the nucleus accumbens and prefrontal cortex in rats. This suggested that 5-HT₃ receptors mediated the stress-dependent activation of dopaminergic neurotransmission [203]. Tropisetron additionally exerted an antidepressant-like effect in FST in rats. This effect was abolished after a pretreatment with mCPGB (1-(m-chlorophenyl)-biguanide), a potent 5-HT₃ receptor agonist (Figure 7) [204].

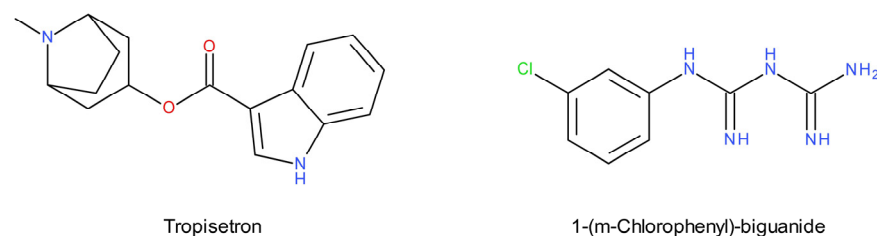


Figure 7. 5-HT₃ receptor ligands: tropisetron and mCPGB.

Some antidepressants with different mechanisms of action exhibit functional 5-HT₃ receptor antagonism [205]. Chronic treatment with fluoxetine desensitizes 5-HT₃ receptors [206], and SERT knockout mice show increased 5-HT₃ receptor density compared to wild-type mice [207]. It has been suggested that the antidepressant effect of SSRIs is partially dependent on the blockade of 5-HT₃ receptors [208]. The relatively new multimodal antidepressant drug vortioxetine [209,210] displays nanomolar binding affinities to the SERT ($K_i = 1.6$ nM) and other serotonin receptors, including 5-HT₃, 5-HT_{1A}, 5-HT₇,

5-HT_{1B} and 5-HT_{1D}, with K_i values of 3.7 nM, 15 nM, 19 nM, 33 nM and 54 nM, respectively [102]. Vortioxetine antagonism at the 5-HT₃ receptor [211] may underlie its faster onset of action [212]. Rodent experiments show that the antidepressant-like effect should be attributed to postsynaptic, rather than presynaptic, 5-HT₃ antagonism, since the presynaptic and somatodendritic 5-HT₃ receptor blockade reduces serotonin levels [203]. The antidepressant and/or anxiolytic effects recently demonstrated by some 5-HT₃ receptor antagonists in animal models of depression may result from the modulation of the hypothalamic–pituitary–adrenal axis, interaction with the serotonergic system, or antioxidant properties [213–218].

The agonism of the 5-HT₃ receptor reduces the antidepressant effect in the FST in rats [219], while the antagonism of the 5-HT₃ receptor reduces the immobility time in the FST [220]. Ondansetron, a 5-HT₃ receptor antagonist, confirms these observations; it exhibits antidepressant properties in the TST (tail suspension test) and FST, also enhancing the effect of fluoxetine [220]. In a model of chronic unpredictable stress in mice, the administration of ondansetron reversed depressive behavior affecting the hypothalamic–pituitary–adrenal axis [221]. Moreover, in mice with streptozotocin-induced diabetes, the drug displayed antidepressant and anxiolytic properties, possibly through the antagonism of the 5-HT₃ receptor [222]. Behavioral studies with ondansetron (and tropisetron) also suggested an interaction of 5-HT₃ and NMDA receptors, as well as an involvement of the nitric oxide–cyclic guanosine monophosphate pathway inhibition in the observed antidepressant-like effects [223,224]. Studies on genetically modified animals confirm the role of 5-HT₃ receptors in the antidepressant effect. The 5-HT₃ receptor knockout mice were reported to display an antidepressant-like phenotype [225].

In vitro electrophysiology studies showed that low-dose citalopram treatment desensitized the 5-HT_{1A} receptor only in the dorsal raphe nucleus of 5-HT₃ knockout mice, while high dose treatment caused similar 5-HT_{1A} autoreceptor desensitization in 5-HT₃ knockout and wild types [225]. Hence, lower doses of citalopram may be effective when 5-HT₃ receptors are deactivated. It has also been shown that the blockade of the 5-HT₃ receptor by ondansetron enhances the effect of citalopram on extracellular serotonin levels in the rat forebrain [102]. The use of combined SSRIs and 5HT₃ receptor antagonists is proposed as an improvement strategy to be tested in the treatment of depressive disorders [226]. The neurochemical, electrophysiological, and behavioral consequences of the repeated administration of this drug combination will need to be assessed.

The properties of 5-HT₃ receptor antagonists have also been used to alleviate substance abuse, which is often associated with most psychiatric disorders, including MDD [227]. The 5-HT₃ receptor antagonists have been reported to be effective in reducing ethanol and morphine intake [228]. It is worth noting that various antipsychotics are non-competitive 5-HT₃ receptor antagonists, and this may contribute to their efficacy [229]. There is likely to be an association between 5-HT₃ receptors and anxiety behavior [230]. The 5-HT₃ antagonists reverse helpless behavior in rats [231] and abolish the emotion-potentiated startle effect in humans [232]:

- Activity towards other neurotransmission systems is the main mechanism of action for 5-HT₃ receptor ligands;
- Rodent experiments show that the antidepressant-like effect should be attributed to postsynaptic rather than presynaptic 5-HT₃ antagonism, since the presynaptic and somatodendritic 5-HT₃ receptor blockade reduces serotonin levels;
- Some antidepressants with different mechanisms of action exhibit functional 5-HT₃ receptor antagonism. The vortioxetine antagonism at the 5-HT₃ receptor may underlie its faster onset of action.

3.8. The 5-HT₄ Receptors

The 5-HT₄ receptors in the CNS are mainly located in the putamen, caudate nucleus, hippocampus, nucleus accumbens, globus pallidus, and substantia nigra. To a lesser extent, these receptors are present in the neocortex, raphe and pontine nuclei, and thalamus [233].

Studies using positron emission tomography show a slightly more limited regional distribution of 5-HT₄ receptors in the human brain, showing a high density of this receptor in the caudate–putamen and much lower densities in the frontal cortex and hippocampus [234]. The 5-HT₄ receptors are coupled to the Gs protein, which activates adenylate cyclase/PKC and increases the intracellular level of cAMP. Regarding peripheral tissues, these receptors play an important role in the heart, gastrointestinal tract, adrenal glands, and urinary bladder [235].

There are reports linking the 5-HT₄ receptor with depressive disorders [236]. Preclinical models of depression, such as the olfactory bulbectomized and glucocorticoid heterozygous receptor mice, show that the expression of 5-HT₄ receptors increased in the ventral hippocampus or striatum, respectively [237], while in the Flinders-sensitive line rat model of depression, the downregulation of 5-HT₄ receptors was observed in the ventral and dorsal hippocampus [238].

The 5-HT₄ receptor subtype is involved in the modulation of synaptic plasticity [239], which is influenced by antidepressants [240]. The signaling of the 5-HT₄ receptor may modulate the function of the dentate gyrus of the hippocampus by increasing the neurogenesis and expression of neurotrophic factors, which may contribute to the antidepressant effects of drugs that enhance serotonergic transmission [241]. The 5-HT₄ receptor interacts with the p11 protein, which determines the antidepressant activity mediated by 5-HT_{1B} and 5-HT₄ receptors [242].

In addition, 5-HT₄ knockout mice show an enhanced response of serotonergic neurons to citalopram [243]. Thus, 5-HT₄ receptors are possibly involved in the activation of 5-HT neurons during SERT inhibition. As observed for 5-HT_{1A} and 5-HT_{2A} receptors [37,40], 5-HT₄ receptors in the PFC control the firing rate of midbrain serotonergic neurons via descending inputs [244]. In addition, 5-HT₄ receptors mediate synaptic transmission between the dentate gyrus and the CA3 field of the hippocampus. Fluoxetine was observed to normalize the mossy fiber pathway by activating 5-HT₄ receptors [245]. Chronic treatment with fluoxetine and venlafaxine (but not reboxetine) decreased the 5-HT₄ receptor density in rat brain [246]. Although the 5-HT₄ receptor antagonist, SB 204070A, showed no independent effect and did not reduce the immobility time in the FST in naive rats [247], another receptor antagonist, GR 125487, blocked fluoxetine activity in a mouse corticosterone-induced depression model [248]. Therefore, this study suggests that the activation of 5-HT₄ receptors mediates the antidepressant-like effects of fluoxetine. It has been shown that a knockout of the 5-HT₄ receptor can induce some adaptive changes in mice, leading to depression and anxiety-like behavior. Moreover, 5-HT₄ receptor knockout mice do not respond to fluoxetine in the olfactory bulbectomized model of depression and anxiety [249]. On the other hand, some studies suggest that the behavioral effects of fluoxetine in the corticosterone-induced model of depression and anxiety do not appear to be dependent on 5-HT₄ receptors [250].

Preclinical studies show that the administration of the 5-HT₄ agonists, RS67333 and prucalopride (Figure 8), reduces the immobility time in the FST, thus demonstrating the potential of the 5-HT₄ receptor as a molecular target of a potential new generation of antidepressants [251]. The agonism of the 5-HT₄ receptor may also play a role in the cognitive deficits associated with MDD. The use of RS67333 in chronic neuroendocrine animal models of depression/anxiety resulted in the restoration of induced learning and memory disorders [252]. Moreover, the studies show that administration of RS67333 and prucalopride causes 5-HT_{1A} autoreceptor desensitization, increased the tonus on hippocampal postsynaptic 5-HT_{1A} receptors, and increased CREB phosphorylation and neurogenesis in the hippocampus [251]. These parameters, which characterize the functioning of the brain, are used in antidepressant therapies. Importantly, these effects are noticeable after 3 days of treatment [251], while they are usually only seen after 2–3 weeks of treatment with SSRIs due to the latency phenomenon. The faster response to 5-HT₄ agonism has been suggested to be a result of the parallel rapid and sustained activation of 5-HT neuronal firing in the dorsal raphe nucleus [253]. Increased serotonergic neuronal firing may also

underlie the apparently superior efficacy of 5-HT₄ agonists over SSRIs because the reuptake inhibitory effect depends on the basal rates of 5-HT cell firing. Since the 5-HT₄ receptor is not expressed in the raphe nuclei, the ability of 5-HT₄ receptors to stimulate the firing of 5-HT neurons appears to involve the activation of receptors located on neurons in the PFC [244]. The identity of the cells expressing 5-HT₄ receptors and their connections to the serotonergic neurons of the dorsal raphe nucleus are not yet well understood. It is possible that they project to other regions, contributing to the antidepressant effect of 5-HT₄ agonists [253].

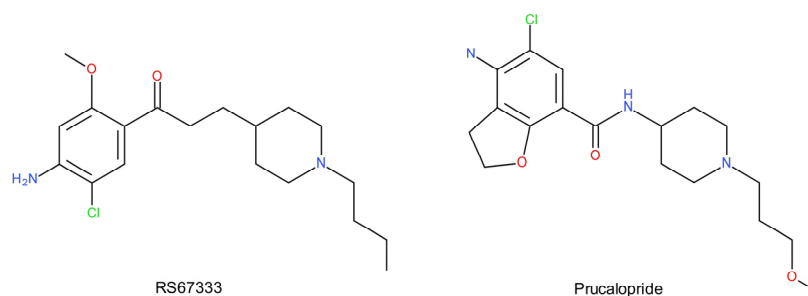


Figure 8. 5-HT₄ receptor agonists: RS67333 and prucalopride.

The activation of the 5-HT₄ receptor may be a useful adjunct to antidepressant therapy, both to accelerate the onset of clinical antidepressant effects and to target cognitive symptoms that are not effectively treated with current therapies [254]:

- There are reports linking the 5-HT₄ receptor with depressive disorders. The 5-HT₄ receptor interacts with the p11 protein, which determines the antidepressant activity mediated by 5-HT_{1B} and 5-HT₄ receptors;
- 5-HT₄ receptor signaling may modulate the function of the dentate gyrus of the hippocampus by increasing the neurogenesis and expression of neurotrophic factors, which may contribute to the antidepressant effects of drugs that enhance serotonergic transmission.
- The activation of the 5-HT₄ receptor may be a useful adjunct to antidepressant therapy, both to accelerate the onset of clinical antidepressant effects and to target cognitive symptoms that are not effectively treated with current therapies.

3.9. The 5-HT₆ Receptors

The 5-HT₆ receptors are the postsynaptic receptors most expressed in the striatum, nucleus accumbens, olfactory tubercle, and cortex. They are also moderately dense in the amygdala, hippocampus, hypothalamus, thalamus, and cerebellum [255].

This serotonin receptor subtype has been found to play a role in learning and memory [256] as well as in the central regulation of hunger and satiety behavior [257]. The 5-HT₆ receptors may, therefore, serve as a novel molecular target for the improvement of cognitive functions [258]. Several of the tricyclic antidepressants (e.g., amitriptyline) and atypical antidepressants (e.g., mianserin) exhibit nanomolar 5-HT₆ binding and antagonistic activity [259]. This fact, as well as the distribution of the 5-HT₆ receptor in the limbic and cortical regions of the brain, may suggest that 5-HT₆ receptors play an important role in the pathogenesis and/or treatment of depression [259]. The 5-HT₆ antagonists (SB-399885, Figure 9) show antidepressant activity in the FST and in the TST in rodents (rats and mice) [260]. In addition, the combination of an ineffective dose of SB-399885 with ineffective doses of imipramine, desipramine, bupropion, or moclobemide has been shown to exert antidepressant effects in the rat FST [261]. This suggests that the inhibition of the 5-HT₆ receptor potentiates the effects of clinically used antidepressants. This synergistic effect is interesting in the search for a multimodal antidepressant therapy with minimized side effects or a faster onset of action. Other preclinical studies show that 5-HT₆ agonism can be used in the treatment of depression. The reduction in the immobility

of mice in the FST after the administration of WAY208466, a selective potent agonist of the 5-HT₆ receptor, has been demonstrated [262]. The 5-HT₆ receptor partial agonist, EMD386088, caused antidepressant- and anxiolytic-like effects after intrahippocampal administration [263]. This also occurred after acute and chronic treatment in rats [264], possibly because it directly stimulated the receptor. The stimulation of the 5-HT₆ receptor may initiate the biochemical and behavioral effects induced by SSRIs (fluoxetine) [122]. On the other hand, the 5-HT₆ receptor agonist LY-586713 increases the expression of BDNF (a marker of cellular antidepressant activity) in the hippocampus after just a single administration [265]. In comparison, SSRIs require multiple applications to produce the same effect [240]. Therefore, it is unclear what functional 5-HT₆ receptor ligand profile (antagonism or agonism) will be more beneficial in the treatment of depression. Moreover, the exact mechanism by which 5-HT₆ ligands induce antidepressant effects is unknown and may include effects on other neurotransmission systems [260,266]:

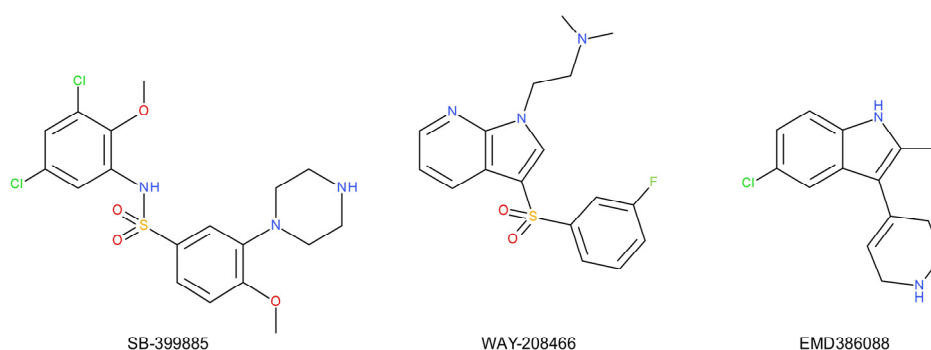


Figure 9. 5-HT₆ receptor ligands: SB-399885, WAY-208466, and EMD386088.

- The distribution of the 5-HT₆ receptor in the limbic and cortical regions of the brain may suggest that 5-HT₆ receptors play an important role in the pathogenesis and/or treatment of depression;
- Several tricyclic and atypical antidepressants exhibit nanomolar 5-HT₆ receptor binding. The inhibition of the 5-HT₆ receptor potentiates the effects of clinically used antidepressants. This synergistic effect is interesting in the search for a multimodal antidepressant therapy with minimized side effects or a faster onset of action;
- It is not exactly clear what functional 5-HT₆ receptor ligand profile (antagonism or agonism) will be more beneficial in the treatment of depression. Moreover, the exact mechanism by which 5-HT₆ ligands induce antidepressant effects is unknown and may include effects on other neurotransmission systems.

3.10. The 5-HT₇ Receptors

The 5-HT₇ receptor is highly expressed in the thalamus, hypothalamus, hippocampus, and cortex [267]. The results of immunolocalization and autoradiography studies are generally consistent with the pattern of mRNA distribution [268,269], suggesting a dominant somatodendritic localization. The physiological role of 5-HT₇ receptors is to regulate circadian rhythm, sleep, and mood [270].

As with the 5-HT₆ receptors, several antidepressants [271] and antipsychotics [272] have been found to have a high affinity for the 5-HT₇ receptor, leading to much further research into its antidepressant activity. One preclinical study in rats showed that several antidepressants, both tricyclic and SSRIs, induce *c-fos* expression in a manner consistent with 5-HT₇ receptor activation within the suprachiasmatic nucleus, and that chronic treatment with antidepressant drugs downregulates 5-HT₇ receptor binding [271].

Preclinical studies also indicate the antidepressant and anxiolytic effects of the selective 5-HT₇ receptor antagonist, SB-269970, in rodents [273], as well as a synergistic interaction between subeffective doses of this agent and antidepressants, leading to a reduction in immobility in both the FST and the TST [274,275]. The intrahippocampal administra-

tion of SB-269970 (Figure 10) induced an antidepressant effect in the FST in rats [276]. The co-administration of citalopram and SB-269970 increased the activity of serotonin neurons in rats and improved the antidepressant effect in the TST [274]. SB-269970 enhanced the antidepressant effect of antidepressants (citalopram, imipramine, desipramine, and moclobemide) in the FST in mice [275]. It was also shown that the administration of SB-269970 for only one week caused the behavioral, electrophysiological, and neuroanatomical changes that usually occur after a long-term treatment with SSRIs. Therefore, 5-HT₇ receptor antagonists might represent a new class of antidepressants with a faster therapeutic effect. JNJ-18038683, another 5-HT₇ receptor antagonist, was also effective in mice TST [277]. Moreover, the compound potentiated serotonin transmission, REM suppression, and antidepressant-like behaviour induced by citalopram in rodents [277]. The above studies indicate that the participation of the 5-HT₇ receptor in the antidepressant-like action, and blockade of the 5-HT₇ receptor may not only induce but accelerate this action.

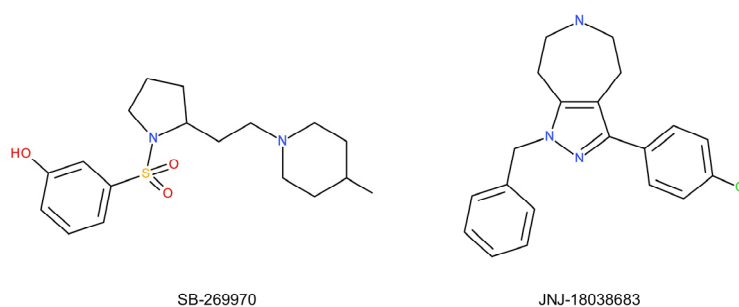


Figure 10. 5-HT₇ receptor antagonists: SB-269970 and JNJ-18038683.

In addition, the genetic and pharmacological inactivation of 5-HT₇ receptors partially reversed phencyclidine-induced deficits of pre-pulse inhibition, an animal model for antipsychotic activity [278]. Similarly, it should also be noted that the atypical antipsychotic aripiprazole, which has a high affinity for the 5-HT₇ receptor, is sometimes used to enhance the effects of traditional antidepressants [279]. Similarly, there are reports that the antidepressant effect of amisulpride is mediated by its action on 5-HT₇ receptors [280].

Vortioxetine is a high affinity inhibitor of the human 5-HT transporter, 5-HT₃ and 5-HT₇ receptors, and a 5-HT_{1A} agonist [281]. Although the affinity of vortioxetine for the rat 5-HT₇ receptor is lower compared to the human receptor [282], subacute administration (within 3 days) of an effective dose of vortioxetine rapidly lowers rat 5-HT₇ receptor levels [283]. This preclinical evidence suggests that vortioxetine has a relatively low affinity for the 5-HT₇ receptor compared to other 5-HT receptor subtypes but inhibits its action with a rapid 5-HT₇ receptor downregulation as an inverse agonist, similar to other 5-HT₇ receptor-inhibiting mood-stabilizing atypical antipsychotics: clozapine, lurasidone, and olanzapine [283,284]. In other words, the rapid-acting antidepressant and anxiolytic actions of 5-HT₇ receptor antagonism are worth reassessing in the context of drug development after future clinical data have been accumulated. Overall, the 5-HT₇ receptor is currently considered a promising target for the development of antidepressants [285]. Recent clinical studies have shown that both the intravenous and oral administration of vortioxetine resulted in a significant improvement in depression (Montgomery Åsberg Depression Rating Scale and Hospital Depression Scale) and anxiety (Hospital Anxiety Scale) after 3 days [77]:

- Several antidepressants have been found to have a high affinity for the 5-HT₇ receptor, leading to much further research into its antidepressant activity;
- The antagonists of the 5-HT₇ receptor might represent a new class of antidepressants with a faster therapeutic effect.
- Preclinical evidence suggests that vortioxetine has a relatively low affinity for the 5-HT₇ receptor compared to other 5-HT receptor subtypes but inhibits its action with a rapid 5-HT₇ receptor downregulation as an inverse agonist. Both the intravenous and

oral administration of vortioxetine resulted in a significant improvement in depression and anxiety after 3 days.

4. Conclusions

The development of new antidepressants is based on monoamine systems. The targeted pharmacological modulation of serotonergic transmission in the brain continues to be a leading strategy in the search for new antidepressants. As can be seen from this review, the serotonergic system offers great potential for the development of new antidepressant therapies based on the combination of SERT inhibition with different pharmacological activities towards the 5-HT system. The careful selection of molecular targets for the proper use of the mechanisms of serotonergic autoregulation and selective/biased activation or the blockade of relevant receptors (e.g., stimulation of postsynaptic 5-HT_{1A}, postsynaptic 5-HT_{1B}, 5-HT_{2B} and 5-HT₄ receptors; or the blockade of presynaptic 5-HT_{1A}, presynaptic 5-HT_{1B}, 5-HT_{2A}, 5-HT₃, and 5-HT₇), which also influences other neurotransmission systems, seems to be the most effective strategy for supplementing the activity of “serotonin-enhancing” drugs in the near future. A better understanding of receptors and the receptor signaling responsible for the effects of serotonin on neurogenesis could also help in the development of new and more effective drugs.

Author Contributions: Conceptualization, G.Ś.; writing—original draft preparation, G.Ś.; writing—review and editing, M.K. and J.T. All authors have read and agreed to the published version of the manuscript.

Funding: This research was supported by Medical University of Warsaw. This research received no external funding.

Institutional Review Board Statement: Not applicable.

Informed Consent Statement: Not applicable.

Data Availability Statement: Data are contained within the article.

Conflicts of Interest: The authors declare no conflict of interest.

References

- James, S.L.; Abate, D.; Abate, K.H.; Abay, S.M.; Abbafati, C.; Abbasi, N.; Abbastabar, H.; Abd-Allah, F.; Abdela, J.; Abdelalim, A.; et al. Global, regional, and national incidence, prevalence, and years lived with disability for 354 diseases and injuries for 195 countries and territories, 1990–2017: A systematic analysis for the Global Burden of Disease Study 2017. *Lancet* **2018**, *392*, 1789–1858. [CrossRef]
- Ögren, S.O.; Eriksson, T.M.; Elvander-Tottie, E.; D’Addario, C.; Ekström, J.C.; Svenningsson, P.; Meister, B.; Kehr, J.; Stiedl, O. The role of 5-HT_{1A} receptors in learning and memory. *Behav. Brain Res.* **2008**, *195*, 54–77. [CrossRef]
- Day, J.J.; Sweatt, J.D. Epigenetic Treatments for Cognitive Impairments. *Neuropsychopharmacology* **2012**, *37*, 247–260. [CrossRef]
- Sheehan, D.V.; Nakagome, K.; Asami, Y.; Pappadopulos, E.A.; Boucher, M. Restoring function in major depressive disorder: A systematic review. *J. Affect. Disord.* **2017**, *215*, 299–313. [CrossRef]
- Sharp, T.; Cowen, P.J. 5-HT and depression: Is the glass half-full? *Curr. Opin. Pharmacol.* **2011**, *11*, 45–51. [CrossRef]
- Wiles, N.J.; Fischer, K.; Cowen, P.; Nutt, D.; Peters, T.J.; Lewis, G.; White, I.R. Allowing for non-adherence to treatment in a randomized controlled trial of two antidepressants (citalopram versus reboxetine): An example from the GENPOD trial. *Psychol. Med.* **2014**, *44*, 2855–2866. [CrossRef]
- Turcotte, J.E.; Debonnel, G.; De Montigny, C.; Hébert, C.; Blier, P. Assessment of the serotonin and norepinephrine reuptake blocking properties of duloxetine in healthy subjects. *Neuropsychopharmacology* **2001**, *24*, 511–521. [CrossRef]
- Cleare, A.; Pariante, C.; Young, A.; Anderson, I.; Christmas, D.; Cowen, P.; Dickens, C.; Ferrier, I.; Geddes, J.; Gilbody, S.; et al. Evidence-based guidelines for treating depressive disorders with antidepressants: A revision of the 2008 British Association for Psychopharmacology guidelines. *J. Psychopharmacol.* **2015**, *29*, 459–525. [CrossRef]
- Bauer, M.; Bschor, T.; Pfennig, A.; Whybrow, P.C.; Angst, J.; Versiani, M.; Möller, H.-J. World Federation of Societies of Biological Psychiatry (WFSBP) Guidelines for Biological Treatment of Unipolar Depressive Disorders in Primary Care. *World J. Biol. Psychiatry* **2007**, *8*, 67–104. [CrossRef]
- Harmer, C.J.; Duman, R.S.; Cowen, P.J. How do antidepressants work? New perspectives for refining future treatment approaches. *Lancet Psychiatry* **2017**, *4*, 409–418. [CrossRef]
- Rana, T.; Behl, T.; Sehgal, A.; Mehta, V.; Singh, S.; Kumar, R.; Bungau, S. Integrating Endocannabinoid Signalling In Depression. *J. Mol. Neurosci.* **2021**. [CrossRef]

12. Rana, T.; Behl, T.; Sehgal, A.; Mehta, V.; Singh, S.; Sharma, N.; Bungau, S. Elucidating the Possible Role of FoxO in Depression. *Neurochem. Res.* **2021**. [CrossRef] [PubMed]
13. Rana, T.; Behl, T.; Sehgal, A.; Sachdeva, M.; Mehta, V.; Sharma, N.; Singh, S.; Bungau, S. Exploring Sonic Hedgehog Cell Signaling in Neurogenesis: Its Potential Role in Depressive Behavior. *Neurochem. Res.* **2021**, *46*, 1589–1602. [CrossRef] [PubMed]
14. Rana, T.; Behl, T.; Sehgal, A.; Srivastava, P.; Bungau, S. Unfolding the Role of BDNF as a Biomarker for Treatment of Depression. *J. Mol. Neurosci.* **2020**. [CrossRef]
15. Millan, M.J. On “polypharmacy” and multi-target agents, complementary strategies for improving the treatment of depression: A comparative appraisal. *Int. J. Neuropsychopharmacol.* **2014**, *17*, 1009–1037. [CrossRef]
16. Duhr, F.; Délérís, P.; Raynaud, F.; Séveno, M.; Morisset-Lopez, S.; Mannoury la Cour, C.; Millan, M.J.; Bockaert, J.; Marin, P.; Chaumont-Dubel, S. Cdk5 induces constitutive activation of 5-HT₆ receptors to promote neurite growth. *Nat. Chem. Biol.* **2014**, *10*, 590–597. [CrossRef]
17. Żmudzka, E.; Sałaciak, K.; Sapa, J.; Pytka, K. Serotonin receptors in depression and anxiety: Insights from animal studies. *Life Sci.* **2018**, *210*, 106–124. [CrossRef]
18. Miller, J.M.; Hesselgrave, N.; Ogden, R.T.; Zanderigo, F.; Oquendo, M.A.; Mann, J.J.; Parsey, R.V. Brain Serotonin 1A Receptor Binding as a Predictor of Treatment Outcome in Major Depressive Disorder. *Biol. Psychiatry* **2013**, *74*, 760–767. [CrossRef]
19. Kaufman, J.; DeLorenzo, C.; Choudhury, S.; Parsey, R.V. The 5-HT_{1A} receptor in Major Depressive Disorder. *Eur. Neuropsychopharmacol.* **2016**, *26*, 397–410. [CrossRef] [PubMed]
20. Artigas, F. Serotonin receptors involved in antidepressant effects. *Pharmacol. Ther.* **2013**, *137*, 119–131. [CrossRef]
21. Artigas, F. Developments in the field of antidepressants, where do we go now? *Eur. Neuropsychopharmacol.* **2015**, *25*, 657–670. [CrossRef]
22. Perez-Caballero, L.; Torres-Sanchez, S.; Romero-López-Alberca, C.; González-Saiz, F.; Mico, J.A.; Berrocoso, E. Monoaminergic system and depression. *Cell Tissue Res.* **2019**, *377*, 107–113. [CrossRef]
23. Albert, P.R.; Vahid-Ansari, F. The 5-HT_{1A} receptor: Signaling to behavior. *Biochimie* **2018**, *161*, 34–45. [CrossRef]
24. Haleem, D.J. Targeting Serotonin1A Receptors for Treating Chronic Pain and Depression. *Curr. Neuropharmacol.* **2019**, *17*, 1098–1108. [CrossRef]
25. Artigas, F.; Bortolozzi, A.; Celada, P. Can we increase speed and efficacy of antidepressant treatments? Part I: General aspects and monoamine-based strategies. *Eur. Neuropsychopharmacol.* **2018**, *28*, 445–456. [CrossRef]
26. Kishi, T.; Meltzer, H.Y.; Matsuda, Y.; Iwata, N. Azapirone 5-HT_{1A} receptor partial agonist treatment for major depressive disorder: Systematic review and meta-analysis. *Psychol. Med.* **2014**, *44*, 2255–2269. [CrossRef]
27. Sahli, Z.T.; Banerjee, P.; Tarazi, F.I. The Preclinical and Clinical Effects of Vilazodone for the Treatment of Major Depressive Disorder. *Expert Opin. Drug Discov.* **2016**, *11*, 515–523. [CrossRef]
28. James Deardorff, W.; Grossberg, G.T. A review of the clinical efficacy, safety and tolerability of the antidepressants vilazodone, levomilnacipran and vortioxetine. *Expert Opin. Pharmacother.* **2014**, *15*, 2525–2542. [CrossRef]
29. Jonnakuty, C.; Gragnoli, C. What do we know about serotonin? *J. Cell. Physiol.* **2008**, *217*, 301–306. [CrossRef]
30. Banerjee, P.; Mehta, M.; Kanjilal, B. *The 5-HT_{1A} Receptor: A Signaling Hub Linked to Emotional Balance*; CRC Press/Taylor & Francis: Boca Raton, FL, USA, 2007; Chapter 7; ISBN 0849339774.
31. Hasegawa, H.; Nakamura, K. Tryptophan Hydroxylase and Serotonin Synthesis Regulation. In *Handbook of Behavioral Neuroscience*; Elsevier B.V.: Amsterdam, The Netherlands, 2010; Volume 21, pp. 183–202. ISBN 9780123746344.
32. Manocha, M.; Khan, W.I. Serotonin and GI Disorders: An Update on Clinical and Experimental Studies. *Clin. Transl. Gastroenterol.* **2012**, *3*, e13. [CrossRef]
33. Savitz, J.; Lucki, I.; Drevets, W.C. 5-HT_{1A} receptor function in major depressive disorder. *Prog. Neurobiol.* **2009**, *88*, 17–31. [CrossRef]
34. Smythies, J. Section V. Serotonin System. *Int. Rev. Neurobiol.* **2005**, *64*, 217–268. [CrossRef]
35. Diksic, M.; Young, S.N. Study of the brain serotonergic system with labeled α -methyl-L-tryptophan. *J. Neurochem.* **2001**, *78*, 1185–1200. [CrossRef] [PubMed]
36. Jacobs, B.L.; Azmitia, E.C. Structure and function of the brain serotonin system. *Physiol. Rev.* **1992**, *72*, 165–229. [CrossRef]
37. Celada, P.; Puig, M.V.; Casanovas, J.M.; Guillazo, G.; Artigas, F. Control of dorsal raphe serotonergic neurons by the medial prefrontal cortex: Involvement of serotonin-1A, GABA(A), and glutamate receptors. *J. Neurosci.* **2001**, *21*, 9917–9929. [CrossRef]
38. O’Leary, O.F.; Bechtholt, A.J.; Crowley, J.J.; Valentino, R.J.; Lucki, I. The role of noradrenergic tone in the dorsal raphe nucleus of the mouse in the acute behavioral effects of antidepressant drugs. *Eur. Neuropsychopharmacol.* **2007**, *17*, 215–226. [CrossRef]
39. Varga, V.; Székely, A.D.; Csillag, A.; Sharp, T.; Hajós, M. Evidence for a role of GABA interneurons in the cortical modulation of midbrain 5-hydroxytryptamine neurones. *Neuroscience* **2001**, *106*, 783–792. [CrossRef]
40. Martín-Ruiz, R.; Ugedo, L.; Honrubia, M.A.; Mengod, G.; Artigas, F. Control of serotonergic neurons in rat brain by dopaminergic receptors outside the dorsal raphe nucleus. *J. Neurochem.* **2001**, *77*, 762–775. [CrossRef]
41. Ohno, Y. *Serotonin Receptors as the Therapeutic Target for Central Nervous System Disorders*; Elsevier Inc.: Amsterdam, The Netherlands, 2019; ISBN 9780128000502.
42. Santana, N.; Bortolozzi, A.; Serrats, J.; Mengod, G.; Artigas, F. Expression of serotonin1A and serotonin2A receptors in pyramidal and GABAergic neurons of the rat prefrontal cortex. *Cereb. Cortex* **2004**, *14*, 1100–1109. [CrossRef]

43. Riad, M.; Garcia, S.; Watkins, K.C.; Jodoin, N.; Doucet, É.; Langlois, X.; El Mestikawy, S.; Hamon, M.; Descarries, L. Somatodendritic localization of 5-HT_{1A} and preterminal axonal localization of 5-HT_{1B} serotonin receptors in adult rat brain. *J. Comp. Neurol.* **2000**, *417*, 181–194. [CrossRef]
44. Liu, Y.F.; Ghahremani, M.H.; Rasenick, M.M.; Jakobs, K.H.; Albert, P.R. Stimulation of cAMP synthesis by G(i)-coupled receptors upon ablation of distinct G α (i) protein expression. G(i) subtype specificity of the 5-HT_{1A} receptor. *J. Biol. Chem.* **1999**, *274*, 16444–16450. [CrossRef]
45. Loucif, A.J.C.; Bonnavion, P.; Macri, B.; Golmard, J.L.; Boni, C.; Melfort, M.; Leonard, G.; Lesch, K.P.; Adrien, J.; Jacquin, T.D. Gender-dependent regulation of G-protein-gated inwardly rectifying potassium current in dorsal raphe neurons in knock-out mice devoid of the 5-hydroxytryptamine transporter. *J. Neurobiol.* **2006**, *66*, 1475–1488. [CrossRef]
46. Halasy, K.; Miettinen, R.; Szabat, E.; Freund, T.F. GABAergic Interneurons are the Major Postsynaptic Targets of Median Raphe Afferents in the Rat Dentate Gyrus. *Eur. J. Neurosci.* **1992**, *4*, 144–153. [CrossRef]
47. Cassel, J.C.; Jeltsch, H. Serotonergic modulation of cholinergic function in the central nervous system: Cognitive implications. *Neuroscience* **1995**, *69*, 1–41. [CrossRef]
48. Jeltsch-David, H.; Koenig, J.; Cassel, J.C. Modulation of cholinergic functions by serotonin and possible implications in memory: General data and focus on 5-HT_{1A} receptors of the medial septum. *Behav. Brain Res.* **2008**, *195*, 86–97. [CrossRef]
49. Lopez-Gil, X.; Artigas, F.; Adell, A. Unraveling Monoamine Receptors Involved in the Action of Typical and Atypical Antipsychotics on Glutamatergic and Serotonergic Transmission in Prefrontal Cortex. *Curr. Pharm. Des.* **2010**, *16*, 502–515. [CrossRef]
50. Di Matteo, V.; Di Giovanni, G.; Pierucci, M.; Esposito, E. Serotonin control of central dopaminergic function: Focus on in vivo microdialysis studies. *Prog. Brain Res.* **2008**, *172*, 7–44. [CrossRef]
51. Andrade, R.; Nicoll, R.A. Pharmacologically distinct actions of serotonin on single pyramidal neurones of the rat hippocampus recorded in vitro. *J. Physiol.* **1987**, *394*, 99–124. [CrossRef]
52. Newman-Tancredi, A. Biased agonism at serotonin 5-HT_{1A} receptors: Preferential postsynaptic activity for improved therapy of CNS disorders. *Neuropsychiatry* **2011**, *1*, 149–164. [CrossRef]
53. Mehta, M.; Ahmed, Z.; Fernando, S.S.; Cano-Sanchez, P.; Adayev, T.; Ziemnicka, D.; Wieraszko, A.; Banerjee, P. Plasticity of 5-HT_{1A} receptor-mediated signaling during early postnatal brain development. *J. Neurochem.* **2007**, *101*, 918–928. [CrossRef]
54. Kushwaha, N.; Albert, P.R. Coupling of 5-HT_{1A} autoreceptors to inhibition of mitogen-activated protein kinase activation via G $\beta\gamma$ subunit signaling. *Eur. J. Neurosci.* **2005**, *21*, 721–732. [CrossRef]
55. Heusler, P.; Pauwels, P.J.; Wurch, T.; Newman-Tancredi, A.; Tytgat, J.; Colpaert, F.C.; Cussac, D. Differential ion current activation by human 5-HT_{1A} receptors in *Xenopus* oocytes: Evidence for agonist-directed trafficking of receptor signalling. *Neuropharmacology* **2005**, *49*, 963–976. [CrossRef]
56. Valdizán, E.M.; Castro, E.; Pazos, A. Agonist-dependent modulation of G-protein coupling and transduction of 5-HT_{1A} receptors in rat dorsal raphe nucleus. *Int. J. Neuropsychopharmacol.* **2010**, *13*, 835–843. [CrossRef]
57. Heisler, L.K.; Chu, H.-M.; Brennan, T.J.; Danao, J.A.; Bajwa, P.; Parsons, L.H.; Tecott, L.H. Elevated anxiety and antidepressant-like responses in serotonin 5-HT_{1A} receptor mutant mice. *Proc. Natl. Acad. Sci. USA* **1998**, *95*, 15049–15054. [CrossRef]
58. Pytka, K.; Podkowa, K.; Rapacz, A.; Podkowa, A.; Zmudzka, E.; Olczyk, A.; Sapa, J.; Filipek, B. The role of serotonergic, adrenergic and dopaminergic receptors in antidepressant-like effect. *Pharmacol. Rep.* **2016**, *68*, 263–274. [CrossRef]
59. Santarelli, L. Requirement of Hippocampal Neurogenesis for the Behavioral Effects of Antidepressants. *Science* **2003**, *301*, 805–809. [CrossRef]
60. Assié, M.B.; Bardin, L.; Auclair, A.L.; Carilla-Durand, E.; Depoortère, R.; Koek, W.; Kleven, M.S.; Colpaert, F.; Vacher, B.; Newman-Tancredi, A. F15599, a highly selective post-synaptic 5-HT_{1A} receptor agonist: In-vivo profile in behavioural models of antidepressant and serotonergic activity. *Int. J. Neuropsychopharmacol.* **2010**, *13*, 1285–1298. [CrossRef]
61. Pytka, K.; Gluch-Lutwin, M.; Kotańska, M.; Żmudzka, E.; Jakubczyk, M.; Waszkielewicz, A.; Janiszewska, P.; Walczak, M. HBK-15 protects mice from stress-induced behavioral disturbances and changes in corticosterone, BDNF, and NGF levels. *Behav. Brain Res.* **2017**, *333*, 54–66. [CrossRef]
62. Depoortère, R.; Auclair, A.L.; Newman-Tancredi, A. NLX-101, a highly selective 5-HT_{1A} receptor biased agonist, mediates antidepressant-like activity in rats via prefrontal cortex 5-HT_{1A} receptors. *Behav. Brain Res.* **2021**, *401*, 113082. [CrossRef]
63. Albert, P.R.; Le François, B.; Millar, A.M. Transcriptional dysregulation of 5-HT_{1A} autoreceptors in mental illness. *Mol. Brain* **2011**, *4*, 1–14. [CrossRef] [PubMed]
64. Terao, T.; Ishii, N.; Hirakawa, H.; Aoshima, E. Is the bell-shaped dose-response curve of the selective serotonin reuptake inhibitor due to 5-HT_{1A} auto-receptors? *Med. Hypotheses* **2020**, *140*, 109681. [CrossRef]
65. Hervás, I.; Vilaró, M.T.; Romero, L.; Scorza, M.C.; Mengod, G.; Artigas, F. Desensitization of 5-HT(1A) autoreceptors by a low chronic fluoxetine dose effect of the concurrent administration of WAY-100635. *Neuropsychopharmacology* **2001**, *24*, 11–20. [CrossRef]
66. Artigas, F.; Celada, P.; Laruelle, M.; Adell, A. How does pindolol improve antidepressant action? *Trends Pharmacol. Sci.* **2001**, *22*, 224–228. [CrossRef]
67. Celada, P.; Artigas, F. Monoamine oxidase inhibitors increase preferentially extracellular 5-hydroxytryptamine in the midbrain raphe nuclei. A brain microdialysis study in the awake rat. *Naunyn-Schmiedeberg Arch. Pharmacol.* **1993**, *347*, 583–590. [CrossRef]
68. Blier, P.; De Montigny, C. Current advances and trends in the treatment of depression. *Trends Pharmacol. Sci.* **1994**, *15*, 220–226. [CrossRef]

69. Romero, L.; Bel, N.; Artigas, F.; De Montigny, C.; Blier, P. Effect of pindolol on the function of pre- and postsynaptic 5-HT_{1A} receptors: In vivo microdialysis and electrophysiological studies in the rat brain. *Neuropsychopharmacology* **1996**, *15*, 349–360. [CrossRef]
70. El Mansari, M.; Sánchez, C.; Chouvet, G.; Renaud, B.; Haddjeri, N. Effects of acute and long-term administration of escitalopram and citalopram on serotonin neurotransmission: An in vivo electrophysiological study in rat brain. *Neuropsychopharmacology* **2005**, *30*, 1269–1277. [CrossRef]
71. Ohno, Y. New Insight into the Therapeutic Role of 5-HT_{1A} Receptors in Central Nervous System Disorders. *Cent. Nerv. Syst. Agents Med. Chem.* **2010**, *10*, 148–157. [CrossRef]
72. Richardson-Jones, J.W.; Craige, C.P.; Guiard, B.P.; Stephen, A.; Metzger, K.L.; Kung, H.F.; Gardier, A.M.; Dranovsky, A.; David, D.J.; Beck, S.G.; et al. 5-HT_{1A} Autoreceptor Levels Determine Vulnerability to Stress and Response to Antidepressants. *Neuron* **2010**, *65*, 40–52. [CrossRef]
73. Whale, R.; Terao, T.; Cowen, P.; Freemantle, N.; Geddes, J. Pindolol augmentation of serotonin reuptake inhibitors for the treatment of depressive disorder: A systematic review. *J. Psychopharmacol.* **2010**, *24*, 513–520. [CrossRef]
74. Arborelius, L.; Linner, L.; Wallsten, C.; Ahlenius, S.; Svensson, T.H. Partial 5-HT_{1A} receptor agonist properties of (-)pindolol in combination with citalopram on serotonergic dorsal raphe cell firing in vivo. *Psychopharmacology* **2000**, *151*, 77–84. [CrossRef]
75. Trivedi, M.H.; Fava, M.; Wisniewski, S.R.; Thase, M.E.; Quitkin, F.; Warden, D.; Ritz, L.; Nierenberg, A.A.; Lebowitz, B.D.; Biggs, M.M.; et al. Medication Augmentation after the Failure of SSRIs for Depression. *N. Engl. J. Med.* **2006**, *354*, 1243–1252. [CrossRef]
76. Shelton, R.C.; Tollefson, G.D.; Tohen, M.; Stahl, S.; Gannon, K.S.; Jacobs, T.G.; Buras, W.R.; Bymaster, F.P.; Zhang, W.; Spencer, K.A.; et al. A novel augmentation strategy for treating resistant major depression. *Am. J. Psychiatry* **2001**, *158*, 131–134. [CrossRef]
77. Vieta, E.; Florea, I.; Schmidt, S.N.; Areberg, J.; Ettrup, A. Intravenous vortioxetine to accelerate onset of effect in major depressive disorder: A 2-week, randomized, double-blind, placebo-controlled study. *Int. Clin. Psychopharmacol.* **2019**, *34*, 153–160. [CrossRef]
78. MacQueen, G.M.; Yucel, K.; Taylor, V.H.; Macdonald, K.; Joffe, R. Posterior Hippocampal Volumes Are Associated with Remission Rates in Patients with Major Depressive Disorder. *Biol. Psychiatry* **2008**, *64*, 880–883. [CrossRef]
79. Bremner, J.D.; Narayan, M.; Anderson, E.R.; Staib, L.H.; Miller, H.L.; Charney, D.S. Hippocampal volume reduction in major depression. *Am. J. Psychiatry* **2000**, *157*, 115–117. [CrossRef] [PubMed]
80. Hong, W.; Fan, J.; Yuan, C.; Zhang, C.; Hu, Y.; Peng, D.; Wang, Y.; Huang, J.; Li, Z.; Yu, S.; et al. Significantly decreased mRNA levels of BDNF and MEK1 genes in treatment-resistant depression. *Neuroreport* **2014**, *25*, 753–755. [CrossRef]
81. Banerjee, R.; Ghosh, A.K.; Ghosh, B.; Bhattacharyya, S.; Mondal, A.C. Decreased mRNA and protein expression of BDNF, NGF, and their receptors in the hippocampus from suicide: An analysis in human postmortem brain. *Clin. Med. Insights Pathol.* **2013**, *1*–11. [CrossRef]
82. Filho, C.B.; Jesse, C.R.; Donato, F.; Giacomeli, R.; Del Fabbro, L.; Da Silva Antunes, M.; De Gomes, M.G.; Goes, A.T.R.; Boeira, S.P.; Prigol, M.; et al. Chronic unpredictable mild stress decreases BDNF and NGF levels and Na_v,K_v-ATPase activity in the hippocampus and prefrontal cortex of mice: Antidepressant effect of chrysin. *Neuroscience* **2015**, *289*, 367–380. [CrossRef]
83. Mao, Q.Q.; Xian, Y.F.; Ip, S.P.; Tsai, S.H.; Che, C.T. Long-term treatment with peony glycosides reverses chronic unpredictable mild stress-induced depressive-like behavior via increasing expression of neurotrophins in rat brain. *Behav. Brain Res.* **2010**, *210*, 171–177. [CrossRef]
84. Su, G.Y.; Yang, J.Y.; Wang, F.; Ma, J.; Zhang, K.; Dong, Y.X.; Song, S.J.; Lu, X.M.; Wu, C.F. Antidepressant-like effects of Xiaochaihutang in a rat model of chronic unpredictable mild stress. *J. Ethnopharmacol.* **2014**, *152*, 217–226. [CrossRef]
85. Antunes, M.S.; Jesse, C.R.; Ruff, J.R.; De Oliveira Espinosa, D.; Gomes, N.S.; Altwater, E.E.T.; Donato, F.; Giacomeli, R.; Boeira, S.P. Hesperidin reverses cognitive and depressive disturbances induced by olfactory bulbectomy in mice by modulating hippocampal neurotrophins and cytokine levels and acetylcholinesterase activity. *Eur. J. Pharmacol.* **2016**, *789*, 411–420. [CrossRef]
86. Noorafshan, A.; Abdollahifar, M.A.; Asadi-Golshan, R.; Rashidian-Rashidabadi, A.; Karbalay-Doust, S. Curcumin and sertraline prevent the reduction of the number of neurons and glial cells and the volume of rats' medial prefrontal cortex induced by stress. *Acta Neurobiol. Exp.* **2014**, *74*, 44–53.
87. Luscombe, G.P.; Martin, K.F.; Hutchins, L.J.; Gosden, J.; Heal, D.J. Mediation of the antidepressant-like effect of 8-OH-DPAT in mice by postsynaptic 5-HT_{1A} receptors. *Br. J. Pharmacol.* **1993**, *108*, 669–677. [CrossRef]
88. Samuels, B.A.; Anacker, C.; Hu, A.; Levinstein, M.R.; Pickenhagen, A.; Tsetsenis, T.; Madroñal, N.; Donaldson, Z.R.; Drew, L.J.; Dranovsky, A.; et al. 5-HT_{1A} receptors on mature dentate gyrus granule cells are critical for the antidepressant response. *Nat. Neurosci.* **2015**, *18*, 1606–1616. [CrossRef]
89. Richardson-Jones, J.W.; Craige, C.P.; Nguyen, T.H.; Kung, H.F.; Gardier, A.M.; Dranovsky, A.; David, D.J.; Guiard, B.P.; Beck, S.G.; Hen, R.; et al. Serotonin-1A autoreceptors are necessary and sufficient for the normal formation of circuits underlying innate anxiety. *J. Neurosci.* **2011**, *31*, 6008–6018. [CrossRef]
90. Vahid-Ansari, F.; Daigle, M.; Manzini, M.C.; Tanaka, K.F.; Hen, R.; Geddes, S.D.; Bèique, J.-C.; James, J.; Merali, Z.; Albert, P.R. Abrogated Freud-1/Cc2d1a Repression of 5-HT_{1A} Autoreceptors Induces Fluoxetine-Resistant Anxiety/Depression-Like Behavior. *J. Neurosci.* **2017**, *37*, 11967–11978. [CrossRef]
91. Stockmeier, C.A.; Shapiro, L.A.; Dilley, G.E.; Kolli, T.N.; Friedman, L.; Rajkowska, G. Increase in serotonin-1A autoreceptors in the midbrain of suicide victims with major depression—Postmortem evidence for decreased serotonin activity. *J. Neurosci.* **1998**, *18*, 7394–7401. [CrossRef]

92. Parsey, R.V.; Oquendo, M.A.; Ogden, R.T.; Olvet, D.M.; Simpson, N.; Huang, Y.Y.; Van Heertum, R.L.; Arango, V.; Mann, J.J. Altered serotonin 1A binding in major depression: A [carbonyl-C-11] WAY100635 positron emission tomography study. *Biol. Psychiatry* **2006**, *59*, 106–113. [CrossRef]
93. Boldrini, M.; Underwood, M.D.; Mann, J.J.; Arango, V. Serotonin-1A autoreceptor binding in the dorsal raphe nucleus of depressed suicides. *J. Psychiatr. Res.* **2008**, *42*, 433–442. [CrossRef]
94. Lemonde, S.; Turecki, G.; Bakish, D.; Du, L.; Hrdina, P.D.; Bown, C.D.; Sequeira, A.; Kushwaha, N.; Morris, S.J.; Basak, A.; et al. Impaired repression at a 5-hydroxytryptamine 1A receptor gene polymorphism associated with major depression and suicide. *J. Neurosci.* **2003**, *23*, 8788–8799. [CrossRef]
95. Neff, C.D.; Abkevich, V.; Packer, J.C.L.; Chen, Y.; Potter, J.; Riley, R.; Davenport, C.; DeGrado Warren, J.; Jammulapati, S.; Bhatena, A.; et al. Evidence for HTR1A and LHPP as interacting genetic risk factors in major depression. *Mol. Psychiatry* **2009**, *14*, 621–630. [CrossRef]
96. Bhagwagar, Z.; Rabiner, E.A.; Sargent, P.A.; Grasby, P.M.; Cowen, P.J. Persistent reduction in brain serotonin1A receptor binding in recovered depressed men measured by positron emission tomography with [11C]WAY-100635. *Mol. Psychiatry* **2004**, *9*, 386–392. [CrossRef]
97. Haddjeri, N.; Blier, P.; De Montigny, C. Long-term antidepressant treatments result in a tonic activation of forebrain 5-HT(1A) receptors. *J. Neurosci.* **1998**, *18*, 10150–10156. [CrossRef]
98. Jacobs, B.; Van Praag, H.; Gage, F. Adult brain neurogenesis and psychiatry a no. *Mol. Psychiatry* **2000**, *5*, 262–269. [CrossRef]
99. Blier, P.; Ward, N.M. Is there a role for 5-HT_{1A} agonists in the treatment of depression? *Biol. Psychiatry* **2003**, *53*, 193–203. [CrossRef]
100. Rabiner, E.A.; Wilkins, M.R.; Turkheimer, F.; Gunn, R.N.; De Haes, J.U.; De Vries, M.; Grasby, P.M. 5-Hydroxytryptamine1A receptor occupancy by novel full antagonist 2-[4-[4-(7-Chloro-2,3-dihydro-1,4-benzodioxyn-5-yl)-1-piperazinyl]butyl] -1,2-benzisothiazol-3-(2H)-one-1,1-dioxide: A [11C][O-methyl-3H]-N-(2-(4-(2-methoxyphenyl)-1-piperazinyl) ethyl)-N-(2-pyridinyl) cyclohexanecarboxamide trihydrochloride (WAY-100635) positron emission tomography study in humans. *J. Pharmacol. Exp. Ther.* **2002**, *301*, 1144–1150. [CrossRef]
101. Scorza, M.; Lladó-Pelfort, L.; Oller, S.; Cortés, R.; Puigdemont, D.; Portella, M.J.; Pérez-Egea, R.; Alvarez, E.; Celada, P.; Pérez, V.; et al. Preclinical and clinical characterization of the selective 5-HT_{1A} receptor antagonist DU-125530 for antidepressant treatment. *Br. J. Pharmacol.* **2012**, *167*, 1021–1034. [CrossRef]
102. Mørk, A.; Pehrson, A.; Brennum, L.T.; Møller Nielsen, S.; Zhong, H.; Lassen, A.B.; Miller, S.; Westrich, L.; Boyle, N.J.; Sánchez, C.; et al. Pharmacological effects of Lu AA21004: A novel multimodal compound for the treatment of major depressive disorder. *J. Pharmacol. Exp. Ther.* **2012**, *340*, 666–675. [CrossRef]
103. Wang, S.-M.; Han, C.; Lee, S.-J.; Patkar, A.A.; Masand, P.S.; Pae, C.-U. Vilazodone for the Treatment of Depression: An Update. *Chonnam Med. J.* **2016**, *52*, 91. [CrossRef]
104. Sowa-Kućma, M.; Pańczyszyn-Trzewik, P.; Misztak, P.; Jaeschke, R.R.; Sendek, K.; Styczeń, K.; Datka, W.; Koperny, M. Vortioxetine: A review of the pharmacology and clinical profile of the novel antidepressant. *Pharmacol. Rep.* **2017**, *69*, 595–601. [CrossRef]
105. Sanchez, C.; Asin, K.E.; Artigas, F. Vortioxetine, a novel antidepressant with multimodal activity: Review of preclinical and clinical data. *Pharmacol. Ther.* **2015**, *145*, 43–57. [CrossRef]
106. Schreiber, R.; De Vry, J. 5-HT_{1A} receptor ligands in animal models of anxiety, impulsivity and depression: Multiple mechanisms of action? *Prog. Neuropsychopharmacol. Biol. Psychiatry* **1993**, *17*, 87–104. [CrossRef]
107. Depoortère, R.; Bardin, L.; Varney, M.A.; Newman-Tancredi, A. Serotonin 5-HT_{1A} Receptor Biased Agonists Display Differential Anxiolytic Activity in a Rat Social Interaction Model. *ACS Chem. Neurosci.* **2019**, *10*, 3101–3107. [CrossRef]
108. Robinson, D.S.; Kajdasz, D.K.; Gallipoli, S.; Whalen, H.; Wamil, A.; Reed, C.R. A 1-year, open-label study assessing the safety and tolerability of vilazodone in patients with major depressive disorder. *J. Clin. Psychopharmacol.* **2011**, *31*, 643–646. [CrossRef] [PubMed]
109. De Boer, S.F.; Koolhaas, J.M. 5-HT_{1A} and 5-HT_{1B} receptor agonists and aggression: A pharmacological challenge of the serotonin deficiency hypothesis. *Eur. J. Pharmacol.* **2005**, *526*, 125–139. [CrossRef] [PubMed]
110. Naranjo, C.A.; Bremner, K.E. Serotonin-altering medications and desire, consumption and effects of alcohol-treatment implications. *EXS* **1994**, *71*, 209–219. [CrossRef]
111. Prinssen, E.P.M.; Colpaert, F.C.; Koek, W. 5-HT_{1A} receptor activation and anti-cataleptic effects: High-efficacy agonists maximally inhibit haloperidol-induced catalepsy. *Eur. J. Pharmacol.* **2002**, *453*, 217–221. [CrossRef]
112. Sari, Y. Serotonin 1B receptors: From protein to physiological function and behavior. *Neurosci. Biobehav. Rev.* **2004**, *28*, 565–582. [CrossRef]
113. Morelli, N.; Gori, S.; Choub, A.; Maluccio, M.R.; Orlandi, G.; Guazzelli, M.; Murri, L. Do 5HT_{1B}/1D Receptor Agonists have an Effect on Mood and Anxiety Disorders? *Cephalalgia* **2007**, *27*, 471–472. [CrossRef]
114. Li, X.; Sun, X.; Sun, J.; Zu, Y.; Zhao, S.; Sun, X.; Li, L.; Zhang, X.; Wang, W.; Liang, Y.; et al. Depressive-like state sensitizes 5-HT_{1A} and 5-HT_{1B} auto-receptors in the dorsal raphe nucleus sub-system. *Behav. Brain Res.* **2020**, *389*. [CrossRef]
115. Carr, G.V.; Lucki, I. The role of serotonin receptor subtypes in treating depression: A review of animal studies. *Psychopharmacology* **2011**, *213*, 265–287. [CrossRef]

116. Banasr, M.; Hery, M.; Printemps, R.; Daszuta, A. Serotonin-induced increases in adult cell proliferation and neurogenesis are mediated through different and common 5-HT receptor subtypes in the dentate gyrus and the subventricular zone. *Neuropsychopharmacology* **2004**, *29*, 450–460. [CrossRef]
117. Nautiyal, K.M.; Tritschler, L.; Ahmari, S.E.; David, D.J.; Gardier, A.M.; Hen, R. A lack of serotonin 1B autoreceptors results in decreased anxiety and depression-related behaviors. *Neuropsychopharmacology* **2016**, *41*, 2941–2950. [CrossRef] [PubMed]
118. Huang, Y.Y.; Oquendo, M.A.; Harkavy Friedman, J.M.; Greenhill, L.L.; Brodsky, B.; Malone, K.M.; Khait, V.; Mann, J.J. Substance abuse disorder and major depression are associated with the human 5-HT_{1B} receptor gene (HTR1B) G861C polymorphism. *Neuropsychopharmacology* **2003**, *28*, 163–169. [CrossRef]
119. Ruf, B.; Bhagwagar, Z. The 5-HT_{1B} Receptor: A Novel Target for the Pathophysiology of Depression (Supplementary Tables). *Curr. Drug Targets* **2009**, *10*, 1118–1138. [CrossRef]
120. Nishiguchi, N.; Shirakawa, O.; Ono, H.; Nishimura, A.; Nushida, H.; Ueno, Y.; Maeda, K. No evidence of an association between 5HT_{1B} receptor gene polymorphism and suicide victims in a Japanese population. *Am. J. Med. Genet. Neuropsychiatr. Genet.* **2001**, *105*, 343–345. [CrossRef] [PubMed]
121. Egeland, M.; Warner-Schmidt, J.; Greengard, P.; Svenningsson, P. Co-expression of serotonin 5-HT_{1B} and 5-HT₄ receptors in p11 containing cells in cerebral cortex, hippocampus, caudate-putamen and cerebellum. *Neuropharmacology* **2011**, *61*, 442–450. [CrossRef] [PubMed]
122. Svenningsson, P.; Tzavara, E.T.; Qi, H.; Carruthers, R.; Witkin, J.M.; Nomikos, G.G.; Greengard, P. Biochemical and behavioral evidence for antidepressant-like effects of 5-HT₆ receptor stimulation. *J. Neurosci.* **2007**, *27*, 4201–4209. [CrossRef]
123. Svenningsson, P. Alterations in 5-HT_{1B} Receptor Function by p11 in Depression-Like States. *Science* **2006**, *311*, 77–80. [CrossRef]
124. Piñeyro, G.; Blier, P. Autoregulation of serotonin neurons: Role in antidepressant drug action. *Pharmacol. Rev.* **1999**, *51*, 533–591.
125. Blier, P.; Chaput, Y.; De Montigny, C. Long-term 5-HT reuptake blockade, but not monoamine oxidase inhibition, decreases the function of terminal 5-HT autoreceptors: An electrophysiological study in the rat brain. *Naunyn-Schmiedeberg's Arch. Pharmacol.* **1988**, *337*, 246–254. [CrossRef]
126. Davidson, C.; Stamford, J.A. The effect of paroxetine on 5-HT efflux in the rat dorsal raphe nucleus is potentiated by both 5-HT_{1A} and 5-HT_{1B} D receptor antagonists. *Neurosci. Lett.* **1995**, *188*, 41–44. [CrossRef]
127. Tatarczyńska, E.; Kłodzińska, A.; Stachowicz, K.; Chojnacka-Wójcik, E. Effects of a selective 5-HT_{1B} receptor agonist and antagonists in animal models of anxiety and depression. *Behav. Pharmacol.* **2004**, *15*, 523–534. [CrossRef]
128. Hervás, I.; Queiroz, C.M.T.; Adell, A.; Artigas, F. Role of uptake inhibition and autoreceptor activation in the control of 5-HT release in the frontal cortex and dorsal hippocampus of the rat. *Br. J. Pharmacol.* **2000**, *130*, 160–166. [CrossRef]
129. Knobelman, D.A.; Hen, R.; Lucki, I. Genetic regulation of extracellular serotonin by 5-hydroxytryptamine(1A) and 5-hydroxytryptamine(1B) autoreceptors in different brain regions of the mouse. *J. Pharmacol. Exp. Ther.* **2001**, *298*, 1083–1091.
130. Dawson, L.A.; Hughes, Z.A.; Starr, K.R.; Storey, J.D.; Bettelini, L.; Bacchi, F.; Arban, R.; Poffe, A.; Melotto, S.; Hagan, J.J.; et al. Characterisation of the selective 5-HT_{1B} receptor antagonist SB-616234-A (1-[6-(cis-3,5-dimethylpiperazin-1-yl)-2,3-dihydro-5-methoxyindol-1-yl]-1-[2'-methyl-4'-(5-methyl-1,2,4-oxadiazol-3-yl)biphenyl-4-yl]methanone hydrochloride): In vivo neurochemical. *Neuropharmacology* **2006**, *50*, 975–983. [CrossRef]
131. Roberts, C.; Watson, J.; Price, G.W.; Middlemiss, D.N. SB-236057-A: A selective 5-HT_{1B} receptor inverse agonist. *CNS Drug Rev.* **2001**, *7*, 433–444. [CrossRef]
132. Chenu, F.; David, D.J.P.; Leroux-Nicollet, I.; Le Maître, E.; Gardier, A.M.; Bourin, M. Serotonin_{1B} heteroreceptor activation induces an antidepressant-like effect in mice with an alteration of the serotonergic system. *J. Psychiatry Neurosci.* **2008**, *33*, 541–550. [PubMed]
133. Tatarczyńska, E.; Antkiewicz-Michaluk, L.; Kłodzińska, A.; Stachowicz, K.; Chojnacka-Wójcik, E. Antidepressant-like effect of the selective 5-HT_{1B} receptor agonist CP 94253: A possible mechanism of action. *Eur. J. Pharmacol.* **2005**, *516*, 46–50. [CrossRef] [PubMed]
134. Tiger, M.; Varnäs, K.; Okubo, Y.; Lundberg, J. The 5-HT_{1B} receptor—A potential target for antidepressant treatment. *Psychopharmacology* **2018**, *235*, 1317–1334. [CrossRef]
135. Neumaier, J.F.; Root, D.C.; Hamblin, M.W. Chronic fluoxetine reduces serotonin transporter mRNA and 5-HT(1B) mRNA in a sequential manner in the rat dorsal raphe nucleus. *Neuropsychopharmacology* **1996**, *15*, 515–522. [CrossRef]
136. Gobert, A.; Dekeyne, A.; Millan, M.J. The ability of WAY100,635 to potentiate the neurochemical and functional actions of fluoxetine is enhanced by co-administration of SB224,289, but not BRL15572. *Neuropharmacology* **2000**, *39*, 1608–1616. [CrossRef]
137. Whale, R.; Clifford, E.M.; Bhagwagar, Z.; Cowen, P.J. Decreased sensitivity of 5-HT_{1D} receptors in melancholic depression. *Br. J. Psychiatry* **2001**, *178*, 454–457. [CrossRef]
138. Lowther, S.; Katona, C.L.E.; Crompton, M.R.; Horton, R.W. 5-HT(1D) and 5-HT(1E/1F) binding sites in depressed suicides: Increased 5-HT(1D) binding in globus pallidus but not cortex. *Mol. Psychiatry* **1997**, *2*, 314–321. [CrossRef]
139. Klein, M.T.; Dukat, M.; Glennon, R.A.; Teitler, M. Toward Selective Drug Development for the Human 5-Hydroxytryptamine 1E Receptor: A Comparison of 5-Hydroxytryptamine 1E and 1F Receptor Structure-Affinity Relationships. *J. Pharmacol. Exp. Ther.* **2011**, *337*, 860–867. [CrossRef]
140. Burnet, P.W.J.; Eastwood, S.L.; Lacey, K.; Harrison, P.J. The distribution of 5-HT_{1A} and 5-HT_{2A} receptor mRNA in human brain. *Brain Res.* **1995**, *676*, 157–168. [CrossRef]

141. López-Giménez, J.F.; Vilaró, M.T.; Palacios, J.M.; Mengod, G. Mapping of 5-HT_{2A} receptors and their mRNA in monkey brain: [3H]MDL100,907 autoradiography and in situ hybridization studies. *J. Comp. Neurol.* **2001**, *429*, 571–589. [CrossRef]
142. Hannon, J.; Hoyer, D. Molecular biology of 5-HT receptors. *Behav. Brain Res.* **2008**, *195*, 198–213. [CrossRef]
143. Bécamel, C.; Berthou, C.; Barre, A.; Marin, P. Growing Evidence for Heterogeneous Synaptic Localization of 5-HT_{2A} Receptors. *ACS Chem. Neurosci.* **2017**, *8*, 897–899. [CrossRef]
144. De Almeida, J.; Mengod, G. Quantitative analysis of glutamatergic and GABAergic neurons expressing 5-HT_{2A} receptors in human and monkey prefrontal cortex. *J. Neurochem.* **2007**, *103*, 475–486. [CrossRef]
145. Mestre, T.A.; Zurowski, M.; Fox, S.H. 5-Hydroxytryptamine 2A receptor antagonists as potential treatment for psychiatric disorders. *Expert Opin. Investig. Drugs* **2013**, *22*, 411–421. [CrossRef]
146. Gawliński, D.; Smaga, I.; Zaniewska, M.; Gawlińska, K.; Faron-Górecka, A.; Filip, M. Adaptive mechanisms following antidepressant drugs: Focus on serotonin 5-HT_{2A} receptors. *Pharmacol. Rep.* **2019**, *71*, 994–1000. [CrossRef] [PubMed]
147. Howland, R.H. Vilazodone: Another novel atypical antidepressant drug. *J. Psychosoc. Nurs. Ment. Health Serv.* **2011**, *49*, 19–22. [CrossRef]
148. Richelson, E. Pharmacology of antidepressants. *Mayo Clin. Proc.* **2001**, *76*, 511–527. [CrossRef]
149. Butler, M.O.; Morinobu, S.; Duman, R.S. Chronic Electroconvulsive Seizures Increase the Expression of Serotonin₂ Receptor mRNA in Rat Frontal Cortex. *J. Neurochem.* **1993**, *61*, 1270–1276. [CrossRef] [PubMed]
150. Carvalho, A.F.; Machado, J.R.; Cavalcante, J.L. Augmentation strategies for treatment-resistant depression. *Curr. Opin. Psychiatry* **2009**, *22*, 7–12. [CrossRef] [PubMed]
151. Carpenter, L.L.; Leon, Z.; Yasmin, S.; Price, L.H. Clinical Experience with Mirtazapine in the Treatment of Panic Disorder. *Ann. Clin. Psychiatry* **1999**, *11*, 81–86. [CrossRef] [PubMed]
152. Marek, G.J.; Carpenter, L.L.; McDougle, C.J.; Price, L.H. Synergistic action of 5-HT_{2A} antagonists and selective serotonin reuptake inhibitors in neuropsychiatric disorders. *Neuropsychopharmacology* **2003**, *28*, 402–412. [CrossRef]
153. Amargós-Bosch, M.; Bortolozzi, A.; Puig, M.V.; Serrats, J.; Adell, A.; Celada, P.; Toth, M.; Mengod, G.; Artigas, F. Co-expression and In Vivo Interaction of Serotonin_{1A} and Serotonin_{2A} Receptors in Pyramidal Neurons of Pre-frontal Cortex. *Cereb. Cortex* **2004**, *14*, 281–299. [CrossRef]
154. Gray, J.A.; Roth, B.L. Paradoxical trafficking and regulation of 5-HT_{2A} receptors by agonists and antagonists. *Brain Res. Bull.* **2001**, *56*, 441–451. [CrossRef]
155. Van Oekelen, D.; Luyten, W.H.M.L.; Leysen, J.E. 5-HT_{2A} and 5-HT_{2C} receptors and their atypical regulation properties. *Life Sci.* **2003**, *72*, 2429–2449. [CrossRef]
156. Bressa, G.M.; Marini, S.; Gregori, S. Serotonin S₂ receptors blockage and generalized anxiety disorders. A double-blind study on ritanserin and lorazepam. *Int. J. Clin. Pharmacol. Res.* **1987**, *7*, 111–119.
157. Blier, P.; El-Mansari, M. Serotonin and beyond: Therapeutics for major depression. *Philos. Trans. R. Soc. B Biol. Sci.* **2013**, *368*. [CrossRef]
158. Szabo, S.T.; Blier, P. Serotonin 1A receptor ligands act on norepinephrine neuron firing through excitatory amino acid and GABA_A receptors: A microiontophoretic study in the rat locus coeruleus. *Synapse* **2001**, *42*, 203–212. [CrossRef]
159. Szabo, S.T.; Blier, P. Response of the norepinephrine system to antidepressant drugs. *CNS Spectr.* **2001**, *6*, 679–684. [CrossRef] [PubMed]
160. Dremencov, E.; El Mansari, M.; Blier, P. Noradrenergic Augmentation of Escitalopram Response by Risperidone: Electrophysiological Studies in the Rat Brain. *Biol. Psychiatry* **2007**, *61*, 671–678. [CrossRef] [PubMed]
161. Kawahara, Y.; Kawahara, H.; Kaneko, F.; Tanaka, M. Long-term administration of citalopram reduces basal and stress-induced extracellular noradrenaline levels in rat brain. *Psychopharmacology* **2007**, *194*, 73–81. [CrossRef] [PubMed]
162. Seager, M.A.; Barth, V.N.; Phebus, L.A.; Rasmussen, K. Chronic coadministration of olanzapine and fluoxetine activates locus coeruleus neurons in rats: Implications for bipolar disorder. *Psychopharmacology* **2005**, *181*, 126–133. [CrossRef]
163. Chernoloz, O.; El Mansari, M.; Blier, P. Electrophysiological studies in the rat brain on the basis for aripiprazole augmentation of antidepressants in major depressive disorder. *Psychopharmacology* **2009**, *206*, 335–344. [CrossRef]
164. Chernoloz, O.; El Mansari, M.; Blier, P. Effects of sustained administration of quetiapine alone and in combination with a serotonin reuptake inhibitor on norepinephrine and serotonin transmission. *Neuropsychopharmacology* **2012**, *37*, 1717–1728. [CrossRef]
165. Patel, J.G.; Bartoszyk, G.D.; Edwards, E.; Ashby, C.R. The Highly Selective 5-Hydroxytryptamine (5-HT)_{2A} Receptor Antagonist, EMD 281014, Significantly Increases Swimming and Decreases Immobility in Male Congenital Learned Helpless Rats in the Forced Swim Test. *Synapse* **2004**, *52*, 73–75. [CrossRef]
166. Albinsson, A.; Björk, A.; Svartengren, J.; Klint, T.; Andersson, G. Preclinical pharmacology of FG5893: A potential anxiolytic drug with high affinity for both 5-HT_{1A} and 5-HT_{2A} receptors. *Eur. J. Pharmacol.* **1994**, *261*, 285–294. [CrossRef]
167. Marek, G.J.; Martin-Ruiz, R.; Abo, A.; Artigas, F. The selective 5-HT_{2A} receptor antagonist M100907 enhances antidepressant-like behavioral effects of the SSRI fluoxetine. *Neuropsychopharmacology* **2005**, *30*, 2205–2215. [CrossRef]
168. Gao, J.; Wu, R.; Davis, C.; Li, M. Activation of 5-HT_{2A} receptor disrupts rat maternal behavior. *Neuropharmacology* **2018**, *128*, 96–105. [CrossRef]
169. Berthou, C.; Barre, A.; Bockaert, J.; Marin, P.; Bécamel, C. Sustained Activation of Postsynaptic 5-HT_{2A} Receptors Gates Plasticity at Prefrontal Cortex Synapses. *Cereb. Cortex* **2019**, *29*, 1659–1669. [CrossRef]

170. Jaggar, M.; Weisstaub, N.; Gingrich, J.A.; Vaidya, V.A. 5-HT_{2A} receptor deficiency alters the metabolic and transcriptional, but not the behavioral, consequences of chronic unpredictable stress. *Neurobiol. Stress* **2017**, *7*, 89–102. [CrossRef]
171. Duxon, M.S.; Flanigan, T.P.; Reavley, T.A.C.; Baxter, T.G.S.; Blackburn, T.P.; Fone, K.C.F. 5-Hydroxytryptamine-2B receptor protein in the rat central nervous system. *Neuroscience* **1997**, *76*, 323–329. [CrossRef]
172. McCorvy, J.D.; Roth, B.L. Structure and function of serotonin G protein-coupled receptors. *Pharmacol. Ther.* **2015**, *150*, 129–142. [CrossRef]
173. Diaz, S.L.; Doly, S.; Narboux-Nme, N.; Fernández, S.; Mazot, P.; Banas, S.M.; Boutourlinsky, K.; Moutkine, I.; Belmer, A.; Roumier, A.; et al. 5-HT 2B receptors are required for serotonin-selective antidepressant actions. *Mol. Psychiatry* **2012**, *17*, 154–163. [CrossRef]
174. Belmer, A.; Quentin, E.; Diaz, S.L.; Guiard, B.P.; Fernandez, S.P.; Doly, S.; Banas, S.M.; Pitychoutis, P.M.; Moutkine, I.; Muzerelle, A.; et al. Positive regulation of raphe serotonin neurons by serotonin 2B receptors. *Neuropsychopharmacology* **2018**, *43*, 1623–1632. [CrossRef]
175. Li, B.; Zhang, S.; Zhang, H.; Nu, W.; Cai, L.; Hertz, L.; Peng, L. Fluoxetine-mediated 5-HT_{2B} receptor stimulation in astrocytes causes EGF receptor transactivation and ERK phosphorylation. *Psychopharmacology* **2008**, *201*, 443–458. [CrossRef] [PubMed]
176. Diaz, S.L.; Narboux-Nême, N.; Boutourlinsky, K.; Doly, S.; Maroteaux, L. Mice lacking the serotonin 5-HT_{2B} receptor as an animal model of resistance to selective serotonin reuptake inhibitors antidepressants. *Eur. Neuropsychopharmacol.* **2016**, *26*, 265–279. [CrossRef]
177. D'Andrea, I.; Béchade, C.; Maroteaux, L. Serotonin and 5-HT_{2B} receptors in microglia control of behavior. *Handb. Behav. Neurosci.* **2020**, *31*, 589–599. [CrossRef]
178. Millan, M.J. Serotonin 5-HT_{2C} receptors as a target for the treatment of depressive and anxious states: Focus on novel therapeutic strategies. *Thérapie* **2005**, *60*, 441–460. [CrossRef]
179. López-Giménez, J.F.; Mengod, G.; Palacios, J.M.; Vilaró, M.T. Regional distribution and cellular localization of 5-HT_{2C} receptor mRNA in monkey brain: Comparison with [3H]mesulergine binding sites and choline acetyltransferase mRNA. *Synapse* **2001**, *42*, 12–26. [CrossRef] [PubMed]
180. Serrats, J.; Mengod, G.; Cortés, R. Expression of serotonin 5-HT_{2C} receptors in GABAergic cells of the anterior raphe nuclei. *J. Chem. Neuroanat.* **2005**, *29*, 83–91. [CrossRef]
181. Liu, S.; Bubar, M.J.; Lanfranco, M.F.; Hillman, G.R.; Cunningham, K.A. Serotonin 2C receptor localization in GABA neurons of the rat medial prefrontal cortex: Implications for understanding the neurobiology of addiction. *Neuroscience* **2007**, *146*, 1677–1688. [CrossRef] [PubMed]
182. Bubar, M.J.; Stutz, S.J.; Cunningham, K.A. 5-HT_{2C} Receptors localize to dopamine and gaba neurons in the rat mesoaccumbens pathway. *PLoS ONE* **2011**, *6*, e20508. [CrossRef] [PubMed]
183. Dekeyne, A.; Mannoury La Cour, C.; Gobert, A.; Brocco, M.; Lejeune, F.; Serres, F.; Sharp, T.; Daszuta, A.; Soumier, A.; Papp, M.; et al. S32006, a novel 5-HT_{2C} receptor antagonist displaying broad-based antidepressant and anxiolytic properties in rodent models. *Psychopharmacology* **2008**, *199*, 549–568. [CrossRef] [PubMed]
184. Dekeyne, A.; Brocco, M.; Loiseau, F.; Gobert, A.; Rivet, J.M.; Di Cara, B.; Cremers, T.I.; Flik, G.; Fone, K.C.F.; Watson, D.J.G.; et al. S32212, a novel serotonin type 2C receptor inverse agonist/ α 2- adrenoceptor antagonist and potential antidepressant: II. A behavioral, neurochemical, and electrophysiological characterization. *J. Pharmacol. Exp. Ther.* **2012**, *340*, 765–780. [CrossRef] [PubMed]
185. Cryan, J.F.; Lucki, I. Antidepressant-like behavioral effects mediated by 5-Hydroxytryptamine(2C) receptors. *J. Pharmacol. Exp. Ther.* **2000**, *295*, 1120–1126.
186. Rosenzweig-Lipson, S.; Sabb, A.; Stack, G.; Mitchell, P.; Lucki, I.; Malberg, J.E.; Grauer, S.; Brennan, J.; Cryan, J.F.; Sukoff Rizzo, S.J.; et al. Antidepressant-like effects of the novel, selective, 5-HT_{2C} receptor agonist WAY-163909 in rodents. *Psychopharmacology* **2007**, *192*, 159–170. [CrossRef] [PubMed]
187. Dunlop, J.; Marquis, K.L.; Lim, H.K.; Leung, L.; Kao, J.; Cheesman, C.; Rosenzweig-Lipson, S. Pharmacological profile of the 5-HT_{2C} receptor agonist WAY-163909; therapeutic potential in multiple indications. *CNS Drug Rev.* **2006**, *12*, 167–177. [CrossRef] [PubMed]
188. Esposito, E. Serotonin-Dopamine Interaction as a Focus of Novel Antidepressant Drugs. *Curr. Drug Targets* **2006**, *7*, 177–185. [CrossRef]
189. Jenck, F.; Moreau, J.; Berendsen, H.H.; Boes, M.; Broekkamp, C.L.; Martin, J.R.; Wichmann, J.; Van Delft, A.M. Antiaversive effects of 5HT_{2C} receptor agonists and fluoxetine in a model of panic-like anxiety in rats. *Eur. Neuropsychopharmacol.* **1998**, *8*, 161–168. [CrossRef]
190. Cremers, T.I.F.H.; Giorgetti, M.; Bosker, F.J.; Hogg, S.; Arnt, J.; Mørk, A.; Honig, G.; Bøgesø, K.P.; Westerink, B.H.C.; Den Boer, H.; et al. Inactivation of 5-HT_{2C} receptors potentiates consequences of serotonin reuptake blockade. *Neuropsychopharmacology* **2004**, *29*, 1782–1789. [CrossRef]
191. Cremers, T.I.F.H.; Rea, K.; Bosker, F.J.; Wikström, H.V.; Hogg, S.; Mørk, A.; Westerink, B.H.C. Augmentation of SSRI effects on serotonin by 5-HT_{2C} antagonists: Mechanistic studies. *Neuropsychopharmacology* **2007**, *32*, 1550–1557. [CrossRef]
192. Clenet, F.; De Vos, A.; Bourin, M. Involvement of 5-HT_{2C} receptors in the anti-immobility effects of antidepressants in the forced swimming test in mice. *Eur. Neuropsychopharmacol.* **2001**, *11*, 145–152. [CrossRef]

193. Gurevich, I.; Tamir, H.; Arango, V.; Dwork, A.J.; Mann, J.J.; Schmauss, C. Altered editing of serotonin 2C receptor pre-mRNA in the prefrontal cortex of depressed suicide victims. *Neuron* **2002**, *34*, 349–356. [CrossRef]
194. Yamauchi, M.; Tatebayashi, T.; Nagase, K.; Kojima, M.; Imanishi, T. Chronic treatment with fluvoxamine desensitizes 5-HT_{2C} receptor-mediated hypolocomotion in rats. *Pharmacol. Biochem. Behav.* **2004**, *78*, 683–689. [CrossRef] [PubMed]
195. Invernizzi, R.W.; Pierucci, M.; Calcagno, E.; Di Giovanni, G.; Di Matteo, V.; Benigno, A.; Esposito, E. Selective activation of 5-HT_{2C} receptors stimulates GABA-ergic function in the rat substantia nigra pars reticulata: A combined in vivo electrophysiological and neurochemical study. *Neuroscience* **2007**, *144*, 1523–1535. [CrossRef]
196. Meltzer, H.Y.; Li, Z.; Kaneda, Y.; Ichikawa, J. Serotonin receptors: Their key role in drugs to treat schizophrenia. *Prog. Neuro-Psychopharmacol. Biol. Psychiatry* **2003**, *27*, 1159–1172. [CrossRef] [PubMed]
197. Demireva, E.Y.; Suri, D.; Morelli, E.; Mahadevia, D.; Chuhma, N.; Teixeira, C.M.; Ziolkowski, A.; Hersh, M.; Fifer, J.; Bagchi, S.; et al. 5-HT_{2C} receptor blockade reverses SSRI-associated basal ganglia dysfunction and potentiates therapeutic efficacy. *Mol. Psychiatry* **2020**, *25*, 3304–3321. [CrossRef]
198. Angel, I.; Schoemaker, H.; Prouteau, M.; Garreau, M.; Langer, S.Z. Litoxetine: A selective 5-HT uptake inhibitor with concomitant 5-HT₃ receptor antagonist and antiemetic properties. *Eur. J. Pharmacol.* **1993**, *232*, 139–145. [CrossRef]
199. Thompson, A.; Lummis, S.R. 5-HT₃ Receptors. *Curr. Pharm. Des.* **2006**, *12*, 3615–3630. [CrossRef]
200. Morales, M.; Bloom, F.E. The 5-HT₃ receptor is present in different subpopulations of GABAergic neurons in the rat telencephalon. *J. Neurosci.* **1997**, *17*, 3157–3167. [CrossRef]
201. Puig, M.V.; Santana, N.; Celada, P.; Mengod, G.; Artigas, F. In vivo excitation of GABA interneurons in the medial prefrontal cortex through 5-HT₃ receptors. *Cereb. Cortex* **2004**, *14*, 1365–1375. [CrossRef]
202. Gupta, D.; Prabhakar, V.; Radhakrishnan, M. 5HT₃ receptors: Target for new antidepressant drugs. *Neurosci. Biobehav. Rev.* **2016**, *64*, 311–325. [CrossRef]
203. Ramamoorthy, R.; Radhakrishnan, M.; Borah, M. Antidepressant-like effects of serotonin type-3 antagonist, ondansetron: An investigation in behaviour-based rodent models. *Behav. Pharmacol.* **2008**, *19*, 29–40. [CrossRef]
204. Bravo, G.; Maswood, S. Acute treatment with 5-HT₃ receptor antagonist, tropisetron, reduces immobility in intact female rats exposed to the forced swim test. *Pharmacol. Biochem. Behav.* **2006**, *85*, 362–368. [CrossRef]
205. Eisensamer, B.; Rammes, G.; Gimpl, G.; Shapa, M.; Ferrari, U.; Hapfelmeier, G.; Bondy, B.; Parsons, C.; Gilling, K.; Zieglgänsberger, W.; et al. Antidepressants are functional antagonists at the serotonin type 3 (5-HT₃) receptor. *Mol. Psychiatry* **2003**, *8*, 994–1007. [CrossRef] [PubMed]
206. Fan, P. Facilitation of 5-hydroxytryptamine₃ receptor desensitization by fluoxetine. *Neuroscience* **1994**, *62*, 515–522. [CrossRef]
207. Mössner, R.; Schmitt, A.; Hennig, T.; Benninghoff, J.; Gerlach, M.; Riederer, P.; Deckert, J.; Lesch, K.P. Quantitation of 5HT₃ receptors in forebrain of serotonin transporter deficient mice. *J. Neural Transm.* **2004**, *111*, 27–35. [CrossRef]
208. Redrobe, J.P.; Bourin, M. Partial role of 5-HT₂ and 5-HT₃ receptors in the activity of antidepressants in the mouse forced swimming test. *Eur. J. Pharmacol.* **1997**, *325*, 129–135. [CrossRef]
209. Alvarez, E.; Perez, V.; Dragheim, M.; Loft, H.; Artigas, F. A double-blind, randomized, placebo-controlled, active reference study of Lu AA21004 in patients with major depressive disorder. *Int. J. Neuropsychopharmacol.* **2012**, *15*, 589–600. [CrossRef]
210. Baldwin, D.S.; Loft, H.; Dragheim, M. A randomised, double-blind, placebo controlled, duloxetine-referenced, fixed-dose study of three dosages of Lu AA21004 in acute treatment of major depressive disorder (MDD). *Eur. Neuropsychopharmacol.* **2012**, *22*, 482–491. [CrossRef]
211. Kelliny, M.; Croarkin, P.E.; Moore, K.M.; Bobo, W.V. Profile of vortioxetine in the treatment of major depressive disorder: An overview of the primary and secondary literature. *Ther. Clin. Risk Manag.* **2015**, *11*, 1193–1212. [CrossRef] [PubMed]
212. Bétry, C.; Pehrson, A.L.; Etiévant, A.; Ebert, B.; Sánchez, C.; Haddjeri, N. The rapid recovery of 5-HT cell firing induced by the antidepressant vortioxetine involves 5-HT₃ receptor antagonism. *Int. J. Neuropsychopharmacol.* **2013**, *16*, 1115–1127. [CrossRef]
213. Gupta, D.; Radhakrishnan, M.; Thangaraj, D.; Kurhe, Y. Antidepressant and anti-anxiety like effects of 4i (N-(3-chloro-2-methylphenyl) quinoxalin-2-carboxamide), a novel 5-HT₃ receptor antagonist in acute and chronic neurobehavioral rodent models. *Eur. J. Pharmacol.* **2014**, *735*, 59–67. [CrossRef]
214. Gupta, D.; Radhakrishnan, M.; Kurhe, Y. Effect of a novel 5-HT₃ receptor antagonist 4i, in corticosterone-induced depression-like behavior and oxidative stress in mice. *Steroids* **2015**, *96*, 95–102. [CrossRef] [PubMed]
215. Gupta, D.; Thangaraj, D.; Radhakrishnan, M. A novel 5HT₃ antagonist 4i (N-(3-chloro-2-methylphenyl)quinoxalin-2-carboxamide) prevents diabetes-induced depressive phenotypes in mice: Modulation of serotonergic system. *Behav. Brain Res.* **2016**, *297*, 41–50. [CrossRef]
216. Dhar, A.K.; Mahesh, R.; Jindal, A.; Bhatt, S. Piperazine analogs of naphthyridine-3-carboxamides and indole-2-carboxamides: Novel 5-HT₃ receptor antagonists with antidepressant-like activity. *Arch. Pharm.* **2015**, *348*, 34–45. [CrossRef]
217. Kurhe, Y.; Radhakrishnan, M.; Gupta, D.; Devadoss, T. QCM-4 a novel 5-HT₃ antagonist attenuates the behavioral and biochemical alterations on chronic unpredictable mild stress model of depression in Swiss albino mice. *J. Pharm. Pharmacol.* **2014**, *66*, 122–132. [CrossRef] [PubMed]
218. Dukat, M.; Alix, K.; Worsham, J.; Khatri, S.; Schulte, M.K. 2-Amino-6-chloro-3,4-dihydroquinazoline: A novel 5-HT₃ receptor antagonist with antidepressant character. *Bioorg. Med. Chem. Lett.* **2013**, *23*, 5945–5948. [CrossRef] [PubMed]
219. Nakagawa, Y.; Ishima, T.; Takashima, T. The 5-HT₃ receptor agonist attenuates the action of antidepressants in the forced swim test in rats. *Brain Res.* **1998**, *786*, 189–193. [CrossRef]

220. Kos, T.; Popik, P.; Pietraszek, M.; Schäfer, D.; Danysz, W.; Dravolina, O.; Blokhina, E.; Galankin, T.; Beshpalov, A.Y. Effect of 5-HT₃ receptor antagonist MDL 72222 on behaviors induced by ketamine in rats and mice. *Eur. Neuropsychopharmacol.* **2006**, *16*, 297–310. [CrossRef] [PubMed]
221. Gupta, D.; Radhakrishnan, M.; Kurhe, Y. 5HT₃ receptor antagonist (ondansetron) reverses depressive behavior evoked by chronic unpredictable stress in mice: Modulation of hypothalamic-pituitary-adrenocortical and brain serotonergic system. *Pharmacol. Biochem. Behav.* **2014**, *124*, 129–136. [CrossRef]
222. Gupta, D.; Radhakrishnan, M.; Kurhe, Y. Ondansetron, a 5HT₃ receptor antagonist reverses depression and anxiety-like behavior in streptozotocin-induced diabetic mice: Possible implication of serotonergic system. *Eur. J. Pharmacol.* **2015**, *744*, 59–66. [CrossRef]
223. Kordjazy, N.; Haj-Mirzaian, A.; Amiri, S.; Ostadhadi, S.; Amini-Khoei, H.; Dehpour, A.R. Involvement of N-methyl-d-aspartate receptors in the antidepressant-like effect of 5-hydroxytryptamine 3 antagonists in mouse forced swimming test and tail suspension test. *Pharmacol. Biochem. Behav.* **2016**, *141*, 1–9. [CrossRef]
224. Haj-Mirzaian, A.; Kordjazy, N.; Amiri, S.; Haj-Mirzaian, A.; Amini-Khoei, H.; Ostadhadi, S.; Dehpour, A.R. Involvement of nitric oxide-cyclic guanosine monophosphate pathway in the antidepressant-like effect of tropisetron and ondansetron in mice forced swimming test and tail suspension test. *Eur. J. Pharmacol.* **2016**, *780*, 71–81. [CrossRef] [PubMed]
225. Martin, V.; Riffaud, A.; Marday, T.; Brouillard, C.; Franc, B.; Tassin, J.P.; Sevoz-Couche, C.; Mongeau, R.; Lanfumey, L. Response of Htr3a knockout mice to antidepressant treatment and chronic stress. *Br. J. Pharmacol.* **2017**, *174*, 2471–2483. [CrossRef] [PubMed]
226. Perez-Palomar, B.; Mollinedo-Gajate, I.; Berrocoso, E.; Meana, J.J.; Ortega, J.E. Serotonin 5-HT₃ receptor antagonism potentiates the antidepressant activity of citalopram. *Neuropharmacology* **2018**, *133*, 491–502. [CrossRef]
227. Ostacher, M.J. Comorbid Alcohol and Substance Abuse Dependence in Depression: Impact on the Outcome of Antidepressant Treatment. *Psychiatr. Clin. N. Am.* **2007**, *30*, 69–76. [CrossRef]
228. Engleman, E.A.; Rodd, Z.A.; Bell, R.L.; Murphy, J.M. The role of 5-HT₃ receptors in drug abuse and as a target for pharmacotherapy. *CNS Neurol. Disord. Drug Targets* **2008**, *7*, 454–467. [CrossRef]
229. Rammes, G.; Eisensamer, B.; Ferrari, U.; Shapa, M.; Gimpl, G.; Gilling, K.; Parsons, C.; Riering, K.; Hapfelmeier, G.; Bondy, B.; et al. Antipsychotic drugs antagonize human serotonin type 3 receptor currents in a noncompetitive manner. *Mol. Psychiatry* **2004**, *9*, 846–858. [CrossRef]
230. Kelley, S.P.; Bratt, A.M.; Hodge, C.W. Targeted gene deletion of the 5-HT_{3A} receptor subunit produces an anxiolytic phenotype in mice. *Eur. J. Pharmacol.* **2003**, *461*, 19–25. [CrossRef]
231. Martin, P.; Gozlan, H.; Puech, A.J. 5-HT₃ receptor antagonists reverse helpless behaviour in rats. *Eur. J. Pharmacol.* **1992**, *212*, 73–78. [CrossRef]
232. Harmer, C.J.; Reid, C.B.; Ray, M.K.; Goodwin, G.M.; Cowen, P.J. 5HT₃ antagonism abolishes the emotion potentiated startle effect in humans. *Psychopharmacology* **2006**, *186*, 18–24. [CrossRef]
233. Varnäs, K.; Halldin, C.; Pike, V.W.; Hall, H. Distribution of 5-HT₄ receptors in the postmortem human brain—An autoradiographic study using [125I]SB 207710. *Eur. Neuropsychopharmacol.* **2003**, *13*, 228–234. [CrossRef]
234. Marnier, L.; Gillings, N.; Madsen, K.; Erritzoe, D.; Baaré, W.F.C.; Svare, C.; Hasselbalch, S.G.; Knudsen, G.M. Brain imaging of serotonin 4 receptors in humans with [11C]SB207145-PET. *Neuroimage* **2010**, *50*, 855–861. [CrossRef]
235. Samuels, B.A.; Mendez-David, I.; Faye, C.; David, S.A.; Pierz, K.A.; Gardier, A.M.; Hen, R.; David, D.J. Serotonin 1A and Serotonin 4 Receptors: Essential Mediators of the Neurogenic and Behavioral Actions of Antidepressants. *Neuroscientist* **2016**, *22*, 26–45. [CrossRef]
236. Vidal, R.; Castro, E.; Pilar-Cuellar, F.; Pascual-Brazo, J.; Diaz, A.; Rojo, M.; Linge, R.; Martin, A.; Valdizan, E.; Pazos, A. Serotonin 5-HT₄ Receptors: A New Strategy for Developing Fast Acting Antidepressants? *Curr. Pharm. Des.* **2014**, *20*, 3751–3762. [CrossRef]
237. Licht, C.L.; Kirkegaard, L.; Zueger, M.; Chourbaji, S.; Gass, P.; Aznar, S.; Knudsen, G.M. Changes in 5-HT₄ receptor and 5-HT transporter binding in olfactory bulbectomized and glucocorticoid receptor heterozygous mice. *Neurochem. Int.* **2010**, *56*, 603–610. [CrossRef]
238. Licht, C.L.; Marcussen, A.B.; Wegener, G.; Overstreet, D.H.; Aznar, S.; Knudsen, G.M. The brain 5-HT₄ receptor binding is down-regulated in the Flinders Sensitive Line depression model and in response to paroxetine administration. *J. Neurochem.* **2009**, *109*, 1363–1374. [CrossRef]
239. Vidal, R.; Pilar-Cuellar, F.; Dos Anjos, S.; Linge, R.; Treceno, B.; Ines Vargas, V.; Rodriguez-Gaztelumendi, A.; Mostany, R.; Castro, E.; Diaz, A.; et al. New Strategies in the Development of Antidepressants: Towards the Modulation of Neuroplasticity Pathways. *Curr. Pharm. Des.* **2011**, *17*, 521–533. [CrossRef]
240. Pittenger, C.; Duman, R.S. Stress, depression, and neuroplasticity: A convergence of mechanisms. *Neuropsychopharmacology* **2008**, *33*, 88–109. [CrossRef]
241. Segi-Nishida, E. The effect of serotonin-targeting antidepressants on neurogenesis and neuronal maturation of the hippocampus mediated via 5-HT_{1A} and 5-HT₄ receptors. *Front. Cell. Neurosci.* **2017**, *11*, 1–7. [CrossRef] [PubMed]
242. Warner-Schmidt, J.L.; Flajolet, M.; Maller, A.; Chen, E.Y.; Qi, H.; Svenningsson, P.; Greengard, P. Role of p11 in cellular and behavioral effects of 5-HT₄ receptor stimulation. *J. Neurosci.* **2009**, *29*, 1937–1946. [CrossRef]
243. Conductier, G.; Dusticier, N.; Lucas, G.; Côté, F.; Debonnel, G.; Daszuta, A.; Dumuis, A.; Nieoullon, A.; Hen, R.; Bockaert, J.; et al. Adaptive changes in serotonin neurons of the raphe nuclei in 5-HT₄ receptor knock-out mouse. *Eur. J. Neurosci.* **2006**, *24*, 1053–1062. [CrossRef]

244. Lucas, G.; Compan, V.; Charnay, Y.; Neve, R.L.; Nestler, E.J.; Bockaert, J.; Barrot, M.; Debonnel, G. Frontocortical 5-HT₄ receptors exert positive feedback on serotonergic activity: Viral transfections, subacute and chronic treatments with 5-HT₄ agonists. *Biol. Psychiatry* **2005**, *57*, 918–925. [CrossRef] [PubMed]
245. Kobayashi, K.; Ikeda, Y.; Haneda, E.; Suzuki, H. Chronic fluoxetine bidirectionally modulates potentiating effects of serotonin on the hippocampal mossy fiber synaptic transmission. *J. Neurosci.* **2008**, *28*, 6272–6280. [CrossRef] [PubMed]
246. Vidal, R.; Valdizan, E.M.; Vilaró, M.T.; Pazos, A.; Castro, E. Reduced signal transduction by 5-HT₄ receptors after long-term venlafaxine treatment in rats. *Br. J. Pharmacol.* **2010**, *161*, 695–706. [CrossRef] [PubMed]
247. Cryan, J.F.; Lucki, I. 5-HT₄ receptors do not mediate the antidepressant-like behavioral effects of fluoxetine in a modified forced swim test. *Eur. J. Pharmacol.* **2000**, *409*, 295–299. [CrossRef]
248. Mendez-David, I.; David, D.J.; Darcet, F.; Wu, M.V.; Kerdine-Römer, S.; Gardier, A.M.; Hen, R. Rapid anxiolytic effects of a 5-HT₄ receptor agonist are mediated by a neurogenesis-independent mechanism. *Neuropsychopharmacology* **2014**, *39*, 1366–1378. [CrossRef]
249. Amigó, J.; Díaz, A.; Pilar-Cuéllar, F.; Vidal, R.; Martín, A.; Compan, V.; Pazos, A.; Castro, E. The absence of 5-HT₄ receptors modulates depression- and anxiety-like responses and influences the response of fluoxetine in olfactory bulbectomised mice: Adaptive changes in hippocampal neuroplasticity markers and 5-HT_{1A} autoreceptor. *Neuropharmacology* **2016**, *111*, 47–58. [CrossRef]
250. Amigo, J.; Garro-Martinez, E.; Vidal Casado, R.; Compan, V.; Pilar-Cuéllar, F.; Pazos, A.; Díaz, A.; Castro, E. 5-HT₄ Receptors Are Not Involved in the Effects of Fluoxetine in the Corticosterone Model of Depression. *ACS Chem. Neurosci.* **2021**, *12*, 2036–2044. [CrossRef]
251. Lucas, G.; Rymar, V.V.; Du, J.; Mnie-Filali, O.; Bisgaard, C.; Manta, S.; Lambas-Senas, L.; Wiborg, O.; Haddjeri, N.; Piñeyro, G.; et al. Serotonin₄ (5-HT₄) Receptor Agonists Are Putative Antidepressants with a Rapid Onset of Action. *Neuron* **2007**, *55*, 712–725. [CrossRef]
252. Darcet, F.; Gardier, A.M.; David, D.J.; Guilloux, J.P. Chronic 5-HT₄ receptor agonist treatment restores learning and memory deficits in a neuroendocrine mouse model of anxiety/depression. *Neurosci. Lett.* **2016**, *616*, 197–203. [CrossRef]
253. Duman, R.S. A Silver Bullet for the Treatment of Depression? *Neuron* **2007**, *55*, 679–681. [CrossRef]
254. Murphy, S.E.; De Cates, A.N.; Gillespie, A.L.; Godlewska, B.R.; Scaife, J.C.; Wright, L.C.; Cowen, P.J.; Harmer, C.J. Translating the promise of 5HT₄ receptor agonists for the treatment of depression. *Psychol. Med.* **2020**, *51*, 1111–1120. [CrossRef] [PubMed]
255. Branchek, T.A.; Blackburn, T.P. 5-HT₆ Receptors as Emerging Targets for Drug Discovery. *Annu. Rev. Pharmacol. Toxicol.* **2000**, *40*, 319–334. [CrossRef] [PubMed]
256. Rosse, G.; Schaffhauser, H. 5-HT₆ Receptor Antagonists as Potential Therapeutics for Cognitive Impairment. *Curr. Top. Med. Chem.* **2010**, *10*, 207–221. [CrossRef]
257. Heal, D.J.; Smith, S.L.; Fisas, A.; Codony, X.; Buschmann, H. Selective 5-HT₆ receptor ligands: Progress in the development of a novel pharmacological approach to the treatment of obesity and related metabolic disorders. *Pharmacol. Ther.* **2008**, *117*, 207–231. [CrossRef] [PubMed]
258. Mitchell, E.S.; Hoplight, B.J.; Lear, S.P.; Neumaier, J.F. BGC20-761, a novel tryptamine analog, enhances memory consolidation and reverses scopolamine-induced memory deficit in social and visuospatial memory tasks through a 5-HT₆ receptor-mediated mechanism. *Neuropharmacology* **2006**, *50*, 412–420. [CrossRef] [PubMed]
259. Monsma, F.J.; Shen, Y.; Ward, R.P.; Hamblin, M.W.; Sibley, D.R. Cloning and expression of a novel serotonin receptor with high affinity for tricyclic psychotropic drugs. *Mol. Pharmacol.* **1993**, *43*, 320–327.
260. Wesołowska, A.; Nikiforuk, A. Effects of the brain-penetrant and selective 5-HT₆ receptor antagonist SB-399885 in animal models of anxiety and depression. *Neuropharmacology* **2007**, *52*, 1274–1283. [CrossRef]
261. Wesołowska, A.; Nikiforuk, A. The selective 5-HT₆ receptor antagonist SB-399885 enhances anti-immobility action of antidepressants in rats. *Eur. J. Pharmacol.* **2008**, *582*, 88–93. [CrossRef]
262. Pereira, M.; Martynhak, B.J.; Andreatini, R.; Svenningsson, P. 5-HT₆ receptor agonism facilitates emotional learning. *Front. Pharmacol.* **2015**, *6*, 1–9. [CrossRef]
263. Nikiforuk, A.; Kos, T.; Wesołowska, A. The 5-HT₆ receptor agonist EMD 386088 produces antidepressant and anxiolytic effects in rats after intrahippocampal administration. *Psychopharmacology* **2011**, *217*, 411–418. [CrossRef] [PubMed]
264. Jastrzębska-Więsek, M.; Siwek, A.; Partyka, A.; Szewczyk, B.; Sowa-Kućma, M.; Wasik, A.; Kołaczkowski, M.; Wesołowska, A. Antidepressant-like activity of EMD 386088, a 5-HT₆ receptor partial agonist, following systemic acute and chronic administration to rats. *Naunyn. Schmiedeberg's Arch. Pharmacol.* **2015**, *388*, 1079–1088. [CrossRef]
265. De Foubert, G.; O'Neill, M.J.; Zetterström, T.S.C. Acute onset by 5-HT₆-receptor activation on rat brain brain-derived neurotrophic factor and activity-regulated cytoskeletal-associated protein mRNA expression. *Neuroscience* **2007**, *147*, 778–785. [CrossRef] [PubMed]
266. Dawson, L.A.; Li, P. Effects of 5-HT₆ receptor blockade on the neurochemical outcome of antidepressant treatment in the frontal cortex of the rat. *J. Neural Transm.* **2003**, *110*, 577–590. [CrossRef] [PubMed]
267. Hedlund, P.B.; Sutcliffe, J.G. Functional, molecular and pharmacological advances in 5-HT₇ receptor research. *Trends Pharmacol. Sci.* **2004**, *25*, 481–486. [CrossRef]
268. Neumaier, J.F.; Sexton, T.J.; Yracheta, J.; Diaz, A.M.; Brownfield, M. Localization of 5-HT₇ receptors in rat brain by immunocytochemistry, in situ hybridization, and agonist stimulated cFos expression. *J. Chem. Neuroanat.* **2001**, *21*, 63–73. [CrossRef]

269. Varnäs, K.; Thomas, D.R.; Tupala, E.; Tiihonen, J.; Hall, H. Distribution of 5-HT₇ receptors in the human brain: A preliminary autoradiographic study using [3H]SB-269970. *Neurosci. Lett.* **2004**, *367*, 313–316. [CrossRef]
270. Hedlund, P.B. The 5-HT₇ receptor and disorders of the nervous system: An overview. *Psychopharmacology* **2009**, *206*, 345–354. [CrossRef] [PubMed]
271. Mullins, U.L.; Gianutsos, G.; Eison, A.S. Effects of antidepressants on 5-HT₇ receptor regulation in the rat hypothalamus. *Neuropsychopharmacology* **1999**, *21*, 352–367. [CrossRef]
272. Roth, B.L.; Craigo, S.C.; Choudhary, M.S.; Uluer, A.; Monsma, F.J.J.; Shen, Y.; Meltzer, H.Y.; Sibley, D.R. Binding of typical and atypical antipsychotic agents to 5-hydroxytryptamine-6 and 5-hydroxytryptamine-7 receptors. *J. Pharmacol. Exp. Ther.* **1994**, *268*, 1403–1410.
273. Wesołowska, A.; Nikiforuk, A.; Stachowicz, K.; Tatarczyńska, E. Effect of the selective 5-HT₇ receptor antagonist SB 269970 in animal models of anxiety and depression. *Neuropharmacology* **2006**, *51*, 578–586. [CrossRef]
274. Bonaventure, P.; Kelly, L.; Aluisio, L.; Shelton, J.; Lord, B.; Galici, R.; Miller, K.; Atack, J.; Lovenberg, T.W.; Dugovic, C. Selective blockade of 5-hydroxytryptamine (5-HT)₇ receptors enhances 5-HT transmission, antidepressant-like behavior, and rapid eye movement sleep suppression induced by citalopram in rodents. *J. Pharmacol. Exp. Ther.* **2007**, *321*, 690–698. [CrossRef] [PubMed]
275. Wesołowska, A.; Tatarczyńska, E.; Nikiforuk, A.; Chojnacka-Wójcik, E. Enhancement of the anti-immobility action of antidepressants by a selective 5-HT₇ receptor antagonist in the forced swimming test in mice. *Eur. J. Pharmacol.* **2007**, *555*, 43–47. [CrossRef]
276. Wesołowska, A.; Nikiforuk, A.; Stachowicz, K. Potential anxiolytic and antidepressant effects of the selective 5-HT₇ receptor antagonist SB 269970 after intrahippocampal administration to rats. *Eur. J. Pharmacol.* **2006**, *553*, 185–190. [CrossRef] [PubMed]
277. Bonaventure, P.; Dugovic, C.; Kramer, M.; De Boer, P.; Singh, J.; Wilson, S.; Bertelsen, K.; Di, J.; Shelton, J.; Aluisio, L.; et al. Translational evaluation of JNJ-18038683, a 5-hydroxytryptamine type 7 receptor antagonist, on rapid eye movement sleep and in major depressive disorder. *J. Pharmacol. Exp. Ther.* **2012**, *342*, 429–440. [CrossRef]
278. Semenova, S.; Geyer, M.A.; Sutcliffe, J.G.; Markou, A.; Hedlund, P.B. Inactivation of the 5-HT₇ Receptor Partially Blocks Phencyclidine-Induced Disruption of Prepulse Inhibition. *Biol. Psychiatry* **2008**, *63*, 98–105. [CrossRef] [PubMed]
279. Berman, R.M.; Fava, M.; Thase, M.E.; Trivedi, M.H.; Swanink, R.; McQuade, R.D.; Carson, W.H.; Adson, D.; Taylor, L.; Hazel, J.; et al. Aripiprazole augmentation in major depressive disorder: A double-blind, placebo-controlled study in patients with inadequate response to antidepressants. *CNS Spectr.* **2009**, *14*, 197–206. [CrossRef] [PubMed]
280. Abbas, A.I.; Hedlund, P.B.; Huang, X.P.; Tran, T.B.; Meltzer, H.Y.; Roth, B.L. Amisulpride is a potent 5-HT₇ antagonist: Relevance for antidepressant actions in vivo. *Psychopharmacology* **2009**, *205*, 119–128. [CrossRef]
281. Okubo, R.; Hasegawa, T.; Fukuyama, K.; Shiroyama, T.; Okada, M. Current Limitations and Candidate Potential of 5-HT₇ Receptor Antagonism in Psychiatric Pharmacotherapy. *Front. Psychiatry* **2021**, *12*, 1–16. [CrossRef] [PubMed]
282. Mørk, A.; Montezinho, L.P.; Miller, S.; Trippodi-Murphy, C.; Plath, N.; Li, Y.; Gulino, M.; Sanchez, C. Vortioxetine (Lu AA21004), a novel multimodal antidepressant, enhances memory in rats. *Pharmacol. Biochem. Behav.* **2013**, *105*, 41–50. [CrossRef]
283. Okada, M.; Matsumoto, R.; Yamamoto, Y.; Fukuyama, K. Effects of subchronic administrations of vortioxetine, lurasidone, and escitalopram on thalamocortical glutamatergic transmission associated with serotonin 5-HT₇ receptor. *Int. J. Mol. Sci.* **2021**, *22*, 1351. [CrossRef]
284. Andressen, K.W.; Manfra, O.; Brevik, C.H.; Ulsund, A.H.; Vanhoenacker, P.; Levy, F.O.; Krobert, K.A. The atypical antipsychotics clozapine and olanzapine promote down-regulation and display functional selectivity at human 5-HT₇ receptors. *Br. J. Pharmacol.* **2015**, *172*, 3846–3860. [CrossRef] [PubMed]
285. Stahl, S.M. The serotonin-7 receptor as a novel therapeutic target. *J. Clin. Psychiatry* **2010**, *71*, 1414–1415. [CrossRef] [PubMed]



Review

Epigenetic Targeting of Histone Deacetylases in Diagnostics and Treatment of Depression

Hyun-Sun Park ^{1,*}, Jongmin Kim ^{2,3} , Seong Hoon Ahn ⁴ and Hong-Yeoul Ryu ^{5,*}

¹ Department of Biochemistry, Inje University College of Medicine, Busan 47392, Korea

² Division of Biological Sciences, Sookmyung Women's University, Seoul 04310, Korea; jkim@sookmyung.ac.kr

³ Research Institute for Women's Health, Sookmyung Women's University, Seoul 04310, Korea

⁴ Department of Molecular and Life Science, College of Science and Convergence Technology, Hanyang University ERICA Campus, Ansan 15588, Korea; hoon320@hanyang.ac.kr

⁵ BK21 FOUR KNU Creative BioResearch Group, School of Life Sciences, College of National Sciences, Kyungpook National University, Daegu 41566, Korea

* Correspondence: hspark@inje.ac.kr (H.-S.P.); rhr4757@knu.ac.kr (H.-Y.R.); Tel.: +82-51-890-6318 (H.-S.P.); +82-53-950-6352 (H.-Y.R.)

Abstract: Depression is a highly prevalent, disabling, and often chronic illness that places substantial burdens on patients, families, healthcare systems, and the economy. A substantial minority of patients are unresponsive to current therapies, so there is an urgent need to develop more broadly effective, accessible, and tolerable therapies. Pharmacological regulation of histone acetylation level has been investigated as one potential clinical strategy. Histone acetylation status is considered a potential diagnostic biomarker for depression, while inhibitors of histone deacetylases (HDACs) have garnered interest as novel therapeutics. This review describes recent advances in our knowledge of histone acetylation status in depression and the therapeutic potential of HDAC inhibitors.

Keywords: histone deacetylase (HDAC); depression; biomarker; anti-depressant therapy

Citation: Park, H.-S.; Kim, J.; Ahn, S.H.; Ryu, H.-Y. Epigenetic Targeting of Histone Deacetylases in Diagnostics and Treatment of Depression. *Int. J. Mol. Sci.* **2021**, *22*, 5398. <https://doi.org/10.3390/ijms22105398>

Academic Editor: Akiyoshi Saitoh

Received: 26 April 2021

Accepted: 18 May 2021

Published: 20 May 2021

Publisher's Note: MDPI stays neutral with regard to jurisdictional claims in published maps and institutional affiliations.



Copyright: © 2021 by the authors. Licensee MDPI, Basel, Switzerland. This article is an open access article distributed under the terms and conditions of the Creative Commons Attribution (CC BY) license (<https://creativecommons.org/licenses/by/4.0/>).

1. Introduction

Depression is characterized by recurrent episodes of sadness and despondency (depressed mood) frequently accompanied by anhedonia, loss of appetite, reduced concentration and energy, excessive guilt, and recurrent suicidal ideation [1]. Despite treatment, more than 50% of patients experience recurrent episodes and approximately 80% of those with a history of two episodes experience another relapse [2]. Both the incidence and prevalence of depression are increasing, and depression is now a major global healthcare burden and cause of lost economic productivity [3]. Current treatment guidelines recommend modulators of monoaminergic transmission such as monoamine oxidase (MAO) inhibitors and specific serotonin reuptake inhibitors (SSRIs) as first-line therapy based on the theory that depression arises from abnormal monoaminergic transmission. However, despite the availability of many monoamine modulators, approximately 50% of patients are unresponsive to these treatments [4].

Indeed, the clinical diagnosis and treatment of depression based on the Diagnostic and Statistical Manual of Mental Disorders (DSM) or the wide-ranging International Statistical Classification of Diseases and Related Health Problems (ICD) have focused on observable behaviors (signs) and self-reported feelings and thoughts (symptoms). Classifying mental disorders according to clinical signs and symptoms has led to a limitation in reflecting the underlying pathophysiology, and to heterogeneity within groups diagnosed with the same psychiatric disease [5]. Thus, attempts have emerged to suggest the novel classification of mental disorders that reflects biological mechanisms, such as Research Domain Criteria (RDoC) and biological classification of mental disorders (BeCOME) study [6,7]. Furthermore, many studies have aimed to identify the pathomechanism of depression to overcome the limitations of other existing tools for its diagnosis and treatment.

In addition to the well-known monoaminergic neurotransmitter dysfunction, altered hypothalamic-pituitary-adrenal (HPA) axis activity, dysfunctional brain network activity, impaired neurotrophic factor signaling, and neuroinflammation have been implicated in depression and studied for potential diagnostic biomarkers and therapeutic targets [8–10]. Additionally, changes in brain structure [11,12], gastrointestinal factors [13,14], oxidative stress [15], and endocannabinoid system components [16] have also been implicated in depression [17]. In addition, correlation studies for the aforementioned biomarkers such as inflammatory factors and brain structural changes also have been conducted in depression [18,19]. Family, twin, and adoption studies suggest that genetic factors account for 30–40% of the variance in depression risk [20], but early genome-wide association studies (GWASs) failed to identify genetic variants strongly associated with depression, suggesting that genetic susceptibility is mediated by heterogeneous combinations of risk alleles [21–23]. However, recent GWASs have identified several genetic loci reproducibly associated with depression [24–28].

The remaining 60–70% of the variation in depression risk appears to be determined by environmental factors [29]. Environmental stressors such as physical, emotional, and sexual abuse, social rejection, and other early adverse experiences and stressful life events such as the death of a loved one, illness, injury, disability, and functional decline are demonstrated risk factors for depression [30–32]. Individual variations in susceptibility to such stimuli may be explained in part by genetic factors. Indeed, a gene-environment interaction model positing that penetrant and complex genetic predispositions interact with environmental factors to determine depression susceptibility is now widely accepted [33].

In this gene-environmental interaction model, epigenetic mechanisms act as a bridge between genes and environmental factors [34]. Epigenetics refers to “heritable, but reversible, regulation of various genomic functions mediated principally through changes in DNA methylation and chromatin structure” [35]. Thus, epigenetic mechanisms are the processes by which various types of cells within the same organism acquire unique transcriptional properties and functions during development [36]. This dynamic and reversible process also contributes to the transcriptional plasticity manifested by the neurons and glia in the brain. Therefore, it is associated with learning and memory, age-related neurodegeneration, cognitive and behavioral effects of early experiences, repeated drug exposure, chronic stress, prolonged changes in nutritional status, and exposure to environmental toxins [37]. The functional analyses of DNA methylation quantitative trait locus (meQTL) and non-coding RNA (ncRNA) in depression-associated single nucleotide polymorphisms (SNPs) revealed that alterations in DNA methylation and ncRNAs interact with genetic factors in depression, which underscores the importance of epigenetic regulation for depression [38]. Thus, the present review provides an overview of the impact of histone deacetylation on the pathophysiology of depression and the therapeutic potential of its modulation.

2. Histone Acetylation

Dynamic acetylation and deacetylation of histone lysine (Lys) residues control the packaging of genomic DNA, thereby influencing DNA replication, transcription, DNA repair, and cell cycle progression [39]. Histone acetyltransferase enzymes (HATs) catalyze the transfer of acetyl groups from acetyl CoA to the ϵ -amino groups of Lys residues within histones [40], while histone deacetylases (HDACs) remove these acetyl groups [41]. Thus, the balance between HAT and HDAC activities determines the net histone acetylation status of the genome. By dynamically modulating the interaction between histones and DNA at the local level, histone acetylation regulates the accessibility of gene promoters to various binding factors such as transcription factors. In addition, acetylation/deacetylation of non-histone proteins modulated by HATs and HDACs also regulates diverse cellular functions [42].

3. Histone Deacetylase (HDAC) Families and Classes

Human HDACs are traditionally divided into two families, the Zn²⁺-dependent amide hydrolases including class I, II, and IV HDACs and the NAD⁺-dependent class III SIRT enzymes (Table 1). To date, 18 HDACs have been identified in humans and are grouped by sequence homology and domain organization [43]. Class I HDACs share structural homology with the yeast transcriptional regulator Rpd3 and typically act as the catalytic subunit within a complex of cognate corepressors to inhibit transcription in the cell nucleus [44]. HDAC1 and 2 are present in NuRD, Sin3, NOD1, CoREST, and MiDAC complexes, while HDAC3 is a component of SMRT and NCoR corepressor complexes [45,46]. In contrast, HDAC8 can function independently without forming a multiprotein complex [47].

Table 1. HDAC classification.

Class	Protein (<i>S. cerevisiae</i>)	Protein (Human)	Subcellular Localization
Class I	Rpd3	HDAC1	Nucleus
		HDAC2	Nucleus
		HDAC3	Nucleus
		HDAC8	Nucleus
Class IIa	Hda1	HDAC4	Nucleus/cytoplasm
		HDAC5	Nucleus/cytoplasm
		HDAC7	Nucleus/cytoplasm
		HDAC9	Nucleus/cytoplasm
Class IIb	Hda1	HDAC6	Cytoplasm
		HDAC10	Cytoplasm
Class IV	Hos3	HDAC11	Nucleus/cytoplasm
Class III	Sir2	SIRT1	Nucleus/cytoplasm
		SIRT2	Nucleus/cytoplasm
		SIRT3	Nucleus/mitochondria
		SIRT4	Mitochondria
		SIRT5	Mitochondria
		SIRT6	Nucleus
		SIRT7	Nucleus

Class II HDACs are highly homologous to yeast Hda1 and are subdivided into two groups [48]. Class IIa HDACs 4, 5, 7, and 9 each have a single catalytic domain and a unique adaptor domain including a transcription factor MEF2-binding motif [49], while class IIb HDACs 6 and 10 contain two catalytic domains, a ubiquitin-binding zinc finger domain and a leucine-rich repeat domain [50–54]. In contrast to class I HDACs, which are exclusively localized in the nucleus, class II enzymes can shuttle between the cytoplasm and nucleus in response to various regulatory cues [49].

HDAC11, a homolog of yeast Hos3, is the only member of Class IV [55]. It is primarily expressed in the brain, skeletal muscle, heart, testis, and kidney, suggesting specific functions in development, inflammation, metabolism [55].

Class III HDACs are homologous to yeast Sir2. Like other HDACs, Class III members are involved in transcriptional silencing but have a deoxyhypusine synthase-like NAD/FAD-binding domain clearly distinct from the catalytic domains of other HDAC classes [56]. Seven Sir2-like proteins (SIRT1–7), referred to as sirtuins, have been identified in humans [57]. These sirtuins possess additional domain(s) such as a mono-ADP-ribosyltransferase domain. SIRT1 has the strongest histone deacetylase activity among sirtuins, while SIRT5 shows weak deacetylase activity but robust lysine desuccinylase and demalonylase activities [58]. These enzymes are differentially localized to the nucleus (SIRT1, 2, 3, 6, and 7), cytoplasm (SIRT1 and 2), and mitochondria (SIRT3, 4, and 5) [43].

4. HDAC and Depression

Among the epigenetic mechanisms, the most well-studied for contributions to depression are DNA methylation mediated by DNA methyltransferases (DNMTs) and histone post-transcriptional modifications (PTMs), including acetylation/deacetylation. Associations between depression and DNA methylation have been suggested in many studies. For example, increased *DNMT3A* levels were found in the nucleus accumbens (NAc), the limbic region regulating reward behavior, in the postmortem brains of depressed patients, and in animal models of depression [59,60]. Data on DNA methylation age (DNAm age) derived from blood and brain tissues indicate that patients with depression displayed higher levels of epigenetic aging than those with normal subjects [61].

Along with DNA methylation, histone acetylation via HAT and deacetylation via HDAC are reported to be crucial for long-term stress adaptation and responses to antidepressant therapy [34]. Further, several studies have suggested a relationship between depression and histone deacetylation. Chronic social defeat stress transiently suppressed histone acetylation in the NAc of mice [62], while HDAC inhibition exerted antidepressant-like effects in animal models of stress-induced depression [62–66]. Moreover, the expression levels of *HDAC2* and *HDAC5* mRNAs in peripheral white blood cells were elevated in depressed patients compared to healthy controls [67]. Singh et al. [68,69] also reported the association between depression and *HDAC6*, which contributes to the stabilization of microtubules in the brain by regulating acetylation of α -tubulin. Interestingly, the effects of early-life stress (e.g., maternal separation) and subsequent environmental enrichment on depressive behavior and HDAC/DNMT activities in the hippocampus and prefrontal cortex (PFC) are sex-dependent, which supports sex differences in the prevalence of depression [70].

Diverse reports have suggested that sirtuins, categorized as class III HDACs, play several roles in the mammalian brain, such as modulating brain structure through axon elongation, outgrowth of neurites, and dendritic branching [71]. Among such sirtuin proteins, SIRT1 is associated with high-order brain function including synaptic plasticity and memory formation [72]. As a result of studies based on these reported functions of SIRT1, many researchers have demonstrated the relationship between SIRT1 and depression. For example, the expression of *SIRT1* in peripheral blood was downregulated in depressed patients compared to healthy controls [73]. Furthermore, these results were reproduced in animal studies; altered activity of SIRT1 in the hippocampus and the NAc provoked depressive-like behaviors in animal models of depression [74,75].

5. HDAC and the Hypothalamic-Pituitary-Adrenal (HPA) Axis

From the epigenetic perspective, stress is considered to be an important factor in the etiology of stress-related disorders such as depression and anxiety [76]. When exposed to social and physical stressors, the paraventricular nucleus (PVN) of the hypothalamus is stimulated to secrete both corticotrophin-releasing hormone (CRH) and arginine vasopressin (AVP) which stimulate the release of adrenocorticotrophic hormone (ACTH) in the pituitary gland. Consequently, mainly cortisol in humans and corticosterone in rodents are produced in the adrenal cortex and released into the bloodstream, exerting their effects through glucocorticoid receptors (GRs) in each tissue. The activation of GRs in the PVN of the hypothalamus and pituitary corticotroph cells inhibits the hypothalamic release of CRH and AVP and contributes to the negative feedback regulation of the HPA axis [77–80]. Additionally, the hippocampus can contribute to feedback regulation of the HPA axis through GR signaling [81]. This regulation is important in handling challenging situations and maintaining homeostasis (Figure 1).

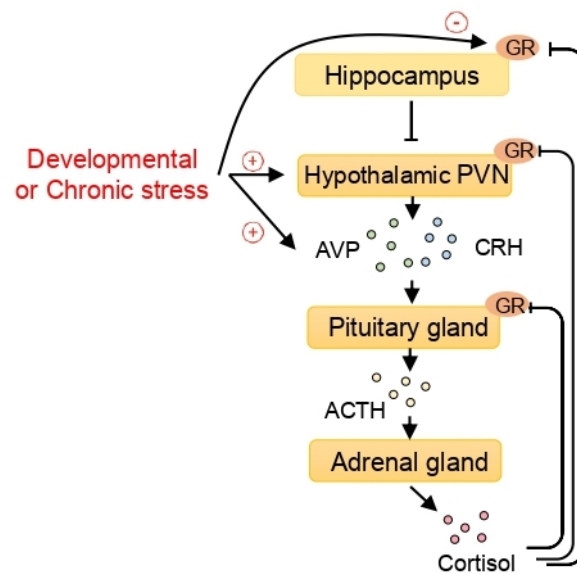


Figure 1. The epigenetic effect of stress on the hypothalamic-pituitary-adrenal (HPA) axis and the epigenetic regulation of arginine vasopressin (AVP) expression. When exposed to stress, corticotrophin-releasing hormone (CRH) and AVP, released from the paraventricular nucleus (PVN) of the hypothalamus, stimulate the pituitary gland to secrete adrenocorticotropic hormone (ACTH). The adrenal glands, activated by ACTH, secrete cortisol. Cortisol exerts its function by binding to the glucocorticoid receptors (GRs). In turn, the GRs in the pituitary gland, the hypothalamic PVN, and the hippocampus play important roles in the feedback regulation of the HPA axis. Developmental or chronic stress, which can program the HPA axis, increases AVP expression and decreases hippocampal GR through epigenetic mechanisms including histone deacetylases (HDACs).

Stress, especially in chronic or developmentally critical periods (i.e., prenatal and postnatal periods), influences various epigenetic mechanisms including DNA methylations and histone modifications, leading to structural and regulatory changes and fine-tunes the neural circuitry [82–84]. For example, researchers reported that early-life stress influences HDAC expression in the mouse brain [85,86]. Given that the HPA axis is one of the main stress responses, many researchers investigated the epigenetic regulation of the HPA axis in depression and identified the indirect effects of HDACs on the HPA axis. Murgatroyd et al. [87] focused on AVP which was reported to be important in the regulation of mood behaviors [88]. The authors demonstrated that early-life stress, represented by maternal deprivation, modulated AVP expression dynamically in the PVN of the hypothalamus initially through methyl CpG binding protein 2 (MeCP2) phosphorylation and later by AVP enhancer hypomethylation [87]. Considering that MeCP2 forms a complex consisting of HDAC and DNMT, consequently inducing gene silencing, HDAC is considered as a modulator of the HPA axis (Figure 2).

Unlike AVP, CRH expression in the hypothalamus, another component of the HPA axis, was not changed by maternal deprivation [87]. However, GR expression in the hippocampus was influenced under early-life stress through epigenetic mechanisms. Maternal deprivation affected DNA methylation status in the promoter of *GR* exons in the hippocampus, which mediates the recruitment of HDAC-containing repressor complexes (e.g., HDAC5) to hypermethylated loci [89,90]. These effects of early-life stress on hippocampal GR were reversed by HDAC inhibitors such as trichostatin A.

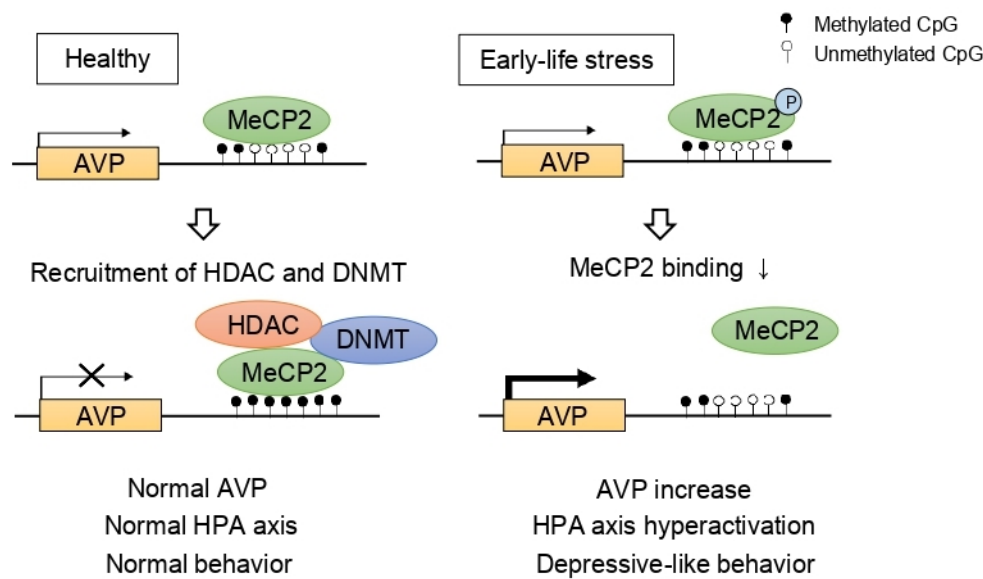


Figure 2. Epigenetic programming of arginine vasopressin (AVP). In normal conditions, AVP expression is repressed by methyl CpG binding protein 2 (MeCP2), DNA methyltransferase (DNMT), and histone deacetylase (HDAC) complex. However, early-life stress induces MeCP2 phosphorylation, inhibiting the recruitment of DNMT and HDAC consequently leading to hypomethylation at the AVP enhancer. As a result, increased AVP levels contribute to hyperactivation of the HPA axis and depressive-like behaviors.

6. HDAC and Brain-Derived Neurotrophic Factor

Brain-derived neurotrophic factor (BDNF) is a critical ligand guiding neurodevelopment and the ongoing neuroplastic processes required for behavioral adaptation, such as neurogenesis, synaptic plasticity, dendritic arborization, and pruning, and dendritic spine maturation [91,92]. Antidepressants and exercise increase endogenous BDNF in rodents, resulting in enhanced neurogenesis, reduced neuronal apoptosis, and inhibition of stress-induced depressive-like behaviors [92], while reduced BDNF is associated with depression as well as other neuropsychiatric and neurologic diseases such as Parkinson's disease and Alzheimer's disease [91]. Further, lower BDNF levels are observed in the PFC and the hippocampus of suicide victims compared to non-victims of suicide with or without depression [93].

Expression of BDNF is influenced by environmental stimuli via histone modification at different promoter sites in distinct brain regions especially during development [94]. Prenatal stress exposure was reported to increase HDAC expression and decrease BDNF expression in the hippocampus, resulting in anxiety- and depression-like behaviors [95]. In addition to prenatal stress, early postnatal stress also induced changes in histone modification and an increase of HDAC in the hippocampus, leading to changes in BDNF expression and behavior in rodents [92]. Not only during development but stress during adulthood also up-regulated MeCP2 levels at the *Bdnf* promoter and *Hdac5* expression in the hippocampus [96]. On the other hand, antidepressants and HDAC inhibitors (e.g., sodium butyrate, trichostatin A, and valproic acid) increased BDNF expression and it was associated with reduced DNA methylation and histone deacetylation around the *Bdnf* promoter region [97–99]. Similar to other HDACs, SIRT1 also can regulate BDNF expression through interaction with MeCP2 [100].

7. HDAC and Neuronal Plasticity

Experience-dependent neuronal plasticity, characterized by sustained changes in synaptic structure and strength, is the neurocellular basis for sensing, adapting, and responding to environmental changes, including stress [101,102]. Thus, it is not surprising that aberrant synaptic plasticity is associated with the pathophysiology of depression.

Indeed, both preclinical models of depression and depressed patients exhibit abnormalities in factors that regulate synaptic plasticity [33,103,104]. One of the strongest factors disrupting normal neuronal plasticity is chronic stress, and severe or chronic stress can reduce the capacity of the brain to respond and adapt to stress, resulting in depression [102,105]. Stressors activate the HPA axis and consequently increase circulating glucocorticoid levels. Chronically elevated glucocorticoid decreases synaptic number, impairs plasticity, and leads to neuronal atrophy, resulting in disrupted neural circuitry within and among regions regulating mood, executive function, and cognition [101]. Moreover, glucocorticoid can alter gene transcription via epigenetic regulation of the GR [89].

Abnormal histone acetylation due to the imbalance between HAT and HDAC activities can also impair synaptic plasticity, thereby reducing cognitive capacity and inducing abnormal behaviors. For instance, histone lysine acetylation can enhance neuronal plasticity while activation of HDAC and concomitant deacetylation can impair neuronal plasticity [106]. The administration of the non-selective HDAC inhibitor sodium butyrate enhanced histone acetylation and long-term potentiation (LTP), a form of synaptic plasticity strongly implicated in learning and memory, and improved memory performance [107]. Conversely, HDAC2 overexpression reduced synaptic number and synaptic plasticity, resulting in long-lasting neural circuit abnormalities and memory impairment. These changes may occur via the inactivation of activity-dependent genes involved in synaptic plasticity. Further, these effects were reversed by the HDAC inhibitor suberoylanilide hydroxamic acid (SAHA) [108].

In addition to HDAC2, HDAC4 is also implicated in the regulation of neuronal plasticity. HDAC4 is a transcriptional repressor that can translocate from the neuronal cytoplasm to the nucleus, bind chromatin, and suppress the expression of transcription factors critical for synaptic plasticity and information processing such as myocyte enhancer factor 2A (MEF2A) and cAMP response element-binding protein (CREB) [109–111]. Brain-specific HDAC4 knockout in mice impaired hippocampus-dependent memory and long-term synaptic plasticity [112]. Chronic cocaine-induced promoter-specific change in HDAC3, which is known as a negative regulator of memory formation, in the NAc and interfering HDAC3 activity restored cocaine-induced synaptic plasticity [113]. In addition, SIRT1 knockout mice also exhibited impaired memory and hippocampal plasticity [72]. Taken together, these findings indicate that appropriate HDAC function is essential for synaptic and neuronal plasticity and that an abnormal shift in histone acetylation status can result in impaired neural plasticity and behavioral dysfunction.

8. Molecular Diagnosis of Depression: An Epigenetic Perspective

Studies on the pathophysiology of depression have identified several promising prognostic and diagnostic biomarkers, including factors associated with the HPA axis (e.g., CRH, ACTH, and cortisol), inflammatory factors (e.g., tumor necrosis factor (TNF)- α , interleukin (IL)-1 β , IL-6, and C-reactive protein (CRP)), neurotrophic factors (e.g., BDNF and glial cell line-derived neurotrophic factor (GDNF)), insulin-like growth factor 1 (IGF-1), and changes in the area or volume of the hippocampus, amygdala, and PFC [17,114,115]. According to Kennis et al. [17], only cortisol in saliva was a significant biomarker for the onset/relapse/recurrence of depression, but careful interpretation is needed given the methodological heterogeneity among included studies.

In addition, several studies have identified the genes encoding the serotonin transporter (SLC6A4) [116,117], IL-1 β [118–120], and FK506 binding protein 5 (FKBP5 or FKBP-51) [116,121] as potential genetic biomarkers for depression. The genetic loci related to depression (e.g., SNPs in *LHPP*, *SIRT1* region) have also been revealed although there are differences between studies [24,26]. Furthermore, there are attempts to identify blood gene expression biomarkers and provide predictive information as well as precise and personalized diagnosis and treatment for depression [117,122]. Recently, researchers have attempted to integrate functional neuroimaging and genetic data (neuroimaging genetics) for depression. Buch et al. [123] found that polymorphisms of the serotonin transporter

(5-HTTLPR) and *BDNF* genes were associated with structural and functional changes in the anterior cingulate cortex, amygdala, and hippocampus, regions of the mesocorticolimbic reward circuit strongly associated with behaviors impaired in depression [124]. These results provide a novel diagnostic strategy for depression and imply that genetic factors contribute to depression by modulating brain structure and function.

The diagnostic biomarkers associated with epigenetic regulation also have been attracted attention in various diseases including neuropsychiatric diseases [121,125]. For instance, an epigenome-wide association study by Jovanova et al. [126] identified the methylation of 3 CpG islands in blood associated with depression. Moreover, hypermethylation of *BDNF* and *SLC6A4* genes have been found in depressed patients [127]. The local regions of histone acetylation may also serve as possible biomarkers for depression, as both animal and human postmortem studies have reported associations between histone modifications in brain tissue and depression. In addition, histone H3 lysine 27 trimethylation (H3K27me3) at the *BDNF* gene promoter IV of peripheral blood was downregulated in an antidepressant-responder group compared to a non-responder group [128]. Also, HDAC5 activity was significantly higher in peripheral leukocytes from drug-free depressive patients and normalized by antidepressant treatment [129]. The plasma levels of acetyl-L-carnitine (LAC), an acetylating agent that can pass through the blood–brain barrier, were decreased in depressed patients compared to control, where the degree of reduction in LAC was much greater in patients with treatment-resistant depression [130].

In recent years, diverse attempts have been conducted to visualize epigenetic factors and utilize them for diagnosis. For example, a positron emission tomography (PET) imaging study in human using [¹¹C] Martinostat, the only selective tracer for class I/IIb HDAC in the central nervous system [131,132], demonstrated that [¹¹C] Martinostat uptake in the dorsolateral PFC of patients with schizophrenia/schizoaffective disorder was lower compared to those of healthy controls, which is inconsistent with the results of postmortem studies [133]. Additionally, low [¹¹C] Martinostat uptake was observed in the frontolimbic areas of patients with bipolar disorder compared with healthy controls [134]. Since no visualization studies have been published related to depression yet and it is still in its infancy, many additional studies are expected to be needed to apply them to a depression diagnosis.

9. Molecular Therapeutics of Depression: An Epigenetic Perspective

The current first-line therapies for depression are tricyclic antidepressants (TCAs), MAO inhibitors, and SSRIs, all of which target the dysfunction of monoaminergic transmission [115]. However, classical antidepressants such as TCAs (e.g., imipramine) and SSRIs (e.g., paroxetine, fluoxetine, and escitalopram) not only bind to monoamine transporters but also have indirect effects on both DNA methylation and histone PTM [135]. For example, the reduced DNA methylation at the *Crh* promoter and increased *Crh* mRNA expression in chronic social defeat stress-induced depression were reversed by chronic imipramine administration [136]. Additionally, the SSRI paroxetine was reported to inhibit DNMTs [98]. Chronic antidepressant administration was also found to increase acetylated histone H3 (AcH3) levels by reducing HDAC expression in several brain regions, including the NAc [137].

DNMT inhibitors are not approved as antidepressant drugs despite their documented antidepressant effects because modulation of global brain methylation can cause cognitive deficits [135]. However, HDAC inhibitors have been examined as novel therapeutics for treatment-resistant depression [34,138,139], and numerous preclinical studies have reported that various HDAC inhibitors exert antidepressant-like effects in animal models of stress-induced depression [62,63,66,140–142] (Table 2). In addition to the antidepressant effect, HDAC inhibitors promoted neuronal rewiring and recovery of motor functions after traumatic brain injury [143]. Also, HDAC inhibitors such as sodium butyrate and SAHA enhanced cognitive function, which may provide therapeutic options for depression that accompanies cognitive impairment [144–146]. A recent drug repositioning study for

precise/personalized medicine in depression using bioinformatic analyses revealed that HDAC inhibitors such as trichostatin A and valproic acid as a new potential antidepressant drug [117].

Table 2. Summary of the antidepressant actions of HDAC inhibitor in animal model.

HDAC Inhibitor	Animal Model	Measurement of Antidepressant Effect	Molecular Mechanisms of Action	Ref.
MS-275	Chronic social defeat stress	Social avoidance, sucrose preference, FST	acH3 ↑ in the NAc	[62]
	Chronic social defeat stress	Sucrose preference test, social avoidance (combined with social enrichment)	acH3 ↑ in the hippocampus	[63]
	Chronic social defeat stress	Social avoidance, FST	acH3 ↑ in the mPFC	[64]
	Chronic social defeat stress	Social avoidance	Rac1 ↑ in the NAc synapse structural plasticity normalization	[141]
SAHA	Chronic social defeat stress	Social avoidance, sucrose preference, FST	acH3 ↑ in the NAc	[62]
	Chronic unpredictable mild stress	Social interaction, sucrose preference test, novelty-suppressed test, FST	HDAC2 inhibition, <i>Gdnf</i> ↑ in the NAc	[140]
Sodium butyrate	Behavioral despair paradigm	TST	acH3 ↑ in the hippocampus, <i>Bdnf</i> ↑ in the frontal cortex	[65]
	Chronic social defeat stress	Social avoidance	HDAC5 inhibition, acH3 ↑ in <i>Bdnf</i> gene P3, P4 promoter	[66]
	Chronic restraint stress	Sucrose preference test, Light/dark test, TST, FST	HDAC2 ↑, pCREB ↑, AcH3 ↑, BDNF ↑ in the hippocampus	[142]

BDNF, brain-derived neurotrophic factor; CREB, cAMP response element-binding protein; FST, forced swim test; GDNF, glial cell-derived neurotrophic factor; HDAC, histone deacetylase; mPFC, medial prefrontal cortex; NAc, nucleus accumbens; Rac1, Rac family small GTPase 1; SAHA, suberoylanilide hydroxamic acid; TST, tail suspension test; ↑ increase.

While these results support the potential of HDAC inhibitors as novel therapeutic drugs for depression, their use in clinical practice is limited by severe side effects including thrombocytopenia and neutropenia [147,148]. Although several HDAC inhibitors, including vorinostat (SAHA), belinostat, panobinostat (LBH-589), romidepsin (FK2280), have been approved by the Food and Drug Agency (United States), the clinical application of these drugs is limited to certain forms of cancers (e.g., T-cell lymphoma and multiple myeloma) [149] and to date, there is no clinical trial evaluating the antidepressant effect of HDAC inhibitors in depression.

Apart from HDAC inhibitors, the acetylating agent LAC also has been reported to be a potential antidepressant that is mediated by neurotransmitter regulations such as serotonin and epigenetic regulation of key genes important for synaptic plasticity (e.g., *BDNF* and metabotropic glutamate receptor of class-2 (*mGlu2*)) [130]. Lactate, a metabolite produced by exercise, induced resilience to social defeat stress and reversed social avoidance behavior and anxiety by modulating the activity of HDAC2 and HDAC3 [150]. In addition, dihydrocaffeic acid (DHCA) and malvidin-3'-O-glucoside (Mal-gluc) induced a resilient state against social stress and attenuated depressive behaviors via epigenetic regulation [151]. In particular, Mal-gluc mediates the increase in histone acetylation of the *Rac1* gene regulatory sequence through HDAC2 inhibition, and as a result, the modulation of synaptic plasticity occurs.

10. Conclusions

Depression is a common and disabling psychiatric disease with high recurrence rates and heterogeneous clinical manifestations, adding to treatment complexity and suggesting that depression is not a unitary disease entity. Indeed, numerous pathomechanisms likely contribute to depression, including abnormal epigenetic changes. Environmental stressors are the primary risk factors for depression, supporting contributions of epigenetic mechanisms to disease pathogenesis and progression. In this review, we summarized the latest knowledge on potential epigenetic mechanisms, especially histone acetylation/deacetylation, underlying disease pathophysiology, the utility of epigenetic markers for diagnosis, and the potential of epigenetic modulators, especially HDAC inhibitors, as therapeutics. Recent studies have shown that HDAC inhibition can upregulate BDNF expression, resulting in enhanced neural/synaptic plasticity, and exert an antidepressant-like effect on behavior. Conventional antidepressants targeting monoaminergic neurotransmission also modulate epigenetic mechanisms, further supporting the contributions of epigenetic dysregulation to the pathophysiology of depression. Thus, HDACs can be regarded as novel diagnostic and therapeutic targets for depression. However, further studies are needed to develop safe and effective HDAC inhibitors for clinical use.

Author Contributions: Conceptualization, H.-S.P.; writing, H.-S.P. and H.-Y.R.; review and editing, J.K., S.H.A., and H.-Y.R.; funding acquisition, H.-Y.R. All authors have read and agreed to the published version of the manuscript.

Funding: This research was supported by Kyungpook National University Research Fund, 2020.

Conflicts of Interest: The authors declare no conflict of interest.

References

1. American Psychiatric Association. *Diagnostic and Statistical Manual of Mental Disorders*, 5th ed.; American Psychiatric Association: Arlington, VA, USA, 2013.
2. Burcusa, S.L.; Iacono, W.G. Risk for recurrence in depression. *Clin. Psychol. Rev.* **2007**, *27*, 959–985. [CrossRef]
3. Liu, Q.; He, H.; Yang, J.; Feng, X.; Zhao, F.; Lyu, J. Changes in the global burden of depression from 1990 to 2017: Findings from the Global Burden of Disease study. *J. Psychiatry Res.* **2020**, *126*, 134–140. [CrossRef] [PubMed]
4. Cipriani, A.; Furukawa, T.A.; Salanti, G.; Chaimani, A.; Atkinson, L.Z.; Ogawa, Y.; Levicht, S.; Ruhe, H.G.; Turner, E.H.; Higgins, J.P.T.; et al. Comparative efficacy and acceptability of 21 antidepressant drugs for the acute treatment of adults with major depressive disorder: A systematic review and network meta-analysis. *Lancet* **2018**, *391*, 1357–1366. [CrossRef]
5. Calabro, M.; Fabbri, C.; Kasper, S.; Zohar, J.; Souery, D.; Montgomery, S.; Albani, D.; Forloni, G.; Ferentinos, P.; Rujescu, D.; et al. Research Domain Criteria (RDoC): A Perspective to Probe the Biological Background behind Treatment Efficacy in Depression. *Curr. Med. Chem.* **2021**, *28*, 1–23. [CrossRef] [PubMed]
6. Insel, T.; Cuthbert, B.; Garvey, M.; Heinssen, R.; Pine, D.S.; Quinn, K.; Sanislow, C.; Wang, P. Research Domain Criteria (RDoC): Toward a New Classification Framework for Research on Mental Disorders. *Am. J. Psychiatry* **2010**, *167*, 748–751. [CrossRef]
7. Bruckl, T.M.; Spoomaker, V.I.; Samann, P.G.; Brem, A.-K.; Henco, L.; Czamara, D.; Elbau, I.; Grandi, N.C.; Jollans, L.; Kuhnel, A.; et al. The biological classification of mental disorders (BeCOME) study: A protocol for an observational deep-phenotyping study for the identification of biological subtypes. *BMC Psychiatry* **2020**, *20*, 213. [CrossRef]
8. Krishnan, V.; Nestler, E.J. The molecular neurobiology of depression. *Nature* **2008**, *455*, 894–902. [CrossRef]
9. Hasler, G. Pathophysiology of depression: Do we have any solid evidence of interest to clinicians? *World Psychiatry* **2010**, *9*, 155–161. [CrossRef] [PubMed]
10. Krishnan, V.; Nestler, E.J. Linking Molecules to Mood: New Insight Into the Biology of Depression. *Am. J. Psychiatry* **2010**, *167*, 1305–1320. [CrossRef]
11. Schlaepfer, T.E.; Cohen, M.X.; Frick, C.; Kosel, M.M.; Brodessa, D.; Axmacher, N.; Joe, A.Y.; Kreft, M.; Lenartz, D.; Sturm, V. Deep Brain Stimulation to Reward Circuitry Alleviates Anhedonia in Refractory Major Depression. *Neuropsychopharmacology* **2007**, *33*, 368–377. [CrossRef]
12. Price, J.L.; Drevets, W.C. Neural circuits underlying the pathophysiology of mood disorders. *Trends Cogn. Sci.* **2012**, *16*, 61–71. [CrossRef]
13. Clapp, M.; Aurora, N.; Herrera, L.; Bhatia, M.; Wilen, E.; Wakefield, S. Gut Microbiota's Effect on Mental Health: The Gut-Brain Axis. *Clin. Pract.* **2017**, *7*, 131–136. [CrossRef] [PubMed]
14. Wallace, C.J.K.; Milev, R. The effects of probiotics on depressive symptoms in humans: A systematic review. *Ann. Gen. Psychiatry* **2017**, *16*, 14. [CrossRef] [PubMed]

15. Black, C.N.; Bot, M.; Scheffer, P.G.; Penninx, B.W.J.H. Oxidative stress in major depressive and anxiety disorders, and the association with antidepressant use; results from a large adult cohort. *Psychol. Med.* **2017**, *47*, 936–948. [CrossRef]
16. Navarrete, F.; Garcia-Gutierrez, M.S.; Jurado-Barba, R.; Rubio, G.; Gasparyan, A.; Austrich-Olivares, A.; Manzanares, J. Endocannabinoid System Components as Potential Biomarkers in Psychiatry. *Front. Psychiatry* **2020**, *11*, 315. [CrossRef] [PubMed]
17. Kennis, M.; Gerritsen, L.; Van Dalen, M.; Williams, A.; Cuijpers, P.; Bockting, C. Prospective biomarkers of major depressive disorder: A systematic review and meta-analysis. *Mol. Psychiatry* **2020**, *25*, 321–338. [CrossRef]
18. Opel, N.; Cearns, M.; Clark, S.; Toben, C.; Grotegerd, D.; Heindel, W.; Kugel, H.; Teuber, A.; Minnerup, H.; Berger, K.; et al. Large-scale evidence for an association between low-grade peripheral inflammation and brain structural alterations in major depression in the BiDirect study. *J. Psychiatry Neurosci.* **2019**, *44*, 423–431. [CrossRef]
19. Green, C.; Shen, X.; Stevenson, A.J.; Conole, E.L.; Harris, M.A.; Barbu, M.C.; Hawkins, E.L.; Adams, M.J.; Hillary, R.F.; Lawrie, S.M.; et al. Structural brain correlates of serum and epigenetic markers of inflammation in major depressive disorder. *Brain Behav. Immun.* **2021**, *92*, 39–48. [CrossRef]
20. Sullivan, P.F.; Neale, M.C.; Kendler, K.S. Genetic Epidemiology of Major Depression: Review and Meta-Analysis. *Am. J. Psychiatry* **2000**, *157*, 1552–1562. [CrossRef]
21. Bosker, F.J.; Hartman, C.A.; Nolte, I.M.; Prins, B.P.; Terpstra, P.; Posthuma, D.; van Veen, T.; Willemsen, G.; DeRijk, R.H.; de Geus, E.J.; et al. Poor replication of candidate genes for major depressive disorder using genome-wide association data. *Mol. Psychiatry* **2010**, *16*, 516–532. [CrossRef] [PubMed]
22. Wray, N.R.; Pergadia, M.L.; Blackwood, D.H.R.; Penninx, B.W.J.H.; Gordon, S.D.; Nyholt, D.R.; Ripke, S.; MacIntyre, D.J.; McGhee, K.A.; Maclean, A.W.; et al. Genome-wide association study of major depressive disorder: New results, meta-analysis, and lessons learned. *Mol. Psychiatry* **2010**, *17*, 36–48. [CrossRef]
23. Uher, R.; Investigators, G.; Investigators, M.; Investigators, S.D. Common Genetic Variation and Antidepressant Efficacy in Major Depressive Disorder: A Meta-Analysis of Three Genome-Wide Pharmacogenetic Studies. *Am. J. Psychiatry* **2013**, *170*, 207–217.
24. Cai, N.; Bigdeli, T.B.; Kretschmar, W.; Li, Y.; Liang, J.; Song, L.; Hu, J.; Li, Q.; Jin, W.; Hu, Z.; et al. Sparse whole-genome sequencing identifies two loci for major depressive disorder. *Nature* **2015**, *523*, 588–591. [CrossRef] [PubMed]
25. Okbay, A.; Baselmans, B.M.L.; De Neve, J.E.; Turley, P.; Nivard, M.G.; Fontana, M.A.; Meddens, S.F.W.; Linner, R.K.; Rietveld, C.A.; Derringer, J.; et al. Genetic variants associated with subjective well-being, depressive symptoms, and neuroticism identified through genome-wide analyses. *Nat. Genet.* **2016**, *48*, 624–633. [CrossRef] [PubMed]
26. Hyde, C.L.; Nagle, M.W.; Tian, C.; Chen, X.; Paciga, S.A.; Wendland, J.R.; Tung, J.Y.; Hinds, D.A.; Perlis, R.H.; Winslow, A.R. Identification of 15 genetic loci associated with risk of major depression in individuals of European descent. *Nat. Genet.* **2016**, *48*, 1031–1036. [CrossRef] [PubMed]
27. Lewis, C. Mega-Analysis of Genome-Wide Association Studies in Major Depressive Disorder: MDD Working Group of the Psychiatric Genomics Consortium. *Eur. Neuropsychopharm.* **2017**, *27*, S119.
28. Howard, D.M.; Adams, M.J.; Shirali, M.; Clarke, T.K.; Marioni, R.E.; Davies, G.; Coleman, J.R.I.; Alloza, C.; Shen, X.Y.; Barbu, M.C.; et al. Genome-wide association study of depression phenotypes in UK Biobank identifies variants in excitatory synaptic pathways. *Nat. Commun.* **2018**, *9*, 1470. [CrossRef]
29. Saveanu, R.V.; Nemeroff, C.B. Etiology of Depression: Genetic and Environmental Factors. *Psychiatry Clin. N. Am.* **2012**, *35*, 51–71. [CrossRef]
30. Bruce, M.L. Psychosocial risk factors for depressive disorders in late life. *Biol. Psychiatry* **2002**, *52*, 175–184. [CrossRef]
31. Cheptou, P.O.; Donohue, K. Epigenetics as a new avenue for the role of inbreeding depression in evolutionary ecology. *Heredity* **2013**, *110*, 205–206. [CrossRef]
32. Shapero, B.G.; Black, S.K.; Liu, R.T.; Klugman, J.; Bender, R.E.; Abramson, L.Y.; Alloy, L.B. Stressful Life Events and Depression Symptoms: The Effect of Childhood Emotional Abuse on Stress Reactivity. *J. Clin. Psychol.* **2014**, *70*, 209–223. [CrossRef] [PubMed]
33. Sun, H.; Kennedy, P.J.; Nestler, E.J. Epigenetics of the Depressed Brain: Role of Histone Acetylation and Methylation. *Neuropsychopharmacology* **2013**, *38*, 124–137. [CrossRef] [PubMed]
34. Lin, E.; Tsai, S.-J. Epigenetics and Depression: An Update. *Psychiatry Investig.* **2019**, *16*, 654–661. [CrossRef] [PubMed]
35. Mill, J.; Petronis, A. Molecular studies of major depressive disorder: The epigenetic perspective. *Mol. Psychiatry* **2007**, *12*, 799–814. [CrossRef]
36. O'Donnell, K.J.; Meaney, M.J. Epigenetics, Development, and Psychopathology. *Annu. Rev. Clin. Psychol.* **2020**, *16*, 327–350. [CrossRef]
37. Meaney, M.J.; Ferguson-Smith, A.C. Epigenetic regulation of the neural transcriptome: The meaning of the marks. *Nat. Neurosci.* **2010**, *13*, 1313–1318. [CrossRef]
38. Ciuculete, D.M.; Voisin, S.; Kular, L.; Jonsson, J.; Rask-Andersen, M.; Mwinyi, J.; Schiøth, H.B. meQTL and ncRNA functional analyses of 102 GWAS-SNPs associated with depression implicate HACE1 and SHANK2 genes. *Clin. Epigenetics* **2020**, *12*, 99. [CrossRef]
39. Wade, P.A.; Pruss, D.; Wolffe, A.P. Histone acetylation: Chromatin in action. *Trends Biochem. Sci.* **1997**, *22*, 128–132. [CrossRef]
40. Roth, S.Y.; Denu, J.M.; Allis, C.D. Histone Acetyltransferases. *Annu. Rev. Biochem.* **2001**, *70*, 81–120. [CrossRef]
41. Marks, P.A.; Miller, T.; Richon, V.M. Histone deacetylases. *Curr. Opin. Pharmacol.* **2003**, *3*, 344–351. [CrossRef]
42. Narita, T.; Weinert, B.T.; Choudhary, C. Functions and mechanisms of non-histone protein acetylation. *Nat. Rev. Mol. Cell Bio.* **2019**, *20*, 156–174. [CrossRef] [PubMed]

43. Seto, E.; Yoshida, M. Erasers of Histone Acetylation: The Histone Deacetylase Enzymes. *Cold Spring Harb. Perspect. Biol.* **2014**, *6*, a018713. [CrossRef]
44. Taunton, J.; Hassig, C.A.; Schreiber, S.L. A Mammalian Histone Deacetylase Related to the Yeast Transcriptional Regulator Rpd3p. *Science* **1996**, *272*, 408–411. [CrossRef] [PubMed]
45. Ayer, D.E. Histone deacetylases: Transcriptional repression with SINers and NuRDs. *Trends Cell Biol.* **1999**, *9*, 193–198. [CrossRef]
46. Wen, Y.D.; Perissi, V.; Staszewski, L.M.; Yang, W.M.; Krones, A.; Glass, C.K.; Rosenfeld, M.G.; Seto, E. The histone deacetylase-3 complex contains nuclear receptor corepressors. *Proc. Natl. Acad. Sci. USA* **2000**, *97*, 7202–7207. [CrossRef]
47. Hu, E.; Chen, Z.X.; Fredrickson, T.; Zhu, Y.; Kirkpatrick, R.; Zhang, G.-F.; Johanson, K.; Sung, C.-M.; Liu, R.G.; Winkler, J. Cloning and Characterization of a Novel Human Class I Histone Deacetylase That Functions as a Transcription Repressor. *J. Biol. Chem.* **2000**, *275*, 15254–15264. [CrossRef]
48. Grozinger, C.M.; Hassig, C.A.; Schreiber, S.L. Three proteins define a class of human histone deacetylases related to yeast Hda1p. *Proc. Natl. Acad. Sci. USA* **1999**, *96*, 4868–4873. [CrossRef]
49. Muslin, A.J.; Xing, H.M. 14-3-3 proteins: Regulation of subcellular localization by molecular interference. *Cell. Signal* **2000**, *12*, 703–709. [CrossRef]
50. Grozinger, C.M.; Schreiber, S.L. Regulation of histone deacetylase 4 and 5 and transcriptional activity by 14-3-3-dependent cellular localization. *Proc. Natl. Acad. Sci. USA* **2000**, *97*, 7835–7840. [CrossRef]
51. Wang, A.H.; Kruhlak, M.J.; Wu, J.; Bertos, N.R.; Vezmar, M.; Posner, B.I.; Bazett-Jones, D.P.; Yang, X.-J. Regulation of Histone Deacetylase 4 by Binding of 14-3-3 Proteins. *Mol. Cell. Biol.* **2000**, *20*, 6904–6912. [CrossRef]
52. McKinsey, T.A.; Zhang, C.L.; Olson, E.N. Activation of the myocyte enhancer factor-2 transcription factor by calcium/calmodulin-dependent protein kinase-stimulated binding of 14-3-3 to histone deacetylase 5. *Proc. Natl. Acad. Sci. USA* **2000**, *97*, 14400–14405. [CrossRef] [PubMed]
53. Kao, H.-Y.; Downes, M.; Ordentlich, P.; Evans, R.M. Isolation of a novel histone deacetylase reveals that class I and class II deacetylases promote SMRT-mediated repression. *Gene Dev.* **2000**, *14*, 55–66.
54. Zhang, H.; Okada, S.; Hatano, M.; Okabe, S.; Tokuhsa, T. A new functional domain of Bcl6 family that recruits histone deacetylases. *Biochim. Biophys. Acta (BBA) Mol. Cell Res.* **2001**, *1540*, 188–200. [CrossRef]
55. Gao, L.; Cueto, M.A.; Asselbergs, F.; Atadja, P. Cloning and Functional Characterization of HDAC11, a Novel Member of the Human Histone Deacetylase Family. *J. Biol. Chem.* **2002**, *277*, 25748–25755. [CrossRef] [PubMed]
56. Brachmann, C.B.; Sherman, J.M.; Devine, S.E.; Cameron, E.E.; Pillus, L.; Boeke, J.D. The SIR2 gene family, conserved from bacteria to humans, functions in silencing, cell-cycle progression, and chromosome stability. *Genes Dev.* **1995**, *9*, 2888–2902. [CrossRef]
57. Frye, R.A. Characterization of Five Human cDNAs with Homology to the Yeast SIR2 Gene: Sir2-like Proteins (Sirtuins) Metabolize NAD and May Have Protein ADP-Ribosyltransferase Activity. *Biochem. Biophys. Res. Commun.* **1999**, *260*, 273–279. [CrossRef] [PubMed]
58. Du, J.; Zhou, Y.; Su, X.; Yu, J.J.; Khan, S.; Jiang, H.; Kim, J.; Woo, J.; Choi, B.H.; He, B.; et al. Sirt5 Is a NAD-Dependent Protein Lysine Demalonylase and Desuccinylase. *Science* **2011**, *334*, 806–809. [CrossRef]
59. LaPlant, Q.; Vialou, V.; Covington, H.E., 3rd; Dumitriu, D.; Feng, J.; Warren, B.L.; Maze, I.; Dietz, D.M.; Watts, E.L.; Iniguez, S.D.; et al. Dnmt3a regulates emotional behavior and spine plasticity in the nucleus accumbens. *Nat. Neurosci.* **2010**, *13*, 1137–1143. [CrossRef]
60. Hodes, G.E.; Pfau, M.L.; Purushothaman, I.; Ahn, H.F.; Golden, S.A.; Christoffel, D.J.; Magida, J.; Brancato, A.; Takahashi, A.; Flanigan, M.E.; et al. Sex Differences in Nucleus Accumbens Transcriptome Profiles Associated with Susceptibility versus Resilience to Subchronic Variable Stress. *J. Neurosci.* **2015**, *35*, 16362–16376. [CrossRef]
61. Han, L.K.M.; Aghajani, M.; Clark, S.L.; Chan, R.F.; Hattab, M.W.; Shabalin, A.A.; Zhao, M.; Kumar, G.; Xie, L.Y.; Jansen, R.; et al. Epigenetic Aging in Major Depressive Disorder. *Am. J. Psychiatry* **2018**, *175*, 774–782. [CrossRef]
62. Covington, H.E.; Maze, I.; LaPlant, Q.C.; Vialou, V.F.; Ohnishi, Y.N.; Berton, O.; Fass, D.M.; Renthal, W.; Rush, A.J.; Wu, E.Y.; et al. Antidepressant Actions of Histone Deacetylase Inhibitors. *J. Neurosci.* **2009**, *29*, 11451–11460. [CrossRef] [PubMed]
63. Covington, H.E.; Vialou, V.F.; LaPlant, Q.; Ohnishi, Y.N.; Nestler, E.J. Hippocampal-dependent antidepressant-like activity of histone deacetylase inhibition. *Neurosci. Lett.* **2011**, *493*, 122–126. [CrossRef]
64. Covington, H.E.; Maze, I.; Vialou, V.; Nestler, E.J. Antidepressant action of HDAC inhibition in the prefrontal cortex. *Neuroscience* **2015**, *298*, 329–335. [CrossRef]
65. Schroeder, F.A.; Lin, C.L.; Crusio, W.E.; Akbarian, S. Antidepressant-Like Effects of the Histone Deacetylase Inhibitor, Sodium Butyrate, in the Mouse. *Biol. Psychiatry* **2007**, *62*, 55–64. [CrossRef] [PubMed]
66. Tsankova, N.M.; Berton, O.; Renthal, W.; Kumar, A.; Neve, R.L.; Nestler, E.J. Sustained hippocampal chromatin regulation in a mouse model of depression and antidepressant action. *Nat. Neurosci.* **2006**, *9*, 519–525. [CrossRef]
67. Hobara, T.; Uchida, S.; Otsuki, K.; Matsubara, T.; Funato, H.; Matsuo, K.; Suetsugi, M.; Watanabe, Y. Altered gene expression of histone deacetylases in mood disorder patients. *J. Psychiatry Res.* **2010**, *44*, 263–270. [CrossRef]
68. Singh, H.; Wray, N.; Schappi, J.M.; Rasenick, M.M. Disruption of lipid-raft localized Galphas/tubulin complexes by antidepressants: A unique feature of HDAC6 inhibitors, SSRI and tricyclic compounds. *Neuropsychopharmacology* **2018**, *43*, 1481–1491. [CrossRef] [PubMed]

69. Singh, H.; Chmura, J.; Bhaumik, R.; Pandey, G.N.; Rasenick, M.M. Membrane-Associated α -Tubulin Is Less Acetylated in Postmortem Prefrontal Cortex from Depressed Subjects Relative to Controls: Cytoskeletal Dynamics, HDAC6, and Depression. *J. Neurosci.* **2020**, *40*, 4033–4041. [CrossRef]
70. Borba, L.A.; Broseghini, L.D.; Manosso, L.M.; de Moura, A.B.; Botelho, M.E.M.; Arent, C.O.; Behenck, J.P.; Hilsendeger, A.; Kammer, L.H.; Valvassori, S.S.; et al. Environmental enrichment improves lifelong persistent behavioral and epigenetic changes induced by early-life stress. *J. Psychiatry Res.* **2021**, *138*, 107–116. [CrossRef]
71. Herskovits, A.Z.; Guarente, L. SIRT1 in Neurodevelopment and Brain Senescence. *Neuron* **2014**, *81*, 471–483. [CrossRef]
72. Michan, S.; Li, Y.; Chou, M.M.; Parrella, E.; Ge, H.; Long, J.M.; Allard, J.S.; Lewis, K.; Miller, M.; Xu, W.; et al. SIRT1 Is Essential for Normal Cognitive Function and Synaptic Plasticity. *J. Neurosci.* **2010**, *30*, 9695–9707. [CrossRef] [PubMed]
73. Kishi, T.; Yoshimura, R.; Kitajima, T.; Okochi, T.; Okumura, T.; Tsunoka, T.; Yamanouchi, Y.; Kinoshita, Y.; Kawashima, K.; Fukuo, Y.; et al. SIRT1 gene is associated with major depressive disorder in the Japanese population. *J. Affect. Disord.* **2010**, *126*, 167–173. [CrossRef] [PubMed]
74. Abe-Higuchi, N.; Uchida, S.; Yamagata, H.; Higuchi, F.; Hobara, T.; Hara, K.; Kobayashi, A.; Watanabe, Y. Hippocampal Sirtuin 1 Signaling Mediates Depression-like Behavior. *Biol. Psychiatry* **2016**, *80*, 815–826. [CrossRef] [PubMed]
75. Kim, H.-D.; Hesterman, J.; Call, T.; Magazu, S.; Keeley, E.; Armenta, K.; Kronman, H.; Neve, R.L.; Nestler, E.J.; Ferguson, D. SIRT1 Mediates Depression-Like Behaviors in the Nucleus Accumbens. *J. Neurosci.* **2016**, *36*, 8441–8452. [CrossRef]
76. Yang, L.; Zhao, Y.; Wang, Y.; Liu, L.; Zhang, X.; Li, B.; Cui, R. The Effects of Psychological Stress on Depression. *Curr. Neuropharmacol.* **2015**, *13*, 494–504. [CrossRef]
77. Murgatroyd, C.; Spengler, D. Epigenetics of Early Child Development. *Front. Psychiatry* **2011**, *2*, 16. [CrossRef]
78. Sandi, C.; Haller, J. Stress and the social brain: Behavioural effects and neurobiological mechanisms. *Nat. Rev. Neurosci.* **2015**, *16*, 290–304. [CrossRef]
79. McEwen, B.S.; Bowles, N.P.; Gray, J.D.; Hill, M.N.; Hunter, R.G.; Karatsoreos, I.N.; Nasca, C. Mechanisms of stress in the brain. *Nat. Neurosci.* **2015**, *18*, 1353–1363. [CrossRef]
80. Godoy, L.D.; Rossignoli, M.T.; Delfino-Pereira, P.; Garcia-Cairasco, N.; de Lima Umeoka, E.H. A Comprehensive Overview on Stress Neurobiology: Basic Concepts and Clinical Implications. *Front. Behav. Neurosci.* **2018**, *12*, 127. [CrossRef]
81. Paul, S.; Jeon, W.K.; Bizon, J.L.; Han, J.S. Interaction of basal forebrain cholinergic neurons with the glucocorticoid system in stress regulation and cognitive impairment. *Front. Aging Neurosci.* **2015**, *7*, 43. [CrossRef]
82. Murgatroyd, C.; Spengler, D. Epigenetic programming of the HPA axis: Early life decides. *Stress* **2011**, *14*, 581–589. [CrossRef] [PubMed]
83. Stankiewicz, A.M.; Swiergiel, A.H.; Lisowski, P. Epigenetics of stress adaptations in the brain. *Brain Res. Bull.* **2013**, *98*, 76–92. [CrossRef]
84. Klengel, T.; Binder, E.B. Epigenetics of Stress-Related Psychiatric Disorders and Gene x Environment Interactions. *Neuron* **2015**, *86*, 1343–1357. [CrossRef]
85. Levine, A.; Worrell, T.R.; Zimnisky, R.; Schmauss, C. Early life stress triggers sustained changes in histone deacetylase expression and histone H4 modifications that alter responsiveness to adolescent antidepressant treatment. *Neurobiol. Dis.* **2012**, *45*, 488–498. [CrossRef]
86. Tesone-Coelho, C.; Morel, L.J.; Bhatt, J.; Estevez, L.; Naudon, L.; Giros, B.; Zwiller, J.; Dauge, V. Vulnerability to opiate intake in maternally deprived rats: Implication of MeCP2 and of histone acetylation. *Addict. Biol.* **2013**, *20*, 120–131. [CrossRef] [PubMed]
87. Murgatroyd, C.; Patchev, A.V.; Wu, Y.; Micale, V.; Bockmuhl, Y.; Fischer, D.; Holsboer, F.; Wotjak, C.T.; Almeida, O.F.; Spengler, D. Dynamic DNA methylation programs persistent adverse effects of early-life stress. *Nat. Neurosci.* **2009**, *12*, 1559–1566. [CrossRef] [PubMed]
88. Neumann, I.D.; Landgraf, R. Balance of brain oxytocin and vasopressin: Implications for anxiety, depression, and social behaviors. *Trends Neurosci.* **2012**, *35*, 649–659. [CrossRef] [PubMed]
89. Zhang, T.Y.; Labonte, B.; Wen, X.L.; Turecki, G.; Meaney, M.J. Epigenetic mechanisms for the early environmental regulation of hippocampal glucocorticoid receptor gene expression in rodents and humans. *Neuropsychopharmacology* **2013**, *38*, 111–123. [CrossRef]
90. Seo, M.K.; Kim, S.G.; Seog, D.H.; Bahk, W.M.; Kim, S.H.; Park, S.W.; Lee, J.G. Effects of Early Life Stress on Epigenetic Changes of the Glucocorticoid Receptor 1 γ Promoter during Adulthood. *Int. J. Mol. Sci.* **2020**, *21*, 6331. [CrossRef]
91. Nagahara, A.H.; Tuszynski, M.H. Potential therapeutic uses of BDNF in neurological and psychiatric disorders. *Nat. Rev. Drug Discov.* **2011**, *10*, 209–219. [CrossRef]
92. Hing, B.; Sathyaputri, L.; Potash, J.B. A comprehensive review of genetic and epigenetic mechanisms that regulate BDNF expression and function with relevance to major depressive disorder. *Am. J. Med. Genet. B* **2018**, *177*, 143–167. [CrossRef] [PubMed]
93. Misztak, P.; Panczyszyn-Trzewik, P.; Nowak, G.; Sowa-Kucma, M. Epigenetic marks and their relationship with BDNF in the brain of suicide victims. *PLoS ONE* **2020**, *15*, e0239335. [CrossRef] [PubMed]
94. Chen, K.-W.; Chen, L.Y. Epigenetic Regulation of BDNF Gene during Development and Diseases. *Int. J. Mol. Sci.* **2017**, *18*, 571. [CrossRef] [PubMed]
95. Zheng, Y.; Fan, W.D.; Zhang, X.Q.; Dong, E.B. Gestational stress induces depressive-like and anxiety-like phenotypes through epigenetic regulation of BDNF expression in offspring hippocampus. *Epigenetics* **2016**, *11*, 150–162. [CrossRef] [PubMed]

96. Seo, M.K.; Ly, N.N.; Lee, C.H.; Cho, H.Y.; Choi, C.M.; Nhu, L.H.; Lee, J.G.; Lee, B.J.; Kim, G.M.; Yoon, B.J.; et al. Early life stress increases stress vulnerability through BDNF gene epigenetic changes in the rat hippocampus. *Neuropharmacology* **2016**, *105*, 388–397. [CrossRef]
97. Su, C.L.; Su, C.W.; Hsiao, Y.H.; Gean, P.W. Epigenetic regulation of BDNF in the learned helplessness-induced animal model of depression. *J. Psychiatry Res.* **2016**, *76*, 101–110. [CrossRef]
98. Gassen, N.C.; Fries, G.R.; Zannas, A.S.; Hartmann, J.; Zschocke, J.; Hafner, K.; Carrillo-Roa, T.; Steinbacher, J.; Preissinger, S.N.; Hoeijmakers, L.; et al. Chaperoning epigenetics: FKBP51 decreases the activity of DNMT1 and mediates epigenetic effects of the antidepressant paroxetine. *Sci. Signal.* **2015**, *8*, ra119. [CrossRef]
99. Varela, R.B.; Resende, W.R.; Dal-Pont, G.C.; Gava, F.F.; Tye, S.J.; Quevedo, J.; Valvassori, S.S. HDAC inhibitors reverse mania-like behavior and modulate epigenetic regulatory enzymes in an animal model of mania induced by Ouabain. *Pharmacol. Biochem. Behav.* **2020**, *193*, 172917. [CrossRef]
100. Zocchi, L.; Sassone-Corsi, P. SIRT1-mediated deacetylation of MeCP2 contributes to BDNF expression. *Epigenetics* **2012**, *7*, 695–700. [CrossRef]
101. Duman, R.S.; Aghajanian, G.K.; Sanacora, G.; Krysta, J.H. Synaptic plasticity and depression: New insights from stress and rapid-acting antidepressants. *Nat. Med.* **2016**, *22*, 238–249. [CrossRef]
102. Uchida, S.; Yamagata, H.; Seki, T.; Watanabe, Y. Epigenetic mechanisms of major depression: Targeting neuronal plasticity. *Psychiatry Clin. Neurosci.* **2018**, *72*, 212–227. [CrossRef] [PubMed]
103. Pena, C.J.; Bagot, R.C.; Labonte, B.; Nestler, E.J. Epigenetic Signaling in Psychiatric Disorders. *J. Mol. Biol.* **2014**, *426*, 3389–3412. [CrossRef] [PubMed]
104. Labonte, B.; Engmann, O.; Purushothaman, I.; Menard, C.; Wang, J.S.; Tan, C.F.; Scarpa, J.R.; Moy, G.; Loh, Y.H.E.; Cahill, M.; et al. Sex-specific transcriptional signatures in human depression. *Nat. Med.* **2017**, *23*, 1102–1111. [CrossRef] [PubMed]
105. de Kloet, E.R.; Oitzl, M.S.; Joels, M. Stress and cognition: Are corticosteroids good or bad guys? *Trends Neurosci.* **1999**, *22*, 422–426. [CrossRef]
106. Guan, Z.H.; Giustetto, M.; Lomvardas, S.; Kim, J.H.; Miniaci, M.C.; Schwartz, J.H.; Thanos, D.; Kandel, E.R. Integration of Long-Term-Memory-Related Synaptic Plasticity Involves Bidirectional Regulation of Gene Expression and Chromatin Structure. *Cell* **2002**, *111*, 483–493. [CrossRef]
107. Levenson, J.M.; O’Riordan, K.J.; Brown, K.D.; Trinh, M.A.; Molfese, D.L.; Sweatt, J.D. Regulation of Histone Acetylation during Memory Formation in the Hippocampus. *J. Biol. Chem.* **2004**, *279*, 40545–40559. [CrossRef]
108. Guan, J.-S.; Haggarty, S.J.; Giacometti, E.; Dannenberg, J.-H.; Joseph, N.; Gao, J.; Nieland, T.J.F.; Zhou, Y.; Wang, X.; Mazitschek, R.; et al. HDAC2 negatively regulates memory formation and synaptic plasticity. *Nature* **2009**, *459*, 55–60. [CrossRef]
109. Bolger, T.A.; Yao, T.P. Intracellular trafficking of histone deacetylase 4 regulates neuronal cell death. *J. Neurosci.* **2005**, *25*, 9544–9553. [CrossRef]
110. Chen, B.; Cepko, C.L. HDAC4 Regulates Neuronal Survival in Normal and Diseased Retinas. *Science* **2009**, *323*, 256–259. [CrossRef]
111. Sando, R.; Gounko, N.; Pieraut, S.; Liao, L.J.; Yates, J.; Maximov, A. HDAC4 Governs a Transcriptional Program Essential for Synaptic Plasticity and Memory. *Cell* **2012**, *151*, 821–834. [CrossRef] [PubMed]
112. Kim, M.S.; Akhtar, M.W.; Adachi, M.; Mahgoub, M.; Bassel-Duby, R.; Kavalali, E.T.; Olson, E.N.; Monteggia, L.M. An Essential Role for Histone Deacetylase 4 in Synaptic Plasticity and Memory Formation. *J. Neurosci.* **2012**, *32*, 10879–10886. [CrossRef]
113. Campbell, R.R.; Kramar, E.A.; Pham, L.; Beardwood, J.H.; Augustynski, A.S.; Lopez, A.J.; Chitnis, O.S.; Delima, G.; Banihani, J.; Matheos, D.P.; et al. HDAC3 Activity within the Nucleus Accumens Regulates Cocaine-Induced Plasticity and Behavior in a Cell-Type-Specific Manner. *J. Neurosci.* **2021**, *41*, 2814–2827. [CrossRef] [PubMed]
114. Schmaal, L.; Pozzi, E.; Ho, T.C.; van Velzen, L.S.; Veer, I.M.; Opel, N.; Van Someren, E.J.W.; Han, L.K.M.; Aftanas, L.; Aleman, A.; et al. ENIGMA MDD: Seven years of global neuroimaging studies of major depression through worldwide data sharing. *Transl. Psychiatry* **2020**, *10*, 172. [CrossRef]
115. Erjavec, G.N.; Sagud, M.; Perkovic, M.N.; Strac, D.S.; Konjevod, M.; Tudor, L.; Uzun, S.; Pivac, N. Depression: Biological markers and treatment. *Prog. Neuro Psychopharmacol. Biol. Psychiatry* **2021**, *105*, 110139. [CrossRef]
116. Gadad, B.S.; Jha, M.K.; Czysz, A.; Furman, J.L.; Mayes, T.L.; Emslie, M.P.; Trivedi, M.H. Peripheral biomarkers of major depression and antidepressant treatment response: Current knowledge and future outlooks. *J. Affect. Disord.* **2018**, *233*, 3–14. [CrossRef] [PubMed]
117. Le-Niculescu, H.; Roseberry, K.; Gill, S.S.; Levey, D.F.; Phalen, P.L.; Mullen, J.; Williams, A.; Bhairo, S.; Voegtline, T.; Davis, H.; et al. Precision medicine for mood disorders: Objective assessment, risk prediction, pharmacogenomics, and repurposed drugs. *Mol. Psychiatry* **2021**, 1–29. [CrossRef]
118. Himmerich, H.; Milenovic, S.; Fulda, S.; Plumakers, B.; Sheldrick, A.J.; Michel, T.M.; Kircher, T.; Rink, L. Regulatory T cells increased while IL-1 beta decreased during antidepressant therapy. *J. Psychiatr. Res.* **2010**, *44*, 1052–1057. [CrossRef] [PubMed]
119. Cattaneo, A.; Gennarelli, M.; Uher, R.; Breen, G.; Farmer, A.; Aitchison, K.J.; Craig, I.W.; Anacker, C.; Zunsztain, P.A.; McGuffin, P.; et al. Candidate Genes Expression Profile Associated with Antidepressants Response in the GENDEP Study: Differentiating between Baseline ‘Predictors’ and Longitudinal ‘Targets’. *Neuropsychopharmacology* **2013**, *38*, 377–385. [CrossRef]

120. Cattaneo, A.; Ferrari, C.; Uher, R.; Bocchio-Chiavetto, L.; Riva, M.A.; Pariante, C.M. Absolute Measurements of Macrophage Migration Inhibitory Factor and Interleukin-1-beta mRNA Levels Accurately Predict Treatment Response in Depressed Patients. *Int. J. Neuropsychoph.* **2016**, *19*, pyw045. [CrossRef]
121. Belzeaux, R.; Lin, R.X.; Ju, C.; Chay, M.A.; Fiori, L.M.; Lutz, P.E.; Turecki, G. Transcriptomic and epigenomic biomarkers of antidepressant response. *J. Affect. Disord.* **2018**, *233*, 36–44. [CrossRef]
122. Le-Niculescu, H.; Kurian, S.M.; Yehyawji, N.; Dike, C.; Patel, S.D.; Edenberg, H.J.; Tsuang, M.T.; Salomon, D.R.; Nurnberger, J.I., Jr.; Niculescu, A.B. Identifying blood biomarkers for mood disorders using convergent functional genomics. *Mol. Psychiatry* **2009**, *14*, 156–174. [CrossRef] [PubMed]
123. Buch, A.M.; Liston, C. Dissecting diagnostic heterogeneity in depression by integrating neuroimaging and genetics. *Neuropsychopharmacology* **2021**, *46*, 156–175. [CrossRef] [PubMed]
124. Miller, E.K.; Cohen, J.D. An Integrative Theory of Prefrontal Cortex Function. *Annu. Rev. Neurosci.* **2001**, *24*, 167–202. [CrossRef] [PubMed]
125. Mueller, T.M.; Meador-Woodruff, J.H. Post-translational protein modifications in schizophrenia. *NPJ Schizophr.* **2020**, *6*, 1–16. [CrossRef]
126. Jovanova, O.S.; Nedeljkovic, I.; Spieler, D.; Walker, R.M.; Liu, C.Y.; Luciano, M.; Bressler, J.; Brody, J.; Drake, A.J.; Evans, K.L.; et al. DNA Methylation Signatures of Depressive Symptoms in Middle-aged and Elderly Persons Meta-analysis of Multiethnic Epigenome-wide Studies. *JAMA Psychiatry* **2018**, *75*, 949–959. [CrossRef]
127. Li, M.; D’Arcy, C.; Li, X.; Zhang, T.; Joobar, R.; Meng, X. What do DNA methylation studies tell us about depression? A systematic review. *Transl. Psychiatry* **2019**, *9*, 68. [CrossRef]
128. Lopez, J.P.; Mamdani, F.; Labonte, B.; Beaulieu, M.M.; Yang, J.P.; Berlim, M.T.; Ernst, C.; Turecki, G. Epigenetic regulation of BDNF expression according to antidepressant response. *Mol. Psychiatry* **2013**, *18*, 398–399. [CrossRef]
129. Iga, J.; Ueno, S.; Yamauchi, K.; Numata, S.; Kinouchi, S.; Tayoshi-Shibuya, S.; Song, H.W.; Ohmori, T. Altered HDAC5 and CREB mRNA expressions in the peripheral leukocytes of major depression. *Prog. Neuro Psychopharmacol. Biol. Psychiatry* **2007**, *31*, 628–632. [CrossRef]
130. Nasca, C.; Bigio, B.; Lee, F.S.; Young, S.P.; Kautz, M.M.; Albright, A.; Beasley, J.; Millington, D.S.; Mathé, A.A.; Kocsis, J.H.; et al. Acetyl-L-carnitine deficiency in patients with major depressive disorder. *Proc. Natl. Acad. Sci. USA* **2018**, *115*, 8627–8632. [CrossRef]
131. Wey, H.-Y.; Wang, C.; Schroeder, F.A.; Logan, J.; Price, J.C.; Hooker, J.M. Kinetic Analysis and Quantification of [11C]Martinostat for in Vivo HDAC Imaging of the Brain. *ACS Chem. Neurosci.* **2015**, *6*, 708–715. [CrossRef]
132. Wey, H.Y.; Gilbert, T.M.; Zurcher, N.R.; She, A.; Bhanot, A.; Taillon, B.D.; Schroeder, F.A.; Wang, C.; Haggarty, S.J.; Hooker, J.M. Insights into neuroepigenetics through human histone deacetylase PET imaging. *Sci. Transl. Med.* **2016**, *8*, 351ra106. [CrossRef] [PubMed]
133. Gilbert, T.M.; Zürcher, N.R.; Wu, C.J.; Bhanot, A.; Hightower, B.G.; Kim, M.; Albrecht, D.S.; Wey, H.-Y.; Schroeder, F.A.; Rodriguez-Thompson, A.; et al. PET neuroimaging reveals histone deacetylase dysregulation in schizophrenia. *J. Clin. Investig.* **2019**, *129*, 364–372. [CrossRef] [PubMed]
134. Tseng, C.-E.J.; Gilbert, T.M.; Catanese, M.C.; Hightower, B.G.; Peters, A.T.; Parmar, A.J.; Kim, M.; Wang, C.; Roffman, J.L.; Brown, H.E.; et al. In vivo human brain expression of histone deacetylases in bipolar disorder. *Transl. Psychiatry* **2020**, *10*, 1–9. [CrossRef] [PubMed]
135. Toth, M. Epigenetic Neuropharmacology: Drugs Affecting the Epigenome in the Brain. *Annu. Rev. Pharmacol. Toxicol.* **2021**, *61*, 181–201. [CrossRef] [PubMed]
136. Elliott, E.; Ezra-Nevo, G.; Regev, L.; Neufeld-Cohen, A.; Chen, A. Resilience to social stress coincides with functional DNA methylation of the Crf gene in adult mice. *Nat. Neurosci.* **2010**, *13*, 1351–1353. [CrossRef]
137. Ookubo, M.; Kanai, H.; Aoki, H.; Yamada, N. Antidepressants and mood stabilizers effects on histone deacetylase expression in C57BL/6 mice: Brain region specific changes. *J. Psychiatry Res.* **2013**, *47*, 1204–1214. [CrossRef]
138. Deussing, J.M.; Jakovcevski, M. Histone Modifications in Major Depressive Disorder and Related Rodent Models. *Adv. Exp. Med. Biol.* **2017**, *978*, 169–183. [CrossRef]
139. Fuchikami, M.; Yamamoto, S.; Morinobu, S.; Okada, S.; Yamawaki, Y.; Yamawaki, S. The potential use of histone deacetylase inhibitors in the treatment of depression. *Prog. Neuro Psychopharmacol. Biol. Psychiatry* **2016**, *64*, 320–324. [CrossRef]
140. Uchida, S.; Hara, K.; Kobayashi, A.; Otsuki, K.; Yamagata, H.; Hobara, T.; Suzuki, T.; Miyata, N.; Watanabe, Y. Epigenetic Status of Gdnf in the Ventral Striatum Determines Susceptibility and Adaptation to Daily Stressful Events. *Neuron* **2011**, *69*, 359–372. [CrossRef]
141. Golden, S.A.; Christoffel, D.J.; Heshmati, M.; Hodes, G.E.; Magida, J.; Davis, K.; Cahill, M.E.; Dias, C.; Ribeiro, E.; Ables, J.L.; et al. Epigenetic regulation of RAC1 induces synaptic remodeling in stress disorders and depression. *Nat. Med.* **2013**, *19*, 337–344. [CrossRef]
142. Han, A.; Sung, Y.-B.; Chung, S.-Y.; Kwon, M.-S. Possible additional antidepressant-like mechanism of sodium butyrate: Targeting the hippocampus. *Neuropharmacology* **2014**, *81*, 292–302. [CrossRef]
143. Sada, N.; Fujita, Y.; Mizuta, N.; Ueno, M.; Furukawa, T.; Yamashita, T. Inhibition of HDAC increases BDNF expression and promotes neuronal rewiring and functional recovery after brain injury. *Cell Death Dis.* **2020**, *11*, 1–15. [CrossRef] [PubMed]

144. Athira, K.V.; Madhana, R.M.; Bais, A.K.; Singh, V.B.; Malik, A.; Sinha, S.; Lahkar, M.; Kumar, P.; Samudrala, P.K. Cognitive Improvement by Vorinostat through Modulation of Endoplasmic Reticulum Stress in a Corticosterone-Induced Chronic Stress Model in Mice. *ACS Chem. Neurosci.* **2020**, *11*, 2649–2657. [CrossRef]
145. Ershadi, A.S.B.; Amini-Khoei, H.; Hosseini, M.-J.; Dehpour, A.R. SAHA Improves Depressive Symptoms, Cognitive Impairment and Oxidative Stress: Rise of a New Antidepressant Class. *Neurochem. Res.* **2021**, *46*, 1252–1263. [CrossRef] [PubMed]
146. Vinarskaya, A.K.; Balaban, P.M.; Roshchin, M.V.; Zuzina, A.B. Sodium butyrate as a selective cognitive enhancer for weak or impaired memory. *Neurobiol. Learn. Mem.* **2021**, *180*, 107414. [CrossRef] [PubMed]
147. Prince, H.M.; Bishton, M.J.; Harrison, S.J. Clinical Studies of Histone Deacetylase Inhibitors. *Clin. Cancer Res.* **2009**, *15*, 3958–3969. [CrossRef]
148. Subramanian, S.; Bates, S.E.; Wright, J.J.; Espinoza-Delgado, I.; Piekarz, R.L. Clinical Toxicities of Histone Deacetylase Inhibitors. *Pharmaceuticals* **2010**, *3*, 2751–2767. [CrossRef]
149. Majchrzak-Celinska, A.; Warych, A.; Szoszkiewicz, M. Novel Approaches to Epigenetic Therapies: From Drug Combinations to Epigenetic Editing. *Genes* **2021**, *12*, 208. [CrossRef]
150. Karnib, N.; El-Ghandour, R.; El Hayek, L.; Nasrallah, P.; Khalifeh, M.; Barmo, N.; Jabre, V.; Ibrahim, P.; Bilen, M.; Stephan, J.; et al. Lactate is an antidepressant that mediates resilience to stress by modulating the hippocampal levels and activity of histone deacetylases. *Neuropsychopharmacology* **2019**, *44*, 1152–1162. [CrossRef]
151. Wang, J.; Hodes, G.E.; Zhang, H.; Zhang, S.; Zhao, W.; Golden, S.A.; Bi, W.; Menard, C.; Kana, V.; Leboeuf, M.; et al. Epigenetic modulation of inflammation and synaptic plasticity promotes resilience against stress in mice. *Nat. Commun.* **2018**, *9*, 477. [CrossRef]



Article

Antitumor Activity and Mechanism of Action of Hormonotoxin, an LHRH Analog Conjugated to Dermaseptin-B2, a Multifunctional Antimicrobial Peptide

Mickael Couty ¹, Marie Dusaud ^{1,†}, Mickael Miro-Padovani ^{1,†}, Liuhui Zhang ^{1,†}, Patricia Zadigue ¹, Loussiné Zargarian ², Olivier Lequin ³, Alexandre de la Taille ¹, Jean Delbe ¹, Yamina Hamma-Kourbali ^{1,‡} and Mohamed Amiche ^{1,*}

¹ INSERM, Institut Mondor de Recherche Biomédicale, Université Paris Est Créteil, F-94010 Créteil, France; mickael.couty@inserm.fr (M.C.); marie.dussaud@gmail.com (M.D.);

mickael.miro-padovani@aphp.fr (M.M.-P.); quingfengxu0716@126.com (L.Z.); zadigue@gmail.com (P.Z.); adelataille@hotmail.com (A.d.l.T.); delbe@u-pec.fr (J.D.); hamma@u-pec.fr (Y.H.-K.)

² LBPA, CNRS UMR 8113 École Normale Supérieure Paris-Saclay, 4 Avenue des Sciences, 91190 Gif-sur-Yvette, France; loussine.zargarian@ens-cachan.fr

³ Sorbonne Université, École Normale Supérieure, PSL University, CNRS, Laboratoire des Biomolécules (LBM), 75005 Paris, France; olivier.lequin@upmc.fr

* Correspondence: mohamed.amiche@sorbonne-universite.fr

† These authors have contributed equally.

‡ Y.H.-K. and M.A. are joint senior authors.

§ Current Address: Sorbonne Université-CNRS, Institut de Biologie Paris-Seine, Laboratoire de Biogenèse des Signaux Peptidiques (BioSiPe), F-75252 Paris, France.

Citation: Couty, M.; Dusaud, M.; Miro-Padovani, M.; Zhang, L.; Zadigue, P.; Zargarian, L.; Lequin, O.; de la Taille, A.; Delbe, J.; Hamma-Kourbali, Y.; et al. Antitumor Activity and Mechanism of Action of Hormonotoxin, an LHRH Analog Conjugated to Dermaseptin-B2, a Multifunctional Antimicrobial Peptide. *Int. J. Mol. Sci.* **2021**, *22*, 11303. <https://doi.org/10.3390/ijms222111303>

Academic Editors: Andrzej Kutner, Geoffrey Brown and Enikő Kallay

Received: 15 September 2021

Accepted: 15 October 2021

Published: 20 October 2021

Publisher's Note: MDPI stays neutral with regard to jurisdictional claims in published maps and institutional affiliations.

Abstract: Prostate cancer is the most common cancer in men. For patients with advanced or metastatic prostate cancer, available treatments can slow down its progression but cannot cure it. The development of innovative drugs resulting from the exploration of biodiversity could open new therapeutic alternatives. Dermaseptin-B2, a natural multifunctional antimicrobial peptide isolated from Amazonian frog skin, has been reported to possess antitumor activity. To improve its pharmacological properties and to decrease its peripheral toxicity and lethality we developed a hormonotoxin molecule composed of dermaseptin-B2 combined with d-Lys⁶-LHRH to target the LHRH receptor. This hormonotoxin has a significant antiproliferative effect on the PC3 tumor cell line, with an IC₅₀ value close to that of dermaseptin-B2. Its antitumor activity has been confirmed in vivo in a xenograft mouse model with PC3 tumors and appears to be better tolerated than dermaseptin-B2. Biophysical experiments showed that the addition of LHRH to dermaseptin-B2 did not alter its secondary structure or biological activity. The combination of different experimental approaches indicated that this hormonotoxin induces cell death by an apoptotic mechanism instead of necrosis, as observed for dermaseptin-B2. These results could explain the lower toxicity observed for this hormonotoxin compared to dermaseptin-B2 and may represent a promising targeting approach for cancer therapy.

Keywords: anticancer drug; antimicrobial peptide (AMP); dermaseptin; frog skin peptides; LHRH; prostate cancer; *Phyllomedusa bicolor*; therapeutic peptides



Copyright: © 2021 by the authors. Licensee MDPI, Basel, Switzerland. This article is an open access article distributed under the terms and conditions of the Creative Commons Attribution (CC BY) license (<https://creativecommons.org/licenses/by/4.0/>).

1. Introduction

Prostate cancer (PCa) is the second most frequent cancer diagnosis made in men and was the fifth leading cause of death worldwide in 2018 [1]. For most men with PCa, their disease will follow an indolent course. The 5-year survival rates are encouraging: 98% and 83% in the USA and Europe, respectively [2]. Localized PCa may be cured with surgery or radionuclide therapy; however, the disease recurs in approximately 20% to 30% of men treated for localized PCa and advanced disease is associated with poor outcomes. Concerning chemotherapy, the current standard treatment for hormone sensitive metastatic PCa is

androgen deprivation by luteinizing hormone-releasing hormone (LHRH) agonists or antagonists that induce castration by blocking the gonadotropic axis. Although most men with metastatic PCa initially respond to this androgen-deprivation therapy (ADT), inevitably their cancer progresses on this treatment to a disease state known as castration-resistant prostate cancer (CRPC). Despite the appearance of a panel of new therapies in this indication since 2010, such as second-generation hormone therapy (abiraterone, enzalutamide), taxane-based chemotherapy (docetaxel, cabazitaxel), immunotherapy (sipuleucel-T), targeted therapy (ipilimumab, an anti-CTLA-4 antibody) and metabolic radiotherapy (Ra-223) for men with bone metastasis, the median survival for men with metastatic castration-resistant prostate cancer (mCRPC) is less than 2 years [2]. In this context, the development of innovative therapies therefore represents a major challenge in the hope of offering to patients a more effective treatment, combining low toxicity, and reduced side effects and resistance associated with conventional therapies.

Among these new molecules, those from biodiversity could represent a particular interest. A group of interesting peptides from natural sources are antimicrobial peptides (AMPs) [3]. Indeed, in recent years, an increasing number of articles show that these AMPs are in fact multifunctional peptides such as anticancer agents, immunomodulators, chemokines, vaccine adjuvants, or regulators of innate defense [4–6]. From this group of AMPs, the cationic antimicrobial peptides (CAPs) offer a concrete development path derived from biodiversity. Characterized for nearly thirty years, they were initially studied for their antimicrobial virtues. Indeed, a growing number of studies have shown that some of these peptides, which are toxic to bacteria but not to normal mammalian cells, have a broad spectrum of cytotoxic activity against cancer cells. Electrostatic interactions between the positive charges carried by CAPs and the anionic components of cell membranes are considered to be the major elements involved in the selective destruction of cancer cells [7]. Among CAPs, dermaseptins B2 and B3 (DRS-B2 and DRS-B3) are two natural antimicrobial peptides isolated from the skin of an Amazonian tree frog of the genus *Phyllomedusa bicolor* [8,9]. Our team initially reported significant antitumor activity of DRS-B2 and DRS-B3 on various human cell lines including prostate cancer, while they had no effect on normal cells [5,10]. Furthermore, the antitumor activity of DRS-B2 was confirmed in vivo in a PC3 prostatic tumor cell line xenografted in an athymic mouse model. Treatment with DRS-B2 at 2.5 mg/kg body weight six times a week in peritumoral mice reduced the tumor growth 50% after 35 days. Concerning the mechanism of action of DRS-B2, our previous studies suggested a rapid mechanism of cell death, with aggregation at the plasma membrane of cancer cells and penetration into the cytoplasm and the nucleus [5,11].

These polycationic peptides, that appear to interact and specifically cross the membrane of the tumor cells, with no effect on normal cells, represent an innovative technological platform for the development and design of original molecules that can be used in the targeted treatment of cancers resistant to current therapies. However, its use in vivo could raise the problem of significant toxicity regarding the doses used. To reduce the toxicity of the pharmacological molecule, a targeted therapy could represent a promising way. The concept of a hormonotoxin (H-B2) was born from this problem, based on tumor targeting by associating DRS-B2 with a hormone (H), the receptor of which is overexpressed on the tumor surface. This concept is related to the immunotoxin approach, which combines a toxin with a monoclonal antibody [12]. The specific interaction of the ligand with its receptor would ideally allow targeting of tumor cells, while optimizing the interaction of the peptide with the membrane. The advantage of peptides is the simplicity of their production by chemical synthesis. Numerous studies have shown that many membrane receptors are overexpressed on the surface of cancer cells and that there are natural or synthetic peptide ligands (agonists or antagonists) that bind to them with very good affinity and selectivity [13]. This is the case for the luteinizing hormone-releasing hormone receptor (LHRH-R), the expression rate of which is greater than 80% in endometrial, ovarian and prostate cancer cells [14]. Available data strongly suggest that about 91% of prostate cancers express LHRH-R high-affinity binding sites [15]. In these cancers, in vitro proliferation

may be inhibited by analogs of LHRH in a dose- and time-dependent manner [15–17]. As a result, LHRH-R appears to be an ideal target for the development of personalized therapeutic treatment of various human cancers. An example is the fusion of LHRH or its analogs with various bacterial and plant toxins that have been used to target and kill cancer cells expressing LHRH receptors [18–22].

In this paper we report the design and synthesis of the chimeric peptide H-B2, a molecule composed of dermaseptin-B2 coupled to an LHRH analog, and studies of its structure and biological activities *in vitro* and *in vivo*, as well as deciphering its antitumor mechanism of action.

2. Results

The hormonotoxin H-B2 and DRS-B2 induce a significant antiproliferative effect on the hormone-resistant prostate tumor cell line PC3 and have low hemolytic activity.

In this study we used four different prostate cell lines (PC3, DU145, 22RV1 and BPH-1) which are presented in Table 1.

Table 1. List of cell lines and their characteristics.

Cell Line	Characteristics
PC3	Adenocarcinoma derived from bone metastasis
DU145	Adenocarcinoma derived from brain metastasis
22Rv1	Adenocarcinoma derived from a PCa primary tumor that was serially transplanted in nude mice.
BPH-1	Benign Prostatic Hyperplasia Cell Line

The PC3, DU145, and 22Rv1 cell lines were used as models for androgen-independent prostate cancer. PC3 and DU145 were derived from bone and brain metastasis, respectively. The 22Rv1 cell line was originally derived from the primary site of an advanced PCa that was serially transplanted in nude mice, and BPH-1 is a prostatic hyperplastic cell line. The primary structure of the synthetic hormonotoxin H-B2 is shown in Figure 1 and its RP-HPLC profile and ESI-MS spectra are reported in the Supplementary Materials (Figure S1A,B).

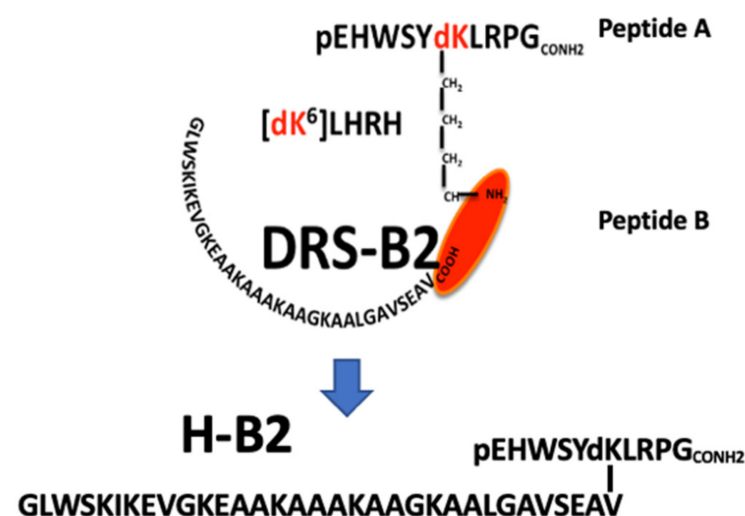


Figure 1. Synthesis of the chimeric H-B2 peptide. Primary structure of the hormonotoxin [D-Lys⁶]-LHRH-dermaseptin B2 (H-B2). The amino acid sequence of dermaseptin B2 is represented as peptide B and the amino sequence of the LHRH analog with a D-Lys (dK) in position 6 is represented as peptide A.

The effect of synthetic H-B2 and DRS-B2 after 48 h of treatment was evaluated on different prostate cell lines. Results show that the viability of all cell lines was reduced dose-dependently by DRS-B2 and H-B2 (Figure 2).

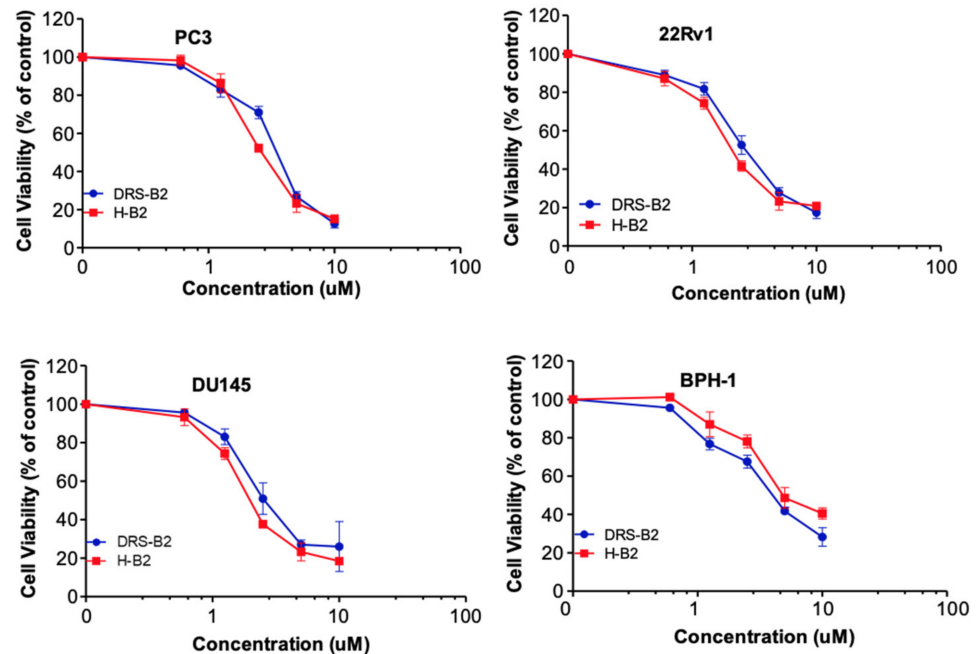


Figure 2. Sensitivity of human PCa cell lines to H-B2 is dependent on LHRH-R expression. The dose-response effect of H-B2 and DRS-B2 (0.1 to 100 μM) on the cell viability of PC3, DU145, 22Rv1 and BPH-1 cells was evaluated using MTT assay. The 100% of cell viability corresponds to cells without treatment.

The concentrations of peptides required to inhibit cell proliferation by 50% (IC_{50}) are reported in Table 2.

Table 2. Comparison of the IC_{50} of H-B2 and DRS-B2 extracted from Figure 1, on the different cell lines.

Cell Lines	IC_{50} (μM)	
	DRS-B2	H-B2
PC3	3.93	2.95
DU145	2.64	2.01
22RV1	2.75	2.23
BPH1	4.05	4.64

Since PC3 cells present a relatively good sensitivity to H-B2 and DRS-B2, we decided to use this cell line for further investigations concerning the in vivo study of H-B2 and exploration of its antiproliferative mechanism of action.

Since CAPs could present hemolytic activity, H-B2 and DRS-B2 were tested on human red blood cells. The hemolytic activity was determined by incubation of DRS-B2 or H-B2 at different doses with human erythrocytes. In parallel, the erythrocytes were incubated in the presence of 0.2% (*v/v*) Triton representing the positive control (100% hemolysis). Results presented in Figure 3 show that DRS-B2 and H-B2 have low hemolytic activity.

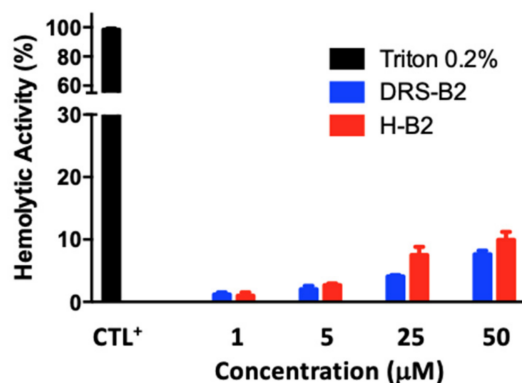


Figure 3. Hemolytic activity of DRS-B2 and H-B2 on human erythrocytes. Human erythrocytes were cultured with different concentrations of DRS-B2 or H-B2 for 1 h at 37 °C. Cells treated with 0.2% Triton X100 were used as a positive control (CTL⁺) and correspond to 100% of the hemolytic activity used as reference.

Indeed, while some cationic antimicrobial peptides show hemolytic activity, DRS-B2 and H-B2 do not cause more than 10% hemolysis at the highest doses tested (50 μM) and could be considered as low cytotoxicity peptides. This finding is encouraging and essential for in vivo testing and for potential therapeutic use.

2.1. Hormonotoxin H-B2 Significantly Inhibits Tumor Growth in Xenografted Mice without Measurable Side Effects

To investigate the antitumor efficacy of H-B2, we performed in vivo experiments using xenografted PC3 tumor cells in nude mice. Fourteen days after injection of PC3 cells, tumors of around 100 mm³ developed. The mice were then randomized into four groups ($n = 6$ mice/group) and treated by IP injection of 2.5 and 5 mg/kg of H-B2 or 2.5 mg/kg of DRS-B2 or vehicle, three times per week for five weeks. The results showed that H-B2 inhibited PC3 tumor growth in a dose-dependent manner (Figure 4). The inhibition of the tumor growth was about 35% and 54% when mice were treated with H-B2 at 2.5 mg/kg and 5 mg/kg, respectively (Figure 4A). At the dose of 2.5 mg/kg, H-B2 had a better antitumor effect (35%) than DRS-B2 (26%) (Figure 4A). Similar results were obtained by analyzing the weights of tumors harvested from tumor-bearing mice (Figure 4B).

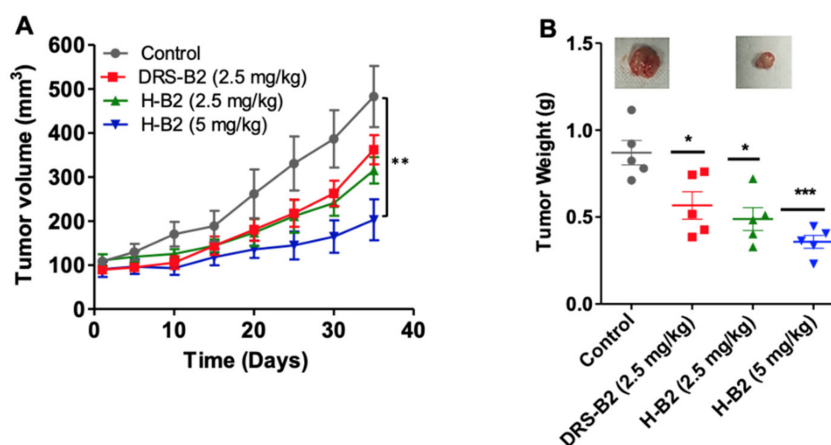


Figure 4. Effect of DRS-B2 and H-B2 on tumor growth in vivo. Nude mice were subcutaneously injected with PC3 cells and treatments began after the xenograft tumor reached 100 mm³. Mice were treated twice a week intraperitoneally with PBS (Control), DRS-B2 (2.5 mg/kg) or H-B2 at 2.5 mg/kg or 5 mg/kg. (A) Effect of tumor volume versus time of treatment. (B) Tumor weight after sacrifice of mice. Data are presented as mean \pm SEM. Differences were considered significant at $p < 0.05$ (*), $p < 0.01$ (**) and $p < 0.001$ (***).

To further define the effect of H-B2 on tumor proliferation in vivo, Ki67 labeling was performed on tumor sections from each group. As shown in Figure 5, the proliferation index was significantly inhibited in H-B2-treated mice (35% inhibition at 2.5 mg/kg and 68% at 5 mg/kg) as compared to the control group.

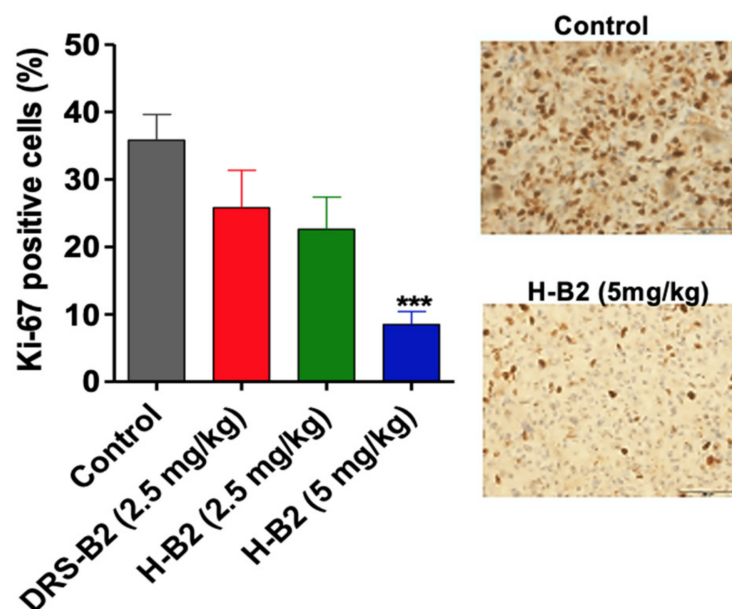


Figure 5. Effect of DRS-B2 and H-B2 on tumor proliferation in vivo. PC3 tumor proliferation was evaluated by Ki67 staining of frozen tissue sections. Proliferation was quantified by image J software analysis of Ki67 positive stained cells on the whole tumor section. The data are mean areas \pm SEM, $p < 0.001$ (***) . Representative tumor section, scale bar, 50 μ m.

Taken together, these results indicate that H-B2 has a better antitumor effect than DRS-B2 and less toxicity in mice (data not shown).

2.2. Mechanism of Antitumor Action of the Hormonotoxin H-B2 in Comparison with DRS-B2

The mechanism of antitumor action of these two peptides was addressed by studying, on the one hand, their bioactive structure by three spectroscopic approaches: CD, fluorescence, and 2D-NMR in the presence of micelles mimicking the plasma membranes of the target cells; and on the other hand, by measuring: the cell viability after double annexin V-FITC and PI staining, the cytotoxic activity by measuring the cytoplasmic LDH released, and the DNA fragmentation induced by these peptides.

Addition of the hormonal analog (d-Lys⁶-LHRH) to DRS-B2 did not alter the secondary structure of the hormonotoxin H-B2.

Preliminary indications of the secondary structures of these peptides, obtained by CD measurements in PBS and in zwitterionic detergent (DPC) at different concentrations, are shown in Figure 6.

The CD spectrum of DRS-B2 and H-B2 in PBS buffer showed that these peptides have very little ordered structure. However, there is a clear change in the spectra of these two peptides as soon as the critical micellar concentration (CMC) of DPC is reached (Figure 6(A1) for DRS-B2 and Figure 6(B1) for H-B2) that indicates an enhanced helical content, with minima at 208 and 222 nm. Deconvolution of the spectra allows us to quantify the relative proportions of the secondary structures of our peptides. Thus, in the absence of micelles in the medium, the observed α -helix ratio is about 11% for DRS-B2 and 10% for HB2 as shown in Figure 6(A2) and Figure 6(B1), respectively. When the concentration of DPC is increased to 5 mM, the α -helicity rates then reach 25% and 55% for H-B2 and DRS-B2, respectively.

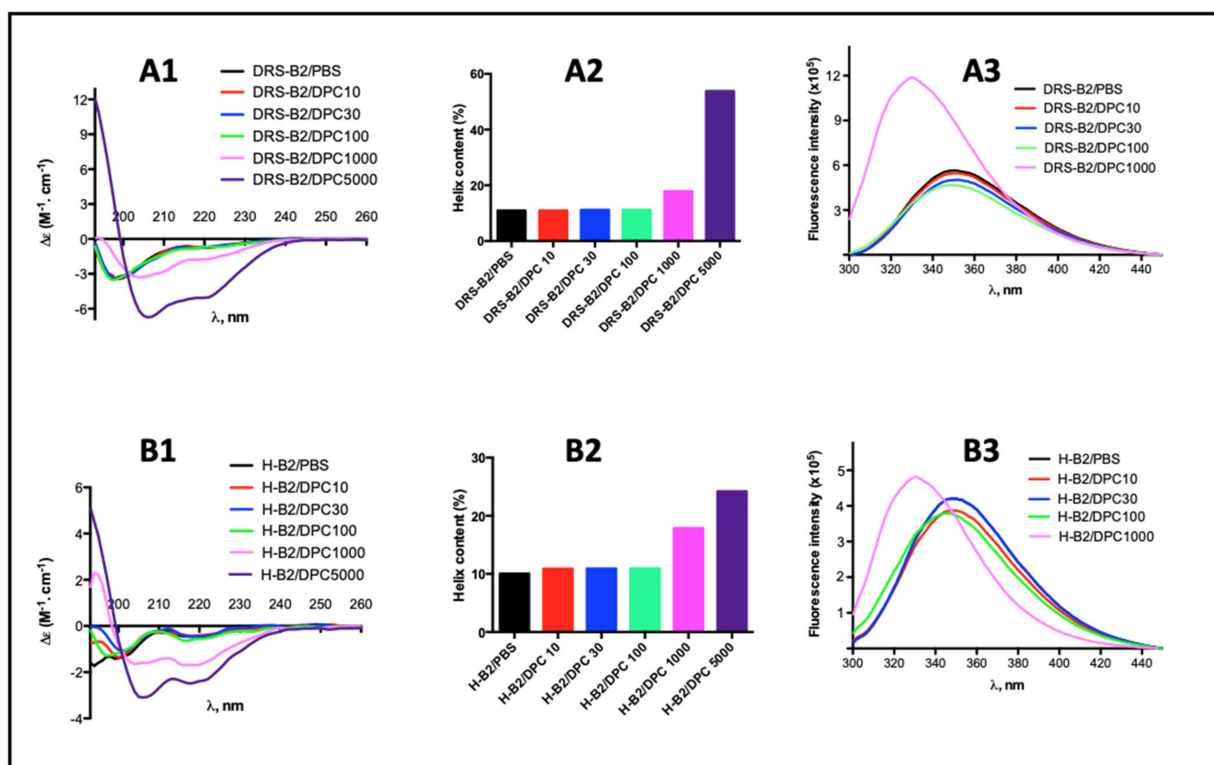


Figure 6. Circular dichroism and fluorescence spectra of DRS-B2 (A1,A3) and H-B2 (B1,B3) alone in PBS or in the presence of increasing concentration of DPC. (A2,B2) represent the percent of helix content in DRS-B2 and H-B2, alone or in presence of an increasing concentration of DPC, respectively.

The presence of a W residue in the sequence of DRS-B2 and H-B2 allows us to study the influence of the microenvironment on the structure of these two peptides. Indeed, the fluorescence emission maximum of W is between 320 and 355 nm when excited at 290 nm, and the maximum emission wavelength reflects the exposure of W to the solvent. This fluorescence is measured in an aqueous solution (PBS 1x) for observation in a nonstructural environment (the peptide does not form an α -helix in water) and in a micellar solution to study the effect of a lipid-like microenvironment (Figure 6(A3,B3)). We observe that beyond 1 mM, which is the CMC of DPC, the fluorescence emission maxima of DRS-B2 and H-B2 shift to shorter wavelengths (“blue shift”) and show a strong increase in fluorescence intensity (hyperchromic shift). These spectral changes reflect a change from a hydrophilic to hydrophobic environment that can be explained either by the burial of the W residue within the hydrophobic layers of DPC micelles, or by burying the W after folding of the peptide following conformational changes.

Finally, the structure of H-B2 was investigated using NMR in a micellar DPC solution. This technique allows a direct analysis of peptide conformation and flexibility at the residue level. For each residue of the peptide chain, the chemical shift deviation (CSD) of the H α protons were calculated (Figure 7A).

This corresponds to the difference between the observed chemical shift of the H α protons and the “random coil” chemical shift (obtained in the absence of structuring and corresponding to values taken from a library of short unstructured peptides). CSD values which deviate from 0 ppm (< -0.1 or $> +0.1$ ppm) are typically used to detect the presence of secondary structures. In the DRS-B2 portion of hormonotoxin H-B2, most residues exhibit significantly negative H α CSD values (average -0.23 ppm), indicating the presence of stable helical conformations, as evidenced by CD. H-B2 forms an α -helix along virtually the entire length of the DRS-B2 part (residues 2–31), with greater stability in the first half of the helix. The CSD values are very close to those observed for DRS-B2 alone, proving that the C-terminal attachment of the LHRH segment does not affect the helical structure of

the DRS-B2 segment. On the other hand, the LHRH segment appears to be less structured, with possibly the formation of turn structures.

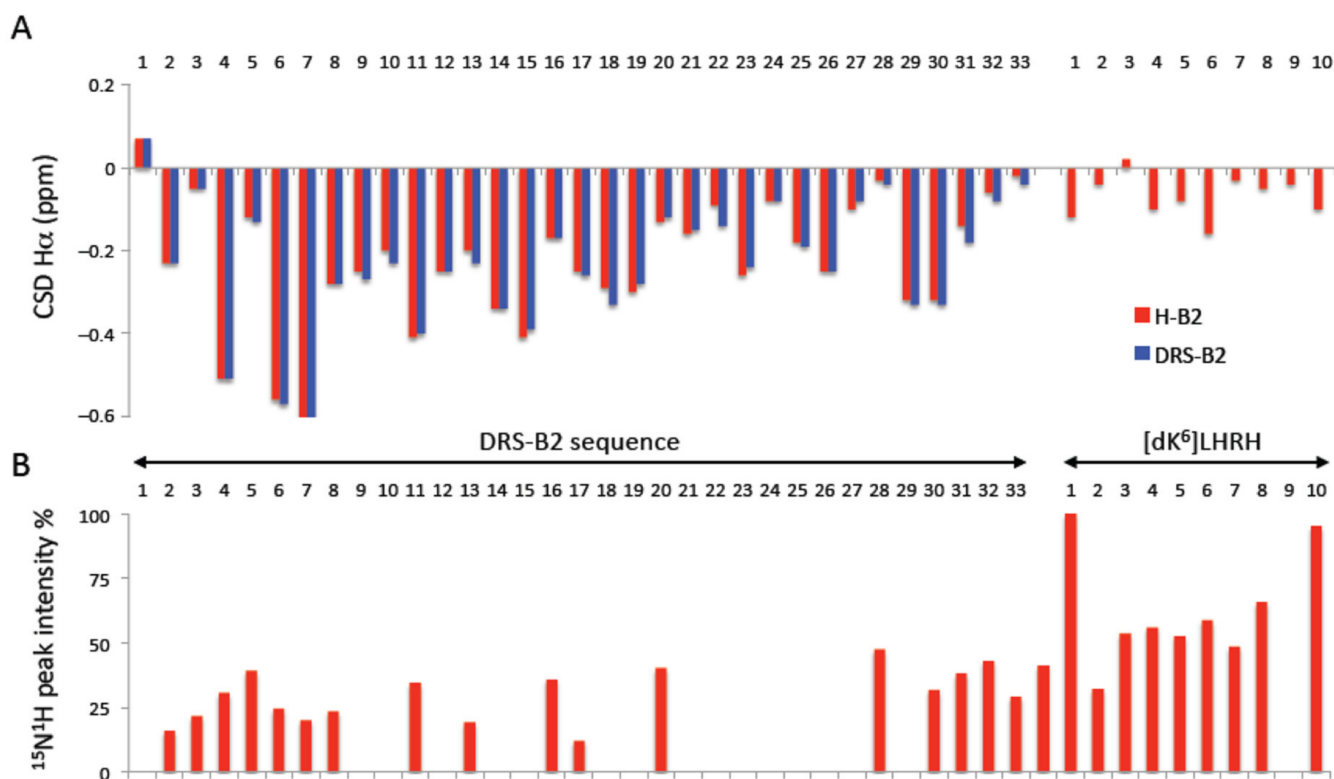


Figure 7. Structure of H-B2 and DRS-B2 analyzed by NMR. (A) Chemical shift deviations (CSDs) of H α protons of DRS-B2 and H-B2 in the presence of DPC. The CSD values were calculated as the difference between observed chemical shifts and random coil chemical shifts. (B) Intensity of ^{15}N - ^1H peaks on 2D ^{15}N - ^1H HSQC. The intensities were normalized to the highest intensity peak. Only well resolved, unambiguously assigned peaks were considered.

The linewidth of HN protons was also analyzed by measuring the intensity of ^{15}N - ^1H cross peaks on the natural abundance ^{15}N - ^1H 2D HSQC spectrum (Figure 7B). The proton linewidth is influenced by peptide dynamics and interaction with the larger molecular weight DPC micelle. The LHRH segment shows a different behavior from the DRS-B2 segment in H-B2, with stronger ^{15}N - ^1H cross peak intensities. This shows that the LHRH segment is more dynamic and does not appear to strongly interact with the micelle.

2.3. The Cell Death Induced by H-B2 and DRS-B2 Uses Two Different Mechanisms That Are Related to Apoptosis and Necrosis, Respectively

To obtain more information about how H-B2 acts on PC3 tumor cells, the antiproliferative mechanism of action of this peptide was studied in comparison with that of DRS-B2. Since the known antiproliferative effect of DRS-B2 on tumor cells resemble more of a membrane killing-like effect, experiments concerning the cytotoxic effect, and the induction of apoptosis or necrosis were investigated with H-B2 in comparison with DRS-B2.

A key feature of cells undergoing apoptosis, necrosis, and other forms of cellular damage could be analyzed by measuring the activity of cytoplasmic lactate dehydrogenase (LDH) released by damaged cells. Previously, we have shown that DRS-2 increased this release [11]. Thus, PC3 cells were treated with different concentrations (1, 5, 7.5 and 10 μM) of H-B2 or DRS-B2 for 24 h and the amount of released cytoplasmic LDH into the medium was measured (Figure 8).

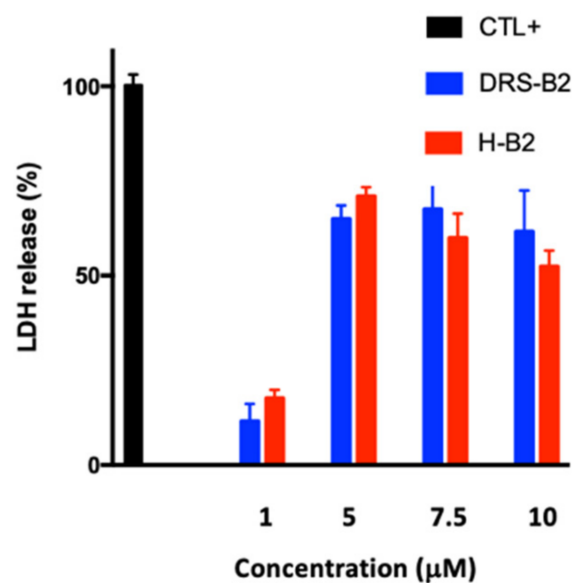


Figure 8. Cytotoxic effect of DRS-B2 on PC3. Twenty-four hours after plating, PC3 cells were single treated with different concentrations of DRS-B2 or H-B2. Triton X100 at 0.9% (*v/v*) was used as an internal positive control. LDH release was measured with a CytoTox 96 kit. Results are expressed in percentage of cytotoxicity versus time of treatment in hours. Results represent the mean \pm SEM of three determinations.

Cells treated with Triton X100 0.9% (*v/v*) were used as an internal positive control. The results show a low release of cytoplasmic LDH when the PC3 cells are treated with 1 μ M of H-B2 or DRS-B2, with 15% and 10% release, respectively. The LDH release is maximal upon addition of 5 μ M or higher doses of these peptides. However, this maximum release was limited to 65–70%. These data suggested that the cytotoxic effect of H-B2 on PC3 cells is comparable to that of DRS-B2.

To further characterize the effect of H-B2 and DRS-B2 on cell death in PC3 cells, we first examined the viability of cells treated with these peptides by flow cytometry using annexin V-FITC and PI double staining of the cells. As shown in Figure 9, flow cytometry analysis showed that H-B2 promoted cell apoptosis in a dose-dependent manner.

Histogram of each population obtained by flow cytometry in the different conditions are presented in the Supplementary Materials (Figure S2) and the percentages of cells in each population are reported in the Table 3.

Table 3. Percentage of PC3 cells in each population extracted from Figure 9.

PC3 (%)	NT	H ₂ O ₂	DRS-B2 (μ M)			H-B2 (μ M)		
			1	2.5	5	1	2.5	5
AV-/PI-	93.9	16.1	91.9	83.7	76.9	84.1	72.2	22.8
AV+/PI-	1.09	63.5	1.44	3.88	9.53	3.81	15.3	63.3
AV+/PI+	4.82	20.2	5.99	12.1	12.8	11.6	11.9	11.5
AV-/PI+	0.2	0.42	0.68	0.42	0.81	0.49	0.64	2.45

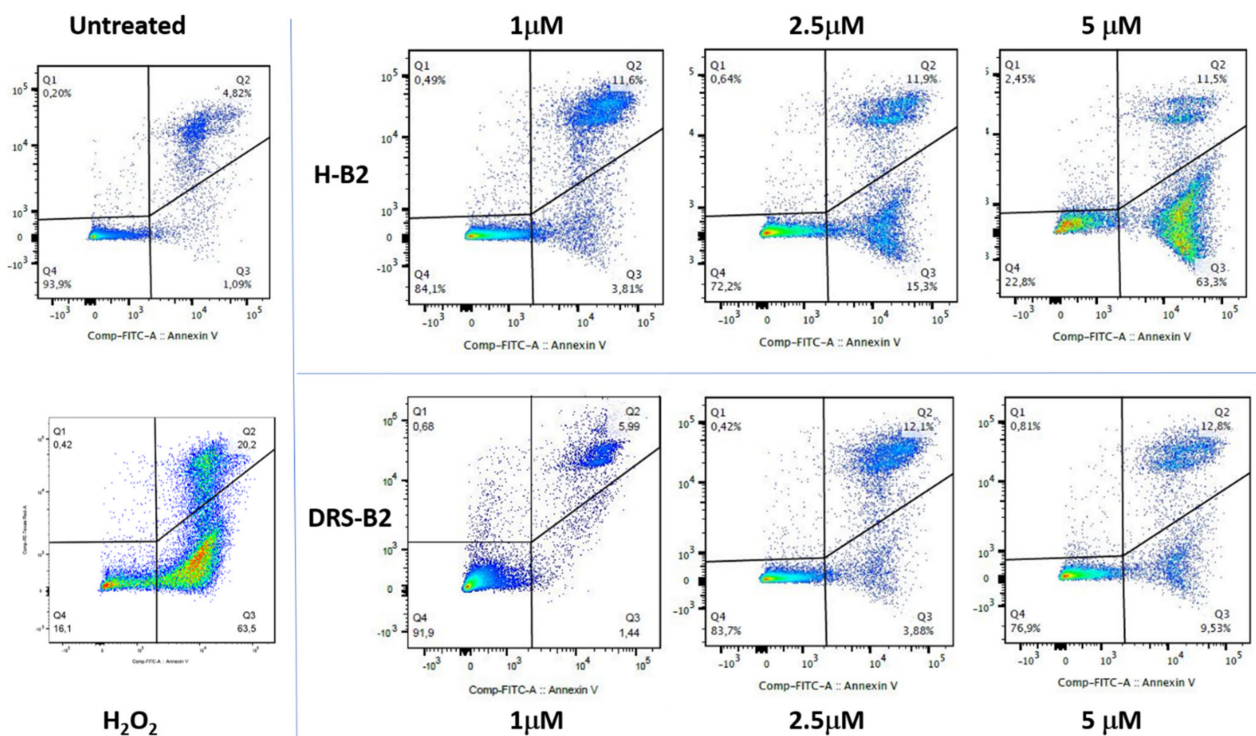


Figure 9. PC3 cell viability after H-B2 and DRS-B2 treatments. PC3 cells were treated with different concentrations of H-B2 or DRS-B2. H_2O_2 was used as a positive control for apoptosis. Twenty-four hours after treatment, cells were double stained with FITC-Annexin-V (A-V) and Propidium Iodide (PI) and analyzed by flow cytometry. The cell viability of PC3 cells was observed by measuring the amount of A-V and PI negative and positive cells. Dot plots of A-V/PI double staining after PC3 treatment with the different concentrations of H-B2 or DRS-B2 for 24 h. All experiments were performed three times.

After being treated with H-B2 for 24 h, 4%, 15%, and 63% of double staining $A-V^+/PI^-$ which corresponds to early apoptotic cells were found in PC3 cells treated with 1 μM , 2.5 μM , and 5 μM , respectively. These values were significantly higher than those of untreated cells (1%) and similar (63.5%) to cells treated with H_2O_2 used as a positive control. DRS-B2 presented a lower effect with only 5.5%, 4% and 9.5% of double staining $A-V^+/PI^-$ when PC3 cells were treated with DRS-B2 at 1 μM , 2.5 μM and 5 μM , which agrees with results described by Van Zogel et al. [11].

DNA fragmentation represents the final stage of apoptosis. To examine apoptosis through DNA fragmentation induced by H-B2 or DRS-B2, we used the terminal deoxynucleotidyl transferase (Tdt) dUTP Nick-End Labeling (TUNEL) assay, in which DNA strand breaks are detected by enzymatic labeling of free 3'-OH ends with modified nucleotides. The analysis of DNA fragmentation in PC3 cells by the TUNEL technique shows that the percentage of fragmented DNA increases with H-B2 treatments. Treatment of PC3 cells with 5 μM H-B2 induces a DNA fragmentation level of 69% compared to untreated cells (1.5%), whereas it reaches only 9% when treated with the same concentration of DRS-B2. (Figure 10).

PC3 cells treated with 10 nM Taxotere or 1 μM of Staurosporine as positive controls show 96% and 86% DNA fragmentation, respectively (Figure 10). These data confirm that the mechanism of PC3 cell death induced by H-B2 is different from that induced by DRS-B2, which is necrotic, and could rather correspond to an apoptotic mechanism, in agreement with the flow cytometry results described previously.

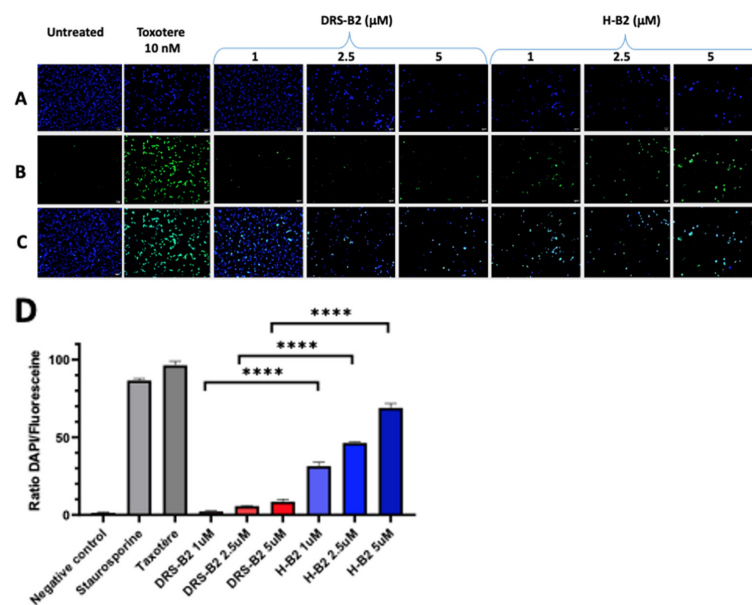


Figure 10. Terminal transferase-mediated dUTP nick end-labeling (TUNEL) in vitro assay of treated PC3 cells. Apoptosis of PC3 cells using TUNEL assay in vitro after DRS-B2 and H-B2 treatment. Cells were treated for 24 h with increasing concentrations of each peptide. Taxotere treatment was performed as a positive control for apoptosis. (A) Cells were stained with DAPI. (B) 3' Hydroxyl-nucleotides of double strand DNA breaks were stained with Fluoresceine. (C) Merged fluorescence of DAPI and fluoresceine showing DNA fragmented cells. (D) Histogram representing percentage of fragmented DNA-containing cells of the total number of cells. $n = 3$ (Mean \pm SD; **** $p < 0.0001$).

3. Discussion

With 1.1 million prostate cancers diagnosed worldwide in 2012, of which approximately 6% are metastatic from the start, the development of treatments for mCPRC is a global necessity with a promising market. The development of treatments for the management of castration-resistant metastatic patients is necessary because currently available treatments only allow a few months of survival gain, mainly due to problems of drug resistance of cancer cells. In this context, the use of natural or synthetic peptides could offer interesting therapeutic approaches. To limit peripheral toxicity and increase local concentrations, numerous cytotoxic molecules conjugated with peptide hormones such as LHRH or somatostatin, the receptors of which are widely overexpressed on the surface of tumor membranes, have been developed [23–27]. Currently, only one cytotoxic peptide is in clinical development (Phase 2 completed), AEZS-108 (zoptarelin doxorubicin) [28].

Starting from our previous studies on the anticancer activity of the CAP dermaseptin-B2 (DRS-B2), a natural peptide issued from biodiversity, we have developed a synthetic chimeric H-B2 peptide combining DRS-B2 and LHRH peptides [5,10,11]. The use of LHRH was justified by the fact that 86% of prostate cancers express the LHRH receptor [14]. A peptide targeting this receptor therefore should increase the specificity for cancer cells and decrease the in vivo toxicity of DRS-B2.

At the structural level, the coupling of the peptide hormone (H) LHRH to the C-terminus of DRS-B2 does not modify the structure of DRS-B2 nor its conformational behavior in a membrane environment. The characteristics essential to the cytotoxic mode of action of these polycationic peptides and to the targeted molecular interaction are therefore preserved. CAPs are supposed to act on cancer cells in which the outer layer of the plasma membrane is highly negatively charged, as for bacterial plasma membranes. In the case of cancer cells, the negatively charged membrane is due to the presence of phosphatidylserine, negatively charged mucin proteins or highly sulfated GAGs (5, 25). After binding, dermaseptin peptides accumulate in a carpet-like manner on the outside of a lipid bilayer until a threshold concentration is reached, causing them to form pores in which

the peptides are inserted with the phospholipid headgroups of the membrane [29–34]. We have shown that H-B2 was structured as a continuous helix in its “toxin” portion (DRS-B2) and that the “hormone” ligand portion remains free to interact with LHRH-R.

In vitro, H-B2 was slightly more effective than DRS-B2 on the proliferation of the various prostate cancer cell lines tested. We could also mention that cells expressing high levels of LHRH receptors, such as PC3 and DU145, presented a modest but significant gain in IC₅₀ when compared with those of DRS-B2 alone. Targeting cancer cells with an overexpressed receptor such as LHRH is a strategy that could permit improvement to the efficiency of a peptide such as DRS-B2 to gain in its ED₅₀. However, in the case of H-B2, this gain is low. We could imagine that even if the LHRH receptor is overexpressed on PC3 cells, its concentration at the surface of the plasma membrane is too low to guide enough DRS-B2 to the membrane to complete its carpet-like structure and further form pores in the plasma membrane. As saturation of the LHRH receptor by H-B2 may not be sufficient to kill cells, an additional part of DRS-B2 in the H-B2 structure may be necessary to do it.

In vivo, H-B2 inhibited tumor growth by more than 50% and significantly decreased proliferation without any major side effects. Since the addition of the hormone peptide to DRS-B2 permits a better tolerance when injected in mice, we could conclude that despite significant improvement in the IC₅₀ on the cell line, the hormone peptide improved the in vivo activity of DRS-B2, as we could treat mice with 5 mg/kg H-B2 without side effects instead of 2.5 mg/kg with DRS-B2. It is interesting to note that the treatment of prostate tumor cells with H-B2 is globally well tolerated. We did not observe any major abnormalities in the blood workup after H-B2 injection. Importantly, at a dose of 10 mg/kg, DRS-B2 is lethal while H-B2 at the same dose was well tolerated in toxicity tests, with no behavioral changes in the mice or weight loss. The design of the H-B2 chimeric peptide, thus made it possible to circumvent the toxicity of DRS-B2 while maintaining its antitumor efficacy.

Concerning the mechanism of action, the combination of different experimental approaches used in this study, such as cell viability by flow cytometry, cytotoxicity by cytoplasmic LDH release, and DNA fragmentation by TUNEL assay, allowed us to show that the mechanism of cell death induced by H-B2 is probably different from that of DRS-B2 and might be similar to apoptosis. Indeed, we showed that both peptides have the same effect on cytoplasmic LDH release but a distinctly different cell labeling when cell viability is analyzed by flow cytometry and DNA fragmentation by TUNEL assays. The differences between the effect of the two peptides observed in the TUNEL assay show that H-B2 induces DNA fragmentation up to 70% in contrast to DRS-B2 which is less than 10%. These results are also in agreement with those obtained in 2012 by Van Zoggel et al. who showed a double Annexin V+/PI+ labeling of PC3 cells treated with DRS-B2, suggesting a necrotic cell death mechanism [11].

Apart from DRS-B2 previously studied in the laboratory, two new members of the dermaseptin family have been recently reported to exhibit antitumor activities: Dermaseptin-PP from *Phyllomedusa palliata* and Dermaseptin-PT9 from *Phyllomedusa tarsius* [35,36]. Both exhibited antiproliferative activity against various human tumor cells, rapid LDH release activity, and an apoptosis-like cell death mechanism. Among these dermaseptins, DRS-B2 presented the higher ED₅₀ on various tumor cells.

Finally, the study of the hemolytic effect of the different peptides allowed us to observe that both DRS-B2 and H-B2 have low hemolytic activity, which is encouraging in the perspective of a therapeutic approach. Further in vivo studies on mice could be necessary to obtain more pharmacokinetic and toxicology information to complete the study.

4. Materials and Methods

Peptide synthesis. The LHRH analog containing a dK residue (d for D configuration of the Lys residue) in position 6 (peptide A: pEHWSY(dK)LRG-amide) and DRS-B2 (peptide B: GLWSKIKEVKGKEAAKAAAKAAGKAALGACSEAV-acid) were synthesized by X'PROCHEM Company (Lille, France). The chimeric peptide H-B2 (Figure 1A), composed

of the peptide A grafted by its epsilon NH₂ of the dK⁶ residue with the COOH-terminal of the peptide B, is determined to be >95% pure by RP-HPLC (Figure S1A) and its molecular weight determined by ESI-mass spectrometry is $[M + 4H]/4 = 1105.2$ (Figure S1). The peptide was dissolved in sterile water for in vitro biological studies and in adequate buffer for the in vivo and structural analysis.

Circular dichroism (CD) spectroscopy of peptides. The helical structures of HB2 and DRS-B2 were analyzed by CD spectroscopy using a Jobin Yvon CD6 dichrograph linked to a PC microprocessor as described in [34]. Briefly, measurements were calibrated with (+)-10-camphorsulfonic acid and performed with 10 μM H-B2 or DRS-B2 diluted in PBS alone or with increasing concentrations of dodecylphosphocholin (DPC) (10, 30, 100, 1000 and 5000 μM) at 25 °C using a quartz cuvette (Hellma) with a path length of 0.1 cm. Spectra, recorded in 1 nm steps, were averaged over five scans, and corrected for the baseline. The CD spectra were deconvoluted using CDNN Software [37]. Circular dichroism measurements are reported as $\Delta\epsilon/n$, where $\Delta\epsilon$ is the dichroic increment ($M^{-1} \text{ cm}^{-1}$) and n is the number of residues in the peptide. The α -helix content of peptides was obtained using the relation: $P\alpha = -[\Delta\epsilon_{222\text{nm}} \times 10]$ ($P\alpha$: percentage of α -helix; $\Delta\epsilon_{222\text{nm}}$: dichroic increment per residue at 222 nm) [38].

Fluorescence of tryptophan-containing peptides was performed as previously described by Dos Santos et al. [5]. Emission spectra were recorded on a Jobin-Yvon Fluoromax II instrument (HORIBA Jobin-Yvon, Montpellier, France) equipped with an Ozone-free 150 W xenon lamp. The excitation wavelength was 290 nm, and the emission spectra were acquired at 300–360 nm. At least five measurements for each titration point were recorded with an integration time of 1 s. The H-B2 and DRS-B2 concentration in PBS was 2 μM, and the DPC concentration varied from 0 to 1000 μM. Tryptophan fluorescence was determined by subtracting spectra without the peptide.

Nuclear Magnetic Resonance (NMR) Spectroscopy. The NMR sample was prepared in 550 μL of H₂O/D₂O (90:10 *v/v*) in the presence of 85 mM DPC-d₃₈ (d₃₈-dodecylphosphocholin, MAPCHO[®]-12-d₃₈, Avanti Polar Lipids) and using a peptide concentration of 1 mM. The pH was set to 4.1 using microliter amounts of NaOH 0.1 M. DSS was added at a concentration of 0.11 mM for chemical shift calibration. The NMR spectra were acquired at 45 °C on a 500 MHz (11.7 T) Avance III Bruker[®] spectrometer equipped with a TCI cryoprobe. The following experiments were recorded: 2D ¹H-¹H TOCSY (66 ms mixing time), 2D ¹H-¹H NOESY (150 ms mixing time), 2D natural abundance ¹⁵N-¹H and 2D ¹³C-¹H HSQC experiments, as described in [34].

Cell culture. Human PCa cell lines, PC3, DU145 and 22Rv1 were purchased from ATCC (American Type Culture Collection) and were cultured in RPMI supplemented with 10% of fetal bovine serum (FBS). The human hyperplastic cell line BPH1 was purchased from the German Collection of Cell Cultures (DSMZ, Braunschweig, Germany). BPH1 were maintained in RPMI 1640 supplemented by 10% FBS, 20 ng/mL testosterone and 1% insulin-transferrin-selenium. Cell cultures were maintained at 37 °C and 5% CO₂ in a humidified atmosphere. All culture reagents were purchased from Life Technologies (Cergy-Pontoise, France). All experiments were performed as previously described by Dos Santos et al. [5]

Cell viability assays. Cells were seeded at a density of 5×10^3 cells/well in 96-multiwell plates in complete medium and incubated for 24 h at 37 °C in a controlled humidified 7% CO₂ environment. Cells were then treated with DRS-B2 or H-B2 as indicated, for 48 h. Cell viability was measured using the 3-(4,5-dimethylthiazol2-yl)-diphenyltetrazolium bromide (MTT) dye method (Sigma, Saint Quentin Fallavier, France) according to the manufacturer's instructions. Each experiment was performed in triplicate with at least three independent experiments, as previously described by Dos Santos et al. [5]. IC₅₀ values were determined by GraphPad Prism 5.0 (GraphPad Software San Diego, CA, USA).

Hemolysis assessment. The hemolytic activity of H-B2 and DRS-B2 was determined using fresh human erythrocytes from a healthy donor that was prepared as follows: 4 mL of

whole blood was collected and centrifuged at $900\times g$ for 10 min at $4\text{ }^{\circ}\text{C}$ to separate plasma from erythrocytes. The pellet was then rinsed with PBS pH 7.4 and centrifuged at $900\times g$ for 10 min at $4\text{ }^{\circ}\text{C}$. After counting and making a red cell solution at 4×10^8 erythrocytes/mL (diluted in PBS pH 7.4), 50 μL of a diluted peptide solution was added in a cascade to which 50 μL of the erythrocyte solution was added (made in triplicate). After 1 h of incubation at $37\text{ }^{\circ}\text{C}$, the tubes were centrifuged at 12,000 rpm for 15 s at $4\text{ }^{\circ}\text{C}$. The supernatant was then recovered. The hemoglobin present in the erythrocytes was determined in the supernatants via a plate reader at 450 nm. A parallel incubation in the presence of 0.2% (*v/v*) Triton was carried out to determine the absorbance associated with 100% hemolysis.

Tumor xenograft studies were performed as previously described by Van Zoggel et al. [11]. PC3 (2×10^6) cells were injected subcutaneously into the right flank of 4-week-old male NMRI nude mice (Janvier, Le Genest-Saint-Isle, France). When the tumor volume reached approximately 100 mm^3 , the mice were randomly divided into four groups ($n = 6$): control (PBS), DRS-B2 (2.5 mg/kg), H-B2 (2.5 mg/kg), H-B2 (5 mg/kg) by intraperitoneal injection twice a week. Tumor size was measured two times per week with a caliper and the tumor volume was calculated with the formula: $V = 4/3\pi \times R1^2 \times R2$ with radius 1 (R1), and radius 2 (R2). At the end of the experiment, the mice were sacrificed, and their body weight was measured. The tumors were isolated, weighted and then fixed in formalin.

Immunohistochemical analysis of the tumors was performed as previously described by Van Zoggel et al. [11]. The fixed tumors were embedded in paraffin and then 6 μm sections were prepared. The tumors sections were deparaffinized, antigen unmasking was performed, and endogenous peroxidase activity was inactivated with a 2% hydrogen peroxide solution for 10 min. Unspecific staining was blocked using Power Block Universal reagent (Biogenex Laboratories/Microm Microtech, Francheville, France) for 10 min at $37\text{ }^{\circ}\text{C}$. Tissues were then incubated 2 h at room temperature with anti-human Ki67 antibody (Mouse monoclonal, M7240, Dako, 1:50) for 2 h. Immuno-complexes were revealed using HRP conjugated secondary antibodies and the DAB substrate. Tissues were then counterstained with hematoxylin and cover slipped with Mowiol mounting medium. Quantification of Ki67 positive stained cells was quantified by image J software analysis on the whole tumor section.

Lactate dehydrogenase (LDH) release assay. The cytoplasm LDH release assay was performed as previously described in [11]. Briefly, PC3 cells were grown in a 96 well plate (1500 cells/well/100 μL) in complete medium and treated with various concentrations of H-B2 or DRS-B2. Cell membrane integrity was evaluated by measuring the LDH activity released into the culture media 24 h after peptide exposure. The CytoTox96 nonradioactive cytotoxicity assay (Promega; Charbonnières-les-Bains, France) was performed according to the manufacturer's instructions and quantified by measuring the absorbance at 490 nm. The 100% cytotoxicity corresponded to the LDH released with treatment of the cells with Triton X100 at 0.9% (*v/v*).

Apoptosis analysis by flow cytometry. For the apoptosis assay, an FITC-Annexin-V (A-V) and Propidium Iodide (PI) double staining method was used. PC3 cells were grown in a 12-well plate and treated or not with H-B2, DRS-B2 or hydrogen peroxide as described previously [5]. At 24 h after exposure, cell viability was evaluated by flow cytometry analysis with FITC-Annexin-V (A-V) and propidium iodide staining. Medium and trypsinized cells were collected and washed with PBS. After centrifugation, cells were suspended in PBS to obtain a cell density of 0.5×10^6 cells per mL. One milliliter of this cell extract was centrifuged, suspended in 200 μL PBS, transferred to a microtiterplate with a round bottom and centrifuged again. The resulting cell pellet was resuspended in 200 μL of Binding Buffer 1x (BD Pharmingen™), containing 5 μL of FITC-Annexin-V (BD Pharmingen™) and incubated for 10 min in the dark at room temperature. The cells were washed with PBS and incubated with 200 μL of Binding Buffer 1x containing PI (final concentration 1 $\mu\text{g}/\text{mL}$) (BD Pharmingen™) for 5 min in the dark at room

temperature. Flow cytometry analysis was performed with an LSR Fortessa X20 analyzer (BD Biosciences, Franklin Lakes, NJ, USA) and FlowJo V10 software.

Terminal transferase-mediated dUTP Nick End-Labeling (TUNEL) assay. PC3 cells were cultured in 6-well plates at 150,000 cells per well in complete medium and treated or not with 1 or 2.5 μM of DRS-B2 or H-B2 and with LHRH (5 μM) or Taxotere (10 nM) and Staurosporine (1 μM) as a positive control. After 24 h of treatment, the supernatant was aspirated and the cells trypsinized and plated on a Superfrost PLUS slide and fixed with a 4% formaldehyde solution without methanol. The cells were then permeabilized with a 0.2% Triton X-100 solution in 1x PBS for 5 min at room temperature. Terminal transferase-mediated dUTP nick end-labeling (TUNEL) was performed according to the DeadEnd™ Fluorometric TUNEL System kit from Promega®. In addition to the fluorescein labeling, a second labeling with DAPI, intercalating DNA was performed by incubating for 15 min at room temperature with a 1 $\mu\text{g}/\text{mL}$ solution. The different labeling steps were performed avoiding any exposure to light.

Imaging was performed with an Axiolmager M2 epifluorescence microscope. The images obtained by microscopy were recorded with Zen 2012 software and analyzed with ImageJ© software. Each image underwent a thresholding of fluorescence calibrated on the positive control, and which was preserved for all the other images. The software then analyzed the number of DAPI and fluorescein fluorescence events to calculate the ratio between the total number of DAPI-labeled cell nuclei and the number of fluorescein-labeled nuclei with fragmented DNA. The experiment was performed in triplicate.

Statistical analysis. The statistical analyses were performed using GraphPad Prism™ version 4.00 software from GraphPad Software Inc. (San Diego, CA, USA). The results are expressed as the means \pm standard deviation (SD) or standard error of the mean (SEM) of at least three determinations for each test from three independent experiments. Statistical analyses were carried out using the unpaired *t*-test. The statistical significance of the differences is given as * $p < 0.05$; ** $p < 0.01$; *** $p < 0.001$; ns: not significant.

Supplementary Materials: The following are available online at <https://www.mdpi.com/article/10.3390/ijms222111303/s1>.

Author Contributions: Conceptualization: J.D., Y.H.-K. and M.A.; formal analysis: M.C., M.D., M.M.-P., L.Z. (Liuhui Zhang), L.Z. (Loussiné Zargarian), O.L., J.D., Y.H.-K. and M.A.; funding acquisition: A.d.l.T., J.D., Y.H.-K. and M.A.; investigation: M.C., M.D., M.M.-P., L.Z. (Liuhui Zhang), P.Z., L.Z. (Loussiné Zargarian) and O.L.; methodology: J.D., Y.H.-K. and M.A.; project administration: A.d.l.T., J.D., Y.H.-K. and M.A.; resources: J.D., Y.H.-K. and M.A.; supervision: J.D., Y.H.-K. and M.A.; validation J.D., Y.H.-K. and M.A.; visualization: J.D., Y.H.-K. and M.A.; writing original draft: J.D., Y.H.-K. and M.A.; writing review and editing: M.C., L.Z. (Loussiné Zargarian), O.L., J.D., Y.H.-K. and M.A. All authors have read and agreed to the published version of the manuscript.

Funding: This research received no external funding.

Institutional Review Board Statement: All mouse experiments were performed according to ARRIVE guidelines on animal care and approved by Charles Darwin Animal Experimentation Ethics Committee (CEEACD/N°5) and conducted in compliance with the European Community.

Acknowledgments: Thanks to the AFU (Association Française d'urologie) and to IMRB which awarded a scholarship to Michaël Miro-Padovani and to Michaël Couty for the realization of a part of this project. We thank Aurelie Guguin and Adeline Henry from the Flow Cytometry facility of IMRB (Institute Mondor de Recherche Biomedicale).

Conflicts of Interest: The authors declare no conflict of interest.

References

1. Rawla, P. Epidemiology of Prostate Cancer. *World J. Oncol.* **2019**, *10*, 63–89. [CrossRef] [PubMed]
2. McNevin, C.S.; Baird, A.-M.; McDermott, R.; Finn, S.P. Diagnostic Strategies for Treatment Selection in Advanced Prostate Cancer. *Diagnostics* **2021**, *11*, 345. [CrossRef] [PubMed]
3. Tornesello, A.L.; Borrelli, A.; Buonaguro, L.; Buonaguro, F.M.; Tornesello, M.L. Antimicrobial Peptides as Anticancer Agents: Functional Properties and Biological Activities. *Molecules* **2020**, *25*, 2850. [CrossRef] [PubMed]

4. Yeung, A.T.Y.; Gellatly, S.L.; Hancock, R.E.W. Multifunctional Cationic Host Defence Peptides and Their Clinical Applications. *Cell. Mol. Life Sci.* **2011**, *68*, 2161. [CrossRef]
5. Dos Santos, C.; Hamadat, S.; Le Saux, K.; Newton, C.; Mazouni, M.; Zargarian, L.; Miro-Padovani, M.; Zadigue, P.; Delbé, J.; Hamma-Kourbali, Y.; et al. Studies of the Antitumor Mechanism of Action of Dermaseptin B2, a Multifunctional Cationic Antimicrobial Peptide, Reveal a Partial Implication of Cell Surface Glycosaminoglycans. *PLoS ONE* **2017**, *12*, e0182926. [CrossRef]
6. Bartels, E.J.H.; Dekker, D.; Amiche, M. Dermaseptins, Multifunctional Antimicrobial Peptides: A Review of Their Pharmacology, Effectivity, Mechanism of Action, and Possible Future Directions. *Front. Pharmacol.* **2019**, *10*, 1421. [CrossRef]
7. Hoskin, D.W.; Ramamoorthy, A. Studies on Anticancer Activities of Antimicrobial Peptides. *Biochim. Biophys. Acta* **2008**, *1778*, 357–375. [CrossRef]
8. Charpentier, S.; Amiche, M.; Mester, J.; Vouille, V.; Le Caer, J.P.; Nicolas, P.; Delfour, A. Structure, Synthesis, and Molecular Cloning of Dermaseptins B, a Family of Skin Peptide Antibiotics. *J. Biol. Chem.* **1998**, *273*, 14690–14697. [CrossRef]
9. Amiche, M.; Ladram, A.; Nicolas, P. A Consistent Nomenclature of Antimicrobial Peptides Isolated from Frogs of the Subfamily Phyllomedusinae. *Peptides* **2008**, *29*, 2074–2082. [CrossRef]
10. Van Zoggel, H.; Hamma-Kourbali, Y.; Galanth, C.; Ladram, A.; Nicolas, P.; Courty, J.; Amiche, M.; Delbé, J. Antitumor and Angiostatic Peptides from Frog Skin Secretions. *Amino Acids* **2010**, *42*, 385–395. [CrossRef]
11. Van Zoggel, H.; Carpentier, G.; Dos Santos, C.; Hamma-Kourbali, Y.; Courty, J.; Amiche, M.; Delbé, J. Antitumor and Angiostatic Activities of the Antimicrobial Peptide Dermaseptin B2. *PLoS ONE* **2012**, *7*, e44351. [CrossRef]
12. Pastan, I.; Hassan, R.; Fitzgerald, D.J.; Kreitman, R.J. Immunotoxin Therapy of Cancer. *Nat. Rev. Cancer* **2006**, *6*, 559–565. [CrossRef]
13. Schally, A.V.; Engel, J.B.; Emons, G.; Block, N.L.; Pinski, J. Use of Analogs of Peptide Hormones Conjugated to Cytotoxic Radicals for Chemotherapy Targeted to Receptors on Tumors. *Curr. Drug Deliv.* **2011**, *8*, 11–25. [CrossRef]
14. Halmos, G.; Arencibia, J.M.; Schally, A.V.; Davis, R.; Bostwick, D.G. High Incidence of Receptors for Luteinizing Hormone-Releasing Hormone (LHRH) and LHRH Receptor Gene Expression in Human Prostate Cancers. *J. Urol.* **2000**, *163*, 623–629. [CrossRef]
15. Engel, J.B.; Schally, A.V. Drug Insight: Clinical Use of Agonists and Antagonists of Luteinizing-Hormone-Releasing Hormone. *Nat. Clin. Pract. Endocrinol. Metab.* **2007**, *3*, 157–167. [CrossRef]
16. Kakar, S.S.; Grizzle, W.E.; Neill, J.D. The Nucleotide Sequences of Human GnRH Receptors in Breast and Ovarian Tumors Are Identical with That Found in Pituitary. *Mol. Cell. Endocrinol.* **1994**, *106*, 145–149. [CrossRef]
17. Völker, P.; Gründker, C.; Schmidt, O.; Schulz, K.-D.; Emons, G. Expression of Receptors for Luteinizing Hormone-Releasing Hormone in Human Ovarian and Endometrial Cancers: Frequency, Autoregulation, and Correlation with Direct Antiproliferative Activity of Luteinizing Hormone-Releasing Hormone Analogues. *Am. J. Obstet. Gynecol.* **2002**, *186*, 171–179. [CrossRef]
18. Yates, C.; Sharp, S.; Jones, J.; Topps, D.; Coleman, M.; Aneja, R.; Jaynes, J.; Turner, T. LHRH-Conjugated Lytic Peptides Directly Target Prostate Cancer Cells. *Biochem. Pharmacol.* **2011**, *81*, 104–110. [CrossRef]
19. Curtis, K.K.; Sarantopoulos, J.; Northfelt, D.W.; Weiss, G.J.; Barnhart, K.M.; Whisnant, J.K.; Leuschner, C.; Alila, H.; Borad, M.J.; Ramanathan, R.K. Novel LHRH-Receptor-Targeted Cytolytic Peptide, EP-100: First-in-Human Phase I Study in Patients with Advanced LHRH-Receptor-Expressing Solid Tumors. *Cancer Chemother. Pharmacol.* **2014**, *73*, 931–941. [CrossRef]
20. Engel, J.B.; Schally, A.V.; Buchholz, S.; Seitz, S.; Emons, G.; Ortmann, O. Targeted Chemotherapy of Endometrial, Ovarian and Breast Cancers with Cytotoxic Analogs of Luteinizing Hormone-Releasing Hormone (LHRH). *Arch. Gynecol. Obstet.* **2012**, *286*, 437–442. [CrossRef]
21. Leuschner, C.; Enright, F.M.; Gawronska-Kozak, B.; Hansel, W. Human Prostate Cancer Cells and Xenografts Are Targeted and Destroyed through Luteinizing Hormone Releasing Hormone Receptors. *Prostate* **2003**, *56*, 239–249. [CrossRef]
22. Zhu, S.; Wang, Q.; Jiang, J.; Luo, Y.; Sun, Z. A Conjugate of Methotrexate and an Analog of Luteinizing Hormone Releasing Hormone Shows Increased Efficacy against Prostate Cancer. *Sci. Rep.* **2016**, *6*, 33894. [CrossRef]
23. Schally, A.V.; Nagy, A. Cancer Chemotherapy Based on Targeting of Cytotoxic Peptide Conjugates to Their Receptors on Tumors. *Eur. J. Endocrinol.* **1999**, *141*, 1–14. [CrossRef]
24. Schally, A.V.; Comaru-Schally, A.M.; Plonowski, A.; Nagy, A.; Halmos, G.; Rekasi, Z. Peptide Analogs in the Therapy of Prostate Cancer. *Prostate* **2000**, *45*, 158–166. [CrossRef]
25. Nagy, A.; Schally, A.V. Targeting of Cytotoxic Luteinizing Hormone-Releasing Hormone Analogs to Breast, Ovarian, Endometrial, and Prostate Cancers. *Biol. Reprod.* **2005**, *73*, 851–859. [CrossRef]
26. Hohla, F.; Buchholz, S.; Schally, A.V.; Krishan, A.; Rick, F.G.; Szalontay, L.; Papadia, A.; Halmos, G.; Koster, F.; Aigner, E.; et al. Targeted Cytotoxic Somatostatin Analog AN-162 Inhibits Growth of Human Colon Carcinomas and Increases Sensitivity of Doxorubicin Resistant Murine Leukemia Cells. *Cancer Lett.* **2010**, *294*, 35–42. [CrossRef]
27. Seitz, S.; Schally, A.V.; Treszl, A.; Papadia, A.; Rick, F.; Szalontay, L.; Szepeshazi, K.; Ortmann, O.; Halmos, G.; Hohla, F.; et al. Preclinical Evaluation of Properties of a New Targeted Cytotoxic Somatostatin Analog, AN-162 (AEZS-124), and Its Effects on Tumor Growth Inhibition. *Anticancer Drugs* **2009**, *20*, 553–558. [CrossRef]
28. Yu, S.S.; Athreya, K.; Liu, S.V.; Schally, A.V.; Tsao-Wei, D.; Groshen, S.; Quinn, D.I.; Dorff, T.B.; Xiong, S.; Engel, J.; et al. A Phase II Trial of AEZS-108 in Castration- and Taxane-Resistant Prostate Cancer. *Clin. Genitourin. Cancer* **2017**, *15*, 742–749. [CrossRef]
29. Shai, Y. Mode of Action of Membrane Active Antimicrobial Peptides. *Biopolymers* **2002**, *66*, 236–248. [CrossRef]

30. Pouny, Y.; Rapaport, D.; Mor, A.; Nicolas, P.; Shai, Y. Interaction of Antimicrobial Dermaseptin and Its Fluorescently Labeled Analogues with Phospholipid Membranes. *Biochemistry* **1992**, *31*, 12416–12423. [CrossRef]
31. Bechinger, B.; Lohner, K. Detergent-like Actions of Linear Amphipathic Cationic Antimicrobial Peptides. *Biochim. Biophys. Acta* **2006**, *1758*, 1529–1539. [CrossRef] [PubMed]
32. Aisenbrey, C.; Bechinger, B.; Gröbner, G. Macromolecular Crowding at Membrane Interfaces: Adsorption and Alignment of Membrane Peptides. *J. Mol. Biol.* **2008**, *375*, 376–385. [CrossRef] [PubMed]
33. Duclohier, H. How Do Channel- and Pore-Forming Helical Peptides Interact with Lipid Membranes and How Does This Account for Their Antimicrobial Activity? *Mini Rev. Med. Chem.* **2002**, *2*, 331–342. [CrossRef] [PubMed]
34. Galanth, C.; Abbassi, F.; Lequin, O.; Ayala-Sanmartin, J.; Ladram, A.; Nicolas, P.; Amiche, M. Mechanism of Antibacterial Action of Dermaseptin B2: Interplay between Helix-Hinge-Helix Structure and Membrane Curvature Strain. *Biochemistry* **2009**, *48*, 313–327. [CrossRef]
35. Dong, Z.; Hu, H.; Yu, X.; Tan, L.; Ma, C.; Xi, X.; Li, L.; Wang, L.; Zhou, M.; Chen, T.; et al. Novel Frog Skin-Derived Peptide Dermaseptin-PP for Lung Cancer Treatment: In Vitro/Vivo Evaluation and Anti-Tumor Mechanisms Study. *Front. Chem.* **2020**, *8*, 476. [CrossRef]
36. Li, M.; Xi, X.; Ma, C.; Chen, X.; Zhou, M.; Burrows, J.F.; Chen, T.; Wang, L. A Novel Dermaseptin Isolated from the Skin Secretion of *Phyllomedusa Tarsius* and Its Cationicity-Enhanced Analogue Exhibiting Effective Antimicrobial and Anti-Proliferative Activities. *Biomolecules* **2019**, *9*, 628. [CrossRef]
37. Böhm, G.; Muhr, R.; Jaenicke, R. Quantitative Analysis of Protein Far UV Circular Dichroism Spectra by Neural Networks. *Protein Eng.* **1992**, *5*, 191–195. [CrossRef]
38. Zhong, L.; Johnson, W.C. Environment Affects Amino Acid Preference for Secondary Structure. *Proc. Natl. Acad. Sci. USA* **1992**, *89*, 4462–4465. [CrossRef]



Article

Stereo-Specific Modulation of the Extracellular Calcium-Sensing Receptor in Colon Cancer Cells

Martin Schepelmann ^{1,*} , Nadja Kupper ¹, Marta Sladczyk ¹, Bethan Mansfield ², Teresa Manhardt ¹, Karina Piatek ¹, Luca Iamartino ^{1,3} , Daniela Riccardi ², Benson M. Kariuki ⁴, Marcella Bassetto ⁵ and Enikő Kallay ^{1,*}

¹ Center for Pathophysiology, Infectiology and Immunology, Institute for Pathophysiology and Allergy Research, Medical University of Vienna, Waehringerguertel 18-20, 1090 Vienna, Austria; nadja.kupper@meduniwien.ac.at (N.K.); marta.sladczyk@gmail.com (M.S.); teresa.manhardt@meduniwien.ac.at (T.M.); karina.piatek@meduniwien.ac.at (K.P.); luca.iamartino@unifi.it (L.I.)

² Cardiff School of Biosciences, Cardiff University, Museum Avenue, Cardiff CF10 3AX, UK; MansfieldB@cardiff.ac.uk (B.M.); Riccardi@cardiff.ac.uk (D.R.)

³ Department of Experimental and Clinical Biomedical Sciences, University of Florence, Viale Pieraccini 18, 50139 Florence, Italy

⁴ School of Chemistry, Cardiff University, Main Building, Park Place, Cardiff CF10 3AT, UK; KariukiB@cardiff.ac.uk

⁵ Department of Chemistry, Faculty of Science and Engineering, Swansea University, Singleton Park Campus, Swansea SA2 8PP, UK; marcella.bassetto@swansea.ac.uk

* Correspondence: martin.schepelmann@meduniwien.ac.at (M.S.); enikoe.kallay@meduniwien.ac.at (E.K.); Tel.: +43-1-40400-51230 (M.S. & E.K.)

Citation: Schepelmann, M.; Kupper, N.; Sladczyk, M.; Mansfield, B.; Manhardt, T.; Piatek, K.; Iamartino, L.; Riccardi, D.; Kariuki, B.M.; Bassetto, M.; et al. Stereo-Specific Modulation of the Extracellular Calcium-Sensing Receptor in Colon Cancer Cells. *Int. J. Mol. Sci.* **2021**, *22*, 10124. <https://doi.org/10.3390/ijms221810124>

Academic Editor: Claudio Bucolo

Received: 10 August 2021

Accepted: 16 September 2021

Published: 19 September 2021

Publisher's Note: MDPI stays neutral with regard to jurisdictional claims in published maps and institutional affiliations.



Copyright: © 2021 by the authors. Licensee MDPI, Basel, Switzerland. This article is an open access article distributed under the terms and conditions of the Creative Commons Attribution (CC BY) license (<https://creativecommons.org/licenses/by/4.0/>).

Abstract: Pharmacological allosteric agonists (calcimimetics) of the extracellular calcium-sensing receptor (CaSR) have substantial gastro-intestinal side effects and induce the expression of inflammatory markers in colon cancer cells. Here, we compared the effects of both CaSR-specific (*R* enantiomers) and -unspecific (*S* enantiomers) enantiomers of a calcimimetic (NPS 568) and a calcilytic (allosteric CaSR antagonists; NPS 2143) to prove that these effects are indeed mediated via the CaSR, rather than via off-target effects, e.g., on β -adrenoceptors or calcium channels, of these drugs. The unspecific *S* enantiomer of NPS 2143 and NPS *S*-2143 was prepared using synthetic chemistry and characterized using crystallography. NPS *S*-2143 was then tested in HEK-293 cells stably transfected with the human CaSR (HEK-CaSR), where it did not inhibit CaSR-mediated intracellular Ca^{2+} signals, as expected. HT29 colon cancer cells transfected with the CaSR were treated with both enantiomers of NPS 568 and NPS 2143 alone or in combination, and the expression of CaSR and the pro-inflammatory cytokine interleukin 8 (IL-8) was measured by RT-qPCR and ELISA. Only the CaSR-selective enantiomers of the calcimimetic NPS 568 and NPS 2143 were able to modulate CaSR and IL-8 expression. We proved that pro-inflammatory effects in colon cancer cells are indeed mediated through CaSR activation. The non-CaSR selective enantiomer NPS *S*-2143 will be a valuable tool for investigations in CaSR-mediated processes.

Keywords: calcium-sensing receptor; enantiomer; calcimimetic; calcilytic; colon cancer; stereospecificity; HT-29; IL-8; inflammation

1. Introduction

The extracellular calcium-sensing receptor (CaSR) is a class C G protein-coupled receptor (GPCR) [1]. Its main and best-described physiological role is monitoring and regulating free ionized blood calcium (Ca^{2+}) concentration [2]. However, the CaSR has several other functions independent of calcium homeostasis. It regulates physiological and pathophysiological processes, such as inflammation, airway constriction, renal and intestinal water transport, cardiovascular effects, neuronal development and function, and

entero-endocrine hormone secretion, etc., in a tissue- and ligand-dependent manner [3]. The CaSR is a multimodal sensor, which has multiple ligand-binding sites for the different orthosteric and allosteric ligands, including divalent and trivalent cations, protons, L-amino acids, polyamines, aminoglycosides, or polycationic molecules [4]. These ligands can activate different G proteins ($G_{q/11}$, $G_{i/o}$, $G_{12/13}$, and in some cases even G_s). Besides the natural ligands, several pharmacological modulators of the CaSR have been developed, drugs that either mimic (calcimimetics) or antagonize (calcilytics) the effects of extracellular Ca^{2+} on the CaSR, as reviewed in [5].

As most of the ligands of the CaSR are able to act through other molecules (receptors and channels), it is very difficult to prove that a certain signaling pathway is indeed mediated by the CaSR. For instance, polycationic peptides can insert into membranes and thus alter G protein activity; aminoglycosides can block voltage-sensitive Ca^{2+} channels; Ca^{2+} itself can also signal through various channels; calcimimetics were originally derived from Ca^{2+} channel blockers, while the amino-alcohol class of calcilytics is similar to beta-blockers. Thus, it is difficult to determine whether a certain effect of a CaSR ligand is indeed mediated via the CaSR or via other routes.

The role of the CaSR in the intestine is not yet clear. Its effect on regulating intestinal inflammatory processes is a point of contention [6]. Several authors suggested a role in preventing inflammation [7,8], while we found a rather pro-inflammatory effect [9,10]. In addition, clinically used calcimimetics have severe gastrointestinal side effects [11], suggesting a role for the intestinal CaSR in mediating these adverse responses. Therefore, in the present study, we tested whether the CaSR has pro- or anti-inflammatory effects, by using positive (NPS 568) and negative (NPS 2143) allosteric modulators of the CaSR and comparing their effects on the expression of the inflammation marker interleukin 8 (IL-8), as several studies suggested that activation of the CaSR leads to the inhibition of IL-8 secretion in colon cancer cells (as reviewed in [6]). To ensure that the results are indeed specific for the CaSR, we used the *R* and *S* enantiomers of both modulators. Enantiomers are “mirror images” of a chemical structure, which only differ in the configuration (stereochemical orientation) of a chiral, i.e., asymmetric atom. The chemical structures of both NPS 568 and NPS 2143 contain one such asymmetric carbon. In both cases, the respective *R* enantiomer binds with much higher affinity to the CaSR than the *S* enantiomer. Previous studies have shown that the *R* enantiomer of NPS 568 is 10-fold more potent than the corresponding *S* enantiomer in inhibiting parathyroid hormone (PTH) secretion from bovine parathyroid cells [12]. To investigate whether the pro-inflammatory effects of calcimimetics in the colon are indeed mediated via the CaSR, we used the colon cancer cell line HT29 transfected either with the CaSR (HT-29^{CaSR-GFP}) or with the empty vector (HT29^{GFP}). These transfections are necessary because colonic epithelial cells, during transformation into cancer cells, lose their native CaSR expression. As there are no reliable native colon epithelial cell lines available, we used these modified cancer cells to study the effect of the CaSR in colonic epithelial cells in vitro where we had already determined that CaSR expression and stimulation using *R*-568 leads to massive changes in their gene expression pattern, including a strong upregulation of pro-inflammatory genes [9].

We were able to prove unequivocally that, in this cell model, the activation of the CaSR by Ca^{2+} or NPS *R*-568 induced the expression of the inflammation marker IL-8, while the calcilytic NPS *R*-2143 was able to prevent this induction. To the best of our knowledge, this is the first study to use both the *R* and *S* forms of a calcimimetic and calcilytic to identify whether a pharmacological effect is indeed mediated via the CaSR. As the non-CaSR selective enantiomer of NPS 2143 (NPS *S*-2143) is not available commercially, we also describe the synthetic route and characterization of this valuable pharmacological tool.

2. Results

As NPS *S*-2143 could not be obtained from any other source, we synthesized and evaluated it in-house.

2.1. Synthetic Chemistry

The pure (*S*) enantiomer of NPS 2143 (NPS *S*-2143) was prepared following a previously described approach for the synthesis of the (*R*) enantiomer [13], according to the synthetic route summarized in Figure 1.

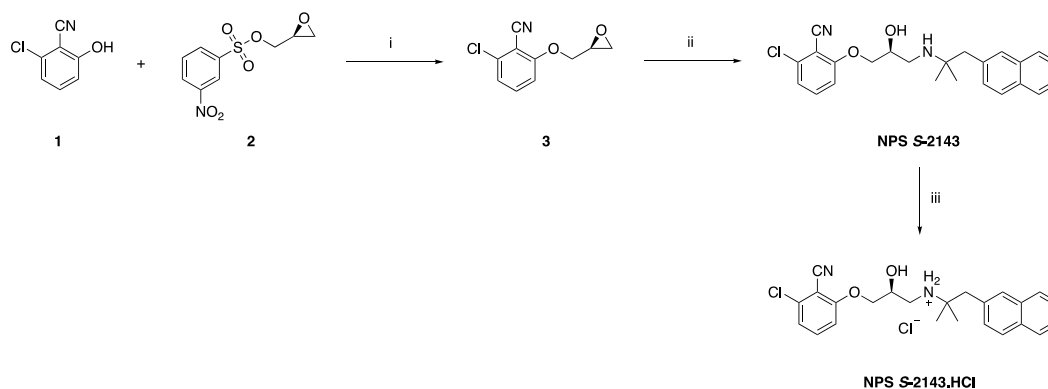


Figure 1. Preparation of NPS *S*-2143 and its hydrochloride salt. Reagents and conditions: (i) K_2CO_3 , acetone, reflux, o.n. (98%); (ii) [1,1-dimethyl-2-(2-naphthalenyl)ethyl]amine, EtOH, 80 °C, 72 h (73%); (iii) conc. HCl, MeOH, r.t., 1 h (quantitative).

Briefly, substituted phenol **1** was deprotonated in refluxing acetone, using an excess of potassium carbonate. Commercially available (*S*)-nosyl epoxide **2** was then added at r.t., and the mixture was refluxed in acetone overnight, to afford the pure intermediate **3** in high yield after flash column chromatography purification. The epoxide ring in **3** was then regioselectively opened with [1,1-dimethyl-2-(2-naphthalenyl)ethyl]amine at the less hindered position, by heating the two reagents in anhydrous EtOH at 80 °C in a sealed tube for 72 h, to afford the enantiomerically pure product NPS *S*-2143 in good yield after flash column chromatography purification. The pure hydrochloride salt of NPS *S*-2143 was finally obtained by treating NPS *S*-2143 with an excess of a concentrated hydrochloric acid solution, while stirring in MeOH at room temperature for 1 h.

2.2. Crystal Structure of NPS *S*-2143.HCl

The crystal structure of NPS *S*-2143.HCl was determined by small molecule crystallography, which confirmed the desired (*S*) absolute configuration of the chiral center. In addition to two independent chloride anions, the asymmetric unit of the crystal structure comprises two independent cations, C1-C24, N1, N2, O1, O2, Cl1 (Figure 2a) and C25-C48, N3, N4, O3, O4, Cl2 (Figure 2b). Both are the cations of NPS *S*-2143 (with chiral centres located on atoms C9 and C33), which differ in their assumption of different conformations, as illustrated by Figure 2 and the torsion angles in Table S1. When packed into the crystal, aromatic rings of the chlorobenzonitrile moieties of neighbouring cations are stacked in the *a*-axis direction with centroid-to-centroid separation of ca. 3.6 Å. The molecules involved are also bridged by N-H...Cl and O-H...Cl hydrogen bonds with each chloride ion interacting with two N-H and one O-H groups (Figure S1 and Table S2).

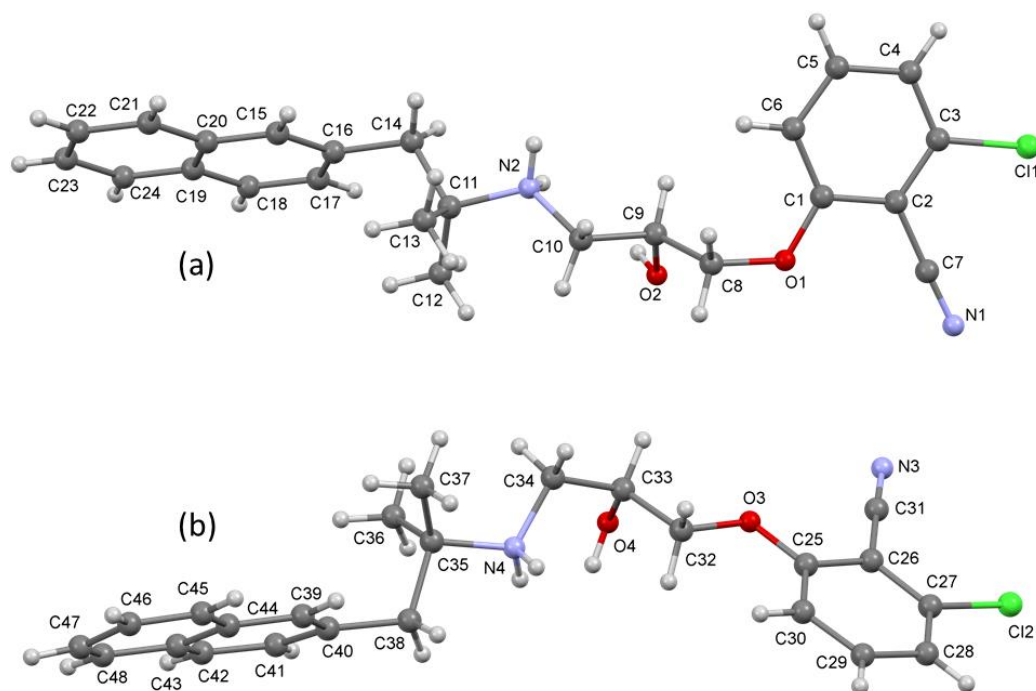


Figure 2. Ball and stick 3D representation of the molecular structure of NPS S-2143, confirming the absolute (*S*) configuration at the asymmetric carbon, showing a comparison of the two independent cations of NPS S-2143 (**a,b**) comprising the crystal, viewed roughly along the C-OH bond, e.g., showing the variation in the torsion angles between the corresponding N2-C10-C9-C8 ($158.5(4)^\circ$) and N4-C34-C33-C32 ($-65.4(5)^\circ$) bonds. Colors denote different atoms: grey = carbon, red = oxygen, green = chlorine, blue = nitrogen, light grey = hydrogen.

2.3. Enantiospecific Inhibition of the CaSR via NPS 2143

With NPS S-2143 now available, we proceeded to test the synthesized compound *in vitro* by individual-cell Ca^{2+} -imaging performed on HEK-293 cells stably transfected with the human CaSR, which is the most common cell model for evaluating the receptor and agents targeting it. Pre-incubation of the cells with a concentration of 100 nmol/L of NPS R-2143 (the selective enantiomer of the compound) significantly suppressed the intracellular Ca^{2+} -response elicited by 5 mmol/L extracellular Ca^{2+} , while the newly synthesized (unselective) NPS S-2143 had no such effect (Figure 3a–d). Together, these results showed that the clean *S* enantiomer of NPS 2143 is indeed not active on the CaSR. It could thus be used for the following specificity experiments in colorectal cancer cell.

2.4. CaSR Gene Induction and Pro-Inflammatory Responses in Colon Cancer Cells Are Mediated through the CaSR

Having established the different activities of the two enantiomers of NPS 2143, we evaluated the specificity of the enantiomers of calcimimetics and calcilytic and their combination in a cell model of colorectal cancer. Here, we used HT29 colon cancer cells, which were modified to stably express the CaSR via lentiviral infection (HT29^{CaSR-GFP}) using empty vector infected cells as the control (HT29^{GFP}).

To test directly whether the calcimimetic-induced effects on CaSR expression were indeed mediated via specific activity of the drug on the receptor or whether unspecific effects of the drug were (partly) responsible as well, we performed a series of tightly controlled single and combination treatment experiments with the selective and non-selective enantiomers of the calcimimetic NPS 568 and the calcilytic NPS 2143. To ensure proper interaction of the calcilytic with the receptor, cells were always pre-treated with NPS 2143 (or vehicle) for 30 min before their treatment with NPS 568 (if applicable). The total treatment time after the addition of NPS 568 was 4 h. Here, we used 1 $\mu\text{mol/L}$ of each compound, as the initial results using NPS R-568 and NPS R-2143 in these transfected

colon cancer cells were obtained using drug concentrations that were previously deemed to be CaSR-selective [5,9,14–16].

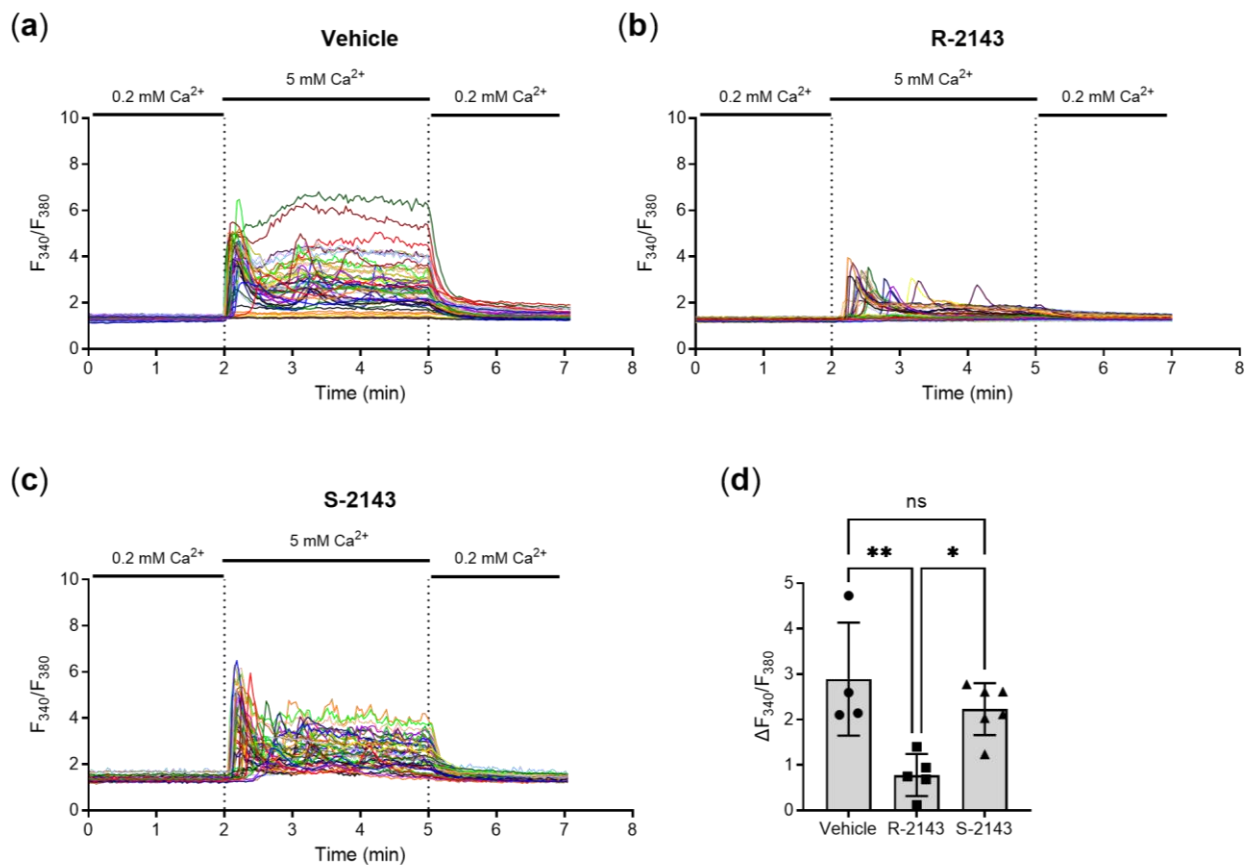


Figure 3. Example traces of the intracellular Ca^{2+} response (shown as fluorescence ratio F_{340}/F_{380} of the Ca^{2+} -dye fura-2 AM) of HEK-293 cells stably transfected with the human calcium-sensing receptor CaSR in response to 5 mmol/L Ca^{2+} , 10 min pre-incubated and perfused with either (a) vehicle control (0.1% DMSO), (b) 100 nmol/L R-2143, or (c) 100 nmol/L S-2143; each colored line represents a single cell. (d) Average maximum intracellular Ca^{2+} response per cell subtracted from its baseline response for all experiments ($N = 4-6$, each N represents the average response of >50 cells). Mean \pm SD, one-way ANOVA with Tukey post-test, ** $p < 0.01$, * $p < 0.05$.

The CaSR has a rather unique property in that its expression increases in response to stimulation (rather than decreases as most receptors do due to desensitization and internalization). This process can be observed directly at the cell membrane, where it is called agonist-driven insertional signaling (ADIS) [17], but also at the mRNA level.

Treatment of HT29^{CaSR-GFP} cells with R-568 evoked a large (~5-fold) increase in *CaSR* gene expression after 4 h of treatment. In contrast, the non-selective enantiomer of the calcimimetic, S-568, did not have any effect on *CaSR* gene expression. Neither the selective nor the non-selective enantiomers of NPS 2143 had any effect on *CaSR* gene expression, either by themselves or in combination. Importantly, pre-treatment with the selective NPS R-2143 completely abolished the *CaSR* gene induction by NPS R-568. On the other hand, pre-treatment with the non-CaSR-selective enantiomer NPS S-2143 did not have any effect on NPS R-568-induced *CaSR* gene expression. The most prominent orthosteric agonist of the CaSR, Ca^{2+} , also upregulated *CaSR* gene expression, and was used as a positive control (Figure 4a). None of the compounds or their combinations had any effect on *CaSR* expression levels in HT29^{GFP} cells, which was expected as the expression levels of the *CaSR* in the non-CaSR transfected HT29^{GFP} cells are negligible (Figure 4b). Taken together, these results showed that both NPS 568 and NPS 2143 affected *CaSR* gene expression in a highly

enantiospecific manner. This strongly indicates that the induction of *CaSR* gene expression is indeed induced directly via the CaSR itself.

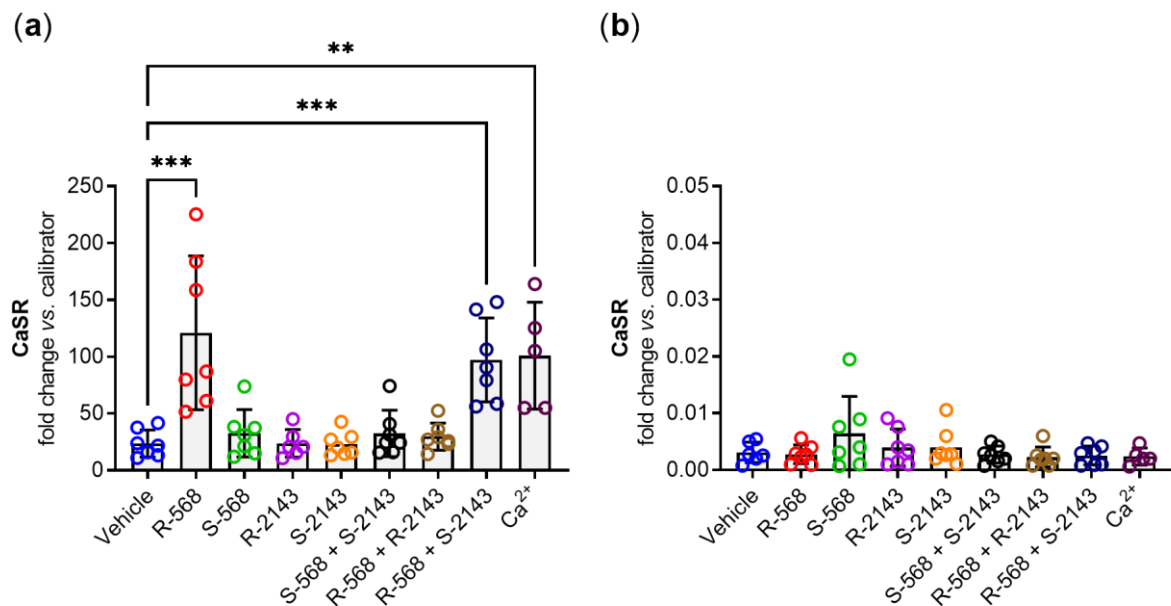


Figure 4. *CaSR* gene expression of (a) HT29^{CaSR-GFP} and (b) HT29^{GFP} cells (note the 5000× smaller scale of the *y*-axis compared to (a) treated for 4 h with either vehicle control (0.1% DMSO) or single treatments with 1 μmol/L of NPS R-568, NPS S-568, NPS R-2143, or NPS S-2143; double treatments with 1 μmol/L of each NPS S-568 + S2143, NPS R-568 + S-2143, or NPS R-568 + R-2143; or with 5 mmol/L of the orthosteric CaSR agonist Ca²⁺). *N* = 5–7, Mean ± SD, one-way ANOVA with Dunnett post-test vs. vehicle, *** *p* < 0.001, ** *p* < 0.01.

Next, we wanted to assess whether the observed enantiospecific effects of CaSR-modulation could be observed on a CaSR-influenced effector gene. As mentioned before, we have recently shown that the modulation of the CaSR with NPS R-568 led to dramatic changes in their gene expression patterns. One of the most strikingly upregulated families of genes were involved in inflammation. Thus, we investigated the effect of the above-mentioned single enantiomers and their combinations on *IL-8* gene expression, as one of the most prominent members of the previously observed pro-inflammatory genes.

We observed the same pattern for *IL-8* gene expression as for *CaSR* in HT29^{CaSR-GFP} cells. NPS R-568 induced a strong upregulation of *IL-8*, while the unspecific NPS S-568 showed no effect whatsoever. Both enantiomers of the calcilytic NPS 2143 did not affect *IL-8* gene expression, and neither did the combination of the two unselective enantiomers NPS S-568 and NPS S-2143. Again, pre-treatment of the cells with NPS R-2143 inhibited NPS R-568-induced *IL-8* gene expression, while NPS S-2143 was not able to suppress this upregulation. The orthosteric CaSR agonist Ca²⁺ also induced a robust upregulation of *IL-8* gene expression (Figure 5a). In HT29^{GFP} cells, none of the substances led to any change in *IL-8* gene expression compared with the vehicle control (Figure 5b).

Finally, we investigated whether changes in *IL-8* gene expression were mirrored by changes at the secreted protein level. We, therefore, performed an ELISA experiment on cell culture supernatants from treated HT29^{CaSR-GFP} and HT29^{GFP} cells and observed the same effect on the protein level as we did on the mRNA level. NPS R-568 and 5 mmol/L Ca²⁺ induced upregulation of IL-8 secretion by the HT29^{CaSR-GFP} cells. The pre-incubation with NPS R-2143 prevented this upregulated secretion, while the unspecific NPS S-2143 did not (Figure 6a). No effects on IL-8 secretion were observed in HT29^{GFP} cells lacking the CaSR (Figure 6b). Interestingly, baseline IL-8 levels were already higher in vehicle-treated HT29^{CaSR-GFP} cells than in HT29^{GFP} cells.

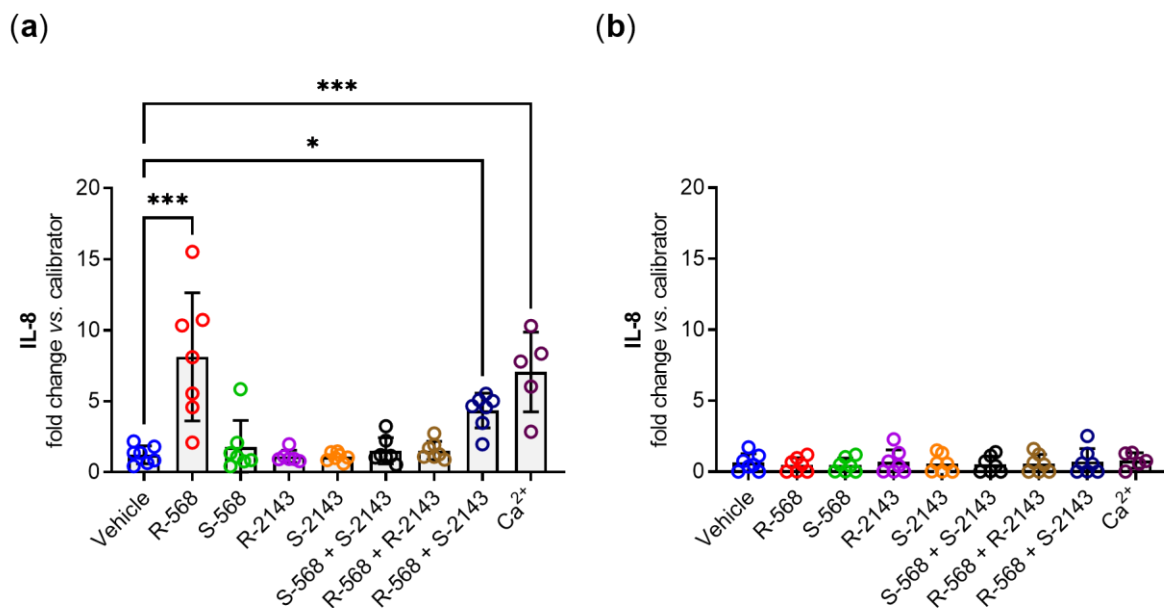


Figure 5. Interleukin 8 (IL-8) gene expression in (a) HT29^{CaSR-GFP} and (b) HT29^{GFP} cells treated for 4 h with either vehicle control (0.1% DMSO) or single treatments with 1 $\mu\text{mol/L}$ of R-568, S-568, R-2143, or S-2143; double treatments with 1 $\mu\text{mol/L}$ of each S-568 + S2143, R-568 + S-2143, or R-568 + R-2143; or with 5 mmol/L of the orthosteric CaSR agonist Ca²⁺. $N = 5\text{--}7$, Mean \pm SD, one-way ANOVA with Dunnett post-test vs. vehicle, *** $p < 0.001$, * $p < 0.05$.

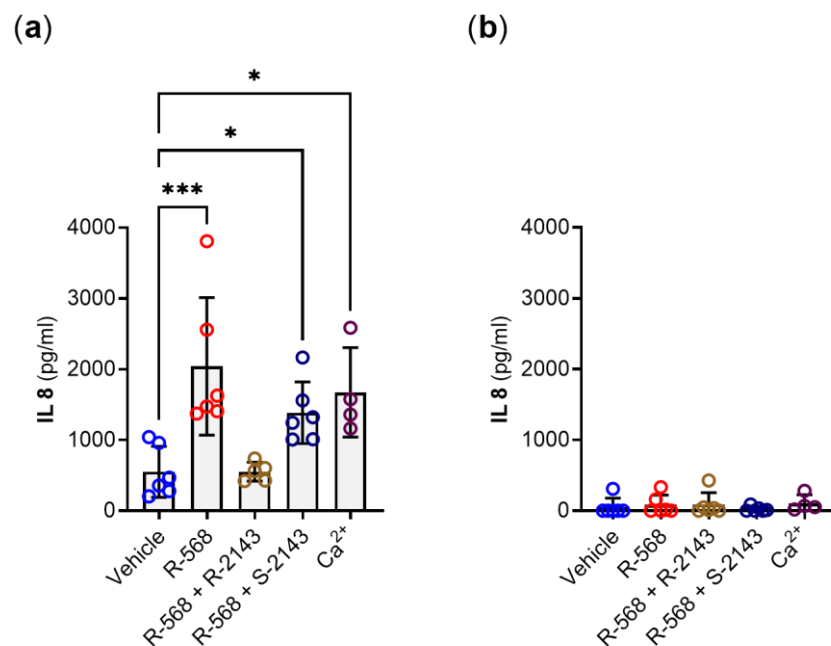


Figure 6. IL-8 protein (ELISA) in cell culture medium of (a) HT29^{CaSR-GFP} and (b) HT29^{GFP} cells treated for 4 h with either vehicle control (0.1% DMSO); 1 $\mu\text{mol/L}$ of R-568; double treatments with 1 $\mu\text{mol/L}$ of each R-568 + S-2143, or R-568 + R-2143; or with 5 mmol/L of the orthosteric CaSR agonist Ca²⁺. $N = 4\text{--}6$, Mean \pm SD, one-way ANOVA with Holm–Sidak post-test vs. vehicle, *** $p < 0.001$, * $p < 0.05$.

3. Discussion

We were able to prove unequivocally that the CaSR mediates the Ca²⁺- and NPS R-568-induced increase in the expression of the inflammation marker IL-8 in HT29^{CaSR-GFP} cells. To verify this, we used both the R and S enantiomers of the calcimimetic NPS 568 and of the calcilytic NPS 2143 and compared their effects in the isogenic cell lines HT29^{CaSR-GFP} and

HT29^{GFP}, differing only in the expression of CaSR. As, to our knowledge, no *S* enantiomer of NPS 2143 was available, we synthesized it and thus obtained a very useful tool for further pharmacological studies on the CaSR.

After ensuring that the synthesized NPS *S*-2143 is indeed significantly less active than *R*-2143 in preventing extracellular Ca²⁺-induced intracellular Ca²⁺ release, we assessed the effectiveness of the modulators in regulating *CaSR* expression, a well-known effect of these compounds. Indeed, extracellular Ca²⁺ and the well-characterized calcimimetic NPS *R*-568 significantly induced *CaSR* expression, which was inhibited by *R*-2143. None of the *S* enantiomers affected *CaSR* expression, proving that the cells were responsive only to the *R* modulators. In the same cells, we measured the IL-8 expression at both the mRNA and protein levels. Numerous studies have shown that IL-8 is a pro-inflammatory cytokine [18] in the intestine [19,20], and thus a valid marker for a pro-inflammatory response in our cell model.

Therefore, we needed to prove that our contradictory observation [9] that the activation of the CaSR induces IL-8 expression is real, and indeed mediated by the CaSR. The results of the Iamartino study [9] were already very convincing, as the observed upregulation of several inflammatory markers was seen only in the cells expressing the CaSR but not in the cells with undetectable CaSR levels. While the observation that *R*-568 induced the expression of these markers suggested that the CaSR mediates this effect, we needed unequivocal proof. Indeed, we could show that only the actively binding *R*-568, at the same concentration of 1 µmol/L as used in the aforementioned study, induced the expression of IL-8, and NPS *S*-568 was unable to do so. The effect of NPS *R*-568 was inhibited by NPS 2143 in a similar stereospecific manner: only *R*-2143 prevented the *R*-568-dependent induction, whereas NPS *S*-2143 did not.

Several studies suggested that calcilytics could be used in the treatment of inflammatory diseases, such as asthma [14,21]. Thus, the newly synthesized *S*-2143 could become a highly useful tool in experiments of proof of principle in other tissues and organs as well.

The first generation of calcimimetics, such as NPS *R*-568, has one chiral carbon and acts stereoselectively on the CaSR. Regardless of the parameter assessed, the *R* enantiomer was always more potent (10- to 100-fold, depending on the measured variable) compared to the *S* enantiomer. At concentrations that maximally activate the CaSR, NPS 568 inhibits ion channels, but this effect is not stereospecific, meaning that both the *R* and *S* enantiomers have similar effects [22]. The calcilytic NPS 2143 also acts on the CaSR in a stereoselective manner and again, the *R* enantiomer is more potent [12,22]. Thus, testing that the compounds used in our experiment produce the expected effect in a stereospecific manner ascertained that the effect was CaSR-mediated. Moreover, none of the compounds had any effect on *IL-8* (or *CaSR*) expression in the HT29^{GFP} cells lacking detectable levels of endogenous CaSR, suggesting that at the concentrations used, the observed effects were not due to the activation of any other possible targets (e.g., voltage-gated Ca²⁺ channels).

To understand the role of the CaSR in a cell is demanding, because Ca²⁺, its main physiological ligand, signals not only through the CaSR, but also by binding to other molecules (e.g., ion channels). Therefore, it is important to combine the right pharmacological approach with the most appropriate experimental design. However, this is challenging in cells where the primary role of the receptor is not clear and Ca²⁺ affects numerous biological processes. The biological process we had to test was given (regulation of the expression of IL-8) and the specificity of the drugs used in this study has already been tested either on parathyroid cells and/or on HEK-CaSR cells (a model broadly used in the field).

Our study is a good example for testing the involvement of the CaSR in molecular processes. It is the first study, to our knowledge, that uses enantiomer pairs and combinations of positive and negative modulators to prove the involvement of a target in the signaling process in intestinal cells. Many natural (endogenous) ligands of the CaSR signal through numerous alternative pathways. Most of the pharmacological modulators have structures very similar to drugs acting on other molecules (e.g., Ca²⁺-channel or β-blockers).

Therefore, it is difficult to exclude the possibility that the effects seen are mediated through other pathways, even more so when the concentrations used are higher than those needed to modulate CaSR activity. The *S* enantiomers could prove very useful in such cases, as they could be used to test if the effect seen is indeed caused by the binding of the drug to the CaSR.

The role of the CaSR in the gastrointestinal tract is complex. The clinical use of calcimimetics, both oral and intravenously applied, is associated with substantial gastrointestinal side effects, such as vomiting and nausea [11], and the U.S. Food and Drug Administration (FDA) has updated the label of cinacalcet to include the risk for upper gastrointestinal bleeding (FDA ID: 4097661). The actual, direct role of the gastrointestinal CaSR in (patho-)physiology and in these adverse effects is, however, still not fully understood. Several studies have shown that the CaSR is directly involved in intestinal fluid secretion [23,24]. However, the involvement of the CaSR in intestinal inflammation is still unclear [6]. The most frequent approaches to verify the role of CaSR in physiology and pathophysiology are either genetic, by comparing the phenotype of the mice lacking the CaSR to their wild type controls [25,26], or pharmacological approaches, using specific CaSR activators (e.g., *R*-568) or inhibitors (e.g., NPS 2143). One of the limitations of the genetic approach is that the organism might develop mechanisms to compensate for the loss of the CaSR. The limitations of the pharmacological approaches are that often the doses of the pharmacological compounds are too high [27], raising the question as to how this affects the specificity of the effect. The potent and selective pharmacological modulators of the CaSR (NPS *R*-568 and NPS *R*-2143) have been proven useful in uncovering new functions of the CaSR at different sites throughout the body [28]. However, it is important to use these compounds in a concentration that is selective to the CaSR, as at high concentrations, they will affect cellular responses independent of the CaSR [22]. In our study, we combined a genetic approach (but instead of knocking out, we introduced the CaSR in the cells) with the pharmacological approach, by using compounds at concentrations that are still specific for the CaSR and taking advantage of the stereospecificity of the used calcimimetic and calcilytic.

Our study demonstrates that in the HT29^{CaSR-GFP} cells, the major activators of the CaSR, Ca²⁺ and *R*-568, induced and did not inhibit the expression of the inflammatory cytokine IL-8. Our results unequivocally confirm the CaSR as a mediator of the enhanced inflammatory gene expression in these cells and are quadruple controlled: (1) a positive CaSR modulator induced inflammatory gene expression, (2) a negative CaSR modulator prevented this upregulation, (3) the unspecific enantiomers of these compounds did not exhibit these effects, and (4) none of these effects were observed in cells not expressing the CaSR.

These data also suggest that in native cells, where no endogenous CaSR is present, the drugs will not affect the expression of these inflammatory markers. This would be in line with our observation in an *in vivo* study, where neither the calcimimetic cinacalcet nor NPS *R*-2143 affected the expression of the inflammatory marker IL-6 in the colon of mice treated per gavage for 2 weeks with these modulators (unpublished results/manuscript in preparation). We now have a better understanding of the role of the CaSR in mediating inflammatory responses and with NPS *S*-2143, a valuable tool for controlling pharmacological CaSR modulation experiments

4. Materials and Methods

4.1. Preparation of NPS *S*-2143—Synthetic Chemistry

All solvents and reagents were used as obtained from commercial sources, unless otherwise indicated. All solvents used for chromatography were HPLC grade (Fisher Scientific, Loughborough, UK). All reactions were performed under a nitrogen atmosphere. ¹H and ¹³C-NMR spectra were recorded with a Bruker Avance III HD spectrometer (Bruker, Coventry, UK) operating at 500 MHz for ¹H and 125 MHz for ¹³C, with Me₄Si as the internal standard. Deuterated chloroform was used as the solvent for NMR experiments.

^1H chemical shifts values (δ) are referenced to the residual non-deuterated components of the NMR solvents ($\delta = 7.26$ ppm for CHCl_3 , etc.). The ^{13}C chemical shifts (δ) are referenced to CDCl_3 (central peak, $\delta = 77.0$ ppm). TLC was performed on silica gel 60 F254 plastic sheets. Normal-phase automated flash column chromatography was performed using a Biotage Isolera system (Biotage, Hengoed, UK). UPLC–MS analysis was conducted on a Waters UPLC system (Waters, Wilmslow, UK) with both Diode Array detection and Electrospray (+ve and –ve ion) MS detection. The stationary phase was a Waters Acquity UPLC BEH C18 1.7 μm 2.1 \times 50 mm column (Waters). The mobile phase was LC–MS grade H_2O containing 0.1% formic acid (A) and LC–MS grade MeCN containing 0.1% formic acid (B). Column temperature: 40 $^\circ\text{C}$. Sample diluent: MeCN or H_2O . Sample concentration: 1 $\mu\text{g}/\text{mL}$. Injection volume: 2 μL . A linear gradient method was used for all analyses performed: 90% A (0.1 min), 90–0% A (1.5 min), 0% A (1.4 min), 90% A (0.1 min); flow rate: 0.5 mL/min. All compounds synthesised were >98% pure.

4.1.1. Synthesis of (S)-2-chloro-6-(oxiran-2-ylmethoxy)benzotrile 3

Potassium carbonate (17.6 mmol, 3 eq.) was added to a stirring solution of 2-chloro-6-hydroxybenzotrile 1 (5.9 mmol, 1 eq.) in dry acetone (60 mL), and the mixture was heated to reflux for 30 min. After cooling to room temperature, commercially available (S)-nosyl epoxide 2 (5.9 mmol, 1 eq.) was added to the reaction, and stirring was continued while heating to reflux overnight. After cooling to room temperature, the reaction mixture was filtered, and the filtrate was dried under vacuum. The crude residue was purified by flash column chromatography on silica gel (*n*-hexane/ethyl acetate 100:0 to *n*-hexane/ethyl acetate 0:100 *v/v*) to afford the pure title compound as a white solid in 98% yield. $^1\text{H-NMR}$ (CDCl_3), δ : 7.46 (dd, $J_1 = 8.9$ Hz, $J_2 = 8.1$ Hz, 1H), 7.12 (dd, $J_1 = 8.1$ Hz, $J_2 = 0.8$ Hz, 1H), 6.96 (dd, $J_1 = 8.9$ Hz, $J_2 = 0.8$ Hz, 1H), 4.42 (dd, $J_1 = 11.4$ Hz, $J_2 = 2.8$ Hz, 1H), 4.14 (dd, $J_1 = 11.4$ Hz, $J_2 = 5.2$ Hz, 1H), 3.43–3.40 (m, 1H), 2.96 (dd, $J_1 = 4.7$ Hz, $J_2 = 4.1$ Hz, 1H), 2.87 (dd, $J_1 = 4.7$ Hz, $J_2 = 2.6$ Hz, 1H). $^{13}\text{C-NMR}$ (CDCl_3), δ : 161.4, 138.1, 134.3, 122.3, 113.4, 110.7, 103.6, 69.8, 49.7, 44.5.

4.1.2. Synthesis of (S)-2-chloro-6-(3-((2,2-dimethyl-3-(naphthalen-2-yl)propyl)amino)-2-hydroxypropoxy) benzotrile (NPS S-2143)

A solution of (S)-epoxide 3 (3.3 mmol, 1 eq.) and [1,1-dimethyl-2-(2-naphthalenyl)ethyl]amine (3.3 mmol, 1 eq.) in dry EtOH (17 mL) was heated to 80 $^\circ\text{C}$ in a sealed tube for 72 h. The mixture was then dried under vacuum, and the crude residue was purified by flash column chromatography on silica gel (*n*-hexane/ethyl acetate 100:0 to *n*-hexane/ethyl acetate 0:100 *v/v*) to afford the pure title compound as a colourless oil in 73% yield. $^1\text{H-NMR}$ (CDCl_3), δ : 7.83–7.76 (m, 3H), 7.64 (s, 1H), 7.48–7.42 (m, 3H), 7.35 (dd, $J_1 = 8.3$ Hz, $J_2 = 1.7$ Hz, 1H), 7.10 (dd, $J_1 = 8.1$ Hz, $J_2 = 0.8$ Hz, 1H), 6.91 (dd, $J_1 = 7.8$ Hz, $J_2 = 0.8$ Hz, 1H), 4.18–4.12 (m, 2H), 4.03–3.98 (m, 1H), 3.06 (dd, $J_1 = 12.1$ Hz, $J_2 = 4.6$ Hz, 1H), 2.94–2.90 (m, 3H), 1.17 (s, 3H), 1.16 (s, 3H). $^{13}\text{C-NMR}$ (CDCl_3), δ : 137.7, 134.4, 133.2, 132.5, 131.8, 129.7, 128.7, 128.1, 127.7, 127.6, 126.3, 126.1, 122.4, 113.6, 110.9, 103.6, 71.2, 65.5, 61.5, 44.9, 44.4, 23.2, 23.0. UPLC–MS: R_t 1.65 min, MS [ESI, *m/z*]: 409.3, 411.3 [M + H].

4.1.3. Synthesis of (S)-2-chloro-6-(3-((2,2-dimethyl-3-(naphthalen-2-yl)propyl)amino)-2-hydroxypropoxy) benzotrile hydrochloride (NPS S-2143.HCl)

(S)-2-Chloro-6-(3-((2,2-dimethyl-3-(naphthalen-2-yl)propyl)amino)-2-hydroxypropoxy) benzotrile (2.4 mmol, 1 eq.) was dissolved in MeOH (15 mL) and added dropwise of a concentrated HCl solution (3 mL), while stirring. Stirring was continued at room temperature for a further 1 h, and the residue was then dried under vacuum to afford the pure title compound as a white solid in quantitative yield. $^1\text{H-NMR}$ (CDCl_3), δ : 9.89 (bs, 1H), 8.37 (bs, 1H), 7.82–7.78 (m, 3H), 7.74 (s, 1H), 7.49–7.45 (m, 2H), 7.39–7.35 (m, 2H), 7.02 (d, $J = 7.9$ Hz, 1H), 6.91 (d, $J = 8.5$ Hz, 1H), 5.67 (d, $J = 5.1$ Hz, 1H), 4.84 (bs, 1H), 4.32–4.26 (m, 2H), 3.57–3.51 (m, 1H), 3.49–3.37 (m, 3H), 1.54 (s, 3H), 1.51 (s, 3H). $^{13}\text{C-NMR}$ (CDCl_3), δ : 161.8, 137.9, 135.8, 134.2, 133.3, 132.1, 129.2, 128.8, 127.5, 127.4, 125.9, 125.4, 122.0, 113.5,

110.5, 103.6, 71.9, 67.9, 53.7, 47.8, 43.9, 27.2, 27.1. UPLC–MS: R_t 1.70 min, MS [ESI, m/z]: 409.3, 411.3 [M + H].

4.2. Crystal Structure Determination

Single-crystal XRD data were collected at room temperature on an Agilent SuperNova Dual Atlas diffractometer (Agilent Technologies XRD Products, Yarnton, UK) with a mirror monochromator using Cu ($\lambda = 1.5418 \text{ \AA}$) radiation. The crystal structure was solved using SHELXS [29] and refined using SHELXL2018 [30]. Non-hydrogen atoms were refined with anisotropic displacement parameters, and hydrogen atoms were inserted in idealized positions. A riding model was used with Uiso(H) set at 1.2 or 1.5 times the $U_{eq}(C,N,O)$ values of the atoms to which the H atoms are bonded. The asymmetric unit contains two cations and two chloride anions. The naphthalene moieties of both independent cations were modelled as disordered, and the components refined to roughly equal occupancy. The crystallographic and refinement parameters are as follows: $C_{24}H_{26}ClN_2O_2^+Cl^-$: FW = 445.37, T = 293(2) K, orthorhombic, $P2_12_12_1$, a = 6.9104(2) \AA , b = 16.3499(5) \AA , c = 40.5957(9) \AA , V = 4586.7(2) \AA^3 , Z = 8, $\rho_{cal} = 1.290 \text{ Mg/m}^3$, $\mu = 2.722 \text{ mm}^{-1}$, F(000) = 1872, crystal size = $0.575 \times 0.114 \times 0.039 \text{ mm}$, reflections collected = 43002, independent reflections = 9164, R(int) = 0.0629, goodness-of-fit on $F^2 = 1.016$, Flack parameter = $-0.009(8)$, largest diff. peak and hole = 0.258 and $-0.256 \text{ e.\AA}^{-3}$, R1 = 0.0522 and wR2 = 0.1311 for $I > 2\sigma(I)$, R1 = 0.0704 and wR2 = 0.1410 for all data.

4.3. Other Compounds and Reagents

NPS R-568 and NPS R-2143 were obtained commercially (Tocris Bioscience/Bio-Techne Ltd., Abingdon, UK), NPS S-568 was a kind gift from Amgen, UK. All basic compounds were obtained from Merck (Darmstadt, DE), unless otherwise stated.

4.4. Calcium Imaging Experiments

HEK293 cells stably transfected with the human CaSR (HEK-CaSR, a kind gift of Dr. Donald Ward [31]) were cultured on poly-D-lysine coated 13 mm coverslips, and calcium imaging experiments were performed as described previously [21]. In brief, the medium of the cells was removed, and cells were loaded with 3 $\mu\text{mol/L}$ Fura 2-AM (Thermo Fisher Scientific, Waltham, MA, USA) in extracellular buffer containing 1.0 mmol/L Ca^{2+} for 45 min at 37 °C. Cells were then washed with ECS at room temperature and pre-incubated with buffer containing 0.2 mmol/L Ca^{2+} and 100 nmol/L NPS R/S-2143 or 0.1% DMSO for 15 min. Cells were imaged on an inverted Olympus IX71 fluorescence microscope (Olympus, Southend-on-Sea, UK). A rapid perfusion system was then used to alter extracellular Ca^{2+} from 0.2 (2 min, baseline) to 5 (3 min, stimulation) to 0.2 mmol/L Ca^{2+} (2 min), with each buffer containing either 100 nmol/L NPS R/S-2143 or 0.1% DMSO. Fluorescence of individual cells (~30–70 per experiment) at 340 and 380 nm was acquired every 2 s. For analysis, the background fluorescence was subtracted for both wavelengths, and the average F340/F380 ratio of the baseline of each cell was then subtracted from the maximum response of each cell during the stimulation phase. The average of these differences in one experiment counted as one biological repetition.

4.5. Colon Cancer Cells

We used lentiviral stably transduced colon cancer cell lines HT29^{CaSR-GFP} and HT29^{GFP} [9]. The parent HT-29 cell line was obtained commercially (HTB-38TM) from the American Type Culture Collection (ATCC, Manassas, VA, USA). Transduced cells were cultured in Dulbecco's Modified Eagle's Medium containing 10% fetal calf serum, 100 U/mL Pen-Strep, 2 mmol/L L-glutamine and 10 mmol/L Hepes. Of note, the medium by itself contains 1.8 mmol/L Ca^{2+} , the complete (FCS supplemented) medium contains ~ 2 mmol/L Ca^{2+} . To select for transduced cells, 0.5 $\mu\text{L/mL}$ puromycin (all Thermo Fisher Scientific) was added to the cell medium. For the treatments, cells were seeded into 6-well plates and grown to

70–80% confluence. 24 h before the treatments, the medium was changed without adding puromycin to let cells recover. All cells were regularly tested negatively for mycoplasma.

4.6. Compound Treatments

70–80% confluent cells in 6-well plates were treated for 4 h with 1 $\mu\text{mol/L}$ of the CaSR modulators alone or in combination, or 5 mmol/L Ca^{2+} (through addition of an 0.25 mol/L aqueous solution of CaCl_2). All compounds were prepared as 2 mmol/L stock solutions in DMSO and were added either by themselves and supplemented with DMSO, or in combination so that DMSO concentration in the medium was 0.1% for all conditions. NPS R/S-2143 was always added 15 min prior to the addition of NPS R/S-568 (pre-incubation period). After incubation, the cells were washed with ice-cold phosphate buffered saline, and finally lysed in Trizol (Thermo Fisher Scientific) by vigorous pipetting for RNA isolation.

4.7. Reverse Transcription Real Time PCR (RT-qPCR)

RNA was isolated from Trizol treated cells according to the manufacturer's protocol. RNA concentrations and purity were measured spectrophotometrically, and integrity was confirmed by gel electrophoresis. Reverse transcription of 1000 ng RNA per sample was performed using the High-Capacity cDNA Reverse Transcription kit (Thermo Fisher Scientific) according to the manufacturer's instructions. RT-qPCR was performed on QuantStudio 12K Flex and QuantStudio 5 real time PCR systems (Thermo Fisher Scientific) with the following program: 2 min 50 $^{\circ}\text{C}$, 10 min 95 $^{\circ}\text{C}$, 40 \times 15 s 95 $^{\circ}\text{C}$ to 1 min 60 $^{\circ}\text{C}$, followed by melting curve analysis 55–95 $^{\circ}\text{C}$, using Power SYBR Green PCR Master Mix (Thermo Fisher Scientific). Relative quantification of the samples was performed using the $\Delta\Delta\text{Ct}$ method, using the average of two housekeeping genes (ribosomal protein lateral stalk subunit P0 [*RPLP0*] & β 2-macroglobulin [*B2m*]), human total RNA calibrator (Takara, Kusatsu, JP) as reference, and the following primer sequences: *RPLP0*: TGGTCATCCAGCAGGTGTTCTGA (fwd), GCAGCAGCTGGCACCTTATTG (rev); *B2m*: GATGAGTATGCCTGCCGTGTG (fwd), CAATCCAAATGCGGCATCT (rev); *CaSR*: GCCAAGAAGGGAGAAAGAC (fwd), CACACTCAAAGCAGCAGG (rev); *IL-8*: CTTGGCAGCCTTCCTGATTT (fwd), TTCTTTAGCACTCCTTGGCAAAA (rev) [9].

4.8. Statistical Analysis

Statistical analysis and visualizations were performed used GraphPad Prism 9.2 (GraphPad Software, San Diego, CA, USA). The applied statistical tests are indicated in the captions of each figure.

Supplementary Materials: The following are available online at <https://www.mdpi.com/article/10.3390/ijms221810124/s1>.

Author Contributions: Conceptualization, M.S. (Martin Schepelmann) and E.K.; methodology, M.S. (Martin Schepelmann), M.B., B.M.K., E.K. and D.R.; formal analysis, M.S. (Martin Schepelmann), B.M.K. and M.B.; investigation, M.S. (Martin Schepelmann), N.K., B.M.K., M.S. (Marta Sladczyk), T.M., K.P., B.M. and M.B.; resources, M.B., B.M.K., L.I., M.B., E.K., and D.R.; data curation, M.S. (Martin Schepelmann), N.K. and B.M.K.; writing—original draft preparation, M.S. (Martin Schepelmann), E.K., B.M.K., D.R. and M.B.; writing—review and editing, M.S. (Martin Schepelmann), N.K., L.I., E.K., D.R., M.B. and B.M.K.; visualization, M.B., B.M.K. and M.S. (Martin Schepelmann); project administration, M.S. (Martin Schepelmann) and E.K.; funding acquisition, M.S. (Martin Schepelmann) and E.K. All authors have read and agreed to the published version of the manuscript.

Funding: This research was funded by the Austrian Science Fund (FWF) and the Herzfelder'sche Familienstiftung, grant number P 32840-B (to M.S., Martin Schepelmann); the Austrian Science Fund (FWF), grant number P 29948-B28 (to E.K.); the European Union Horizon 2020 research and innovation programme, grant number 675228 (to E.K.); and the Welsh Government through the Knowledge Economy Skills Scholarship 2, grant number 516062 (to D.R.).

Data Availability Statement: Supplementary crystallographic data are available at CCDC 2097408.

Acknowledgments: The authors wish to thank Amgen and Donald Ward from the University of Manchester for providing reagents and cells. Open Access Funding by the Austrian Science Fund (FWF).

Conflicts of Interest: The authors declare no conflict of interest. The funders had no role in the design of the study; in the collection, analyses, or interpretation of data; in the writing of the manuscript, or in the decision to publish the results.

References

- Brown, E.M.; Gamba, G.; Riccardi, D.; Lombardi, M.; Butters, R.; Kifor, O.; Sun, A.; Hediger, M.A.; Lytton, J.; Hebert, S.C. Cloning and characterization of an extracellular Ca^{2+} -sensing receptor from bovine parathyroid. *Nature* **1993**, *366*, 575–580. [CrossRef]
- Brown, E.M. Role of the calcium-sensing receptor in extracellular calcium homeostasis. *Best Pract. Res. Clin. Endocrinol. Metab.* **2013**, *27*, 333–343. [CrossRef] [PubMed]
- Hannan, F.M.; Kallay, E.; Chang, W.; Brandi, M.L.; Thakker, R.V. The calcium-sensing receptor in physiology and in calcitropic and noncalcitropic diseases. *Nat. Rev. Endocrinol.* **2018**, *15*, 33–51. [CrossRef]
- Leach, K.; Hannan, F.M.; Josephs, T.M.; Keller, A.N.; Møller, T.C.; Ward, D.T.; Kallay, E.; Mason, R.S.; Thakker, R.V.; Riccardi, D.; et al. International Union of Basic and Clinical Pharmacology. CVIII. Calcium-Sensing Receptor Nomenclature, Pharmacology, and Function. *Pharmacol. Rev.* **2020**, *72*, 558–604. [CrossRef] [PubMed]
- Nemeth, E.F.; Van Wagenen, B.C.; Balandrin, M.F. Discovery and Development of Calcimimetic and Calcilytic Compounds. *Prog. Med. Chem.* **2018**, *57*, 1–86. [CrossRef] [PubMed]
- Iamartino, L.; Elajnaf, T.; Kallay, E.; Schepelmann, M. Calcium-sensing receptor in colorectal inflammation and cancer: Current insights and future perspectives. *World J. Gastroenterol.* **2018**, *24*, 4119–4131. [CrossRef]
- Mine, Y.; Zhang, H. Anti-inflammatory Effects of Poly-l-lysine in Intestinal Mucosal System Mediated by Calcium-Sensing Receptor Activation. *J. Agric. Food Chem.* **2015**, *63*, 10437–10447. [CrossRef]
- Zhang, H.; Kovacs-Nolan, J.; Kodera, T.; Eto, Y.; Mine, Y. γ -Glutamyl cysteine and γ -glutamyl valine inhibit TNF- α signaling in intestinal epithelial cells and reduce inflammation in a mouse model of colitis via allosteric activation of the calcium-sensing receptor. *Biochim. Biophys. Acta BBA Mol. Basis Dis.* **2015**, *1852*, 792–804. [CrossRef]
- Iamartino, L.; Elajnaf, T.; Gall, K.; David, J.; Manhardt, T.; Heffeter, P.; Grusch, M.; Derdak, S.; Baumgartner-Parzer, S.; Schepelmann, M.; et al. Effects of pharmacological calcimimetics on colorectal cancer cells over-expressing the human calcium-sensing receptor. *Biochim. Biophys. Acta (BBA) Bioenerg.* **2020**, *1867*, 118836. [CrossRef] [PubMed]
- Elajnaf, T.; Iamartino, L.; Mesteri, I.; Müller, C.; Bassetto, M.; Manhardt, T.; Baumgartner-Parzer, S.; Kallay, E.; Schepelmann, M. Nutritional and Pharmacological Targeting of the Calcium-Sensing Receptor Influences Chemically Induced Colitis in Mice. *Nutrients* **2019**, *11*, 3072. [CrossRef] [PubMed]
- Block, G.A.; Bushinsky, D.A.; Cheng, S.; Cunningham, J.; Dehmel, B.; Druke, T.B.; Ketteler, M.; KewalRamani, R.; Martin, K.J.; Moe, S.M.; et al. Effect of Etelcalcetide vs Cinacalcet on Serum Parathyroid Hormone in Patients Receiving Hemodialysis with Secondary Hyperparathyroidism: A Randomized Clinical Trial. *JAMA* **2017**, *317*, 156–164. [CrossRef] [PubMed]
- Nemeth, E.F.; Steffey, M.E.; Hammerland, L.G.; Hung, B.C.P.; Van Wagenen, B.C.; DelMar, E.G.; Balandrin, M.F. Calcimimetics with potent and selective activity on the parathyroid calcium receptor. *Proc. Natl. Acad. Sci. USA* **1998**, *95*, 4040–4045. [CrossRef] [PubMed]
- Marquis, R.W.; Lago, A.M.; Callahan, J.F.; Trout, R.E.L.; Gowen, M.; DelMar, E.G.; Van Wagenen, B.C.; Logan, S.; Shimizu, S.; Fox, J.; et al. Antagonists of the Calcium Receptor I. Amino Alcohol-Based Parathyroid Hormone Secretagogues. *J. Med. Chem.* **2009**, *52*, 3982–3993. [CrossRef] [PubMed]
- Yarova, P.L.; Huang, P.; Schepelmann, M.W.; Bruce, R.; Ecker, R.; Nica, R.; Telezhkin, V.S.; Traini, D.; Dos Reis, L.G.; Kidd, E.J.; et al. Characterization of Negative Allosteric Modulators of the Calcium-Sensing Receptor for Repurposing as a Treatment of Asthma. *J. Pharmacol. Exp. Ther.* **2021**, *376*, 51–63. [CrossRef] [PubMed]
- Cayzac, S.H.; Rocher, A.; Obeso, A.; Gonzalez, C.; Riccardi, D.; Kemp, P. Spermine attenuates carotid body glomus cell oxygen sensing by inhibiting L-type Ca^{2+} channels. *Respir. Physiol. Neurobiol.* **2011**, *175*, 80–89. [CrossRef]
- Finney, B.A.; Del Moral, P.M.; Wilkinson, W.J.; Cayzac, S.; Cole, M.; Warburton, D.; Kemp, P.J.; Riccardi, D. Regulation of mouse lung development by the extracellular calcium-sensing receptor, CaR. *J. Physiol.* **2008**, *586*, 6007–6019. [CrossRef]
- Grant, M.P.; Stepanchick, A.; Cavanaugh, A.; Breitwieser, G.E. Agonist-Driven Maturation and Plasma Membrane Insertion of Calcium-Sensing Receptors Dynamically Control Signal Amplitude. *Sci. Signal.* **2011**, *4*, ra78. [CrossRef]
- Subramanian, S.; Rhodes, J.M.; Hart, A.C.; Tam, B.; Roberts, C.L.; Smith, S.L.; Corkill, J.E.; Winstanley, C.; Virji, M.; Campbell, B.J. Characterization of epithelial IL-8 response to inflammatory bowel disease mucosal E. coli and its inhibition by mesalamine. *Inflamm. Bowel Dis.* **2008**, *14*, 162–175. [CrossRef]
- Martin-Viñas, J.J.; Quigley, E.M.M. Immune response in irritable bowel syndrome: A systematic review of systemic and mucosal inflammatory mediators. *J. Dig. Dis.* **2016**, *17*, 572–581. [CrossRef]
- Pedersen, G. Development, validation and implementation of an in vitro model for the study of metabolic and immune function in normal and inflamed human colonic epithelium. *Dan Med. J.* **2015**, *62*, B4973.

21. Yarova, P.L.; Stewart, A.L.; Sathish, V.; Britt, R.D., Jr.; Thompson, M.A.; Lowe, A.; Freeman, M.; Aravamudan, B.; Kita, H.; Brennan, S.; et al. Calcium-sensing receptor antagonists abrogate airway hyperresponsiveness and inflammation in allergic asthma. *Sci. Transl. Med.* **2015**, *7*, 284ra60. [CrossRef]
22. Nemeth, E. Calcimimetic and calcilytic drugs: Just for parathyroid cells? *Cell Calcium* **2004**, *35*, 283–289. [CrossRef]
23. Cheng, S.X.; Okuda, M.; Hall, A.E.; Geibel, J.P.; Hebert, S.C. Expression of calcium-sensing receptor in rat colonic epithelium: Evidence for modulation of fluid secretion. *Am. J. Physiol. Gastrointest. Liver Physiol.* **2002**, *283*, G240–G250. [CrossRef] [PubMed]
24. Geibel, J.; Sritharan, K.; Geibel, R.; Geibel, P.; Persing, J.S.; Seeger, A.; Roepke, T.K.; Deichstetter, M.; Prinz, C.; Cheng, S.X.; et al. Calcium-sensing receptor abrogates secretagogue-induced increases in intestinal net fluid secretion by enhancing cyclic nucleotide destruction. *Proc. Natl. Acad. Sci. USA* **2006**, *103*, 9390–9397. [CrossRef]
25. MacLeod, R.J. Extracellular calcium-sensing receptor/PTH knockout mice colons have increased Wnt/ β -catenin signaling, reduced non-canonical Wnt signaling, and increased susceptibility to azoxymethane-induced aberrant crypt foci. *Lab. Investig.* **2013**, *93*, 520–527. [CrossRef]
26. Cheng, S.X.; Lightfoot, Y.L.; Yang, T.; Zadeh, M.; Tang, L.; Sahay, B.; Wang, G.P.; Owen, J.L.; Mohamadzadeh, M. Epithelial CaSR deficiency alters intestinal integrity and promotes proinflammatory immune responses. *FEBS Lett.* **2014**, *588*, 4158–4166. [CrossRef]
27. Wang, S.; Qiu, L.; Song, H.; Dang, N. NPS-2143 (hydrochloride) inhibits melanoma cancer cell proliferation and induces autophagy and apoptosis. *Méd. Sci.* **2018**, *34*, 87–93. [CrossRef] [PubMed]
28. Nemeth, E.F.; Goodman, W.G. Calcimimetic and Calcilytic Drugs: Feats, Flops, and Futures. *Calcif. Tissue Int.* **2016**, *98*, 341–358. [CrossRef] [PubMed]
29. Sheldrick, G.M. A short history of SHELX. *Acta Crystallogr. Sect. A Found. Crystallogr.* **2008**, *64*, 112–122. [CrossRef]
30. Sheldrick, G.M. Crystal structure refinement with SHELXL. *Acta Crystallogr. Sect. C Struct. Chem.* **2015**, *71*, 3–8. [CrossRef]
31. Ward, D.T.; Mughal, M.Z.; Ranieri, M.; Dvorak-Ewell, M.M.; Valenti, G.; Riccardi, D. Molecular and clinical analysis of a neonatal severe hyperparathyroidism case caused by a stop mutation in the calcium-sensing receptor extracellular domain representing in effect a human 'knockout'. *Eur. J. Endocrinol.* **2013**, *169*, K1–K7. [CrossRef] [PubMed]



Article

In Vitro and In Silico Characterization of an Antimalarial Compound with Antitumor Activity Targeting Human DNA Topoisomerase IB

Bini Chhetri Soren ^{1,†}, Jagadish Babu Dasari ^{1,†,‡}, Alessio Ottaviani ^{1,*} , Beatrice Messina ¹, Giada Andreotti ¹, Alice Romeo ¹ , Federico Iacovelli ¹ , Mattia Falconi ¹ , Alessandro Desideri ¹ and Paola Fiorani ^{1,2}

¹ Department of Biology, University of Rome Tor Vergata, Via della Ricerca Scientifica 1, 00133 Rome, Italy; binichhetri.14@gmail.com (B.C.S.); jagadishdrdasari@gmail.com (J.B.D.); beatrice.messina702@gmail.com (B.M.); giada0404@gmail.com (G.A.); alice.romeo@uniroma2.it (A.R.); federico.iacovelli@uniroma2.it (F.I.); falconi@uniroma2.it (M.F.); desideria@uniroma2.it (A.D.); paola.fiorani@uniroma2.it (P.F.)

² Institute of Translational Pharmacology, National Research Council, CNR, Via del Fosso del Cavaliere 100, 00133 Rome, Italy

* Correspondence: alessio.ottaviani@uniroma2.it; Tel.: +39-06-72594358

† The authors contributed equally to this work.

‡ Present address: Diagnostic BioSystems USA Pvt. Ltd. 612, Eden Square, St. John's Road, Secunderabad 500003, India.

Citation: Soren, B.C.; Babu Dasari, J.; Ottaviani, A.; Messina, B.; Andreotti, G.; Romeo, A.; Iacovelli, F.; Falconi, M.; Desideri, A.; Fiorani, P. In Vitro and In Silico Characterization of an Antimalarial Compound with Antitumor Activity Targeting Human DNA Topoisomerase IB. *Int. J. Mol. Sci.* **2021**, *22*, 7455. <https://doi.org/10.3390/ijms22147455>

Academic Editors: Geoffrey Brown, Andrzej Kutner and Enikő Kallay

Received: 16 June 2021

Accepted: 7 July 2021

Published: 12 July 2021

Publisher's Note: MDPI stays neutral with regard to jurisdictional claims in published maps and institutional affiliations.



Copyright: © 2021 by the authors. Licensee MDPI, Basel, Switzerland. This article is an open access article distributed under the terms and conditions of the Creative Commons Attribution (CC BY) license (<https://creativecommons.org/licenses/by/4.0/>).

Abstract: Human DNA topoisomerase IB controls the topological state of supercoiled DNA through a complex catalytic cycle that consists of cleavage and religation reactions, allowing the progression of fundamental DNA metabolism. The catalytic steps of human DNA topoisomerase IB were analyzed in the presence of a drug, obtained by the open-access drug bank Medicines for Malaria Venture. The experiments indicate that the compound strongly and irreversibly inhibits the cleavage step of the enzyme reaction and reduces the cell viability of three different cancer cell lines. Molecular docking and molecular dynamics simulations suggest that the drug binds to the human DNA topoisomerase IB-DNA complex sitting inside the catalytic site of the enzyme, providing a molecular explanation for the cleavage-inhibition effect. For all these reasons, the aforementioned drug could be a possible lead compound for the development of an efficient anti-tumor molecule targeting human DNA topoisomerase IB.

Keywords: human DNA topoisomerase; cancer; drug; molecular docking

1. Introduction

Biologically, topoisomerases play a vital role in the maintenance of genomic integrity inside the cell by controlling DNA torsional stress [1]. This is accomplished by transiently breaking and rejoining DNA strands. Human DNA topoisomerase IB (htopIB) is one of six different topoisomerases that exist in humans [2]. HtopIB is a nuclear enzyme and, with type IA topoisomerase, belongs to the topoisomerase I subfamily that cuts only one DNA strand. The type IA topoisomerases bind covalently to the 5' end of the cleaved DNA, whereas the type IB are attached to the 3' end during the catalytic cycle. Among topoisomerase families there are also type II topoisomerases that cut both DNA strands [2].

HtopIB is a monomeric 91 kDa enzyme consisting of 765 amino acids and is composed of four domains: the N-terminal domain (residues 1–214), which is never crystallized due to a high degree of flexibility and which contains nuclear localization signals; the core domain (residues 215–635) which can be further divided into subdomains I, II, and III; linker domain (residues 636–712) connecting subdomain III with the C-terminal; and the C-terminal domain (residues 713–765) containing the catalytic residue Tyr723 [3,4]. The linker domain, formed by two long helices, is involved in controlling the relaxation

mechanism. Due to its shape and its positive charge, this domain interacts with the DNA downstream of the cleavage site and drives relaxation through a controlled rotation [5–8]. The enzyme relaxes both positive and negative supercoils by creating a nick on one strand of the DNA duplex, forming a transient phospho-tyrosine bond [3]. This transient bond occurs through a nucleophilic attack on DNA by Tyr723 that breaks one of the DNA strands, leaving the enzyme covalently attached to the 3'-phosphate and forming a protein–DNA covalent complex called “cleavage complex”. At this point, the cut DNA strand can rotate around the other one, changing the linking number and consequently the DNA topology. The htopIB catalytic cycle can be summarized in five steps: (1) non-covalent DNA binding; (2) nucleophilic attack by the Tyr723 residue; (3) strand rotation of the nicked strand around the intact strand to relax the supercoiled DNA; (4) religation of the DNA strand; and (5) enzyme release [4].

HtopIB is the unique target of a class of anticancer compounds belonging to the camptothecin (CPT) family [9,10]. CPT, a pentacyclic alkaloid extracted from the plant *Camptotheca acuminata*, is an E-ring lactone that is poorly soluble and toxic for the organism, but a series of more soluble derivatives have been developed [11] and two of them, topotecan (TPT) and irinotecan, are in clinical use as a second line therapy for ovarian, lung, and colorectal cancers [12–14]. Once the enzyme has cut a supercoiled DNA to form the protein–DNA complex, CPT binds to this transient complex by intercalating in the cleavage site and slowing down the religation step [15–17]. The increased lifetime of the covalent complex leads to the collapse of the replicative fork with the formation of double strand breaks and, if not repaired, consequent cell death. The CPT inhibition is called a poison because it causes the stalling of the protein on DNA that leads to cell death. Other htopIB poisons are the indenoisoquinolines which the planar polycyclic cores allow the intercalation of at the strand breakage site in a CPT-like manner. However, indenoisoquinolines are less reversible than CPT and thus their pharmacokinetics enable the formation of persistent cleavage complexes and potential shorter infusion times [18]. Besides poisons, other types of htopIB inhibitors are catalytic inhibitors that act by preventing the enzyme's binding to DNA or cleavage step. Among them we can count erybraedin C, which is a cleavage inhibitor [19], or benzoxazines, such as 1,4-benzoxazin-3-ones and 2,4-Dihydroxy-1,4-benzoxazin-3-one, which prevent enzyme binding to DNA [11]. Erybraedin C contains a tetracyclic ring system and is characterized by the presence of two hydroxy groups and two prenyl groups [19], while benzoxazines are a group of heterocyclic chemical compounds that consist of a benzene ring fused to an oxazine ring [11].

DNA topoisomerases have been shown to be a promising therapeutic target not only against cancer but also against bacteria and parasites [20–22]. An example is the topoisomerase from apicomplexan parasites, like *Plasmodium falciparum*, which may be a striking target for drug development [23,24].

Open-access drug banks are an interesting source of compounds for a wide range of different diseases since, they contain hundreds of drugs for which a target is still unknown [25]. Among them, Pathogen Box by Medicines for Malaria Venture is a product development partnership with the aim of reducing the burden of malaria by delivering novel, efficient and reasonably priced anti-malarial drugs for disease-endemic countries.

The Pathogen Box contains 400 different drug-like molecules active in neglected diseases (including malaria, tuberculosis, dengue, and kinetoplastids). These compounds were designed as drugs for the treatment of neglected diseases, but, as history has taught us, a drug designed for a specific pathology has sometimes proved to be much more effective in treating a completely different one. For this reason, we considered that among them there could be a novel compound to be used as an anti-tumor drug. We then screened the activity of 125 compounds designed for malaria treatment against htopIB, due to the similarity of *Plasmodium falciparum* topoisomerase with its human counterpart [26].

During the screening, we selected one compound, MMV024937 (Figure 1), which efficiently inhibits htopIB.

In this paper we investigated the effect of MMV024937 on the catalytic cycle of htopIB through experimental and computational approaches, and we tested its effect on

three different cancer cell lines. The results indicate that the compound inhibits the htopIB cleavage activity in vitro by binding to the enzyme's active site. Furthermore, it strongly reduced cell viability at concentrations between 50 and 100 μM .

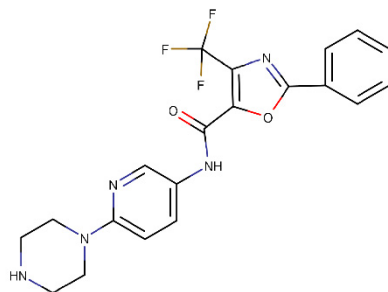


Figure 1. Molecular structure of MMV024937.

2. Results

2.1. MMV024937 Inhibits the Catalytic Activity of htopIB

The inhibitory effect of MMV024937 on htopIB activity was assessed by a plasmid relaxation assay (Figure 2A). Wild-type protein was incubated with a supercoiled plasmid in the absence or presence of increasing concentrations of MMV024937, and the relaxation activity was monitored after 1 h. The results indicated that MMV024937 inhibited the relaxation activity of htopIB in a dose-dependent manner (Figure 2A). Addition of MMV024937 to the enzyme and DNA determined an inhibition of the relaxation activity that was already observable at a concentration of 20 μM (Figure 2A, lane 3) and became maximal at a concentration of 150/200 μM (Figure 2A, lanes 9 and 10). Since MMV024937 is dissolved in DMSO, we evaluated the enzyme activity in the presence of an identical concentration of solvent without MMV024937, demonstrating that DMSO does not affect the relaxation activity of htopIB (Figure 2A, lane 1). In addition, the compound's effect on the electrophoretic mobility of DNA in absence of htopIB was evaluated (Figure 2A, lane 11).

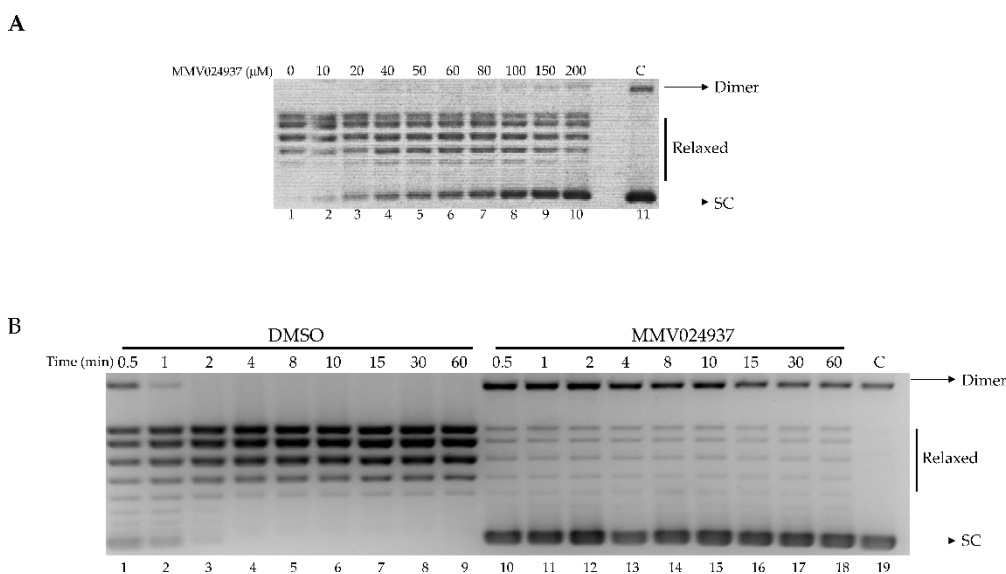


Figure 2. Relaxation of supercoiled DNA. **(A)** Relaxation of a negatively supercoiled plasmid DNA by htopIB at increasing concentrations of MMV024937 (lanes 2–10); lane 1: no drug added and lane 11: no protein added. **(B)** Relaxation of negative supercoiled plasmid DNA in a time course experiment with DMSO (lanes 1–9), 100 μM MMV024937 dissolved in DMSO (lanes 10–18), lane 19, no protein added. The reaction products are resolved on agarose gel and visualized with ethidium bromide. Dimer indicates dimer supercoiled plasmid DNA; SC indicates supercoiled plasmid DNA.

The assay was carried out as a function of time in the presence of MMV024937 at a concentration of 100 μ M. This experiment showed that the inhibitory effect is maintained over time (Figure 2B, lanes 10–18), to minimally 1 h, indicating an irreversible inhibition of the enzyme's catalytic activity. As a control, the relaxation assay was performed in the presence of DMSO alone (Figure 2B, lanes 1–9).

2.2. Cleavage with CL14/CP25 Suicide Substrate

The cleavage activity of the htopIB was analyzed in a time course experiment using a CL14/CP25 suicide cleavage substrate. In detail, a 5'-end radiolabeled oligonucleotide CL14 (5'-GAAAAAAGACTTAG-3') was annealed to the CP25 (5'-TAAAAATTTTCTAAGTCTTTTTTC-3') complementary strand to produce a duplex with an 11 base 5' single-strand overhang (Figure 3A).

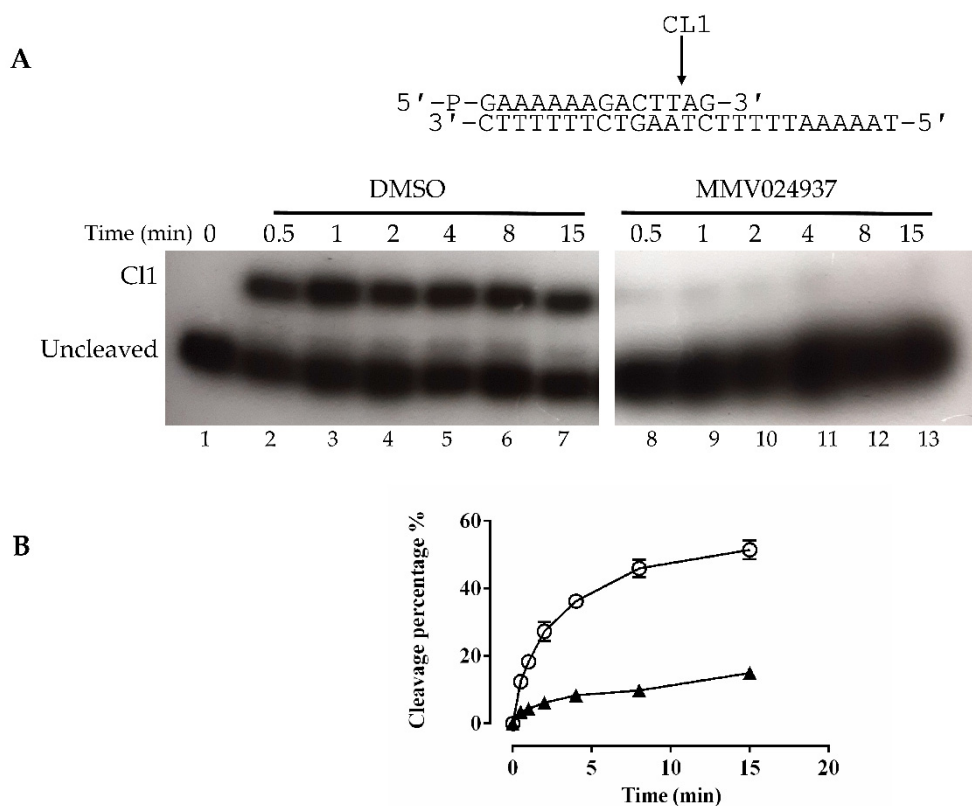


Figure 3. Cleavage kinetics. **(A)** Cleavage reaction of the enzyme with the CL14/CP25 suicide substrate, shown at the top of the figure, in a time course experiment in the presence of only DMSO (lanes 2–7), or MMV024937 dissolved in DMSO (lanes 8–13). In lane 1 the protein was not added. CL1 represents the DNA strand cleaved by the enzymes at the preferred cleavage site, indicated by an arrow. **(B)** Percentage of cleaved suicide substrate, normalized to the total amount of each lane, plotted against time for the reaction with only DMSO (circles) and MMV024937 dissolved in DMSO (triangles). Data are means \pm SD obtained from three independent experiments.

In this experiment the religation step was precluded because the AG-3' dinucleotide is too short to be religated, leaving the enzyme covalently attached to the 12 oligonucleotide 3'-end. Three units of wild-type enzyme were incubated in the absence and presence of MMV024937, and the reactions were stopped at increasing time intervals ranging from 0.5 min to 15 min. Samples were precipitated by using 100% ethanol, then digested by trypsin, and the products were resolved on a denaturing urea polyacrylamide gel (Figure 3A). Figure 3A shows that in the presence of MMV024937 the cleavage does not occur at all (lanes 8–13), while the control, in the presence of DMSO, showed a typical cleavage kinetics (Figure 3A, lanes 2–7). The percentage of the cleaved fragment (CL1), normalized to the total radioactivity in each lane plotted against time for DMSO (Figure 3B,

circle) and MMV024937 incubation (Figure 3B, triangle), confirmed the full inhibitory effect of the MMV024937 compound.

2.3. Cell Viability Assay

The cytotoxic effect of MMV024937 on the colon carcinoma cancer cell line (Caco-2), non-small cell lung cancer cell line (A-549), and ovarian cancer cell line (SKOV-3) was evaluated via an MTT assay in comparison to TPT. The drugs were tested at various concentrations, ranging from 12.5 μM to 100 μM in a 96-well plate, containing 10^4 cells/well. The cells were incubated in the presence of various concentrations of the drug, or in the presence of the same amount of DMSO as a control, for 48 h at 37 °C under 5% CO₂ and 95% air. After the incubation, the medium was removed and 200 μL of fresh media supplemented with MTT reagent at a final concentration of 0.5 mg/mL was added for 4 h. The reagent was then replaced with 100 μL DMSO and incubated at room temperature, covered from light, on a shaking plate for 15 min, and the absorbance was measured at 570 nm using a microplate reader. The MMV024937 compound affected cell viability in a dose-dependent manner with an inhibition, at 50 and 100 μM stronger than TPT, which displays a constant inhibition from 12.5 to 100 μM (Figure 4). The compound exhibited a larger cytotoxic effect on the SKOV-3 cell line, where cell viability started to decrease at 25 μM , indicating that MMV024937 had a cell line-dependent effect (Figure 4).

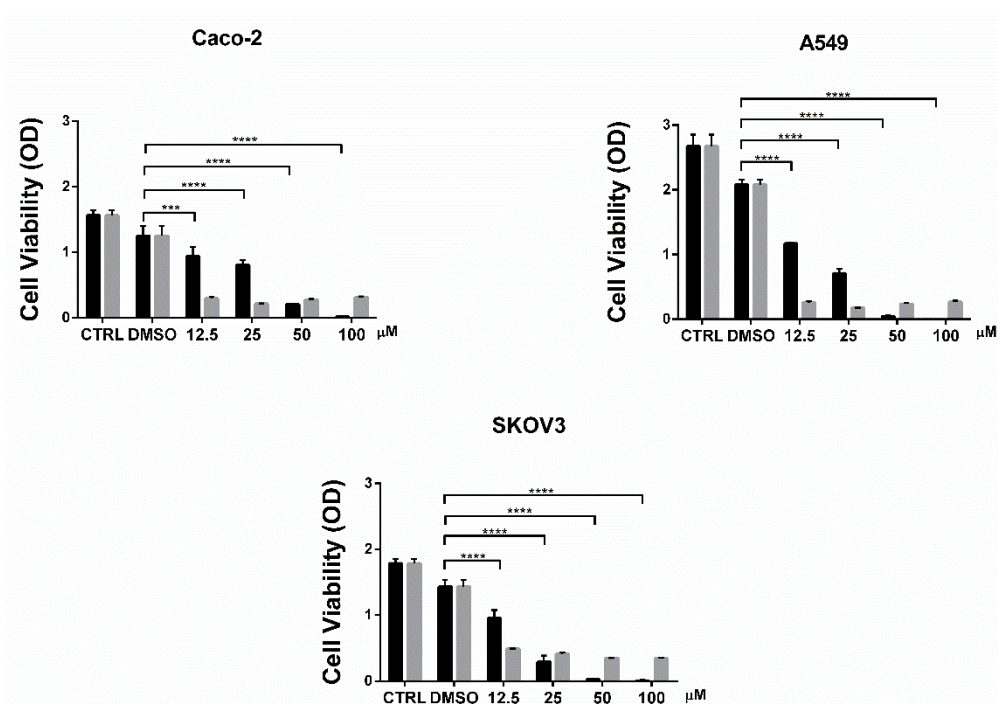


Figure 4. Cell viability assay in the presence of MMV024937 and TPT. Cytotoxicity of MMV024937 (black) and TPT (gray) were tested on three different cancer cell lines; Caco-2 (top left panel), A-549 (top right panel), and SKOV-3 (bottom panel). The figure reports cumulative data analyzed by a two-way ANOVA test, with mean \pm SD values. **** $p < 0.0001$ and *** $p < 0.001$.

2.4. Molecular Docking Simulations

Molecular docking simulations were performed to structurally evaluate the interaction of MMV024937 with a DNA-bound htopIB structure (PDBID: 1T8I) [27], mimicking the experimental conditions of simultaneous incubation of the enzyme, the drug, and the DNA. All the molecular docking simulations performed indicated that the drug interacts with the htopIB-DNA complex with a high average energy of about -12.0 kcal/mol, achieving binding at two preferential locations within the htopIB-DNA binding cavity.

In most of the obtained binding poses the drug localizes at the center of the cavity, inserted among the catalytic pentad of the enzyme. Figure 5A represents the best binding pose, named “non-intercalated configuration”, that shows an interaction energy of -12.4 kcal/mol. In this pose the drug establishes five hydrogen bonds and five hydrophobic interactions with the surrounding residues (Figure 5B).

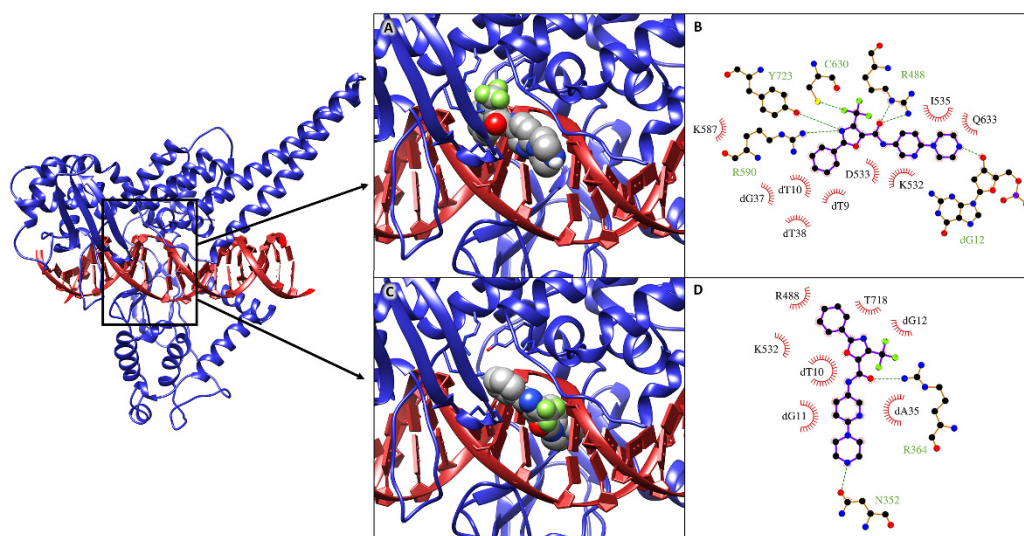


Figure 5. On the left: 3D structure of the htopIB-DNA complex (PDBID: 1T8I), used as receptor for the molecular docking simulations. The binding site is highlighted by a rectangular box. The htopIB structure is represented as a blue cartoon, while the DNA is shown as a red ribbon. (A,C) 3D best binding poses obtained for the drug MMV024937 in “non intercalated” (A) and “intercalated” (C) configuration. The MMV024937 compound is shown in a space fill model, colored by atom type, with carbon atoms in grey, while htopIB catalytic residues are shown as stick models, colored by atom type, with carbon atoms in blue. The pictures were obtained using the Chimera program [28]. (B,D) 2D schematic view of the interactions between the drug and the htopIB-DNA complex in “non intercalated” (B) and “intercalated” (D) configuration. Hydrogen bonds between the drug molecule and the interacting residue/base are shown as dashed lines. Hydrophobic interactions are shown as radial half-circles. Labels indicate base or residue names in one-letter code and their numbering in the structure. The pictures were created using the LigPlot+ 1.4 software [29].

In particular, the oxazole-5-carboxamide group and the trifluoromethyl group of MMV024937 insert within the catalytic site of the enzyme (Figure 5A), establishing hydrogen bonds with Arg488, Arg590, and Tyr723 and setting up hydrophobic interactions with Lys532 (Figure 5B). The drug also contacts the nearest DNA major groove, establishing four hydrophobic contacts and one hydrogen bond with the underlying nucleotides (Figure 5A,B). In the remaining binding poses, the drug intercalates within the structural distortion generated between the dT10 and dG11 nucleotides after htopIB binding. Figure 5C shows the best binding pose, named “intercalated configuration”, which reaches an interaction energy of -11.7 kcal/mol. The interaction pattern evaluated for this pose highlights two hydrogen bonds and three hydrophobic interactions with surrounding residues, in particular with Arg488 and Lys532 of the catalytic site, and four hydrophobic interactions with the nucleotides located below (Figure 5D).

2.5. Molecular Dynamics Simulations and MM/GBSA Analysis

The two best complexes obtained for the non-intercalated and intercalated drug configurations were further analyzed by performing 100 ns of classical molecular dynamics (MD) simulations to further validate the stability of the obtained complexes and to accurately evaluate the interaction energies between the htopIB-DNA complex and the drug. MM/GBSA analyses confirmed the strong interaction between MMV024937 and the htopIB-

DNA complex, showing interaction free energies of -49.0 and -55.1 kcal/mol for the non-intercalated and intercalated drug configurations, respectively (Table 1).

Table 1. Results of the MM/GBSA analyses of the MD trajectories of the htopIB-DNA complex with the drug in non-intercalated (Figure 5A) or intercalated (Figure 5C) configuration.

Drug Binding Configuration	VdW (kcal/mol)	Electrostatic (kcal/mol)	Interaction Energy (kcal/mol)
non-intercalated	-63.7 ± 2.8	-14.4 ± 9.5	-49.0 ± 3.4
intercalated	-67.1 ± 2.9	-64.0 ± 12.3	-55.1 ± 4.0

Both VdW and electrostatic interactions contribute importantly to the binding, although the electrostatic contribution is predominant in the intercalated configuration due to its close interactions with the charged DNA. MM/GBSA per-residue decomposition analyses, which allowed for estimating the contribution given by single residues or DNA bases to the total binding energy of the drug, confirmed that the drug in non-intercalated configuration closely interacts with htopIB catalytic site residues and also with some of the underlying DNA bases (Table 2). On the other hand, the intercalated drug only establishes minor contacts with the catalytic region but can strongly interact with surrounding DNA bases (Table 2).

Table 2. MM/GBSA per-nucleotide/residue decomposition analyses performed for the MD trajectories of the htopIB-DNA complexes bound to the drug in non-intercalated (Figure 5A) and intercalated (Figure 5C) configurations. Interaction energies were evaluated between the drug and surrounding DNA bases or htopIB active site residues.

Nucleotide/Residue	Non-Intercalated Drug Binding Energy (kcal/mol)	Intercalated Drug Binding Energy (kcal/mol)
dT10	-2.0 ± 0.5	-3.0 ± 1.8
dG11	-0.1 ± 0.1	-5.8 ± 0.9
dG12	-3.0 ± 1.1	-0.4 ± 0.2
dA13	-2.1 ± 1.7	$+0.1 \pm 0.0$
dC34	$+0.1 \pm 0.0$	-4.4 ± 1.0
dA35	0.0 ± 0.0	-6.1 ± 1.0
dA36	-0.1 ± 0.1	-0.7 ± 0.2
dG37	-0.7 ± 0.4	-0.2 ± 0.2
Arg488	-0.8 ± 0.6	-0.9 ± 0.5
Lys532	-2.7 ± 0.6	-0.8 ± 1.0
Arg590	$+0.1 \pm 0.4$	-0.1 ± 0.1
His632	-1.8 ± 0.4	-0.2 ± 0.2
Tyr723	-1.3 ± 0.5	-0.3 ± 0.2

The high-interaction free energies indicate that MMV024937 could interfere with htopIB catalytic activity when DNA binding has already occurred, occupying the catalytic site of the enzyme and, due to the favorable electrostatic energy, altering the interactions between the negatively charged DNA and the mostly positively charged protein, which are crucial for the controlled rotation mechanism that leads to the final DNA relaxation [30].

2.6. Principal Component Analysis

To better characterize the collective motions of different regions of the htopIB structure and to highlight if the presence of the drug could induce changes in the structural dynamics of the htopIB-DNA complexes, dynamic cross-correlation maps (DCCM), based on the atomic fluctuations of 565 C α atoms of htopIB and on the 42 P atoms of DNA, were generated for each MD trajectory. Positive values indicate that the motion between two residues/bases is correlated, with residues/bases moving in the same direction, while

negative values represent an anti-correlated motion, with residues/bases moving in opposite directions. A 100 ns MD simulation of the htopIB-DNA complex in the unbound state was also performed and analyzed as reference. MD simulations indicate remarkable differences between the unbound and bound complexes, and highlight the presence of functional structural motions in the htopIB unbound structure (Figure 6A,B).

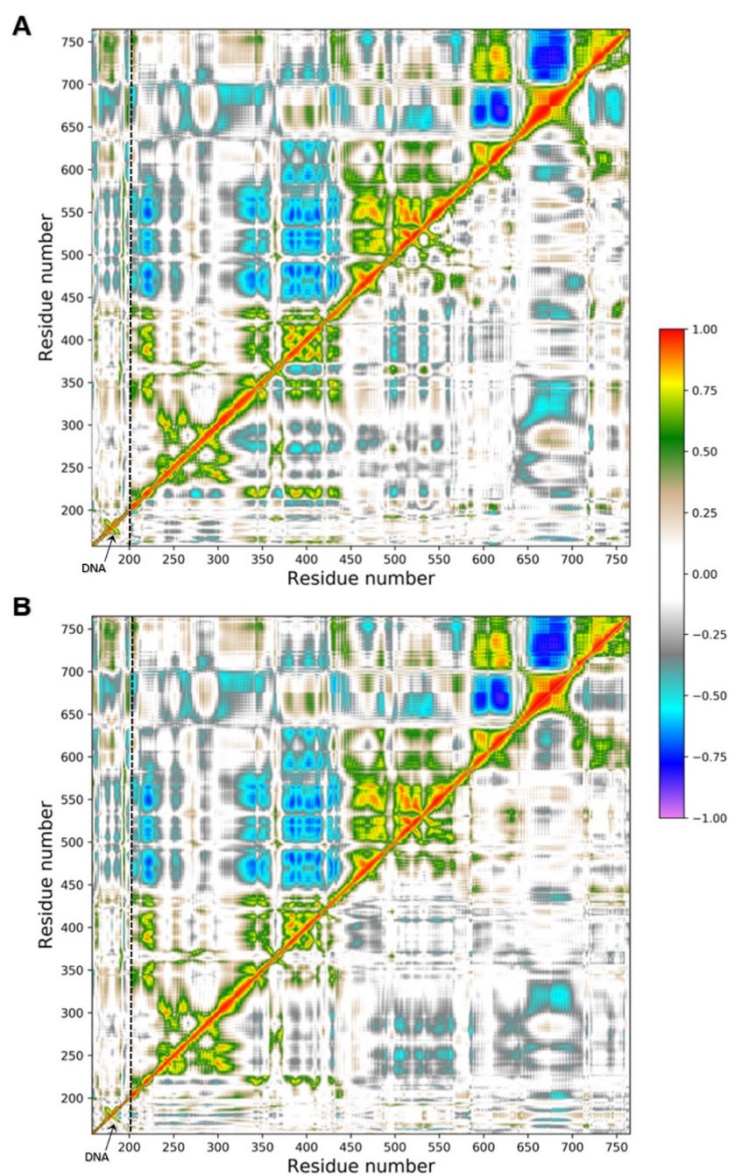


Figure 6. DCCMs obtained for the three simulated systems. The upper-left triangles of both graphs (A,B) represent the DCCM obtained for the unbound htopIB-DNA complex, while the lower-right triangles show the DCCMs for the non-intercalated (A) and intercalated (B) drug complexes, respectively. Color coding is reported in the legend. Positive values between two residues indicate a correlated motion, while negative values indicate an anti-correlated motion. DNA regions are indicated by labels and separated from the protein regions by dotted lines.

The unbound htopIB-DNA simulation is characterized by highly anti-correlated motions between subdomain I (residues 215–232 and 320–433) and subdomain III (residues 450–635) of the htopIB core domain (Figure 6A,B; upper-left triangles). Strong anti-correlated motions are also present between the end region of subdomain III (residues 575–635) and the linker region (residues 650–700), and between the linker region and the htopIB C-terminal domain (residues 715–765). Similarly, correlated motions can be sparsely

observed between the subdomains I, II and III (residues 200–635), and between subdomain III (residues 575–635) and the C-terminal domain (residues 715–765). As previously reported, correlated internal motions represent an important feature of the DNA-bound htopIB structure and highlight the important role played by protein-protein domain communications and conformational changes in the functional processes of this enzyme [16]. Subdomain III (residues 450–635), containing four of the five htopIB catalytic residues, the linker (residues 650–700), and the C-terminal regions also show mild positively and negatively correlated motions with the DNA region (Figure 6A,B; upper-left triangles).

The presence of the drug within the binding pocket completely abolishes these correlated motions in both the non-intercalated and intercalated binding configurations (Figure 6A,B; lower-right triangles). In fact, in the presence of the drug, DNA motions and intra- and inter-domain protein motions become completely uncorrelated, except for a small anti-correlated movement between subdomain I (residues 300–350) and the linker region (residues 636–712), and sparse positively and negatively correlated motions within the three subdomains of the htopIB core region (residues 250–575), which was observed in both binding configurations.

To further characterize the main regions showing different flexibilities in the bound and unbound htopIB-DNA complexes, principal component analysis (PCA) was performed for each MD trajectory [31]. This technique allows for the isolation of the major fluctuations that contribute to the dynamics of each structure, identifying the principal 3 N directions along which the majority of the protein and DNA motion is defined. Atomic displacements, calculated for each C α atom of htopIB and P atom of DNA along the first eigenvector, indicate that the unbound htopIB structure shows an overall higher degree of flexibility, mainly in the linker domain, in subdomain III, and in the C-terminal domain (Figure 7). Interestingly, the htopIB-DNA structure, complexed with the intercalated drug, shows a stronger rigidity within subdomain I that is not observed in the presence of the non-intercalated drug. The linker domain is the most flexible region of htopIB in both the unbound and bound systems, although in the unbound system this region shows about two-fold the flexibility observed in the two bound states. These data confirm the strongly correlated motions observed between the three main htopIB domains in the unbound complex DCCM (Figure 6A,B; upper-left triangles), and also validate the finding that the presence of the drug induces an evident structural rigidity in the protein, particularly in those residues directly facing the DNA region (residues 488–500, 532–535, 631–640, 713–722) (Figure 7).

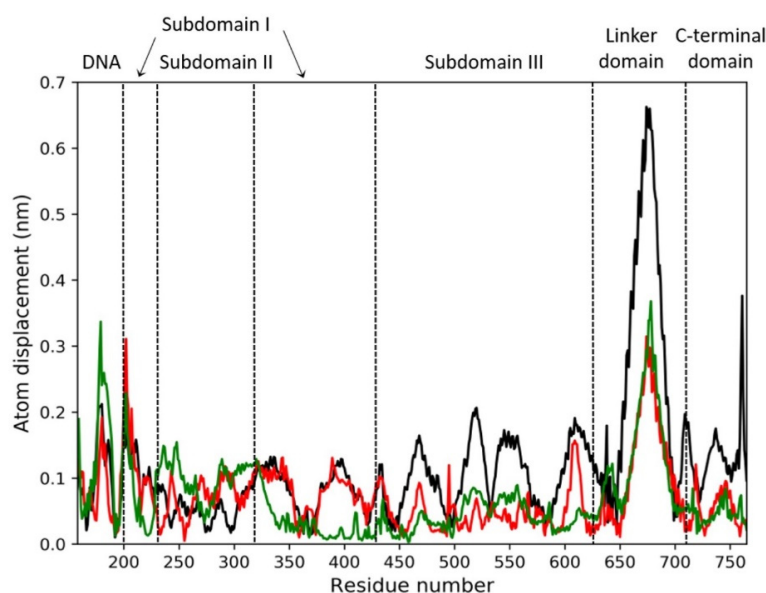


Figure 7. Atomic displacement calculated for each of the 565 C-alpha atoms of htopIB and each of

the 42 P atoms of DNA, computed along the direction of the first eigenvector for the three MD trajectories. The black line indicates the unbound htopIB-DNA complex, while the red and green lines indicate the complexes with the non-intercalated or intercalated drug bound, respectively. Dotted lines separate the DNA region from the different htopIB domains, as indicated by the labels.

3. Discussion

Despite the fact that cancer knowledge has been growing in recent decades, the problem of cancerous disease persists, and these decades of scientific findings are still insufficient to solve it. The remarkable progresses made in cancer prevention, early detection, and treatment are still not sufficiently specific and effective. HtopIB plays essential roles in cell division by regulating all topological DNA stresses that arise during transcription or replication. For these reasons, htopIB is an interesting target for cancer treatment. In this work we screened a library of antimalarial compounds, adopting a drug-repositioning screening, based on the evidence of *Plasmodium falciparum* topoisomerase homology with its human counterpart. In detail, we have characterized the effect of MMV024937 as a new drug, provided by the open-access drug bank MMV, on htopIB through experimental and computational approaches. To test MMV024937's inhibition of htopIB activity, whether as a poison, in a CPT-like manner, or as a catalytic inhibitor such as erybraedin C, we performed in vitro assays. We demonstrated that MMV024937 affects htopIB as a catalytic inhibitor, and also in an irreversible manner (Figure 2B).

The efficiency of MMV024937 as a potential anti-tumor drug was tested on cancer cell lines in comparison with TPT, a drug currently used in clinics for cancer treatment (Figure 4). We observed that the effect of MMV024937 is stronger than TPT at high concentrations, likely due to the fact that MMV024937 can act on pathways other than htopIB alone. Indeed, a previous work has demonstrated that MMV024937 is closely related to a series of human diacylglycerol acyltransferase-1 (DGAT-1) inhibitors [32]. DGAT-1 inhibition causes cancer cell death by inducing mitochondrial damage and elevated ROS formation, supporting the use of MMV024937 as a promising anti-tumor drug [33].

To better understand these results we also performed a computational analysis (Figure 5). Molecular docking and molecular dynamics simulations of MMV024937 modeled over the htopIB-DNA complex strongly support the observed inhibition effect, although they cannot provide information on its irreversibility. Computational results indicate that MMV024937 binds the htopIB-DNA complex sitting inside the catalytic site of the enzyme or intercalating within the DNA. Interaction analyses shows that the drug contacts several htopIB residues, including residues of the catalytic pentad such as Arg488, Lys532, Arg590, and Tyr723, as well as the neighbor DNA bases (Tables 1 and 2). The persistent stability of the complexes and the strongly negative free energies of binding displayed by the drug during the 100 ns MD simulations provide a clear molecular explanation for the cleavage inhibition. The drug can exert its inhibitory activity, preventing DNA and htopIB contacts, by establishing a steric hindrance within the htopIB-DNA cleft and strong hydrophobic and electrostatic interactions with surrounding residues and DNA bases. Furthermore, in both the evaluated binding configurations, the presence of a single drug molecule can strongly influence the structural dynamics of htopIB-DNA structure. It is known that intra- and inter-domain communications are fundamental for htopIB's catalytic activity and that DNA strand rotation is strongly dependent on the enzyme's conformation and dynamics [34]. In particular, a different flexibility of the linker domain was shown to correlate with the rate of DNA religation reactions. Indeed, this region has a role in slowing the religation step, allowing the enzyme to remain associated to DNA for a larger number of cleavage/religation rounds, and it is also fundamental for DNA-controlled rotation [35,36]. During MD simulations we observed that the presence of the drug within the binding pocket almost completely abolished correlated motions of the complex, and strongly reduced htopIB linker flexibility. This is likely due to the strong interactions established by the drug with surrounding residues and DNA bases that decrease the protein-DNA structural movements and anchor the complex in an expected inactive state. Considering these results, we hypothesize that the structural stability induced by

the drug should prevent the occurrence of the large conformational changes leading to the correct unwinding and relaxation of supercoiled DNA.

Despite MMV024937 may have additional targets beside htopIB; the evidence for relaxation and cleavage inhibition identifies this molecule as an interesting and valuable candidate in targeting htopIB in the context of cancer treatment.

4. Materials and Methods

4.1. Chemicals, Cells, Yeast Strains and Plasmids

MMV024937 were kindly provide by Malaria for Medicine Venture, Anti-FLAG M2 monoclonal affinity gel, FLAG peptide, Anti-FLAG M2 monoclonal antibodies, topotecan, 3-(4,5-Dimethyl-2-thiazolyl)-2,5-diphenyl-2H-tetrazolium bromide (MTT,) and dimethyl sulfoxide (DMSO) were purchased from MERCK (Darmstadt, Germany). In order to express the htopIB enzyme we used *Saccharomyces cerevisiae* Top1 null strain EKY3 (ura3–52, his3Δ200, leu2Δ1, trp1Δ63, top1::TRP1, MATα). Single copy plasmid YCpGAL-e- hTop1 was used to express the enzyme under a galactose-inducible promoter. The N-terminal sequence of the epitope-tagged construct YCp-GAL-e-, indicated as 'e', contains a FLAG sequence, DYKDDDY, and it is recognized by the M2 monoclonal antibody. The cloning reaction was transformed into XL10-Gold E. coli cells (Agilent Technologies, Santa Clara, CA, USA), and a positive clone was identified by sequencing the extracted plasmid DNA. Oligonucleotides for radioactive assays were purchased from Eurofins Genomics. [γ -32P] ATP was purchased from PERKIN Elmer (Waltham, MA, USA).

Dulbecco's modified Eagle's medium high glucose, RPMI 1640 medium, fetal bovine serum (FBS), L-glutamine, penicillin/streptomycin, and non-essential amino acids were purchased from Euroclone (Pero, Italy). Complete media (CM) were supplemented with 10% FBS, 2 mM L-glutamine, 0.1 mg/mL streptomycin, and 100 U/mL penicillin. The ovarian cancer cell line SKOV-3 was purchased from Cell Biolabs, Inc. and maintained in DMEM-high glucose, CM supplemented with 1X non-essential amino acids; colorectal adenocarcinoma cell line, Caco-2, was maintained in RPMI 1640, CM; and non-small-cell-lung cancer cell line, A-549, was maintained in DMEM high glucose, CM. Caco-2 and A-549 cell lines were kindly provided by Dr. Giuseppe Sconocchia (Institute of Translational Pharmacology, CNR, Rome, Italy). The cells were tested for mycoplasma using the PCR detection Kit (Euroclone). The cells were kept in culture for a maximum of eight passages.

4.2. Protein Purification

In order to purify htopIB, the enzyme was cloned in a single copy plasmid YCpGAL under a galactose-inducible promoter. The purification was carried out by using the lithium acetate procedure, and the transformation was made in top1 null EKY3. Transformed cells were grown on SC-Uracil, with added 2% dextrose. Subsequently, the cells were diluted 1:100 in SC-Uracil with 2% raffinose until an optical density of $A_{600} = 1$ was reached, and then the transformed cells were induced with 2% galactose for 6 h. A washing with cold water occurred after the harvesting of the cells. In the next step the cells were resuspended in 2 mL/g cells using a buffer made up by 50 mM Tris/HCl, pH 7.4, 1 mM EDTA, 1 mM EGTA, 10% (v/v) glycerol, protease inhibitor cocktail, and supplemented with 10 mg/mL sodium bisulfite and 40 mg/mL sodium fluoride, 1 mM PMSF, and 1 mM DTT. The cells were disrupted by adding of 0.5 volume of 425–600 mm diameter glass beads, and by vortexing the solution for 30 s, alternating with 30 s on ice. In order to separate the glass beads from the supernatant, the solution was centrifuged at 12,000 rpm for 30 min. The column was then washed with TBS (50 mM Tris/HCl and 150 mM KCl, pH 7.4) and the ANTI-FLAG M2 affinity gel (MERCK, Darmstadt, Germany) was equilibrated. Several elutions of the protein were obtained by adding five columns volume of a solution containing the FLAG peptide, whereupon 500 μ L of htopIB were supplemented with 40% glycerol and stored at -20 °C. In order to test the integrity of the protein, the fractions were resolved by SDS-PAGE and then shown through the immunoblot.

4.3. Relaxation Assay

The activity of the htopIB was assessed through the relaxation of negatively pBlue-Script KSII (-) DNA. The reaction was carried out in a final volume of 30 μ L containing a buffer composed of 20 mM Tris-HCl pH 7.5, 0.1 mM EDTA, 10 mM $MgCl_2$, 50 μ g/m acetylated bovine serum albumin, 150 mM KCl, and ddH₂O. The reaction was stopped after 1 h incubation at 37 °C by adding 0.5% SDS stop dye. The samples were resolved in 1% agarose gel and in a running buffer containing 48 mM Tris, 45.5 mM boric acid, 1 mM EDTA. The enzyme's ability to relax supercoiled DNA was visualized through a UV transilluminator after a gel staining in 0.5 μ g/mL ethidium bromide and destaining in dH₂O.

4.4. Cleavage Kinetics Using CL14/CP25 Oligonucleotide Substrate

In order to analyze the cleavage kinetics a CL14 (5'-GAAAAAAGACTTAG-3') was radiolabeled with [γ -32P] ATP at its 5' end through a 30 min incubation of 10 pmol of CL14 with a T4 kinase (New England Biolabs, Ipswich, MA, USA) buffer, 10 μ L of [γ -32P] ATP and T4 kinase in a final volume of 50 μ L at 37 °C. The radiolabeled oligonucleotide has been purified with MicroSpin g-25 (Amersham Biosciences, Amersham, United Kingdom). The CL14 oligonucleotide contains a htopIB high affinity cleavage site. CL14 was annealed to a complementary oligonucleotide called CP25 (5'-TAAAAATTTTTCTAAGTCTTTTTTC-3') that was phosphorylated with ATP at its 5' end. The annealing between the oligonucleotides was carried out by incubating 10 pmol of CL14 with 20 pmol of CP25 in the presence of an Annealing Buffer at 95 °C for 5 min and then overnight at 4 °C.

The suicide cleavage reaction was carried out by incubating 20 nM of the duplex CL14/CL25 with htopIB in a buffer containing 10 mM Tris (pH 7.5), 5 mM $MgCl_2$, 5 mM $CaCl_2$, and 150 mM KCl at 25 °C in a final volume of 60 μ L. After adding the enzyme, aliquots of 5 μ L were removed at different times and the reactions were stopped by adding 0.5% SDS. After a precipitation with ethanol, the samples were resuspended in 5 μ L of 1 mg/mL of trypsin and incubated at 37 °C for 1 h. The samples were analyzed by electrophoresis on denaturing polyacrylamide gel (7 M urea, 20% Acrylamide) in TBE running buffer (48 mM Tris, 45.5 mM Boric Acid and 1 mM EDTA). The percentage of cleaved substrate (CL1) has been evaluated.

4.5. Cell Viability Assay

To evaluate cell viability 1×10^4 tumor cells (Caco-2, A-549 and SKOV-3) were seeded in a 96-well plate for 24 h at 37 °C, 5% CO₂, and 95% humidity. The day after, each cell line was treated with a different amount of MMV024937 or topotecan, ranging from 12.5 μ M to 100 μ M. As a control, the cells were treated with the same amount of DMSO as well. The plates were then incubated for 48 h at 37 °C under 5% CO₂. After the incubation, the medium was removed and 200 μ L of fresh CM supplemented with MTT reagent at final concentration of 0.5 mg/mL was added and incubated again for 4 h at 37 °C and 5% CO₂. The reagent was then replaced with 100 μ L per well of DMSO and incubated at room temperature for 15 min on a shaking plate, covered from light. The absorbance was measured within an hour at 570 nm using a microplate reader; the data was analyzed with GraphPad Prism.

4.6. Molecular Docking Simulations

A crystal structure of the DNA-bound htopIB, lacking the N-terminal domain (residues 1–200), was obtained from the PDB database (PDB ID: 1T8I) [27] and used as a receptor for molecular docking simulations. The gap between nucleotides dT10 and dG11 was repaired. The tleap module of the AmberTools19 program [37], the parmbsc1 force field [38], and the Chimera software [28], were used to reconstruct the two nucleotides and the missing phosphodiester bond. A CPT molecule, originally bound to the crystal structure, was removed from the complex. The structure of the drug MMV024937 was retrieved from the PubChem compound database (PubChem CID: 44528432) [39]. Receptor and drug

structure files were converted into pdbqt format using the `prepare_receptor4.py` and `prepare_ligand4.py` tools of the AutoDockTools4 program [40]. Protein-ligand molecular docking simulations were performed using the AutoDock Vina program [41]. Ten molecular docking simulations, each including ten docking runs, were performed using a box of size $x = 27.4 \text{ \AA}$; $y = 27.4 \text{ \AA}$; $z = 23.3 \text{ \AA}$, centered over the htopIB-DNA binding site. To increase the accuracy of binding pose estimation, 10 receptor residue side chains around the binding site were regarded as flexible (Arg364, Arg488, Lys532, Asp533, Ile535, Arg590, Asn631, His632, Thr718 and Tyr723). The final interaction energies were calculated as an average over the 10 replicas of the docking simulations. Interaction analyses on the best binding poses obtained were performed using the Ligplot+ software [29].

4.7. Classical Molecular Dynamics Simulations and Trajectory Analysis

Topologies and coordinates files for the two best complexes obtained from molecular docking simulations and for the unbound htopIB-DNA structure (PDB ID: 1T8I) [27], simulated as reference, were generated using the `tleap` module of the AmberTools19 program [37]. The AMBER `ff19SB` [42] and `parmbsc1` [38] force fields were used to parametrize the htopIB and DNA, while ligand parameters were generated using the `antechamber` module of the AmberTools19 program [37] and the general Amber force field [43]. Each complex were inserted in a box of TIP3P water molecules [44] and 0.15 mol/L of NaCl, setting a minimum distance of 12.0 \AA from the box sides. To remove unfavorable interactions, four minimization cycles were performed for the three structures, each composed of 500 steps of the steepest descent minimization, followed by 1500 steps of conjugated gradient. A starting restraint of $20.0 \text{ kcal}\cdot\text{mol}^{-1}\cdot\text{\AA}^{-2}$ was imposed on the protein, DNA, and ligand atoms; it was then slowly reduced and removed in the last minimization cycle. Systems temperature was gradually increased from 0 to 300 K in an NVT ensemble, using the Langevin thermostat [45], over a period of 2.0 ns. A starting restraint of $0.5 \text{ kcal}\cdot\text{mol}^{-1}\cdot\text{\AA}^{-2}$ was imposed on the protein, DNA, and ligand atoms and then gradually decreased to slowly relax the system. Systems were then simulated in an isobaric-isothermal (NPT) ensemble for 2.0 ns using the Langevin barostat [46], imposing a pressure of 1.0 atm and maintaining the temperature to 300 K. The SHAKE algorithm [47] was used to constrain covalent bonds involving hydrogen atoms. Production runs of 100 ns were generated for each system using the `pmemd.cuda` module of the AMBER16 software [48] and a timestep of 2.0 fs. System coordinates were written every 1000 steps. Long-range interactions were recalculated using the PME method [49], while a cut-off of 9.0 \AA was imposed for short-range interactions.

4.8. Trajectory Analysis

Principal component analysis (PCA) [30] has been performed for each trajectory on $C\alpha$ atoms of the htopIB and P atoms of DNA using the GROMACS 2019 program [50]. This analysis is based on the diagonalization of a covariance matrix, generated for each trajectory using the `covar` module of GROMACS [50], and built from the atomic fluctuations of $C\alpha$ atoms and P atoms after the removal of translational and rotational movements. PCA analyses showed that, for all three systems, the main motion is dispersed over 1821 eigenvectors, but 80% of the total protein and DNA motion can be described by the first 6 eigenvectors for the unbound system and by the first 17 and 16 eigenvectors for the non-intercalated and intercalated systems, respectively. In particular, the first eigenvector, with the largest eigenvalue, accounted for 58% of the total motion for the unbound htopIB-DNA complex and for 32% and 34% of the total motion for the htopIB-DNA complexes bound to the non-intercalated and intercalated drug, respectively. Dynamic cross-correlation maps (DCCMs) were computed from the covariance matrices generated for each trajectory using code written in-house. Plots were realized using the matplotlib Python 3 library. Molecular mechanics/generalized Born and surface area continuum solvation (MM/GBSA) analyses [51] were performed over the last 50 ns of each trajectory, using the `MMPBSA.py.MPI` program implemented in the AMBER16 software [48] on three nodes of the of ENEA HPC cluster CRESCO6 [52], setting the ionic strength to 0.15 M. Per-residue decomposition

analysis was performed on DNA bases surrounding the drug (nucleotides dT10, dG11, dG12, dA13, dC34, dA35, dA36, dG37) and on htopIB active site residues (residues Arg488, Lys532, Arg590, His632, Tyr723).

Author Contributions: Conceptualization, P.F., A.D.; investigation, J.B.D. has performed the relaxation assay, B.C.S. has performed the cleavage assay, A.O. has performed the cell viability assay, B.M. and G.A. have performed the relaxation assay; software, M.F., A.R. and F.I. have performed the molecular docking; writing, P.F., A.O., M.F. and A.D.; supervision, P.F. and A.D.; funding acquisition, A.O. and A.D. All authors have read and agreed to the published version of the manuscript.

Funding: This research and AO were supported by PNRA (the Italian National Antarctic Research Program) awarded by the Ministry for the Education, University and Scientific Research (MIUR), grant number PNRA18_00005-D.

Acknowledgments: The computing resources and the related technical support were provided by CRESCO/ENEAGRID High Performance Computing infrastructure. CRESCO/ENEAGRID High Performance Computing infrastructure is funded by ENEA, the Italian National Agency for New Technologies, Energy and Sustainable Economic Development and by Italian and European research programs, see <http://www.cresco.enea.it/english> (accessed on 1 June 2021) for information. We thank Giuseppe Sconocchia from Institute of Translational Pharmacology, National Research Council, CNR, Rome, Italy, for providing cancer cell lines. Blasco Morozzo della Rocca for reviewing and editing the manuscript. We acknowledge MMV (Medicine of Malaria Venture) for support, designing and supplying the Pathogen Box.

Conflicts of Interest: The authors have no commercial, proprietary, or financial interest in the products or companies described in this article.

References

1. Wang, J.C. DNA topoisomerases. *Annu. Rev. Biochem.* **1996**, *65*, 635–692. [CrossRef]
2. Leppard, J.B.; Champoux, J.J. Human DNA topoisomerase I: Relaxation, roles, and damage control. *Chromosoma* **2005**, *114*, 75–85. [CrossRef] [PubMed]
3. Champoux, J.J. DNA topoisomerases: Structure, function, and mechanism. *Annu. Rev. Biochem.* **2001**, *70*, 369–413. [CrossRef] [PubMed]
4. Soren, B.C.; Dasari, J.B.; Ottaviani, A.; Lacovelli, F.; Fiorani, P. Topoisomerase IB: A relaxing enzyme for stressed DNA. *Cancer Drug Resist.* **2019**, 18–25. [CrossRef]
5. Fiorani, P.; Tesauro, C.; Mancini, G.; Chillemi, G.; D’Annessa, I.; Graziani, G.; Tentori, L.; Muzi, A.; Desideri, A. Evidence of the crucial role of the linker domain on the catalytic activity of human topoisomerase I by experimental and simulative characterization of the Lys681Ala mutant. *Nucleic Acids Res.* **2009**, *37*, 6849–6858. [CrossRef]
6. Stewart, L.; Ireton, G.C.; Champoux, J.J. A Functional Linker in Human Topoisomerase I Is Required for Maximum Sensitivity to Camptothecin in a DNA Relaxation Assay. *J. Biol. Chem.* **1999**, *274*, 32950–32960. [CrossRef]
7. Wang, Z.; D’Annessa, I.; Tesauro, C.; Croce, S.; Ottaviani, A.; Fiorani, P.; Desideri, A. Mutation of Gly717Phe in human topoisomerase IB has an effect on enzymatic function, reactivity to the camptothecin anticancer drug and on the linker domain orientation. *Biochim. Biophys. Acta* **2015**, *1854*, 860–868. [CrossRef] [PubMed]
8. Chillemi, G.; Fiorani, P.; Benedetti, P.; Desideri, A. Protein concerted motions in the DNA-human topoisomerase I complex. *Nucleic Acids Res.* **2003**, *31*, 1525–1535. [CrossRef] [PubMed]
9. Wall, M.E.; Wani, M.C. Camptothecin and taxol: From discovery to clinic. *Cancer Res.* **1995**, *51*, 753–760. [CrossRef]
10. Pizzolato, J.F.; Saltz, L.B. The camptothecins. *Lancet* **2003**, *361*, 2235–2242. [CrossRef]
11. Ottaviani, A.; Iacovelli, F.; Fiorani, P.; Desideri, A. Natural compounds as therapeutic agents: The case of human topoisomerase *ib*. *Int. J. Mol. Sci.* **2021**, *22*, 4138. [CrossRef] [PubMed]
12. Paton, F.; Paulden, M.; Saramago, P.; Manca, A.; Misso, K.; Palmer, S.; Eastwood, A. Topotecan for the treatment of recurrent and stage IVB carcinoma of the cervix. *Health Technol. Assess.* **2010**, *14* (Suppl. S1), 55–62. [CrossRef] [PubMed]
13. Crea, F.; Giovannetti, E.; Cortesi, F.; Mey, V.; Nannizzi, S.; Gallegos Ruiz, M.I.; Ricciardi, S.; Del Tacca, M.; Peters, G.J.; Danesi, R. Epigenetic mechanisms of irinotecan sensitivity in colorectal cancer cell lines. *Mol. Cancer Ther.* **2009**, *8*, 1964–1973. [CrossRef] [PubMed]
14. Ando, Y.; Figg, W.D. Irinotecan in Small-Cell Lung Cancer. *N. Engl. J. Med.* **2002**, *346*, 1414–1415. [CrossRef] [PubMed]
15. Fiorani, P.; Amatruda, J.F.; Silvestri, A.; Butler, R.H.; Bjornsti, M.A.; Benedetti, P. Domain interactions affecting human DNA topoisomerase I catalysis and camptothecin sensitivity. *Mol. Pharmacol.* **1999**, *56*, 1105–1115. [CrossRef] [PubMed]
16. Tesauro, C.; Morozzo della Rocca, B.; Ottaviani, A.; Coletta, A.; Zuccaro, L.; Arnò, B.; D’Annessa, I.; Fiorani, P.; Desideri, A. Molecular mechanism of the camptothecin resistance of Glu710Gly topoisomerase IB mutant analyzed in vitro and in silico. *Mol. Cancer* **2013**, *12*, 100. [CrossRef] [PubMed]

17. D'Annessa, I.; Tesauro, C.; Fiorani, P.; Chillemi, G.; Castelli, S.; Vassallo, O.; Capranico, G.; Desideri, A. Role of Flexibility in Protein-DNA-Drug Recognition: The Case of Asp677Gly-Val703Ile Topoisomerase Mutant Hypersensitive to Camptothecin. *J. Amino Acids* **2012**, *2012*, 206083. [CrossRef]
18. Pommier, Y. Topoisomerase I inhibitors: Camptothecins and beyond. *Nat. Rev. Cancer* **2006**, *6*, 789–802. [CrossRef] [PubMed]
19. Tesauro, C.; Fiorani, P.; D'Annessa, I.; Chillemi, G.; Turchi, G.; Desideri, A. Erybraedin C, a natural compound from the plant *Bituminaria bituminosa*, inhibits both the cleavage and religation activities of human topoisomerase I. *Biochem. J.* **2010**, *425*, 531–539. [CrossRef]
20. Pommier, Y.; Leo, E.; Zhang, H.; Marchand, C. DNA Topoisomerases and Their Poisoning by Anticancer and Antibacterial Drugs. *Chem. Biol.* **2010**, *17*, 421–433. [CrossRef] [PubMed]
21. Delgado, J.L.; Hsieh, C.M.; Chan, N.L.; Hiasa, H. Topoisomerases as anticancer targets. *Biochem. J.* **2018**, *475*, 373–398. [CrossRef] [PubMed]
22. Chowdhury, S.R.; Majumder, H.K. DNA Topoisomerases in Unicellular Pathogens: Structure, Function, and Druggability. *Trends Biochem. Sci.* **2019**, *44*, 415–432. [CrossRef]
23. García-Estrada, C.; Prada, C.F.; Fernández-Rubio, C.; Rojo-Vázquez, F.; Balaña-Fouce, R. DNA topoisomerases in apicomplexan parasites: Promising targets for drug discovery. *Proc. Biol. Sci.* **2010**, *277*, 1777–1787. [CrossRef]
24. Tesauro, C.; Juul, S.; Arnò, B.; Nielsen, C.J.F.; Fiorani, P.; Fröhlich, R.F.; Andersen, F.F.; Desideri, A.; Stougaard, M.; Petersen, E.; et al. Specific detection of topoisomerase I from the malaria causing *P. falciparum* parasite using isothermal rolling circle amplification. In Proceedings of the 2012 Annual International Conference of the IEEE Engineering in Medicine and Biology Society, San Diego, CA, USA, 28 August–1 September 2012; pp. 2416–2419. [CrossRef]
25. Duffy, S.; Sykes, M.L.; Jones, A.J.; Shelper, T.B.; Simpson, M.; Lang, R.; Poulsen, S.A.; Sleebs, B.E.; Avery, V.M. Screening the medicines for malaria venture pathogen box across multiple pathogens reclassifies starting points for open-source drug discovery. *Antimicrob. Agents Chemother* **2017**, *61*. [CrossRef]
26. Arnò, B.; D'Annessa, I.; Tesauro, C.; Zuccaro, L.; Ottaviani, A.; Knudsen, B.; Fiorani, P.; Desideri, A. Replacement of the human topoisomerase linker domain with the plasmodial counterpart renders the enzyme camptothecin resistant. *PLoS ONE* **2013**, *8*, e68404. [CrossRef] [PubMed]
27. Staker, B.L.; Feese, M.D.; Cushman, M.; Pommier, Y.; Zembower, D.; Stewart, L.; Burgin, A.B. Structures of three classes of anticancer agents bound to the human topoisomerase I-DNA covalent complex. *J. Med. Chem.* **2005**, *48*, 2336–2345. [CrossRef] [PubMed]
28. Pettersen, E.F.; Goddard, T.D.; Huang, C.C.; Couch, G.S.; Greenblatt, D.M.; Meng, E.C.; Ferrin, T.E. UCSF Chimera—a visualization system for exploratory research and analysis. *J. Comput. Chem.* **2004**, *25*, 1605–1612. [CrossRef] [PubMed]
29. Laskowski, R.A.; Swindells, M.B. LigPlot+: Multiple ligand-protein interaction diagrams for drug discovery. *J. Chem. Inf. Model* **2011**, *51*, 2778–2786. [CrossRef] [PubMed]
30. Stewart, L. A Model for the Mechanism of Human Topoisomerase I. *Science* **1998**, *279*, 1534–1541. [CrossRef]
31. Amadei, A.; Linssen, A.B.M.; Berendsen, H.J.C. Essential dynamics of proteins. *Proteins Struct. Funct. Genet.* **1993**, *17*, 412–425. [CrossRef] [PubMed]
32. Veale, C.G.L. Unpacking the Pathogen Box—An Open Source Tool for Fighting Neglected Tropical Disease. *ChemMedChem* **2019**, *14*, 386–453. [CrossRef] [PubMed]
33. Cheng, X.; Geng, F.; Guo, D. DGAT1 protects tumor from lipotoxicity, emerging as a promising metabolic target for cancer therapy. *Mol. Cell. Oncol.* **2020**, *7*, 4–6. [CrossRef]
34. Chillemi, G.; Fiorani, P.; Castelli, S.; Bruselles, A.; Benedetti, P.; Desideri, A. Effect on DNA relaxation of the single Thr718Ala mutation in human topoisomerase I: A functional and molecular dynamics study. *Nucleic Acids Res.* **2005**, *33*, 3339–3350. [CrossRef]
35. Fiorani, P.; Bruselles, A.; Falconi, M.; Chillemi, G.; Desideri, A.; Benedetti, P. Single mutation in the linker domain confers protein flexibility and camptothecin resistance to human topoisomerase I. *J. Biol. Chem.* **2003**, *278*, 43268–43275. [CrossRef] [PubMed]
36. Ireton, G.C.; Stewart, L.; Parker, L.H.; Champoux, J.J. Expression of human topoisomerase I with a partial deletion of the linker region yields monomeric and dimeric enzymes that respond differently to camptothecin. *J. Biol. Chem.* **2000**, *275*, 25820–25830. [CrossRef] [PubMed]
37. Salomon-Ferrer, R.; Case, D.A.; Walker, R.C. An Overview of the Amber Biomolecular Simulation Package. *WIREs Comput. Mol. Sci.* **2013**, *3*, 198–210. [CrossRef]
38. Ivani, I.; Dans, P.D.; Noy, A.; Pérez, A.; Faustino, I.; Hospital, A.; Walther, J.; Andrio, P.; Goñi, R.; Balaceanu, A.; et al. Parmbsc1: A refined force field for DNA simulations. *Nat. Methods* **2015**, *13*, 55–58. [CrossRef]
39. PubChem. Available online: <https://pubchem.ncbi.nlm.nih.gov/> (accessed on 1 June 2021).
40. Morris, G.M.; Ruth, H.; Lindstrom, W.; Sanner, M.F.; Belew, R.K.; Goodsell, D.S.; Olson, A.J. Software news and updates AutoDock4 and AutoDockTools4: Automated docking with selective receptor flexibility. *J. Comput. Chem.* **2009**, *30*, 2785–2791. [CrossRef] [PubMed]
41. Trott, O.; Olson, A.J. AutoDock Vina: Improving the speed and accuracy of docking with a new scoring function, efficient optimization, and multithreading. *J. Comput. Chem.* **2009**, *31*. [CrossRef]

42. Tian, C.; Kasavajhala, K.; Belfon, K.A.A.; Raguette, L.; Huang, H.; Miguez, A.N.; Bickel, J.; Wang, Y.; Pincay, J.; Wu, Q.; et al. Ff19SB: Amino-Acid-Specific Protein Backbone Parameters Trained against Quantum Mechanics Energy Surfaces in Solution. *J. Chem. Theory Comput.* **2020**, *16*, 528–552. [CrossRef] [PubMed]
43. Wang, J.; Wolf, R.M.; Caldwell, J.W.; Kollman, P.A.; Case, D.A. Development and testing of a general Amber force field. *J. Comput. Chem.* **2004**, *25*, 1157–1174. [CrossRef]
44. Jorgensen, W.L.; Chandrasekhar, J.; Madura, J.D.; Impey, R.W.; Klein, M.L. Comparison of simple potential functions for simulating liquid water. *J. Chem. Phys.* **1983**, *79*, 926–935. [CrossRef]
45. Goga, N.; Rzepiela, A.J.; De Vries, A.H.; Marrink, S.J.; Berendsen, H.J.C. Efficient algorithms for langevin and DPD dynamics. *J. Chem. Theory Comput.* **2012**, *8*, 3637–3649. [CrossRef]
46. Aoki, K.M.; Yoneya, M.; Yokoyama, H. Constant pressure MD simulation method. *Mol. Cryst. Liq. Cryst.* **2004**, *413*, 109–116. [CrossRef]
47. Ryckaert, J.P.; Ciccotti, G.; Berendsen, H.J.C. Numerical integration of the cartesian equations of motion of a system with constraints: Molecular dynamics of n-alkanes. *J. Comput. Phys.* **1977**, *23*, 327–341. [CrossRef]
48. Case, D.A.; Cheatham, T.E.; Darden, T.; Gohlke, H.; Luo, R.; Merz, K.M.; Onufriev, A.; Simmerling, C.; Wang, B.; Woods, R.J. The Amber biomolecular simulation programs. *J. Comput. Chem.* **2005**, *26*, 1668–1688. [CrossRef] [PubMed]
49. Darden, T.; York, D.; Pedersen, L. Particle mesh Ewald: An N·log(N) method for Ewald sums in large systems. *J. Chem. Phys.* **1993**, *98*, 10089–10092. [CrossRef]
50. Abraham, M.J.; Murtola, T.; Schulz, R.; Páll, S.; Smith, J.C.; Hess, B.; Lindahl, E. Gromacs: High performance molecular simulations through multi-level parallelism from laptops to supercomputers. *SoftwareX* **2015**, *1–2*, 19–25. [CrossRef]
51. Genheden, S.; Ryde, U. The MM/PBSA and MM/GBSA methods to estimate ligand-binding affinities. *Expert Opin. Drug Discov.* **2015**, *10*, 449–461. [CrossRef]
52. Iannone, F.; Ambrosino, F.; Bracco, G.; De Rosa, M.; Funel, A.; Guarnieri, G.; Migliori, S.; Palombi, F.; Ponti, G.; Santomauro, G.; et al. CRESCO ENEA HPC clusters: A working example of a multifabric GPFS Spectrum Scale layout. In *Proceedings of the 2019 International Conference on High Performance Computing and Simulation, HPCS 2019*; Institute of Electrical and Electronics Engineers Inc.: Dublin, Ireland, 2019; pp. 1051–1052.

MDPI
St. Alban-Anlage 66
4052 Basel
Switzerland
Tel. +41 61 683 77 34
Fax +41 61 302 89 18
www.mdpi.com

International Journal of Molecular Sciences Editorial Office

E-mail: ijms@mdpi.com
www.mdpi.com/journal/ijms



MDPI
St. Alban-Anlage 66
4052 Basel
Switzerland
Tel: +41 61 683 77 34
www.mdpi.com



ISBN 978-3-0365-4645-2